Gang Huang
Editor

Nuclear Medicine in Oncology

Molecular Imaging and Target Therapy

上海交通大學出版社
SHANGHAI JIAO TONG UNIVERSITY PRESS

Springer

Nuclear Medicine in Oncology

Gang Huang
Editor

Nuclear Medicine in Oncology

Molecular Imaging and Target Therapy

上海交通大學出版社
Shanghai Jiao Tong University Press

Springer

Editor
Gang Huang
Shanghai Key Laboratory of Molecular Imaging
Shanghai University of Medicine and Health Sciences
Shanghai
P. R. China

ISBN 978-981-13-7457-9 ISBN 978-981-13-7458-6 (eBook)
https://doi.org/10.1007/978-981-13-7458-6

The print edition is not for sale in China Mainland. Customers from China Mainland please order the print book from: Shanghai Jiao Tong University Press.

This Springer imprint is published by the registered company Springer Nature Singapore Pte Ltd.
The registered company address is: 152 Beach Road, #21-01/04 Gateway East, Singapore 189721, Singapore

Preface

With the latest development of electronics and computer sciences, medical imaging has become a multidisciplinary clinical science characterized by the use of computed tomography (CT), magnetic resonance imaging (MRI), nuclear medicine, and ultrasound imaging. This book aims to provide professional suggestions on clinical study and practice, by using images from multiple clinical case studies, informing this ever-evolving specialty. This book mainly focuses on nuclear medicine and therapy, molecular imaging, and imaging-based therapy evaluation. It contains 20 chapters covering a variety of topics on medical physics and instruments, nuclear medicine, and its application in multiple diseases both in the areas of diagnosis and therapy.

In the early part of the book, a brief introduction of the ^{18}F-FDG positron emission tomography (PET) technique and its application in clinical cancer studies are given, which include breast cancers, non-small-cell lung cancers, lymphoma, genitourinary cancers, gastrointestinal cancers, head and neck cancers, melanoma, and pediatric cancers. This book then discusses the current applications of molecular imaging for various clinical studies proposed, including metabolic imaging, receptor imaging and therapy, immuno-imaging and therapy, imaging of apoptosis, imaging of gene expression, radioactive iodine imaging and therapy, neuroimaging and therapy, and cardiac imaging and therapy. The latter part of the book focuses on the latest research findings of the medical physics and the molecular imaging, highlighting the application of novel molecular probes in clinical studies and its potential impacts. As a component of medical imaging, nuclear medicine and molecular imaging could be used as an important approach in evaluating human physiological profiles, including assessing organic functions, metabolism, blood flow, receptor density, and gene expression at both molecular and functional levels. The modality of nuclear medicine and molecular imaging would also provide the quantitative analysis to help early disease diagnosis and to evaluate disease progression, prognosis, and therapy outcomes. These novel techniques could be incorporated with other reliable analytical data to reach the goal of precision and molecular medicine.

By presenting the latest findings in molecular imaging with validated clinical data, this book may serve as a useful tool for nuclear medicine physicians, nuclear radiologists, residents, and graduate students in nuclear medicine to help with their learning and teaching processes.

Special thanks are given to all the scholars and colleagues who contributed to the preparation of this book. Finally but not least, special gratitude to their families for their unfailing support in making this book a reality.

Shanghai, P. R. China — Gang Huang

Contents

Abbreviations

ACS	Acute coronary syndrome
BC	Bladder cancer
CABG	Coronary artery bypass grafting
CAD	Coronary artery disease
CAG	Coronary angiography
CHF	Congestive heart failure
CMR	Cardiovascular magnetic resonance
CTCA	Computed tomography coronary angiography
CVD	Cardiovascular disease
DTPA	Diethylenetriaminepentaacetic acid
ERNA	Equilibrium radionuclide angiocardiography
FDG	Fluorodeoxyglucose
FPRNA	First-pass radionuclide angiocardiography
GLUT1	Glucose transporter type 1
HLA	Horizontal long axis
IHD	Ischemic heart disease
LAD	Left anterior descending artery
LCX	Left circumflex artery
LDHA	Lactate dehydrogenase A
LEAP	Low-energy all-purpose
LEHR	Low-energy high-resolution
LM	Left main artery
LV	Left ventricular
LVEDV	End-diastolic volume of LV
LVEF	Ejection fraction of LV
LVESV	End-systolic volume of LV
LVSV	Stroke volume of LV
MCTs	Monocarboxylate transporters
MI	Myocardial infarction
MIBI	2-Methoxy-isobutyl-isonitrile
MPI	Myocardial perfusion imaging
MRCA	Magnetic resonance coronary angiography
MRI	Magnetic resonance imaging
MUGA	Multiple-gated acquisitions
PCI	Percutaneous coronary interventions
PTCA	Percutaneous transluminal coronary angioplasty
RCA	Right coronary artery
RCC	Renal cell carcinoma
RNA	Radionuclide angiocardiography
ROI	Region of interest
SA	Short axis
SCE	Severe cardiac event

SDS	Summed difference score
SRS	Summed rest score
SSS	Summed stress score
TLG	Total lesion glycolysis
VLA	Vertical long axis

About the Editor

Gang Huang is a Professor and the President of Shanghai University of Medicine & Health Sciences (SUMHS). He is also the Elected President of the Asia Oceania Federation of Nuclear Medicine and Biology; Dean of Asia School of Nuclear Medicine; Editor in Chief, *Chinese Journal of Nuclear Medicine and Molecular Imaging*; and the Predecessor President of the Chinese Society of Nuclear Medicine.

Glucose Metabolism Imaging

1

Liang Shi and Jianjun Liu

1.1 Glucose Metabolism

The metabolism of carbohydrates includes glycolysis, aerobic oxidation, pentose phosphate pathway, glycogen synthesis, and gluconeogenesis. Glucose metabolism has two major functions: providing energy for living organisms and supplying a huge array of metabolic intermediates for biosynthetic reactions [1].

1.1.1 Glucose Metabolism Pathway and Flux Analysis

Glycolysis is an anaerobic catabolic pathway in which a molecule of glucose is broken down into two molecules of lactate with the concurrent generation of two molecules of ATP. In the cytosol, glucose is initially converted into pyruvate, and then the latter is catalyzed into lactate by lactate dehydrogenase with concurrent regeneration of NAD^+ from NADH. Alternatively, pyruvate, as an important metabolic intermediate, harbors several potential fates. Pyruvate can then entrance into the mitochondria and join in the tricarboxylic acid (TCA) cycle to produce NADH and $FADH_2$. The mitochondrial electron transport chain (ETC) subsequently uses the electrons donated from these reducing agents to the complex V ATP synthase of the mitochondrial inner membrane with a generation of an additional 34 molecules of ATP per glucose. This process of glucose conversion to CO_2 and water with liberation of energy as the form of ATP is named as aerobic oxidation. The reactions and the enzymes related to TCA cycle are located in the mitochondrial matrix. TCA cycle acts as the final pathway for the oxidation of glucose. Pentose phosphate pathway supplies ribose 5-phosphate for biosynthesis of nucleic acid and NADPH for the synthesis of fatty acids, amino acids, cholesterol, etc. The process of glycogenesis occurs mainly in cytosol of the liver and skeletal muscle. Lactate, glycerol, pyruvate, glucogenic amino acid, and other noncarbohydrates can be transformed to glucose or glycogen mainly in the liver and kidney. This process is termed as gluconeogenesis. This pathway is essentially a reversal of glycolysis; however, there are three different energy barriers obstructing the reversal process.

Proliferating malignant cells prefer aerobic glycolysis pathway even in the presence of oxygen, whereas nonmalignant cells would choose mitochondrial respiration in an oxygen-rich environment. Glycolysis may provide additional biosynthetic precursors to support rapid proliferation of cancer cell. Tumor cells need glycolysis to support higher rates of nucleotide synthesis for DNA replication and RNA transcription, phospholipid synthesis for membrane production, and amino acid synthesis for protein translation. Thus, an increased flux through glycolysis is essential for the proliferation of most cancer cells, by providing additional energy in the form of ATP and metabolic intermediates derived from glucose for lipid, nucleotide, and protein biosynthesis. Accordingly, positron emission tomography (PET) scanning has been exploited in clinical practice, using fluorinated glucose analogs such as ^{18}F-deoxyglucose, to detect tumors with the shifting metabolism toward glycolysis.

Measurements of metabolites offer an opportunity to obtain steady-state data on the levels of all detectable metabolic reactions within the cell. Mass spectrometry (MS) or nuclear magnetic resonance (NMR) spectrometry with unlabeled metabolites or ^{13}C-labeled metabolites can be used to quantify this metabolic information. As fluctuant flux through any of its associated metabolic pathways can influence the source and exit of almost all the metabolic intermediates, using metabolite concentrations for extrapolation of flux information is difficult. However, adding a labeled standard for the metabolite of interest to make an absolute quantification of an unlabeled metabolite before MS analysis is a reasonable way. For example, decreased serine biosynthesis

L. Shi · J. Liu (✉)
Department of Nuclear Medicine, RenJi Hospital, School of Medicine, Shanghai JiaoTong University, Shanghai, P. R. China

G. Huang (ed.), *Nuclear Medicine in Oncology*, https://doi.org/10.1007/978-981-13-7458-6_1

resulting from PKM2 silencing was identified by metabolite profiling [2]. Nowadays, using stable isotope-labeled glucose as the nutrient source to analyze glucose metabolic flux of cells may help to detect the metabolism characteristics of metabolic-related diseases [3]. Any of the six carbons within a glucose molecule can be replaced by stable isotope ^{13}C. [U-$^{13}C_6$]-glucose, which is replaced by ^{13}C at all six carbons, is often used to trace the glucose in the TCA cycle. [1, 2-$^{13}C_2$]-glucose can be used for glycolytic pathway metabolite measurements [4]. In addition, [U-$^{13}C_6$]-glucose cannot well define carbon flux through the pentose phosphate pathway. Instead, [1, 2-$^{13}C_2$]-glucose distinguishes metabolites that have gone through this pathway from those that have gone directly through glycolysis because it loses one ^{13}C during its passing through the pentose phosphate pathway. There is a competition between the labeled glucose and unlabeled glucose within the media for being absorbed into cells. Therefore, cells should be cultured in [U-$^{13}C_6$]-glucose- or [1, 2-$^{13}C_2$]-glucose-supplemented media for 24 h before metabolite extraction and flux analysis. The release of ^3H_2O from [5-^{3}H]-glucose is another way to obtain glycolytic flux [5]. Enolase catalyzes and removes a single tritium at C5 of glucose by a condensation reaction in the ninth step of glycolysis, with the production of ^3H_2O, which diffuses freely out of cell. A liquid scintillation counter is used to quantify the ^3H_2O in culture medium. Studies to track changes in glucose metabolic flux and its collateral anabolic pathways can reveal and quantify the metabolic alterations that underlie malignant cell proliferation. Glycolysis and other metabolic pathways that regulate tumor cell proliferation may represent valuable targets for therapeutic interventions and diagnostic procedures.

1.1.2 Biochemical of Glucose Metabolism

The initial procedure of glucose metabolism is glycolysis, in which glucose is converted to pyruvic acid. All the enzymes and ten reactions related to glycolysis locate in cytosol. This pathway is composed of three stages. Stage 1 is the conversion of glucose into fructose-1,6-bisphosphate (F-1,6-BP). This stage consists of three reactions with two phosphorylation and isomerization reactions. The meaning of first stage in glycolysis is to trap the glucose in the cell as well as generate a compound, which is readily cleaved into phosphorylated three-carbon units. In stage 2, F-1, 6-BP is cleaved into two three-carbon fragments. These resulting three-carbon units are readily interconvertible. The final stage is the generation of ATP during the oxidization of the three-carbon fragments to pyruvate.

Glucose enters cell through specific transport proteins, glucose transporters (GLUT). Then glucose is phosphorylated to form glucose 6-phosphate (G-6P), which cannot diffuse through the membrane because of its negative charges. At the same time, glucose is destabilized by the addition of the phosphoryl group, facilitating its further metabolism. Hexokinase (HK) catalyzes the transfer of the phosphoryl group donated from ATP to the hydroxyl group on carbon 6 of glucose. Then, glucose 6-phosphate is isomerized to fructose 6-phosphate (F-6P). This process is a conversion of an aldose into a ketose catalyzed by phosphoglucose isomerase which first opens the six-membered ring of glucose 6-phosphate, catalyzes the isomerization, and promotes the production of the five-membered ring of fructose 6-phosphate. F-6P is phosphorylated to fructose-1,6-bisphosphate (F-1,6-BP). This step is a key reaction of glycolysis and catalyzed by phosphofructokinase (PFK), an allosteric enzyme. This enzyme plays a crucial role in the integration of metabolism. A molecule of glucose consumes two molecules of ATP in stage 1. Then, in the second stage, fructose-1,6-bisphosphate is split into two kinds of three-carbon units, glyceraldehyde 3-phosphate (GAP) and dihydroxyacetone phosphate (DHAP), both of which can be converted to each other. Aldolase catalyzes this reaction. The reaction is readily reversible under intracellular conditions. The conversion of glyceraldehyde 3-phosphate into 1,3-bisphosphoglycerate (1,3-BPG) is catalyzed by glyceraldehyde 3-phosphate dehydrogenase. The third stage in glycolysis is the production of ATP from the phosphorylated three-carbon metabolites of glucose. The transfer of the phosphoryl group from the acyl phosphate of 1,3-bisphosphoglycerate to ADP is catalyzed by phosphoglycerate kinase. The products of this reaction are ATP and 3-phosphoglycerate. 3-Phosphoglycerate is then transferred into phosphoenol pyruvate (PEP) under the catalysis of mutase and enolase. Phosphoenol pyruvate releases a molecule of ATP and then transformed into pyruvate. This means that one molecule of glucose generated two molecules of pyruvic acid with the release of two molecules of ATP. Electrons generated in the process of GAP oxidation are accepted by NAD+, which guarantees the continuity of glycolysis.

There are three key enzymes which catalyze irreversible reactions: hexokinase (HK), phosphofructokinase (PFK), and pyruvate kinase (PK). The most important rate-limiting step of the glycolysis pathway is the reaction catalyzed by PFK. High ATP and citric acid concentration can inhibit PFK-1 activity, while AMP and fructose-2, 6-diphosphate can activate it. PFK is activated when cells are in the need of energy or synthetic ingredients. HK is inhibited by its product glucose-6-phosphate (G-6-P), which is increased when fructose phosphate kinase is inactive. PK activity is regulated by allosteric regulation. ATP and alanine act as allosteric inhibitors. So when the cells are in a low energy demand and produce much glycogenolytic intermediates, pyruvate kinase activity is high. PK can be phosphorylated to inhibit its activity.

1.1.3 Abnormal Glucose Metabolism and Related Diseases

Blood glucose balance is maintained by several factors, including hormone, enzyme, substrate system, etc. Hyperglycemia means that blood glucose level is more than 130 mg/dL, which is a major symptom of diabetes. Hypoglycemia is characterized by blood glucose level equal to or less than 50 mg/dL and the presence of clinical symptoms, such as confusion and aberrant behavior. Severe hypoglycemia can cause side effects on the brain, even leading to coma and brain death.

Fasting for a long time can cause liver glycogen synthesis and reduce peripheral tissue glucose consumption. The brain uses ketone bodies as a compensation source of glucose to provide energy during a chronic fasting. After long-term fasting and in type 2 diabetes, glucose cannot be fully utilized. This state is called insulin resistance. Insulin resistance can be caused by decreased ability of target tissue to respond to normal (or elevated) circulating concentrations of insulin. If the glycogen synthesis and glycogen degradation accelerate, muscle and adipose tissues glucose utilization rate is reduced, which results in extracellular glucose concentration and in turn leads to hyperglycemia. On the contrary, too much insulin secretion or insulinoma can increase peripheral glucose consumption and lead to hypoglycemia and coma if accompanied by glycogen synthesis inhibition.

Insulin plays an important role in the regulation of glucose balance. Insulin can inhibit glycogen synthesis in the liver and increase glucose uptake by skeletal muscle, cardiac muscle, and adipose tissue; therefore, it can decrease serum glucose level. On the contrary, if the body lacks insulin, catabolism hormone (adrenaline, cortisol, glucagon) will be dominant, which can cause the increased release of liver glucose and decreased glucose uptake by peripheral muscle and adipose tissue. For instance, in type 2 diabetes, disproportionate hepatic glucose output and peripheral glucose consumption can cause hyperglycemia.

Renal glucose metabolism also plays a great role in glucose balance and ranks only second to the liver. Glucose production of the proximal renal tubule and non-insulin-dependent glucose uptake of other nephrons are balanced. Renal generates much more glucose only in the conditions of lactic acidosis and decompensation of liver glucose synthesis.

Under the condition of hyperglycemia, the kidney has a key function of eliminating glucose from the cardiovascular system. Normally most glucose in the renal glomerular filtrate can be reabsorbed into the blood. If glucose concentration exceeds the renal glucose threshold, glycosuria occurs.

1.2 Glucose Metabolism and Tumor

1.2.1 Cancer (Tumor Suppressor) Gene and Glucose Metabolism

Compared to normal cells, malignant cells are associated with a higher glycolysis metabolic rate and higher lactate releasing rate, namely, Warburg effect [6], which was proposed by Otto Warburg in 1956. Many cancers frequently harbor a metabolic characteristic of enhanced glycolysis. It is known that activation of oncogenes and the inactivation of tumor suppressor genes constitute in vivo. These classical oncogenic genes also participate in the regulation of the Warburg effect.

The proto-oncogene *MYC* encodes the Myc transcription factor, which can bind DNA and alter gene expression. Accumulated evidence showed that Myc plays key roles in regulating cancer cell metabolism [7]. The *MYC* proto-oncogene is frequently overexpressed in over half of human cancers [8]. Myc activates many genes involving in cellular processes, including transcription, translation, chromatin modification, and protein degradation. In *Drosophila*, glucose activates insulin signaling, which activates TOR through PI3K/Akt pathway and suppresses FOXO. Myc is a downstream of TOR and FOXO signaling in response to nutrients. When glucose is abundant, Myc protein is rapidly increased by the activated TOR. Conversely, under fasting conditions, Myc expression is directly inhibited by derepressed FOXO [9]. In colon cancer cells, Myc activity was inhibited by FOXO3a which could induce Myc antagonist Mxi1 proteins. Thus, Myc seems to be a well evolutionary conserved nutrient sensor, which is critical in the process of utilizing extracellular nutritional substrates. Many glucose metabolic genes have been documented to be the downstream targets of Myc. Myc enhances genes encoding glucose transporters (GLUT) and hexokinase (HK), resulting in an increase of glucose uptake [10]. The expression of many other glycolytic genes can be activated by Myc. They are phosphoglucose isomerase, phosphofructokinase, glyceraldehyde-3-phosphate dehydrogenase, phosphoglycerate kinase, and enolase [10]. Using [U-$^{(13)}$C]-glucose as the tracer, Myc expression increased both glucose consumption and lactate production in a *MYC*-inducible human Burkitt lymphoma model, suggesting Myc overexpression increases overall glycolytic flux [11]. Myc also upregulates lactate dehydrogenase A (LDHA) which generates NAD+, a cofactor required for maintaining the high flux of glycolysis [12]. Moreover, oncogenic transcription factor Myc upregulates transcription of polypyrimidine tract binding protein (PTB) and heterogeneous nuclear ribonucleoproteins (hnRNPA1 and hnRNPA2). PTB, hnRNPA1, and hnRNPA2 promote mutually exclusive alternative splicing of the PKM pre-mRNA, ensuring a high PKM2/PKM1 ratio [13]. There are two distinct isoforms of pyruvate kinase:

PKM2 promotes aerobic glycolysis, whereas PKM1 favors oxidative phosphorylation. Thus Myc ensures high flux of glycolysis by regulating alternative splicing of the rate-limiting enzyme pyruvate kinase. Furthermore, overexpressed Myc, PTB, hnRNPA1, and hnRNPA2 levels are correlated with PKM2 expression level in human gliomas.

Hypoxia happens in a number of physiological and pathophysiological processes, particularly when rapid tissue growth exceeds blood supply. For example, malignant tumor cells reside in a pathophysiological "hypoxic" environment. Hypoxia-inducible factors (HIFs) are the primary transcriptional regulators for cellular metabolic adaptation. Hypoxia-inducible factor-1(HIF1), as a master hypoxic regulator, plays a crucial role in glucose metabolism regulation in cancer cells. HIF-1 is able to bind to the hypoxia response element DNA sequence in mammalian cells cultured under reduced O_2 tension [14]. HIF-1 is essential to activate many glycolytic enzymes under hypoxic conditions. HIF-1 directly activates the gene encoding pyruvate dehydrogenase kinase 1 (PDK1) [15]. PDK1 inactivates the TCA cycle enzyme, pyruvate dehydrogenase (PDH), which catalyzes the conversion from pyruvate to acetyl-CoA. HIF-1 promotes a hypoxia-induced glucose metabolic switch from the mitochondrial TCA cycle to glycolysis to maintain ATP production. HIF-1 upregulates mRNA and protein expression of MCT4 (monocarboxylate transporter), which transports lactate out of cancer cells reducing intracellular lactic acidification [16]. HIF-1 induces the expression of glucose transporter 1, 3 (Glut1, Glut3), LDHA, which are associated with the increased glucose uptake and lactate production in tumors. Sodium-hydrogen exchanger NHE1 and carbonic anhydrase 9 (CA9) are frequently overexpressed in cancer cells, which are able to maintain both an alkaline intracellular pH and an acidic extracellular pH. Expression of the NHE1 and CA9 genes is also induced by HIF1. It has been observed that HIF-1 is accumulated in many cancers, including astrocytomas, superficial urothelial bladder carcinoma, breast cancer, cervical cancer, gastroesophageal adenocarcinomas, non-small cell lung cancer, and malignant melanoma. Furthermore, elevated HIF1 expression is associated with poor prognosis of tumor patients.

The *KRAS* oncogene encodes a 21-kDa small GTPase, which transforms between the inactive guanosine diphosphate-bound state and the active guanosine triphosphate-bound state. Recently, a number of studies have shown that the oncogene *KRAS* plays a prominent role in regulating cancer metabolism by reprogramming multiple metabolic pathways [17]. Oncogenic activation of *KRAS* can influence cellular morphology, survival, and proliferation by activating its downstream pathways, such as the MAPK and PI3K/AKT/mTOR pathways [18, 19]. It has been reported that KRAS signaling takes part in the modulation of aerobic glycolysis in several types of cancer. *KRAS*-driven cancers harbor great possibility to resist to therapeutic intervention. Mutation of KRAS happens in a variety of human tumors, especially frequently in colorectal cancer (CRC), pancreatic ductal cell carcinoma (PDCA), and non-small cell lung cancer (NSCLC). In CRC cell lines, KRAS and BRA*F* mutations increase the GLUT1 expression and glucose uptake. CRC cells with mutated *KRAS* or *BRAF* were able to survive long term in low-glucose culture environments, which suggests that enhanced glucose metabolic alteration induced by KRAS mutation could provide a significant survival advantage for tumor cells [20]. In retrospective studies with primary and metastatic CRCs, ^{18}F-FDG accumulation in CRC tissues of *KRAS*-mutant CRC patients was significantly higher than that of *KRAS* wild-type CRC patients [21]. It is suggested that FDG accumulation may reflect the mutational status of *KRAS* in CRC [22]. *KRAS* mutation occurs in >90% of pancreatic carcinoma cases. *KRAS* mutations play a great role in pancreatic malignant progression from intraepithelial neoplasia to invasive malignant tumor. Studies, using this *KRAS* ^{G12D}-driven PDCA mouse model, have shown that mutated *KRAS* maintains tumor growth by stimulating glucose uptake. Mutated *KRAS* enhances the expression of glucose transporter-1 (GLUT1) and several rate-limiting glycolytic enzymes, including hexokinase (HK2) and lactate dehydrogenase (LDH), which channels glucose intermediates into the non-oxidative pentose phosphate pathway (PPP) and hexosamine biosynthesis pathway (HBP). As a result, *KRAS* mutations promote protein glycosylation through HBP and ribose production through non-oxidative PPP [23]. Conversely, silencing either the HBP gene (*Gfpt1*) or non-oxidative PPP genes (*Rpia* or *Rpe*) results in a suppression of KRAS-dependent tumor growth in vivo, implying a potential therapeutic strategy. Hexokinases catalyze the first committed step of glucose metabolism. HK2 deletion in *KRAS*-driven NSCLC cells reduces glucose-derived ribonucleotide synthesis and inhibits the incorporation of glutamine-derived carbon into TCA cycle intermediates [24].

Tumor-suppressor protein p53 prevents cancer development through various mechanisms, including the induction of apoptosis, cell-cycle arrest, and the maintenance of genome stability. p53 inactivation induces Warburg effect by affecting HIF-1 and a number of glycolytic enzymes' function. In hypoxic conditions, p53 induces the expression of Ras-related associated with diabetes (RRAD), which blocks membrane localization of GLUT1, resulting in an inhibition of glycolysis. p53 decreases the rate of aerobic glycolysis and upregulates GLUT3 through the IKK-NF-kappaB pathway suppression of glycolysis [25]. Inactivation of tumor suppressor p53 activates HK2 to maintain a high glycolytic phenotype [26]. TP53-induced glycolysis and apoptosis regulator (TIGAR) is one of the downstream glycolytic targets of p53. TIGAR can lower fructose-2,6-bisphosphate protein levels in cells, resulting in a downregulation of glycolysis and a decrease in intracellular reactive oxygen species (ROS) levels by regulating PPP pathway [27]. The RING finger protein MDM2 is a transcriptional target of p53. As MDM2 also ubiquitinates the tumor suppressor

p53, p53 may regulate glycolysis by posttranscription via its target *MDM2*. Moreover, MDM2 gene amplification is observed in certain cancers.

1.2.2 Glucose Enzyme and Tumor

Tumor glucose metabolic change is a complex process, and metabolic enzymes are the direct executors following oncogene activation and tumor-suppressor gene inactivation [28]. The first step of glucose metabolism is to transport glucose across the plasma membrane, which is mediated by GLUT proteins. Many studies have reported that GLUT1 is upregulated in cancers, which directly enhances glucose metabolism. PI3K/Akt signaling functions as a master regulator for cancer cells to uptake glucose. PI3K/Akt signaling increases the expression of glucose transporter GLUT1 mRNA and promotes the translocation of GLUT1 protein from the endomembrane to the cell surface [29]. Besides the PI3K/Akt signaling module, other oncogenic stimuli also play a role in regulating the expression and translocation of GLUT1 protein. Oncogenic protein Ras has been reported to upregulate mRNA expression of GLUT1 and increase cellar glucose uptake.

HK, mediating the critical first reaction of glycolysis, catalyzes the phosphorylation of glucose to glucose-6-phosphate (G6P). G-6P may enter into either the glycolic pathway or the pentose phosphate pathway for glycogen synthesis in tumor cells. There are four mammalian isoforms of HK, designated as HK-1 to HK-4. HK-2 is predominantly expressed in cancer cells. Clinical studies have showed that the expression of hexokinase-2 protein is upregulated in a number of cancers, including breast, lung, and liver cancers. Studies have revealed that deletion of HK2 inhibits the tumor progression by shutting down glucose flux at the earliest step in glucose metabolism. HK2 interacts with voltage-dependent anion channel (VDAC), which is located in the outer membrane of mitochondria. This interaction promotes the production of glycolytic fuel through ATP generated from mitochondria. Combined expression of a plasma membrane glucose transporter GLUT1 and hexokinase (HK) provides a survival advantage for cells cultured in a growth factor-deprived medium.

It also has been well established that PFK, as the second rate-limiting enzyme, controls the glycolytic pathway by its allosteric regulation. The activity of PFKFB3 can be regulated by the oncogenic Ras signaling pathway. In breast cancer cells, PFK expression is increased by constitutive HER2 expression.

Downregulation of PFK expression leads to a reduction in glycolytic flux and suppresses tumor proliferation.

PK is another glycolytic enzyme, which converts PEP into pyruvate in the final step of glycolysis. PK has two isoforms, PKM1 and PKM2. PKM2 is detected in embryonic tissues and many tumors, while PKM1 is expressed in normal adult tissues. Studies have found that mice injected with the PKM2-expressing cells showed a faster tumor growth rate and a larger tumor size than those injected with PKM1-expressing cells, which suggesting that PKM2 provides a growth advantage for tumor cells in vivo. Proteomic studies have showed that PKM2 constitutively shifted its active tetrameric structure by multiple additional posttranslational regulations, which leads to the regulation of pyruvate kinase activity. PKM2 activity is inhibited by the displacement of the activating cofactor fructose-1,6-bisphosphate followed by PKM2 directly binding to phosphotyrosine peptides. Phosphoproteomic study of PKM2 showed that phosphorylation disrupts its interaction with fructose-1,6-bisphosphate and inhibits the formation of the active tetrameric form. Glucose stimulated K305 acetylation of PKM2, and PKM2 activity is inhibited by subsequent autophagic degradation, which results in enhanced tumorigenicity. Immunohistological staining using anti-PKM2 antibodies revealed a strong staining of PKM2 in almost all kinds of solid tumor tissues [30]. Collectively, a variety of studies have shown that PKM2 promotes glucose metabolic flux and contributes to cancer cell proliferation.

Lactate dehydrogenase A (LDHA) plays a critical role in tumor development. It catalyzes the final step of the glycolytic pathway, to produce lactate and NADP from pyruvate and NADPH. LDHA, as the direct target gene of *MYC* and *HIF1*, promotes glucose uptake and lactate generation of cancer cells. A large number of studies have reported that silencing LDHA protein in tumor cells increases mitochondrial respiration, decreases the proliferation, and leads to cell death in both normal and hypoxic environments. It has been well known that many human tumors have higher LDHA levels than surrounding normal tissues. Because abolishing LDHA has no significant effect on normal tissue, it suggests that LDHA may be a promising therapeutic target in cancer.

G6PD catalyzes the formation of glucono-D-lactone-6-phosphate and NADPH via the oxidation of glucose-6-phosphate with NADP. Glucose-6-phosphate dehydrogenase (G6PD) is the rate-limiting enzyme in the pentose phosphate pathway. It has been reported that G6PD overexpression promoted fibrosarcoma growth in nude mice. Knockdown G6PD in melanoma cells decreases proliferation and promotes apoptosis. Clinically, G6PD is overexpressed in many human cancers, including breast, bladder, cervical, ovarian, and prostate cancer. Moreover, G6PD is an independent prognosis predictor in breast and gastric cancer.

Isocitrate dehydrogenase 1 (IDH1) and isocitrate dehydrogenase 2 (IDH2) mutations have been identified in several human cancers, such as low-grade glioma, cholangiocarcinoma, chondrosarcoma, and acute myeloid leukemia (AML). IDH1 or IDH2 with mutant alleles harbors an unusual neomorphic enzymatic function. Mutant IDH prefers to catalyze a-ketoglutarate to D-enantiomer of 2-hydroxyglutarate (2-HG), whereas the wild-type IDH catalyzes the converse reaction

from TCA cycle metabolite isocitrate to a-ketoglutarate. A prominent CpG island hypermethylation was observed in IDH-driven glioma, leukemia, and chondrosarcoma. Notably, normal hematopoietic cells or chondrocytes with a mutant IDH1 allele knock-in can show an aberrant expansion.

Glyceraldehyde-3-phosphate dehydrogenase (GAPDH) catalyzes the reversible conversion of glyceraldehydes-3-phosphate (G-3-P) to 1,3-diphosphoglycerate in glycolytic metabolism. Recent studies show GAPDH is also a pro-apoptotic agent. Remarkably increased GAPDH in many human cancer types are often correlated with reduced survival. Several cancerous factors, such as HIF-1, p53, insulin, nitric oxide (NO), and acetylated histone, not only regulate GAPDH gene expression but also modulate its protein functions [31].

Phosphoglycerate mutase 1 (PGAM1) is a vital enzyme in the glycolytic pathway catalyzing the conversion of 3-phosphoglycerate (3-PG) to 2-phosphoglycerate (2-PG) [32]. It has been reported that PGAM1 is upregulated in diverse cancers, including lung squamous carcinoma, hepatoma, and cholangiocarcinoma. Ablation of PGAM1 results in blocking aerobic glycolysis and oxidative pentose phosphate pathway (PPP), which consequently inhibits cancer cell proliferation.

1.2.3 Glucose Metabolism and Targeted Therapy

Enhanced glycolysis is a metabolic characteristic of many cancers. It is confirmed that dysregulation of oncogenes and glycolytic enzymes is directly linked to the aerobic glycolysis and oxidative pentose phosphate pathway, which are essential to cancer cell proliferation. Thus, it is believed that the inhibition glycolysis pathway may be a promising therapeutic approach.

The transcription factors HIF-1 orchestrate multiple metabolic-related enzymes and promote tumor growth via enhancing glucose uptake and utilization in tumor cells. As a consequence, inhibition of HIF-1 is an attractive anticancer strategy. Many anticancer drugs being tested in clinical trials of cancer patients are now recognized as HIF-1 inhibitors. The expression of HIF-1α mRNA can be induced by topoisomerase 1 (TOP1), so that TOP1 inhibitors, for example, topotecan and irinotecan, downregulate HIF-1α expression. TOP1 inhibitors are being studied in cancer clinical trials to assess its anticancer effects. There are more HIF-1 inhibitors being tested in oncology clinical trials. HSP90 inhibitor ganetespib impairs HIF-1α stability. Digoxin, an antiarrhythmic drug, inhibits HIF-1α translation. Proteasome inhibitor bortezomib inhibits HIF-1α transactivation. Although many agents can inhibit cancer growth in a HIF-1-dependent way, preclinical and clinical studies about these agents have been stopped for toxicity or safety problems.

Some of the drugs that target glycolytic related oncogenes, enzymes, and transporters of glycolytic products are under clinical investigation. For example, silibinin (also known as silybin), one of the GLUT1 inhibitors, is being tested clinically. A novel representative inhibitor of GLUT1, WZB117, is a small-molecule inhibitor of *SLC2A1*. WZB117 decreases GLUT1 protein expression levels and represses activity of GLUT1. Its effect has been extensively tested in vitro and in vivo. WZB117 inhibits glucose uptake in cancer cells in a dose-dependent manner [33]. In vitro studies, WZB117 inhibits glucose transport of lung cancer A549 cell lines rapidly, starting 1 min after treatment. Furthermore, WZB117 significantly inhibited the proliferation of lung cancer cells by 50%, 48 h after treatment. However, WZB117 showed no such obvious effects in the NL20 noncancerous lung cell line. The levels of cyclins and phosphorylated retinoblastoma protein (RB1) of A549 cells were also blocked 6 h after WZB117 treatment, as well as prominent cell-cycle arrest and senescence within 24 h. Finally WZB117 treatment induced a necrosis within 48 h. WZB117 not only inhibited cancer cell growth in vitro study but also inhibited subcutaneously implanted tumor growth in a nude mouse mode. In in vivo studies, injection of WZB117 into nude mice for 10 weeks reduced the tumor growth of A549 cell xenografts by 70% when compared with grafts from mice mock treated [34]. In addition to testing GLUT1 inhibitor alone as an anticancer agent, researches are also performed to assess the effectivity of combining use of GLUT1 inhibition and other cancer therapeutics. WZB117 showed a stronger synergistic antitumor effect when administered in vitro along with the anticancer drug cisplatin or paclitaxel in lung cancer cell lines A549 and H1229 and breast cancer MCF7 cells than when they were tested alone. Another natural inhibitor of a GLUT1, phloretin, presented a better antitumor effect if administered in combination with daunorubicin. In in vitro study, combining use of inhibiting cisplatin with shRNA-GLUT1, which stably knock down GLUT1 protein expression, has a stronger antitumor effect in head and neck carcinoma cells under both normoxic and hypoxic conditions. Although these studies show promising effects of GLUT1 inhibitor in combination with other anticancer treatment, more researches are needed to explore the underlying mechanism for the synergistic antitumor activity in the combined therapy.

The important role of HK2 in glycolysis makes it an important therapeutic target for designing agents against cancer. 2-Deoxyglucose (2-DG) and 3-bromopyruvate (3-BrPA) are two well-known inhibitors of HK2. 2-Deoxidation-D-glucose (2-DG) is a kind of glucose analog and functions as a competitive inhibitor of HK2. 2-DG is phosphorylated by hexokinase (HK) to generate 2-DG-6-phosphate. The latter is not metabolized further, which inhibits phosphohexoisomerase and glucose-6-phosphate

dehydrogenase and finally reduces the output from glycolysis (ATP) and the pentose phosphate pathway. Systemic deletion of HK2 in breast and NSCLC cancer mouse models inhibited tumor initiation, implying HK2 as an attractive target for these tumors. Clinical trial has been initiated to evaluate the therapeutic effectiveness of using 2-DG in combination with other chemotherapeutics [35]. 3-Bromine pyruvate (3-BrPA) is a lactose analog. It directly inhibits the activity of HK2 in a particular way different from 2-DG by alkylation thiol in HK2. 3-Bromopyruvate (3-BrPA) was highly effective on the xenografts derived from CRC cells with mutated *KRAS* or *BRAF* [21]. 3-BrPA has been proposed as an anticancer agent as well as a chemosensitizer for use in combination with anticancer drugs [36]. Lonidamine, a small-molecule inhibitor, has been reported to inhibit HK activity. The interaction of HK and VDAC can be interrupted by various azoles and their derivatives, such as clotrimazole and bifonazole. Methyl jasmonate, a plant lipid derivative, is reported to impair the interaction of HK2 and VDAC. Therefore, HK2 seems to be a potential target for the therapeutic agent designing.

6-Phosphofructo-2-kinase (PFKFB3) is also a key regulator of glycolysis. PFKFB3 catalyzes the synthesis of fructose-2,6-bisphosphate (F26BP), which is an activator of 6-phosphofructo-1-kinase, a key step of glycolysis. A small-molecule inhibitor of PFKFB3, 3-(3-pyridinyl)-1-(4-pyridinyl)-2-propen-1-one (3PO), suppresses PFKFB3 activity, reduces glucose uptake, and decreases the intracellular concentration of Fru-2,6-BP, lactate, and ATP. Then, one small molecule, 1-(4-pyridinyl)-3-(2-quinolinyl)-2-propen-1-one (PFK15), which is selected from synthesized 73 derivatives of 3PO, exhibits a strong activity against recombinant PFKFB3 [37]. PFK15 was further used in preclinical trials to evaluate its antimetabolic, antineoplastic, and pharmacokinetic properties in vitro and in vivo. PFK15 induces apoptosis, suppresses the glucose uptake and growth of Lewis lung carcinomas, and has adequate pharmacokinetic properties in syngeneic mice. PFK15 inhibits the growth of human cancers in xenograft model mice.

Pyruvate is an attractive target for anticancer therapy because of its dual functions in both ATP generation and biosynthetic reactions. TT-232, a structural somatostatin analog, has been studied in clinical trials. TT-232 inhibits PKM2 dimerization, which leads to its activity decrease. In addition, TT-232 also promotes nuclear translocation of PKM2 resulting in a caspase-independent cell death [38].

LDHA inhibition for anticancer treatment is a safe therapeutic target because a complete abolishment of LDHA protein in humans by hereditarily deleting *LDHA* gene only induces non-life-threatening and a few cases of exertional myoglobinuria. 3-Dihydroxy-6-methyl-7-(phenylmethyl)-4-propylnaphthalene-1-carboxylic acid (FX11) is a small and specific inhibitor of LDHA. FX11 blocks cellular energy metabolism via inhibition of glycolysis; thereby targeted tumor types are those with glycolysis metabolic phenotype. In addition to inhibition of glycolysis, FX11 also elevates oxygen intake and ROS generation and induces apoptosis and cell death in P493 human lymphoma B cells in vitro. The xenograft growth rate of P493 lymphoma B cells and P198 human pancreatic cancer cells in mice is significantly reduced by FX11 treatment. Besides FX11, other molecules agents, such as galloflavin and *N*-hydroxyindole, have been identified to inhibit LDHA. Although initial efficiency of these novel antitumor agents has been revealed, more studies are needed to investigate their underlying mechanisms for cancer therapy.

The Warburg effect also generates lactate followed by preferential use of the glycolytic pathway [12]. Overexpressed MCT1 in cancer and disrupting lactate transport indicate a promising approach for therapeutic targeting. AZD3965 is a selective MCT1 inhibitor that exhibits growth-inhibitory activity in small cell lung cancer tumor xenografts. Phase I and progressing to phase II clinical trials for AZD3965 have been initiated in the UK.

Dichloroacetate (DCA), a pyruvate analog, can stimulate pyruvate dehydrogenase which promotes the conversion of pyruvate into acetyl-CoA, significantly shifting the metabolic flux in glycolytic cancer cells with impaired mitochondrial activity and increasing mitochondrial apoptosis. Clinical studies have been performed in patients with glioma to verify the efficacy of DCA and its adverse effects.

Although almost all cancer cells prefer glycolysis pathway, mitochondrial metabolism is also essential to some types of tumors. Therefore, mitochondrial metabolic products or enzymes offer a variety of attractive targets for anticancer therapy. To date, a number of drugs that interfere with oxidative phosphorylation (OXPHOS) are being investigated as anticancer drugs. A key example is metformin, which interferes with OXPHOS by inhibiting NADH-coenzyme Q oxidoreductase (complex I). Metformin can reduce gluconeogenesis in the liver and is recognized as an important drug for the type 2 diabetes mellitus treatment. Some epidemiological studies have found metformin treatment reduced risk of cancer in patients of diabetes, which remains controversial. As thus, the use of metformin as an anticancer agent has been deeply studied, and metformin has showed anticancer effect activity in clinical trials. Metformin treatment at physiological doses induced apoptosis prominently in breast cancer cells in vitro. This effect is more significant under low-glucose concentration conditions. Clinical trials have supported the anticancer effects of metformin in patients with breast, prostate, and endometrial cancer. Metformin is widely assessed in many clinical trials of non-diabetic cancer patients.

The following table contains the inhibitors that target glucose metabolism (Table 1.1).

Table 1.1 Glucose metabolic inhibitors

Target protein	Agent	Mechanism	Development stage	Observations
Transcription factors				
HIF-1	Irinotecan, topotecan	• TOP1 inhibitor • Downregulates HIF-1α mRNA expression	Clinical studies	Anticancer effect but with toxicity or safety problems
	Ganetespib	• HSP90 inhibitor • Impairs HIF-1α stability	Preclinical, clinical studies	
	Digoxin	Inhibits HIF-1α translation	Preclinical, clinical studies	
	Bortezomib	• Proteasome inhibitor • Inhibits HIF-1α transactivation	Preclinical, clinical studies	
Glycolysis				
GLUT1	Silibinin	GLUT1 inhibitor	Clinical studies	
	WZB117	• SLC2A1 inhibitor • Decreases GLUT1 protein expression levels • Inhibits the proliferation of lung cancer cells • Induces tumor cells necrosis	Preclinical, clinical studies	In vitro, presented a better effect if administered in combination with cisplatin or paclitaxel in lung cancer
	Phloretin	GLUT1 inhibitor	Preclinical, clinical studies	Better antitumor effect with daunorubicin
HK2	2-DG	• Glucose analog • HK2 competitive inhibitor • Inhibits tumor initiation	Preclinical, clinical studies	
	3-BrPA	• Lactose analog • Inhibits the activity of HK2	Preclinical, clinical studies	• Anticancer agent • Chemosensitizer
	Lonidamine	Inhibits HK activity	Preclinical, clinical studies	
	Clotrimazole, bifonazole	Interrupts the interaction of HK and VDAC	Preclinical, clinical studies	
	Methyl jasmonate	Impairs the interaction of HK2 and VDAC	Preclinical, clinical studies	
PFKFB3	3PO,PFK15	• PFKFB3 inhibitor • Reduces glucose uptake • Induces apoptosis	Preclinical, clinical study	• Antimetabolic • Antineoplastic • Pharmacokinetic
LDHA	FX11, galloflavin, *N*-hydroxyindole	• LDHA inhibitor • Inhibits glycolysis, elevates oxygen intake and ROS generation • Induces apoptosis	Preclinical study	
TCA cycle				
Pyruvate	TT-232	• Structural somatostatin analog • Inhibits PKM2 dimerization • Promotes nuclear translocation of PKM2	Clinical study	Leads caspase-independent cell death
PDK1	DCA	• Pyruvate analog • Stimulates pyruvate dehydrogenase • Promotes mitochondrial apoptosis	Clinical study	
Lactate				
MCT1	AZD3965	• Selective MCT1 inhibitor • Inhibits growth activity	Phase I, phase II clinical study	
Mitochondrial metabolism				
Mitochondrial complex I	Metformin	• Mitochondrial complex I inhibitor • Interferes with OXPHOS • Reduces gluconeogenesis in the liver	Preclinical, clinical study	• An important drug for the type 2 diabetes mellitus • Clinical trials have supported the anticancer effects in patients with breast, prostate, and endometrial cancer

1.3 ^{18}F-FDG PET/CT Scanning

1.3.1 Glucose and ^{18}F-Fluorodeoxyglucose (^{18}F-FDG)

^{18}F-FDG is a small-molecule probe with a structural similarity to glucose. ^{18}F, a kind of positron emission radioisotope, can substitute the second position hydroxyl group to make ^{18}F-FDG (Fig. 1.1). ^{18}F-FDG enters the tumor cells by using the same facilitated transport mechanism as glucose via cell surface glucose transporter proteins, such as GLUT1 and GLUT3. Once inside the cell, ^{18}F-FDG is phosphorylated by hexokinase into ^{18}F-FDG-6-phosphate (^{18}F-FDG-6-PO_4). Phosphofructokinase and other enzymes, which further metabolize glucose-6-phosphate, cannot use ^{18}F-FDG-6-PO_4 as a substrate; and phosphorylation increases the molecular polarity, so ^{18}F-FDG-6-PO_4 could not diffuse back out of the cell. As thus, ^{18}F-FDG can accumulate in the cell.

1.3.2 ^{18}F-FDG PET/CT Scanning

^{18}F-FDG PET/CT scanning is a molecular imaging technique that uses a radioactively labeled glucose (^{18}F-FDG) with PET/CT to visualize fundamental molecular and biochemical processes of glucose in the body. Preference to glycolysis pathway is the most common phenotype of malignant tumor energy metabolism disorder. ^{18}F-FDG PET/CT imaging can show the malignant tumors with high level of glycolysis. ^{18}F-FDG PET/CT imaging analysis is normally performed by two methods: visually qualitative interpretation and/or using quantitative parameters. Standardized uptake value (SUV) is the most commonly used quantitative analytical parameter in clinical practice. The SUV allows comparisons of ^{18}F-FDG uptake to be made between the target tissues and normal tissues. PET/CT imaging shows the glucose uptake and distribution in body organs, tissues, and cells. Cortical gray matter, nuclei, and thalamus in the basal ganglia and the cerebellar gray matter have more intense uptake of FDG; white matter and ventricular system are associated with less intense or absent FDG uptake. Uptake in the palatal tonsils, adenoids, and brown fat can be shown. Mild-to-moderate uptake within parotid gland, submandibular gland, and thyroid gland is also a physiological finding. There would be an intense uptake in the eye muscles, facial muscles (vocal cords, masseter, lingualis), and neck muscles (sternocleidomastoid and prevertebral muscles) due to exercise or stress. The uptake of FDG within the heart is extremely variable from low to high glucose uptake level under different physiological conditions; there is a mild uptake in mediastinum due to a large amount of blood in great vessels. Normal lung tissue uptake is low due to being filled with a large amount of gas; hilar lymph node uptake is a common finding especially in the old; and mild physiologic uptake is often seen in the thymus which is not completely degraded, secretory mammary gland and normal esophagus. The uptake within the stomach and intestines can be variable, and the distribution of the imaging agent is consecutive and consistent with the outline of digestive tract. The liver usually shows diffused uptake from mild to moderate levels, with a clear boundary; the spleen also has a diffused uptake of ^{18}F-FDG but a little lower uptake level than that of the liver. ^{18}F-FDG is filtered through the kidney and could not be reabsorbed by the renal tubule. Therefore, the kidneys, ureters, and bladder have intense uptake of ^{18}F-FDG (urinary retention). The prostate normally shows little uptake. There is a variable uptake in the uterus and ovaries due to the women menstrual cycle.

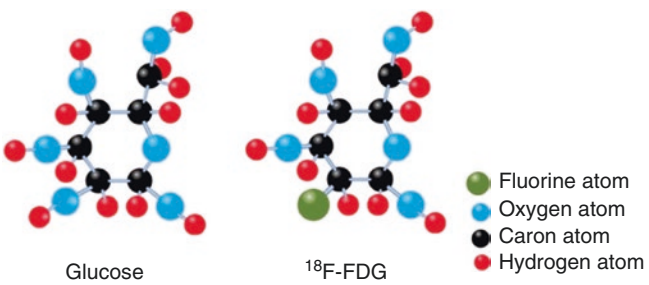

Fig. 1.1 Chemical structure of glucose (left) and 18F-FDG (right)

1.3.3 Clinical Utility of ^{18}F-FDG PET/CT Scanning

Nowadays, ^{18}F-FDG PET/CT has been widely used to detect malignant tumors; to make differential diagnosis, clinical stage, and prognosis; and to monitor therapeutic response. The uptake of imaging agent ^{18}F-FDG into the malignant tissue is related to the tumor histologic type and differentiation grade, etc. Most of the common tumors, such as squamous cell carcinomas, colorectal cancer, and malignant lymphoma, avidly uptake ^{18}F-FDG. Some benign tumors such as thyroid papillary adenoma, parotid gland tumor (Warthin's tumor, polycrystal adenomas), adenomatous polyposis coli, pastel adenoma, and leiomyoma may also demonstrate high ^{18}F-FDG uptake in PET/CT imaging. Increased ^{18}F-FDG uptake also occurs in acute inflammation caused by various causes, such as surgery, radiotherapy, or infection; granulomatous inflammation, such as sarcoidosis, fungal disease, or tuberculous disease; and chronic inflammatory diseases such as ulcerative colitis and systemic lymphadenopathy. These nonmalignant tumor diseases can cause potential confusion in clinical application, and other imaging information or pathological examinations are required to make a differential diagnosis. In clinical practice, ^{18}F-FDG PET/CT scanning also can be used in neurology, cardiology, neuropsychology, and psychiatry.

References

1. Ferrier DR (2011) Biochemistry, 5th edn. Lippincott Williams & Wilkins, Philadelphia, pp 91–154
2. Chaneton B, Hillmann P, Zheng L et al (2012) Serine is a natural ligand and allosteric activator of pyruvate kinase M2. Nature 491(7424):458–462
3. Benjamin DI, Cravatt BF, Nomura DK (2012) Global profiling strategies for mapping dysregulated metabolic pathways in cancer. Cell Metab 16(5):565–577
4. Metallo CM, Walther JL, Stephanopoulos G (2009) Evaluation of 13C isotopic tracers for metabolic flux analysis in mammalian cells. J Biotechnol 144(3):167–174
5. Neely JR, Denton RM, England PJ et al (1972) The effects of increased heart work on the tricarboxylate cycle and its interactions with glycolysis in the perfused rat heart. Biochem J 128(1):147–159
6. Warburg O (1956) On respiratory impairment in cancer cells. Science 124(3215):269–270
7. Hsieh AL, Walton ZE, Altman BJ et al (2015) MYC and metabolism on the path to cancer. Semin Cell Dev Biol 43:11–21
8. Dang CV (2012) MYC on the path to cancer. Cell 149(1):22–35
9. Teleman AA, Hietakangas V, Sayadian AC et al (2008) Nutritional control of protein biosynthetic capacity by insulin via Myc in Drosophila. Cell Metab 7(1):21–32
10. Osthus RC, Shim H, Kim S et al (2000) Deregulation of glucose transporter 1 and glycolytic gene expression by c-Myc. J Biol Chem 275(29):21797–21800
11. Le A, Lane AN, Hamaker M et al (2012) Glucose-independent glutamine metabolism via TCA cycling for proliferation and survival in B cells. Cell Metab 15(1):110–121
12. Le A, Cooper CR, Gouw AM et al (2010) Inhibition of lactate dehydrogenase A induces oxidative stress and inhibits tumor progression. Proc Natl Acad Sci U S A 107(5):2037–2042
13. David CJ, Chen M, Assanah M et al (2010) HnRNP proteins controlled by c-Myc deregulate pyruvate kinase mRNA splicing in cancer. Nature 463(7279):364–368
14. Wang GL, Jiang BH, Rue EA et al (1995) Hypoxia-inducible factor 1 is a basic-helix-loop-helix-PAS heterodimer regulated by cellular O2 tension. Proc Natl Acad Sci U S A 92(12):5510–5514
15. Kim JW, Tchernyshyov I, Semenza GL et al (2006) HIF-1-mediated expression of pyruvate dehydrogenase kinase: a metabolic switch required for cellular adaptation to hypoxia. Cell Metab 3(3):177–185
16. Kennedy KM, Dewhirst MW (2010) Tumor metabolism of lactate: the influence and therapeutic potential for MCT and CD147 regulation. Future Oncol 6(1):127–148
17. Kawada K, Toda K, Sakai Y (2017) Targeting metabolic reprogramming in KRAS-driven cancers. Int J Clin Oncol 22(4):651–659
18. Gysin S, Salt M, Young A et al (2011) Therapeutic strategies for targeting ras proteins. Genes Cancer 2(3):359–372
19. Karnoub AE, Weinberg RA (2008) Ras oncogenes: split personalities. Nat Rev Mol Cell Biol 9(7):517–531
20. Yun J, Rago C, Cheong I et al (2009) Glucose deprivation contributes to the development of KRAS pathway mutations in tumor cells. Science 325(5947):1555–1559
21. Kawada K, Nakamoto Y, Kawada M et al (2012) Relationship between 18F-fluorodeoxyglucose accumulation and KRAS/BRAF mutations in colorectal cancer. Clin Cancer Res 18(6):1696–1703
22. Miles KA, Ganeshan B, Rodriguez-Justo M et al (2014) Multifunctional imaging signature for V-KI-RAS2 Kirsten rat sarcoma viral oncogene homolog (KRAS) mutations in colorectal cancer. J Nucl Med 55(3):386–391
23. Ying H, Kimmelman AC, Lyssiotis CA et al (2012) Oncogenic Kras maintains pancreatic tumors through regulation of anabolic glucose metabolism. Cell 149(3):656–670
24. Patra KC, Wang Q, Bhaskar PT et al (2013) Hexokinase 2 is required for tumor initiation and maintenance and its systemic deletion is therapeutic in mouse models of cancer. Cancer Cell 24(2):213–228
25. Kawauchi K, Araki K, Tobiume K et al (2008) p53 regulates glucose metabolism through an IKK-NF-kappaB pathway and inhibits cell transformation. Nat Cell Biol 10(5):611–618
26. Mathupala SP, Heese C, Pedersen PL (1997) Glucose catabolism in cancer cells. The type II hexokinase promoter contains functionally active response elements for the tumor suppressor p53. J Biol Chem 272(36):22776–22780
27. Bensaad K, Tsuruta A, Selak MA et al (2006) TIGAR, a p53-inducible regulator of glycolysis and apoptosis. Cell 126(1):107–120
28. Baig MH, Adil M, Khan R, et al (2017) Enzyme targeting strategies for prevention and treatment of cancer: implications for cancer therapy. Semin Cancer Biol. https://doi.org/10.1016/j.semcancer.2017.12.003. [Epub ahead of print]
29. Pavlova NN, Thompson CB (2016) The emerging hallmarks of cancer metabolism. Cell Metab 23(1):27–47
30. Mazurek S (2011) Pyruvate kinase type M2: a key regulator of the metabolic budget system in tumor cells. Int J Biochem Cell Biol 43(7):969–980
31. Zhang JY, Zhang F, Hong CQ et al (2015) Critical protein GAPDH and its regulatory mechanisms in cancer cells. Cancer Biol Med 12(1):10–22
32. Peng XC, Gong FM, Chen Y et al (2016) Proteomics identification of PGAM1 as a potential therapeutic target for urothelial bladder cancer. J Proteomics 132:85–92
33. Liu Y, Cao Y, Zhang W et al (2012) A small-molecule inhibitor of glucose transporter 1 downregulates glycolysis, induces cell-cycle arrest, and inhibits cancer cell growth in vitro and in vivo. Mol Cancer Ther 11(8):1672–1682
34. Ooi AT, Gomperts BN (2015) Molecular pathways: targeting cellular energy metabolism in cancer via inhibition of SLC2A1 and LDHA [J]. Clin Cancer Res 21(11):2440–2444
35. Raez LE, Papadopoulos K, Ricart AD et al (2013) A phase I dose-escalation trial of 2-deoxy-D-glucose alone or combined with docetaxel in patients with advanced solid tumors. Cancer Chemother Pharmacol 71(2):523–530
36. Chong D, Ma L, Liu F et al (2017) Synergistic antitumor effect of 3-bromopyruvate and 5-fluorouracil against human colorectal cancer through cell cycle arrest and induction of apoptosis. Anticancer Drugs 28(8):831–840
37. Clem BF, O'neal J, Tapolsky G et al (2013) Targeting 6-phosphofructo-2-kinase (PFKFB3) as a therapeutic strategy against cancer. Mol Cancer Ther 12(8):1461–1470
38. Keri G, Erchegyi J, Horvath A et al (1996) A tumor-selective somatostatin analog (TT-232) with strong in vitro and in vivo antitumor activity. Proc Natl Acad Sci U S A 93(22):12513–12518

Clinical Utility of PET/CT in Breast Cancer Management and Targeted Therapy

2

Xinzhong Hao, Xiaxia Meng, and Zhifang Wu

2.1 Introduction

Breast cancer is currently the most prevalent malignant disease affecting women's health. Breast cancer is a highly heterogeneous tumor, comprising multiple entities associated with distinctive histological and biological features, clinical presentations, and responses to therapy. In addition to traditional treatment approaches, such as surgery, radiotherapy, endocrine therapy, and chemotherapy, targeted therapy is another emerging approach for breast cancer treatment. With the breakthrough in molecular biology and pharmacology research, new targeted drugs have been continuously applied in clinic and have achieved good clinical results.

2.1.1 Epidemiology

Breast cancer is the leading cause of cancer-related death for women in both developed and developing countries [1]. In 2012, 1.7 million women were diagnosed with breast cancer, and 522,000 died from it at the same year [1]. From 1989 to 2012, breast cancer death rates decreased by 36% in the United States [2]. But in China, the incidence of breast cancer is still slowly rising [3].

According to the study by Lei Fan [3] from China, breast cancer is now still the most common cancer in Chinese women. With more than 1.6 million people are diagnosed with breast cancer and 1.2 million people die every year in China, accounts for 12.2% of all newly diagnosed cancers and 9.6% of all cancer deaths worldwide [3]. There is still a long way for China in the prevention and treatment of breast cancer.

There are regional differences in the incidence of breast cancer, and urban areas are higher than rural areas. The average age at diagnosis of breast cancer in China is 45–55 years old, younger than Western women.

Some risk factors are thought to contribute to the development of breast cancer. Currently, recognized risk factors include early age at first menstruation, late childbearing or not at all, older age, prior history of breast cancer, family history, obesity, lack of physical exercise, drinking alcohol, smoking tobacco, hormone replacement therapy during menopause, and ionizing radiation. Genes are also thought to be a major factor in 5–10% of cases [4], including BRCA1 and BRCA2, among others.

2.1.2 Molecular Subtypes and Gene Expression Tests in Breast Cancer

Most of the malignant breast tumors are adenocarcinomas, usually called as breast cancer. Breast cancer is a highly heterogeneous tumor, comprising distinctive entities associated with its own clinical, histological, molecular, and genic characteristics.

At the gross histopathology level, breast cancer can be divided into carcinoma in situ, and invasive carcinoma depended on whether tumor breaks through the basement membrane or not. According to the growth location of tumors in the breast, it can be divided into ductal carcinoma and lobular carcinoma (such as intralobular carcinoma in situ, ductal carcinoma in situ).

In clinic, infiltrating ductal carcinomas are most common, accounting for 70–80% of invasive breasts, followed by infiltrating lobular carcinoma accounting for 5–10%. In addition, there are some rare types of invasive breast cancer histology, such as tubular, mucinous, and medullary carcinoma. Compared with infiltrating ductal carcinomas, infiltrating lobular carcinomas tend to be multicentric and/or bilateral. Inflammatory breast cancer and Paget's disease are two specific types of breast cancer, with particularly pathological and clinical features.

Over the years, new molecular diagnostic technology have been studied, which aims to find new biomarkers to

X. Hao · X. Meng · Z. Wu (✉)
The First Hospital of Shanxi Medical University, Shanxi, P. R. China

G. Huang (ed.), *Nuclear Medicine in Oncology*, https://doi.org/10.1007/978-981-13-7458-6_2

better describe and distinguish entities. The development of new biomarkers provides clinicians with a reference for diagnosis of breast cancer, risk stratification, staging, treatment options, and finally helps to achieve precise and individualized treatment for patients.

According to the characteristics of immunohistochemistry (IHC), breast cancer can be divided into three major subtypes: tumors expressing the estrogen receptors (ERs), progesterone receptors (PRs), and human epidermal growth factor receptor 2 (HER2) breast cancer. The remaining group is commonly referred to as triple-negative breast cancer (TNBC) due to lack of expression of ERs, PRs, and HER2. TNBC itself contains many different entities that have been identified through gene expression tests.

The seminal discovery of breast cancer research over the last two decades was the description of the intrinsic breast cancer subtypes. Perou et al. [5] analyzed gene expression patterns of breast cancer employing microarray-based gene expression profiling, identifying four major intrinsic gene signatures: luminal, triple-negative/basal-like, HER2-positive-enriched, and normal-like. Subsequent studies led to subdivision of luminal tumors into luminal A and luminal B subgroups. Table 2.1 demonstrates the classification of these subtypes and the specific immunohistochemical expression patterns [6].

Of mammary carcinogenesis, perhaps the most extensively studied are BRCA1, BRCA2, and TP53 genes. These are associated with a high risk of developing breast cancer in carriers, and hence they are referred to as high penetrance genes. However, it should be noted that among breast cancer patients with a strong family history, only 40% are thought to be caused by the above three genes [7]. This suggests that in the remaining 60% of cases, apart from sporadic breast cancers, other genetic pathways are likely involved.

In recent years, five novel gene expression prognostic tests [8] for breast cancer have been developed: MammaPrint, MapQuant Dx, Oncotype DX, PAM50, and Theros Breast Cancer Index. The development of multigene-based prognostic tests is not only to add prognostic and predictive information to conventional biomarkers but to provide more reliable and reproducible techniques than the IHC-based assays, which in turn reduces the technical errors and subjective interpretation [9].

Table 2.1 Breast cancer intrinsic subtypes with prevalent immunohistochemical profiles [6]

Intrinsic subtype	Immunohistochemistry
Luminal A	ER- and/or PR-positive, HER2-negative with Ki-67 < 14%
Luminal B	ER- and/or PR-positive, HER2-negative with Ki-67 ≥ 14%
	ER- and/or PR-positive, HER2-positive with any Ki-67
HER2-enriched	ER- and PR-negative, HER2-positive
Basal-like	ER- and PR-negative, HER2-negative

In spite of their demonstrated efficacy, there are still large regional differences in the application of these tests, probably reflecting variations in economies, health systems, and physician training. Therefore, in many hospitals, immunohistochemical evaluation remains the primary method for the classification of breast cancer.

2.1.3 Targeted Therapy for Breast Cancer

Targeted therapy is a new treatment method in addition to the four traditional treatments of surgery, radiotherapy, endocrine therapy, and chemotherapy. With the deepening of pharmacology and molecular biology research, many molecular targets have been identified, and breakthroughs have also been made in the research and application of new targeted drugs.

Generally, according to the mechanism of action, targeted drugs can be classified into two categories. One of the categories acts on tumor cells, such as antihuman epidermal growth factor receptor 2 (HER2), PI3K/AKT/mTOR inhibitor, CDK4/6 inhibitor, and Poly (ADP-ribose) polymerase (PARP) inhibitor. Another category acts on the microenvironment, such as angiogenesis inhibitors.

2.1.3.1 Anti-HER2 Targeted Therapy

Human epidermal growth factor receptor 2 (HER-2) is not expressed in normal tissues but is overexpressed in tumor tissues. Twenty to thirty percent of breast cancer patients found HER-2 gene overexpression, and the high expression of HER-2 is closely related to the occurrence, development, prognosis, and metastasis of breast tumors. This type of breast cancer is usually highly invasive and has a poor prognosis.

According to the molecular mechanism, drugs targeting HER2 are mainly divided into three categories: Category 1 is a monoclonal antibody, including trastuzumab and pertuzumab, which specifically binds to the extracellular region IV or II of the HER2 receptor and inhibits HER2 receptor activation; Category 2 is a small molecule tyrosine-kinase inhibitor, representing the drug lapatinib, which reversibly interacts with the epidermal growth factor receptor (EGFR) and adenosine triphosphate (ATP) site of HER2 receptor tyrosine kinase regions and inhibit its tyrosine kinase activity; Category 3 is a monoclonal antibody. The representative drug is an antibody-conjugated drug, such as trastuzumab emtansine (TDM1), which is a combination of trastuzumab and anti-tubulin chemotherapeutic drugs through a disulfide bond. It can selectively bring chemotherapeutic drugs into cancer cells and enhance the induction of cancer cell apoptosis.

Numerous studies have shown that trastuzumab is the basic treatment for HER2-positive breast cancer, whether using trastuzumab alone or in combination with chemotherapy drugs, it can bring survival benefits to patients. However, in clinical practice, 70% HER2-positive breast cancer is resistant to trastuzumab, and almost all patients are relayed for resistance during treatment

[10]. How to overcome trastuzumab resistance has become a key issue to be addressed in anti-HER2 targeted therapy.

Several large clinical studies have demonstrated that trastuzumab combined with chemotherapy can reduce the risk of disease recurrence and death in patients with HER2-positive early breast cancer, significantly improving patient outcomes.

2.1.3.2 Anti-angiogenic Targeted Therapy

Angiogenesis is the main cause of tumor growth and metastasis. Therefore, the treatment of targeted angiogenesis is also one of the important strategies. Currently, anti-angiogenic drugs for breast cancer include bevacizumab (targeting vascular endothelial growth factor, VEGF), ramucirumab (targeting vascular endothelial growth factor receptor 2, VEGFR 2), and multiple target of sorafenib and sunitinib. The application of anti-angiogenic targeted drugs in the treatment of advanced breast cancer is controversial. The treatment of anti-angiogenic targeted drugs in breast cancer needs to be further explored. In the future, it is necessary to find a therapeutic target and optimize the benefit population.

2.1.3.3 PI3K/AKT/mTOR Pathway Inhibitor

The PI3K/AKT/mTOR pathway plays an important role in the development of breast cancer. On the one hand, it is downstream of the HER2 pathway, and the activation of the PI3K/AKT/mTOR pathway is involved in the resistance mechanism of trastuzumab; on the other hand, it also interacts with the estrogen receptor (ER) signaling pathway and is involved in the pathogenesis of endocrine therapy resistance.

Everolimus is an inhibitor of mTOR target protein, and a large number of studies have demonstrated that everolimus reverses the activity of the aromatase inhibitor by inhibiting the activity of the PI3K/AKT/mTOR pathway. For postmenopausal women with advanced breast cancer, patients with aromatase inhibitor treatment failure, use of other endocrine drugs in combination with everolimus will become a new strategy to reverse endocrine therapy resistance.

2.1.3.4 Other Targeted Therapy

There are still some other targeted drugs which had been developed, such as cell cycle inhibitors CDK4/6 and PARP inhibitors. CDK4/6 is a representative cell cycle blocker. Phase II study showed that the CDK4/6 inhibitor palbociclib combined with letrozole versus single-agent letrozole for the treatment of postmenopausal ER-positive, HER2-negative advanced breast cancer patients, PFS significantly benefited (20.2 month vs 10.2 months, $P < 0.001$) [11]. In 2015, the FDA approved palbociclib combined with letrozole as an initial regimen for the treatment of postmenopausal ER-positive, HER2-negative advanced breast cancer. For postmenopausal women with advanced breast cancer, patients who failed aromatase inhibitor therapy, use of other endocrine drugs in combination with everolimus will become a new strategy to reverse endocrine therapy resistance.

PARP mainly affects the repair of damaged DNA, resulting in the accumulation of damaged DNA, and ultimately induces tumor cell apoptosis. Currently, iniparib, olaparib, and veliparib are representatives of PARP inhibitors and are undergoing relevant clinical trials.

With the development of molecular biology, breast cancer has entered the era of targeted therapy. As new targeted drugs continue to be developed, prospective studies are needed to determine predictive outcomes, further optimizing the benefit population and maximizing the efficacy of targeted therapy.

2.2 Clinical Utility of ^{18}F-FDG PET/CT in Breast Cancer

The application of PET/CT has been extensively studied in the management of patients with breast cancer, but not applied as a clinical routine in the diagnosis of primary breast cancer. PET/CT cannot replace the sentinel node biopsy in the diagnosis of breast cancer clinically. However, for the detection of supraclavicular, mediastinal, and internal mammary metastatic lymph nodes, PET/CT performs better than other imaging methods. Lymph nodes in these areas may be easily missed in routine CT and MRI study. In the detection of distant metastases, PET/CT has a better accuracy in detecting lytic bone metastases compared to bone scintigraphy. PET/CT is recommended in clinic when advanced-stage disease is suspected and conventional modalities are inconclusive. For the monitoring of locoregional recurrence, PET/CT has a high sensitivity and specificity. Numerous studies support the role of PET/CT in prediction of response to neoadjuvant radiation or chemotherapy. With further research on the treatment planning and evaluation of patients with breast cancer, the role of PET/CT can be further extended.

2.2.1 The Heterogeneity and ^{18}F-FDG Uptake in Breast Cancer

Breast cancer is a highly heterogeneous tumor disease. It is well-known that the glycolysis activity of tumor cells affects ^{18}F-FDG uptake. In general, glycolytic rates of cancer cells are correlated with HIF-1a and c-Myc expression resulting in considerable variability in glycolytic activity. Researches have already shown that the extent of ^{18}F-FDG uptake in breast cancer is affected by a variety of factors.

A larger primary tumor, a positive axillary lymph node status, and higher TNM stage were all significantly associated with a higher SUVmax [12]. The uptake of ^{18}F-FDG is also correlative with the pathological types and cell phenotype of breast cancer. Infiltrating ductal carcinoma has higher ^{18}F-FDG uptake than infiltrating lobular carcinoma even for the same size tumors. The higher ^{18}F-FDG accumulation also correlates with the higher histological grade and the higher expression of

the proliferation marker Ki-67 [13, 14]. ER negativity, PR negativity, HER2 positivity, and high Ki-67 expression were also significantly correlated with a higher SUVmax. Basu et al. [15] and Kitajima et al. [12] found that tumors with a triple-negative phenotype had a higher FDG uptake. Breast cancers with a p53 mutation were repeatedly shown to be associated with poorer prognosis. Several studies [14, 16, 17] demonstrated the positive correlation between FDG uptake and p53 status, but another study by Buck A [18] showed that there was no correlation between these two indexes.

2.2.2 Detection and Differentiation of Primary Breast Cancer

Both mammography and ultrasound are most commonly used imaging methods in detection, differential diagnosis, the measurement of tumor size, and extent of breast cancer. MR has a high soft tissue resolution and has shown high sensitivity and specialty in the several aspects mentioned above. In addition, MR may find some additional breast cancer lesions, which may do not be displayed on other conventional imaging. Due to the many advantages of MR, it is increasingly being used in clinical practice.

^{18}F-FDG PET/CT can be used for detection and visualization of the primary tumor. However, due to the limited resolution of PET scanners and the influence of some breast cancer pathological characteristics (e.g., low ^{18}F-FDG uptake in high-grade cancer and/or in lobular cancer), PET has poor sensitivity for detection of small lesions. In a study by Avril et al. [19], while PET imaging detected 92% of pT2 lesions (>20 mm, but <50 mm) (see Fig. 2.1), only 68% of pT1 lesions (<20 mm) were detected. And 65% of lobular carcinomas had false-negative results, compared with ductal

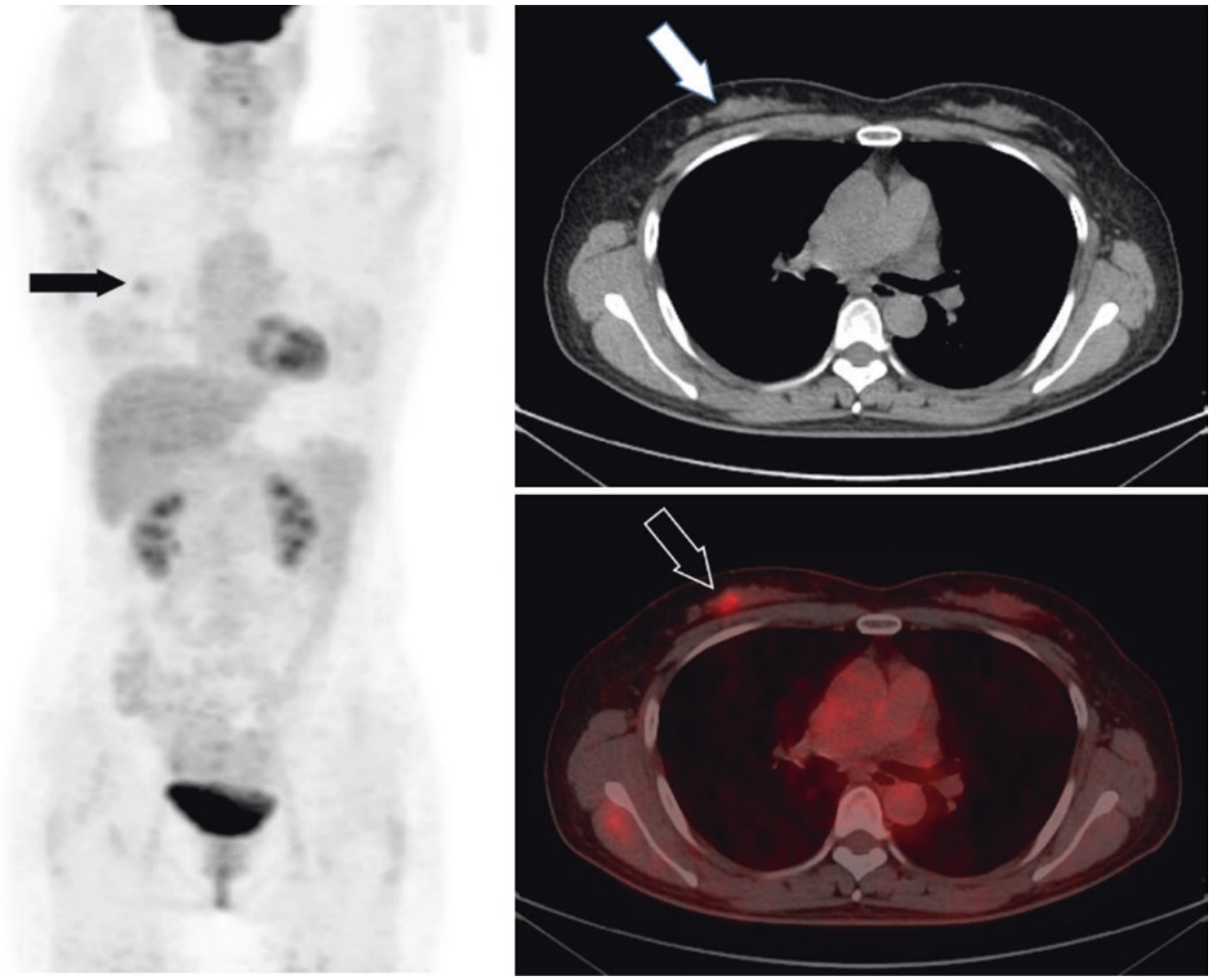

Fig. 2.1 A 56-year-old woman with suspicious left lung adenocarcinoma (*no increased activity*) undergoing ^{18}F-FDG PET/CT for tumor staging. An incidental ^{18}F-FDG focus (*black solid arrow*) was seen in the upper and medial quadrant of the right breast on coronal maximum intensity projection (MIP) PET image and fuse imaging (*white hollow arrow*), pathologically confirmed as invasive ductal adenocarcinoma with a maximum diameter of 2.6 cm. No obvious abnormality was found at CT image (*white solid arrow*)

carcinomas (24% false-negative) [20]. Studies have also shown that FDG-PET has poor sensitivity for submillimeter breast cancer lesions, and the sensitivity of detection is less than 50% [21, 22]. As mentioned above, infiltrating lobular carcinoma is more likely to be missed.

Positron emission mammography (PEM) is a breast-dedicated PET device, which with a high spatial resolution (even less than 2 mm) has showed promising results. It has dramatic improvements of sensitivity and specificity for detecting breast cancer lesions (especially for small lesions), compared to conventional whole-body PET. In the study of Kalinyak et al. [23], 109 primary invasive breast cancers (the average size 1.6 ± 0.8 cm) were enrolled. They found that the detection rates obtained with PEM and conventional PET/CT were 95% and 87%, respectively ($p < 0.029$). A meta-analysis [21] that evaluated eight studies comprising 873 breast lesions (the size ranged from 0.1 to 10 cm) showed a pooled sensitivity of 85% (95% CI, 83–88%) and a specificity of 79% (95% CI, 74–83%) on a lesion basis, using FDG PEM in women with suspected breast malignancy. Another report by Lima et al. [24] also showed similar results. A total of 80 lesions (the size ranged from 0.4 to 11.2 cm, mean 2.6 cm, included 76 breast cancers and 4 benign lesions) were enrolled; 63/76 breast cancer lesions was detected by PEM (the C-shape scanner); the lesion-based sensitivity was 83% (63/76), and this was increased to 90% (63/70) after excluding lesions outside the field of view.

A multicenter comparative study [25] determined the efficacy of PEM and DCE-MRI on ipsilateral pre-surgery planning, including 388 patients who undertook MRI and PEM, showed that a total of 116 malignant lesions were found after surgery, 61 of 116 malignant lesions (53%) were raised by MR for suspicious malignancy; 47 of these (41%) were raised as suspicious on PEM ($P = 0.04$), and only 24 lesions (21%) were raised as suspicious on conventional imaging. This result demonstrates that MR is superior to PEM in detecting breast cancer lesions.

Some benign lesions of the breast may also show the concentrated FDG uptake and sometimes are not easy to be differentiated from breast cancer. The following review will help us understand the uptake of breast lesions. The meta-analysis [26] reviewed the significance of incidental FDG uptake (from whole-body PET) in breast; the pooled risk of malignancy of incidental FDG uptake was 48% (95% CI, 38–58%), and the pooled risk of malignancy of incidental FDG uptake with histological examination was 60% (95% CI, 53–66%).

False-positive uptake caused by benign lesions had been reported, such as breast fibrocystic disease, fibroadenomas, papilloma, silicone leakage, fat necrosis, inflammatory, and infectious diseases. Breast fibrocystic disease usually does not exhibit very high FDG uptake, and higher FDG uptake generally indicates higher risk of malignancy. Lobulated contour, crab-like edge, ill-defined, and clustered granular calcification are typical morphological characteristics of breast cancer. In contrast-enhanced MR imaging, enhanced patterns of breast cancer, such as time-signal curves, contribute to the differentiation of benign diseases and breast cancer.

In addition, it has been reported that dual-time-point PET/CT imaging helps to increase the specificity and to better differentiate primary breast cancer from benign tumors or inflammatory processes [27, 28]. However, its usefulness has not yet been demonstrated in large series.

2.2.3 Initial Staging

Accurate and reliable initial staging is the premise for determining breast cancer treatment options and the basis for prognosis assessment. Once breast cancer is diagnosed, staging of the breast cancer must be performed. Currently, the TNM staging system (Tables 2.2 and 2.3) is widely used in clinic. Current evidence suggests that ^{18}F-FDG PET/CT has a good performance for patients with clinical stage IIB and higher stage, and its performance is not affected by the breast cancer cell phenotype, tumor grade, and patient's age.

2.2.3.1 T Staging

The size of the tumor lesion, tumor's relationship with the adjacent structure, and whether tumor are multicenter lesions are the important indicators for breast cancer T staging, which is an especially important consideration for planning of optimal breast conservation surgery.

Duo to the low spatial resolution of PET, PET remains inadequate for accurately defining the size and involved rang of breast cancer. To a certain extent, CT imaging in PET/CT can make up for this shortcoming. However, despite a high-density resolution of CT, small breast cancers (especially those in dense breasts) are often not well displayed by CT. When the breast cancer lesion grows to a certain size, CT can show its advantages in the measurement of lesion size and in judging the relationship between breast cancer and intercostal muscles and ribs.

US and mammography have relatively high sensitivity for the detection of small breast cancer lesions, high accuracy for measuring lesion size, and are easy to use and low in cost. But the size and extent of breast cancer are frequently underestimated by mammography and ultrasound.

MR can clearly display the contour of the lesion, so that accurate measurement of the lesion size can be performed, and determine the relationship between the lesion and the adjacent tissue. As it was reported in the study [28], FDG PET had less sensitivity than dynamic contrast-enhanced magnetic resonance imaging (DCE-MRI) in the determination of the delineation of the primary tumor and in screening

Table 2.2 TNM staging system for breast cancer according to the AJCC cancer staging manual [29]

TNM category	Clinical data
Primary tumor	
TX	Primary tumor cannot be assessed
T0	No evidence of primary tumor
Tis	Carcinoma in situ
T1	Tumor ≤2 cm in greatest dimension
T2	Tumor >2 cm but not ≤5 cm in greatest dimension
T3	Tumor >5 cm in greatest dimension
T4	Tumor of any size with direct extension to the chest wall and/or to the skin (ulceration or skin nodules)
T4a	Extension to the chest wall, not including only pectoralis muscle adherence/invasion
T4b	Ulceration and/or ipsilateral satellite nodules and/or edema (including peau d'orange) of the skin, which do not meet the criteria for inflammatory carcinoma
T4c	Both T4a and T4b
T4d	Inflammatory carcinoma
Regional lymph nodes	
NX	Regional lymph nodes cannot be assessed (e.g., previously removed)
N0	No regional lymph node metastasis
N1	Metastases to movable ipsilateral level I and II axillary lymph nodes
N2	Metastases in ipsilateral level I and II axillary lymph nodes that are clinically fixed or matted or in clinically detected ipsilateral internal mammary nodes in the *absence* of clinically evident axillary lymph node metastases[a]
N3	Metastases in ipsilateral infraclavicular (level III axillary) lymph nodes with or without level I and II axillary lymph node involvement, or in clinically detected ipsilateral internal mammary lymph nodes with clinically evident level I and II axillary lymph node metastases, or metastases in ipsilateral supraclavicular lymph nodes with or without axillary or internal mammary lymph node involvement[a]
N3a	Metastases in ipsilateral infraclavicular lymph nodes
N3b	Metastases in ipsilateral internal mammary lymph nodes and axillary lymph nodes
N3c	Metastases in ipsilateral supraclavicular lymph nodes
Distant metastasis	
M0	No distant metastasis
M1	Distant metastasis

[a]A clinically detected lymph node is defined as one detected by using imaging studies (excluding lymphoscintigraphy) or by using clinical examination and having characteristics highly suggestive of malignancy or a presumed pathologic macro-metastasis on the basis of results of fine-needle aspiration biopsy with cytological examination

Table 2.3 TNM stage grouping for breast cancer according to the AJCC cancer staging manual [29]

Stage	T category	N category	M category
0	Tis	N0	M0
IA	T1[a]	N0	M0
IB	T0	N1mi	M0
	T1[a]	N1mi	M0
IIA	T0	N1[b]	M0
	T1[a]	N1[b]	M0
	T2	N0	M0
IIB	T2	N1	M0
	T3	N0	M0
IIIA	T0	N2	M0
	T1[a]	N2	M0
	T2	N2	M0
	T3	N1	M0
	T3	N2	M0
IIIB	T4	N0	M0
	T4	N1	M0
	T4	N2	M0
IIIC	Any T	N3	M0
IV	Any T	Any N	M1

Note: *N1mi* nodal micrometastases
[a]T1 includes T1mi
[b]T0 and T1 tumors with nodal micrometastases only are excluded from stage IIA and are classified as stage IB

for multifocality. Forty patients underwent PET/CT and DCE-MRI [28]; MR imaging aided classification of the T staging correctly in 77% of cases while PET/CT only in 54% of cases ($P = 0.001$).

Because of the high sensitivity of PEM, the T stage of breast cancer may be altered by the discovery of multicenter tumors and extensive intraductal breast cancer. A multicenter comparative study [25] on the effects of PEM and MR on ipsilateral presurgical planning, which included 388 patients who undertook DCE-MRI and PEM, showed that MR imaging had greater lesion-level sensitivity and detection accuracy for mastectomy. In total 89 women with breast cancer required more extensive surgery; only 41 (46%, 41/89) were identified with PEM ($P = 0.003$); 61 (69%, 61/89) were identified with MR imaging. From the above data, it can be seen that DCE-MRI is superior to PEM in the detection of intraductal infiltration and multicenter breast cancer.

2.2.3.2 Axillary Lymph Node Staging

Axillary lymph node status is an essential consideration; it affects clinical decision-making and prognosis of breast cancer. In recent years, sentinel lymph node biopsy (SLNB) has become widely accepted as a less invasive alternative to

axillary lymph node dissection (ALND) and has become the standard procedure for patients with small primary breast cancers [20].

In a prospective multicenter study [30], FDG PET (without the CT component) was performed in 360 female patients with newly diagnosed invasive breast cancer. For detection of metastatic axillary nodal, the sensitivity and specificity of PET were, respectively, 61% and 80% [30]. Another meta-analysis also yielded similar results. In the meta-analysis [31], researchers evaluated the diagnostic accuracy of PET (with or without CT). Nineteen studies from PET (n = 1729) showed mean sensitivity was 66% (range, 50–79%), and mean specificity was 93% (range, 89–96%). Seven studies from PET/CT (n = 862) showed that mean sensitivity was 56% (range, 44–67%), mean specificity was 96% (range, 90–99%), and the mean sensitivity to micrometastases (≤2 mm) is 11% (5–22%) [31].

Although FDG PET/CT has a relatively high specificity in detecting axillary lymph node involvement but has less sensitivity, PET/CT cannot replace sentinel node biopsy in patients with breast cancer. In a study by Veronesi et al. [32] including 236 patients with clinically negative findings for axillary involvement, only 37% of patients with positive results of sentinel node biopsy had positive findings at PET [32].

^{18}F-FDG uptake of axillary lymph nodes in the drainage area of breast cancer does not all mean metastasis, and there is a possibility of false-positive uptake. Such false positive was also mentioned in the study by Verones et al. [32] on the value of PET for axillary metastases. In all 43 patients with positive axillary lymph nodes on PET, 5 patients were confirmed to be nonmetastatic lymph nodes by surgical resection. This situation needs to be brought to the attention of nuclear medicine and clinical physicians. Reactive hyperplasia lymph nodes is the main cause of false-positive results, and their FDG uptake is often lower.

In addition to proliferative lymph nodes, FDG leakage at injection site is also the cause of false-positive uptake of axillary lymph nodes (because of the injection technology, FDG leaks into the subcutaneous tissue space at the injection site and is drained back to the axillary lymph nodes through the ipsilateral lymphatic vessels, resulting in increased FDG physiological uptake in these lymph nodes). For patients with unilateral breast cancer, it is suggested that intravenous injection of radiopharmaceuticals should be performed on the contralateral upper limb vessel, to reduce the interference of this physiological uptake in the diagnosis of axillary lymph node metastasis. Fundamentally, avoiding leakage of injection site through improving injection technology is the best choice to solve the problem.

Diagnostic performance of PET/CT for axillary lymph node metastasis does not seem to be superior to that of US or MRI. Ahn et al. [33] demonstrated that for detection of lymph node metastasis, the diagnostic accuracy of US was 78.8% and that of FDG-PET was 76.4%. As shown by the meta-analysis [34], for detection of lymph node metastasis, the mean sensitivity and specificity of gadolinium-enhanced MR was 88% (95% CI, 78%–94%) and 73% (95% CI, 63%–81%), respectively.

PET/CT was not able to reliably identify axillary lymph node involvement; it is not routinely recommended for axillary staging of patients with newly diagnosed breast cancer.

2.2.3.3 Staging in Stage II–III Disease and Inflammatory Breast Cancer

Axillary clearance is usually limited to Berg I and Berg II levels. Whether lymph nodes involvement at Berg level III (infraclavicular) or in extra-axillary local-regional nodes (such as supraclavicular or internal mammary) have important implications for clinical decision-making, especially in surgery and radiotherapy. Lymph node involvement in the axillary Berg level III area, in the supraclavicular area, or in the internal mammary area is classified as an N3 (stage IIIC) lesion according to the recently revised 8th edition of the *AJCC Cancer Staging Manual* [29]. Data from the national cancer institute database in 2001–2002 showed that women patients with stage IIIC disease had poor prognosis, and the 5-year survival rate was only 49%.

In a study [35] of 39 patients with stages II–III breast carcinoma, PET/CT successfully found 3 patients of extra-axillary lymph node involvement which were missed in conventional imaging method. According to the results of PET/CT, the extent of surgical dissection and radiation therapy fields were modified in all three patients. In another study [36], also involving patients with stages II-III breast carcinoma, radiation therapy planning was altered in seven patients with extra-axillary lymph node involvement (account for 12% of the total number of patients) not detected by US examination.

A prospective study from Groheux et al. [37] also reported the value of ^{18}F-FDG PET/CT in the evaluation of breast cancer staging. A total of 131 consecutive patients were enrolled. They underwent physical examination, mammogram, ultrasound, and magnetic resonance imaging before the ^{18}F-FDG PET/CT examination. Of these, 36 were classified as clinical stage IIA cancer, 48 were classified as clinical stage IIB, and 47 were classified as clinical stage IIIA cancer. ^{18}F-FDG PET/CT results helped clinicians modify staging for 5.6% of patients with stage IIA cancer, for 14.6% of patients with stage IIB cancer, and for 27.6% of patients with stage IIIA cancer. Segaert [38] and Bourgeois [39], respectively, reported the value of preoperative PET/CT for stage IIB and IIIA breast cancer, similar results for locally advanced breast cancer had been obtained.

As for the patients with clinical IIB stage and more advanced stage breast cancer, PET/CT often provides critical information and is considered to be superior to conventional staging (see Fig. 2.2).

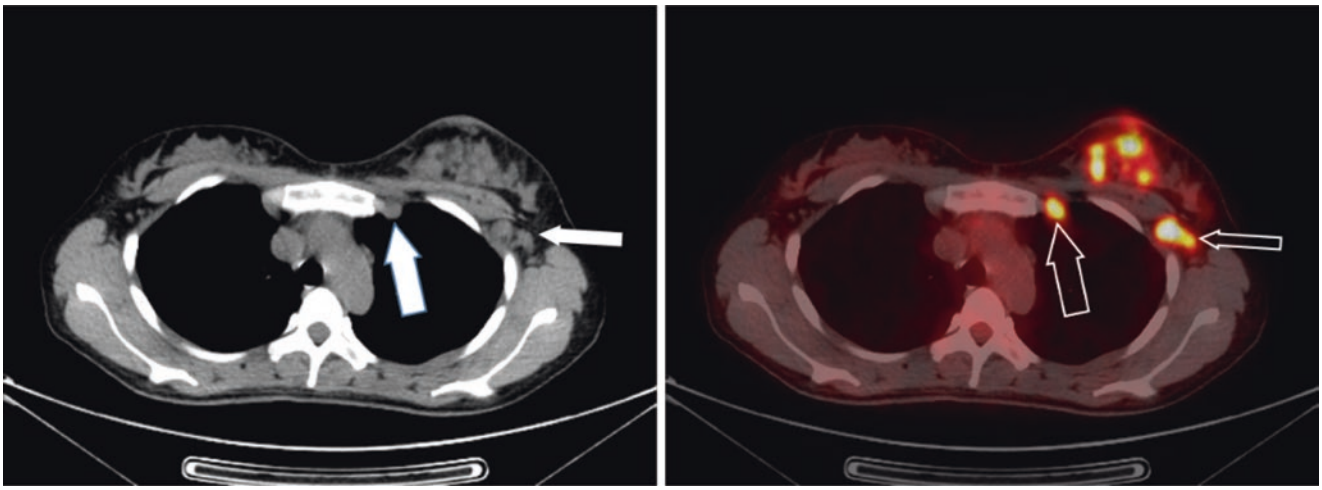

Fig. 2.2 A 31-year-old woman with breast cancer undergoing FDG PET/CT for tumor staging. Left internal mammary lymph nodes (*thick solid arrow*) are easily misdiagnosed as normal costal cartilage on CT image, but increased ^{18}F-FDG activity (*thick hollow arrow*) was seen on fuse imaging. In addition, multiple enlarged lymph nodes with increased ^{18}F-FDG activity can be seen in the left axillary (*thin solid/hollow arrow*)

Inflammatory breast cancer is a special and highly aggressive form of breast cancer, characterized by high rate of local recurrence, distant metastases, and mortality, which has the poorest prognosis among primary breast cancers. Most patients had axillary and/or supraclavicular lymph node metastases, almost 30% of patients have distant metastases at the time of diagnosis [40]. A study from Alberini [40] include 59 patients with inflammatory breast cancer, shown that the detection rate of PET/CT for primary tumors of inflammatory breast cancer was 100%. Three studies [40–42] have reported the value of PET for lymph node involvement in inflammatory breast cancer. PET found more metastatic lymph nodes than conventional images, with about 15–56% more.

PET/CT is useful for diagnosis of the lymph node metastases at extra-axillary sites, such as the internal mammary lymph nodes, subclavian lymph nodes, supraclavicular, and the intrathoracic lymph nodes. Whether these regional lymph nodes are involved or not will directly impact on the staging and the subsequent treatment strategies.

2.2.3.4 Distant Metastases of Breast Cancer

Currently, there is no evidence to prove that the use of PET/CT to further clarify distant metastases can benefit patients with ductal carcinoma in situ or clinical stage I or stage IIA.

The common distant metastatic sites of breast cancer are skeleton and lung, followed by lung, liver, brain, and ovary. Whether distant metastasis has occurred, there is a direct impact on the patient's treatment planning and prognosis, and early definite diagnosis benefits disease outcome in patients.

Skeleton Metastases

Generally, according to the density difference between bone metastases and normal bone tissue at CT, bone metastases can be divided into osteolytic, osteogenic, and mixed types (both osteogenesis and osteolysis). At CT, there is another type of bone metastasis which is called invisible-type bone metastasis, which is not displayed because they do not cause visible bone destruction or osteogenic abnormality.

Bone scintigraphy is widely used in the detection of bone metastases, and it is a whole-body examination with relatively high sensitivity, especially those with active osteogenic activity. Bone scintigraphy sensitivity ranges from 62 to 100%, and its specificity is between 78 and 100% [43].

However, in some cases, it shows its disadvantage. The bone scintigraphy may present false negative for purely osteolytic bone metastases, and it may present false-positive uptake for some benign diseases, such as osteoporotic fracture, infectious diseases, arthritis, primary bone tumors, and tumor-like diseases.

SPECT/CT scanner equipped with simultaneous CT furtherly improves the specificity and the susceptibility, compared with those of conventional bone scintigraphy. However, the part of invisible-type metastases may still be missed in SPECT/CT examination. For the kind of metastasis, PET/CT have high sensitivity and specificity (see Fig. 2.3).

Studies also suggest that ^{18}F-FDG PET outperforms CT and bone scintigraphy in detection of invisible-type, osteolytic, and mixed bone metastases [44–47]. But ^{18}F-FDG PET may miss purely sclerotic metastases, which often contain fewer tumor cell. The additional anatomical information provided by the CT component of PET/CT often helps to

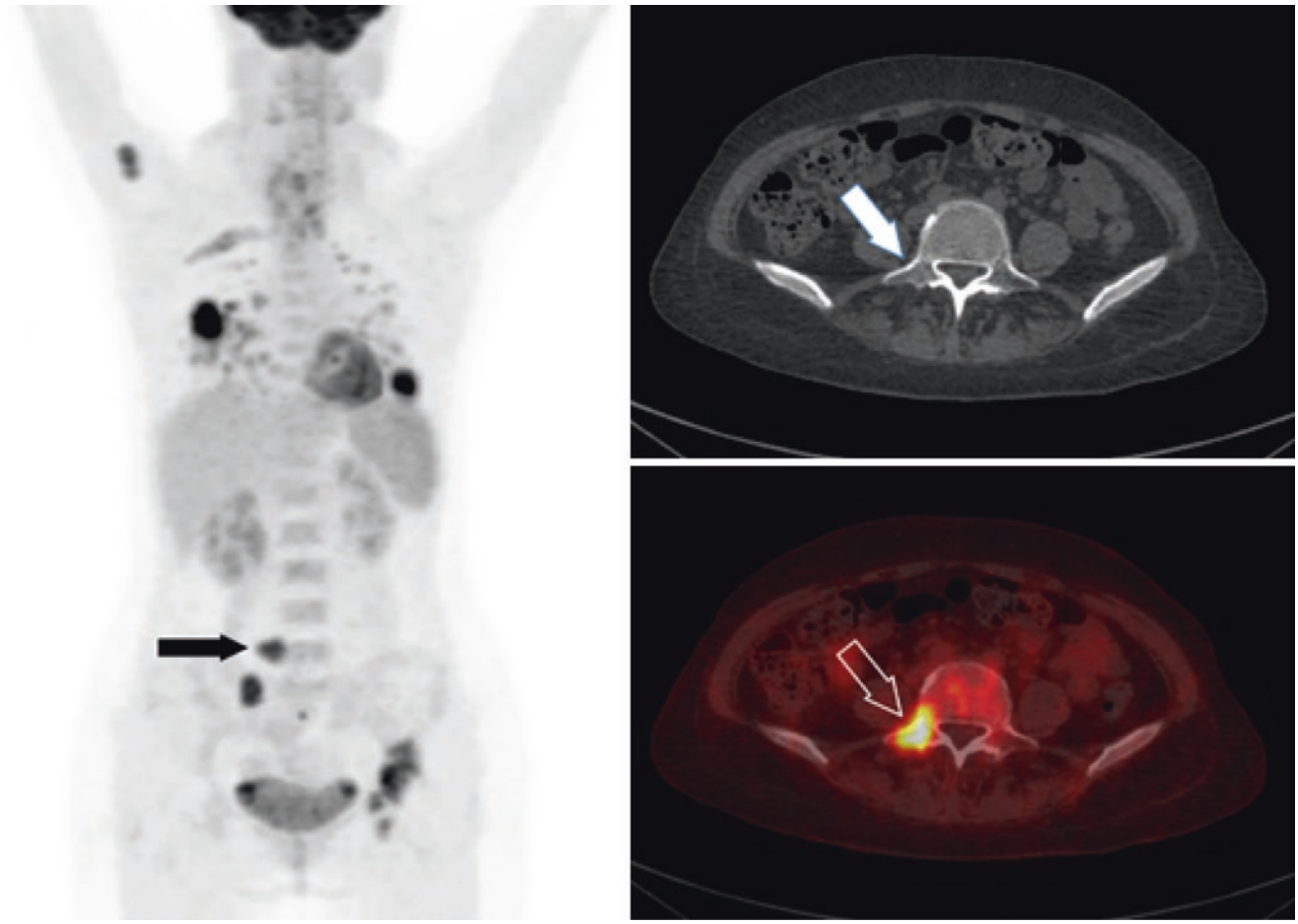

Fig. 2.3 A 58-year-old woman with right breast cancer (*invasive ductal carcinoma*) undergoing ^{18}F-FDG PET/CT for tumor staging. PET/CT showed multiple bone and bilateral lung metastatic. A ^{18}F-FDG focus was seen in transverse process of the third lumbar on coronal maximum intensity projection (MIP) PET image (*black solid arrow*) and fuse imaging (*white hollow arrow*), no clear abnormality was seen on axial CT images of the same site (*white solid arrow*)

improve sensitivity for the detection of purely sclerotic bone lesions (see Fig. 2.4).

A study [46] for comparison of ^{18}F-FDG PET/CT and bone scintigraphy for detection of bone metastases in breast cancer showed that the sensitivity of bone scintigraphy was 76% (53/70) compared to 96% (67/70) for ^{18}F-FDG PET/CT.

^{18}F-Fluoride is a highly sensitive bone-seeking PET tracer used for detection of skeletal abnormalities. With the popularization of PET/CT, ^{18}F-NaF PET/CT bone scan is increasingly used clinically. ^{18}F-NaF PET/CT has shown higher sensitivity for detection of bone metastases in breast cancer, compared to ^{99m}Tc-MDP SPECT bone scan. The sensitivity and specificity of ^{18}F-NaF PET/CT in evaluating bone metastases were, respectively, 91% and 91% [48]. In addition, studies showed that combined ^{18}F-FDG and ^{18}F-NaF PET/CT was superior to ^{18}F-FDG PET/CT alone for the detection of skeletal/marrow metastases in breast cancer [49, 50].

Extra-skeletal Metastases

The timely detection of pulmonary metastasis is important for accurate staging and assessing the likelihood of surgical clearance. CT is routinely performed on patients with higher risk of pulmonary metastases. Compared to standalone CT, the metabolic information provided by the ^{18}F-FDG PET/CT can increase the specificity of the study and can facilitate the classification of suspicious indeterminate lesions, especially if they are more than 8 mm in diameter. Also, the reported physicians need to be alert to the potential risk of false-positive PET/CT findings mainly due to radiation pneumonitis, bacterial pneumonia, and granulomatous disease.

The physiological uptake of the liver limits the diagnostic accuracy of the PET/CT in detecting liver metastases. Adrenal metastatic lesions often show a very high ^{18}F-FDG uptake; however, there are also a number of benign reasons leading to high ^{18}F-FDG uptake of adrenal, such as stress, adrenal hyperplasia, adrenocortical adenoma, etc. Further

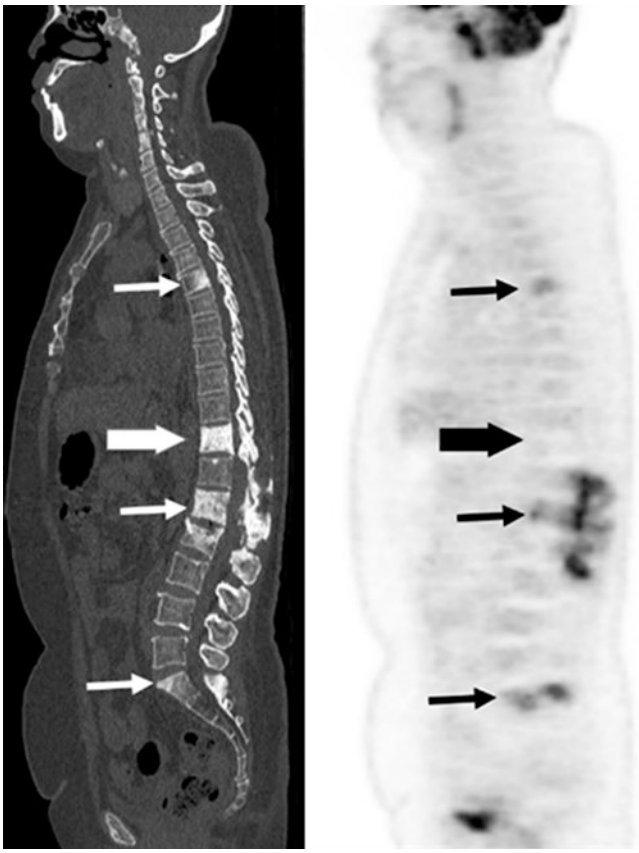

Fig. 2.4 A 53-year-old woman with left breast cancer and multiple bone metastases. PET/CT showed multiple bone metastases. In sagittal CT images, metastatic lesions of the 11th thoracic spine demonstrated complete osteopetrosis (*thick white arrow*), no increased ^{18}F-FDG uptake was observed (*thick solid arrow*). The remaining bone metastases also showed osteosclerosis with different degrees of increased ^{18}F-FDG uptake (*thin white/black arrows*)

confirmation is recommended. As for the diagnosis of brain metastases, the usefulness of ^{18}F-FDG is seriously limited by the highly physiological uptake in the normal brain, especially in the cortex, enhanced MR should be a most choice.

2.2.4 Response Assessment

Traditional morphological imaging is mainly based on changes of the tumor size before and after treatment for response assessment. Different from traditional imaging, metabolic parameters in ^{18}F-FDG PET is commonly used as an index of response evaluation, such as SUVmax, SUVlean, ΔSUVmax, total lesion glycolysis (TLG), metabolic tumor volume (MTV), etc. As we all know, changes in metabolic activity generally occur earlier than changes in tumor size; ^{18}F-FDG PET as a metabolic and functional imaging can be used to evaluate early response of treatment.

2.2.4.1 Early Response Assessment

Early and reliable prediction of treatment response of the primary breast cancer may allow changing the treatment strategy in case of an ineffective therapy and decreasing unnecessary side effects.

Some results had shown a correlation between early changes in SUV (after one or two cycles of chemotherapy) and the histopathologic response at completion of chemotherapy. A study [51], including 66 patients with HER2-positive breast cancer, showed that ASUVmax in patients with pathologic complete response (pCR) had significantly greater reductions at weeks 2 and 6 ($P = 0.02$ for both time points), compared to SUVmax in those without a pCR. Mean SUVmax reductions were 54.3% versus 32.8% at week 2 and 61.5% versus 34.1% at week 6 for pCR and non-pCR.

The time of therapy assessment for NAC has an influence on the accuracy of response assessment. PET imaging has a better performance for the prediction of pathological response when it is performed after the second cycle of NAC. A multicenter study [52] including 104 patients (receiving one or two cycles of chemotherapy) shown pathologic nonresponders were identified with a negative predictive value of 90%, using a threshold of 45% decrease in SUV after the first cycle of chemotherapy. When using more than 55% reduction in SUV as the threshold after the second cycle, similar results is achieved [52]. Another study [53] showed, when using a threshold of 60% decrease in SUV, the sensitivity, specificity, and negative predictive value of FDG PET were 61%, 96%, and 68% after one cycle of NAC, 89%, 95%, and 85% after two cycles, and 88%, 73%, and 83% after three cycles, respectively. A subgroup study from a meta-analysis by Fangfang Tian [54] for response to neoadjuvant chemotherapy also has shown similar result. With pCR as the reference standard, ^{18}F-FDG PET after two cycles and with at least a 50% reduction of the SUVmax as a threshold demonstrated the sensitivity of 85% (77–91%) and the specificity of 79% (69–86%).

For response assessment of breast cancer, there are following issues that need to be noted. Response assessment using ^{18}F-FDG PET/CT is more meaningful for tumors with higher SUV. Low metabolic tumors may suggest resistance to chemotherapy. In the study by Schwarz-Dose [52], none of the 23 patients with initial SUV less than three achieved a complete histopathologic response.

2.2.4.2 Post-therapy Evaluation

Endocrine therapy has become an important part of systemic breast cancer therapy in women with ER-positive breast cancer. It should be noted that metabolic flares phenomenon may occur after endocrine therapy, which are manifested as sudden, aggravation of tumor-related symptoms and potential signs of disease progression in imaging, such as ^{18}F-FDG avid lymphadenopathy. The metabolic flare phenomenon occurs usually after week 1 or 2 of endocrine therapy; it is

caused by the initial agonist effect of tamoxifen and considered an effective sign of treatment [55].

Due to the limited data, the significance of ^{18}F-PET/CT for the evaluation of response after the completion of treatment is not clear. The combination of PET and CT seems to be especially helpful in evaluating bone metastases. Additionally, to avoid false-negative interference caused by "metabolic stunning" of residual tissue, it is advised to wait at least 4–6 weeks after completion of the therapy. However, further multicenter studies need to be performed to deepen our understanding.

2.2.5 Monitoring Recurrence

Early detection of the extent and characters of recurrent disease can help clinician to adopt an optimal and reasonable treatment program and improve the prognosis of patients.

Clinical symptoms, biological markers (such as CA153, CEA), and routine radiological examination are commonly used methods to determine the recurrence of breast cancer. ^{18}F-FDG PET/CT seems to perform better than routine imaging for detecting locoregional recurrence, especially the thoracic wall and extra-axillary lymph nodes, which are superior to CT and MR [56–58]. PET also has advantages in differentiating tumors from posttreatment scar or fibrosis, while it is often difficult to differentiate between them in conventional imaging.

A meta-analysis [59] showed that in breast cancer patients with elevated clinical tumor markers, the sensitivity, specificity, and accuracy of ^{18}F-FDG PET for detecting recurrent tumors were 87.8%, 69.3%, and 82.8%, respectively.

^{18}F-FDG PET/CT is superior to conventional imaging in the evaluation of disease relapse in breast cancer patients. A study by Champion, L [60], 187 true recurrences in 228 patients with increasing CA153 and/ or CEA were diagnosed by PET/CT. Compared with the standard work-up available in 67 patients with increasing tumor marker, PET/CT had a higher sensitivity and accuracy (94.5% vs 33% and 94% vs 48%, respectively). According to a study [57] including seven literatures, the sensitivity, specificity, and accuracy of the restaging of breast malignant tumors using PET/CT were, respectively, 85%–97%, 52%–100%, and 60%–98%. Two studies [61, 62] have also shown that PET/CT is more accurate in diagnosing breast cancer recurrence than enhanced CT or alone PET.

2.2.6 Prognostic Assessment

The prognosis of breast cancer is affected by many factors, such as pathological type, immunohistochemistry phenotype, tumor staging, and rationality of treatment.

Studies have shown that early response in patients receiving neoadjuvant chemotherapy before surgery is a good predictor for posttreatment response. In a study by Kenny [63], absence of response in the primary tumor at week 2 was predictive of nonresponse at week 6 (at least a 15% reduction of the SUVmax were considered responding), with a negative predictive value of 90% (18/20 patients). The presence of response at week 2 was predictive of response at week 6, with a positive predictive value of 78.5% (33/42 patients).

Based on the advantage of PET/CT staging, PET/CT can evaluate the prognosis of patients. One study [64] reported the value of PET/CT in evaluating the prognosis of patients with clinical II and stage III breast cancer. Sufficient follow-up was conducted for 189 patients with IIB and higher stages, and it was found that the 3-year disease-specific survival of patients with distant metastasis was significantly shorter than that of patients without distant metastasis (57% vs 88%, $P < 0.001$).

Several literatures reported that the degree of FDG uptake in primary tumor was of prognostic value. High FDG uptake was associated with poor outcome. In the study by Inoue et al. [65], FDG PET was performed preoperatively in 81 patients. With using SUV equal to 4.0 as the cutoff, the patients were randomly divided into the high SUV group and the low SUV group. Five-year disease-free survival rates in the high SUV group were significantly lower than that in the low SUV group (75.0% vs 95.1%, $P = 0.011$).

2.3 Clinical Application of ^{18}F-Fluoroestradiol PET

^{18}F-fluoroestradiol (^{18}F-FES) is an estrogen receptor imaging agent, targets ER, and image tissue expressing ER receptors in vivo. Approximately 75% of newly diagnosed breast cancer has ER-positive expression [2]. Clinical studies have shown that ^{18}F-FES PET can quantify ER expression in vivo and has the ability to predict the efficacy of ER-targeted or endocrine therapy.

2.3.1 ^{18}F-FES Uptake and Tumor ER Expression

Multiple studies have shown a correlation between FES uptake and ER expression by in vitro test in tumor lesions. Peterson et al. [66] reported, using SUV equal to 1.1 as a threshold to characterize ER-negative tumors and ER-positive tumors, the correlation between SUV and IHC index was 0.73. ^{18}F-FES PET SUV is significantly associated with the size of primary breast tumors, and comparing with large

breast tumors, ^{18}F-FES PET has lower sensitivity [67]. Other factors may also affect FES uptake, such as premenopausal circulating estrogen levels, plasma sex hormone-binding globulin levels, and injected activity.

2.3.2 Ability of ^{18}F-FES PET to Assess Heterogeneity of Disease

The main advantage of ^{18}F-FES PET is its ability to evaluate the ER expression status of all tumor lesions simultaneously.

Traditionally, the state of ER expression in breast cancer is performed by quantitative or semiquantitative immunohistochemical staining on tissue specimens from local tissue biopsy and is easily limited by sampling error and tumor heterogeneity. Additionally, although primary breast tumors are positive for ER expression, its metastatic lesions may no longer express ER or express nonfunctional ER. Therefore, the results of local histological specimens cannot reliably represent the ER expression status of all lesions, but it is unrealistic to perform biopsy on all metastatic lesions.

In contrast, ^{18}F-FES PET can assess ER expression over all tumor sites and provide a more comprehensive profile of the patient's overall ER expression status. Clinical studies on ^{18}F-FES PET have shown that ^{18}F-FES uptake of all metastases sites (i.e., ^{18}F-FES-positive and ^{18}F-FES-negative lesions) are usually consistent with primary tumor in the same patient; there are a small number of patients demonstrated highly nonuniform ^{18}F-FES uptake between primary tumor and metastases lesions and among different metastases lesions.

Potential differences in tumor ER status and ^{18}F-FES uptake are particularly important in women with recurrent or metastatic disease.

2.3.3 Assess of Response to Endocrine Therapy

For ER-positive breast cancer patients, endocrine therapy achieves good results and has fewer side effects than traditional chemotherapy. Although ER-negative in vitro test suggests a lower likelihood of response and a poor prognosis, ER-positive does not ensure that it is effective to endocrine therapy.

Studies have shown that the efficacy of endocrine therapy is closely related to the FES uptake before treatment. The SUV of baseline ^{18}F-FES PET can predict endocrine therapy response. Mortimer et al. [55] reported that the positive predictive value and negative predictive value were, respectively, 79%–87% and 88%–100%, when 2.0 was used as the threshold of SUV on baseline ^{18}F-FES PET.

Both Linden et al. and Dehdashti et al. reported that ^{18}F-FES PET for response assessment had a poor positive predictive value of 34%–50% [68, 69]. A recent study [70] by van Kruchten reported that the positive and negative predictive value of ^{18}F-FES PET for response to therapy were 60% (95% CI: 31–83%) and 80% (95% CI: 38–96%), respectively, using SUVmax = 1.5 as a threshold.

Some studies supporting ^{18}F-FES PET before therapy and early series of ^{18}F-FDG PET to predict the response of endocrine therapy have cause debates about which method is more suitable for clinical use. Both tracers have high negative predictive value for endocrine therapy, but ^{18}F-FDG PET has a higher positive predictive value.

The future workflow may be the combined of two methods. The first, the status of tumor ER expression is evaluated by ^{18}F-FES PET, and then the response is evaluated by the series of FDG PET.

2.3.4 Application of ^{18}F-FES PET in Non-breast Tumor

In addition to breast cancer, some diseases also have varying degrees of ER expression, such as endometrial cancer, epithelial ovarian cancer, and meningioma. In the future, ^{18}F-FES PET could play an important role in confirming patients with epithelial ovarian cancer who would benefit from endocrine therapy for these.

References

1. Ferlay J et al (2015) Cancer incidence and mortality worldwide: sources, methods and major patterns in GLOBOCAN 2012. Int J Cancer 136(5):E359–E386
2. DeSantis CE et al (2016) Breast cancer statistics, 2015: convergence of incidence rates between black and white women. CA Cancer J Clin 66(1):31–42
3. Fan L et al (2014) Breast cancer in China. Lancet Oncol 15(7):e279–e289
4. Gage M, Wattendorf D, Henry LR (2012) Translational advances regarding hereditary breast cancer syndromes. J Surg Oncol 105(5):444–451
5. Perou CM et al (2000) Molecular portraits of human breast tumours. Nature 406(6797):747–752
6. Sorlie T et al (2001) Gene expression patterns of breast carcinomas distinguish tumor subclasses with clinical implications. Proc Natl Acad Sci U S A 98(19):10869–10874
7. Ford D et al (1998) Genetic heterogeneity and penetrance analysis of the BRCA1 and BRCA2 genes in breast cancer families. The Breast Cancer Linkage Consortium. Am J Hum Genet 62(3):676–689
8. Toss A, Cristofanilli M (2015) Molecular characterization and targeted therapeutic approaches in breast cancer. Breast Cancer Res 17:60
9. Prat A, Ellis MJ, Perou CM (2011) Practical implications of gene-expression-based assays for breast oncologists. Nat Rev Clin Oncol 9(1):48–57

10. Brufsky AM (2014) Current approaches and emerging directions in HER2-resistant breast cancer. Breast Cancer (Auckl) 8:109–118
11. Finn RS et al (2015) The cyclin-dependent kinase 4/6 inhibitor palbociclib in combination with letrozole versus letrozole alone as first-line treatment of oestrogen receptor-positive, HER2-negative, advanced breast cancer (PALOMA-1/TRIO-18): a randomised phase 2 study. Lancet Oncol 16(1):25–35
12. Kitajima K et al (2015) Association between (1)(8)F-FDG uptake and molecular subtype of breast cancer. Eur J Nucl Med Mol Imaging 42(9):1371–1377
13. Groheux D et al (2013) Performance of FDG PET/CT in the clinical management of breast cancer. Radiology 266(2):388–405
14. Gil-Rendo A et al (2009) Association between [18F]fluorodeoxyglucose uptake and prognostic parameters in breast cancer. Br J Surg 96(2):166–170
15. Basu S et al (2008) Comparison of triple-negative and estrogen receptor-positive/progesterone receptor-positive/HER2-negative breast carcinoma using quantitative fluorine-18 fluorodeoxyglucose/positron emission tomography imaging parameters: a potentially useful method for disease characterization. Cancer 112(5):995–1000
16. Avril N et al (2001) Glucose metabolism of breast cancer assessed by 18F-FDG PET: histologic and immunohistochemical tissue analysis. J Nucl Med 42(1):9–16
17. Crippa F et al (1998) Association between [18F]fluorodeoxyglucose uptake and postoperative histopathology, hormone receptor status, thymidine labelling index and p53 in primary breast cancer: a preliminary observation. Eur J Nucl Med 25(10):1429–1434
18. Buck A et al (2002) FDG uptake in breast cancer: correlation with biological and clinical prognostic parameters. Eur J Nucl Med Mol Imaging 29(10):1317–1323
19. Avril N et al (2000) Breast imaging with positron emission tomography and fluorine-18 fluorodeoxyglucose: use and limitations. J Clin Oncol 18(20):3495–3502
20. Hindié E et al (2011) The sentinel node procedure in breast cancer: nuclear medicine as the starting point. J Nucl Med 52(3):405–414
21. Caldarella C, Treglia G, Giordano A (2014) Diagnostic performance of dedicated positron emission mammography using fluorine-18-fluorodeoxyglucose in women with suspicious breast lesions: a meta-analysis. Clin Breast Cancer 14(4):241–248
22. Ueda S et al (2008) Clinicopathological and prognostic relevance of uptake level using 18F-fluorodeoxyglucose positron emission tomography/computed tomography fusion imaging (18F-FDG PET/CT) in primary breast cancer. Jpn J Clin Oncol 38(4): 250–258
23. Kalinyak JE et al (2014) Breast cancer detection using high-resolution breast PET compared to whole-body PET or PET/CT. Eur J Nucl Med Mol Imaging 41(2):260–275
24. Iima M et al (2012) Clinical performance of 2 dedicated PET scanners for breast imaging: initial evaluation. J Nucl Med 53(10):1534–1542
25. Berg WA et al (2011) Breast cancer: comparative effectiveness of positron emission mammography and MR imaging in presurgical planning for the ipsilateral breast. Radiology 258(1):59–72
26. Bertagna F et al (2014) Prevalence and clinical significance of incidental F18-FDG breast uptake: a systematic review and meta-analysis. Jpn J Radiol 32(2):59–68
27. Kumar R et al (2005) Potential of dual-time-point imaging to improve breast cancer diagnosis with (18)F-FDG PET. J Nucl Med 46(11):1819–1824
28. Heusner TA et al (2008) Breast cancer staging in a single session: whole-body PET/CT mammography. J Nucl Med 49(8):1215–1222
29. Amin MB, Edge S, Greene FL (2016) AJCC cancer staging manual. Springer, New York
30. Wahl RL et al (2004) Prospective multicenter study of axillary nodal staging by positron emission tomography in breast cancer: a report of the staging breast cancer with PET Study Group. J Clin Oncol 22(2):277–285
31. Cooper KL et al (2011) Positron emission tomography (PET) for assessment of axillary lymph node status in early breast cancer: a systematic review and meta-analysis. Eur J Surg Oncol 37(3):187–198
32. Veronesi U et al (2007) A comparative study on the value of FDG-PET and sentinel node biopsy to identify occult axillary metastases. Ann Oncol 18(3):473–478
33. Ahn JH et al (2010) The role of ultrasonography and FDG-PET in axillary lymph node staging of breast cancer. Acta Radiol 51(8):859–865
34. Cooper KL et al (2011) Positron emission tomography (PET) and magnetic resonance imaging (MRI) for the assessment of axillary lymph node metastases in early breast cancer: systematic review and economic evaluation. Health Technol Assess 15(4):iii–iv, 1–134
35. Groheux D et al (2008) Effect of (18)F-FDG PET/CT imaging in patients with clinical Stage II and III breast cancer. Int J Radiat Oncol Biol Phys 71(3):695–704
36. Aukema TS et al (2010) Detection of extra-axillary lymph node involvement with FDG PET/CT in patients with stage II-III breast cancer. Eur J Cancer 46(18):3205–3210
37. Groheux D et al (2011) The yield of 18F-FDG PET/CT in patients with clinical stage IIA, IIB, or IIIA breast cancer: a prospective study. J Nucl Med 52(10):1526–1534
38. Segaert I et al (2010) Additional value of PET-CT in staging of clinical stage IIB and III breast cancer. Breast J 16(6):617–624
39. Bourgeois AC et al (2013) Role of positron emission tomography/computed tomography in breast cancer. Radiol Clin North Am 51(5):781–798
40. Alberini JL et al (2009) 18F-fluorodeoxyglucose positron emission tomography/computed tomography (FDG-PET/CT) imaging in the staging and prognosis of inflammatory breast cancer. Cancer 115(21):5038–5047
41. Carkaci S et al (2009) Retrospective study of 18F-FDG PET/CT in the diagnosis of inflammatory breast cancer: preliminary data. J Nucl Med 50(2):231–238
42. Yang WT et al (2008) Inflammatory breast cancer: PET/CT, MRI, mammography, and sonography findings. Breast Cancer Res Treat 109(3):417–426
43. Hamaoka T et al (2004) Bone imaging in metastatic breast cancer. J Clin Oncol 22(14):2942–2953
44. Schirrmeister H (2007) Detection of bone metastases in breast cancer by positron emission tomography. Radiol Clin North Am 45(4):669–676, vi.
45. Even-Sapir E (2005) Imaging of malignant bone involvement by morphologic, scintigraphic, and hybrid modalities. J Nucl Med 46(8):1356–1367
46. Hahn S et al (2011) Comparison of FDG-PET/CT and bone scintigraphy for detection of bone metastases in breast cancer. Acta Radiol 52(9):1009–1014
47. Nakai T et al (2005) Pitfalls of FDG-PET for the diagnosis of osteoblastic bone metastases in patients with breast cancer. Eur J Nucl Med Mol Imaging 32(11):1253–1258
48. Gaeta CM et al (2013) Recurrent and metastatic breast cancer PET, PET/CT, PET/MRI: FDG and new biomarkers. Q J Nucl Med Mol Imaging 57(4):352–366
49. Roop MJ et al (2017) Incremental value of cocktail 18F-FDG and 18F-NaF PET/CT over 18F-FDG PET/CT alone for characterization of skeletal metastases in breast cancer. Clin Nucl Med 42(5):335–340
50. Minamimoto R et al (2015) Prospective comparison of 99mTc-MDP scintigraphy, combined 18F-NaF and 18F-FDG PET/CT, and whole-body MRI in patients with breast and prostate cancer. J Nucl Med 56(12):1862–1868

51. Gebhart G et al (2013) 18F-FDG PET/CT for early prediction of response to neoadjuvant lapatinib, trastuzumab, and their combination in HER2-positive breast cancer: results from Neo-ALTTO. J Nucl Med 54(11):1862–1868
52. Schwarz-Dose J et al (2009) Monitoring primary systemic therapy of large and locally advanced breast cancer by using sequential positron emission tomography imaging with [18F]fluorodeoxyglucose. J Clin Oncol 27(4):535–541
53. Rousseau C et al (2006) Monitoring of early response to neoadjuvant chemotherapy in stage II and III breast cancer by [18F] fluorodeoxyglucose positron emission tomography. J Clin Oncol 24(34):5366–5372
54. Tian F et al (2017) The accuracy of (18)F-FDG PET/CT in predicting the pathological response to neoadjuvant chemotherapy in patients with breast cancer: a meta-analysis and systematic review. Eur Radiol 27(11):4786–4796
55. Mortimer JE et al (2001) Metabolic flare: indicator of hormone responsiveness in advanced breast cancer. J Clin Oncol 19(11):2797–2803
56. Schmidt GP et al (2008) Comprehensive imaging of tumor recurrence in breast cancer patients using whole-body MRI at 1.5 and 3 T compared to FDG-PET-CT. Eur J Radiol 65(1):47–58
57. Dirisamer A et al (2010) Integrated contrast-enhanced diagnostic whole-body PET/CT as a first-line restaging modality in patients with suspected metastatic recurrence of breast cancer. Eur J Radiol 73(2):294–299
58. Aukema TS et al (2010) The role of FDG PET/CT in patients with locoregional breast cancer recurrence: a comparison to conventional imaging techniques. Eur J Surg Oncol 36(4):387–392
59. Evangelista L et al (2012) Tumor marker-guided PET in breast cancer patients-a recipe for a perfect wedding: a systematic literature review and meta-analysis. Clin Nucl Med 37(5):467–474
60. Champion L et al (2011) Breast cancer recurrence diagnosis suspected on tumor marker rising: value of whole-body 18FDG-PET/CT imaging and impact on patient management. Cancer 117(8):1621–1629
61. Haug AR et al (2007) F-18-fluoro-2-deoxyglucose positron emission tomography/computed tomography in the follow-up of breast cancer with elevated levels of tumor markers. J Comput Assist Tomogr 31(4):629–634
62. Veit-Haibach P et al (2007) FDG-PET/CT in restaging of patients with recurrent breast cancer: possible impact on staging and therapy. Br J Radiol 80(955):508–515
63. Kenny LM (2013) 18F-FDG PET/CT for early prediction of response to neoadjuvant lapatinib, trastuzumab, and their combination in HER2-positive breast cancer: results from Neo-ALTTO. J Nucl Med 54(11):1855–1856
64. Groheux D et al (2012) Prognostic impact of (18)FDG-PET-CT findings in clinical stage III and IIB breast cancer. J Natl Cancer Inst 104(24):1879–1887
65. Inoue T et al (2004) Preoperative evaluation of prognosis in breast cancer patients by [(18)F]2-Deoxy-2-fluoro-D-glucose-positron emission tomography. J Cancer Res Clin Oncol 130(5): 273–278
66. Peterson LM et al (2008) Quantitative imaging of estrogen receptor expression in breast cancer with PET and 18F-fluoroestradiol. J Nucl Med 49(3):367–374
67. Gemignani ML et al (2013) Feasibility and predictability of perioperative PET and estrogen receptor ligand in patients with invasive breast cancer. J Nucl Med 54(10):1697–1702
68. Linden HM et al (2006) Quantitative fluoroestradiol positron emission tomography imaging predicts response to endocrine treatment in breast cancer. J Clin Oncol 24(18): 2793–2799
69. Dehdashti F et al (2009) PET-based estradiol challenge as a predictive biomarker of response to endocrine therapy in women with estrogen-receptor-positive breast cancer. Breast Cancer Res Treat 113(3):509–517
70. van Kruchten M et al (2015) Positron emission tomography of tumour [(18)F]fluoroestradiol uptake in patients with acquired hormone-resistant metastatic breast cancer prior to oestradiol therapy. Eur J Nucl Med Mol Imaging 42(11):1674–1681

Using ^{18}F-FDG PET/CT to Diagnose and Treat Non-small Cell Lung Cancer

3

Liu Liu, Maomei Ruan, and Wenhui Xie

3.1 Overview

Primary lung cancer is the leading cause of cancer-related death worldwide and is the most incident cancer, causing about 1.37 million deaths per year globally [1]. In China, both the incidence and the mortality rates of lung cancer also rank first, and the incidence of lung cancer is higher in males than in females, with a sex ratio (male/female) of 3–5:1. In recent years, the incidence of lung cancer in females has increased markedly; most of these patients are older than 40 years. In urban settings, both the incidence and mortality rates of lung cancer are slightly higher than in rural settings, whereas an opposite result was observed after age standardization. Most lung cancer is derived from the epithelium of the tunica mucosa bronchiorum. Lung cancer is classified as non-small cell lung cancer (NSCLC) and small-cell lung cancer (SCLC). NSCLC is the most common type, accounting for ~85% of lung cancers, including squamous carcinoma (SQCC), adenocarcinoma (ADC), and large cell carcinoma. The incidence of SCLC has been decreasing for decades [1].

The pathogenesis of lung cancer remains unclear; however, long-term and frequent tobacco smoking is recognized as the major risk factor. The burning of cigarettes and tobacco releases dangerous carcinogens, resulting in malignant differentiation of lung cells. Approximately 70% of lung cancer-related deaths are caused by tobacco smoking [1]. The distinct distribution pattern of lung cancer could reflect the difference in tobacco consumption patterns, resulting in geographical or temporal differences. The incidence of newly occurring lung cancer is declining, probably because of effective tobacco control in men, while the incidence of female lung cancer has reached a plateau. However, approximately 0.4 million lung cancer-related deaths happen each year in never-smoking patients. Besides smoking, the continuous exposure to certain carcinogens, including asbestos, chrome, arsenic, copper, and radioactive substances, is also recognized as risk factor for lung cancer. Outdoor air pollution might also explain the relatively high incidence of lung cancer in cities compared with that in the countryside, while indoor air pollution, such as cooking fumes and coal-fuel stoves, might explain the relatively high incidence of lung cancer in certain never-smoking female patients.

L. Liu · M. Ruan · W. Xie (✉)
Department of Nuclear Medicine, Shanghai Chest Hospital, Shanghai, P. R. China

3.2 Using ^{18}F-FDG PET/CT to Diagnose Non-small Cell Lung Cancer

As the most fatal malignant tumor worldwide, NSCLC is almost always diagnosed with locally advanced or metastatic disease, thus losing the chance of curative resection. The early diagnosis and tumor-necrosis-metastasis (TNM) staging of NSCLC is essential for appropriate tumor therapy.

3.2.1 Diagnosing Primary Non-small Cell Lung Cancer

Positron emission tomography (PET) was introduced in the 1970s, while PET combined with computed tomography (PET/CT) has been used clinically since the 1990s. The invention of PET/CT was honored as one of the three inventions of the year by *Time* magazine, because PET/CT provides both functional and anatomical information, revealing precise biochemistry changes in vivo. ^{18}F-fluorodeoxyglucose (^{18}F-FDG) is the best-known imaging agent, which assesses glucose accumulation in tumor cells and thus reflects their growth activity. ^{18}F-FDG PET/CT is widely used in diagnosis, TNM staging, chemo- or radiotherapy effect evaluation, and recurrence monitoring of NSCLC.

^{18}F-FDG PET/CT is widely used in the diagnosis of lung cancer, obtaining glucose metabolic and anatomical images

G. Huang (ed.), *Nuclear Medicine in Oncology*, https://doi.org/10.1007/978-981-13-7458-6_3

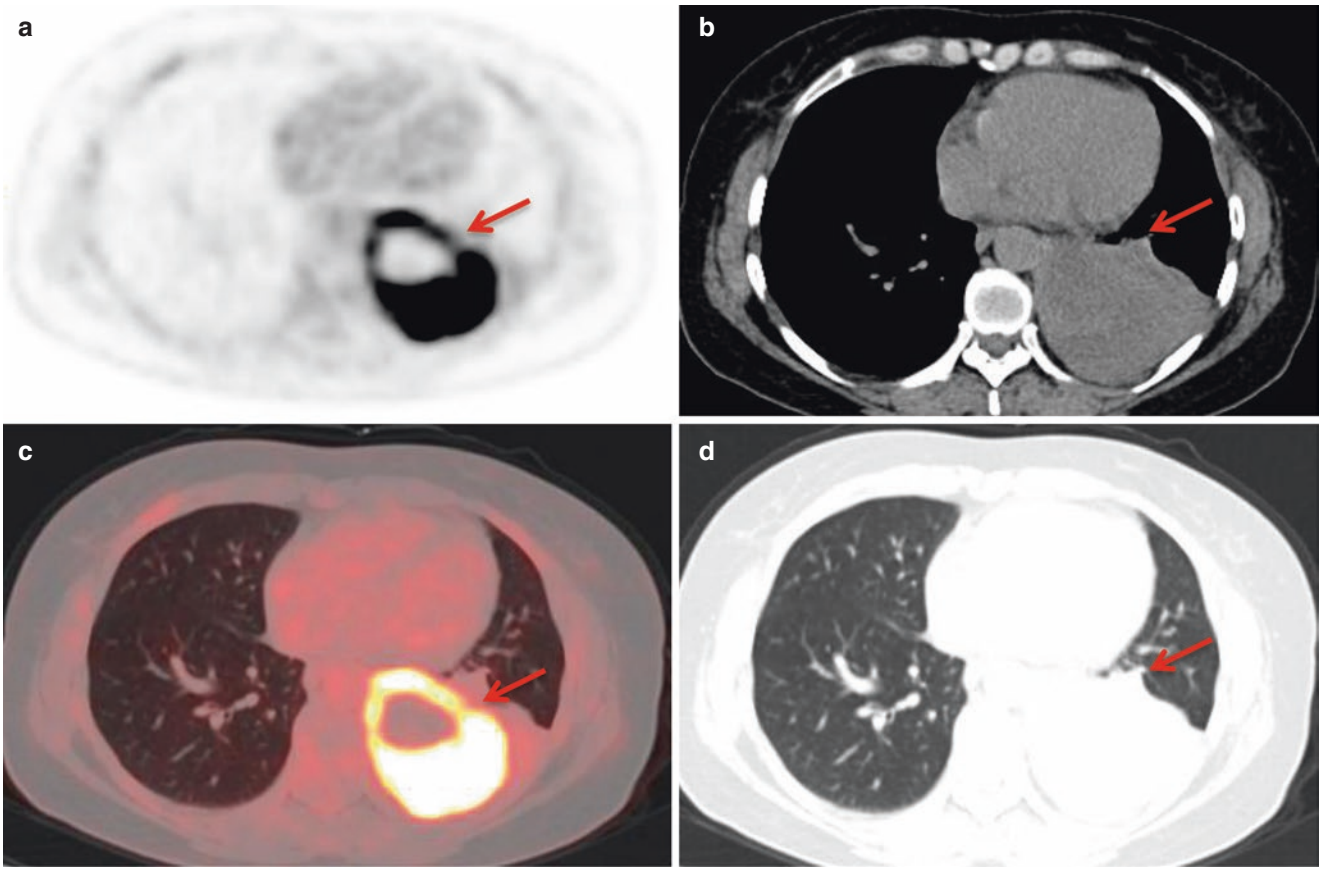

Fig. 3.1 Axial ^{18}F-FDG PET/CT revealing a hypermetabolic mass with ^{18}F-FDG uptake (SUVmax = 11.0) with central necrosis and atelectasis around the left lower lung lobe of a 54-year-old woman. A histological examination confirmed lung adenocarcinoma. (**a**), axial PET image; (**b**),axial CT image (mediastinal window); (**c**), axial fused PET/CT image; (**d**), axial CT image (lung window)

simultaneously. Most NSCLC tissue shows enhanced ^{18}F-FDG uptake compared with that of normal lung tissues. Relatively high uptake of ^{18}F-FDG in primary NSCLC tissues always predicts poor prognosis in patients. ^{18}F-FDG uptake is also strongly correlated with large tumor size, lymph node metastasis, and late TNM stage of patients with NSCLC. Compared to PET or CT scanning, the combination of PET and CT increases both the sensitivity and specificity of NSCLC diagnosis [2].

Traditional medical imaging techniques are still essential for the diagnosis and clinical staging of NSCLC, including X-ray, CT, and magnetic resonance imaging (MRI). Among them, chest CT is the most commonly used imaging technique to display lesions in the chest, while contrast-enhanced CT is considered the standard imaging technique to detect lung tumors currently. MRI is also necessary to diagnose superior sulcus or mediastinal invasive chest tumors, via observing the anatomical relationship of lesion with the heart and vessels. In post-obstructive atelectasis or consolidation cases, the relative high sensitivity and specificity of ^{18}F-FDG PET/CT in tumor imaging makes it superior to CT/MRI for tumor size assessment. In lung cancer with surrounding consolidation or collapse, ^{18}F-FDG PET/CT is better than CT, with both soft tissue and lung windows showing high ^{18}F-FDG uptake in primary NSCLC tissue (Fig. 3.1). However, PET may not be reliable to diagnose some ADC cases, because in situ or minimally invasive ADC in situ shows little or no ^{18}F-FDG accumulation.

Malignant cells exhibit increased glucose metabolism, which promotes cancer cell proliferation and a relative higher standardized uptake value (SUV) of ^{18}F-FDG (Fig. 3.2). In tumor tissues, abnormal glucose accumulation and the subsequent tumorigenic glucose metabolism can induce angiogenesis, resulting in tumor metastasis and a short survival time in patients. Glucose is the main substance providing the energy and macromolecules to sustain cell growth. However, in a malignant tumor, the blood and the energy supplements are insufficient to sustain its uncontrolled growth, resulting in oxygen delivery reduction, which is also called tumor hypoxia. To adapt to the hypoxic microenvironment, cancer cells overexpress glucose transporter 1 (GLUT1) to accumulate much more glucose, which triggers aerobic glycolysis, the best-known feature of malignant cancer, termed the Warburg effect, which can explain the relative high SUV value in larger tumors.

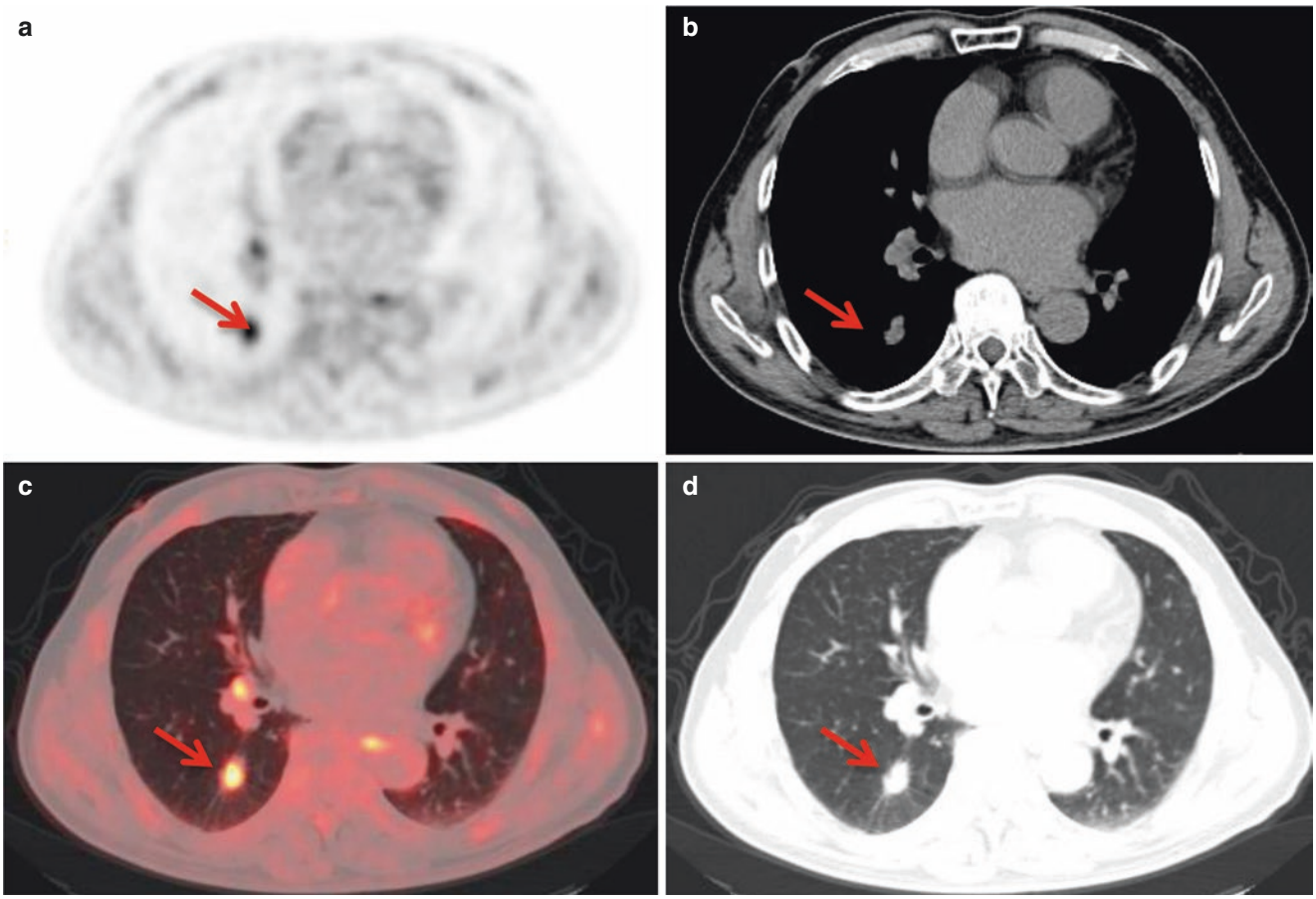

Fig. 3.2 Axial [18]F-FDG PET/CT revealing a hypermetabolic nodule with lobulated and spicule signs in the right lung lobe of a 65-year-old man. A histological examination confirmed lung adenocarcinoma. (**a**), axial PET image; (**b**), axial CT image (mediastinal window); (**c**), axial fused PET/CT image; (**d**), axial CT image (lung window)

A strong positive relationship has been established between the [18]F-FDG uptake level and primary NSCLC tumor size. However, the findings of current research vary because of the difference in patient population size, histological subtypes, and other clinicopathological parameters of different patient groups. Compared with relative small tumors, large NSCLC tissue has a higher accumulation of [18]F-FDG and shows a relative high SUV (Figs. 3.3 and 3.4). In addition, high [18]F-FDG uptake also correlates with late TNM stage, especially in adenocarcinomas, as well as with poor prognosis. The [18]F-FDG uptake of SQCC and ADC, the two main subtypes of NSCLC, also show significant differences: SQCC always accumulates much more [18]F-FDG than ADC. The relatively high expression of glucose transporter type 1 (GLUT1) in SQCC compared with that in ADC might explain this difference. Besides the pathological subtype, NSCLC with different epidermal growth factor receptor (EGFR) phenotypes also have different glucose uptake abilities, such that NSCLC with an EGFR mutation accumulates relatively little glucose and thus shows relatively low SUV compared with that of NSCLC with wild-type EGFR; however, the mechanism remains elusive.

Intracellular glucose accumulation is directly mediated by glucose transporters, in which the transmembrane GLUT1 is always overexpressed in malignant tumors, resulting in abnormal glucose accumulation, and triggers tumor progression. GLUT1 overexpression is also observed in NSCLC and is related to high [18]F-FDG uptake. The trans-glucose function of GLUT1 can be regulated at both the transcriptional and posttranslational levels. GLUT1 is encoded by *solute carrier family 2 member 1 (SLC2A1)*, which is transcriptionally unregulated by hypoxia inducible factor-1 alpha (HIF-1a) and c-MYC. Intracellular glucose transported by GLUT1 is converted into lactic acid by the rate-limiting enzymes hexokinase-II (HK-II) and glucose-6-phosphatase. The overexpression and activation of these enzymes also correlate with [18]F-FDG uptake in some types of tumors. Besides these glucose metabolism regulators at the molecular level, local blood flow, intra-tumoral microvessel density, tumor doubling time, tumor proliferation rates, and viable tumor cell numbers of the tumor lesion also influence the glucose uptake of tumor tissues. The relatively high expression of GLUT1 in SQCC compared with that in ADC might explain the relative high [18]F-FDG uptake of SQCC. The

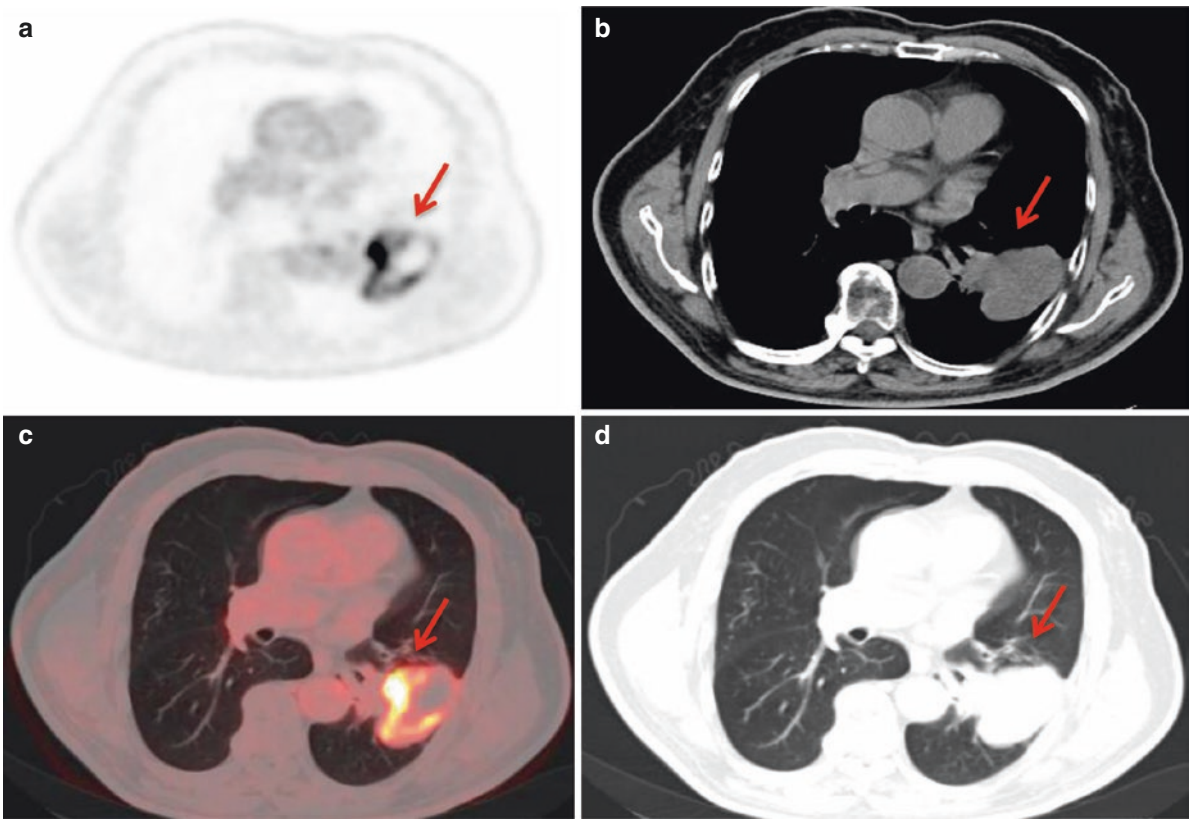

Fig. 3.3 ^{18}F-FDG PET/CT imaging of an 83-year-old man showing uptake (SUVmax = 9.13) with local necrosis in a lung mass in the left lower lobe. A histological examination confirmed the lung mass was primary pulmonary squamous carcinoma. (**a**), axial PET image; (**b**), axial CT image (mediastinal window); (**c**),axial fused PET/CT image; (**d**), axial CT image (lung window)

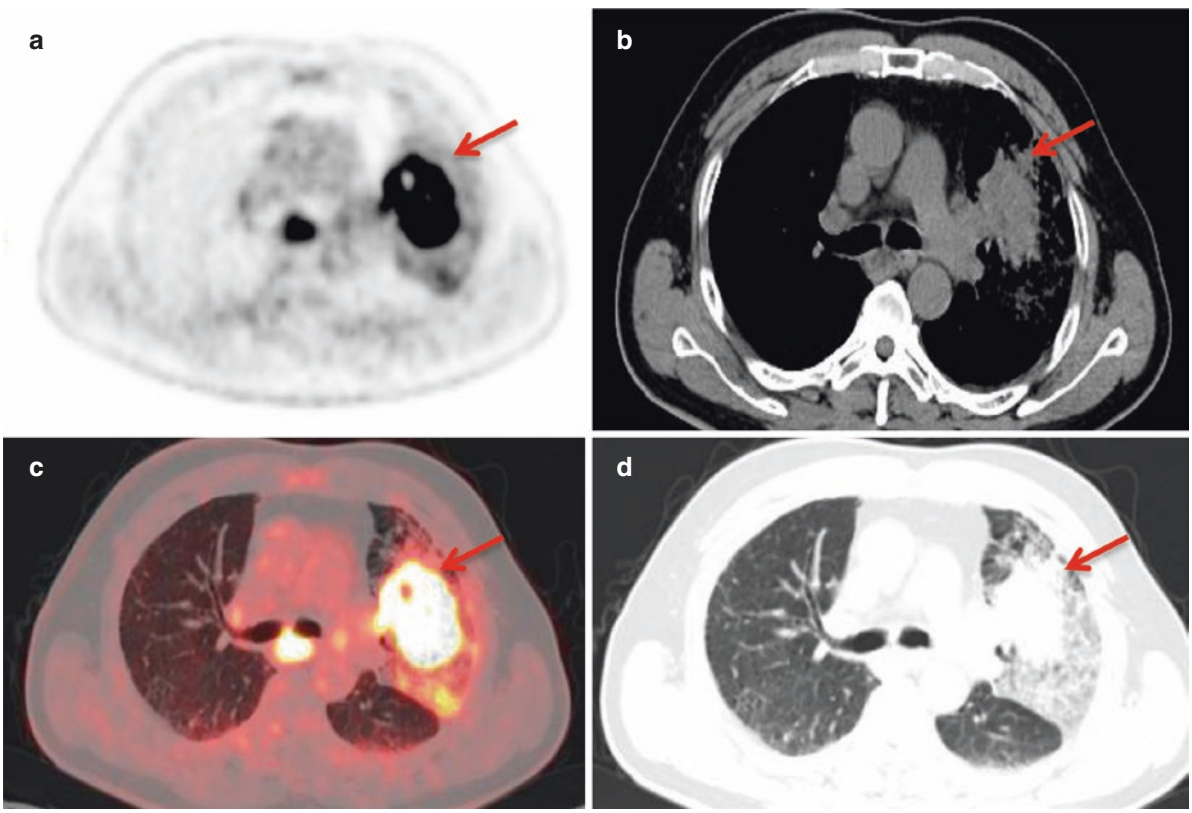

Fig. 3.4 Axial ^{18}F-FDG PET/CT revealing a hypermetabolic mass (SUVmax = 18.5) with obstructive pneumonia in the left upper lung lobe and enlarged lymph nodes at station 7 of a 64-year-old man. A histological examination confirmed pulmonary squamous carcinoma. (**a**), axial PET image; (**b**), axial CT image (soft tissue window); (**c**), axial fused PET/CT image; (**d**), axial CT image (lung window)

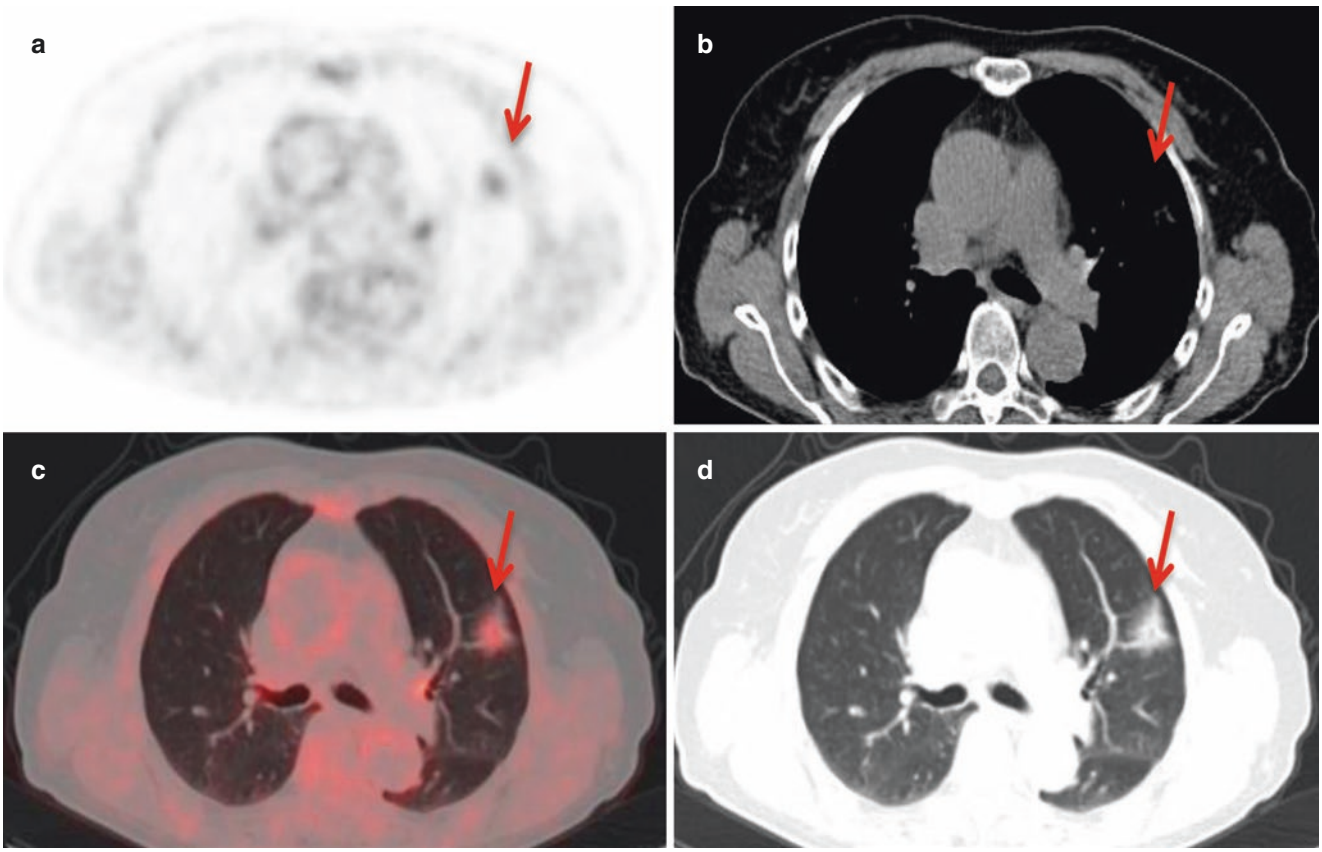

Fig. 3.5 Axial ^{18}F-FDG PET/CT revealing a pure ground glass opacity with mild ^{18}F-FDG uptake (SUVmax = 2.4) in the left upper lung lobe of a 69-year-old woman. A histological examination confirmed lung adenocarcinoma. (**a**), axial PET image; (**b**), axial CT image (mediastinal window); (**c**), axial fused PET/CT image; (**d**), axial CT image (lung window)

differences in ^{18}F-FDG uptake in NSCLC with different tumor sizes and TNM stages might also be explained by the changes in the tumor microenvironment, which induces hypoxia, promoting the transcriptional ability of glucose transporters transcript factor HIF-1a or c-MYC.

The maximum SUV (SUVmax) is an important semi-quantitative parameter to assess intracellular ^{18}F-FDG uptake via PET/CT scanning in vivo. NSCLC with high GLUT1 expression, a rapid doubling time, oxygen supplement deficiency, and poor differential subtype always accumulate much more ^{18}F-FDG than other NSCLC tissues. The clinical stage of NSCLC is classified as TNM stages I to IV by the American Joint Committee on Cancer (AJCC), among which, NSCLC tissues from curable TNM stage I patients have the lowest SUVmax, which can be explained by the differences in tumor size and local microvascular or pleural invasion. The high ^{18}F-FDG uptake of primary NSCLC tumors indicates the high malignancy of the tumor and the poor prognosis of patients. Patients with NSCLC whose primary lung tumor tissues have very high ^{18}F-FDG uptake might need more timely and thorough treatment to improve their overall survival.

Although the total sensitivity and specificity of ^{18}F-FDG PET/CT in NSCLC diagnosis are higher than traditional imaging techniques, such as X-ray, CT, or MRI, the sensitivity of ^{18}F-FDG PET/CT to diagnose both bronchoalveolar carcinoma (BAC, a subtype of adenocarcinoma) and ground glass opacities (GGO) is lower than for other NSCLC subtypes (Fig. 3.5). The sensitivities of PET to BAC and GGO in different studies varied from ~38 to 75% and from 20 to 33%, respectively. The low expression of GLUT1, or its inactivation, resulted in decreased membrane location, and the relative fewer number of tumor cells, which might explain the relatively low ^{18}F-FDG uptake by BAC and GGO.

Solitary pulmonary nodule (SPN) is a well-defined single mass in the lung, with an opaque image in CT scanning, the diameter of which is equal or less than 3 cm, surrounded by gas-containing lung tissue, without atelectasis, enlarged hilar and mediastinal lymph nodes, pneumonia, or pleural effusion. In SPNs, nodules smaller than 1 cm are defined as small SPNs, the diagnosis of which remains a challenge because of the unavoidable physical disadvantages of PET scanning, including the partial volumetric effect, respiratory motion, and the relative low resolution of PET (~7 mm). The combination of CT with PET is important to increase the diagnostic sensitivity for small SPNs, because it is difficult for PET to detect relative small nodules without the correction of CT [3, 4]. The diagnostic value of ^{18}F-FDG-CT in small SPNs

showed large variations in different studies. The diagnostic sensitivity of ^{18}F-FDG PET for small tumors varied from 0 to 93% in different reports, which might be explained by the varied definitions of PET-positive-small SPNs in the different studies. When the ^{18}F-FDG uptake of the SPNs (T = tumor), the mediastinal blood pool, and the normal lung tissue (N = normal) are taken into consideration for the diagnosis of SPNs, a $(T - N)/(T + N) \geq 0.4$ or a relative high ^{18}F-FDG uptake >~2.3 times that of normal lung tissue can be recognized as a PET-positive nodule. An invasive percutaneous biopsy is recognized as an effective diagnostic method for PET-negative nodules. However, negative PET imaging reduces the anxiety of a patient concerning malignant tumors, as well as avoiding other unnecessary invasive or costly diagnostic procedures.

With the development of modern imaging techniques, the disadvantages of PET mentioned above have been substantially reduced but have not disappeared. The physical disadvantages of ^{18}F-FDG PET/CT may result in mistaken diagnosis in some cases of pure glass opacity (pGGO) and mixed GGO (mGGO) as BAC. Appropriate noninvasive supplementary programs, such as contrast-enhanced CT (CECT) and MRI, are suggested in the assessment of lung nodules. Again, invasive percutaneous biopsies will be needed for suspicious metastases nodules from tumors derived in other systems outside the lung, such as gastrointestinal cancer, brain cancer, or ovarian cancer, especially in those patients with a history of lung cancer history.

The discrimination of a malignant tumor from inflammation is important for SPNs diagnosis. The use of early and delayed (dual-time-point) ^{18}F-FDG PET/CT can improve the diagnostic accuracy, because malignant tumor cells continually increase intracellular ^{18}F-FDG accumulation over time, whereas in inflamed or benign tissues, the increase in ^{18}F-FDG uptake only persists for several hours after ^{18}F-FDG injection. However, the improved sensitivity of dual-time-point ^{18}F-FDG PET/CT compared with single-time-point ^{18}F-FDG PET/CT in malignant SPN diagnosis requires confirmation [5]. The added diagnostic value of the dual-time-point ^{18}F-FDG PET/CT in SPNs is also questionable. Additionally, dual-time-point ^{18}F-FDG PET/CT increases the complexity of clinical workflow issues, thus lowering efficiency. Taken together, it remains difficult to add delayed ^{18}F-FDG PET/CT into early scanning as a routine PET scanning model and is only recommended for patients with equivocal or suspicious images in early scanning.

Nowadays, ^{18}F-FDG PET/CT is known as a promising molecular imaging technique for the diagnosis, staging, monitoring tumor reoccurrence, and therapeutic effect of NSCLC. However, there are still some disadvantages that should be taken into consideration in the application of ^{18}F-FDG PET/CT. The use of ^{18}F-FDG PET in small SPNs is limited because of its relative low sensitivity and specificity. In addition, relatively low-grade malignant tumors with low glucose uptake and glycolysis, such as benign tumors and bronchiole-alveolar cancer, always show ^{18}F-FDG-negative images. Conversely, some acute or chronic infections (Fig. 3.6) and inflammatory conditions (Figs. 3.7 and 3.8) with locally high glucose accumulation show ^{18}F-FDG-positive images. These limitations should be considered in the clinical diagnosis in SPNs via ^{18}F-FDG PET/CT to improve diagnostic accuracy.

3.2.2 Identifying the TNM Stage

The accurate staging of primary tumor, regional nodes, and distant sites (TNM staging) before therapy is important for treatment planning as well as prognosis prediction. In NSCLC patients, PET/CT scanning before operation helps to avoid unnecessary thoracotomy and thoracotomy via relative accurate locoregional staging. The whole-body imaging model of PET/CT is superior in TNM staging to detect both the locoregional and the distant lesions in a single scanning. As a sensitive functional imaging tool, PET/CT can detect invisible lesions than other traditional imaging modalities, such as CT and MRI, and thus will directly influence the treatment planning and improve patients' outcome. Currently, PET/CT is becoming a standard tool for staging of patients who were already diagnosed with malignant tumor.

3.2.2.1 Nodal Metastasis

Currently, the nodal metastasis (N) stage of NSCLC is classified as N0 to N3: N0 means no lymph node metastasis, N1 means local ipsilateral hilar or/and peribronchial lymph node metastasis, N2 means subcarinal or/and ipsilateral mediastinal lymph node metastasis, and N3 means supraclavicular or/and contralateral mediastinal lymph node metastasis. The status of lymph node metastasis (N) is strongly correlated with the prognosis of patients with lung cancer. In NSCLC, the accurate staging of mediastinal lymph nodes is very important, because it can directly help clinicians to formulate the optimum therapeutic plan. The presence of metastasis in mediastinal lymph nodes directly changes the clinical treatment approach in patients with lung cancer.

In the evaluation of intra- and extra-thoracic metastases from primary lung cancer, CT is the most widely and commonly used imaging modality. Lymph nodes with a short axis longer than 1 cm measured via a transverse CT scan are recognized as suspicious metastasis lymph nodes, which is the most widely used criteria to diagnose N stage in NSCLC. Many other criteria assessed via CT are also used in node metastasis assessment. However, the staging ability of CT imaging is limited if CT is the only modality used to evaluate the mediastinum for metastases. In recent years,

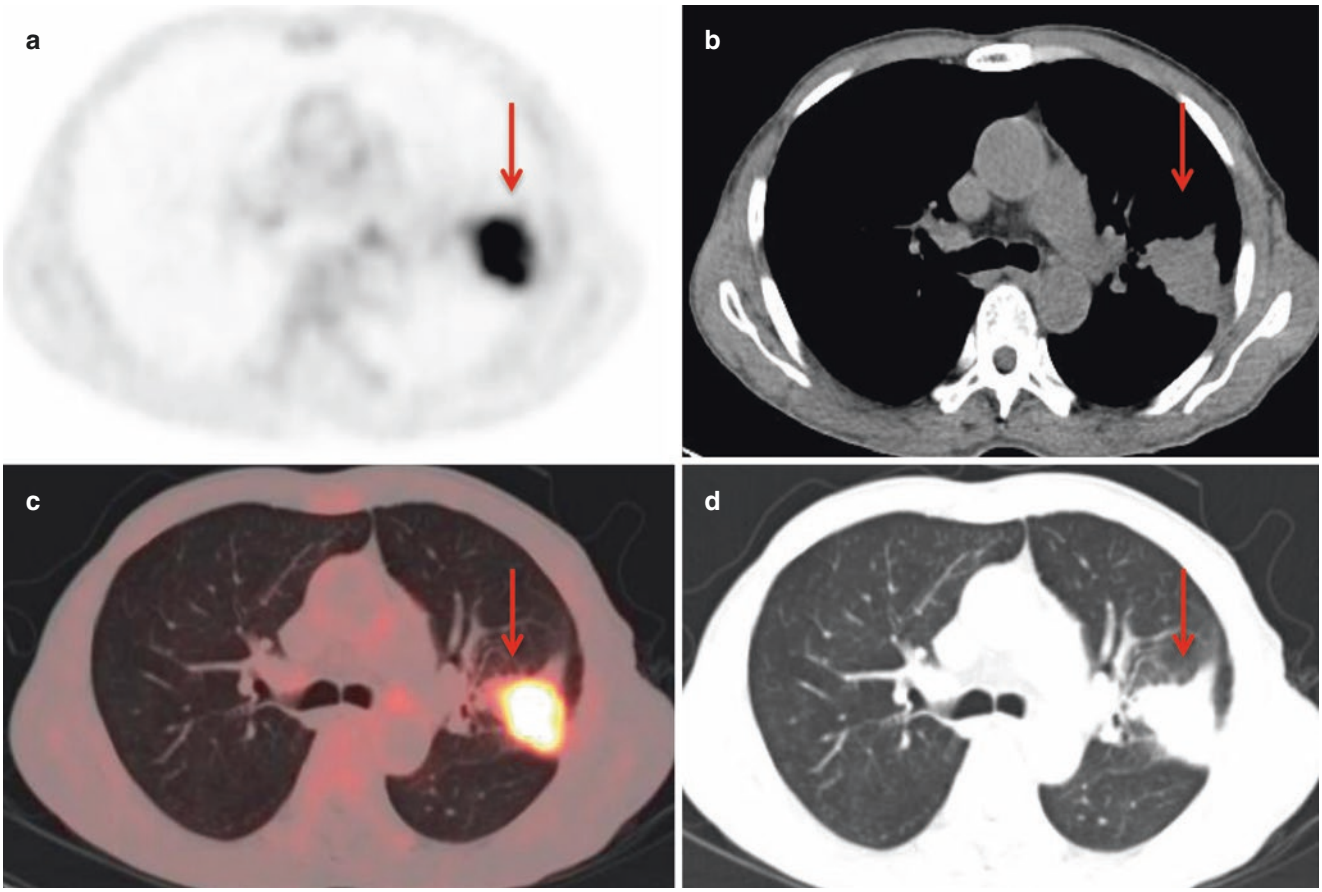

Fig. 3.6 Axial ^{18}F-FDG PET/CT revealing a hypermetabolic mass with lobulated signs in the left upper lung lobe of a 65-year-old man. A histological examination confirmed tuberculosis. (**a**), axial PET image; (**b**), axial CT image (mediastinal window); (**c**), axial fused PET/CT image; (**d**), axial CT image (lung window)

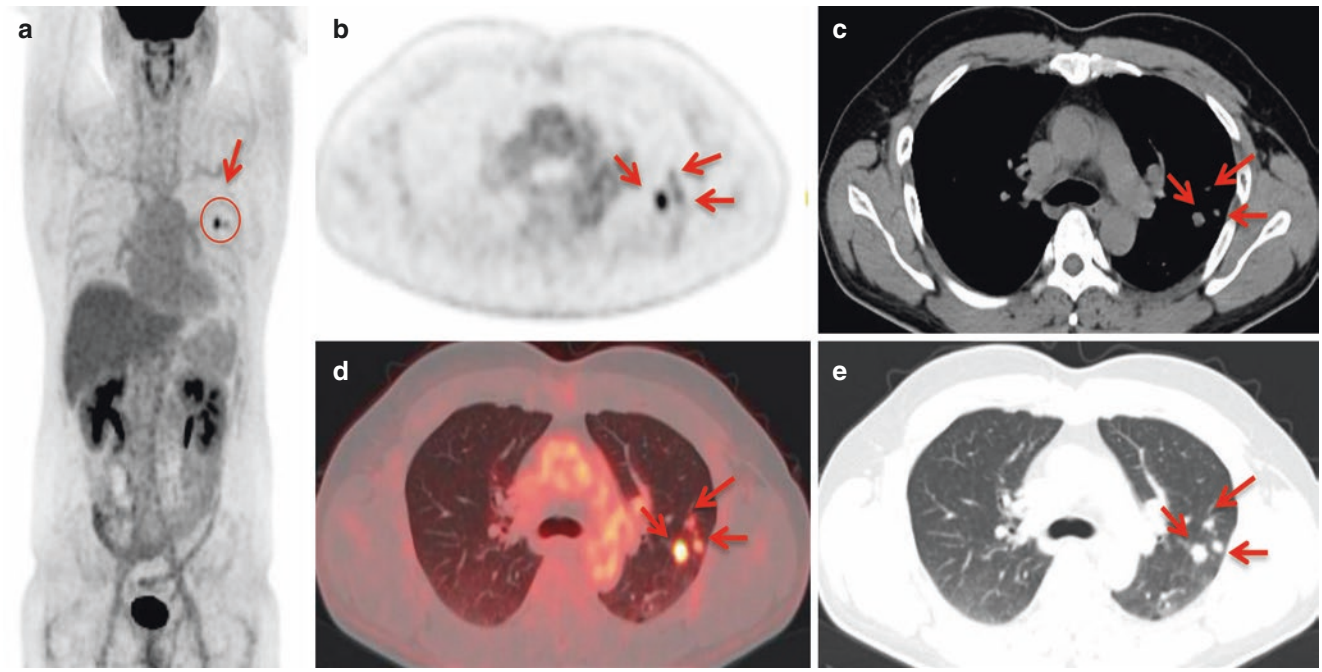

Fig. 3.7 ^{18}F-FDG PET/CT imaging (**a**, maximum intensity projection image; **b**–**e**, axial images) in a 44-year-old man showing uptake (SUVmax = 7.9) in multiple small lung nodules in the left upper lung lobe. A histological examination confirmed that the lung nodules were pulmonary fungal granuloma. (**a**), maximum intensity projection image; (**b**), axial PET image; (**c**), axial CT image (mediastinal window); (**d**), axial fused PET/CT image; (**e**), axial CT image (lung window)

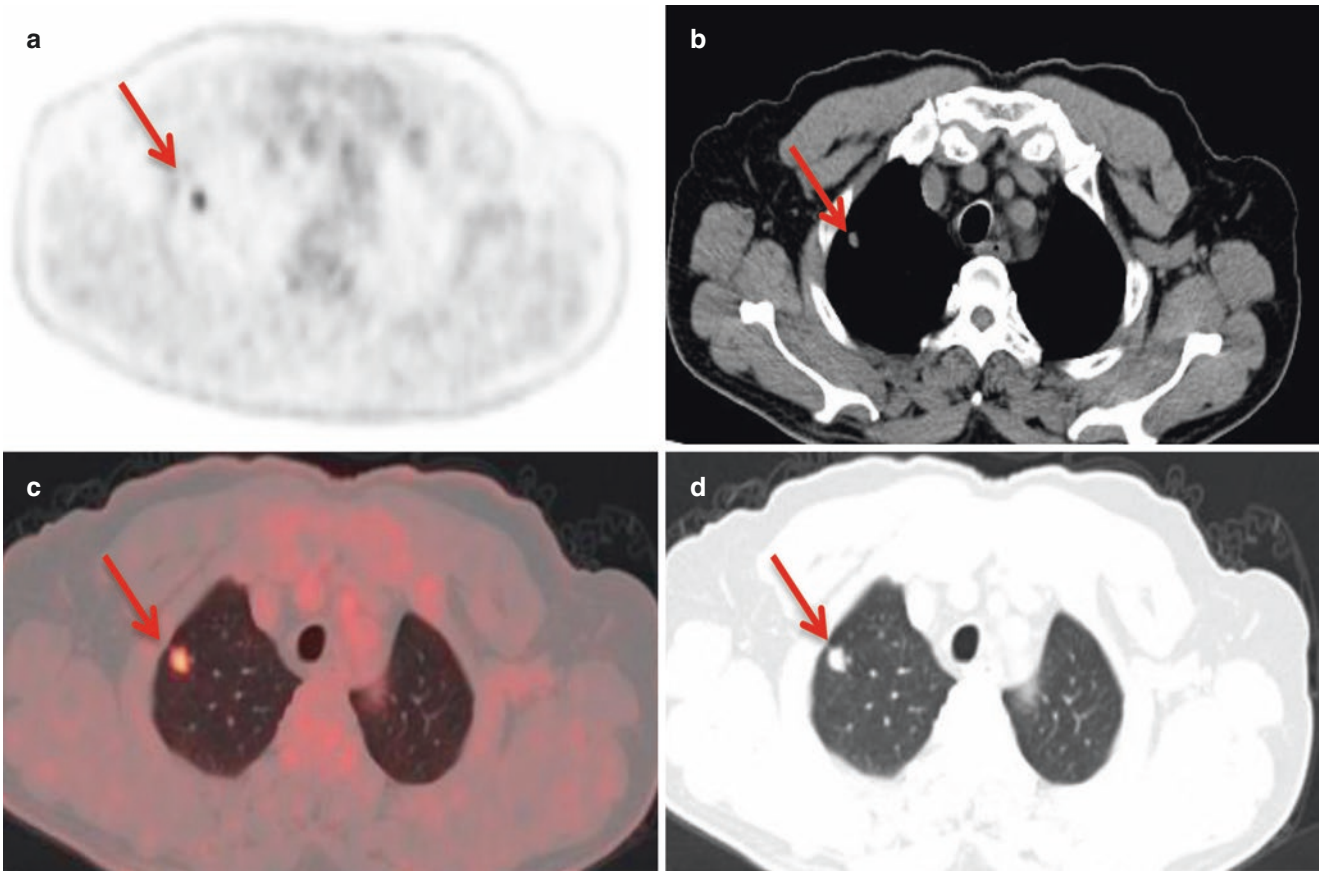

Fig. 3.8 Axial ^{18}F-FDG PET/CT showing a hypermetabolic nodule with lobulated and spicule signs in the right lung lobe of a 64-year-old man. A histological examination confirmed an inflammatory nodule. (**a**), axial PET image; (**b**), axial CT image (mediastinal window); (**c**), axial fused PET/CT image; (**d**), axial CT image (lung window)

with advances in the development of molecular imaging modalities, the combination of ^{18}F-FDG PET with CT has dramatically improved the sensitivity of node staging in lung cancer diagnosis, which is widely used in tumor diagnosis (Fig. 3.9).

Compared with stand-alone CT scanning, ^{18}F-FDG PET/CT is presently recognized as a standard tool for accurate node staging in many types of malignant tumor. In NSCLC, the sensitivity of ^{18}F-FDG PET/CT in detecting mediastinal lymph node metastasis ranged from 78 to 93%, with the specificity ranging from 83 to 93%, the positive predictive value (PPV) ranging from 82 to 95%, and the negative predictive value (NPV) ranging from 88 to 95%. The data mentioned above, assessed from ^{18}F-FDG PET/CT scanning, are all higher than those obtained by CT scanning only, for which the sensitivity, specificity, the positive predictive value (PPV), and the negative predictive value (NPV) in mediastinal staging detection were ~57, ~82, ~56, and ~83%, respectively. Besides enhanced sensitivity and specificity, the accuracy of nodal staging of lung cancer is also improved by the application of ^{18}F-FDG PET/CT (ranging from 69.0 to 87.3%) compared with that of stand-alone CT (ranging from 79.2 to 84.0%).

Moreover, ^{18}F-FDG PET/CT could identify the metastatic lesions in lymph nodes that may not be imaged via traditional scanning tools. The advantage of PET/CT in detecting very small metastatic lymph nodes is important for tumor staging, because the relatively small metastatic lesions in N2 staging nodes (the most expansive node group, including 2R, 2L, 3A, 3P, 4R, 4L, 5, 6) and posterior subcarinal area may be difficult to image using traditional scanning techniques. The application of ^{18}F-FDG PET/CT scanning can detect the suspected metastatic lesions at the mediastinum, which always shows high ^{18}F-FDG uptake, thus enhancing the accuracy of tumor staging. Additionally, the highly suspicious PET-positive nodes can be recognized as the punctual node for oncologists, resulting in more accurate pathological diagnosis.

However, there are still some disadvantages of ^{18}F-FDG PET, with or without the combination of CT scan. A variety of endemic granulomatous malignant diseases also show ^{18}F-FDG PET-positive nodes, which is the main reason for interfering with the diagnostic accuracy of N staging of a tumor. Endemic granulomatous diseases, such as HIV infection, sarcoidosis, and fungal disease, increase the rate of false-positive mediastinal nodes because of increased glucose

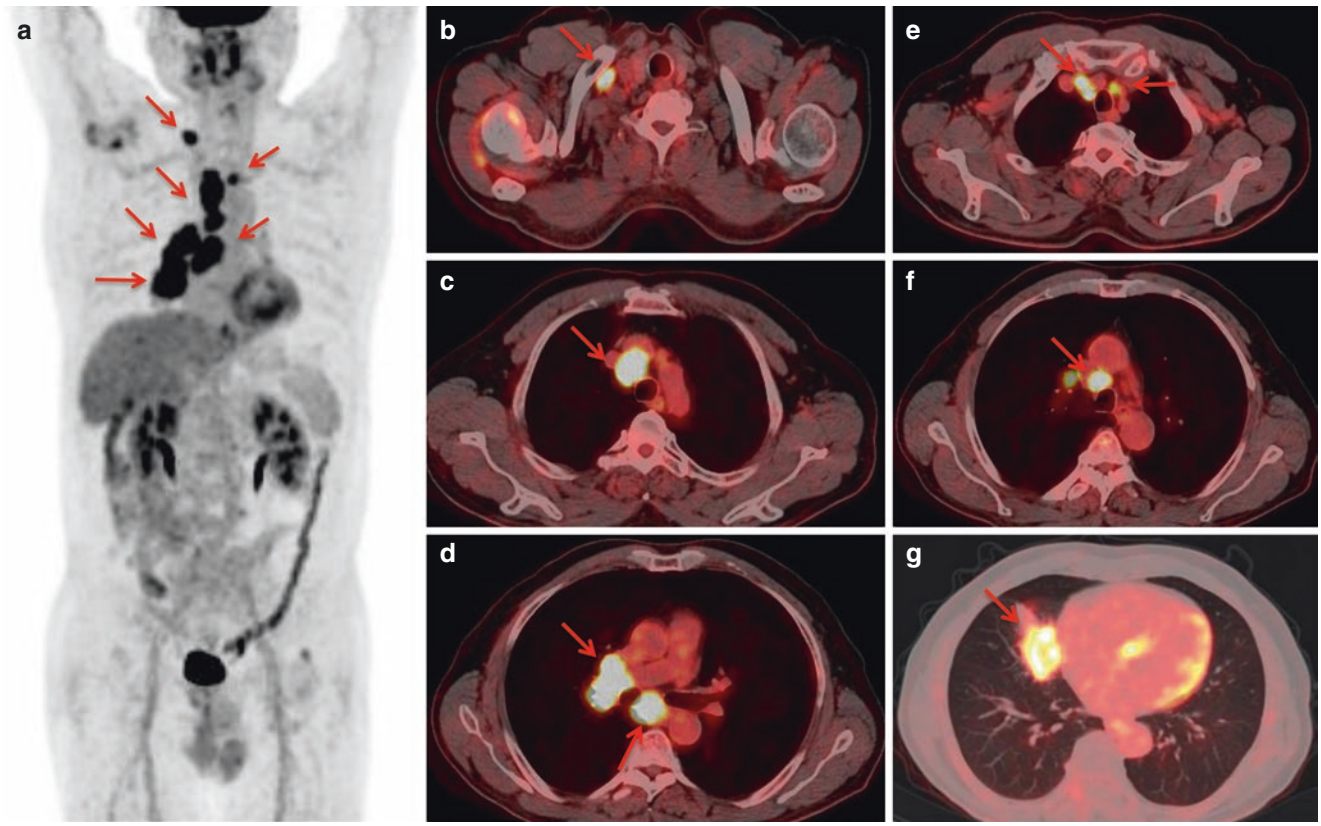

Fig. 3.9 A 68-year-old man with lung squamous carcinoma and multiple lymph node metastases. (**a**–**f**) ^{18}F-FDG PET/CT imaging (**a**), maximum intensity projection image; (**b**–**f**), axial fusion images showing uptake (SUVmax = 15.6) in his enlarged lymph nodes at stations 1R, 2R, 2L, 4R, 7, and 10R. A histological examination confirmed lymph nodes metastases. (**g**), axial fused PET/CT images showing uptake (SUVmax = 14.2) in a lung mass in the right middle lobe. A histological examination confirmed lung squamous carcinoma

metabolism in N2 staging nodes. A false-positive mediastinal node observed via PET can incorrectly upstage the clinical stage of lung cancer, resulting in inappropriate surgery and/or non-operative therapy, which may be hazardous to health. Hence, it is very important for clinicians to understand the limitations of PET, as well as the comprehensive medical history of the patients, to minimize the incorrect N staging of lung cancer.

Biopsy examination is recognized as the gold standard for the diagnosis of both primary and metastatic tumors. To diagnose suspicious metastatic nodes, biopsy is commonly used before surgery. However, before PET/CT scanning, local interventions (such as endobronchial ultrasound (EBUS), biopsy, and surgery) should be avoided, because the invasive interventions might result in false-positive-PET images, which may interfere with the judgment of clinicians.

3.2.2.2 Distant Metastasis

The early diagnosis of extra-thoracic metastasis is essential for tumor therapy; the underestimated distant metastasis (M) score always results in poor prognosis for patients with NSCLC. The distant metastatic sites of lung cancer are the brain, bones, liver, adrenal gland, abdominal lymph nodes, and kidneys. The distant metastasis of lung cancer is commonly transferred via a hematogenous pathway or via a lymphatic pathway. As a whole-body scanning tool with high sensitivity in detecting distant metastatic lesions, ^{18}F-FDG PET/CT is widely used in clinical staging of primary NSCLC and is also considered as an invaluable scanning technique in patients whose primary tumor lies outside the chest.

3.2.2.3 Bone Metastasis

Lung cancer has been the most common malignancy worldwide, with ~1.8 million new cases resulting in one tumor-related death in five (1.59 million deaths, 19.4% of total) annually [6]. The bone is recognized as the most common distant metastatic site of lung cancer, which occurs in about 30–60% of patients. A significant proportion of patients with lung cancer with bone metastasis experience skeletal-related events (SREs), as a result of the osteolytic hyperkalemia, pathological fractures, local radiotherapy, and/or therapeutic orthopedic surgery. The occurrence of SREs always predicts a poor quality of life, which significantly affects the clinical outcomes of patients. The median

survival time of patients with lung cancer with SREs was reported to be as low as 4.1 months but can also be costly [7]. Male gender and a score of 3 or 4 by the Eastern Cooperative Oncology Group (ECOG) criteria are recognized as predictive factors for poor prognosis after bone metastasis. By contrast, other studies found that female gender, performance status of 0 or 1, single bone metastasis, and presentation with EGFR mutation also indicated good prognosis for lung cancer after bone metastasis [8–10]. In patients with lung cancer in TNM stages I and II who underwent tumor resection, tumor recurrence in bone occurred in approximately 10% of patients [11].

The correct diagnosis and the precise position of bone metastasis are the key prerequisites for clinicians to develop a reasonable and valid treatment strategy, which is essential for the survival or improvement of patients with lung cancer. To detect a possible skeletal metastatic lesion, ^{99m}Tc-methylene diphosphonate (MDP) bone scintigraphy is the most routinely used modality to evaluate the tumor stage, the working mechanism of which is the changes in absorption of MDP in metastatic tissues. However, bone metastasis lesions in the very early stage, small lesions, and certain pure osteolytic metastatic lesions without or with little osteoplastic response remain invisible under MDP scanning. Besides the poor sensitivity, the specificity of bone scanning is also low because of the high occurrence of false-positive images, whereas healing fractures, extra-bone benign or malignant calcification lesions, some benign neoplasms, and pleural effusions or ascites can all result in abnormal local MDP accumulation, thus producing false-positive results. MRI is a major scanning modality for diagnosing bone metastasis because of its high contrast and spatial resolution of the soft tissues, with relative high sensitivity and specificity in diagnosing bone metastasis compared with MDP scanning. However, MDP bone scanning is still an irreplaceable modality to establish the possible metastatic bone lesions via the whole-body viewpoint.

^{18}F-FDG uptake in disease lesions with abnormal intracellular glucose accumulation is recognized as an effective non-invasive modality for bone metastasis diagnosis, especially in patients with osteolytic metastatic carcinoma (Fig. 3.10). The high sensitivity and accuracy of ^{18}F-FDG PET/CT in detecting osteolytic metastatic lesions make it an indispensable additional staging method for patients with tumors in addition to MDP bone scanning. Among the three most used scanning modalities (MRI, bone scanning, and ^{18}F-FDG

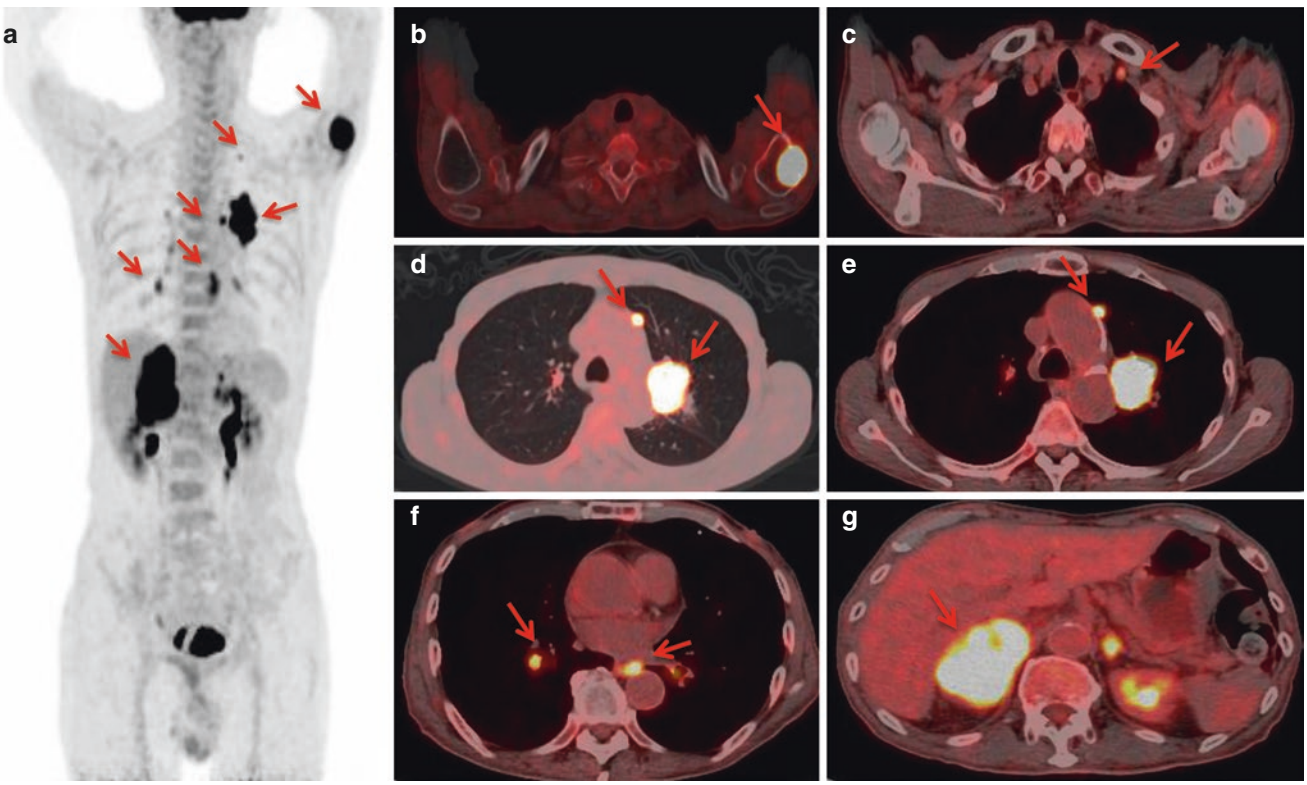

Fig. 3.10 An 84-year-old man with suspected lung carcinoma and mediastinal lymph node, bone, and right adrenal gland metastases. (**a**–**g**) ^{18}F-FDG PET/CT imaging (**a**), maximum intensity projection image; (**b**–**g**), axial PET/CT images showing uptake (SUVmax = 24.1) in a lung mass in the left upper lobe (**d** and **e**), uptake (SUVmax = 7.4) in the mediastinal lymph nodes (**c**, **e**, and **f**), uptake (SUVmax = 23.2) in the left humerus (**b**), and uptake (SUVmax = 21.9) in the right adrenal gland, which were all highly suspicious of metastases (**g**). A histological examination confirmed that the lung mass was lung adenocarcinoma

PET/CT) to diagnose bone metastasis in patients with lung cancer, ^{18}F-FDG PET/CT shows the highest specificity (~96%), sensitivity (~98%), and diagnostic odds ratio (449.17), and has the highest value for diagnosing bone metastatic lesions in patients with lung cancer.

^{18}F-FDG PET/CT can detect bone metastatic lesions even smaller than 1 cm because of its high sensitivity and is recognized as a good imaging method to detect metastatic skeletal sites in patients with lung cancer. Some metastatic lesions in bone, which are invisible via traditional imaging modality, such as CT and MRI, can be easily detected by ^{18}F-FDG PET/CT. However, ^{18}F-FDG PET/CT cannot be used alone to diagnose tumors, because MRI still has advantages in bone metastasis diagnosis to ensure the diagnostic accuracy, while a high-quality CT image is also essential for clinicians to localize the disease site. Both MRI and a high-quality CT scans can make up for the limitation of ^{18}F-FDG PET in anatomical resolution, thus providing precise information on bone metastatic lesions, including the site, size, and the extent of the lesions. Additionally, osteoblastic metastatic lesions, which might show a false-negative PET image, can be detected by PET combined with CT. Thus, the combination of ^{18}F-FDG PET/CT with other imaging modalities is an effective strategy to assess bone metastasis in patients with lung cancer.

3.2.2.4 Brain Metastasis

Extra-thoracic metastasis is the most common reason for lung cancer-related death, and the brain is the most common metastatic site of lung cancer. Brain metastasis (BM) occurs in almost one half of patients with lung cancer in the progression stage, resulting in poor quality of life and short survival time. The median survival time of patients with BM from in lung cancer is less than 6 months, and treating BM to improve outcome remains a huge challenge. Recently, the occurrence of BM in patients with lung cancer has increased, which might be explained by the advances in BM diagnostic methods, the increased lifespan in the general population, the increase in advanced clinic staging, and the prolonged totally survival time of patients with lung cancer, as a result of developments in tumor therapeutic drugs.

Although the development of modern diagnostic techniques has improved the early diagnosis of BM, patients with lung cancer and BM still have a poor prognosis. The normal blood-brain barrier (BBB) limits the use of some therapeutic macromolecular agents to treat BM lesions located in the brain parenchyma, making them not applicable to treat lung cancer-associated BM. Age $\leq$ 60 years, the non-SQCC subtype, non-SQCC patients in pIIIA-N2 stage who underwent complete resection, a mediastinal lymph node length of >2 cm, and a lymph node ratio (LNR) of $\geq$30% have been identified as high-risk factors for BM in patients with lung cancer and always predict poor prognosis. Prophylactic cranial irradiation is necessary for patients with high-risk factors for BM. Besides cranial irradiation, appropriate chemotherapy and close radiological follow-up are also important to prevent BM occurrence. The effective control of primary tumor lesions, isolated cranial metastasis, and a Karnofsky performance status greater than 70% all correlate with longer survival of patients with lung cancer with BM [12, 13]. Differences in tumor-driving gene phenotypes result in different outcomes in lung cancer. Tumor-driving genes such as *EGFR*, Kirsten rat sarcoma viral oncogene homolog (*KRAS*), serine/threonine *kinase11* (*STK11*), and anaplastic lymphoma kinase (*ALK*) are essential for lung cancer progression; however, the relationship between the activation of these genes and BM is unclear.

The brain is always the only metastatic site in patients with lung cancer; left untreated, BM results in a poor median survival time of less than 3 months. Prophylactic cranial radiotherapy extended the median survival time of patients with lung cancer brain metastasis (LCBM) to approximately 8 months. Early diagnosis and the precise location of BM lesions are essential for early intervention for tumor therapy. Thus, cerebral imaging is recommended as a routine examination in the early staging of lung cancer. For patients with lung cancer in stage III or IV, cerebral staging is recommended regardless of the preoperative TNM stage and the therapeutic strategy. Lesion resection and gamma knife treatment can improve the survival time of patients with lung cancer with a solitary BM lesion. For patients with multiple BM lesions <3 cm or with BM lesions that are hard to resect, whole-brain radiotherapy is the best therapeutic choice.

High-quality imaging plays pivotal role in BM diagnosis. Diagnosis of the BM stage of NSCLC provides key clues to clinicians, allowing them to choose the most reasonable and effective individual therapeutic strategies. Initial cerebral staging is recommended whether the patient has neurological symptoms or not, because early intervention in patients with LCBM can apparently improve their overall survival especially in patients without obvious neurological symptoms. Although PET/CT can provide whole-body information for patients with lung cancer and is recommended as a routine scanning tool in the early staging of patients with lung cancer because of its higher sensitivity and specificity compared with traditional imaging techniques, MRI is still the best imaging modality to detect BM lesions. Brain tissues consume large amounts of glucose to meet basic energy needs. The physiological uptake of ^{18}F-FDG in the brain may mask the metastatic lesions located in the brain, which can be both hypermetabolic and hypometabolic compared with surrounding tissue (Fig. 3.11), or may be too small to be detected by ^{18}F-FDG PET or PET/CT. False-positive hypometabolic lesions detected by ^{18}F-FDG PET can be caused by previous infarction, age-related atrophy, dementia disorders, benign cysts

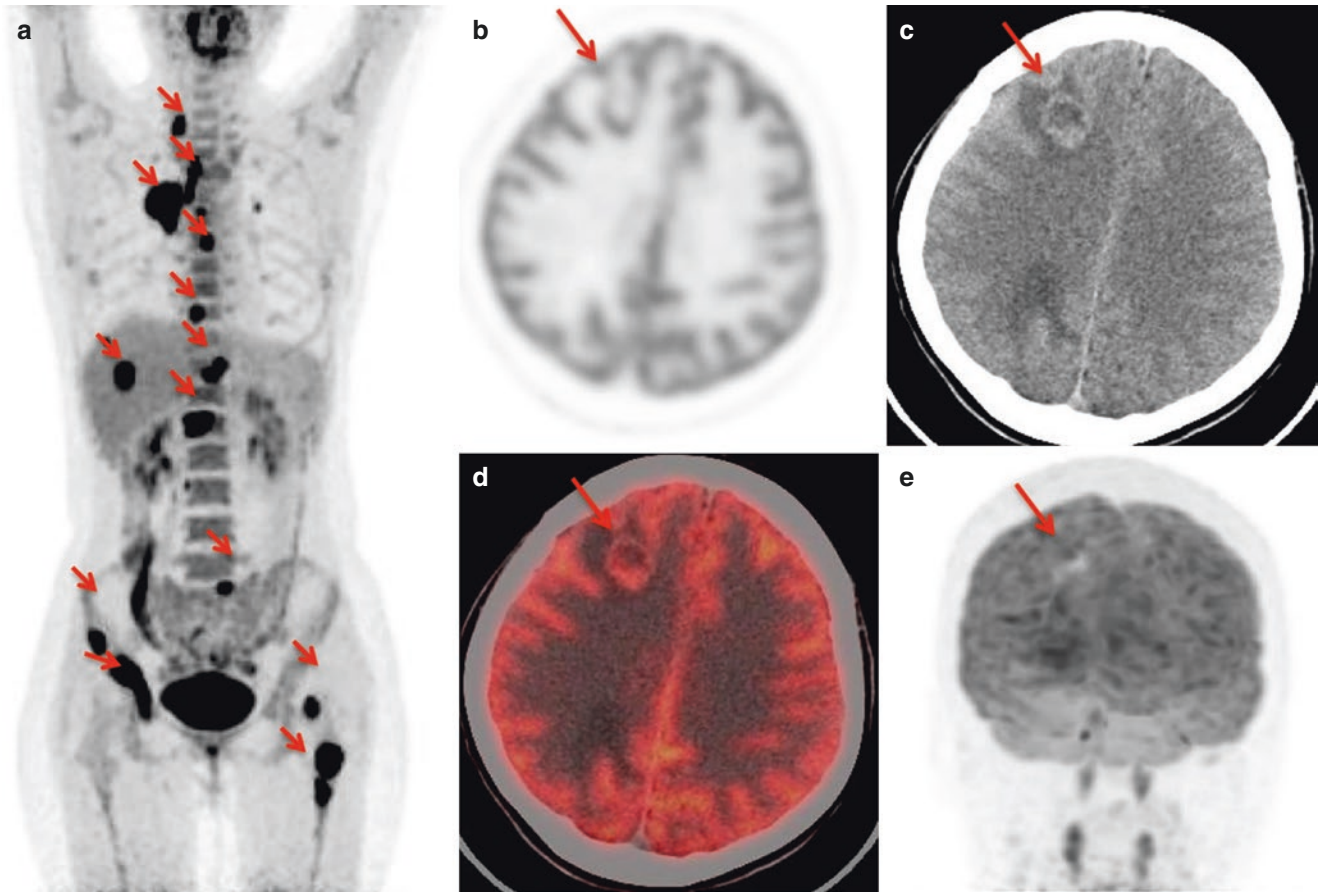

Fig. 3.11 A 41-year-old woman with suspected lung carcinoma, right supraclavicular lymph node, right lung hilum lymph node, mediastinal lymph nodes, and liver, brain, and bone metastases. (**a**–**e**), ^{18}F-FDG PET/CT imaging (**a**) maximum intensity projection image showing uptake in a lung mass in the right upper lobe and uptake in the right supraclavicular lymph node, right lung hilum lymph node, mediastinal lymph nodes, liver, and bone, which were all highly suspicious of metastases (**b**–**e**), both axial and coronal PET images showing a hypermetabolic area in the right frontal lobe (**b**, **e**) and axial CT (**c**) showing a tumor surrounded by edema in the same area of PET imaging (shown in fused image **d**), which was highly suspicious of brain metastasis. Histological examinations confirmed that the lung mass was lung adenocarcinoma

or other benign space-occupying processes, and previous cerebral surgery. The most common cause of false-positive hypermetabolic findings is probably variations in gray matter activity mimicking focal lesions.

The application of modern techniques in oncological imaging systems improves the accuracy of tumor diagnosis. Recently, with the development of modern imaging modalities, the combination of PET with MRI (PET/MR) has become a focus in the field of imaging techniques. However, the integration of PET with MRI does not overcome the limitation of the sole use of PET or MRI, such as the partial volume effect of PET and the incapability of quantification of MRI. Thus, for the initial whole-body staging of patients with lung cancer, ^{18}F-FDG PET/CT has proved its particular equivalence and cannot be replaced by PET/MR, whereas for cerebral staging of patients with lung cancer, MRI alone is still recognized as the "gold standard" imaging technique.

3.2.2.5 Adrenal Metastasis

In patients with lung cancer, the adrenals are not an uncommon site of metastases. The accurate restaging of patients with lung cancer with a solitary adrenal mass is very important for tumor therapy. Aggressive intervention, such as surgery or stereotactic body radiotherapy, may significantly improve the overcome of patients with solitary adrenal metastasis.

However, the diagnosis of adrenal metastasis in lung cancer is challenging because both neoplastic and nonneoplastic masses of the adrenals occur frequently. Delayed contrast-enhanced computed tomography (CT) can aid the differentiation of benign and malignant adrenal lesions. However, patients with lung cancer often do not undergo delayed contrast-enhanced CT, which is not sensitive to the differentiation of benign from malignant lesions because of too much overlap in the mean attenuation between the two groups. In addition, MRI has not shown definite superiority

to CT because of the considerable overlaps between the signal intensities of benign and malignant lesions.

As a functional imaging modality that provides glucose metabolic information on malignant tumors, ^{18}F-FDG PET has shown encouraging results in differentiating metastatic lesions from benign adrenal disease in lung cancer. However, occasionally, PET cannot clearly identify the location of functional abnormalities, especially if the adrenal lesions are adjacent to the liver. Compared with PET, integrated PET/CT can acquire both anatomical and functional information almost simultaneously, which minimizes the adverse effect of internal organ motion, such as diaphragmatic movement, on the accurate location of functional abnormalities in an anatomical site. ^{18}F-FDG PET/CT has a high ability to detect adrenal metastasis from lung cancer, with a reported sensitivity of more than 88% and a high specificity of more than 90% to exclude adrenal metastasis in lung cancer with adrenal masses compared with CT or MRI [14]. However, it should be noted that ^{18}F-FDG PET/CT possibly shows false-positive or false-negative results for adrenal metastasis in patients with lung cancer. According to the available data from studies included in a meta-analysis, false-negative findings (approximately 10%) may mainly be caused to small lesions, necrosis, or hemorrhage. However, the most frequent cause of false-positive findings (approximately 10%) is likely to be adrenal functional adenomas, other pheochromocytomas, or endothelial cysts.

3.2.2.6 Liver Metastasis

The frequencies of liver metastasis in different subtypes of NSCLC are very similar, ranging from 2.9 to 4.1%, whereas the frequency of liver metastasis in SCLC patients is higher than that in NSCLC, at 17.5 to 20.3% [15, 16]. Metastatic lesions in the liver always accumulate much more glucose than adjacent normal liver tissues and thus can be easily detected using ^{18}F-FDG PET as hypermetabolic areas. Compared with contrast-enhanced CT, which is traditionally used to find hypervascular liver metastatic lesions, ^{18}F-FDG PET/CT is superior to detect untreated metastatic lesions in the liver because of its high sensitivity. The combination of ^{18}F-FDG PET with CT added the sensitivity of 87.9% and the specificity of 16.7% of solely CT application to 97% and 75% in the diagnosis of hepatic metastasis, respectively [17]. False-positive imaging caused by infection, benign neoplasms, or local abscesses remains a problem in ^{18}F-FDG PET/CT evaluation. False-negative metastatic lesions in the liver have also been observed in a few patients with lung cancer, mainly because of the low resolution of ^{18}F-FDG PET and the small size of the metastatic lesions.

3.2.2.7 Pleural Involvement

The pleural cavity is also a common site that can be directly invaded or metastasized by lung cancer. The involvement of lung cancer in the pleural cavity is defined as the M1 stage, which is hard to resect curatively by surgery. The thickened pleura and the pleural nodules can be detected by conventional CT and MRI scanning, whereas the capacity of CT and MRI to differentiate malignant from benign pleural disease is limited because of their imaging characteristics. Some cases of benign effusion resulting in obstructive pulmonary disease might be mistakenly diagnosed as malignant metastatic disease, which should be distinguished from pleural metastasis. Metastatic pleural lesions always accumulate much more glucose than benign tissues and thus can be sensitively detected by ^{18}F-FDG PET. Thus, ^{18}F-FDG PET/CT is recognized as a reliable imaging tool for the diagnosis of pleural metastasis, because of its high sensitivity (88.8–100%), specificity (76–94.1%), and accuracy (8491.4%) to distinguish malignant pleural metastasis in patients with lung cancer from benign pleural disease [18, 19]. In addition to noninvasive imaging modalities, invasive methods, such as pleural fluid cytology, thoracentesis, and thoracoscopy, are also very important for the definitive diagnosis of malignant pleural effusion. The integration of all examinations helps clinicians to correctly identify the distant metastatic site of patients with lung cancer, thus providing clues for tumor therapy.

Correct TNM staging and curative tumor resection of lung cancer in the early stages can significantly improve patient outcome. However, a large number of patients with lung cancer have undetected occult metastatic diseases at the time of tumor resection. For these patients, curative surgery is not the best therapeutic strategy and may even be harmful to some extent, being termed futile treatment, which should be avoided at the early stage of tumor therapy. Up to 20% of patients with lung cancer undergo futile treatment because of an underestimated M stage.

Occult metastasis of lung cancer is hard to detect using current examination methods because of the limited resolution of certain imaging modalities, which will mislead therapeutic planning in tumor treatment and is thus the main reason for futile treatment. Pre-operational ^{18}F-FDG PET/CT scanning increased the positive rate of occult metastasis that was not detected by traditional tools, which helped clinicians to formulate more reasonable therapeutic strategies and thus prevented unnecessary or futile therapy [20–28]. ^{18}F-FDG PET/CT can effectively demonstrate the primary tumor size, the local extension, the relation of the primary lesion to adjacent tissue, lymph node metastasis, and the distant metastasis in patients with lung cancer. The additional application of ^{18}F-FDG PET/CT to other examination tools, such as bone scanning, CT, and MRI, significantly decreased the rate of futile tumor resection in patients with lung cancer; about one in five futile operations could be prevented by the use of ^{18}F-FDG PET/CT. In nonsurgical patients with lung cancer, the ^{18}F-FDG PET/CT-detected occult metastasis

lesions, which were not found by other imaging tools, also helped physicians to develop more reasonable chemo- or/and radiotherapy planning for tumor therapy. The advantage of ^{18}F-FDG PET/CT in avoiding unnecessary thoracotomies in patients with lung cancer is still a matter of debate and should be further studied in the future.

3.2.3 Identifying the Recurrence of Lung Cancer and Restaging

NSCLC recurrence means the regrowth of the tumor after curative therapy, including local-regional and distant recurrences. Local-regional recurrence is limited to the same side of the chest as the primary tumor, containing the ipsilateral mediastinal or hilar lymph nodes, pleura, bronchial stump or anastomosis, and the chest wall. Distant recurrence mainly occurs in the same site of the initial distant metastatic lesions. Combinations of tumor resection, chemo- and radiotherapy, immune therapy, and gene-targeted treatment have improved the total curative rate of lung cancer. However, tumor recurrence is still an unavoidable event in the progression of lung cancer, which occurs in about 20–80% of patients with lung cancer, resulting in poor prognosis. The result of initial ^{18}F-FDG PET/CT scanning might predict tumor recurrence after surgery. A high standardized uptake value (SUV) of ^{18}F-FDG in primary NSCLC tissue increases the possibility of post-surgical recurrence.

For the past decade, research has focused on the pathophysiological mechanisms that induce lung cancer recurrence, an understanding of which is essential to expand therapeutic strategies. Curative resection cannot avoid the recurrence of lung cancer, even at an early TNM stage. It was reported that about 30–55% of patients with NSCLC that underwent complete tumor resection finally succumbed to tumor recurrence-related death [29]. The under-staging of patients with lung cancer because of undetected occult metastasis lesions in the pre-operational period and the spread of lung cancer cells caused by surgery might explain the postoperational recurrence of lung cancer. Regular follow-up after initial curative therapy is essential for the early detection of tumor recurrence in patients with lung cancer. Besides the standard imaging modalities (chest X-ray, CT, or MRI) or/and tumor marker testing, ^{18}F-FDG PET/CT is now recommended as a useful modality to assess tumor recurrences and restage the TNM stage in the follow-up period and has advantages in terms of sensitivity over other follow-up methods (Fig. 3.12).

3.2.3.1 Diagnosis of NSCLC Recurrence

In NSCLC, ^{18}F-FDG PET/CT is recommended for routine follow-up after initial therapy and provides key information to guide subsequent therapeutic planning. Its high sensitivity in tumor detection means that ^{18}F-FDG PET/CT can visualize occult metastatic recurrence lesions that cannot be detected by the sole use of CT and is thus conducive to the accurate restaging of patients with lung cancer during follow-up. Moreover, ^{18}F-FDG PET/CT can reflect the glucose metabolism changes in a local recurrence site before anatomical changes occur, thereby visualizing tumor recurrence at a very early stage after initial chemo-/radiotherapy or surgery. Compared with a negative recurrence result of ^{18}F-FDG PET/CT, a positive recurrence result always predicts relatively poor outcome of patients with lung cancer. Appropriate

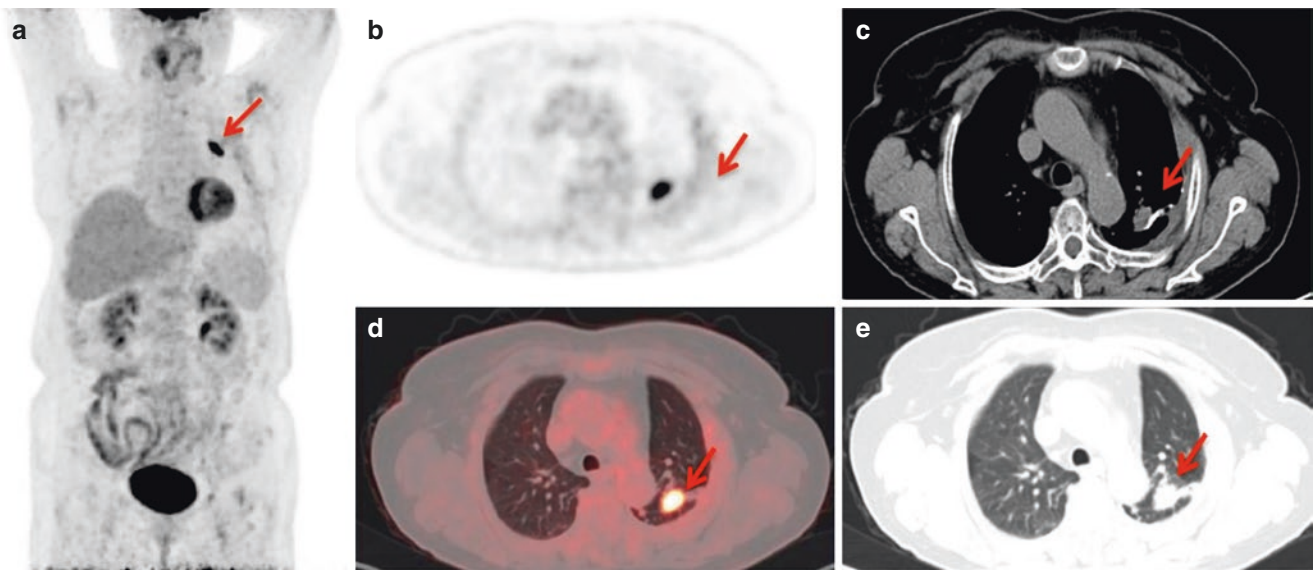

Fig. 3.12 ^{18}F-FDG PET/CT imaging (**a**, maximum intensity projection image; **b**–**e**, axial images) of a 75-year-old woman showing uptake (SUVmax = 10.9) in small lung nodules in the left upper lung lobe with a suture shadow, 6 months after surgery, indicating tumor recurrence (**b**), axial PET image; (**c**), axial CT image (mediastinal window); (**d**), axial fused PET/ CT image; (**e**), axial CT image (lung window)

aggressive therapy is suggested for patients with recurrent NSCLC to improve their survival time; ^{18}F-FDG PET/CT is superior in identifying these patients compared with traditional imaging modalities and is thus recommended for routine use during NSCLC follow-up after initial therapy.

^{18}F-FDG PET/CT in NSCLC has a well-known role in restaging. For those equivocal recurrent lesions detected by traditional CT or MRI, which are hard to distinguish from tumor-therapy-induced benign diseases, ^{18}F-FDG PET/CT is recommended and helpful to diagnose recurrence [30]. ^{18}F-FDG PET/CT can easily detect local or distant recurrence lesions after tumor resection, local ablation, local radiotherapy, or whole-body chemotherapy, thus restaging NSCLC in the follow-up period. Accurate restaging of patients with NSCLC using ^{18}F-FDG PET/CT helps clinicians to develop appropriate treatment plans and avoids unnecessary aggressive therapy, thus benefiting patients clinically and economically. In addition, the application of ^{18}F-FDG PET/CT could reduce the number of traditional invasive histological procedures, such as thoracotomies and futile thoracotomies, which might have no effect on improving patients' prognosis. However, brain scanning via MRI remains an essential additional imaging modality to ^{18}F-FDG PET/CT for the accurate staging of patients with stage II–IV lung cancer.

3.2.3.2 Surveillance of NSCLC Recurrence

Besides surgical or nonsurgical treatment, regular recurrence surveillance is another basic principle of the management of patients with lung cancer. In raising the point of NSCLC recurrence surveillance, we should realize the key role of appropriative and regular tumor monitoring after initial therapy to detect and locate the recurrent tumor lesions in a timely manner, thus promoting early treatment to improve patient prognosis during follow-up. Of course, the differential diagnosis of newly developed primary tumors or tumor therapy-related benign disease complications compared with tumor recurrence is very important in the monitoring period, thus providing assistance for rational treatment design.

In recurrence monitoring, the diagnostic methods and the interval of review are the two most important issues, which are still a matter of debate. For patients with lung cancer who undergo curative therapy, the first 2 years after tumor therapy is the high-risk period for recurrence; therefore, they must be closely followed up for at least 2 years. However, there is still no consensus on the interval of imaging review and the total follow-up period for these patients. The recommended imaging review models vary according to the different overall or/and pulmonary status of these patients. For patients with lung cancer in the early stage and with a relatively good status, chest X-ray or CT every 6 months in the first 2 years posttreatment and subsequent yearly scanning is recommended.

Currently, both PET/CT and MRI are not recommended as routine monitoring methods in patients with lung cancer. The application of ^{18}F-FDG PET/CT in tumor monitoring apparently did not improve the global survival time of patients with lung cancer. However, whole-body ^{18}F-FDG PET/CT is superior because of its high diagnostic accuracy and its multisystem scope in NSCLC recurrence compared with the routine use of local CT scans (Fig. 3.13). For patients with lung cancer without suspicion of recurrence reviewed

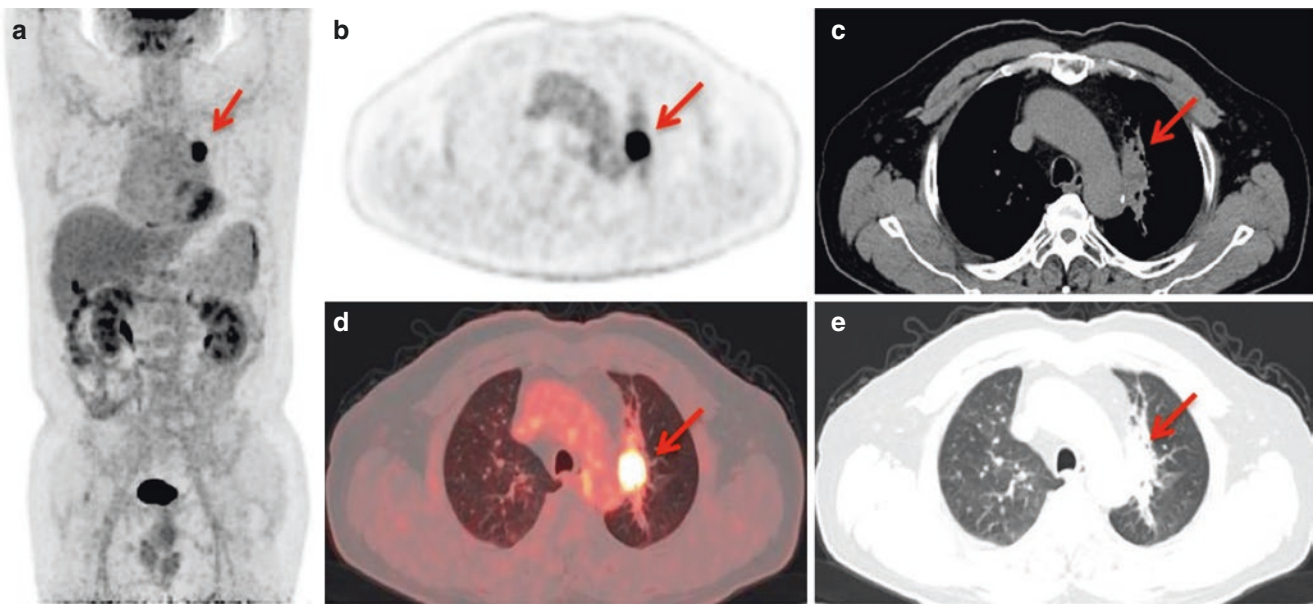

Fig. 3.13 A 66-year-old man with lung squamous carcinoma in the left superior lobe treated with chemo-radiotherapy for 1 year. ^{18}F-FDG PET/CT (**a**: maximum intensity projection image; **b**–**e**: axial images) showing lesion recurrence with radiation pneumonitis. (**b**), axial PET image; (**c**), axial CT image (mediastinal window); (**d**), axial fused PET/CT image; (**e**), axial CT image (lung window)

by traditional imaging methods, ^{18}F-FDG PET/CT can identify more than 40% of cases of recurrence and can rule out more than 20% of non-recurrence. For patients who are suspected to have suspicious recurrence, as assessed by CT scanning, the addition of ^{18}F-FDG PET/CT scanning changed the therapeutic strategy in about 30% of cases. The additional application of MRI is also recommended for patients with suspicious brain recurrence lesions.

How to use ^{18}F-FDG PET/CT as a helpful follow-up modality in lung cancer is a key question that should be discussed scientifically. The high glucose metabolism of primary lung cancer tumors before therapy always predicts poor patient outcome [31]. The glucose metabolism level can be indirectly quantified by parameters included in ^{18}F-FDG PET/CT, such as SUVmax, the metabolic tumor volume (MTV), and the total lesion glycolysis (TLG). High ^{18}F-FDG accumulation in primary tumor lesions is correlates closely with the increased risk of tumor invasiveness, tumor recurrence, and tumor-related death of surgically treated patients with lung cancer [32]. An ^{18}F-FDG PET/CT scan before surgery helps to screen patients whose primary tumor has abnormally high glucose metabolism, which might require more aggressive treatment after tumor resection [33].

The utility of ^{18}F-FDG PET/CT follow-up for nonsurgically treated patients with lung cancer is another key question, especially in locoregional recurrence monitoring in patients who underwent local radiotherapy. Although ^{18}F-FDG PET/CT increased the sensitivity of tumor detection compared with traditional CT, it still has disadvantages in post-radiotherapy monitoring. Local inflammation or fibrosis induced by radiotherapy are detected as PET-positive sites, which may be misleading in the diagnosis of tumor recurrence in primary or/and adjacent lesions or local lymph nodes, thus influencing tumor staging during follow-up. The two-time-point ^{18}F-FDG PET/CT scanning model might help to distinguish genuine local recurrence from inflammation or/and fibrosis, because recurrent lesions show a continually high uptake of ^{18}F-FDG, whereas the ^{18}F-FDG uptake level in benign lesions always decreases in delayed scanning.

In conclusion, ^{18}F-FDG PET/CT can sensitively detect suspicious recurrent lesions with abnormally high glucose metabolism in lung cancer follow-up. However, the value of ^{18}F-FDG PET/CT in lung cancer recurrence surveillance remains controversial. Determining how ^{18}F-FDG PET/CT can be used more reasonably and effectively in tumor monitoring should be addressed in future studies to maximize its clinical value.

3.2.3.3 Future Perspectives

^{18}F-FDG PET/CT has superiority in detecting glucose metabolic changes in recurrent lesions, which can be sensitively observed by PET before anatomical changes can be observed via other imaging modalities. Local inflammation induced by surgery or local radiotherapy is the main reason for false-positive recurrence results using ^{18}F-FDG PET, which limit the routine application of ^{18}F-FDG PET in tumor posttreatment monitoring. To prolong the total survival time of patients with lung cancer, regular review via all available examination methods is unavoidable in the follow-up period, especially in those patients in the early stage and with good body status. Future research should focus on the development of more effective molecular imaging agents, scanning models, and measurements to improve the diagnostic accuracy of ^{18}F-FDG PET/CT for tumor-related diseases, to effectively distinguish tumor recurrence from tumor-therapy-related benign diseases.

3.3 ^{18}F-FDG PET/CT for Non-small Cell Lung Cancer Therapy

Cancer treatment has significantly progressed over the past few decades. The combination of surgery and other modern nonsurgical treatment modalities has successfully made previously intractable malignancies curable. Radio- and chemotherapy are essential for tumor therapy. The monitoring of the early response of lung cancer to tumor therapy and possible recurrence during the follow-up period can affect individual management decisions.

3.3.1 Auxiliary Precise Radio-/Chemotherapy

The precise location of tumor lesions is the basis of local radical radiotherapy for almost all malignant tumors. In lung cancer, in addition to an accurate location, the precise estimation of the target tumor volume and the safe and effective therapeutic dose are essential for precise radiotherapy. The integration of multiple imaging modalities can help to achieve these goals. The most important advantage in scanning techniques for precious local radiotherapy is the introduction of computer-controlled multi-leaf collimator systems to CT scanning. Modern techniques, such as intensity-modulated radiotherapy (IMRT), three-dimensional conformal radiotherapy (3D-CRT), and volumetric arc radiotherapy (VMAT), which were derived from the combination of CT with multi-leaf collimator systems, help clinicians to accurately define the target volume, leading to a more effective and precise local radiotherapeutic strategy. Recently, MRI has also been applied in target volume delineation because of its high soft tissue resolution.

However, conventional CT and MRI cannot reflect all the changing features that occur in tumor lesions. ^{18}F-FDG PET provides an additional choice for tumor volume assessment at the biological (glucose metabolic) level. The standardized

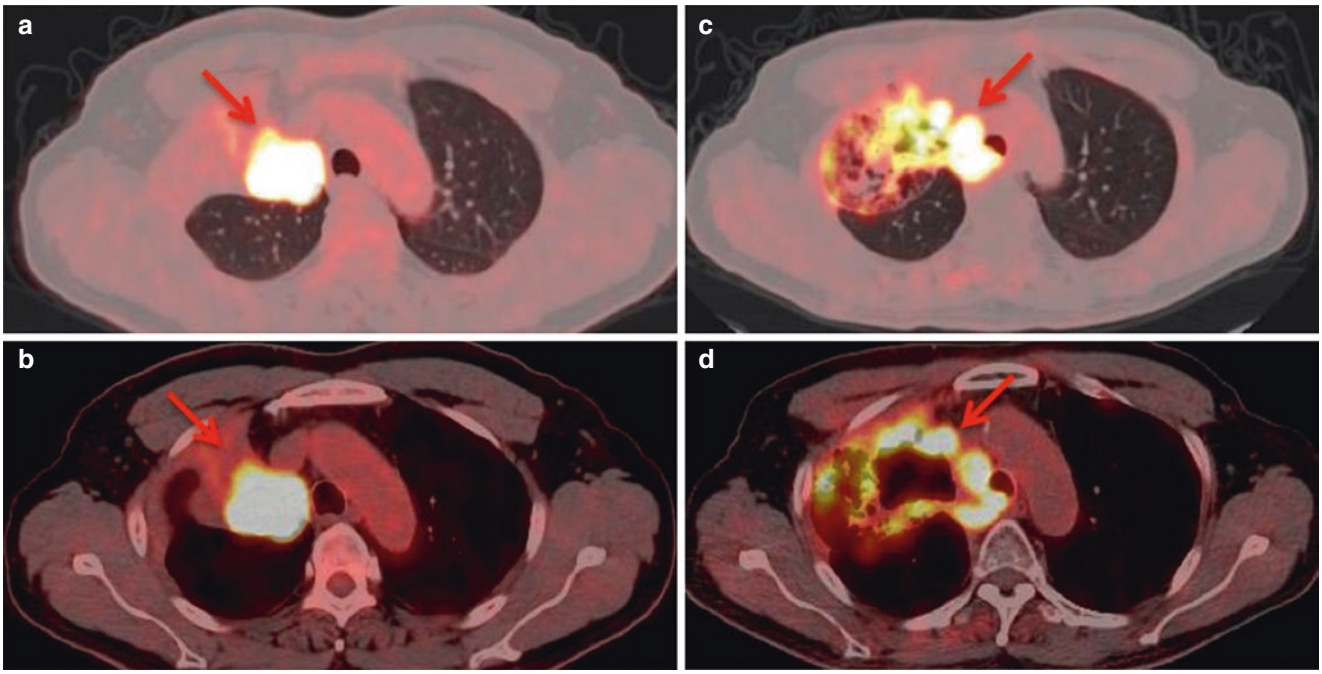

Fig. 3.14 A 53-year-old man with lung squamous carcinoma in the right upper lung lobe. Baseline axial fused (**a**) and (**b**) ^{18}F-FDGPET/CT images showing intense metabolic activity in a lung mass localized to the right upper lung lobe with obstructive atelectasis. Axial fused (**c**) and (**d**) ^{18}F-FDG PET/CT images obtained 1 month after completion of radiotherapy (total dose, 60 Gy) showing interval improvements in the lung mass with radiation-induced inflammation

lesion delineation (GTV) value of a tumor measured by ^{18}F-FDG PET/CT is the most valuable parameter to determine the tumor volume of lung cancer lesions. Different thresholds used in tumor contouring might lead to different results of GTV, and a threshold SUV of 2 ± 0.4 is most commonly used in tumor volume assessment [34, 35].

Compared with standard CT, ^{18}F-FDG PET/CT can more accurately evaluate the metabolically active tumor volume, which helps to minimize the local radiological dose, resulting as little damage as possible to the adjacent normal tissue. ^{18}F-FDG PET/CT can effectively distinguish malignant and atelectasis lesions, which might mistakenly be diagnosed as tumor tissues and induce unnecessary radiotherapy [36]. Moreover, ^{18}F-FDG PET/CT can detect metastatic lymph nodes sensitively, which might be invisible by traditional CT scanning, as well as ruling out suspicious mediastinal or hilar node metastasis of lung cancer detected by other imaging modalities [37]. Although the application of ^{18}F-FDG PET/CT did not improve the therapeutic effect of involved-field radiotherapy (IFRT) in patients with local lymph node metastasis, accurate ^{18}F-FDG PET/CT-based staging before radiotherapy significantly improved the prognosis of patients with lung cancer compared with that of traditional CT-based staging [38, 39]; therefore, ^{18}F-FDG PET/CT is suggested to replace traditional CT or MRI scanning before radiotherapy.

In addition to tumor volume assessment before radiotherapy, the evaluation of the curative effect of neoadjuvant chemotherapy (NC) in patients with lung cancer before surgery is also a key value of ^{18}F-FDG PET/CT in planning tumor therapeutic strategies. Patients with lung cancer whose primary tumors persistently accumulate ^{18}F-FDG after radio- or chemotherapy always have a relatively poor outcome compared with patients whose primary tumors show decreased ^{18}F-FDG after treatment. In some cases, the high uptake of ^{18}F-FDG post-therapy in tumor lesions might overlap with high ^{18}F-FDG uptake before treatment [40], and the increase in high ^{18}F-FDG uptake in tumor tissues after therapy might reflect the tumor's resistance to current radio- and chemotherapy. In other cases, locally persistent ^{18}F-FDG accumulation after therapy might be associated with inflammation or fibrotic lesions induced by radio- or chemotherapy (Fig. 3.14), which can persist for more than a year after tumor treatment [41].

3.3.2 Curative Effect Evaluation

About one-third of patients with lung cancer will suffer from malignant progression in the period of first-line chemotherapy. ^{18}F-FDG PET/CT is recommended as an ideal follow-up modality to evaluate the curative effect on lung cancer. The early metabolic response determined by ^{18}F-FDG PET in the second week after initial chemo-radiotherapy might predict the therapeutic effect of the therapeutic program, thus

providing reliable information to guide subsequent management decisions, as well as predicting patient outcome.

In addition to the well-known WHO criteria and the response evaluation criteria in solid tumors (RECIST), PET response criteria in solid tumors (PERCIST) calculated using the standard uptake value normalized to the lean body mass (SULpeak) are also recommended in lung cancer response assessment, comparing the ^{18}F-FDG uptake levels before and after therapy. In patients with lung cancer, the tumor metabolic response can also be determined using five-point scale PET-based response criteria, in which the ^{18}F-FDG uptake of the mediastinal blood pool and liver are recognized as standards. In this criteria system, focal ^{18}F-FDG uptake of tumor lesions less than or equal to that of the mediastinal blood pool is scored as 1, while uptake greater than that of the mediastinal blood pool, but less than that of the liver, is scored as 2, both of which are considered as a complete response. Diffuse ^{18}F-FDG uptake of tumor lesions greater than that of the mediastinal blood pool or liver is scored as 3 and is considered to represent inflammatory changes. Focal ^{18}F-FDG uptake of tumor lesions greater than that of the liver is scored as 4, while focal and intense ^{18}F-FDG uptake in tumor lesions greater than that of the liver is scored as 5, both of which are considered to indicate residual tumors. This five-point response system via ^{18}F-FDG PET has shown high accuracy in predicting patients' prognosis in multiple solid malignant tumors, whereas its application in lung cancer curative monitoring is still under investigation.

Although the high accuracy of ^{18}F-FDG PET/CT in the metabolic response evaluation in patients with lung cancer has been confirmed by many studies and ^{18}F-FDG PET/CT follow-up within 6 months after tumor therapy has been performed as an ideal modality to evaluate the curative response, the differences among the studies, such as the patients' features, imaging conditions, response evaluation criteria, and the analysis methods, make it hard to summarize an effective evaluation system for response assessment. Larger standard prospective global trials should be performed to identify accurate indexes derived from ^{18}F-FDG PET/CT to effectively evaluate the tumor response.

3.3.3 Effect of Treatment Response Assessed by ^{18}F-FDG PET/CT on Patient Management

^{18}F-FDG PET/CT can assess the early response of a malignant tumor to curative treatment and predicts the potential effect on current management, thus providing an opportunity to change ineffective therapeutic strategies during the early period of treatment and helping patients with lung cancer to achieve relatively long-term survival. For patients with lung cancer who need further aggressive treatment after surgery, the additional application of ^{18}F-FDG PET/CT within 6 months after tumor resection can effectively predict the validity of current treatment and tailor an ineffective management program in time [33, 42, 43]. In patients with lung cancer who lost the chance of surgical resection, early treatment response evaluation using ^{18}F-FDG PET/CT after nonsurgical treatment also helps clinicians to judge the efficiency of current therapy and influences the planning of subsequent treatment (Fig. 3.15).

The definition of nodal metastatic status before the development of surgical planning is necessary to select patients with stage III lung cancer who may benefit from surgery after intimal induction chemotherapy, especially for the appropriate treatment planning for patients with N2 or N3 disease. Although traditional CT is widely used in lymph node staging, it still has a relative high false-negative rate of 33% compared with that of ^{18}F-FDG PET (25%). Biopsy techniques, including mediastinoscopy, ultrasound (EBUS)-guided fine-needle aspiration, and primary mediastinoscopy, can reduce the false-negative rate of lymph node metastasis to 22%, 14%, and 9% [44], respectively. However, biopsy is invasive, and an accurate diagnosis sometimes requires repeated sampling. Inflammatory disease of the lymph node and surrounding fibrosis and adhesions might mislead physicians to puncture the wrong benign lesion, thus providing a false-negative diagnosis. As a noninvasive imaging modality, ^{18}F-FDG PET can be applied before biopsy to help locate the suspicious metastatic lymph nodes, thus improving the positive rate of biopsy and improving the accuracy of N staging before the next step in treatment planning.

Currently, invasive biopsy is still recommended as the gold standard for postsurgical diagnosis; the routine application of ^{18}F-FDG PET/CT in NSCLC restaging after antitumor therapy remains a matter of controversy, and there is insufficient evidence to prove the accurate tracing effect of ^{18}F-FDG PET/CT for metastatic lymph nodes. Sophisticated assessments, such as ^{18}F-FDG PET/CT combined with enhanced CT, MRI, EBUS or/and endoscopic ultrasound, can significantly improve the diagnostic accuracy of NSCLC restaging.

The value of ^{18}F-FDG PET/CT in NSCLC response assessment of chemo-/radiotherapy is acknowledged. However, the criteria for ^{18}F-FDG PET/CT-based response evaluation are still in development. Currently, the most frequently used evaluation guideline is the PET response evaluation criteria in solid tumors (PRECIST) criteria. However, PRECIST does not provide standard scanning processes, clear harmonization, accurate quantitative parameters, and specific cutoff values for ^{18}F-FDG PET/CT to evaluate a tumor's response to treatment. The different evaluation reference parameters from different institutions should be standardized globally to define an ideal ^{18}F-FDG PET evaluation system for tumor response.

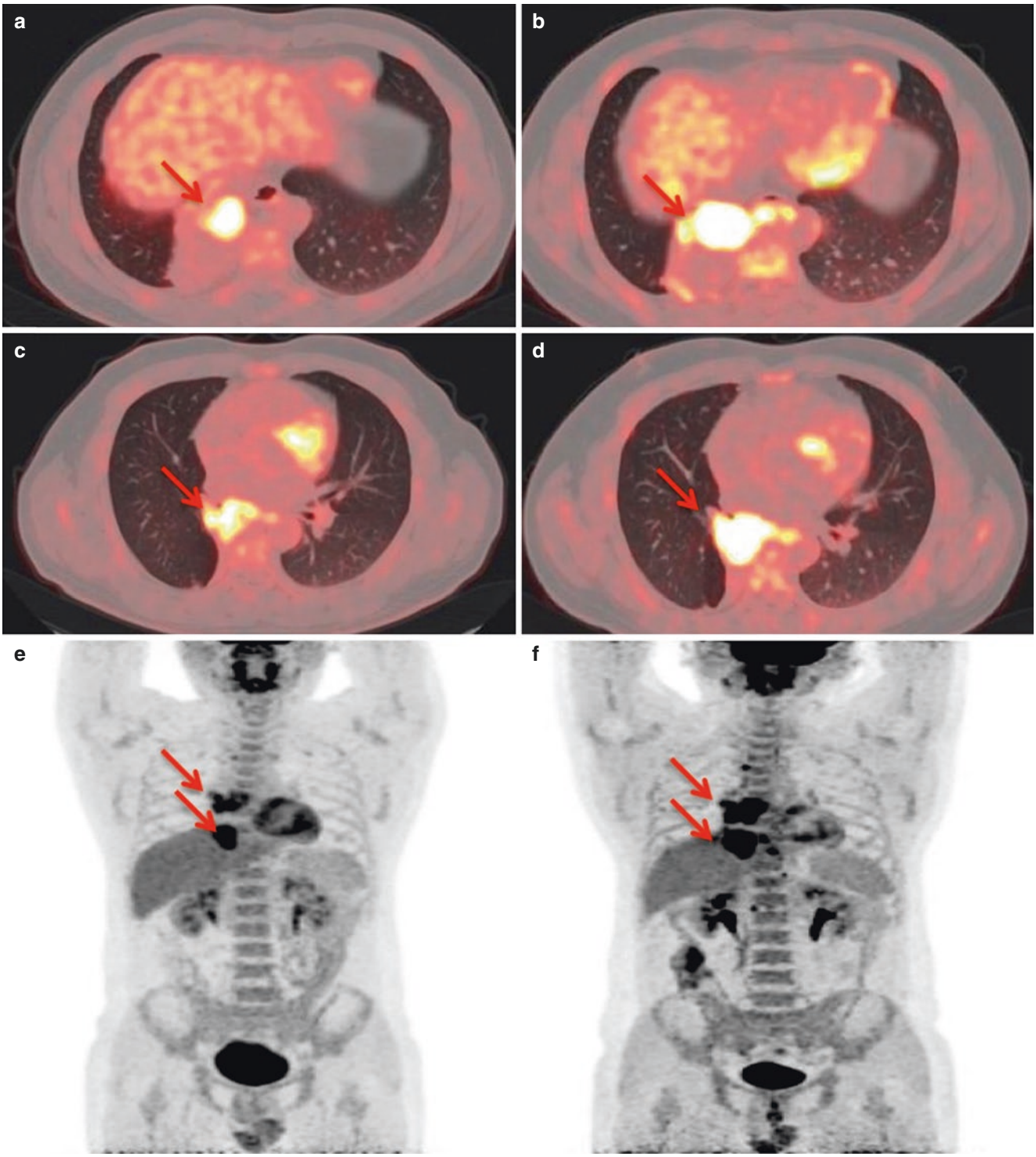

Fig. 3.15 A 38-year-old man with lung adenocarcinoma in the right lower lung lobe. Baseline [18]F-FDG PET/CT (**a** and **c**, axial fusion images; **e**, maximum intensity projection image) images showing intense metabolic activity in a lung mass localized to the right lower lung lobe with obstructive atelectasis. [18]F-FDG PET/CT images (**b** and **d**, axial fusion images; **f**, maximum intensity projection image) obtained 1 month after completion of five cycles of chemotherapy, showing progressive disease with enlarged lesions in a lung mass with obstructive atelectasis

Besides response evaluation accuracy, optimizing cost-effectiveness is another issue that must be considered. The standardized timing and frequency of ^{18}F-FDG PET scanning in NSCLC follow-up should also be defined in the future. The ^{18}F-FDG uptake features detected by PET correlate with pathological subtype, genotype, and the different biological behavior of NSCLC, for example, SQCC always accumulates more ^{18}F-FDG than ADC, NSCLC with an *EGFR* mutation showed lower ^{18}F-FDG uptake than NSCLC with wild-type *EGFR*, and a high level of ^{18}F-FDG always predicts worse prognosis. Thus, the evaluation criteria should vary according to the different genomic and clinicopathological profiles of NSCLC.

Future research will focus on gaining a comprehensive understanding of the glucose metabolic response of different subtypes of NSCLC in response to diverse therapeutic schemes, which will promote the development of standard PET response evaluation criteria for NSCLC.

References

1. Jemal A, Bray F, Center MM, Ferlay J, Ward E, Forman D (2011) Global cancer statistics. CA Cancer J Clin 61:69–90
2. Kim SK, Allen-Auerbach M, Goldin J, Fueger BJ, Dahlbom M, Brown M, Czernin J, Schiepers C (2007) Accuracy of PET/CT in characterization of solitary pulmonary lesions. J Nucl Med 48:214–220
3. Herder GJ, Golding RP, Hoekstra OS, Comans EF, Teule GJ, Postmus PE, Smit EF (2004) The performance of(18)F-fluorodeoxyglucose positron emission tomography in small solitary pulmonary nodules. Eur J Nucl Med Mol Imaging 31:1231–1236
4. Nomori H, Watanabe K, Ohtsuka T, Naruke T, Suemasu K, Uno K (2004) Evaluation of F-18 fluorodeoxyglucose (FDG) PET scanning for pulmonary nodules less than 3 cm in diameter, with special reference to the CT images. Lung Cancer 45:19–27
5. Lin YY, Chen JH, Ding HJ, Liang JA, Yeh JJ, Kao CH (2012) Potential value of dual-time-point (1)(8)F-FDG PET compared with initial single-time-point imaging in differentiating malignant from benign pulmonary nodules: a systematic review and meta-analysis. Nucl Med Commun 33:1011–1018
6. Ferlay J, Soerjomataram I, Dikshit R, Eser S, Mathers C, Rebelo M, Parkin DM, Forman D, Bray F (2015) Cancer incidence and mortality worldwide: sources, methods and major patterns in GLOBOCAN 2012. Int J Cancer 136:E359–E386
7. Delea T, Langer C, McKiernan J, Liss M, Edelsberg J, Brandman J, Sung J, Raut M, Oster G (2004) The cost of treatment of skeletal-related events in patients with bone metastases from lung cancer. Oncology 67:390–396
8. Ulas A, Bilici A, Durnali A, Tokluoglu S, Akinci S, Silay K, Oksuzoglu B, Alkis N (2016) Risk factors for skeletal-related events (SREs) and factors affecting SRE-free survival for non-small cell lung cancer patients with bone metastases. Tumour Biol 37:1131–1140
9. Bae HM, Lee SH, Kim TM, Kim DW, Yang SC, Wu HG, Kim YW, Heo DS (2012) Prognostic factors for non-small cell lung cancer with bone metastasis at the time of diagnosis. Lung Cancer 77:572–577
10. Nakamura H, Ando K, Shinmyo T, Morita K, Mochizuki A, Kurimoto N, Tatsunami S (2011) Female gender is an independent prognostic factor in non-small-cell lung cancer: a meta-analysis. Ann Thorac Cardiovasc Surg 17:469–480
11. Schirrmeister H, Arslandemir C, Glatting G, Mayer-Steinacker R, Bommer M, Dreinhofer K, Buck A, Hetzel M (2004) Omission of bone scanning according to staging guidelines leads to futile therapy in non-small cell lung cancer. Eur J Nucl Med Mol Imaging 31:964–968
12. Gaspar L, Scott C, Rotman M, Asbell S, Phillips T, Wasserman T, McKenna WG, Byhardt R (1997) Recursive partitioning analysis (RPA) of prognostic factors in three Radiation Therapy Oncology Group (RTOG) brain metastases trials. Int J Radiat Oncol Biol Phys 37:745–751
13. Hanibuchi M, Kim SJ, Fidler IJ, Nishioka Y (2014) The molecular biology of lung cancer brain metastasis: an overview of current comprehensions and future perspectives. J Med Invest 61:241–253
14. Dinnes J, Bancos I, Ferrante di Ruffano L, Chortis V, Davenport C, Bayliss S, Sahdev A, Guest P, Fassnacht M, Deeks JJ, Arlt W (2016) MANAGEMENT OF ENDOCRINE DISEASE: imaging for the diagnosis of malignancy in incidentally discovered adrenal masses: a systematic review and meta-analysis. Eur J Endocrinol 175:R51–R64
15. Stenbygaard LE, Sorensen JB, Larsen H, Dombernowsky P (1999) Metastatic pattern in non-resectable non-small cell lung cancer. Acta Oncol 38:993–998
16. Kagohashi K, Satoh H, Ishikawa H, Ohtsuka M, Sekizawa K (2003) Liver metastasis at the time of initial diagnosis of lung cancer. Med Oncol 20:25–28
17. D'Souza MM, Sharma R, Mondal A, Jaimini A, Tripathi M, Saw SK, Singh D, Mishra A, Tripathi RP (2009) Prospective evaluation of CECT and 18F-FDG-PET/CT in detection of hepatic metastases. Nucl Med Commun 30:117–125
18. Erasmus JJ, McAdams HP, Rossi SE, Goodman PC, Coleman RE, Patz EF (2000) FDG PET of pleural effusions in patients with non-small cell lung cancer. AJR Am J Roentgenol 175:245–249
19. Schaffler GJ, Wolf G, Schoellnast H, Groell R, Maier A, Smolle-Juttner FM, Woltsche M, Fasching G, Nicoletti R, Aigner RM (2004) Non-small cell lung cancer: evaluation of pleural abnormalities on CT scans with 18F FDG PET. Radiology 231:858–865
20. Herder GJ, Kramer H, Hoekstra OS, Smit EF, Pruim J, van Tinteren H, Comans EF, Verboom P, Uyl-de Groot CA, Welling A, Paul MA, Boers M, Postmus PE, Teule GJ, Groen HJ, POORT Study Group (2006) Traditional versus up-front [18F] fluorodeoxyglucose-positron emission tomography staging of non-small-cell lung cancer: a Dutch cooperative randomized study. J Clin Oncol 24:1800–1806
21. Viney RC, Boyer MJ, King MT, Kenny PM, Pollicino CA, McLean JM, McCaughan BC, Fulham MJ (2004) Randomized controlled trial of the role of positron emission tomography in the management of stage I and II non-small-cell lung cancer. J Clin Oncol 22:2357–2362
22. Maziak DE, Darling GE, Inculet RI, Gulenchyn KY, Driedger AA, Ung YC, Miller JD, Gu CS, Cline KJ, Evans WK, Levine MN (2009) Positron emission tomography in staging early lung cancer: a randomized trial. Ann Intern Med 151:221–8, W-248
23. Fischer B, Lassen U, Mortensen J, Larsen S, Loft A, Bertelsen A, Ravn J, Clementsen P, Hogholm A, Larsen K, Rasmussen T, Keiding S, Dirksen A, Gerke O, Skov B, Steffensen I, Hansen H, Vilmann P, Jacobsen G, Backer V, Maltbaek N, Pedersen J, Madsen H, Nielsen H, Hojgaard L (2009) Preoperative staging of lung cancer with combined PET-CT. N Engl J Med 361:32–39
24. MacManus MP, Hicks RJ, Matthews JP, Hogg A, McKenzie AF, Wirth A, Ware RE, Ball DL (2001) High rate of detection of unsuspected distant metastases by pet in apparent stage III non-small-cell lung cancer: implications for radical radiation therapy. Int J Radiat Oncol Biol Phys 50:287–293

25. Reed CE, Harpole DH, Posther KE, Woolson SL, Downey RJ, Meyers BF, Heelan RT, MacApinlac HA, Jung SH, Silvestri GA, Siegel BA, Rusch VW, American College of Surgeons Oncology Group Z0050 Trial (2003) Results of the American College of Surgeons Oncology Group Z0050 trial: the utility of positron emission tomography in staging potentially operable non-small cell lung cancer. J Thorac Cardiovasc Surg 126:1943–1951
26. Lardinois D, Weder W, Hany TF, Kamel EM, Korom S, Seifert B, von Schulthess GK, Steinert HC (2003) Staging of non-small-cell lung cancer with integrated positron-emission tomography and computed tomography. N Engl J Med 348:2500–2507
27. Kozower BD, Meyers BF, Reed CE, Jones DR, Decker PA, Putnam JB Jr (2008) Does positron emission tomography prevent nontherapeutic pulmonary resections for clinical stage IA lung cancer? Ann Thorac Surg 85:1166–1169; discussion 1169–1170.
28. De Wever W, Ceyssens S, Mortelmans L, Stroobants S, Marchal G, Bogaert J, Verschakelen JA (2007) Additional value of PET-CT in the staging of lung cancer: comparison with CT alone, PET alone and visual correlation of PET and CT. Eur Radiol 17:23–32
29. Carnio S, Novello S, Papotti M, Loiacono M, Scagliotti GV (2013) Prognostic and predictive biomarkers in early stage non-small cell lung cancer: tumor based approaches including gene signatures. Transl Lung Cancer Res 2:372–381
30. Jimenez-Bonilla JF, Quirce R, Martinez-Rodriguez I, Banzo I, Rubio-Vassallo AS, Del Castillo-Matos R, Ortega-Nava F, Martinez-Amador N, Ibanez-Bravo S, Carril JM (2013) Diagnosis of recurrence and assessment of post-recurrence survival in patients with extracranial non-small cell lung cancer evaluated by 18F-FDG PET/CT. Lung Cancer 81:71–76
31. Liu J, Dong M, Sun X, Li W, Xing L, Yu J (2016) Prognostic value of 18F-FDG PET/CT in surgical non-small cell lung cancer: a meta-analysis. PLoS One 11:e0146195
32. Ito R, Iwano S, Kishimoto M, Ito S, Kato K, Naganawa S (2015) Correlation between FDG-PET/CT findings and solid type non-small cell cancer prognostic factors: are there differences between adenocarcinoma and squamous cell carcinoma? Ann Nucl Med 29:897–905
33. Chaft JE, Dunphy M, Naidoo J, Travis WD, Hellmann M, Woo K, Downey R, Rusch V, Ginsberg MS, Azzoli CG, Kris MG (2016) Adaptive neoadjuvant chemotherapy guided by (18)F-FDG PET in resectable non-small cell lung cancers: the NEOSCAN trial. J Thorac Oncol 11:537–544
34. Ciernik IF, Dizendorf E, Baumert BG, Reiner B, Burger C, Davis JB, Lutolf UM, Steinert HC, Von Schulthess GK (2003) Radiation treatment planning with an integrated positron emission and computer tomography (PET/CT): a feasibility study. Int J Radiat Oncol Biol Phys 57:853–863
35. Erdi YE, Rosenzweig K, Erdi AK, Macapinlac HA, Hu YC, Braban LE, Humm JL, Squire OD, Chui CS, Larson SM, Yorke ED (2002) Radiotherapy treatment planning for patients with non-small cell lung cancer using positron emission tomography (PET). Radiother Oncol 62:51–60
36. Hellwig D, Baum RP, Kirsch C (2009) FDG-PET, PET/CT and conventional nuclear medicine procedures in the evaluation of lung cancer: a systematic review. Nuklearmedizin 48:59–69, quiz N58–59.
37. De Wever W, Stroobants S, Coolen J, Verschakelen JA (2009) Integrated PET/CT in the staging of nonsmall cell lung cancer: technical aspects and clinical integration. Eur Respir J 33:201–212
38. Rosenzweig KE, Sura S, Jackson A, Yorke E (2007) Involved-field radiation therapy for inoperable non small-cell lung cancer. J Clin Oncol 25:5557–5561
39. Grills IS, Hope AJ, Guckenberger M, Kestin LL, Werner-Wasik M, Yan D, Sonke JJ, Bissonnette JP, Wilbert J, Xiao Y, Belderbos J (2012) A collaborative analysis of stereotactic lung radiotherapy outcomes for early-stage non-small-cell lung cancer using daily online cone-beam computed tomography image-guided radiotherapy. J Thorac Oncol 7:1382–1393
40. Aerts HJ, van Baardwijk AA, Petit SF, Offermann C, Loon J, Houben R, Dingemans AM, Wanders R, Boersma L, Borger J, Bootsma G, Geraedts W, Pitz C, Simons J, Wouters BG, Oellers M, Lambin P, Bosmans G, Dekker AL, De Ruysscher D (2009) Identification of residual metabolic-active areas within individual NSCLC tumours using a pre-radiotherapy (18)Fluorodeoxyglucose-PET-CT scan. Radiother Oncol 91:386–392
41. Larici AR, del Ciello A, Maggi F, Santoro SI, Meduri B, Valentini V, Giordano A, Bonomo L (2011) Lung abnormalities at multimodality imaging after radiation therapy for non-small cell lung cancer. Radiographics 31:771–789
42. William WN Jr, Pataer A, Kalhor N, Correa AM, Rice DC, Wistuba II, Heymach J, Lee JJ, Kim ES, Munden R, Gold KA, Papadimitrakopoulou V, Swisher SG, Erasmus JJ, University of Texas M.D. Anderson Lung Cancer Collaborative Research Group (2013) Computed tomography RECIST assessment of histopathologic response and prediction of survival in patients with resectable non-small-cell lung cancer after neoadjuvant chemotherapy. J Thorac Oncol 8:222–228
43. van Loon J, Grutters JP, Wanders R, Boersma L, Dingemans AM, Bootsma G, Geraedts W, Pitz C, Simons J, Brans B, Snoep G, Hochstenbag M, Lambin P, De Ruysscher D (2010) 18FDG-PET-CT in the follow-up of non-small cell lung cancer patients after radical radiotherapy with or without chemotherapy: an economic evaluation. Eur J Cancer 46:110–119
44. de Cabanyes Candela S, Detterbeck FC (2010) A systematic review of restaging after induction therapy for stage IIIa lung cancer: prediction of pathologic stage. J Thorac Oncol 5:389–398

Clinical Application of ^{18}F-FDG PET/CT in Lymphoma

4

Xiaoli Lan, Altine Bouhari, Khamis Hassan Bakari, and Alexandre Niyonkuru

4.1 Introduction

Lymphoma is one of the medical diseases which has more than 80% successful treatment, and it is one of the frequent carcinogenic healthcare conditions. The treatment efficacy of lymphoma is rendered possible by combination therapy such as chemotherapy with radiotherapy or sometimes chemotherapy alone. Thomas Hodgkin first introduced this disease in 1832 by reviewing seven cases. The immunohistochemistry (IHC) examination of these cases lately revealed that two different types of lymphoma were actually described in his paper. By today's standard techniques, most cases described in his original paper were "Hodgkin's lymphomas (HL)," while only one case was recognized as "non-Hodgkin's lymphoma" (NHL) [1].

Over the past 60 years, many competing lymphoma classifications have been introduced, and the classification of lymphoma is a historical issue. The development of new medical instrument and the advance of medical field achieved great success in diagnosing and treatment of lymphoma. Medical imaging instruments, such as CT, MRI, and PET/CT, have played important roles in the management of lymphoma patients. PET/CT with ^{18}F-FDG is nowadays one of the prominent and necessary tools in diagnosis, staging, and therapy evaluation of lymphoma.

4.1.1 Epidemiology of Lymphoma

The prevalence of lymphoma varies based on the geographical location of patient population. Lymphoma is commonly found in the developed countries. The prevalence of all types of lymphomas represented 5.3% of malignant diseases and 55.6% of blood malignant tumors in America. A report from the US NIH has suggested lymphoma and HL account for 5% and less than 1% of malignant tumors, respectively [2]. The immune cells are an essential part of the circulation system, and patients with immune deficiency caused by virus infection or drugs tend to have a high risk of developing lymphoma.

4.1.2 Clinical Features of Lymphoma

The clinical manifestations of patient with lymphoma may be presented with certain nonspecific symptoms. Lymphadenopathy or swelling of lymph nodes is the primary presentation in lymphoma. Hematopoietic B-cell symptoms, systemic symptoms, can be associated with both HL and NHL; these symptoms are fever, night sweats, and weight loss. Other symptoms may be loss of appetite or anorexia, fatigue, respiratory distress or dyspnea, and itching.

4.1.3 Diagnosis of Lymphoma

The gold-standard diagnosis method of lymphoma is the pathological diagnosis, which is done by lymph node or involved lesion biopsy. This test indicates the histopathological features that may conclude lymphoma. After lymphoma has been confirmed, a variety of tests may be carried out to look for specific features characteristic of different types of lymphoma. These tests include IHC, immunophenotyping, flow cytometry, and fluorescence in situ hybridization.

4.2 Clinical Pathology Types and Metabolic Features of Lymphoma

4.2.1 Pathological Types of Lymphoma

Several classification systems have existed for lymphoma, which use histological and other findings to divide lymphoma

X. Lan (✉) · A. Bouhari · K. H. Bakari · A. Niyonkuru
Department of Nuclear Medicine, Union Hospital, Tongji Medical College, Huazhong University of Science and Technology, Wuhan, P. R. China
e-mail: 2006xh0807@hust.edu.cn

G. Huang (ed.), *Nuclear Medicine in Oncology*, https://doi.org/10.1007/978-981-13-7458-6_4

into different categories. The classification of a lymphoma can affect treatment and prognosis. Classification systems generally classify lymphoma according to:

1. Whether it is a HL or NHL
2. Whether the cell that is replicating is a T cell or B cell
3. The site from which the cell arises

4.2.1.1 Hodgkin's Lymphoma

HL was described in 1898 and 1902 by Carl Sternberg and Dorothy Reed as doubled nucleated giant cells called Reed-Sternberg cells. Therefore, RS cells are used as the histopathological characteristics of HD. The origin of typical RS cells is unclear. Some studies related them to follicular B-cell origin from highly mutant cells, and other studies believed that they belonged to T cells or dendritic cells. HL is divided into nodular lymphocyte-predominant Hodgkin's lymphoma (NLPHL) and classical Hodgkin's lymphoma. The latter includes four types: nodular sclerosis (NSHL; Lukers and Butler 1960), mixed cellularity type (MCHL), lymphocyte depletion type (LDHL), and lymphocyte-rich type.

4.2.1.2 Non-Hodgkin's Lymphoma

NHLs are large group of heterogeneous diseases. They are differentiated by histopathologic morphology and cell pattern among different types, which can be derived from B-lymphocyte set and T-lymphocyte set. In recent decades, the pathological research of malignant lymphoma has made great progress due to the application of new technologies such as immunohistochemistry, chemistry, cell quantitative analysis, molecular biology, and molecular genetics. NHL was classified from the Rappaport classification (1966) to the Lukes and Collins classification (1975), the international NHL classification (1982), and then the new Kiel classification (1992), REAL (1994), and WHO classification (2000). The classification progress was shown from simple morphology to morphology and function of the combination, then the clinical classification which include morphology, immunophenotyping, and cytogenetics combined with the evolutional processes. The work of classification of lymphoma developed by WHO was accepted and applied by pathologists and clinicians from all over the world. The typing method has good reproducibility, and it can be divided into low grade, moderate malignant, and highly malignant. It can better indicate the prognosis and make corresponding treatment plan. Different from HL, NHL is the result of cell monoclone, so the involved lymph nodes have single component under the electron microscope, mainly based on one cell type. We can determine the source of tumor cells according to their different types, which is the most important basis for classification.

4.2.2 Characteristics of Glucose Metabolism in Some Common Lymphoma

4.2.2.1 Hodgkin's Lymphoma

The lymphocytes of HL are believed to be mostly derived from B-cell germinal centers, and most of HL have higher ^{18}F-FDG uptake. Hutching M and others [3] pointed out that ^{18}F-FDG uptake in involved lesions significantly increased in HL patients but the mean value of SUVmax is different in various clinical subtypes. The mean SUVmax of classical HL (CHL) lesions was significantly higher than that of nodular lymphocyte-predominant (NLP) lymphoma. Similarly, the mean SUVmax of nodular sclerosis (NS) lymphoma was also significantly higher than NLP but lower than that of mixed cell (MC)-type lymphoma lesion. The studies of Döbert N et al. [4] showed that the mean SUVmax of NS lymphoma is twice higher than that of NLP and the mean SUVmax of MC lymphoma is slightly higher than that of NLP. Although the ^{18}F-FDG uptake of classical lymphomas is higher than that of NLP, the different glucose metabolic degree among different types of HL is not consistent.

4.2.2.2 Non-Hodgkin's Lymphoma

NHL is consisted of different tissue types. This differentiated tissue types determined the degree of malignancy which are shown by a quite different ^{18}F-FDG uptake in PET/CT. Hoffmann et al. [5] indicated in their research that SUV can be used to differentiate aggressive from indolent lymphoma. Histology of subtypes of lymphoma tissue was used to explain the correlation with PET/CT images. They found that the SUV value in non-transformed follicular lymphoma (FL) was much higher than that of other types of indolent lymphoma (MZL or SLL/CLL), and most of indolent lymphomas which underwent transformation had higher SUV value than non-transformed ones. The studies of Elstrom R and Weiler-Sagie M [6, 7] showed that the PET/CT-positive rate was 100% in diffuse large B-cell lymphoma (DLBCL) and mantle cell lymphoma (MCL), 98% in HL and FL, only 67% in lymph node marginal zone B-cell lymphoma (MZBCL), and 40% in peripheral T-cell lymphoma (PTCL). PET/CT is not the best method to detect whether the bone marrow is involved. There are few bone marrow abnormalities which could not be detected by PET/CT in DLBCL and HL, only a small proportion of confirmed bone marrow lesions could be detected in FL, and the abnormal bone marrow lesions could be hardly detected in MCL or MZL. Schoder H [8] presented other types of classification of invasive, indolent lymphoma and MCL. The SUV range of indolent lymphoma was 2.3–13.0, invasive lymphoma was from 3.2 to 43.0, and in group of MCL was 4.7–8.7. An obvious uptake of ^{18}F-FDG was detected in more aggressive lymphomas (SUV > 13 in this study), which suggested the characteristic of tumor invasion.

However, lower ^{18}F-FDG uptake does not indicate the indolent lymphoma or lower invasive features. In this study, cases with lower ^{18}F-FDG uptake (SUV < 13) accounted of 22/63 (35%) of invasive lymphoma patients, and the lesions with SUV < 10 include 81% of indolent lymphoma. In indolent lymphoma, when the SUV values increase significantly, the type of lymphoma should be highly associated to transform to invasive lymphoma. Therefore, it is suggested that the corresponding high metabolic lesions should be taken out for biopsy and the type or subtype of lymphoma should be identified to guide the treatment regimens. Most of the studies have pointed out that the ^{18}F-FDG uptake is associated with the degree of malignancy of the lesion and provided the best site of biopsy through PET/CT. Jerusalem G et al. [9] assessed that for the patients with indolent lymphoma, PET can only detect part of the involved lesions (40–98%). In patients with small lymphocytic lymphoma (SLL), only 58% of CT-detected abnormal lesions can be detected by PET. Some relevant studies suggested the limitations of PET in mantle-zone lymphoma (MZL) and peripheral T-cell lymphoma (PTCL).

4.3 Clinical Application of ^{18}F-FDG PET/CT in Lymphoma

4.3.1 ^{18}F-FDG PET/CT for Diagnosis of Lymphoma

PET is a noninvasive imaging modality that uses a radiopharmaceutical to target a certain physiological function such as glucose metabolism, amino acid metabolism, DNA synthesis, etc. The most commonly used radiopharmaceutical during PET imaging is the radiolabeled glucose analog fluorine-18-deoxyglucose (^{18}F-FDG).

Recently, PET has emerged as the most essential tool in the assessment of lymphoma. The sensitivity and specificity of PET has been described to be higher in HL and in majority subtypes of indolent and aggressive NHL. Isasi et al. narrated that in various lymphoma, ^{18}F-FDG PET has the median sensitivity and specificity of 90% and 91%, respectively, and 93% and 88%, respectively, in Hodgkin's lymphoma [10].

PET has also been shown to have higher sensitivity, specificity, and diagnostic accuracy in detection of primary splenic lymphoma (PSL). Several authors have documented that the sensitivity and specificity of detecting splenic involvement in malignant lymphoma were 100% and 95%, respectively [11], and also the sensitivity, specificity, and accuracy for detection of splenic involvement in lymphoma were 100%, 100%, and 100%, respectively.

Karunanithi et al. [12] in their study of PSL found that the overall sensitivity, specificity, and accuracy were 96.2%, 91.7%, and 94%, respectively. The two false-positive PET/CTs and one false-negative PET/CT all belong to the restaging group. The two false-positive studies were due to liver lesions (hepatitis-related ^{18}F-FDG uptake on biochemical imaging), and the one false-negative study was due to splenic enlargement, although ^{18}F-FDG uptake was not elevated. Therefore, ^{18}F-FDG uptake in lymphoma relies on histopathological type, grade, and Ki-67 index of the tumor [13].

^{18}F-FDG PET false-positive findings of lymphoma are due to either infection or inflammatory changes presumably therapy induced. Inflammatory tissue usually contains neutrophils and activated macrophages that are ^{18}F-FDG avid and very difficult to distinguish from viable residual tumor during FDG PET scanning. Consequently, low-grade lymphoma depicting poor ^{18}F-FDG avidity may cause false-negative findings.

Various detection rates of ^{18}F-FDG PET/CT in gastric mucosa-associated lymphoid tissue (MALT) lymphoma have been described. Numerous authors have shown that the detection rate of ^{18}F-FDG PET/CT in gastric MALT lymphoma were 50% [14], 62% [15], and 60% [16].

Regarding bone marrow involvement, ^{18}F-FDG PET/CT has been shown to significantly improve its detection with a twofold increase in the diagnosis of bone marrow involvement in HL compared to diagnosis by histopathology alone. Published reports have indicated that PET diffusely increases ^{18}F-FDG uptake in the axial skeleton or in the long bones [17], the sensitivity of ^{18}FDG PET/CT in the diagnosis of bone marrow involvement is close to 97%, and the percentage of ^{18}F-FDG PET/CT-negative patients with a positive biopsy among all subjects stands at around 1.1% [18]. Moreover, PET/CT may aid in providing relevant information in determining the appropriate site for target biopsy in patients with suspected transformation of indolent disease to aggressive histology, due to the fact that aggressive lymphoma is more FDG avid than indolent ones.

In addition, ^{18}F-FDG PET/CT is a valuable imaging tool in differentiating between HIV-related brain infection such as toxoplasmosis and primary central nervous system lymphoma (PCNSL) [19]. Primary brain lymphoma has been shown to have increased ^{18}F-FDG uptake as a result of elevated cellular density and heightened glucose metabolism [20].

4.3.2 ^{18}F-FDG PET/CT for Staging of Lymphoma

Treatment of lymphoma patients depends on the histological subtype, pretreatment identification of disease risk factors, and accurate staging. Staging refers to determining the extent of tumor metastases whether locally or to distant sites. The main aim of staging is assessment, promotion of better patient management, establishment of more effective

therapies, and adoption of new treatment protocols by relevant regulatory authorities. Historically, staging of lymphoma was based on a number of assumptions. In its initial stage, HL usually spreads to its adjacent sites; the treatment of choice is the extended field radiation while chemotherapy is preserved for advanced disease due to its unrecognized efficacy and significant toxicity.

Initially, several classification systems of lymphoma have existed which are Rye classification of 1966 [21], Ann Arbor classification of 1971, [22] and WHO classification first published in 2001 and updated in 2008 [23]. Currently, the Ann Arbor staging system is routinely used for staging of both HL and NHL (Table 4.1).

Lymphoma can also metastasize to the central nervous system usually around brain meninges which is referred to as lymphomatous meningitis [24]. Staging of lymphoproliferative process is carried out according to bone marrow biopsy and CT intravenous contrast. Nonetheless, in the last decade, ^{18}F-FDG PET/CT has shown better diagnostic ability in detecting lymph node and extra lymph node involvement prior to treatment, hence permitting more accurate and effective staging of lymphomas based on Ann Arbor classification with the Cotswolds modification (Table 4.1).

Table 4.1 Ann Arbor classification (Cotswolds modification) for staging of lymphomas

Stages	Descriptions
Stage I	Involvement of a single lymph node region or lymphoid structure (i.e., spleen, thymus, Waldeyer's ring) (Fig. 4.1)
Stage II	Involvement of two or more lymph node regions on the same side of the diaphragm (the mediastinum is a single site: the hilum includes one on each side); the number of sites is indicated with a subset (i.e., II3)
Stage III	Involvement of lymphatic regions or lymphatic structures on both sides of the diaphragm (Fig. 4.2)
III_1	Upper abdomen (splenic, celiac, portal)
III_2	Lower abdomen (para-aortic, mesenteric)
Stage IV	Involvement of extranodal sites beyond those indicated as visceral involvement (Fig. 4.3)
Applicable to any stage	
A	No B symptoms
B	Fever, nocturnal sweats, loss of more than 10% of body weight in the previous 6 months
X	Bulky disease: mediastinal widening ˃1/3 measured at the T5–T6 level or mass ˃10 cm
E	Involvement of a single extranodal site contiguous next to the known lymph node localization
S	Splenic involvement

Recently, ^{18}F-FDG PET/CT has been used as a standard imaging modality for staging, restaging, surveillance of recurrence, and evaluation of therapy response of lymphoma. Compared to conventional imaging modalities, ^{18}F-FDG PET/CT is much more sensitive, accurate, and reliable in evaluating therapeutic responses in lymphoma. Unlike CT, which solely focus on anatomical characteristics of a tumor, ^{18}F-FDG PET/CT shows both metabolic and functional status of the lesions which can be semi-quantified by SUV. Hybrid PET/CT provides more advantages in staging compared to CT or PET alone, by expressing a greater number of lesions, mostly at an extra lymph node level in HD, DLBCL, FL, and mantle cell lymphoma (MCL).

Previous published data has observed that the pooled sensitivity and a false-positive rate of ^{18}F-FDG PET/CT in staging lymphoma were 91% and 10%, respectively [10]. Several studies have also identified that, for lesion-based analysis, the maximum joint sensitivity and specificity of ^{18}F-FDG PET/CT was found to be 96% exceeding the corresponding values for contrast-enhanced CT (CECT) [25]. ^{18}F-FDG PET/CT has also been shown to upstage as many as 30% of patients [10]. In another study by Schaefer et al., they showed that the sensitivity and specificity of PET/CT and CECT for both nodal disease in HL and aggressive NHL were higher than that of CT, 94% vs. 88% and 100 vs. 86%, respectively [26]. Regarding extranodal involvement, the sensitivity of PET/CT was almost twice than that of CECT, and the specificities were similar, 88% vs. 50% and 100% vs. 90%, respectively [26]. CECT is a valuable diagnostic tool for

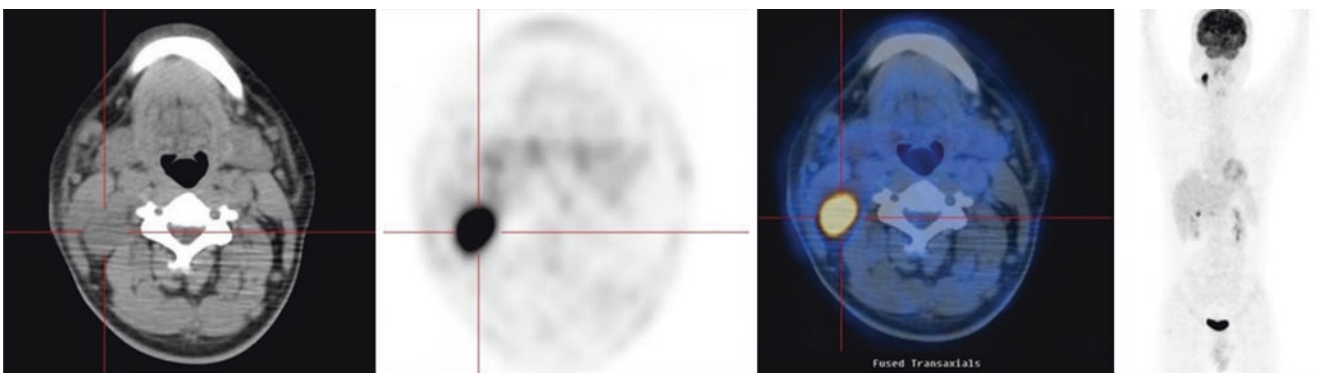

Fig. 4.1 A 34-year-old male, HL, only one lymph node involved (stage I)

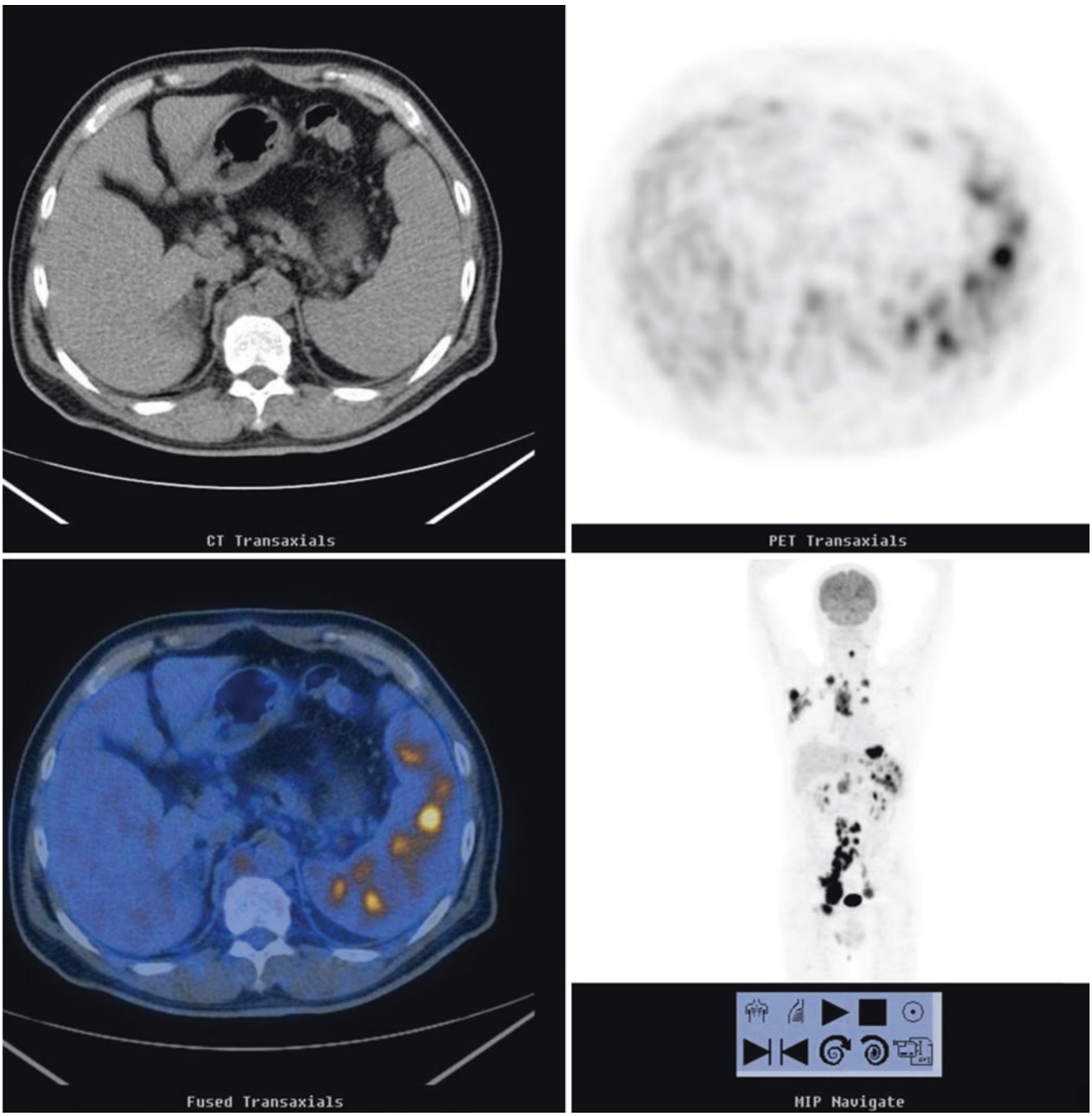

Fig. 4.2 A 64-year-old male, DLBCL, involvement of lymphatic regions or lymphatic structures on both sides of the diaphragm, the spleen also involved (stage III)

differentiating lymph nodes from vessels and unopacified bowel loops in the abdomen and pelvis. In Kwee TC et al. research, in initial staging of lymphoma, the sensitivity of ^{18}F-FDG PET/CT was almost similar to that of CT, 85.6% vs. 87.5%, while its specificity was higher than that of CT, 100% vs. 87.5% [27].

However, numerous literatures have also indicated that ^{18}F-FDG PET/CT has a lower sensitivity of 25–30% in indolent NHL subtypes depending on the low grade and density of malignant cells [25]. Previous reports have also mentioned that indolent lymphomas appear to have variable avidity for ^{18}F-FDG with less avidity compared with that of aggressive HD and NHL. Thus, some authors recommended the exclusive usage of initial diagnostic CT for staging of indolent NHL, such as marginal zone small cell lymphocytic lymphomas and that associated with the mucosa (MALT), while performing ^{18}F-FDG PET/CT only in clinical researches.

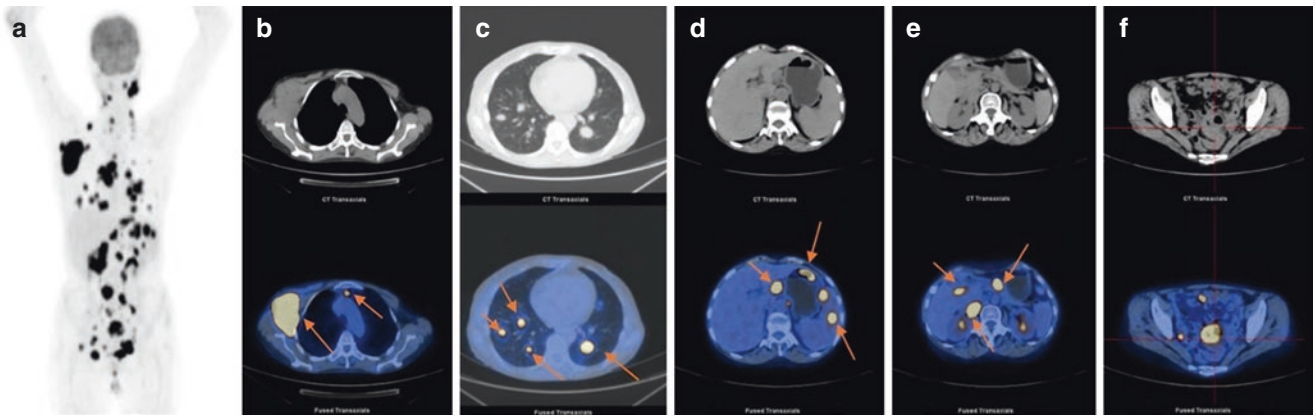

Fig. 4.3 A 60-year-old female, B-cell lymphoma, except for lymph nodes, some organs also involved, such as the lung, liver, pancreas, and small intestine (stage IV)

Furthermore, PET has also been recognized to possess good capacity of analyzing bone marrow involvement by lymphoma, even in cases with a negative biopsy results. On the other hand, when the bone marrow involvement is limited or in indolent lymphomas, the yield of functional imaging is generally poorer [28]. However, the sensitivity and specificity of PET/CT in evaluating bone marrow involvement of limited or indolent lymphomas were found to be 91% and 90%, respectively, thus influencing the best choice for the localization of biopsy [25]. In HD, widespread uptakes of the bone marrow prior to therapy doesn't necessarily mean involvement of the same but rather due to the presence of focal reactive hyperplasia.

Regarding the CT component of PET/CT, the use of intravenous contrast in the staging of lymphoma is still refutable. Different studies [29] have found the existence of high similarities between the low-dose CT findings (approximately 80 mAs in the hybrid PET/CT study) and those of standard- and contrast-dose CT (kappa 0.9), hence concluding that PET/CT could be indicated for the staging of lymphomas using a low-dose CT component without intravenous contrast. This will significantly reduce the exposure of patients to unnecessary radiation mainly in HD, FL, and DLBCL, thereby limiting the use of higher-dose and contrast-enhanced CT for selected patients.

Another option is the incorporation of PET/CT with intravenous contrast for initial staging and then proceeds with the follow-up of these patients with low-dose studies devoid of contrast, with the exception of cases with negative PET findings at the onset.

Published literatures have reported that primary hepatic MALT lymphoma had positive ^{18}F-FDG PET/CT showing ^{18}F-FDG uptake (average SUVmax was 5.62 ± 1.6) at corresponding liver lesion and that ^{18}F-FDG PET/CT was crucial in evaluating treatment response of chemotherapy and radiotherapy in these patients [30]. Treglia et al. in their study have also described that MALT lymphomas especially those located in the bronchus, head, and neck were generally ^{18}F-FDG-avid tumors [31]. Furthermore, earlier study has shown that, out of the 69 histologically confirmed gastric MALT lymphoma patients who underwent initial staging using ^{18}F-FDG PET/CT, 36 patients (52%) had a positive ^{18}F-FDG PET/CT with average SUVmax of 9 ± 6.7 at the corresponding gastric lesion with the remaining 33 patients showing negative ^{18}F-FDG PET/CT findings [32].

The importance of ^{18}F-FDG PET/CT in the initial staging and restaging following therapy of patients with primary cutaneous lymphoma cannot be ignored. A study by Kumar et al. [33] has indicated that for initial staging of primary cutaneous lymphoma, ^{18}F-FDG PET had a sensitivity of 82% for evaluation of local disease and 80% for the detection of distance metastases. While for restaging of cutaneous lymphoma, ^{18}F-FDG PET was found to have a sensitivity of 86% and a specificity of 92% for local recurrence/residual disease and a sensitivity of 100% and specificity of 100% for distant metastases.

4.3.3 ^{18}F-FDG PET/CT for Monitoring Therapy Response of Lymphoma

Lymphomas are well managed by medical imaging tools, especially with advanced technology such as ^{18}F-FDG PET/CT. This imaging modality takes care of patients with lymphoma by monitoring therapeutic response. Its outcome of therapeutic effect of lymphoma is shown very early, as patients with NHL are reimaged after short intervals (often every 6 weeks) with whole-body imaging of PET/CT.

Many studies have shown the utility of PET/CT in monitoring of patient therapeutic response of lymphoma types. Years ago, response criteria of malignant lymphomas varied among study groups and cancer centers with value to the size of a normal lymph node, the repeated assessment and

the time that is taken for the response assessment to be made, the ways the responses are assessed prospectively or retrospectively, the increase of number of cases required for disease progression, and many other factors [34]. Relatively minor differences in the definition of normal size of a lymph node can have a major influence on response rates [35]. Therefore 1999 was the year that therapy monitoring of lymphoma has gotten standard interpretation criteria that radiologist follow to interpret and to give more accurate information of the therapeutic method which is chosen. In 1999, an international working group (IWG) of clinicians, radiologists, and pathologists with expertise in the evaluation and management of patients with non-Hodgkin's lymphoma (NHL) published guidelines for response assessment and outcomes measurement [34]. From then on, many difference evaluation criteria arise. ^{18}F-FDG PET/CT imaging was also included into the interpretation criteria, for example, International Harmonization Project (IHP), European Organization for Research and Treatment of Cancer (EORTC), PET Response Criteria in Solid Tumors (PERCIST), and Deauville criteria.

The ^{18}F-FDG PET/CT therapy monitoring criteria provided uniformity and harmonization in the evaluation of patient with lymphoma in different medical centers. These criteria are the reference criteria in the management of treatment of patient with lymphomas (Table 4.2).

^{18}F-FDG PET has emerged as a powerful functional imaging tool for staging, restaging, and response assessment of lymphomas. The advantage of PET over conventional imaging techniques such as computed tomography (CT) or magnetic resonance imaging is its ability to distinguish between viable tumor and necrosis or fibrosis in residual mass(es) often present after treatment [36]. Therefore, ^{18}F-FDG PET/CT provide explicit findings in the assessment of therapeutic effect of different chemotherapy regimens on patient with lymphoma. The use of PET therapy criteria is based on visual assessment which is currently considered adequate for determining whether a PET scan is positive or negative, and use of the standardized uptake value (SUV) is not sometimes necessary. A more extensive description of interpretation of PET scans is provided in the consensus guidelines of the Imaging Subcommittee [37]. The standardized criteria of ^{18}F-FDG PET/CT used for therapy monitoring from the above table can be described as follows:

Table 4.2 Four different criteria definitions of ^{18}F-FDG PET/CT-positive findings and ^{18}F-FDG PET/CT-negative findings in lymphoma

Criteria	Positive findings	Negative findings
IHP	PD, stable disease, PR	CR
EORTC	PMD, SMD, PMR	CMR
PERCIST 1.0	PMD, SMD, PMR	CMR
Deauville	Score 4: Uptake of lesion is moderately higher than that of liver Score 5: Uptake of lesion is markedly higher than that of the liver and/or new lesions	Score 1: No residual uptake Score 2: Uptake of lesion is lower than that of the mediastinum Score 3: Uptake of lesion is higher than that of the mediastinum but lower than that of the liver

Note: *CMR* complete metabolic response, *PD* progressive disease, *PMD* progressive metabolic disease, *PMR* partial metabolic response, *CR* complete response, *PR* partial remission, *SMD* stable metabolic disease

4.3.3.1 International Harmonization Project Criterion

Positive findings are defined as the increased focal or diffuse uptake of ^{18}F-FDG in the lymphoid tissue which consist of lymphoma; a very high uptake is shown on the area of the lymphoma**.** A positive scan represents focal or diffuse ^{18}F-FDG uptake above surroundings in a location incompatible with normal anatomy or physiology, without a specific SUV cutoff but higher. In therapy assessment of lymphoma after chemotherapy or radiation therapy, the evaluation is done in a manner to observe whether there is or isn't ^{18}F-FDG uptake in the involved areas.

The IHP criterion of positive and negative finding of PET/CT of lymphoma are based on complete response (CR), partial remission (PR), stable disease (SD), and progressive disease (PD), which are further explained.

Complete Response (CR)

The identification of patient with CR is confirmed when the following four points are observed:

- No previous clinical evidence or symptoms of disease was found prior to the treatment.
- Typical FDG-avid lymphoma was shown in patients without PET scan before therapy or without findings on PET scan result. Posttreatment residuals with negative findings on PET scan result are also included (Fig. 4.4).
- Varied unknown FDG-avid/FDG-avid lymphoma: patients who did not receive PET scan before therapy or with a negative pretreatment PET scan result present a CT regression of lymph nodes and nodules back to normal sizes. Previously identified nodes that range from 11 to 15 mm in the long axis and more than 10 mm in the shorter axis before treatment should regress to 10 mm or lesser in the shorter axis posttreatment.
- Abnormal morphological appearances of the spleen and/or liver such as splenomegaly and/or hepatomegaly that were seen before therapy during physical examination or CT scan should disappear and decrease to normal size in

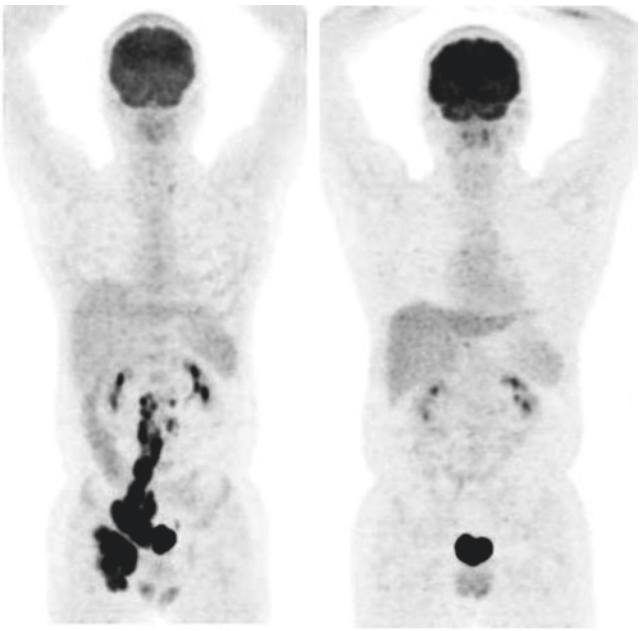

Fig. 4.4 A 54-year-old male, HL, after treatment, no positive lesions found (CR or CMR)

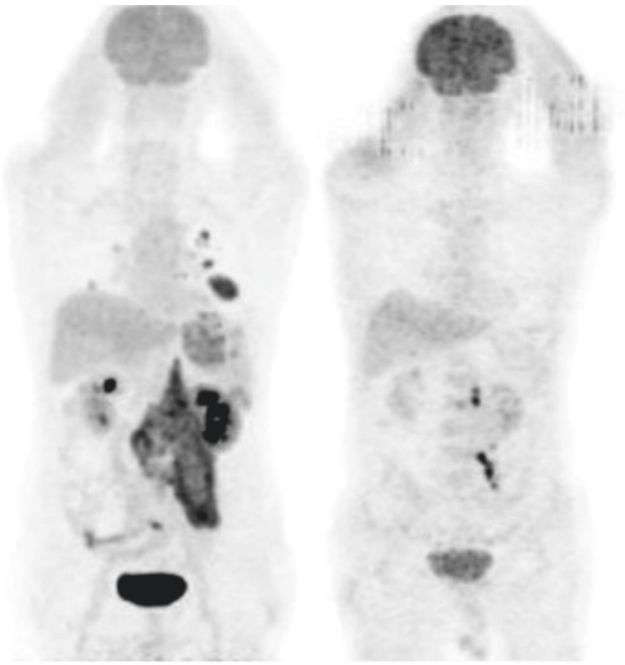

Fig. 4.5 A 64-year-old male, DLBCL, after four cycles of chemotherapy, most high FDG uptake lesions disappeared, but small lesions remained (PR)

posttreatment images. Lymph nodes should also disappear. However, the splenomegaly is not a good index as other factors which can also conduct to splenomegaly, and a normal spleen can't mean the presence of lymphoma.

- No infiltrate is shown on revised acceptable biopsy sample after treatment when the bone marrow had pretreatment involvements of lymphoma. In addition, the morphological outcomes should not show any abnormal sign on IHC. Therefore, a CR is considered on a sample when it has a normal appearance on IHC and sometimes with a few proliferative lymphocytes on flow cytometry.

Partial Remission (PR)

- There is at least a 50% decrease in sum of the product of the diameters (SPD) of up to six of the largest dominant nodes or nodal masses. These nodes or masses should be selected according to all of the following: they should be clearly measurable in at least two perpendicular dimensions; if possible, they should be from disparate regions of the body; and they should include mediastinal and retroperitoneal areas of disease whenever these sites are involved.
- No increase should be observed in the size of the other nodes, liver, or spleen.
- Splenic and hepatic nodules must regress by ≥50% in their SPD or, for single nodules, in the greatest transverse diameter.
- With the exception of splenic and hepatic nodules, involvement of other organs is usually assessable, and no measurable disease should be present.
- Bone marrow assessment is irrelevant for determination of a PR if the sample was positive before treatment. However, if positive, the cell type should be specified (e.g., large-cell lymphoma or small neoplastic B cells). Patients who achieve a CR by the above criteria but who have persistent morphologic bone marrow involvement will be considered partial responders.

When the bone marrow was involved before therapy and a clinical CR was achieved, but with no bone marrow assessment after treatment, patients should be considered partial responders.

- No new sites of disease should be observed.
- Typically, FDG-avid lymphoma: for patients with no pretreatment PET scan or if the PET scan was positive before therapy, the posttreatment PET should be positive in at least one previously involved site.
- Variably FDG-avid lymphomas/FDG avidity unknown: for patients without a pretreatment PET scan, or if a pretreatment PET scan was negative, CT criteria should be used (Fig. 4.5).

In patients with follicular lymphoma or mantle cell lymphoma, a PET scan is only indicated with one or at most two residual masses that have regressed by more than 50% on CT; those with more than two residual lesions are unlikely to be PET negative and should be considered partial responders.

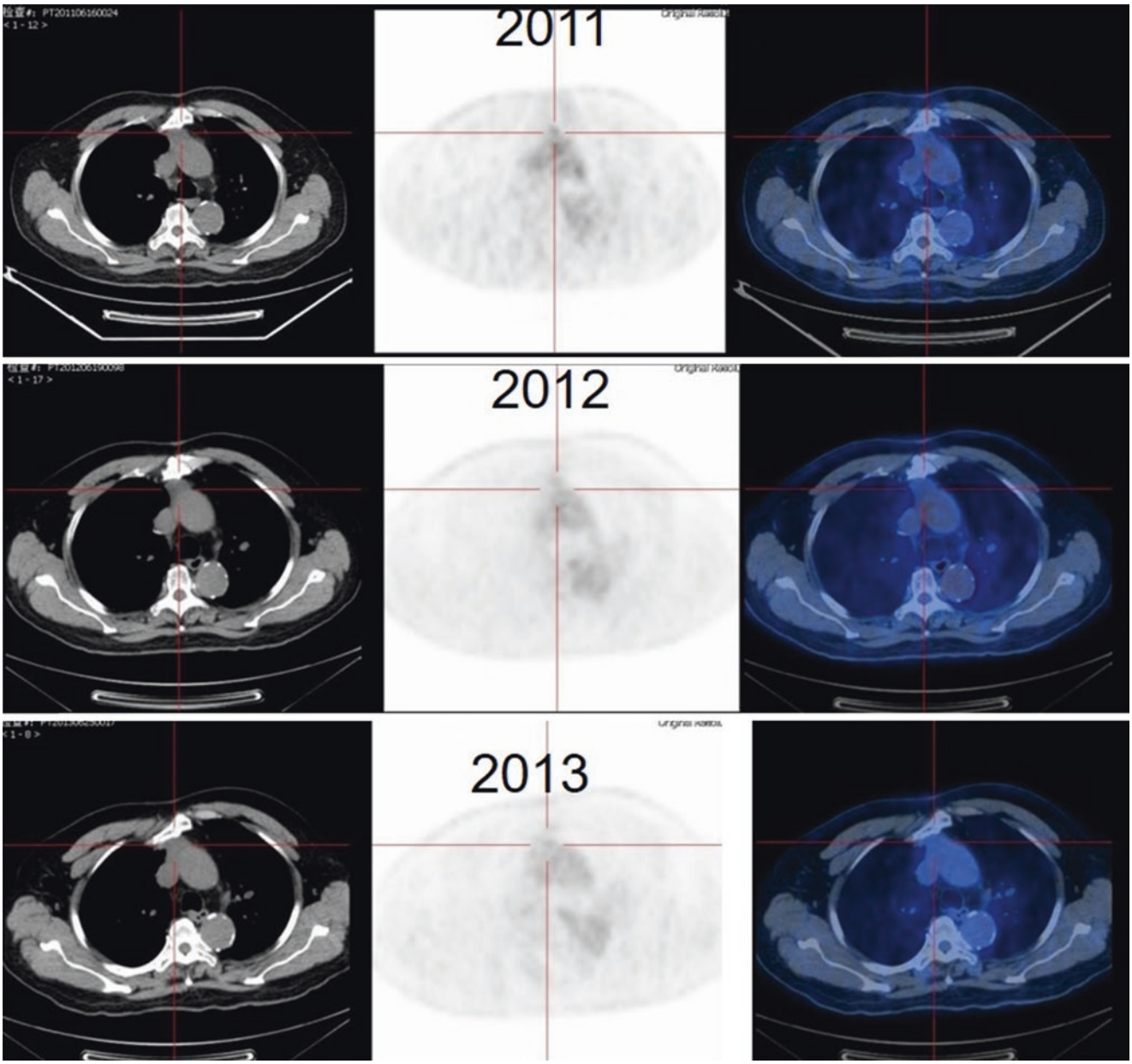

Fig. 4.6 Male, 78 years old, with DLBCL, after therapy. ^{18}F-FDG PET/CT shows a mass in the anterior superior mediastinum with no obvious uptake of ^{18}F-FDG for 3 years (SD)

Stable Disease (SD)

- SD is considered when a patient does not fall into the criteria of CR, PR, or progressive disease.
- Patients with typical FDG-avid lymphomas: the FDG uptake should be positive on the previous lesion without having any new lesions identified on CT or PET after therapy.
- Patients with varied FDG uptake lymphomas: no changes of the size of previous lesions were observed on posttreatment CT if the patient did not perform a pretreatment PET scan or with no sign of PET scan result (Fig. 4.6).

Progressive Disease (PD or PR)

PD or PR criteria are characterized by the lymph node sizes associated to the type of lymphoma. Lymph nodes are reported as abnormal when the long axis is more than 15 mm without considering the short axis. When range of the long axis is from 11 to 15 mm, the lymph nodes are considered as abnormal if their short axis is more than 10 mm. Lymph nodes $\leq 10 \times \leq 10$ mm will be reported as normal for relapse or progressive disease.

- PD or PR is considered when any new nodules greater than 15 mm in both axes during or posttreatment are

found, regardless of therapeutic response. The increase of FDG on previously nonaffected site is not sufficient to determine PD or PR; it needed reassessment by other modalities. For example, new pulmonary nodules found on CT in patients without primary findings of pulmonary lymphoma are often benign. However, single PET scan is not used for therapeutic decision-making, but the histological results should confirm the findings.

- Any lesion presented typically with FDG-avid lymphoma is positive in PET before therapy only if the nodule is smaller to be detected, less than 15 mm in the long axis on CT scan (Fig. 4.7).

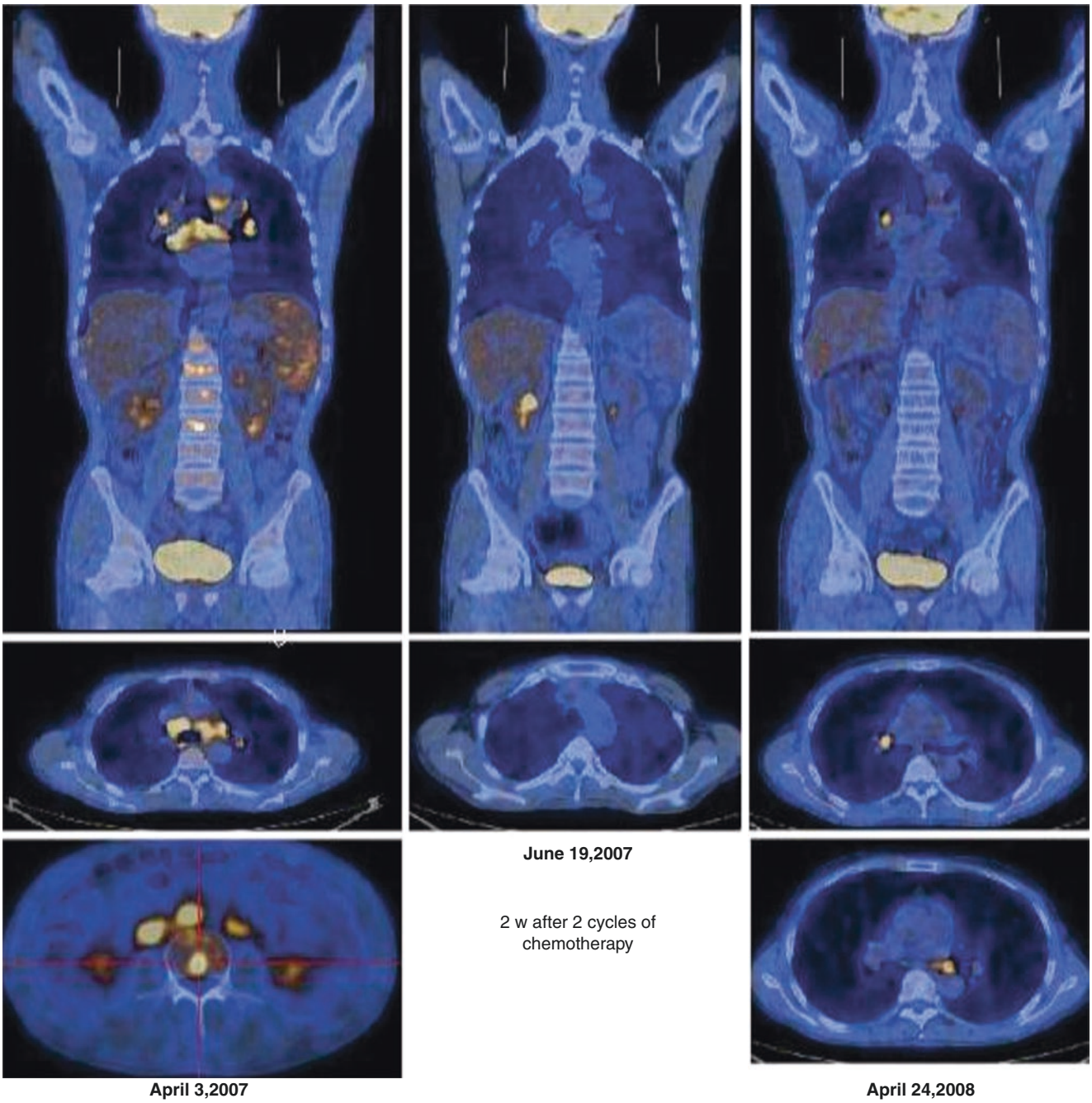

Fig. 4.7 Male, 60 years old, anaplastic large-cell lymphoma. Left column, ^{18}F-FDG PET/CT of before therapy shows high uptake of lymph nodes in the regions of the mediastinum and retroperitoneal and some bones; middle column, ^{18}F-FDG PET/CT of 2 weeks after two cycles of chemotherapy shows nearly no obvious uptake lesions; right column, ^{18}F-FDG PET/CT after half year of ten cycles of chemotherapy shows high uptake in the mediastinum and suggested relapse (PD)

The splenic disorder is considered as nodal lesion. The nodal and extranodal diseases are evaluated using the same method. The clinical findings including imaging reported lesions such as pleural effusions and bone lesions will be recorded even if they are histologically found negative.

In clinical trials where most of the patients have CT instead of PET or in patient where PET cannot be used, CT can be considered to classify whether the patient is PD or PR. Residual masses are considered partial responses not CR.

4.3.3.2 Deauville Criterion

The five-point scoring system (5 PS) of Deauville criterion was a simple, reproducible scoring method, with the flexibility to change the threshold between good and poor response according to the clinical context and/or treatment strategy [37]. This criterion was presented as follows:

- Score 1. No tumor uptake
- Score 2. Tumor uptake inferior or equal to that of the mediastinum
- Score 3. Tumor uptake superior to that of the mediastinum but inferior or equal to the liver
- Score 4. Tumor uptake moderately higher than the liver
- Score 5. Tumor uptake markedly higher than the liver and/or new lesions
- X. New areas of uptake unlikely to be related to lymphoma

This criterion was used like other criteria in ^{18}F-FDG PET/CT suited to assess different degrees of response at the middle and end of treatment and has been developed to score images (scores 1, 2, 3, 4, and 5) [38]. It was recommended as the standard reporting tool at the First International Workshop on PET in Lymphoma in Deauville, France, in 2009, and these so-called Deauville criteria have been widely applied in trials in preference to earlier criteria [39].

Deauville criterion (DC) improves the positive predictive value of PET reporting compared to IHP and other criteria [40]. Therefore, there was no doubt that physician working on PET to be aware of this and to interpret using the Deauville score (DS) for objective reports and convenient clinical management of lymphoma treatment.

However, there is a caveat: if treatment is to be de-escalated, to avoid the risk of undertreatment, some investigators have preferred to use the mediastinum (equivalent to DS 2) to define CMR or a "negative" scan.

4.3.3.3 Standardized Uptake Value Changes

Quantitative applications of ^{18}F-FDG PET/CT are recognized as objective tools for response monitoring, although accurate measurement relies on consistent methods of acquisition, processing, and rigorous quality assurance of equipment for widespread application.

Lower SUVmax compared to background in liver uptake corresponded to DS 1, 2, or 3. DS 3 in a patient receiving standard treatment more likely represents CMR. Some aggressive lymphoma showed high SUVmax which may predict good response to therapy. DS 4 and 5 patient tended to show higher SUVmax. Quantitative verification is of particular importance for discrimination between DS 4 and DS 5. Currently published studies have shown that DS 5 has three or more times SUVmax in the liver in the UK NCRI group trials and two or more times SUVmax in the liver in the French and Belgian Lymphoma Studies Association and Italian groups. According to updated guidelines of 2014, it was recommended that DS 5 be applied to uptake two to three times the uptake in the normal liver [41]. Indolent low-grade lymphoma usually shows lower SUVmax; in this type of tumor, it is possible to keep control of the disease for longtime treatment regimens since therapy doesn't really work.

4.3.4 ^{18}F-FDG PET/CT for Predicting Prognosis of Lymphoma

The IPI extensively evaluated and showed several risk factors which play crucial role in HL treatment outcomes including male gender, age (more than 45 years old), stage IV HL, an albumin concentration lesser than 4.0 g/dL, a hemoglobin concentration lesser than 10.5 g/dL, a higher level of WBC concentration of 15,000/mL, and low lymphocyte concentration lesser than 600/mL or lesser than 8% of total WBC. Modulating these risk factors has shown an improvement in therapeutic outcomes in patients with HL. The nonexistence of any of these seven risk factors showed better prognosis (84%) when compared to controls. The presence of five or all risk factors decreased the disease control rate to 42%. An early study has reported that the outcomes for these patients were related to the treatment they received and newer treatments may improve these predicted outcomes. Furthermore, new treatments are being developed for patients with greater risk factors.

Previous ^{18}F-FDG PET/CT Deauville criterion had reported that patients with DS 5 have significantly bad prognosis than patients with DS 4 at the interim evaluation. In stage I HL, death or high risk of progression is more bound to DS 5 than DS 1–4, independently to the pretreatment prognostic DS [42]. DS 5 predicts a low PFS in the advanced-stage HL [43]. However, DS 4 has shown good prognosis in primary mediastinal BCL, probably due to the hypertrophy of the residual mediastinal masses which is typical for this

disease, while DS 5 patients have higher risk of disease relapse [44].

The IPI is used in NHL for prognosis prediction. Five risk factors are associated with NHL, including patients more than 60 years old, with stage III or IV disease, with a high lactate dehydrogenase LDH level, with more than one affected extranodal site, and with a poor performance status. Therefore, the therapy outcomes are evaluated based on the above factors.

- Patients who present no more than one risk factor account as low risk, having a 5-year OS of around 73%.
- Patients who present two risk factors account as low-intermediate risk, having a 5-year OS of around 50%.
- Patients who present three risk factors account as high-intermediate risk, having a 5-year OS of around 43%.
- Patients who present more than three risk factors account as high risk, having a 5-year OS of around 26%.

The LDH level is a factor used to evaluate the tumor proliferation. A LDH level in patients higher than normal (140–280 units/L) often reflects fast-growing lymphomas and a more advanced disease state. Therefore, a good prognosis is found in lymphoma patient with normal LDH than the one with higher LDH. In addition, in fast-growing NHL patients, LDH often tends to be higher.

The prognostic models reported above have been used in groups of patients and proven to be useful in developing therapeutic strategies. However, it is noticed that individual patient might present with heterogeneous results than these reported data. There are specific IPIs for certain subtypes of this disease, such as FL or DLBC.

Additionally, ^{18}F-FDG PET/CT has relevant findings in prediction of therapy rate. It is predictable of PFS rates in different types of lymphoma. A PFS rate of 89% was reported on patients with negative PET and 59% and 16%, respectively, in patients with fewest residual FDG and in patients with higher FDG on PET results in high-grade NHL. In aggressive NHL, patients with early ^{18}F-FDG PET-positive results have a 1-year PFS that ranges from 10 to 50%, while patients with negative results have a 1-year PFS which is between 79 and 100%. Regardless of the tumor stage, patients with early ^{18}F-FDG PET-positive results tend to have a high relapse rate.

Comparison of interim ^{18}F-FDG PET image with the International Prognostic Index (IPI) in a multivariate analysis, at mid treatment, is regarded as with a strong prognostic factor for PFS and OS than the International Prognostic Index (P, 0.03, and P, 0.58, respectively). Previous published studies have documented that early metabolic changes after 1–3 cycles of chemotherapy for aggressive NHL and HL are highly predictive of the final treatment response and PFS [45, 46].

4.4 Conclusion

^{18}F-FDG PET/CT is better discriminators than CT with respect to disease-free interval and overall survival. Therefore, the prognosis of lymphoma by this advanced medical imaging machine is quite interesting. The diagnostic procedure of ^{18}F-FDG PET/CT has played an important role in the management of patients with lymphoma because it provides information on prognosis, and nowadays, there are multiple chemotherapy regimens available in management of the different histologic types of lymphoma. It has to rule out and recognize the importance of PET/CT even though it is valuable in restaging and prognosis of lymphoma. More attention should be given to these very advanced medical imaging techniques.

References

1. Poston JN (1999) Positive Leu-MI immuno-histochemistry and diagnosis of the lymphoma cases described by Hodgkin in 1832. Appl Immunohistochem Mol Morphol 7:6–8
2. Horner MJ, Ries LA, Krapcho M, Neyman N, Aminou R, Howlader N, Altekruse SF, Feuer EJ, Huang L, Mariotto A, Miller BA, Lewis DR, Eisner MP, Stinchcomb DG, Edwards BK (eds) (2009) SEER Cancer Statistics Review, 1975-2006. National Cancer Institute, Bethesda. http://seer.cancer.gov/csr/1975_2006/ based on November 2008 SEER data submission, posted to the SEER web site
3. Hutchings M, Loft A, Hansen M et al (2006) Different histopathological subtypes of Hodgkin lymphoma show significantly different levels of FDG uptake. Hematol Oncol 24(3):146–150
4. Döbert N, Menzel C, Hamscho N et al (2004) Atypical thoracic and supraclavicular FDG-uptake in patients with Hodgkin's and non-Hodgkin's lymphoma. Q J Nucl Med Mol Imaging 48(1):33–38
5. Hoffmann M, Kletter K, Diemling M et al (1999) Positron emission tomography with fluorine-18-2-fluoro-2-deoxy-D-glucose (F18-FDG) does not visualize extranodal B-cell lymphoma of the mucosa-associated lymphoid tissue (MALT)-type. Ann Oncol 10:1185–1189
6. Elstrom R (2003) Utility of FDG-PET scanning in lymphoma by WHO classification. Blood 101(10):3875–3876
7. Weiler-Sagie M, Bushelev O, Epelbaum R et al (2010) 18F-FDG avidity in lymphoma readdressed: a study of 766 patients. J Nucl Med 51(1):25–30
8. Schoder H, Noy A, Gonen M et al (2005) Intensity of 18fluorodeoxyglucose uptake in positron emission tomography distinguishes between indolent and aggressive non-Hodgkin's lymphoma. J Clin Oncol 23(21):4643–4651
9. Jerusalem G, Beguin Y (2006) The place of positron emission tomography imaging in the management of patients with malignant lymphoma. Haematologica 91(4):442–444
10. Isasi CR, Lu P, Blaufox MD (2005) A meta-analysis of 18F-2-deoxy-2-fluro-D-glucose positron emission tomography in the staging and restaging of patients with lymphoma. Cancer 104(5):1066–1074
11. De Jong PA, van Ufford HM, Baarslag HJ et al (2009) CT and 18F-FDG PET for noninvasive detection of splenic involvement in patients with malignant lymphoma. AJR Am J Roentgenol 192(3):745–753
12. Karunanithi S, Sharma P, Roy SG et al (2014) Use of 18F-FDG PET/CT imaging for evaluation of patients with primary splenic lymphoma. Clin Nucl Med 39(9):772–776

13. Chang CC, Cho SF, Chen YW et al (2012) SUV on dual-phase FDG PET/CT correlates with the Ki-67 proliferation index in patients with newly diagnosed non-Hodgkin lymphoma. Clin Nucl Med 37:e189–e195
14. Hwang JW, Jee SR, Lee SH et al (2016) Efficacy of positron emission tomography/computed tomography in gastric mucosa-associated lymphoid tissue lymphoma. Korean J Gastroenterol 67:183–188
15. Hirose Y, Kaida H, Ishibashi M et al (2012) Comparison between endoscopic macroscopic classification and F-18 FDG PET findings in gastric mucosa-associated lymphoid tissue lymphoma patients. Clin Nucl Med 37:152–157
16. Beal KP, Yeung HW, Yahalom J (2005) FDG-PET scanning for detection and staging of extranodal marginal zone lymphomas of the MALT type: a report of 42 cases. Ann Oncol 16:473–480
17. Pelosi E, Penna D, Douroukas A et al (2011) Bone marrow disease detection with FDG-PET/CT and bone marrow biopsy during the staging of malignant lymphoma: results from a large multicenter study. Q J Nucl Med Mol Imaging 55:469–475
18. Adams HJ, Kwe TC, Keizer B et al (2014) Systemic review and meta-analysis on the diagnostic performance of FDG-PET/CT in detecting bone marrow involvement in newly diagnosed Hodgkin lymphoma: is bone marrow biopsy still necessary? Ann Oncol 25:921–927
19. Hoffman JM, Waskin HA, Schifter T et al (1993) FDG-PET in differentiating lymphoma from nonmalignant central nervous system lesions in patients with AIDS. J Nucl Med 34(4):567–575
20. Makino K, Hirai T, Nakamura H et al (2011) Does adding FDG-PET to MRI improve the differentiation between primary cerebral lymphoma and glioblastoma? Observer performance study. Ann Nucl Med 25(6):432–438
21. Rosenberg SA (1996) Report of the committee on the staging of Hodgkin's disease. Cancer Res 26:1310
22. Rosenberg SA, Boiron M, DeVita VT Jr et al (1971) Report of the committee on Hodgkin's disease staging procedures. Cancer Res 31:1862–1863
23. Swerdlow SH, International Agency for Research on Cancer, World Health Organization (2008) WHO classification of tumours of haematopoietic and lymphoid tissues. World Health Organization of Tumours 2, 4th edn. International Agency for Research on Cancer. ISBN 9789283224310
24. Canova F, Marino D, Trentin C et al (2011) Intrathecal chemotherapy in lymphomatous meningitis. Crit Rev Oncol Hematol 79(2):127–134
25. Seam P, Juweid ME, Cheson BD (2007) The role of FDG-PET scans in patients with lymphoma. Blood 110:3507–3516
26. Schaefer NG, Hany TF, Tavena C et al (2004) Non-Hodgkin lymphoma and Hodgkin disease: coregistered FDG PET and CT at staging and restaging: do we need contrast-enhanced CT. Radiology 232:823–829
27. Kwee TC, Kwee RM, Nievelstein RA (2008) Imaging in staging of malignant lymphoma: a systematic review. Blood 111:504–516
28. Mittal BR, Manohar K, Malhotra P et al (2011) Can flourodeoxyglucose positron emission tomography/computed tomography avoid negative iliac crest biopsies in evaluation of marrow involvement by lymphoma at time of initial staging? Leuk Lymphoma 52:2111–2116
29. Rodriguez-Vigil Junco B, Gomez Leon N et al (2011) Non-Hodgkin's lymphoma staging: a prospective study of the value of positron emission tomography/computed tomography (PET/CT) versus PET and CT. Med Clin 137:383–389
30. Albano D, Giubbini R, Bertagna F (2016) 18F-FDG PET/CT and primary hepatic MALT: a case series. Abdom Radiol (NY) 41(10):1956–1959
31. Treglia G, Zucca E, Sadeghi R et al (2015) Detection rate of fluorine-18-fluorodeoxyglucose positron emission tomography in patients with marginal zone lymphoma of MALT type: a meta-analysis. Hematol Oncol 33:113–124
32. Albano D, Bertoli M, Ferro P et al (2017) ^{18}F-FDG EPT/CT in gastric MALT lymphoma: a bicentric experience. Eur J Nucl Med Mol Imaging 44(4):589–597
33. Kumar R, Xiu Y, Zhuang HM et al (2006) ^{18}F-flourodeoxyglucose-positron emission tomography in evaluation of primary cutaneous lymphoma. Br J Dermatol 155(2):357–363
34. Cheson BD, Horning SJ, Coiffier B et al (1999) Report of an International Workshop to standardize response criteria for non-Hodgkin's lymphomas. J Clin Oncol 17(4):1244
35. Grillo-López AJ, Cheson BD, Horning SJ et al (2000) Response criteria for NHL: importance of "normal" lymph node size and correlations with response rates. Ann Oncol 11(4):399–408
36. Spaepen K, Stroobants S, Dupont P et al (2001) Prognostic value of positron emission tomography (PET) with fluorine-18 fluorodeoxyglucose ([18F] FDG) after first-line chemotherapy in non-Hodgkin's lymphoma: is [18F] FDG-PET a valid alternative to conventional diagnostic methods? J Clin Oncol 19(2): 414–419
37. Juweid ME, Stroobants S, Hoekstra OS et al (2007) Use of positron emission tomography for response assessment of lymphoma: consensus recommendations of the Imaging Subcommittee of the International Harmonization Project in Lymphoma. J Clin Oncol 25(5):571–578
38. Barrington SF, Qian W, Somer EJ et al (2010) Concordance between four European centres of PET reporting criteria designed for use in multicenter trials in Hodgkin lymphoma. Eur J Nucl Med Mol Imaging 37(10):1824–1833
39. Meignan M, Gallamini A, Haioun C (2009) Report on the first international workshop on interim-PET scan in lymphoma. Leuk Lymphoma 50(8):1257–1260
40. Le Roux PY, Gastinne T, Le Gouill S et al (2011) Prognostic value of interim FDG PET/CT in Hodgkin's lymphoma patients treated with interim response adapted strategy: comparison of International Harmonization Project (IHP), Gallamini and London criteria. Eur J Nucl Med Mol Imaging 38:1064–1071
41. Bourguet P, Blanc-Vincent MP, Boneu A et al (2003) Summary of the standards, options and recommendations for the use of positron emission tomography with 2-[18F] fluoro-2-deoxy-D-glucose (FDG-PET scanning) in oncology. Br J Cancer 89(Suppl 1):S84–S91
42. Annunziata S, Cuccaro A, Calcagni ML et al (2016) Interim FDG-PET/CT in Hodgkin lymphoma: the prognostic role of the ratio between target lesion and liver SUVmax (rPET). Ann Nucl Med 30:588–592
43. Hutchings M, Loft A, Hansen M et al (2006) FDG-PET after two cycles of chemotherapy Predicts treatment failure and progression-free survival in Hodgkin lymphoma. Blood 107: 52–59
44. Zinzani PL, Tani M, Fanti S et al (2006) Early positron emission tomography (PET) restaging: a predictive final response in Hodgkin's disease patients. Ann Oncol 17:1296–1300
45. Kostakoglu L, Goldsmith SJ, Leonard JP et al (2006) FDG-PET after 1 cycle of therapy predicts outcome in diffuse large cell lymphoma and classic Hodgkin disease. Cancer 107: 2678–2687
46. Hutchings M, Mikhaeel NG, Fields PA, Nunan T, Timothy AR (2005) Prognostic value of interim FDG-PET after two or three cycles of chemotherapy in Hodgkin lymphoma. Ann Oncol 16:1160–1168

Clinical Utility of ^{18}F-FDG PET/CT Scanning in Urological Cancers Management

5

Xiang Zhou and Gang Huang

5.1 Introduction

Positron emission tomography/computed tomography (PET/CT) has become an important method for the diagnosis/identification, staging, follow-up monitoring, and efficacy and prognosis determination of malignant tumors. The glucose analog ^{18}F-deoxyglucose (FDG) is the most mature and widely used imaging agent for PET. Since most malignant cells show a high glucose metabolism, they can accumulate more ^{18}F-FDG than do normal tissues and organs, which can be detected by PET/CT and distinguished from normal tissues. ^{18}F-FDG-PET/CT imaging has good sensitivity and accuracy for the diagnosis and evaluation of most malignant tumors. However, ^{18}F-FDG-PET/CT has limited application in primary urinary tumors (prostate cancer, renal clear-cell carcinoma, and bladder cancer [BC]). Initial studies evaluating the role of ^{18}F-FDG-PET in kidney and bladder malignancies showed disappointingly low sensitivity. The main reason is that FDG is mainly excreted through the urinary system, thereby masking the FDG uptake of primary renal and BCs. Many researchers are trying to improve the sensitivity and specificity of PET/CT in urological malignancies through a variety of techniques, including bladder irrigation and delayed imaging. Recent studies using PET/CT instead of PET and some improved protocol techniques have shown better sensitivity and specificity, and PET/CT now appears to be more useful in the staging and follow-up of urinary malignancies than originally reported.

X. Zhou
Department of Nuclear Medicine, RenJi Hospital, School of Medicine, Shanghai JiaoTong University, Shanghai, P. R. China

G. Huang (✉)
Shanghai Key Laboratory of Molecular Imaging, Shanghai University of Medicine and Health Sciences, Shanghai, P. R. China

5.2 Bladder Cancer

5.2.1 Overview of Bladder Cancer

BC is the ninth most common cancer in the world and the most common type of cancer of the urinary system. Painless hematuria is the most common symptom of BC. More than 90% of BC cases are of urinary tract epithelial (transitional cell) cancer, 5% of squamous cell carcinoma, and less than 2% of adenocarcinoma [1]. The main method for the diagnosis of BC is cystoscopy and biopsy under cystoscopy for pathological analysis. Approximately 30% of patients show muscle invasion. Prolonged metastases of BC are common, and the most important metastatic sites include the liver, lung, bone, and adrenal gland. In general, BC with muscle invasion is treated with cystectomy and pelvic lymphadenectomy (PLND), while metastatic disease is treated with cisplatin-based combination chemotherapy.

5.2.2 Glucose Metabolism in Bladder Cancer

The metabolism of malignant tumor cells mainly comprises anaerobic glycolysis of glucose; these cells also show decreased TCA activity. Cancer cells in the urinary tract rely on a special transformation of aerobic glycolysis-dependent metabolism (Warburg effect) to provide a rapid supply of ATP, thereby maintaining the primary source of energy for uncontrolled proliferation. Therefore, high glycolysis flux is dependent on glycolysis-related genes (glucose transporter type 1 [GLUT1], lactate dehydrogenase A [LDHA], hexokinase 1 [HK1], pyruvate kinase type M [PKM2], hypoxia-inducible factor 1-α [HIF-1α]), etc., resulting in excessive production of pyruvic acid and lactic acid. In addition, activation of the PTEN/PI3K/AKT/mTOR signaling pathway in BC also activates tumor glucose metabolism and suppresses oxidative phosphorylation by promoting anaerobic glycolysis.

G. Huang (ed.), *Nuclear Medicine in Oncology*, https://doi.org/10.1007/978-981-13-7458-6_5

5.2.3 Clinical Utility of ^{18}F-FDG-PET/CT Scanning in BC

5.2.3.1 ^{18}F-FDG-PET/CT for Diagnosis of Primary BC

In the past, the use of FDG-PET/CT for the diagnosis of primary BC was limited because it was difficult to distinguish the radiotracer activity from the urine from the tumor activity in the bladder. There are several ways to overcome radioactive interference in the urine, such as delayed imaging after urination, diuretic interventional imaging, and bladder irrigation after catheterization. These methods significantly reduce the physiological uptake of FDG in the bladder and improve the detection rate of the primary BC (Figs. 5.1 and 5.2). A recent

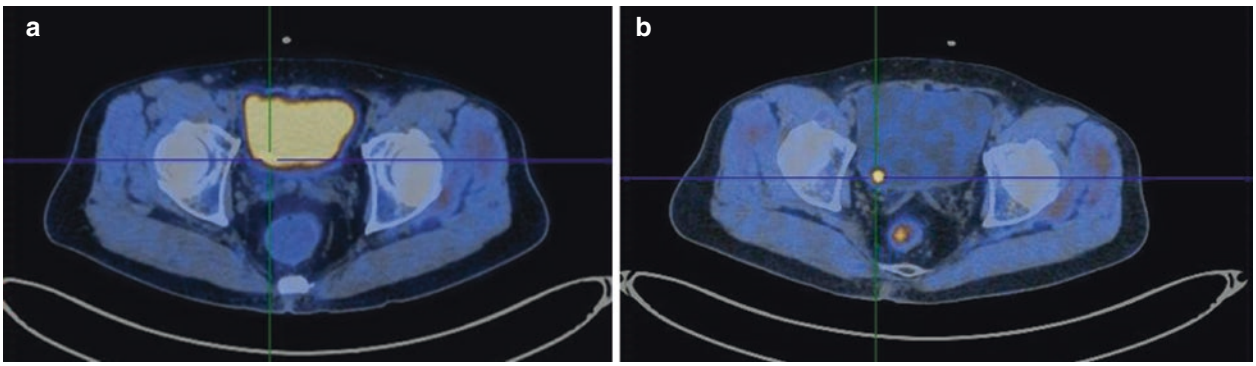

Fig. 5.1 Dual-phase ^{18}F-fluorodeoxyglucose positron emission tomography/computed tomography during forced diuresis. (**a**) Before diuresis; (**b**) after diuresis

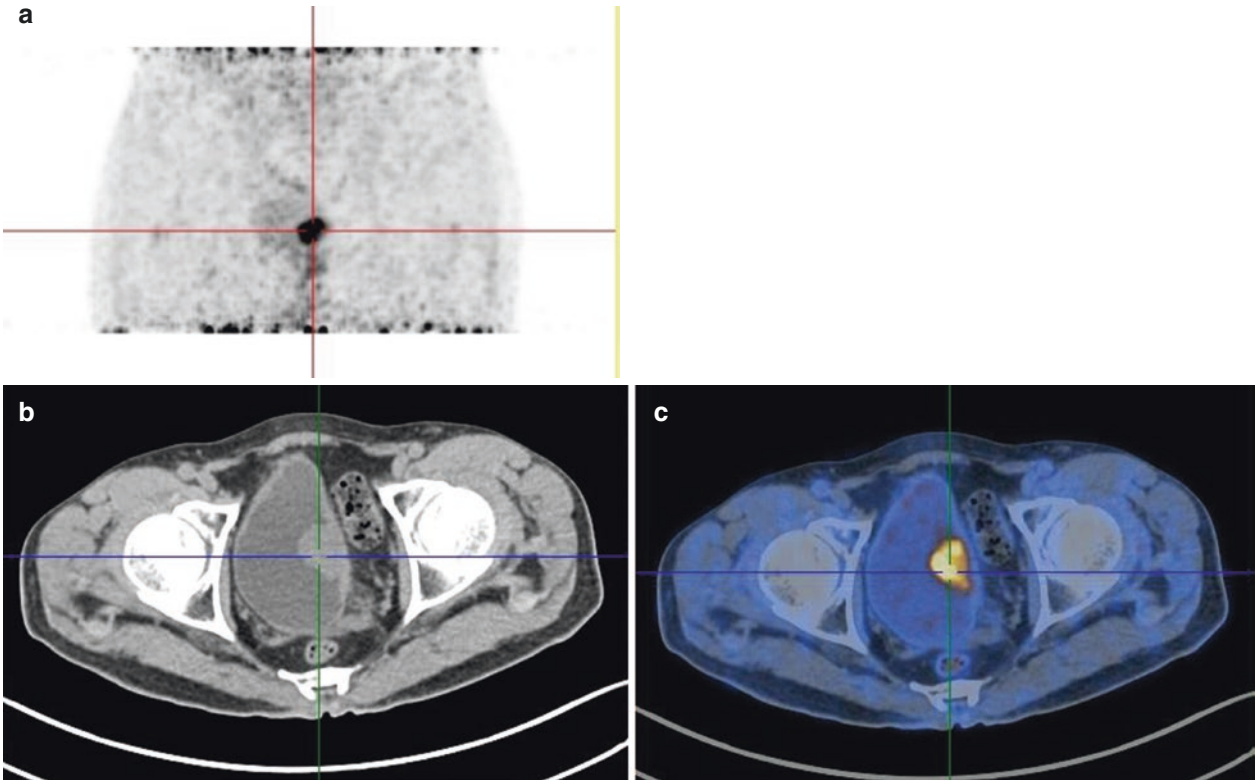

Fig. 5.2 Primary tumor in the left bladder wall could be visualized with FDG-PET after diuresis. (**a**) The MIP of FDG-PET shows abnormal FDG uptake in the pelvis after diuresis; (**b**) CT of FDG-PET/CT and (**c**) PET/CT showed high FDG uptake of primary tumor in the bladder wall

meta-analysis evaluated the accuracy of FDG PET/CT in the diagnosis of bladder lesions. Six studies met the inclusion criteria. The sensitivity and specificity of BC for PET or PET/CT detection are 80.0% and 84.0%, respectively [2]. Compared to magnetic resonance imaging (MRI) and CT, FDG-PET/CT showed no advantage in detecting local bladder lesions.

5.2.3.2 ^{18}F-FDG-PET/CT for Staging of BCs

CT and MRI can help determine whether lymph node (LN) metastasis is mainly based on the size and shape of the LNs. However, the rate of misdiagnosis of LNs with normal-sized metastasis is very high. Therefore, both the imaging methods have very low sensitivity for the detection of LN metastases. The specificity of the two methods for the detection of LN metastases is also low. Moreover, the rate of misdiagnosis is higher, because lymphadenopathy may be caused by benign diseases, such as inflammatory hyperplasia of the LNs. Metastases of BC, such as LN metastasis, also have metabolic properties similar to those of the primary tumor; therefore, LNs or distant metastatic lesions with high metabolic activity outside the bladder are detected by PET (Fig. 5.3). A recent meta-analysis of FDG-PET/CT for BC staging and re-segmentation found that the sensitivity, specificity, and accuracy of PET/CT for BC staging were 82%, 89%, and 92%, respectively [3]. In 20–40% of patients, FDG-PET/CT detected more malignant diseases than conventional CT/MRI, and FDG-PET/CT may change the clinical treatment plan in 68% of patients [4]. Some authors believe that FDG-PET/CT

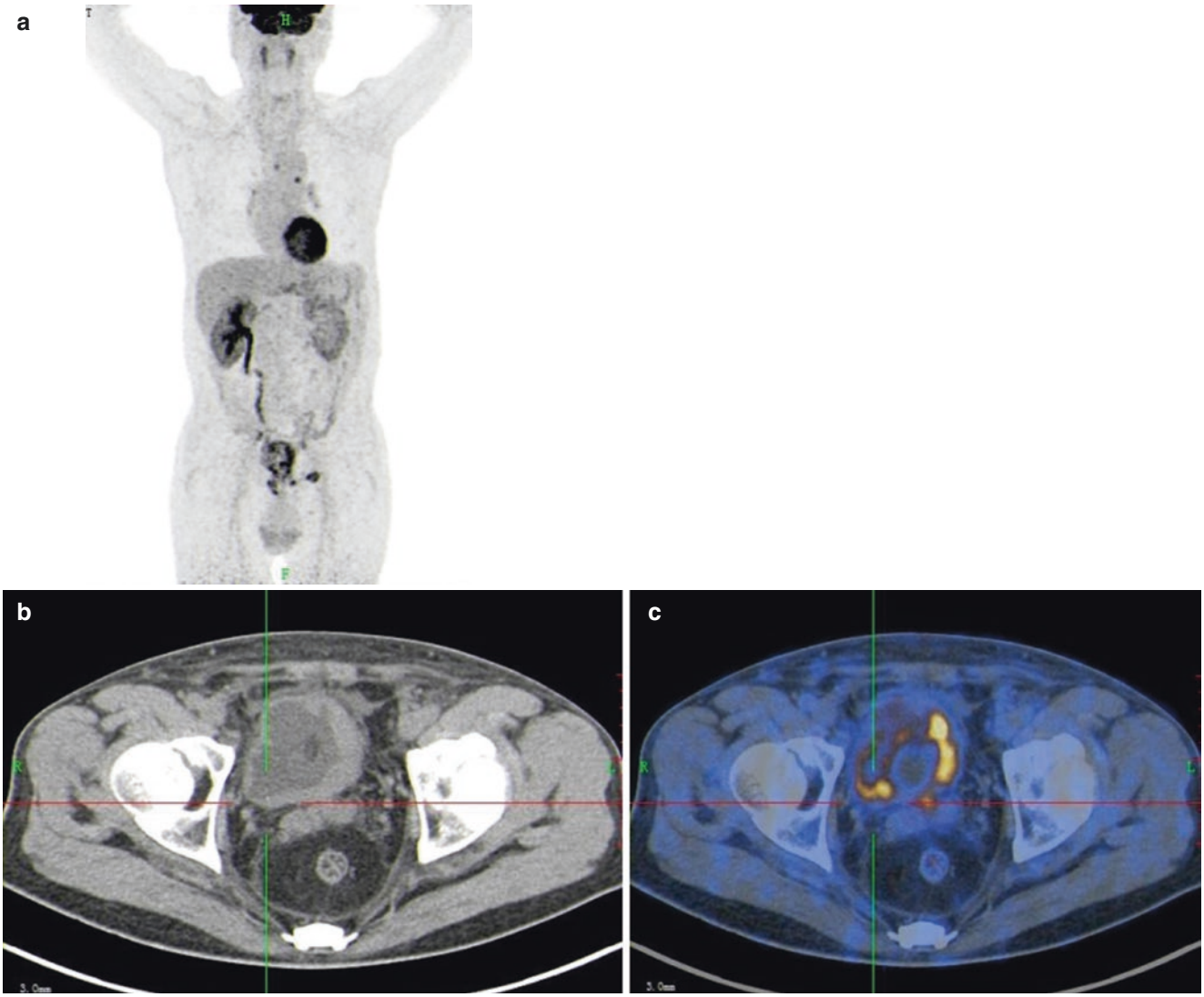

Fig. 5.3 Images of a patient with diagnosed muscle-invasive bladder cancer. (**a**) The MIP of FDG-PET; (**b**) CT of FDG-PET/CT and (**c**) PET/CT showed high FDG uptake of primary tumor in the bladder wall after diuresis. A lymph node metastasis is seen in the right side of the pelvis on CT of FDG-PET/CT (**d**) and PET/CT (**e**). Bone metastasis in pubic bone can be seen on CT of FDG-PET/CT (**f**) and PET/CT (**g**)

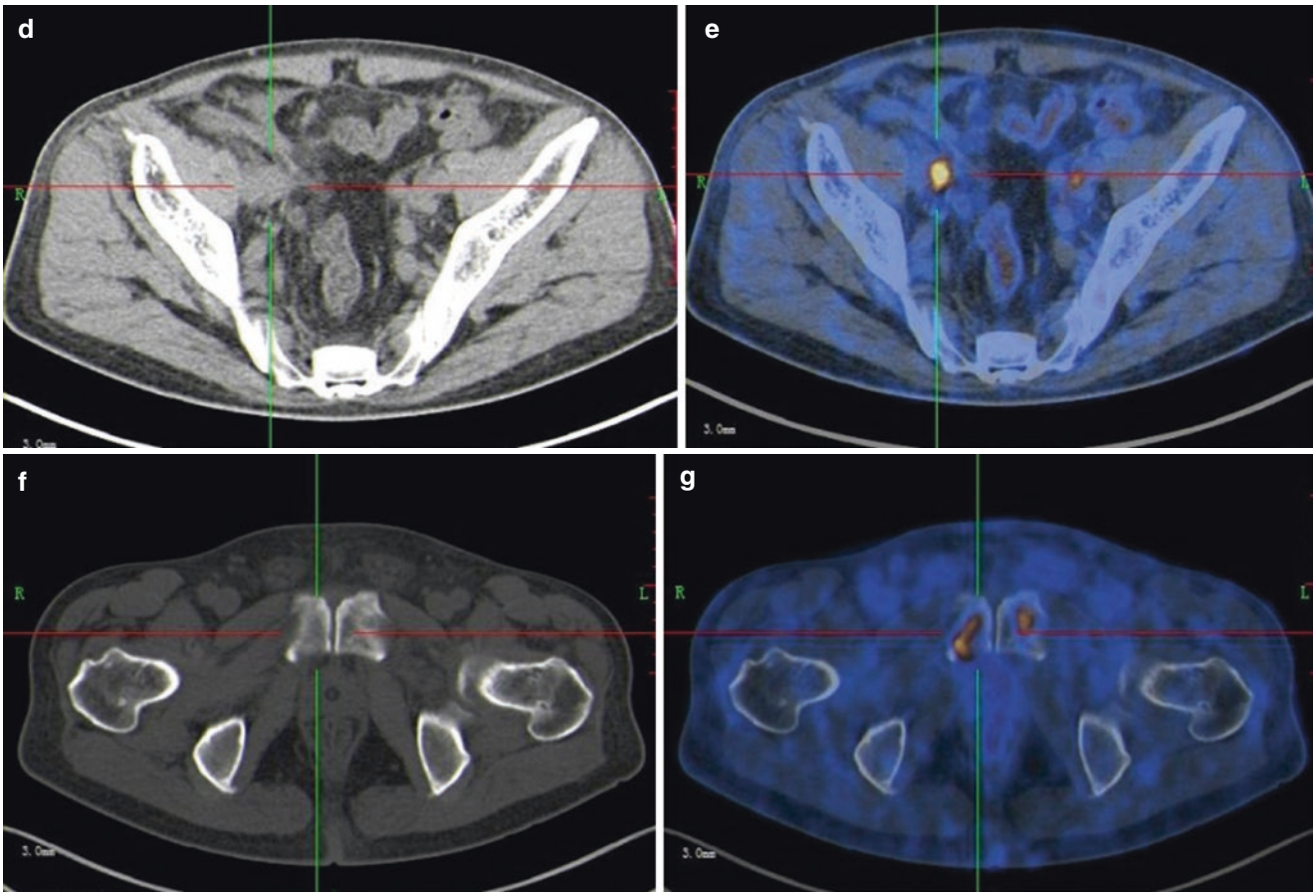

Fig. 5.3 (continued)

diagnosis of LN metastasis is not significantly better than CT. Swinnen et al. reported that the accuracy, sensitivity, and specificity of FDG-PET/CT for diagnosing LN metastasis of BC were 84%, 46%, and 97%, respectively [5]. The corresponding values when CT results were analyzed separately were 80, 46, and 92%. The study considered that compared to CT alone, the combination of FDG-PET/CT afforded no advantage in the staging of invasive BC and LN metastases.

5.2.3.3 ^{18}F-FDG-PET/CT for Restaging of BCs

The prognosis of recurrent BC is very poor. Early detection and active treatment remain very important for prolonging the survival time of patients and improving their quality of life. Considering that recurrent BC patients may require expensive targeted therapies and immunotherapy, precise re-segmentation is particularly important. FDG-PET/CT can be used for whole-body imaging, and in most instances of recurrence, BC shows higher FDG uptake; thus, FDG-PET/CT can be used for an accurate diagnosis of BC (Fig. 5.4). Jadvar et al. retrospectively evaluated the ability of FDG-PET or PET/CT to diagnose recurrent and metastatic BC. In their study, all 35 patients had previously been treated for the primary disease. The sites of metastasis detected in the study included the mediastinum, lungs, and bone. FDG-PET/CT had an impact on the clinical treatment of 17% of patients by facilitating the proposal of additional treatment or waiting for an observational strategy [6]. FDG-PET can also be used to detect recurrent tumors in the pelvis and distinguish between local recurrence and post- or postradiation fibrosis/necrosis and distant metastasis.

5.2.3.4 ^{18}F-FDG-PET/CT for Determining the Response to Therapy

In bladder muscle-invasive BC, neoadjuvant chemotherapy is the standard treatment, which can improve the overall survival rate of patients with BC. Patients with significantly reduced LNs after neoadjuvant chemotherapy can further choose surgery and reduce the recurrence rate. However, we should also recognize that some BCs are not responsive to neoadjuvant chemotherapy. It is often difficult and inaccurate

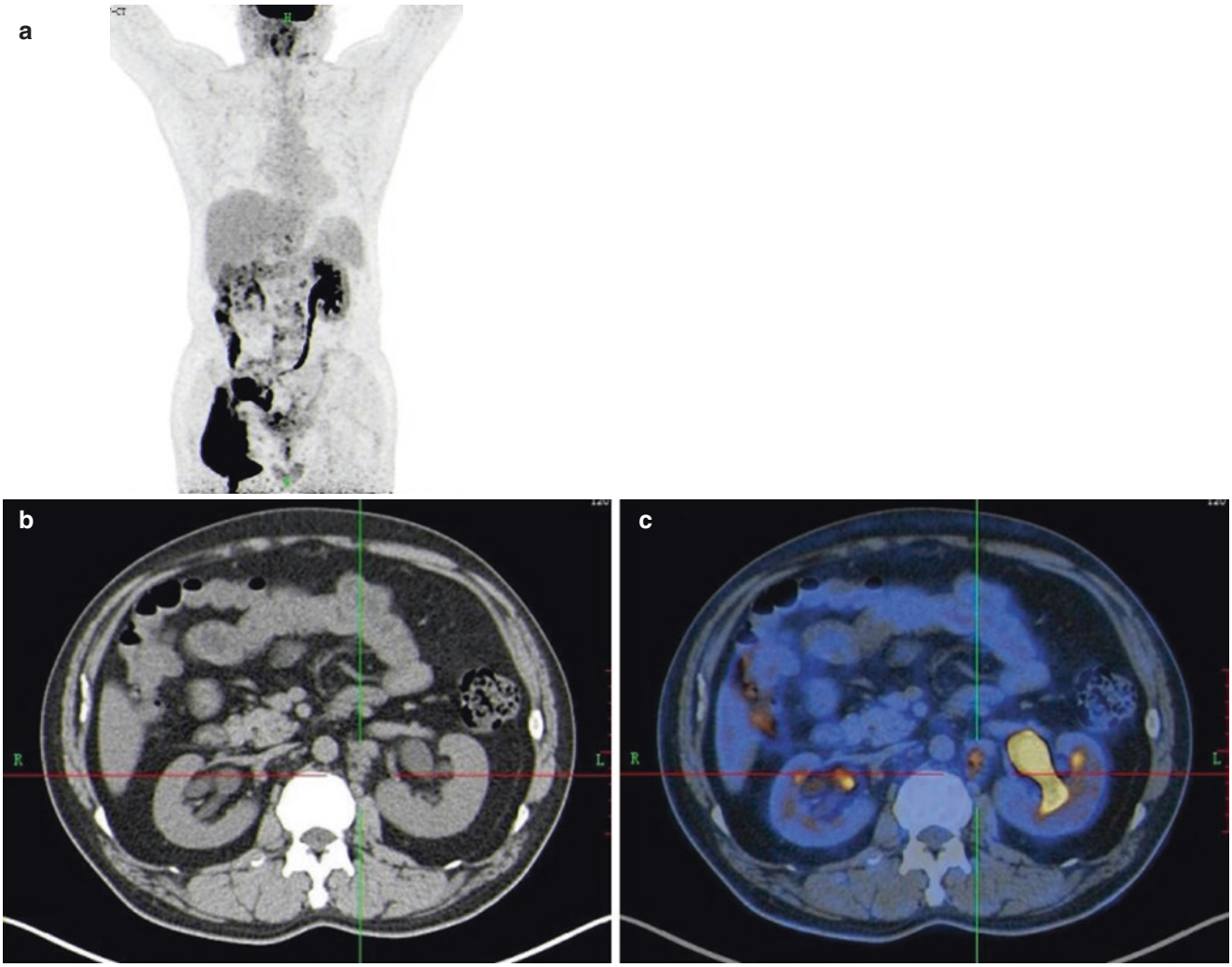

Fig. 5.4 Images of a patient with bladder cancer who developed lymph node metastasis after operation and chemotherapy. (**a**) The MIP of FDG-PET. A lymph node metastasis is seen in the side of abdominal aorta on CT of FDG-PET/CT (**b**) and PET/CT (**c**)

to use conventional imaging modalities such as CT to assess the responsiveness of LN to neoadjuvant chemotherapy. This is mainly due to the difficulty in identified surviving tumors in residual (necrotic) masses and small-tumor deposits in normal-sized LNs. FDG-PET/CT is currently used to monitor the response of pelvic LN metastasis to BC neoadjuvant chemotherapy. According to the European Cancer Research and Treatment Organization (EORTC) recommendations, metabolic responses are assessed based on changes in FDG uptake. Reactivity was assessed on CT according to Reaction Assessment Criteria in Solid Tumors (RECIST). All patients underwent a histopathological examination for PLND. PET/CT and CT correctly distinguished between nonresponders (79%) and complete responders (68%) among disabled patients (63%). At present, it is commonly believed that PET/CT is suitable for evaluating the response of LN to neoadjuvant chemotherapy. However, this belief needs to be confirmed in large clinical trials [7] (Fig. 5.5).

5.3 Renal Cell Carcinoma

5.3.1 Overview of Renal Cell Carcinoma

Renal cell carcinoma (RCC) accounts for about 3% of human cancers, most of which are well differentiated and cured by surgical resection. However, poorly differentiated kidney cancer is highly invasive and remains the main cause of cancer-related death. Kidney cancer is divided into clear-cell carcinomas (60–80%), papillary carcinomas (10%), chromophobe cell carcinoma (5%), and other tumors such as sarcomatoid carcinomas, squamous cell carcinomas, and leiomyosarcomas [8]. Because some RCCs are highly fatal, it is important to identify, recognize, and grade them and then to monitor them during treatment. Ten years ago, PET had little to do with RCC. In recent years, a more comprehensive understanding of the clinical application of FDG-PET in RCC has been gained.

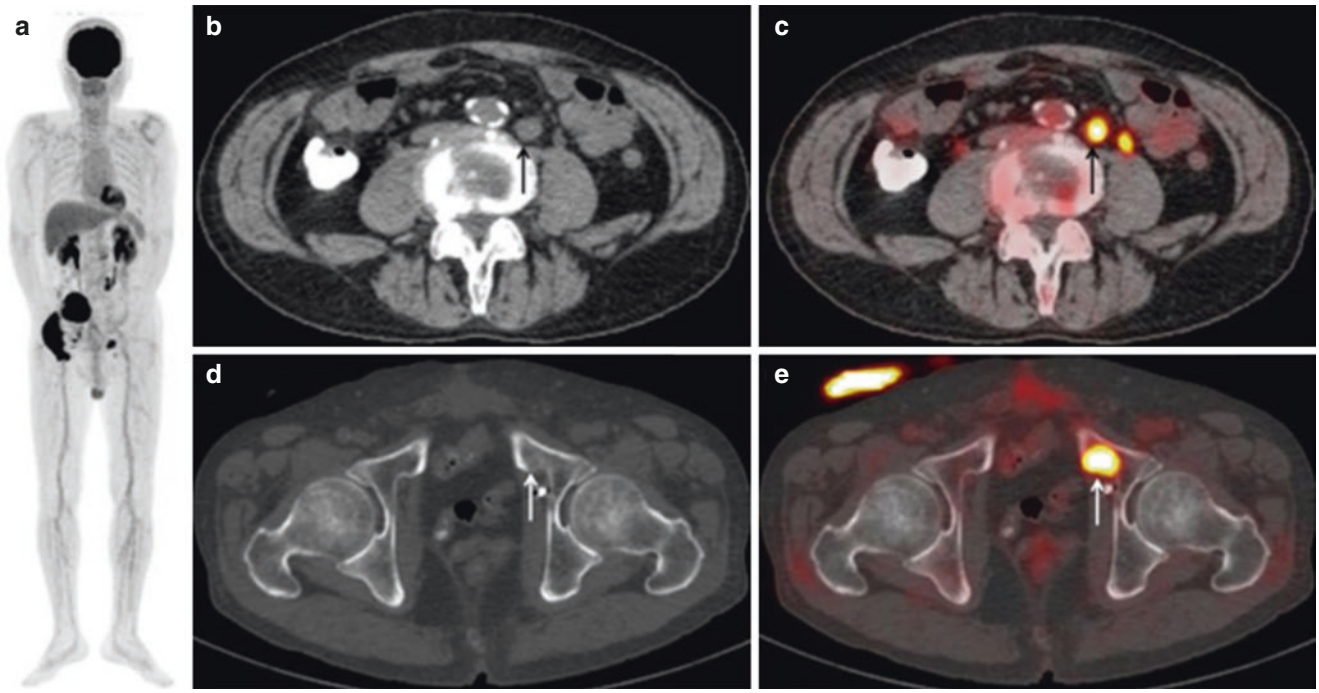

Fig. 5.5 A 66-year-old male patient with bladder cancer (cT3N1) developed lymph node metastasis and bone metastasis after neoadjuvant chemotherapy and radical cystectomy. (**a**) The maximum intensity projection (MIP) of FDG-PET shows two regions of abnormal FDG uptake in the pelvis. (**b**) CT of FDG-PET/CT and (**c**) PET/CT showed moderate FDG uptake (SUVmax, 7.2) corresponding to a 1.5-cm enlarged para-aortic lymph node (arrow), suggesting lymph node recurrence. The little FDG uptake on the left side of the lymph node recurrence lesion is a physiological excretion in the left ureter. CT of FDG-PET/CT and (**e**) PET/CT showed strong FDG uptake (SUVmax, 13.0) corresponding to a mild sclerosis of the left pubic symphysis (arrow), suggesting bone metastasis. It is difficult to detect this bone metastasis only by (**d**) CT

5.3.2 Glucose Metabolism of Renal Cell Carcinoma

RCC glucose metabolism is active at the cellular level and exhibits the classic Warburg effect. Increased levels of GLUT 1 in clear-cell renal cell carcinoma (ccRCC) tumors compared to those in normal control tissues indicate increased glucose uptake. In addition, metabolomics, proteomics, and transcriptomics studies have shown increased levels of glycolytic metabolites and enzymes, such as hexokinase, pyruvate kinase 2, and lactate dehydrogenase A (LDHA) in ccRCC cells and tissues, indicating increased glucose utilization in renal cancer; the lactic acid product of anaerobic glycolysis increases accordingly. On the other hand, the kidney is an important organ of gluconeogenesis, and fructose 1,6-bisphosphatase 1 (FBP1) is highly expressed in the kidney and can antagonize glycolysis. However, the expression of FBP1 that antagonizes glycolysis in renal cancer is reduced or even disappears in the tumor. Studies have shown that overexpression of FBP1 in tumors can inhibit ccRCC tumor growth, indicating glycolysis and the closely related gluconeogenesis play an important role in the occurrence and development of kidney cancer. In addition, many studies have confirmed that the levels of pyruvate carboxylase and pyruvate dehydrogenase (i.e., enzymes that catabolize pyruvate to facilitate the TCA cycle) also significantly reduce in ccRCC, further indicating that these tumors are dependent on glycolysis (Table 5.1) [9].

5.3.3 Clinical Utility of ^{18}F-FDG-PET/CT Scanning in RCC

5.3.3.1 ^{18}F-FDG-PET/CT for Diagnosis of Primary RCC

It is generally believed that the value of FDG-PET in the diagnosis of primary RCC is little. The accuracy of CT-based diagnosis of renal cancer can reach 95%. CT scans of RCC are characterized by a soft tissue mass in the renal parenchyma, showing a uniform or uneven density, a slightly higher density, or a slightly lower density lesion, which may have cystic changes and calcification. FDG-PET/CT sensitivity is only about 60% in RCC, although its specificity for malignancy is 90% [4]. In clinical practice, RCC has relatively low FDG uptake, especially in well-differentiated ccRCC. The low sensitivity of ^{18}F-FDG-PET/CT for renal cancer diagnosis may be related to the following factors: RCC is mostly clear-cell carcinoma, especially of grades I–II; low expression of GLUT-1 in tumor tissue, which reduces the glucose uptake ability of the tumor; gluconeogenesis in some well-differentiated renal cancers, and high glucose-6-phosphatase activity in the tumor, so that the

Table 5.1 Renal cancer-related oncogenes and tumor suppressor genes

Gene	Effect on metabolic pathways	Correlation with RCC
VHL	Inhibition of the Warburg effect by inactivating HIF	Loss of function found in >90% of RCC patients
p53	• Downregulation glycolysis by inactivating of GLUT 1/4 and upregulation of TIGAR • Upregulates glutamine metabolism by increasing the transcription of glutaminase 2	p53 mutation is rare in RCC
PTEN	Inhibition of glycolysis by inactivating AKT	• In RCC patients, 2.6% had double-allele loss and 16.6% had PTEN single-allele loss • Loss of PTEN is associated with high staging and staging of RCC
TSC1/2	Warburg effect deficiency and glutamine addiction by activating mTOR	Mutation is a risk factor for RCC
AKT	Up regulation of glycolysis by kinases including hexokinase	• AKT mutations are rare in RCC, but AKT is activated due to loss of PTEN • AKT inhibitors are being tested in RCC clinical trials

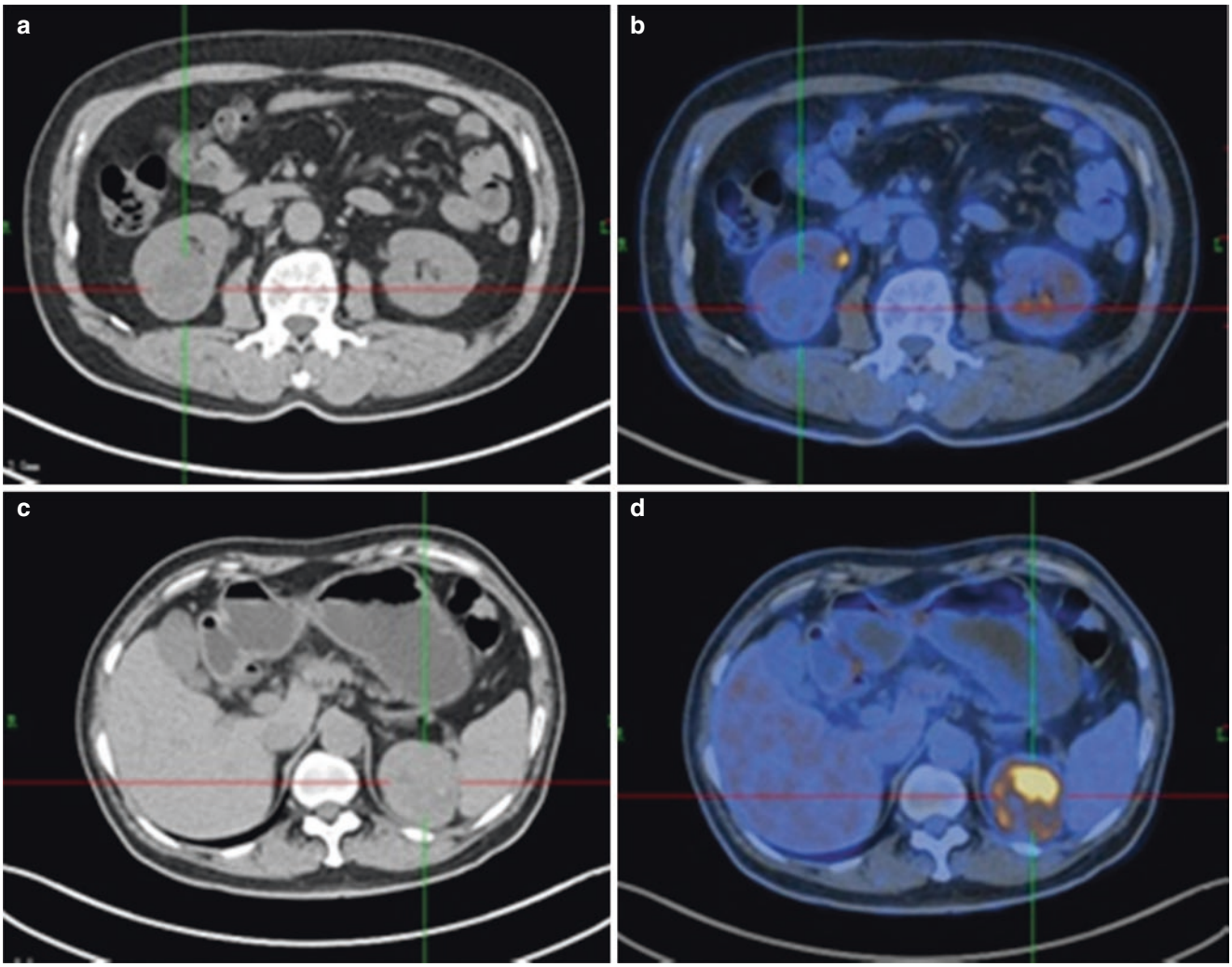

Fig. 5.6 Primary RCC could be visualized with FDG-PET. (**a**) CT of FDG-PET/CT and (**b**) PET/CT showed solitary renal cancer in the right lower pole (SUVmax = 2.9). (**c**) CT of FDG-PET/CT and (**d**) PET/CT showed renal cancer in the left upper pole (SUVmax = 8.1)

phosphorylated FDG regenerates free FDG and discharges the tumor cells; and the effect of intrarenal urine radioactivity on tumor detection. These factors make it difficult to distinguish between FDC uptake in RCC tumor tissue and physiological FDG uptake in renal parenchyma. In addition, the uptake of FDG in renal tumors also depends on tumor size (Fig. 5.6). FDG is sensitive and specific for poorly differentiated clear-cell carcinomas, such as those of grades III and IV, which may be related to decreased gluconeogenesis and enhanced glycolysis in poorly differentiated renal

cancer. Ferda et al. found that patients with the highest FDG intake had a tumor grade of IV and SUVmax was more than 10 in these patients [10].

5.3.3.2 ^{18}F-FDG-PET/CT for the Staging of RCC

FDG-PET plays a minor role in the diagnosis of primary renal cancer. Enhanced CT and/or MRI usually detects the primary lesion well, and if identification is difficult, it can be further punctured to pinpoint the pathology. FDG plays an important role in the diagnosis of specific kidney cancer subtypes such as type II papillary and sarcomatoid cancers, and FDG-PET plays a relatively minor role in the initial staging of RCC. Currently, there is a higher risk, and larger tumors are more studied in FDG-PET. For local staging, FDG-PET has been found to be able to determine whether the thrombus in the renal vein and inferior vena cava is malignant or benign. When isolated lesions are detected, FDG-PET can diagnose metastatic disease based on the metabolic properties of the lesion (Figs. 5.7 and 5.8). However, FDG PET is not widely used in RCC staging.

5.3.3.3 ^{18}F-FDG-PET/CT for Response to Therapy

FDG-PET is also commonly used to monitor and evaluate RCC sensitivity to novel targeted therapies. Kidney cancer does not respond to conventional chemotherapy, so this treatment approach is rarely used. A variety of targeted therapies, including tyrosine kinase inhibitors such as sorafenib and sunitinib (with anti-angiogenic mechanisms) and mTOR

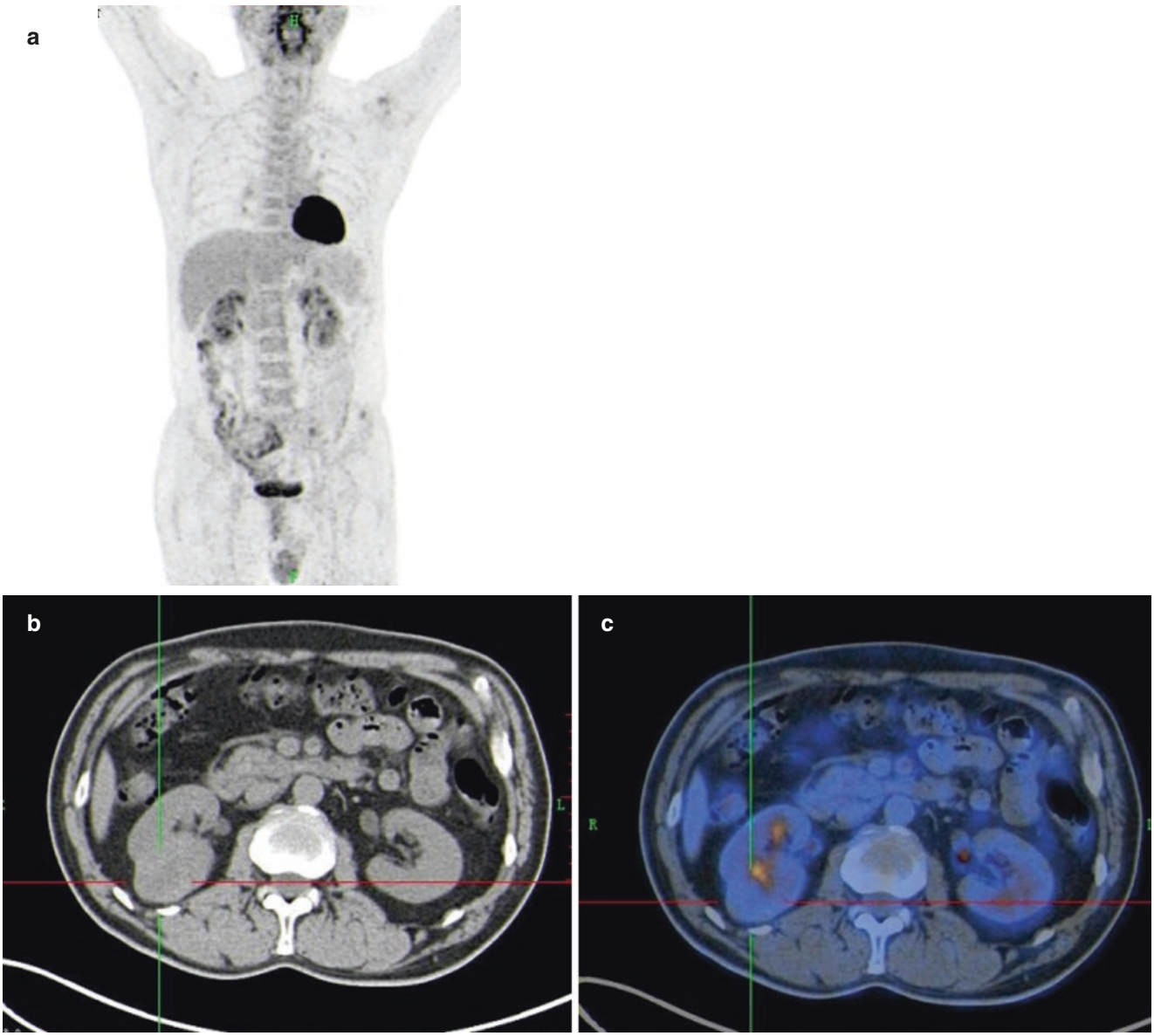

Fig. 5.7 Patient with diagnosed RCC. (**a**) The MIP of FDG-PET; (**b**) CT of FDG-PET/CT and (**c**) PET/CT show primary tumor in the right renal; (**d**) CT of FDG-PET/CT and (**e**) PET/CT show lung metastasis

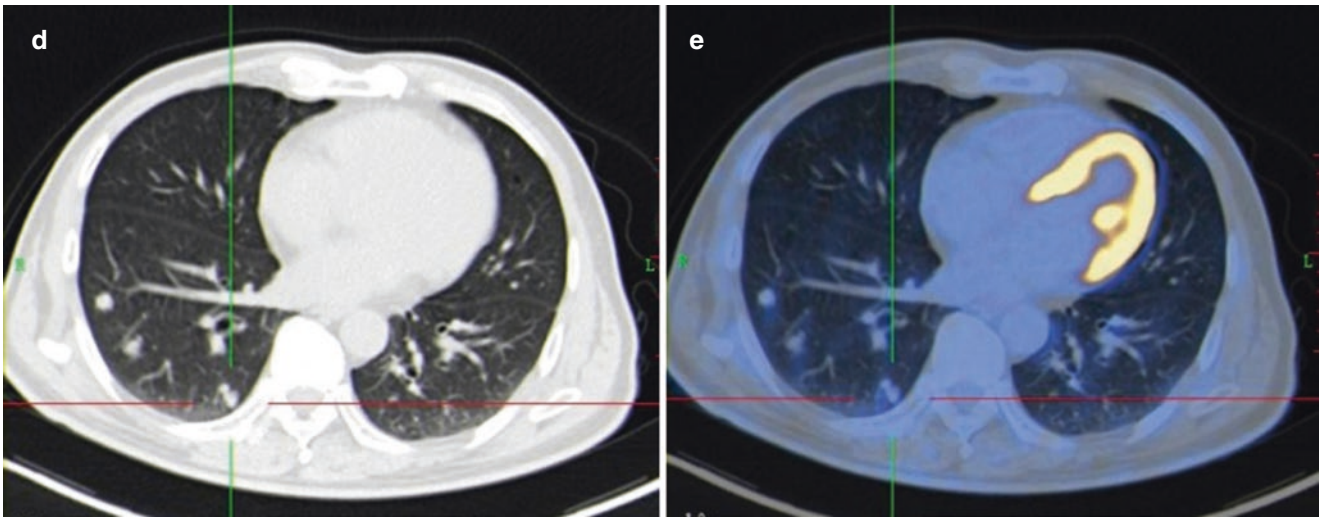

Fig. 5.7 (continued)

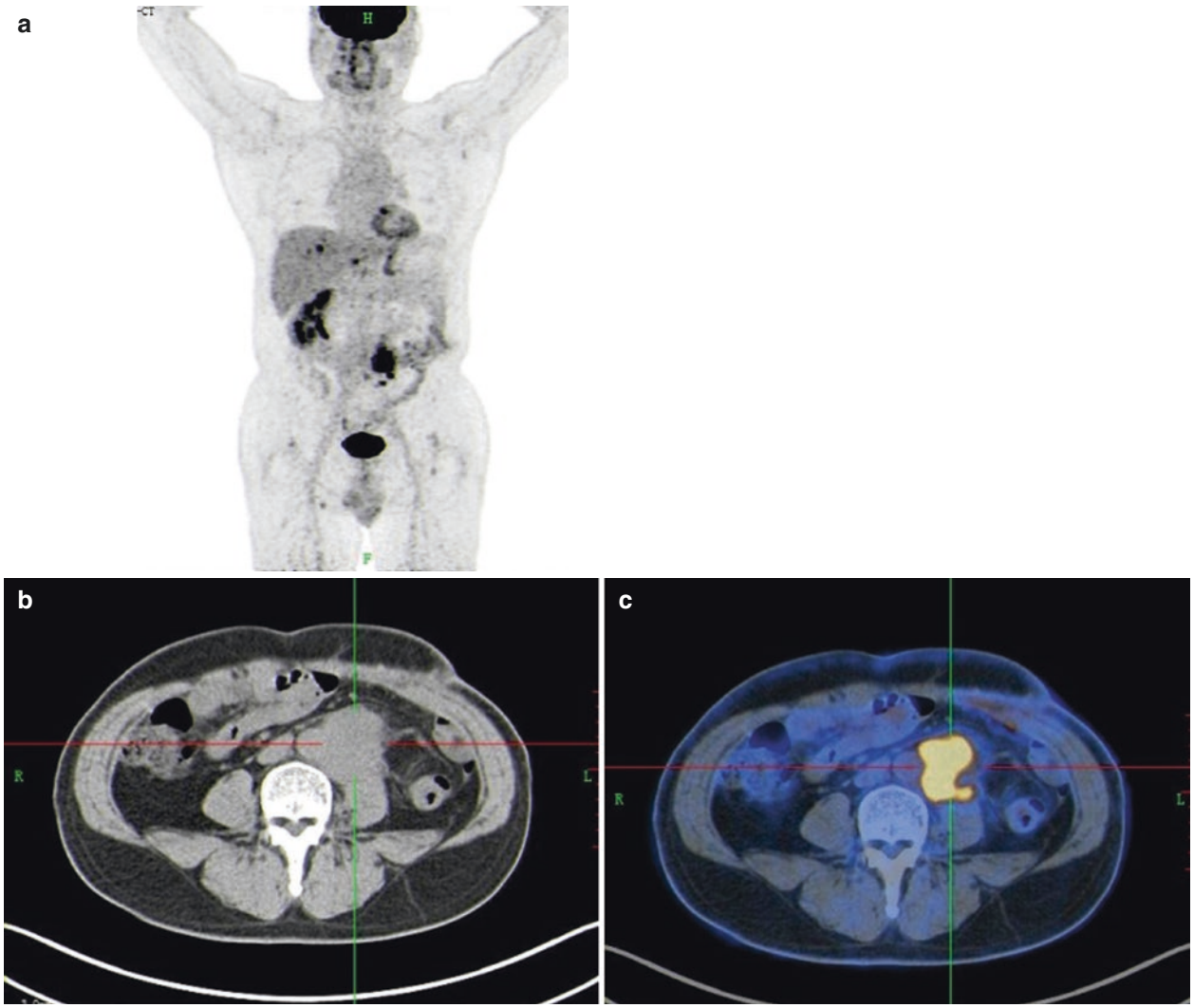

Fig. 5.8 Clear-cell renal cancer recurrence after operation. (**a**) The MIP of FDG-PET shows regions of abnormal FDG uptake on whole body. Lymph node metastasis is seen in the side of abdominal aorta on (**b**) CT of FDG-PET/CT and (**c**) PET/CT. Liver metastasis is seen in the right lobe of liver on (**d**) CT of FDG-PET/CT and (**e**) PET/CT. Bone metastasis is seen in sacrum on (**f**) CT of FDG-PET/CT and (**g**) PET/CT

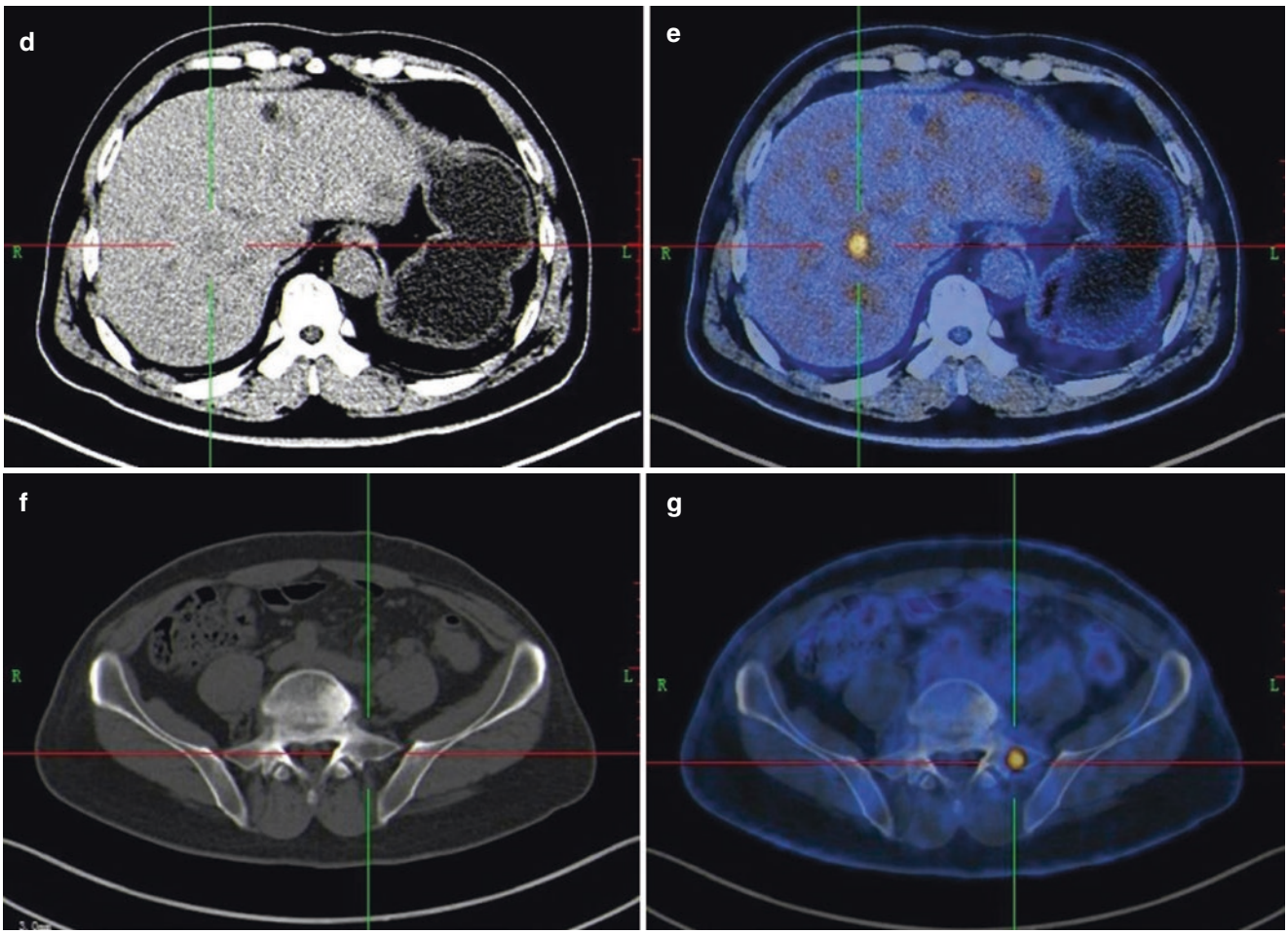

Fig. 5.8 (continued)

inhibitors (such as everolimus), have shown good curative effects. Although measurement of the tumor size with the RECIST criteria has been attempted to monitor chemotherapy effects, tumor size typically does not change much in targeted therapies. Evaluation of FDG-PET metabolic activity can allow better monitoring of the effectiveness of targeted therapy with tyrosine kinase inhibitors. Ferda et al. demonstrated that FGF uptake was associated with the prognosis in pretreatment tumors, and patients with a renal tumor SUVmax >10 had a significantly lower survival rate than those with an SUVmax <10. A reduction in FDG uptake is also closely related to the effect of targeted therapy, regardless of the location of the lesion (e.g., bone, lung, LNs, etc.). The extent of the SUVmax decline was associated with progression-free survival and overall survival (OS). The advantage of FDG-PET over conventional methods is most pronounced in bone and musculoskeletal metastases, which are difficult to assess on CT and MRI because bone damage persists even if targeted therapy was effective for the lesion. Some investigators used the total metabolic mass and total disease glycolysis (TLG) as an overall measure of disease burden rather than a separate SUVmax score. This is calculated by multiplying by SUVmax and the number of lesions. Therefore, FDG-PET is being increasingly used to monitor the therapeutic effects in patients with metastatic disease receiving tyrosine kinase inhibitors and other targeted therapies.

5.4 Prostate Cancer

5.4.1 Overview of Prostate Cancer

Prostate cancer is the second most common malignant tumor in men and the fifth leading cause of cancer-related death in men worldwide. At present, a prostate biopsy is still the only way to provide a definitive diagnosis of prostate cancer.

Other diagnostic methods for prostate cancer include measurement of serum prostate-specific antigen (PSA) levels, ultrasound (US) and MRI examinations, and PET. The current clinical challenge in the management of this disease is improving the accuracy of biopsy for diagnosis and identification of aggressive prostate cancer to avoid overdiagnosis and overtreatment. Accurate staging is another major challenge in the diagnosis of prostate cancer. Accurate staging of prostate cancer on the basis of imaging data can avoid unnecessary LN dissection and reduce the related complications.

5.4.2 Glucose Metabolism in Prostate Cancer

Prostate tissue cells show lower levels of anaerobic glycolysis. Early prostate cancer cells rely more on lipids and other energy molecules to produce energy than they do on aerobic respiration. Therefore, the Warburg effect is not consistent in the pathogenesis of prostate cancer, and most prostate tumor cells do not show a high glycolytic ability. Clinically, many prostate tumor lesions show negative findings on FDG-PET scans. Only some poorly differentiated, advanced prostate cancers will begin to exhibit the Warburg effect and show high glucose uptake. Late prostate cancer lesions show increased lactate concentrations, expressing monocarboxylate transporters (MCTs) to transport intracellular lactate. Studies have shown that the phenotype of MCT is associated with the aggressiveness of the cancer and the prognosis. By blocking MCT activity, tumor cells can accumulate toxic metabolites at a faster rate. Thus, expression of the lactate shuttle in prostate cancer represents a potential therapeutic target as well as a potential diagnostic and prognostic indicator.

5.4.3 Clinical Utility of ^{18}F-FDG-PET/CT Scanning in Prostate Cancer

5.4.3.1 ^{18}F-FDG-PET/CT for Diagnosis of Primary Prostate Cancer

In 2008, Jadvar et al. [11] studied the glucose metabolism of the normal prostate in 145 normal male patients who underwent FDG-PET/CT imaging. They found a mean SUV of 1.3 for the prostate and an average SUVmax of 1.6. In 2010, Minamimoto et al. [12] performed FDG-PET examinations before prostate biopsy in 50 patients with elevated PSA levels. The patients' median age was 68 years and their median PSA level was 15.9 ng/mL. The investigators reported that FDG-PET assessments diagnosed prostate cancer with a sensitivity of 51.9% and a specificity of 75.7%. Shiiba et al. [13] reported a prospective study comparing 20 male patients with elevated PSA levels who were assessed for prostate cancer. These patients underwent 11 C-methionine and FDG imaging. Their median age was 72.4 years, and the median PSA level was 181.3 ng/mL. In their study, the sensitivity and specificity of FDG-PET/CT for the diagnosis of prostate cancer were 35.8% and 92.3%, respectively. The researchers concluded that the two tracers performed the same in patients with a high Gleason score, although FDG-PET/CT findings were poor when the Gleason score was lower than 8. In 2012, Minamimoto and colleagues [14] reported the findings for a total of 155,456 investigations, and FDG-PET/CT showed positive findings in 16,955. Of these, 1912 were diagnosed with cancer, and 165 of them had prostate cancer. The overall sensitivity of FDG-PET/CT for detecting cancer was 78% (1491/1912), but the detection rate for prostate cancer was only 37%. Therefore, FDG-PET is not suitable as the main diagnostic method for prostate cancer (Fig. 5.9).

5.4.3.2 ^{18}F-FDG-PET/CT for the Staging of Prostate Cancers

FDG-PET shows some value in the staging of prostate cancer (Fig. 5.10). In 2010, Tiwari et al. [15] examined 16 cases involving FDG-PET/CT and bone imaging and found 197 bone lesions by FDG-PET/CT imaging, of which 97 (49%) were also detected using conventional bone imaging. Most of the lesions (i.e., 95%) shown by FDG-PET/CT showed matched lesions in bone imaging. Yu et al. [16] compared the findings of FDG and ^{11}C-acetate PET/CT imaging in eight patients. In their study, ^{11}C-acetate PET/CT showed more metastases than FDG-PET/CT in most patients. In 2013, Damle et al. [17] compared FDG-PET/CT, ^{18}F-sodium fluoride PET/CT, and bone imaging for their effectiveness in detecting bone metastasis of prostate cancer, lung cancer, and breast cancer. In assessments for 49 patients with prostate cancer, they found that the sensitivity, specificity, and accuracy of FDG-PET/CT were 71.9%, 100%, and 81.6%, respectively.

5.4.3.3 ^{18}F-FDG-PET/CT for Restaging of Prostate Cancers

Many clinical studies have assessed the use of FDG-PET/CT for prostate cancer re-segmentation. Most of these studies compared FDG to another PET tracer. Garcia et al. [18] studied 38 patients and found that FDG-PET/CT diagnosed recurrent lesions with a sensitivity of 34% and ^{11}C-choline PET/CT showed a sensitivity of 68%. Therefore, the researchers concluded that FDG-PET/CT has limited value for prostate cancer re-segmentation. However, a study by the National Cancer PET Registry is

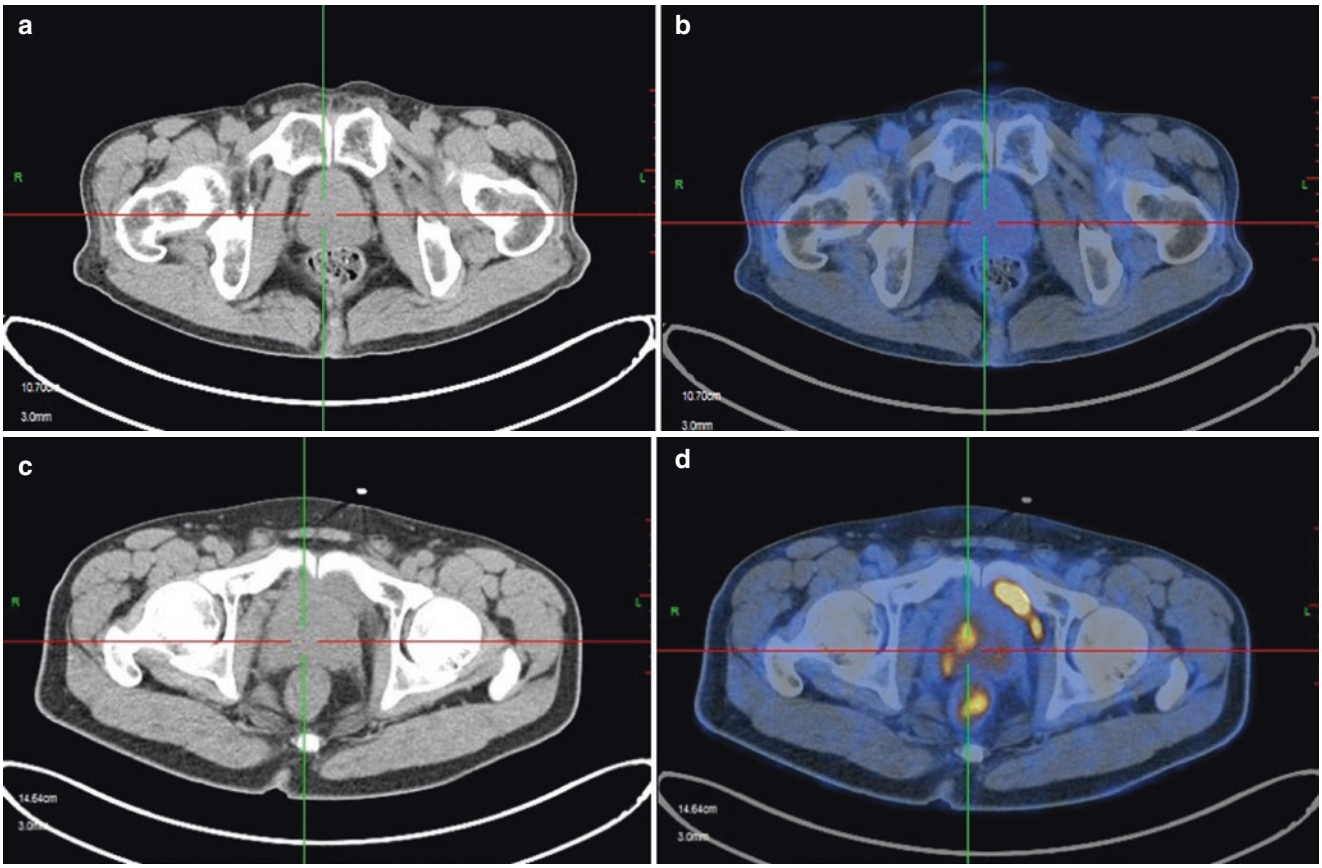

Fig. 5.9 FDG PET can show primary prostate cancer. (**a**, **b**) PET/CT showed a slight FDG uptake corresponding to the prostate (SUVmax = 2.2). (**c**, **d**) PET/CT showed strong FDG uptake corresponding to the prostate (SUVmax = 6.2)

worth mentioning in this context. This study used scans for pathologically confirmed cancer patients to determine the stage or suspected recurrence (Fig. 5.11). A total of 40,863 FDG-PET and FDG-PET/CT scans were included, of which 5309 were performed in men with prostate cancer (i.e., 2042 for initial staging, 1477 for re-segmentation, and 1790 for suspected recurrence) [19]. These scans resulted in an expected cancer treatment change in 35.1% of cases: 25.3% from untreated to treatment and 9.7% from treatment to untreated. The rates of staging, reclassification, or detection of subgroup changes in treatment plans due to suspected recurrence were 32.0%, 34.0%, and 39.4%, respectively.

5.4.3.4 ^{18}F-FDG-PET/CT to Determine the Prognosis of Prostate Cancers

One study explored the value of FDG-PET/CT in determining the prognosis of prostate cancer. The study was published in 2013 by Jadvar et al. and included 87 patients with metastatic prostate cancer after castration and antiandrogen therapy [20]. The median follow-up period was 22.2 months, and 61 patients died. The authors tested the SUVmax values by univariate and multivariate Cox regression analyses of continuous PET parameters adjusted for the standard clinical parameters (age, serum PSA levels, alkaline phosphatase

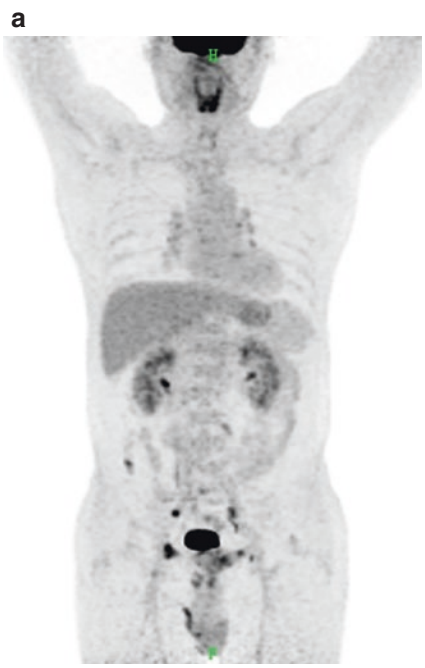

Fig. 5.10 Patients diagnosed with prostate cancer. (**a**) The MIP of FDG-PET. Primary tumors in the prostate can be visualized on CT (**b**) and FDG PET/CT (**c**). Lymph nodes on the metastatic side of the iliac arteries can be seen on CT (**d**) and FDG PET/CT (**e**). Pubic bone metastases can be seen on CT (**f**) and FDG PET/CT (**g**)

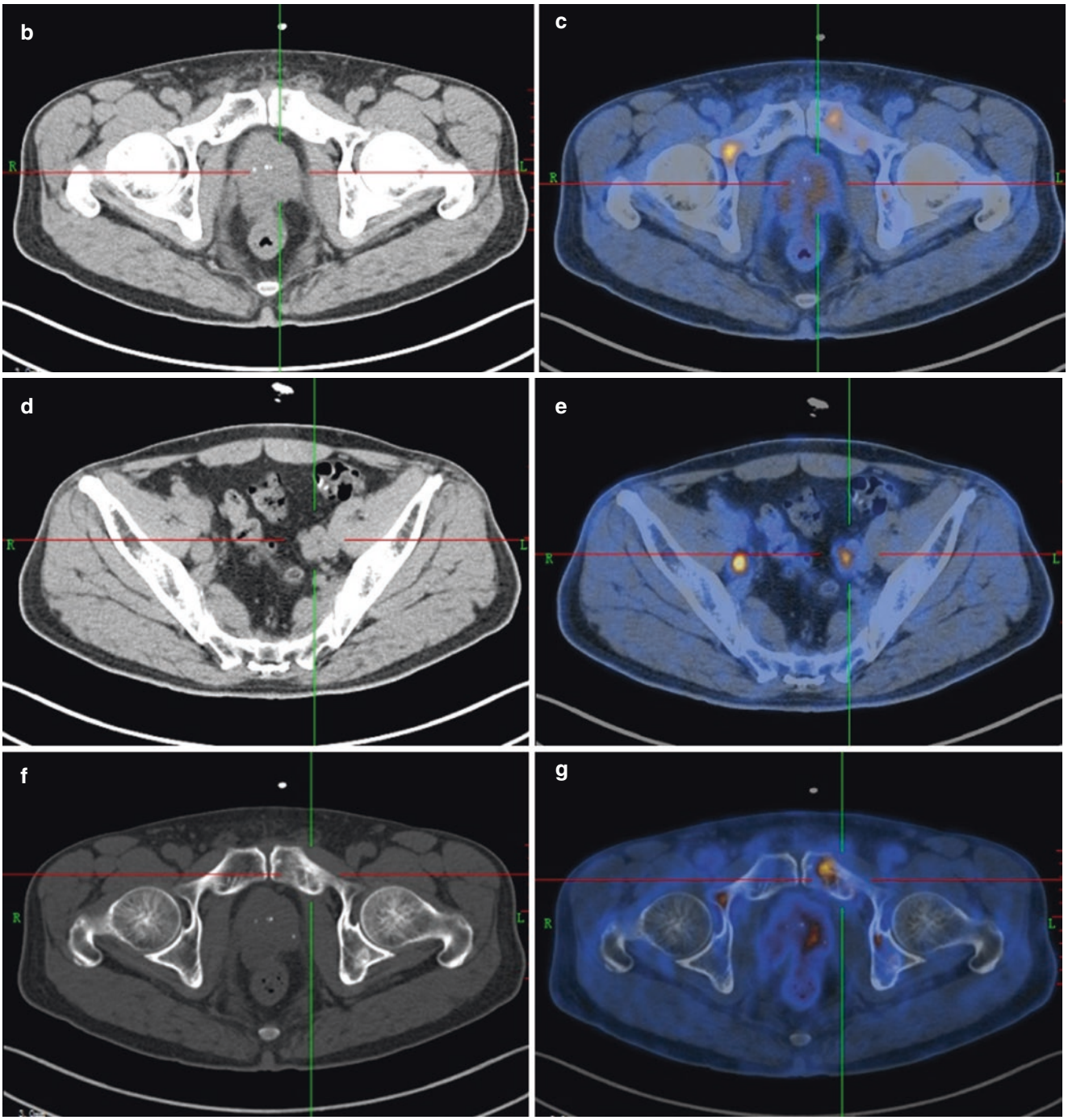

Fig. 5.10 (continued)

levels, analgesics, previous chemotherapy, and Gleason score at initial diagnosis). In their study, the sum of the SUVmax and average SUVmax influenced the OS, and the sum of the SUVmax values of all metabolically active lesions (after deducting patient-specific background—the average SUV of the liver) provided independent prognostic information for the OS of metastatic prostate cancer in castrated men. This information may be useful in assessing various traditions and the effectiveness of emerging treatment strategies.

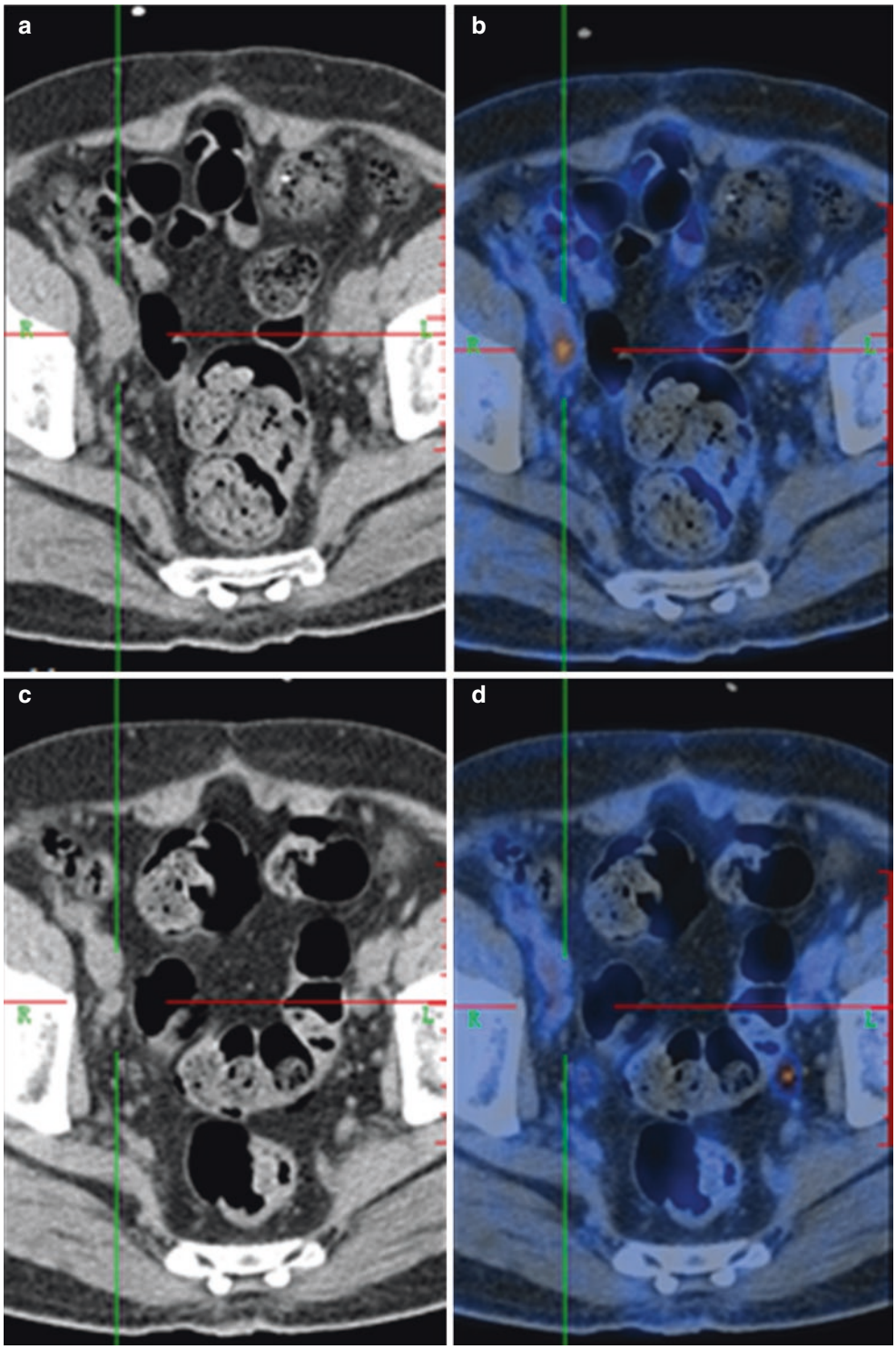

Fig. 5.11 Patients who received androgen deprivation therapy. (**a**, **b**) FDG PET/CT showed lymph node metastasis on the right side of the pelvis after androgen deprivation therapy; (**c**, **d**) FDG PET showed no lymph node metastasis in the pelvis prior to androgen deprivation therapy

5.5 Summary

At present, FDG-PET/CT is not the main imaging method for diagnosing urinary system tumors, mainly because of its low sensitivity, which may be caused by disturbances in physiological excretion and the low level of tumor glucose metabolism in these tumor cells. In kidney cancer, FDG-PET/CT may play a new role in the selection of surgery and targeted therapy during the initiation and follow-up periods in TKI treatment. In BC, FDG-PET/CT can be used for staging and re-segmentation, and its clinical value in prostate cancer remains doubtful. With regard to the three main types of cancers of the urinary system, there is a need to study the potential of FDG or other tracers in PET/CT more systematically.

References

1. Apolo AB, Riches J, Schoder H, Akin O, Trout A, Milowsky MI, Bajorin DF (2010) Clinical value of fluorine-18 2-fluoro-2-deoxy-D-glucose positron emission tomography/computed tomography in bladder cancer. J Clin Oncol 28(25):3973–3978
2. Avery R, Kuo PH (2013) 18F sodium fluoride PET/CT detects osseous metastases from breast cancer missed on FDG PET/CT with marrow rebound. Clin Nucl Med 38(9):746–748
3. Bouchelouche K (2012) PET/CT and MRI in bladder cancer. J Cancer Sci Ther s14(1):7692–7709
4. Caldarella C, Muoio B, Isgro MA, Porfiri E, Treglia G, Giovanella L (2014) The role of fluorine-18-fluorodeoxyglucose positron emission tomography in evaluating the response to tyrosine-kinase inhibitors in patients with metastatic primary renal cell carcinoma. Radiol Oncol 48(3):219–227
5. Ferda J, Ferdova E, Hora M, Hes O, Finek J, Topolcan O, Kreuzberg B (2013) 18F-FDG-PET/CT in potentially advanced renal cell carcinoma: a role in treatment decisions and prognosis estimation. Anticancer Res 33(6):2665–2672
6. Garcia JR, Soler M, Blanch MA, Ramirez I, Riera E, Lozano P, Perez X, Delgado E, Carrio I, Lomena F (2009) [PET/CT with (11)C-choline and (18)F-FDG in patients with elevated PSA after radical treatment of a prostate cancer]. Rev Esp Med Nucl 28(3): 95–100
7. Hillner BE, Siegel BA, Shields AF, Liu D, Gareen IF, Hunt E, Coleman RE (2008) Relationship between cancer type and impact of PET and PET/CT on intended management: findings of the national oncologic PET registry. J Nucl Med 49(12): 1928–1935
8. Sahni VA, Silverman SG (2014) Imaging management of incidentally detected small renal masses. Semin Intervent Radiol 31(1):9–19
9. Jadvar H, Quan V, Henderson RW, Conti PS (2008) [F-18]-Fluorodeoxyglucose PET and PET-CT in diagnostic imaging evaluation of locally recurrent and metastatic bladder transitional cell carcinoma. Int J Clin Oncol 13(1):42–47
10. Lu YY, Chen JH, Liang JA, Wang HY, Lin CC, Lin WY, Kao CH (2012) Clinical value of FDG PET or PET/CT in urinary bladder cancer: a systemic review and meta-analysis. Eur J Radiol 81(9):2411–2416
11. Jadvar H, Ye W, Groshen S, Cibtut PS (2008) [F-18]-fluorodeoxyglucose PET-CT of the normal prostate gland. Ann Nucl Med 22:787–793
12. Minamimoto R, Uemura H, Sano F, Terao H, Nagashima Y, Yamanaka S, Shizukuishi K, Tateishi U, Kubota Y, Inoue T (2011) The potential of FDG-PET/CT for detecting prostate cancer in patients with an elevated serum PSA level. Ann Nucl Med 25(1):21–27
13. Minamimoto R, Uemura H, Sano F, Terao H, Nagashima Y, Yamanaka S, Shizukuishi K, Tateishi U, Kubota Y, Inoue T (2011) The potential of FDG-PET/CT for detecting prostate cancer in patients with an elevated serum PSA level. Ann Nucl Med 25(1):21–27
14. Minamimoto R, Senda M, Jinnouchi S, Terauchi T, Yoshida T, Murano T, Fukuda H, Iinuma T, Uno K, Nishizawa S, Tsukamoto E, Iwata H, Inoue T, Oguchi K, Nakashima R, Inoue T (2013) The current status of an FDG-PET cancer screening program in Japan, based on a 4-year (2006-2009) nationwide survey. Ann Nucl Med 27(1):46–57
15. Tiwari BP, Jangra S, Nair N, Tongaonkar HB, Basu S (2010) Complimentary role of FDG-PET imaging and skeletal scintigraphy in the evaluation of patients of prostate carcinoma. Indian J Cancer 47(4):385–390
16. Yu EY, Muzi M, Hackenbracht JA, Rezvani BB, Link JM, Montgomery RB, Higano CS, Eary JF, Mankoff DA (2011) C11-acetate and F-18 FDG PET for men with prostate cancer bone metastases: relative findings and response to therapy. Clin Nucl Med 36(3):192–198
17. Damle NA, Bal C, Bandopadhyaya GP, Kumar L, Kumar P, Malhotra A, Lata S (2013) The role of 18F-fluoride PET-CT in the detection of bone metastases in patients with breast, lung and prostate carcinoma: a comparison with FDG PET/CT and 99mTc-MDP bone scan. Jpn J Radiol 31(4):262–269
18. Wang N, Jiang P, Lu Y (2014) Is fluorine-18 fluorodeoxyglucose positron emission tomography useful for detecting bladder lesions? A meta-analysis of the literature. Urol Int 92(2):143–149
19. Wettersten HI, Aboud OA, Lara PJ, Weiss RH (2017) Metabolic reprogramming in clear cell renal cell carcinoma. Nat Rev Nephrol 13(7):410–419
20. Jadvar H, Desai B, Ji L, Conti PS, Dorff TB, Groshen SG, Pinski JK, Quinn DI (2013) Baseline 18F-FDG PET/CT parameters as imaging biomarkers of overall survival in castrate-resistant metastatic prostate cancer. J Nucl Med 54(8):1195–1201

Gynecologic Tumor PET/CT Imaging

6

Qian Xia and Gang Huang

6.1 Introduction

PET/CT is a mature noninvasive molecular imaging tool in modern oncology that can detect changes in tissue biology, and functional changes usually occur earlier than structural changes. PET/CT can also provide quantitative information that plays an important role in monitoring disease status over time or in treatment. At present, the most commonly used radiotracer for PET/CT is ^{18}F-FDG. ^{18}F-FDG is a glucose analog that is abnormally active in malignant tissue relative to normal tissues, and ^{18}F-FDG accumulates in malignant tumors. In addition, many oncogenes of malignant tumors are abnormally activated and form tumor-specific expression markers, which also provide additional targets for PET/CT molecular imaging. Designed targeted imaging agents have been widely used in gynecological malignancies, including ^{11}C-methionine, ^{18}F-fluoro-17-β-estradiol (^{18}F-FES), and ^{60}Cu-diacetyl-bis (N4 methylthiosemicarbazide) (ATSM) and ^{64}Cu-ATSM. However, ^{18}F-FDG is still the most important tracer currently used. Below we will mainly discuss the clinical application of ^{18}F-FDG PET/CT in gynecological tumors.

6.2 Cervical Cancer

6.2.1 Epidemiology, Clinical Presentation, and Prognosis

Cervical cancer is the third most common tumor in women worldwide. Risk factors include human papillomavirus (HPV) infection, increased number of sexual partners, underaged sexual intercourse, smoking, and diethylstilbestrol exposure. Recent studies have shown that HPV infection is the leading cause of cervical cancer, accounting for 75% of cases [1]. The most common histological types are squamous cell carcinoma (75%) and adenocarcinoma subtypes (such as clear cells, small cells, and glandular squamous cells) [2]. Clinically, patients usually have bleeding after intercourse, and then there is uterine bleeding or menorrhagia. The later stages are associated with chronic anemia, followed by rectal or bladder and symptoms associated with both. The most important prognostic parameters at diagnosis include tumor size, parametrial infiltration, and lymph node spread (especially adjacent to the aorta). If the disease is confined to the primary site, the 5-year survival rate is about 90.9%, but if there appears regional lymph node metastasis, the 5-year survival rate is about 57.1%. If there is distant metastasis, this number will get worse; the 5-year survival rate is only 16.1% [3, 4].

6.2.2 Clinical Staging and Pattern of Spread

The most widely used clinical stage of cervical cancer is the International Federation of Gynecology and Obstetrics (FIGO) staging system. Early-stage cervical cancer is treated by surgery, but advanced disease is treated by radiation or combination chemotherapy. Para-aortic lymph node metastasis was observed in approximately one-third of patients with locally advanced cervical cancer (FIGO II Phase B) [5]. Advanced imaging modalities such as PET/CT, CT, and MRI have been used to overcome the limitations of traditional diagnostic methods and provide important prognostic information. In a multicenter clinical trial in the Gynecologic Oncology Group, which included the evaluation of tumor staging by imaging, the most important prognostic factor in patients with stage I-IVA cervical cancer is the status of the para-aortic lymph nodes, followed by tumor size. The National Comprehensive Cancer Network (NCCN) now recommends ^{18}F-FDG PET/CT imaging as a pre-treatment check for cervical cancer in clinical stage IB2 or higher.

Q. Xia
Department of Nuclear Medicine, RenJi Hospital, School of Medicine, Shanghai JiaoTong University, Shanghai, P. R. China

G. Huang (✉)
Shanghai Key Laboratory of Molecular Imaging, Shanghai University of Medicine and Health Sciences, Shanghai, P. R. China

G. Huang (ed.), *Nuclear Medicine in Oncology*, https://doi.org/10.1007/978-981-13-7458-6_6

Judging the tumor diffusion pattern helps to better stage and judge prognosis. Cervical cancer is mainly confined to the squamous column junction in the early stage of infiltration, and then the cancer invades the cervical stroma, which in turn directly invades the parametrium, uterus, and vagina. As the disease progressed, the tumor is primarily metastasized through three lymphatic pathways: a lateral pathway along the external iliac vessels, a lower abdomen pathway along the iliac vessels, and an anterior iliac ligament along the iliac ligament. All three pathways eventually flow into the common lymph nodes, which then lead to para-aortic lymph node metastasis and eventually to the supraclavicular lymph nodes. Blood-borne transmission is rare, with only 5% of cases occurring. The most common sites of metastasis are the lungs, liver, and bones. Although distal organ metastases may occur at any stage, this probability is low in the absence of pelvic lymph nodes [6].

6.2.3 ^{18}F-FDG PET/CT for the Initial Treatment Strategy

Diagnosis and primary lesion assessment cervical cancer is primarily tested by the Papanicolaou screening test (Pap test). Cervical cancer usually has a high level of ^{18}F-FDG uptake, and it has been reported that the level of glucose metabolism in primary tumors is higher in squamous cell carcinoma than non-squamous cell carcinoma, and the glucose metabolism in poorly differentiated tumors is more active (Fig. 6.1). Despite this, ^{18}F-FDG PET/CT is not routinely used for the initial assessment of the primary lesion. ^{18}F-FDG PET/CT may also have false negatives for the identification of smaller (i.e., sub-cm) and superficial invasive tumors. MRI is more recommended because of the higher spatial resolution of MRI. However, studies show that the level of metabolic activity in primary cervical lesions can provide more information on prognosis. In 51 patients with diagnosed advanced cervical cancer, Miller and Grisby found that the metabolic volume of PET obtained by using the simple counting threshold method was more correlated with patient survival and basic progression than tumor volume. The study also reported that the level of metabolic activity of primary cervical cancer was higher. With the SUV_{max} increased, the 5-year overall survival rate decreased: SUV_{max} was 5.2, the 5-year survival rate was 95%, and SUV_{max} was 5.2–13.3, the 5-year survival rate was 70%, while the SUV_{max} was 13.3, the 5-year survival rate was only 44% [7, 8]. Lee et al. reported that SUV_{max} was also an independent predictor of recurrence after surgery. Kidd et al. found a correlation between the SUV_{max} of the primary lesion and the probability of tumorigenic lymph node metastasis [9]. It has also been reported that the sensitivity of FDG-PET/CT for detection of para-aortic lymph node metastasis is as high as 95%. In patients with locally advanced disease, the SUV_{max} of the aortic metastatic lymph nodes is >3.3, and the tumor recurrence rate is higher, and the survival rate is lower than that of the metastatic lymph nodes with SUV_{max} < 3.3. In addition, FDG-PET/CT has been found to more accurately assess local lymph node metastasis than contrast-enhanced CT and MRI and is subsequently used to guide laparoscopic staging [10]. The main limitation of these studies is the lack of histopathological findings as a gold standard, the study of small populations, and the lack of survival-related research. Long-term metastasis assessment of the distal part of cervical cancer patients with metastasis is the left supraclavicular region. In 186 newly diagnosed cervical cancer patients, Tran et al. found that 14 (8%) patients had hidden supraclavicular lymph node metastasis due to ^{18}F-FDG PET/CT, and all patients were confirmed by pathology [11]. In this study, 40% of patients showed a para-aortic lymph node metastasis by ^{18}F-FDG PET/CT, and the overall prognosis was poor.

6.2.4 ^{18}F-FDG-PET/CT for the Subsequent Treatment Strategy

Detection of recurrent disease, namely, detection of recurrent cervical cancer, is defined as tumor progression at least 6 months after the malignant lesion has subsided. The reported recurrence rate is as high as 28–35% in patients with uterine infiltration or aortic metastasis or with both. Local recurrent cervical cancer occurs mainly in the vaginal vault but can extend to the parauterine and pelvic sidewalls. Distal metastases occur in 70% of patients with recurrent disease. Lymph node metastasis often occurs in the para-aortic lymph nodes (11%), the abdominal cavity (8%), and the supraclavicular lymph nodes (7%). There is also a bloody transfer to the liver, adrenal gland (15%), lung (21%), and bone (20%). Adrenal metastasis may also occur in cervical adenocarcinoma. Bodurka-Bevers et al. [12] retrospectively evaluated 133 patients and found that patients with asymptomatic recurrent cervical cancer had a higher overall survival (42 months) than symptomatic patients (11 months). FDG-PET/CT is superior to other imaging diagnostic techniques for detecting cervical cancer with local recurrence. Blood tumor markers, such as carcinoembryonic antigens, CA-199 and CA-125, can help identify asymptomatic patients with recurrence; however, they do not have disease specific and cannot indicate the recurrence extent or the disease progression. Enhanced CT and MRI with high sensitivity are often difficult to distinguish between possible postoperative or postradiation tumor recurrence areas, but it is at the expense of specificity. The role of CT and MRI in detecting lymph node metastasis is also limited. Because the size of lymph nodes is below standard, it is considered

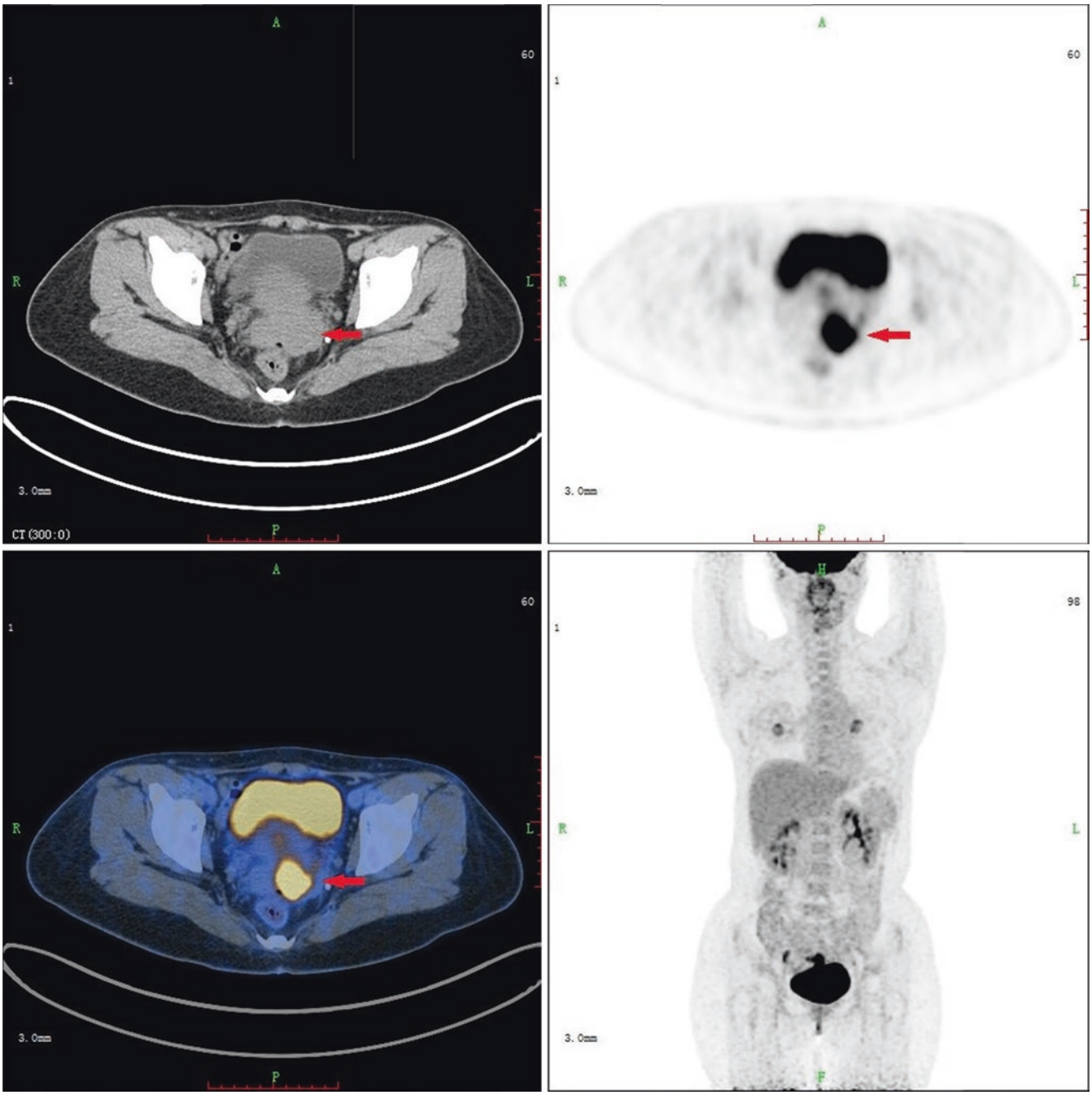

Fig. 6.1 Cervical cancer has a high level of ^{18}F-FDG uptake. Intense ^{18}F-FDG uptake is seen in the primary cervical mass with SUV_{max} 19.8 (cross). Intense but physiological ^{18}F-FDG activity is seen in the bladder anterior to the cervical mass (arrows). No FDG-avid locoregional or distant metastases were identified

normal, but the actual situation is that these lymph nodes are also likely to be associated with metastasis. In contrast, the metabolism of recurrent malignancies is usually higher than the scar formation after treatment, and ^{18}F-FDG PET and PET/CT have been shown to be effective in detecting recurrent tumors (Fig. 6.2). The study included different patient populations and different techniques for meta-analysis (^{18}F-FDG PET vs. PET/CT only).

However, overall, the study reported that ^{18}F-FDG PET (/CT) is relatively sensitive (90–95%) for detecting recurrent cervical cancer, with a specificity of 76–93%, and positive predictive value (PPV) is 35–96%, and negative predictive value (NPV) is 87–98%. A large number of PPVs were associated with a study that investigated the use of ^{18}F-FDG PET to detect early recurrence in patients without clinical evidence of recurrence, in which we could assume

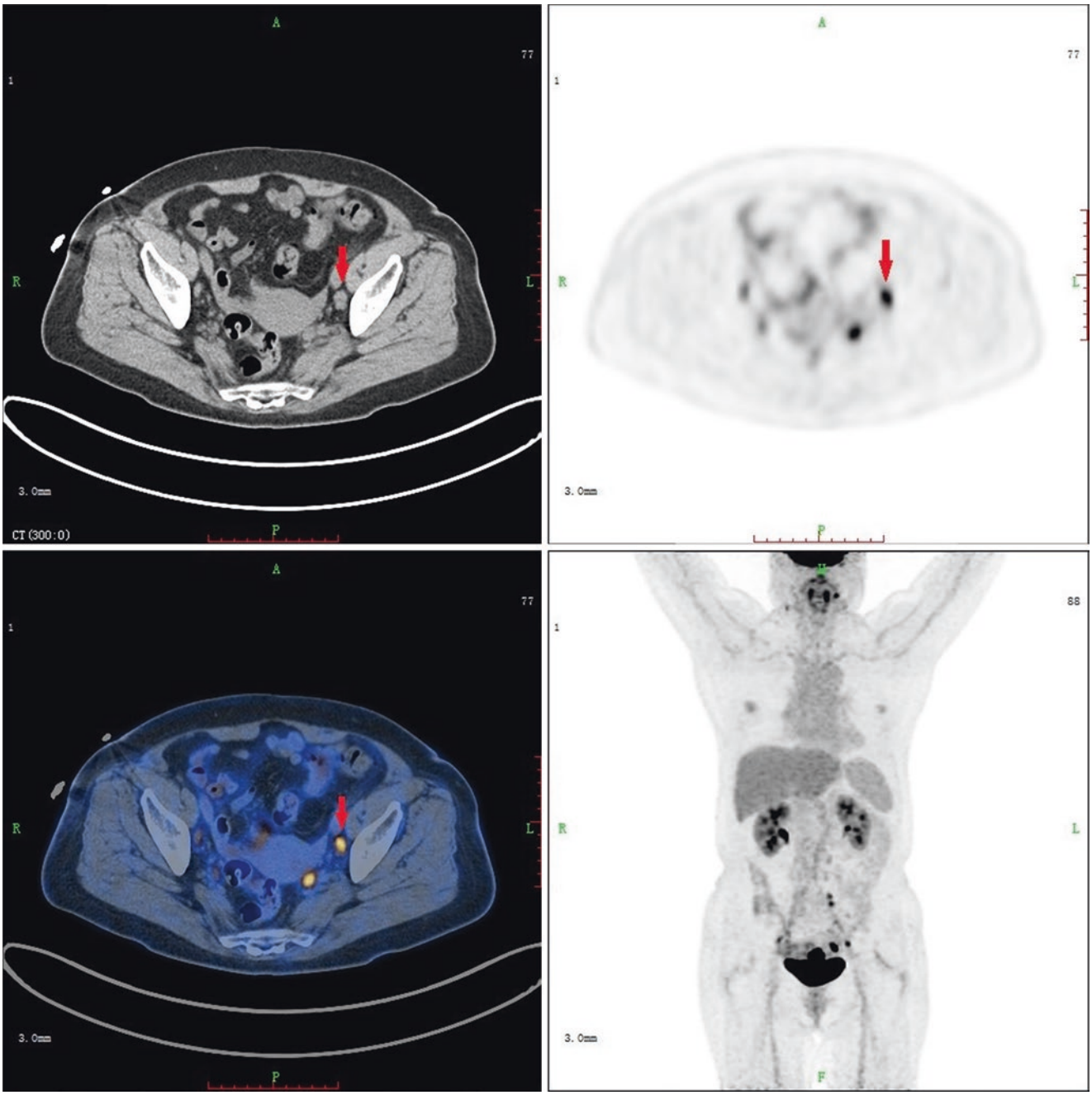

Fig. 6.2 Cervical cancer with local recurrence. There was one of some ^{18}F-FDG-avid bilateral external iliac lymph nodes (cross) which were only borderline abnormal size on diagnostic CT

a higher false positive rate. In Van der Veldt et al. research [13], the sensitivity to local and regional recurrence was higher (87–100%) than distant metastasis (75%). Regardless of the location of the recurrent disease, the specificity is similar, and ^{18}F-FDG PET/CT can significantly improve the diagnostic accuracy. Meads et al. recently published a meta-analysis to determine the added value of ^{18}F-FDG PET/CT in CT or MRI, including three cases: routine follow-up of asymptomatic cervical cancer patients after treatment, detecting recurrence in symptomatic women, and detecting recurrence to determine treatment strategies. Only 15 studies were included in the final analysis, 9 of which included FDG-PET/CT, and the sensitivity and specificity of ^{18}F-FDG PET/CT for detecting recurrence were higher than that of CT. The current NCCN guidelines recommend ^{18}F-FDG PET/CT for cervical cancer surveillance and are also used to detect tumor recurrence [14]. It has been reported that the use of ^{18}F-FDG PET/CT in suspected

recurrences may have an impact on subsequent treatment strategies. Chung et al. showed that 40% of asymptomatic pelvic recurrences and no distant metastases can be cured by surgical resection. After ^{18}F-FDG PET/CT imaging, treatment strategies have changed in approximately 25% of patients [15]. Monitoring treatment response although not used for cervical cancer, Nishiyama et al. evaluated the role of ^{18}F-FDG PET in monitoring neoadjuvant response in patients with advanced gynecologic cancer. The study showed that after chemotherapy or radiotherapy, the SUV_{max} of primary tumors decreased by more than 65%, indicating that the tumors responded better to radiotherapy and chemotherapy, and the accuracy of predicting treatment response was 85% [16]. Schwarz et al. analyzed 92 subjects with cervical cancer who underwent external beam radiotherapy, brachytherapy, and concurrent chemotherapy, followed by chemotherapy in the midline of the 3 months after treatment; an ^{18}F-FDG PET/CT examination after chemotherapy was performed. The results of the study were divided into complete metabolic reactions, partial reactions, or new abnormal ^{18}F-FDG hypermetabolic lesions. The 3-year survival rates were 78%, 33%, and 0%, respectively ($P < 0.05$) [17].

6.2.5 ^{18}F-FDG PET/CT: Radiation Therapy Planning

Chao et al. confirmed the application of ^{18}F-FDG PET/CT in the radiotherapy program for assisted cervical cancer [18]. Since ^{18}F-FDG PET/CT has been shown to be more accurate in detecting diseases of lymph nodes and distant lesions, it is considered a useful tool to guide radiotherapists during intensity-modulated radiation therapy (IMRT). The inclusion of ^{18}F-FDG PET/CT data in the IMRT program allows for reduced doses to surrounding healthy tissue and dose escalation to treatment needs. In other studies, IMRT significantly reduced grade 2 gastrointestinal toxicity and reduced the use of antidiarrheals.

6.2.6 Summary

There is more and more evidence to support the initial staging of FDG-PET/CT for patients with cervical cancer. This leads to NCCN recommending clinical stage IB2 or higher cervical cancer should use ^{18}F-FDG PET/CT examination before treatment. ^{18}F-FDG PET/CT has the advantage in detecting recurrent disease and may be found earlier than CT/MRI, which can significantly affect clinical treatment plans. In addition, ^{18}F-FDG PET/CT has been shown to help guide radiation therapy planning for cervical cancer.

6.3 Ovarian Cancer

6.3.1 Epidemiology, Clinical Presentation, and Prognosis

Ovarian cancer is the sixth most common malignant tumor in the world, and it ranks second in gynecologic malignancies. Although it accounts for only 3% of all female cancers, it is the highest among gynecological cancers. About 10% of ovarian cancers are autosomal inheritance, 90% of which are caused by mutations in the BRCA-1 and BRCA-2 genes, and about 10% are caused by Lynch syndrome (hereditary nonpolyposis colon cancer syndrome) [19]. By the age of 70, 18–54% of BRCA-1 mutation carriers and 2.4–19% of BRCA-2 mutation carriers are diagnosed with ovarian cancer. The lifetime risk of ovarian cancer in Lynch syndrome is as high as 10–15% [20]. Other common risk factors for ovarian cancer are age (more than one-third in postmenopausal patients), family history, non-fertility, early menarche, and late menopause. The reported protective factors are oral contraceptives, parity, and bilateral oophorectomy. Typical signs and symptoms of ovarian cancer are abdominal pain, irregular menstruation, and indigestion. As the disease progresses, bloating may occur, and respiratory symptoms may occur due to an increase in intra-abdominal pressure caused by ascites. Pathologically, the majority (90%) of ovarian cancers is epithelial tumors, and the remaining 10% originate from the source of germ, germ, or mixed cells. Epithelial tumors are subdivided into serous, mucinous, endometrioid, clear cells and undifferentiated. Epithelial serous carcinoma accounts for about 80% of all ovarian cancers and can be divided into highly differentiated, poorly differentiated. Standard treatment for ovarian cancer consists primarily of cytoreductive surgery, followed by chemotherapy, usually paclitaxel and platinum-based cytotoxic chemotherapy. Patients with early diagnosis (stage I) had a significantly better prognosis than patients with advanced diagnosis (stages III and IV), with 5-year survival rates estimated at 90% and 25%, respectively [21].

6.3.2 Clinical Staging and Pattern of Spread

Unlike cervical cancer, ovarian cancer usually spreads directly into the peritoneal cavity. Lymphatic and bloodborne spread is relatively small. The usual route of diffusion is to penetrate the ovarian sac and directly invade adjacent organs or the pelvic peritoneum. Tumors can also spread to the contralateral ovaries, uterus, and peritoneum. The cells can then enter the abdomen through the peritoneal fluid. This diffusion will follow the normal cycle from the pelvis to the abdomen in a clockwise direction. Initially it is at the right side of the colon and then to the upper right area around the

liver and diaphragm and then transferred to the greater omentum and the left side of the colon. Usually it disseminates the surface of the greater omentum, small omentum, mesentery, and liver, intestines, and spleen. The spread of the diaphragm to the pleura is also very common after peritoneal implantation. Serous papillary carcinoma and poorly differentiated adenocarcinoma are the most common histological subtypes of peritoneal cancer. Diffusion along the lymphatic vessels to the pelvic lymph nodes can pass through the wide ligaments and along the aorta along the gonadal vessels. The entry of the retroperitoneal lymph nodes into the diaphragm through the lymphatic passage can lead to the spread of the supraclavicular lymph nodes, which spread to the intramammary lymph nodes. The incidence of stage I patients with lymph node metastasis in the first operation was 25%, the incidence of stage II disease was 50%, and the incidence of stage III–IV disease was 74%. Blood-borne metastases at diagnosis are uncommon but are most common in the liver, the lungs, and the pleura. Only 2–3% of patients have lung metastases or liver metastases at the time of diagnosis. The most common manifestation of stage IV disease is pleural effusion, followed by substantial liver metastases [22].

6.3.3 FDG-PET/CT for the Initial Treatment Strategy

Ultrasound (US) is the main primary screening method for ovarian cancer. The tumor marker CA-125 is commonly used for early detection; however, CA-125 has neither ovarian cancer specificity nor sensitivity. CA-125 expression does not increase in about 20% of ovarian cancers. Most ovarian masses in premenopausal women are benign, but lumps cannot resolve. The clinician should pay attention to it and require further examination. In contrast, ovarian masses in postmenopausal women are usually malignant. The postmenopausal attachment mass and CA-125 levels increase more than 200 IU/mL; the probability of ovarian cancer is 97%. Some authors evaluated the role of ^{18}F-FDG PET/CT in distinguishing between benign and malignant ovarian masses [23]. Nam et al. conducted a prospective study of 133 patients with suspected ovarian cancer who were compared for the diagnostic performance of ^{18}F-FDG PET/CT, CT, or MRI by using surgery as a gold standard. The accuracy of ^{18}F-FDG PET/CT is higher than the accuracy of pelvic US, CT, or MRI [24]. Castellucci et al. used SUV_{max} to distinguish benign and malignant ovarian lesions. When the focal SUV_{max} in the ovary was greater than or equal to 3, it was considered to be positive for ovarian malignant tumors and was considered to be benign tumors when it was less than or equal to 2.7. Its sensitivity was 87% and specificity was 100%. Despite this, ^{18}F-FDG PET/CT is not principally used for screening or diagnosing primary ovarian malignancies because of false positives and false negatives. In the same study, 19 (21%) of 91 benign ovarian masses had abnormal ^{18}F-FDG uptake, including cyst adenoma, endometrioma, hydrosalpinx, benign germ cell tumor, granuloma, abscess, and coma. Increased FDG uptake has also been described in endometriosis, which is important because ovaries are the most common anatomical location of endometriosis [25]. The specificity of ^{18}F-FDG PET/CT can be increased when combined with elevated postmenopausal status and increased level of CA-125. Risum et al. used US to evaluate the ^{18}F-FDG PET/CT in 101 menopausal women with elevated serum CA-125 levels and ovarian masses. ^{18}F-FDG PET/CT has 100% sensitive and 92% specific in distinguishing between malignant and benign or borderline tumors. Therefore, in clinically suspected or high-risk surgical cases, ^{18}F-FDG PET/CT can play an important role in confirming the diagnosis of malignant tumors. ^{18}F-FDG PET/CT may be false negative in small, necrotic, mucous, cystic, or low-grade tumors. Another limitation is the ability of ^{18}F-FDG PET/CT to recognize lesions of less than 1 cm, particularly lesions of less than 5 mm. In a study by Castellucci et al., there were three false-negative results in four ^{18}F-FDG PET/CT scans with a primary tumor measurement of less than 5 mm. At present, the ^{18}F-FDG PET/CT staging study shows that ^{18}F-FDG PET/CT can improve the accuracy of pretreatment staging to 69–75%, while the accuracy of CT alone is 53–55%. Nam et al. performed a prospective assessment of 91 patients before surgical staging. In 16% of patients, PET/CT imaging revealed extra-abdominal lymph node metastasis, but the surgical staging was not recognized. In addition, they found malignancies in five other patients, including thyroid, breast, and pancreatic neuroendocrine, further confirming the potential value of ^{18}F-FDG PET/CT imaging in initial treatment strategies for patients with ovarian cancer [25].

6.3.4 ^{18}F-FDG PET/CT for the Subsequent Treatment Strategy

Up to 75% of patients with ovarian cancer detect residual and recurrence mainly in the peritoneal and retroperitoneal lymph nodes. A number of studies have evaluated the role of ^{18}F-FDG PET and PET/CT in detecting recurrent ovarian cancer. In a meta-analysis, Gu et al. reported that ^{18}F-FDG PET/CT was more sensitive (69%) than CA-125, but CA-125 had higher specificity (93% vs. ^{18}F-FDG PET/CT 88%). In the same meta-analysis, both ^{18}F-FDG PET and PET/CT have higher sensitivity and specificity than CT and MRI [26]. Sebastian et al. reported that using ^{18}F-FDG PET/CT to detect recurrent ovarian cancer was more effective than using CT alone. Kim et al. used MRI and ^{18}F-FDG PET/CT to detect 36 patients with suspected recurrent ovarian cancer,

20 of whom underwent laparotomy after 2–35 days after imaging. The authors concluded that MRI and ^{18}F-FDG PET/CT had a higher overall sensitivity (91% vs. 73%) with similar specificity, NPV, and PPV [27]. However, lesion-based analysis shows that MRI is more sensitive because it better detects peritoneal lesions. ^{18}F-FDG PET/CT is more sensitive to lymph node metastasis. It is now generally accepted that combining CA-125 assays with imaging (CT, MRI, and ^{18}F-FDG PET/CT) can better detect recurrence. Although ^{18}F-FDG PET/CT has limitations in detecting small lesions or diffuse peritoneal metastases, some small lesions may also have higher ^{18}F-FDG uptake, which helps us to differentiate the diagnosis. In examining tumor recurrence, many studies report ^{18}F-FDG PET/CT sensitivity ranging from 65 to 100%, specificity from 60 to 100%, PPV from 85 to 100%, and NPV from 67 to 100%. Risum et al. prospectively studied 60 patients who had remission 3 months or more after initial treatment and who were suspected of recurrent ovarian cancer at a physical examination or elevated US or CA-125 level and were found with ^{18}F-FDG PET/CT (97%) that was more sensitive than US (66%) and CT (81%) ($P < 0.001$) [28]. Some authors and reviews report that the results of ^{18}F-FDG PET/CT are mostly consistent with elevated levels of CA-125, and the results of CT or MRI are often ambiguous, making it difficult to give doctors an accurate judgment [28, 29]. Fulham et al. found that ^{18}F-FDG PET/CT can find recurrent ovarian cancer 6 months earlier before CT. Evidence based on ^{18}F-FDG PET/CT findings can alter the treatment of recurrent ovarian cancer in as many as 37–63% of patients. These studies are consistent with the results reported by the National Oncology Registry, which includes more than 3000 patients with ovarian or uterine cancer [30]. Some authors evaluated a second procedure after first-line treatment with ^{18}F-FDG PET/CT. Overall; ^{18}F-FDG PET/CT detects clinically occult residual disease and contributes to surgical planning. There is not much research on the role of ^{18}F-FDG PET/CT in examining the response of ovarian cancer to treatment. A prospective study by Avril et al. evaluated the association between ^{18}F-FDG PET/CT response and total survival in 33 patients with advanced ovarian cancer (stages III_C–IV) who received neoadjuvant carboplatin chemotherapy before cytoreductive surgery. After chemotherapy first (the threshold for a 20% reduction in SUV_{max}) and the third cycle (a threshold for a 55% decrease in SUV_{max}), a correlation was compared between overall survival and ^{18}F-FDG PET/CT metabolic response. For patients who showed metabolic response to treatment, the median overall survival was 38.3 months, compared with 23.1 months for patients who did not exhibit metabolic response. No correlation was found between clinical or CA-125 response and overall survival [31]. Nishiyama et al. evaluated the role of ^{18}F-FDG PET in monitoring neoadjuvant therapy in patients with advanced gynecologic cancer, and 8 of 21 patients had ovarian cancer. After treatment, with a cutoff of $SUV_{max} = 3.8$, PET sensitivity was 90%, the specificity was 64%, and the accuracy was 76%. If the arbitrary rate of change in SUV_{max} was applied to the cutoff value (SUV_{max} was reduced by 65%), the specificity and accuracy were further increased to 82% and 86%, respectively. Although the results of these studies are exciting, relatively studies are few, and more large-scale prospective studies are needed [16].

6.3.5 Summary

Currently, ^{18}F-FDG PET/CT imaging has no positive value in screening for ovarian cancer. Although studies have shown that ^{18}F-FDG PET/CT is highly sensitive for detecting primary ovarian cancer, its use is still limited due to the presence of false positive and negative results. In the development of the protocol, ^{18}F-FDG PET/CT may confirm the diagnosis with high clinical suspicion, assess the degree of disease progression, and more accurately stage, which is very useful for optimizing cytoreductive surgery and prognosis. The most common use of ^{18}F-FDG PET/CT is for patients with clinically suspected recurrent ovarian cancer, especially those with elevated levels of CA-125 (over 35 U/mL or the lowest point after initial treatment). There is data showing that ^{18}F-FDG PET/CT is superior to CT detection in the detection of recurrent ovarian cancer. Many retrospective studies have demonstrated that ^{18}F-FDG PET/CT imaging has limitations in lesions with a maximum diameter of less than 5–10 mm. The role of ^{18}F-FDG PET/CT imaging in the treatment response of ovarian cancer, although the initial results are exciting, but has not been extensively studied, more evidence is needed to prove.

6.4 Endometrial Cancer

6.4.1 Epidemiology, Clinical Presentation, and Prognosis

Endometrial cancer is a common invasive gynecological malignancy. There are two major subtypes, endometrioid (80–90%) and non-endometrial. The most common histological morphology is adenocarcinoma, which is usually a well or moderately differentiated cell. A less common non-endometrioid subtype, which is characterized by serous and clear cells, has a poor prognosis. Unlike ovarian cancer, up to 25% of cases occur in premenopausal patients. The main risk factor is the increase in estrogen resistance, which is associated with menopause, non-fertility, obesity, anovulation, and polycystic ovary syndrome. The risk of endometrial cancer in patients with Lynch syndrome also increases. In postmenopausal patients, dysfunctional

bleeding can usually be detected early. Since it was found to be in the early stages, more than 70% of patients are in stage I when symptoms appeared. Serous and clear cell carcinoma has a tendency to muscle layer infiltration, vascular invasion, and peritoneal cancer. The prognosis is related to the staging and grading of the tumor at the time of diagnosis. The 5-year overall survival rate of stage I is 80–90%, the stage II is 70–80%, and the stages III–IV is 20–60% [32].

6.4.2 Clinical Staging and Pattern of Spread

FIGO staging is usually performed by exploratory laparotomy, total abdominal hysterectomy, bilateral salpingo-oophorectomy, and peritoneal lavage. Lymph node dissection is also recommended for high-risk stage I disease and patients with serous or clear cell carcinoma to help assess whether adjuvant diffusion is required to invade the cervix through the myometrium or invade the ovaries from the fallopian tubes and then locally invade the other pelvis organs. As the depth of myometrial invasion increases, the likelihood of lymph node spread increases. Tumors from the lower middle uterus will be transferred to the side of the palace and to the closed hole. Tumors from the proximal and base are transferred to the common iliac artery and the aorta.

6.4.3 ^{18}F-FDG PET/CT for the Initial Treatment Strategy

US and MRI are the main ways to diagnose endometrial cancer. In postmenopausal bleeding patients, the Society of Ultrasound Radiologists found that the sensitivity of diagnosis is 96% with a threshold of 5 mm [33]. MRI is considered to be the most accurate imaging technique for preoperative assessment of myometrial invasion. Due to the limitation of resolution, ^{18}F-FDG PET/CT is unlikely to replace ultrasound or MRI. The main role of ^{18}F-FDG PET/CT in the initial treatment strategy for endometrial cancer is to define lymph node metastasis and distant metastasis, which helps to more accurately perform clinical staging and guide the development of later treatment options. Suzuki et al. found that the sensitivity of ^{18}F-FDG PET in distant metastatic lesions was 83.3%, while CT and MRI were only 66.7%. As with other malignancies, the sensitivity of PET/CT decreases as the size of the tumor decreases [34]. Kitajima et al. found that ^{18}F-FDG PET/CT had a sensitivity of 93.3% for detecting tumors larger than 10 mm in lymph nodes, but the sensitivity decreased to 66.7% for lesions of 5–9 mm and decreased to 16.7% for lesions smaller than 4 mm [35, 36].

6.4.4 FDG-PET/CT for the Subsequent Treatment Strategy

Another major contribution of ^{18}F-FDG PET/CT in the evaluation of endometrial cancer is the detection of tumor recurrence after treatment. Local recurrence of the patient usually occurs at the blind end of the vagina. ^{18}F-FDG PET/CT detected recurrent endometrial cancer and found sensitivity and specificity of 93%–100% and 78%–93%, respectively. In another study, Park et al. showed that ^{18}F-FDG PET/CT resulted in a change in treatment plans in 21.9% of 64 patients with recurrent disease [37].

6.5 Other Gynecological Cancer

There are also some clinically rare tumors, such as uterine sarcoma, vaginal and vulvar cancer, etc. We have summarized some of the ^{18}F-FDG PET/CT imaging of these tumors.

6.5.1 Uterine Sarcoma

Uterine sarcoma is invasive, accounting for about 2–8% of uterine malignancies. Uterine sarcoma is divided into three subtypes: carcinosarcoma, leiomyosarcoma, and endometrial sarcoma. Yamada et al. retrospectively studied 62 patients after surgery and found that 61% of them had blood-borne metastasis, which was similar to the biological characteristics of endometrial cancer, which led to a poor prognosis of uterine sarcoma [38]. Regarding FDG-PET/CT imaging of uterine sarcoma, they found that the uterine sarcoma SUV_{max} was between 3 and 6.3. ^{18}F-FDG PET/CT can be used to distinguish between low-grade and high-grade uterine sarcomas and assess posttreatment responses and tumor residuals. It has been reported that ^{18}F-FDG PET/CT has a higher detection rate than CT alone and can be used to detect extra-pelvic recurrence. The sensitivity of PET/CT is 100%, while the CT is 85.7%. Park et al. evaluated 36 patients and found that the sensitivity, specificity, accuracy, PPV, and NPV of ^{18}F-FDG PET/CT in symptomatic patients were 92.9%, 100%, 94.4%, 100%, and 80%, respectively while in asymptomatic patients were 87.5%, 95.5%, 93.3%, 87.5%, and 95.5%, respectively. They also found that FDG-PET/CT changed the treatment plan for 33.3% patients with suspected recurrence [39].

6.5.2 Vaginal Carcinoma

Among all gynecological malignancies, vaginal cancer accounts for less than 3%, of which squamous cell carcinoma is the main cause, accounting for about 80%. These risk factors include multiple sexual partners, smoking,

diethylstilbestrol exposure, and HPV infection. Tumor spread is usually a local invasion, or it may be a blood-borne spread to the lungs and lymphatic spread. The lymph node metastasis pathway varies according to the location of the tumor. One-third of the upper vagina's tumors usually spread to the obturator and the internal and external axillary lymph nodes. One-third of the primary tumor in the lower part of the vagina often flows to the femoral and inguinal lymph nodes. There are currently few documents using ^{18}F-FDG PET/CT in vaginal cancer. Lamoreaux et al. compared CT and ^{18}F-FDG PET/CT alone in 23 patients. ^{18}F-FDG PET/CT has a sensitivity of 100% for primary tumors, while CT has only 43% sensitivity. ^{18}F-FDG PET/CT also detected metastatic lymph nodes in 35% patients, while CT only detected 17% [40].

6.5.3 Vulvar Carcinoma

Vulvar cancer accounts for about 4% of all gynecologic malignancies, and most are squamous cell carcinoma. The typical mode of spread is lymph node metastasis, which is mainly transferred to the ipsilateral inguinal lymph nodes. If the tumor infiltrates into the midline or clitoris, it may metastasize to the bilateral inguinal lymph nodes and spread to the pelvic lymph nodes. Even if the primary lesion is small, the lymph node metastasis rate of the vulvar cancer is high. For example, in up to 20% of cases, lymph node metastasis can occur in tumors of 5 mm or less. Lymph node metastasis is an important poor prognostic factor for vulvar cancer. Progress from stage I (no lymph node involvement) to stage III (lymph node involvement) reduces the 5-year overall survival rate from 97 to 50% [40]. The role of ^{18}F-FDG PET/CT in patients with vulvar cancer is few reported in the literature. Due to the high incidence of regional metastases, it can be used for clinical staging of invasive vulvar tumors. Vulvar squamous cell carcinoma has the same biological characteristics as cervical squamous cell carcinoma, and the ^{18}F-FDG metabolic pattern of the tumor is similar.

6.6 Conclusion

^{18}F-FDG PET/CT has been evaluated in a variety of settings and in a variety of gynecologic malignancies, and CMS approved initial and follow-up treatment strategies for these malignancies. In cervical cancer, ^{18}F-FDG PET/CT has a high clinical value for the development of treatment options. For ovarian cancer, the greatest value of ^{18}F-FDG PET/CT seems to be used to raise the level of CA-125, but other imaging studies are difficult to identify recurrent lesions. In addition, ^{18}F-FDG PET/CT has a high clinical value for assessing the response to treatment, and of course, further study in this area is still needed.

References

1. Jemal A, Bray F, Center MM et al (2011) Global cancer statistics. CA Cancer J Clin 61(2):69–90
2. Wang SS, Carreon JD, Gomez SL et al (2010) Cervical cancer incidence among 6 Asian ethnic groups in the United States,1996 through 2004. Cancer 116:949–956
3. Howlader N, Noone AM, Krapcho M et al (2013) SEER cancer statistics review, 1975-2010. National Cancer Institute. http://seer.cancer.gov/csr/1975_2010/
4. Marnitz S, Köhler C, Roth C et al (2005) Is there a benefit of pretreatment laparoscopic transperitoneal surgical staging in patients with advanced cervical cancer? Gynecol Oncol 99:536–544
5. Yildirim Y, Sehirali S, Avci ME et al (2008) Integrated PET/CT for the evaluation of para-aortic nodal metastasis in locally advanced cervical cancer patients with negative conventional CT findings. Gynecol Oncol 108(1):154–159
6. UEG week 2015 poster presentations (2015) United Eur Gastroenterol J 3(5 suppl):146–687. https://doi.org/10.1177/2050640615601623.
7. Sironi S, Buda A, Picchio M et al (2006) Lymph node metastasis in patients with clinical early-stage cervical cancer: detection with integrated FDG PET/CT. Radiology 238:272–279
8. Kidd EA, Siegel BA, Dehdashti F et al (2007) The standardized uptake value for F-18 fluorodeoxyglucose is a sensitive predictive bio-marker for cervical cancer treatment response and survival. Cancer 110(8):1738–1744
9. Lee YY, Choi CH, Kim CJ (2009) The prognostic significance of the SUVmax (maximum standardized uptake value for F-18 fluorodeoxyglucose) of the cervical tumor in PET imaging for early cervical cancer: preliminary results. Gynecol Oncol 115(1):65–68
10. Yen TC, See LC, Lai CH et al (2008) Standardized up-take value in paraaortic lymph nodes is a significant prognostic factor in patients with primary advanced squamous cervical cancer. Eur J Nucl Med Mol Imaging 35(3):493–501
11. Tran BN, Grigsby PW, Dehdashti F et al (2003) Occult supraclavicular lymph node metastasis identified by FDG-PET in patients with carcinoma of the uterine cervix. Gynecol Oncol 90:572–576
12. Bodurka-Bevers D, Morris M, Eifel P et al (2000) Post-therapy surveillance of women with cervical cancer: an outcomes analysis. Gynecol Oncol 78:187–193
13. Van der Veldt AA, Buist MR, van Baal MW et al (2008) Clarifying the diagnosis of clinically suspected recurrence of cervical cancer: impact of 18F-FDG PET. J Nucl Med 49(12):1936–1943
14. Meads C, Davenport C, Małysiak S et al (2014) Evaluating PET-CT in the detection and management of recurrent cervical cancer: systematic reviews of diagnostic accuracy and subjective elicitation. BJOG 121(4):398–407
15. Chung HH, Kim SK, Kim TH et al (2006) Clinical impact of FDG-PET imaging in post-therapy surveillance of uterine cervical cancer: from diagnosis to prognosis. Gynecol Oncol 103:165–170
16. Nishiyama Y, Yamamoto Y, Kanenishi K et al (2008) Monitoring the neoadjuvant therapy response in gynecological cancer patients using FDG PET. Eur J Nucl Med Mol Imaging 35(2):287–295
17. Schwarz JK, Siegel BA, Dehdashti F et al (2007) Association of post therapy positron emission tomography with tumor response and survival in cervical carcinoma. JAMA 298(19):2289–2295
18. Chao A, Ho KC, Wang CC et al (2008) Positron emission tomography in evaluating the feasibility of curative intent in cervical cancer patients with limited distant lymph node metastases. Gynecol Oncol 110(2):172–178
19. Mourits MJ, de Bock GH (2009) Managing hereditary ovarian cancer. Maturitas 64(3):172–176 52

20. Malander S, Rambech E, Kristoffersson U et al (2006) The contribution of the hereditary nonpolyposis colorectal cancer syndrome to the development of ovarian cancer. Gynecol Oncol 101(2):238–243
21. Barnholtz-Sloan JS, Schwartz AG, Qureshi F et al (2003) Ovarian cancer: changes in patterns at diagnosis and relative survival over the last three decades. Am J Obstet Gynecol 189(4):1120–1127
22. Shaaban A, Rezvani M (2009) Ovarian cancer: detection and radiologic staging. Clin Obstet Gynecol 52:73–93
23. Mironov S, Akin O, Pandit-Taskar N et al (2007) Ovarian cancer. Radiol Clin North Am 45:149–166
24. Santillan A, Garg R, Zahurak ML et al (2005) Risk of epithelial ovarian cancer recurrence in patients with rising serum CA-125 levels within the normal range. J Clin Oncol 23(36):9338–9343
25. Nam EJ, Yun MJ, Oh YT et al (2010) Diagnosis and staging of primary ovarian cancer: correlation between PET/CT, Doppler US, and CT or MRI. Gynecol Oncol 116:389–394
26. Gu P, Pan LL, Wu SQ et al (2009) CA125, PET alone, PET-CT, CT and MRI in diagnosing recurrent ovarian carcinoma: a systematic review and meta-analysis. Eur J Radiol 71(1):164–174
27. Sebastian S, Lee SI, Horowitz NS et al (2008) PET-CT vs. CT alone in ovarian cancer recurrence. Abdom Imaging 33(1):112–118
28. Kim CK, Park BK, Choi JY et al (2007) Detection of recurrent ovarian cancer at MRI: comparison with integrated PET/CT. J Comput Assist Tomogr 31(6):868–875
29. Risum S, Høgdall C, Markova E et al (2009) Influenceof2-(18F) fluoro-2-deoxy-D-glucose positron emission tomography/computed tomography on recurrent ovarian cancer diagnosis and on selection of patients for secondary cytoreductive surgery. Int J Gynecol Cancer 19:600–604
30. Fulham MJ, Carter J, Baldey A et al (2009) The impact of PET-CT in suspected recurrent ovarian cancer: a prospective multi-centre study as part of the Australian PET Data Collection Project. Gynecol Oncol 112:462–468
31. Avril N, Sassen S, Schmalfeldt B et al (2005) Prediction of response to neoadjuvant chemotherapy by sequential F-18-fluorodeoxyglucose positron emission tomography in patients with advanced-stage ovarian cancer. J Clin Oncol 23:7445–7453
32. Mendivil A, Schuler KM, Gehrig PA (2009) Non-endometrioid adenocarcinoma of the uterine corpus: a review of selected histological subtypes. Cancer Control 16:46–52
33. Smith-Bindman R, Kerlikowske K, Feldstein VA et al (1998) Endovaginal ultrasound to exclude endometrial cancer and other endometrial abnormalities. J Am Med Assoc 280:1510–1517
34. Suzuki R, Miyagi E, Takahashi N et al (2007) Validity of positron emission tomography using fluoro-2-deoxyglucose for the preoperative evaluation of endometrial cancer. Int J Gynecol Cancer 17(4):890–896
35. Suzuki R, Miyagi E, Takahashi N et al (2007) Validity of positron emission tomography using fluoro-2-deoxyglucose for the preoperative evaluation of endometrial cancer. Int J Gynecol Cancer 17(4):890–896
36. Kitajima K, Murakami K, Yamasaki E et al (2008) Accuracy of 18F-FDG PET/ CT in detecting pelvic and paraaortic lymph node metastasis in patients with endometrial cancer. AJR Am J Roentgenol 190(6):1652–1658
37. Park JY, Kim EN, Kim DY et al (2008) Clinical impact of positron emission tomography or positron emission tomography/computed tomography in the post-therapy surveillance of endometrial carcinoma: evaluation of 88 patients. Int J Gynecol Cancer 18(6):1332–1338
38. Yamada SD, Burger RA, Brewster WR et al (2000) Pathologic variables and adjuvant therapy as predictors of recurrence and survival for patients with surgically evaluated carcinosarcoma of the uterus. Cancer 88(12):2782–2786
39. Lamoreaux WT, Grigsby PW, Dehdashti F et al (2005) FDG-PET evaluation of vaginal carcinoma. Int J Radiat Oncol Biol Phys 62(3):733–737
40. Stehman FB, Look KY (2006) Carcinoma of the vulva. Obstet Gynecol 107(3):719–733

Molecular Imaging and Targeted Therapy of Gastrointestinal Cancer

7

Menghui Yuan and Hua Pang

7.1 Generality of Gastrointestinal Cancer

Gastrointestinal (GI) cancer constitutes an important health issue worldwide and is responsible for most cancer-related fatalities in both genders. GI malignancies such as colorectal, gastric, and esophageal tumors are on the rise. Multiple treatment approaches are currently used for GI cancer but with limited effect.

GI incidence and mortality have markedly decreased lately. However, GI carcinoma still ranks fourth among major cancers and represents a leading cause of cancer-associated fatalities around the world. Different demographic trends are observed according to the location and histology of the lesions.

7.1.1 Hepatocellular Carcinoma

Hepatocellular carcinoma (HCC) represents the most frequently detected primary liver cancer and is a common malignancy around the world. HCC ranks sixth among cancers and third among the most lethal malignancies in industrial nations; indeed, the death toll associated with HCC exceeds a million individuals yearly in the West. In countries with elevated chronic hepatitis B virus (HBV) or chronic hepatitis C virus (HCV) rates, approximately 15/100,000 cases of HCC are detected yearly, versus an incidence of 3/100,000 in Western nations. The 30 past years have witnessed increased HCC incidence in America, which is likely due to increased HCV infection incidence and current migration patterns worldwide. HCC is likely tightly associated with sex, affecting 2–8 times more males in comparison with females. Elevated HCC incidence in male individuals can be explained by higher rates of related risk factors. Generally, HCC incidence increases with age; meanwhile, individuals in regions with high incidence tend to develop HCC earlier [1]. Additionally, HCC might aggregate in families.

7.1.2 Biliary Tract Tumor

Cholangiocarcinoma comprises multiple epithelial lesions characterized by the differentiation of cholangiocytes. Cholangiocarcinoma classes based on anatomical location include intrahepatic (iCCA), perihilar (pCCA), and distal (dCCA) subtypes, each with distinct epidemiological, biological, prognostic, and management features. Cholangiocarcinoma, especially iCCA, has shown increased incidence in the last few decades worldwide.

Gallbladder cancer (GBC), as a biliary tract cancer, is rarely diagnosed in industrialized nations but commonly found in poor areas worldwide. GBC shows no symptoms at the initial stage, making it difficult to diagnose and treat. Despite the global GBC occurrence below 2/100,000 people, great variance has been noted.

7.1.3 Pancreatic Cancer

Pancreatic cancer (PC) ranks fourth among the deadliest malignancies in America, following pulmonary, prostate/breast, and colorectal cancers. However, PC shows worst survival among all solid tumors. PC incidence and death rates are slightly higher in the male population, and the majority of cases are 65–80 years old at first diagnosis [2]. Approximately 53,070 newly diagnosed PC cases and 41,780 PC-related fatalities were reported in 2016, and 5-year survival in this malignancy only increased from 3 to 8% in the last four decades. Despite intensive scientific efforts, PC still claims many lives, and only a small number of cases can be cured.

M. Yuan (✉)
Tangdu Hospital of the Forth Military and Medical University, Xi'an, P. R. China

H. Pang (✉)
The First Affiliated Hospital of Chongqing Medical University, Chongqing, P. R. China

G. Huang (ed.), *Nuclear Medicine in Oncology*, https://doi.org/10.1007/978-981-13-7458-6_7

7.2 Diagnosis

7.2.1 Hepatocellular Carcinoma

HCC is mostly caused by HBV, HCV, nonalcoholic fatty liver disease, aflatoxin consumption, and tobacco smoking. Clinical presentations vary, from the absence of symptoms to symptomatology extending from right upper abdominal quadrant pain and decreased weight to obstructive jaundice and lethargy. HCC is mainly diagnosed by imaging and laboratory assays. Imaging methods of diagnosis, therapy planning, management, and follow-up in HCC include ultrasonography (US), computed tomography (CT), and magnetic resonance imaging (MRI) (Fig. 7.1).

Alpha-fetoprotein (AFP) represents the major serological biomarker of HCC. However, it has low sensitivity and detects only 25% of lesions <3 cm in diameter and 50% of larger ones. Recently described serum markers and IgM immune complexes failed in diagnosing HCC accurately. Nevertheless, using these biomarkers in combination may increase sensitivity. Although currently available management guidelines for HCC require biopsy for diagnostic confirmation, lesions >2 cm on MRI or computed tomography angiography (CTA), with AFP either >400 ng/mL or increasing after sequential assessments, certainly represent based on the European Association for the Study of the Liver (EASL) guidelines. In cases with no chronic liver disease, liver biopsy is highly recommended for final diagnosis and adequate therapy planning.

7.2.2 Biliary Tract Cancer

Biliary tract cancer should be diagnosed based on radiological (MRI and CT) findings and pathomorphological features according to the World Health Organization classification from a biopsy, fine needle aspiration, or biliary brush cytology. Definite pathological diagnosis is required before chemotherapy, radiotherapy, or other non-surgical treatment, however, but not essential for planning operations in cases showing characteristic features of resectable biliary cancer.

7.2.3 Pancreatic Cancer

The detection of PC was delayed due to the absence of early specific symptoms. Pancreatic lesions were generally hypovascular; enhanced scan, CT arterial, and venous enhancement can also improve the assessment of lesions and the extent of disease involvement. Thin slices and high resolution images have improved the assessment of vascular involvement, such as the celiac axis, the superior mesenteric artery, and the portal vein that determines whether tumors can be removed. However, enhanced scan has its limitations, especially in the identification of non-cancerous tissues around the pancreas or chronic pancreatitis. In addition, enhanced CT cannot effectively detect liver metastasis and early lymph node metastasis. Magnetic resonance imaging has higher sensitivity in the detection of metastatic lesions. Endoscopic ultrasound is critical for the diagnosis and treatment of PC, which could measure the depth of lesions and guide fine-needle biopsy for tissue diagnosis without surgery.

The use of tumor biomarkers in the diagnosis of PC is limited. The expression of CA 19-9 in PC is often increased, with a sensitivity of 70–92% and a specificity of 68–92%. In cases where Lewis antigen is not expressed (5–10% of individuals), CA 19-9 is not produced and cannot serve as a valuable index. Meanwhile, CA 19-9 is also highly expressed in a variety of benign lesions. Other biomarkers, including macrophage inhibitory cellular factor 1 (MIC), osteopontin,

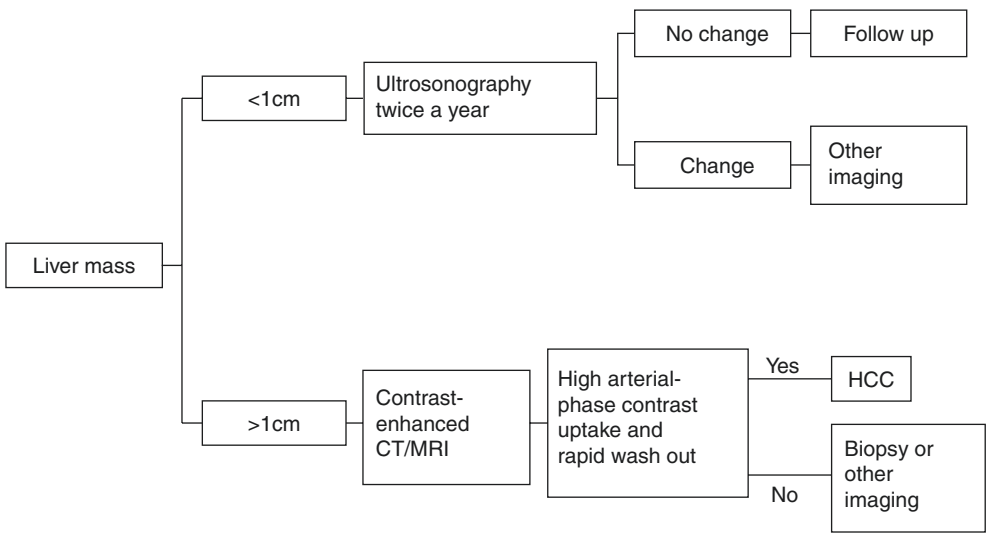

Fig. 7.1 Imaging methods of HCC diagnosis, therapy planning, management, and follow-up

metalloproteinases tissue inhibitor of protein 1, and hepatocarcinoma-intestine-pancreas assessment in preclinical studies, cannot replace the CA 19-9.

7.3 The Application of ^{18}F-FDG-PET/CT in Gastrointestinal Cancer

Morphological imaging efficiently determines TN staging, except for small metastatic lymph nodes, but does not accurately reveal distant metastases. Fluorine-18 fluorodeoxyglucose positron emission tomography (FDG-PET) has been increasingly applied in the past two decades, especially after the advent of PET/CT combination. FDG-PET/CT is employed in gastrointestinal cancer for detection, grading, follow-up, and recurrence assessment.

7.3.1 The Application of Primary Hepatocellular Carcinoma

Various glucose-6-phosphatase activity and glucose transporter levels have been found in HCC, resulting in different FDG uptake amounts. With a 50–65% sensitivity, FDG-PET/CT is not suitable for HCC detection, although adding CT images could help, since 70% and 20% of HCC tumors appear in unenhanced CT as hypodense and hyperdense lesions, respectively. However, it was recently suggested that FDG-PET uptake might help in tumor characterization, therapeutic response evaluation, and prognosis; indeed, elevated FDG uptake is correlated with higher-grade tumors and poorer prognosis (Fig. 7.2). The later conclusion requires further validation.

Furthermore, tumor metabolism evaluated by FDG-PET/CT independently predicts response to transarterial chemoembolization, with reduced OS in cases with high pretreatment SUVmax ratio in comparison with those with low SUVmax ratio. FDG-PET/CT and other imaging modalities, including CT and MRI, should be compared in a comprehensive manner.

Moreover, FDG-PET/CT improves clinical management in HCC cases by allowing the selection of liver transplantation candidates. According to the FFCD, NCCN, and ESMO guidelines, PET/CT is not recommended for HCC diagnosis, grading, or management. However, it could be applied for recurrence detection in cases with increased AFP amounts [3].

7.3.2 The Application of Cholangiocarcinoma and Gallbladder Carcinoma

FDG-PET/CT shows no remarkable benefit over contrast-enhanced CT or MRI in detecting primary biliary lesions; however, it is useful for detecting regional and distal metastases, which could affect the management of patients by excluding

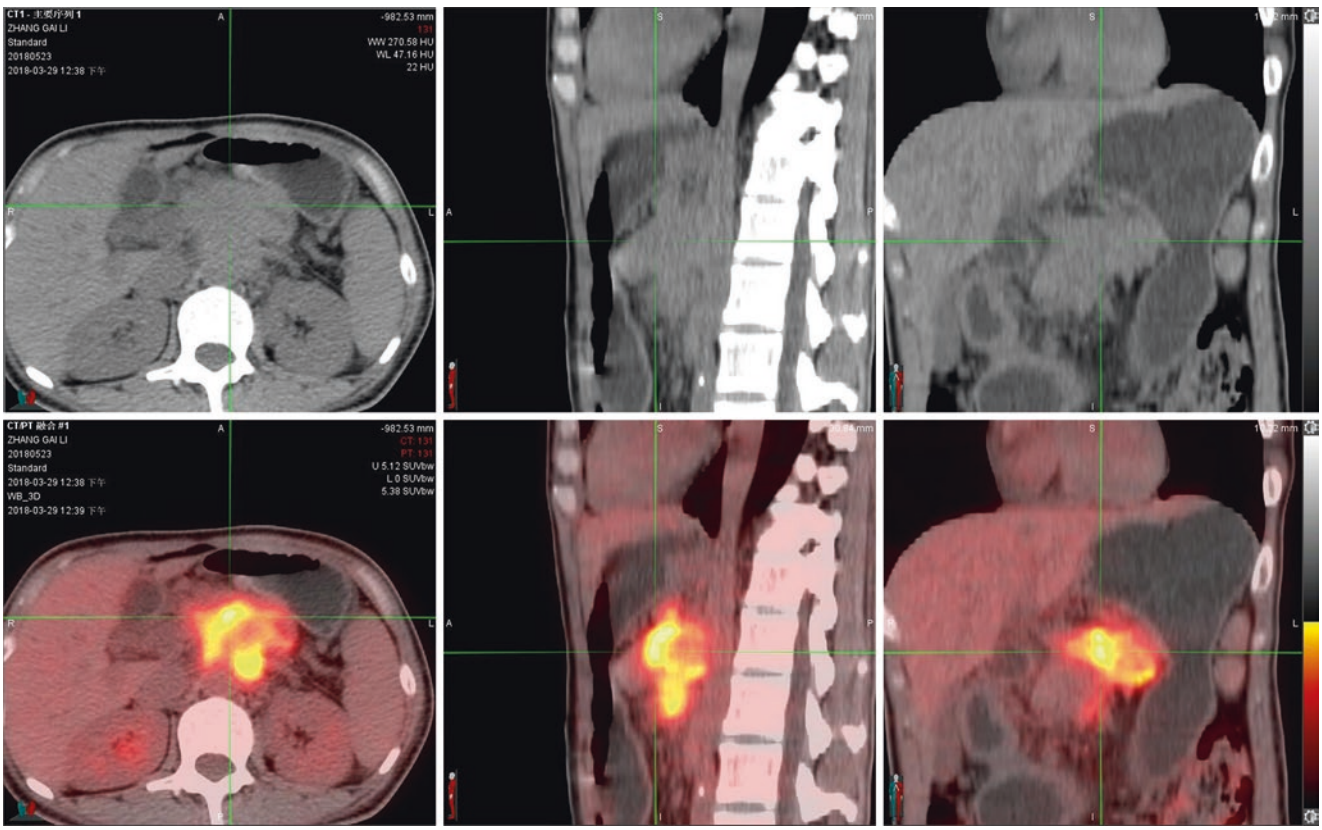

Fig. 7.2 Mild differentiated pancreatic cancer, SUVmax5.3

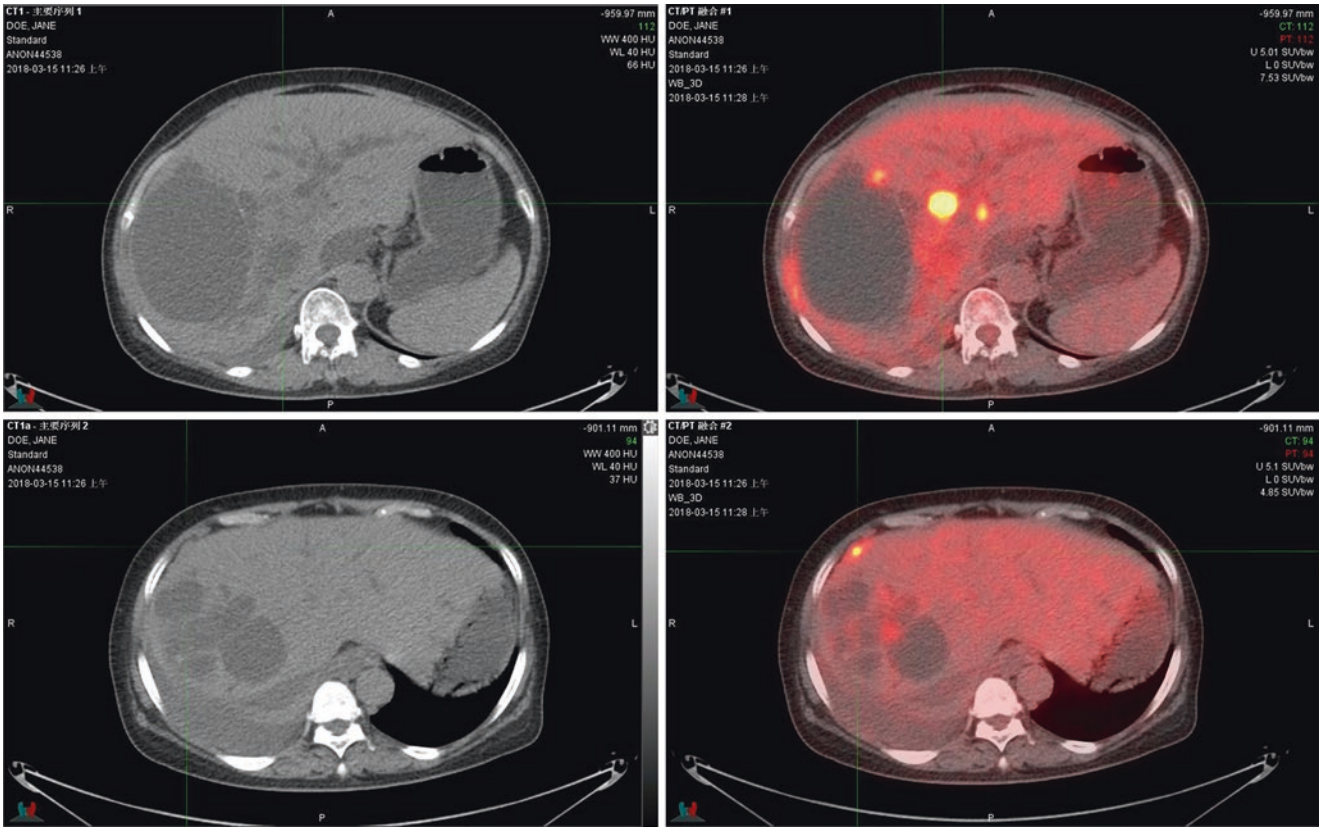

Fig. 7.3 Cholangiocarcinoma with peritoneal metastasis

them from surgery (Fig. 7.3). FDG-PET has good sensitivity (75–100%) and specificity (80–89%) for detecting primary gallbladder cancer. However, findings in support of PET application in gallbladder carcinoma are limited, and trials enrolling large numbers of patients are required to determine whether these methods affect patient outcomes.

Despite emerging evidence indicating a role for PET in the initial grading of cholangiocarcinoma and gallbladder carcinoma, this technique is not presently recommended for such cancers [4].

7.3.3 The Application of Pancreatic Cancer

Contrast-enhanced CT (CECT) represents the mostly employed tool for pancreatic cancer diagnosis. Routinely, CT, transabdominal ultrasound, endoscopic ultrasound, endoscopic retrograde cholangiopancreatography, MRI, MR cholangiopancreatography, PET, and PET/CT are used for imaging pancreatic processes [5].

7.3.3.1 PET/CT Application in Initial Management of Pancreatic Cancer

CT and MRI, especially CECT, are currently recommended for the evaluation of cases with clinically suspected PC. Multiphase CT or MRI is suitable for suspected pancreatic neuroendocrine lesions. Recent evidence supports a role for PET/CT in the initial management of PC, especially for characterizing lesions, disease staging, and preoperative and pre-radiotherapy planning. PET/CT can detect isodense/isointense lesions that are not obvious on conventional imaging (Fig. 7.4). Such lesions are more easily detected by PET in comparison with CT or MR, as tumor-associated hypermetabolism may precede actual anatomic changes. PET/CT and CECT have comparable sensitivities and specificities in PC diagnosis (89–91% vs. 88%, respectively).

PET/CT clearly differentiates chronic pancreatitis from PC. In chronic pancreatitis, the pancreas shows diffuse and reduced ^{18}F-FDG uptake compared with a more focal uptake and higher maximum SUV (SUV_{max}) in case of cancer (Fig. 7.5). Imaging-guided biopsies can be precisely obtained based on PET/CT data. Targeted biopsy of the most hypermetabolic part of the lesion could allow increased diagnostic yield, which is of particular importance in heterogeneous necrotic lesions, tumors with considerable cystic components, and lesions with equivocal findings from CT-guided biopsies. In the specific case of PC, inflammatory and desmoplastic reactions accompanying the lesions might be similar to the primary masses themselves on conventional imaging. This indicates that PET/CT may participate in targeting the most ^{18}F-FDG-avid lesion areas, improving tissue diagnosis.

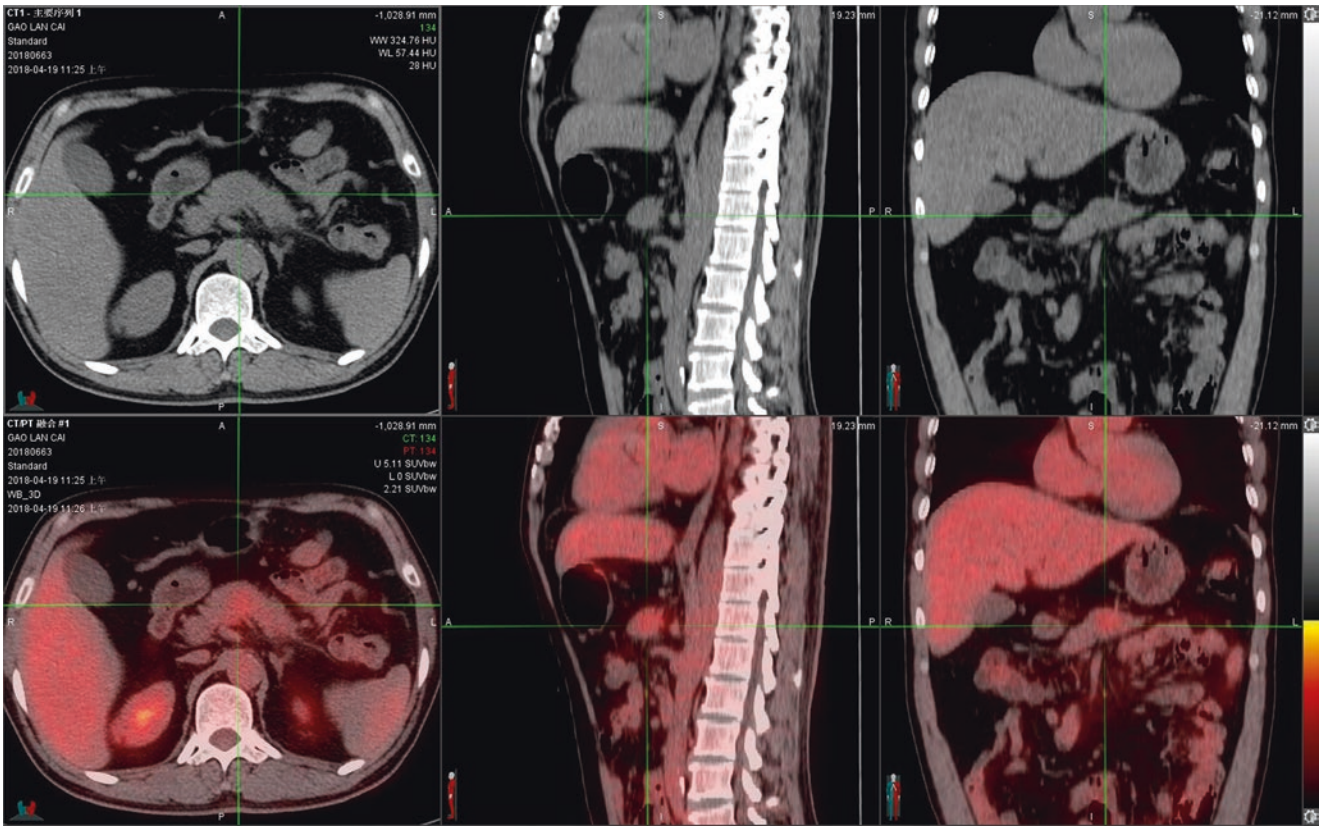

Fig. 7.4 Isodense pancreatic cancer with mild ^{18}F-FDG uptake

7.3.3.2 PET/CT Application in Staging and Presurgical Planning of Pancreatic Cancer

Determining resectability is critical in therapeutic planning for PC. Ideally, an imaging tool should detect nodal and distant metastases (Fig. 7.5), as well as invasion of adjacent important neurovascular structures such as the superior mesenteric artery and vein, the portal vein, and the celiac, hepatic, and gastroduodenal arteries. Although most of this is achieved by CECT, PET shows superiority in initial lesion grading, detecting both lymph node and distant metastases. Based on PET/CT findings, disease management is altered in 41% patients, with 33% occurring at initial grading and 43% cases at subsequent imaging, all secondary to upstaging disease.

7.3.3.3 PET/CT Application in Radiotherapy Planning of Pancreatic Cancer

PET/CT can help estimate the tumor volume and plan the conformal radiation field in cases of undergoing radiotherapy, with ameliorated demarcation of lesion margins, in comparison with CT alone. A single-center trial combining PET and CT found a gross tumor volume increase approximating 30%, due to additional lymph node metastases incorporated as well as primary volume extension compared with CT.

7.3.3.4 PET/CT Application in Prognosis, Response to Therapy, and Recurrence of Pancreatic Cancer

Schellenberg et al. reported SUVs derived from pretreatment PET/CT could predict survival in cases with unresectable PC, even after controlling for age, CA19-9 amounts, and chemotherapy type (single or combination). The greater the baseline SUV_{max}, the higher the odds of recurrence early after operation. SUV_{max} might also independently predict overall survival in cases with locally advanced PC. Pre- and post-chemotherapy PET/CT can be comparatively assessed to estimate chemotherapeutic effects and predict survival. Finally, PET/CT improves cancer recurrence assessment, especially in cases with high CA19-9 amounts and those with non-remarkable or uncertain CT findings [6].

7.3.4 The Application of Esophageal Cancer

Esophageal cancer accounted for 4% in all gastrointestinal tumor, the main symptoms include dysphagia, odynophagia, and hematemesis. Many patients have distant metastasis once they are diagnosed with cancer. Therefore the overall prognosis is poor. The 5-year survival rate is less than 25%, and the worldwide incidence increased year by year. PET/

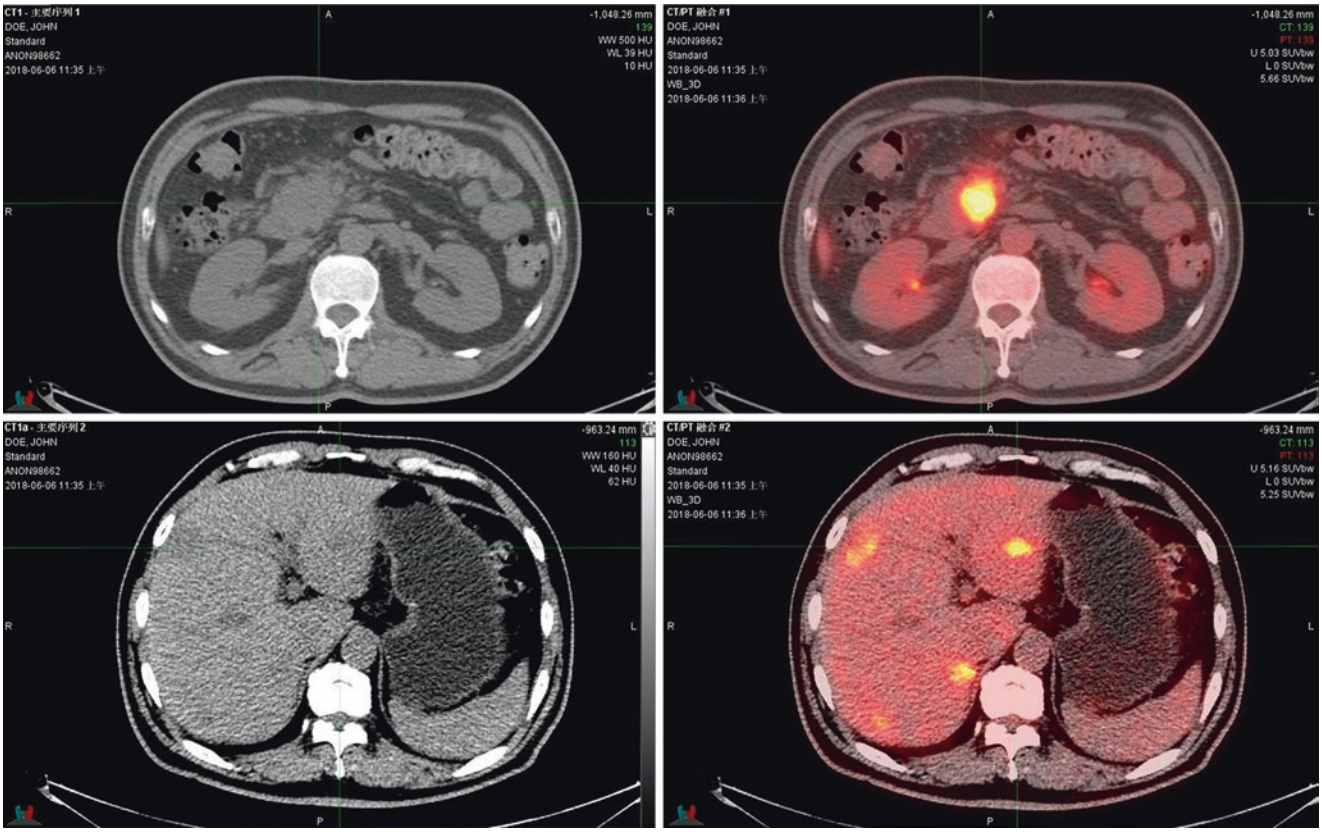

Fig. 7.5 Pancreatic cancer with intrahepatic metastasis

CT breaks through the confinement of traditional imaging methods based on morphological changes and plays an important role in the diagnosis, staging, and evaluation of curative effect of esophageal cancer.

Primary esophageal cancer usually shows a high concentration of ^{18}F-FDG. The degree of concentration is about the expression of glucose transporter protein one (glucose transporter, GLUT1) and the upregulation of hexosapride II (type II hexo kinase, HK-II). PET/CT can accurately locate abnormal metabolic disorders and reflect the metabolic characteristics of normal and abnormal anatomical structures. However, some esophageal cancer of small volume and early stage are still likely to be missed. In addition, some of the limited physiological uptake, benign lesions of the esophagus, and early malignant lesions of the esophagus are also easily confused. The sensitivity of ^{18}F-FDG-PET/CT to the diagnosis of primary esophageal carcinoma was 77.8–91%, the specificity was 92.9%, and the accuracy was 84.4%. For esophageal cancer, the advantage of PET/CT is to detect distant metastases, find metastatic lymph nodes, and carry out TNM staging to provide a basis for the determination of the operative plan. In particular, the diagnosis of cervical, upper mediastinum, and abdominal lymph nodes metastasis is more accurate. About 22% of patients have changed their treatments (Fig. 7.6).

Although the recurrence of esophageal cancer is common, the early diagnosis and appropriate treatment are beneficial to prolong the survival time of the patients with esophageal cancer. Some traditional imaging techniques, such as CT, ultrasound endoscopy, and MRI, are routinely used to detect the recurrence of esophageal cancer. However, these morphological imaging techniques are limited to identify the differentiation of the recurrence and inflammation, edema, and fibrosis after treatments which could result in the thicker wall of the esophagus. As a functional imaging technology, ^{18}F-FDG-PET can provide metabolic information of the tissues. Therefore, it can overcome some shortcomings of traditional imaging and reliably identify malignant lesions and inflammatory reactions or tissue edema (Fig. 7.7). ^{18}F-FDG can not only be absorbed by tumor cells but also can be absorbed by restoration tissue or inflammatory cell, which results in the limited specificity of PET and the difficulty of differential diagnosis. In addition, the physiological uptake of smooth muscle cells, esophageal mucosa, and anastomotic stoma also causes false-positive ^{18}F-FDG uptake. PET/CT, combinating metabolic and anatomical images, improves the accuracy of recurrent diagnosis to a certain extent by localization the lesion of ^{18}F-FDG uptake accurately.

^{18}F-FDG-PET/CT is more accurate than conventional images in delineation of the boundary of the lesion, and it is

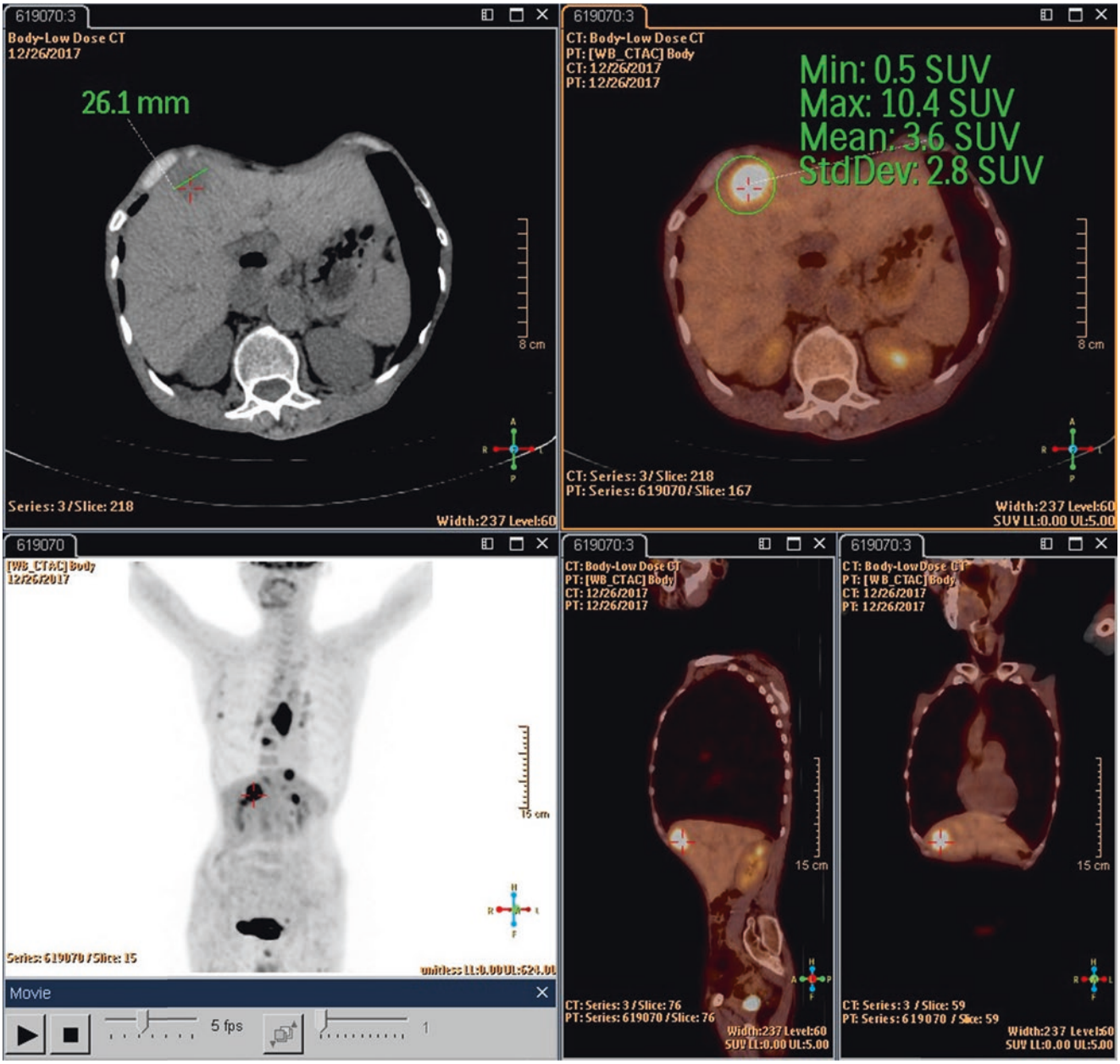

Fig. 7.6 Live, bone, and lymph nodes metastasis with midpiece esophageal cancer

beneficial to delineate gross tumor volume (GTV) of esophageal cancer in making radiotherapy plan. PET/CT also plays an important role in evaluating the curative effect of radiotherapy and chemotherapy and differentiating the local tumor recurrence and fibrosis after radiotherapy and chemotherapy. Because of the metabolic activity of granulocytes and macrophages after radiotherapy, it is not easy for PET/CT to identify the difference between esophagitis, esophageal ulcer, and tumor recurrence; therefore, choosing the right time to assess the therapeutic effect becomes more important; and it is considered appropriate to carry out PET/CT within 14 days after radiotherapy and chemotherapy.

7.3.5 The Application of Gastric Cancer

Gastric cancer is a common malignant tumor in the digestive system, and its morbidity and mortality are among the highest in China. The prognosis of gastric cancer in advanced stage was poor, and the 5-year survival rate was less than 61%, while the 5-year survival rate of early gastric cancer was 84–99%. ^{18}F-FDG-PET/CT was used to detect gastric cancer from the perspective of functional and morphology and showed certain guiding value in preoperative staging, prognosis evaluation, and monitoring of gastric cancer.

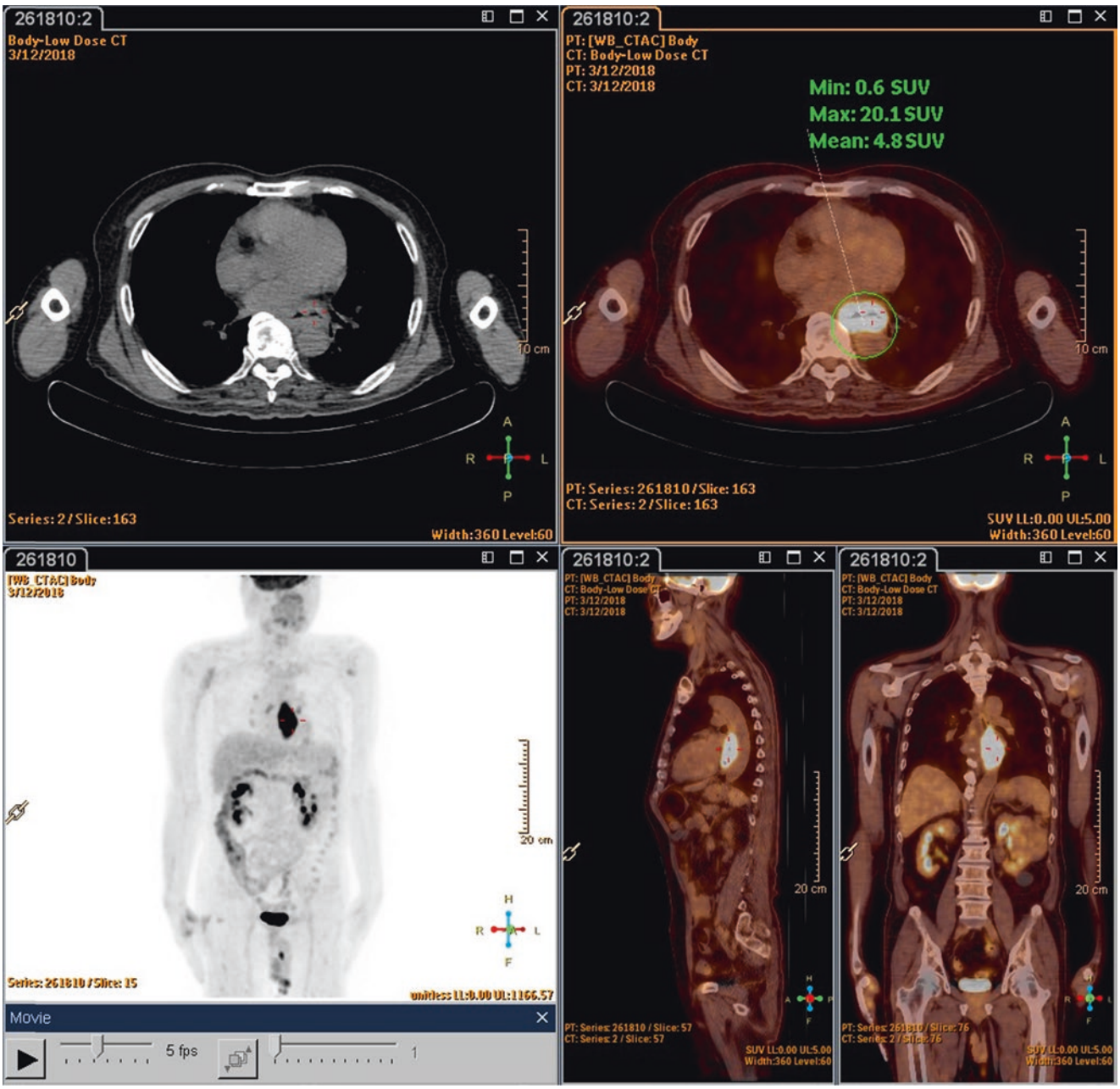

Fig. 7.7 Recurrence of esophageal cancer after chemotherapy

^{18}F-FDG-PET/CT can be used to determine the primary foci of gastric cancer, lymph node metastasis, and distant tissue metastasis, and it has certain reference value for TNM staging of tumor (Fig. 7.8). SUVmax uptake of primary gastric cancer was significantly correlated with tumor size and tumor invasion, indicating that SUVmax was closely related to tumor progression. However, the sensitivity of PET imaging in the diagnosis of early gastric cancer is low, which is mainly due to false positive and false negative. False positive is associated with normal physiological uptake of the stomach wall and/or mucosal inflammation. False negative is related to the limited spatial resolution of PET, also to mucinous adenocarcinoma, signet ring cell carcinoma, and poorly differentiated adenocarcinoma, which is usually associated with low metabolism or no uptake of ^{18}F-FDG (this is related to variation in the amount and metabolic function of glucose transporter protein-1 on the surface of tumor cells, resulting in excessive ^{18}F-FDG uptake or excessive elimination). All of these may interfere with the correct diagnosis of PET.

^{18}F-FDG-PET/CT was low in early gastric cancer screening and T_1 detection rate but had high positive predictive value. For the advanced gastric cancer (T_2–T_4) and local

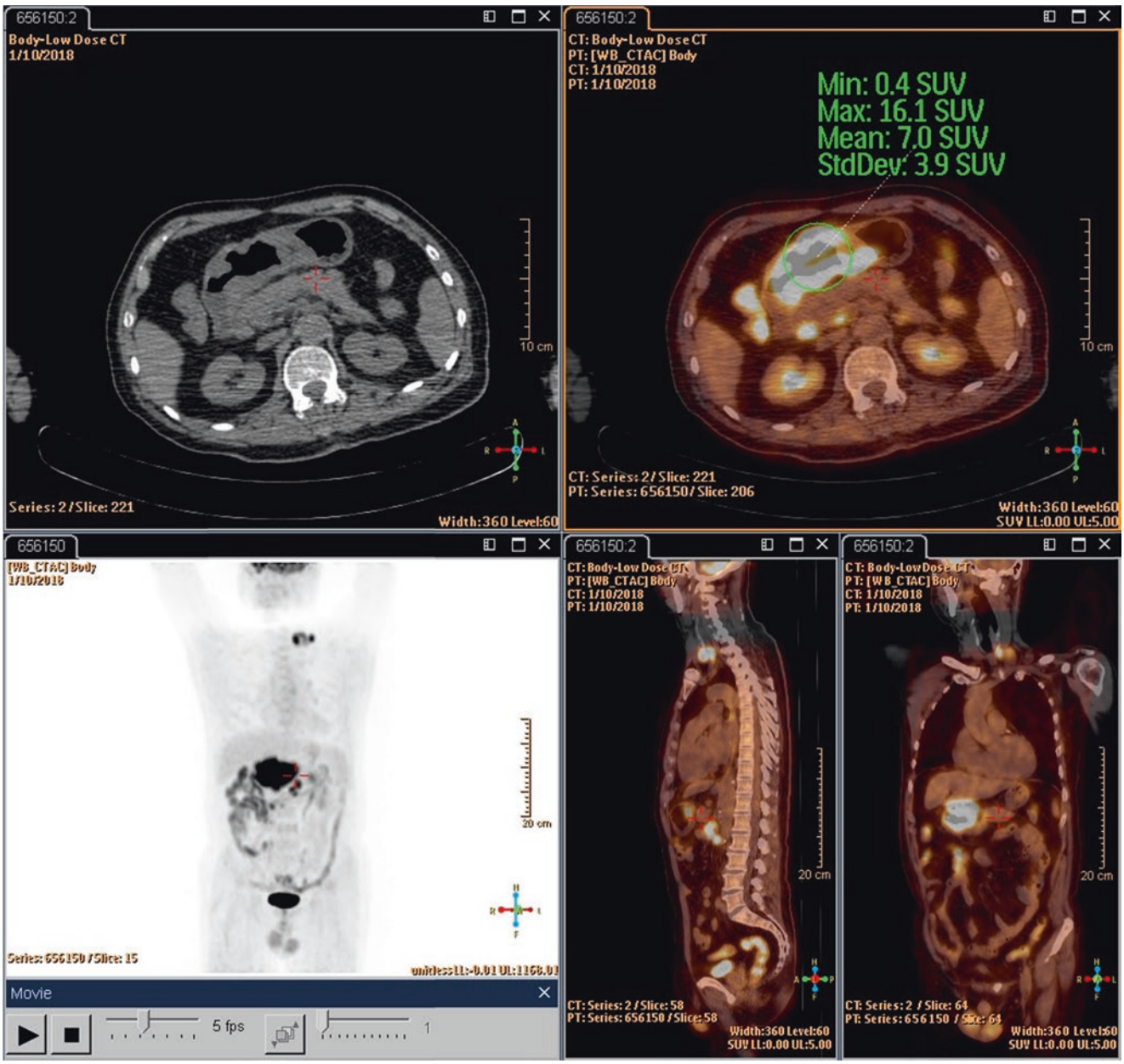

Fig. 7.8 Gastric cancer with multiple retroperitoneal lymph nodes metastasis

lymph node metastasis, PET/CT has a higher detection rate and similar accuracy than enhanced CT. In addition, PET/CT may also detect occult metastatic lesions, which can significantly change the staging and clinical treatment of gastric cancer; for the recurrence of the lesions, PET/CT has a high positive predictive value, which can guide clinical treatment planning. Besides, in the early evaluation of the curative effect of gastric cancer, PET/CT can assess tumor tissue metabolism and monitor the efficacy of tumor tissue for sensitive chemotherapy drugs by SUV or tumor size. In the improvement of gastric cancer detection method, ^{18}F-FLT-PET/CT imaging could be selected to improve the sensitivity of gastric cancer detection. And gradually mature PET/MRI examination method is expected to significantly improve the accuracy of monitoring gastric cancer staging.

7.3.6 The Application of Colorectal Cancer

^{18}F-FDG-PET/CT is more valuable in staging, relapse, and metastasis of colorectal cancer and can accurately guide postoperative radiotherapy. For the diagnosis of primary tumor, although various research results are different, most reports affirm the value of ^{18}F-FDG-PET/CT. For primary

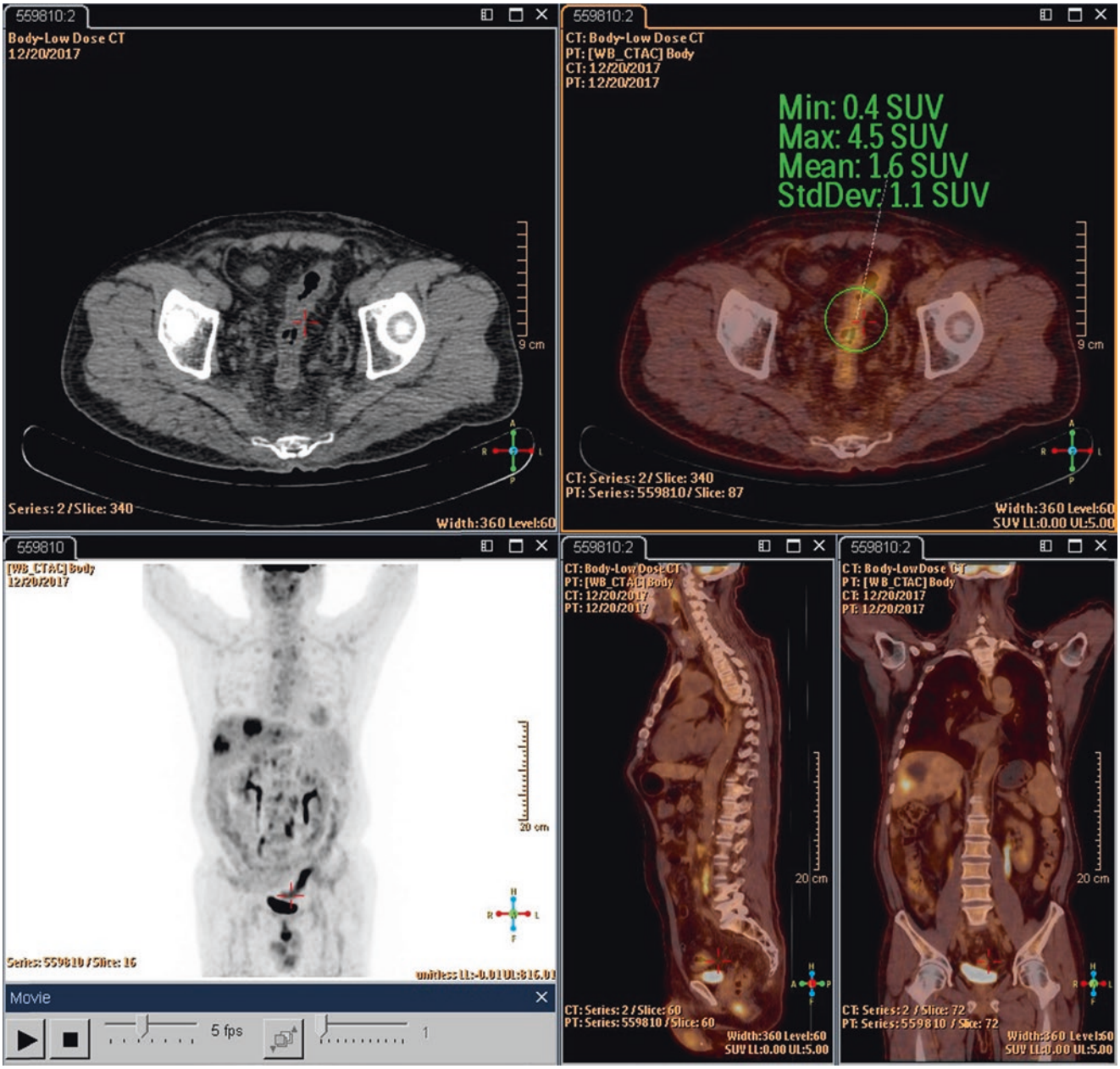

Fig. 7.9 Live metastasis with colorectal cancer

lesions of colorectal cancer, ^{18}F-FDG-PET has high sensitivity and low specificity. The advantages of ^{18}F-FDG-PET/CT are the detection of liver and extrahepatic metastasis and the identification of tumor recurrence and scar. Comparative studies showed that the accuracy of ^{18}F-FDG-PET in detection of hepatic metastasis and of colonic carcinoma was 92%, while conventional CT was 78%, and CT angiography was 80%. The PET detection rate of extrahepatic metastasis was 92%, and CT was 71%. A study of 378 patients with colorectal cancer showed that 27% patients found new undetected metastases in other detection by ^{18}F-FDG-PET/CT, and 37% patients modified therapeutic schedule because of PET results (Fig. 7.9). The sensitivity of ^{18}F-FDG-PET in diagnosis of local recurrence was 90.3–100%, and the specificity was 90–100%. In clinic, it is necessary to carry out PET/CT examination for patients with high serum CEA and negative imaging examination results (Fig. 7.10).

The clinical application of ^{18}F-FDG-PET/CT in colorectal cancer has the following shortcomings:

1. The sensitivity of PET to small lesions was significantly decreased, such as some metastases in live with a diameter less than 0.5 cm.

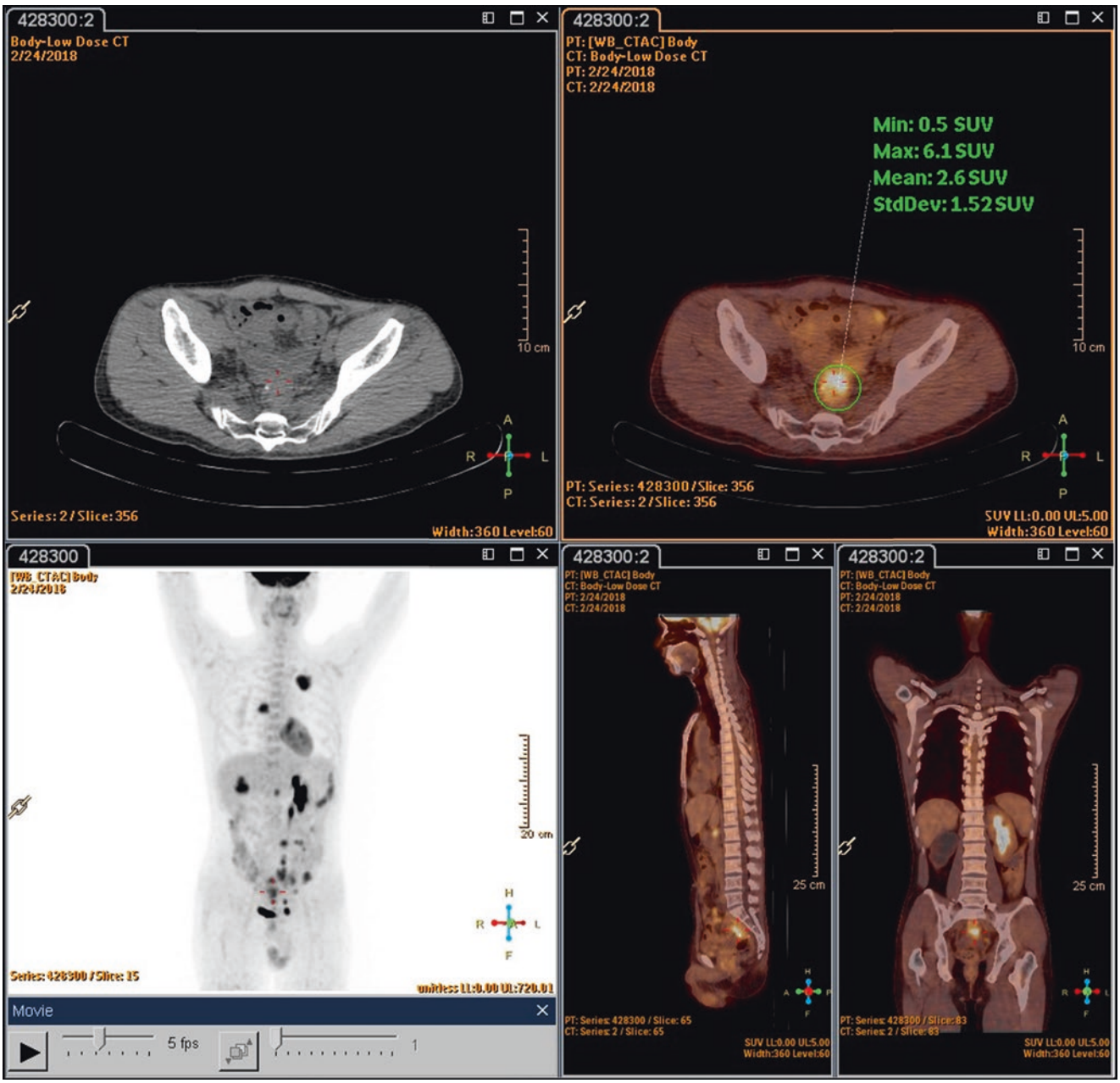

Fig. 7.10 Live, bone, and lymph nodes metastasis with colorectal cancer

2. Tumor tissues with necrotic tissues are often diagnosed as benign lesions. For example, the mucus in rectal mucinous adenocarcinoma is often deposited into the mucous lake, and its internal cell content is very small. Therefore, PET shows that the uptake of ^{18}F-FDG is very low, even none, and the result is false negative.
3. Because active macrophages have high uptake of ^{18}F-FDG, the recent surgical incision, drainage tube, enterostomy, and intestinal inflammation all showed ^{18}F-FDG hypermetabolism in PET, and false positive occurred.
4. Physiological radioactive uptake caused by intestinal peristalsis influences image analysis, which is important to affect the detection rate of primary tumor of colorectal cancer. Discrimination of false-negative or false-positive lesions should be closely combined with the history, and more fully use spiral CT which can be used for the thin layer scanning of the interest area and even the target scanning and multiplanar reconstruction, etc. There is also hope for the development of specific new imaging agents. The delay imaging can usually solve the problem of the image quality caused by intestinal physiological metabolism.

7.4 The Application in Targeted Therapy of Gastrointestinal Cancer

7.4.1 Targeted Therapy of Hepatocellular Carcinoma

HCC resection is considered the primary therapeutic option for cases with single lesions and well-compensated Child A cirrhosis. The 5-year survival exceeds 50%, while about 70% recurrent cases are found within 5 years in patients after lesion removal by surgery.

Liver transplantation (LT) represents the ideal therapy in HCC, especially in case of an underlying liver disease, eliminating the lesion and curing the associated cirrhotic liver, which promotes HCC development. However, LT is seriously hampered by organ shortage, which results in huge dropout (12–25%). Early HCC cases not eligible for surgery or LT should be administered local ablative therapy (LAT), which uses thermal ablation, e.g., microwave ablation (MWA) and laser-induced interstitial thermotherapy, or chemicals, e.g., percutaneous alcohol injection (PEI). Under US or CT guidance, PEI is performed directly to lesions.

HCC is often detected in the late stage, with underlying chronic liver disease. This reduces cure options, and palliative methods dominate as treatment tools, with the aim of downstaging or alleviating a locally advanced disease. Few treatment options are available in advanced HCC because of chemoresistance. Systemic administration of doxorubicin or cisplatin produces low objective response rates, while combining drugs might improve disease control but does not enhance survival. Meanwhile, because of chronic liver disease and underlying hepatic dysfunction, HCC cases show reduced tolerance to full-dose poly-chemotherapy. Indeed, low response rates and the absence of survival benefits are due to cytotoxic chemotherapeutics.

7.4.2 Targeted Therapy of Biliary Tract Cancer

For cholangiocarcinoma, surgical removal is the main potential curative therapy for all three subtypes; meanwhile, liver transplantation following neoadjuvant chemoradiation is only performed in few cases with early pCCA [7]. In advanced-stage or unresectable disease, locoregional and systemic chemotherapies are the primary therapeutic options. Improved external-beam radiation has ameliorated cholangiocarcinoma treatment. In addition, improved whole-exome and transcriptome sequencing tools comprehensively define the genetic landscapes of various cholangiocarcinoma subtypes [8]. Therefore, promising molecular targets for precision medicine have been reported and are under clinical evaluation. Biomarker-driven studies with patient stratification based on anatomical cholangiocarcinoma subtype and genetic alterations are critical for developing targeted treatments. Targeting the rich tumor stroma of cholangiocarcinomas alongside targeted treatments might also be useful.

In gallbladder carcinoma, radical resection should be applied for cases with incidental GBC stage T_{1b} (muscle layer invasion) or higher. Cases showing T_{1a} lesions (lamina propria invasion) have no further improvement after re-resection if the gallbladder was removed intact [III, B]. Supplemental administration of fluorouracil-containing chemotherapeutics yields some survival benefit following non-curative removal of gallbladder lesions [II, B]. Postsurgical therapy following non-curative cholangiocarcinoma removal by surgery is highly controversial, and both supportive care/palliative chemotherapy and/or radiotherapy might be considered. Jaundice can be alleviated by endoscopic or percutaneous stenting of the biliary tree or via surgical biliary-enteric bypass. Urgent biliary drainage as well as broad-spectrum antibiotics is critical for cholangitis cases resulting from obstructive jaundice.

7.4.3 Targeted Therapy of Pancreatic Cancer

Patients with PC always delayed because of non-specific symptoms present. Under contrast-enhanced imaging often showed hypovascular, CECT imaging is preferred in the clinical practice and can provide an assessment of local and regional disease extent. However, there still remain clinical limitations, delayed enhancement, difficult to differentiate tumors from the normal surrounding or chronic pancreatitis, and also difficult to detect liver or early lymph node metastasis. There, MRI is useful in the situations.

Tumors markers for PC are not useful in diagnosing disease. CA199 is the most commonly evaluated maker in PC and has a higher sensitivity and specificity ranged of 70–92% and 68–92%. Others such as MIC-1, osteopontin, tissue inhibitor of metalloproteinase 1, and hepatocarcinoma-intestine-pancreas protein have been studied but not replaced CA199 in the clinical study.

7.4.4 Targeted Therapy of Esophageal Cancer

More than half of patients with esophageal cancer have found little chance for radical surgery, and recurrence and metastasis of esophageal cancer are common; for these patients, palliative radiotherapy, chemotherapy, biological therapy, traditional Chinese medicine, and other comprehensive treatments are mostly used for such patients. Although a certain effect has been achieved, the prognosis is still poor. In recent years, basic and clinical researches on molecular-targeted therapy for esophageal cancer have attracted more and more attention and provided new treatment methods for esophageal cancer patients.

Targeted therapy for epidermal growth factor receptor (EGFR): There are two main types of drugs for this target, which are anti-EGFR monoclonal antibodies and small molecule tyrosine kinase inhibitors. Monoclonal antibodies mainly include nimotuzumab, cetuximab, and panitumumab. Small molecule tyrosine kinase inhibitors mainly include gefitinib and erlotinib. Targeted treatment of human epidermal growth factor receptor 2 (Her-2): Trastuzumab is an anti-Her-2 monoclonal antibody that blocks the attachment of human epidermal growth factor on Her-2 by attaching to Her-2, thereby blocking the growth of cancer cells. Targeted therapy for vascular endothelial growth factor (VEGF): Bevacizumab is a representative drug for antiangiogenic drugs. In a phase II clinical trial, bevacizumab combined with docetaxel, carboplatin, and fluorouracil increased PFS (progress-free survival) and OS (overall survival). In April 2014, the US Food and Drug Administration approved the human VEGF-2 antagonist ramucirumab for the treatment of advanced gastric cancer or adenocarcinoma of the gastroesophageal junction. Targeted treatment of mesenchymal epidermal transformation factor (c-MET): Ramucirumab is a fully humanized monoclonal antibody that neutralizes HGF and is a new targeted drug that inhibits the HGF/MET signaling pathway in patients with MET-positive gastric and gastroesophageal junction cancers.

How to combine the use of targeted drugs with multiple targets, especially monoclonal antibodies combined with new cytotoxic drugs and combined radiotherapy to achieve the best efficacy, is the focus of future research. In addition, molecular-targeted therapy is easy to produce drug resistance, and how to prevent drug resistance in advance is also an important research direction, which also requires further basic and clinical research.

7.4.5 Targeted Therapy of Gastric Cancer

In recent years, we have found that molecular-targeted therapy using HER-2 and VEGFR2 can prolong the overall survival of advanced gastric cancer by in-depth studies of the molecular biology of gastric carcinoma.

Targeting epidermal growth factor receptor (EGFR), the EGFR family includes four members of HER-1, HER-2, HER-3, and HER-4. HER-2 and HER-1 are major targets of gastric carcinoma. Therapeutic drugs targeting human epidermal growth factor-2 (HER-2) are common with trastuzumab and lapatinib; the therapeutic drugs targeting HER-1 are common with cetuximab, eulottini, and gefitinib. Similar to esophageal cancer, bevacizumab and ramucirumab are often used as an antiangiogenic drug in the treatment of gastric cancer, in addition to other drugs such as apatinib, sunitinib, and sorafenib.

Other targeted therapies, such as targeting signaling pathway of c-MET and PI3K inhibitors, PARP (Poly ADP-ribose polymerase) inhibitors, etc., are being or about to enter clinical trials in recent years. The Cancer Genome Atlas (TCGA) recently proposed a new molecular classification of gastric carcinoma. It further illustrates the molecular mechanism of the heterogeneity of gastric carcinoma and GEJ adenocarcinoma and open up broad prospects for identifying the occurrence, developing gastric cancer, driving genes, guiding individualized treatment, and providing new molecularly targeted therapeutics.

7.4.6 Targeted Therapy of Colorectal Cancer

At present, the targeted drugs for the treatment of colorectal cancer mainly act on vascular endothelial growth factor (VEGF) and its receptor, such as bevacizumab, zaltrap, regorafenib, cyclooxygenase-2 (COX-2) selective inhibitor, and celecoxib. As for the epidermal growth factor receptor (EGFR) molecular-targeting drugs, cetuximab and panitumumab are common. Recent studies have found that the hessaitin can also be used for the treatment of colorectal cancer. It is an inhibitor of HER-2 amplification of molecular-targeted drug.

The occurrence and development of colorectal cancer involve many genes, and the genes that play a leading role in different stages are different. Molecular-targeted therapy is also a multi-target treatment. At the present, the molecular-targeted drugs for clinical selection are limited. Therefore, molecular-targeting drugs need to be further studied and developed to play a more important role in the comprehensive treatment of colorectal cancer.

References

1. Alan PV, Christos P, Junji F et al (2010) The incidence and epidemiology of hepatocellular carcinoma: a global and regional perspective. Oncologist 15(Suppl 4):5–13
2. Federico I, Kouros O, Nancy LC et al (2012) A genome-wide association study of overall survival in pancreatic cancer patients treated with gemcitabine in CALGB 80303. Clin Cancer Res 18:577–584
3. Castilla-Lièvre M-A, Franco D, Gervais P et al (2016) Diagnostic value of combining 11C-choline and 18F-FDG PET/CT in hepatocellular carcinoma. Eur J Nucl Med Mol Imaging 43:852–859
4. Valle JW, Borbath I, Khan SA et al (2016) Biliary cancer: ESMO Clinical Practice Guidelines for diagnosis, treatment and follow-up. Ann Oncol 27(suppl_5):v28–v37
5. Priyanka J, Bijan B (2015) PET/CT for pancreatic malignancy: potential and pitfalls. J Nucl Med Technol 43:92–97
6. Woohyun J, Jin-Young J, Mee Joo K (2016) The clinical usefulness of 18F-fluorodeoxyglucose positron emission tomography–computed tomography (PET–CT) in follow-up of curatively resected pancreatic cancer patients. HPB 18:57–64
7. Khan SA, Davidson BR, Goldin RD et al (2012) Guidelines for the diagnosis and treatment of cholangiocarcinoma: an update. Gut 61(12):1657–1669
8. Brito AF, Abrantes AM, Encarnacao JC et al (2015) Cholangiocarcinoma: from molecular biology to treatment. Med Oncol 32(11):245

Head and Neck Cancer

8

Hubing Wu and Shaoli Song

8.1 Nasopharyngeal Carcinoma

Nasopharyngeal carcinoma (NPC) is a carcinoma arising from the nasopharyngeal mucosa and notorious for its highly malignant behavior, often presenting with intensive locoregional infiltration, regional lymph node metastasis, and distant metastasis. Radiotherapy is the most important treatment modality for NPC. As a sensitive imaging modality, ^{18}F-FDG PET/CT plays an important role in diagnosing and staging of NPC, which is useful for making an individualized treatment for NPC patient.

8.1.1 Epidemiology and Etiology

8.1.1.1 Epidemiology

NPC has a global incidence of annual 3.16/million and a mortality of 1.53/million. Incidence of NPC has obvious geographical aggregation, racial susceptibility, and familial tendency. It is popular in Inuit, Northern African, and southern China but rare in European and North American people. Nearly 80% of NPC patients live in Asia. In the popular places, the annual disease' incidence is high with 20–30/million in men and 8–15/million in women. In China, there is also an obvious geographical aggregation of the disease, with a high incidence in southern China, including Guangdong, Guangxi, Jiangxi, Hunan, Fujian, Taiwan, Hainan Provinces, etc., especially Guangdong Province, but a low incidence in northern China. The incident rate in the men is 2–3 times higher than that in the women. NPC affects predominately the adults, with the highest onset age section of 40–60 years, and rare cases are seen in pediatric population [1].

H. Wu (✉)
Nanfang PET center, Nanfang Hospital, Southern Medical University, Guangzhou, P. R. China

S. Song (✉)
Department of Nuclear Medicine, Fudan University Shanghai Cancer Hospital, Shanghai, P. R. China

8.1.1.2 Etiology

Causative carcinogens have not yet been definitely identified, but the inheritance, Epstein-Barr virus (EBV) infection, diet, and environment are likely contributed factors for NPC. Serum EBV-DNA could be detected in 96% of the patients with NPC, but only 7% in the normal population [1]. EBV has a strong association with the NK-NPC, especially in endemic regions. Conversely, EBV is generally absent in keratinized NPC (K-NPC). A high consumption of salted and fermented foods, which have high nitrosamine content, is also suggested to be related to NK-NPC. In the other hand, tobacco smoking and alcohol consumption are associated with K-NPC. Other environmental factors, such as occupational exposure to wood dust, formaldehyde, heat, smoke, dust, and chemical fume, have been proposed as possible contributing or causative factors [1].

8.1.2 Pathological Diagnosis and Biological Behavior

8.1.2.1 Microscopy

NPC lesion can present as a smooth bulge in the mucosa, a discrete raised nodule, a surface ulceration, or a frankly infiltrative fungating mass. Among them, nodular type is the most common one, followed by infiltrative fungating type. However, the morphological abnormality in early stage of the disease is often slight, which can only be presented as a localized and thicken mucous membrane or a mild protrusion without grossly visible lesion. In some patients, the lesion can infiltrate under the mucosa with intact nasopharynx mucosa, which is easy to be missed by the nasopharyngoscope.

8.1.2.2 Histopathology

In 2017, World Health Organization (WHO) [1] classified NPC into three types on the histopathology: keratinized squamous cell carcinoma (K-NPC), nonkeratinized squamous cell carcinoma (NK-NPC), and basaloid squamous cell carcinoma. NK-NPC is a most common one of NPC, which has two subtypes: undifferentiated NK-NPC and differenti-

G. Huang (ed.), *Nuclear Medicine in Oncology*, https://doi.org/10.1007/978-981-13-7458-6_8

ated NK-NPC. The undifferentiated NK-NPC is more common and often has abundant lymphocytic infiltration.

Nasopharyngeal papillary adenocarcinoma, which was one type of NPC, is now classified as another independent type of nasopharyngeal malignant tumor [1]. Approximately 96.71% of NPCs are NK-NPC, 2.32% are keratinized one, while only 0.84 and 0.13% are adenocarcinoma and carcinoma in situ.

8.1.2.3 Tumor Spread

1. Locoregional Infiltration
   NPC is notorious for its highly malignant behavior, which can not only invade the skull base and intracranial space (upper invasion) but also oropharynx and laryngeal cavity (descending invasion). It often presented with intensive locoregional infiltration, such as erosion of skull base and paranasal sinuses, spreading into intracranial space, infiltration of cranial nerves, and extension to adjacent structures (e.g., infratemporal fossa, orbit, and hypopharynx). The commonly involved structures are listed on Table 8.1.
2. Regional Lymph Node Metastasis
   Due to the rich lymphatic plexus in the nasopharynx, lymphatic spread occurs early in the course of disease. NPC can spread to retropharyngeal and cervical lymph nodes. Cervical palpable node is often a first presentation when the patients visit the doctor. Poor prognosis is often found in the patients with large lymph node metastasis greater than 6.0 cm or that locates below the cricoid cartilage.
3. Distant Metastasis
   Approximately 10–15% of the NPC patients develop the distant metastasis. The most common sites of distant metastasis are bone, lung, liver, and distant nodes.

Table 8.1 Structure involved by NPC tumor

Structure involved		
Adjacent soft tissues	Bony erosion/paranasal sinus	Extensive/intracranial extension
Nasal cavity Oropharyngeal wall, soft palate Parapharyngeal space, carotid space Pterygoid muscle (medial, lateral) Prevertebral muscle	Nasal septum Pterygoid plate(s), pterygomaxillary fissure, pterygopalatine fossa Maxillary antrum Ethmoid sinus Sphenoid sinus, sphenoid bone Foramina lacerum, ovale, and rotundum Clivus Petrous bone, petro-occipital fissure Jugular foramen, hypoglossal canal Pituitary fossa/gland	Cavernous sinus Cerebrum, meninges, cisterns Infratemporal fossa Orbit, orbit fissure(s) Hypopharynx

8.1.3 Clinical Presentation

Being familiar with the clinical manifestations of NPC is useful for understanding the imaging changes of PET/CT. The common clinical presentations of NPC include epistaxis or nasal bleeding, nasal obstruction, ear symptoms, headache, ocular symptoms, symptoms of cranial nerve damage, cervical lymph node enlargement, and symptoms caused by distant metastases or cachexia, etc. Most of the symptoms are related to the locoregional invasion of the tumor. Table 8.2 lists the detailed clinical presentations and their causes.

8.1.4 Diagnosis, Stage, and Treatment

8.1.4.1 Diagnosis

Histopathology is the diagnostic gold standard of NPC. The sample is often obtained by the biopsy under the guidance of nasopharyngoscope.

8.1.4.2 Stage

The staging of NPC is very important for designing a personalized treatment protocol for individual patient. Chinese 2017 edition of NPC staging [2] is in accordance with the eighth edition of the Union for International Cancer Control (UICC)/National Cancer Joint Committee (American Joint Committee on Cancer). The detailed description of Chinese 2017 edition of NPC staging is presented in Table 8.3.

8.1.4.3 Treatment

Radiotherapy is the most important treatment modality for NPC, especially the intensity-modulated radiation therapy (IMRT). The local control rate for tumor is larger than 80%. For early-stage (I, II stage) NPC, the disease is mainly treated with IMRT. However, for the advanced-stage NPC, combination with chemotherapy and radiotherapy is needed. Concurrent chemoradiotherapy or platinum-based induction chemotherapy combined with nasopharynx and neck radiotherapy is often recommended as the standard treatment for the metastatic NPC. NPCs often show good response to chemotherapy. At present, platinum combined with fluorouracil, paclitaxel, and gemcitabine is often chosen to be the first line of chemotherapy protocol.

The average 5-year survival rate after radiotherapy is 50–60%; however, it can reach 75–90% in the early-stage disease. Elderly age, local invasion and distant metastasis are correlated with the poor prognosis.

Table 8.2 Clinical presentation of NPC

Presentation	Cause
Epistaxis or Nasal bleeding	Mild hemorrhage caused by microvascular rupture in the tumor Massive hemorrhage caused by vascular rupture in the tumor in the advanced stage
Nasal obstruction	Most of them are unilateral nasal obstruction, mainly due to the obstruction of one side of the nostrils by the tumor Bilateral nasal obstruction can occur when the tumor is very large and block the bilateral posterior nostrils
Ear symptoms (tinnitus, ear stuffiness, ear inflammation, or hearing loss)	Tinnitus, ear stuffiness and ear inflammation are caused by the tumor blockage of the orifice of pharynx drum Hearing loss is often caused by the involvement of auditory nerve in advanced disease
Headache (unilateral, continuous, and fixed)	It is often related to the invasion of skull base and nerves by the tumor
Ocular symptoms (exophthalmos, limitation of the eye motion, visual impairment, visual field defect, diplopia, and trophic keratitis)	Ocular symptoms are mainly caused by the invasion of orbital cavity or eyeball related nerves by tumor
Symptoms of cranial nerve damage (facial numbness, diplopia, eyelid ptosis, hoarseness, muscle atrophy, dysphagia, and tongue deflection)	Facial numbness: trigeminal nerve damage Diplopia: trochlear and/or abduction nerve damage Eyelid ptosis: oculomotor nerve damage Hoarseness, muscle atrophy, dysphagia, and tongue deflection: glossopharyngeal, vagus, accessory, and sublingual nerve damage Olfactory nerve, facial nerve, and auditory nerve were seldom involved
Cervical lymph node enlargement (unilateral or bilateral, hard texture and poor mobility, painless, and fused)	Unilateral or bilateral lymph nodes metastasis
Symptoms caused by distant metastases or cachexia	The symptoms caused by distant metastasis are related to the location, size, and lesion number of the tumors Cachexia is due to the consumption of a large amount of nutrient substance or malnutrition

Table 8.3 Chinese 2017 edition of NPC staging

TNM classification		Stage grouping			
T-primary tumor		Stage 0	Tis	N0	M0
Tx	Primary tumor can't be assessed	StageI	T1	N0	M0
T0	No evidence of primary tumor	StageII	T1	N1	M0
Tis	Carcinoma in situ	Stage III	T2	N0–N1	M0
T1	Tumor confined to nasopharynx or extends to oropharynx and/or nasal cavity	Stage IVA	T1–T2	N2	M0
T2	Tumor with parapharyngeal extension (which denotes posterolateral infiltration of	Stage IVB	T3	N0-2	M0
T3	tumor)	Stage IVC	T4	N2	M0
T4	Tumor invades bone structure of skull base and/or paranasal sinuses		Any T	N3	M0
	Tumor with intracranial extension and/or involvement of cranial nerves infratemporal fossa, hypopharynx, orbit, or masticator space		Any T	Any N	M1
N-regional lymph nodes (i.e., the cervical node)					
Nx	Regional lymph nodes can't be assessed				
N0	No regional lymph node metastasis				
N1	Unilateral metastasis in lymph node(s), and/or unilateral or bilateral metastasis in				
N2	retropharyngeal lymph node, ≤6 cm in greatest dimension, above the				
N3	supraclavicular fossa				
N3a	Bilateral metastasis in cervical lymph node, ≤6 cm in greatest dimension, above				
N3b	the supraclavicular fossa				
	Metastasis in cervical lymph node, >6 cm in greatest dimension, and/or in the supraclavicular fossa				
	>6 cm, in greatest dimension in the supraclavicular fossa				
	Note: midline nodes are considered ipsilateral nodes				
M-distant metastasis					
M0	No distant metastasis				
M1	Distant metastasis				

8.1.5 Anatomy of Nasopharynx and Regional Lymph Node Level

8.1.5.1 Anatomy of Nasopharynx

The upper respiratory tract includes nasal cavity, pharyngeal cavity, and laryngeal cavity. Nasopharynx, as a part of pharyngeal, refers to the cavity between the sphenoid base, occipital slope, and soft palate, which opens forward into the nasal cavity through posterior naris. In each side of nasopharyngeal lateral wall, about 1 cm behind the posterior end of the inferior turbinate, there is the eustachian tube orifice, which opens to the tympanic chamber of the middle ear with the function of maintaining the air pressure balance on both sides of the tympanic membrane and drainage liquid for the middle ear. The anterior and posterior of the eustachian tube contain the tensor veli palatine muscle and levator veli palatini muscle, which have the functions to open the eustachian tube, and tighten and raise the upper palate to prevent nasal fluid from returning. Around the front, upper, and back sides of eustachian tube orifice, there is an arched protuberate called torus tubarius. Located between the back of the tubal torus and the posterior wall of the pharynx, there is a deep longitudinal recess known as pharyngeal recess, which is the most commonly originated site of NPC (Fig. 8.1).

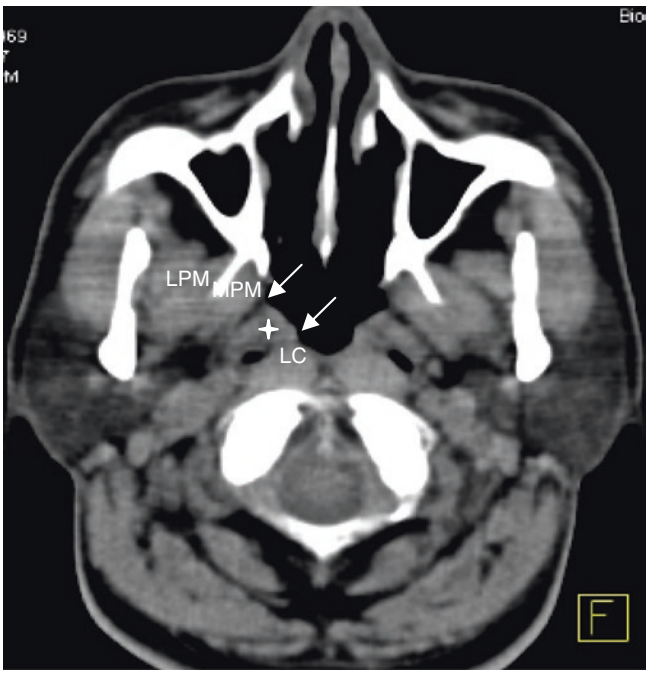

Fig. 8.1 Normal nasopharynx on CT. Eustachian tube orifice (arrow in front), torus tubarius (*), and lateral pharyngeal recess (arrow behind) around the lateral wall of nasopharynx are showed on the axial non-enhanced contrast CT image. In front of eustachian tube, there are lateral pterygoid muscle (LPM) and medial pterygoid muscle (MPM), which are attached to the lateral side of the pterygoid process. The longus capitis (LC) muscle is located deep to posterior wall of nasopharynx

Normally, nasopharynx is symmetrical on both sides. Under the calm breathing status, nasopharynx presents four different forms: square, rectangle, trapezium, and double trapezoid. However, in some individuals, the pharyngeal recess can also be asymmetrical or even closed on one side.

8.1.5.2 Regional Lymph Node Level

The status of the regional lymph nodes in head and neck cancer is of such prognostic importance that the cervical nodes must be assessed for each patient and tumor. The lymph nodes may be subdivided into specific anatomic subsites and grouped into seven levels for ease of description. The detailed information of lymph node group and description is presented on Table 8.4 and Fig. 8.2.

8.1.6 ^{18}F-FDG PET/CT Imaging Findings

8.1.6.1 ^{18}F-FDG PET/CT Image of Normal Nasopharynx

Under normal condition, nasopharynx is symmetrical on both sides. Symmetrical square, rectangular, trapezoid, and double trapezoid of the nasopharyngeal cavity can be seen on CT images, and the eustachian tube can be clearly visualized. The radioactivity distribution in the nasopharyngeal tissue is minimal on PET, which is similar to the surrounding normal tissues.

8.1.6.2 ^{18}F-FDG PET/CT Image of NPC

NPC is a highly aggressive tumor with a rapid growing, which needs a large amount of glucose to meet the requirement for growth. As a result, most of NPC lesions have intense ^{18}F-FDG uptake. NPC tumor can be clearly visualized on PET/CT because the radioactivity in the lesion is significantly higher than that of normal nasopharyngeal tissue. ^{18}F-FDG uptake is reported to be positively related with the tumor size. ^{18}F-FDG uptake was observed to be lower in the tumor ≤1.5 cm than those of lesions with the size between 1.5 and 3.0 cm or >3.0 cm. However, there is not a significant difference of ^{18}F-FDG uptake between the lesions 1.5–3.0 cm and >3.0 cm [3]. ^{18}F-FDG uptake was also found to be significantly different between different pathological subtype tumors. The undifferentiated NPC was observed to have much higher ^{18}F-FDG uptake than poorly differentiated squamous cell carcinoma (SUVmax: 8.41 ± 1.71 vs. 5.58 ± 1.48, $P < 0.001$). Compare to that of nasopharyngeal inflammation, ^{18}F-FDG uptake in NPC tumors was significant higher (SUVave, 3.97 ± 1.28 vs. 2.43 ± 0.51, $t = 5.53$, $P < 0.01$) [3], which indicated that ^{18}F-FDG PET/CT helps to differentiate NPC from nasopharyngeal inflammation.

Table 8.4 The group of cervical lymph node and its description

Lymph node group	Description
Level IA	Lymph nodes within the triangular boundary of the anterior belly of the digastric muscles and the hyoid bone
Level IB	Lymph nodes within the boundaries of the anterior and posterior bellies of the digastric muscle, the stylohyoid muscle, and the body of the mandible
Level IIA and IIB	Lymph nodes located around the upper third of the internal jugular vein and adjacent spinal accessory nerve extending from the level of the skull base (above) to the level of the inferior border of the hyoid bone (below). The anterior (medial) boundary is stylohyoid muscle (the radiologic correlate is the vertical plane defined by the posterior surface of the submandibular gland), and the posterior (lateral) boundary is the posterior border of the sternocleidomastoid muscle. Sublevel IIA nodes are located anterior (medial) to the vertical plane defined by the spinal accessory nerve. Sublevel IIB nodes are located posterior lateral to the vertical plane defined by the spinal accessory nerve
Level III	Lymph nodes located around the middle third of the internal jugular vein extending from the inferior border of the hyoid bone (above) to the inferior border of the cricoid cartilage (below). The anterior (medial) boundary is the lateral border of the sternohyoid muscle, and the posterior (lateral) boundary is the posterior border of the sternocleidomastoid muscle
Level IV	Lymph nodes located around the lower third of the internal jugular vein extending from the inferior border of the cricoid cartilage (above) to the clavicle below. The anterior (medial) boundary is the lateral border of the sternohyoid muscle, and the posterior (lateral) boundary is the posterior border of the sternocleidomastoid muscle
Level VA and VB	Lymph nodes located along the lower half of the spinal accessory nerve and the transverse cervical artery. The supraclavicular nodes are also included in posterior triangle group. The superior boundary is the apex formed by convergence of the sternocleidomastoid and trapezius muscles; the inferior boundary is the clavicle; the anterior (medial) boundary is the posterior border of the sternocleidomastoid muscle, and the posterior (lateral) boundary is the anterior border of the trapezius muscle. Sublevel VA includes the spinal accessory nodes, whereas sublevel VB includes the nodes following the transverse cervical vessels and the supraclavicular nodes, with the exception of the Virchow node, which is located in level IV
Level VI	Lymph nodes in this compartment include the pretracheal and paratracheal nodes, precricoid (Delphian) node, and the perithyroidal nodes including the lymph nodes along the recurrent laryngeal nerves. The superior boundary is the hyoid bone; the inferior boundary is the suprasternal notch, and the lateral boundaries are the common carotid arteries
Level VII	Lymph nodes in this group include pretracheal, paratracheal, and esophageal groove lymph nodes, extending from the level of the suprasternal notch cephalad and up to the innominate artery caudad

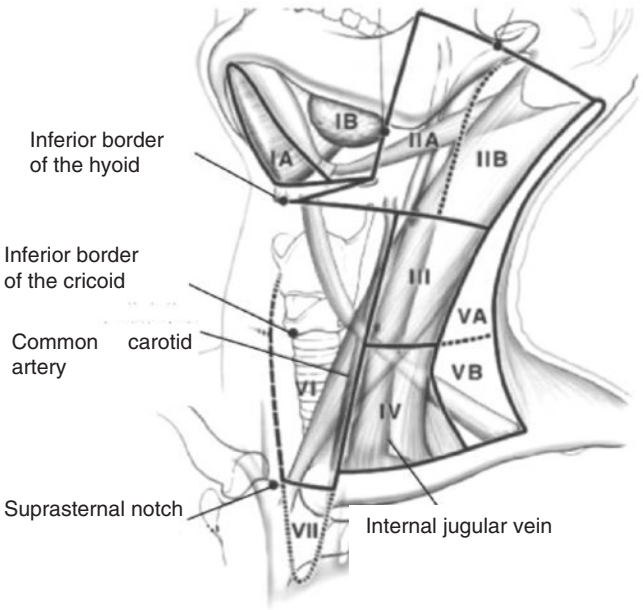

Fig. 8.2 Group of cervical lymph node and some important anatomic markers

NPC can present as a nodular or massive high metabolic lesion on PET images (Figs. 8.3 and 8.4). Because the uptake of NPC is always significantly higher than that of surrounding normal tissue, the tumor can be clearly visualized, and the margin of lesion is easy to determine. However, in the very early-stage NPC, there is only mildly increased ^{18}F-FDG uptake on the surface of mucosa, which is easy to be misdiagnosed as inflammation.

Most of NPC lesions are presented as the soft tissue nodule or mass on the CT image. The existence of the tumor often leads to the obvious asymmetry of both walls of the nasopharyngeal cavity. In early stage of the disease, the change of morphology is always subtle, which can appear as the localized protuberance on the surface of mucosa or only flattening or shallowing of the eustachian tube.

Pharyngeal recess (fossa of Rosenmüller) is the most common site of origin of NPC (Fig. 8.3), followed by the superior posterior wall of nasopharynx (Fig. 8.4). With the development of the tumor, the lesion can invade to other walls of nasopharynx cavity and spread to nasal cavity, parapharyngeal tissue space, and skull base.

A presentation of a soft tissue nodule or mass with intense uptake of ^{18}F-FDG, which locates at the soft tissue of nasopharynx, accompanied with obvious asymmetry of both walls of the nasopharyngeal cavity, is the typical imaging manifestation of NPC on PET/CT.

8.1.7 Differential Diagnosis

NPC should be differentiated from some diseases, such as nasopharyngeal inflammation, lymphoma, and normal physiological intake.

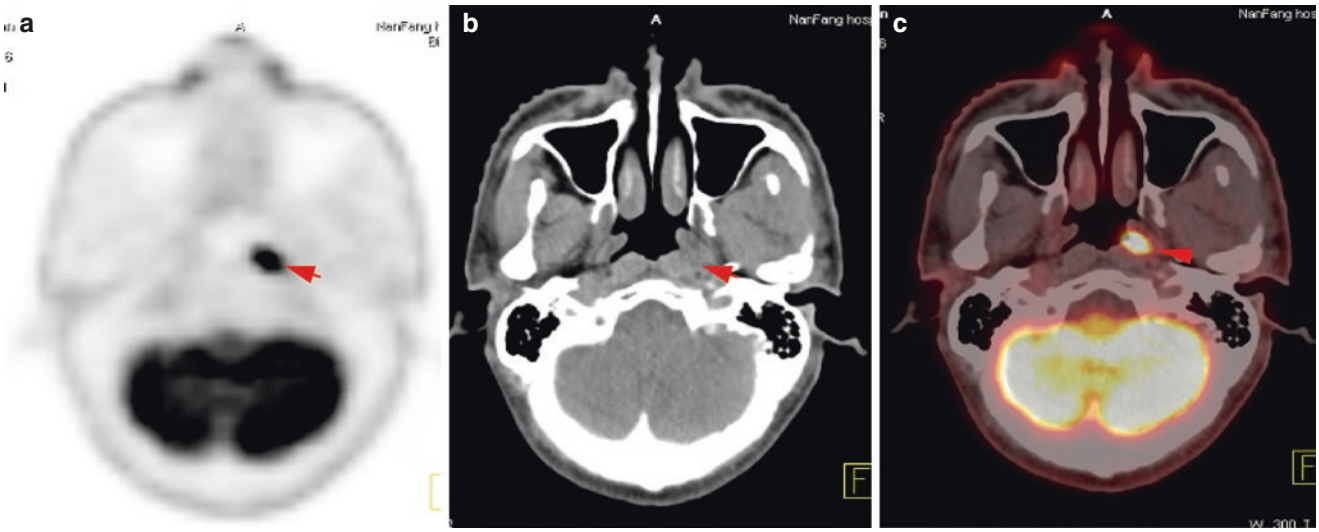

Fig. 8.3 A 31-year-old man complained of enlargement of lymph nodes in the left neck for 2 months. Lymph node metastasis was identified by biopsy. ^{18}F-FDG PET/CT was referred for searching the tumor origin. PET/CT showed a small hypermetabolic lesion (tumor size, 1.4 × 1.3 cm; SUVmax, 15.7) in the left pharyngeal recess (**a**, **c**, arrow), suggesting NPC. Disappearance of left pharyngeal recess was noted on corresponding non-enhanced CT image (**b**, arrow). The lesion was finally diagnosed to be nonkeratinized undifferentiated NPC by histopathology

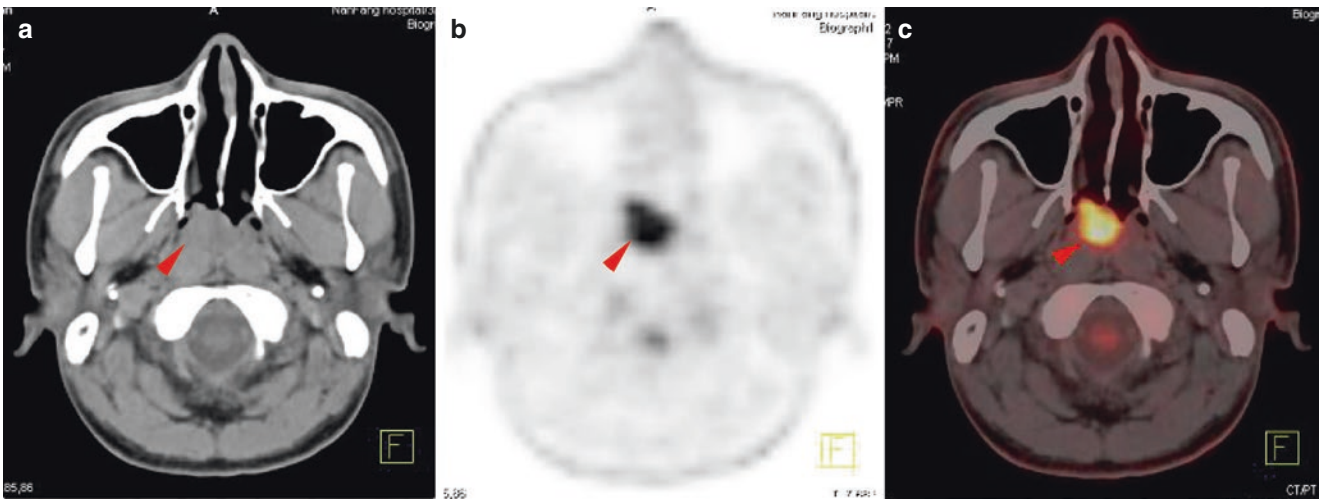

Fig. 8.4 A 52-year-old man suffered from epistaxis and nasal obstruction for about 3 weeks. The diagnosis of nonkeratinized undifferentiated NPC was established by biopsy under the guidance of the nasopharyngoscope. ^{18}F-FDG PET/CT was referred for staging the disease. A soft tissue mass (2.3 × 2.0 cm) in the posterior wall of the nasopharynx was detected by non-enhanced CT (**a**, arrow). Intense uptake of ^{18}F-FDG (SUVmax, 8.3) was observed in the corresponding region on PET (**b**, arrow) and fused PET/CT images (**c**, arrow). No any other metabolic abnormality was found in the other parts of the whole body

8.1.7.1 Nasopharyngeal Inflammation

Acute nasopharyngeal inflammation can also take up ^{18}F-FDG, however, the uptake is often mild. As a result, most of them can be easily distinguished from NPC. However, some lesions can take up high level of ^{18}F-FDG and may be falsely diagnosed as NPC. In these statuses, the shape of the lesions must be carefully analyzed. The infiltration of the inflammatory cells in the mucosa is relatively light and shallow, so the inflammatory lesions often present as hypermetabolic lesions with the shapes liking "thin strip," "willow leaf," or "thin arc" along the mucosa of one or both sides of pharyngeal recess, accompanied with the involvement of the mucosa in posterior wall of nasopharynx. On the contrast, NPC lesions often presented as nodular or mass hypermetabolic lesion [3]. Nevertheless, the inflammatory lesions can also present as nodular or mass lesions in sometimes, which can't be accurately distinguished from NPC. In this situation, biopsy under the guidance of the nasopharyngoscope should be referred for further differentiation.

8.1.7.2 Nasopharyngeal Lymphoma

Incidence of nasopharyngeal lymphoma is high, which is only next to tonsillar lymphoma among the head and neck lymphomas. Diffuse large B-cell lymphoma and natural killer cell/T cell (NK/T cell) are the common pathological types. ^{18}F-FDG uptake in nasopharyngeal lymphoma is very high, similar to that of NPC. However, there are some differences between them, which are useful for differentiation. These differences present as follows:

1. Lymphoma lesion often appears as a large soft tissue mass with expansive, symmetrical involvement to all the walls of nasopharynx (Fig. 8.5). On the other hand, NPC tumor often originates from one side of nasopharyngeal cavity with a localized invasion.
2. In some nasopharyngeal lymphoma, the pharyngeal recess is not affected and keeps intact. However, the pharyngeal recess is always invaded by NPC and disappears.
3. Nasopharyngeal lymphoma often protrudes into nasopharyngeal, nasal, and oropharyngeal cavity, rather than invades into neighboring deep tissues. On the contrary, NPC tumor often invades the deep nasopharynx tissues, parapharyngeal tissue, and the skull base.
4. Whole-body scan can provide more information for differentiation. Lymphoma disease often has a systemic involvement of lymph nodes. On the contrary, positive lymph nodes of NPC are always confined to bilateral necks.

8.1.7.3 Adenoid Hypertrophy

Adenoid is the lymphatic tissue, which is located at the apex of the posterior wall of the nasopharyngeal cavity. It can gradually enlarge since infancy but begins to atrophy after 10 years old. During the teenage period, glandular hyperplasia can occur due to the inflammatory stimulation in some patients. High ^{18}F-FDG uptake is always noted in the hyperplasia adenoids on PET imaging. On CT images, adenoid hypertrophy always presents as a smooth and well-defined soft tissue nodule. The diagnosis is easy to make based on the specific onset age of adenoid hypertrophy**.** Adenoid hypertrophy often occurs in teenage and infancy. On the contrary, in this age section, NPC rarely occurs.

8.1.8 Clinical Application of ^{18}F-FDG PET/CT for NPC

A large number of literatures have confirmed that ^{18}F-FDG PET or PET/CT can be useful in diagnosis, staging, recurrence monitoring, treatment response evaluation, and prognosis prediction for NPC, especially in detection of distant metastasis and recurrent tumor [4–16]. Based on nearly 20 years of clinical practice, the Chinese Association of Nuclear Medicine proposed an expert consensus to develop the recommendations for application of ^{18}F-FDG PET/CT in NPC under the evidence-based background in 2015 (Table 8.5) [17]. The application of ^{18}F-FDG PET/CT in N and M staging for newly diagnosed patients, in diagnosis of recurrent tumor and metastasis, and in detection of unknown origin tumor are highly recommended with grade I and A level of evidence [11]. Although ^{18}F-FDG PET/CT is also clinically useful in assessment of the treatment response, diagnosis of the primary tumor, and delineation of gross tumor volume (GTV), its role is not very outstanding comparing to other image modalities; therefore, it is recommended with the grade of II in these fields [17].

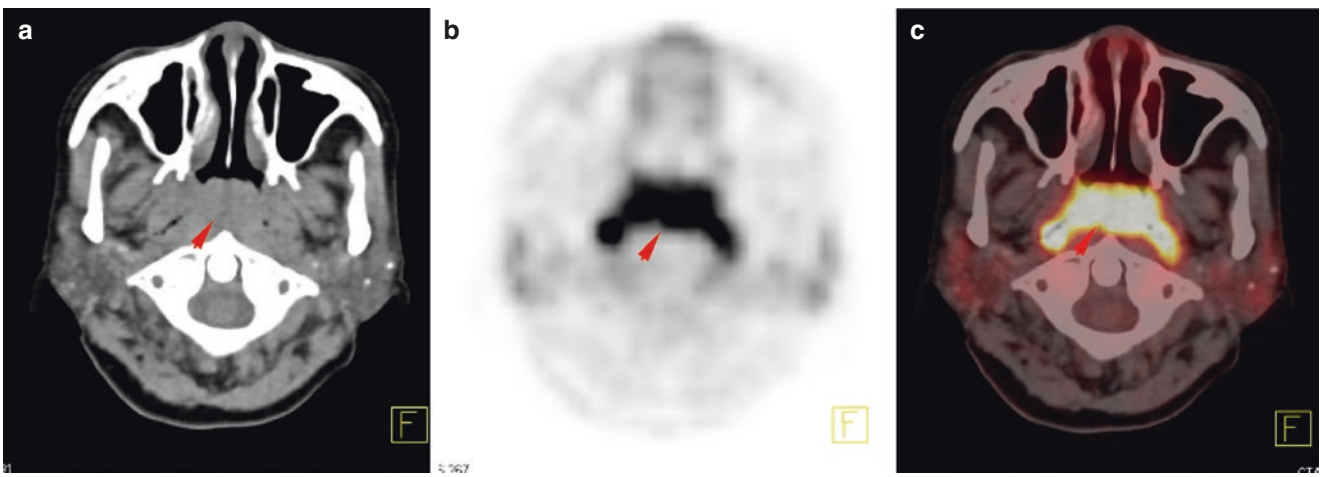

Fig. 8.5 A 61-year-old woman suffered from discontinuous epistaxis and cough for 1 year. ^{18}F-FDG PET/CT was referred for identifying the cause. On CT image, diffusely thickened soft tissue was found in the posterior wall of the nasopharynx (a, arrow) with intact pharyngeal recess was noted. Intense and diffuse uptake of ^{18}F-FDG (SUVmax, 9.4) was observed in the corresponding region on PET (**b**, arrow) and fused PET/CT images(**c**, arrow). The disease was diagnosed to be mucosa-associated lymphoid tissue lymphoma (extranodal marginal zone)

8.1.8.1 Diagnosis and T Staging of ^{18}F-FDG PET/CT for NPC

Diagnosis

Most of NPC lesions have intense uptake of ^{18}F-FDG, which yields a high sensitivity of PET and is helpful to detect occult early-stage NPC. Our study demonstrated that the diagnostic sensitivity and specificity of ^{18}F-FDG PET/CT for NPC were 96.0% and 85.7%, respectively, if intense uptake of ^{18}F-FDG in a nodule or mass in nasopharynx was considered an indicator for NPC [3, 18]. The diagnostic efficiencies reported by other authors are similar [4–6]. In total, ^{18}F-FDG PET/CT imaging has a high diagnostic sensitivity for NPC (94.7–100%), but the specificity is moderate (76.9–98%), which is resulted from the specific uptake of ^{18}F-FDG in some inflammations.

Table 8.5 Clinical applied recommendations of ^{18}F-FDG PET/CT for NPC by Chinese Association of Nuclear Medicine

No.	Recommendation	Grade	Level of evidence
1	Evaluation of distant metastasis (M staging)	I	A
2	Diagnosis of recurrent tumor and metastasis	I	A
3	Detection of unknown origin tumor	I	A
4	Evaluation of the regional lymph node metastasis (N staging)	I	A
5	Assessment of the treatment response	II	A
6	Diagnosis of the primary tumor	II	A
7	Delineation of gross tumor volume (GTV)	II	B

T Staging

Determining gross tumor volume (GTV) accurately is crucial for the radiotherapy, which help to achieve a good therapeutic effect and minimize the side effects of radiation to neighboring normal tissue. Determining GTV depends on the imaging modality to delineate the invasion of NPC (T staging).

For T stage of NPC, ^{18}F-FDG PET/CT is useful. The uptake of ^{18}F-FDG in NPC lesion is intense, while that in the surrounding nasopharynx tissue is minimal, which can yield a high tumor/background ratio for NPC lesion. As a result, the boundary of NPC can be easily defined on PET (Fig. 8.6). When PET images are co-registered on CT, the tumor and its margin can be accurately recognized and delineated on PET/CT images. Therefore, ^{18}F-FDG PET/CT is more accurate than CT in T staging of NPC. However, ^{18}F-FDG PET/CT is still inferior to MRI in T staging of NPC. MRI has perfect soft tissue resolution, which can provide detailed information of lesion and show a very clear margin of tumor tissue. Up to now, MRI still serves as a first line and the most important imaging modality for T staging of NPC although it has the deficiency in defining the bone structure. Compared to MRI, ^{18}F-FDG PET/CT has a lower soft tissue resolution. In addition, ^{18}F-FDG PET/CT has not enough sensitivity to detect the invasion of the tumor to skull base, and intracanial or intraorbital space due to high uptake of ^{18}F-FDG in normal tissue of brain and in ocular muscles. In these situations, PET/CT is easy to understage the disease in T4-staged NPC patients [7, 8]. Nevertheless, in some patients, PET/CT can still play a complementary role for T staging when MRI is difficult to identify the lesion boundaries.

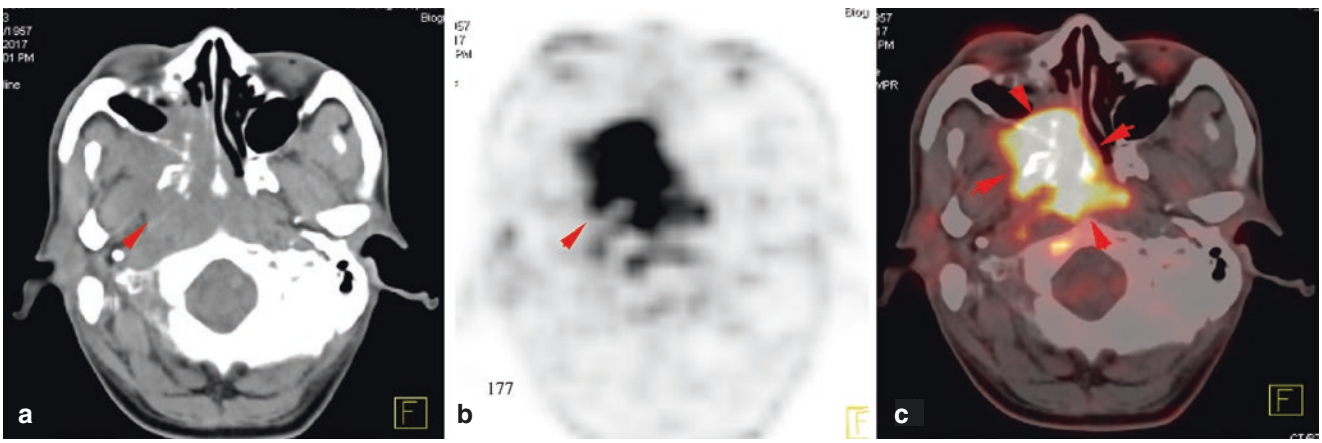

Fig. 8.6 Nasopharyngeal carcinoma invaded the surrounding tissue. CT detected a soft tissue mass in the nasopharynx, which grew into the nasal cavity and invaded the nasal septum, the right pterygus, the medial and lateral wall of the maxillary sinus, the right infratemporal fossa, the lateral and medial pterygoid muscle, and the right pterygopalatine fossa with a unclear margin (**a**, arrow). Increased uptake of ^{18}F-FDG in the lesion (SUVmax, 19.2) was found on corresponding PET (**b**, arrow). Fused PET/CT image revealed a clearer invaded margin of the tumor than CT, which can distinguished the tumor from the neighboring chronic inflammation. The disease was diagnosed to be nonkeratinized undifferentiated NPC

Understading the common invasion routes of NPC and its image manifestations on PET/CT imaging is helpful for making an accurate diagnosis for T staging. The common invasive routes of NPC include:

1. Parapharyngeal space invasion. The parapharyngeal space is the most common invasive site of NPC. Approximately 80% NPC lesion originates from one side of the pharyngeal recess and invades to the adjacent parapharyngeal space and/or infratemporal fossa. The tumor can also invade the neighboring medical and lateral pterygoid muscles, which will cause dehisce difficulty. When the tumor progresses, it can grow into the anterior and posterior area of styloid process and invades to the posterior group of cranial nerves.
2. Lateral wall invasion. The lateral wall of nasopharyngeal cavity is also a common involved structure, and the invasion of the tumor can often obstruct the opening of eustachian tube, which will result in tinnitus, stuffiness, and inflammation of suffered ear, or hearing loss.
3. Nasal cavity invasion. The tumor can expand forward into the nasal cavity, which will cause the nasal obstruction, nasal stress, or dyspnea. The tumor can also infiltrate the adjacent pterygoid process and/or involve the maxillary sinus, sphenoid sinus, and pterygopalatine fossa. As a special situation, the tumor can extend into the lamina cribosa and anterior cranial fossa. When the tumor invades the pterygopalatine fossa, superior and inferior spehenoidal fissure, orbital floor, and intraorbital space, it will bring about eyeball protrusion, visual impairment, and some nerve symptoms due to the damage of the oculomotor nerve, trigeminal nerve, trochlear nerve, and abducens nerve.
4. Skull base and intracranial invasion. NPC is easy to invade the skull base and intracranial space (Fig. 8.7). The commonly involved skull base includes occipital slope, basal part of occipital bone, basal part of sphenoid bone, petrous apex, pterygoid, alae temporalis, ossis sphenoidalis, sella, etc. When the bones of skull base are

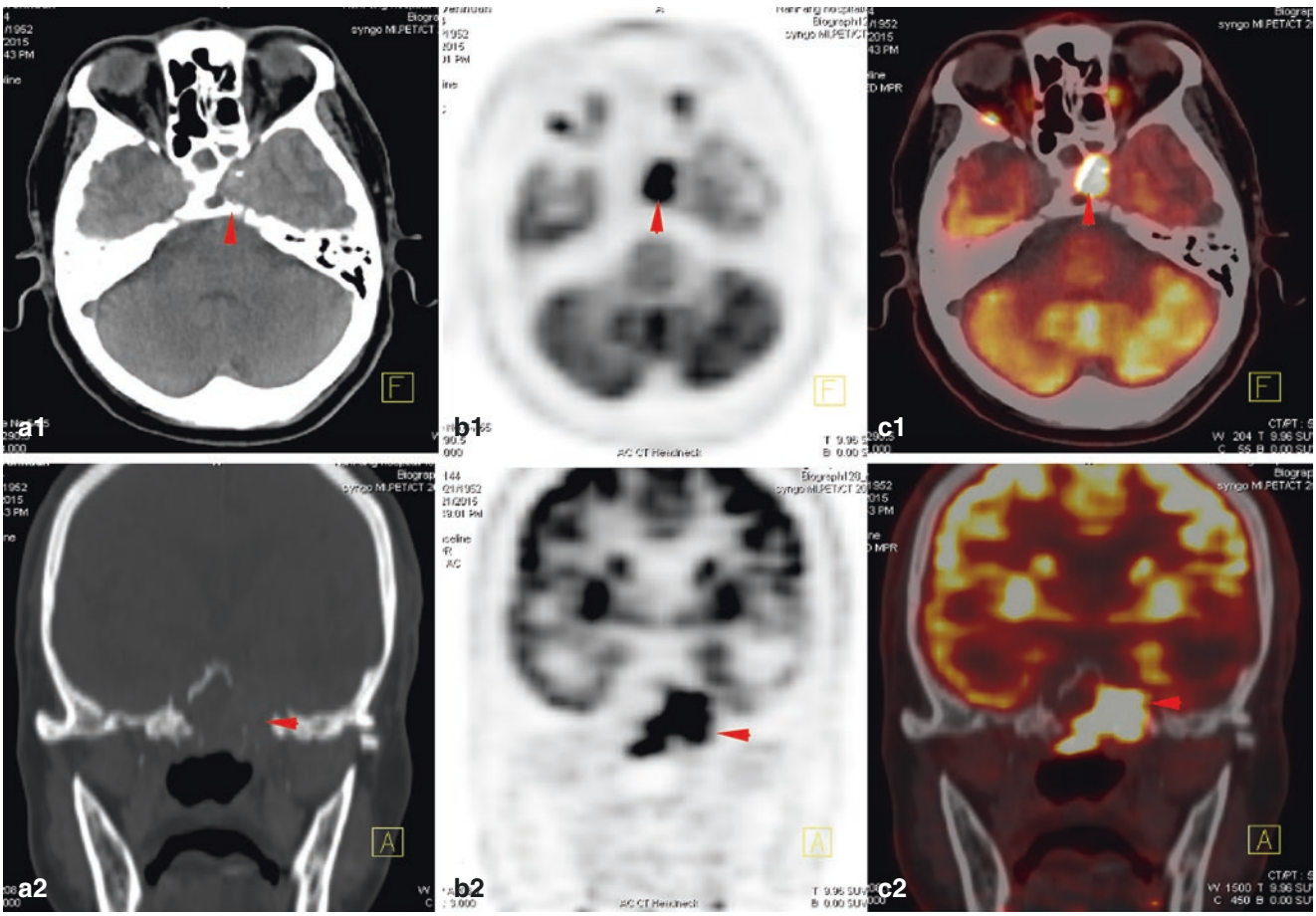

Fig. 8.7 Nasopharyngeal carcinoma invaded skull base and cavernous sinus. A soft tissue mass was detected in the top wall of the nasopharynx, skull base, and left cavernous sinus, accompanied with bone destruction of skull base bones by CT (**a1**, **a2**, arrow). Intense uptake of ^{18}F-FDG (SUVmax, 20.3) was noted in the lesion (**b1**, **b2**, arrow) on corresponding PET. ^{18}F-FDG PET/CT showed that tumor originated from the top wall of the nasopharynx, infiltrated into the left cavernous sinus along left rupture hole, and destructed the skull base bones (**c1**, **c2**, arrow). The infiltration path was visualized clearly on fused PET/CT image (**c2**, arrow)

involved, it will result in persistent, fixed headaches. The cavernous sinus is the most involved intracranial structure. The tumor can infiltrate into the fossae cranial via the following routes: (1) invades into frontal lobes by destroying the anterior cranial fossa, (2) invades into the cavernous sinus, hypophyseal fossa, or middle cranial fossa through the ruptured hole, (3) invades into hypophyseal fossa and bilateral cavernous sinus through the sphenoid sinus and sella, and (4) invades into the posterior cranial fossa through the occipital slope and large occipital hole.

5. The involvement of cranial nerve often occurs when NPC invades into intracranial spaces. NPC tumor can infiltrate the optic chiasma and causes binocular visual abnormalities through the hypophyseal fossa. It also can invade the zone of cavernous sinus through a ruptured hole and infiltrates II–VI cranial nerves, which locate in the zone of the cavernous sinus. Abnormal sensation will appear when the maxillary and the mandibular nerve, second and third branch of the trigeminal nerve, are infiltrated. This phenomenon can present if the round and the oval hole are invaded by tumor. The tumor can also invade the jugular foramen and the glossopharyngeal, vagus, accessory, and hypoglossal nerves nearby and leads to the following symptoms, such as the voice hoarseness, muscle atrophy, dysphagia, tongue muscle atrophy, tongue deflection, etc.
6. Posterior nasopharyngeal invasion. NPC can invade into the posterior nasopharyngeal space and involves the occipital slope, the basilar part of the occipital bone, the cervical spine, the cervical spinal cord, etc.
7. Oropharyngeal cavity invasion. NPC tumor can grow downward and invade the soft palate, tonsil, tongue, and even the epiglottis and larynx, which can cause the symptoms of dysphagia, sore throat, trismus, etc.

N Staging

The lymphatic networks of the nasopharyngeal cavity are extremely rich and intersect each other between both sides of nasopharynx, which drain the lymph liquid into the retropharyngeal lymph node. The lymph liquid then passes by the carotid sheath and flows into the rear part of the deep cervical lymph node. The lymph liquid of nasopharynx can also flow directly into the deep cervical lymph node or parapharyngeal lymph node chain.

The cells of NPC are prone to spread to cervical lymph nodes. The cervical lymph node metastasis occurs in approximately 76% of NPC patients. It is also the first presentation of disease in more than half of patients.

The lymph node spreading of NPC shows some regular patterns as follows: (1) first of all, the lymph node metastasis often spreads orderly downward along the lymphatic chain, and the quantity of them also decreases gradually. The most involved ones are the lymph nodes in level II, followed by those in retropharyngeal space and next by those in level III, IV, and V. Lymph node in level I B group is seldom involved, and nearly none occurs in level Ia and VI group. The retropharyngeal space is the first lymph node spreading station of NPC, where most of the lymph node metastases firstly arise. However, some lymph node metastases can appear firstly in level II group, but not retropharyngeal space. (2) Secondly, only a few salutatory metastases (4.6–6.5%) were presented in the patients with NPC. (3) Thirdly, bilateral cervical lymph node metastases occur in approximately 1/3 NPCs [9, 10].

It is very important to identify the location of regional lymph node metastasis and N stage of NPC, which is crucial for the designing the treatment protocol and predicting the prognosis of the patient. The diagnosis of regional lymph node metastasis is mainly depended on the findings of imaging modalities. MRI is the traditional and most commonly used imaging modality at present. MRI is superior to CT in the diagnosis of regional lymph node metastasis, especially for retropharyngeal lymph node metastasis. The positive lymph node diagnosed by MRI is proposed as follows: (1) the smallest diameter of the lymph node on the cross-sectional image ≥10 mm; (2) the lymph node with central necrosis or ring enhancement, (3) more than three lymph nodes in a same high-risk area with the smallest axial diameter of largest one ≥8 mm on the cross-sectional image, (4) the lymph node with extracapsular spread, and (5) the smallest diameter of retropharyngeal lymph node ≥5 mm.

The diagnosis of lymph node metastasis on ^{18}F-FDG PET/CT is established mainly based on the uptake intensity of ^{18}F-FDG. The enlarged lymph nodes with intense uptake of ^{18}F-FDG are often considered positive (Figs. 8.8 and 8.9), while those lesions with no or slight uptake of ^{18}F-FDG uptake are often considered negative. However, the size, distribution, and morphology of lymph nodes are also combined for analysis when the diagnosis is made. ^{18}F-FDG PET/CT is more sensitive for detection of lymph node metastases ≤1.0 cm than CT and MRI. It is also useful to differentiate the lymph node metastases from the inflammatory ones for those lesions ≥1.0 cm in diameter. In totally, the sensitivity and specificity of ^{18}F-FDG PET/CT in diagnosing cervical lymph node metastasis are 91.8% and 82.2%, respectively.

Compared to MRI, ^{18}F-FDG PET/CT is superior to detect occult cervical lymph node metastasis but is inferior to detect retropharyngeal lymph node metastasis [11–13].

For detection of retropharyngeal lymph node metastasis, the study of Su Y et al. showed that the positive detection of CT, MRI, and ^{18}F-FDG PET/CT were 39.6%, 45.3%, and 20.8%, respectively, in 53 patients when the smallest diameter of retropharyngeal lymph node ≥4 mm was considered positive one. The detections of CT and MRI were not significantly different, but both were higher than ^{18}F-FDG PET/CT

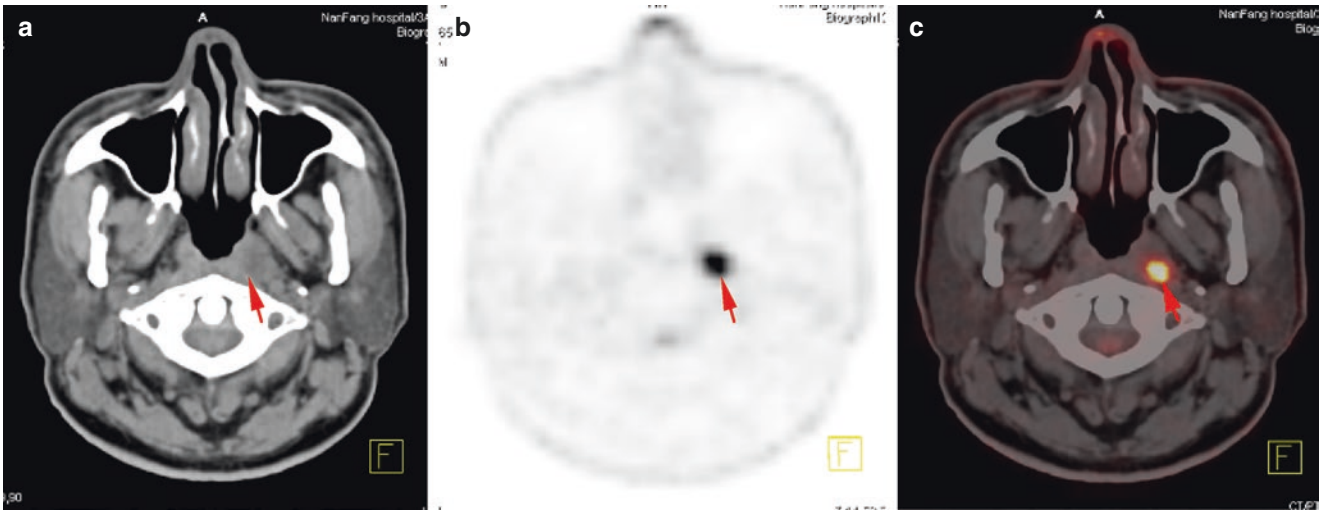

Fig. 8.8 Lymph node metastasis of nonkeratinized undifferentiated NPC in retropharyngeal space. Soft tissue incrassation was found in left retropharyngeal space with an unclear margin on non-enhanced CT (**a**, arrow). Focal uptake of ^{18}F-FDG (SUVmax, 25.1) was observed in corresponding region on PET image (**b**, arrow) and fused PET/CT (**c**, arrow). A clearer margin of the lesion was seen on PET/CT (**c**, arrow) compared to CT

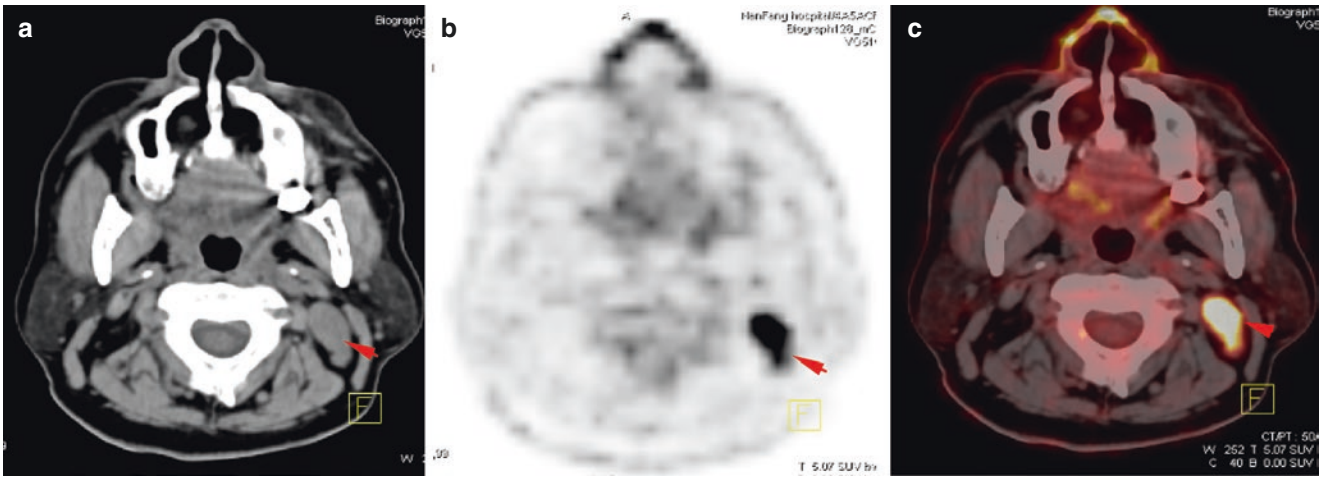

Fig. 8.9 Lymph node metastasis of nonkeratinized undifferentiated NPC in the left neck. Enlarged lymph node was found in left cervical II level on non-enhanced CT (**a**, arrow). Focal uptake of ^{18}F-FDG (SUVmax, 25.1) was observed in corresponding region on PET image (**b**, arrow) and fused PET/CT (**c**, arrow)

($P < 0.01$) [19]. The results of Ng SH et al. confirmed that the sensitivity of ^{18}F-FDG PET/CT for detection of retropharyngeal lymph node metastasis was inferior to that of MRI ($P < 0.01$) [11].

For detection of cervical lymph node metastasis, many studies have been done to discover the role of ^{18}F-FDG PET/CT. Hu WH et al. compared the diagnosis of ^{18}F-FDG PET/CT and MRI for cervical N staging in 105 patients with NPC. They found that the diagnosis of ^{18}F-FDG PET/CT was not consistent with that of MRI in 35 patients. Of 30 positive lymph nodes on PET/CT but negative on MRI, 25 were identified to be lymph node metastasis by the clinical follow-up. On the contrary, of 37 negative lymph nodes on PET/CT but positive on MRI, 21 were finally proved to be benign lymph nodes [12]. The results of Lin XP et al. demonstrated that PET/CT was more sensitive than MRI in the detection of cervical lymph node metastasis. In 68 patients with NPC, PET/CT detected 138 positive lymph nodes less than 1.0 cm in diameter; however, MRI had a positive detection in only 28.0% of them. Fine needle biopsy was performed to confirm the findings of PET/CT imaging. Of the ten patients, 87.5% (16/18) of positive lymph nodes on PET/CT were finally identified to be lymph node metastases by histopathological examination [13].

Shen G performed a meta-analysis to assess the diagnostic performance of positron emission tomography (PET) or

PET/CT for detecting lymph node metastases in patients with NPC. In total, 18 articles were included. On a per-patient basis, the overall pooled sensitivity and specificity of PET or PET/CT in N and M staging of NPC were 0.89 [95% confidence interval (CI), 0.86–0.91] and 0.96 (95% CI, 0.95–0.96), respectively. The further analysis showed that AUC and Q* index were 0.9734 and 0.9255. This meta-analysis showed that PET or PET/CT has excellent diagnostic performance for detecting lymph node and distant metastases in patients with NPC [15].

Although ^{18}F-FDG PET/CT helps to detect small lymph node metastases less than 1.0 cm in diameter, its positive detection is also limited to the finite resolution of PET/CT. There is a certain relationship between the positive detection of PET/CT and the size of lymph node metastasis. Peng H et al. investigated the capacity of PET/CT for detecting small lymph node metastases less than 1.0 cm in diameter. Their study indicated that the diagnostic sensitivity of ^{18}F-FDG PET/CT increased from 3.5%, 8.0%, 31.3%, and 60.0% to 83.9% when the diameters of the lymph node metastasis increased from 5–6 mm, 6–7 mm, 7–8 mm, and 8–9 mm to 9–10 mm ($P < 0.001$). PET/CT changed the N staging in 28.7% patients [14].

Acute inflammatory is a main factor which influences the diagnostic specificity of ^{18}F-FDG PET/CT because some acute inflammatory lymph nodes can also have increased uptake of ^{18}F-FDG. At some times, it is actually difficult to differentiate the inflammatory lymph node from lymph node metastasis. For those patients with NPC accompanied by acute inflammation, such as acute tonsillitis, the diagnosis should be cautiously make for the cervical lymph node with ^{18}F-FDG uptake, especially for the lesion with slightly uptake.

^{18}F-FDG PET/CT for Detection of Distant Metastasis

IMRT is now widely used in the treatment of NPC. The local control rate of NPC by IMRT is larger than 80%. Distant metastasis has become the main cause for the failure of treatment. Distant metastasis occurs in 10–15% of newly diagnosed NPC and in 15–30% of relapsed patients. Our research demonstrated that the distant metastasis was occurred in 14% (37/264) of NPC patients. The common disseminated organs were the bone (22/37), followed by liver (15/37), lung (12/37), and mediastinal lymph node (12/37). Distant metastasis was rarely found in other organs (4/37). Positive EB virus (OR = 13.1, 95% CI: 1.61, 106.80), tumor T stage (OR = 2.16, 95% CI: 1.10, 4.24), and N stage (OR = 3.05, 95% CI: 1.41, 6.63) were closely related to the incidence of distant metastasis. EBV-DNA ≥9000 copies/mL, N2/N3, and T3/T4 are three risk factors of M staging. For those patients with above three risk factors or two high-risk factors, whole-body ^{18}F-FDG PET/CT is highly recommended for detection of distant metastasis [16].

Detection of distant metastasis sensitively and comprehensively is very important for making a treatment plan for metastatic NPC. Imaging modalities are important instruments for M staging of NPC. Conventional M staging work-up (CWU) includes chest radiography or CT, abdominal ultrasonography, and skeletal scintigraphy. Compared to CWU, ^{18}F-FDG PET/CT has two advantages in detecting the distant metastases. First of all, PET/CT is a positive imaging technology for the tumor, which can yield a high detective sensitivity because the malignant tumor often presents as a "hot point" with a low background on PET. Therefore, PET/CT can detect some occult lesions which often missed by CWU [4]. Secondly, it is convenient to perform a whole-body scan for the patients (Figs. 8.10 and 8.11), which can provide a whole picture of systemic tumor load. Yen RF et al. reported that the sensitivity, specificity, and accuracy of ^{18}F-FDG PET in the diagnosis of recurrence and metastasis of NPC and second primary cancers were 92%, 90%, and 92%, respectively [20]. Yen TC et al. reported the diagnostic sensitivity and specificity of ^{18}F-FDG PET were 100% and 86.9%, respectively. They found ^{18}F-FDG PET detected 26 "unsuspected" metastatic tumors in 18 patients [21]. In our study, the sensitivity and specificity of ^{18}F-FDG PET for detection of distant metastasis were 91.9% and 97.8%, respectively [18]. A meta-analysis of eight representative articles published from 1996 to 2011 [22] showed that the overall sensitivity and specificity of ^{18}F-FDG PET/CT for the detection of distant metastasis of NPC were 83% (77.0%–88.0%) and 97% (95.0%–98.0%), respectively. In addition, ^{18}F-FDG PET/CT imaging is also helpful in detecting second primary cancers.

Due to the advantage of ^{18}F-FDG PET/CT in detection of metastatic tumor, the Chinese Expert Consensus on Recurrent NPC and Metastasis, which was published in Chinese Journal of radiation oncology in 2018, recommended the utility of PET-CT for M staging on the patients who are highly suspected to have recurrent and metastatic NPC [23].

^{18}F-FDG PET/CT for Detection of Residual and Recurrent Tumor

Although IMRT and chemotherapy have made a great progress in the treatment of NPC, tumor recurrence still occurs in 10–15% of patients. Approximately 50% and 80–90% of recurrent tumors take place within 2 years and 5 years after successful treatment. After 5 years later, few tumors recur. Therefore, the time interval of 2 years after radical treatment is often considered a high-risk period of tumor relapses, while 2–5 years is a middle-risk period and 5 years later a low-risk period.

Imaging modalities are the important diagnostic techniques for detection of locally recurrent NPC. CT is the most commonly used imaging modality. However, CT is inferior to MRI in differentiating the recurrent tumor from inflammation and in visualizing the skull or skull base involvement. Nevertheless, MRI still has limitation in distinguishing the

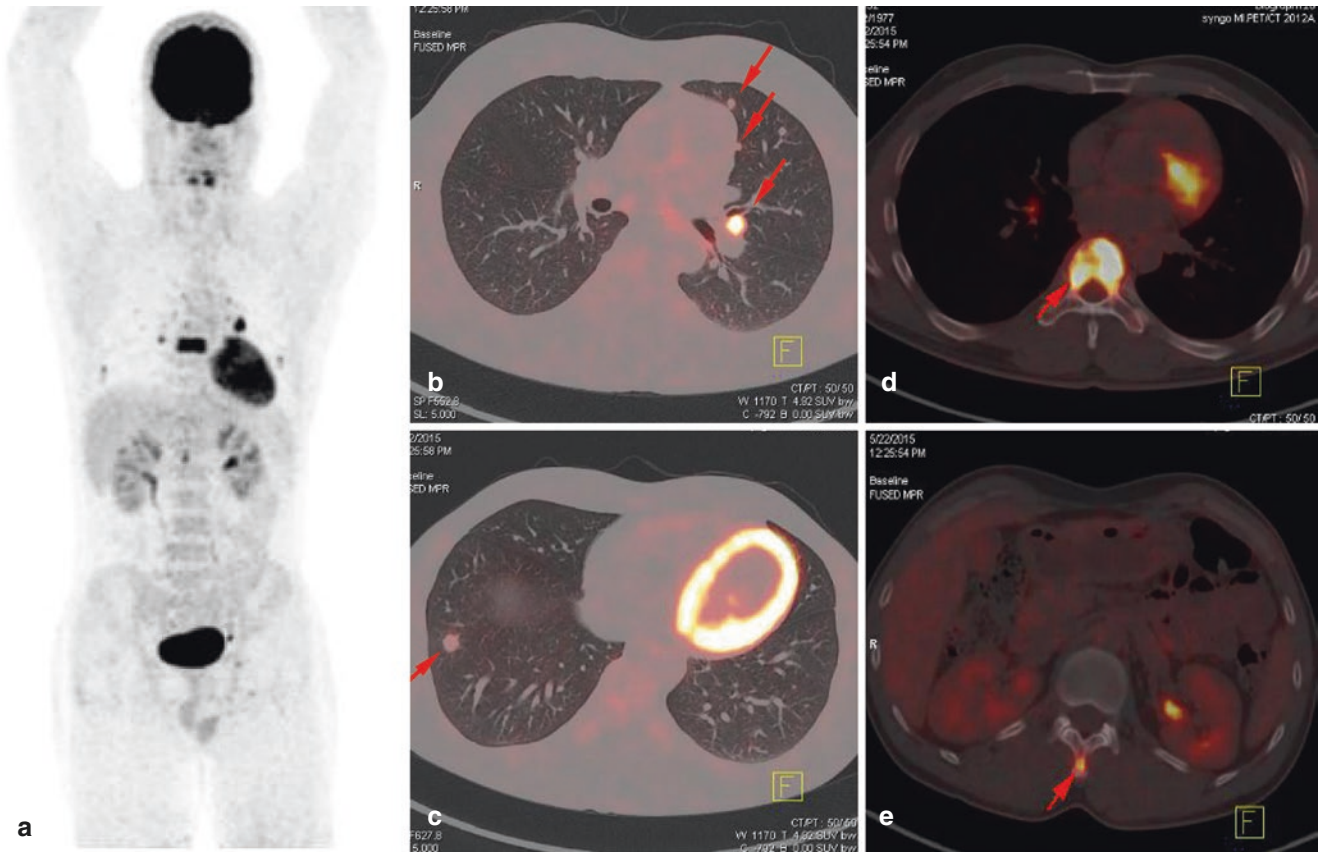

Fig. 8.10 ^{18}F-FDG PET/CT of metastatic NPC. A 38-year-old patient was highly suspected to have distant metastases at 9 months after treatment. ^{18}F-FDG PET/CT showed distant metastases (**a**) in both lungs (**b**, **c**, arrow), hilus of left lung (**a**, arrow), and bones (7th thoracic vertebrae and 12th thoracic spinous process) (**d**, **e**, arrow)

recurrent tumor from hypertrophic scar tissue after radiotherapy. In addition, it is also difficult to discriminate bone involvement from chronic osteomyelitis or osteonecrosis. The clinical value of ^{18}F-FDG PET/CT in the diagnosis of recurrent NPC has been affirmed (Fig. 8.12). Yen RF et al. reported that the sensitivity, specificity, and accuracy of ^{18}F-FDG PET in the diagnosis of recurrence and metastasis of NPC and second primary cancers were 92%, 90%, and 92%, respectively [20]. NG SH performed ^{18}F-FDG PET/CT study in the patients with suspected recurrent NPC on MRI and found that ^{18}F-FDG PET/CT had a diagnostic sensitivity and specificity of 91.6% and 76.0%, respectively [24]. The systematic meta-analysis concerning 17 studies was performed by Wei J et al. Their study found that the overall sensitivity and specificity of ^{18}F-FDG PET/CT for diagnosing recurrent NPC were 90% and 93%, respectively, which were higher than those (77% and 76%) for MRI (P = 0.096 and P = 0.033) [19]. Therefore, the Chinese expert consensus on recurrent NPC and metastasis, which was published in Chinese Journal of radiation oncology in 2018, recommended the utility of PET-CT for detection of recurrent tumor.

It is very important to set up a suitable time window to use PET/CT for detecting residual tumor. The study based on the meta-analysis of 51 articles with 2335 head and neck tumors patients including NPC revealed that the sensitivity and specificity of PET/CT for diagnosing residual tumors were 73.6% (64.8–81.2%) and specificity (85.2–88.6% 91.4%) within 12 weeks after the end of treatment. On the contrary, the sensitivity and specificity reached 91.9% (82.7–97.1%) and 86.9% (82.8–90.4%) after 12 weeks later [25]. Therefore, 3 months after the treatment is the most appropriate time for referring PET/CT scan, which help to avoid the potential false positive or negative due to the treatment response.

Others

^{18}F-FDG PET/CT is also useful for predicting the prognosis, evaluation of treatment response, determining the gross tumor volume (GTV), and guiding the radiotherapy. Decrease of ^{18}F-FDG uptake in lesion is a good indicator for good response. However, because radiation therapy is the first line of treatment modality and most NPC has a good response, ^{18}F-FDG PET/CT is little used for evaluating the response of radiation therapy in the medium term. Meanwhile, because ^{18}F-FDG PET/CT is inferior to MRI in T staging, it is only used as a supplement of MRI in determining the GTV.

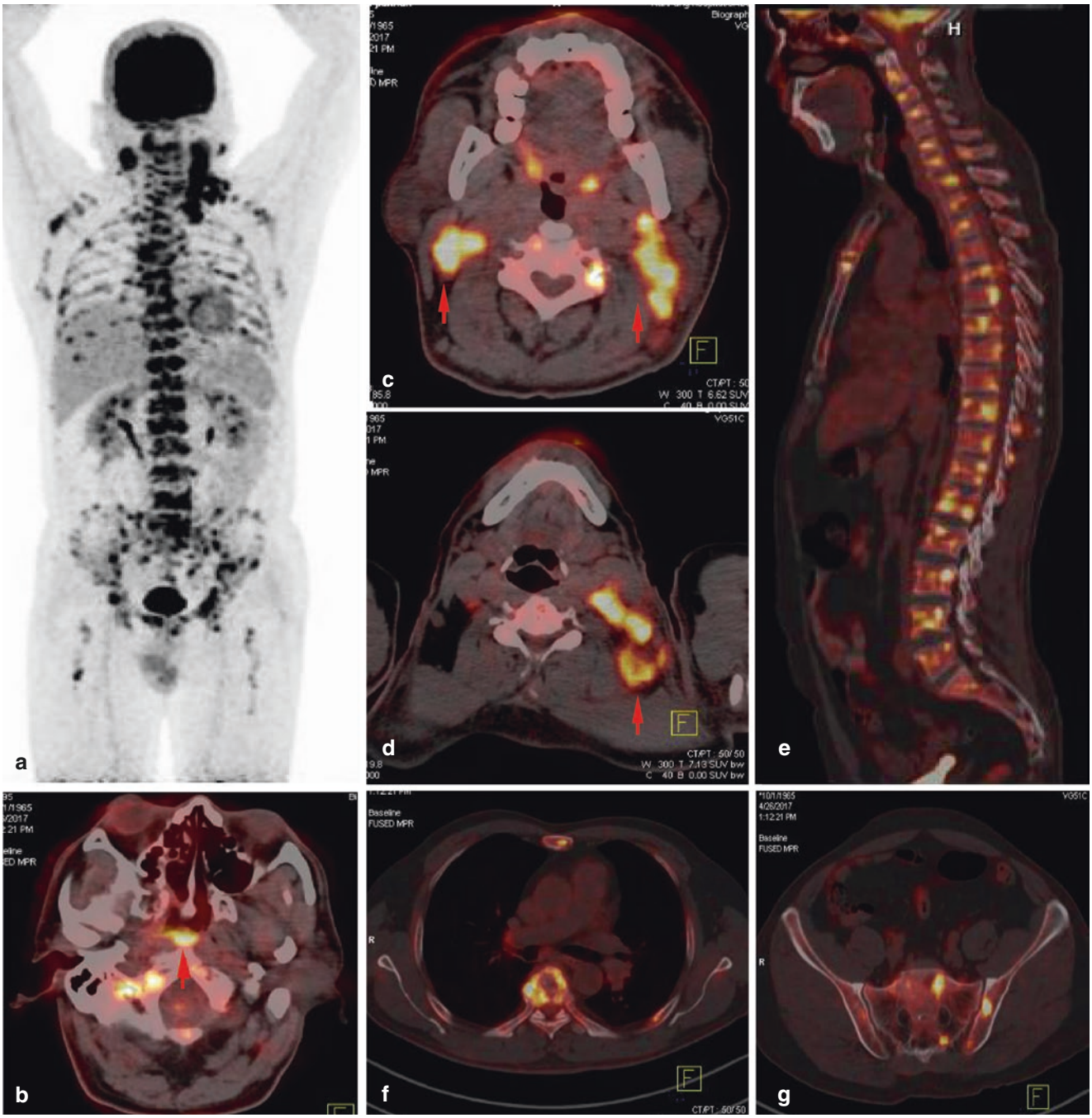

Fig. 8.11 ^{18}F-FDG PET/CT of widespread metastatic NPC (**a**). ^{18}F-FDG PET/CT showed an NPC tumor in posterior nasopharyngeal wall (**b**, arrow), bilateral cervical lymph node metastases (**c**, **d**, arrow), and extensive bone metastases (**e**–**g**)

8.2 Other Head and Neck Cancers

This chapter is mainly focused on the advances in the imaging work-up of head and neck cancer patients. CT and MRI are the cornerstones of the diagnostic work-up and have been used for decades. However, these morphologic imaging approaches have distinct limitations when they are used for accurately identifying viable tumor tissues within distorted structures, for identifying small tumor deposits, and for characterizing secondary enlarged inflammatory lymph nodes or second primary malignancies in the posttreatment setting. Functional imaging modality ^{18}F-FDG PET/CT scanning has been increasingly used for detecting and staging head and neck cancers, providing more accurate diagnosis and improved patient management. ^{18}F-FDG PET/CT scanning can provide both structural and metabolic information, where

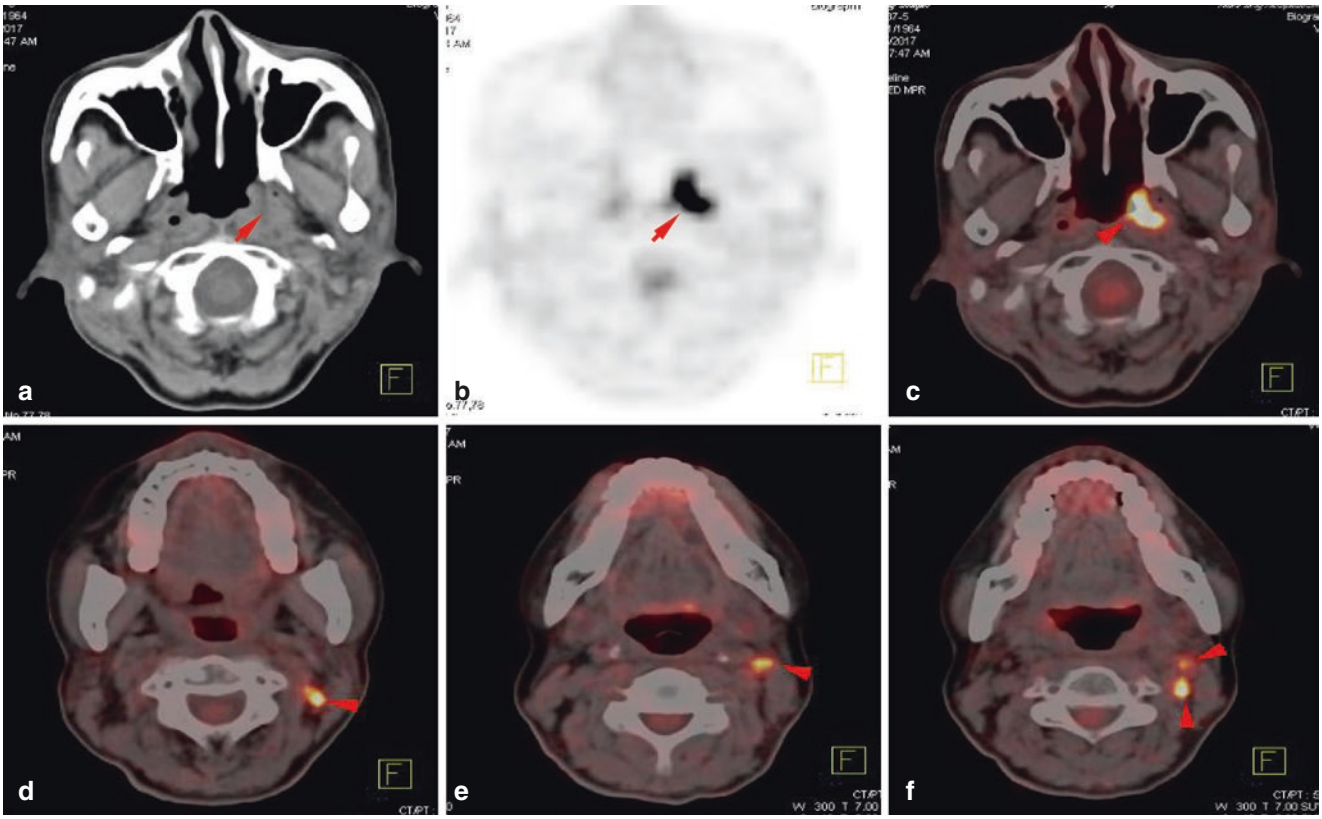

Fig. 8.12 ^{18}F-FDG PET/CT images of recurrent NPC. A 52-year-old man was suspected to have recurrent NPC. ^{18}F-FDG PET/CT demonstrated that hypermetabolic lesion in the left pharyngeal recess of the nasopharynx (SUVmax, 16.2) (**a**–**c**, arrows) indicating the recurrent tumor. Meanwhile, multiple lymph node metastases with intense uptake of ^{18}F-FDG in the left neck were also detected by PET/CT (**d**–**f**, arrows). Recurrent nonkeratinized undifferentiated NPC was identified by biopsy

the metabolic information relies on the detection of glucose metabolism in cancer cells and is complementary to the structural features provided by CT. With further application of newer parameters as well as technical improvements, the role of ^{18}F-FDG PET/CT in the management of patients with head and neck cancers will become even more important in the foreseeable future. A detailed introduction and discussion of anatomy of head and neck is beyond the scope of the present review; we therefore focus on the value of ^{18}F-FDG PET/CT imaging in detecting and staging of head and neck cancers and also discuss the potential pitfalls of ^{18}F-FDG PET/CT imaging in these conditions.

8.2.1 Epidemiology of Head and Neck Cancers

Head and neck cancers are usually divided into two major groups: the largest group, namely, the head and neck squamous cell carcinoma (HNSCC), arises from the mucosal membranes of the upper aerodigestive tract and accounts for more than 90% of all head and neck neoplasms, and the second group is the "glandular neoplasms," which mainly arise from the thyroid but also from the salivary glands. Besides these two cancer types, skin cancers are generally considered as a separate entity and so are the non-melanoma skin cancers of the head and neck, which mainly include squamous cell carcinoma (SCC) and basal cell carcinoma. Other infrequent head and neck malignancies include lymphoma, soft tissue sarcoma, bone sarcoma, and neuroectodermal tissue tumors (olfactory neuroblastoma, paraganglioma, malignant melanoma, and neuroendocrine carcinoma). In the USA, the estimated new malignant cases for tongue, mouth, pharynx, and other oral cavity in 2017 were 49,670 (35,720 cases for men and 13,950 for women), accounting for 3% of all estimated new cancer cases in 2017 [26]. When we compare the two largest groups (i.e., HNSCC and thyroid cancers), we could find predominant gender differences in the incidence of these two malignancies. While the incidence of laryngeal SCC has a male-to-female ratio of 6:1, the corresponding ratio for thyroid cancer is 1:3.

Although the most common cancer type of paranasal sinuses is SCC, several other cancer types can arise from paranasal sinuses, including melanoma, sarcoma, inverting papilloma, and midline granulomas. SCC is generally believed to be the most frequent malignant histologic type

and accounts for more than half of all the malignancies. Occupational factors (such as occupational exposures to nickel, chromium, Thorotrast, and radium) are associated with an increased risk of SCC. The prognosis of this cohort is overall poor (5-year survival rate is reported to be 40%), worsened by aggressive histologic findings and involvement of critical anatomical areas. Inverted papilloma (IP) is an uncommon, benign epithelial tumor of the sinonasal cavity and accounts for 0.5–4% of all nasal tumors [27]. It is characterized by local aggressiveness with propensity toward local invasion and with a high rate of recurrence and association with SCC. Medical imaging plays a vital role in planning treatment approaches, in selecting tumors which are amenable to purely endoscopic resection, in staging advanced malignant tumors, and also in assessing tumor invasion into the crucial anatomic areas.

Laryngeal cancer is the second most common respiratory cancer secondary to lung cancer in the USA. The majority of laryngeal tumors arise from the surface epithelium, and therefore most laryngeal tumors are SCCs. It has been reported that laryngeal cancers occur more commonly in men than in women (5.8 cases per 100,000 vs. 1.2 per 100,000, respectively). In 2017, an estimated 13,360 patients with laryngeal cancers will be diagnosed with approximately 3660 of them dying from the disease [26]. Unfortunately, approximately 60% of laryngeal cancer patients present with advanced (stage III or IV) diseases at the time of diagnosis. Several risk factors, such as use of tobacco and alcohol consumption, have been implicated in the pathogenesis and development of laryngeal cancers. Although the human papillomavirus (HPV) has been proven to be a driver of the majority of cancers of the oropharynx, the role of HPV in the initiation and development of laryngeal cancer remain elusive. In addition, while dietary factors like salted meat and total fat seem to be associated with an elevated risk of laryngeal cancer, intake of raw leafy vegetables and fresh legumes may have a preventative and protective effect.

Thyroid cancer is the most common endocrine malignancy and accounts for ~1% of all malignancies and causes around 0.5% of all cancer deaths. Thyroid cancer is the most commonly diagnosed cancer before the age of 30 among women in China, and dramatic rise in thyroid cancer incidence was also found in other countries, especially in South Korea. Increased use of new screening technologies and routine physical examination may lead to increased detection and diagnosis of thyroid cancers, but we are still unable to rule out a real increase in the incidence. While dietary, environmental, and genetic factors can contribute to initiation and development of thyroid cancer, there is a definite and linear dose-response relationship between radiation exposure and development of thyroid cancers. Medullary thyroid cancer (MTC) arises from parafollicular C cells and tends to be multifocal. Seventy-five percent of MTC cases are in the sporadic form, and the remaining 25% of cases have a hereditary form. MEN IIa is a hereditary syndrome occurs in the second or third decade. MEN IIa is characterized by MTC, pheochromocytoma, parathyroid hyperplasia (or adenomas), and occasionally cutaneous lichen amyloidosis. MEN IIb is much more aggressive and occurs in early childhood. Although the incidence of anaplastic thyroid cancer (ATC) is very rare (2% of all thyroid malignancies), it is highly aggressive and is a clinical challenge, causing the majority of deaths from thyroid cancers.

8.2.2 ^{18}F-FDG PET/CT in the Diagnosis of Head and Neck Tumor

The role of ^{18}F-FDG PET/CT in the management of head and neck cancers can be summarized as follows: ^{18}F-FDG PET/CT is the modality of choice for accurate staging patients with head and neck cancers, especially for patients with T3 and T4 diseases and/or distant metastases; ^{18}F-FDG PET/CT is a supplement to facilitate metabolism information guided tissue sampling; ^{18}F-FDG PET/CT is superior to conventional imaging modalities when it comes to planning radiation treatment protocols and could therefore facilitate accurate delineating of the target volume and sparing of normal tissues; ^{18}F-FDG PET/CT is useful for staging and restaging head and neck cancers and for monitoring therapeutic response following local and/or systemic treatments.

8.2.2.1 Paranasal Sinus Cancer

Paranasal sinuses are hollow, air-filled spaces that surround the nasal cavity. Mucus produced within these sinuses could humidify and heat the inhaled air and keep the inside of the nose from drying during breathing. Detailed understanding and knowledge of the anatomy (such as the orbit, anterior skull base, and masticator space) is very important to interpret all the anatomic and metabolic information provided by imaging examinations, not only at the initial staging phase but also during the subsequent follow-up. As a general rule, MRI has unsurpassed contrast resolution and is the technique of choice for the detection and evaluation of paranasal sinus tumors. In comparison, CT is preferred in the assessment of fibrous dysplasia and osteoma because of its excellent spatial resolution, which enables the precise assessment of the relationships between the suspicious lesion and sinus drainage pathways and skull base neurovascular foramina. The role of ^{18}F-FDG PET or PET/CT lies in refining surgical planning and in predicting the presence and location of a coexisting malignancy such as SCC.

Although the definitive diagnosis of paranasal sinus cancers is based on histological examination, continuous and unilateral nasal sinus symptoms and/or specific features such as bone lysis or a heterogeneous opacity on medical images

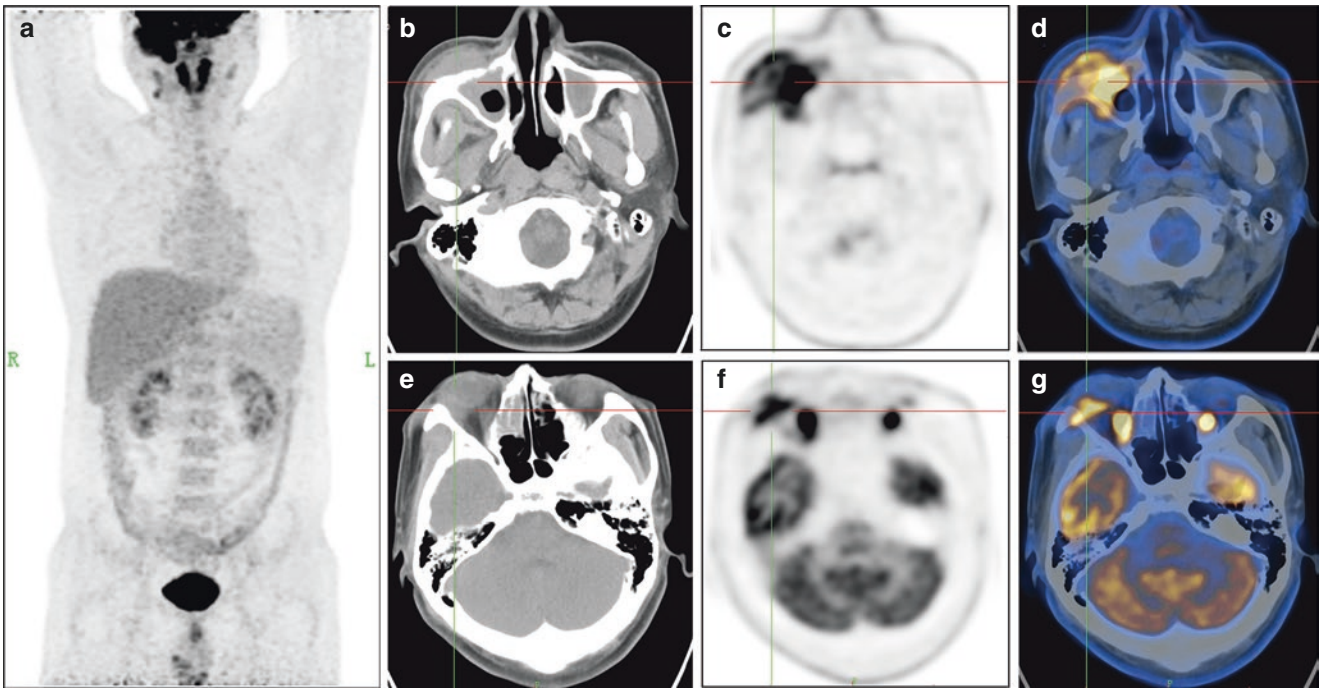

Fig. 8.13 A 35-year-old male patient, with repeated nasal obstruction and purulent discharge for 4 months; symptoms aggravated for 1 month. FESS biopsy demonstrated the right maxillary squamous cell carcinoma. ^{18}F-FDG PET/CT maximum intensity projection (MIP) image (**a**) demonstrated abnormal uptake of the radiotracer in the right side of the neck and in the right maxillary sinus. CT (**b**), PET (**c**), and fused PET/CT (**d**) images demonstrated soft tissue infiltration of the bilateral maxillary sinuses, with the right maxillary sinus showing significantly increased concentration of ^{18}F-FDG (SUVmax = 17.5) and destruction of the right maxillary sinus walls. Furthermore, the tumor has invaded the adjacent right orbit (**e**–**g**)

may indicate the occurrence of paranasal sinus cancers. The majority of SCC arises from maxillary sinus, and then from the nasal cavity, SCC rarely arises from the ethmoid, frontal, or sphenoid sinus. Currently, there is still no consensus on the place of ^{18}F-FDG PET or PET/CT in the management of paranasal sinus cancers. PET may be performed for initial staging assessment, or for restaging purpose (Fig. 8.13). As we mentioned above, IP originates from the Schneiderian membrane of the mucosa, which lines the nasal cavity and paranasal sinuses (most frequently in the maxillary antrum). Due to the association of IP and SCC and the very high recurrence rate of IP, endoscopic surgery is the mainstay of treatment for IP patients. Shojaku et al. reported that the SUVmax values for the 3 IP patients without SCC ranged from 4.9 to 7.3, whereas the corresponding values of 2 IP patients with SCC were 8.9 and 20.9, respectively [28]. SUVmax values for two benign IP patients were 8.2 and 7.8, respectively. In these two cases, MR imaging demonstrated a convoluted cerebriform pattern (CCP). In six patients with coexistent IP and SCC, the maximum SUVs ranged from 13.3 to 31.9; MR imaging demonstrated a diffuse CCP in two but no obvious CCP in the remaining three cases [29]. In addition, application of ^{18}F-FDG PET/CT may further leads to the successful delineation of recurrence of IP. Taken together, these results indicate a potential role of ^{18}F-FDG PET/CT in the evaluation of malignant transformation of IP and in the delineation of recurrent IP. However, other studies demonstrated that ^{18}F-FDG PET/CT is not a reliable predictor of potential malignancy in patients with sinonasal IP. In addition, radiotherapy together with chemotherapy is an effective, well-tolerated, and feasible treatment option for patients with paranasal sinus carcinomas, and ^{18}F-FDG PET/CT is of great value in detecting disease recurrence in the post-therapy settings.

Mucosal malignant melanomas (MMM) of the head and neck are rare and account for only 1.3% of all melanomas arising in the USA [30]. The most commonly involved sites include the head and neck area and urinary, female genital, and gastrointestinal tract. Of all sinonasal malignancies, the incidence of sinonasal malignant melanoma (SNMM) was about 10%. An initial study from Goerres et al. showed that all MMM were visible in staging ^{18}F-FDG PET examinations and ^{18}F-FDG uptake was dependent on lesion size and anatomic site [31]. More importantly, locoregional and distant metastases can be evaluated much like those of cutaneous malignant melanoma. In a study which included ten patients suffering from SNMM, ^{18}F-FDG PET/CT scanning depicted all primary tumors and all regional and distant metastases except one cerebral metastasis [32]. Post-radiotherapy PET avidity is reported to be associated with

local disease control and greater overall survival. Apart from ^{18}F-FDG PET/CT, recent studies have elucidated that ^{18}F-FLT PET/CT imaging is useful in predicting the therapeutic outcome of carbon ion radiotherapy, and C-choline PET/CT imaging was of certain value in diagnosing SNMM which was negative on ^{18}F-FDG PET/CT imaging.

8.2.2.2 Oral Carcinoma

The "pathology" of oral cavity contains all relevant benign lesions, inflammatory conditions, benign neoplasms, and more importantly malignant neoplasms. In the current chapter, we mainly focus on the most frequent malignant neoplasm of the oral cavity, oral squamous cell cancer (OSCC). OSCC originates from the mucosa and predominantly affects old men aged 50–70-year-old. Because the lower lip is the most common site for OSCC and local extension of the tumor can be easily detected and biopsied, cross-sectional imaging is not needed for most of the cases unless very large tumors or distant metastases are suspected. Apartment from the lips, the floor of the mouth, the ventrolateral tongue, and the retromolar trigone are three other intraoral sites that can be affected. Generally, CT and MR images are used to delineate tumor mass and to accurately staging OSCC according to the TNM system. A soft tissue mass is a direct sign of the malignancy and can be visualized on both CT and MRI images. Moreover, CT images with a bone window setting could also detect bony structure changes and cortical tumor infiltration, such as erosion and/or lysis of the adjacent bone cortex. Furthermore, OSCC tends to invade nerves and vessels of the neurovascular bundles, resulting in a greater risk of distant as well as local lymph node metastases. In this setting, pre-contrast together with fat-saturated contrast-enhanced T1-weighted MRI is very helpful to detect tumor extension along nerve routes.

Although CT and MRI have greatly improved staging and monitoring of OSCC, small metastatic lesions and early recurrent disease can still be underestimated. In addition, artifacts generated by dental amalgams and implants may lead to failed diagnosis of mandibular involvement. To overcome these disadvantages, ^{18}F-FDG PET/CT has been increasingly used for the evaluation and management of OSCC. ^{18}F-FDG PET/CT had a sensitivity of 97% in the detection of primary HNSCC in a large series of 167 patients (54 of them were with oral cavity cancers), higher than that of CT (86%) and MRI (without STIR-technique; 88%) [33]. After reviewing 16 studies and analyzing a total of 302 patients suffering from cervical metastases from unknown primary tumors, Rusthoven et al. reported that ^{18}F-FDG PET/CT detected 24.5% of primary tumors that were not apparent on conventional imaging examinations [34].

^{18}F-FDG PET/CT imaging is superior to CT and MRI in detecting and confirming lymph node metastases from OSCC (Fig. 8.14). This is of great importance because nodal metastasis is the most important prognostic factor for SCC

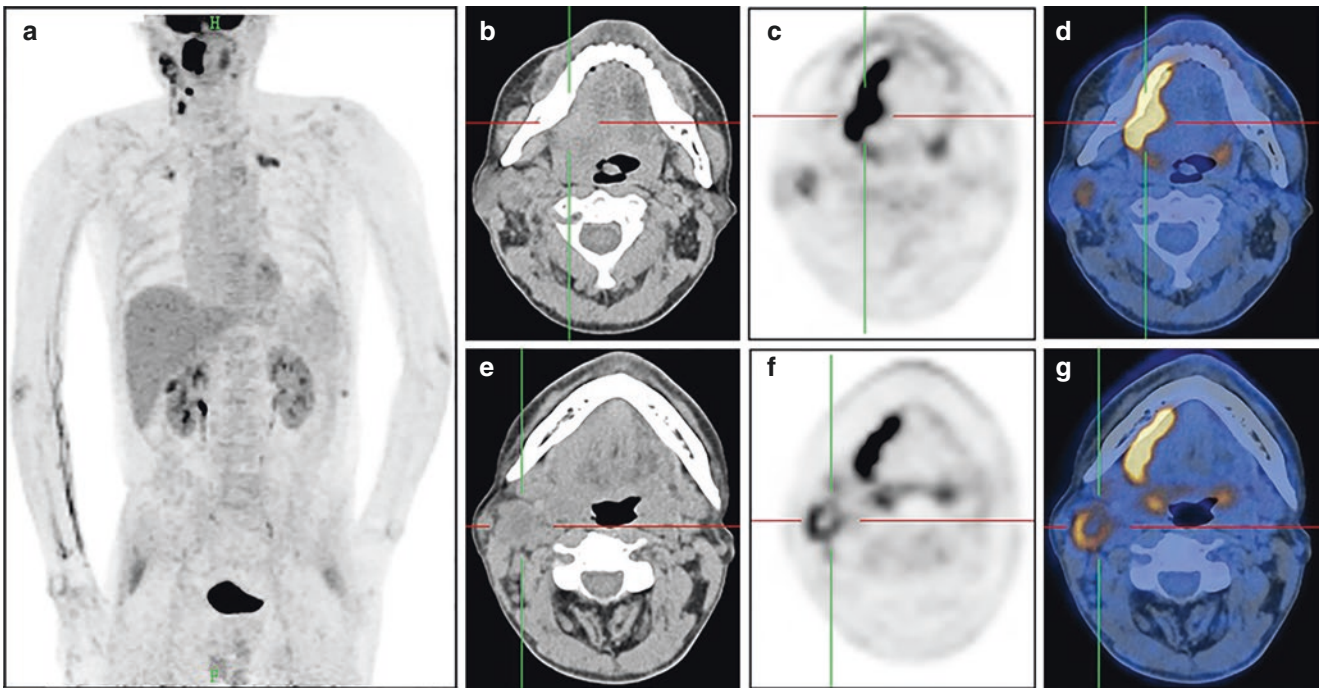

Fig. 8.14 A 58-year-old male patient who found right tongue lump for 3 months. Tumor biopsy proved to be squamous cell carcinoma. The patient had undergone chemotherapy before receiving ^{18}F-FDG PET/CT examination (**a**). Although CT image (**b**) failed to clearly visualize the primary tumor, PET (**c**) and fused PET/CT (**d**) images showed intense FDG uptake in the right side of the tongue base (primary site, SUVmax = 16.3) and in the right side of the neck (**e**–g), a finding that represented a level II lymph node metastasis

and negatively affects the 5-year survival rate by 40–50% [35]. The reported incidence of the clinically identified distant metastases from HNSCC at initial diagnosis varies from 2 to 18% [36], which is too low to warrant routine ^{18}F-FDG PET/CT screening. In a multicenter prospective study, the data of 92 evaluable HNSCC patients who developed distant metastases or who had a follow-up of at least 12 months, ^{18}F-FDG PET showed a higher sensitivity (53% vs. 37%) and positive predictive value (80% vs. 75%) when compared with CT [37]. This study indicated that pretreatment chest CT screening of distant metastases from HNSCC is improved by addition of ^{18}F-FDG PET imaging, but one concern of using ^{18}F-FDG PET for screening is its expensive costs. SUV of SCC is significantly associated with the outcome of SCC, and higher uptake of FDG should be considered for more aggressive treatment approaches.

8.2.2.3 Laryngeal Cancer

To precisely assess and treat neoplastic diseases, the larynx is divided into three parts: the supraglottis, the glottis, and the subglottis. The majority of supraglottic cancer arise from the epiglottis and tend to spread locally to the pre-epiglottic space, which can be sensitively detected by unenhanced T1-weighted MRI when the high signal intensity of fat is replaced by a mass with lower signal intensity and when enhancement of the pre-epiglottic mass is observed. As the contralateral undissected neck is a common cause of surgical failure in patients with SCC of the supraglottic larynx, therefore, it is reasonable that routine bilateral neck dissection may decrease cervical recurrence and further improve survival of patients with supraglottic cancer. Cancers originating from glottic or true vocal cord often demonstrate infiltrative growth patterns. And about 2/3 of these cancers are confined to the vocal folds (glottis), with the majority of these diseases confined to the anterior 2/3 of that structure. When vocal cord malignancies progress, they may invade and penetrate the subglottic region, infiltrate through the thyroid cartilage, penetrate the thyrohyoid membrane, or expand superiorly to infiltrate the base of the tongue. Although tumors arising in the subglottic area of the larynx are quite rare, they are often quite aggressive and infiltrative. A broad range of other benign and malignant tumors of non-squamous cell origin may also affect the larynx, such as chondrosarcoma, lymphoma, hemangioma, and paraganglioma.

Considering the unique physiological function of the larynx, several symptoms should prompt timely work-up for laryngeal cancer. The symptoms may include but not limited to hoarseness, dysphonia, dyspnea, and swallowing dysfunction. After initial evaluation and physical examination, flexible nasopharyngoscopy is usually performed to observe and/or biopsy the larynx and mucosal surfaces. However, it is worthwhile to mention that this procedure is not always adequate for submucosal tumor extension and needs anesthesia in the operating room. Accurate staging detailed anatomic structures and metabolic information provided by CT, MRI, and PET/CT examinations are imperative for laryngeal carcinomas, because differences in tumor size, location, infiltrative, and metabolic information may have a significant impact on initial patient stratification and subsequent use of treatment options. When cross-sectional imaging was applied to visualize a laryngeal or hypopharyngeal tumor, several questions should be answered. First of all, should the exact structures/organs involved by the tumor be identified? Second, are there any invasions of the adjacent spaces (paraglottic space or pre-epiglottic space) or cartilages? Third, are there any local lymph node metastases or distant metastases on cross-sectional images?

CT staging of the head and neck cancers has an excellent reported accuracy of >80% with comparable results with that of MRI, and CT typically demonstrates a higher specificity in identifying thyroid cartilage invasion when compared with MRI, but this imaging modality has a relatively lower sensitivity. However, for patients with small T1 larynx cancers, use of CT may not be recommended because it did not change the staging or failed to detect these early T1 larynx cancers. Barbera et al. further found that 54% of T1 larynx cancers had no abnormality on CT images [38]. In patients with primary laryngeal cancer or recurrence diseases in which CT was considered inadequate, ^{18}F-FDG PET/CT scanning and dynamic MRI, especially the former imaging modality, have high diagnostic values in the evaluation of primary, residual, and recurrent diseases (Fig. 8.15). In a retrospective study, Fleming et al. reported that proper use of ^{18}F-FDG PET/CT changed the treatment plans in 38 of 123 patients (30.9%) with laryngeal cancer. Altered treatments included upstaging, diagnosing distant and unresectable disease, and working-up second primary malignancies. ^{18}F-FDG PET/CT imaging has also demonstrated a utility in clinical staging as well as in detecting metastatic lesions. For laryngeal cancer patients who underwent definitive radiotherapy/radical surgery with or without chemotherapy, SUVmax is a significantly unfavorable factor for progression-free survival. Thanks to the additional structural information provided by CT, PET/CT is more accurate and precise than PET alone in the detection and anatomic localization of head and neck cancers.

More recently, PET/MRI has been applied to the diagnosis of laryngeal cancers. Cavaliere et al. demonstrated that PET/CT SUV parameters highly correlated with that derived by PET/MRI and that functional MRI parameters may further help improve patient's treatment planning [39]. In addition to abovementioned imaging methods, ^{18}F-FLT PET and ^{11}C-methionine were potential imaging approaches for laryngeal cancers, but further studies in larger cohorts are still needed to confirm these preliminary results.

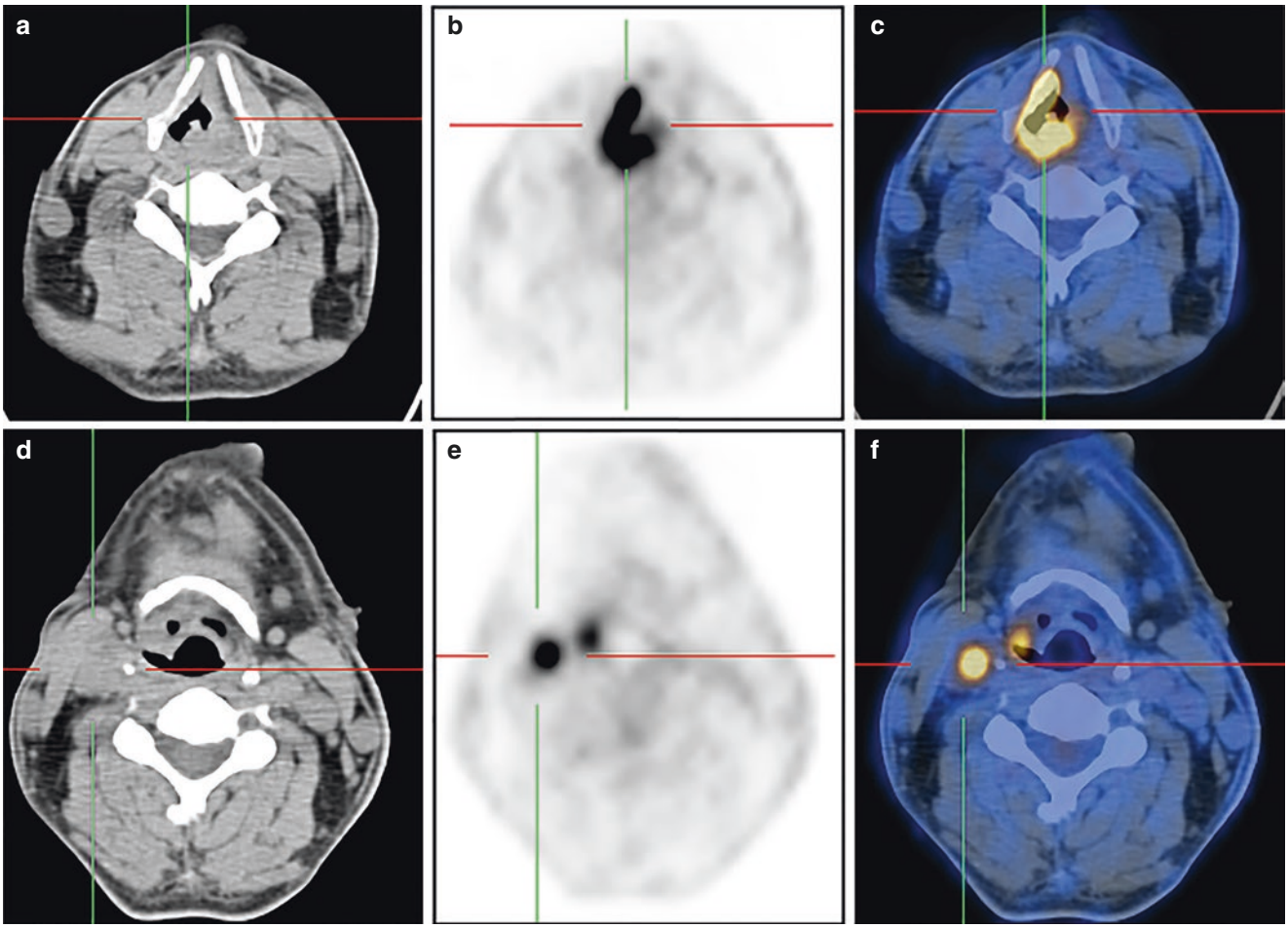

Fig. 8.15 Glottic cancer with invasion of supraglottis, subglottis, thyroid cartilage, and lymph node metastasis in a 63-year-old male patient. (**a**) Axial CT image at the supraglottic level showed a tumor mass arising from the right vocal cord with invasion of the thyroid cartilage and extension into the right aryepiglottic folds. PET (**b**) and fused PET/CT (**c**) images showed that the corresponding tumor tissues had intense FDG uptake with SUVmax of 19.2. (**d**–**f**) PET-CT scanning also revealed intensely increased FDG accumulation in the right side of the neck, a finding that was interpreted as lymph node metastasis

8.2.2.4 Thyroid Carcinoma

Differentiated thyroid cancer (DTC) contains two subtypes: papillary thyroid cancer (PTC) and follicular thyroid cancer (FTC). DTC is the most commonly diagnosed endocrine malignancy, and its incidence has been increasing in the past three decades. The first-line therapeutic methods for DTC consist of thyroidectomy, radioactive iodine treatment, and levothyroxine replacement therapy. However, about 30–40% of patients with either local thyroid cancer or distant metastatic thyroid cancer develop resistance to radioactive iodine therapy due to tumor dedifferentiation. For patients with radioiodine-refractory DTC (RR-DTC), molecularly targeted therapy specifically inhibiting oncogenic pathways has greatly changed the therapeutic landscape in the past decade.

An important aspect in clinical management of thyroid cancers is the visualization and localization of diseases by imaging. Ultrasonography (US) and fine needle aspiration biopsy (FNAB) are the major approaches to assess thyroid nodules. In addition, ^{18}F-FDG PET/CT is the most useful method to detect RR-DTC and other aggressive thyroid cancers. For whole-body scan (WBS) negative thyroid cancer patients with persistently elevated level of thyroglobulin (Tg), studies demonstrated that ^{18}F-FDG PET/CT scanning may detect residual and/or metastatic diseases in approximately 40–70% of patients [40]. Usually, patients with ^{18}F-FDG-positive lesions have significantly higher Tg values than patients with a negative PET/CT. According to our own experience and literature report, ^{18}F-FDG PET/CT scanning has a good diagnostic performance for PTC patients with negative Tg, negative ^{131}I-WBS, and progressively increased TgAb level and therefore may be performed routinely for these patients. However, it is difficult to establish exact Tg cutoff to achieve the maximum sensitivity and specificity for ^{18}F-FDG PET/CT scanning, as rhTSH-stimulated PET/CT detected ^{18}F-FDG-positive lesions in 20% patients with Tg less than 10 ng/mL [41]. Recombinant human TSH (rhTSH)

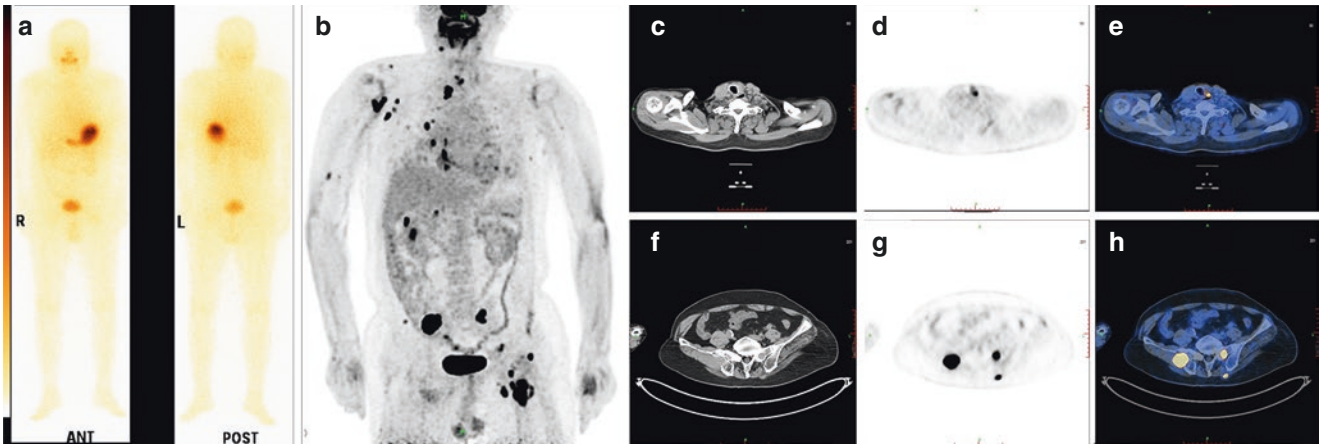

Fig. 8.16 74-year-old male with papillary thyroid carcinoma (PTC). Iodine-131 whole-body scan showed no obvious abnormal uptake lesions across the body (**a**). But whole-body ^{18}F-FDG PET/CT scanning showed the metastatic lesions in multiple lymph nodes, right kidney, and bone (**b**). The metastatic upper left clavicle lymph node had high uptake of ^{18}F-FDG (**c**–**e**). Representative ^{18}F-FDG PET/CT images showed that the metastatic lesions in the pelvis bone had high uptake of ^{18}F-FDG (**f**–**h**)

stimulation prior to PET/CT examination might further improve the diagnostic sensitivity, increase the number of thyroid cancers detected, direct surgical interventions, and thus refine the clinical management in a small percentage of cases. Although integrated ^{131}I SPECT/CT is a useful and cost-effective tool for the diagnosis, staging, risk stratification, and follow-up of patients with DTC, combinational use of ^{18}F-FDG PET/CT and ^{131}I SPECT/CT may provide superior information in the management of the distant metastases from thyroid cancer. These results indicate that ^{18}F-FDG PET/CT is useful in evaluating patients affected by DTC, especially those with positive thyroglobulin level and negative ^{131}I whole-body scan (Fig. 8.16), as a result, providing important additional information not available with conventional follow-up methods and refining subsequent risk stratification and management strategies.

Incidentally, ^{18}F-FDG uptake within the thyroid is associated with significantly higher risk of thyroid cancer, and special attention should be given to these patients. Specifically, Hassan et al. reported that 173 out of 10,012 ^{18}F-FDG PET/CT scans showed incidental thyroid uptake, and 29 of them were malignant. Focal ^{18}F-FDG uptake rather than diffuse ^{18}F-FDG uptake was associated with a higher prevalence of malignant thyroid nodule [42].

Notably, ^{18}F-FDG PET/CT has long been the imaging agent of choice for MTC, ATC, and primary thyroid lymphoma (PTL). MTC accounts for 3–9% of all thyroid cancers and cause around 13% of thyroid cancer-related deaths. The reported sensitivity and specificity of ^{18}F-FDG PET/CT imaging for localizing MTC metastases are above 70% when calcitonin levels are raised. ATC is very aggressive and usually presents as a rapidly expanding hard neck mass, and ATC is often associated with symptoms caused by local invasion and compression. Therefore, one of the most important management considerations in ATC patients is to accurately assess the disease burden by medical imaging examinations. CT and MRI of the neck and chest should be obtained to assess the extent of the tumor itself, and more importantly the invasion of the tumor into adjacent structures. As all patients with ATC are considered to have stage IV disease, ^{18}F-FDG PET/CT is very useful for staging local disease and distant metastases. Additionally, high ^{18}F-FDG uptake on PET images is closely correlated with poor survival in patients with ATC.

In addition, advances in molecular imaging and development of novel imaging agents have led to the development of new thyroid cancer-specific tracer like ^{18}F-tetrafluoroborate (^{18}F-TFB), which is transported through the sodium-iodide symporter (NIS) and has been validated in a clinical setting. ^{18}F-TFB had a biodistribution similar to that of ^{99m}Tc-pertechnetate and was pharmacologically and radiobiologically safe in humans, but clinical trials are urgently needed to confirm the diagnostic efficacy of this novel probe. Furthermore, ^{124}I PET/CT scanning was more sensitive in detecting metastatic disease than SPECT imaging with ^{131}I or ^{123}I. Apart from these thyroid-specific probes, recent studies have shown that prostate-specific membrane antigen was frequently expressed in microvessels of thyroid tumors, and PSMA-targeted PET agents could delineate the PTCs, FTCs, as well as follicular adenomas. These initial results indicate that PSMA-targeted theranostic approaches may open a new horizon in the management of thyroid cancer, especially RR-DTC.

8.2.3 ^{18}F-FDG PET/CT in Staging of Head and Neck Cancer

The American Joint Committee on Cancer (AJCC) published the eighth edition of the AJCC/tumor-node-metastasis (TNM) cancer staging system, replacing the seventh edition

which has been in use since 2009. The TNM classification system has been proven to be a very effective and useful tool in clinical practice to facilitate many elements of prognostication and cancer control. The prognosis and outcome of head and neck cancers are determined by several factors such as patient, tumor, and relevant healthcare system.

Assessment of the tumor stage does not limit to measurement of the size of the primary lesion, the depth of invasion (DOI), and the involvement of the surrounding structures, and midline crossing should be taken into consideration as well. However, CT and MRI could be suboptimal in assessing mandibular bone invasion by oral cancers, partially due to the artifacts generated by dental amalgams and implants. In recent years, momentum to include other non-anatomic factors, such as metabolic, biological, and genetic information, has gained sustained attention, partly because it is well-recognized that anatomic extent of the malignancy does not embrace all dimensions of prognosis. Indeed, there is an urgent need in clinical practice to exploit biological processes such as glucose metabolism to permit more personalized treatment and interventions for patients with heterogeneous head and neck cancer. Moreover, more than 50% of patients with HNSCC have regional lymph node metastases at initial diagnosis. In this setting, ^{18}F-FDG PET/CT imaging has been increasingly used to delineate mandibular involvement. More importantly, this imaging modality is superior to CT and MRI in the detection of metastatic diseases involving the cervical lymph nodes. Although the incidence of distant metastases of HNSCC at the initial presentation is quite low, ^{18}F-FDG PET/CT is more sensitive and specific than these conventional imaging modalities (e.g., CT and MRI) in the early detection and localization of distant and skeletal metastases, and even secondary primary malignancies.

The recently released eighth edition of the AJCC Staging Manual introduced significant modifications regarding head and neck section. For oral cavity cancers, this most recent edition acknowledges the different biological behaviors of these small but deeply invasive tumors and therefore incorporates DOI into the staging system (Table 8.6). DOI is distinct from tumor thickness and affects T category [43]. Currently, assessment of DOI can be achieved by clinical examination and pathology. ^{18}F-FDG PET/CT imaging has a good accuracy in determining the extension and/or DOI of the oral cavity cancers and could therefore facilitate staging and detecting of oral cavity cancers.

As for thyroid cancers, in the eighth edition, the major change in T category is the definition of T3, and the remaining T categories remain unchanged in content (Table 8.7). In the seventh edition, T3 category included any tumor >4 cm in greatest dimension, but the tumor is limited to the thyroid and tumors of any size with minimal extrathyroidal extension (or abbreviated as ETE, which is defined as extension to sternothyroid muscle or perithyroidal soft tissue). Based on the most recent update, minor ETE identified only on histological examination is no longer a variable in determining the T category. Although this change to the definition of T3 category was prompted by several evidence-based studies, a retrospective analysis of 241,118 patients with DTC demonstrated that

Table 8.6 T category for oral cavity cancer, eighth edition staging manual

T category for oral cavity cancer	
T category	T criteria
TX	Primary tumor cannot be assessed
Tis	Carcinoma in situ
T1	Tumor ≤2 cm, ≤5 mm depth of invasion (DOI) (DOI is depth of invasion and not tumor thickness)
T2	Tumor ≤2 cm, DOI >5 mm and ≤10 mm or tumor >2 cm but ≤4 cm and DOI ≤ 10 mm
T3	Tumor >4 cm or any tumor >10 mm DOI
T4	Moderately advanced or very advanced local disease
T4a	Moderately advanced local disease: (lip) tumor invades through cortical bone or involves the inferior alveolar nerve, floor of mouth, or skin of face (i.e., chin or nose); (oral cavity) tumor invades adjacent structures only (e.g., through cortical bone of the mandible or maxilla, or involves the maxillary sinus or skin of the face); note that superficial erosion of bone/tooth socket (alone) by a gingival primary is not sufficient to classify a tumor as T4
T4b	Very advanced local disease; tumor invades masticator space, pterygoid plates, or skull base and/or encases the internal carotid artery

Table 8.7 T Category definitions for papillary, follicular, poorly differentiated, Hurthle cell, and anaplastic thyroid carcinomas

Definition of primary tumor (T)	
T category	T criteria
TX	Primary tumor cannot be assessed
T0	No evidence of primary tumor
T1	Tumor ≤2 cm in greatest dimension limited to the thyroid
T1a	Tumor ≤1 cm in greatest dimension limited to the thyroid
T1b	Tumor >1 cm but ≤2 cm in greatest dimension limited to the thyroid
T2	Tumor >2 cm but ≤4 cm in greatest dimension limited to the thyroid
T3[a]	Tumor >4 cm limited to the thyroid or gross extrathyroidal extension invading only strap muscles
T3a[a]	Tumor >4 cm limited to the thyroid
T3b[a]	Gross extrathyroidal extension invading only strap muscles (sternohyoid, sternothyroid, thyrohyoid, or omohyoid muscles) from a tumor of any size
T4	Includes gross extrathyroidal extension into major neck structures
T4a	Gross extrathyroidal extension invading subcutaneous soft tissues, larynx, trachea, esophagus, or recurrent laryngeal nerve from a tumor of any size
T4b	Gross extrathyroidal extension invading prevertebral fascia or encasing carotid artery or mediastinal vessels from a tumor of any size

Table 8.8 N and M category definitions for differentiated and anaplastic thyroid cancer and anaplastic thyroid carcinomas

Definition of regional lymph node (N)	
N category	N criteria
NX	Regional lymph nodes cannot be assessed
N0	No evidence of regional lymph nodes metastasis
N0a[a]	One or more cytologic or histologically confirmed benign lymph node
N0b[a]	No radiologic or clinical evidence of locoregional lymph node metastasis
N1[a]	Metastasis to regional nodes
N1a[a]	Metastasis to level VI or VII (pretracheal, paratracheal, or prelaryngeal/Delphian, or upper mediastinal) lymph nodes; this can be unilateral or bilateral disease
N1b[a]	Metastasis to unilateral, bilateral, or contralateral lateral neck lymph nodes (levels I, II, III, IV, or V) or retropharyngeal lymph nodes
Definition of distant metastasis (M)	
M category	M criteria
M0	No distant metastasis
M1	Distant metastasis

[a]All categories may be subdivided: (s) solitary tumor and (m) multifocal tumor (the largest tumor determines the classification)

minimal ETE was accompanied by cervical lymph node metastases in 67% of the cases, and minimal ETE was further associated with a statistically significant decrease in 5-year survival [44]. The eighth edition provides more details about N0 category and has changed the upper mediastinal lymph nodes (cervical level VII) to N1a (central neck) category. The definitions for the M category are the same in the eighth edition as in previous editions (Table 8.8). The change of the upper mediastinal lymph nodes to N1a, therefore, acknowledges the anatomic continuum between the low cervical neck and the upper mediastinum and the lack of data differentiating the prognostic importance of upper mediastinal nodes from lower cervical central neck nodes. In addition, the age for poor prognosis of thyroid cancer has changed from 45 to 55 years, and all patients younger than 55 years are considered to have stage I disease unless they are suffering from distant metastases, in which case their disease is stage II [45]. For patients aged 55 years or older, the presence of distant metastases confers stage IVB, while cases without distant metastases are further categorized based on the presence/absence of gross extrathyroidal extension, tumor size, and lymph node status (Table 8.9). By moving the age cutoff from 45 to 55 years, 10–30% of the patient population was downstaged to a lower risk category without significant impact on the survival curves; however, a small proportion of DTC patients with relatively high-risk diseases will be downstaged into the lower stages at the same time. The role of ^{18}F-FDG PET/CT in the staging of thyroid cancers according to *AJCC Cancer Staging Manual*, eighth edition remains to be determined by future studies.

Table 8.9 Prognostic stage definitions for differentiated thyroid cancer

Stages of differentiated thyroid cancer				
Age at diagnosis	T category	N category	M category	Stage
<55 years	Any T	Any N	M0	I
	Any T	Any N	M1	II
≥55 years	T1	N0/NX	M0	I
	T1	N1	M0	II
	T2	N0/NX	M0	I
	T2	N1	M0	II
	T3a/T3b	Any N	M0	II
	T4a	Any N	M0	III
	T4b	Any N	M0	IVA
	Any T	Any N	M1	IVB

8.2.4 ^{18}F-FDG PET/CT in the Detection and Diagnosis of Recurrent Head and Neck Cancers

In our experience, one of the most powerful applications of ^{18}F-FDG PET/CT examination lies in detecting residual or recurrent head and neck neoplasms after initial treatment (Fig. 8.17). Neck dissection, flap reconstruction, and radiation therapy unavoidably change and distort the normal neck anatomy, making detection of recurrent neoplasms very challenging with traditional imaging methods. Despite the fact that stability of a lesion over several months on CT and MRI images suggests scar rather than residual or recurrent neoplasm, the main criterion for tumor recurrence (tumor growth over time) at conventional CT or MR imaging may occur as a normal post-radiotherapy effect. ^{18}F-FDG PET or PET/CT is a useful imaging approach for detecting tumor and differentiating recurrent tumor tissues from post-therapy necrosis.

Initial results showed that the sensitivity and specificity of ^{18}F-FDG PET/CT imaging in detecting recurrent head and neck neoplasms were >90% and >60%, respectively [46]. However, locally recurrent HNSCCs are often more difficult to diagnose than primary SCCs, and radiotherapy/chemotherapy inevitably induce morphological and metabolic changes, which are thus difficult to interpret and to differentiate from these recurrent diseases. For example, it has been reported that recurrent glottic carcinomas tend to recur submucosally with multicentric tumor foci, a growth pattern that often understaged by traditional imaging studies and endoscopy [47]. In a prospective study which included 116 histologically proven HNSCC patients who had no recurrence during a 6-month follow-up, Robin et al. reported that of the 34 patients with positive ^{18}F-FDG PET/CT findings, 22 of them had relapsed diseases, whereas the remaining 12 cases did not show evidence of recurrence. In comparison, of the 82 cases with negative ^{18}F-FDG PET/CT findings, only 1 patient had a recurrence, resulting in excellent sensitivity of

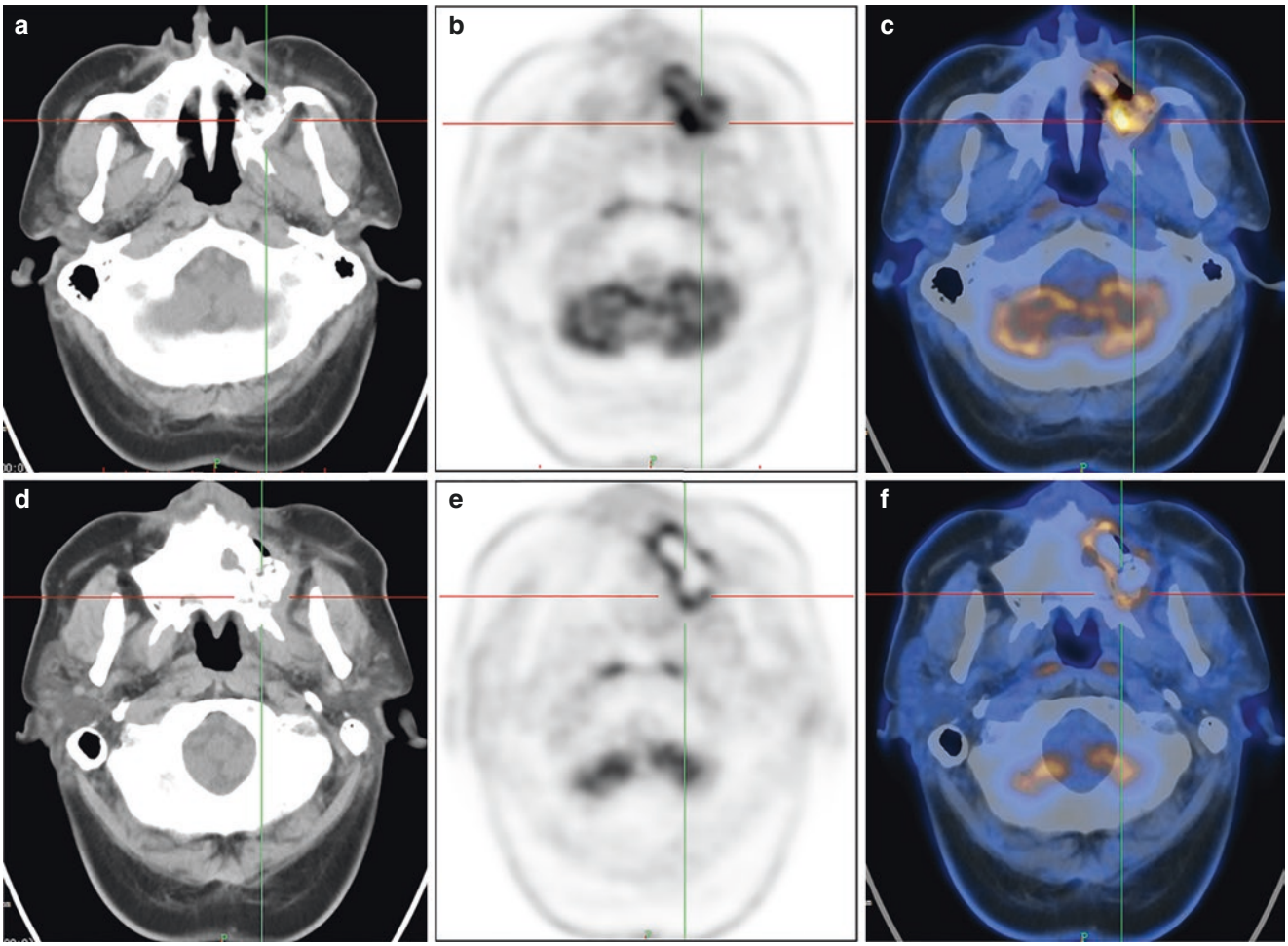

Fig. 8.17 Recurrence of left maxillary adenoid cystic carcinoma in a 64-year-old male patient. The patient initially received surgical resection of the primary tumor and then received local radiotherapy for 4 years. The patient presented with new left-sided facial pain. (**a**–**c**) ^{18}F-FDG PET/CT showed concomitant sclerosis and destruction of the left maxillary sinus walls with SUVmax of 9.9, thereby representing recurrence of maxillary adenoid cystic carcinoma. (**d**–**f**) ^{18}F-FDG PET/CT scanning also showed a circle area of FDG uptake in the left maxilla. Although neoplasm was suspected, this kind of FDG uptake needed to be differentiated from a dental abscess

96% (22/23) and specificity of 87% (81/93) for ^{18}F-FDG PET/CT examination in this cohort [48].

In addition, a combination of ^{18}F-FDG PET/CT and MRI with DWI sequence can provide additional diagnostic certainty in difficult posttreatment situations. And combining PET with MRI is technically and clinically feasible. Becker et al. recently performed a prospective study which included 74 consecutive HNSCC patients, who previously received radiotherapy/chemotherapy and for whom tumor recurrence or radiation-induced complications were highly suspected. The authors reported that 43 locally recurrent tumors were present in 38 patients, of which 32 recurrent lesions were missed by endoscopy as no obvious mucosal abnormality observed [49]. Statistically, sensitivity, specificity, and positive and negative predictive value of PET/MRI-DWI examination were 97.4%, 91.7%, 92.5%, and 97.1% per patient and 93.0%, 93.5%, 90.9%, and 95.1% per lesion, respectively. The authors suggested false-positive ^{18}F-FDG PET assessments could be avoided by restriction information and features on DWI and MRI, and false-positive DWI or MRI assessments could be avoided by absent focal ^{18}F-FDG uptake or ADC value [49]. According to this study, locally recurrent tumors have lower ADCmean or ADCmin value but higher SUVmean or SUVmax value than those benign post-therapeutic lesions or complications, indicating that combined use of ADC and SUV values is reproducible and is useful for detecting primary and recurrent tumors. However, since the hybrid PET/MRI examination is much less cost-effective and available than ^{18}F-FDG PET/CT examination, and may involve longer scanning time, the usefulness of PET/MRI in routine clinical practice needs to be carefully determined. We should note that contrast-enhanced PET/MRI may not yield higher diagnostic accuracy than non-enhanced PET/MRI. Furthermore, accurate SUV quantification using PET/MRI system is not achieved at the moment, although visual analysis of focal FDG accumulation without

semiquantitative criteria was reported to be sufficient for the diagnosis of local recurrence of head and neck cancers.

Timely detection and visualization of recurrent laryngeal cancers is a useful predictive factor for curation and preservation of laryngeal function. Although direct laryngoscopy under general anesthesia with taking of biopsies is the standard approach to detect suspected recurrence, this method is invasive and lacks repeatability. In addition, careful assessment of the risk of occult nodal disease is important before performing a neck dissection, because salvage laryngectomy is already associated with impaired wound healing, wound-related complications, and even increased morbidity. Therefore, noninvasive methods that can identify those patients at high risk of regional failure are important. ^{18}F-FDG PET/CT scanning can provide both anatomic features and glucose metabolism information; therefore, there is a growing interest in the use of this imaging modality for tumor contouring and precise delineation of the target volume. More importantly, the sensitivity of ^{18}F-FDG PET/CT in localizing recurrent head and neck cancers is about 95% [50], and the negative predictive of this imaging method for viable diseases in a residual anatomic abnormality was as high as 97%. However, the value of ^{18}F-FDG PET/CT in mapping distant bone metastases equaled to that of bone scintigraphy. Gilbert et al. analyzed 15 patients who received PET/CT scans prior to neck dissections for recurrent laryngeal cancers, and the authors found that ^{18}F-FDG PET/CT had a sensitivity of 70% and a negative predictive value of 62.5% in predicting the pathologic status [51]. However, after retrospectively reviewing 46 clinically and radiographically N0 patients with recurrent laryngeal cancer who underwent ^{18}F-FDG PET/CT examination before surgery, Rosko et al. reported that ^{18}F-FDG PET/CT only detected 2 of 12 patients with recurrent diseases with a poor sensitivity of 16.7% and identified 33 of 34 patients without recurrent diseases with a specificity of 97.1% [52]. The substantially lower sensitivity reported in this study was likely because of the restrict inclusion criteria, as the authors only included patients with laryngeal cancers previously treated with radiotherapy or concurrent chemoradiotherapy. And these treatments inevitably altered the lymphatics with decreased vascularity and reduced size of the residual diseases, leading to omission of those small pathologically positive lesions by ^{18}F-FDG PET/CT.

Thyroid cancers may have variable^{18}F-FDG uptake, which largely depends on the differentiation status with DTCs take up less ^{18}F-FDG than those undifferentiated or poorly differentiated thyroid cancers. In an initial study which included eight thyroid cancer patients undergoing ^{18}F-FDG PET/CT scanning, Zimmer et al. reported that half of these cases demonstrated recurrent neoplasms on PET images, with initial histologic findings of three PTC cases and one MTC case. Eight lesions in three patients were sampled, and 75% of sampled lesions were recurrent neoplasms [53]. A recent study showed that ^{18}F-FDG avidity of the primary thyroid cancers is one of the significant predictors in predicting tumor recurrence, and PTC patients with ^{18}F-FDG-avid tumors had higher lymph node stage, larger tumor size, and more frequent extrathyroidal extension [54]. Although routine ^{18}F-FDG PET/CT imaging is not recommended for initial evaluation of newly detected thyroid nodules, ^{18}F-FDG PET/CT scanning may be considered in high-risk DTC patients, especially for patients with elevated serum Tg (generally >10 ng/mL) and negative RAI imaging. ^{18}F-FDG PET/CT imaging should be included as a routine examination for patients with poorly differentiated thyroid cancer or ATC.

In addition to recurrent diseases and distant metastases, it is notable that second primary cancers are found even in patients with early-stage head and neck cancers. Kim et al. staged 349 patients with previously untreated head and neck cancers using ^{18}F-FDG PET/CT [55]. Most of the included cases were squamous cell carcinoma (81.1%), and the most common histological type is laryngeal cancer (32.1%), followed by cancers in the oral cavity, oropharynx, nasopharynx, and hypopharynx. During a mean follow-up period of 15 months, the incidence of distant metastases in this cohort was 7.4%. Of the 26 patients suffering from distant metastases, only 8 patients were detected by pretreatment ^{18}F-FDG PET/CT scanning, resulting in a low sensitivity of 30.7%. Importantly, initial ^{18}F-FDG PET/CT imaging revealed 10 of the 14 second primary tumors developed in this period. In a prospective cohort study which included 307 patients with oral, pharyngeal, or laryngeal cancer, Rohde et al. reported that ^{18}F-FDG PET/CT imaging had a significantly higher diagnostic rate in detecting distant metastases or synchronous cancers than imaging strategies used in current guidelines [56]. To be more specific, while chest x-ray/head and neck MRI (CXR/MRI) and chest CT/head and neck MRI (CHCT/MRI) detected 3 (1%) and 11 (4%) patients with distant metastases, ^{18}F-FDG PET/CT detected 18 (6%) patients. Also, ^{18}F-FDG PET/CT correctly identified 25 (8%) synchronous cancers, which was significantly higher than that detected by CXR/MRI (3 patients, 1%) or by CHCT/MRI (6 patients, 2%). Currently, the National Comprehensive Cancer Network (NCCN) guidelines recommend concomitant use of chest CT and MRI for all HNSCC patients and conditional use of ^{18}F-FDG PET/CT for clinical stage 3–4 patients (https://oralcancerfoundation.org/wp-content/uploads/2016/09/head-and-neck.pdf). However, these above results indicate that combined ^{18}F-FDG PET/CT is useful as a primary method for detecting both second cancers and distant metastases in patients with HNSCC regardless of clinical evidence of nodal metastases. Enhanced assessment of metastatic disease and second primary cancers would thus facilitate more appropriate decisions regarding the optimal treatment strategy and prognosis prediction.

To conclude, ^{18}F-FDG PET/CT imaging has dramatically changed head and neck cancer imaging and management. Despite the superior accuracy and sensitivity of ^{18}F-FDG PET/CT examination, there are limitations and pitfalls of this imaging modality where a misinterpretation of ^{18}F-FDG uptake may be unavoidable. Possible reasons that may cause false-positive or false-negative findings include, but not limited to, physiologic ^{18}F-FDG uptake (such as Waldeyer's ring, the salivary glands, and the muscles of mastication), inflammatory changes (such as periodontal disease, dental infection, active atherosclerotic plaques or tuberculosis), brown adipose fat, benign thyroid nodules, unilateral cranial nerve palsy, radiotherapy, chemotherapy, surgery, low ^{18}F-FDG uptake of the tumors, obscuration of ^{18}F-FDG uptake by dental hardware, inadequate PET scanner resolution, and so on. Under the circumstances, cross-sectional imaging and further approaches such as biopsy are needed to make the differential diagnosis. And we should always remember that familiarity with key imaging features of physiological and nonphysiological ^{18}F-FDG uptake, detailed anatomy of the head and neck, and unusual ^{18}F-FDG uptake patterns is essential to delineate actual pathology and to avoid misdiagnosis of benign conditions as malignancy.

References

1. El-Naggar AK, Chan JKC, Grandis JR et al (2017) WHO classification of head and neck tumours, 4th edn. The International Agency for Research on Cancer (IARC), Lyon Cedex, pp 65–70
2. Chinese Committee for Staging of Nasopharyngeal Carcinoma (2017) The 2017 edition for staging of nasopharyngeal carcinoma in China (The Chinese 2008 expert consensus on staging revision of nasopharyngeal carcinoma). Chin J Radiat Oncol 26(10):1119–1125. [Article in Chinese]
3. Hu-bing W, Quan-shi W, Ming-fang W et al (2005) The imaging manifestation and clinical value of PET/CT in nasopharyngeal carcinoma. Chin J Nucl Med 25:347–349. [Article in Chinese]
4. Ng SH, Chan SC, Yen TC et al (2009) Staging of untreated nasopharyngeal carcinoma with PET/CT: comparison with conventional imaging work-up. Eur J Nucl Med Mol Imaging 36(1):12–22
5. Liu FY, Lin CY, Chang JT et al (2007) ^{18}F-FDG PET can replace conventional work-up in primary M staging of nonkeratinizing nasopharyngeal carcinoma. J Nucl Med 48(10):1614–1619
6. King AD, Ma BB, Yau YY et al (2008) The impact of ^{18}F-FDG PET/CT on assessment of nasopharyngeal carcinoma at diagnosis. Br J Radiol 81(964):291–298
7. Chan SC, Yeh CH, Yen TC et al (2018) Clinical utility of simultaneous whole-body ^{18}F-FDG PET/MRI as a single-step imaging modality in the staging of primary nasopharyngeal carcinoma. Eur J Nucl Med Mol Imaging 45(8):1297–1308
8. Wu H-b, Wang Q-s, Wang M-f et al (2011) Preliminary study of ^{11}C-choline PET/CT for T staging of locally advanced nasopharyngeal carcinoma: comparison with ^{18}F-FDG PET/CT. J Nucl Med 52(3):341–346
9. Ng SH, Chang JT, Chan SC et al (2004) Nodal metastases of nasopharyngeal carcinoma: patterns of disease on MRI and FDG PET. Eur J Nucl Med Mol Imaging 31(8):1073–1080
10. Sun Y, Ma J, Lu TX et al (2004) Regulation for distribution of metastatic cervical lymph nodes of 512 cases of nasopharyngeal carcinoma. Ai Zheng 23(11 Suppl):1523–1527. [Article in Chinese]
11. Su Y, Zhao C, Xie CM et al (2006) Evaluation of CT, MRI and PET-CT in detecting retropharyngeal lymph node metastasis in nasopharyngeal carcinoma. Ai Zheng 25(5):521–525. [Article in Chinese]
12. Hu WH, Zhang GY, Liu LZ et al (2005) Comparison between PET-CT and MRI in diagnosing nodal metastasis of nasopharyngeal carcinoma. Ai Zheng 24(7):855–860. [Article in Chinese]
13. Lin XP, Zhao C, Chen MY et al (2008) Role of ^{18}F-FDG PET/CT in diagnosis and staging of nasopharyngeal carcinoma. Ai Zheng 27(9):974–978
14. Peng H, Chen L, Tang LL et al (2017) Significant value of ^{18}F-FDG-PET/CT in diagnosing small cervical lymph node metastases in patients with nasopharyngeal carcinoma treated with intensity-modulated radiotherapy. Chin J Cancer 36(1):95
15. Shen G, Zhang W, Jia Z et al (2014) Meta-analysis of diagnostic value of ^{18}F-FDG PET or PET/CT for detecting lymph node and distant metastases in patients with nasopharyngeal carcinoma. Br J Radiol 87(1044):20140296
16. Ren YY, Li YC, Wu HB et al (2017) Whole-body ^{18}F-FDG PET/CT for M staging in the patient with newly diagnosed nasopharyngeal carcinoma: who needs? Eur J Radiol 89:200–207
17. Gan H (2016) Guidelines for the clinical application of nuclear medicine and molecular imaging. People's Health Press, Beijing, pp 65–70
18. Hu-bing W, Quan-shi W, Zhu-han H et al (2002) Clinical application of ^{18}F-FDG PET in diagnosis and staging of patients with nasopharyngeal tumor. Chin J Nucl Med 22(4):137–138. [Article in Chinese]
19. Wei J, Pei S, Zhu X (2016) Comparison of ^{18}F-FDG PET/CT, MRI and SPECT in the diagnosis of local residual/recurrent nasopharyngeal carcinoma: a meta-analysis. Oral Oncol 52:11–17
20. Yen RF, Hong RL, Tzen KY et al (2005) Whole-body ^{18}F-FDG PET in recurrent or metastatic nasopharyngeal carcinoma. J Nucl Med 46(5):770–774
21. Yen TC, Chang JT, Ng SH et al (2005) The value of 18F-FDG PET in the detection of stage M0 carcinoma of the nasopharynx. J Nucl Med 46(3):405–410
22. Chang MC, Chen JH, Liang JA et al (2013) Accuracy of whole-body FDG-PET and FDG-PET/CT in M staging of nasopharyngeal carcinoma: a systematic review and meta-analysis. Eur J Radiol 82(2):366–373
23. Committee of Nasopharyngeal Cancer of Chinese Anti-Cancer Association, Xiaozhong C, Jingao L, Shaojun L, Chaosu H (2018) Expert consensus on the treatment of metastasis nasopharyngeal carcinoma. Chin J Radiat Oncol 27(1):7–15. [Article in Chinese].
24. Ng SH, Joseph CT, Chan SC et al (2004) Clinical usefulness of ^{18}F-FDG PET in nasopharyngeal carcinoma patients with questionable MRI findings for recurrence. J Nucl Med 45(10):1669–1676
25. Gupta T, Master Z, Kannan S et al (2011) Diagnostic performance of post-treatment FDG PET or FDG PET/CT imaging in head and neck cancer: a systematic review and meta-analysis. Eur J Nucl Med Mol Imaging 38(11):2083–2095
26. Siegel RL, Miller KD, Jemal A (2017) Cancer statistics, 2017. CA Cancer J Clin 67(1):7–30
27. Melroy CT, Senior BA (2006) Benign sinonasal neoplasms: a focus on inverting papilloma. Otolaryngol Clin North Am 39(3):601–617, x.
28. Shojaku H, Fujisaka M, Yasumura S et al (2007) Positron emission tomography for predicting malignancy of sinonasal inverted papilloma. Clin Nucl Med 32(4):275–278
29. Jeon TY, Kim HJ, Choi JY et al (2009) 18F-FDG PET/CT findings of sinonasal inverted papilloma with or without coexistent malig-

nancy: comparison with MR imaging findings in eight patients. Neuroradiology 51(4):265–271
30. Chang AE, Karnell LH, Menck HR (1998) The National Cancer Data Base report on cutaneous and noncutaneous melanoma: a summary of 84,836 cases from the past decade. The American College of Surgeons Commission on Cancer and the American Cancer Society. Cancer 83(8):1664–1678
31. Goerres GW, Stoeckli SJ, von Schulthess GK et al (2002) FDG PET for mucosal malignant melanoma of the head and neck. Laryngoscope 112(2):381–385
32. Haerle SK, Soyka MB, Fischer DR et al (2012) The value of 18F-FDG-PET/CT imaging for sinonasal malignant melanoma. Eur Arch Otorhinolaryngol 269(1):127–133
33. Roh JL, Yeo NK, Kim JS et al (2007) Utility of 2-[18F] fluoro-2-deoxy-D-glucose positron emission tomography and positron emission tomography/computed tomography imaging in the preoperative staging of head and neck squamous cell carcinoma. Oral Oncol 43(9):887–893
34. Rusthoven KE, Koshy M, Paulino AC (2004) The role of fluorodeoxyglucose positron emission tomography in cervical lymph node metastases from an unknown primary tumor. Cancer 101(11):2641–2649
35. Layland MK, Sessions DG, Lenox J (2005) The influence of lymph node metastasis in the treatment of squamous cell carcinoma of the oral cavity, oropharynx, larynx, and hypopharynx: N0 versus N+. Laryngoscope 115(4):629–639
36. de Bree R, Castelijns JA, Hoekstra OS et al (2009) Advances in imaging in the work-up of head and neck cancer patients. Oral Oncol 45(11):930–935
37. Senft A, de Bree R, Hoekstra OS et al (2008) Screening for distant metastases in head and neck cancer patients by chest CT or whole body FDG-PET: a prospective multicenter trial. Radiother Oncol 87(2):221–229
38. Barbera L, Groome PA, Mackillop WJ et al (2001) The role of computed tomography in the T classification of laryngeal carcinoma. Cancer 91(2):394–407
39. Cavaliere C, Romeo V, Aiello M et al (2017) Multiparametric evaluation by simultaneous PET-MRI examination in patients with histologically proven laryngeal cancer. Eur J Radiol 88:47–55
40. Bertagna F, Albano D, Bosio G et al (2016) 18F-FDG-PET/CT in patients affected by differentiated thyroid carcinoma with positive thyroglobulin level and negative 131I whole body scan. It's value confirmed by a bicentric experience. Curr Radiopharm 9(3):228–234
41. Vera P, Kuhn-Lansoy C, Edet-Sanson A et al (2010) Does recombinant human thyrotropin-stimulated positron emission tomography with [18F]fluoro-2-deoxy-D-glucose improve detection of recurrence of well-differentiated thyroid carcinoma in patients with low serum thyroglobulin? Thyroid 20(1):15–23
42. Hassan A, Riaz S, Zafar W (2016) Fluorine-18 fluorodeoxyglucose avid thyroid incidentalomas on PET/CT scan in cancer patients: how sinister are they? Nucl Med Commun 37(10):1069–1073
43. International Consortium for Outcome Research (ICOR) in Head and Neck Cancer, Ebrahimi A et al (2014) Primary tumor staging for oral cancer and a proposed modification incorporating depth of invasion: an international multicenter retrospective study. JAMA Otolaryngol Head Neck Surg 140(12):1138–1148
44. Youngwirth LM, Adam MA, Scheri RP et al (2017) Extrathyroidal extension is associated with compromised survival in patients with thyroid cancer. Thyroid 27(5):626–631
45. Perrier ND, Brierley JD, Tuttle RM (2018) Differentiated and anaplastic thyroid carcinoma: major changes in the American Joint Committee on Cancer eighth edition cancer staging manual. CA Cancer J Clin 68(1):55–63
46. Wong RJ, Lin DT, Schoder H et al (2002) Diagnostic and prognostic value of [(18)F]fluorodeoxyglucose positron emission tomography for recurrent head and neck squamous cell carcinoma. J Clin Oncol 20(20):4199–4208
47. Zbaren P, Nuyens M, Curschmann J et al (2007) Histologic characteristics and tumor spread of recurrent glottic carcinoma: analysis on whole-organ sections and comparison with tumor spread of primary glottic carcinomas. Head Neck 29(1):26–32
48. Robin P, Abgral R, Valette G et al (2015) Diagnostic performance of FDG PET/CT to detect subclinical HNSCC recurrence 6 months after the end of treatment. Eur J Nucl Med Mol Imaging 42(1):72–78
49. Becker M, Varoquaux AD, Combescure C et al (2018) Local recurrence of squamous cell carcinoma of the head and neck after radio(chemo)therapy: diagnostic performance of FDG-PET/MRI with diffusion-weighted sequences. Eur Radiol 28(2):651–663
50. Zimmer LA, Snyderman C, Fukui MB et al (2005) The use of combined PET/CT for localizing recurrent head and neck cancer: the Pittsburgh experience. Ear Nose Throat J 84(2):104, 106, 108–110
51. Gilbert MR, Branstetter BF, Kim S (2012) Utility of positron-emission tomography/computed tomography imaging in the management of the neck in recurrent laryngeal cancer. Laryngoscope 122(4):821–825
52. Rosko A, Birkeland A, Shuman A et al (2017) Positron emission tomography-CT prediction of occult nodal metastasis in recurrent laryngeal cancer. Head Neck 39(5):980–987
53. Zimmer LA, McCook B, Meltzer C et al (2003) Combined positron emission tomography/computed tomography imaging of recurrent thyroid cancer. Otolaryngol Head Neck Surg 128(2):178–184
54. Kim SK, So Y, Chung HW et al (2016) Analysis of predictability of F-18 fluorodeoxyglucose-PET/CT in the recurrence of papillary thyroid carcinoma. Cancer Med 5(10):2756–2762
55. Kim SY, Roh JL, Yeo NK et al (2007) Combined 18F-fluorodeoxyglucose-positron emission tomography and computed tomography as a primary screening method for detecting second primary cancers and distant metastases in patients with head and neck cancer. Ann Oncol 18(10):1698–1703
56. Rohde M, Nielsen AL, Johansen J et al (2017) Head-to-head comparison of chest X-ray/head and neck MRI, chest CT/head and neck MRI, and (18)F-FDG PET/CT for detection of distant metastases and synchronous cancer in oral, pharyngeal, and laryngeal cancer. J Nucl Med 58(12):1919–1924

Molecular Imaging and Targeted Therapy for Malignant Melanoma

9

Bin Zhang

9.1 General of Malignant Melanoma

Malignant melanoma is a tumor produced by the melanocytes of the skin and other organs. Skin melanoma shows a significant change in pigmented skin lesions for months or years. Most malignant melanoma occurs in adults. Although the incidence of malignant melanoma is low, its malignant degree is high, the metastasis is early, and the mortality is high, so early diagnosis and early treatment are very important.

9.1.1 Etiology

The cause of disease is not yet fully elucidated. Some research data suggest that its occurrence is related to the following risk factors, gene, environment, and genetic/environmental factors, for example, atypical nevus or family history of melanoma, light-induced pigmented skin, hard to tan skin, strong intermittent sunlight exposure, sunburn, and multiple melanocytic nevus. Many factors in the gene/environment cause malignant transformation of melanoma. Key cellular pathways of malignant transformation are Rb pathway, p53 pathway, PI3K/AKT pathway, RAS/MAPK pathway, etc.

9.1.2 Clinical Manifestation

The clinical symptoms of a malignant melanoma of the skin, includes bleeding, pruritus, tenderness, ulcers, etc. In general, the symptoms of melanoma are associated with the age of the disease. Young patients are generally manifested in pruritus, skin lesion color changes, and enlargement. Ulcers usually appear in skin lesions in elderly patients, usually suggesting poor prognosis.

The skin lesion of malignant melanoma of the skin is associated with the anatomical location and the tumor growth pattern, which is related to the histologic type. The types of histology vary greatly from age, type, and race. Different types of melanoma have different etiological and genetic background. At present, the Clark classification of the clinical histologic type of melanoma is used, including four types: malignant freckles nevus melanoma (LMM), superficial diffuse melanoma, acral freckle-like melanoma/mucosal melanoma, and tuberous melanoma (NM).

9.1.3 Diagnosis

Diagnosis requires surgical removal of a full-thickness lesion, including some margins, for biopsy. Melanoma histology reports should include at least the following information: type of melanoma, maximum vertical thickness (mm), mitotic rate under pT1, presence and extent of ulcers or degeneration, and clearance of surgical margins. Physical examination is necessary, with attention to other suspicious pigmented lesions and local LN and distant metastasis. In low-risk melanoma (pT1a), other examinations may not be performed, but in higher tumor stages, imaging is recommended for appropriate staging [1, 2].

The ABCDE standard can be used to judge the suspicious skin lesions. A (Asymmey) represents asymmetry. B (Border irregularity) represents irregular boundaries. C (Color variegation) represents color diversity. D (Diameter > 6 mm) represents diameter greater than 6 mm, and E (Elevation, 6 mm) represents skin damage uplift and progress. If the skin damage conforms to the ABCDE standard, it is highly suspected of malignant melanoma, and biopsy should be taken for histopathological examination to further confirm the diagnosis. However, some subtypes, such as nodular melanoma, cannot be judged by the ABCDE standard.

B. Zhang (✉)
The First Affiliated Hospital of Soochow University, Suzhou, P. R. China

G. Huang (ed.), *Nuclear Medicine in Oncology*, https://doi.org/10.1007/978-981-13-7458-6_9

9.1.4 Histopathology

Melanocytes are abnormal, and some cell nests are formed in the epidermis or epidermis-dermis. These cell nests are different in size and can be fused with each other. The size and shape of the melanocytes in the nests, as well as the shape of the nuclei, vary in varying degrees. Mitosis (including abnormal mitosis) in malignant melanoma cells is more common than benign pigmented nevus, and there are pigment granules in the cytoplasm of tumor cells. In invasive malignant melanoma, the tumor cells infiltrate into the dermis or subcutaneous tissue. Immunohistochemical staining includes S100-positive tumor cells, HMB45 positive, and Melan-A positive.

9.1.5 Pathological Grading

9.1.5.1 Invasion Depth Classification

After Clark (1969) studying the relationship between the invasion depth of the melanoma and the prognosis, the melanoma was divided into five levels according to the depth of the invasion. The higher the grade, the worse the prognosis.

- Grade I: the tumor cells are confined to the epidermis above the basement membrane.
- Grade II: tumor cells break through the basilar membrane to the dermal papilla layer.
- Grade III: the tumor cells are filled with the dermal papilla layer and further infringe, but not to the dermis reticular layer.
- Grade IV: tumor cells have encroached on the dermis reticular layer.
- Grade V: the tumor cells have passed through the dermal reticular layer and infringe on the subcutaneous fat layer.

9.1.5.2 Vertical Thickness Classification

Breslow (1970) studied the relationship between the vertical thickness of melanoma and prognosis. According to the thickest part of melanoma (the thickness from the granular layer to the deepest part of melanoma), the melanoma was divided into five grades.

- Grade I: Less than 0.75 malignant melanoma of the skin.
- Grade II: 0.76–1.50 malignant melanoma of the skin.
- Grade III: 1.51–3.00 malignant melanoma of the skin.
- Grade IV: 3.01–4.50 malignant melanoma of the skin.
- Grade V: More than 4.50 malignant melanoma of the skin.

The greater the thickness, the worse the prognosis, and this classification method has been proved to be of great value in judging the prognosis.

9.1.6 Treatment

Surgical removal of early nonmetastatic lesions should be performed. The normal skin around the lesion need cut off, and the range of the normal skin should be determined according to the depth of Breslow standard. If it is a malignant melanoma of the finger/toes, the finger/toe truncation could be used. Metastatic lymph nodes should be removed, but prophylactic lymph node dissection is still controversial. It is effective to treat limb melanoma by instillation of against mitotic drugs by limb artery. Combined chemotherapy and radiation therapy can be used for people with extensive metastasis. Biochemical therapy and molecular targeted therapy have great prospects.

9.1.7 Prognosis

The prognosis depends on the staging of the diagnosis. Only local focus, no lymph node and distant metastasis have better prognosis. The survival rate of women in stage I/II was higher than that of men. The prognosis of primary melanoma in the trunk or head and neck was lower than that of the extremities. Age is inversely proportional to the survival rate of melanoma. Stage III melanoma has distinct different prognosis: the number of ulceration and lymph node metastasis suggests poor prognosis. The important prognostic factor of stage IV melanoma is the location of distant metastasis, and the prognosis of visceral metastasis is worse than that of non-visceral (skin and distal lymph node) metastasis.

9.2 Targeted Therapy of Malignant Melanoma

Patients with early stage melanoma could be cured by surgical excision. But the treatment of metastatic malignant melanoma turns to be difficult, and patients' prognosis was poor. In advanced cases with metastases, palliative treatment may start with well-tolerated cell inhibitors including dacarbazine (DTIC), taxanes, cytokines (interferon, interleukin-2), and combined treatments [2]. The FDA has approved the use of interferon, interleukin-2, and DTIC in the treatment of melanoma. Interferon and interleukin-2 have been shown to stimulate the immune response to reach the antitumor effect; however, the clinical application is limited by the low response rate and toxicity.

9.2.1 Selective BRAF Inhibitors

Many targeted inhibitors have been developed and are in clinical trials. Activation mutations of serine/threonine-protein kinase B-RAF (BRAF) were found in about 50% of

patients with advanced melanoma. Several highly selective inhibitors have been developed for this target. Vemurafenib (PLX4032) has been approved for the treatment of melanoma in the United States and the European Union and shows a high rate of rapid tumor response (about 50%) in patients with V600E mutation [3].

Another BRAF inhibitor dabrafenib (GSK2118436) showed similar effectively as vemurafenib, and a patient with $BRAF^{V600E}$-mutated metastatic malignant melanoma achieved a complete metabolic response after 7 months of treatment with the combination of dabrafenib and trametinib. About 46 months later after the beginning of treatment, PET scans have showed a complete metabolic remission [4].

9.2.2 Selective MEK Inhibitors

The regulatory role of MAP/extracellular signal-regulated kinase (MEK) 1/2 in the Ras/Raf/MEK/ERK pathway makes it a promising target for melanoma treatment.

Tramebinib (GSK1120212) is a selective MEK inhibitor approved by FDA in 2013. In a phase III clinical trial, metastatic melanoma patients who carry a BRAF mutation were given 2 mg of trametinib or chemotherapy treatment every day during the trial. The median PFS of patients was longer in the trametinib group (4.8 months) than those in the chemotherapy group (1.5 months). After 6 months of treatment, patients in the trametinib group has a higher OS rate than those in the chemotherapy group (81% vs. 67%) [5].

Selumetinib (also known as AZD6244/ARRY-142886) is an effective, selective, and allosteric MEK 1/2 inhibitor for melanoma treatment. In a phase II multicenter clinical trial for unresectable stage III/IV melanomas, they found that among six patients who had partially responded to selumetinib, five of them were BRAF mutation carriers [6].

9.2.3 Immunotherapy

Immune checkpoint inhibitors induce antitumor immune responses by disinhibiting native immunity. FDA has approved several immune checkpoint inhibitors for the treatment of unresectable or metastatic melanoma. Ipilimumab, an antibody against cytotoxic T-lymphocyte-associated protein 4 (CTLA-4), blocks immune inhibitory interactions between CTLA-4 and B7. Nivolumab and pembrolizumab, antibodies that target programmed cell death receptor 1 (PD-1), inhibit interactions between this receptor and its ligand (PD-L1) [7]. These agents have revolutionized the care of patients with advanced cutaneous melanoma and also induce durable objective responses in a wide spectrum of malignances.

Ipilimumab, the first immune checkpoint inhibitor approved by FDA, is a monoclonal antibody (mAb) against human immunoglobulin (Ig) G1. It has been used to block cytotoxic T lymphocyte antigen (CTLA)-4 in metastatic melanoma. Both of ipilimumab and high dose IL-2 showed good and persistent responses in melanoma. Compared with IL-2, ipilimumab is more tolerant but with a lower response rate. In an ipilimumab study with 1861 melanoma patients, about 20% of the patients survived after 3 years. Importantly, most of patients who survived at the 3-year time point remained to survive for up to 10 years. Since the tumor response patterns are often varied during immunotherapy, it is suggested that survival follow-up data may serve as a better index for evaluating immunotherapy response.

Objective responses to single-agent PD-1 antibody therapy appear to be most common in tumors that have pretreatment tumor infiltration with cytotoxic lymphocytes and intratumoral expression of markers of T-cell exhaustion, including PD-L1. Although these immune checkpoint inhibitors have demonstrated substantial activity in advanced cutaneous melanoma, their role in uveal melanoma has not yet been defined. In cutaneous melanoma, ipilimumab induces objective responses in 11–19% of patients, with a 2-year OS rate of 24%. Anti-PD-1 monotherapy with pembrolizumab or nivolumab confers objective responses and durable remissions in 30–40% of patients with cutaneous melanoma and has a favorable toxicity profile.

Antibodies against programmed death receptor 1 (PD-1) is a promising treatment for advanced cutaneous melanoma. The efficacy and safety of PD-1 antibodies in melanoma were evaluated in a multicenter clinical recruiting stage IV uveal melanoma patients who received PD-1 (pembrolizumab or nivolumab) or PD-L1 (atezolizumab) antibodies treatment. The treatment was well tolerated, and only one patient stopped treatment due to drug toxicity. In total eligible 56 patients, the median PFS and OS were 2.6 months and 7.6 months, respectively. However, this study found that PD-1 and PD-L1 treatment rarely result in lasting remission in metastatic uveal melanoma [8].

9.3 The Application of PET/CT Imaging in Patients with Malignant Melanoma [9]

9.3.1 Recommendations and Guidelines

Malignant melanoma is a rare type of cancer; however, it accounts for 90% of skin cancer-related deaths [1]. According to the 2008 American Joint Cancer Commission (AJCC) melanoma staging database, the stage IA melanoma patients have a 5-year survival rate of 97%, while the rate drops to 15–20% in patients with stage IV melanoma. PET/CT

imaging has been suggested as an important approach for melanoma staging, especially for patients with III and IV stages [1–3].

9.3.2 PET/CT for Initial Staging and Preoperative Assessment

^{18}F-FDG-PET/CT is useful for the detection of melanoma metastases, especially in patients with stage III and IV melanoma, while the application of ^{18}F-FDG-PET/CT in patients with stage I and II melanoma is limited [10]. The pooled sensitivity and specificity of ^{18}F-FDG-PET/CT are 83% and 85%, respectively. In general, the diagnostic performance of PET/CT is better than other imaging methods. In addition, the combination of CT and PET can provide more accurate staging information than using PET only.

A meta-analysis included 74 studies and more than 10,000 patients was performed to investigate the use of CT, PET, and PET/CT for the staging and surveillance of melanoma patients [11]. The results suggested that PET/CT had a better performance in detecting distant metastasis for staging when compared to use PET or CT only [11]. For staging of distant metastases, PET/CT had the highest sensitivity (80%), specificity (87%), and diagnostic odds ratio (25). Meanwhile, the limited benefit of PET/CT in stages I and II diseases was confirmed [12, 13], because ^{18}F-FDG PET/CT imaging demonstrated very low sensitivity and positive predictive value for localizing the subclinical nodal metastases [13].

Reported in Chinese reference, the pooled sensitivity, specificity, and accuracy of ^{18}F-FDG PET/CT in the diagnosis of primary malignant melanoma are 90.9% (40/44 cases), 88.2% (15/17 cases), and 90.2% (55/61 cases), respectively [14, 15]. ^{18}F-FDG PET/CT has a better performance during whole-body staging other than detecting primary site of lymph node metastases in malignant melanoma [15].

Cutaneous melanoma and non-cutaneous melanoma have different tumor features. Non-cutaneous melanoma is associated with fewer BRAF mutations and worse prognosis. A patient, male, age 84, was admitted to hospital because of intermittent hemoptysis for 3 months, which aggravated for 1 week. The patient had no history of pulmonary tuberculosis and no fever. A malignant tumor of the lungs was considered, and PET/CT imaging was performed for initial staging. Right lung mass with increased glucose metabolism was found in PET/CT imaging, and SUVmax of the mass was 11.66 (Fig. 9.1a). Bilateral hilar lymph nodes were also found with increased glucose metabolism, and SUVmax was 3.67 (Fig. 9.1b). Pathological findings were in accordance with malignant melanoma, with metastases to hilar lymph nodes.

9.3.3 PET/CT for Follow-Up and Assessment of Recurrence

Danielsen et al. summarized seven studies on the diagnostic role of PET/CT in asymptomatic patients at high risk of recurrence and concluded that PET/CT is not only helpful in detecting tumor recurrence with high positive predictive value but also helpful in identifying tumor-free patients with high negative predictive value [16]. Thus, PET/CT imaging can be used as a prognostic method. In 90 patients, the risk of melanoma-related death was significantly higher in PET-positive patients than in serum protein S100B-positive patients. Therefore, the effect of PET/CT imaging is better than that of clinical often-used serum protein S100B [17].

Bastiaannet et al. studied the relationship between standardized uptake value (SUV) of PET and disease-free survival rate in 80 patients with stage III B. The results showed that ^{18}F-FDG uptake in tumors was negatively correlated with disease-free survival rate [18]. Rueth et al. compared the effectiveness of CT and PET/CT imaging in detecting life expectancy related melanoma recurrence. Compared with CT alone, the false-positive rate of PET/CT was lower (9–20%) [19]. It is worth noting that the high diagnostic performance of PET/CT imaging for distant metastases may lead to better choice of treatment options for patients with resectable diseases [20, 21]. Bronstein et al. reported that unexpected metastases were found in 12% of examinations for melanoma patients, which changed the clinical treatment regimen [20].

According to autopsy, the most common metastasis site of non-cutaneous malignant melanoma was the liver (93%), followed by the lung and bone (24% and 16%, respectively) mainly due to hematogenous spread [22]. Behavior of liver metastases of ocular melanoma appears to be different from that of cutaneous melanoma. Strobel et al. studied the value of ^{18}F-FDG PET/CT and serum protein S100B in detecting liver metastasis of cutaneous and uveal melanoma and found that both PET/CT and S100B were less sensitive to liver metastasis of uveal melanoma than to metastatic diseases of cutaneous melanoma. It should be emphasized that the absence of intravenous contrast agents in the above studies may reduce the diagnostic performance of PET/CT. Maximum standardized uptake value (SUVmax) of liver metastases from uveal melanoma was significantly lower than that from cutaneous melanoma [23]. Although several authors reported the better role of PET/CT in the diagnosis of liver metastasis of uveal melanoma [24, 25], comparative studies of PET/CT and liver MRI can conclude that liver MRI is superior to PET/CT in the diagnosis of liver metastasis, especially in small lesions [26, 27].

Reported in Chinese reference, the sensitivity, specificity, and accuracy of ^{18}F-FDG-PET/CT in detecting recurrence or metastasis of malignant melanoma were 100.0% (19/19),

85.7% (12/14), and 93.9% (31/33), respectively, in patients with malignant melanoma after radical operation [14]. Therefore, ^{18}F-FDG PET/CT is a valuable imaging method for detecting residual, recurrent, and metastatic tumors in patients with melanoma.

In a patient, male, age 54, right foot and hip tumor lump excision was performed 2 years ago, and pathological findings were in accordance with malignant melanoma. After this operation, inguinal lymph node dissection was performed 2 months later, and 6 times of DTIC plus DDP chemotherapy were carried out. Extensive resection of right foot tumor mass was performed 1 year ago, and local chemotherapy was used after operation. PET/CT imaging was performed in our department for evaluating treatment effect and searching for metastasis. Left axillary lymph nodes, right abdominal lymph nodes, pelvic lymph nodes, and bilateral inguinal lymph nodes were enlarged. These lymph nodes with increased glucose metabolism were found in PET/CT imaging, and SUVmax of the

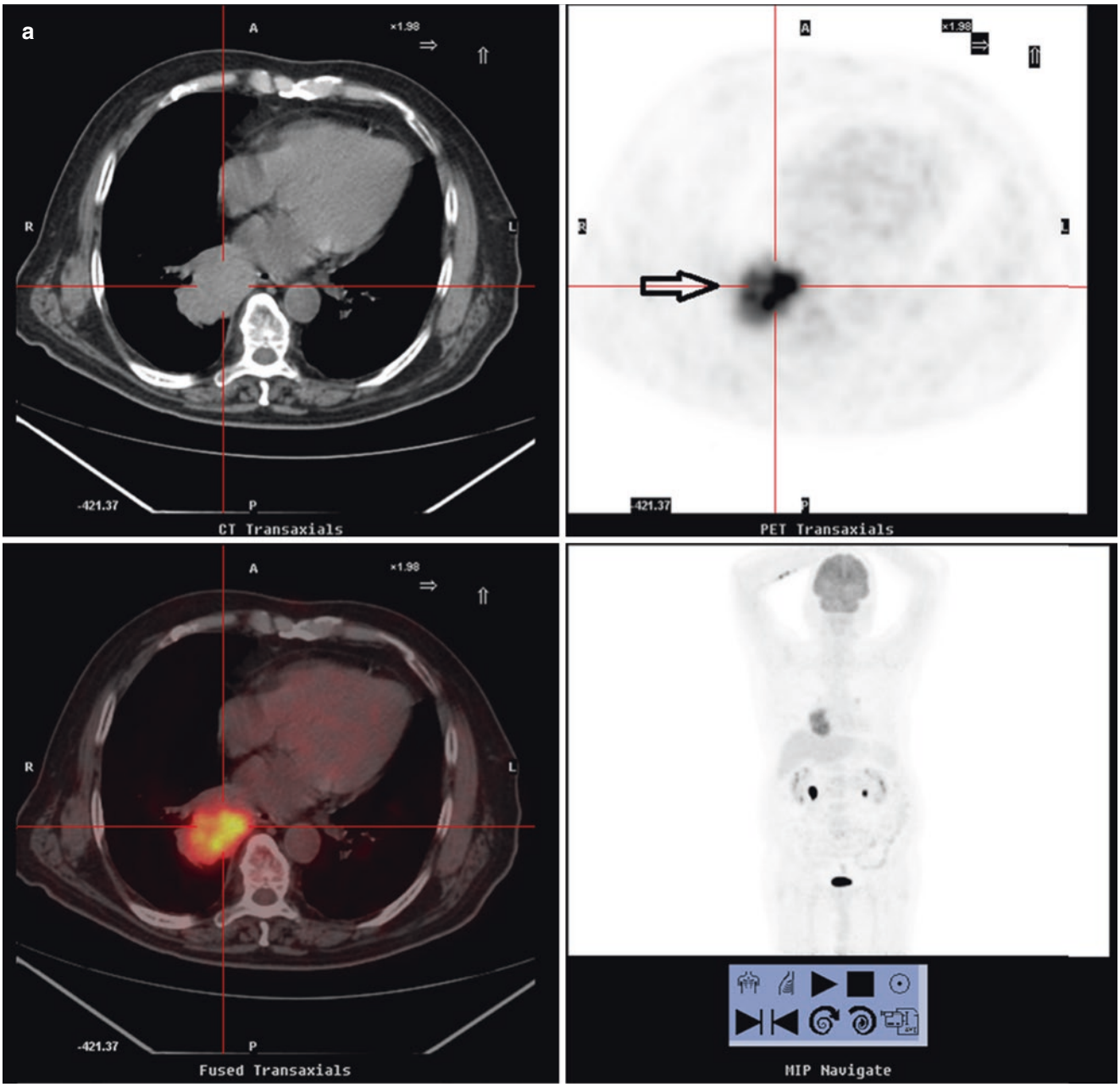

Fig. 9.1 (**a**, **b**) ^{18}F-FDG PET/CT imaging of a patient with lung malignant melanoma

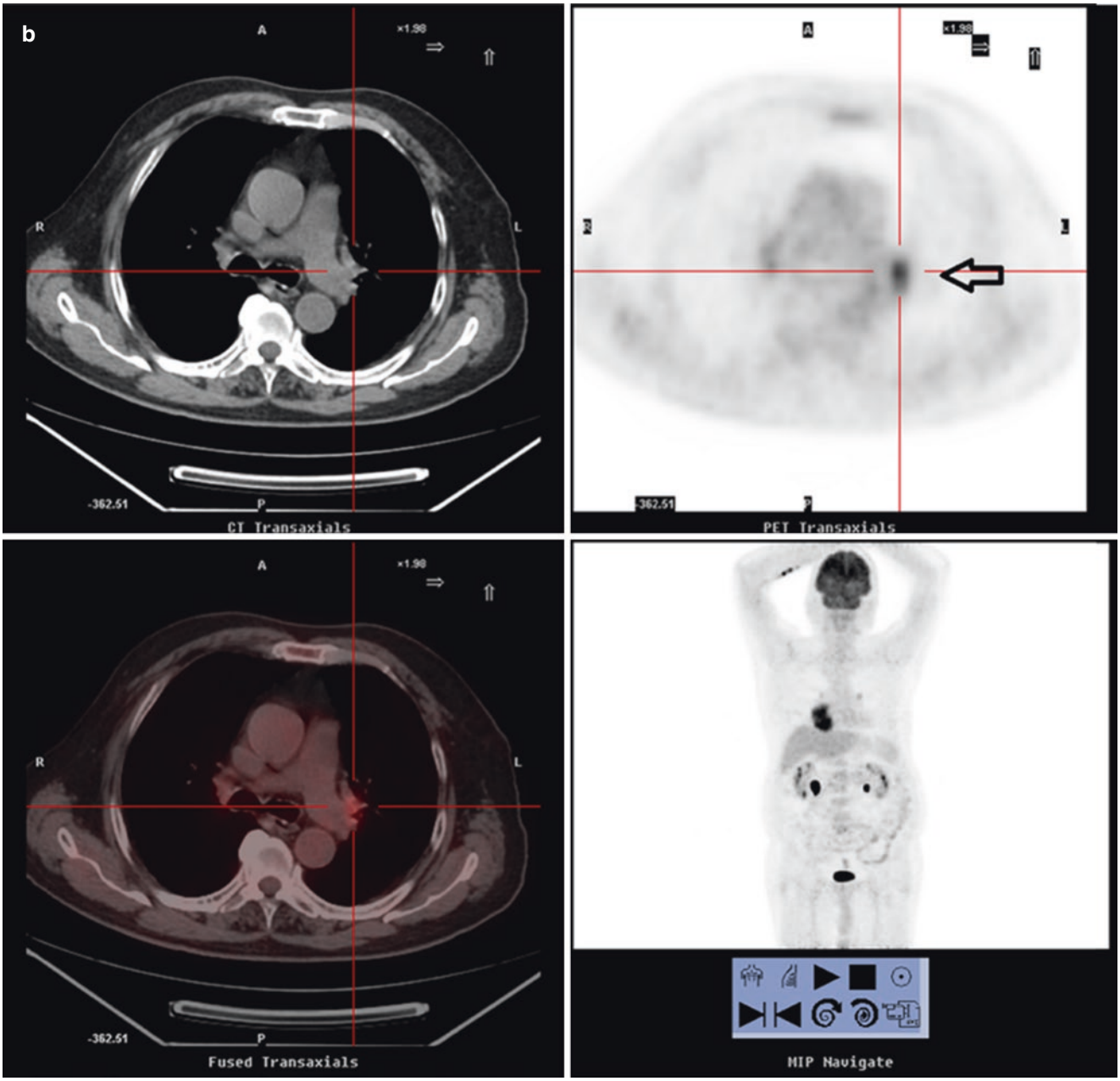

Fig. 9.1 (continued)

right inguinal mass was 10.39 (Fig. 9.2a). Multiple subcutaneous soft tissue shadows were seen on the right hip and right lower extremities in PET/CT imaging, and SUVmax of the focus in the right calf was 6.10 (Fig. 9.2b).

9.3.4 Therapy Assessment of Targeted Therapies

Wolchok et al. reported an evaluation criterion for immunotherapy response in a phase II clinical trial of ipilimumab [28]. After ipilimumab monotherapy treatment, four different response patterns were observed, including reduction of baseline lesions, durable stable diseases, response after increased overall tumor burden, and response to new lesions. Since these four patterns are accompanied by favorable survival, new immune-related response evaluation criteria need to be introduced to explain these increased response patterns. PLX4032 (also known as RG7204) is an orally available mutant BRAF inhibitor, which has been reported to have a rapid complete or partial regression in the treatment of metastatic melanoma [29]. ^{18}F-FDG PET/CT plays a good role in

response assessment after conventional chemotherapy or early response assessment after two cycles of chemotherapy [30, 31]. Also, PET/CT can evaluate the therapeutic response of BRAF inhibitors very early in preclinical studies and may be used as a new biomarker and dose adjustment index [32, 33]. Since new targeted therapies are accompanied by a series of side effects, some of which are more serious, early response assessment is helpful. Because some side effects manifest as inflammatory changes, it is important to understand the image characteristics and clinical significance of PET/CT and other imaging techniques. Especially, sarcoid-like patterns cannot be mistaken for disease progression [9].

9.3.5 Other Targets and PET Tracers in Melanoma

New methods and targets for melanoma therapy and PET imaging are being studied, some of which may be located in signaling pathways involved in tumor angiogenesis. Integrins are a family of transmembrane receptor proteins that promote cell survival and differentiation and are essential for the growth and metastasis of tumors. Integrin $\alpha_v\beta_3$ is expressed in 86% of tumorigenic vertical growth phase melanomas and 96% of metastatic lesions and has a high affinity for arginine-glycine-aspartate (RGD) tripeptide sequence. In

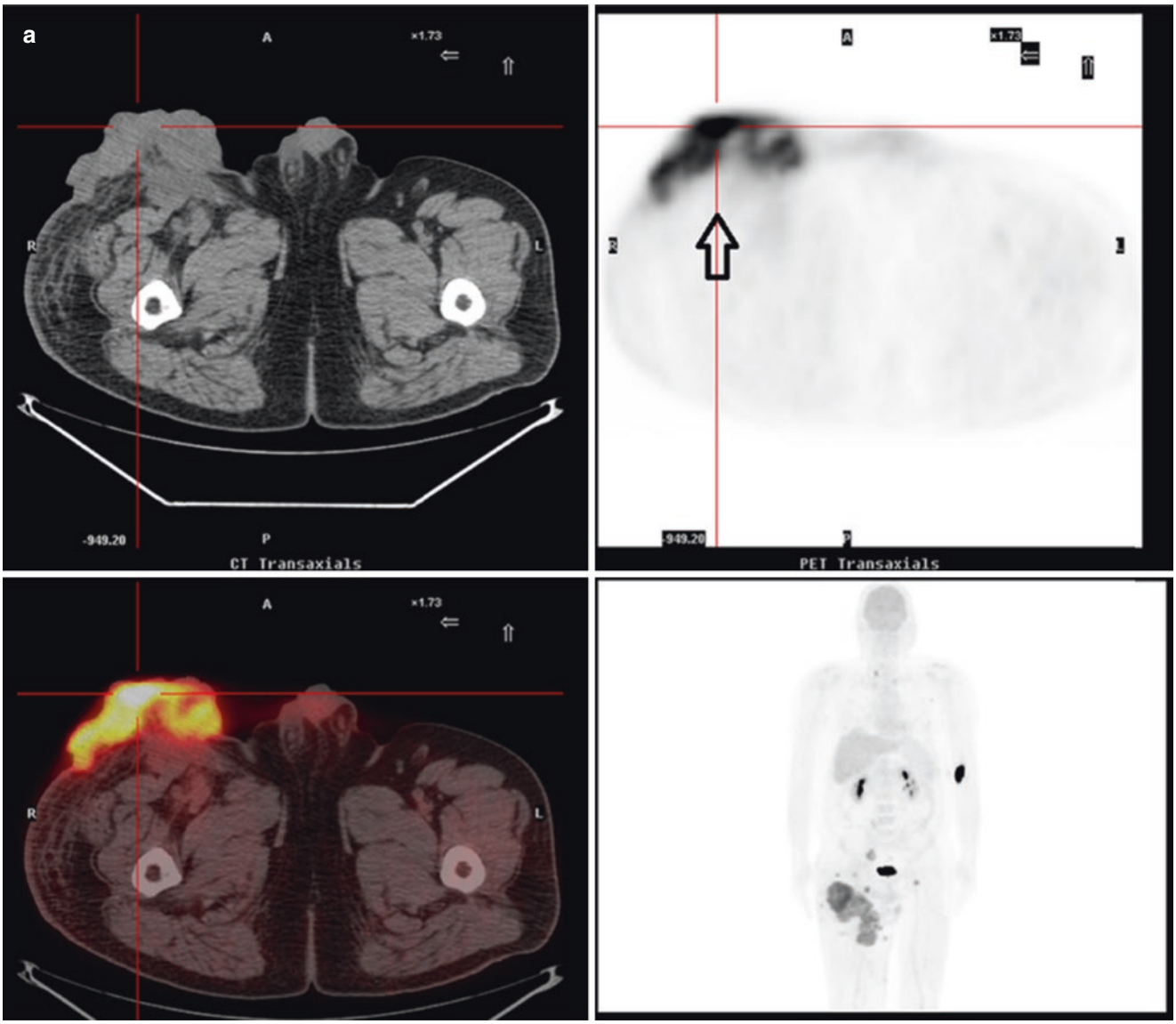

Fig. 9.2 (**a**, **b**) ^{18}F-FDG PET/CT imaging of a patient with recurrence and metastases

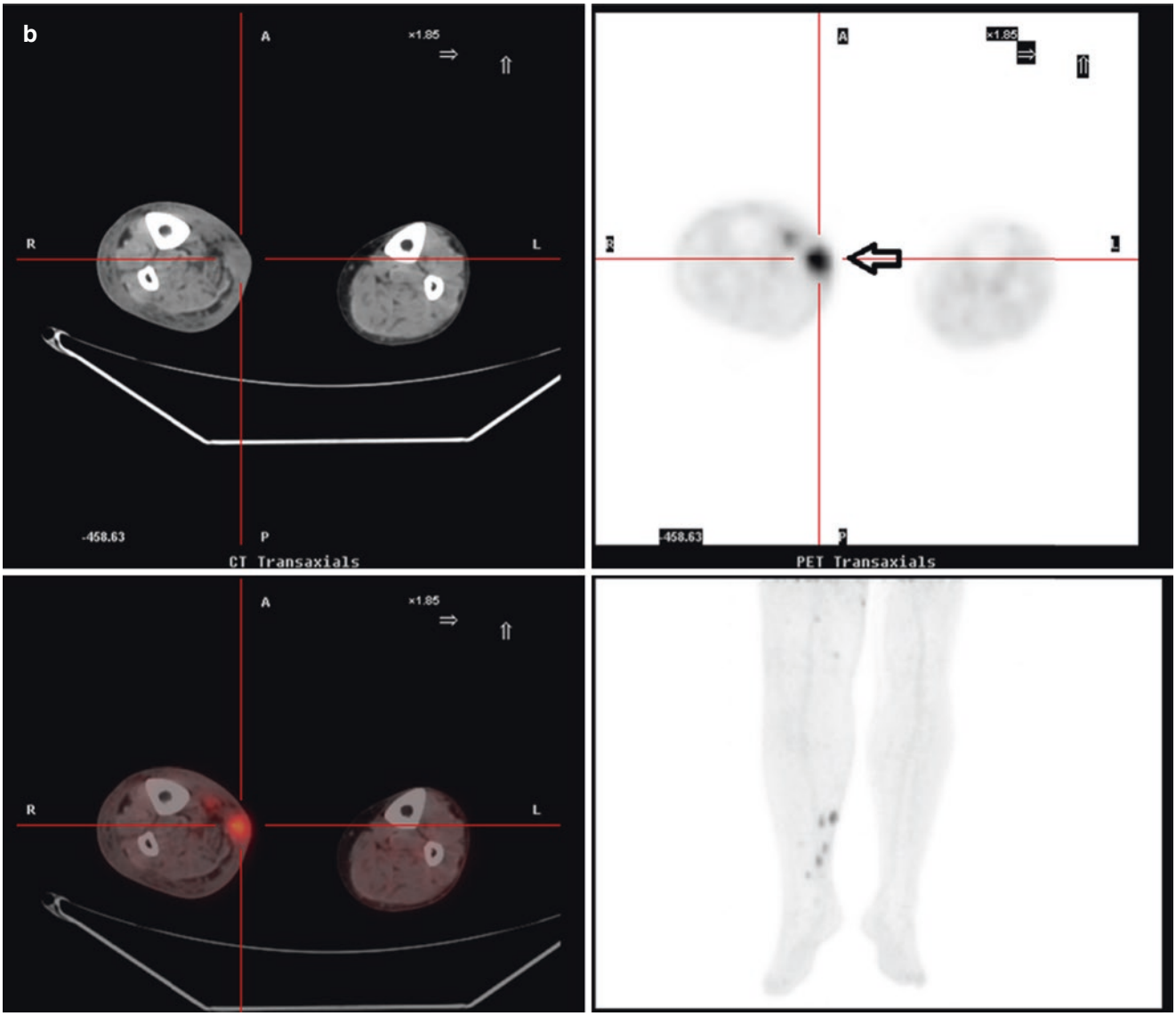

Fig. 9.2 (continued)

terms of treatment, substances that inhibit these integrins have been reported [34, 35]. ^{18}F-fluciclatide is a synthetic cyclic polypeptide with high affinity for RGD binding sites integrins $\alpha_v\beta_3$ and $\alpha_v\beta_5$. Mana et al. reported measurable uptake of melanoma focus in six melanoma patients [36]. These types of tracers can detect the expression of integrins and help physicians to plan anti-angiogenesis therapies.

As a radionuclide produced by cyclotron, ^{64}Cu emits both beta + and beta- radiation with an intermediate half-life of 12.7 h, which makes it suitable for the integrated diagnosis and treatment of melanoma (PET imaging and radionuclide therapy), so-called theranostic approaches. Qin et al. proposed a tracer $^{64}CuCl_2$ that binds to human copper transporter 1 (CTR1) [37]. CTR1 is overexpressed in a lot of cancer cells, including two melanoma cell lines (B16F10 and A375M). Feasibility studies on animals have been successfully carried out, and it laid a foundation for the research of transformational medicine.

^{18}F-FDG is not a tumor-specific imaging agent, and it can accumulate in tissues with high levels of glucose uptake and metabolism, especially in inflammatory tissues. Therefore, more specific radiotracers for tumors, such as ^{18}F-FLT [32] and ^{18}F-5-FPN [38], deserve attention. The new radiotracer ^{18}F-FITM, 4-^{18}F-N-[4-[6-(isopropylamino)pyrimidin-4-yl]-1, 3-thiazol-2-yl]-N-methylbenzamide, specifically targets metabotropic glutamate-1, a receptor that induces melanocyte carcinogenesis, and has a good target/nontarget ratio in the imaging of metabotropic glutamate-1 positive melanoma-bearing mice [39].

9.3.6 Conclusions

PET/CT imaging is recommended for patients with melanoma in the initial preoperative staging of stage III and IV diseases. With the emergence of new therapies, the interpretation of imaging needs to be further improved and adapted.

References

1. Dummer R, Hauschild A, Lindenblatt N et al (2015) Cutaneous melanoma: ESMO clinical practice guidelines for diagnosis, treatment and follow-up. Ann Oncol 26(S5):v126–v132
2. Dummer R, Hauschild A, Guggenheim M et al (2010) Melanoma: ESMO clinical practice guidelines for diagnosis, treatment and follow-up. Ann Oncol 21(S5):v194–v197
3. Garbe C, Peris K, Hauschild A et al (2012) Diagnosis and treatment of melanoma. European consensus-based interdisciplinary guideline—update 2012. Eur J Cancer 48(15):2375–2390
4. Brugnara S, Sicher M, Bonandini EM et al (2018) Treatment with combined dabrafenib and trametinib in $BRAF^{V600E}$-mutated metastatic malignant melanoma: a case of long-term complete response after treatment cessation. Drugs Context 7:212515
5. Flaherrty K, Robert C, Hersey P et al (2012) Improved survival with MEK inhibition in BRAF-mutated melanoma. N Engl J Med 367:107–114
6. Kirkwood J, Bastholt L, Robert C et al (2012) Phase II, open-label, randomized trial of the MEK 1/2 inhibitor selumetinib as monotherapy versus temozolomide in patients with advanced melanoma. Clin Cancer Res 18:555–567
7. Mahoney KM, Freeman GJ, McDermott DF (2015) The next immune-checkpoint inhibitors: PD-1/PD-L1 blockade in melanoma. Clin Ther 37(4):764–782
8. Algazi AP, Tsai KK, Shoushtari AN et al (2016) Clinical outcomes in metastatic uveal melanoma treated with PD-1 and PD-L1 antibodies. Cancer 122:3344–3353
9. Schwenzer NF, Pfannenberg AC (2015) PET/CT, MR, and PET/MR in lymphoma and melanoma. Semin Nucl Med 45:322–331
10. Krug B, Crott R, Lonneux M et al (2008) Role of PET in the initial staging of cutaneous malignant melanoma: systematic review. Radiology 249(3):836–844
11. Xing Y, Bronstein Y, Ross MI et al (2011) Contemporary diagnostic imaging modalities for the staging and surveillance of melanoma patients: a meta-analysis. J Natl Cancer Inst 103(2):129–142
12. Veithaibach P, Vogt FM, Jablonka R et al (2009) Diagnostic accuracy of contrast-enhanced FDG-PET/CT in primary staging of cutaneous malignant melanoma. Eur J Nucl Med Mol Imaging 36(6):910–918
13. Singh B, Ezziddin S, Palmedo H et al (2008) Preoperative 18F-FDG-PET/CT imaging and sentinel node biopsy in the detection of regional lymph node metastases in malignant melanoma. Melanoma Res 18(5):346–352
14. Li DL, Li HS, Wang QS et al (2008) Clinical value of ^{18}F-FDG PET/CT in detection of malignant melanoma. Chin J Nucl Med 28(5):295–298
15. Hu YY, Lin XP, Liang PY et al (2009) Application of ^{18}F-FDG PET/CT in diagnosis and staging of malignant melanoma. Chin J Med Imag Technol 25(4):685–688
16. Danielsen M, Hojgaard L, Kjar A et al (2013) Positron emission tomography in the follow-up of cutaneous malignant melanoma patients: a systematic review. Am J Nucl Med Mol Imaging 4(1):17–28
17. Wieder HA, Tekin G, Rosenbaum-krumme S et al (2013) ^{18}FDG-PET to assess recurrence and long term survival in patients with malignant melanoma. Nuklearmedizin 52(5):198–203
18. Bastiaannet E, Hoekstra OS, de Jong JR et al (2012) Prognostic value of the standardized uptake value for 18F-fluorodeoxyglucose in patients with stage IIIB melanoma. Eur J Nucl Med Mol Imaging 39(10):1592–1598
19. Rueth NM, Xing Y, Chiang YJ et al (2014) Is surveillance imaging effective for detecting surgically treatable recurrences in patients with melanoma? A comparative analysis of stage-specific surveillance strategies. Ann Surg 259(6):1215–1222
20. Bronstein Y, Ng CS, Rohren E et al (2012) PET/CT in the management of patients with stage IIIC and IV metastatic melanoma considered candidates for surgery:evaluation of the additive value after conventional imaging. Am J Roentgenol 198(4):902–908
21. Harris MT, Berlangieri SU, Cebon JS et al (2005) Impact of 2-deoxy-2[F-18] fluoro-D-glucose positron emission tomography on the management of patients with advanced melanoma. Mol Imaging Biol 7(4):304–308
22. Willson JK, Albert DM, Diener-West M et al (2001) Assessment of metastatic disease status at death in 435 patients with large choroidal melanoma in the Collaborative Ocular Melanoma Study (COMS): COMS report no. 15. Arch Ophthalmol 119(5):670–676
23. Strobel K, Bode B, Dummer R et al (2009) Limited value of 18F-FDG PET/CT and S-100B tumour marker in the detection of liver metastases from uveal melanoma compared to liver metastases from cutaneous melanoma. Eur J Nucl Med Mol Imaging 36(11):1774–1782
24. Klingenstein A, Haug AR, Nentwich MM et al (2010) Whole-body F-18-fluoro-2- deoxyglucose positron emission tomography/computed tomography imaging in the follow-up of metastatic uveal melanoma. Melanoma Res 20(6):511–516
25. Francken AB, Fulham MJ, Millward MJ et al (2006) Detection of metastatic disease in patients with uveal melanoma using positron emission tomography. Eur J Surg Oncol 32(7):780–784
26. Servois V, Mariani P, Malhaire C et al (2010) Preoperative staging of liver metastases from uveal melanoma by magnetic resonance imaging (MRI) and fluorodeoxyglucose-positron emission tomography (FDG-PET). Eur J Surg Oncol 36(2):189–194
27. Orcurto V, Denys A, Voelter V et al (2012) ^{18}F-fluorodeoxyglucose positron emission tomography/computed tomography and magnetic resonance imaging in patients with liver metastases from uveal melanoma: results from a pilot study. Melanoma Res 22(1):63–69
28. Wolchok JD, Hoos A, O'Day S et al (2009) Guidelines for the evaluation of immune therapy activity in solid tumors: immune-related response criteria. Clin Cancer Res 15(23):7412–7420
29. Flaherty KT, Puzanov I, Kim KB et al (2010) Inhibition of mutated, activated BRAF in metastatic melanoma. N Engl J Med 363(9):809–819
30. Strobel K, Skalsky J, Steinert HC et al (2007) S-100B and FDG-PET/CT in therapy response assessment of melanoma patients. Dermatology 215(3):192–201
31. Hofman MS, Constantinidou A, Acland K et al (2007) Assessing response to chemotherapy in metastatic melanoma with FDG PET: early experience. Nucl Med Commun 28(12):902–906
32. Geven EJ, Evers S, Nayak TK et al (2015) Therapy response monitoring of the early effects of a new BRAF inhibitor on melanoma xenograft in mice: evaluation of F-FDG-PET and F-FLT-PET. Contrast Media Mol Imaging 10(3):203–210
33. Guerreschi P, Scalbert C, Qassemyar A et al (2013) Patient-derived tumor xenograft model to guide the use of BRAF inhibitors in metastatic melanoma. Melanoma Res 23:373–380
34. O'Day S, Pavlick A, Loquai C et al (2011) A randomised, phase II study of intetumumab, an anti-alphav-integrin mAb, alone and with dacarbazine in stage IV melanoma. Br J Cancer 105(3):346–352

35. Kim KB, Prieto V, Joseph RW et al (2012) A randomized phase II study of cilengitide (EMD 121974) in patients with metastatic melanoma. Melanoma Res 22(4):294–301
36. Mena E, Owenius R, Turkbey B et al (2014) [^{18}F]fluciclatide in the in vivo evaluation of human melanoma and renal tumors expressing αvβ 3 and α vβ 5 integrins. Eur J Nucl Med Mol Imaging 41(10):1879–1888
37. Qin C, Liu H, Chen K et al (2014) Theranostics of malignant melanoma with $^{64}CuCl_2$. J Nucl Med 55(5):812–817
38. Wang Y, Li M, Zhang Y et al (2017) Detection of melanoma metastases with PET-comparison of ^{18}F-5-FPN with ^{18}F-FDG. Nucl Med Biol 50:33–38
39. Xie L, Yui J, Fujinaga M et al (2014) Molecular imaging of ectopic metabotropic glutamate 1 receptor in melanoma with a positron emission tomography radioprobe 18F-FITM. Int J Cancer 135(8):1852–1859

Role of ^{18}F-FDG PET/CT in Pediatric Oncology

10

Hongliang Fu, Suyun Chen, and Hui Wang

PET has been recognized as a powerful imaging modality for a variety of diseases in adults, mainly cancer. PET is also emerging as an increasingly important tool in diagnosis, staging, treatment assessment, and surveillance in children and adolescents with cancer. This chapter reviews the clinical role of ^{18}F-FDG PET/CT in pediatric oncology and its radiation safety.

10.1 Brief Introduction of Pediatric Malignancies

Although cancer can be considered much less common in children than in adults, it is the second most common cause of death among children in the United States [1]. The incidence of pediatric cancer has been increasing slightly by 0.6% per year since 1975. Among children and adolescents ages 0–19 years, 1 in 285 children was diagnosed with cancer in 2014 and 43 children per day are expected to be diagnosed with malignant disease in the United States [1]. The cancer mortality rate has continuously declined by more than 50% from 1975–1977 to 2010–2014. For several types of cancer, the improvement has been dramatic, especially acute lymphoblastic leukemia, while outcome remains dismal for some cancers and for some age groups. The crude incidence of childhood cancer was 129 per million among children and adolescents ages 0–15 years in Shanghai between 2009 and 2011 [2].

There is marked variation in the incidence rates of cancer types at different ages in children. The most common types of cancer diagnosed in children ages 0–14 years are leukemias, which accounts for 29–36% of all childhood cancers [2]. Brain and other nervous system tumors (26%), lymphomas, and reticuloendothelial neoplasms (11%) are the second and third most common cancer type, respectively, followed by neuroblastoma (6%), soft-tissue sarcomas (6%), and Wilms tumors (5%) [1].

Adolescents (aged 15–19 years) are often diagnosed with different types of cancer. The most common cancer types diagnosed in adolescents are lymphomas (21%), followed by brain and other central nervous system tumors (17%), leukemias (14%), germ cell tumors (12%), thyroid carcinoma (11%), and melanoma (5%) [1].

10.2 Clinical Application of ^{18}F-FDG PET/CT in Pediatric Malignancies

10.2.1 Physiological Uptake

Proper interpretation of pediatric ^{18}F-FDG PET/CT requires thorough knowledge of the physiological ^{18}F-FDG uptake in children, which may differ from that in adults. Markedly high FDG uptake typically can be seen in Waldeyer rings due to high physiological activities of the lymphatic tissues that peak at 6–8 years [3] (Fig. 10.1). Diffuse and homogeneous FDG uptake in the thymus is common in healthy children. It may extend superior to the left brachiocephalic vein and anterior to the brachiocephalic artery or left common carotid artery and appears as a soft-tissue nodule [4] (Fig. 10.2). FDG activity of the thymus change with a time-dependent pattern following chemotherapy. The lowest thymic volume and FDG uptake is at cessation of chemotherapy, rebounds afterward, and peaks on average 10 months after therapy [5]. Intense FDG uptake in the diaphragm, the crura of the diaphragm, and the intercostal muscles is commonly seen in children who have been crying during the uptake

H. Fu (✉) · S. Chen · H. Wang
Department of Nuclear Medicine, Xinhua Hospital Shanghai Jiao Tong University, School of Medicine, Shanghai, P. R. China

G. Huang (ed.), *Nuclear Medicine in Oncology*, https://doi.org/10.1007/978-981-13-7458-6_10

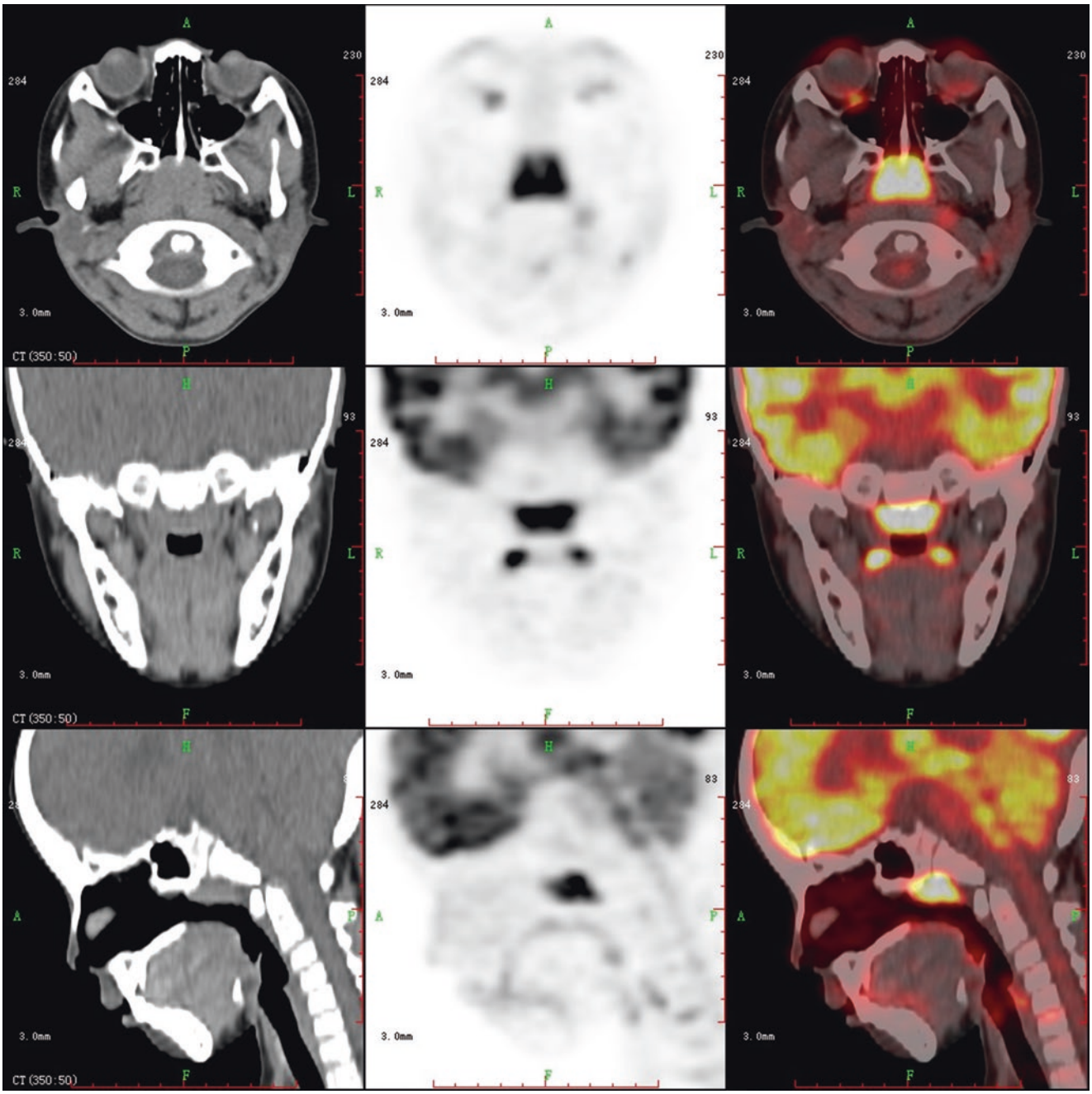

Fig. 10.1 Transverse, coronal, and sagittal PET/CT images show increased FDG uptake in adenoid in a 5-year-old boy as well as symmetric uptake in normal tonsils

phase [3] (Fig. 10.3). Physiological linear uptake in physes and apophyses (skeletal growth centers) could be identified in skeletally immature pediatric patients (Fig. 10.4). FDG uptake in spinal cord is significantly higher at cervical and lower thoracic levels than that at upper thoracic level [6].

Knowledge of physiological ^{18}F-FDG activity in pediatric patients is essential for a correct interpretation of PET/CT scans to avoid potential pitfalls.

10.2.2 Lymphoma

Hodgkin's lymphoma (HL) and non-Hodgkin lymphoma (NHL) account for 10–15% of pediatric malignancies. HL makes up about 40% of cases and NHL about 60%. HL is the most common childhood cancer during adolescence. The two major types are nodular sclerosing and mixed cellularity HL. It appears rarely widespread at the time of diagnosis. On

the contrary, pediatric NHL is often a rapidly progressing disease and widely spreads at diagnosis. It differs markedly from the adult forms of NHL. The most common types are as follows: Burkitt lymphoma, lymphoblastic lymphoma, diffuse large B-cell lymphoma, anaplastic large cell lymphoma, and primary mediastinal B-cell lymphoma.

Most childhood lymphoma types show intensive FDG avidity [7]. Comparisons between ^{18}F-FDG PET or PET/CT and conventional imaging methods in staging of pediatric HL resulted higher sensitivity and specificity (^{18}F-FDG PET: 96.5% vs. 87.5% for sensitivity, 96.7% vs. 85.2% for specificity; ^{18}F-FDG PET/CT: 98% vs. 77% for sensitivity, 99.6% vs. 98.7% for specificity) [8, 9]. Multifocal patterns of bone marrow involvement are typical in HL and are often missed by regular iliac bone marrow biopsy. In a large prospective clinical trial evaluating the role of ^{18}F-FDG PET/CT to detect bone marrow involvement in pediatric HL, ^{18}F-FDG PET/CT shows a higher sensitivity than bone marrow biopsy, and they suggest that PET can be substituted for a routine bone marrow biopsy [10]. Based on our study of 93 pediatric NHL patients, all of the aggressive types had intense FDG uptake higher than the liver. Anaplastic large cell lymphoma showed the most intense FDG activity with SUV_{max} of 21.0, followed by mature B-cell NHL. Lymphoblastic lymphoma had the lowest SUV_{max} of 6.7 [11]. In NHL, due to insufficient data available, the International Pediatric Non-Hodgkin Lymphoma Staging System suggested that PET should be used with caution for staging and PET results should be

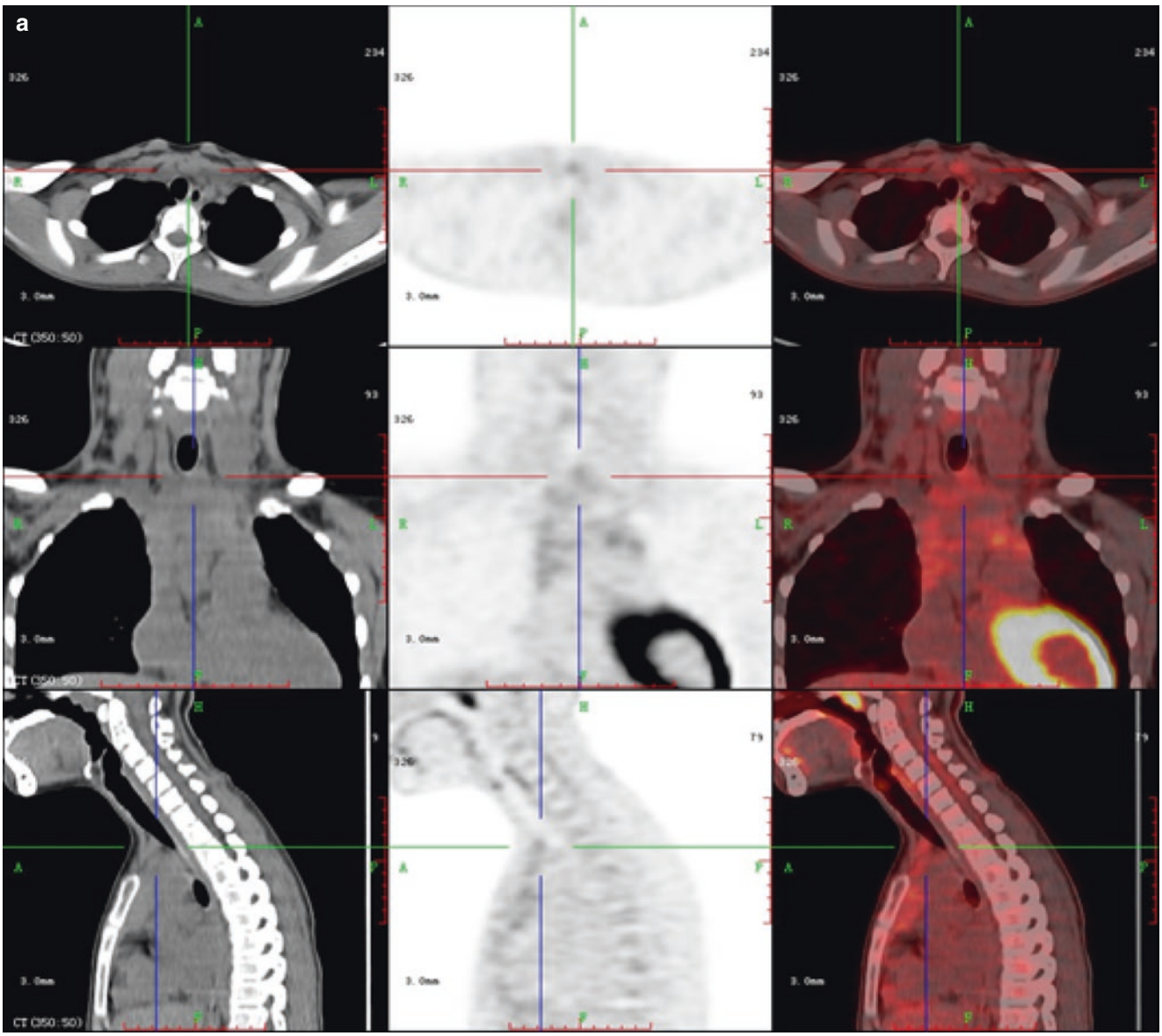

Fig. 10.2 FDG PET scan shows diffuse increased ^{18}F-FDG uptake in the thymus with an inverted V shape. It may extend to the lower cervical and appear as a soft-tissue nodule (**a**), which could show no obvious connection with the thymus (**b**)

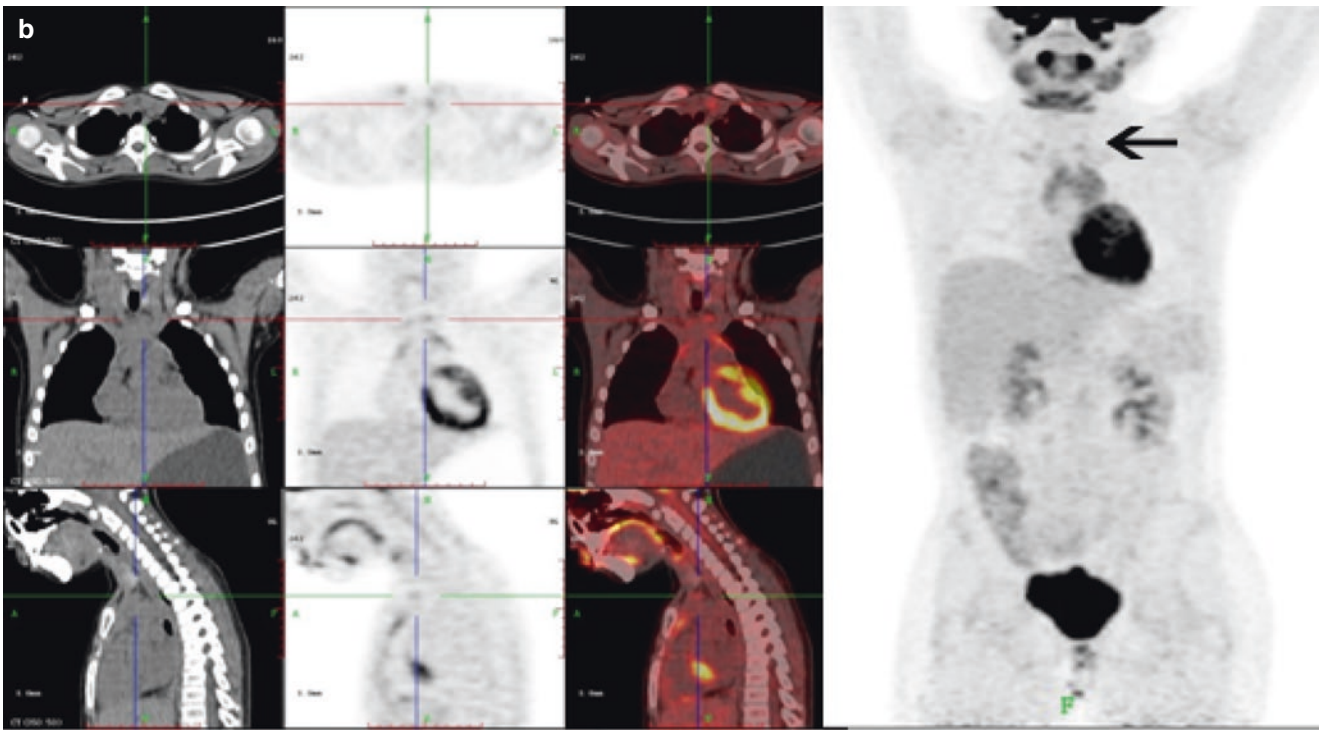

Fig. 10.2 (continued)

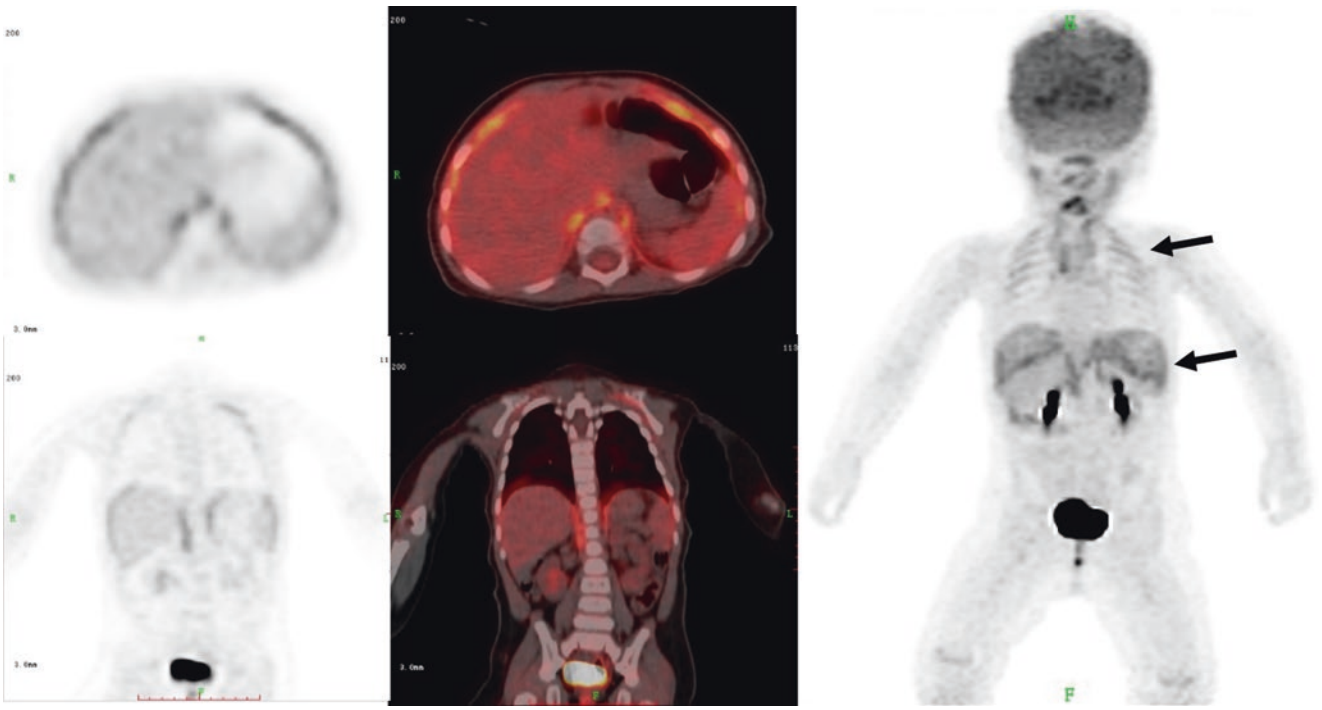

Fig. 10.3 Transverse, coronal, and maximum-intensity-projection (MIP) ^{18}F-FDG PET images show marked linear uptake (arrows) corresponding to the intercostal muscle and diaphragm in a 1-year-old girl who was crying after ^{18}F-FDG injection

compared and discussed in light of other imaging approaches [12]. Nevertheless, we found that ^{18}F-FDG PET/CT upstaged 13% pediatric patients with newly diagnosed NHL [11]. We also suggested PET/CT was highly accurate for detecting bone marrow involvement in pediatric patients with NHL. Bone marrow biopsy might be omitted in selected patients: cases with bone marrow FDG uptake less intense than the liver are unlikely to have bone marrow involvement;

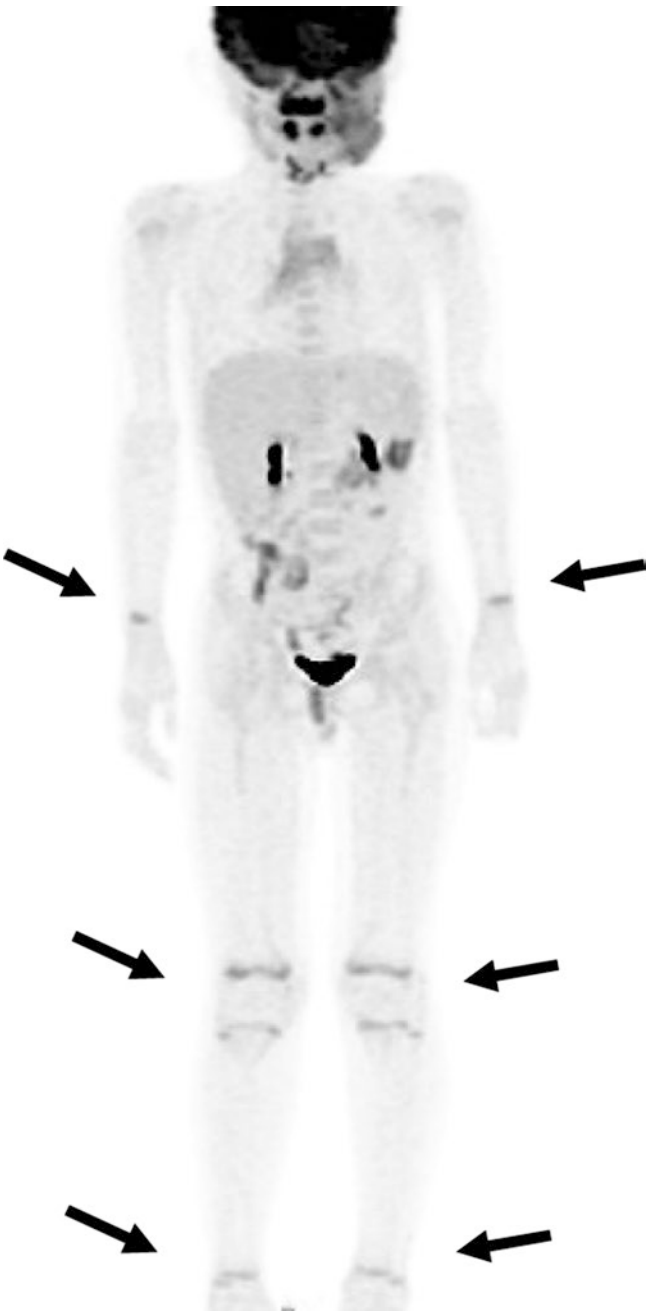

Fig. 10.4 MIP FDG PET image of a 4-year-old boy with B-cell lymphoblastic lymphoma shows symmetrical linear ^{18}F-FDG uptake in the physes of the distal radius and femora and both proximal and distal tibiae

cases with limited focal deposits (<10 lesions) distant from the iliac crest are similarly unlikely to gain from bone marrow biopsy [11]. In 45 patients presenting homogeneously increased bone marrow uptake, positive bone marrow biopsy was achieved in 93% (14/15) of patients with FDG uptake expanding to the distal portion of extremities, compared to 7% (2/30) of those without (Fig. 10.5).

Dramatic progress has been achieved for childhood lymphomas, with estimated 5-year survival rates exceeding 98% for HL and higher than 80% for NHL, respectively. After chemotherapy, absence of FDG uptake in a residual mass is predictive of complete remission, while increased FDG uptake may indicate residual or recurrent tumor. Studies have shown that negative findings on an early interim FDG PET during the course of chemotherapy are associated with an excellent prognosis in childhood HL, whereas children with positive interim PET findings had a significantly higher relapse rate [13]. With increasing concerns about second malignancies in childhood cancer survivors, the focus of treatment approaches for pediatric HL has been shifted to minimizing toxicity and possible late effects while preserving high cure rates. ^{18}F-FDG PET-guided treatment adaptation has been increasingly studied in clinical trials. The five-point Deauville score (5PS), which is widely used as a treatment response standard, defines that a score of 3 or less in adult trials using intensive chemotherapy regimens indicates complete metabolic response. The definitions for PET response assessment in pediatric HL adopted a threshold of 5PS of 4 for PET positivity in EuroNet-PHL-C2 trial, with the aim to increase the portion of patients in whom radiotherapy could be omitted.

Compared with adulthood NHL, experience in ^{18}F-FDG PET/CT imaging in pediatric NHL is relatively sparse. In 2015, international standardized criteria for treatment response assessment in children and adolescents with NHL was developed. Negative PET findings (5PS of 1–3) are considered complete response or complete response unconfirmed [14] (Fig. 10.6). Data containing 18 childhood NHL show that a negative ^{18}F-FDG PET/CT finding is a good indicator of complete remission, while false positivity of PET relating to necrosis or inflammation is relatively common (40%) [15]. Thus, biopsy and close monitoring are suggested for accurate determination of residual disease in pediatric NHL with positive PET findings.

In conclusion, ^{18}F-FDG PET/CT is a valuable modality for pediatric lymphoma and now being used widely for disease evaluation and treatment response assessment; however, more prospective data are required for stronger evidence.

10.2.3 Bone and Soft-Tissue Sarcomas

Pediatric sarcomas account for 13% of childhood malignancies. The most common types are osteosarcoma, Ewing sarcoma, and rhabdomyosarcoma. Other histologic subtypes, including malignant peripheral nerve sheath tumor, synovial sarcoma, and desmoplastic small round cell tumor, are grouped under the classification of non-rhabdomyosarcoma soft-tissue sarcoma. Event-free survival rates are approximately 70% for children and adolescents with localized osteosarcoma or Ewing sarcoma, while recurrent or metastatic disease has a poor prognosis with overall survival rates between 10 and 40%. The prognosis of rhabdomyosarcoma

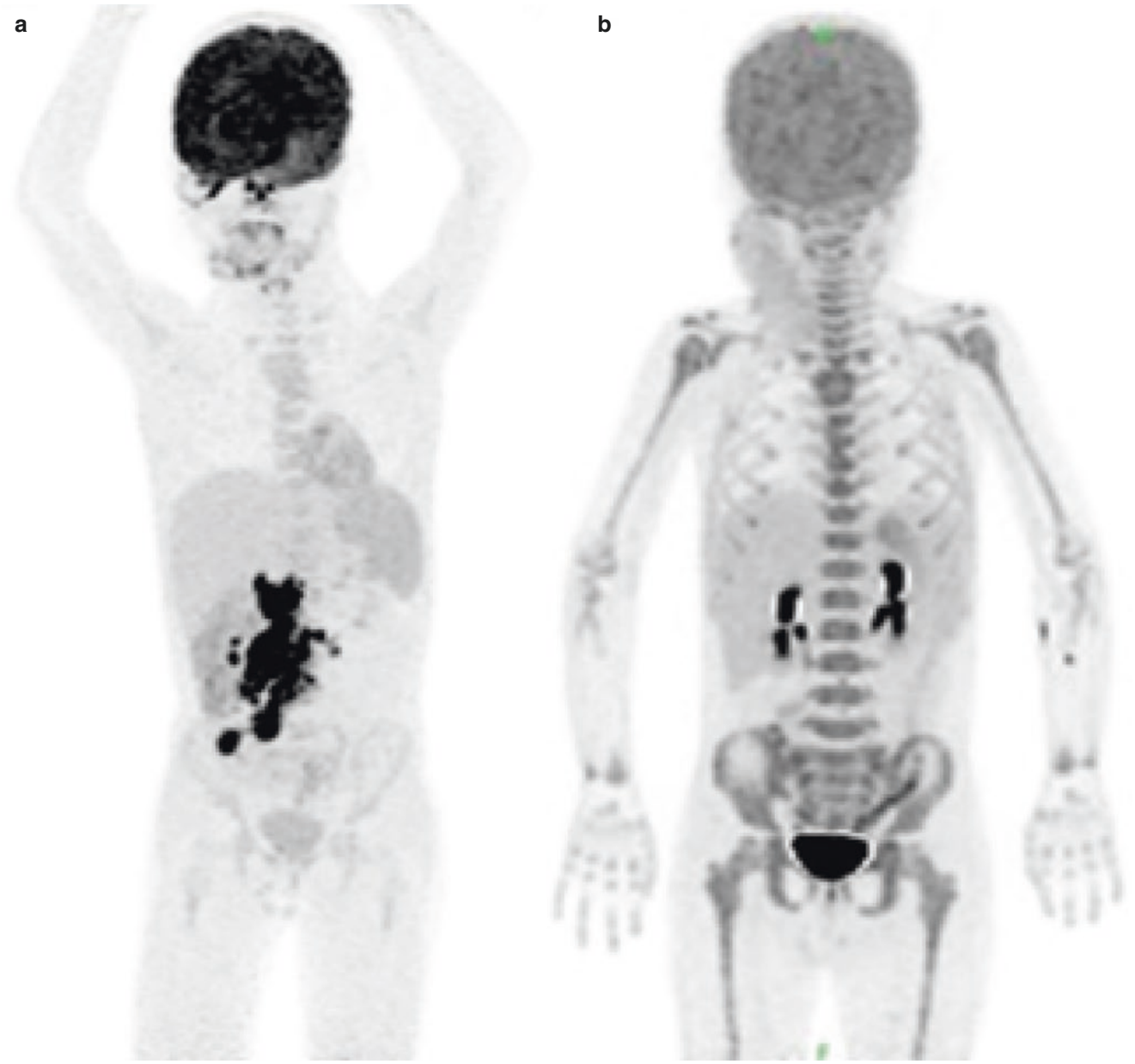

Fig. 10.5 Representative MIP images of homogeneously increased FDG uptake in bone marrow. (**a**) FDG uptake in the bone marrow with an intensity higher than liver activity within the axial skeleton while sparing the distal portion of extremities: a 7-year-old boy with Burkitt lymphoma and a negative bone marrow biopsy. (**b**) Homogeneously and diffusely increased FDG uptake involving both the axial skeleton and distal portion of extremities: a 5-year-old boy with B-cell lymphoblastic lymphoma/leukemia and a positive bone marrow biopsy

is determined based on a risk classification system (TNM stage, histologic subtype, and primary tumor location), with event-free survival of 90%, 65%, and 30% for low-risk, intermediate-risk, and high-risk, respectively.

The role of ^{18}F-FDG PET/CT in pediatric sarcomas has been studied. At the time of initial diagnosis, ^{18}F-FDG PET/CT was found to have higher sensitivity to detect distant bone metastases as compared to bone scintigraphy (93–95% vs. 73–76% for osteosarcoma [16, 17]; 88% vs. 37% for Ewing sarcoma [18]). For surveillance follow-up, PET/CT also demonstrates high accuracy for the detection of recurrence both in pediatric patients with osteosarcoma [19] and Ewing sarcoma [20] and provides higher accuracy than conventional imaging (95% vs. 67% for CT and 86% for MRI) [19]. In the case of rhabdomyosarcoma, PET/CT is reported to be effective in identifying lymph node, bone, and marrow diseases as compared to conventional imaging techniques, with sensitivities and specificities of 89–100% for detection of nodal diseases and 95–100% and 80–100%, respectively, for detection of distant metastases [14, 21].

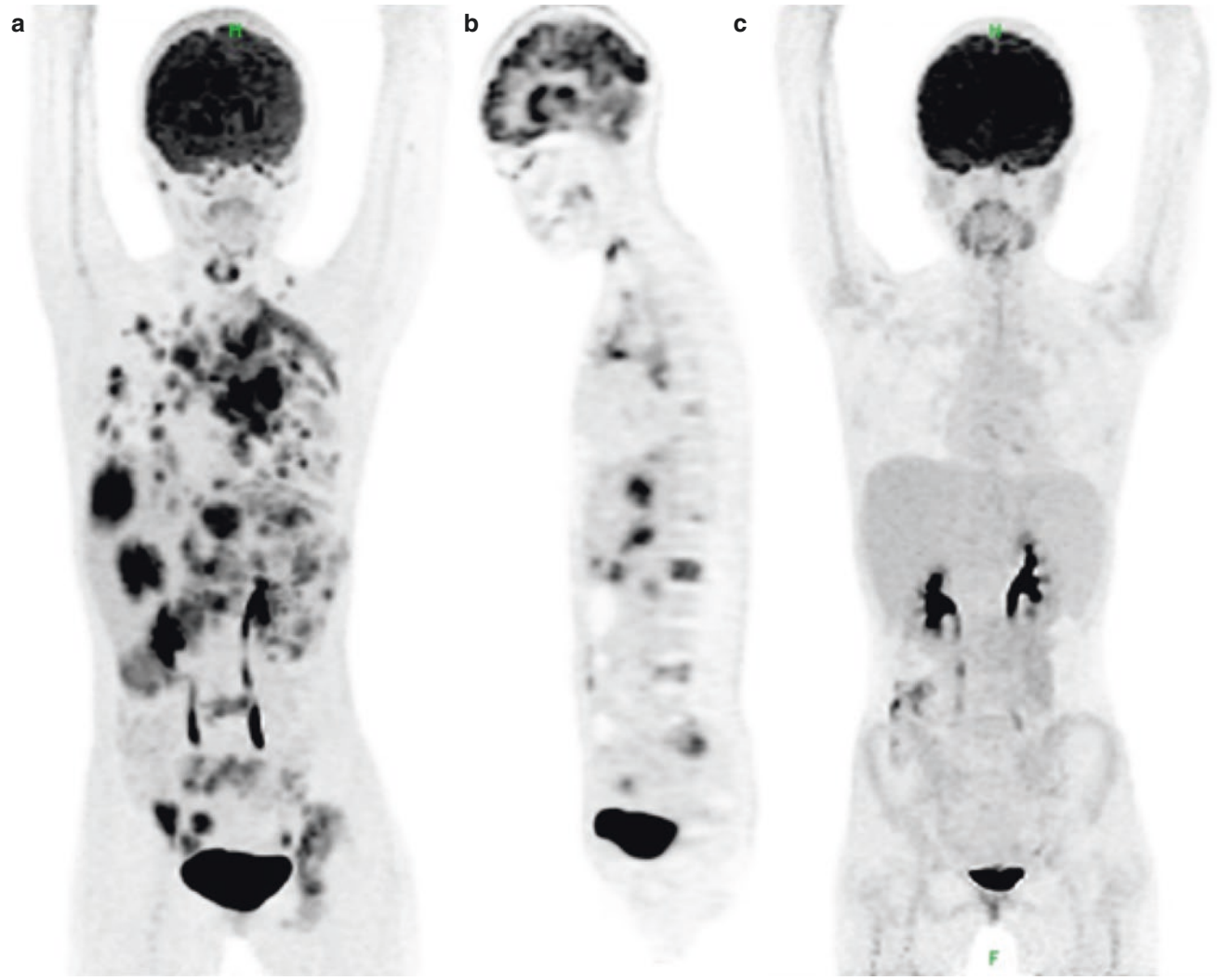

Fig. 10.6 11-year-old girl with DLBCL. (**a**) MIP images of ^{18}F-FDG PET/CT show extensive disease involvement. (**b**) Sagittal images show multifocal increased FDG uptake in bone marrow. (**c**) Interim PET/CT reveals excellent response with 5PS of 3 after four cycles of chemotherapy. Two years follow-up showed no relapse

Metabolic activity of the primary tumor on ^{18}F-FDG PET/CT scan predicts outcome in pediatric patients with sarcomas at diagnosis [22–24]. Rhabdomyosarcomas show variable intensity of FDG uptake (Fig. 10.7). In a study of 41 rhabdomyosarcoma cases, higher FDG uptake of the primary tumor with $SUV_{max}/SUV_{liver} > 4.6$ correlated with poor outcome, on the contrary, all patients with FDG uptake of the primary tumor less than the liver activity survived during follow-up [22]. Our results are in agreement with others; we found that the high SUV_{max} of pediatric alveolar rhabdomyosarcoma indicated worse prognosis [24]. Ewing sarcoma usually presents intense FDG uptake and widespread disease (Fig. 10.8). In patients with Ewing sarcoma, a cutoff threshold of 11.6 was suggested to predict low survival rate [23].

Metabolic response assessment by ^{18}F-FDG PET/CT correlates with histologic response and survival outcome following neoadjuvant chemotherapy in patients with bone and soft-tissue sarcomas. In osteosarcoma, SUV_{max} on posttreatment PET scans are reported to predict tumor response more accurately than change of tumor volume [25, 26]. A reduction of SUV_{max} by 62–75% from baseline to interim PET is also an indicator of treatment responders and better survival outcome [26, 27]. For pediatric patients with rhabdomyosarcoma, a complete metabolic response on PET following induction chemotherapy was reported to correlate with longer survival [28]. By contrast, the role of PET for treatment response assessment in Ewing sarcoma is not yet clear due to contradicting results. SUV_{max} during or after neoadjuvant chemotherapy was found to be associated with survival in retrospective studies [29, 30], whereas it failed to predict outcome in a prospective study [26].

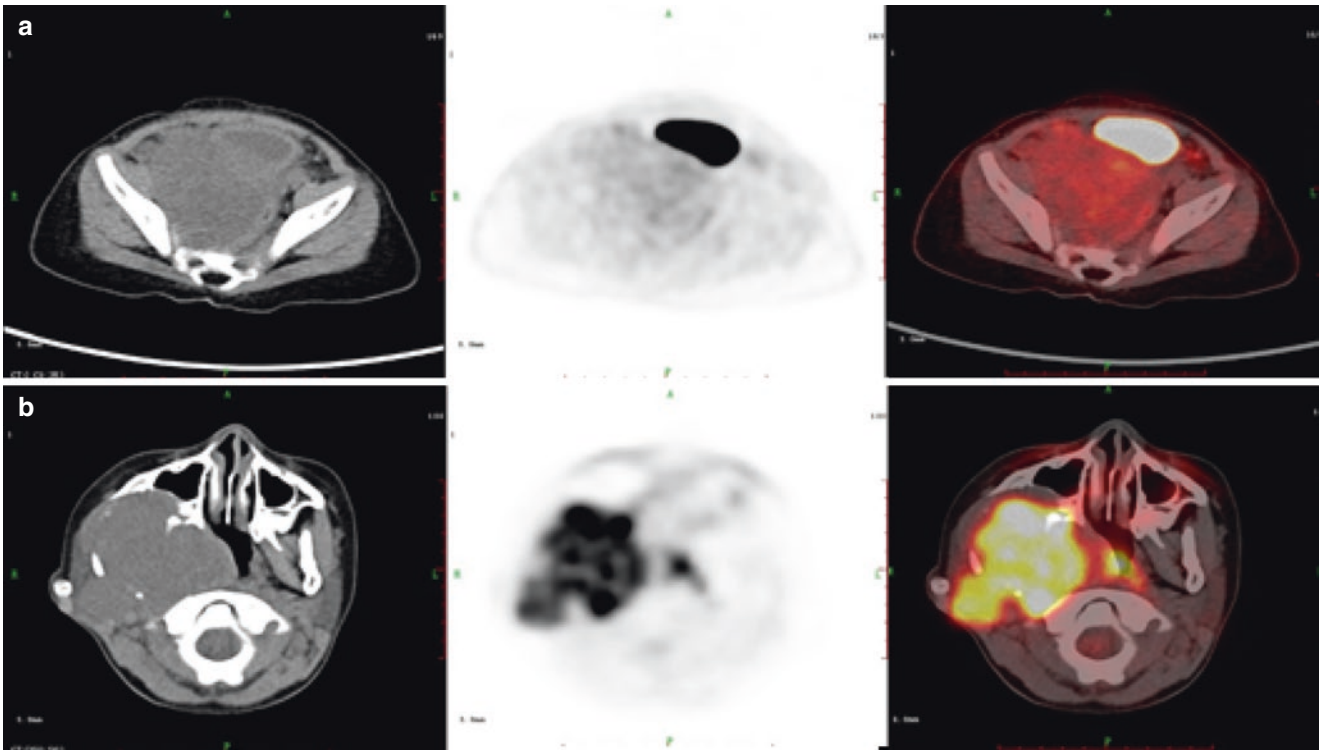

Fig. 10.7 PET/CT images of rhabdomyosarcoma with variable degrees of FDG uptake. (**a**) SUV_{max} of the bladder embryonal rhabdomyosarcoma in a 2-year-old boy with 3.3; (**b**) SUV_{max} of the alveolar rhabdomyosarcoma in an 8-year-old boy was 9.5

10.2.4 Neuroblastoma

Neuroblastoma, an embryonal tumor derived from the peripheral sympathetic nervous system, is the most common pediatric extracranial solid tumor. Approximately 70–80% patients older than 18 months have metastatic diseases at the time of diagnosis. Age, stage, and phenotype features are prognostic factors and are used for risk stratification and treatment assignment. Although patients with low- or intermediate-risk disease have excellent prognosis, those with high-risk or metastatic diseases have long-term survival of less than 40%.

^{123}I-metaiodobenzylguanidine (MIBG) is the fundamental approach in the staging of neuroblastoma, evaluation for ^{131}I therapy, treatment response assessment, and surveillance follow-up. Because most neuroblastomas (about 90%), especially those high-risk ones, are metabolically active [31], ^{18}F-FDG PET/CT has become an important approach complementary to MIBG imaging (Fig. 10.9). Study showed that ^{18}F-FDG PET was superior in depicting stage I and II neuroblastoma, while ^{123}I-MIBG was superior in the evaluation of stage IV disease [32, 33]. However, PET/CT better delineated disease extent. Other studies suggest the superiority of PET to detect neuroblastoma lesions compared to ^{123}I-MIBG or CT [34, 35]. A combined PET/CT approach leads to more accurate detection of metastatic lymph nodes and bone or bone marrow lesions than ^{131}I-MIBG scintigraphy [36]. Furthermore, ^{18}F-FDG PET/CT provides additional prognostic information in patients with neuroblastoma that SUV_{max} of the tumor independently correlated with survival [31, 37]. Progression-free survival rates were over 80.0% in patients with low FDG uptake, while it was less than 30% in those with high FDG uptake [37]. Based on 47 pediatric patients with newly diagnosed neuroblastoma in our institution, we concluded that pretreatment ^{18}F-FDG PET/CT had significant prognostic value for neuroblastoma patients. High metabolic tumor volume, total lesion glycolysis, or focal/multifocal bone marrow uptake on PET indicated inferior survival outcomes [38].

In conclusion, both ^{123}I-MIBG and ^{18}F-FDG PET/CT provide staging and prognosis information in neuroblastoma. Since MIBG has not been proved by the China Food and Drug Administration yet, FDG PET/CT becomes a valuable imaging tool for staging, restaging, and response to therapy for neuroblastoma in China. The future role of non-FDG PET/CT, such as radiolabeled DOTA-peptides, needs to be developed and determined.

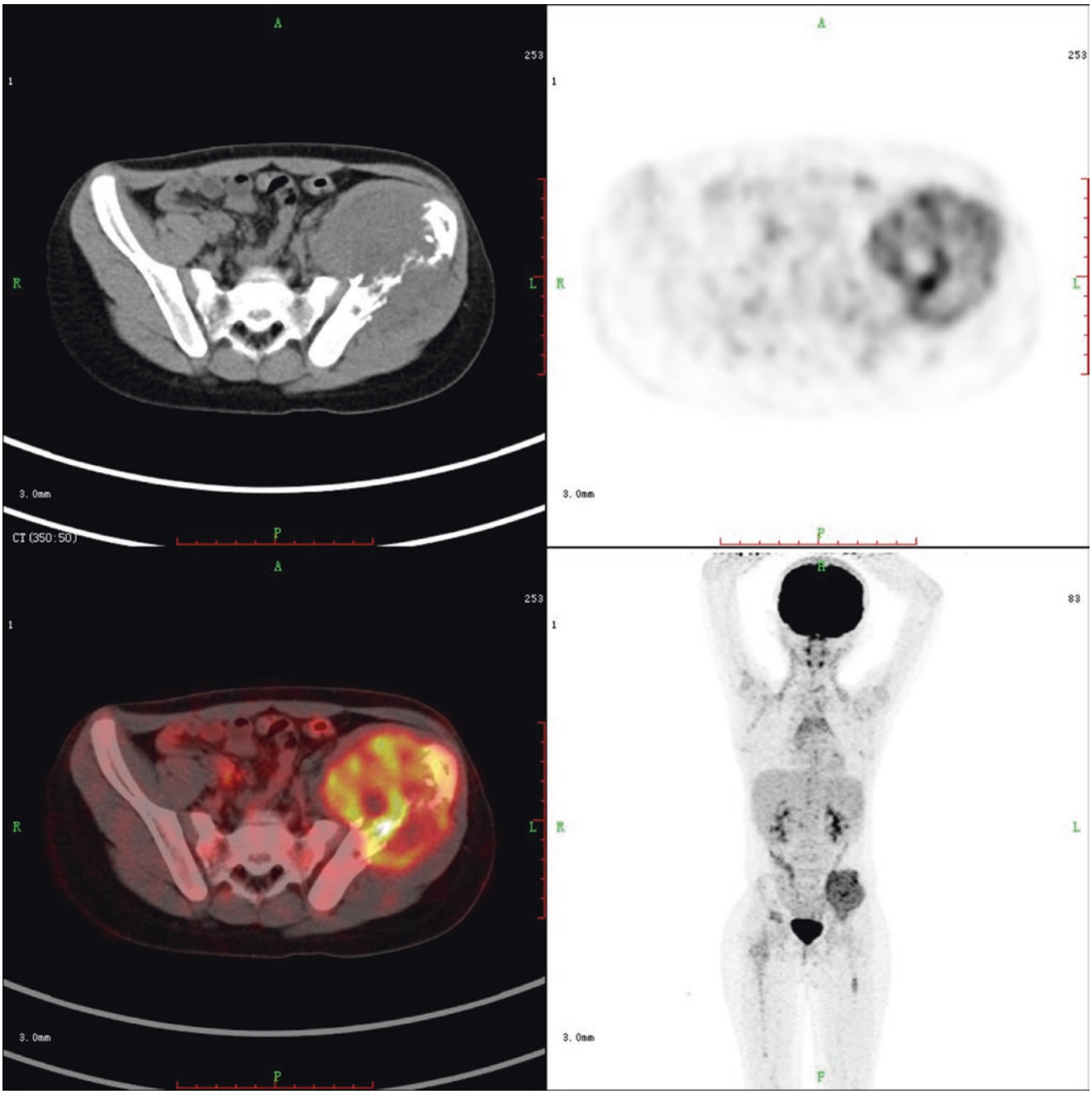

Fig. 10.8 An-8-year-old boy with metastatic Ewing sarcoma of the left ilium. MIP shows multiple bone metastasis

10.2.5 Wilms Tumor

Wilms tumor is the most common renal malignancy in children. The overall 5-year survival rate exceeds 90% [39]. At first diagnosis, the standard imaging modalities include a CT or MRI scan of the abdomen and pelvis and a Doppler ultrasound to evaluate tumor thrombus in the renal vein and inferior vena cava.

Uptake of FDG by Wilms tumor has been described in small cohorts of pediatric patients [40–42]. Comparing with conventional imaging staging modality, FDG PET showed concordant results for staging of Wilms tumor and SUV_{max} was correlated with histological differentiation [43]. In 26 patients with Wilms tumor, we found that the average SUV_{max} of the primary tumor was 5.5, and sensitivity and specificity for staging was 95 and 71%, respectively

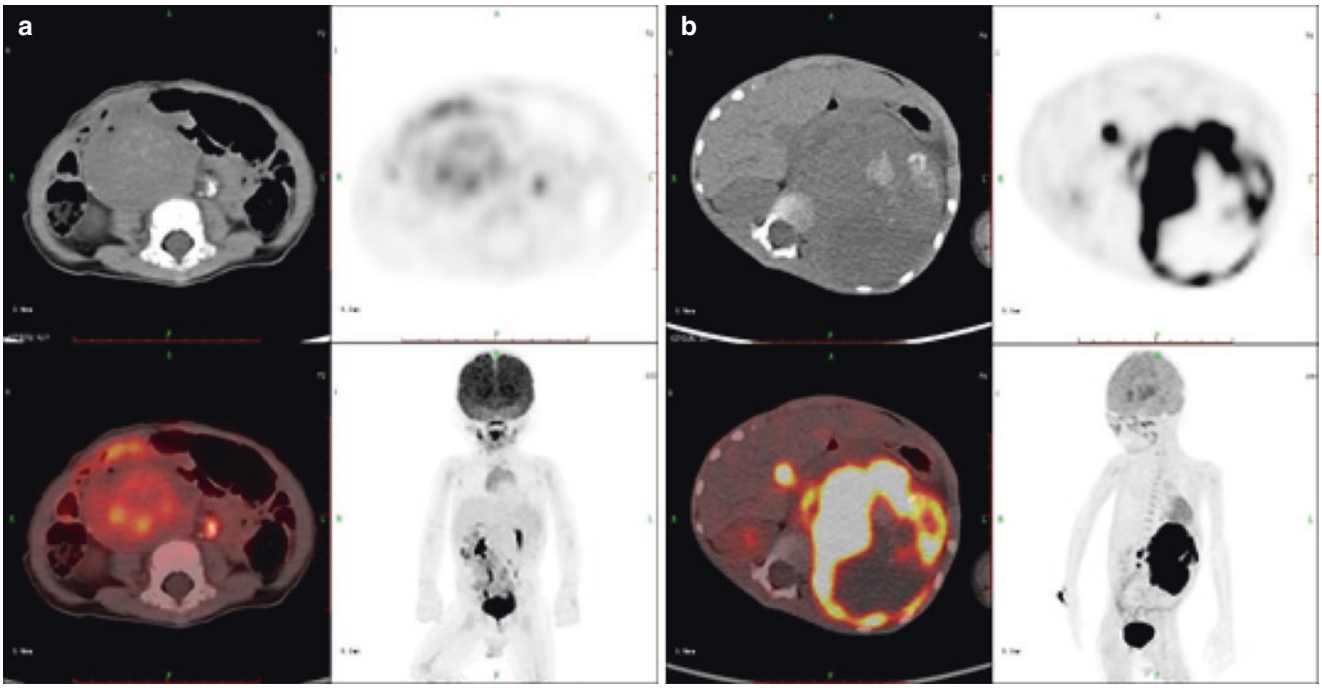

Fig. 10.9 PET/CT images of neuroblastoma with variable levels of ^{18}F-FDG intensity. (**a**) A 12-month-old boy with well-differentiated neuroblastoma (SUV_{max}, 2.9); (**b**) PET/CT images of a 3-year-old boy with poorly differentiated neuroblastoma (SUV_{max}, 22.0). Patient died 20 months after initial diagnosis despite intensive multimodality therapy

(Fig. 10.10). For assessment of induction chemotherapy response, FDG PET was advantageous in ruling out residual disease, and higher SUV ($SUV_{max} > 5$) following chemotherapy suggested histologically high-risk disease [42, 43].

10.2.6 Brain Tumor

Brain tumors are the leading cause of cancer mortality in children and accounts for 20–25% of all childhood cancers. The most common types are as follows: astrocytoma, medulloblastoma, ependymoma, and brain stem glioma.

MRI and CT are the fundamental imaging modalities used in staging and follow-up in children with brain tumors. The use of ^{18}F-FDG for brain tumor imaging is limited by physiological uptake in the normal cortex. However, ^{18}F-FDG PET/CT may reflect malignancy grade and predict survival in pediatric patients with brain tumor (Fig. 10.11). Generally, FDG uptake of the primary tumor positively correlated with WHO graded malignancy [44]. Glioblastoma multiforme and medulloblastoma had intense FDG uptake, whereas ependymoma had low uptake throughout the tumor [45]. Tumors with high FDG accumulation are more likely to demonstrate aggressive behavior and disease progression; on the contrary, clinical outcome is significantly better for patients with hypometabolic tumors [46, 47]. In brain stem glioma, FDG uptake of the tumor higher than the gray matter or FDG uptake involving greater than half the tumor suggests poorer survival outcome [48]. However, despite its poor outcome, approximately one-half of brain stem gliomas have low uptake (Fig. 10.12). Furthermore, in refractory/recurrent brain stem gliomas, ^{18}F-FDG uptake could not predict survival, which may be attributed to concurrent tissue breakdown and development of new lesions at sites of treatment [45]. Noteworthy, some benign tumors can also present intensive FDG uptake: juvenile pilocytic astrocytomas [49], choroid plexus papilloma [50], and pleomorphic xanthoastrocytoma [51].

10.3 Radiation Safety of ^{18}F-FDG PET/CT in Children

10.3.1 Radiation Exposure Hazards in Children

Radiologic imaging modality is a double-edged sword. Although the use of radiologic imaging has profoundly improved diagnostic and treatment capabilities, its use comes with risks related to the ionizing radiation [52]. This is particularly concerning for children because they are much more sensitive to radiation than adults due to a rapid rate of cell division and they have a longer expected life span during which to develop hazardous effect of radiation such as cancer. Miglioretti et al. [53] estimated that four million pediatric CT scans performed each year in the United States are projected to cause 4870 future cancers. An infant is 10 times more sensitive than middle-aged adults [52]. Girls have approximately

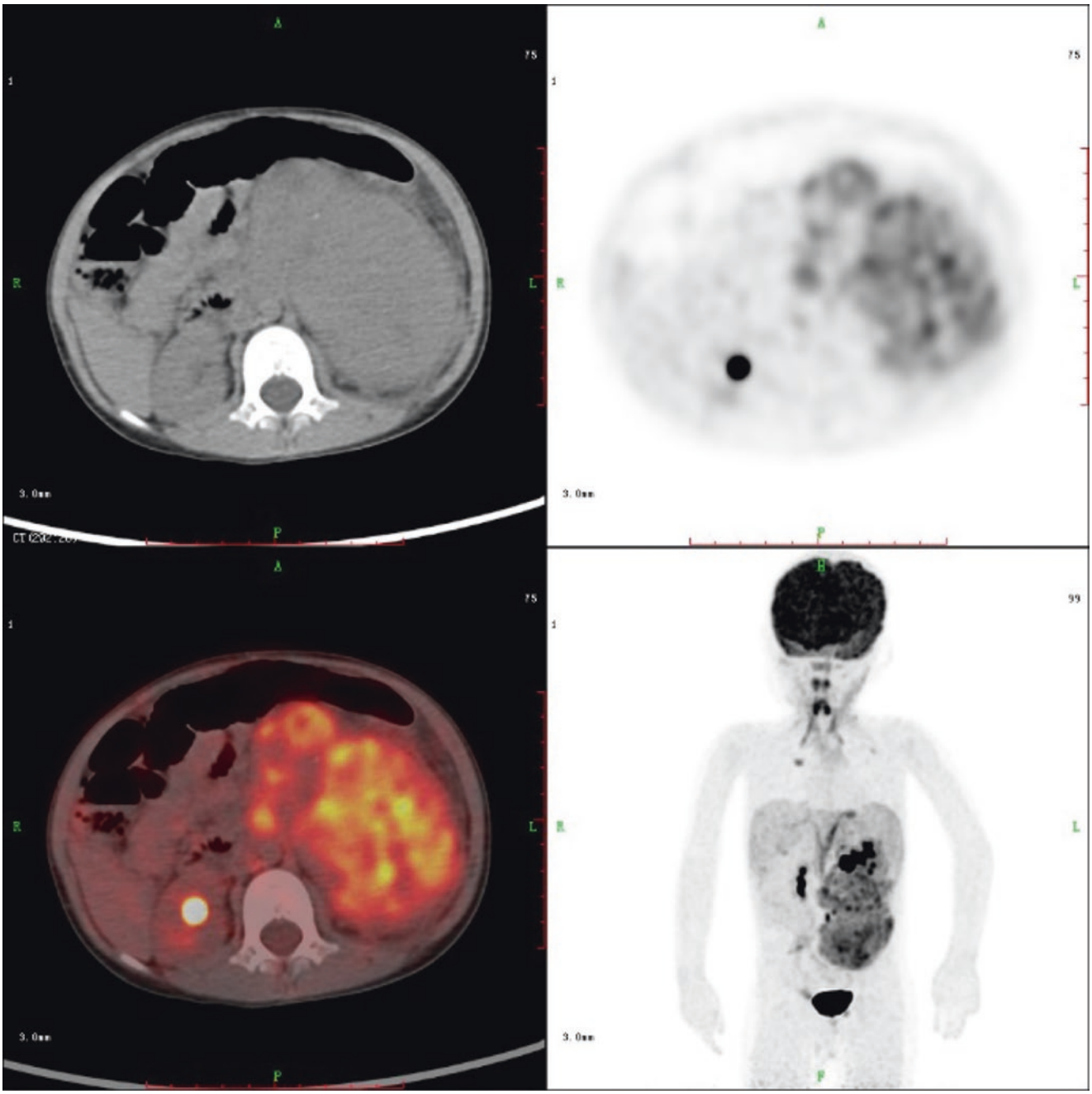

Fig. 10.10 PET/CT image of a 3-year-old boy with left kidney Wilms tumor. SUV_{max} of the primary tumor was 6.6

50% higher risk for cancer induced by radiation than boys, largely attribute to an excess risk of breast cancer [54]. For CT scans, effective doses were highest for abdomen/pelvis scans, with the mean dose of 10.6 mSv and 14.8 mSv among toddlers (≤5 years) and teenagers (10–14 years), respectively [53]. The average dose per ^{18}F-FDG PET/CT scan was estimated to be 24.8 mSv and an average cumulative dose was 78 mSv (range, 6.2–399 mSv) received from ^{18}F-FDG PET/CT in pediatric patients treated for cancer [55]. Therefore, attention to radiation safety for pediatric patients is paramount.

10.3.2 Principle of Radiation Protection and Protective Measures

The concept of ALARA, an acronym for "as low as reasonably achievable," should always be utilized. It means making every reasonable effort to maintain exposures to ionizing radiation as low as possible. Several strategies can be used to minimize the radiation dose to a pediatric patient receiving a PET/CT scan.

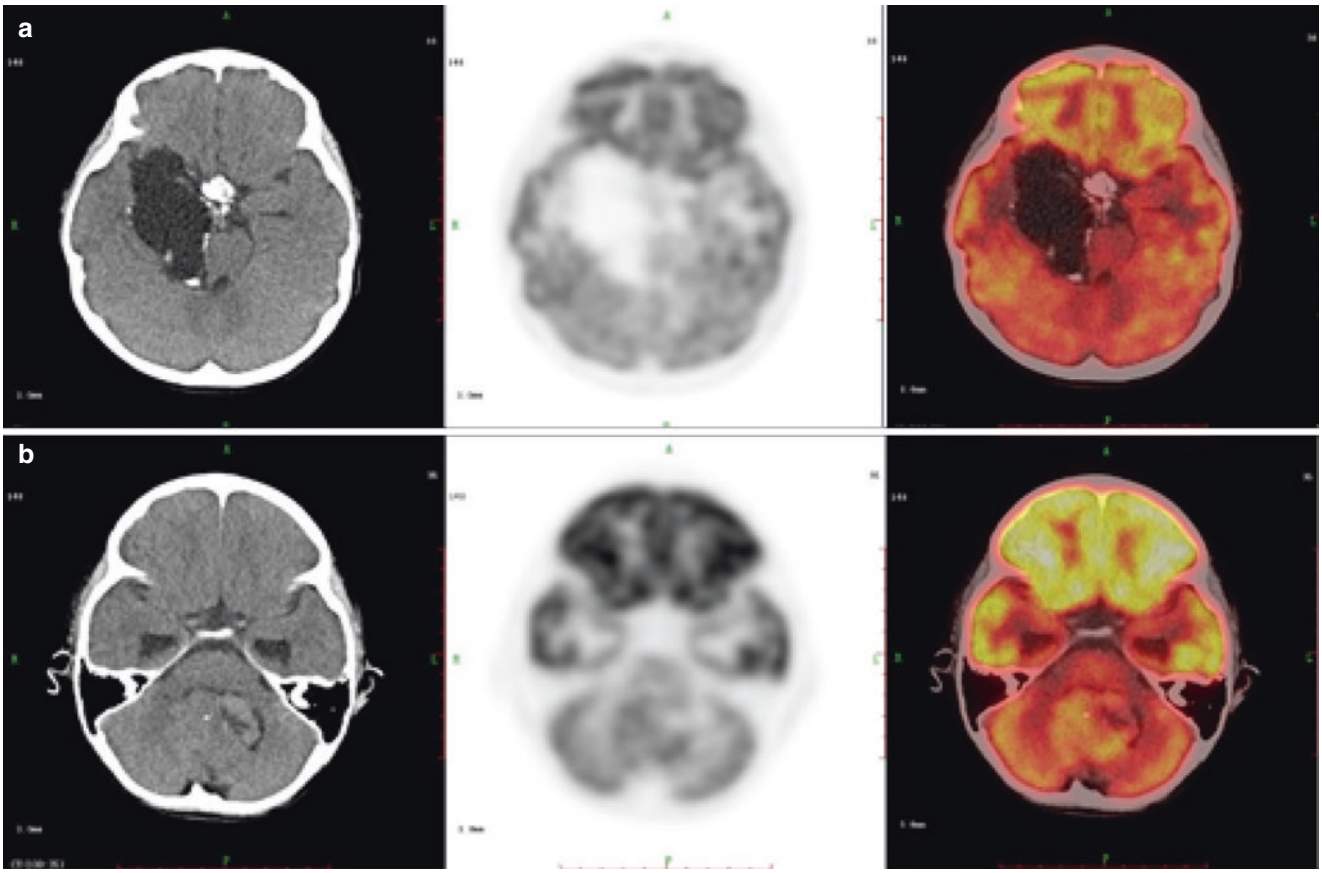

Fig. 10.11 ^{18}F-FDG PET/CT images of pediatric patients with brain tumor. (**a**) A 6-year-old boy with craniopharyngioma (WHO grade I) which shows no FDG uptake; (**b**) a 5-year-old boy with medulloblastoma (WHO grade IV) which shows increased uptake with SUV_{max} of 4.1

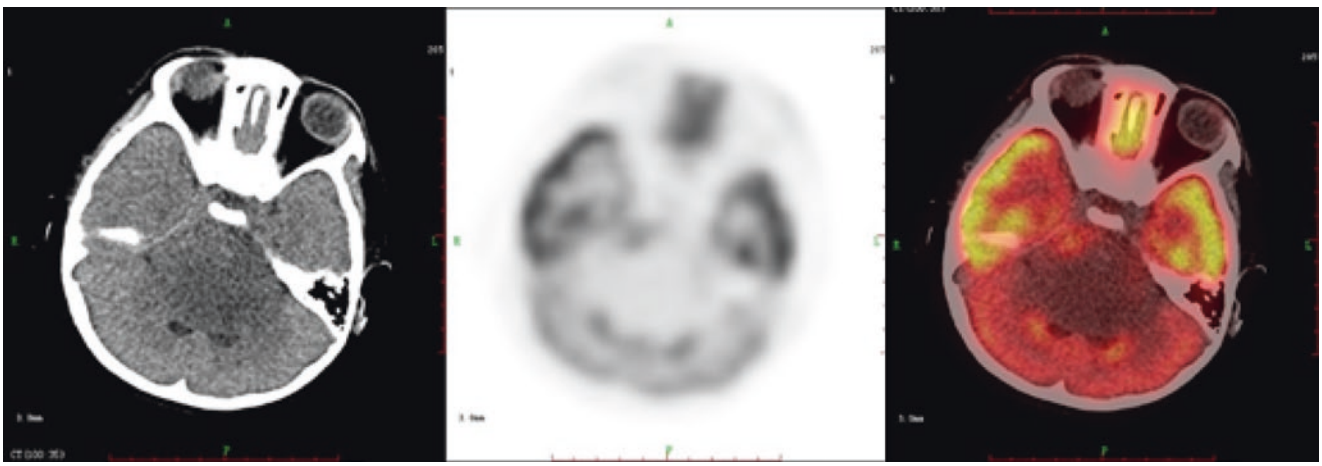

Fig. 10.12 ^{18}F-FDG PET/CT images of a 5-year-old boy with diffuse intrinsic pontine glioma (WHO grade III) which has low ^{18}F-FDG uptake with SUV_{max} of 1.5

Firstly, avoid PET/CT scans when unnecessary: A PET/CT examination should be performed only if it is appropriate for answering a specific clinical question. Use alternative diagnostic methods that do not produce radiation, such as ultrasound or MRI, when possible.

Secondly, for the PET component, reduce the injected ^{18}F-FDG dose while maintaining the image quality. Several groups have presented recommendations on pediatric ^{18}F-FDG dosing [56–58]. The mostly recommended dose of ^{18}F-FDG is around 0.14–0.15 mCi/Kg, which is based on adult protocols. Alessio et al. [59] suggested an injected activity of 0.09 mCi/kg with a scan duration of 5 min/FOV for patients more than 22 kg providing equivalent image quality, leading to 40% of reduction of FDG dose. Other methods to improve

the image quality with low inject activity are as follows: by acquiring PET data in 3D mode, by increasing the axial extent, and by scanning in time-of-flight mode. Good hydration and rapid drainage of radioactive urine also help to reduce radiation dose. Combining the strategies results in more than 50–75% of dose reduction.

Thirdly, for the CT component, several approaches lead to minimize radiation dose to the pediatric patient. Lower radiation dose delivered by CT can be obtained by a lower tube voltage (kVp) or tube current (mA), a greater pitch, and a faster rotation speed. In children who already recently underwent diagnostic quality CT or contrast-enhanced CT scans, the decision to use the CT component of the PET/CT scan solely for attenuation correction for whole-body PET and anatomical land marking rather than for diagnostic purpose can be made. In this regard, an adequate CT-based attenuation correction can be obtained with CT acquisition parameters as low as 80 kVp, 5 mAs, and a pitch of 1.5:1. Such strategy leads to 100-fold dose reduction relative to diagnostic CT [60]. Finally, the use of bismuth breast shields reduces the dose to the patient's breast by a maximum of 20% without impacting image quality.

Finally, with the introduction of PET/MR, the ionizing radiation produced by CT component in PET/CT studies can be eliminated [61]. Preliminary reports have demonstrated that the radiation exposure from a single hybrid imaging PET/MR scan is approximately reduced by 80% compared to PET/CT study, with an effective dose of 4.6 mSv per scan [55, 62].

In conclusion, under appropriate clinical conditions, the benefit of ^{18}F-FDG PET/CT significantly outweighs the potential risks induced by ionizing radiation. It is essential that minimization of radiation dose does not come at the expense of jeopardizing the quality of the clinical information necessary for the patient's care. When a PET/CT scan is appropriate for the patient's care, it is important to give the least radiation necessary to obtain the scan.

References

1. Siegel RL, Miller KD, Jemal A (2017) Cancer statistics, 2017. CA Cancer J Clin 67:7–30
2. Pingping B, Chunxiao W, Kai G et al (2016) Incidence trend of malignant tumors in children in Shanghai. Chin J Epidemiol 37:106–110
3. Shammas A, Lim R, Charron M (2009) Pediatric FDG PET/CT: physiologic uptake, normal variants, and benign conditions. Radiographics 29:1467–1486
4. Cory DA, Cohen MD, Smith JA (1987) Thymus in the superior mediastinum simulating adenopathy: appearance on CT. Radiology 162:457–459
5. Goethals I, Hoste P, De Vriendt C, Smeets P, Verlooy J, Ham H (2010) Time-dependent changes in 18F-FDG activity in the thymus and bone marrow following combination chemotherapy in paediatric patients with lymphoma. Eur J Nucl Med Mol Imaging 37:462–467
6. Taralli S, Leccisotti L, Mattoli MV et al (2015) Physiological activity of spinal cord in children: an 18F-FDG PET-CT study. Spine (Phila Pa 1976) 40:E647–E652
7. Weiler-Sagie M, Bushelev O, Epelbaum R et al (2010) (18)F-FDG avidity in lymphoma readdressed: a study of 766 patients. J Nucl Med 51:25–30
8. London K, Cross S, Onikul E, Dalla-Pozza L, Howman-Giles R (2011) 18F-FDG PET/CT in paediatric lymphoma: comparison with conventional imaging. Eur J Nucl Med Mol Imaging 38:274–284
9. Kabickova E, Sumerauer D, Cumlivska E et al (2006) Comparison of 18F-FDG-PET and standard procedures for the pretreatment staging of children and adolescents with Hodgkin's disease. Eur J Nucl Med Mol Imaging 33:1025–1031
10. Purz S, Mauz-Korholz C, Korholz D et al (2011) [18F] Fluorodeoxyglucose positron emission tomography for detection of bone marrow involvement in children and adolescents with Hodgkin's lymphoma. J Clin Oncol 29:3523–3528
11. Chen S, Wang S, He K, Ma C, Fu H, Wang H (2018) PET/CT predicts bone marrow involvement in paediatric non-Hodgkin lymphoma and may preclude the need for bone marrow biopsy in selected patients. Eur Radiol 28:2942–2950
12. Rosolen A, Perkins SL, Pinkerton CR et al (2015) Revised International pediatric non-Hodgkin lymphoma staging system. J Clin Oncol 33:2112–2118
13. Furth C, Steffen IG, Amthauer H et al (2009) Early and late therapy response assessment with [18F]fluorodeoxyglucose positron emission tomography in pediatric Hodgkin's lymphoma: analysis of a prospective multicenter trial. J Clin Oncol 27:4385–4391
14. Sandlund JT et al (2015) International pediatric non-Hodgkin lymphoma response criteria. J Clin Oncol 33(18):2106–2111
15. Bhojwani D, McCarville MB, Choi JK et al (2015) The role of FDG-PET/CT in the evaluation of residual disease in paediatric non-Hodgkin lymphoma. Br J Haematol 168:845–853
16. Byun BH, Kong CB, Lim I et al (2013) Comparison of (18)F-FDG PET/CT and (99 m)Tc-MDP bone scintigraphy for detection of bone metastasis in osteosarcoma. Skeletal Radiol 42:1673–1681
17. Hurley C, McCarville MB, Shulkin BL et al (2016) Comparison of (18) F-FDG-PET-CT and bone scintigraphy for evaluation of osseous metastases in newly diagnosed and recurrent osteosarcoma. Pediatr Blood Cancer 63:1381–1386
18. Volker T, Denecke T, Steffen I et al (2007) Positron emission tomography for staging of pediatric sarcoma patients: results of a prospective multicenter trial. J Clin Oncol 25:5435–5441
19. Quartuccio N, Fox J, Kuk D et al (2015) Pediatric bone sarcoma: diagnostic performance of (1)(8)F-FDG PET/CT versus conventional imaging for initial staging and follow-up. Am J Roentgenol 204:153–160
20. Sharma P, Khangembam BC, Suman KC et al (2013) Diagnostic accuracy of 18F-FDG PET/CT for detecting recurrence in patients with primary skeletal Ewing sarcoma. Eur J Nucl Med Mol Imaging 40:1036–1043
21. Dharmarajan KV, Wexler LH, Gavane S et al (2012) Positron emission tomography (PET) evaluation after initial chemotherapy and radiation therapy predicts local control in rhabdomyosarcoma. Int J Radiat Oncol Biol Phys 84:996–1002
22. Baum SH, Fruhwald M, Rahbar K, Wessling J, Schober O, Weckesser M (2011) Contribution of PET/CT to prediction of outcome in children and young adults with rhabdomyosarcoma. J Nucl Med 52:1535–1540
23. Salem U et al (2017) 18F-FDG PET/CT as an indicator of survival in Ewing sarcoma of bone. J Cancer 8(15):2892–2898
24. Dong Y, Zhang X, Wang S, Chen S, Ma C (2017) 18F-FDG PET/CT is useful in initial staging, restaging for pediatric rhabdomyosarcoma. Q J Nucl Med Mol Imaging 61:438–446
25. Kong CB et al (2013) (1)(8)F-FDG PET SUVmax as an indicator of histopathologic response after neoadjuvant chemotherapy in

extremity osteosarcoma. Eur J Nucl Med Mol Imaging 40(5): 728–736
26. Denecke T, Hundsdorfer P, Misch D et al (2010) Assessment of histological response of paediatric bone sarcomas using FDG PET in comparison to morphological volume measurement and standardized MRI parameters. Eur J Nucl Med Mol Imaging 37: 1842–1853
27. Hawkins DS, Conrad EU III, Butrynski JE, Schuetze SM, Eary JF (2009) [F-18]-fluorodeoxy-D-glucose-positron emission tomography response is associated with outcome for extremity osteosarcoma in children and young adults. Cancer 115:3519–3525
28. Casey DL, Wexler LH, Fox JJ et al (2014) Predicting outcome in patients with rhabdomyosarcoma: role of [(18)f]fluorodeoxyglucose positron emission tomography. Int J Radiat Oncol Biol Phys 90:1136–1142
29. Hawkins DS, Schuetze SM, Butrynski JE et al (2005) [18F] Fluorodeoxyglucose positron emission tomography predicts outcome for Ewing sarcoma family of tumors. J Clin Oncol 23:8828–8834
30. Raciborska A et al (2016) Response to chemotherapy estimates by FDG PET is an important prognostic factor in patients with Ewing sarcoma. Clin Transl Oncol 18(2):189–195
31. Papathanasiou ND, Gaze MN, Sullivan K et al (2011) 18F-FDG PET/CT and 123I-metaiodobenzylguanidine imaging in high-risk neuroblastoma: diagnostic comparison and survival analysis. J Nucl Med 52:519–525
32. Sharp SE, Shulkin BL, Gelfand MJ, Salisbury S, Furman WL (2009) 123I-MIBG scintigraphy and 18F-FDG PET in neuroblastoma. J Nucl Med 50:1237–1243
33. Taggart DR, Han MM, Quach A et al (2009) Comparison of iodine-123 metaiodobenzylguanidine (MIBG) scan and [18F]fluorodeoxyglucose positron emission tomography to evaluate response after iodine-131 MIBG therapy for relapsed neuroblastoma. J Clin Oncol 27:5343–5349
34. Melzer HI, Coppenrath E, Schmid I et al (2011) (1)(2)(3)I-MIBG scintigraphy/SPECT versus (1)(8)F-FDG PET in paediatric neuroblastoma. Eur J Nucl Med Mol Imaging 38:1648–1658
35. Choi YJ et al (2014) (18)F-FDG PET as a single imaging modality in pediatric neuroblastoma: comparison with abdomen CT and bone scintigraphy. Ann Nucl Med 28(4):304–313
36. Dhull VS et al (2015) Diagnostic value of 18F-FDG PET/CT in paediatric neuroblastoma: comparison with 131I-MIBG scintigraphy. Nucl Med Commun 36(10):1007–1013
37. Lee JW, Cho A, Yun M, Lee JD, Lyu CJ, Kang WJ (2015) Prognostic value of pretreatment FDG PET in pediatric neuroblastoma. Eur J Radiol 84:2633–2639
38. Li C, Zhang J, Chen S et al (2017) Prognostic value of metabolic indices and bone marrow uptake pattern on preoperative 18F–FDG PET/CT in pediatric patients with neuroblastoma. Eur J Nucl Med Mol Imaging 45:306–315
39. Smith MA, Seibel NL, Altekruse SF et al (2010) Outcomes for children and adolescents with cancer: challenges for the twenty-first century. J Clin Oncol 28:2625–2634
40. Shulkin BL, Mitchell DS, Ungar DR et al (1995) Neoplasms in a pediatric population: 2-[F-18]-fluoro-2-deoxy-D-glucose PET studies. Radiology 194:495–500
41. Moinul Hossain AK et al (2010) FDG positron emission tomography/computed tomography studies of Wilms' tumor. Eur J Nucl Med Mol Imaging 37(7):1300–1308
42. Begent J, Sebire NJ, Levitt G et al (2011) Pilot study of F(18)-Fluorodeoxyglucose positron emission tomography/computerised tomography in Wilms' tumour: correlation with conventional imaging, pathology and immunohistochemistry. Eur J Cancer 47:389–396
43. Misch D, Steffen IG, Schonberger S et al (2008) Use of positron emission tomography for staging, preoperative response assessment and posttherapeutic evaluation in children with Wilms tumour. Eur J Nucl Med Mol Imaging 35:1642–1650
44. Borgwardt L, Hojgaard L, Carstensen H et al (2005) Increased fluorine-18 2-fluoro-2-deoxy-D-glucose (FDG) uptake in childhood CNS tumors is correlated with malignancy grade: a study with FDG positron emission tomography/magnetic resonance imaging coregistration and image fusion. J Clin Oncol 23:3030–3037
45. Zukotynski K, Fahey F, Kocak M et al (2014) 18F-FDG PET and MR imaging associations across a spectrum of pediatric brain tumors: a report from the pediatric brain tumor consortium. J Nucl Med 55:1473–1480
46. Kruer MC, Kaplan AM, Etzl MM Jr et al (2009) The value of positron emission tomography and proliferation index in predicting progression in low-grade astrocytomas of childhood. J Neurooncol 95:239–245
47. Pirotte BJ, Lubansu A, Massager N, Wikler D, Goldman S, Levivier M (2007) Results of positron emission tomography guidance and reassessment of the utility of and indications for stereotactic biopsy in children with infiltrative brainstem tumors. J Neurosurg 107:392–399
48. Zukotynski KA et al (2011) Evaluation of 18F-FDG PET and MRI associations in pediatric diffuse intrinsic brain stem glioma: a report from the Pediatric Brain Tumor Consortium. J Nucl Med 52(2):188–195
49. Fulham MJ, Melisi JW, Nishimiya J, Dwyer AJ, Di Chiro G (1993) Neuroimaging of juvenile pilocytic astrocytomas: an enigma. Radiology 189:221–225
50. Sunada I, Tsuyuguchi N, Hara M, Ochi H (2002) 18F-FDG and 11C-methionine PET in choroid plexus papilloma--report of three cases. Radiat Med 20:97–100
51. Tsuyuguchi N, Matsuoka Y, Sunada I, Matsusaka Y, Haque M (2001) Evaluation of pleomorphic xanthoastrocytoma by use of positron emission tomography with. AJNR Am J Neuroradiol 22:311–313
52. Preston DL, Ron E, Tokuoka S et al (2007) Solid cancer incidence in atomic bomb survivors: 1958-1998. Radiat Res 168:1–64
53. Miglioretti DL, Johnson E, Williams A et al (2013) The use of computed tomography in pediatrics and the associated radiation exposure and estimated cancer risk. JAMA Pediatr 167:700–707
54. Fahey FH, Treves ST, Adelstein SJ (2012) Minimizing and communicating radiation risk in pediatric nuclear medicine. J Nucl Med Technol 40(1):13–24
55. Chawla SC, Federman N, Zhang D et al (2010) Estimated cumulative radiation dose from PET/CT in children with malignancies: a 5-year retrospective review. Pediatr Radiol 40:681–686
56. Stauss J, Franzius C, Pfluger T et al (2008) Guidelines for 18F-FDG PET and PET-CT imaging in paediatric oncology. Eur J Nucl Med Mol Imaging 35:1581–1588
57. Alessio AM et al (2009) Weight-based, low-dose pediatric whole-body PET/CT protocols. J Nucl Med 50(10):1570–1577
58. Accorsi R, Karp JS, Surti S (2010) Improved dose regimen in pediatric PET. J Nucl Med 51:293–300
59. Alessio AM, Sammer M, Phillips GS, Manchanda V, Mohr BC, Parisi MT (2011) Evaluation of optimal acquisition duration or injected activity for pediatric 18F-FDG PET/CT. J Nucl Med 52:1028–1034
60. Fahey FH, Palmer MR, Strauss KJ, Zimmerman RE, Badawi RD, Treves ST (2007) Dosimetry and adequacy of CT-based attenuation correction for pediatric PET: phantom study. Radiology 243:96–104
61. Pichler BJ et al (2010) PET/MRI: paving the way for the next generation of clinical multimodality imaging applications. J Nucl Med 51(3):333–336
62. Hirsch FW, Sattler B, Sorge I et al (2013) PET/MR in children. Initial clinical experience in paediatric oncology using an integrated PET/MR scanner. Pediatr Radiol 43:860–875

Molecular Imaging

11

Hubing Wu, DeWei Tang, XiaoPing Zhao, Gengbiao Yuan, and Xinhui Su

11.1 Metabolic Imaging of Fatty Acid

The most prominent metabolic alteration in cancer is a high rate of glycolysis. Liking glucose metabolism, lipid metabolism is also pivotal for tumor proliferation, energy storage, and the generation of signaling molecules. Metabolic imaging of fatty acid can visualize the lipid metabolism of the tumor in vivo by PET/CT, which now plays an important role in the diagnosing and staging for tumors.

11.1.1 Lipid Metabolism, Membrane Biosynthesis, and Tumor Proliferation

Altered energy metabolism is a biochemical fingerprint of cancer cells [1]. The metabolic properties of cancer cells are different from those of normal cells. As rapid growing cells, cancer cells have an enhanced energy metabolism, which is rewired to the demands for cell growth and survival. This metabolic reprogramming can produce the massive intermediates for the synthesis of cellular building blocks and signaling molecules [1]. The most prominent metabolic alteration in cancer is high aerobic glycolysis, called the "Warburg effect." In normal cells, energy is primarily produced through mitochondrial oxidative phosphorylation. However, in most cancer cells, a high rate of glycolysis becomes a predominant pathway for cells to generate energy even in the presence of abundant oxygen. According to "Warburg effect," ^{18}F-fluorodeoxyglucose (^{18}F-FDG), an analog of glucose, has been developed to be a PET imaging agent that reflects glucose metabolism in tumors. It has been widely adopted for the detection, staging, and therapy monitoring of malignant tumors. Another important metabolic alteration in cancer is high rate of lipid uptake. Similar to the glucose metabolism, high rate of lipid metabolism in cancer cells has also been associated with cellular proliferation, energy demand and the generation of signaling molecules that supports the cancer growth [1]. Overexpression of fatty acid synthase (FASN) in several cancers has been observed and provided the evidences of a de novo lipogenesis in tumors [1, 2].

Most lipids are synthesized from fatty acids. An important metabolic intermediate that provides the substrate for fatty acids and cholesterol biosynthesis is acetyl coenzyme A (CoA), which is produced through multiple pathways. Acetyl CoA is commonly generated from pyruvate by the enzyme pyruvate dehydrogenase under aerobic conditions or generated from citrate by cytoplasmic adenosine triphosphate (ATP)-citrate lyase. Acetyl CoA can also be synthesized from acetate, which can be obtained from the environment or intracellular sources. Acetate is an essential intermediate in catabolic and biosynthetic processes, and its intracellular fate is diverse. On one hand, it is transported into cells via the monocarboxylate transporter and is further metabolized to CO_2 via the tricarboxylic acid cycle. However, acetate use in cancer cells is governed predominantly by another metabolic process for membrane biosynthesis [2]. Cancer cells have an increased requirement for cell membrane lipids, and acetate is a very important intermediate for its biosynthesis [2]. Free acetate is taken up by cells and activated to acetyl CoA in both the cytosol and

H. Wu (✉)
Nanfang PET center, Nanfang Hospital, Southern Medical University, Guangzhou, P. R. China

D. Tang (✉) · X. Zhao
Department of Nuclear Medicine, RenJi Hospital, School of Medicine, Shanghai JiaoTong University, Shanghai, P. R. China

G. Yuan (✉)
Department of Nuclear Medicine, The Second Affiliated Hospital of Chongqing Medical University, Chongqing, P. R. China

X. Su (✉)
Department of Nuclear Medicine, Zhongshan Hospital Xiamen University, Xiamen, P. R. China

G. Huang (ed.), *Nuclear Medicine in Oncology*, https://doi.org/10.1007/978-981-13-7458-6_11

mitochondria by acetyl CoA synthetase (Fig. 11.1). The rate-limiting enzyme in this pathway is fatty acid synthase (FAS), which due to increased expression promotes de novo fatty acid synthesis from CoA, malonyl-CoA, and nicotinamide adenine dinucleotide phosphate in normal and abnormal tissues and meets the increased demand for membrane lipids [2].

Besides acetate, choline is also an important precursor for the biosynthesis of membrane phospholipids [2]. As a key membrane phospholipid, a large number of phosphatidylcholine (PtdCho) is needed to meet the increased requirements of biological membrane building during cancer cell turnover [3]. PtdCho is biosynthesized via the Kennedy pathway. Choline kinase (ChoK), choline phosphate cytidylyltransferase (CCT), and diacylglycerol cholinephosphotransferase (CPT) are three key enzymes which regulate this pathway. Free choline is first taken up into the cytoplasm via the cell membrane by a number of choline transporters. In the cytoplasm, free choline is rapidly phosphorylated to phosphorylcholine by ChoK, which is then conversed to cytidine diphosphate choline (CDP-choline) by CCT. After that, cytidine monophosphate is replaced with 1,2-sn-diacylglycerol (DAG) by CPT, and finally PtdCho is synthesized. Therefore, in the Kennedy pathway, choline serves as a synthetic precursor for PtdCho production (Fig. 11.2). Free choline also can be incorporated into a variety of other important cellular components in the cell, such as acetylcholine, betaine, platelet activating factor, or sphingomyelin.

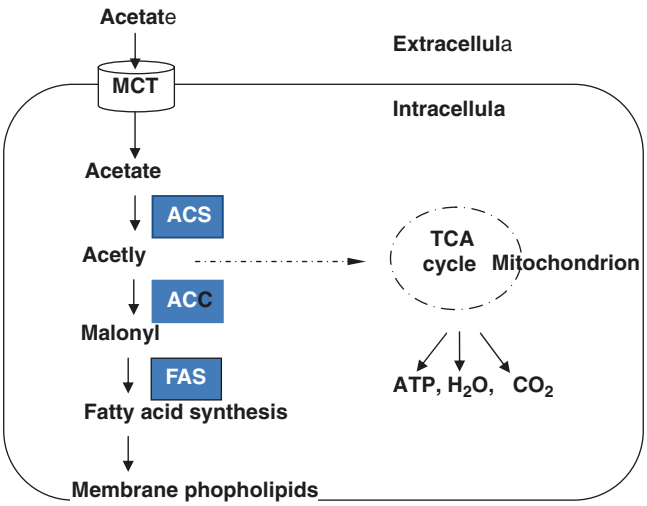

Fig. 11.1 Metabolism and the production of membrane phospholipids. *MCT* monocarboxylate transporter; *ACS* acetyl CoA synthase; *ACC* acetyl CoA carboxylase; *FAS* fatty acid synthase; *TCA* tricarboxylic acid

11.1.2 Lipid PET Probes and Their Molecular Biology

Currently, the commonly used lipid PET probes are ^{11}C-choline, ^{18}F-choline, and ^{11}C-acetate.

11.1.2.1 Molecular Biology of ^{11}C-Choline and ^{18}F-Choline

Elevated phosphorylcholine and phosphocholine turnover were found not only in prostate cancer (PCa) and hepatocellular carcinoma (HCC) but also in other tumors. Corresponding to the high levels of phosphorylcholine and phosphocholine, some key enzymes of choline metabolism, such as ChoK and CCT, have been observed to be upregulated in malignant lesions.

^{11}C-labeled choline (^{11}C-choline) was first developed by Hara et al. in 1997, with a primary purpose for overcoming the limitations of ^{18}F-FDG in diagnosing prostate cancer.

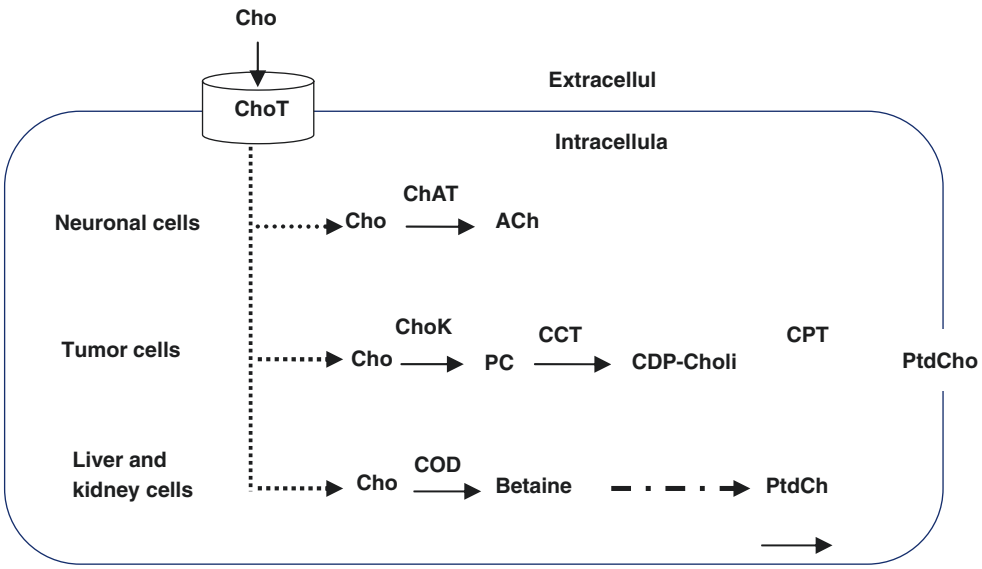

Fig. 11.2 Choline metabolism and the production of membrane phospholipids. *ChoT* choline transporter; *Cho* choline; *PC* phosphocholine; *PtdCho* phosphatidylcholine; *CDP-choline* cytidine diphosphate choline; *Ach* acetylcholine; *ChoK* choline kinase; *CCT* choline phosphate cytidylyltransferase; *CPT* cholinephosphotransferase; *ChAT* choline acetyltransferase; *COD* choline oxidase

Now, it is also adopted as a supplement of ^{18}F-FDG imaging in the detection of HCC and other tumors.

In HCC [3], the activities of both ChoK and CCT were significantly higher than that in the surrounding hepatic tissues. The major metabolites of ^{11}C-choline were phosphocholine in HCC and betaine and choline in the surrounding hepatic tissues at 12 min after injection. In HCC, phosphocholine rapidly converted to phosphatidylcholine at 30 min after injection. Therefore, in the high proliferative tumor, ^{11}C-choline was mainly used as a precursor for membrane phospholipids, and high uptake of ^{11}C-choline can reflect the proliferation of the tumor to some extent.

^{18}F-Fluorocholine (or ^{18}F-choline) is another PET tracer of choline metabolism, which has similar biological characteristics to ^{11}C-choline in vivo. However, it owns some advantages of ^{18}F compared to ^{11}C, such as a longer half-life (~110 min) and a shorter positron range. Longer half-life allows transportation to centers without a cyclotron, and a shorter positron range can produce a slightly higher-quality image in terms of spatial resolution.

11.1.2.2 Molecular Biology of ^{11}C-Acetate

The first synthesis of ^{11}C-acetate dates back to 1943, when Buchanan et al. labeled acetic, propionic, and butyric acids with ^{11}C to determine contributions to liver glycogen synthesis.

^{11}C-Acetate was originally used for PET measurements of myocardial oxidative metabolism. In normal myocardium, ^{11}C-acetate was found to enter the Krebs cycle after conversion to acetyl coenzyme A (CoA) to meet cellular energy demands. ^{11}C-Acetate is rapidly taken up by myocardium and metabolized to CO_2 and water via the monocarboxylate transporter (MCT) after intravenous injection (Fig. 11.1). The clearance of the tracer is a direct reflection of TCA cycle activity, which is coupled to myocardial oxygen consumption. It can be used to evaluate ischemia and myocardial infraction.

In tumor, however, increased cellular uptake of ^{11}C-acetate reflects the increased membrane lipid demands of proliferating tissues. Different from its metabolism in the myocardium, ^{11}C-acetate serves as a precursor for lipid and cholesterol synthesis in tumor. It is predominantly converted into fatty acids by a key enzyme FAS, which is then incorporated into intracellular phosphatidylcholine membrane microdomains to meet the demands of tumor proliferation (Fig. 11.1).

11.1.3 Application of Lipid PET Probes in the Diagnosis of Malignant Tumors

Lipid metabolic PET imaging, as an important complement to glucose metabolism PET imaging, has been widely used in clinical practice.

11.1.3.1 Clinical Application of ^{11}C-Choline PET/CT Imaging

1. Normal Physiological Uptake

   In normal subjects, high physiological uptake of this tracer is noted in the intracranial choroid, pituitary, salivary glands, liver, pancreas, spleen, and gastrointestinal tract. The main excretory pathway is the urinary system, which contributes to high uptake of ^{11}C-choline in both kidneys (Fig. 11.3). However, the clearance of ^{11}C-choline from both kidneys is slow, so the radioactivity in bladder

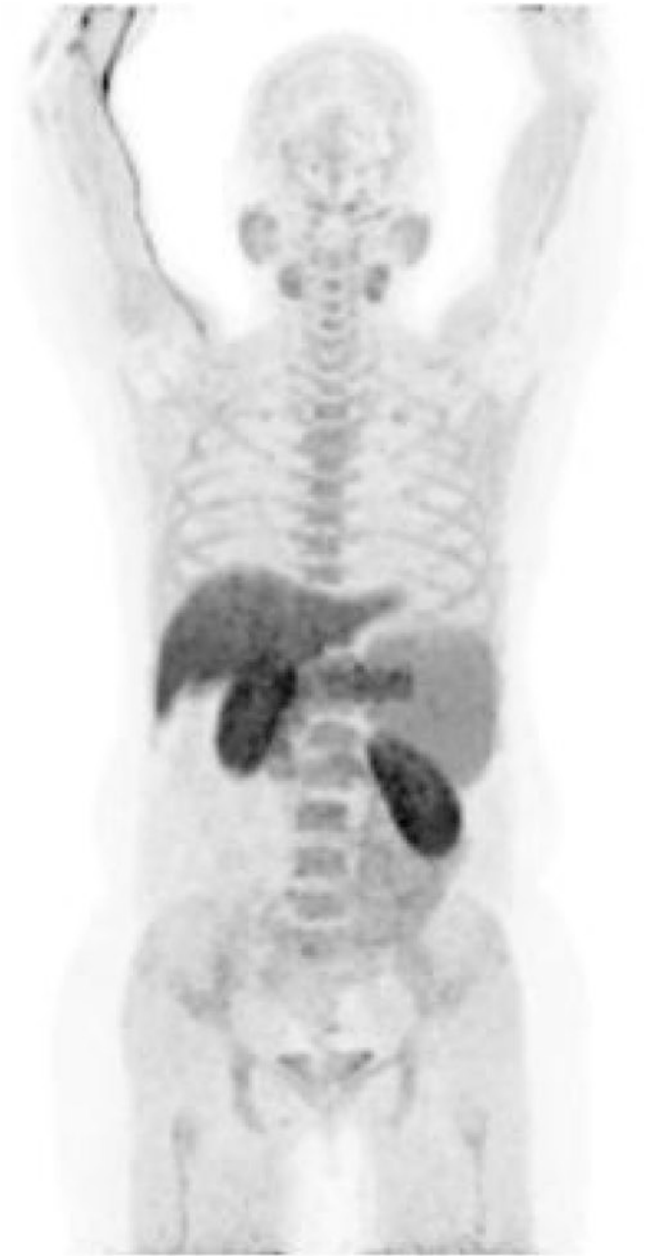

Fig. 11.3 Normal physiological uptake of ^{11}C-choline. High uptake of ^{11}C-choline is found in both kidneys, liver, and spleen, while slight and moderate uptake was noted in the intracranial choroid, pituitary, salivary glands, and bone. The radioactivity in bladder and prostate is low

is low in the first 10 min after injection of tracer (Fig. 11.3), which is of benefit for the detection of the tumor in the bladder or prostate. The uptake in the normal brain parenchyma is minimal. Low uptake is also found in the head and neck apart from the salivary glands, heart, lungs, bone, muscle, etc.

2. Prostatic Cancer
   (a) Primary Tumor
   Prostate cancer (PCa) is a relatively low-grade tumor, especially a well-differentiated one. As a result, PCa is prone to be false negative on ^{18}F-FDG PET/CT. Although ^{11}C-choline is showed to be avid in PCa tumors (Fig. 11.4) and has a higher detection of PCa than ^{18}F-FDG, there has been some debate regarding its clinical value. For primary tumor evaluation, ^{11}C-choline has a limited sensitivity due to a low uptake in small-sized tumor and the limited resolution of PET. Meanwhile, ^{11}C-choline and ^{18}F-choline don't have enough specificity for diagnosing PCa. Benign processes, such as prostate hyperplasia, chronic prostatitis, and high-grade intraepithelial neoplasia, have also been observed to have high uptake of tracer sometimes. In staging untreated primary PCa, on a per-patient basis, pooled sensitivity, specificity, and diagnostic confidence interval odds ratio (DOR) were reported to be 84% (95% [CI], 68–93%), 79% (95% CI, 53–93%), and 20.4 (95% CI, 9.9–42.0), respectively, by a meta-analysis. On a per-lesion basis, lower pooled sensitivity (66% [95% CI, 56–75%]) was reported, even though the pooled specificity and DOR were high [92% (95% CI, 78–97%) and 22.7 (95% CI, 8.9–58.0), respectively] [4]. In the detection of lymph node metastases prior to surgery in PCa patients, ^{11}C-choline and ^{18}F-choline have also demonstrated a high specificity. However, a low sensitivity was also reported. A meta-analysis analyzed 10 selected studies with a total of 441 patients and showed a high pooled diagnostic specificity of 95% (95% CI, 92–97.1) and a low pooled sensitivity of 49.2% (95% confidence interval [CI], 39.9–58.4) [5].
   (b) Recurrent Tumor
   Most studies are focused on the role of ^{11}C-choline and ^{18}F-choline PET/CT in the restaging of PCa patients with biochemical relapse. In a study with large patient size, 52.8% of ^{11}C-choline PET/CT scans (2337/4426) and 54.8% of the patients (1755/3203) were reported to be positive [6]. In 29.4% of the cases, at least one distant finding was observed. ^{11}C-Choline PET/CT changes the management in approximately half of the patients. However, the sensitivity of ^{11}C-choline PET/CT for restaging PCa patients with biochemical relapse depends on the level of serum PSA. Currently, it is recommended that ^{11}C-choline PET/CT should be performed in patient with a PSA level less than 2 ng/mL.
   Utility of ^{11}C-choline PET/CT in patients with low serum PSA is controversial. In the patients with biochemical relapse of PCa and serum PSA <1 ng/mL, ^{11}C-choline PET/CT proved its usefulness in demonstrating tumor in only 14% of patients with therapeutic implications.
3. Hepatocellular Carcinoma
   The feasibility of detecting HCC using ^{11}C-choline or ^{18}F-Choline PET has been shown despite constitutively high parenchymal choline metabolism in the liver. In 2008, Yamamoto [7] performed ^{11}C-choline and ^{18}F-FDG PET/CT in 12 patients with 16 HCC lesions. In their

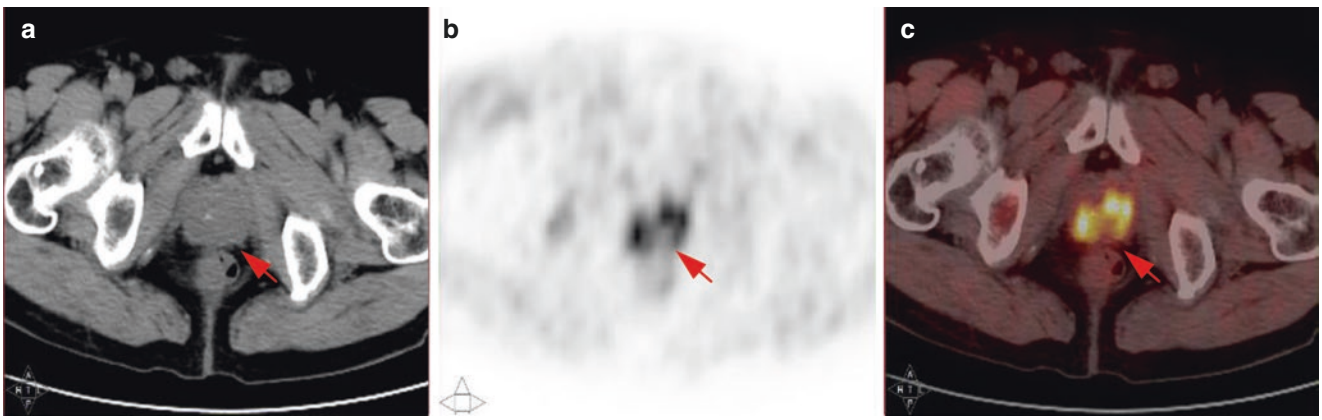

Fig. 11.4 Positive ^{11}C-choline PET/CT in the prostate cancer. A 77-year-old man complained with difficulty in urination for more than 1 year. Ultrasound showed an enlarged prostate. Serum TPSA (13.26 ng/mL) and cPSA (12.20 ng/mL) were increased. Enlarged prostate with punctate calcification was found on non-enhanced CT (**a**, arrow). ^{11}C-Choline uptake in the part of the prostate was observed to be high on PET (**b**, arrow) and PET/CT fused image (**c**, arrow). Well- and moderately differentiated prostate carcinoma was identified by histopathology with Gleason score of 3 + 4

study, ^{11}C-choline and ^{18}F-FDG are complementary. ^{11}C-choline PET seemed to be more sensitive in the detection of moderately differentiated HCC compared to ^{18}F-FDG (75% vs. 42%, respectively). In contrast, ^{18}F-FDG PET exhibited a better detection rate for poorly differentiated HCC than ^{11}C-choline (75% vs. 25%, respectively). Importantly, by combination of these two modalities, all 16 HCC lesions could be detected. Our team confirmed that a high sensitivity (89.5%) of PET/CT for detection of HCC can be achieved when ^{11}C-choline was combined with ^{18}F-FDG PET/CT.

^{18}F-choline has a similar detectability for HCC. A study reported by Talbot JN demonstrated ^{18}F-choline PET/CT had a high detection rate (12/12) for both newly diagnosed and recurrent HCC [8]. When compared to ^{18}F-FDG, a higher sensitivity was observed when using ^{18}F-choline (9/9 vs. 5/9, respectively). The diagnostic accuracy of ^{18}F-choline PET/CT for intra- and extrahepatic HCC was also studied by Bieze M [9]. ^{18}F-Choline PET was positive in 48 of 53 intrahepatic lesions with a sensitivity of 88% and a specificity of 100%. PET/CT detected true positive in 18 extrahepatic lesions and true negative in 3 benign lesions with an accuracy of 100%. Choline PET/CT appeared less specific than ^{18}F-FDG PET/CT due to the high uptake of ^{11}C-choline or ^{18}F-choline in FNH.

4. Other Tumors

The utilities of ^{11}C-choline and ^{18}F-choline in other tumors were also explored. The clinical studies suggested that ^{11}C-choline or ^{18}F-choline PET/CT could be used to diagnose intracranial tumors, nasopharyngeal carcinoma, lung cancer, esophageal cancer, and soft tissue tumors.

^{11}C-Choline PET/CT was superior to ^{18}F-FDG imaging in detection of brain metastasis because high uptake of ^{11}C-choline in brain metastasis and glioma, but not in the normal brain parenchyma, can yield a high tumor/non-tumor ratio (Fig. 11.5). ^{11}C-Choline PET/CT was helpful in diagnosing upper ureteral cancer and bladder cancer in that there was minimal radioactivity in the ureteral and bladder in the first 10 min after intravenous administration.

11.1.3.2 Clinical Application of ^{11}C-Acetate PET/CT Imaging

1. Normal Physiological Uptake

After intravenous administration, early tracer accumulation can be found in the myocardium, kidneys, pancreas, spleen, and bone marrow. Myocardial and normal renal tissue showed rapid washout consistent with predominant oxidation to CO_2 via the tricarboxylic acid cycle. At 20 min after administration, normal uptake of ^{11}C-acetate can be found in the pancreas, liver, spleen, and suprarenal gland in PET. ^{11}C-Acetate is mainly excreted via the intestines and little via the urinary tract. Low activity in the bladder allows PET to detect the ^{11}C-acetate-avid tumor in the pelvis.

2. Ischemic Myocardium

^{11}C-Acetate was firstly used for delineation of myocardial oxygen utilization. Because the metabolism of acetate needs the oxygen, the oxidation of acetate is consistent with the consumption of oxygen in cells. Therefore, measurement of myocardial ^{11}C-acetate kinetics allows noninvasive determination of cardiac oxygen consumption. PET with ^{11}C-acetate and dobutamine stress have been suggested to be a promising approach for the evaluation of regional myocardial oxidative metabolic reserve in patients with cardiac diseases of diverse etiologies. Besides, uptake of ^{11}C-acetate was suggested to be represents the pathological state of the mitochondria, which is the organelle where the metabolism of ^{11}C-acetate takes place and its function influences the fate of ^{11}C-acetate.

3. Prostate Carcinoma

^{11}C-Acetate has a manner similar to ^{11}C-choline, and it has been introduced for the evaluation of PCa. Like ^{11}C-choline, ^{11}C-acetate does not have a sufficient diagnostic accuracy for the staging of primary PCa. The diagnostic capacity of ^{11}C-acetate PET/CT was reported to be inferior to that of multiparametric MRI. On a sector-based analysis, ^{11}C-acetate PET/CT demonstrated a sensitivity and specificity of 61.6% and 80.0%, respectively, which were significantly lower than that of MRI (82.3% and 95.1%, respectively) [10]. False positive results can occur in benign processes, such as BPH, due to a considerable overlap of the tracer uptake in primary PCa and benign processes. For evaluation of nodal staging before radical prostatectomy, the sensitivity, specificity, and positive and negative predictive values of ^{11}C-acetate PET/CT were 68.0%, 78.1%, 48.6%, and 88.9%, respectively.

^{11}C-Acetate imaging was reported to be sensitive in the detection of recurrent PCa. However, its positive detection rate is closely related with the level of serum PSA, similar to ^{11}C-choline. When a PSA level greater than 1.24 ng/mL was used as the threshold defining positive findings in ^{11}C-acetate PET/CT imaging of recurrent PCa, the putative sensitivity and specificity were 86.6% and 65.8%, respectively. In the patients with very low PSA levels at relapse (PSA level < 1.0 ng/mL) after RP, the sensitivity of ^{11}C-acetate PET/CT for detecting local recurrence is 66%, which is lower than the endorectal coil MRI (82%) [11].

4. Hepatocellular Carcinoma

An interesting application of ^{11}C-acetate is its role as a useful supplement of ^{18}F-FDG in diagnosing HCC. It is well-known that ^{18}F-FDG PET/CT are always negative in detection of well- or moderately differentiated HCC. In 2003, Ho CL et al. investigated the application of ^{11}C-acetate combined with ^{18}F-FDG in diagnosing HCC in 39 patients.

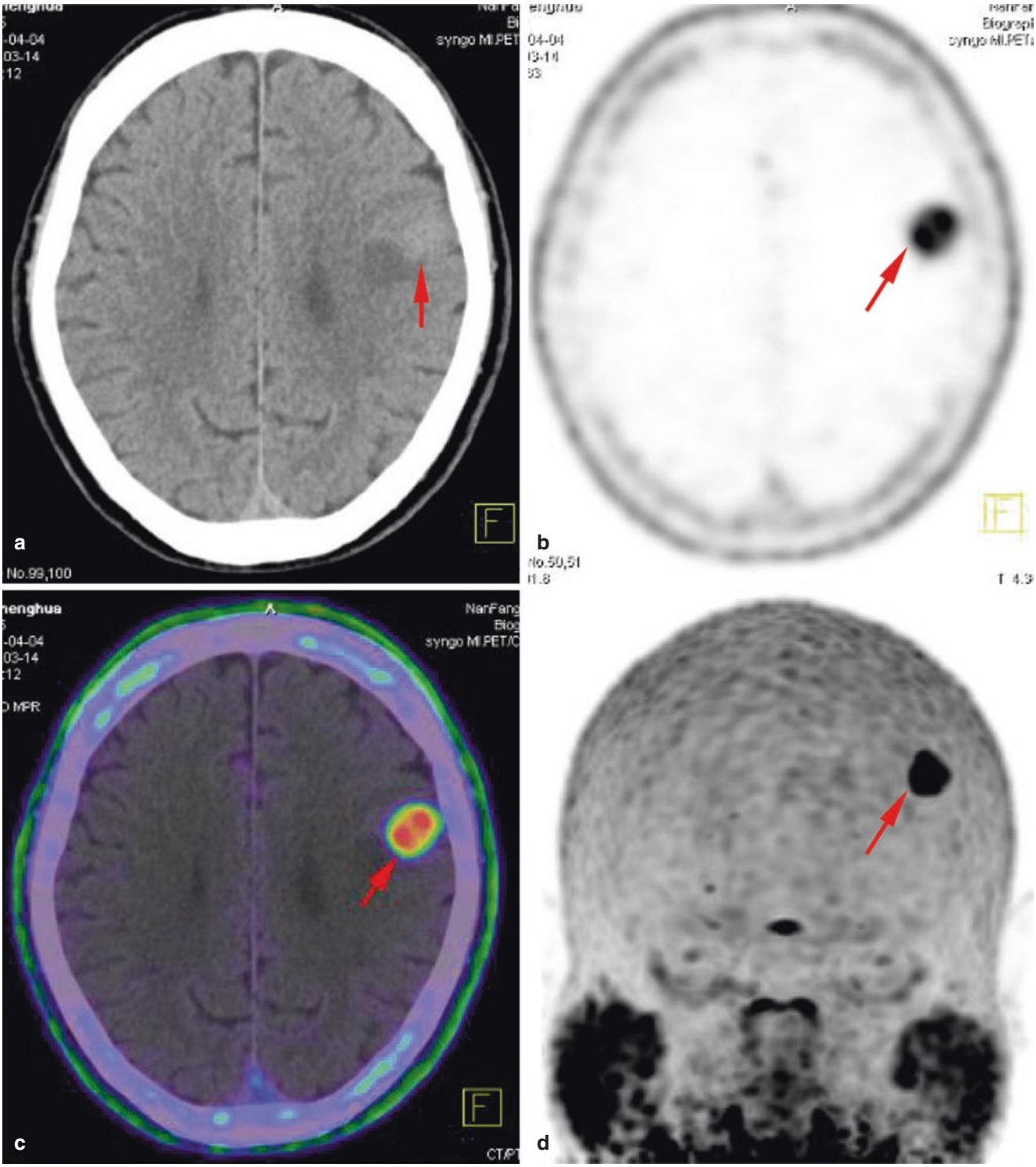

Fig. 11.5 ^{11}C-choline PET/CT of brain metastasis. An occupying lesion with slightly high density and unclear margin, accompanied by peripheral cerebral edema, was detected in the left frontal lobe by non-enhanced CT (**a**, arrow). Intense ^{11}C-choline uptake was noted in the lesion on PET (**b**, arrow) and fused PET/CT (**c**, arrow) and MIP images (**d**, arrow). Minimal uptake of ^{11}C-choline was observed in the normal brain (**b**, **c**, and **d**)

They found ^{11}C-acetate was positive in 87.3% of HCC, whereas the sensitivity of ^{18}F-FDG PET/CT was only 47.3%. Combined with both modalities, the sensitivity increased to 100%. ^{18}F-FDG imaging is superior to ^{11}C-acetate imaging in the detection of poorly and moderately differentiated HCC, while ^{11}C-acetate imaging was more sensitive in detection of well- and moderately differentiated HCC. ^{11}C-Acetate was negative in the liver metas-

tases and cholangiocarcinoma (CCC) [12]. The study by Park confirmed the findings of Ho CL that the combination of ^{18}F-FDG and ^{11}C-acetate imaging could improve the sensitivity of PET for detection of HCC. In 90 patients involving 110 HCC lesions, the study showed that the sensitivities of ^{18}F-FDG and ^{11}C-acetate and combination of both modalities for detection of HCC were 60.9%, 75.4%, and 82.7%, respectively. ^{11}C-Acetate is prone to be positive in the patients with large or multiple lesions. When the size of the lesions were divided into three groups of 1–2 cm, 2–5 cm, and > 5 cm, the positive detection and ^{11}C-acetate were 27.2%, 47.8%, and 92.8% for ^{18}F-FDG and 31.8%, 78.2%, and 95.2% for ^{11}C-acetate, respectively. Combination of ^{18}F-FDG and ^{11}C- acetate was also used to detection the extrahepatic metastases [13]. The research by Ho CL et al. [14] demonstrated that high diagnostic potential was gained with the sensitivity of 98%, specificity of 86%, and accuracy of 96% in 121 patients with metastatic HCC. Combination of ^{11}C-acetate and ^{18}F-FDG PET/CT may also be useful in patient selection for liver transplantation (LT). Cheung TT used ^{11}C-acetate combined with ^{18}F-FDG PET/CT for selection of the patients with HCC for liver transplantation (LT) and partial hepatectomy (PH) [15]. Their research demonstrated that dual-tracer PET/CT had high sensitivity and specificity in both LT and PH for HCC detection (94.1% vs. 95.8%) and TNM staging (90.9% vs. 90.5%). Dual-tracer PET/CT showed not only a significantly higher sensitivity compared to that of contrast CT for patient selection for LT (96.8% vs. 41.9%, $P < 0.05$) but also the specificity (91.7% vs. 33.0%, $P < 0.05$). However, ^{11}C-acetate had limitation in differentiation of HCC from focal nodular hyperplasia (FNH), which was also avid on ^{11}C-acetate PET/CT.

5. Other Tumors
   ^{11}C-Acetate PET/CT can also be used to diagnose renal cell carcinoma, bladder urothelial carcinoma, glioma, lung bronchioloalveolar carcinoma, and multiple myeloma. Although it has some advantages in evaluation of above tumors, comparing to ^{18}F-FDG PET/CT, it is still not widely applied in the clinic for these tumors.

11.2 Amino Acid PET Imaging

11.2.1 Characteristics and Pathways of Amino Acid Metabolism

Amino acids (AAs) are organic compounds containing amine (-NH_2) and carboxyl (-COOH) functional groups, along with a side chain (R group) specific to each amino acid. All 20 of the amino acids present in proteins are essential for health. Humans can synthesize 12 of the 20 common amino acids from the intermediates of glycolysis and of the citric acid cycle.

11.2.1.1 Source of Amino Acids

1. Metabolic Pool of Amino Acid
   Exogenous amino acids are derived from the degradation of proteins in foods. In vivo synthesis of nonessential amino acids and amino acids from human protein degradation is collectively referred to as endogenous amino acids. Exogenous amino acids and endogenous amino acids mixed together are a metabolic pool, distributed in the body and involved in cell metabolism.

   Metabolic pool of amino acid is usually calculated as the total amount of free amino acids. The amino acids are unable to free pass through the cell membrane, so the body distribution is not uniform. Muscle accounts for more than 50% of the total amino acids, the liver accounts for about 10%, the kidney accounts for about 4%, and plasma accounts for about 1–6%. The catabolism of most amino acids such as alanine and aromatic amino acids is mainly in the liver. Branched-chain amino acid catabolism is mainly occurred in skeletal muscle.
2. Protein Turnover to Generate Amino Acids
   Proteins are essential nutrients for the human body. The human proteins are in a state of equilibrium of synthesis and degradation. Each day humans turn over 1–2% of their total body protein, principally muscle protein. Approximately 70–80% of the amino acids produced by protein degradation are reused.

   Different proteins have different rates of degradation. The rate of protein degradation varies with physiological circumstances. The high rate of protein degradation occurs in tissues that undergo structural rearrangement, such as uterine tissue during pregnancy or skeletal muscle when starved. The degraded protein is expressed in terms of its half-life ($t_{1/2}$), which is the time it takes to reduce its concentration to half its original value. The half-life of liver proteins varies from 30 min to more than 150 h. In order to meet the physiological needs, it can accelerate or delay the degradation of key enzymes, thereby changing the enzyme content, to further change the metabolite flux and metabolite levels.

   There are two major ways to degrade proteins in eukaryotes. (1) Proteins are degraded in lysosomes through ATP-independent manner. Lysosomes are the main sites of digestion. It is the intracellular digestive organs. Lysosomes contain a variety of proteases. These proteases have poor selectivity for degrading proteins and mainly degrade extracellular proteins, membrane proteins, and intracellular long-half-life proteins. Proteins are degraded by this pathway without consuming ATP. (2) Proteins are degraded by proteasomes in an ATP-dependent manner. Ubiquitin is necessary for the degradation of proteins by this pathway. Ubiquitin is a 76 amino acid polypeptide that is named for its widespread presence in eukaryotic cells. Ubiquitin-mediated protein degradation is a complex process. First, ubiquitin forms a

covalent linkage to the protein that is selected for degradation, allowing it to be labeled and activated, and then the proteasome specifically recognizes and degrades the marked protein. Ubiquitination involves a three-step reaction involving three enzymes (El, E2, and E3) and consumes ATP. Ubiquitinated proteins are degraded to peptides containing 7–9 amino acid residues that are further hydrolyzed to amino acids.

11.2.1.2 Transamination of Amino Acids

1. Interconversion Between α-Amino Acid and α-Keto Acid
   Transaminases catalyze the transamination to reversibly transfer the amino group of an α-amino acid to an α-keto acid, resulting in the deamination of the amino acid to the corresponding α-keto acid while the original α-keto acid becomes another type of amino acid. All protein amino acids except lysine, threonine, proline, and hydroxyproline are involved in transamination. Transaminases are widely distributed in various tissues, most abundant in the liver and heart. A variety of transaminases exist in the body. Transamination between α-amino acids and α-keto acids can only be catalyzed by a specific aminotransferase. Transaminases have the same coenzyme and mechanism of action. Pyridoxal phosphates are their coenzyme. During transamination, bound PLP serves as a carrier of amino groups. Among various aminotransferases, glutamate-pyruvate transaminase (GPT) also known as alanine aminotransferase (ALT) and glutamate oxaloacetate aminotransferase (GOT) also known as aspartate aminotransferase (AST) are the most important.
2. Oxidation of L-Glutamate by L-Glutamate Dehydrogenase
   The reactions of transamination of amino acids can be focused on L-glutamate. This is important because L-glutamate is the only amino acid that undergoes oxidative deamination by L-glutamate dehydrogenase in human tissues. L-Glutamate dehydrogenase is widespread in the liver, kidneys, and brain tissue. L-Glutamate dehydrogenase catalyzes the oxidative deamination of L-glutamine to α-ketoglutarate and ammonia. L-Glutamate dehydrogenase is the only enzyme that uses NAD and NADP as reducing equivalents.
3. Transamination by Purine Nucleotide Cycle
   L-Glutamate dehydrogenase activity in the myocardium and skeletal muscle is weak. Therefore, the transamination of amino acids in these tissues is by another pathway.

   In these tissues, amino acids are primarily deaminated by purine nucleotide cycle. In this process, aspartic acid is first produced by successive transamination of the amino acid into oxaloacetate. Aspartate reacts with inosine monophosphate (IMP) to generate adenylosuccinate, which cleaves to release fumarate and produce adenine nucleotide (AMP). AMP adenosine deaminase catalytic the final deamination step. Therefore, purine nucleotide cycle can also be seen as another joint deamination process.
4. Transamination by Amino Acid Oxidase
   Most of the ammonia released from L-glutamate reflects the combined effect of aminotransferases and L-glutamate dehydrogenase. Liver and kidney tissues also contain L-amino acid oxidase using FMN or FAD as a coenzyme. L-amino acid oxidases of the liver and kidney convert amino acids to α-amino acid that decomposes to an α-keto acid with release of ammonium ion. The reduced flavin is reoxidized by molecular oxygen, forming hydrogen peroxide (H_2O_2), which then is split to O_2 and H_2O by catalase.

11.2.1.3 Metabolism of Amino Acid Carbon Backbone

After deamination, *α-keto acid* can be metabolized in three pathways. (1) α-keto acid can completely undergo oxidative decomposition to provide energy. α-keto acid is converted to CO_2 and H_2O through TCA cycle with releasing energy to support physiological activity. As such, amino acids are also a class of energy substances. (2) α-keto acid is used to produce nonessential amino acids. Some of α-keto acids are derived from the products of glucose metabolism and TCA cycle. For example, pyruvate, oxaloacetate, oxaloacetate, and α-ketoglutarate can be converted to alanine, aspartic acid, and glutamate. (3) α-keto acid can be used to produce glucose and lipids. It includes glucogenic amino acid, ketogenic amino acid, and glucogenic and ketogenic amino acid.

1. Ammonia Metabolism
   (a) Transportation of Ammonia
   Ammonia is a toxic substance. Ammonia is mainly transported as alanine and glutamine in the blood.

   Through the alanine-glucose cycle, ammonia is delivered from the muscle to the liver. In the muscle, amino acids are converted by aminotransferases into pyruvate to produce alanine and transported by the blood to the liver. In the liver, alanine is converted to pyruvate with release of ammonia. Ammonia is used to synthesize urea, and pyruvate is converted to glucose by gluconeogenesis. Glucose is transported to the muscle by the blood and is converted to pyruvate by glycolysis. The pyruvate is then converted to alanine again. Through this cycle, muscle ammonia is delivered to the liver as a nontoxic alanine, while liver provides pyruvate to the muscle to produce glucose.

   Through glutamine, ammonia is delivered from the brain and muscle to the liver or kidney. Glutamine is another transporter of ammonia. In the brain and muscle tissue, glutamine synthetase catalyzes the synthesis of glutamine from ammonia and glutamate.

Glutamate is transported by the blood to the liver or kidney. It is catalyzed by glutaminase to produce glutamate and ammonia.

(b) Ornithine Cycle

Under normal circumstances, the most of ammonia is synthesized as urea in the liver. And only a small portion of ammonia is excreted through urine as ammonium salts. Ammonia is converted to urea through ornithine cycle. The entire process converts two amino groups, one from $NH4^+$ and one from Asp, and a carbon atom from HCO_3^-, to the relatively nontoxic excretion product urea at the cost of four "high-energy" phosphate bonds (three ATP hydrolyzed to two ADP and one AMP). The conversion from ammonia to urea happens in five main steps. (1) NH_3, CO_2, and ATP are condensed into carbamoyl phosphate. The reaction is catalyzed by carbamoyl phosphate synthetase I (CPS-I), which is a rate-limiting enzyme in ornithine cycle. (2) Carbamoyl phosphate reacts with ornithine to form citrulline. The carbamoyl moiety of the carbamoyl phosphate is transferred to ornithine catalyzed by ornithine carbamoyl transferase (OCT) to form citrulline. (3) Citrulline reacts with aspartic acid to form argininosuccinate. After mitochondrial synthesis, citrulline is transported to the cytoplasm. In the cytoplasm, citrulline is acted with aspartate to form argininosuccinate by argininosuccinate synthetase. Aspartate provides the second nitrogen of the urea. (4) Argininosuccinate cleaves into arginine and fumarate. Argininosuccinate is cleaved by argininosuccinate lyase. (5) Arginine hydrolysis releases urea and regenerates ornithine. In the cytoplasm, arginine is catalyzed by arginase and hydrolyzed to produce urea and ornithine. Ornithine enters the mitochondria through a carrier localized on mitochondrial inner membrane to produce citrulline. Urea is excreted as an end product of metabolism.

2. Metabolism of Individual Amino Acids

In addition to the common metabolic pathways, amino acids have their own special metabolic pathways due to their different side chains. This section describes only a few important amino acid metabolic pathways.

(a) The decarboxylation of amino acids produces amines. Some amino acids can be decarboxylated into the corresponding amine. The enzyme catalyzing decarboxylation is called decarboxylase. Pyridoxal phosphate is a coenzyme of amino acid decarboxylase. The level of amine in vivo is low but has important physiological functions. Amine content is not high but has important physiological functions. Amine oxidase can oxidase amine to the corresponding aldehyde, NH_3 and H_2O. The aldehyde is then oxidized to a carboxylic acid, which is then reoxidized to carbon dioxide and water, or in urine to avoid amine accumulation.

Glutamate is decarboxylated to γ-aminobutyric acid (GABA) catalyzed by L-glutamate decarboxylase. This enzyme is highly active in brain and kidney tissue. Therefore, GABA is highly concentrated in the tissues. GABA is an inhibitory neurotransmitter that inhibits the central nervous system.

Histidine is decarboxylated to histamine by histidine decarboxylase. Histamine is widely distributed in the body, breast, lung, liver, muscle, and gastric mucosa. Histamine is a powerful vasodilator that increases capillary permeability. Histamine can cause bronchospasm or promote gastric mucosal cells to secrete pepsinogen and gastric acid.

Tryptophan was first catalyzed by tryptophan hydroxylase to produce 5-hydroxytryptophan and then by 5-hydroxytryptophan decarboxylase to produce 5-hydroxytryptamine (5-HT). 5-HT is widely distributed in various tissues, in addition to nerve tissue, but also to the gastrointestinal tract, platelets, and breast cells. 5-HT is a neurotransmitter with an inhibitory effect that directly affects nerve conduction. In peripheral tissues, 5-HT has a strong vasoconstrictor effect.

(b) One-Carbon Metabolism

One-carbon unit refers to carbon-containing groups generated during some amino acid catabolism including methyl ($-CH_3$), methyl ($-CH_2-$), methyl (-CH-~), formyl (-CHO), and iminomethyl (-CH-~NH). One-carbon unit is often associated with tetrahydrofolate (FH_4) for transportation and metabolism. FH_4 is a carrier of one-carbon unit. One-carbon unit is mainly derived from the catabolism of cysteine, glycine, histidine, and tryptophan. One-carbon unit produced from amino acids is interconvertible. One-carbon unit can bind to N5 and N10 positions of tetrahydrofolate. N5 of tetrahydrofolic acid is bound to methyl or iminomethyl, N5 and N10 are bound to methyl or methyl, and N5 or N10 is bound to formyl.

The main function of the one-carbon unit is to participate in the synthesis of purines and pyrimidines. One-carbon units establish a close relationship between amino acid metabolism and nucleotide metabolism. Metabolic disorders or lack of FH4 can cause megaloblastic anemia and other diseases. Application of methotrexate and other folic acid analogs can inhibit the formation of FH4, thereby inhibiting the synthesis of nucleic acids to achieve anticancer effect.

(c) Sulfur-Containing Amino Acid Metabolism

Sulfur-containing amino acids include methionine, cysteine, and cystine. Methionine can be converted to

cysteine and cystine. Cysteine and cystine can be transformed into each other, but cannot be converted to methionine. Therefore, methionine is an essential amino acid.

Methionine contains S-methyl molecules, through a variety of methyl transfer that can generate a variety of methyl-containing physiologically active substances, such as epinephrine, carnitine, choline, creatine, and so on. Methionine must react with ATP catalyzed by adenosyltransferse to produce adenosylmethionine (SAM) prior to methyl transfer. The methyl group in SAM is called active methyl, and the SAM is called active methionine. SAM is the most important methyl donor in vivo. SAM is catalyzed by methyltransferase to transfer to substrate, called methylation. After methylation, SAM is converted to S-adenosyl homocysteine, which is converted to homocysteine with release of adenosine. Homocysteine then receives methyl group from N^5-CH_3-FH_4 to regenerate methionine.

(d) Catabolism of Aromatic Amino Acid Metabolism Can Produce Neurotransmitters

Aromatic amino acids include phenylalanine, tyrosine, and tryptophan. Tyrosine can be produced by phenylalanine via hydroxylation. Phenylalanine and tryptophan are essential amino acids. Tyrosine can be used to synthesis of neurotransmitters, hormones, and melanin.

Tyrosine can be converted to 3,4-dihydroxyphenylalanine (DOPA) by tyrosine hydroxylase. DOPA is decarboxlated into dopamine DOPA decarboxylase. In the adrenal medulla, the carbons of the dopamine side chain are hydroxylated, producing norepinephrine, and methylated to epinephrine. Dopamine, norepinephrine, and epinephrine are collectively known as catecholamines. Tyrosine hydroxylase is the rate-limiting enzyme in catecholamine synthesis and is regulated by the feedback of the final product.

Another pathway of tyrosine metabolism is to synthesize melanin. In melanocytes, tyrosine is hydroxylated by tyrosinase to produce DOPA, which is converted to indoloquinones by oxidation, decarboxylation, and other reactions. Finally, indoloquinone polymerizes into melanin. Patients with congenital tyrosinase deficiency are called albinism.

11.2.2 Amino Acid Transportation System and Amino Acid PET Imaging

The clinical nuclear medicine uses a variety of imaging modalities to profile the diseases at the molecular level. The typical modalities for nuclear molecular imaging include positron-emission tomography (PET) and single-photon emission computed tomography (SPECT). For both PET and SPECT, the radiotracers are crucial for the disease characterization. By introducing radionuclide into the scaffold of natural or synthesized compounds, different radiotracers were developed for disease diagnosis and therapy recently. Of these probes, radiolabeled amino acids (AAs) have been introduced in a broad range of clinical applications, frequently labeled with the suitable radionuclides including C-11 ($t_{1/2}$ 20.4 min), N-13 ($t_{1/2}$ 10.0 min), F-18 ($t_{1/2}$ 110 min), and I-124 ($t_{1/2}$ 4.2 days).

L-AAs are essential substances playing an important role in maintaining cell growth and nitrogen balance, as well as a variety of roles in biological processes, including protein synthesis and cell signaling. Besides that, AAs can also serve as alternative energy source to glucose for tissues or cells in many biologic processes. All amino acids are hydrophilic and cannot transverse the cell membrane without the help of certain membrane proteins called AA transporters. Tumor cells often features overexpression of specific AA transporters and increased AA uptake to support their fast proliferation. Due to the imperative role of their consumption in many cellular processes, radiolabeled AAs have become an appealing class of compounds to be used as PET tracers for cancer imaging.

Based on the transporting mechanisms, the AA transporters can be divided into several systems, including sodium dependence, substrate specificity, tissue expression patterns, and sensitivity to pH or hormones. Normally different transport systems co-exist in the cell plasma membranes, including generally existed transport systems (such as systems A, system N, ASC, L, y^+ and $X_{AG}-$, X_C^-) and tissue-specific transport systems (such as systems B^0 and $b^{0,+}$).

Na^+-independent system L is the major transporter that uptakes branched and aromatic AAs from the extracellular space. Many cancer 1.7cells use system L transporters to acquire essential AAs. The AAs transported by system L transporter include isoleucine, valine, methionine, histidine, phenylalanine, and tryptophan. Four subtypes of system L have been isolated, including L-type AA transporters 1 (LAT1), LAT2, LAT3, and LAT4. LAT1 and LAT2 are obligatory AA transporter, while LAT3 and LAT4 mainly mediate AA perfusion. In cancer, LAT1 has a more crucial role when compared with other three transporters. It has a specific role in carcinogenesis and expression type in a variety of cancers, including lung, colon, brain, breast, prostate cancer, and T-cell acute lymphoblastic leukemia (T-ALL).

System ASC (alanine-serine-cysteine) is a Na^+-dependent transporter capable of mediating net influx or efflux, with substrates (L-alanine, L-serine, L-cysteine, and L-glutamine). It belongs to a member of the solute carrier 1(*SLC1*) family with two subtypes isolated as ASC-Type AA transporter 1 (ASCT1) and ASC-Type AA transporter 2 (ASCT2). ASCT2

utilizes an intracellular gradient of AAs, efflux of intracellular AAs in exchange for extracellular AAs. Glutamine is a key substrate of ASCT2 with important roles in tumor metabolism. ASCT2 is overexpressed in many human cancers including non-small cell lung cancer (NSCLC), prostate cancer, breast cancer, glioma, liver cancer, and many other tumors. ASCT2 overexpression is also closely related to prognosis, demonstrating a significant role for cancer imaging.

System X_C^- is a sodium-independent and Cl^--dependent AA antiporter. It mediates the exchange of extracellular L-cystine and intracellular L-glutamate across the cellular plasma membrane at 1:1 ratio. It consists of the transporter subunit SLC7A11 and the regulatory subunit SLC3A2. In many cells, the import of L-cystine through this transporter is critical to glutathione production and oxidative protection. The exchange-mediated export of L-glutamate takes on added significance within the CNS, as it represents a nonvesicular route of release through which this excitatory neurotransmitter can participate in either neuronal signaling or pathology. It is not only a potential target for therapy but also a potential PET biomarker for imaging the system X_C^- activity of cancer and other diseases.

The transporter systems can serve as the target for PET imaging as for their significant role in disease diagnosis and therapy evaluation, especially for LAT1, ASCT2, and xCT. Both ASCT2 and LAT1 are upregulated in most tumor tissues. Tumor cell accumulation of AA PET tracers mainly depends on the rate and mechanism of AA transport. Based on the overexpression of AA transporters, the uptake of AA PET tracers in tumor cells is greater than that in normal cells.

11.2.3 AA PET Tracers

AAs are most frequently radiolabeled with radionuclides including ^{11}C and ^{18}F. However, the short half-life for ^{11}C (20 min, 100% of beta positron decay) makes it not a suitable radionuclide for PET imaging. To overcome the limitations of ^{11}C, a series of ^{18}F-labeled AAs (half-life of 110 min, 97% of beta positron decay) were developed. The radiolabeled amino acids can be classified into two categories, the structure-changed and structure-unchanged labeled AAs. Normally the radiolabeling process does not change the chemical structure of a specific AA and thus produced the structure-unchanged labeled AAs, like ^{11}C-Met. These specific radiotracers can still maintain the same pharmacodynamics and pharmacokinetics profiles as the natural AAs. On the contrary, structure-changed AA tracers (such as ^{18}F-FET and S-(^{11}C)-methyl-L-cysteine) can be produced by using unnatural nuclides (like ^{18}F nuclides) or structure-modified AA precursors. These AA tracers cannot have the same structure as the natural AA and thus cannot be incorporated into protein synthesis. However, like structure-changed labeled AAs, these nonnatural AA tracers can be transported via the AA transport and thus can be employed for the characterization of specific AAs transportation or metabolism for different diseases. Recently, specific radiotracers including^{18}F-FAMT, ^{18}F-FET, ^{18}F-D-FMT, ^{18}F-FDOPA, ^{18}F-FMT, ^{18}F-Cis-FPro, ^{18}F-OMFD, ^{18}F-FACBC, ^{18}F-FACPC, ^{11}C-HTP, ^{11}C-DOPA, BAY 94–9392, BAY85–8050, and ^{18}F-(2*S*, 4*R*)4F-GLN have been used in clinical PET imaging of tumors.

11.2.4 Clinical Applications

AA PET tracers were used initially to profile the protein synthesis in vivo. These AA PET tracers include ^{11}C-labeled natural AAs, such as L-leucine, L-methionine, L-phenylalanine, and L-tyrosine. Meanwhile, AA transporters can also serve as the main targets for tumor metabolism imaging in vivo. For this purpose, a wide range of ^{11}C and ^{18}F AAs have been developed. These established AA tracers are used for imaging of brain tumors, neuroendocrine tumors, breast and prostate cancer, and many other tumors.

11.2.4.1 Brain Tumors

Cerebral gliomas are the most common primary brain tumors in adults with an incidence of 5–6 in 100,000. The brain metastasis is more frequently observed in clinic with an incidence of 8–14 in 100,000. ^{18}F-FDG in clinic has significant limitations for brain tumor imaging, due to the high metabolism of glucose in the healthy brain. In contrast, the AA tracers have a lower uptake in the healthy brain and a higher tumor-to-background ratio, thus providing a better tumor boundary characterization. AA tracers including ^{18}F-FET, ^{11}C-MET, and ^{18}F-FDOPA are often employed for brain tumor diagnosis, surgical interventions, targeting biopsies, as well as radiation therapy. They can play important role in excluding pseudoprogression and radionecrosis for both brain tumor primary diagnosis and following treatment response evaluation.

Compared to ^{18}F-FDG, the superior diagnostic accuracy of ^{11}C-MET has been demonstrated in detecting, grading, delineating, and searching recurrences, prediction of prognosis, and evaluation of response to treatment. It demonstrated a significantly higher sensitivity for brain tumor biopsy guidance when compared to ^{18}F-FDG. However, the short half-life of ^{11}C limits its clinical use as for the requirement of the on-site cyclotron. The sensitivity of ^{11}C-MET was also lower in the studies with high proportions of low-grade glioma, which is the most universal type of primary brain tumor. Moreover, there is not yet enough evidence about grading glioma, and its use in differentiating tumor recurrences from radiation necrosis is controversial [16–18].

The two most common amino acid PET radiopharmaceuticals labeled with ^{18}F (109.8 min half-life) are O-(2-[^{18}F] fluoroethyl)-L-tyrosine (FET) and 3,4-dihydroxy-6-[18F]-fluoro-L-phenylalanine (FDOPA). ^{18}F-FET and ^{18}F-FDOPA are derivatives of ^{18}F-labeled L-phenylalanine and L-tyrosine, which target system L transporters to detect brain tumors. ^{18}F-FET provides both good-contrast PET images of brain tumors [19–21] and valuable information about differentiating low-grade from high-grade tumor. Dynamic ^{18}F-FET examinations show high diagnostic accuracy in patients with suspected tumor progression or recurrence in clinical settings [20, 21]. ^{18}F-FET also can differentiate recurrent brain tumor from pseudoprogression and radiation necrosis. Additionally, ^{18}F-FET has a lower uptake by inflammatory cells than ^{11}C-MET or ^{18}F-FDG, and it clearly delineates tumors from inflammation.

^{18}F-FDOPA is an analog of L-DOPA, and ^{18}F-OMFD is a major metabolite of ^{18}F-FDOPA. ^{18}F-FDOPA has been used to investigate the activity of aromatic L-AA decarboxylase and to evaluate the dopaminergic system functioning in brain tumors and neuroendocrine tumors. ^{18}F-FDOPA has been used for detecting primary, metastatic, and recurrent brain tumors and provides valuable information on the delineation of tumor volume, the determination of proliferative activities, and grading [22, 23]. The uptake of ^{18}F-FDOPA correlates with the glioma grade; thus, it plays an important role for managing patients in clinical settings [22].

There are several AA PET tracers of imaging glutaminolysis, such as L-[5-^{11}C]-glutamine, 4-^{18}F-(2S,4R)-fluoroglutamine (^{18}F-FGln), and (2S,4S)-4-(3-^{18}F-fluoropropyl)glutamine (^{18}F-FPGln). In glioma patients, the tracer ^{18}F-FGln showed tumor-to-background contrast different from that of ^{18}F-FDG and differences in uptake in glioma patients with clinical progression of disease versus stable disease (tumor-to-brain ratio 3.7 in clinically active glioma tumors, minimal or no specific uptake in clinically stable tumors) [24]. This indicates ^{18}F-FGln PET may be a new tool for probing in vivo metabolism of glutamine in cancer patients and for guiding glutamine-targeted therapeutics.

11.2.4.2 Neuroendocrine Tumors

Neuroendocrine tumors (NETs) are a heterogeneous group of neoplasms comprising at one end of the spectrum well-differentiated and slowly growing tumors. ^{18}F-FDG, the most commonly used radiotrancer, features low uptake for most of NETs, demonstrating no significant advantage for NETs imaging.

In many NETs the serotonin pathway is overactive. Therefore, the development of a PET tracer for NETs exploiting this pathway is of invaluable importance. At present, a carbon-11-labeled tracer has been developed for the serotonin pathway, ^{11}C-5-HTP [25]. ^{11}C-HTP is useful for detecting small tumors and early recurrences; however, the 20-min half-life of ^{11}C and difficulty for synthesis limit its wide clinical use.

NETs have an increase activity of aromatic AA decarboxylase (AADC) and a favorable imaging property and a high accumulation of ^{18}F-DOPA. ^{18}F-FDOPA is a favorable AA tracer for diagnosing NETs with high accuracy, such as pheochromocytomas, pancreatic pheochromocytoma, and insulinomas, and for staging carcinoids, which cannot be detected by CT, MRI, or other imaging tracers. Additionally, ^{18}F-FDOPA is a highly sensitive marker in patients with functional carcinoid tumors and has low sensitivity for malignant NETs, such as medullary thyroid cancer and pancreatic islet cell tumors.

One study compared ^{11}C-HTP PET and ^{18}F-FDOPA PET in patients with gastrointestinal NET and pancreatic NET. ^{18}F-FDOPA was found to be more sensitive than ^{11}C-HTP (98 vs. 89%, respectively) for gastrointestinal NET. However, for pancreatic NET, the result was opposite (80 vs. 96%, respectively) [26].

11.2.4.3 Breast Tumors

^{18}F-FDG has multiple limitations in breast cancer imaging, including difficulty distinguishing malignant from benign primary breast lesions and variable sensitivity and specificity of breast cancer lesions, depending on tumor and patient characteristics and limited utility in the evaluation of the breast and axilla. In particular, invasive lobular carcinoma (ILC) features a lower ^{18}F-FDG uptake when compared with the most common invasive ductal carcinoma (IDC) in both the primary and metastatic breast tumors.

^{18}F-Fluciclovine (^{18}F-FACBC), an L-leucine analog, is a nonnaturally occurring amino acid analog. ^{18}F-Fluciclovine (^{18}F-FACBC) PET/CT can visualize malignant tumors ILC and IDC. In a study with 12 women, ^{18}F-fluciclovine has a fourfold higher uptake in malignant breast lesions than in benign lesions, with the greatest uptake found in the highest-grade malignancies, indicating that ^{18}F-fluciclovine can be used for breast cancer PET/CT imaging. Changes in ^{18}F-fluciclovine avidity were strongly associated with a reduction in the percentage of tumor on pathology caused by treatment [27]. In addition to detecting and locating breast cancer, ^{18}F-fluciclovine may provide a new tool for the exploration of amino acid transport and metabolism in breast cancer. ^{18}F-fluciclovine also detected lymph nodes and bone metastases, but liver metastases were less effective due to the high physiological uptake of the tracer in liver parenchyma.

The AA transporter system Xc^- is also upregulated in some breast cancers. Amino acid analog (4S)-4-(3-[^{18}F] fluoropropyl)-L-glutamate (^{18}F-FSPG) has been introduced to

evaluate Xc activity and provide PET/CT imaging of tumors. ^{18}F-FSPG PET imaging has been performed both in preclinical and clinical studies, although uptake in breast cancer lesions was lower and not appreciated in all breast tumors [28]. Recently, preclinical studies of ^{18}F-fluoroaminosuberic acid, another cysteine/glutamate analog, also demonstrate a high tumor uptake in multiple breast cancer cell lines and a great potential for clinical breast cancer imaging.

11.2.4.4 Prostate Tumors

Prostate cancer is a complex and biologically heterogeneous tumor. It is the most common non-cutaneous malignancy in men and second leading cause of cancer-related death in the United States and Europe. ^{18}F-FDG in prostate cancer is very low. It is not an adequate tracer for differentiating prostate cancer, benign hyperplasia lesion, and normal prostate, and it is not useful for initial staging and is of limited utility in the clinical setting of biochemical failure after prior definitive therapy for primary cancer. ^{11}C-MET is a helpful tracer for imaging the prostate in patients with increased PSA levels. Short dynamic scanning limits the wide clinical use of ^{11}C-MET for imaging prostate cancer.

Many amino acid transporter systems are overexpressed in prostate cancer, predominantly large neutral amino acid transporters (L systems: LAT1, LAT3, and LAT4) and alanine-serine-cysteine transporters (ASC systems: ASCT1, ASCT2). Prostate cancer may be imaged using both radiolabeled natural and synthetic amino acids. Naturally occurring amino acids like ^{11}C-methionine are not optimal for imaging because of the accumulation of metabolites in nontarget organs, whereas radiolabeled synthetic, nonmetabolized amino acid analogs are preferred owing to simpler kinetics and the ability to radiolabel with longer-lived radionuclides.

^{18}F-Fluciclovine (^{18}F-FACBC) is used frequently in the clinical studies for prostate cancer. ^{18}F-FACBC is predominantly transported via ASCT2 and LAT1. Because these transporters mediate both influx and efflux of amino acids, peak uptake in tumors occurs at 5–20 min after injection with variable washout [29]. ^{18}F-FACBC is only minimally eliminated by the kidneys during the typical imaging time course. Due to its low urinary excretion after injection, it has advantages in the imaging of prostate cancer when compare with ^{18}F-FDG [30]. Prostate cancer, within the prostate or in pelvic lymph node metastases, can be detected using ^{18}F-FACBC with high sensitivity and specificity. ^{18}F-FACBC is highly useful in the detection of recurrent prostate cancer even in the presence of negative or equivocal conventional imaging [29]. ^{18}F-FACPC, as an analog of ^{18}F-FACBC, is a helpful tracer for imaging prostate cancer, but ^{18}F-FACPC is not a good tracer for imaging pelvic lymph node metastases compared to ^{18}F-FACBC.

11.2.4.5 Other Tumors

Human hepatocellular carcinoma can be imaged using ^{18}F-FSPG and demonstrated a significantly greater tumor-to-liver background ratios compared with ^{11}C-acetate. The use of ^{18}F-FAMT PET/CT for bone metastasis detection regardless of the lesion phenotype was demonstrated, indicating ^{18}F-FAMT PET/CT has the potential to complement ^{18}F-FDG PET/CT for the detection of bone metastases [31]. ^{18}F-D-FMT (BAY 86–9596), a derivative of ^{18}F-labeled tyrosine and transported via the system L transporter 1 (LAT-1), showed a lower sensitivity but higher specificity for ^{18}F-D-FMT than ^{18}F-FDG in patients with NSCLC and head and neck squamous cell cancer [32].

11.3 Nucleotide Metabolism Imaging

11.3.1 Introduction

A nucleotide is a structural component of DNA and RNA (Fig. 11.6), also known as building block. It consists of a base one of the chemicals adenine (A), thymine (T), uracil (U) guanine (G), and cytosine (C) plus a molecule of sugar and one of phosphoric acid, where C, T, and U are called **pyrimidines** and each has a single nitrogen-containing ring. On the other hand, A and G are called **purines**, and each has two nitrogen-containing rings, where U only exists in RNA and T only exists in DNA.

Nucleic acid metabolism is the process in which nucleic acids (DNA and RNA) are synthesized and degraded. Nucleic acids are polymers of nucleotides. Synthesis is an anabolic mechanism involving the chemical reaction of phosphate, pentose sugar, and a nitrogenous base where degradation of nucleic acids is a catabolic reaction. Additionally, parts of the nucleotides or nucleobases can be salvaged to recreate new nucleotides. Both synthesis and degradation reactions require enzymes to facilitate the event. Defects or deficiencies in these enzymes can lead to a variety of diseases including cancer [33].

Once synthesis takes place, they can exchange phosphates among one another in order to create mono-, di-, and triphosphate molecules. The conversion of a nucleoside diphosphate (NDP) to a nucleoside triphosphate (NTP) is catalyzed by nucleoside diphosphate kinase, which uses ATP as the phosphate donor. Similarly, nucleoside monophosphate kinase carries out the phosphorylation of nucleoside monophosphates. Adenylate kinase is a specific nucleoside monophosphate kinase that functions only on adenosine monophosphate (AMP) [33, 34].

DNA and RNA have a variety of biological functions: to form energy in the body, to participate in metabolic and

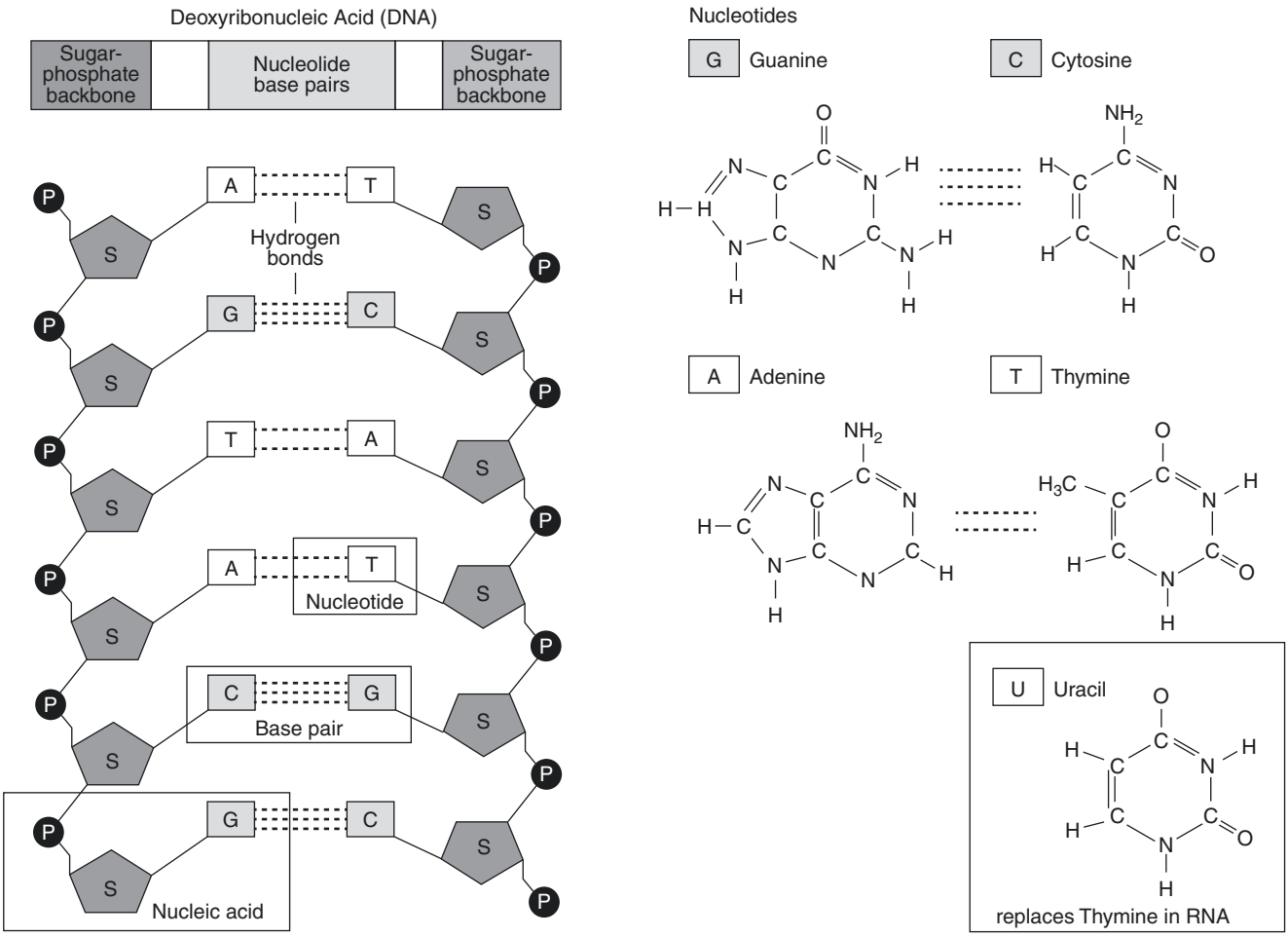

Fig. 11.6 Structure of nucleotides and nucleic acids (DNA and RNA)

physiological regulation in the human body, composition of coenzyme, and activation of intermediate metabolites for various body activities.

11.3.2 Role of Nucleotide Metabolism in Various Diseases Including Cancer

All nucleotides are essential for a variety of cellular processes. It has been well-known that imbalances in nucleotide levels lead to a variety of human diseases, like cancer immunodeficiency [35], aging, kidney diseases [36], gout, and a number of mitochondrial pathologies [37].

11.3.2.1 Synthesis of Nucleotides

There are two pathways for the synthesis of nucleotides: the de novo synthesis pathway and the salvage synthesis pathway. In the de novo pathway, glucose and glutamine are the major nutrients needed to synthesize nucleotides [38]. Glucose is converted to ribose-5-phosphate during the pentose phosphate pathway, which is used for both purine and pyrimidine syntheses [39]. Glutamine is necessary for supplying nitrogen [40]. Purines and pyrimidines are synthesized in two distinct ways [40]. Purines are made by directly assembling the atoms that comprise the purine ring onto ribose-5-phosphate through 11 steps. This yields inosine monophosphate (IMP), which is further modified to produce adenosine monophosphate (AMP) and guanosine monophosphate (GMP). In contrast, during pyrimidine synthesis, the pyrimidine ring is completed before addition of the ribose-5-phosphate moiety. Pyrimidines are made through a six-step process, which produces uridine monophosphate (UMP). UMP can then be converted into cytidine triphosphate (CTP). Thymine is synthesized after uridine diphosphate (UDP) and cytidine diphosphate (CDP) are reduced, and thymidylate synthase (TS) is necessary for dTTP synthesis [40].

On the other hand, salvage pathway exists for both purine and pyrimidines [40]. Normal cells undergo turnover and degradation of cellular materials, leading to release of free

purines or substrates that compose the pyrimidine ring [40]. These can be converted back into dNTPs by a variety of enzymes in both the cytosol and mitochondria [40]. Interestingly, pyrimidine salvage is more efficient than purine salvage [40].

11.3.2.2 Synthesis of Deoxyribonucleotides

One particular type of nucleotide named 2′-deoxyribonucleoside 5′-triphosphates (dNTPs) is necessary for both DNA replication and repair [40, 41]. Without the correct levels of dNTPs, cells can't faithfully replicate either nuclear or mitochondrial DNA, and DNA damage can't be repaired [42]. The rate-limiting step in dNTP synthesis is reduction of ribonucleoside di- or triphosphates (NDPs/NTPs) at the 2′ position of ribose sugar to deoxyribonucleotide di- or triphosphates (dNDPs/dNTPS) by ribonucleotide reductase (RNR) [40, 41]. During reduction of ribonucleosides, RNR is oxidized and then reduced by either thioredoxin or glutathione [41]. Nicotinamide adenine dinucleotide phosphate (NADPH) is the ultimate source of the electrons. RNR reduces all four rNDPs/rNTPs (i.e., ADP/ATP, GDP/GTP, UDP/UTP, and CDP/CTP) [40]. RNR activity is tightly regulated by allosteric regulation and enzyme specificity [41]. RNR is a tetrameric complex consisting of two large catalytic subunits (R1, ribonucleotide reductase M1, RRM1) and two small regulatory subunits (R2, ribonucleotide reductase M2 and RRM2 or p53R2/RRM2B) [40, 41]. RRM1 contains both the catalytic site and the allosteric regulatory sites [41]. RRM1 is expressed throughout all phases of the cell cycle [43]. The R2 subunit contains the tyrosyl radical, the site necessary for the reduction reaction [41]. RRM2 is the R2 subunit that controls reduction during S phase of the cell cycle when dNTPs are needed for DNA replication [43]. Therefore, RRM2 expression is rate limiting for RNR activity [41]. In contrast, p53R2 is involved in supplying dNTPs for DNA repair and mitochondrial DNA synthesis in the G0/G1 phase of the cell cycle [44].

It is clear that changes in nucleotide metabolism can cause transformation and variety of human diseases including tumorigenesis. Therefore, many studies have sought to determine whether components of the nucleotide metabolic pathway are either prognostic or *diagnostic biomarkers* in a variety of human diseases including cancers.

11.3.3 Applications of Radionuclide-Labeled Nucleotide (DNA and RNA) Probes

As discussed earlier that nucleotide metabolism can lead as *diagnostic biomarkers* for variety of diseases including tumorigenesis.

Development of new diagnostic, patient stratification, and treatment-monitoring approaches will accelerate the implementation of personalized therapy in cancer. Positron-emission tomography (PET) using fluorodeoxyglucose (^{18}F-FDG) measures drug-induced changes in tumor glucose metabolism that correlate with clinical end points of treatment efficacy. Such "metabolic responses" are detected earlier than changes in tumor volumes assessed by computed tomography (CT) [45]. ^{18}F-FDG PET has been validated as an indicator of therapeutic responses in gastrointestinal stromal tumors [46], high-grade soft tissue sarcomas [47], metastatic breast cancer [48], lung cancer [49], and adenocarcinoma of the esophagogastric junction [50]. In addition to treatment monitoring, PET may also prove useful in guiding therapeutic decisions before treatment initiation. Measurements of estrogen receptor expression by using ^{18}F-fluoroestradiol PET could be useful for stratifying breast cancer patients for estrogen-based therapy [51]. PET using ^{18}F-fluorobenzaldehyde-conjugated aminooxy-protein scaffolds has been used in small animal models to detect tumoral Her2 expression [52]. Similar approaches could guide the selection of chemotherapy regimes.

However, PET probes that can measure the activity of proteins or biochemical pathways targeted by common chemotherapy drugs are lacking. If available, such probes could enable pretherapeutic stratification of patients and reduce the frequency of ineffective chemotherapy. To develop PET probes and assays that are predictive of responses to chemotherapy, this chapter is focused on a class of pyrimidine and purine nucleoside prodrugs. However, there are so many researches are ongoing and still have to approve. So, in this chapter only approved applications are going to be discussed. These applications are as follows.

11.3.4 Application of PET/CT

11.3.4.1 Applications of 3′-Deoxy-3′-[^{18}F] Fluorothymidine (^{18}F-FLT) in Oncology

The most established tracer for PET applications is 2-[^{18}F]-fluoro-2-deoxy-D-glucose (^{18}F-FDG), whose uptake is regulated by glucose metabolism. Due to the Warburg effect, uptake of ^{18}F-FDG in tumors is generally high, making it a good candidate for visualization of neoplastic lesions. On the other hand, metabolically active organs like the heart and brain and glycolytic cells in inflammatory lesions accumulate this tracer as well. To overcome the drawbacks of ^{18}F FDG, Shields et al. proposed 3′-deoxy-3′-[^{18}F] fluorothymidine (^{18}F-FLT) as a radiotracer for imaging actively proliferating cells. ^{18}F-FLT is taken up by cells by the same mechanism as the nucleoside thymidine. This transport step is facilitated by nucleoside transporters, especially by the human equilibrative nucleoside transporter 1 (hENT1). Once within

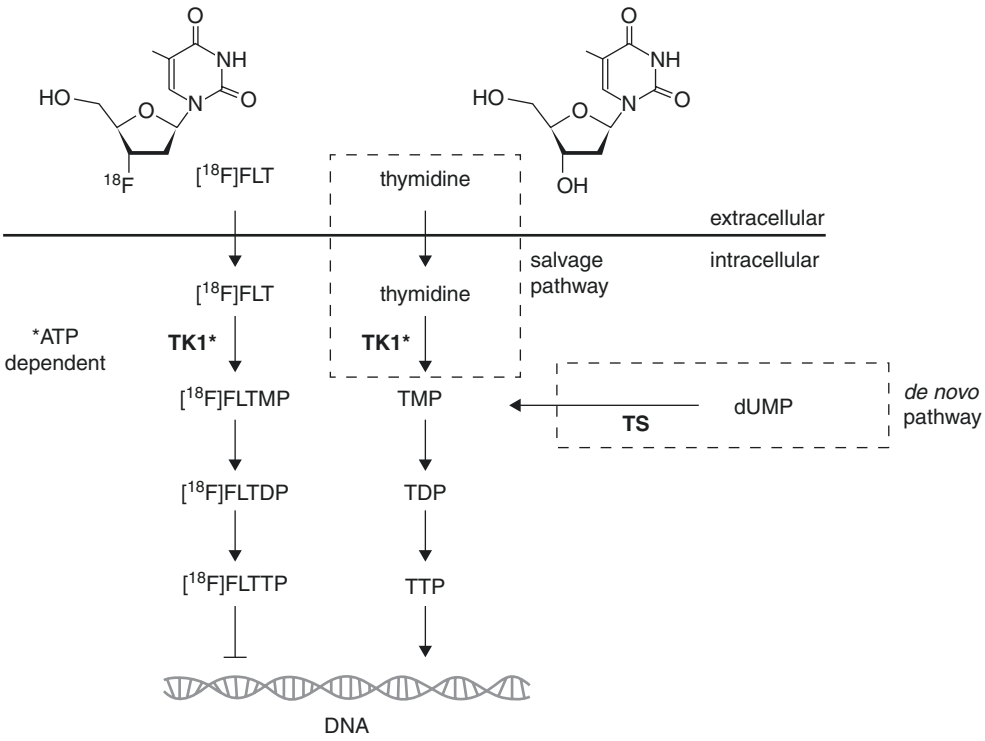

Fig. 11.7 Mechanisms of cellular ^{18}F-FLT retention (Redrawn from [53]

the cell, ^{18}F-FLT is phosphorylated by the enzyme thymidine kinase 1 (TK1), which results in the intracellular accumulation of the tracer. Accumulation of ^{18}F-FLT reflects the thymidine salvage pathway, specifically activity of the cytoplasmic form of TK1, which in turn is considered to be tightly linked to the S phase of the cell proliferation cycle (Fig. 11.7). The other important thymidine-to-DNA pathway is the de novo DNA synthesis pathway [53].

Similar to thymidine in the salvage pathway, ^{18}F-FLT is taken up from the extracellular milieu by specialized nucleoside transporters or via passive diffusion. Within the cell ^{18}F-FLT is phosphorylated by thymidine kinase 1 (TK1), the enzyme also responsible for phosphorylation of thymidine. TK1 activity is dependent on adenosine triphosphate (ATP).

The phosphorylated form of thymidine (TMP) is further phosphorylated to thymidine diphosphate (TDP) and thymidine triphosphate (TTP), which is subsequently incorporated into the DNA. The phosphorylated form of ^{18}F-FLT cannot be incorporated into DNA but is trapped within the cell. Techniques like PET or gamma counter measurements are capable of quantifying the rate of accumulation of ^{18}F-FLT within cells [53].^{18}F-FLT PET holds promise as a therapy response assessment tool in cancer patients. Moreover, it reports on completely different biology than does the more clinically familiar tracer ^{18}F-FDG, which accumulates in glycolytic inflammatory cells and cancer cells. Hence, ^{18}F-FLT accumulation and its changes should be further explored as an imaging biomarker in treatment response studies in the clinical situation [53].

11.3.4.2 Applications of 1-(2′-Deoxy-2′-[^{18}F] Fluoro-β-D-Arabinofuranosyl) Cytosine (^{18}F-FAC)

Actually, the ability to measure tumor determinants of response to nucleoside analog chemotherapy agents such as gemcitabine and related compounds could significantly affect the management of several types of cancer. The accumulation of PET tracer 1-(29-deoxy29-^{18}F-fluoro-b-D-arabinofuranosyl) cytosine (^{18}F-FAC) is predictive of responses to gemcitabine. Its retention in cells requires deoxycytidine kinase (dCK), a rate-limiting enzyme in the deoxyribonucleoside salvage metabolism, and in gemcitabine conversion from an inactive prodrug to a cytotoxic compound. PET using these probes is useful for guiding the selection of NA chemotherapeutic agents. A more in-depth consideration of the advantages and limitations of these PET probes together with other imaging modalities such as MRI will further the role of imaging in personalized, predictive medicine [54].

It is useful in visualization of lymphoid organs and is sensitive to localized immune activation. It can also detect early changes in lymphoid mass in systemic autoimmunity and allow evaluation of immunosuppressive therapy. It suggests a wide range of clinical applications in immune disorders and in certain types of cancer [55].

11.3.4.3 Applications of ^{11}C-labeled ^{11}C-Methionine, ^{11}C-Flumazenil, and ^{11}C-4DST

^{11}C-methionine, ^{11}C-flumazenil, and ^{11}C-4DST probes for PET/CT are very sensitive in patients with progressive multifocal leukoencephalopathy (PML) [56]. ^{11}C-labeled

thymidine analog, 4′-[methyl- ^{11}C] thiothymidine (^{11}C-4DST), also became available as an in vivo cell proliferation positron-emission tomography (PET) tracer. Thymidine analog can be labeled with ^{11}C at either the pyridine methyl position or the urea carbonyl. In a study in human brain tumors, ^{11}C-4DST showed little uptake in normal brain tissue, resulting in low-background activity for imaging brain tumors. It demonstrated rapid uptake in aggressive tumor masses, whereas no uptake was seen in clinically stable disease.

11.3.5 Conclusion

Identification and validation of new therapeutic targets in cancer metabolism are currently areas of intense, renewed investigation. While most efforts in the field have recently focused on identifying strategies to target glucose, amino acid, and lipid metabolism in tumors, much less emphasis is presently placed on *targeting nucleotide metabolism for DNA synthesis*. New, more targeted and rationally designed approaches to target the metabolic pathways that fuel DNA replication and repair in tumors are needed.

Several ^{18}F-labeled nucleosides such as ^{18}F -fluorothymidine, ^{18}F-(fluoroarabinofuranosyl) cytosine and ^{11}C-labeled nucleosides such as ^{11}C-methionine, ^{11}C-flumazenil, ^{11}C-4DST, have been accomplished within the last two decades, but a number of potentially interesting nucleoside-based biomarkers are not yet available for automated good manufacturing practice production due to the lack of fast and efficient synthetic methods. In order to meet recent demands for new PET-based biomarkers in various clinical applications, appropriate precursors which can easily be fluorinated and deprotected need to be developed. Finally, more clinical applications of nucleotide metabolism imaging require our further study and exploration.

11.4 Oxygen Metabolism

Oxygen metabolism is the basic energy-supplying way in vital movement. As oxygen supply is inadequate (also known as tissue hypoxia), oxygen metabolism may disturb, resulting in damage and dysfunction of tissues and organs. Tissue hypoxia is a key characteristic of many disease resulting in morbidity and mortality, including stroke, ischemic heart disease, and cancer. The ability to determine hypoxia has been an interesting field for a long time, since it not only closely correlated with the progression, infiltration, and migration of tumors but also with poor outcome in cancer patients. The chapter reviewed the physiology and pathophysiology of oxygen metabolism, the role of oxygen metabolism in tumor development, and tumor hypoxia imaging.

11.4.1 Physiology, Biochemistry, and Pathophysiology of Oxygen Metabolism

Oxygen is life. It is essential for living well and living younger, and so critical nature programmed your body to take it in automatically with every breath. With plenty of oxygen, your body pulses with energy. A human adult at rest needs a continuous supply of energy equivalent to about 150 watts, enough to power a large light bulb. Oxidizing foodstuffs with molecular oxygen generates this energy. Oxygen consumption at rest is around 200–250 mL/min in our body, while minute volume (tidal volume multiplied by breaths per minute) is around 6000 mL/min. If our oxygen supply is interrupted for more than a few minutes, irreversible damage, including cell dysfunction, injury, and/or death, is done to some tissues, notably the brain.

Eight percent of the oxygen is used for energy generation in the human body. Complex nutrient molecules, including carbohydrate, lipid, and protein, are catabolized into simpler end products, such as carbon dioxide, water, and ammonia, accompanied by the synthesis of ATP (adenosine triphosphate). ATP is always called as the "energy currency" of cells as it can be transported to those sites in the cell where it is utilized for several cellular functions, such as synthesis of protein, RNA, DNA for growth, adaptation and repair, transport of ions against a gradient, performance of mechanical work, etc. The rate of ATP synthesis fluctuates on a daily basis from 80 moles (around 40 kg) in a resting state to 1800 moles (around 910 kg) under an exercising state in the human body. Generally, majority of cellular energy is powered by ATP synthesis via a multistep pathway.

The first process is glycolysis, and this term refers to the process of breaking down of sugars. During this process, glucose is broken down via multiple enzymes and being converted into two molecular of pyruvates. Glycolysis itself is an energy demanding process which requires the consumption of two ATP molecules. Four new ATP molecules were generated at the end, which makes a net yield of two ATP molecules during the glycolytic reactions. In addition, two molecules of electron carriers NADH are generated as well.

Glycolysis is one of the primary pathways for energy production which does not require the involvement of oxygen, while the presence of oxygen in turn determines the path of pyruvate metabolism. When the oxygen is absent, pyruvate would not be fully converted into carbon dioxide, which results in the following accumulation of other metabolic intermediates in the cells. One classic example is that skeletal muscle cells predominately adopt glycolytic pathway to generate ATPs to meet intense energy needs during muscle contractions, which further causes an increased accumulation of lactic acid and results in muscle stiffness and soreness.

The second major pathway of ATP production is tricarboxylic acid (TCA) cycle. When there is enough oxygen in tissues, pyruvates in the cytoplasm are transferred via mitochondrial inner membrane and being converted into acetyl CoA. During the TCA cycle, the third carbon of acetyl CoA combines with oxygen and generates carbon dioxide. Meanwhile, high-energy carriers NADH, $FADH_2$, and GTP are released in the TCA cycle.

The third part of ATP production is called oxidative phosphorylation. NADH and $FADH_2$ generated from TCA cycle carry high-energy electrons and pass them to a chain of protein complexes located on the mitochondrial inner membrane, named electronic transport chain (ETC). These electrons were passed down via a stepwise manner and ultimately bind to oxygen to form water, and three molecules of ATP are produced at the final complex in ETC. In general, the citric acid cycle yields 15 times more energy than glycolytic pathway. In total, the whole process of TCA cycle and oxidative phosphorylation is known as cellular respiration, in which oxygen is being consumed and carbon dioxide is being generated.

11.4.1.1 Pathophysiology of Oxygen Metabolism

When oxygen is absent, accumulation of metabolic waste results in damage and dysfunction of tissues and organs. At the beginning of anoxia, cells primarily use glycogen (stored glucose) and the remaining oxygen to maintain aerobic metabolism until the oxygen is further depleted. In order to meet energy needs, cells turn to using glycolytic pathway as a main source for ATP when there is not sufficient oxygen available. However, glycolysis is less efficient compared to aerobic metabolism and results in an accumulation of lactic acid and further intracellular acidosis.

Hypoxia is a complex process with many physiological and pathological events being involved, including affection of cellular processes, generation of free radicals, imbalance of cellular osmosis, accumulation of metabolic wastes, and release of lysosomal enzymes. Short period of anoxia can cause minor recoverable damages, while longer term of anoxia will lead to irreversible cell damage and cause cell death. The hypoxia tolerance in tissues or organs is based on these factors: (1) the amount of the available energy pool in storage, (2) the energy required per time unit, and (3) the efficiency of energy generation via anaerobic metabolism. The maximum time of tolerance for hypoxia in the heart, liver, and brain is shown to be around 30–45 min, 30–60, and less than 5 min, respectively. Beyond these time limits, there can be irreversible damages. Even if oxygen supply for tissues is re-established, total function cannot recover in these damaged tissues. In addition, functional loss occurs prior to cell death. One example is that myocardial tissues could remain viable for 30–60 min during ischemia; cardiac contractility is found to be lost within 1 min. Similarly, neurons cannot survive without oxygen for a few minutes, but cognitive deficit occurs almost immediately after the oxygen supply is suddenly interrupted in the brain.

11.4.2 The Role of Oxygen Metabolism in Tumorigenesis and Tumor Development

The oxygenation in normal tissues varies since they have different blood supply and metabolic capacity. In human, oxygen levels in organs differ between around 9.5% in the renal cortex and 4.6% in the brain. Hemoglobin concentrations beyond 8 g/dL are enough to maintain an adequate oxygenation. If hemoglobin is between 4 and 8 g/dL, human body can compensate for O_2 deficiencies through regulating blood supply to maintain an adequate oxygenation of normal tissues. In contrast, tumors cannot balance the reduction in O_2 availability and thus result in the development of hypoxia.

Fast-growing tumors have to develop their own vascular network to ensure its blood supply once its diameter is over around 1.0 mm. Compared with normal vasculature, tumor vessels are often highly abnormal, with distended capillaries, leaky walls, and slow flow, resulting oxygen deficit and the development of hypoxia in tumor tissues. Protection against hypoxia is an important step in tumor development and progression. Hypoxia would result in dysfunctional vascularization and acquire an epithelial-to-mesenchymal transition phenotype in tumors, which in turn could further increase cell mobility and metastasis. Several pathways including HIF-1, PI3K, MAPK, and NFκB pathways have been shown to participate in the changes of cell metabolism and the development of therapy resistance in hypoxia tumors. Therefore, better understanding of the role of hypoxia in cancer development and progression will be a new field for the discovery of novel therapeutical and imaging agents targeting tumor hypoxic and acidic microenvironments.

11.4.3 Tumor Hypoxia Imaging

More than half of solid tumors have heterogeneously hypoxic/anoxic areas. Hypoxia could induce genetic mutation in tumor cells and result in a serial of events, including affecting cell cycle arrest, cell differentiation, and apoptosis. Moreover, it also can promote tumor growth by helping tumor to survive nutritive deprivation, to get away from the immune surveillance, and to promote unlimited cell proliferation. In general, hypoxia plays a role in tumor growth rates and metastasis, as well as tumor response to chemotherapy and radiotherapy. Hence, evaluating hypoxia status before initial therapy will greatly improve the management in cancer treatment.

Consequently, different methods have been used to measure the levels of oxygen in tumor tissues in recent decades. These methods are generally classified into invasive direct measurements, including polarographic oxygen electrodes and immunohistochemical (IHC) staining, and noninvasive, mainly based on imaging approaches including magnetic resonance imaging (MRI), optical imaging (near-IR imaging), and radionuclide imaging [single-photon emission computed tomography (SPECT) and positron-emission tomography (PET)]. Dynamic contract MRI, magnetic resonance spectroscopy (MRS), and blood oxygen level-dependent (BOLD) imaging are representative imaging models of MRI. However, these imaging methods all have their own limitations. BOLD cannot determine the oxygen level in tissues or reflex the molecular changes in tumor cells. MRS has poor sensitivity and spatial resolution. Near-IR imaging has limitations in penetrating depth and therefore hinders its application in relatively large animal models or in human tumors. Despite their resolution limitations, SPECT and PET still present a much higher sensitivity than MRI. The characteristics and limitations of different imaging techniques are shown in Table 11.1 [57].

Developing SPECT or PET imaging agents for noninvasive hypoxia imaging has gained great interest recently. Tumor hypoxia imaging using SPECT or PET is known as an important molecular imaging approach for evaluating hypoxia in clinical practice.

11.4.3.1 SPECT Imaging of Hypoxia

Single-photon emitters include ^{123}I, ^{125}I, ^{131}I, and ^{99m}Tc labeled with hypoxia-specific compounds that produce signals in SPECT which reveal the hypoxic parts of tumors. In 1996, Urtasun RC et al. reported that ^{123}I-labeled hypoxia-specific agent iodoazomycinarabinoside (^{123}I-IAZA) may identify tumor hypoxia tissues in cancer patients. This method is safe and can be applied repeatedly as a routine imaging procedure for cancer outpatients during the initial visit and follow-up [58]. Later, modifications have been applied on iodinated azomycin arabinosides due to the inconsistent uptake of ^{123}I-IAZA in various tumors. Several IAZA analogs, such as iodoazomycin pyranoside (IAZP), beta-D-iodinatedazomycin galactopyranoside (IAZGP), and iodoazomycinxylopyranoside (IAZXP), have been created as novel imaging agents on the basis of the azomycin-nucleoside structure. A preclinical study has examined the ^{131}I-IAZGP imaging in HT29 colorectal cancer mice tumors, revealing a high accumulation of ^{131}I-IAZGP in tumor. This finding suggested that ^{131}I-IAZGP may serve as a clinical imaging agent for hypoxia imaging in cancer patients. One type of SPECT hypoxia-selective radiotracers incorporated with ^{99m}Tc has gained popularity. Two agents, nitroimidazoles and non-nitroimidazoles, labeled with ^{99m}Tc have been used for the imaging of tumor hypoxia, such as BMS-181321, BRU 59–21, and HL91. BMS-181321 labeled with ^{99m}Tc was first used to detect ischemic and hypoxic myocardium. ^{99m}Tc-

Table 11.1 The principal characteristics and limitations of imaging techniques

Modality		Technique	Limitations
Optical imaging	Phosphorescence	Injection of water-soluble phosphor probes into the vasculature	The measurement represents the vascular pO_2, not tissue pO_2
	Near-infrared spectroscopy (NIRS)	Hemoglobin (Hb) saturation assessment	The measurement represents the vascular oxygenation, but not on tissue pO_2
MRI	Blood oxygen level-dependent (BOLD) MRI	BOLD shows deoxyhemoglobin change in the blood	The measurement represents the changes in blood oxygenation, but not on tissue pO_2
	^{19}F-MRI	^{19}F spin lattice relaxation rate (R1) is linear relation with the dissolved oxygen concentration	The relaxation rate of ^{19}F is based on other physiological factors present in the tissue and not only on O_2 concentration
	Electron paramagnetic resonance imaging (EPRI)	Injection of paramagnetic particulates or soluble probes that physically interact with oxygen	The molecules predominantly distribute in the vasculature, thus biasing in part measurements of tissue oxygenation
	Proton-electron double resonance imaging (PEDRI)	Injection of a probe with unpaired electrons and use of a strong EPR impulse	The molecules predominantly distribute in the vasculature, thus biasing in part measurements of tissue oxygenation
	Dynamic Gd-DTPA-enhanced MRI	Injection of contrast agent	Low specificity, because the information measured are both vascular and tissue oxygenation
Nuclear-based	Single-photon emission computed tomography (SPECT)	Injection of radiopharmaceutical agents targeting hypoxic tissue. High specificity	Limited resolution
	Positron-emission tomography (PET)	Injection of positron (β+)-emitting radiopharmaceutical agents targeting hypoxic tissue. High specificity	Limited resolution compared to MRI but superior to SPECT

Redrawn from [57]

BMS-181321 is not an optimal agent for tumor hypoxia imaging due to its instability, slow blood clearance, and high normal tissue background. ^{99m}Tc-BRU59–21 has a better stability and faster clearance compared with ^{99m}Tc-BMS-181321. ^{99m}Tc-BRU59–21 is also shown to be suitable for tumor hypoxia imaging due to its high tumor uptake [59]. ^{99m}Tc-HL91 is a SPECT radiotracer for hypoxia imaging that is without a nitroimidazole unit. It has been shown that hypoxic tumor tissues have hight accumulation of ^{99m}Tc-HL91, which is positive correlation with hypoxia status. Furthermore, ^{99m}Tc-HL91 uptake also has a positive correlation with the levels of GLUT1 expression in tumors [59]. Cook et al. reported that SPECT imaging showed visible uptake of ^{99m}Tc-HL91 in the tumor area which could be clearly identified by ^{18}F-FDG PET imaging in the patients with various tumors. ^{99m}Tc-HL91 did not accumulate in any benign tumor in which ^{18}F-FDG had weakly positive imaging [60]. Li et al. showed that ^{99m}Tc-HL91 imaging was able to detect the hypoxia state and changes following the radiotherapy in lung cancer patients. ^{99m}Tc-HL91 hypoxia imaging can be used to predict tumor response, radiosensitivity, and outcome in cancer patients prior to the administration of radiotherapy [61].

11.4.3.2 PET Imaging of Hypoxia

Compared with SPECT, PET has a better performance regarding sensitivity, spatial resolution, and quantification ability. PET recently has gained its advantages over SPECT in the aspects of availability and numbers of hypoxia imaging agents. $^{15}O_2$ PET imaging is known as the "gold standard" for noninvasive imaging of tissue oxygen levels. However, the short half-life of $^{15}O_2$, which is about 2 min, hampers its clinical application.

Another type of PET radiotracer contains a radioisotope and an active biomolecule which specifically targets tumor hypoxia. The commonly used radioisotopes for tumor hypoxia imaging include ^{18}F, ^{124}I, and $^{60/64}$Cu. 2-Nitroimidazoles (such as fluoromisonidazole (FMISO), EF5, and fluoroetanidazole (FETA)) and nucleoside conjugates (such as iodoazomycinarabinoside (IAZA) and diacetyl-bis(N^4- methylthiosemicarbazone) (ATSM)) are often combined with above isotopes for hypoxia PET imaging. These molecules have high affinity to hypoxic cells to form PET-detectable stable adducts. Then, they could be quickly oxidized and cleared from cells to create a good demarcation between hypoxic and normoxia areas. Major radiopharmaceuticals used in PET imaging of tumor hypoxia are summarized in Table 11.2 [57]. Among these PET traces, ^{18}F-FMISO is a first-generation nitroimidazole compound that is widely used as a hypoxia imaging agent for PET. It can specifically bind to hypoxia cells, and a mild hypoxic status (<10 mmHg) can result in a significant uptake of ^{18}F-FMISO. ^{18}F-FMISO hypoxia imaging has been investigated in several human cancers, such as gliomas, head and neck carcinoma, breast cancer, and renal carcinoma. ^{18}F-FMISO uptake was found closely related with the measurements of pO_2, hence suggested to be a good representative of intracellular pO_2. A significant correlation has also been shown between ^{18}F-FMISO accumulation and the hypoxic-inducible factor-1 (HIF-1) expression in several tumors. Lee et al. have studied the data of 300 cancer patients and suggested ^{18}F-FMISO to be a good index for predicting treatment response and disease prognosis [62]. Compared with ^{18}F-FDG, ^{18}F-FMISO imaging had a similar or better predictive performance for disease outcome, as hypoxia indicates poor local control and metastasis of tumors. Sequential ^{18}F-FMISO PET could reveal increased oxygen and reduced hypoxia distribution during tumor treatment. Thus, performing serial ^{18}F-FMISO PET imaging during the course of treatment would provide more information on boosting radiation therapy to persistent hypoxic subvolumes, comparing to baseline volumes.

^{18}F-FAZA, one of the second-generation nitroimidazoles, is a second commonly used PET tracer for imaging hypoxia, showing an improved contrast and reduced background signals compared with ^{18}F-FMISO. Servagi-Vernat et al. have performed a prospective clinical study on ^{18}F-FAZA and suggested its role in quantifying tumor hypoxia before and during radiation therapy. ^{18}F-FAZA PET imaging also allows to delineate hypoxic volumes in planning protocols [63].

11.4.4 Tumor Hypoxia PET Imaging-Guided Radiation Therapy

Radiation therapy is one of the major therapeutic options for cancer treatment. The accuracy and safety of radiation therapy have been significantly improved with latest technological progressions. The effectiveness of radiotherapy is determined by multiple factors. Oxygen deficiency (hypoxia) has been known as a major factor for radiation resistance since it can weaken the indirect effect of ionizing radiation on the DNA by reducing the production of free radical. Cells irradiated in the presence of oxygen are about three times sensitive than severely hypoxic cells [64]. Moreover, HIF-1 activation has been found to be involved in the development of radioresistance in tumors. Hypoxia induces the activation of HIF-1 and subsequently upregulates gene expressions in multiple pathways, including cell metabolism, pH regulation, blood vessel formation, cell invasion, DNA synthesis, protein synthesis, and treatment resistance [65].

As the association has been determined between tumor hypoxia and patient treatment response, PET imaging of tumor hypoxia may modify radiation therapy planning to improve patient prognosis. Dose escalation, namely, dose painting, can increase local tumor control and consequently

Table 11.2 Major radiopharmaceuticals used in PET imaging of tumor hypoxia (redrawn from [57])

Uptake mechanism	Tracer	Tumors imaged	Benefits	Benefits
Nitroimidazole-like uptake: reduction of RNO_2 radicals to RNHOH compounds that bind covalently to intracellular macromolecules and remain within the tumor cell	^{18}F-MISO (^{18}F-fluoromisonidazole)	Head and neck tumors Locally advanced HNSCC Glioblastoma multiforme (GBM) Breast cancer NSCLC	Broadest evidence of value as a hypoxia tracer Good correlation with low intracellular oxygen concentration Good availability	Lack of correlation in all tumors Low tumor-to-background ratio Variable reproducibility
	^{18}F-FAZA (^{18}F-fluoroazomycin-arabinozide)	Head and neck tumors. Cervical cancer Prostate cancer NSCLC Rectal cancer	Good correlation with low intracellular oxygen concentration Higher selective accumulation in hypoxic tumors than ^{18}F-MISO	More limited evidence compared to ^{18}F-MISO
	^{18}F-FETNIM (^{18}F-fluoroerythronitroimidazole)	NSCLC Esophageal cancer	Promising tracer with possible correlation with patient outcome Higher selective accumulation in hypoxic tumors than ^{18}F-MISO	Limited evidence compared to ^{18}F-MISO
	^{18}F-EF5 (^{18}F-2-nitroimidazolpentafluoropropyl acetamide)	Brain tumors Soft tissue sarcoma Head and neck tumors	Promising tracer with possible correlation with patient outcome	Limited evidence
	^{18}F-EF3 (^{18}F-2-nitroimidazol-trifluoropropyl acetamide)	Rats bearing syngeneic rhabdomyosarcoma tumors Head and neck tumors	Promising tracer	Very limited evidence, mostly preclinical
	^{18}F-FETA (^{18}F-fluoroetanidazole)	Mice bearing MCF-7, RIF-1, EMT6, HT1080/26.6, and HT1080/1-3C xenografts	Promising tracer with better biodistribution than 18F-MISO	Preclinical evidence
	^{124}I-IAZG (^{124}I-iodoazomycin galactopyranoside)	Hepatocellular carcinoma	Promising tracer	Preclinical evidence
	^{68}Ga-labeled nitroimidazole analogs (^{68}Ga-NOTA-nitroimidazole, ^{68}Ga-DOTA-nitroimidazole, ^{68}Ga-SCN-NOTA-nitroimidazole)	Tumor xenografted mice	Promising tracer	Preclinical evidence
Reduction of Cu(II)-ATSM complex into an unstable [Cu(I)-ATSM]-complex in hypoxic conditions	^{60,61,62,64}Cu-ATSM (^{60,61,62,64}Cu-diacetyl-bis(*N*4-methylthiosemicarbazone)	NSCLC Head and neck tumors Cervical cancer Rectal cancer Brain tumors	Good correlation with low intracellular oxygen concentration Good image contrast with high tissue-to-muscle ratio (T/M) Possibility for late acquisition with ^{64}Cu-ATSM Possibility for radio-nuclide therapy with ^{64}Cu-ATSM	Evidence more limited compared to ^{18}F-MISO Less clear mechanism of uptake in tumor hypoxia compared to nitroimidazole-like compounds
Recognizes carbonic anhydrase IX (CA IX)	^{124}I-cG250 (^{124}I-chimeric mAb G250)	Renal cell carcinoma	Promising tracer	Preclinical evidence
	^{89}Zr-cG250-F(ab′)$_2$ (^{89}Zr-chimeric G250 F(a- b′)$_2$)	Head and neck tumors	Promising tracer	Preclinical evidence

improve overall survival by increasing the biological effective dose to hypoxic sub-volumes. Among advanced molecular imaging, PET imaging is required to determine plan for a hypoxia radiation "boost treatment" in current clinical practice. Hendrickson et al. reported that ^{18}F-FMISO PET imaging could identify tumor hypoxic sub-volumes and made a plan to simulate boosts of additional 10 Gy on the prescribed 70 Gy to the primary tumor via intensity-modulated radiation therapy (IMRT) based on ^{18}F-FMISO imaging. This study was to investigate the feasibility and efficacy of ^{18}F-FMISO imaging-guided IMRT. There was a significant increase of 17% in local tumor control probability (LTCP)

without unacceptable increases in normal tissue complication probability (NTCP), suggesting ^{18}F-FMISO imaging allows to deliver a higher dose to hypoxic regions with better LTCP without increasing expected complications [66]. Lee et al. studied the treatment planning feasibility in 11 patients with head and neck cancer (HNC). They found that, based on ^{18}F-FMISO PET results, it was possible to dose escalate the hypoxic sub-volumes (GTV) to 84 Gy and even 105 Gy without exceeding the normal tissue tolerance [67, 68]. These studies have demonstrated that subsequent hypoxia PET imaging-guided IMRT can improve locoregional control in tumor patients.

It is import to assess the dynamic features of tumor oxygenation with cycling hypoxia during the course of IMRT and modifying IMRT dose painting plans based on hypoxia imaging. Several studies have evaluated the overtime variance of pretreatment PET hypoxia images by performing two separated PET hypoxia scans during radiotherapy. A preliminary clinical study by Nehmeh SA et al. has shown a great variability in the tumor uptake of ^{18}F-FMISO in patients with head and neck cancer between the pretreatment initial scan and the second scan during treatment. Their findings suggested that changes between series of ^{18}F-FMISO PET/CT imaging can identify changes in the hypoxia distribution during treatment. ^{18}F-FMISO PET/CT-guided dose painting IMRT may be used to increase the dose to hypoxia tumor volume within the tumor volume (without increasing expected complications) and thus reduce gross tumor volume radiation resistance and improve local control [69]. Moreover, Lin et al. have used serial ^{18}F-FMISO PET/CT imaging to determine the impact of hypoxia distribution on the efficacy of IMRT dose painting in seven patients with head and neck cancer, in order to circumvent hypoxia-induced radioresistance [70]. Compared with the first ^{18}F-FMISO PET/CT imaging (before radiotherapy), the second ^{18}F-FMISO PET/CT imaging scan (during treatment) showed a reduction of coverage of hypoxic volumes, and EUD (equivalent uniform dose) decreased from 87 to 80 Gy. Based on the changes of tumor hypoxia shown by serial ^{8}F-FMISO PET imaging, the coverage of hypoxic tumor was compromised by dose painting. Therefore, performing serial hypoxia imaging before and throughout therapy may be helpful to monitor potential changes in the hypoxic volume as treatment progresses and real-time adjust the intensity-modulated radiotherapy plans.

References

1. Kuhajda FP (2006) Fatty acid synthase and cancer: new application of an old pathway. Cancer Res 66(12):5977–5980
2. Mori N, Wildes F, Takagi T, Glunde K, Bhujwalla ZM (2016) The tumor microenvironment modulates choline and lipid metabolism. Front Oncol 6:262. https://doi.org/10.3389/fonc.2016.00262. eCollection
3. Kolthammer JA, Corn DJ, Tenley N, Wu C et al (2011) PET imaging of hepatocellular carcinoma with 18F-fluoroethylcholine and 11C-choline. Eur J Nucl Med Mol Imaging 38(7):1248–1256
4. Umbehr MH, Müntener M, Hany T, Sulser T, Bachmann LM (2013) The role of ^{11}C-choline and ^{18}F-fluorocholine positron emission tomography (PET) and PET/CT in prostate cancer: a systematic review and meta-analysis. Eur Urol 64(1):106–117
5. Evangelista L, Guttilla A, Zattoni F, Muzzio PC, Zattoni F (2013) Utility of choline positron emission tomography/computed tomography for lymph node involvement identification in intermediate- to high-risk prostate cancer: a systematic literature review and meta-analysis. Eur Urol 63(6):1040–1048
6. Graziani T, Ceci F, Castellucci P, Polverari G et al (2016) (11) C-Choline PET/CT for restaging prostate cancer. Results from 4,426 scans in a single-centre patient series. Eur J Nucl Med Mol Imaging 43(11):1971–1979
7. Yamamoto Y, Nishiyama Y, Kameyama R, Okano K et al (2008) Detection of hepatocellular carcinoma using ^{11}C-choline PET: comparison with ^{18}F-FDG PET. J Nucl Med 49(8):1245–1248
8. Mena E, Turkbey B, Mani H, Adler S et al (2012) ^{11}C-Acetate PET/CT in localized prostate cancer: a study with MRI and histopathologic correlation. J Nucl Med 53(4):538–545
9. Ho CL, Yu SC, Yeung DW (2003) 11C-acetate PET imaging in hepatocellular carcinoma and other liver masses. J Nucl Med 44(2):213–221
10. Park JW, Kim JH, Kim SK, Kang KW et al (2008) A prospective evaluation of ^{18}F-FDG and ^{11}C-acetate PET/CT for detection of primary and metastatic hepatocellular carcinoma. J Nucl Med 49(12):1912–1921
11. Cheung TT, Ho CL, Lo CM, Chen S et al (2013) ^{11}C-acetate and ^{18}F-FDG PET/CT for clinical staging and selection of patients with hepatocellular carcinoma for liver transplantation on the basis of Milan criteria: surgeon's perspective. J Nucl Med 54(2):192–200
12. Washburn LC, Sun TT, Anon JB, Hayes RL (1978) Effect of structure on tumor specificity of alicyclic alpha-amino acids. Cancer Res 38:2271–2273
13. De Vis K, Schelstraete K, Deman J, Vermeulen FL, Sambre J, Goethals P, Van Haver D, Slegers G, Vandecasteele C, De Schryver A (1987) Clinical comparison of 11C-ACPC (aminocyclopentane carboxylic acid) and 13N-ammonia as tumour tracers. Acta Oncol 26:105–111
14. Ho CL, Chen S, Yeung DW, Cheng TK (2007) Dual-tracer PET/CT imaging in evaluation of metastatic hepatocellular carcinoma. J Nucl Med 48(6):902–909
15. Prenant C, Theobald A, Haberkorn U, Bellemann ME, Weber K, Oberdorfer F (1996) Feasibility of labeled alpha-acetamido-aminoisobutyric acid as new tracer compound for kinetic labeling of neutral amino acid transport: preparation of alpha-(N-[1-11C] acetyl)- and alpha-(N-[1-14C]acetyl)-aminoisobutyric acid. Nucl Med Biol 23:359–363
16. Nakagawa M, Kuwabara Y, Sasaki M, Koga H, Chen T, Kaneko O, Hayashi K, Morioka T, Masuda K (2002) 11C-methionine uptake in cerebrovascular disease: a comparison with 18F-fDG PET and 99mTc-HMPAO SPECT. Ann Nucl Med 16:207–211
17. Tsuyuguchi N, Takami T, Sunada I, Iwai Y, Yamanaka K, Tanaka K, Nishikawa M, Ohata K, Torii K, Morino M, Nishio A, Hara M (2004) Methionine positron emission tomography for differentiation of recurrent brain tumor and radiation necrosis after stereotactic radiosurgery--in malignant glioma. Ann Nucl Med 18:291–296
18. Minamimoto R, Saginoya T, Kondo C, Tomura N, Ito K, Matsuo Y, Matsunaga S, Shuto T, Akabane A, Miyata Y, Sakai S, Kubota K (2015) Differentiation of brain tumor recurrence from post-radiotherapy necrosis with 11C-methionine PET: visual assessment versus quantitative assessment. PLoS One 10:e0132515
19. Langen KJ, Hamacher K, Weckesser M, Floeth F, Stoffels G, Bauer D, Coenen HH, Pauleit D (2006) O-(2-[18F]fluoroethyl)-L-

tyrosine: uptake mechanisms and clinical applications. Nucl Med Biol 33:287–294
20. Lau EW, Drummond KJ, Ware RE, Drummond E, Hogg A, Ryan G, Grigg A, Callahan J, Hicks RJ (2010) Comparative PET study using F-18 FET and F-18 FDG for the evaluation of patients with suspected brain tumour. J Clin Neurosci 17:43–49
21. Dunet V, Rossier C, Buck A, Stupp R, Prior JO (2012) Performance of 18F-fluoro-ethyl-tyrosine (18F-FET) PET for the differential diagnosis of primary brain tumor: a systematic review and meta-analysis. J Nucl Med 53:207–214
22. Pafundi DH, Laack NN, Youland RS, Parney IF, Lowe VJ, Giannini C, Kemp BJ, Grams MP, Morris JM, Hoover JM, Hu LS, Sarkaria JN, Brinkmann DH (2013) Biopsy validation of 18F-DOPA PET and biodistribution in gliomas for neurosurgical planning and radiotherapy target delineation: results of a prospective pilot study. Neuro Oncol 15:1058–1067
23. Juhasz C, Dwivedi S, Kamson DO, Michelhaugh SK, Mittal S (2014) Comparison of amino acid positron emission tomographic radiotracers for molecular imaging of primary and metastatic brain tumors. Mol Imaging 13
24. Zhu L, Ploessl K, Zhou R, Mankoff D, Kung HF (2017) Metabolic imaging of glutamine in cancer. J Nucl Med 58:533–537
25. Koopmans KP, Glaudemans AW (2014) Other PET tracers for neuroendocrine tumors. PET Clin 9:57–62
26. Toumpanakis C, Kim MK, Rinke A, Bergestuen DS, Thirlwell C, Khan MS, Salazar R, Oberg K (2014) Combination of cross-sectional and molecular imaging studies in the localization of gastroenteropancreatic neuroendocrine tumors. Neuroendocrinology 99:63–74
27. Huang C, McConathy J (2013) Fluorine-18 labeled amino acids for oncologic imaging with positron emission tomography. Curr Top Med Chem 13:871–891
28. Baek S, Choi CM, Ahn SH, Lee JW, Gong G, Ryu JS, Oh SJ, Bacher-Stier C, Fels L, Koglin N, Hultsch C, Schatz CA, Dinkelborg LM, Mittra ES, Gambhir SS, Moon DH (2012) Exploratory clinical trial of (4S)-4-(3-[18F]fluoropropyl)-L-glutamate for imaging xC-transporter using positron emission tomography in patients with non-small cell lung or breast cancer. Clin Cancer Res 18:5427–5437
29. Savir-Baruch B, Zanoni L, Schuster DM (2018) Imaging of prostate cancer using fluciclovine. Urol Clin North Am 45:489–502
30. Picchio M, Mapelli P, Panebianco V, Castellucci P, Incerti E, Briganti A, Gandaglia G, Kirienko M, Barchetti F, Nanni C, Montorsi F, Gianolli L, Fanti S (2015) Imaging biomarkers in prostate cancer: role of PET/CT and MRI. Eur J Nucl Med Mol Imaging 42:644–655
31. Morita M, Higuchi T, Achmad A, Tokue A, Arisaka Y, Tsushima Y (2013) Complementary roles of tumour specific PET tracer (1)(8)F-FAMT to (1)(8)F-FDG PET/CT for the assessment of bone metastasis. Eur J Nucl Med Mol Imaging 40:1672–1681
32. Burger IA, Zitzmann-Kolbe S, Pruim J, Friebe M, Graham K, Stephens A, Dinkelborg L, Kowal K, Schibli R, Luurtsema G, Maas B, Horn-Tutic M, Haerle SK, Wiegers J, Schaefer NG, Hany TF, von Schulthess GK (2014) First clinical results of (D)-18F-fluoromethyltyrosine (BAY 86-9596) PET/CT in patients with non-small cell lung cancer and head and neck squamous cell carcinoma. J Nucl Med 55:1778–1785
33. Voet D, Voet J, Pratt C (2008) Fundamentals of biochemistry: life at the molecular level, 3rd edn. Wiley, Hoboken, NJ. ISBN 9780470129302
34. "Nucleotide metabolism". The medical biochemistry. Accessed 20 Oct 2014
35. Ammann AJ (1985) Purine nucleotide imbalance in immunodeficiency disorders. Basic Life Sci 31:487–502
36. Kimura T, Takeda S, Sagiya Y, Gotoh M, Nakamura Y, Arakawa H (2003) Impaired function of p53R2 in Rrm2b-null mice causes severe renal failure through attenuation of dNTP pools. Nat Genet 34:440–445
37. El-Hattab AW, Scaglia F (2013) Mitochondrial DNA depletion syndromes: review and updates of genetic basis, manifestations, and therapeutic options. Neurotherapeutics 10:186–198
38. Dang CV (2012) Links between metabolism and cancer. Genes Dev 26:877–890
39. Hartman SC, Buchanan JM (1959) Nucleic acids, purines, pyrimidines (nucleotide synthesis). Annu Rev Biochem 28:365–410
40. Reichard P (1988) Interactions between deoxyribonucleotide and DNA synthesis. Annu Rev Biochem 57:349–374
41. Nordlund P, Reichard P (2006) Ribonucleotide reductases. Annu Rev Biochem 75:681–706
42. Anglana M, Apiou F, Bensimon A, Debatisse M (2003) Dynamics of DNA replication in mammalian somatic cells: nucleotide pool modulates origin choice and interorigin spacing. Cell 114:385–394
43. Engstrom Y, Eriksson S, Jildevik I, Skog S, Thelander L, Tribukait B (1985) Cell cycle-dependent expression of mammalian ribonucleotide reductase. Differential regulation of the two subunits. J Biol Chem 260:9114–9116
44. Hakansson P, Hofer A, Thelander L (2006) Regulation of mammalian ribonucleotide reduction and dNTP pools after DNA damage and in resting cells. J Biol Chem 281:7834–7841
45. Weber WA, Czernin J, Phelps ME, Herschman HR (2008) Technology insight: novel imaging of molecular targets is an emerging area crucial to the development of targeted drugs. Nat Clin Pract 5:44–54
46. Gayed I et al (2004) The role of 18F-FDG PET in staging and early prediction of response to therapy of recurrent gastrointestinal stromal tumors. J Nucl Med 45:17–21
47. Evilevitch V et al (2008) Reduction of glucose metabolic activity is more accurate than change in size at predicting histopathologic response to neoadjuvant therapy in high-grade soft-tissue sarcomas. Clin Cancer Res 14:715–720
48. Dose Schwarz J et al (2005) Early prediction of response to chemotherapy in metastatic breast cancer using sequential 18F-FDG PET. J Nucl Med 46:1144–1150
49. Weber WA et al (2003) Positron emission tomography in non-small-cell lung cancer: prediction of response to chemotherapy by quantitative assessment of glucose use. J Clin Oncol 21:2651–2657
50. Lordick F et al (2007) PET to assess early metabolic response and to guide treatment of adenocarcinoma of the oesophagogastric junction: the MUNICON phase II trial. Lancet Oncol 8:797–805
51. Peterson LM et al (2008) Quantitative imaging of estrogen receptor expression in breast cancer with PET and ^{18}F-fluoroestradiol. J Nucl Med 49:367–374
52. Cheng Z et al (2008) Small-animal PET imaging of human epidermal growth factor receptor type 2 expression with site-specific 18F-labeled protein scaffold molecules. J Nucl Med 49:804–813
53. Schelhaas S et al (2017) Preclinical applications of 3′-Deoxy-3′-[^{18}F] fluorothymidine in oncology - a systematic review. Theranostics 7(1):40–50
54. Lee JT et al (2012) Stratification of nucleoside analog chemotherapy using 1-(2′-Deoxy-2′-^{18}F-fluoro-β-D-arabinofuranosyl) cytosine and 1-(2′-Deoxy-2′-^{18}F-fluoro-β-L-arabinofuranosyl)-5-methylcytosine PET. J Nucl Med 53(2):275–280
55. Nair-Gill E et al (2010) PET probes for distinct metabolic pathways have different cell specificities during immune responses in mice. J Clin Invest 120(6):2005–2015
56. Ishibashi K et al (2017) PET imaging of ^{18}F-FDG, ^{11}C-methionine, ^{11}C-flumazenil, and ^{11}C-4DST in progressive multifocal leukoencephalopathy. Intern Med 56(10):1219–1223
57. Lopci E, Grassi I, Chiti A et al (2014) PET radiopharmaceuticals for imaging of tumor hypoxia: a review of the evidence. Am J Nucl Med Mol Imaging 4(4):365–384
58. Urtasun RC, Parliament MB, McEwan AJ et al (1996) Measurement of hypoxia in human tumours by non-invasive spect imaging of iodoazomycin arabinoside. Br J Cancer Suppl 27:S209–S212

59. Mees G, Dierckx R, Vangestel C et al (2009) Molecular imaging of hypoxia with radiolabelled agents. Eur J Nucl Med Mol Imaging 36:1674–1686
60. Cook GJ, Houston S, Barrington SF et al (1998) Technetium-99m-labeled HL91 to identify tumor hypoxia: correlation with fluorine-18-FDG. J Nucl Med 39:99–103
61. Li L, Yu J, Xing L et al (2006) Serial hypoxia imaging with ^{99m}Tc-HL91 SPE- CT to predict radiotherapy response in non-small cell lung cancer. Am J Clin Oncol 29(6):628–633
62. Lee ST, Scott AM (2007) Hypoxia positron emission tomography imaging with 18f-fluoromisonidazole. Semin Nucl Med 37:451–461
63. Servagi-Vernat S, Differding S, Hanin FX et al (2014) A prospective clinical study of 18 F-FAZA PET-CT hypoxia imaging in head and neck squamous cell carcinoma before and during radiation therapy. Eur J Nucl Med Mol Imaging 41(8):1544–1552
64. Horsman MR, Overgaard J (2016) The impact of hypoxia and its modification of the outcome of radiotherapy. J Radiat Res 57(Suppl 1):i90–i98
65. Tamaki N, Hirata K (2016) Tumor hypoxia: a new PET imaging biomarker in clinical oncology. Int J Clin Oncol 21(4):619–625
66. Hendrickson K, Phillips M, Smith W et al (2011) Hypoxia imaging with [F-18] FMISO-PET in head and neck cancer: potential for guidingintensity modulated radiation therapy in overcominghypoxia-induced treatment resistance. Radiother Oncol 101:369–375
67. Lee CT, Boss MK, Dewhirst MW (2014) Imaging tumor hypoxia to advance radiation oncology. Antioxid Redox Signal 21(2):313–337
68. Lee NY, Mechalakos JG, Nehmeh S et al (2008) Fluorine-18-labeled fluoromisonidazole positron emission andcomputed tomography-guided intensity-modulated radiotherapyfor head and neck cancer: a feasibility study. Int J Radiat Oncol Biol Phys 70:2–13
69. Nehmeh SA, Lee NY, Schroder H et al (2008) Reproducibility of intratumordistribution of (18)F-fluoromisonidazole in head and neckcancer. Int J Radiat Oncol Biol Phys 70:235–242
70. Lin Z, Mechalakos J, Nehmeh S et al (2008) The influence of changes in tumor hypoxia on dose-painting treatment plans based on 18F-FMISO positron emission tomography. Int J Radiat Oncol Biol Phys 70:1219–1228

12 Receptor-Targeted Radionuclide Imaging (RTRI) and Peptide Receptor Radionuclide Therapy (PRRT)

Weidong Yang, Cheng Wang, and Gang Huang

12.1 Folate-Based Radiotracers for Nuclear Medicine Imaging

Increased amount of folate is needed for cells under rapid proliferation such as cancer cells. Folate receptors (FRs) are shown to be overexpressed on the surface of tumor cells under low folate conditions and viewed as tumor-associated antigen. The FRs could specifically bind folate and folate conjugates with very high affinity and then transport these molecules into cells through an endocytic mechanism. The fact that various tumors are folate dependent has been applied to improve tumor diagnosis and treatment, developing anti-FRa antibodies, high-affinity antifolates, folate-conjugated drugs and toxins, and folate-based imaging agents.

There are four FR proteins known as FR-α, FR-β, FR-γ, and FR-δ. Among these four isoforms, FR-α isoform exerts a great value for nuclear medicine imaging using folate-based radiotracers as FR-α is overexpressed on various solid tumors. Furthermore, folic acid radiopharmaceuticals have great application potential as they could target FR-β on activated macrophages and hence be able to image inflammatory diseases. Therefore, emerging researches focus on folate conjugates which radiolabeled molecular probes with radionuclides such as ^{99m}Tc, ^{111}In, ^{18}F, and ^{68}Ga for nuclear medicine imaging (such as single-photon emission computed tomography (SPECT) and positron emission tomography (PET)), and many radiolabeling methods and technologies were developed. Either these folate molecular probes or these radiolabeling methods and technologies are applied not only in cancers but in inflammatory diseases. Therefore, folic acid-based imaging agents can be useful in patient selection for testing new therapeutic concept or monitoring treatment responses.

12.1.1 Folate Receptor and Folic Acid

Among these FR subtypes, FR-α and FR-β are glycophosphatidyl inositol-anchored membrane proteins that bind folic acid and folate conjugates with high affinity and are internalized by endocytosis. What's more important is that the FR-α is overexpressed on the cellular surface of different kinds of tumors, including the ovaries, uterus, brain, lungs, kidneys, breast, and colon-rectum, while only limited expression of FR-α is found in normal tissues. FR-α consists of a deep open folate-binding pocket containing conservative residues expressed in all isoforms. The globular structure of FR-α is stabilized by eight disulfide bonds. The folate pteroate moiety is located inside the deep open folate-binding pocket, as the glutamate moiety sticks out of the pocket entrance, which enables the conjugation between FR-α and drugs without affecting its binding with the receptor inside the pocket. The pocket receptors and ligand combination of FR enable its high affinity with folate analogues. In addition, it provides an important template for developing radiopharmaceuticals and drug delivery systems targeting the FRs, while the FR-β is specifically overexpressed on activated macrophages and hence could be used as a marker for inflammatory diseases such as rheumatoid arthritis. In normal tissue, the FRs was found expressed on the apical side of polarized epithelial cells in the lung, choroid plexus, salivary glands, and the placenta. Since FRs are expressed in the proximal tubules, the kidney also is an important folate targeting organ. Due to a very high affinity (KD < 10^{-9} M) between the folic acid and the FRs (FR-α and FR-β), its nontoxic, non-immunogenic properties, chemical modification, and high temperature resistance in radiolabeling proce-

W. Yang
Department of Nuclear Medicine, Xijing Hospital, The Fourth Military Medical University, Xi'an, P. R. China

C. Wang
Department of Nuclear Medicine, RenJi Hospital, School of Medicine, Shanghai JiaoTong University, Shanghai, P. R. China

G. Huang (✉)
Shanghai Key Laboratory of Molecular Imaging, Shanghai University of Medicine and Health Sciences, Shanghai, P. R. China

G. Huang (ed.), *Nuclear Medicine in Oncology*, https://doi.org/10.1007/978-981-13-7458-6_12

dures made folic acid being viewed as an almost perfect targeting agent for cancer and inflammatory diseases imagining (Fig. 12.1) [1].

12.1.2 Folate Metabolism

Folates are important one-carbon donors for the purines and thymidine synthesis, which are essential building components of nucleic acids. Folates also indirectly involve in the processes of S-adenosyl methionine (SAM) synthesis and the methylation of DNA, proteins, and lipids. Folate coenzymes mediate the transportation of one-carbon units. Folate coenzymes function as acceptors and donors of one-carbon units in many critical metabolic reactions during nucleic acid and amino acid metabolism.

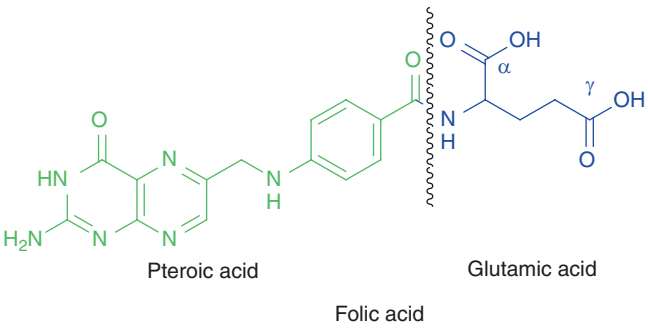

Fig. 12.1 The structure of folic acid

The primary function of folate coenzymes is to accept or donate one-carbon units in metabolic pathways (see Fig. 12.2). The continuous reduction of folic acid by dihydrofolate reductase to produce tetrahydrofolate (THF) is the first step in cyclic metabolism. Tetrahydrofolate, also known as coenzyme F (CoF), is an active coenzyme form of folic acid. 3-carbon of serine is used as the main carbon source to oxidize tetrahydrofolate (THF) to 5, 10-methylene-THF via pyridoxal phosphate (PLP)-dependent serine hydroxymethyltransferase (SHMT). While in the transformation, serine is converted to glycine. A portion of the 5, 10-methylenetetrahydrofolate undergoes irreversible enzymatic reduction to 5-methyl-THF by methylene tetrahydrofolate reductase (MTHFR). Meanwhile, MTHFR serves a key role in one-carbon metabolism by converting methylene-THF to 5-methyl-THF. The N-5 methyl group of 5-methyl-THF can only be used metabolically and transferred to homocysteine to (re)generate methionine. In the methionine synthase reaction, a methyl group is removed from 5-methyl-THF, which functions as a substrate, and is sequentially transferred to the vitamin B-12 coenzyme before homocysteine, thus forming methionine. Dihydrofolate reductase, which converts folic acid, dihydrofolate, and tetrahydrofolate into each other, has caught a lot of attention of researchers in recent years. It is clearly the site of action of antineoplastic drugs, including methotrexate and aminotrexate. These molecules

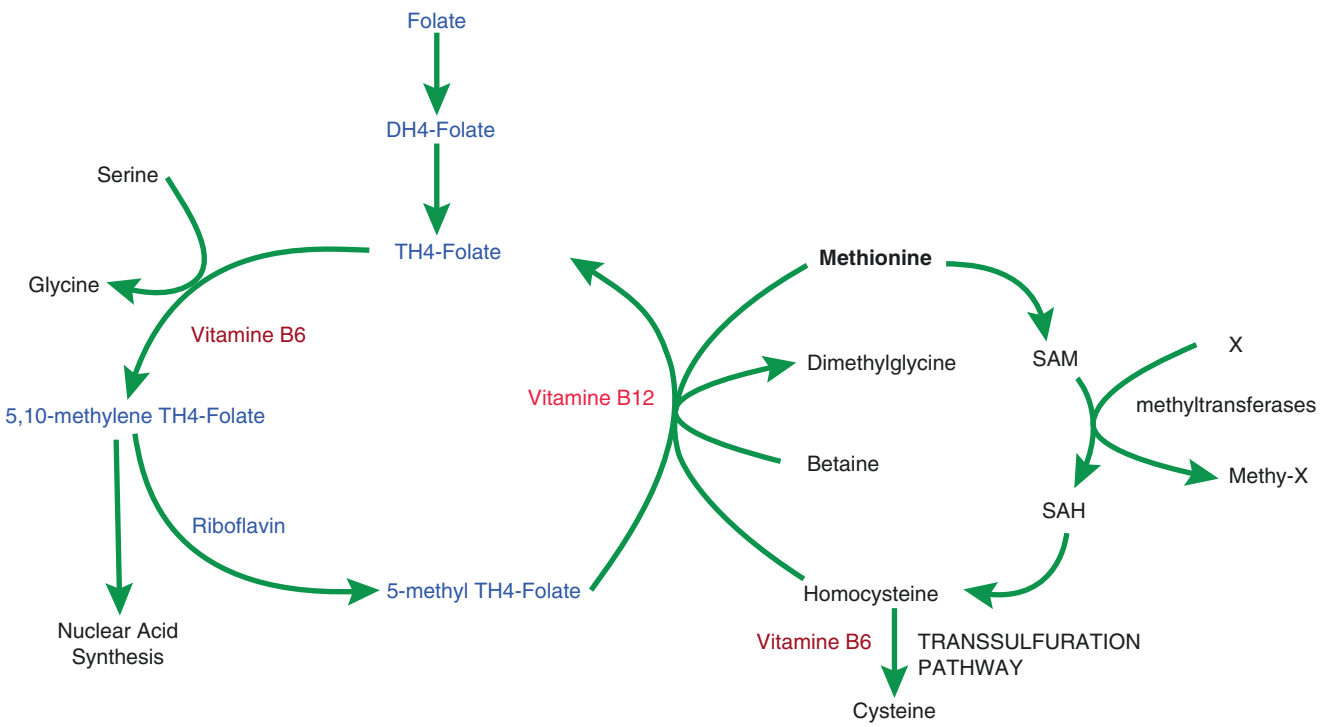

Fig. 12.2 The metabolic pathway of folic acid

are potent inhibitors of dihydrofolate reductase. Because cell growth requires a carbon unit of THF compounds for the synthesis of purine and thymine, methotrexate and its analogues are used as effective inhibitors of tumor growth. However, these drugs are also toxic to normal cells, and methotrexate can only be used for short-term treatment. Folate deficiency has been linked with many diseases, including fetal neural tube defects, cardiovascular disease, cancers, and Alzheimer's disease [2].

12.1.2.1 Nucleic Acid Metabolism

Folate coenzymes actively participate in the DNA metabolism via involving the formation of DNA precursors (thymidine and purines) or the synthesis of methionine from homocysteine. Homocysteine is essential for the SAM synthesis. SAM is an important regulator for various biological methylation reactions, such as DNA and RNA methylation, amino acid, and phospholipid metabolism. The biosynthetic pathway for methionine, steroids, and thymine relies on the incorporation of one-carbon unit from the tetrahydrofolate derivative. The methyl group of methionine is obtained from 5-methyl-THF via a vitamin B12-dependent manner. In the process of thymidylate synthase, a methyl group is introduced at the C-5 position of the deoxyuridine monophosphate (dUMP) to form deoxythymidine nucleotides (dTMP). 10-formyl-THF and 5, 10-methylene-THF are formyl donors for the transformylase reaction. Since folic acid is involved in the synthesis of nucleic acids, when folic acid or vitamin B12 is deficient, the synthesis of dTMP is restricted and further leads to DNA synthesis disorders. When folic acid is deficient, DNA synthesis is inhibited, resulting in reduced DNA synthesis in bone marrow macrocyte, decreased cell division rate, large cell volume, and loose chromatin in the nucleus. Most of this red blood cell is destroyed before it matures in the bone marrow, resulting in the giant red cell anemia. Therefore, folic acid is used for the treatment of macrocytic anemia.

12.1.2.2 Amino Acid Metabolism

Folate coenzymes are essential for the amino acid metabolism, especially methionine, cysteine, serine, glycine, and histidine. Folic acid is important for the metabolism of histidine. THF deficiency results in the accumulation of formiminoglutamic acid (FIGLU). FIGLU is a metabolite of histidine. THF is required to convert FIGLU to glutamic acid. Normal people have very little or no FIGLU in their urine. When folic acid is deficient, the excretion of urinary imine methyl glutamate increases without causing symptoms, which can be used as an evidence of folate deficiency. Folic acid also promotes the mutual conversion of glycine and serine, the conversion of phenylalanine to tyrosine, the conversion of histidine to glutamic acid, and the conversion of cysteine to methionine. Elevated blood levels of homocysteine have been reported to be a risk factor for chronic diseases such as cardiovascular disease and dementia.

12.1.3 The Isotopes and the Structures of the Folate Radiotracers

In recent years, researchers have used small molecule ligands to specifically bind to folate receptors on the surface of tumors and then deliver them into cells via the endocytosis mechanism. Besides, folate molecule itself serves as a good ligand. It has been found that when the carboxylic acid of the gamma isomer of the folate is covalently linked to other macromolecules, the affinity of folic acid to the cell surface receptor does not change. Moreover, the small molecule of the ligand is smaller than the size of the antibody and is easier to be removed from the body. Folate receptors are potential molecular targets, including radiolabeled folate chelate delivery for diagnostic imaging. Although these folate receptor-targeted radioactive molecular probes have not been shown to have a comparable clinical efficacy as diagnostic tools, they provide a feasible approach to noninvasively assess the levels of folate receptor in tissues by external radionuclide imaging.

Today's clinical practice of nuclear medicine focuses on the use of whole-body gamma or positron-emitting radiopharmaceuticals as imaging diagnostic or therapeutic tools. In this case, the chemical content of such radiopharmaceuticals is very small (10^{-6}–10^{-8} M). Currently, clinical radionuclide imaging techniques for diagnosis include single-photon emission computed tomography (SPECT) and positron emission tomography (PET). This is based on the nuclide properties of different nuclides. Different imaging methods are applied based on different properties of the radionuclide properties. Isotopes that have been conjugated with folate conjugates are shown in Table 12.1. The structure of folate conjugates is shown in Table 12.2. Folate receptors are promising molecular targets for radionuclide delivery because they are overexpressed on the surface of many tumor types, but not in normal tissues. The selection criteria for radionuclides for the preparation of radiopharmaceuticals for targeting folate receptors are as follows: (1) the decay mode of radionuclides and photon energy/energy, (2) physical half-life (usually giving priority to the shortest half-life nuclide), (3) availability for regular production or shipment to hospitals, (4) cost, (5) preparation of radiopharmaceuticals by simple modular chemical synthesis, so that sterile, nonthermal can be prepared routinely and reliably [3].

Most imaging agents targeting folate receptors are based on the structure of folate molecules as templates. On this basis, the glutamic acid moiety on the folic acid molecule is modified. If the selected labeling nuclides are metal nuclides, then a portion of the spacers on the gamma carboxyl group are then subjected to ligand modification. Common ligands are deferoxamine (DF), hydrazinonicotinamide (HYNIC), diethylenetriamine pentaacetic acid (DTPA), 1,4,7,10-tetraazacyclododecane-N,N′,N″,N‴-

Table 12.1 Properties of selected radionuclides commonly used in radiopharmaceutical labeling [4, 5]

Isotope	Half-life	Decay mode	Gamma energy (abundance)	Means of production
^{99m}Tc	6.01 h	Isomeric transition	140 keV (87%)	Generator
^{67}Ga	78 h	Electron capture	93 keV (38%) 185 keV (24%) 300 keV (17%) 394 keV (4%)	Cyclotron
^{111}In	67.4 h	Electron capture	171 keV (91%)	Cyclotron
^{123}I	13.3 h	Electron capture	159 keV (83%)	Cyclotron
^{131}I	8.05d	β−	364 keV (81%) 637 keV (7%) 284 keV (6%	Reactor
^{18}F	110 m	β+	511 keV	Cyclotron
^{64}Cu	12.7 h	β + (18%) β− (37%)	511 keV	Cyclotron or reactor
^{67}Cu	2.58d	β−	141 keV	Cyclotron
^{66}Ga	9.5 h	β+	511 keV	Cyclotron
^{68}Ga	68 m	β+	511 keV	Generator
^{44}Sc	3.97 h	β+	511 keV	Generator or cyclotron
^{152}Tb	17.5 h	β+	511 keV	High-energy proton-induced spallation of tantalum targets (ISOLDE/CERN)
^{124}I	4.2d	β+	511 keV	Cyclotron

Table 12.2 Folate radiotracers and structures

Radiotracers	Structures
Deferoxamine (α)-folate	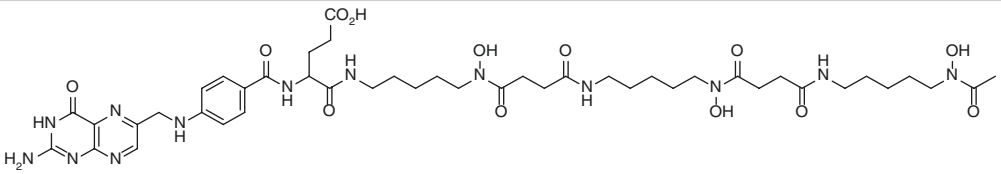
Deferoxamine (γ)-folate	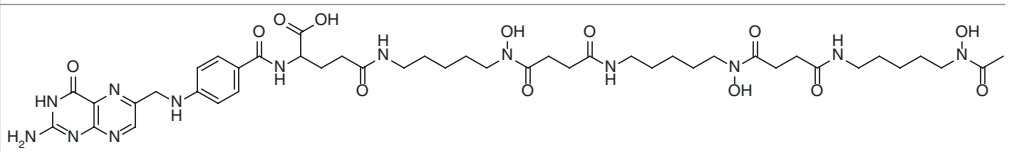
^{111}In-DTPA-folate (γ)	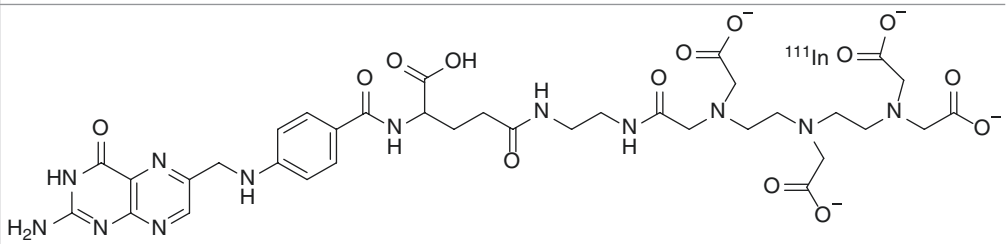
^{99m}Tc-EC20 (^{99m}Tc-Cys-Asp-Dap-D-Glu-Pte)	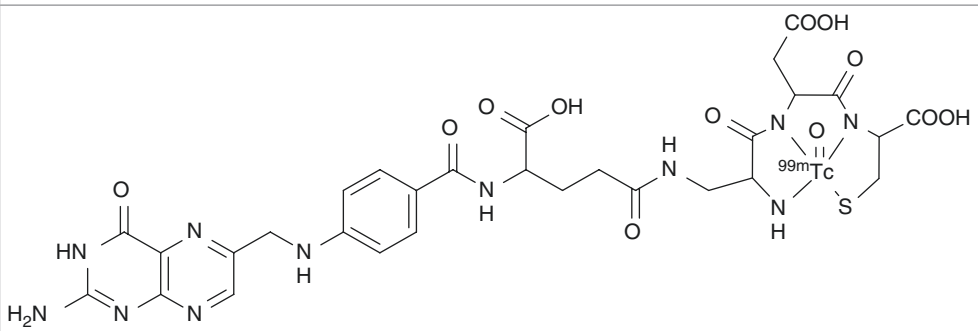

Table 12.2 (continued)

Radiotracers	Structures
HYNIC-folate (γ)	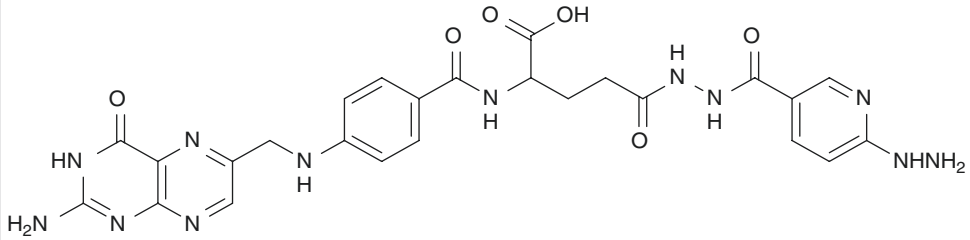
[^{18}F]FBA-(γ)-folate	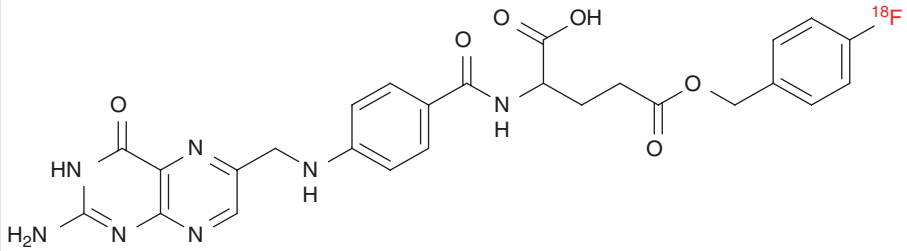
[^{18}F] fluorobenzene-carbohydrazide-folates	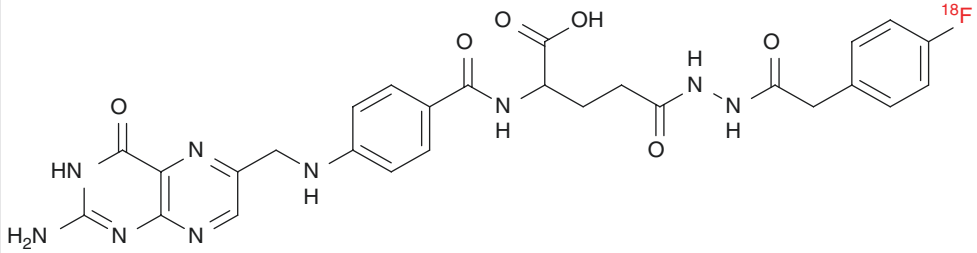
[^{18}F] fluoropyridinecarbohydrazide-folate	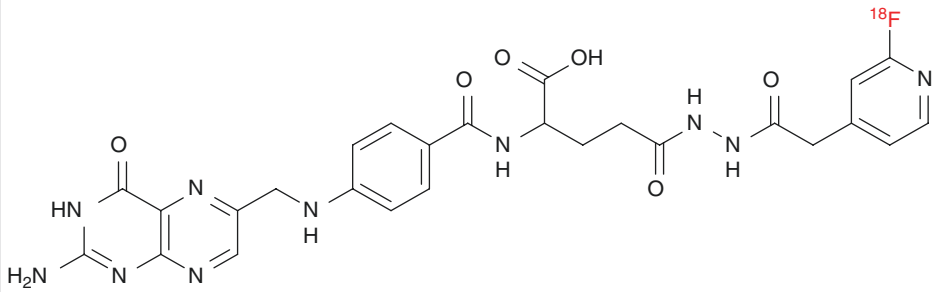
[^{18}F] fluoropyridinecarbohydrazide-methotrexate	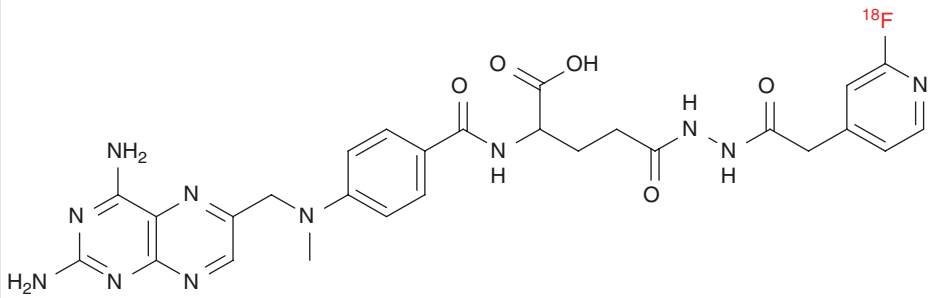
[^{18}F] fluoropyridinecarbohydrazide-methotrexate	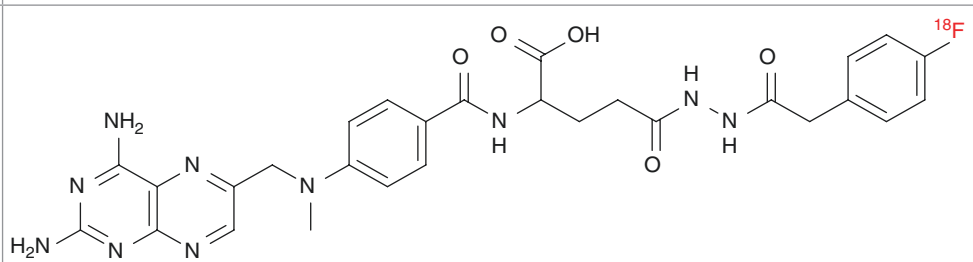

(continued)

Table 12.2 (continued)

Radiotracers	Structures
[^{18}F]fluoro-click- folate	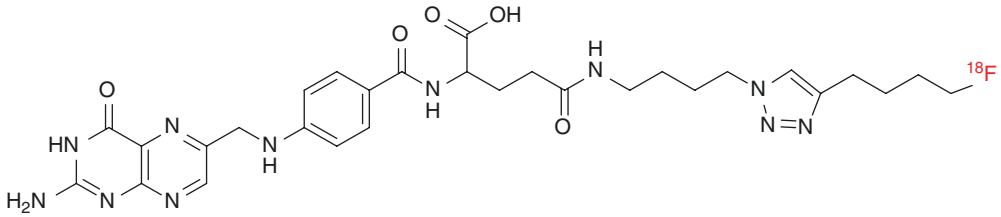
[^{18}F]FDG-folate	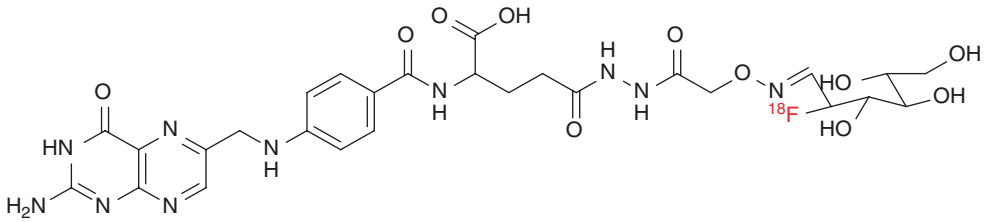
[^{18}F]FDG-methotrexate	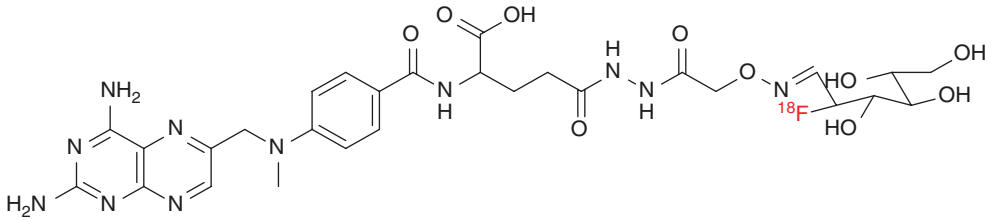
[^{18}F] fluoro-deoxy-glucose-folate	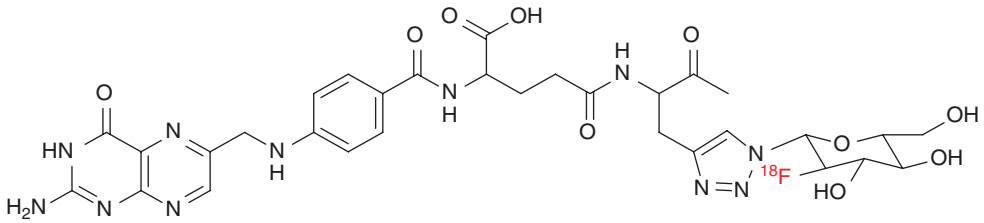
2′-[^{18}F]fluorofolic acid	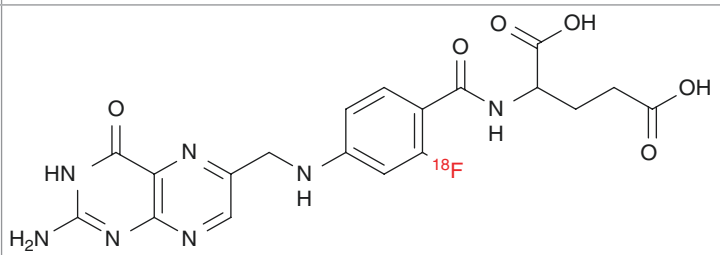
3′-aza-2′-[^{18}F]fluorofolic acid	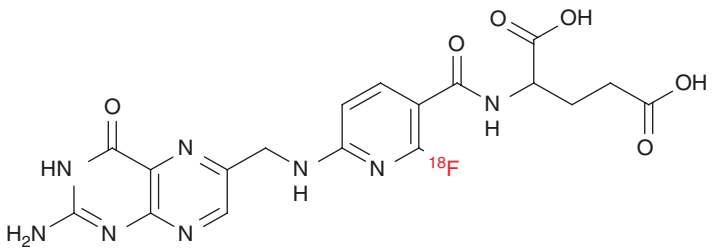

Table 12.2 (continued)

Radiotracers	Structures
DOTA-folate P3026	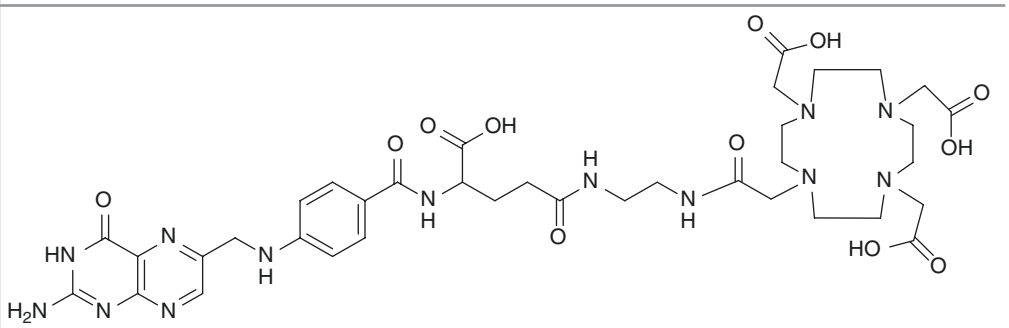
DOTA-folate P1254	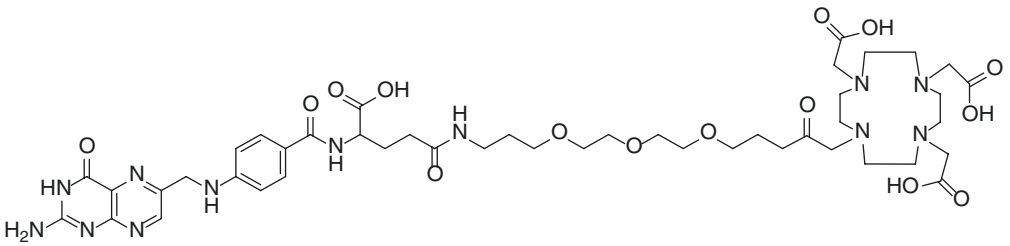
EC0800	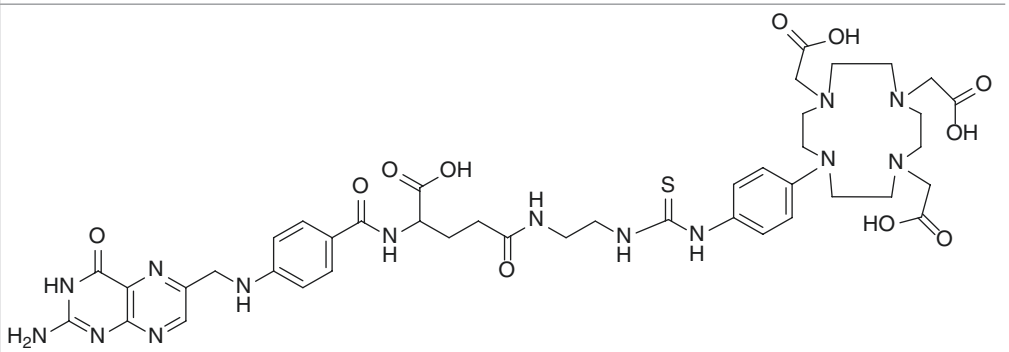
NODAGA-folate P3246	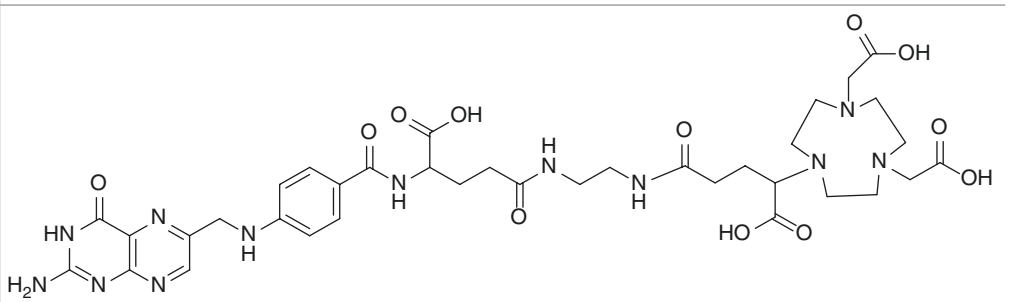
NODAGA-dideaza-folate P3238	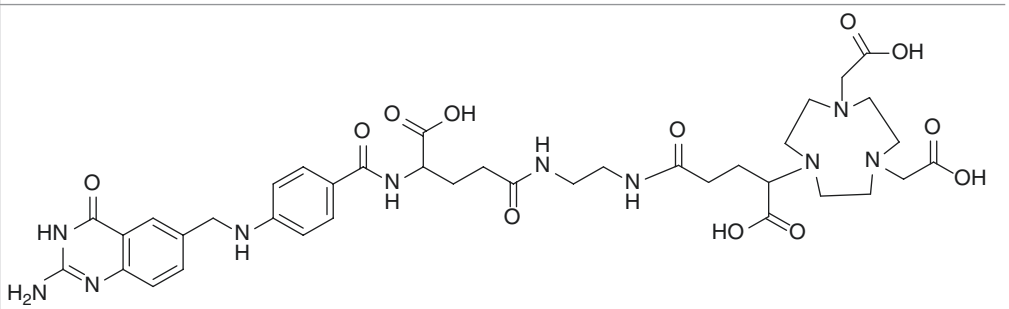

(continued)

Table 12.2 (continued)

Radiotracers	Structures
Cm09	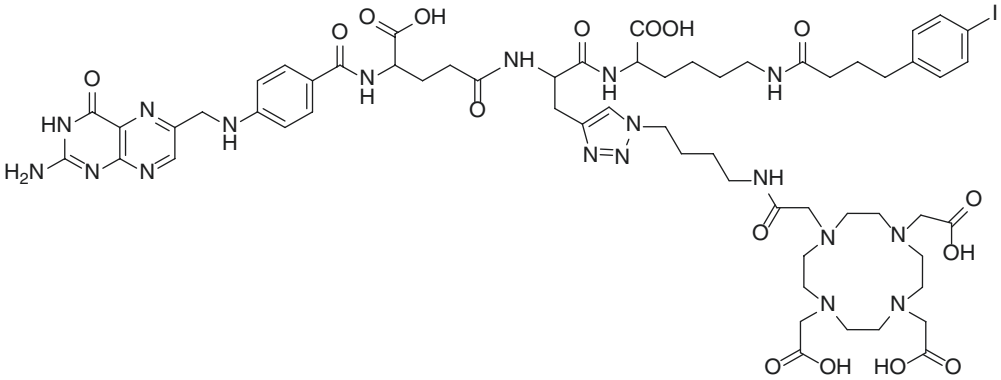
Folate-NOTA	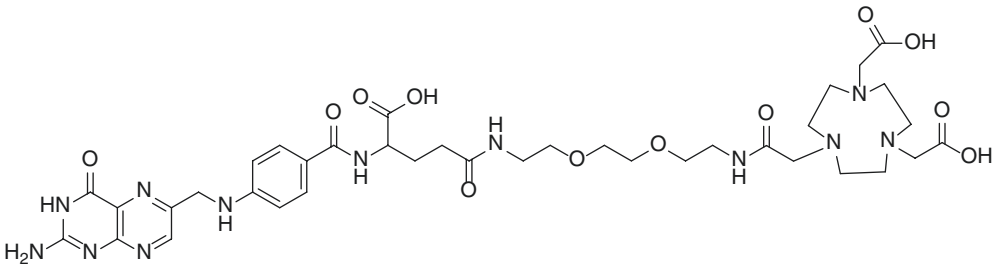
Folate-PEG12-NOTA	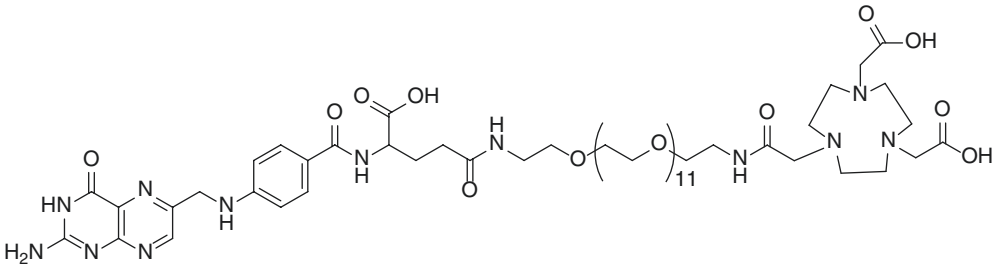
N-succinimidyl-p-[^{124}I]-iodobenzoate ([^{124}I]-SIB)	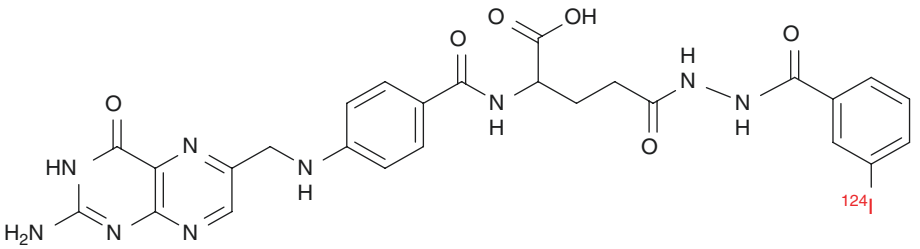
N-succinimidyl-[124I]-iodopyridine carboxylates ([124I]-SIP)	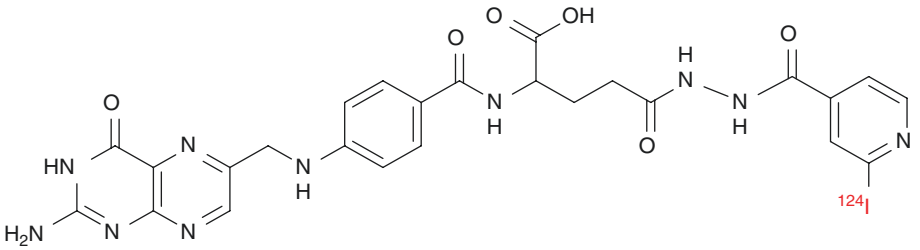

Table 12.2 (continued)

Radiotracers	Structures
HYNIC-D1-FA2	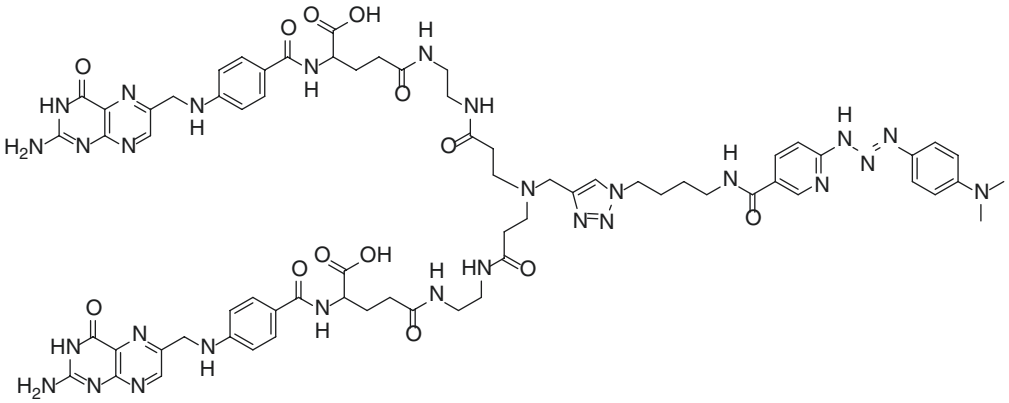

tetraacetic acid (DOTA), 1,4,7-triazacyclononane-1,4,7-triacetic acid (NOTA), and others. For the labeling of other nonmetallic radionuclides, C-X covalent bonds (such as C-F bonds and C-I bonds) are formed. The manner of biconjugating is varied, and the common labeling method is indirect labeling, in which the radioactive synthon is first prepared, and then the synthon is coupled to the γ-carboxyl group on the folic acid. Of course, direct labeling has recently been found for the nucleophilic substitution of the phenyl ring on the folic acid backbone of folic acid. However, the radiochemical yield is very low.

12.1.4 Folate Conjugate for Metallic Nuclides Labeling

Since the expression level of FR-α has been correlated with the invasion of specific cancer types, folic acid-based radiotracers have received great attention. Folate receptors have successfully targeted various radioactive metal chelates that bind to folate derivatives. The reported agents used a range of radionuclides that have considerable nuclear properties. Radionuclide imaging has allowed noninvasive detection of the expression of folate receptors of tumors in animal models and patients. Over the past two decades, various folate conjugates have been developed for PET and SPECT nuclear imaging. However, only two of these folate-based radioconjugates (^{111}In-DTPA-folate and ^{99m}Tc-EC20) have been tested in clinical trials. As an imaging agent for ovarian cancer diagnosis, ^{111}In-DTPA-folic acid has been initially evaluated for safety, biodistribution, and possible efficacy in humans. ^{99m}Tc-EC20 is currently being used in selecting patients who may benefit from FR-targeted therapy [6].

12.1.4.1 Deferoxamine-Folate

Deferoxamine is a high-affinity chelating agent for Fe(III) and also has a strong affinity to trivalent metals such as Ga(III) cations. A large excess of folic acid is coupled to the DF amine end by DCC to give an α-carboxyl and γ-carboxy conjugated chelating ligands. The affinity of the two DF-folate isoforms was determined by competition for folic acid, using folate receptor-expressing human KB tumor cells. The semi-inhibition constant experiment has found that the combination of γ-isomerDF-folate is similar to that of free folic acid. However, the α-isomerDF-folate has almost no affinity for folate receptors on cell surface.

The Ga(III)-DF-folate (γ) conjugate can be radiolabeled at high specific activity with ^{66}Ga, ^{67}Ga, and ^{68}Ga. The ^{67}Ga-DF-folate (γ) conjugate delivered 5.2 ± 1.5% of the injected dose per gram (%ID/g) of tumor at 4 h post-injection, with tumor-to-blood ratios as high as 409 ± 195 and 2.6 ± 0.9 for tumor/kidney. Tumor uptake of ^{67}Ga-DF-folate (γ) was effectively blocked by co-injection of free folic acid. In the tumor-bearing mouse model, when the dose of DF-folate is greater than 0.29 mg/kg, the amount of ^{67}Ga-DF-folate absorbed by the tumor is significantly decreased. The combination of receptor and DF-folate probably resulted in an inhibition of tumor absorption of ^{67}Ga-DF-folate. When the amount of DF-folate is 2.8 mg/kg, the target/nontarget ratio is the highest, and the metering of more than 20% is discharged from the urinary system. However, the tracer is excreted through the liver and gallbladder, so the radioactive concentration in the abdomen is remarkable [7]. Since the compound is a small molecule, it quickly reaches the tumor cells and enters the cells via endocytosis. However, this compound has a mild non-specific adhesion to the cell surface.

12.1.4.2 DTPA-Folate

In order to synthesize a more hydrophilic tracer, DTPA was selected as a chelating agent to couple with folic acid. The chelating ligand DTPA is covalently linked to the carboxylic acid of folic acid through the amide bond linked to ethylenediamine spacer. The affinity of DTPA-folate conjugates to folate receptors seems to be slightly lower than that of folate.

Biological distribution studies using KB cell xenograft model have demonstrated that the ^{111}In-DTPA-folate (γ) was

basically concentrated in the tumor. Except for the kidney, all tissues observed excellent tumor versus nontarget tissue distribution within 4 h (tumor/blood = 350 ± 100, tumor/kidney = 1.00 ± 0.34). The promising results with ^{111}In-DTPA-folate (γ) in the mouse xenograft model led to following phase I–II clinical trial to test this agent for detecting ovarian cancer in human [8]. SPECT imaging diagnosis was used for the diagnosis of 35 patients with ovarian cancer. The results of imaging were compared with surgical and pathological examinations. This study has found that, in a small range of subjects, all malignant tumors had high absorption rate of ^{111}In-DTPA-folate (γ). The sensitivity of the newly diagnosed malignant ovarian solid tumor was 100%, and the specificity was about 80%. For recurrent or suspected recurrent ovarian or endometrial malignant solid tumors, the sensitivity of ^{111}In-DTPA-folate (γ) is no more than 90%. The main reason for the diagnosis of recurrent or suspected recurrent ovarian or endometrial malignant solid tumors is that the solid tumor is much smaller than the newly emerging solid tumor.

^{111}In-DTPA-folate has been used in phase I and II clinical trials in the United States. Although better data of human distribution and imaging results of ovarian cancer have been obtained, there are many obstacles to further commercial promotion of the drug, such as high-cost radionuclide ^{111}In, longer radiochemical half-life, and unsatisfactory clinical results. Due to the low production cost of nuclides ^{99m}Tc and its superior radionuclide physical properties, more and more research groups have chosen to use ^{99m}Tc-labeled folate chelate. It is also found that small molecule imaging agents need short half-life radionuclides to be rapidly absorbed by specific tissue and rapidly discharged from the blood.

The DTPA-folate (γ) conjugate has also been employed to prepare two ^{99m}Tc radiopharmaceuticals: ^{99m}Tc-DTPA-folate (γ) and ^{99m}Tc $(CO)_3$-DTPA-folate (γ). ^{99m}Tc-DTPA-folate (γ) was prepared by reducing stannous chloride in [^{99m}Tc] sodium perrhenate in an aqueous solution of DTPA-folate (γ) with a radiochemical yield greater than 97%. The pharmacokinetics of ^{99m}Tc-DTPA-folate (γ) was evaluated by assessing the biodistribution of the tracer at 5 min, 1 h, and 4 h. The tumor uptake of ^{99m}Tc at 4 h was significantly higher than that at 5 min, while the renal level of the radiotracer did not change significantly within 4 h. Overall, the pharmacokinetic behaviors of ^{99m}Tc-DTPA-folate (γ) and ^{111}In-DTPA-folate (γ) in the mouse tumor model are very similar [9].

Although the pharmacokinetic behavior and biological distribution of ^{99m}Tc-DTPA-folate (γ) and ^{111}In-DTPA-folate (γ) in rat tumor models are similar, The radiochemical purity and stability of ^{99m}Tc-DTPA-folate (γ) were not very good when the amount of DTPA-folate (γ) was less than 200 mg. The water- and air-stable organometallic complex, ^{99m}Tc $(H_2O)_3(CO)_3^+$, has been proven to be a very versatile reagent for labeling various bioconjugates of ^{99m}Tc at low conjugation concentrations. A ^{99m}Tc(CO)3-DTPA-folate (γ) radiopharmaceutical was prepared by reacting DTPA-folate (γ) with a $^{99m}Tc(CO)_3(H_2O)_3^+$ intermediate with at least greater than 98% of radiochemical purity. In KB cell tumor-bearing model, biological distribution analysis has shown that the radioactivity uptakes in tumors at 5, 30 min, and 4 h post-injection (p.i.) were 0.8 ± 0.4, 1.8 ± 0.5, and 3.3 ± 0.2% ID/g, respectively. The radiotracer in the kidney increased from 5 min to 4 h p.i. However, the radiotracer uptake in the liver decreased from that time [10]. Although ^{99m}Tc(CO)3-DTPA-folate (γ) has good selectivity for folate receptors, it is concentrated in nontarget tissues with higher folate receptors. Therefore, ^{99m}Tc(CO)3-DTPA-folate (γ) has no obvious superiority compared with other folate chelates.

12.1.4.3 EC20 (Cys-Asp-Dap-D-Glu-Pte)

The EC20 is a pteroic acid derivative with the natural L-glutamate of folate replaced by D-glutamate. Additional metabolic protection was provided against tissue-resident γ-glutamyl hydrolases, followed by extension of the β-L-diaminopropionate (Dap)-L-Asp-L-Cys peptide chain from the γ-carboxylate of the glutamate. The peptide chain can be coordinated as a tetradentate ligand to the center of the Tc(V), which is produced by reducing the [^{99m}Tc] sodium perrhenate with α-D-glucoheptonate and tin (II) chloride. The FR binding affinity of 99mTc-EC20 in KB cells was reported to be 1.1 nm. At 4 h p.i., biodistribution studies showed that radioactivity uptake of ^{99m}Tc-EC20 was mainly in tumor (17.2 ± 1.0% ID/g) and kidney (138 ± 12% ID/g) in Balb/c mice with folate receptor-positive M109 tumors. The uptake of ^{99m}Tc-EC20 in tumor and renal in this animal model was very similar to that of ^{111}In-DTPA-folate (γ) [11]. A clinical study of 154 patients with malignant tumors has studied the expression of ^{99m}Tc-EC20 in tumor tissues, reporting positive and negative agreement with FR expression of 72% and 38%, respectively.

12.1.4.4 HYNIC-Folate (γ)

The HYNIC (hydrazinonicotinamide)-modified folate derivative, a monodentate ligand for the octahedral ^{99m}Tc center, allows high radiolabeling purity of more than 95%. However, in the preparation of r^{99m}Tc-HYNIC-folate (γ), co-ligands, tricine, and trisodium triphenylphosphine-3,3′,3″-trisulfonate (TPPTS) are also learned to bind multiple coordinators. Tissue biodistribution of ^{99m}Tc-HYNIC-folate (γ) in mice implanted with 24JK-FBP cells had demonstrated that the radioactivity uptakes in kidney and tumor at 4 h p.i. were 61 ± 34 and 18 ± 11% ID/g, respectively [12], while the tumor-to-blood was 55 at 4 h p.i.

HYNIC-D1-FA2 is a dimeric conjugated compound of folic acid. Using tricine and TPPTS as co-ligands, HYNIC-D1-FA2 was conjugate with ^{99m}Tc to generate ^{99m}Tc-HYNIC-D1-FA2. ^{99m}Tc-HYNIC-D1-FA2 uptake in the KB tumor

reached 10.16% ± 1.16%ID/g at 2 h p.i. and reached a remarkable value of 56.69% ± 3.12%ID/g at 4 h p.i. in the kidney. The tumor-to-kidney ratio was changed from 0.19 at 2 h to 0.16 at 4 h [13].

12.1.4.5 DOTA-Folates

Macrocyclic chelator DOTA (1,4,7,10-tetraazacyclododecane-N,N′,N″,N‴-tetraacetic acid) was employed to synthesis DOTA-folates for conjugating with diagnosis and therapeutic radioisotopes. These DOTA-folates include P3026 (with a 1,2-diaminoethane linker), P1254 (with a 3-{2-[2-(3-aminopropoxy)-ethoxy]-ethoxy}-propylamine linker), and EC0800 (DOTA-Bz-EDA-folate conjugate). The tumor uptake of $^{67/68}$Ga-DOTA-folate conjugates (P3026 and P1254) showed similar results with 10% ID/g at 2 h p.i.. However, the radioactivity uptakes of P3026 and P1254 in kidney were 87.78 ± 12.37% ID/g and 98.43 ± 15.40% ID/g, respectively. The tumor-to-kidney ratios of these two radiotracers were between 0.08 and 0.14 [14]. The radioactivity uptakes of 67Ga-EC0800 in KB tumor xenografts and kidneys were 6.08 ± 0.89% ID/g and 84.53 ± 14.10% ID/g, respectively, at 4 h p.i., and the tumor-to-kidney ratio was 0.07 [15].

In order to enhance the blood circulation time, an albumin-binding entity was introduced into the DOTA-folate molecule's backbone, named cm09. This DOTA-folate conjugate was labeled with ^{152}Tb, ^{177}Lu, and ^{44}Sc, respectively. All of these metallic nuclides labeling radiochemical yields were over 96% at elevated temperature for 15 min. Uptake of radioactivity in KB tumor xenografts was 14.1 ± 0.6%ID/g at 1 h p.i. Renal retention of these tracers was in the range of 19–23%ID/g in 24 h, and the tumor-to-kidney ratios reached values between 0.45 and 0.65 [16].

12.1.4.6 NODAGA-Folates

Folic acid and 5,8-dideaza folic acid were conjugated with 1,4,7-triazacyclononane,1-glutaric acid-4,7-acetic acid (NODAGA) to generate folate conjugates P3246 and P3238, respectively. Radiolabeling these conjugates with ^{68}Ga generates ^{68}Ga-P3246 and ^{68}Ga-P3238 with more than 95% labeling yields and 30 GBq/micromol specific activities within 10 min at room temperature. Radioactivity uptakes of ^{68}Ga-P3246 and ^{68}Ga-P3238 in KB tumor xenografts at 4 h p.i. reached 16% ID/g and 15% ID/g, respectively. Similar to the previous SPECT nuclides labeling, the radioactivity uptake in the kidney was high and the tumor-to-kidney ratio was less than 0.18 at all time-points of investigation. The most remarkable difference between these two derivatives was the uptake in the liver. The liver uptake of ^{68}Ga-P3238 was 2.49 ± 0.21% ID/g compared to the ^{68}Ga-P3246 uptake of 1.07 ± 0.18% ID/g at 4 h p.i. This is because the nitrogen atom in the conjugated compound P3246 easily forms a hydrogen bond with the water molecule to enhance the water solubility thereof, and the carbon atom in the conjugated compound P3238 is less likely to easily form a hydrogen bond with the water molecule, and thus its fat solubility is enhanced [17].

12.1.4.7 NOTA-Folates

Folate-NOTA (1,4,7-triazacyclononane-1,4,7-triacetic acid) and folate-PEG12-NOTA were NOTA-modified folate conjugates. These NOTA-functionalized folate conjugates can be labeled with the $(Al\text{-}^{18}F)^{2+}$ species to generate folate-NOTA-Al^{18}F and folate-PEG12-NOTA-Al^{18}F. The radioactivity uptakes of these two tracers in KB tumors were 10.9% ID/g and 9.20 ± 0.62% IA/g at 90 min p.i., respectively. And the tumor-to-kidney ratios were 0.12 ± 0.03 and 0.18 ± 0.02, respectively. But the radioactivity uptake of folate-PEG12-NOTA-Al^{18}F in liver was over twofold reduced than folate-NOTA-Al^{18}F. This is because the modification of PEG enhances the water solubility of the conjugated compound, resulting in a change in the metabolic pathway of the drug [18, 19].

12.1.5 Halogen-Labeled Folic Acid Radiotracer

The key to halogen-labeled folic acid is the formation of a halogen-carbon covalent bond. Currently, there are two methods for halogen labeling folic acid, one of which is the modification of two carboxyl groups on glutamic acid in folic acid. The most important labeling method is the prosthetic group approach. Another method of labeling is the modification of the folic acid backbone in folic acid. The labeling method is mainly nucleophilic substitution approach.

12.1.5.1 Prosthetic Group Approach

Prosthetic groups approach is a type of indirect labeling method. In the preparation of the radiolabeled compound, the radionuclide is first labeled with a small molecule compound to form a labeled intermediate, also named synthon. The synthon is then combined with the targeting molecule to synthesize the radiopharmaceutical by simple and rapid organic chemical synthesis. This method is commonly applied to the labeling process of nonmetallic radionuclides. The most common synthons used for folate labeling include [^{18}F]fluorobenzylamine ([^{18}F]FBA), 4-[^{18}F]fluorobenzoate, 2-[^{18}F]fluoro-4-pyridinecarboxylate, [^{18}F]fluoro-glucose, N-succinimidyl-p-[^{124}I]-iodobenzoate carboxylates ([^{124}I]-SIB), and N-succinimidyl-[^{124}I]-iodopyridine carboxylates ([^{124}I]-SIP).

[^{18}F]Fluorobenzylamine-Folates

[^{18}F]FBA was synthesized with the radiochemical yield of 8%–13%. In the conjugating step, [^{18}F]FBA reacts with unprotected folic acid and produces [^{18}F]FBA-α/γ-folate.

The total radiochemical yields were between 1.2% and 5.7% with a specific activity of 7–24 GBq/μmol, and the ratio of α-andγ-isomers was 1:4. The radioactivity uptake in KB-31 tumor xenografts amounted to 6.56 ± 1.80% ID/g at 125 min p.i. vs. 40.65 ± 12.81%ID/g in the kidney. Therefore, tumor-to-kidney ratio was only 0.16. Blocking experiment, carried out by injecting 200 μg of folic acid before the injection of radioactive tracers, has showed the uptake reduced to 1.07 ± 0.38%ID/g in tumor and reduced to 1.16 ± 0.41%ID/g in the kidney. However, the tumor-to-kidney ratio was increased to 0.92 [20].

[^{18}F]Fluorobenzene-Folates

4-[^{18}F]fluorobenzoate was reacted with hydrazine hydrate to give the labeling intermediate 4-[^{18}F]fluorobenzenecarbohydrazide, which was subsequently conjugated with NHS-activated folic acid or antifolate methotrexate to generate [^{18}F]fluorobenzenecarbohydrazide-folates or [^{18}F]fluoropyridinecarbohydrazide-methotrexate. The radioactivity uptakes of these two tracers in KB tumors were 5.94 ± 1.16%ID/g and 0.81 ± 0.09% ID/g at 60 min p.i., respectively. And the kidney uptakes of these two tracers were 19.70 ± 2.25%ID/g and 4.01 ± 0.80%ID/g, respectively. The tumor-to-kidney ratios were 0.3 and 0.2, respectively [21, 22].

[^{18}F]Fluoropyridinecarbohydrazide-Folates

Similar to the preparation of 4-[^{18}F]fluorobenzenecarbohydrazide, 2-[^{18}F]fluoro-4-pyridinecarboxylate was reacted with hydrazine hydrate to give 2-[^{18}F]fluoropyridine-4-carbohydrazide, which was subsequently conjugated with NHS-activated folic acid and methotrexate to generate [^{18}F]fluoropyridinecarbohydrazide-folates or [^{18}F]fluoropyridinecarbohydrazide-methotrexate. The radioactivity uptakes of these two radiotracers in KB tumors were 5.74 ± 0.16%ID/g and 1.00 ± 0.19% ID/g at 60 min p.i., respectively. And the kidney uptakes were 7.90 ± 1.25%ID/g and 5.04 ± 0.25%ID/g, respectively. The tumor-to-kidney ratios were 0.7 and 0.2, respectively. However, the radioactivity uptake of [^{18}F]fluoropyridinecarbohydrazide-folates was sixfold higher in the tumor than that of [^{18}F]fluoropyridinecarbohydrazide-methotrexates, as well as the [^{18}F]fluorobenzenecarbohydrazide derivatives [21, 22]. This may be due to the change of the pteroic acid in the folate molecule structure, which affects the affinity between the folic acid receptor, pocket-packed structure, and pteroic acid.

[^{18}F]Fluoro-Glucose-Folates

As a prosthetic group, [^{18}F]FDG has a strong water solubility. Based on this, a more hydrophilic folate-based ^{18}F-radiotracer was designed. As oxime-forming synthon, [^{18}F]FDG was conjugated with aminoxy-folate and methotrexate derivatives to produce [^{18}F]FDG-folate, [^{18}F]FDG-methotrexate, and [^{18}F]fluoro-deoxy-glucose-folate. The distribution study in KB tumor-bearing mice has showed the radioactive uptakes of [^{18}F]FDG-folate, [^{18}F]FDG-methotrexate, and [^{18}F]fluoro-deoxy-glucose-folate in tumor were 3.32 ± 0.32% ID/g, 1.10 ± 0.21% ID/g, and 10.03 ± 1.12% ID/g, respectively, at 60 min p.i. vs. 1.49 ± 0.05% ID/g, 0.82 ± 0.05% ID/g, and 42.94 ± 2.04% ID/g, respectively, in the kidney. The tumor-to-kidney ratios were of these tracers 2.2, 1.4, and 0.23, respectively. Among current folate-based ^{18}F-tracers, [^{18}F]fluoro-deoxy-glucose-folate is one of the most promising radiotracers for clinical use [23, 24].

[^{18}F]Fluoro-Click-Folate

Radioactive synthon 6-[^{18}F]fluoro-1-hexyne is coupled to an azide-derivatized folate precursor via the Cu(I)-catalyzed 1,3-dipolar cycloaddition to produce [^{18}F]fluoro-click-folate. In vivo tissue distribution data showed that the tumor uptakes of [^{18}F]fluoro-click-folate was 3.13 ± 0.83% ID/g at 45 min p.i. in KB tumor xenografts and 16.53 ± 2.22% ID/g in the kidney. The tumor-to-kidney ratio was just 0.19. High radioactivity uptake was discovered in gallbladder (1.71 ± 0.14% ID/g) and in intestines (19.59 ± 5.26% ID/g), which indicated that the fat solubility of this ^{18}F-click folate was enhanced when the alkane chain linker was added [25].

[^{124}I]iodobenzene and Pyridine Carbohydrazide-Folate Conjugates

[^{124}I]iodobenzene and pyridine carbohydrazide-folate conjugates were prepared by the reaction of ^{124}I-labeled intermediates N-succinimidyl-p-[^{124}I]-iodobenzoate carboxylates ([^{124}I]-SIB) or N-succinimidyl-[^{124}I]-iodopyridine carboxylates ([^{124}I]-SIP) with folate-hydrazide. The radioactivity uptakes of [^{124}I]SIB- and [^{124}I]SIP-folate conjugates in kidneys in normal mice were 2.31 ± 0.74%ID/g and 0.72 ± 0.36% ID/g at 60 min p.i., respectively. While in KB tumor-bearing mice, the uptakes of [^{124}I]SIP-folate in tumor and kidneys were 1.48 ± 0.12%ID/g and 1.47 ± 0.21%ID/g, respectively. Hence its tumor-to-kidney ratio was almost close to 1. However, the literature did not report the uptake of [^{124}I]SIB-folate in tumor models [26].

12.1.5.2 Nucleophilic Substitution Approach

The most important method to generate ^{18}F-labeled compounds is nucleophilic substitution based on n.c.a. [^{18}F]fluoride, which is directly conjugated to the target molecules. The typical leaving groups were NO_2, TfO, TsO, and the halogen (I, Br, F). The key of this method is to prepare the suitable precursor for nucleophilic substitution within a short time (usually within three nuclides half-lives). The preparation of the [^{18}F]fluorine-labeled folic acid derivatives by this method comprises two steps: (1) nucleophilic substitution reaction of the labeled precursor and (2) deprotection of the [^{18}F]fluorine-labeled intermediate.

For the direct labeling method, two labeling precursors, N2-(N, N-dimethylaminomethylene)-2′-nitrofolic acid di-tert-butylester and N2-acetyl-3′-aza-2′-chlorofolic acid di-tert-butylester, were prepared. Then the n.c.a. [^{18}F]fluoride was conjugated to the target molecule by a direct nucleophilic aromatic substitution of the 2′-nitro group or Cl atom under anhydrous solvent and high temperature. The radiochemical yields were 4% in 80 min and 3–9% in 110 min after the preparation started. Biodistribution data of 2′-[^{18}F] fluorofolic acid in KB tumor xenografts mouse models demonstrate that the radioactivity uptakes in tumor and kidney were 11.50 ± 0.28% ID/g and 35.73 ± 0.25% ID/g, respectively, at 75 min p.i. Hence, the tumor-to-kidney ratio was 0.32. However, the 3′-aza-2′-[^{18}F]fluorofolic acid uptake in KB tumor xenografts was 12.59 ± 1.77% ID/g and 57.33 ± 8.40 ID/g in the kidney at 90 min p.i., with a tumor-to-kidney ratio of 0.21. The substitution of a nitrogen atom for a carbon atom in the tracer enhances the hydrophilicity of the radiopharmaceutical, thereby enhancing its water solubility. Therefore, the uptake in the kidney was significantly enhanced [27, 28].

12.1.6 Summary and Outlook

It has been more than 20 years since metal radionuclide gallium-labeled folic acid derivative was used for the preparation of radioactive probes targeting folic acid receptors, which were highly expressed on the surface of tumors. From the initial coordination labeling of metal radionuclide to the covalent bond formation labeling of halogen, from direct labeling to indirect labeling by means of labeling intermediates, nearly 40 molecular probes targeting folate receptors have been prepared by various nuclides and methods. Moreover, these probes do not include labeled probes based on nanomaterials as carriers. The metal radionuclide-labeled folate derivative is characterized by the formation of coordinate bonds, which has the advantages of simplicity and high efficiency. However, the disadvantage is that the labeling precursor and product are more difficult to separate by HPLC and therefore have a lower specific activity. Halogens, especially ^{18}F-labeled folate derivatives, are characterized by the formation of covalent bonds, which are limited by the time-consuming procedure and low labeling yields. However, since the n.c.a. fluoride is used and the product is separated by HPLC, the specific activity has been generally improved. The current limitation of these folate-based molecular probes is the high concentration of radioactivity uptake in the kidney due to the presence of folate receptors in the kidney, which could result in a poor imaging by SPECT or PET scan in animal or clinical studies. Therefore, the accurate diagnosis of abdominal tumors remains to be a great challenge for future studies.

The simultaneous radioactivity uptake at the knees of cancer patients is another concern. Further examination revealed that these patients also had arthritic diseases. Further studies found that these radioactive uptakes of folate-based targeting agents are mediated by FR-β on the surface of macrophage, which is activated by the inflammatory process. Therefore, the development of a clinically useful folate-based tracer has considerable potential for early diagnosis, staging, and prognosis monitoring of inflammatory diseases, which may involve the activation of macrophages. In addition, considering the high resolution and sensitivity of PET, developing a potential folic acid derivative-based PET tracer for monitoring and quantifying the sites of activated macrophages in inflammatory diseases will result in a beneficial impact in clinical practice. With the rapid development of PET imaging probes, folic acid derivatives will certainly have great potential to become an effective tool in the field of nuclear medicine.

12.2 RTRI and PRRT for Neuroendocrine Tumors

Somatostatin receptors (SSTRs) are G-protein-coupled receptor abnormally expressed in various neuroendocrine tumors. Somatostatin or its analog can specifically bind to SSTRs with high affinity, which makes the SSTRs as ideal targets for neuroendocrine tumor (NET) diagnosis and therapy. Somatostatin receptor imaging (SRI) and peptide receptor radionuclide therapy (PRRT) based on the radioisotope-labeled somatostatin analog (SSA) have been successfully developed in NET theranostic in the past two decades. Various radioisotopes have been used to label SSA, for example ^{111}In, ^{99m}Tc labeled SSA usually used for SPECT imaging, while ^{68}Ga, ^{64}Cu used for PET imaging. SRI is more sensitive and specific in detecting NETs compared with other traditional imaging modality. Higher energy of β particle for ^{90}Y and ^{177}Lu with a reasonable tissue penetration has been broadly used for PRRT. The accuracy of diagnoses and efficacy of treatment for SSTRs over expressed NETs have been significantly improved by SRI and PRRT based on the radioisotope-labeled SSA.

12.2.1 Somatostatin Receptor, Somatostatin, and Somatostatin Analog

Somatostatin receptors (SSTRs) are G-protein-coupled receptors highly expressed in various NETs and can specifically bind with somatostatin. However, the natural somatostatin can be easily degraded with a short half-life and makes it hard to be used in clinic. To expand its clinical application, somatostatin analogues with longer half-life and specific binding to SSTRs have been developed.

12.2.1.1 Somatostatin Receptors (SSTRs)

Somatostatin receptors (SSTRs) are one of the seven transmembrane domain families of G-protein-coupled receptors [29]. The SSTRs family includes five subtypes (SSTR1–5), with SSTR2 being the most highly expressed subtype, followed by SSTR1, SSTR5, SSTR3, and SSTR4 [30]. They are broadly expressed on cells of neuroendocrine origin, as well as on a few types of tumors such as breast cancer, lung cancer, and lymphoma. SSTRs can be detected in cells under physiological or pathological processes, while the overexpression of SSTRs is often seen on the surface of cancer cells. Different cell types usually express varied amounts of different SSTRs subtypes.

12.2.1.2 Somatostatin (SST)

Somatostatin (SST) is a regulatory peptide hormone which was first successfully isolated from sheep hypothalamus in 1973. SST could be further processed into two active forms as SST-14 and SST-28 through an alternative proteolytic processing from a single precursor [31]. Somatostatin degrades rapidly in vivo with a short half-life of 2–4 min. Four amino acids, Phe, Trp, Lys, and Thr, of somatostatin are important for its biological activity. Trp and Lys are necessary for maintaining the biological functions of SST, while Phe and Thr could be replaced by other amino acids without significantly impacting biological activity of SST. Somatostatin specifically binds to its target receptor SSTRs and then triggers SSTRs to reduce secretion of cyclic AMP and cytosolic calcium (Fig. 12.3).

12.2.1.3 Somatostatin Analogue (SSA)

Since family members of SSTR (SSTR1-5) are over-expressed on well-differentiated NETs, especially the SSTR2. Therefore the over-expressed SSTR could be severed as an ideal target in diagnosing and therapying for NETs. However, endogenous somatostatin undergoes rapid degradation in vivo, and the shortcoming of the relative short half-life of SST strongly limits its clinical application. To overcome this shortcoming, the native somatostatin has been modified in many different ways. Somatostatin analogue (SSA) has been developed by introducing D-amino acids and shortening the molecule to improve its biological characteristics, which makes it more resistant to the in vivo degradation. Several effective somatostatin analogues with longer half-lives have been synthesized since the 1980s, such as octreotide, octreotate, vapreotide, lanreotide, RC-160, and MK-678. Octreotide is the most typical SSA first synthesized by Wilfried Bauer. It is an octapeptide with eight amino acids D-Phe-c[Cys-Phe-D-Trp-Lys-Thr-Cys]-Thr(ol) that mimics natural somatostatin pharmacologically. The octreotide is more stable to enzymatic degradation compared with the native somatostatin, with a half-life of 90 min, which is 30 times longer than the half-life of native somatostatin. Octreotate (octreotide acid) is another form of somatostatin analogue with an amino acid sequence similar to octreotide. It is produced by replacing amino acid Thr for the corresponding amino alcohol Thr(ol) at the C terminus of octreotide. Vapreotide is a synthetic somatostatin analog with an eight-residue peptide, and its amino acid sequence is H-D-Phe-Cys(1)-Tyr-D-Trp-Lys-Val-Cys(1)-Trp-NH2. Other SSA includes lanreotide, RC-160 and MK678. As listed in Table 12.3, each of these somatostatin analogs has different binding affinity with different subtypes of somatostatin receptors. Structures of several typical somatostatin analogs are showed in Fig. 12.4. These somatostatin analogues have significantly broadened the clinical application of SSA, and some of them are used for the diagnosis and treatment of various diseases [32, 33].

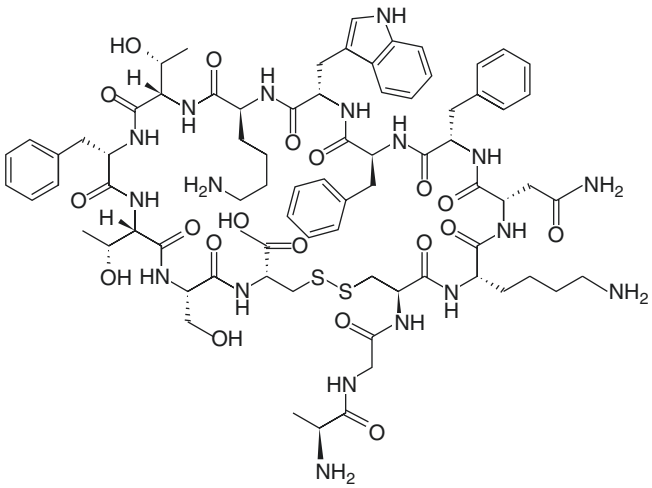

Fig. 12.3 The structure of somatostatin

12.2.2 Somatostatin Receptor Scintigraphy (SRS)

Based on the principle that SSA specifically binds to SSTRs, various radioisotopes have been successfully labeled with SSA in NETs imaging. ^{111}In- or ^{99m}Tc-labeled SSA are used for SPECT, and ^{18}F- or ^{68}Ga-labeled SSA are used for PET imaging. Somatostatin receptor scintigraphy (SRS) has a valuable technique for detecting NETs [34].

12.2.2.1 Radiotracer for Somatostatin Receptor Imaging

The abnormal expression of SSTRs on NET cell surfaces makes them ideal targets for NET imaging using radionuclide-labeled SSA. The radionuclide-labeled SSA can be used for imaging tumors with elevated somatostatin receptor. Compared to SST, SSA has a longer half-life and specifically binds to SSTRs with a higher affinity, which makes it easier to deliver the radionuclide to the site of NETs. Different

Table 12.3 Characteristic of SST or SSA binding with hSSTRs (IC_{50} in nM)

SST or SSA	SSTR1	SSTR2	SSTR3	SSTR4	SSTR5
SST-14	1.10	1.30	1.60	0.53	0.90
SST-28	2.20	4.10	6.40	1.10	0.07
Lanreotide	>1000	1.80	43	66	0.62
RC-160	>1000	5.40	31	45	0.70
MK-678	>1000	0.5	21	>1000	12
Octreotide	>1000	2.10	4.40	>1000	5.60
[DOTA,Tyr^3]-Octreotide	>1000	14	880	>1000	393
[DTPA,Tyr^3]-Octreotate	>1000	3.9	>1000	>1000	>1000
[DOTA,Tyr^3]-Octreotate	>1000	1.5	>1000	453	547

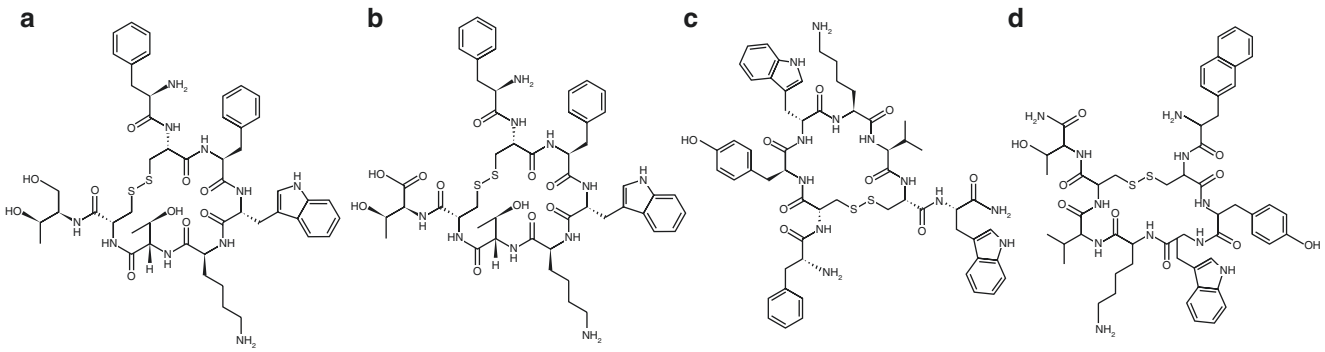

Fig. 12.4 The structure of typical somatostatin analog. (**a**) Octreotide; (**b**) octreotate; (**c**) vapreotide; (**d**) lanreotide

radionuclides have been successfully conjugated to various SSA, and some of them have already been used in clinic for detecting NETs.

I-123 tyr3-octreotide is the first SSTR radionuclide imaging agent. Iodine-123 was used to label many probes with a half-life of 13.22 h. However, synthesis of I-123 tyr3-octreotide has always been a high cost and time-consuming process, and its low quality of imaging further limits the clinical application of I-123 tyr3-octreotide. Since then, other types of radioisotope-labeled SSA have been synthesized for either SPECT (SPECT/CT) or PET (PET/CT) imaging. Usually, the radionuclide complex is formed between a radionuclide and organic ligands or chelators such as DOTA or DTPA. Various α-emitter, β-emitter, or γ-emitter radionuclides have been used in labeling SSA. Among them, ^{111}In-, ^{99m}Tc-, ^{18}F-, ^{68}Ga-, ^{18}F-, and ^{64}Gu-labeled SSA are used for imaging, and ^{111}In, ^{177}Lu, ^{90}Y, and ^{213}Bi are used for treatment. Among these radionuclides, both ^{111}In and ^{177}Lu can produce rays for imaging and treatment.

1. Indium-111(^{111}In)-labeled SSA
   By using the DTPA as chelator, ^{111}In can be easily used for labeling SSA. ^{111}In-DTPA-D-Phe1-octreotide (OctreoScan Mallinckrodt Inc.) was the first radiopharmaceutical containing a SSA, and it was approved by the FDA in 1994 for the diagnosis of neuroendocrine tumors. It used to be the gold standard for the diagnosis and staging of SSTR-positive tumors with SPECT. However, OctreoScan only has highly affinity to sstr2 and sstr5, which makes it unsuitable for imaging tumors expressing other types of somatostatin receptors [35].
2. Technetium-99 m (^{99m}Tc)-labeled SSA
   Technetium-99 m is the most commonly used radioactive tracer in clinic. It is well suited to label SSA, since it emits readily detectable gamma rays with a photon energy of 140 keV. ^{99m}Tc-Depreotide is made by direct labeling, while the direct labeling process may affect the biological activity of SSA. Using HYNIC as the chelator, SSA can be easily labeled with high activity. ^{99m}Tc-hydrazinonicotinyl-Tyr3-octreotide (HYNIC-TOC) has a better performance in the evaluation of several different types of malignancies, showing a higher tumor-to-normal tissue ratio than ^{111}In-labeled SSA.
3. Fluorine-18 (^{18}F)-labeled SSA
   Compared to SPECT/CT, PET/CT has the advantages of a higher spatial resolution and a better quantification. Radiolabeled SSAs that are used for PET imaging have been rapidly developed as the most commonly used radioisotope in clinic. ^{18}F has several advantages compared with another commonly used PET radioisotope

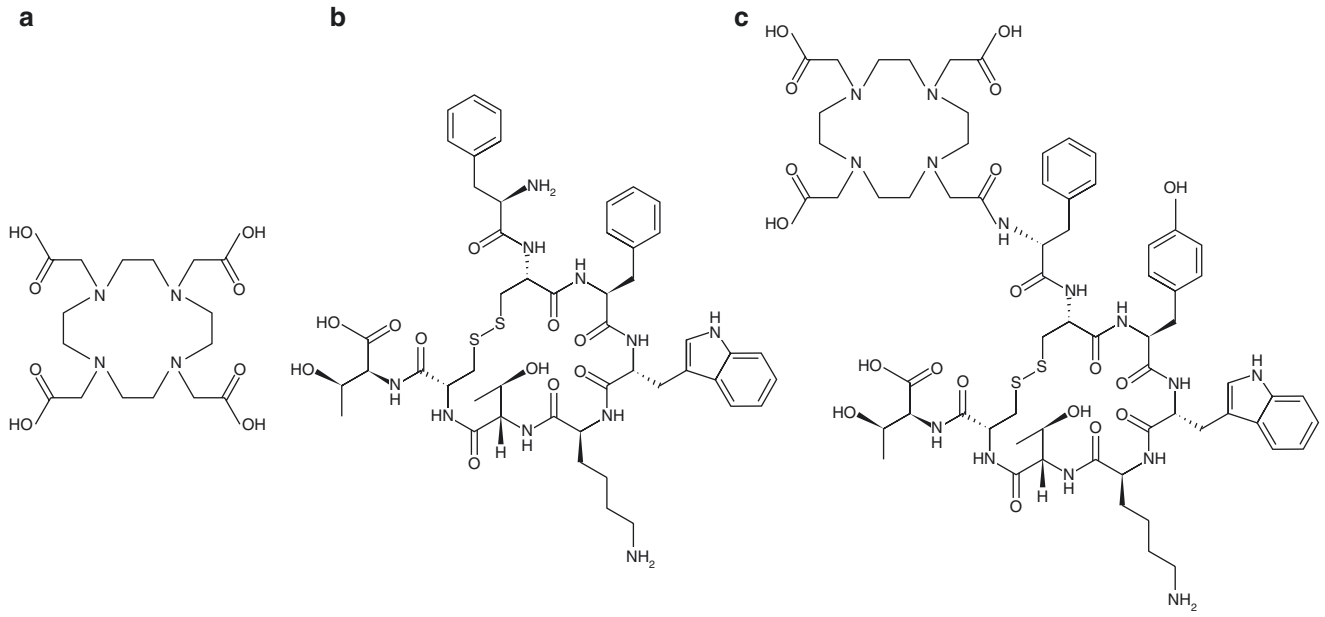

Fig. 12.5 Structure of (**a**) DOTA, (**b**) octreotate (TATE), (**c**) NOTA-TATE

^{68}Ga, for example, the half-life of ^{18}F is 110 min, which is longer than ^{68}Ga. An interesting approach consists of labeling peptides with Al^{18}F via radiometalation chemistry which has been used for labeling octreotide.

4. Gallium-68 (^{68}Ga)-labeled SSA
   Unlike the most common radioisotopes such as ^{18}F, ^{64}Cu needs to be produced by cyclotron for PET imaging. ^{68}Ga can be obtained by a generator, which makes it more easily available. By using DOTA or other chelators, the ^{68}Ga labeling with peptide is becoming simple. Therefore the ^{68}Ga-labeled SSA has gained more attention in recent years, and it moved a step forward with the introduction of DOTA as the chelator [36]. Several ^{68}Ga-labeled SSAs have been successfully used in clinic. Tyr3-octreotide, Tyr3-octreotate, and l-Nal3-octreotide are the most frequently used SSA. By labeling them with ^{68}Ga using DOTA as chelator, they are named ^{68}Ga-DOTA-Tyr3-octreotide (^{68}Ga-DOTATOC), ^{68}Ga-DOTA-Tyr3-octreotate (^{68}Ga-DOTATATE), and ^{68}Ga-DOTA-l-Nal3-octreotide (^{68}Ga-DOTANOC). The structure of the DOTA bind to TATE is shown in Fig. 12.5.
5. Copper-64 (^{64}Cu)-labeled SSA
   ^{64}Cu is another PET radioisotope with a longer half-life (12.7 h) and a lower positron energy. Because of its longer half-life and a stable complex formation with chelating molecules, ^{64}Cu-labeled SSA such as ^{64}Cu-CPTA-D-Phe1–octreotide, ^{64}Cu-TETA-D-Phe1–octreotide, and ^{64}Cu-TETA-Tyr3–octreotate is promising in SRI.

12.2.2.2 SPECT Imaging of NETs

Computed tomography (CT) and magnetic resonance imaging (MRI) are commonly used to detect NETs with a sensitivity between 50 and 80%. In comparison, functional imaging modalities including PET and SPECT have shown higher sensitivity and specificity in visualizing primary tumors and their metastases. During the past two decades, SRI has been widely used for the diagnosis and staging of NETs. ^{111}In-labeled SSA with the DPTA as the chelator was developed and soon been approved by FDA. ^{111}In-DTPA-octreotide (OctreoScan) became the most commonly used agent for SRI. OctreoScan could detect lesions that were often missed by CT or MRI. A study by Chiti et al. has identified new lesions in 28% of patients with OctreoScan, and other two studies in detecting of NET metastases also showed that OctreoScan detected new lesions in 47% and 4.6% of cases, respectively, which were missed by CT or MRI. By combining with CT, the anatomic localization of tumor and the accuracy of SPECT/CT will be dramatically improved. The combined use of OctreoScan and CT is shown to improve clinical management in about 15% of patients, comparing to the planar OctreoScan images only.

^{111}In-pentetreotide is more sensitive for the diagnosis of detecting gastroenteropancreatic tumor. Normally, the sensitivity of ^{111}In-DTPA-octreotide in detecting the NETs is between 67 and 100%. The common indications for ^{111}In-DTPA-octreotide imaging include the detection and localization of tumors and their metastases, tumor staging, and patient follow-up. In addition, it is also useful for selecting potential responsive patients for octreotide therapy or patients with inoperable and/or metastatic tumors for peptide receptor radionuclide therapy (PRRT).

^{111}In-DTPA-octreotide was used to be considered as the gold standard for NETs imaging; it is an important part of the diagnostic work-up of patients with NETs in the consensus guidelines of the European Neuroendocrine Tumor Society.

However there are some NETs that show low uptake of ^{111}In-DTPA-octreotide and some other NETs even negative. After ^{111}In-DTPA-octreotide, ^{99m}Tc-depreotide is another commercially available radiotracer in detecting SSTR subtypes, especially for SSTR2, SSTR3, and SSTR5. It has shown promise in detecting a variety of tumor types, including some OctreoScan negative NETs. Followed by ^{99m}Tc-Depreotide, other ^{99m}Tc-labeled somatostatin analogs have been also developed, by using HYNIC as the chelator to label hydrazinonicotinyl-Tyr3-octreotide, and synthesized the new SPECT imaging radiotracer ^{99m}Tc-HYNIC-TOC; a study reported that ^{99m}Tc-HYNIC-TOC is more sensitive than ^{111}In-labeled SSA in localizing somatostatin receptor-positive tumors. So we can anticipate that with new radiotracer developed, the specificity and sensitivity of SPECT in diagnosing NETs will be greatly improved.

12.2.2.3 PET Imaging of NETs

Other than the use of SPECT imaging in detecting NETs, PET/CT with higher spatial resolution can detect the NETs with a better sensitive. ^{68}Ga labeled several SSA PET/CT imaging have been used in clinic in detecting NETs (^{68}Ga-DOTANOC ,^{68}Ga-DOTANOC etc.).

1. PET/CT imaging of NETs
   The spatial resolution of PET/CT is higher than SPECT, PET can detect millimeters lesion, while SPECT can only detect lesion more than 1 cm. Three ^{68}Ga-labeled somatostatin analogs including ^{68}Ga-DOTATOC, ^{68}Ga-DOTANOC, and ^{68}Ga-DOTATATE have been successfully used in clinic. Since then the detection of SSTR-positive tumor has made remarkable progress.

   ^{68}Ga-labeled SSA are sensitive in detecting the NETs. However, in different NETs, with the different type and expression amount of SSTR, the sensitivity of PET imaging for each NETs may be different. Hofmann et al. has reported a sensitivity of 100% for ^{68}Ga-DOTATOC in detecting eight GEP NET patients. Gabriel et al. showed a sensitivity of 97% for the 50 NETs patients. Versari et al. showed a high sensitivity of 92% but a low specificity of 83% in 19 patients with duodenopancreatic NETs. However, Ambrosini et al. reported 100% sensitivity and 100% specificity for ^{68}Ga-DOTANOC in nine patients with typical, well-differentiated pulmonary NETs. On the other hand, by using ^{68}Ga-DOTATATE, Kayani et al. reported a slightly lower sensitivity of 72% for pulmonary NETs.

   Except for the primary tumors, tumor metastases can be also clearly detected by PET/CT with the ^{68}Ga-labeled SSA. For the liver metastases, ^{68}Ga-DOTANOC and ^{68}Ga-DOTATOC both exhibit an almost threefold higher tumor-to-normal tissue uptake ratio compared to ^{18}F-FDG PET. Wild et al. conducted a lesion-to-lesion analysis in 18 patients showing a better detection rate of ^{68}Ga-DOTANOC PET/CT (tumor-to-background ratio of 2.7) in liver lesions compared to ^{68}Ga-DOTATATE (tumor-to-background ratio of 2.0). The bone is another most common target organ for metastases, and precise detection of bone metastases is critical for monitoring and predicting the prognosis. ^{99m}Tc-dicarboxy propane diphosphonate is considered as the gold standard for detecting bone metastases. ^{68}Ga-DOTATOC has been reported with a sensitivity of 97% and a specificity of 92% for the detection of bone metastases, indicating that ^{68}Ga-DOTATOC PET is a better diagnostic tool than CT and bone scintigraphy. Wild et al. also suggested ^{68}Ga-DOTATATE as a better tracer for bone lesion detection than ^{68}Ga-DOTANOC. They found a reduced ^{68}Ga-DOTATATE accumulation in the bone marrow than ^{68}Ga-DOTANOC, which makes ^{68}Ga-DOTATATE having a higher tumor-to-background for bone metastases.
2. PET/CT Versus Other Imaging Techniques
   Many clinical studies have been performed in the past several years to compare the ^{68}Ga-PET with other imaging methods. Comparison of ^{68}Ga-DOTANOC PET/CT and conventional imaging (mainly CT and MRI) has been investigated; ^{68}Ga-DOTANOC PET/CT was a good diagnostic accuracy for detecting NETs, with high sensitivity, specificity, positive predictive value (PPV), and negative predictive value (NPC). Study showed that contrast-enhanced ^{68}Ga-DOTATATE PET/CT is significantly sensitivity than contrast-enhanced CT (94% vs. 63%) and more accurate than contrast-enhanced CT (87% vs. 68%). Another study also showed that ^{68}Ga-DOTATATE PET/CT was able to detect the occult lesion in more than half of the patients who had the lesions missed by CT. ^{68}Ga-DOTATATE PET/CT also has a better performance than ^{111}In-DTPA-octreotide in detecting small lesions with a low density of SSTRs. Buchmann et al. reported that ^{68}Ga-DOTATOC has a better detection rate for NET lesions in 27 patients than ^{111}In-DTPA-octreotide SPECT (279 vs. 157 NET lesions, respectively). Gabriel et al. further confirmed that ^{68}Ga-DOTATOC PET can detect more lesions compared with conventional SRI and diagnostic CT. In their study, the ^{68}Ga-DOTATOC PET has a sensitivity of 97% and a specificity of 92%, while SPECT has a low sensitivity of 52%. In another study with 109 patients, the sensitivity of ^{68}Ga-DOTANOC was better than CT, MRI, and ultrasound. For primary tumors, the sensitivity of ^{68}Ga-DOTANOC (78.3%) was higher than the sensitivity of conventional imaging (63.8%). ^{68}Ga-DOTANOC had a sensitivity of 97.4% for the diagnosis of metastases, and a sensitivity of 81.8% was reported using conventional. Above all the ^{68}Ga PET is sensitive in detecting the NETs and superior to other conventional imaging techniques and may play a more important role in management of NETs.

3. Comparison of various ^{68}Ga-labeled SSA
   Each SSA shows different binding affinity to SSTRs; ^{68}Ga-DOTATATE is SSTR2 selective with tenfold higher affinity for SSTR2 in vitro than that of ^{68}Ga-DOTATOC. ^{68}Ga-DOTANOC has a wider receptor binding profile, able to specifically bind to SSTR2, SSTR3, and SSTR5. The affinity profiles are different between ^{68}Ga-DOTATOC, ^{68}Ga-DOTATATE, and ^{68}Ga-DOTANOC. The efficiency of NET lesion detection could be affected due to different binding affinity [37, 38]. A recent meta-analysis showed that both ^{68}Ga-DOTATOC (Sen 93%, Spe 85%) and ^{68}Ga-DOTATATE (Sen 96%, Spe 100%) have high diagnostic accuracy. Poeppel T.D. et al. studied 40 patients with metastatic NETs. The diagnostic accuracy was almost the same between these two radiotracers; however the within and between group tumor uptake differs due to difference in SSTR subtype profile of individuals. For tumors expressing broader SSTR subtypes, ^{68}Ga-DOTANOC may be more efficient; Wild et al. study showed that the SSTR2-, SSTR3-, and SSTR5-specific radiotracer ^{68}Ga-DOTANOC detected significantly more lesions than the SSTR2 selective radiotracer ^{68}Ga-DOTATATE for those patients. All of all, PET imaging with ^{68}Ga-labeled SSA offers higher sensitivity and specificity compared with SRI and conventional imaging modalities.
4. Clinical Application of ^{68}Ga-labeled SSA
   ^{68}Ga-labeled SSA PET/CT imaging has been broadly used for management of NETs, the indications for SRI including primary lesion detection, staging and restaging, evaluating the treatment response, guiding surgery, follow-up, and selecting patients for peptide receptor radionuclide therapy (PRRT). With the coming of this new imaging modality, the prognosis of the NETs is gradually improved.

   In diagnosing, ^{68}Ga-labeled SSA PET/CT is an effective method in detecting both the primary lesion and metastases with high sensitivity and specificity. It is also superior to other convention imaging techniques as CT, MRI, and ultrasound. Although each radiotracer has its own property, most of the time the sensitivity and specificity are above or close to 90%. Because of the higher spatial resolution, it can even detect the small lesions. In brief, the ^{68}Ga-labeled SSA PET/CT can diagnose the NETs earlier and more accurately. For the staging and restaging, ^{68}Ga-labeled SSA PET/CT is more accurate in staging the NETs and also an effective method for restaging of NETs. Gabriel et al. compared the SPECT with ^{68}Ga-DOTANOC PET in 84 patients, compared with SRI SPECT. ^{68}Ga-DOTATOC has been shown to provide extra clinical information in 21.4% of patients, which resulted in the change of treatment plans in three patients who previously were not detected with the widespread metastases. ^{68}Ga-labeled SSA PET imaging is also showing its promise and potential in monitoring treatment response to NETs; ^{68}Ga-labeled SSA uptake significantly decreases after effective therapy. Based on ^{68}Ga PET imaging, further treatment plan can be made; this could ensure the suitable treatment for the NETs to improve the treatment. ^{68}Ga-labeled SSA can also been used for surgery-guiding; ^{68}Ga-labeled SSA radioguided surgery (RGS) has also been done in various SSTR-positive tumor, such as lung tumors (pulmonary NETs, non-small cell lung cancer), gliomas, and breast cancer. As such, RGS results in better long-term outcomes for patients with SSTR-positive tumor.

   ^{68}Ga-labeled SSA PET imaging was also effective in therapeutic decisionmaking and theranostics. For example, low-gradetumors can be considered to treat by surgery. High-grade tumors are treated mainly by chemotherapy and peptide receptor radionuclide therapy (PRRT) which is always used for the unresectable tumor highly uptake the SSA. PRRT is an effective method for NET treatment, however it is only efficient to SSTR-positive NETs. To ensure effective treatment, ^{68}Ga PET should be done before PRRT; if PET imaging is positive, it will be suitable for PRRT, but if it is negative it should not treat with PRRT; normally the more ^{68}Ga-SSA uptake in tumor, the better treatment of PRRT will be.

   As mentioned above, ^{68}Ga PET is used in diagnosing, staging, and evaluating treatment response, so it is clearly that ^{68}Ga PET was broadly used in every step of the theranostics. It anticipated that the correct use of ^{68}Ga PET imaging for NET management will effectively improve its treatment.
5. Limitation of ^{68}Ga-labeled SSA PET
   ^{68}Ga PET/CT is increasingly recognized as the best imaging modality for the evaluation of well-differentiated NETs. However, SSR is not an exclusive marker for NETs. A variety of tumors with negative SSR will lead to a significant risk of false-positive PET/CT results. This reminds us that we should be more careful in interpreting the ^{68}Ga PET imaging.

12.2.3 Peptide Receptor Radionuclide Therapy (PRRT)

Radionuclide-labeled synthesized peptide which specifically binds to its target receptor highly expressed in malignant tissues can effectively destroy the tumor cells and inhibit the growth of tumor tissue. Several peptides such as TOC, NOC, TATE targeted SSTR2 have been used for treatment of NETs.

12.2.3.1 Principle of PRRT

Peptide receptor radionuclide therapy (PRRT) is based on α- or β-emitting radioisotope-labeled SSA which specifically binds to SSTRs abnormally expressed in NETs and their metastases for treatment of well-differentiated unresectable or metastatic NETs. The radioisotope-labeled complex is stable and is internalized into the cell for the irradiation. Furthermore, the long half-life of the analog would help to maintain a persistent therapeutic effect. Several radioisotopes have been used for PRRT such as ^{111}In, ^{90}Y, and ^{177}Lu, and more recently ^{231}Bi or ^{225}Ac have been explored; the detailed information of the radiotracers are showed as follows.

12.2.3.2 Radiotracer for Peptide Receptor Radionuclide Therapy (PRRT)

The overexpression of SSTRs in NETs has made it as a very important target for radionuclide therapy; several radionuclides have been enrolled in labeling SSAs for PRRT. Radionuclide-produced Auger electrons as ^{111}In, and *β*-rays as ^{90}Y and ^{177}Lu, have been used for NET treatment; more recently α-emitter radionuclide such as ^{213}Bi was also used for PRRT. Characteristic of those radionuclide were listed in Table 12.4 and the radionuclide-labeled SSA were introduced as follows.

1. Indium-111 (^{111}In)-labeled SSA
   ^{111}In emits both *γ*-radiation and therapeutic Auger and conversion electrons. *γ*-Ray can be used for SPECT imaging, while the Auger and conversion electrons can be used for treatment. Therefore ^{111}In is a radioisotope that can be used for both imaging and therapy. However, the energy of the Auger and conversion electrons is slightly weak resulting in a short tissue penetration; usually, it can only penetrate 10 μm local tissue which limited its efficacy to larger tumor. ^{111}In-DTPA-octreotide is one of the typical ^{111}In-labeled SSAs that has been used for SRI, since other higher-energy *β*-emitters are used for labeling SSA, but ^{111}In-DTPA-octreotide is not an ideal option for PRRT.
2. Yttrium-90 (^{90}Y)-labeled SSA
   ^{90}Y is a *β*-particle emitter with a maximum energy of 2.3 MeV and a maximum range of 12 mm in tissue; it can effectively inhibit the growth of the tumor, especially to those larger-volume tumors. Normally it is combined with a more stable chelator such as DOTA and a modified SST analog such as TOC, NOC, and TATE. ^{90}Y-DOTATOC has superior therapeutic efficacy since adequate dose of radiation can be delivered to tumors to cause cell damage, the structure of ^{90}Y-DOTATOC as shown in Fig. 12.6.
3. Lutetium-177 (^{177}Lu)-labeled SSA

Table 12.4 Characteristic of radioisotope used for peptide receptor radionuclide therapy

Radioisotope	Half-life	Type of ray	Decay energy	Originated	Example of radiotracer	Penetrating depth
Indium-111 (^{111}In)	2.8 d	γ Auger electrons	0.2454 MeV 3.6&19 Kev	Cyclotron	^{111}In-DTPA-D-Phe1-octreotide	10 μm
Yttrium-90 (^{90}Y)	64.1 h	β	2.28 MeV	Reactors	^{90}Y-DOTATOC	10 mm
Lutetium-177 (^{177}Lu)	6.7 d	β	497Kev(78.6%) 384Kev(9.1%) 176Kev(12.2%)	Reactors	^{177}Lu-DOTATATE	2 mm
Bismuth-213 (^{213}Bi)	65.6 min	α	8.32 MeV	Generator	^{213}Bi-DOTATOC	40–50 μm

EC electron capture; *h* hour; *min* minutes; *d* days

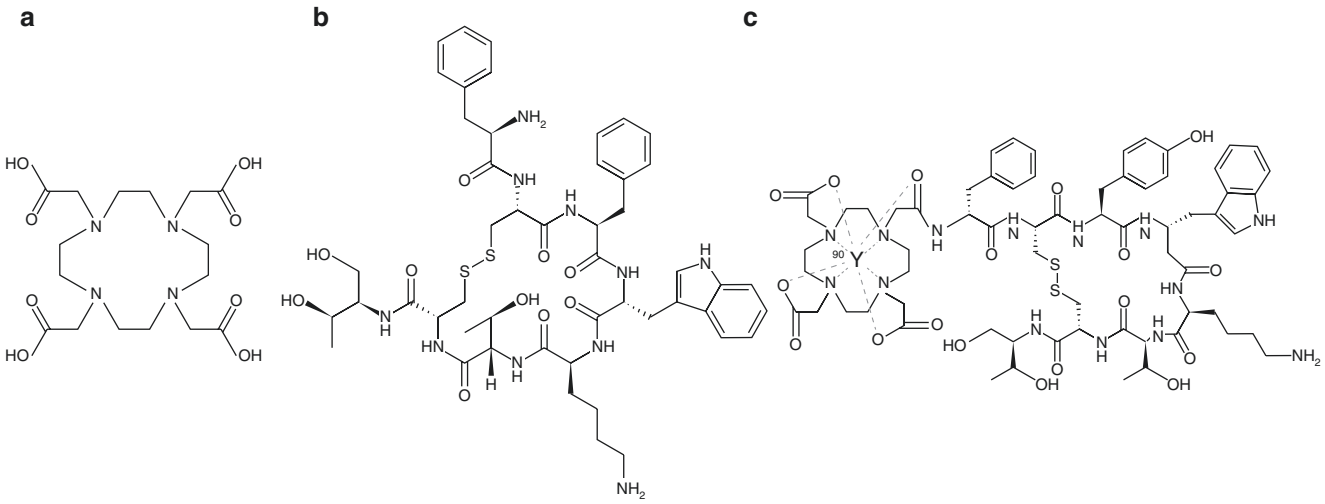

Fig. 12.6 Structure of ^{90}Y-DOTATOC. (**a**) DOTA; (**b**) TATE; (**c**) ^{90}Y-DOTATOC

Table 12.5 Different studies of ^{111}In-labeled SSA treatment to NETs

Researcher	Years	Patient number	Treatment Dose (GBq)	Treatment response PR	MR	SD	PD
Valkema et al.	2002	26	4.7–160.0	0 (0%)	2 (8%)	15 (58%)	9 (35%)
Anthony et al.	2002	26	6.7–46.6	2 (8%)	0 (0%)	21 (81%)	3 (11%)
Buscombe et al.	2003	12	3.1–36.6	2 (17%)	0 (0%)	7 (58%)	3 (25%)

PR partial response; *MR* minor response; *SD* stable disease; *PD* progressive disease

^{177}Lu is a median energy β-emitter (0.5 MeV) with small tissue penetrating range (2 mm). This allows for higher radiation dose delivered to smaller tumors and less damage to surrounding tissues than the radionuclide ^{90}Y. Except the β ray, ^{177}Lu also emits γ-rays with the energy of 150Kev which is suitable for SPECT imaging. So ^{177}Lu is another radioisotope used for both SPECT imaging and PRRT after ^{111}In. ^{177}Lu can also be conjugated with SSA by using DOTA as the chelator, and different SSAs can be labeled with ^{177}Lu. Among those radiotracers, ^{177}Lu-DOTATATE are impressive since its binding affinity to SSTR2 is significantly higher than others.

4. Bismuth-213(213Bi)-labeled SSA
   α-Ray is a high linear energy transfer (LET). It could easily cause double-strand DNA breaks and make irreversible DNA damage. Recent studies suggest that radioisotope treatment with high LET radiation may have better therapeutic results compared to conventional low LET emissions. So the application of α-emitters such as ^{213}Bi is arousing immense interest in PRRT recently. ^{213}Bi emit higher energy (8.32 MeV) compared with β-emitters and had a short path length of only 40–50 μm, which can increase the local antitumor effect without affecting untargeted tissues. Several SSAs have been labeled by ^{213}Bi or other α-emitting isotopes. ^{213}Bi-DOTATOC has been investigated in preclinical studies which showed its great potency and limited toxicity of targeted α-therapy in NETs.

12.2.3.3 The Treatment of NETs with PRRT

Several radionuclides with different radiation rays have been used for PRRT in treating NETs; ^{90}Y and ^{177}Lu are most commonly used for PRRT. For each different radionuclide-labeled SSA will cause different results.

1. Treatment of NETs with ^{111}In-DTPA-Octreotide Octreotide
   ^{111}In-DTPA-octreotide is the first radiolabeled somatostatin analog therapy in NETs. A study by Valkema has reported that more than half of patients resulted in a stabilization of their metastatic disease following the treatment of ^{111}In -DTPA-octreotide, and about 10% of patients had minor remission. Some other studies performed with high radioactivity doses of ^{111}In-DTPA-octreotide in patients with metastatic NETs showed a significant symptom relief. Other researchers conducted several clinical experiments with ^{111}In-DTPA-octreotide as shown in Table 12.5. In fact all the studies did not show the significant tumor shrink which suggested that the antitumor effect of ^{111}In-octreotide is limited for PRRT, at least for visible NETs. The most possible reason is that the energy of the Auger and conversion electrons is slightly weak resulting in a short tissue penetration (10 μm) which limited its efficacy.
2. Treatment of NETs with ^{90}Y-labeled SSA
   Considering the limitation of ^{111}In-labeled SSA, ^{90}Y was naturally considered as a better candidate radioisotope for PRRT due to its high energy and wide-range β-particle emitter. ^{90}Y-DOTATOC and ^{90}Y-DOTATATE were explored in clinical trials followed by ^{111}In-DTPA-octreotide. Valkema R. et al. [39] conducted a clinic experiment in 58 NET patients with ^{90}Y-DOTATOC, and after treatment, 5 were partial remission (PR), 7 minor response (MR), 29 stable disease (SD), and 17 progressive disease (PD). Overall, more than half of the patients showed improvements in their disease status. The median overall survival (OS) was 36.7 months, and the median progression-free survival was 29.3 months. Patients with NETs who had received the ^{90}Y-DOTATOC treatment showed a significantly better OS than patients with ^{111}In-DTPA-octreotide treatment. Forrer et al. also treated 116 metastatic NET patients with ^{90}Y-DOTATOC, and the response rate was found in 31 patients (26%), including 4% complete remission (CR) and 22% partial response (PR). Seventy-two patients (62%) showed stabilization of their diseases and the remaining patients (11%) were still progressive. No serious side effects occurred and the toxicity was well tolerated. Other reported articles assessing the therapeutic effects of ^{90}Y-DOTATOC showed similar results with tumor response approximately 20–28% in patients with NETs. All these results indicated that ^{90}Y-DOTATOC is a useful radiopharmaceutical in treating of inoperable and/or metastatic NETs.

   Except ^{90}Y-DOTATOC, ^{90}Y-DOTATATE and other ^{90}Y-labeled SSA have also been broadly studied, ^{90}Y-DOTATATE has been used for treatment in 75 NETs, 28 out of 75 (37%) had PR, and 39 (52%) had SD. ^{90}Y-DOTA-lanreotide was used to treat 39 NETs, as a result 8 out of 39 (20%) patients had MR, 17 (44%) had

Table 12.6 Treatment of NETs with ^{90}Y-labeled SSA

^{90}Y-labeled SSA	Patient number	Treatment response					
		CR	PR	MR	SD	PD	CR + PR
^{90}Y-DOTATOC	180	4 (2%)	37 (21%)	7 (4%)	106 (59%)	26 (14%)	41 (23%)
^{90}Y-DOTA Lanreotide	39	0 (0%)	0 (0%)	8 (20%)	17 (44%)	14 (36%)	0 (0%)
^{90}Y-DOTATATE	75	0 (0%)	28 (37%)	0 (0%)	39 (52%)	8 (11%)	28 (37%)

CR complete response; *PR* partial response; *MR* minor response; *SD* stable disease; *PD* progressive disease

Table 12.7 Treatment of NETs with ^{177}Lu-DOTA,Tyr3-octreotate

Researcher	Years	Patient number	Treatment response				
			CR	PR	MR	SD	PD
Kwekkeboom et al.	2005	131	3 (2%)	32 (26%)	24 (19%)	44 (35%)	22 (18%)
Kwekkeboom et al.	2008	310	5 (2%)	86 (26%)	51 (16%)	107 (35%)	61 (20%)
Ezziddin S et al.	2014	74	0 (0%)	27 (36.5%)	13 (17.6%)	26 (35.1)	8 (10.8%)

SD. Table 12.6 listed several studies that use various ^{90}Y-labeled SSA; all these radiotracers are promising in NET treatment.

3. Treatment of NETs with ^{177}Lu-labeled SSA

   ^{177}Lu is a β-emitter with median energy (0.5 MeV) and small tissue penetrating depth (2 mm). The short tissue penetration may result in a less efficacy in treating a larger size lesion; however it allows for higher radiation dose delivered to smaller tumors and less damage to surrounding tissues than the radionuclide ^{90}Y. ^{90}Y and ^{177}Lu are most commonly used radioisotope to label SSA for PRRT; ^{177}Lu-DOTATATE has been wildly investigated for PRRT [40]. Kwekkeboom group conducted several clinical studies. One of their studies treated 310 NETs with 27.8–29.6 GBq of ^{177}Lu-DOTATATE over 4 cycles performed 6 to 10 weeks apart. CR was observed in 2% of patients, with PR shown in 26% of patients and MR shown in 16% of patients. The average time to progression was 40 months and median OS was 128 months. More recently a study retrospectively analyzed a consecutive cohort of 74 NETs underwent ^{177}Lu-DOTATATE treatment with 7.9 GBq per cycle, and the result for PR was 36.5%, MR was 17.6%, SD was 35.1%, and 10.8% for PD. NETs respond differently; for pancreatic NETs 54.5% were PR, 18.2% MR, 18.2% SD, and 9.1% PD and for nonpancreatic NETS 22.0% were PR, 17.1% MR, 48.8% SD, and 12.2% PD. The median PFS and OS were 26 months and 55 months, respectively (Table 12.7).

   ^{177}Lu also emits γ-rays; therefore ^{177}Lu-labeled SSA can be also used for dosimetry calculation and monitoring of tumor response. In this point, ^{177}Lu-labeled SSA is really a good candidate for theranostic and pretty much close to the precision medicine by personalized patient preparation prior to and after PRRT.

   The characteristic of ^{90}Y and ^{177}Lu are different, especially the energy of β particle produced by these two radioisotope, the higher energy of ^{90}Y can penetrate longer in tissues, while the median energy of ^{177}Lu can only pass through less tissues. This suggested that ^{90}Y-labeled SSA will be more effective for larger tumor and ^{177}Lu-labeled SSA for smaller tumor and metastases. Since most solid malignant tumors are heterogeneous, therefore the combination treatment of ^{90}Y- and ^{177}Lu-labeled SSA seems a reasonable option for managing tumors of varying sizes and SSTR subtypes [41, 42]. One study reported that 310 NETs with 27.8–29.6 GBq of ^{177}Lu-DOTATATE over four cycles performed 6 to10 weeks apart. CR was observed in 2% of patients, with PR was shown in 26% of patients, and MR shown in 16% of patients. The average time to progression was 40 months and median OS was 128 months. More recently a study retrospectively analyzed a consecutive cohort of 74 NETs underwent ^{177}Lu-DOTATATE treatment with 7.9 GBq per cycle, and the result for PR was 36.5%, MR was 17.6%, SD was 35.1% and 10.8% for PD. Each differently NETs response differently, for pancreatic NETs 54.5% were PR, 18.2% MR, 18.2% SD, and 9.1% PD; and 22.0% PR, for nonpancreatic NETS 17.1% were MR, 48.8% SD, and 12.2% PD. The median PFS and OS were 26 months and 55 months, respectively.

4. Treatment of NETs with ^{213}Bi-Labeled SSA

   Although PRRT with ^{90}Y- and ^{177}Lu-labeled SSA has been promising for NET treatment, there are still amount of tumors that are not sensitive to this treatment. On the contrary, α-ray is a high LET that leads to a complete or non-repairable DNA damage; SSA labeled with α-emitting isotopes may provide an alternative therapy for NETs resistant to PRRT with β-emitting radionuclides. The application of α-emitters such as ^{213}Bi or its mother radionuclide ^{225}Ac is arousing great interest in PRRT. Several preclinical studies have shown the potency of targeted α-therapy in NETs. In a pilot study in three patients, no short-term adverse side effects on the kidney or bone marrow were found after ^{213}Bi-DOTATOC.

Table 12.8 NET responses to different radiolabeled SSA

Radiotracer	Patient number	Treatment response			
		CR	PR	SD	PD
^{111}In-DTPA-octreotide	26	0 (0%)	2 (8%)	44 (35%)	22 (18%)
^{90}Y-DOTATOC	116	5 (4%)	26 (22%)	72 (62%)	13 (11%)
^{177}Lu-DOTATATE	310	5 (2%)	86 (28%)	158 (51%)	61 (20%)
^{90}Y-DOTATATE and ^{177}Lu-DOTATATE	26	2 (7.7%)	9 (34.6%)	11 (42.3%)	4 (15.4%)
^{213}Bi-DOTATOC	7	1 (14%)	2 (28%)	3 (44%)	NA

NA not available

Because of different physical characteristics of each radioisotope, the efficacy of treatment is also different, and Table 12.8 showed NET response with different radiotracers. In clinic to get the best treatment result, the right radiotracer and its dosage should be chosen according to the type of SSTRs; the size of the lesion and the tolerance of the patient should also be carefully concerned.

12.3 Conclusion

Based on the specific and high binding to the SSTRs which is abnormally expressed in NETs, SSA specific binding to the SSTRs has been successfully labeled with various radionuclides and applied to tumor imaging and treatment. The new radiotracer for SPECT or PET has significantly improved the accuracy in diagnosing the NETs. And the PRRT has been broadly used for treatment of NETs in clinic and become an irreplaceable method in treating NETs after the chemotherapy, surgery, and radiotherapy. The coming of the SRI and PRRT opens a new way for NETs, and we can anticipate that with the more ideal radiotracer coming out, the theranostic to the NETs will be further greatly improved.

References

1. Bailey LB, Gregory JF (1999) Folate metabolism and requirements. J Nutr 129(4):779–782
2. Lucock M (2000) Folic acid: nutritional biochemistry, molecular biology, and role in disease processes. Mol Genet Metab 71(1–2):121–138
3. Sudimack J, Lee RJ (2002) Targeted drug delivery via the folate receptor. Adv Drug Deliv Rev 41(2):147–162
4. Ke CY, Mathias CJ, Green MA (2004) Folate-receptor-targeted radionuclide imaging agents. Adv Drug Deliv Rev 56(8):1143–1160
5. Müller C (2013) Folate-based radiotracers for PET imaging--update and perspectives. Molecules 18(5):5005–5031
6. Müller C, Schibli R (2011) Folic acid conjugates for nuclear imaging of folate receptor-positive cancer. J Nucl Med 52(1):1–4
7. Mathias CJ, Lewis MR, Reichert DE et al (2003) Preparation of ^{66}Ga- and ^{68}Ga-labeled Ga(III)-deferoxamine-folate as potential folate-receptor-targeted PET radiopharmaceuticals. Nucl Med Biol 30(7):725–731
8. Wang S, Luo J, Lantrip DA et al (1997) Design and synthesis of [^{111}In]DTPA-folate for use as a tumor-targeted radiopharmaceutical. Bioconjug Chem 8(5):673–679
9. Mathias CJ, Hubers D, And PSL et al (2000) Synthesis of [^{99m}Tc]DTPA-Folate and its evaluation as a Folate-receptor-targeted radiopharmaceutical. Bioconjug Chem 11(2):253–257
10. Trump DP, Mathias CJ, Yang Z et al (2002) Synthesis and evaluation of ^{99m}Tc(CO)$_3$-DTPA-folate as a folate-receptor-targeted radiopharmaceutical. Nucl Med Biol 29(5):569–573
11. Leamon CP, Parker MA, Vlahov IR et al (2002) Synthesis and biological evaluation of EC20: a new folate-derived, ^{99m}Tc-based radiopharmaceutical. Bioconjug Chem 13(6):1200–1210
12. Guo W, Hinkle GH, Lee RJ (1999) ^{99m}Tc-HYNIC-folate: a novel receptor-based targeted radiopharmaceutical for tumor imaging. J Nucl Med 40(9):1563–1569
13. Guo Z, Gao M, Song M et al (2016) Synthesis and evaluation of ^{99m}Tc-Labeled Dimeric folic acid for FR-targeting. Molecules 21(6):817
14. Fani M, Wang X, Nicolas G et al (2011) Development of new folate-based PET radiotracers: preclinical evaluation of ^{68}Ga-DOTA-folate conjugates. Eur J Nucl Med Mol Imaging 38(1):108–119
15. Müller C, Vlahov IR, Santhapuram HK et al (2011) Tumor targeting using ^{67}Ga-DOTA-Bz-folate--investigations of methods to improve the tissue distribution of radiofolates. Nucl Med Biol 38(5):715–723
16. Müller C, Zhernosekov K, Köster U et al (2012) A unique matched quadruplet of terbium radioisotopes for PET and SPECT and for α- and β- radionuclide therapy: an in vivo proof-of-concept study with a new receptor-targeted folate derivative. J Nucl Med 53(12):1951–1959
17. Fani M, Tamma ML, Nicolas GP et al (2012) In vivo imaging of Folate receptor positive tumor Xenografts using novel ^{68}Ga-NODAGA-Folate conjugates. Mol Pharm 9(5):1136–1145
18. Chen Q, Meng X, Mcquade P et al (2017) Folate-PEG-NOTA-Al^{18}F, a new folate based radiotracer for PET imaging of folate receptor-positive tumors. Mol Pharm 14:4353–4361
19. Chen Q, Meng X, Mcquade P et al (2016) Synthesis and preclinical evaluation of Folate-NOTA-Al^{18}F for PET imaging of Folate-receptor-positive Tumors. Mol Pharm 13(5):1520–1527
20. Bettio A, Honer M, Müller C et al (2006) Synthesis and preclinical evaluation of a folic acid derivative labeled with ^{18}F for PET imaging of folate receptor-positive tumors. J Nucl Med 47(7):1153–1160
21. Al Jammaz I, Al-Otaibi B, Okarvi S et al (2010) Novel synthesis of [^{18}F]-fluorobenzene and pyridinecarbohydrazide-folates as potential PET radiopharmaceuticals. J Label Compd Radiopharm 49(2):125–137
22. Al Jammaz I, Al-Otaibi B, Okarvi S (2011) Rapid synthesis and in vitro and in vivo evaluation of folic acid derivatives labeled with fluorine-18 for PET imaging of folate receptor-positive tumors. Nucl Med Bio 38(7):1019–1028
23. Al Jammaz I, Al-Otaibi B, Amer S et al (2012) Novel synthesis and preclinical evaluation of folic acid derivatives labeled with [^{18}F]FDG for PET imaging of folate receptor-positive tumors. Nucl Med Biol 39(6):864–870
24. Fischer CR, Müller C, Reber J et al (2012) [^{18}F]fluoro-deoxy-glucose folate: a novel PET radiotracer with improved in vivo properties for folate receptor targeting. Bioconjug Chem 23(4):805–813
25. Ross TL, Honer M, Lam PYH et al (2008) Fluorine-18 click Radiosynthesis and preclinical evaluation of a new ^{18}F-Labeled folic acid derivative. Bioconjug Chem 19(12):2462–2470
26. Aljammaz I, Al-Otaibi B, Al-Rumayan F et al (2014) Development and preclinical evaluation of new ^{124}I-folate conjugates for PET

imaging of folate receptor-positive tumors. Nucl Med Biol 41(6):457–463
27. Ross TL, Honer M, Müller C et al (2010) A new ^{18}F-labeled folic acid derivative with improved properties for the PET imaging of folate receptor-positive tumors. J Nucl Med 51(51):1756–1762
28. Betzel T, Müller C, Groehn V et al (2013) Radiosynthesis and preclinical evaluation of 3′-Aza-2′-[^{18}F]fluorofolic acid: a novel PET radiotracer for Folate receptor targeting. Bioconjug Chem 24(2):205–214
29. Koch BD, Schonbrunn A (1984) The somatostatin receptor is directly coupled to adenylate cyclase in GH4C1 pituitary cell membranes. Endocrinology 114(5):1784–1790
30. Vanetti M et al (1992) Cloning and expression of a novel mouse somatostatin receptor (SSTR2B). FEBS Lett 311(3):290–294
31. Patel YC (1999) Somatostatin and its receptor family. Front Neuroendocrinol 20:157–198
32. Pawlikowski M (2007) Somatostatin analogs in diagnostics and therapy. Landes Bioscience, Austin
33. Lamberts SWJ, Krenning EP, Reubi JC (1991) The role of somatostatin and its analogs in the diagnosis and treatment of tumors. Endocr Rev 12:450–482
34. Balon HR, Brown TL, Goldsmith SJ et al (2011) The SNM practice guideline for somatostatin receptor scintigraphy 2.0. J Nucl Med Technol 39(4):317–324
35. Krenning EP, Bakker WH, Kooij PPM et al (1992) Somatostatin receptor scintigraphy with Indium-111-DTPA-D-Phe-1-Oman: metabolism, dosimetry and comparison with iodine-123-Tyr-3-octreotide. J Nucl Med 33(5):652–658
36. Buchmann I, Henze M, Engelbrecht S et al (2007) Comparison of 68 Ga-DOTATOC PET and 111In-DTPAOC (Octreoscan) SPECT in patients with neuroendocrine tumours. Eur J Nucl Med Mol Imaging 34(10):1617–1626
37. Wild D, Bomanji JB, Benkert P et al (2013) Comparison of 68Ga-DOTANOC and 68Ga-DOTATATE PET/CT within patients with gastroenteropancreatic neuroendocrine tumors. J Nucl Med 54(3):364–372
38. Ambrosini V, Campana D, Tomassetti P, Fanti S (2012) 68 Ga-labelled peptides for diagnosis of gastroenteropancreatic NET. Eur J Nucl Med Mol Imaging 39:s52–s60
39. Valkema R, Pauwels S, Kvols LK et al (2006) Survival and response after peptide receptor radionuclide therapy with [90Y-DOTA0, Tyr3]octreotide in patients with advanced gastroenteropancreatic neuroendocrine tumors. Semin Nucl Med 36(2):147–156
40. Ezziddin S, Attassi M, Yong-Hing CJ et al (2014) Predictors of long-term outcome in patients with well-differentiated gastroenteropancreatic neuroendocrine tumors after peptide receptor radionuclide therapy with 177Lu-octreotate. J Nucl Med 55(2):183–190
41. de Jong M, Breeman WA, Valkema R, Bernard BF, Krenning EP (2005) Combination radionuclide therapy using 177 Lu and 90 Y-labeled somatostatin analogs. J Nucl Med 46:13S–17S
42. Romer A, Seiler D, Marincek N et al (2014) Somatostatin-based radiopeptide therapy with [177 Lu-DOTA]-TOC versus [90 Y-DOTA]-TOC in neuroendocrine tumours. Eur J Nucl Med Mol Imaging 41(2):214–222

Radioimmunoimaging and Targeted Therapy

13

Yafu Yin and Steven Rowe

More than 20 years ago, Dr. Zhu from China said, "As the world-renowned achievements of radioimmunoassay for trace substance detection are attributed to the multidisciplinary effect of nuclear medicine and immunology, likewise, success of radioimmunoimaging (RII) and radioimmunotherapy (RIT) are dependent on the interaction of these two disciplines, which opens up a new way for the diagnosis and treatment of cancer." RII and RIT, together termed radioimmunotheranostics, are characterized by radioisotope-labeled antibody or fragments which can recognize some specific antigen; the ultimate goal of which is to diagnose or treat cancer or other diseases. Radioimmunotheranostics has a 70-year history of development, and numerous scholars who came from diverse fields including medicine, immunology, bioengineering, etc. dedicated in this field made unremittent efforts for human health. With the rapid development of medical and bioengineering technology, novel theranostic probes, which can recognize a specific antigen on the cancer cell or are associated with the tumor microenvironment, are not limited to antibodies but include some small-molecule ligands. In this chapter, we would also give some introduction of radionuclide-labeled non-antibody imaging and therapy, while the major focus will be on traditional RII and RIT.

13.1 Basic Physiology, Biochemistry, and Pathophysiology of Immunology

Immunology is a discipline that studies the immune system, immune response to microbial pathogens and damaged tissues, and the roles of immune system in disease. As we know, immunity refers to the body's resistance to disease, especially infectious disease, which is mediated by the collection of cells, tissues, and molecules called immune system, and the coordinated reaction of these cells and molecules to the infectious microbes is termed as immune response.

The most important physiologic function of the immune system is to prevent or eradicate infections. The immune system does not only provide protection against infections but also prevent the growth of some tumors, and some cancers can be treated by stimulating immune responses against tumor cells. Immune responses also participate in the clearance of dead cells and initiating tissue repair. In addition, the immune system can injure cells and induce pathologic inflammation and recognizes and responds to tissue grafts and newly introduced proteins.

Immunity includes innate immunity, which provides immediate protection against microbial invasion and adaptive immunity, which develops more slowly and provides more specialized defense against infections. The adaptive immune system consists of lymphocytes and their products, such as **antibodies**. The substance that is specifically recognized by lymphocytes or antibodies is named **antigen**. Antigens are "targeted" by antibodies. The antibody's paratope is specific for one specific epitope on an antigen, which results in antibody and antigen binding together with precision. An antigen usually contains different epitopes along its surface arranged discontinuously, and dominant epitopes on a given antigen are called determinants. On the basis of binding mechanism, an antibody can recognize a microbe or an infected cell for attack by other parts of the immune system or can neutralize its target directly.

The properties of adaptive immune responses are crucial for the effectiveness of responses in fighting against infections, which include **specificity**, **diversity**, **memory**, **clonal expansion**, **specialization**, **contraction and homeostasis**, and **nonreactivity to self**.

Y. Yin (✉)
Department of Nuclear Medicine, Xinhua Hospital, Shanghai Jiao Tong University School of Medicine, Shanghai, P. R. China

S. Rowe
The Russell H. Morgan Department of Radiology and Radiological Science, Johns Hopkins University School of Medicine, Baltimore, MD, USA

G. Huang (ed.), *Nuclear Medicine in Oncology*, https://doi.org/10.1007/978-981-13-7458-6_13

13.2 Immune Responses in Tumorigenesis and Development

Tumor immunology is the study of the complex interaction between a human host and a neoplasm, which causes the death of the host unless adequately treated. The immune system plays a critical role in surveillance and prevention of malignancy. There are many complex mechanisms in this field, which are not understood well until now.

The modern era of tumor immunology was created in the 1950s; at that time the role of T-cell responses in tissue allograft rejection was firstly recognized. Since that time, tumors occurrence was confirmed in association with impaired function of T cells, which indicated the importance of the immune system in the development and progression of cancer [1]. The use of the immune system to treat cancer was based on the identification of tumor-associated antigens, the role of regulatory and suppressor T-cell populations, and the knowledge of effector T-cell responses.

The immune system has three primary roles in preventing tumors. One is that, as we know, the immune system can eliminate or suppress viral infections, so it can protect the host from virus-induced tumors. Furtherly, the immune system can impede the establishment of inflammatory environment which is conducive to tumorigenesis by timely eliminating the pathogens and inflammation. The third is that in the light of their expression of tumor-specific antigens or molecules induced by cellular stress, which is referred to as tumor immune surveillance, the immune system can specifically identify and eliminate tumor cells.

13.2.1 Immune Surveillance

As we know, one of the physiologic functions of the adaptive immune system is to prevent the outcome of transformed cells and eliminate these cells before they become malignant tumors. The role of the immune system that controls and eliminates the malignant cells is called **immune surveillance**. Now it is realized that once the tumor exists, the immune response to it is often dominated by tolerance or regulation, not by effective immunity. The field of tumor immunology has focused on defining the kinds of tumor antigens, against which the immune system reacts and the nature of the immune responses, and developing strategies for maximally enhancing antitumor immunity.

13.2.2 Tumor Antigens

Malignant tumors express various types of molecules that may be recognized by the immune system as foreign antigens. If the immune system is able to react against a tumor in the individual, the tumor must express antigens that are recognized as non-self by the individual's immune system. The common tumor antigens are usually classified into a couple of groups: products of diverse mutated genes, products of oncogenes or mutated tumor suppressor genes, aberrantly expressed proteins, and viral antigens.

13.3 Radioimmunoimaging

RII refers to the use of radiolabeled antibodies and/or fragments for the in vivo detection of cancer and other disease, such as myocardial infarction and infections. The development of RII is a history of the discovery and synthesis of labeled antibodies, which is the key factor of RIT.

At the beginning of the twentieth century, Ehrlich suggested that a "magic bullet" might seek out and eradicate the spirochete of syphilis without affecting normal tissues. This type of disease targeting has been a goal of medicine throughout its history. One of the earliest applications of radionuclide-labeled antibodies for the purpose of detecting neoplasms was reported by Pressman and Keighley in 1948 [2]. They found that antibodies developed in rabbits to rat kidney could be successfully labeled with ^{131}I without changing affinity and would localize in the rat kidney in vivo. The importance of this early development can be appreciated in terms of specificity. During the 1950s, methods with greater specificity for tumors were further developed that used radiolabeled antibodies to tumor-associated antigens or products.

Labeled antibodies for the diagnosis of cancer were pioneered by Pressman and Keighley in 1948; 12 years later, Bale and Spar investigated radiation therapy of tumors with ^{131}I-labeled antibodies to fibrin which happened nearly 60 years ago. The potential clinical utilities of these approaches have been demonstrated in the following two decades, but their success has been limited by inadequate specificity of labeled antibodies, in part because of their polyclonal source.

13.3.1 Development of Radioisotope-Labeled Antibodies

The hybridoma technology was firstly introduced by Kohler and Milstein in 1975, which made it possible that a defined specificity of monoclonal antibodies (mAbs) could be produced in unlimited quantities to practically bind to any antigen and were more easily standardized. However, mAbs face several difficulties, for example, human anti-mouse antibody (HAMA), which is due to the murine origin when administrated to human, limits their clinical applications, in addition to mAbs-producing technology which is very laborious and time-consuming. Moreover, as the development of

the sensitive assay, the need of the high-affinity antibody to particular antigen could not be satisfied by small mammals like mice.

As times are evolving and new technologies are constantly emerging, the recombinant DNA technology and antibody engineering make it come true that antibody genes can be cloned and expressed successfully as a fragment in bacteria, mammalian cells, yeasts, plants, and also insect cells. One advantage of this new technology is that they could retain the intact antigen-binding site (paratope) while reducing the size of the antibody molecule. Moreover, it enabled the expression of the functional antibody and their fusion in bacteria and displayed on a filamentous phage. Additionally, the combination of small antibody molecule and the efficient microbial production systems enabled the production of sufficient homogenous protein for diagnostic and therapeutic aims including structural studies.

With the development of the updated technology, a huge variety of genetically engineered antibodies have been produced and were reviewed by many researchers, which include antigen-binding (Fab) fragments [3], Fv (variable domain) fragments, or scFv antibodies. And the minimized antibody molecule, as a building block for the construction of new recombinant proteins for different purposes, was provided, such as bivalent antibodies, multivalent antibodies, domain antibodies, affibodies, nanobodies, and anticalins. Nanobodies, which are single-domain antigen-binding fragments, were produced by bioengineering technique and applied in molecular imaging. Due to the superior features, such as fast blood clearance, rapid targeting, high stability, high solubility, and the capability of binding to cavities and difficult-to-access antigens, nanobodies with smaller size (~15 kDa) and suitable configuration of the complementarity determining regions (CDRs) are suitable for imaging applications. Some imaging techniques, using nanobody-based probes, for instance, radionuclide-based, optical, and ultrasound, have been implied for visualization of target expression in various disease models [4]. But these promising imaging agents still have a long way to translate to the clinic.

RII and RIT rely on the coordination of information and efforts shared by a broad variety of scientific disciplines, including immunology, biochemistry, bioengineering, radiochemistry, oncology, radiotherapy, and nuclear medicine.

13.3.2 Molecular Probes and Clinical Application of RII

Since Dr. Goldenberg performed the first RII with radiolabeled antibody to CEA in hamster and human in 1974 and 1978 [5, 6], the researchers in the world did unremitting studies for the "magic bullet" targeted imaging and treatment, and it's still one of the hot topics in nuclear medicine research, although there are many problems to be solved for clinical application till today.

13.3.2.1 Application of CEA-Targeted RII

For the clinical application, it started in 1982, mAb against CEA was labeled by ^{131}I and used for detecting gastrointestinal and medullary thyroid cancers. By SPECT imaging 94% tumor sites (16/17) were identified, while only 43% tumor sites (9/21) were detected by rectilinear scintigraphy. It represents a very important first step for CEA-targeted RII in the clinic.

Since then, SPECT imaging with several antibodies against CEA was reported. For instance, ^{111}In-labeled ZCE-025 was researched in a number of studies for detecting primary, metastatic, or recurrent colorectal carcinomas. For primary lung cancer, an ^{111}In-labeled anti-CEA mAb (F023C5i) was performed for RII in 1991. Many ^{99m}Tc-labeled anti-CEA antibodies (e.g., BW431/26, IMMU-4, and 88BV59) were applied in clinical research for RII in colorectal, breast, and lung cancer. In 1998, in a phase III clinical trial, a ^{99m}Tc-labeled fully humanized mAb 88BV59 was used to detect recurrent, metastatic, or occult colorectal cancer, which provided important and accurate information about the presence and location of malignant lesions that could not be identified by morphological CT imaging. It is concluded that RII with SPECT is a suitable method for cancer diagnosis, especially for recurrences.

In 1992, the US Food and Drug Administration (FDA) approved the first RII agent ^{111}In-B72.3 (also called OncoScint CR/OV, satumomab pendetide) for clinical application. B72.3 is a murine IgG mAb to CEA, which reacts with human colorectal, breast, lung, pancreatic, gastric, and ovarian tumors.

Four years later, another anti-CEA agent for RII, ^{99m}Tc-CEA-Scan, was also approved by the US FDA for colorectal cancer imaging. CEA-Scan (also called CEA-Fab', IMMU-4 Fab', arcitumomab) which is a murine anti-CEA Fab' fragment has the advantages in rapid tumor detection, and fast clearance from the blood and normal organs allowed the use of short-lived radionuclides, such as ^{123}I and ^{99m}Tc. RII with CEA-Scan has also been used to detect other CEA-positive cancers, for instance, breast cancer, medullary thyroid cancer, and lung cancer.

Also in 1996, the first high-affinity scFv directed against CEA, MFE-23 was selected by a bacteriophage library. MFE-23 labeled with ^{123}I was evaluated in normal and colorectal carcinoma patients. Compared to conventional imaging modalities, such as CT, it exhibited better diagnostic characteristics for detecting hepatic or abdominal metastases which were not found by any other modalities. RII with ^{123}I-MFE-23 was more sensitive than CT was due to the high tumor-to-blood ratios. Soon afterward, ^{125}I- MFE-23 was used for image-guided surgery. The overall diagnostic

accuracy was 84% when compared with histology which showed ^{125}I- MFE-23 with good properties of tumor localization. Due to short time interval between operation and injection, no significant toxicity and easily produced technique in bacteria, MFE-23, was highly responsible for image-guided surgery. A study of dosimetry estimation using ^{125}I-scFv-Fc indicated that ^{131}I-H310A/H435Q could be a promising candidate for RIT. Definitely, for tumor targeting and imaging, bivalent antibody fragments are superior to the monovalent analogs (e.g., Fab' and scFv) in several aspects. In addition, a number of other forms of antibody fragments have also been tested for CEA-targeted RII.

In addition to SPECT imaging agents, a variety of isotopes for PET imaging have been selected to label mAbs for RII-PET. For example, ^{124}I-labeled mAb against CEA with a physical half-life of 4.2 days was adopted for PET imaging performed on mice xenografted with CEA-positive tumors. The studies suggested that RII-PET could provide more accurate radiation dosimetry estimation for RIT, in addition to potentially more precise diagnosis. Other positron emitting isotopes such as ^{76}Br ($t_{1/2}$: 16.0 h) and ^{64}Cu ($t_{1/2}$: 12.7 h) were also used to label anti-CEA antibodies.

13.3.2.2 Non-anti-CEA RII

In addition to the anti-CEA RII agents, there are many other mAbs targeting different tumor antigens. For example, one of two mAbs approved by the US FDA at the end of the twentieth century, is ^{99m}Tc-NR-LU-10-Fab, also called nofetumomab or Verluma, which is a Fab fragment of the pancarcinoma antibody NR-LU-10 labeled with ^{99m}Tc. NR-LU-10 is a murine IgG2b immunoglobulin directed against a 40 kD carcinoma-associated glycoprotein antigen. The NR-LU-10 antibody reacts in vitro with cancers derived from the breast, colon, ovary, prostate, pancreas, and kidney. ^{99m}Tc-NR-LU-10-Fab was approved by the US FDA for small-cell lung cancer in 1996.

The other one is ^{111}In-CYT-356 (capromab pendetide, ProstaScintst, Cytogen Corporation, Princeton, NJ), a murine mAb 7E11-C5.3 conjugate directed to a glycoprotein found primarily on the cell membrane of prostate tissue, which was approved by the US FDA for localizing recurrent prostate cancer (PCa) in 1999.

Among others, well-studied targets are epidermal growth factor receptor (EGFR), human epidermal growth factor receptor 2 (HER2), folate receptor (FR), PD-L1, CD20, and prostate-specific membrane antigen (PSMA) in recent decade.

1. Epidermal Growth Factor Receptor
   EGFR is overexpressed in different tumors, including lung, breast, colon, head and neck, pancreatic, and brain, favoring tumor growth and progression. In 2009, a preclinical evaluation of ^{111}In-panitumumab (a mAb targeting the EGFR) showed the efficiency in tumor targeting and low normal tissue uptake that make ^{111}In-panitumumab effective targeting component for RII and RIT. However, inherent and acquired resistances are serious problems and are responsible for limited clinical efficacy and tumor recurrence. Recently, some anti-EGFR mAb therapy and imaging based on RIT in mice give us promising results. The predictive value of ^{89}Zr-labeled cetuximab in advanced head and neck cancer patients was performed in an ongoing phase II study (ARTFORCE). A RII-PET imaging based on RIT in head and neck squamous cell carcinoma (HNSCC) model, which was reported in 2017, showed that theranostic radiopharmaceutical, ^{64}Cu-/^{177}Lu-PCTA-cetuximab had the potential of targeted RII-PET imaging and targeted therapy by RIT in EGFR expressing cetuximab-resistant HNSCC [7].
2. HER2
   HER2, also called Neu, ErbB-2, CD340, or p185, which is a protein that in humans is encoded by the ERBB2 genes, is a member of the human EGFR family. Trastuzumab, a humanized IgG1 mAb targeting HER2, has exhibited significant activity in HER2-positive breast cancer patients. Several researches have evaluated the application of trastuzumab labeled with ^{111}In, ^{64}Cu, or ^{89}Zr for detecting HER2 expression in vivo in primary and metastatic breast cancer. Preliminary clinical studies have indicated the activity of ^{111}In-pertuzumab in liver metastases in patients with HER2-positive breast cancer [8].
3. CD20
   CD20 is a kind of surface antigen which is expressed on B-cell hematological malignancies. Rituximab is a chimeric mAb targeted against CD20, which has shown high activity in non-Hodgkin's lymphoma (NHL). In despite of the high response rate to rituximab, a number of patients experienced primary or acquired resistance in some way. Based on the remarkable radiosensitivity of NHL, two kinds of radiolabeled murine mAbs against CD20 were developed for RIT, ^{90}Y-ibritumomab tiuxetan (Zevalin) and ^{131}I-tositumomab (Bexxar), which would be introduced in next section of RIT. Anti-CD20 mAbs RIT of NHL is representative of the "radiotheranostic" approach, for tumors detected by ^{111}In-mAbs and patients selecting for RIT on the basis of imaging results, which expose the extent of not only tumor uptake but also normal organ. This approach was tested early in the introduction of ^{90}Y-Zevalin, although the imaging was no longer routinely performed, for the safety and dosing of this agent has now been well-established.
4. PD-L1
   Programmed cell death protein 1 (PD-1) is expressed on the cell membrane of T cells, and the interaction with its ligand PD-L1 (programmed cell death-ligand 1) acti-

vates inhibitory pathways and downregulates the immune system favoring cancer growth and progression. PD-L1 is overexpressed in several tumors, and anti-PD-1 or anti-PD-L1 mAbs have exhibited promising activity. ^{111}In-PD-L1-mAb and ^{111}In-NIR-PD-L1-mAb could evaluate different levels of PD-L1 expression in tumor xenografts which indicated the potential of in vivo PD-L1 assessment [9].

5. FR

   FR is expressed in different types of epithelial tumors, such as ovarian, non-small cell lung, endometrial, and breast cancer. Its expression is possibly related to chemotherapy resistance. Farletuzumab (MORAb-003) is a fully humanized FRα-binding mAb, and MOv18 IgE is a novel mouse/human chimeric IgE mAb engineered against FRα; both of them are used for immunotherapy, but no radionuclide-labeled mAb was reported [10].
6. PSMA will be stated in the last section in detail.

13.4 Targeted Radioimmunotherapy

RIT refers to the use of appropriately radiolabeled antibodies for therapeutic purposes, especially in the treatment of cancer. RIT is a molecular targeted radionuclide therapy in which low-dose irradiation from radionuclides is delivered to tumor cells by antibodies binding to tumor antigens. Both radiobiological and immunological processes were involved in the cytotoxic mechanisms.

The radiolabeled antibodies are formulated in sterile and pyrogen-free form and can be intravenously injected, or injected directly into the tumor, or compartmentally into a body cavity such as the peritoneum, pleura, or intrathecal space. After being injected, they can be distributed by blood flow, diffusion, or convection to its natural target: an antigen-binding site on tumor cells. The cells were irradiated for high amounts of energy in forms of photons or charged particles, promoting the direct macromolecular damage and the production of reactive oxygen and/or nitrogen species. As we know, free radicals and molecular oxygen both damage DNA strand, which results in apoptosis and programmed necrosis. Due to the ranges of ionizing radiations in tissue being much larger than a typical cell size, uniform binding of the radioimmunoconjugates is not a prerequisite for its efficacy. That means, the adjacent cells without tumor antigens expression also can be killed by the physical cross-fire effect, which is the reason why continuous low-dose irradiation can cause fatal effects on nearby normal cells. The relative radiosensitivity or radioresistance is an intrinsic property of the tumor cells and correlates best with the cell of origin. Furthermore, hypoxia and the ability to rapidly repair radiation-induced damage are additional factors increasing radiation resistance.

13.4.1 Radiopharmaceuticals of RIT

Selection of the optimal cell surface antigen and targeting antibody are critical to the success of a therapeutic program. An ideal antigen for RIT is expressed at a high, uniform density on the surface of all tumor cells, not expressed on normal cells, or in the bloodstream.

It's well known that the first systemic radiotherapy was using radioisotope, ^{131}I, which was performed by Hertz to a patient with Graves' disease for clinical application in 1941. After that, the researches about using favorable radioisotope-labeled antibodies emerged in the early 1950s. Direct radioiodine labeling antibodies was the main technology in the original clinical studies, as well as chelation chemistry which made a number of metal radioisotopes with inherent radiation properties available. And in vivo label of tumor-binding mAbs by conjugation-pretargeting method was developed in addition to the direct label of mAbs.

For RIT, α- or β-particle emitters are preferable, while Auger electrons emitters are also available, although they need to be localized close to DNA due to the very short range of these radiations. If the radioisotopes can emit γ rays simultaneously, they are suitable for imaging because γ rays can be well used for measuring pharmacokinetic parameters and calculating dosimetry of the radioimmunoconjugates. The radioisotopes commonly used for RIT are listed in Table 13.1. ^{131}I, yttrium-90 (^{90}Y), and lutetium-177 (^{177}Lu), all β-particle emitters, are mostly employed and well-studied practical radioisotopes. Both radiophysical properties (energy and half-life) and the labeling chemistry are the basis of selecting radioisotope for RIT. ^{90}Y is often preferred for higher β-particle *E*max and a shorter half-life compared with ^{131}I, but ^{131}I can form a carbon-iodine bond directly with antibodies which is much better, in this way, than ^{90}Y for conjugating via chelating agent. ^{177}Lu possesses radiophysical properties similar to ^{131}I and radiolabeling chemistry similar to ^{90}Y. And ^{186}Re and ^{188}Re have desirable particulate emis-

Table 13.1 Radioisotopes for radioimmunotherapy

Radioisotope	Particles	$Energy_{max}$ (MeV)	Range	Half-life
^{67}Cu	$\beta-$	0.58	2.1 mm	2.6 days
^{90}Y	$\beta-$	2.28	12.0 mm	2.7 days
^{125}I	Auger electron		2 ~ 500 nm	60.5 days
^{131}I	$\beta-$, γ	0.61	2.0 mm	8.0 days
^{177}Lu	$\beta-$, γ	0.50	1.5 mm	6.7 days
^{186}Re	$\beta-$, EC	1.07	4.5 mm	3.7 days
^{188}Re	$\beta-$, γ	2.12	10.4 mm	16.9 h
^{211}At	$\alpha-$, γ	6.8	80 μm	7.2 h
^{213}Bi	$\alpha-$, $\beta-$, γ	8.3	84 μm	46 min
^{223}Ra	$\alpha-$, $\beta-$, γ	5.78	<100 μm	11.43 days
^{225}Ac	$\alpha-$, γ	6.0 ~ 8.0	60 ~ 90 μm	10.0 days

sion characteristics for RIT and are characterized by a very rich chemistry, which is suitable for different radiolabeling methods. A few α-particle emitters are considered suitable for in vivo applications of RIT, which include bismuth-213 (^{213}Bi), astatine-211 (^{211}At), actinium-225 (^{225}Ac), and radium-223 (^{223}Ra).

13.4.2 Clinical Application of RIT

1. Lymphoma
   It is well reported that the anticancer responses of RIT in lymphoma is better than other tumors. ^{90}Y-ibritumomab tiuxetan (Zevalin) and ^{131}I-tositumomab (Bexxar) are two US FDA-approved radiolabeled anti-CD20 murine antibodies that have been administered to patients with NHL. RIT with ^{90}Y-Zevalin and ^{131}I-Bexxar were shown to be effective in relapsed indolent B-cell lymphomas with a response rate of 50–80%, as well as in rituximab refractory patients. However, the production of ^{131}I-Bexxar has been discontinued, though ^{90}Y-Zevalin remains available. A clinical trial showed the results with 100% of the overall response rate (ORR) in 20 patients with diffuse large B-cell lymphoma who received ^{90}Y-Zevalin treatment after 6 cycles of CHOPand the complete response rate (CRR) increased from 75 to 95% after CHOP. ^{90}Y-Zevalin has also been shown to be more effective in another clinical trial with 143 NHL patients compared to rituximab. ^{90}Y-Zevalin group had significantly higher response rates, with an ORR of 80% vs. 56%, and a CRR of 34% vs. 20%.

   Several other radiolabeled antibodies have been investigated in hematological cancers. ^{131}I-rituximab (anti-CD20 mAb) and ^{90}Y-epratuzumab tetraxetan (anti-CD22 mAb) are in advanced clinical trials. Although ^{213}Bi-labeled anti-CD33 IgG was previously performed in myeloid leukemia, the short physical half-life of ^{213}Bi which is a shortcoming for conjugate preparation limited its application in clinical field.
2. Breast Cancer/Ovarian Cancer
   It's well known that overexpression of HER2 is commonly associated with breast and ovarian cancers. Trastuzumab labeled with radioisotopes such as ^{90}Y, ^{111}In, ^{177}Lu, ^{188}Re, ^{211}At, and ^{212}Pb has been applied for clinical study of breast and ovarian cancers. MUC-1, a mucin epitope, is expressed on the surface of breast cancer cells and ovarian cancers. In a clinical trial phase I, the murine ^{90}Y-DTPA-BrE-3 and autologous stem cell were used in patients with breast cancer; the rate of objective partial response to the therapy was 50%. For ovarian cancer, mixed results have been reported. A phase I/II clinical trial assessing intraperitoneal ^{90}Y-HMFG1 reported extended progression-free survival (PFS) in subjects, while a randomized multinational phase III trial with ^{90}Y-HMFG1 found that RIT did not extend survival or time to relapse in epithelial ovarian cancer patients who had attained complete clinical remission after cytoreductive surgery and chemotherapy. A phase I study evaluating intraperitoneal α-particle RIT with ^{211}At-MX35 F(ab′)$_2$ (anti-OC antibody) was performed in recurrent ovarian cancer patients, reporting no observed or estimated toxicity, suggesting this might be an avenue for clinical investigation.
3. Prostate Cancer
   As described in breast cancer, MUC-1 has also been shown to be expressed in androgen-independent PCa cells, indicating it is a good target for RIT. ^{90}Y-m170, a murine mAb, was examined in patients with metastatic, hormone-refractory PCa. Many patients who complain of pain reported a remarkable reduction in pain after therapy. A phase I study using ^{90}Y-2IT-BAD-m170 combined with low-dose paclitaxel was also performed by the same group of investigators. J591 is an IgG mAb against the extracellular domain of PSMA. A number of J591 constructs were labeled with ^{90}Y, ^{177}Lu, and ^{213}Bi, which have also been used in patients with PCa.
4. Colorectal Cancer
   CEA has been the most common target in colorectal cancer for RIT as for RII. In 1999, the preclinical evaluation and the initial results of a phase I clinical study in comparison to standard chemotherapy showed encouraging results with a single injection of ^{131}I-labeled humanized version of MN-14 (anti-CEA mAb) in 12 colorectal cancer patients with small-volume liver metastases. The subsequent phase II trial showed an objective response rate of 16% and an overall response rate of 58%, suggesting that RIT has potential as an adjuvant treatment for colorectal cancer. Further, another phase II trial reported that RIT using ^{131}I-labetuzumab (anti-CEA) after salvage resection of colorectal metastases in liver improved the overall survival, supporting the utility of RIT in an adjuvant setting.

   A phase I trial of ^{90}Y-cT84.66 (a chimeric IgG against the A3 epitope of CEA) RIT in patients with metastatic colorectal cancer was reported by Wong et al. in 2003, though the results showed only a minor effect on tumor regression. Additionally, several other murine anti-CEA RIT agents have demonstrated modest effects in clinical trial studies including ^{131}I-NP-4, ^{131}I-F6 F(ab′)$_2$, ^{131}I-A5B7, ^{131}I-COL-1, and ^{186}Re-NR-CO-02F(ab′)$_2$.

   Another popular target for RIT in colorectal cancer, TAG-72, has been adopted in several clinical trials. A phase I trial of 24 metastatic colon carcinoma patients treated with ^{131}I-CC49 (murine anti-TAG-72 antibody) found that 25% of patients exhibited stable disease or a minor response, but all patients developed HAMAs. A phase II trial conducted in 15 patients with colorectal

cancer receiving ^{131}I-CC49 yielded similar results, with minor responses reported in 20% of patients, with all but 1 patient developing HAMAs. Other clinical trials evaluating ^{177}Lu-CC49, ^{90}Y-CC49, and ^{131}I-chimeric B72.3 also reported a minor response to RIT.

Epithelial cellular adhesion molecule (Ep-CAM) and A33 are another two antigens highly expressed on colorectal cancer. Several studies about RIT with anti-Ep-CAM and anti-A33 antibodies labeled by radioisotopes were reported with faint effects.

Essentially, most results were disappointing; nevertheless some studies demonstrated promising potential for RIT in colorectal cancer.

The anti-TAG-72 mAb CC49 has also been evaluated in breast cancer and ovarian cancer, as well as the anti-CEA and anti-CA-125 mAbs. L6 is another antigen highly expressed in breast cancer as well as in ovarian, prostate, some lung, and vascular endothelial cancers. ^{131}I-chL6 RIT has been performed in clinical trials with promising results in breast cancer patients.

For RIT of tumor, two radiopharmaceuticals have been approved by the Chinese State Food and Drug Administration. One is ^{131}I-chTNT-1/B mAb (Cotara®), a genetically engineered chimeric mAb that specifically binds to DNA-bound histone H1, a universal intracellular antigen found in the necrotic core of solid tumors, which was approved for the treatment of advanced lung cancer in China. A phase II trial using ^{131}I-chTNT-1/B mAB for treatment of advanced lung cancer demonstrated that RIT with ^{131}I-chTNT-1/B mAB was well-tolerated and can be used systemically or locally to treat refractory tumors of the lung [11]. A phase I trial demonstrated ^{131}I-chTNT-1/B mAB was well-tolerated when administrated systemically for treatment of colorectal cancer.

The other one is ^{131} I-metuximab (Licartin), which is an ^{131}I-labeled murine mAb HAb18 F(ab')2 fragment against the HCC-associated antigen HAb18G/CD147. Both a phase I clinical trial in 28 patients who were randomly assigned to receive the injection in four different doses of Licartin by hepatic artery infusion and a multicenter phase II trial in 106 patients who received the injection (27.75 MBq/kg) per cycle demonstrated the ^{131}I-metuximab injection was safe and effective for HCC patients.

The developments of radiolabeled immunoconjugates and the use of innovative radionuclides, such as ^{177}Lu, ^{67}Cu, and ^{211}At, can improve efficacy for RIT of hematopathy and solid tumors, particularly at the stage of minimal disease. RIT may have the added potential of killing chemoresistant and radioresistant tumor stem cells [12].

Seventeen years ago, the former President of European Association of Nuclear Medicine (EANM), Prof. A. B. Delaloye, said that he firmly believed in the future of RIT, which he predicted would become standard therapy of patients with malignancies. RII and RIT, which together comprise the field of radioimmunotheranostics, will help transform the field of nuclear medicine if sufficient economic and scientific power is made available for their further evolution [13].

13.5 Clinical Application and Advances in PSMA-Targeted Imaging and Therapy

PSMA known as folate hydrolase I or glutamate carboxypeptidase II is a 750 amino acid type II transmembrane protein with a unique three-part structure composed of a major extracellular domain, a transmembrane portion, and an intracellular component that shows a significant overexpression (about 1000 times higher than normal prostate cells) in PCa cells (5–10% of prostate cancers without expression of PSMA glycoprotein) but a low expression in normal tissues. It was first identified on the human PCa cell line LNCaP [14]. Due to PSMA showing significantly high expression in PCa compared to benign prostatic tissue and low expression in nontarget tissues, it is considered an ideal target for both diagnostic and therapeutic applications. However, the exact function of PSMA on PCa cells is not yet clear; it has been known that PSMA undergoes constitutive receptor-mediated endocytosis via clathrin-coated pits. PSMA also plays a role in cell migration, survival, and proliferation. PSMA is not completely prostate specific, which is also expressed in other cells including the proximal small intestine, kidney, and salivary glands.

13.5.1 PSMA-Targeted Imaging Agents

Recently, a number of antibodies, as well as small molecules with high affinity to the extracellular domain of PSMA, have been developed. Among them, the urea-based small-molecule inhibitors of PSMA are considered the most promising for their good pharmacokinetic features and rapid blood clearance resulting in low background activity. A variety of radionuclides used to label the PSMA-targeted radiotracers have been reported, which include ^{111}In, ^{99m}Tc, ^{123}I, ^{89}Zr, ^{68}Ga, and ^{18}F. Some agents are currently used clinically to test their potential in detecting PCa lesions, for instance, the urea-based PSMA ligands $^{123/124/131}$I-MIP-1072/−1095, ^{99m}Tc-MIP-1404/-1405, ^{68}Ga-HBED-CC-PSMA, ^{68}Ga/^{177}Lu-PSMA-I&T, ^{68}Ga/^{177}Lu-PSMA-617, ^{18}F-DCFBC, ^{18}F-DCFPyL, and ^{18}F-PSMA-1007. Among these tracers, ^{68}Ga- and ^{18}F-labeled compounds are particularly promising for diagnostic purposes, as they can be used for PET imaging, which have been successfully translated to clinical

applications. On the contrary, in some situations that PET is not available, using the radioisotopes for scintigraphy and SPECT to label PSMA ligands, such as ^{123}I or ^{99m}Tc, is practical and valuable.

^{123}I-MIP-1072 and ^{123}I-MIP-1095 were the first two agents, followed by ^{99m}Tc-MIP-1404 and ^{99m}Tc-MIP-1405 for clinically SPECT imaging. *N*-[*N*-[(*S*)-1,3-dicarboxypropyl] carbamoyl]-4-^{18}F-fluorobenzyl-L-cysteine (^{18}F-DCFBC) [15] and ^{68}Ga-PSMA-11 (^{68}Ga-PSMA–*N,N′*-bis-[2-hydroxy-5-(carboxyethyl)benzyl]ethylenediamine-*N,N′*-diacetic acid) were the first two agents for PET imaging. Premier therapeutic studies were performed with ^{131}I-MIP-1095, which was soon replaced by chelator-based PSMA-617 and another PSMA inhibitor for imaging and therapy, PSMA-I&T [16], which are theranostic agents capable of being labeled with PET, SPECT, or therapeutic radionuclides.

^{68}Ga-PSMA-11 (also known as ^{68}Ga-PSMA-HBED, ^{68}Ga-PSMA-HBED-CC, and ^{68}Ga-PSMA-Glu-urea-Lys-(Ahx)-HBED-CC) was initially introduced by the German Cancer Research Center (Heidelberg, Germany) in 2012. This radiotracer currently has been used most widely for PSMA-targeted imaging, especially in Europe and Asia. In imaging of normal populations, ^{68}Ga-PSMA-11 was observed with high concentration in the kidney cortex, duodenum, parotid, and submandibular salivary glands followed by moderate concentration in the spleen, lacrimal glands, and liver. While ^{68}Ga-PSMA-11 and other most current PSMA-targeted radiotracer are not good at detecting the lesions around the prostate gland, especially the small local recurrences, which is related to high levels of radiotracer excretion and urinary bladder activity that may mask small foci in this vicinity.

^{18}F-DCFBC, which was first introduced in 2008 by researchers from Johns Hopkins University, has persistent high blood pool activity and relatively low tumor-to-background ratios [17]. And a second-generation, ^{18}F-labeled, small-molecule urea derivative known as 2-(3-{1-carboxy-5-[(6-^{18}F-fluoro-pyridine-3-carbonyl)-amino]-pentyl}-ureido)-pentanedioic acid (^{18}F-DCFPyL) overcame the first-generation's limitations becoming more popular [18]. The favorable dosimetry, biodistribution, and safety of ^{18}F-DCFPyL were identified in the first-in-human study of nine patients with known metastatic PC [19]. Initial data on the biodistribution and radiation dosimetry of ^{18}F-DCFPyL showed a more rapid renal excretion, higher tumor-to-blood and tumor-to-muscle ratios, and lower uptake in the liver. Similar to ^{68}Ga-PSMA-11 and possibly all other small-molecule PSMA ligands, physiologic accumulation of ^{18}F-DCFPyL is observed in the salivary glands, lacrimal glands, kidneys, liver, spleen, small intestine, and urinary collecting system (Fig. 13.1). Most recently, ^{18}F-PSMA-1007 [20] was reported as another ^{18}F-labeled agent with very low urine excretion and potentially improved detection of the prostatic bed. ^{18}F-labeled radiotracers also have a longer half-life and potentially easier centralized production and distribution than ^{68}Ga-labeled agents.

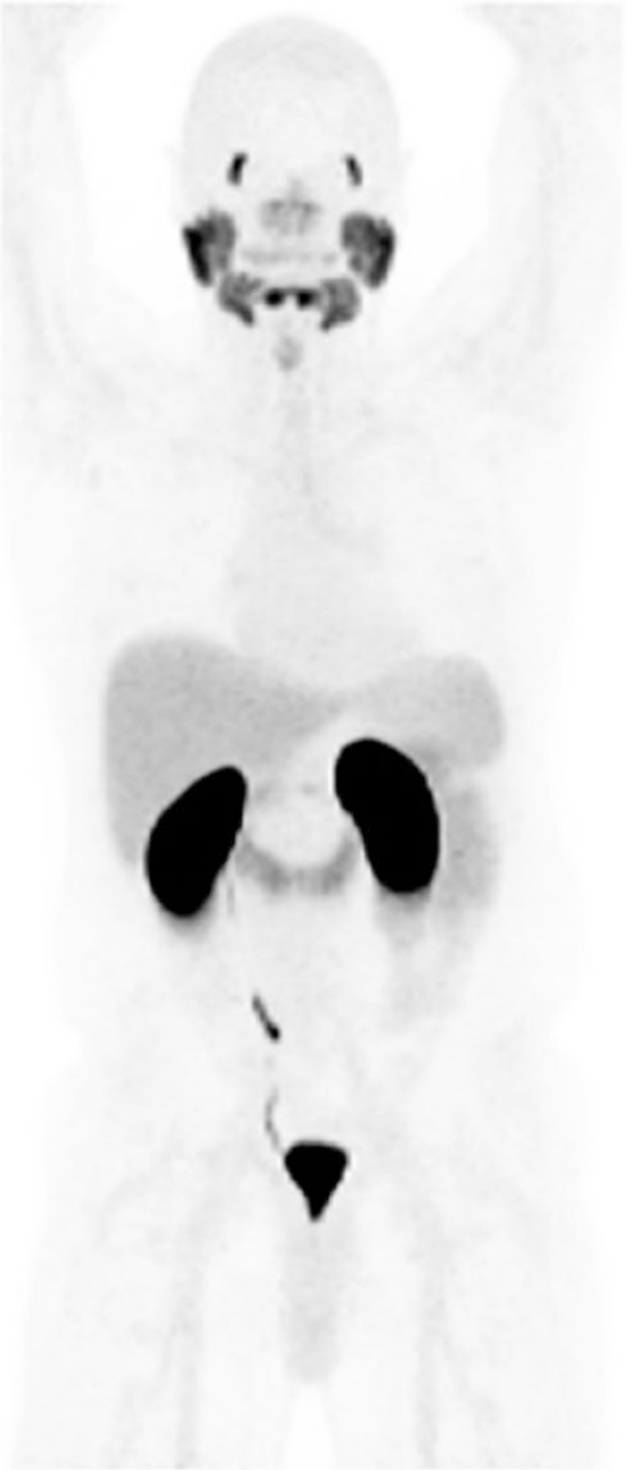

Fig. 13.1 PET whole-body maximum-intensity-projection image with ^{18}F-DCFPyL. Normal radiotracer uptake is seen in the lacrimal glands, salivary glands, liver, spleen, kidneys, small intestine, and urinary collecting system

With the unexpected potential of ^{99m}Tc-PSMA-I&S as SPECT imaging agent, an alternative to the use of

^{111}In-PSMA-I&T for PSMA-radioguided surgery is now available and may permit fast, convenient, kit-like labeling [21].

13.5.2 PSMA-Targeted Imaging

The most popular application of PSMA-targeted imaging is in PCa since PSMA represents an excellent target for molecular imaging of PCa. Yet, recent reports on the application of PSMA-targeted imaging in non-prostatic tumors have emerged in large numbers.

13.5.3 PSMA-Targeted Therapy

13.5.3.1 Application in Prostate Cancer

1. ^{68}Ga-Labeled PSMA-Targeted Imaging
   An increasing number of studies on ^{68}Ga-labeled PSMA imaging have emerged and yielded promising results for the clinical application of PSMA-targeted imaging. ^{68}Ga-PSMA PET imaging has already been used as a part of the routine diagnostic workup of PCa at some centers in Europe. A number of studies have paid more attention to the accuracy of ^{68}Ga-PSMA-11 PET/CT for primary PCa staging. In a retrospective analysis of 130 patients with intermediate- to high-risk PCa and subsequent pelvic lymph nodes dissection, ^{68}Ga-PSMA-11 PET was shown to be superior to standard routine imaging [22]. The sensitivity of ^{68}Ga-PSMA-11 PET/CT was 65.9%, while conventional imaging was 43.9%, at the patient level. Moreover, ^{68}Ga-PSMA-11 PET was shown to have a high specificity 98.9% and high accuracy 88.5%, superior to morphological imaging.

   On the detection of bone metastases, ^{68}Ga-PSMA-11 PET was definitely proven superior to bone scanning in a clinical trial of 126 PCa patients [23]. Currently, a prospective multicenter trial to assess the diagnostic accuracy and management impact of ^{68}Ga-PSMA-11 PET scanning in PCa patients compared with conventional imaging (CT and bone scanning) is ongoing (ANZCTR 12617000005358).

   A retrospective analysis of 1007 consecutive patients with recurrent PCa showed a high percentage of 79.5% detected by ^{68}Ga-PSMA-11 PET/CT [24]. Recently, a systematic review and meta-analysis evaluating ^{68}Ga-PSMA PET/CT for PCa, which included 15 ^{68}Ga-PSMA PET/CT studies with 1256 patients, showed a sensitivity of 61–70% and a specificity of 84–97% based on published reports comparing ^{68}Ga-PSMA PET/CT and PET/MRI to conventional imaging, and restaging ^{68}Ga-PSMA PET/CT had a detection rate of 50% for an early rise in PSA [25]. It has been shown that salvage therapy initiated before PSA > 0.5 ng/mL improves prognosis in PCa patients. In a number of studies, the detection rate in such patients by ^{68}Ga-PSMA-11 PET/CT was reported to be 50.0–57.9%, which is higher than other imaging modalities. Therefore, ^{68}Ga-PSMA PET imaging potentially offers more effective selection for salvage treatment.
2. ^{18}F-Labeled PSMA-Targeted Imaging
   In 2012, Johns Hopkins University School of Medicine conducted the first-in-human clinical study of ^{18}F-DCFBC in five patients with metastatic PCa demonstrating favorable dosimetry and biodistribution for the detection of PCa [15]. Soon afterward, detection rates and sensitivity of ^{18}F-DCFBC PET were reported superior to conventional imaging in hormone-naïve and castration-resistant metastatic PCa [26, 27]. The first-in-human study of ^{18}F-DCFPyL was reported in 2015, which was performed in nine metastatic PCa patients [19]. Subsequent studies indicated increased detection efficiency of lesions compared with conventional imaging [28]. ^{18}F-DCFPyL was shown to possess over five times greater affinity for PSMA relative to ^{18}F-DCFBC, with a markedly higher uptake in presumed primary and metastatic PCa (Fig. 13.2). These features remarkably improve the detection of suspected metastatic foci in PCa. Rowe et al. showed that ^{18}F-DCFPyL PET can detect multiple sites of recurrent disease that were occult or equivocal on conventional imaging modalities (Figs. 13.2 and 13.3), which is very important in the detection of pelvic/peri-prostatic tissues and subcentimeter lymph node foci (Fig. 13.4). In addition, ^{18}F-DCFPyL PET was also shown to be superior to conventional imaging modalities in evaluation of primary infiltrative or lytic bone foci, which may be visually occult on contrast-enhanced CT or have low uptake on bone scanning [28].

   Recently, the preliminary clinical application of ^{18}F-PSMA-1007 PET/CT and PET/MR has been reported in small cohort of PCa [20, 29–31], showing promising results with high potential for localization of recurrent disease and accurate local staging of PCa.

13.5.3.2 Application in Non-prostatic Tumor

Beyond its applications in PCa, the expression of PSMA in non-PCa tumor neovasculature that has long been established in the pathology literature suggested that PSMA-targeted imaging would be able to effectively image other tumor types, including sarcomas, as well as renal, bladder, colon, neuroendocrine, pancreatic, lung cancer, and most breast cancers. Recent reports also confirmed that certain non-PCa tumors may express PSMA directly on cancer cells in addition to the neovasculature [32].

The most widely explored non-prostatic tumor with PSMA-targeted imaging is clear cell renal cell carcinoma (RCC). Immunohistochemistry studies have shown PSMA is

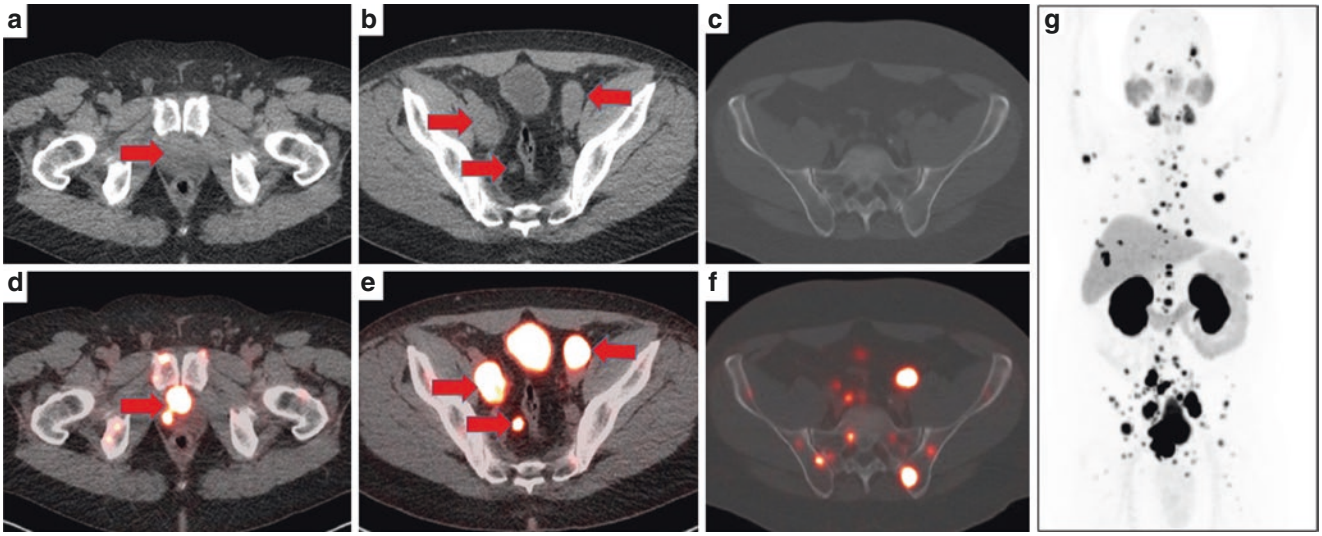

Fig. 13.2 ^{18}F-DCFPyL PET/CT images of patient with recurrent PCa. (**a**–**c**) CT scanning. (**d**–**f**) ^{18}F-DCFPyL PET/CT fusion images. (**g**) MIP of ^{18}F-DCFPyL PET indicated numerous metastases with high uptake of ^{18}F-DCFPyL. Avid uptake of ^{18}F-DCFPyL was observed in prostate bed (**d**), pelvic mass and lymph nodes (**e**) and bones (**f**) indicating prostate cancer with multiple metastasis, while CT scanning only showed metastatic pelvic mass and lymph nodes (**b**), no metastatic evidence in prostate bed (**a**) and bones (**c**)

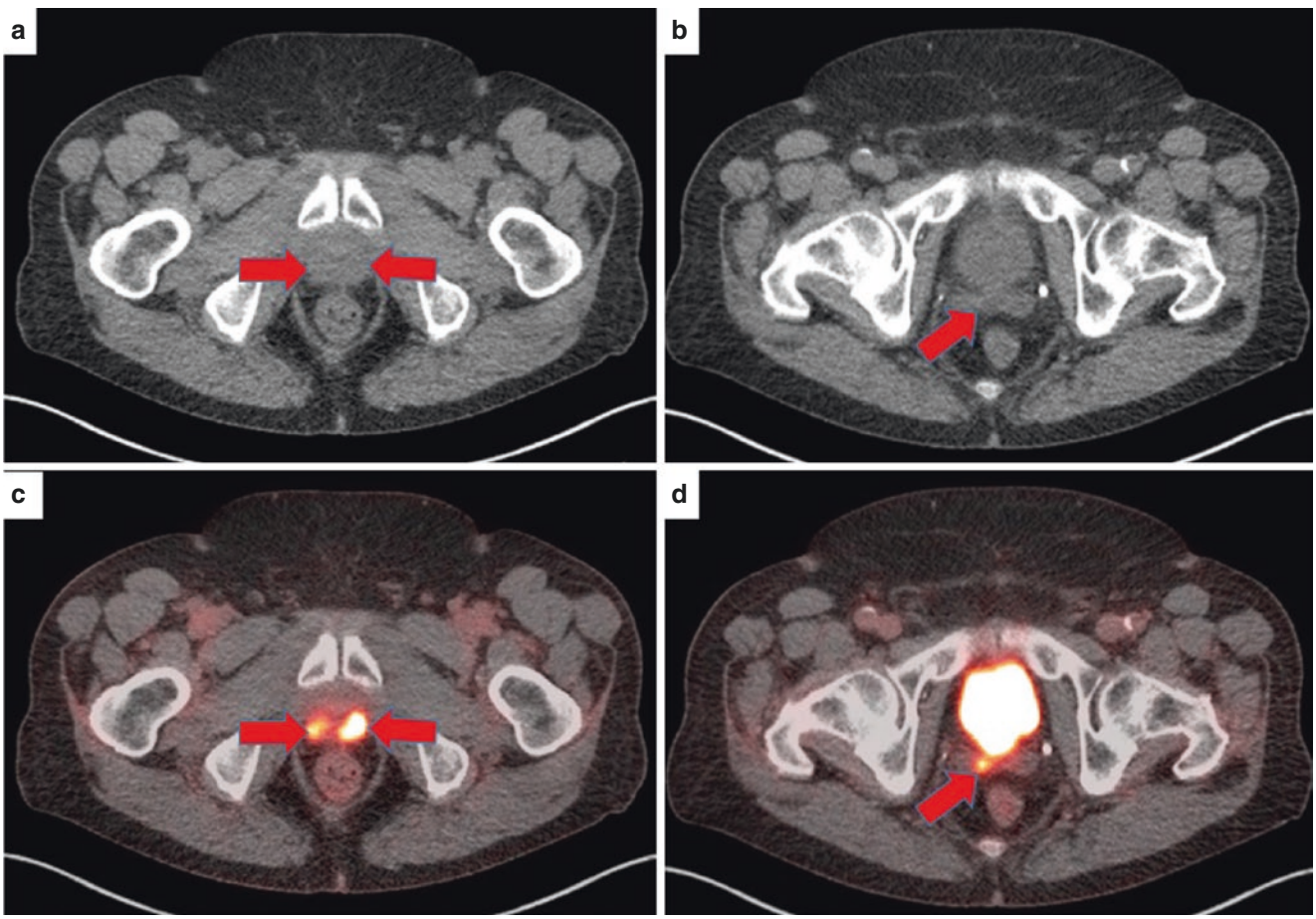

Fig. 13.3 ^{18}F-DCFPyL PET/CT imaging showed avid uptake of ^{18}F-DCFPyL in prostate bed (**c**) and right seminal vesicle (**d**) which indicated recurrent prostate cancer and metastasis to the right seminal vesicle. (**a**, **b**) On CT scanning no evidence was observed to diagnose recurrent disease or metastasis

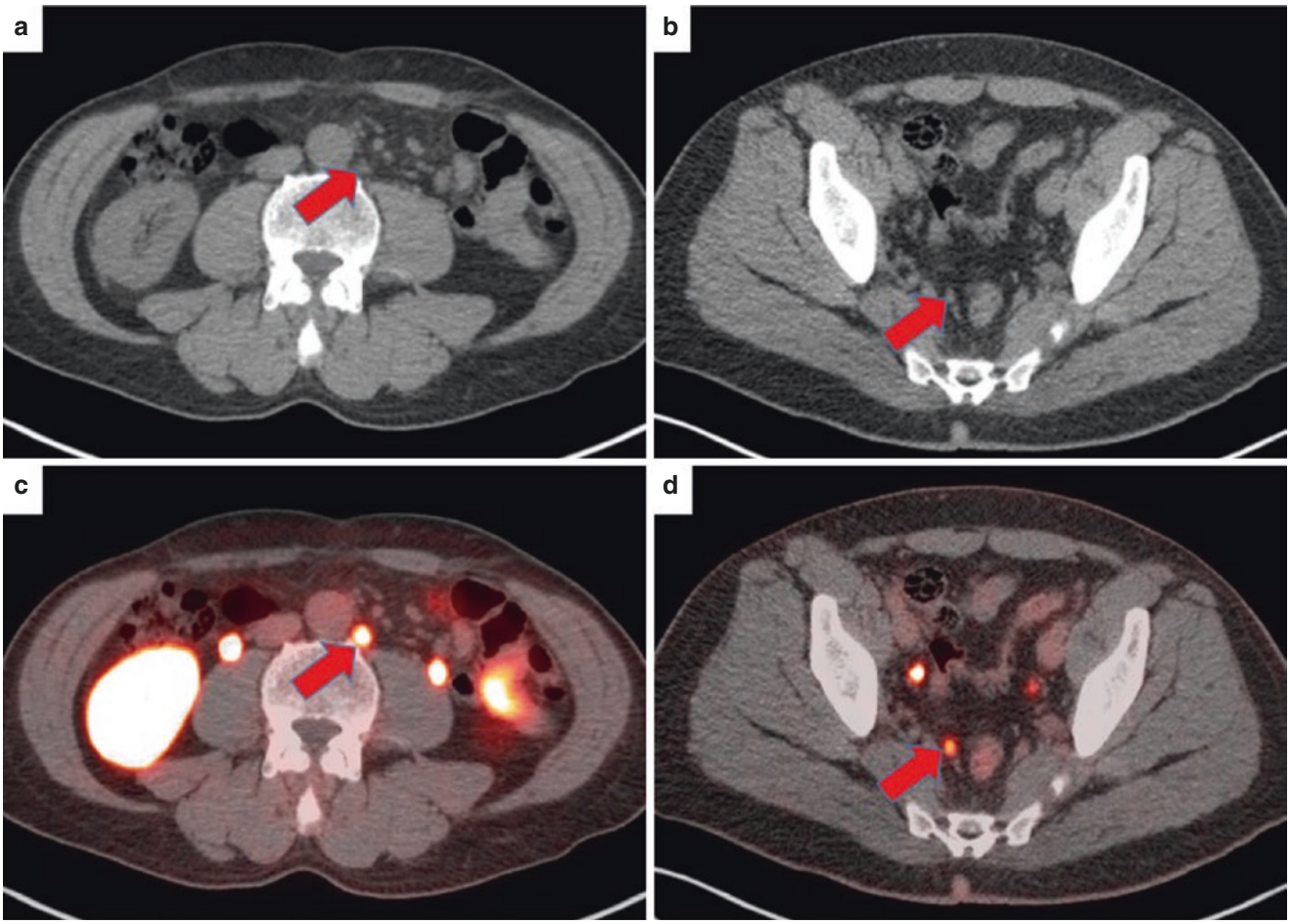

Fig. 13.4 ^{18}F-DCFPyL PET/CT images of a potoperative patient with PCa. Avid uptake of ^{18}F-DCFPyL was observed in retroperitoneal (**c**) and pelvic lymph nodes (**d**) indicating lymph nodes metastasis, while CT only showed tiny lymph nodes without metastatic evidence (**a**, **b**)

differentially expressed in the tumor-associated neovasculature in different renal tumors; the most diffuse and intense PSMA expression pattern was identified in clear cell RCC while rarely detectable in papillary RCC and angiomyolipoma. Recently, some case reports and clinical pilot studies suggest the potential role of PET/CT with ^{18}F-DCFPyL and ^{68}Ga-PSMA-11 in the evaluation of advanced RCC, though they mostly focused on the clear cell subtype. PSMA-targeted PET/CT shows promising efficacy in RCC staging and timely and accurate detection of occult metastatic lesions on conventional imaging. The sensitivity of PSMA-targeted PET/CT was reported to be superior to conventional imaging in detecting sites of metastatic RCC [33, 34]. One potential limitation of PSMA-targeted PET/CT imaging in RCC is with regard to the assessment of primary tumors due to intense uptake of PSMA tracers in normal renal parenchyma.

In addition to the application of PSMA-targeted imaging in renal cell carcinoma, there have been reports of its utility in breast cancer, gastrointestinal cancer, lymphoma, liver carcinoma, lung cancer, thyroid cancer, adenoid cystic carcinoma, brain tumor, neurofibromas, gastrointestinal stromal tumor, thymoma, and some benign lesions [35]. Most of these reports are usually case reports or small case series, and none revealed the similar outcomes as in PCa.

In conclusion, PSMA-targeted PET imaging has been shown to support high sensitivity and specificity in identifying the sites of PCa. Regardless of the excellent performance features reported in the literature, we must pay attention to the uptake of PSMA-targeted radiotracers in a number of non-prostate malignancies as well as many types of benign lesions. Furthermore, even when used to detect PCa, the degree of radiotracer uptake can be very variable depending on the level of PSMA expression as well as the size and location of lesions. In order to facilitate the collection of data for large prospective trials as well as allow for an accurate and efficient means of relaying findings to referring providers, Dr. Rowe proposed a structured reporting system, termed PSMA-RADS version 1.0, for reporting the findings on PSMA-targeted PET studies [36]. In short words, PSMA-RADS gives a framework for classifying PSMA-targeted PET imaging and individual findings into categories that

could clearly provide the likelihood of the presence of PCa. PSMA-RADS version 1.0 is composed of a five-point scale, with higher numbers indicating a higher probability of PCa.

PSMA-RADS version 1.0: PSMA-RADS-1 (benign) comprises PSMA-RADS-1A and PSMA-RADS-1B, which describe a benign lesion characterized by biopsy or a pathognomonic finding on anatomic imaging without or with abnormal radiotracer uptake. PSMA-RADS-2 (likely benign) designates lesions with equivocal (focal but low level such as blood pool or lower) uptake that are likely benign but have not been biopsied or are not definitively identifiable as a specific entity on the anatomic imaging. PSMA-RADS-3 (equivocal, further workup can be considered) includes four designations suggesting that either further workup or follow-up imaging may be valuable to more completely characterize the findings: PSMA-RADS-3A and PSMA-RADS-3B represent either soft tissue, such as lymph nodes or bone lesions with equivocal uptake that are suggestive of but not definitive for PCa; PSMA-RADS-3C indicates lesions with intense radiotracer uptake that have a high likelihood of representing a non-prostate malignancy or other benign tumor; and the PSMA-RADS-3D designation is reserved for lesions that are suspicious for malignancy on the basis of anatomical imaging but lack radiotracer uptake, which include non-prostate malignancies, neuroendocrine PCa, and the uncommon prostate adenocarcinoma that fails to express PSMA. PSMA-RADS-4 (prostate cancer highly likely) represents lesions with intense uptake that have a high likelihood of being PCa but do not have confirmatory findings on anatomic imaging or bone scans. PSMA-RADS-5 (prostate cancer almost certainly present) indicates lesions that are diagnosed with PCa as definitive findings are found on both PSMA-based PET (intense uptake) and conventional imaging.

13.5.4 PSMA-Targeted Therapy

The efficacy of radionuclide therapy using radiolabeled PSMA ligands has been evaluated in a number of clinical studies. PSMA ligands include antibodies, with the most used antibody for PSMA RIT in advanced PCa being the humanized IgG monoclonal antibody J591. Since PSMA-targeted radiopharmaceuticals also include some small molecules, PSMA-targeted therapy comprises more than just RIT.

^{177}Lu-J591, the radiolabeled anti-PSMA antibody, targets the extracellular domain of PSMA. A phase II study revealed that nearly 60% of patients experienced a PSA decline following single treatment, though only 11% experienced a greater than 50% decline in PSA, and all experienced reversible hematologic toxicity, with grade 4 thrombocytopenia occurring in about 47% of cases, which limits clinical application [37]. The slow diffusion of antibodies into solid lesions, which peaks at 6 or 7 days after injection, also limits radiolabeled antibody therapy [38]. Small-molecule PSMA ligands for radionuclide therapy were first applied in 28 patients with progressive PCa by Zechmann et al., with a single therapeutic dose of ^{131}I-MIP-1095 (2–7.2 GBq) following conventional treatments [39]. They found that more than half of the patients experienced considerable symptom relief and a decline of over 50% in PSA after a single dose of ^{131}I-MIP-1095, with mild hematological toxicities.

Since 2013, ^{131}I-related PSMA therapy has largely been replaced by therapy with ^{177}Lu- and ^{225}Ac-labeled therapeutic ligands, such as PSMA-617. ^{225}Ac-labeled PSMA-targeted therapy is currently available only in Heidelberg, Germany. ^{177}Lu-PSMA-617 has been increasingly used for radionuclide therapy in metastatic PCa patients in different countries. An increasing number of studies reported the preliminary clinical application of ^{177}Lu-labeled PSMA-targeted radiotherapies, concentrating mainly on efficacy evaluations of ^{177}Lu-PSMA-617 and ^{177}Lu-(DOTAGA-(I-y)fk(Sub-KuE) (also called ^{177}Lu-PSMA-I&T). The results were promising in that 30–60% of patients experienced a decrease of PSA of more than 50% after radionuclide therapy of metastatic castration-resistant prostate cancer (mCRPC). A large retrospective case series evaluating the toxicity of ^{177}Lu-PSMA-617 and PSA response in 145 patients with mCRPC was reported by the German Society of Nuclear Medicine [40]. Patients from 12 German Nuclear Medicine Clinics received a median of two cycles (range 1–4) of ^{177}Lu-PSMA radionuclide therapy. Thirteen percent of patients with 5.5–6.5 GBq experienced toxic response, and 18% of patients with >6.5 GBq during the first radionuclide therapy experienced grade 3–4 toxicity. Over the entire follow-up period with 16 weeks in median (range, 2–30 weeks), 45 of 99 (45%) patients demonstrated a PSA decline of over 50% and were considered biochemically responsive. Patients receiving a third or fourth cycle of therapy showed a PSA decline over 50% in 13 of 20 (65%) and 3 of 3 (100%) cases, respectively.

The largest series on radionuclide therapy of ^{177}Lu-PSMA I&T was reported by Baum et al. [41] in which 56 mCRPC patients underwent 1–5 cycles of ^{177}Lu-PSMA I&T (3.6–8.7 GBq). All patients tolerated the therapy without any acute adverse effects, including thrombocytopenia. 80.4% of patients experienced a decrease in serum PSA, and more than half who were monitored for over 6 months after receiving at least two cycles of therapy obtained partial remission on PET/CT with a median PFS period of 13.7 months. In another study performed in 22 mCRPC patients evaluating the safety and efficacy of ^{177}Lu-PSMA I&T, none experienced grade 3/4 toxicities. Five percent of patients got complete remission, based on combined assessment of bone and soft tissue metastases, stable disease was reported in 63%, and disease progression occurred in 32%.

More recently a new approach focused on the treatment of PCa using alpha-emitters ^{225}Ac or ^{213}Bi-labeled PSMA-617 has been developed [42, 43]. For advanced PCa patients, a treatment of ^{225}Ac-PSMA-617 (100 kBq/kg/cycle) repeated every 8 weeks showed promising antitumor efficacy and presented a reasonable trade-off between toxicity and biochemical response. Nevertheless, severe xerostomia occurred when treatment activity exceeded 100 kBq/kg, which indicated a dose-limiting effect [43]. The first-in-human treatment with ^{213}Bi-PSMA-617 was performed on a patient with mCRPC who was refractory to conventional therapy [44]. The patient was treated with two cycles of ^{213}Bi-PSMA-617 (cumulative activity: 592 MBq). Restaging with ^{68}Ga-PSMA PET/CT demonstrated remarkable molecular imaging response, and biochemical response (PSA level decreased to 43 μg/L from 237 μg/L) was also observed 11 months after therapy. Another study evaluating radiation dosimetry and empiric dosing for ^{213}Bi-PSMA-617 radionuclide therapy in three metastatic PCa patients showed dosimetry to be in a range traditionally considered promising for clinical application, but compared to ^{225}Ac-PSMA-617, its therapeutic index for PCa appears inferior.

PSMA-targeted imaging and therapy have been applied clinically at an unheard-of rate, with a noticeable increase in research publications. Up to now, the evidences from the literature strongly indicate that PSMA-targeted PET imaging may have a promising effect on the management of early recurrent or primary PCa. In terms of PSMA-targeted therapy, the use of ^{177}Lu-PSMA has been shown to be beneficial for the treatment of advanced disease, with further advancement expected from the use of α-emitters.

13.5.5 PSMA-Based Radioguided Surgery (PSMA-RGS)

With improvement of tumor localization with PSMA ligands, which are capable of detecting tiny, occult, and often atypically located lesions not routinely visualized reliably during surgery, the new techniques are expected to make intraoperative detection of small tumor in real time to become true. In 2015, a PSMA-RGS for metastatic lymph nodes in PCa was reported [45]. One patient with primary PCa and lymph node metastases and four patients with recurrent PCa and regional lymph node metastases on ^{68}Ga-PSMA-11 PET received an intravenous injection of 146 MBq of ^{111}In-PSMA-I&T 24 h before surgery. All lymph nodes that showed positive radiosignals in vivo were detected using a hand-held gamma detector to be PSMA-expressing metastatic disease confirmed by ex vivo histopathology. The detection of subcentimeter metastatic lymph nodes was enabled by PSMA-RGS, and in two patients, additional lesions, which were not observed on preoperative ^{68}Ga-PSMA-11 PET imaging, were detected. Overall, this study showed the feasibility of this PSMA-based radio-guided surgical approach. Later, a study that summarized the data from 31 patients with localized recurrent PCa undergoing salvage PSMA-RGS using ^{111}In-PSMA-I&T [46] revealed declines in PSA of over 50% and over 90% in 76.7% and 53.3% of patients, respectively. There were also 4 false-negative and 6 false-positive compared with histological findings among 48 metastasis and 87 cancer-free specimens by ^{111}In-PSMA-RGS ex vivo measurements. Although evidence suggests that ^{111}In-PSMA-I&T RGS could support a beneficial effect on disease progression, the selection of suitable patients on the basis of PSMA-targeted PET imaging as well as clinical variables is very important and necessary for satisfactory results. Currently, some researchers are focusing on PSMA ligands suitable for real-time near-infrared fluorescence imaging of surgical margins and fluorescence-guided resection of tumor residues [47].

In summary, PSMA-guided surgery for prostate cancer lesions appears to be an attractive approach for detection of metastasis, especially tiny lesions.

References

1. Lachmann PJ (1984) Tumour immunology: a review. J R Soc Med 77:1023–1029
2. Pressman D, Keighley G (1948) The zone of activity of antibodies as determined by the use of radioactive tracers; the zone of activity of nephrotoxic antikidney serum. J Immunol 59:141–146
3. Hust M, Jostock T, Menzel C et al (2007) Single chain Fab (scFab) fragment. BMC Biotechnol 7:14
4. Chakravarty R, Goel S, Cai W (2014) Nanobody: the "magic bullet" for molecular imaging? Theranostics 4:386–398
5. Goldenberg DM, Preston DF, Primus FJ et al (1974) Photoscan localization of GW-39 tumors in hamsters using radiolabeled anticarcinoembryonic antigen immunoglobulin G. Cancer Res 34:1–9
6. Goldenberg DM, Deland F, Kim E et al (1978) Use of radiolabeled antibodies to carcinoembryonic antigen for the detection and localization of diverse cancers by external photoscanning. N Engl J Med 298:1384–1386
7. Song IH, Noh Y, Kwon J et al (2017) Immuno-PET imaging based radioimmunotherapy in head and neck squamous cell carcinoma model. Oncotarget 8:92090–92105
8. Colombo I, Overchuk M, Chen J et al (2017) Molecular imaging in drug development: update and challenges for radiolabeled antibodies and nanotechnology. Methods 130:23–35
9. Chatterjee S, Lesniak WG, Gabrielson M et al (2016) A humanized antibody for imaging immune checkpoint ligand PD-L1 expression in tumors. Oncotarget 7:10215–10227
10. Ledermann JA, Canevari S, Thigpen T (2015) Targeting the folate receptor: diagnostic and therapeutic approaches to personalize cancer treatments. Ann Oncol 26:2034–2043
11. Chen S, Yu L, Jiang C et al (2005) Pivotal study of iodine-131-labeled chimeric tumor necrosis treatment radioimmunotherapy in patients with advanced lung cancer. J Clin Oncol 23:1538–1547
12. Kraeber-Bodere F, Rousseau C, Bodet-Milin C et al (2015) Tumor immunotargeting using innovative radionuclides. Int J Mol Sci 16:3932–3954
13. Mottaghy FM (2014) Can radioimmunotherapy promote from an orphan drug to daily clinical practice? Eur J Nucl Med Mol Imaging 41:865–866

14. Israeli RS, Powell CT, Fair WR et al (1993) Molecular cloning of a complementary DNA encoding a prostate-specific membrane antigen. Cancer Res 53:227–230
15. Cho SY, Gage KL, Mease RC et al (2012) Biodistribution, tumor detection, and radiation dosimetry of 18F-DCFBC, a low-molecular-weight inhibitor of prostate-specific membrane antigen, in patients with metastatic prostate cancer. J Nucl Med 53:1883–1891
16. Weineisen M, Schottelius M, Simecek J et al (2015) 68Ga- and 177Lu-labeled PSMA I&T: optimization of a PSMA-targeted theranostic concept and first proof-of-concept human studies. J Nucl Med 56:1169–1176
17. Mease RC, Dusich CL, Foss CA et al (2008) N-[N-[(S)-1,3-dicarboxypropyl]carbamoyl]-4-[18F]fluorobenzyl-L-cysteine, [18F]DCFBC: a new imaging probe for prostate cancer. Clin Cancer Res 14:3036–3043
18. Chen Y, Pullambhatla M, Foss CA et al (2011) 2-(3-{1-Carboxy-5-[(6-[18F]fluoro-pyridine-3-carbonyl)-amino]-pentyl}-ureido)-pentanedioic acid, [18F]DCFPyL, a PSMA-based PET imaging agent for prostate cancer. Clin Cancer Res 17:7645–7653
19. Szabo Z, Mena E, Rowe SP et al (2015) Initial evaluation of [(18)F] DCFPyL for prostate-specific membrane antigen (PSMA)-targeted PET imaging of prostate cancer. Mol Imaging Biol 17:565–574
20. Giesel FL, Hadaschik B, Cardinale J et al (2017) F-18 labelled PSMA-1007: biodistribution, radiation dosimetry and histopathological validation of tumor lesions in prostate cancer patients. Eur J Nucl Med Mol Imaging 44:678–688
21. Robu S, Schottelius M, Eiber M et al (2017) Preclinical evaluation and first patient application of 99mTc-PSMA-I&S for SPECT imaging and radioguided surgery in prostate cancer. J Nucl Med 58:235–242
22. Maurer T, Gschwend JE, Rauscher I et al (2016) Diagnostic efficacy of (68)gallium-PSMA positron emission tomography compared to conventional imaging for lymph node staging of 130 consecutive patients with intermediate to high risk prostate cancer. J Urol 195:1436–1443
23. Pyka T, Okamoto S, Dahlbender M et al (2016) Comparison of bone scintigraphy and (68)Ga-PSMA PET for skeletal staging in prostate cancer. Eur J Nucl Med Mol Imaging 43:2114–2121
24. Afshar-Oromieh A, Holland-Letz T, Giesel FL et al (2017) Diagnostic performance of (68)Ga-PSMA-11 (HBED-CC) PET/CT in patients with recurrent prostate cancer: evaluation in 1007 patients. Eur J Nucl Med Mol Imaging 44:1258–1268
25. Von Eyben FE, Picchio M, Von Eyben R et al (2018) (68)Ga-labeled prostate-specific membrane antigen ligand positron emission tomography/computed tomography for prostate cancer: a systematic review and meta-analysis. Eur Urol Focus 4(5):686–693
26. Rowe SP, Gorin MA, Salas Fragomeni RA et al (2017) Clinical experience with (18)F-labeled small molecule inhibitors of prostate-specific membrane antigen. PET Clin 12:235–241
27. Rowe SP, Macura KJ, Ciarallo A et al (2016) Comparison of prostate-specific membrane antigen-based 18F-DCFBC PET/CT to conventional imaging modalities for detection of hormone-naive and castration-resistant metastatic prostate cancer. J Nucl Med 57:46–53
28. Rowe SP, Macura KJ, Mena E et al (2016) PSMA-based [(18)F] DCFPyL PET/CT is superior to conventional imaging for lesion detection in patients with metastatic prostate cancer. Mol Imaging Biol 18:411–419
29. Giesel FL, Kesch C, Yun M et al (2017) 18F-PSMA-1007 PET/CT detects micrometastases in a patient with biochemically recurrent prostate cancer. Clin Genitourin Cancer 15:e497–e499
30. Freitag MT, Kesch C, Cardinale J et al (2018) Simultaneous whole-body (18)F-PSMA-1007-PET/MRI with integrated high-resolution multiparametric imaging of the prostatic fossa for comprehensive oncological staging of patients with prostate cancer: a pilot study. Eur J Nucl Med Mol Imaging 45:340–347
31. Giesel FL, Will L, Kesch C et al (2018) Biochemical recurrence of prostate cancer: initial results with [(18)F]PSMA-1007 PET/CT. J Nucl Med 59:632–635
32. Nimmagadda S, Pullambhatla M, Chen Y et al (2018) Low level endogenous prostate-specific membrane antigen (PSMA) expression in non-prostatic tumor xenografts is sufficient for in vivo tumor targeting and imaging. J Nucl Med 59(3):486–493
33. Rowe SP, Gorin MA, Hammers HJ et al (2015) Imaging of metastatic clear cell renal cell carcinoma with PSMA-targeted (1)(8) F-DCFPyL PET/CT. Ann Nucl Med 29:877–882
34. Rhee H, Blazak J, Tham CM et al (2016) Pilot study: use of gallium-68 PSMA PET for detection of metastatic lesions in patients with renal tumour. EJNMMI Res 6:76
35. Sheikhbahaei S, Afshar-Oromieh A, Eiber M et al (2017) Pearls and pitfalls in clinical interpretation of prostate-specific membrane antigen (PSMA)-targeted PET imaging. Eur J Nucl Med Mol Imaging 44:2117–2136
36. Rowe SP, Pienta KJ, Pomper MG et al (2018) Proposal of a structured reporting system for prostate-specific membrane antigen (PSMA)-targeted PET imaging: PSMA-RADS version 1.0. J Nucl Med 59(3):479–485
37. Tagawa ST, Milowsky MI, Morris M et al (2013) Phase II study of Lutetium-177-labeled anti-prostate-specific membrane antigen monoclonal antibody J591 for metastatic castration-resistant prostate cancer. Clin Cancer Res 19:5182–5191
38. Vallabhajosula S, Nikolopoulou A, Jhanwar YS et al (2016) Radioimmunotherapy of metastatic prostate cancer with (1)(7)(7) lu-DOTAhuJ591 anti prostate specific membrane antigen specific monoclonal antibody. Curr Radiopharm 9:44–53
39. Zechmann CM, Afshar-Oromieh A, Armor T et al (2014) Radiation dosimetry and first therapy results with a (124)I/ (131)I-labeled small molecule (MIP-1095) targeting PSMA for prostate cancer therapy. Eur J Nucl Med Mol Imaging 41:1280–1292
40. Rahbar K, Ahmadzadehfar H, Kratochwil C et al (2017) German multicenter study investigating 177Lu-PSMA-617 radioligand therapy in advanced prostate cancer patients. J Nucl Med 58:85–90
41. Baum RP, Kulkarni HR, Schuchardt C et al (2016) 177Lu-labeled prostate-specific membrane antigen radioligand therapy of metastatic castration-resistant prostate cancer: safety and efficacy. J Nucl Med 57:1006–1013
42. Kratochwil C, Schmidt K, Afshar-Oromieh A et al (2018) Targeted alpha therapy of mCRPC: dosimetry estimate of (213)bismuth-PSMA-617. Eur J Nucl Med Mol Imaging 45:31–37
43. Kratochwil C, Bruchertseifer F, Rathke H et al (2017) Targeted alpha-therapy of metastatic castration-resistant prostate cancer with (225)ac-PSMA-617: dosimetry estimate and empiric dose finding. J Nucl Med 58:1624–1631
44. Sathekge M, Knoesen O, Meckel M et al (2017) (213) Bi-PSMA-617 targeted alpha-radionuclide therapy in metastatic castration-resistant prostate cancer. Eur J Nucl Med Mol Imaging 44:1099–1100
45. Maurer T, Weirich G, Schottelius M et al (2015) Prostate-specific membrane antigen-radioguided surgery for metastatic lymph nodes in prostate cancer. Eur Urol 68:530–534
46. Rauscher I, Duwel C, Wirtz M et al (2017) Value of (111)In-prostate-specific membrane antigen (PSMA)-radioguided surgery for salvage lymphadenectomy in recurrent prostate cancer: correlation with histopathology and clinical follow-up. BJU Int 120:40–47
47. Neuman BP, Eifler JB, Castanares M et al (2015) Real-time, near-infrared fluorescence imaging with an optimized dye/light source/camera combination for surgical guidance of prostate cancer. Clin Cancer Res 21:771–780

Apoptosis Imaging

14

Hui Wang and Xiao-Jun Zhang

Apoptosis, which was first proposed by Kerr in 1972, is a basic physiological mechanism of life, and it is also the pathological basis for the development of many diseases [1]. With the deepening of research, increasingly explicit about mechanism of apoptosis was considered to be one of the most important progresses in biological field in recent decades. In the field of cancer treatment, apoptosis has a broad application prospect in the observation of curative effect or new drug evaluation. Radionuclide imaging using radiopharmaceuticals detects apoptosis by targeting apoptotic cells with high sensitivity and specificity. With decades of effort, the radioactive probes for different targets of the apoptotic cells were developed and evaluated. Many kinds of probes have been applied in clinical research [2].

14.1 Basic Physiology, Biology, and Pathophysiology of Apoptosis

The physiological, biological, and pathophysiological characteristics of apoptosis differ substantially from other cell death patterns.

14.1.1 Definition of Apoptosis

The term "apoptosis" contains two Greek roots "apo" and "ptosis," which means "from" and "falling," respectively. Apoptosis is known as programmed cell death that participates in cell growth, differentiation, the immune system regulation, and clearing abnormal cells [3]. Dysregulated apoptotic progress would result in harmful effects on normal tissues in various conditions, including tumor development that is due to too little apoptosis or neurodegenerative diseases and autoimmune disorder because of too much apoptosis [4].

14.1.2 Molecular Biological Mechanism

The mechanism of cell apoptosis is precise and complex, which belongs to the cascade reaction of energy-consuming molecules. The apoptotic process is mainly induced by two well-defined cellular pathways, the intrinsic pathway and the extrinsic pathway. Infection, radiation, heat, nutrient deprivation, glucocorticoids, or exorbitant intracellular calcium concentration can cause the release of apoptotic signals in cells, and extracellular signals were usually induced by toxic nitric oxide. Two distinct but convergent pathways can initiate apoptotic receptor pathways. Both apoptotic pathways shared a common cascade named caspases, consisting of cysteine-dependent aspartate-specific proteases. Executioner caspases degrade intercellular components in order to induce the morphological changes for apoptosis, finally disposed by macrophages. This program protects the microenvironment from proteolytic enzymes and cytosolic material during apoptosis. Multiple inducements of apoptosis are known, including growth factor withdrawal, chemotherapy, DNA damage, immunoreaction, and ischemic injury. The interval between the trigger of apoptosis and the time of detectable biologic reactions largely depends on the type of cells, the degree and the lasting time of trigger, and the microenvironment [5].

14.1.3 Biochemical and Morphological Changes

Apoptosis is a suicide procedure that widely existed in multicellular organisms, which consumes energy but does not cause inflammatory reaction. Cells are broken into fragments and swallowed up by adjacent cells or macrophages

H. Wang (✉)
Nuclear Medicine Department, Hainan Branch of the Chinese PLA General Hospital, Sanya, P. R. China

X.-J. Zhang
Nuclear Medicine Department, The Chinese PLA General Hospital, Beijing, P. R. China

G. Huang (ed.), *Nuclear Medicine in Oncology*, https://doi.org/10.1007/978-981-13-7458-6_14

rapidly. Apoptosis is characterized by the double-stranded breaks in the nucleosome junction region, leading to the DNA fragment formation and multiple gene and protein expressions [6].

The first morphological changes of apoptotic cells include densification and separation of nuclear chromatin and condensation of cytoplasm. The plasma membrane convolutes or blebs, shaping in apoptotic bodies. These apoptotic bodies are membrane-bounded fragments containing nuclear components. The apoptotic bodies are quickly devoured by phagocyte cells and degrade within their lysosomes, and no inflammation is involved [7].

Tumor cells can escape apoptosis through many ways. The inactivation of p53 pathway plays a vital role in multiple stages of tumor proliferation. Studies revealed that p53-mutant mice had greater tumor load than p53-deficient mice. The mutation of p53 dominant was more favorable for tumor cell growth [8].

14.1.4 Apoptosis and Multisystem Diseases

Apoptosis is an important process essential for life. Imbalanced regulation between proliferation and death of cells plays a role in various conditions, such as infections, autoimmune disorder, neurodegenerative diseases, and cancer. Apoptosis participates in pathological processes in two ways: On one side, damage of major healthy, functional cells can lead to an increase in apoptotic levels, such as stroke, myocardial infarction, or allograft rejection reaction. Explicit delineation of the injured region with distinction of reversibly and irreversibly damaged cells may benefit the risk classification of patients with apoptosis-related diseases. On the other side, the reduction or even elimination of apoptosis goes hand in hand with the cancer formation and progression. Thus, apoptosis has a vital function for the development and homeostasis of normal tissues and has a profound impact on the growth and progression of tumors [9, 10].

14.2 Multimodality Apoptosis Imaging and Imaging Principle

Majority of anticancer treatment induce cell apoptosis and cell death to remove tumor cells, while deregulated apoptosis helps tumor cells to escape cell death and results in uncontrolled tumor proliferation, resistance to treatment, and recurrence. The major resistance targets include Mcl-1 and Bcl-2 proteins, autophagy pathway, necrosis and necrosis process, heat shock protein signaling, proteasome pathways, epigenetic modifications, and dysregulated nuclear output signals [11].

Newly developing targeted therapeutics provide an opportunity to improve the survival and response rates of refractory cancers. Tumor growth is usually associated with insufficient apoptosis. The tumor necrosis factor-related apoptosis-inducing ligand (TNF-related apoptosis-inducing ligand) is a type II transmembrane protein in the TNF family, and it is one of the most effective proapoptotic targeted biological therapy agents [12].

It is not until a few weeks after the end of the treatment that traditional imaging can be used to monitor the response to a particular treatment. Rapid evaluation of therapeutic response within days will help guide individuals to receive the most effective treatment [13]. Hence, inducing apoptosis in tumor cells represents an attractive target to curative effect of cancer. To achieve the clinical translation of in vivo apoptotic imaging, a few imaging techniques using various probes have been developed. Fluorescent-labeled inhibitors have been designed as affinity labels for caspase activity sites and showed promising results in vitro and in vivo [14].

Molecular imaging is dedicated to noninvasive in vivo characterization at cellular and molecular levels by clinical imaging methods. Visualization of diagnosis and treatment processes will provide more accurate information about disease progression after treatment and guide personalized treatment. Molecular events during cell death have been used as biomarkers for molecular imaging. Determining early response after treatment by apoptotic molecular imaging would improve patient management and treatment selection and also reduce adverse effects and medical expenses [15].

On the basis of the characteristics of molecular imaging, cell death imaging agents can be classified into five major categories, including phosphatidylserine ectropion, effector caspase activation, mitochondrial membrane depolarization, plasma membrane depolarization, and DNA fragmentation (Fig. 14.1).

The negatively charged phosphatidylserine loses asymmetric distribution accompanied by phosphatidylserine exposure which is the early hallmark of apoptosis. Phosphatidylserine accounts for 2–10% of total cell phospholipids, which makes it an effective and feasible target for apoptosis imaging. The intrinsic and extrinsic pathways of apoptosis are concentrated in a small amount of executor caspases, such as caspase-3, caspase-7, and caspase-9. Several caspase inhibitors have been labeled and tracked in vivo for imaging the activated (cleaved) caspases. The depolarization of mitochondrial electrochemical potential is one of the central events of apoptosis. Because cells contain a large number of mitochondria, it is a potential target of apoptosis. The caspase-activated DNase (CAD), which is activated by caspase-3 during apoptosis, is responsible for DNA fragmentation, another biochemical hallmark of apoptosis [16].

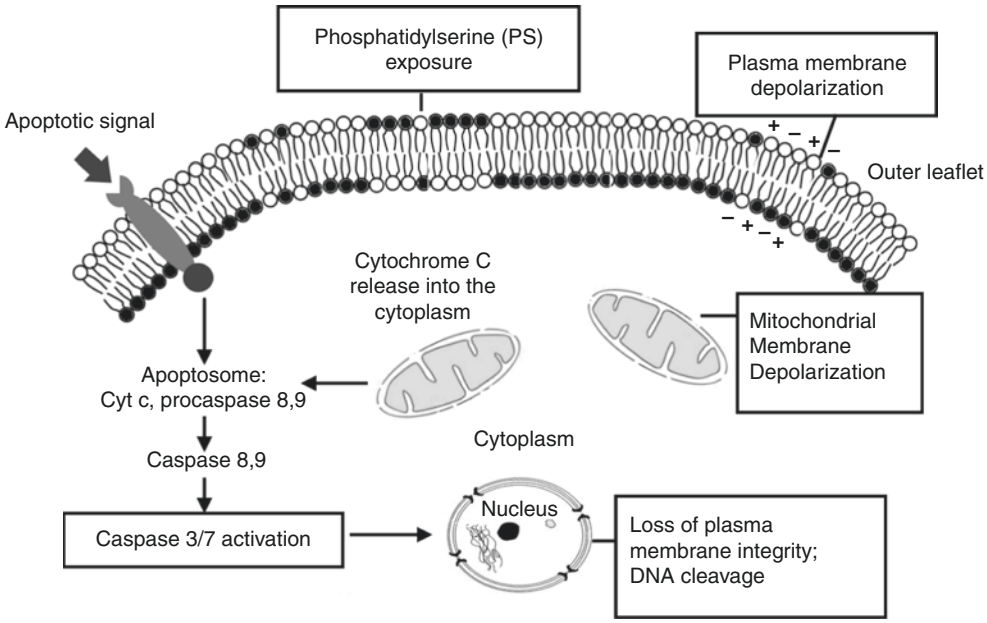

Fig. 14.1 Illustration of the main cellular events exploited to date for imaging cell apoptosis

14.3 Development of Apoptosis Imaging

Based on the well-defined biomarkers for apoptosis, a number of probes and strategies that enable visualized detection of apoptosis have been developed with various imaging modalities in preclinical and clinical studies.

14.3.1 Radiotracers Based on Proteins and Peptides

14.3.1.1 Annexin V-Based Proteins

Annexin V, a recombinant phosphatidylserine-binding protein, specifically binds to membrane-bound PS with high affinity in a Ca^{2+}-dependent manner. A variety of radionuclides can be coupled to annexin V for PET or SPECT scanning. Technetium-99 m is the most widely used medical radioisotope, and its labeled compounds are used in a great quantity of medical diagnostic procedures, which accounted for more than 80% of the annual nuclear medicine examination around the world. ^{99m}Tc-labeled annexin A5 has been the most widely used radiopharmaceutical for laboratory and clinical studies. The researchers used different ligands to link ^{99m}Tc and annexin V. The first ^{99m}Tc-labeled and clinically evaluated ^{99}mTc-annexin V probe was ^{99m}Tc-BTAP-annexin V. Clinical trial indicated that patients with lung or breast cancer or lymphoma showed no subsequent objective clinical response if lesions did not show any changes in radiotracer uptake after the first dose of therapy. Patients with effective treatment increased radiation uptake from 20 to 48 h after chemotherapy [17]. However, complex labeling procedures and relatively low radiochemical yield limit its further application. ^{99m}Tc-HYNIC-annexin V (^{99m}Tc-hydrazinamide-annexin V), labeled with a bifunctional chelating agent of HYNIC, is the most widely investigated apoptosis tracer. PET imaging with healthy humans showed a quick radioactivity clearance of blood with a half-life of 24 min. The probe was mainly metabolized by the kidneys, but radioactive uptake by the liver, spleen, and bone marrow was high. The biologic half-life of the activity registered over the whole body was 69 h [18]. Among patients with different tumor types, such as lymphoma, non-small cell lung cancer, and head and neck squamous cell carcinoma, ^{99m}Tc-HYNIC-annexin V can accurately separate treatment respondents from nonrespondents within 3 days after the initial treatment [19]. Meanwhile, ^{99m}Tc-HYNIC-annexin V is a promising tracer to image infectious foci and, perhaps, to distinguish between infection and inflammation. In addition, a variety of chelating agents such as MAG_3 (mercaptoacetyltriglycine), EC (ethylenedicysteine), and iminothiolane were used to connect ^{99m}Tc and annexin V, but biological experiments showed that these probes had no obvious advantage over ^{99m}Tc-HYNIC-annexin V [20]. Compared with ^{99m}Tc-HYNIC-annexin V, the site-specific labeling of annexin V-117 and annexin V-128 with ^{99m}Tc has a 75% decreased radiotracer uptake in renal and a twofold improved specific localization to sites of apoptosis in phase I/II clinical trial [21]. Although many ^{99m}Tc-labeled annexin V probes have undergone extensive clinical studies, this type of probes has the disadvantage of high nonspecific liver, kidney, and spleen uptake and low T/NT ratio. A meta-analysis (1999–2015) about ^{99m}Tc-annexin V probes demonstrated a high pooled

positive PPV of 100% (95%CI 92–100%) and a moderate pooled NPV of 70% (95%CI 55–82%) for predicting tumor response following the initial round of chemotherapy/radiotherapy in terms of ΔU% [22].

The formation of ^{18}F-SFB-annexin V (N-succinimidyl-4-[^{18}F]fluorobenzoate-annexin V) was performed through a labeling strategy lacking specificity that ^{18}F-SFB randomly reacts with 22 lysine residues or N-terminal amine of annexin V, which results in reduction of PS affinity and quantitative difficulties in uptake of tumor [23]. Another study obtained ^{18}F-FBEM-annexin V by site-specific alkylation reaction. Compared with ^{18}F-SFB-annexin V, ^{18}F-FBEM-annexin V showed similar ability to detect apoptotic EL4 cells. This finding suggests that site-specific ^{18}F-labeled strategy had no significant effect on the binding affinity of ^{18}F-labeled wild-type annexin V to PS in apoptotic cells [24].

Although annexin V probes typically have nanomolar affinity to PS with ideal results in in vitro studies, and in vivo experiments exhibit lack of immunogenicity and toxicity of annexin V-based probes, radiolabeled annexin V probes have several issues that limit further clinical use, including suboptimal pharmacokinetics, slow activity clearance in blood, high background activity in the abdominal region, high application cost, and Ca^{2+}-dependent binding affinity. Most importantly, because phosphatidylserine is also exposed during necrosis subsequent to apoptosis due to the destruction of cell membrane integrity, annexin V cannot distinguish between apoptosis and necrosis. The focus on such probes (preclinical and clinical research) was mainly concentrated in the years 2000 to 2010. In recent years, studies have turned to polypeptides and small-molecule probes with simple labeling methods and better biological characteristics.

14.3.1.2 Phosphatidylserine-Binding Peptide Probes

Syt I (synaptotagmin I) is a membrane-bound protein on synaptic vesicles of neurons. The C2A protein is one of the membrane-spanning cytoplasmic fragments of Syt I. C2A can insert into negatively charged membrane phospholipids such as PS in a Ca^{2+}-dependent mechanism. Few studies have been executed with the ^{99m}Tc-labeled C2A. The PET counterpart of C2A was prepared by labeling with ^{18}F-SFB. ^{18}F-C2A-GST, like ^{18}F-annexin V, has the ability to determine apoptosis in the same tumor cells and animal models. The major limitation for these compounds was a significant uptake in the spleen, liver, bone, and lungs, which cause high background activity in the abdominal region [25].

Song et al. found a 14-mer peptide SAAC-(M) FNFRLKAGQKIRFG (SAAC-(Re)-PSBP-6 that showed a nanomolar binding affinity (26 nM) to phosphatidylserine. Early chemotherapeutic effects in lymphoma and melanoma tumor models have been assessed by comparing ^{99m}Tc-labeled PSBP with ^{18}F-FDG. The increase in SAAC-(^{99m}Tc)-PSBP-6 uptake due to increased apoptosis was significantly associated with a decrease in uptake of ^{18}F-FDG due to reduced metabolism ($r = -0.79$, $P < 0.05$) [26]. SAAC-(^{99m}Tc)-PSBP-6 might bind with both apoptotic and necrotic cells, while the high abdomen background signal makes it difficult to detect liver and gastrointestinal lesions.

14.3.1.3 Phosphatidylethanolamine-Binding Peptide Probes

Another biochemical change in early stage of apoptosis is the externalization of PE, which occurs with PS exposure simultaneously. Duramycin is a disulfide cross-linked peptide containing 19 amino acids. It binds to PE with high affinity, selectivity, and specificity at a molar ratio of 1:1 (K_d = 5 nM). In vitro experiments with ^{99m}Tc-HYNIC-duramycin showed that the radioactive uptake of apoptotic cells was 30 times higher than that of the control group. The SPECT imaging results of mice with acute myocardial necrosis showed rapid diffusion rates and blood-pool clearance rates ($T_{1/2}$ = 4 min). The uptake of ^{99m}Tc-HYNIC-duramycin in the liver and gastrointestinal tract is low. SPECT imaging results also showed renal excretion and rapidly accumulation of apoptotic myocardial cells. A single-step kit formulation with high labeling rate and radiochemical purity of ^{99m}Tc-duramycin was developed due to its favorable pharmacokinetic features [27]. In addition, ^{99m}Tc-duramycin can be used for detecting ischemia/reperfusion injury in myocardium using the pig model, ApoE−/− knockout mice model of artery atheromatous plaque, oxidative lung injury, breast cancer-bearing nude mouse models, and side effect of radiotherapy for susceptible tissues. In all cases, ^{99m}Tc-duramycin could detect apoptotic cells and was useful for the estimation of the degree of the symptoms [28]. However, more complicated synthesis of ^{18}F-labeled duramycin and high accumulation in the liver and spleen significantly limit its clinical application [29].

14.3.1.4 Caspase-3 Activity Imaging Peptide Agents

The caspases play a key role in the start and execution of apoptotic procedures. Among them, caspase-3 is a key executive molecule that activated in the early phases of apoptosis, but caspase-3 activity of cells is significantly decreased during the late stages of apoptosis or death stages. Therefore, caspase-3 should be an attractive biomarker for early evaluation and real-time detection of apoptosis.

D-E-V-D (Asp-Glu-Val-Asp) is an effector caspase-3 recognition sequence. ^{18}F-CP-18 was designed to facilitate membrane transport into cells with a polyethylene glycol (PEG) chain as a caspase-3 peptide substrate with the tetrapeptidic caspase-3 recognition sequence D-E-V-D. Mechanistically, ^{18}F-CP-18 freely permeates cell membranes and enzyme substrates detached from the active

site by caspase-3, leading to signal enhancement. Animal experiments showed that the probe is quickly cleared from the circulation, mostly through renal excretion, and has a very low hepatic uptake (60 min, 0.27% ID/g), which provides a better signal-noise ratio in the abdomen [30]; Zhang Bao-shi et al. used ^{18}F-CP-18 to evaluate the early apoptosis of A549 tumor-bearing mice after chemotherapy, indicating that ^{18}F-CP-18 can reflect the tumor response to chemotherapy earlier and more accurately than ^{18}F-FDG [31]. The results of PET imaging in healthy individuals confirmed that ^{18}F-CP-18 was rapidly excreted into the bladder through the renal system and the received radiation activity of urinary bladder wall being the highest in the whole body [32]. Wang Hui et al. showed that ^{18}F-CP-18 could reflect the apoptosis of A549 tumor-bearing mice after radiotherapy. Further phase II/III studies are required to assess the efficacy of this promising apoptosis imaging agent.

14.3.2 Small-Molecule Probes

With the thoroughly studies on macromolecule such as large protein and peptide molecules for apoptosis imaging, it has been found that there are some inherent disadvantages, including complex labeling method, difficult purification of products, and suboptimal pharmacokinetics. No ideal imaging agent has yet been accepted into routine clinical practice. Compared with macromolecule probes, small molecules have excellent potentials for clinical translation, such as well-designed structure and optimized pharmacokinetic characters including good in vivo distribution, fast diffusion rates, and blood-pool clearance rates. Many potential small-molecule imaging agents have been developed and become the hotspot of the current studies.

14.3.2.1 PS-Target Small-Molecule Probes

Binuclear Zn (II) complexes of zinc dipicolylamine (Zn^{2+}-DPA) are known as an effective binding motif for phosphate anion. Cooperative association of the anionic headgroup of membrane-bound PS and the dipicolylamine ligand was mediated by Zn^{2+} ions, which is similar to the way that Ca^{2+} ions assist annexin V-binding membrane. Zhonglin Liu reported ^{99m}Tc-HYNIC-ZnDPA and $^{99m}Tc(CO)_3$-ZnDPA as cell death imaging agents for SPECT. Using anti-Fas hepatocyte apoptosis and myocardial ischemia-reperfusion injury mouse models, selective accumulation of two tracers could be detected in risk areas, which is related to the histological evidence of cell death. The results showed the ability of ^{99m}Tc-labeled Zn^{2+}-DPA complexes to detect cell death [33]. Expanding on this molecular design strategy, several ^{18}F-prosthetic groups can be conjugated to Zn cyclen for PET imaging, including ^{18}F-SFB (N-succinimidyl-4-[^{18}F] fluorobenzoate), ^{18}F-NFP (4-nitrophenyl-2-[^{18}F]fluoro propionate), ^{18}F-FET ([^{18}F]fluoroethyl p-toluenesulfonic acid), and Al^{18}F ([^{18}F]aluminum fluoride) with radiochemical yields of 85%, 76%, 15%, and 10%, respectively. The PET imaging and fluorescence microscopy results suggest that ^{18}F-FB-$DPAZn_2$ targets both the apoptotic and necrotic cells in tumors [34]. However, to overcome the limitations of high retention of radionuclide-labeled ZnDPA and Zn cyclen probes in the liver and intestine, the pharmacokinetics need to be further optimized prior to clinical trials.

14.3.2.2 Caspase-3/Caspace-7 Target Probes

The previous study has discovered a species of small molecules based mostly on the isatin sulfonamide moiety as selective, non-peptidic inhibitors of recombinant caspase-3 by high-throughput screening (K_i = 0.5 μM). X-ray co-crystal studies of an enzyme-inhibitor complex revealed that the carbonyl group at the three positions of isatin is covalently bound with the cysteine-163 thiolate to form the tetrahedral intermediate thiohemiacetal anion [35]. In recent years, isatin sulfonamides have been developed along with more than 230 different derivatives which have been reported for targeting the executing caspases in vitro and in vivo [36]. The ^{11}C labeling method of isatin sulfonamides used in PET imaging is mainly direct methylation by ^{11}C-CH_3I. ^{11}C-WC-98, a unique ^{11}C-labeled isatin analogue, was in vivo evaluated in the FAS-mediated hepatic cell apoptosis model; the result showed increased uptake in caspase-3 activated mice compared with the control [37]. However, a major disadvantage of ^{11}C-WC-98 is the relatively short physical half-life of 20.4 min, and isatin analogues were unable to distinguish different caspase-3 levels in vivo, like ^{18}F-WC-II-89 [38]. Studies showed that the liver and spleen accumulation of ^{18}F-WC-II-89 in cycloheximide-treated rats was twice as high as that of control group and correlated well with caspase-3 activity. ^{18}F-ICMT-11 is a promising imaging agent based on the isatin structure with EC50 of 0.5 nM for caspase-3 and 2.2 nM for caspase-7. The automated radiosynthesis of ^{18}F-ICMT-11 under GMP conditions has been verified to accord with clinical use criteria. In a stage I clinical study, the safety, biodistribution, and radiation dosimetry profiles of ^{18}F-ICMT-11 were evaluated in healthy controls [39]. After intravenous injection, ^{18}F-ICMT-11 radioactivity was rapidly accumulated in the kidneys and liver, subsequently excreted via renal and hepatobiliary routes within 3 h, which performed in accordance with the biodistribution in mice. Besides, relatively high gallbladder uptake was detected, following by a slowly washout into the gastrointestinal tract. The mean effective dose for whole-body irradiation was evaluated as 0.025 ± 0.004 mSv/MBq with no serious adverse events. The promising mechanistic and safety profile encourage the further clinical research to determine the potency of ^{18}F-ICMT-11 in tumor apoptosis caused by treatments.

Biodistribution studies and micro-PET findings suggested that ^{18}F-WC-4-116 could serve as a noninvasive imaging agent for detecting caspase activity during myocardial apoptosis in vivo [40]. However, as cell-penetrating agents, isatin-based agents have amphipathic character and are prefer to clear through the hepatobiliary route, which leads to high abdominal uptake in the gallbladder, liver, and intestine, exhibiting a suboptimal biodistribution profile. Moreover, caspase-detecting probes based on caspase inhibitor structure usually lack selectivity owing to nonspecific inhibition of various cathepsins, which dampens the enthusiasm for these probes.

14.3.2.3 Imaging of Apoptotic Membrane Imprint

The ApoSense family is a set of novel small non-peptidic fluorescent probes including DCC, NST-732, and dansyl-ML-10. It developed on the basis of Gla structure that is designed for apoptosis imaging without a fully elucidated mechanism. A widely accepted interpretation of the binding principle is that these ApoSense probes detect the apoptotic membrane imprint, including plasma membrane depolarization, acidification of the external cytosolic leaflet of plasma membrane, and the membrane phospholipid scramblase system activation, which took place early in the apoptotic process. In addition to the fluorescence properties, several ApoSense molecules have a fluorine atom that enables the radiolabeling with ^{18}F isotope for PET, such as ^{18}F-NST-732 and ^{18}F-ML-10 [41, 42]. Among them, ^{18}F-ML-10 is the most notable as a rationally designed molecule with an amphipathic compact structure and a molecular weight of 206 Da [43]. Preclinical studies using ^{18}F-ML-10 reported no specific accumulation of organs in the animals except the kidney and selective uptake by apoptotic cells. A phase I trial of ^{18}F-ML-10 on healthy volunteers showed high stability, favorable dosimetry of 15.4 ± 3.7 μSv/MBq, and suitable biodistribution, with predominantly renal excretion and fast clearance from nontarget organs in accordance with the mice, supporting further clinical development [44]. The application of ^{18}F-ML-10 was evaluated in ten patients to assess the treatment response of brain metastases following the radiation therapy in the brain. All patients received ^{18}F-ML-10 PET scan before radiotherapy as the baseline scan, and the follow-up scan was performed after nine or ten fractions of radiotherapy. An average change of 69.9% (36.3–100%) was found in early stage of ^{18}F-ML-10 uptake in the volume of interest (VOI) by voxel-based analysis, which was highly related to later changes in tumor anatomical dimensions obtained by MRI in 6–8 weeks after the final treatment ($r = 0.919$, $P < 0.001$) (Fig. 14.2) [45]. Another research demonstrated a methodology for measuring therapeutic response in patients with malignant glioblastoma multiforme (GBM) that underwent ^{18}F-ML-10 PET scans. It proposed a multimodal (^{18}F-ML-10 PET and MRI), multi-time point (baseline and early therapy assessment) approach to assess therapy response of GBM and may provide a novel approach for early response assessment and provide optimal management for cancer patients [46]. However, several defects were raised during the clinical application of ^{18}F-ML-10, including a weak affinity for apoptotic, a low absolute uptake values, a high baseline uptake due to excessive accumulation in tumors, and no significant uptake change of therapeutic evaluation in nude mice model of NSCL and lymphoma [47]. Therefore, further study is necessary to understand the cell-binding mechanism and to help validate the specificity of ^{18}F-ML-10.

14.3.2.4 Imaging Mitochondrial Membrane Potential

The mitochondrial membrane potential is formed due to the redox transformations during TCA cycle activity, and it also presents as an intermediate storage form of cellular energy during ATP synthesis. At the initiating phase of apoptosis, before the major morphology and biochemistry changes including externalization of membranous PS, the mitochondrial membrane potential decreases along with caspase cascade activation, providing a new method to assess apoptosis [48]. Because the mitochondria membrane potential is the highest in normal cells, phosphonium cations with sufficiently lipophilic and delocalized positive charge can penetrate the membrane lipid bilayer and accumulate in the inner membrane of the mitochondria. Consequently, loss of $\Delta\Psi$m caused by apoptosis results in a decline of phosphonium cation uptake. ^{18}F-Fluorobenzyl triphenylphosphonium (^{18}F-FBnTP), a PET voltage sensor, was first reported in 2007 by Madar et al [49] In vitro experiments showed that the dependence of ^{18}F-FBnTP uptake on membrane potential, including the $\Delta\Psi$m-dependent, plasma membrane potential ($\Delta\Psi$p)-dependent, and nonspecific binding, were about 80%, 10%, and 10%, respectively, which indicate that ^{18}F-FBnTP could mainly reflect the $\Delta\Psi$m changes. In vivo study of ^{18}F-FBnTP has been sued for detecting docetaxel-induced apoptosis in prostatic carcinoma models, revealing a 50% reduction in tumor radio-uptake 48 h after chemotherapy. In contrast, ^{18}F-FDG showed no significant change in tumor uptake on treatment response. Similarly, chemotherapy of breast cancer and lung cancer resulted in a significant decrease in tumor uptake of ^{18}F-FBnTP compared to the control group [50]. Other probes such as ^{18}F-MitoPhos_01 and ^{18}F-FPTP that target loss of $\Delta\Psi$m have also been described and evaluated, which showed the dependence on $\Delta\Psi$m and the potential for the detection of apoptosis. However, mitochondria-rich tissues can also concentrate probes, leading to high accumulation of radioactive in the stomach, spleen, intestine, and testis, especially in the heart. In addition, these probes present negative imaging on induction of apoptosis that are technically less attractive in contrast to the positive imaging with other PET apoptosis probes.

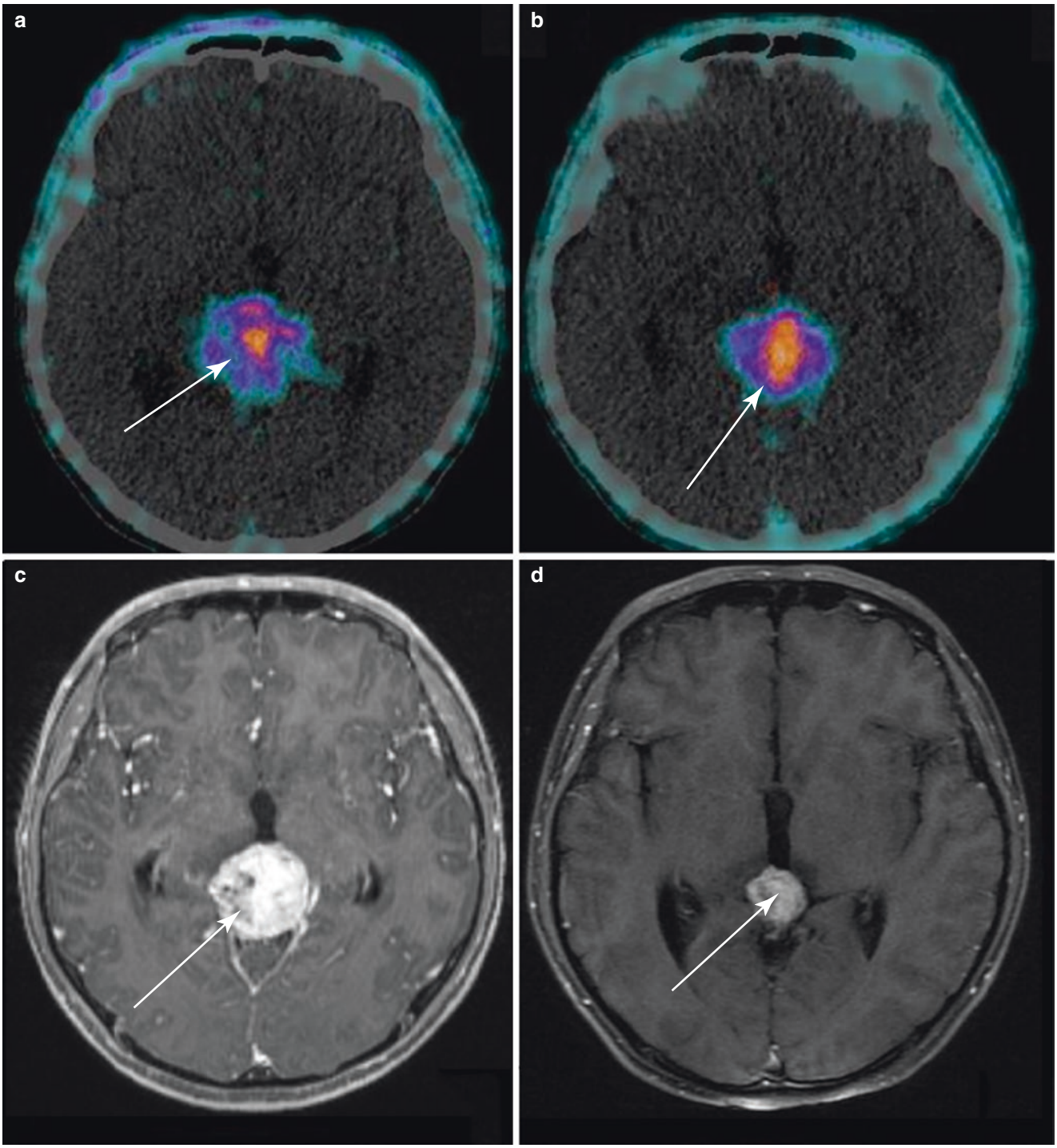

Fig. 14.2 The use of ^{18}F-ML-10 PET to assess apoptosis change in a patient with brain metastasis from germ cell cancer before and early after therapy (**a**, **b**, **c**, **d**, white arrows). (**a**) ^{18}F-ML-10 uptake at baseline PET of a patient shows a high tracer uptake of the third ventricle (SUVmean = 3.58). (**b**) After 24 h of CyberKnife therapy, the ^{18}F-ML-10 PET imaging shows a remarkably higher radioactivity uptake of the brain metastasis (SUVmean = 4.91). (**c**) T1-MRI at the baseline shows space-occupying lesion in the third ventricle corresponding to PET images with a gross tumor volume of 32.8 cm^3. (**d**) After 3 months of therapy, a reduced tumor volume was detected by T1-MRI (GTV = 16.5 cm^3) [45]

14.4 Summary

Cell death is an essential biological process. Apoptosis and necrosis are two distinctive processes of cell death with complex cross-talks. Necrosis is a casual, passive, and unregulated process of cellular death that is due to mechanical trauma and sudden metabolic failure, which are characterized by increased cytoplasmic vacuolation, organelle degeneration, condensation of chromatin into irregular patches, and rapid cytoplasmic swelling. In contrast, apoptosis is a highly controlled and regulated process without causing inflammation. From the receipt of apoptotic signals to the formation of apoptotic bodies, several characteristics in morphologic and biochemical events in cells have been researched extensively, including exposure of phosphatidylserine, activation of effector caspases, depolarization of the plasma and mitochondrial membranes, cytoplasmic shrinkage, nuclear condensation, and degradation of nuclear DNA. Apoptosis is associated with several diseases and responses to therapy. Apoptosis imaging could contribute to early evaluation of treatment effects, especially in cancer treatment. Nuclear imaging techniques such as PET and SPECT provide extremely deep tissue penetration and impressive sensitivity, and, therefore, their clinical application in many aspects is very attractive.

According to the molecular weight of the radiotracers, cell apoptosis imaging agents mainly fall into three categories: proteins, peptides, and small molecules. Radiolabeled protein probes, such as ^{99m}Tc-labeled annexin V, are the first to be investigated as apoptosis-detecting radioligands. Preclinical and clinical studies have confirmed that the accumulation of PS-directed probes correlates with apoptotic cells after therapy. However, the large molecular weight of protein limits its ability to penetrate the cell membrane; thus, protein probes are usually designed to binding with the biomarker on the surfaces of cells, such as PS and PE, which occurred both in apoptosis and necrosis. Another drawback of protein probes is suboptimal pharmacokinetic properties. Compared with protein, peptide probes and small molecules have been developed for detecting the intra- or extracellular hallmarks along the apoptotic cascade with advantageous clinical translation potentials. With favorable pharmacokinetic profile and a kit-based synthesis, radiolabeled duramycin is promising for further clinical application. ^{18}F-ML-10 is the first small-molecule agent for clinical imaging of apoptosis, showing exciting results in a few phase II clinical studies. ^{18}F-CP18, a peptide probe for caspase-3/caspase-7 imaging, has also showed good application prospects in clinical studies. Because of the favorable pharmacokinetic and safety characteristic of ^{18}F-ICMT-11, the QuIC-ConCePT project has selected it as a candidate radiotracer for clinical application. Although a lot of promising radiotracers for apoptosis imaging have been developed during the past decade, no apoptosis imaging agent has been approved for clinical application. A few features should be integrated to obtain to have an optimal tracer for clinical apoptosis imaging. The tracer should bind apoptotic cells with high affinity and specificity and detect apoptotic cells in forepart of the death process by preferably distinguishing with necrotic cells. Furthermore, the tracer should be suitable for in vivo use with minimal metabolism, which implies rapid distribution throughout the body and high accumulation in the apoptotic cells in vivo with the minimization of nonspecific tissue binding. Moreover, the probe should not have immunogenicity and toxicity. Finally, the probe should be adapted to daily clinical setting with feasibility of economical production. To achieve a high-quality image, in addition to desirable radiopharmaceuticals, the precise detection of the spatiotemporal occurrence of apoptosis remains highly a challenge to overcome. Addressing these challenges should be important to help promote future clinical application of one or more noninvasive probes for apoptosis imaging.

References

1. Kerr JF, Wyllie AH, Currie AR (1972) Apoptosis: a basic biological phenomenon with wide-ranging implications in tissue kinetics. Br J Cancer 26(4):239–257
2. Zeng W, Wang X, Xu P, Liu G, Eden HS, Chen X (2015) Molecular imaging of apoptosis: from micro to macro. Theranostics 5(6):559–582
3. Blankenberg FG (2008) In vivo detection of apoptosis. J Nucl Med 49(2):81S–95S
4. Tan ML, Ooi JP, Ismail N et al (2009) Programmed cell death pathways and current antitumor targets. Pharm Res 26(7):1547–1560
5. Galluzzi L, Bravo-San Pedro JM, Vitale I, Aaronson SA, Abrams JM, Adam D, Alnemri ES, Altucci L, Andrews D, Annicchiarico-Petruzzelli M et al (2015) Essential versus accessory aspects of cell death: recommendations of the NCCD. Cell Death Differ 22:58–73
6. Cotter TG (2009) Apoptosis and cancer: the genesis of a research field. Nat Rev Cancer 9(7):501–507
7. Tan ML, Ooi JP, Ismail N, Moad AI, Muhammad TS (2009) Programmed cell death pathways and current antitumor targets. Pharm Res 26(7):1547–1560
8. Goh AM, Xue Y, Leushacke M, Li L, Wong JS, Chiam PC, Rahmat SA, Mann MB, Mann KM, Barker N, Lozano G, Terzian T, Lane DP (2015) Mutant p53 accumulates in cycling and proliferating cells in the normal tissues of p53 R172H mutant mice. Oncotarget 6(20):17968–17980
9. Peng Y-T, Chen P, Ouyang R-Y, Song L (2015) Multifaceted role of prohibitin in cell survival and apoptosis. Apoptosis 20(9):1135–1149
10. Kiraz Y, Adan A, Kartal YM, Baran Y (2016) Major apoptotic mechanisms and genes involved in apoptosis. Tumour Biol 37(7):8471–8486
11. Fulda S (2009) Tumor resistance to apoptosis. Int J Cancer 124(3):511–515
12. Mohammad RM, Muqbil I, Lowe L et al (2015) Broad targeting of resistance to apoptosis in cancer. Semin Cancer Biol 35(Supplement):S78–S103
13. Heneweer C, Grimm J (2011) Clinical applications in molecular imaging. Pediatr Radiol 41(2):199–207

14. Lee BW, Olin MR, Johnson GL, Griffin RJ (2008) In vitro and in vivo apoptosis detection using membrane permeant fluorescent labeled inhibitors of caspases. Methods Mol Biol 414:109–135
15. Niu G, Chen X (2010) Apoptosis imaging: beyond annexin V. J Nucl Med 51(11):1659–1662
16. Galluzzi L, Vitale I, Abrams JM et al (2012) Molecular definitions of cell death subroutines: recommendations of the Nomenclature Committee on Cell Death. Cell Death Differ 19(19):107–120
17. Cai J, Li F (2013) Single-photon emission computed tomography tracers for predicting and monitoring cancer therapy. Curr Pharm Biotechnol 14(7):693–707
18. Kemerink GJ, Liu X, Kieffer D et al (2003) Safety, biodistribution, and dosimetry of ^{99m}Tc-HYNIC-annexin V, a novel human recombinant annexin V for human application. J Nucl Med 44(6):947–952
19. Rottey S, Slegers G, Van Belle S, Goethals I, Van de Wiele C (2006) Sequential ^{99m}Tc-hydrazinonicotinamide-annexin V imaging for predicting response to chemotherapy. J Nucl Med 47(11):1813–1818
20. Schaper FL, Reutelingsperger CP (2013) ^{99m}Tc-HYNIC-annexin A5 in oncology: evaluating efficacy of anti-cancer therapies. Cancer 5(2):550–568
21. Hardy JW, Levashova Z, Schmidt TL, Contag CH, Blankenberg FG (2015) ^{99m}Tc-annexin V-128 SPECT monitoring of splenic and disseminated listeriosis in mice: a model of imaging sepsis. Mol Imaging Biol 17(3):345–354
22. Belhocine TZ, Blankenberg FG, Kartachova MS et al (2015) ^{99m}Tc-Annexin A5 quantification of apoptotic tumor response: a systematic review and meta-analysis of clinical imaging trials. Eur J Nucl Med Mol Imaging 42(13):2083–2097
23. Perreault A, Knight JC, Wang M, Way J, Wuest F (2016) ^{18}F-labeled wild-type annexin V: comparison of random and site-selective radiolabeling methods. Amino Acids 48(1):65–74
24. Lu C, Jiang Q, Hu M, Tan C, Yu H, Hua Z (2015) Preliminary biological evaluation of ^{18}F-FBEM-Cys-Annexin V a novel apoptosis imaging agent. Molecules 20(3):4902–4914
25. Yanjie H, Biao L, Zizheng W et al (2010) Automatic synthesis of N-succinimidyl 4-^{18}F-fluorobenzoate and its utility for ^{18}F labeled C2A donain of synaptotagmin I. Chin J Nucl Med Mol Imaging 30(6):414–418
26. Song S, Xiong C, Lu W, Ku G, Huang G, Li C (2013) Apoptosis imaging probe predicts early chemotherapy response in preclinical models: a comparative study with ^{18}F-FDG PET. J Nucl Med 54(1):104–110
27. Zhao M, Li Z (2012) A single-step kit formulation for the ^{99m}Tc-labeling of HYNIC-Duramycin. Nucl Med Biol 39(7):1006–1011
28. Elvas F, Vangestel C, Pak K et al (2016) Early prediction of tumor response to treatment: preclinical validation of ^{99m}Tc-Duramycin. J Nucl Med 57(5):805–811
29. Yao S, Hu K, Tang G et al (2014) Positron emission tomography imaging of cell death with ^{18}F-FPDuramycin. Apoptosis 19(5):841–850
30. Xia CF, Chen G, Gangadharmath U et al (2013) In vitro and in vivo evaluation of the caspase-3 substrate-based radiotracer ^{18}F-CP18 for PET imaging of apoptosis in tumors. Mol Imaging Biol 15(6):748–757
31. Bao-shi Z, Nai-kang Z, Hui W et al (2011) Imaging of apoptosis with ^{18}F-FP-peptide focused on the evaluation of tumor response to chemotherapy. Chin J Nucl Med Mol Imaging 2:84–89. [中文发表]
32. Doss M, Kolb HC, Walsh JC et al (2013) Biodistribution and radiation dosimetry of ^{18}F-CP-18, a potential apoptosis imaging agent, as determined from PET/CT scans in healthy volunteers. J Nucl Med 54(12):2087–2092
33. Wyffels L, Gray BD, Barber C et al (2011) Synthesis and preliminary evaluation of radiolabeled bis (zinc(II)-dipicolylamine) coordination complexes as cell death imaging agents. Bioorg Med Chem 19(11):3425–3433
34. Sun T, Tang G, Tian H et al (2015) Positron emission tomography imaging of cardiomyocyte apoptosis with a novel molecule probe ^{18}F-FP-DPAZn2. Oncotarget 6(31):30579–30591
35. Lee D, Long SA, Adams JL et al (2000) Potent and selective nonpeptide inhibitors of caspases 3 and 7 inhibit apoptosis and maintain cell functionality. J Biol Chem 275(21):16007–16014
36. Limpachayaporn P, Schafers M, Haufe G (2015) Isatin sulfonamides: potent caspases-3 and -7 inhibitors, and promising PET and SPECT radiotracers for apoptosis imaging. Future Med Chem 7(9):1173–1196
37. Chen DL, Zhou D, Chu W et al (2012) Radiolabeled isatin binding to caspase-3 activation induced by anti-Fas antibody. Nucl Med Biol 39(1):137–144
38. Zhou D, Chu W, Rothfuss J et al (2006) Synthesis, radiolabeling, and in vivo evaluation of an ^{18}F-labeled isatin analog for imaging caspase-3 activation in apoptosis. Bioorg Med Chem Lett 16(19):5041–5046
39. Challapalli A, Kenny LM, Hallett WA et al (2013) ^{18}F-ICMT-11, a caspase-3-specific PET tracer for apoptosis: biodistribution and radiation dosimetry. J Nucl Med 54(9):1551–1556
40. Thukkani AK, Shoghi KI, Zhou D et al (2016) PET imaging of in vivo caspase-3/7 activity following myocardial ischemia-reperfusion injury with the radiolabeled isatin sulfonamide analogue ^{18}F-WC-4-116. Am J Nucl Med Mol Imaging 6(2):110–119
41. Xiaojun Z, Li Y, Jian L et al (2016) Preparation and biodistribution of 2-(5-[18F]fluoro-pentyl)-2-methyl-malonic acid and its primary clinical application[J]. Chin J Nucl Med Mol Imaging 36(2):131–136. [中文发表]
42. Basuli F, Wu H, Shi ZD et al (2012) Synthesis of ApoSense compound [^{18}F]2-(5-(dimethylamino)naphthalene-1-sulfonamido)-2-(fluoromethyl)butanoic acid ([^{18}F]-NST732) by nucleophilic ring opening of an aziridine precursor. Nucl Med Biol 39(5):687–696
43. Cohen A, Shirvan A, Levin G, Grimberg H, Reshef A, Ziv I (2009) From the Gla domain to a novel small-molecule detector of apoptosis. Cell Res 19(5):625–637
44. Hoglund J, Shirvan A, Antoni G et al (2011) ^{18}F-ML-10, a PET tracer for apoptosis: first human study. J Nucl Med 52(5):720–725
45. Sun L, Zhou K, Wang W et al (2018) ^{18}F-ML-10 imaging for assessment of apoptosis response of intracranial tumor early after radiotherapy by PET/CT. Contrast Media Mol Imaging 2018(3):1–9
46. Oborski MJ, Laymon CM, Qian Y, Lieberman FS, Nelson AD, Mountz JM (2014) Challenges and approaches to quantitative therapy response assessment in glioblastoma multiforme using the novel apoptosis positron emission tomography tracer F-18 ML-10. Transl Oncol 7(1):111–119
47. Bauwens M, De Saint-Hubert M, Cleynhens J, Vandeputte C, Li J, Devos E (2013) In vitro and in vivo comparison of ^{18}F and ^{123}I-labeled ML10 with ^{68}Ga-Cys2-AnxA5 for molecular imaging of apoptosis. Q J Nucl Med Mol Imaging 57(2):187–200
48. Ly JD, Grubb DR, Lawen A (2003) The mitochondrial membrane potential (deltapsi(m)) in apoptosis; an update. Apoptosis 8(2):115–128
49. Madar I, Ravert H, Nelkin B et al (2007) Characterization of membrane potential-dependent uptake of the novel PET tracer ^{18}F-fluorobenzyl triphenylphosphonium cation. Eur J Nucl Med Mol Imaging 34(12):2057–2065
50. Madar I, Huang Y, Ravert H et al (2009) Detection and quantification of the evolution dynamics of apoptosis using the PET voltage sensor ^{18}F-fluorobenzyl triphenyl phosphonium. J Nucl Med 50(5):774–780

Radionuclide Gene and Reporter Gene Imaging

15

Xiaoli Lan, Min Ye, Pengxin Qiao, and Wenxia Wang

15.1 Antisense Gene Imaging

In the 1970s, the Johns Hopkins University School of Medicine (JHUSOM) and Harvard Medical School discovered that antisense oligonucleotides (ASON) could actually block the expression of specific genes. Since then, a new genetic engineering technology—antisense technology—has emerged. According to the principle of complementary base pairing, ASON is specifically used to bind the genes or mRNA in cells and regulate gene expression by blocking the transcription of gene or translation of mRNA. After the artificially synthesized radionuclide-labeled ASON is introduced into the body, it binds specifically to intracellular target genes or mRNAs through the principle of complementary base pairing, and then an imaging instrument is used to display the target genes or tissue that is overexpressed in genes, thereby forming a new diagnosis method—radionuclide antisense gene imaging [1, 2].

15.1.1 Antisense Targeting and Radionuclide Antisense Imaging

In 1954, Watson-Crick and Hoogsteen proposed the Watson-Crick model and the principle of complementary base pairing; they point out that DNA is usually double-stranded and the two chains use phosphate sugar as backbone, running in opposite directions. The nucleobases can be hybridized by the creation of hydrogen bonds, which are formed between adenine (A) and thymidine (T), and guanine (G) and cytosine (C). The introduction of this nucleic acid pairing model has brought epoch-making significance to the development of biomedicine; one of the innovative ideas was the antisense treatment proposed by Belikova AM in 1967, that is, use of shorter oligonucleotide sequences to specifically bind the DNA or mRNA sequences of certain genes that cause the disease, thereby rendering them inhibited.

Oligonucleotides (SON) are small chains of a few nucleotides which have only 20 bases in length, which are the elementary units of nucleic acid (DNA or RNA), and have a molecular weight of about 4000–10,000 daltons. ASON is an unmodified or chemically modified single oligomer that is designed to contain a sequence complementary to a targeting nucleic acid. The idea of antisense targeting is based on the specific complementary pairing of nucleic acids which is participating in the regulation of the expression of related genes by means of base pairing binding with ASON and target RNA.

According to the mechanism of antisense targeting, introducing labeled antisense oligonucleotides as radiotracers into the human body; specific binding of the target gene in vivo by the principle of base pair complementary pairing, real-time dynamic monitoring of diseased tissue gene expression can be achieved at the overall level with an appropriate radionuclide imaging equipment. Antisense imaging reveals changes in the molecular level of organisms, and the first step in many diseases is the change of genes. Therefore, antisense imaging has been achieved earlier and is a more accurate diagnosis of disease. The principle of radionuclide antisense imaging is shown in Fig. 15.1.

15.1.2 Molecular Probes of Antisense Imaging

The design of successful radionuclide antisense imaging and probes needs to consider the following elements: (1) prepare ASON fragments that specifically bind to the target gene; (2) select radionuclide that is suitable for imaging and a simple effective labeling method; (3) antisense imaging requires stable delivery of ASON, for example, to be able to withstand the degradation of enzymes, such as nucleases, and to maintain a lower binding rate to matrix proteins in the circulation; (4) radiolabeled antisense probes need to escape the body's immune system, localize in cells of interest, and hybridize to the target mRNA; and (5) antisense imaging

X. Lan (✉) · M. Ye · P. Qiao · W. Wang
Department of Nuclear Medicine, Union Hospital, Tongji Medical College, Huazhong University of Science and Technology, Wuhan, P. R. China

G. Huang (ed.), *Nuclear Medicine in Oncology*, https://doi.org/10.1007/978-981-13-7458-6_15

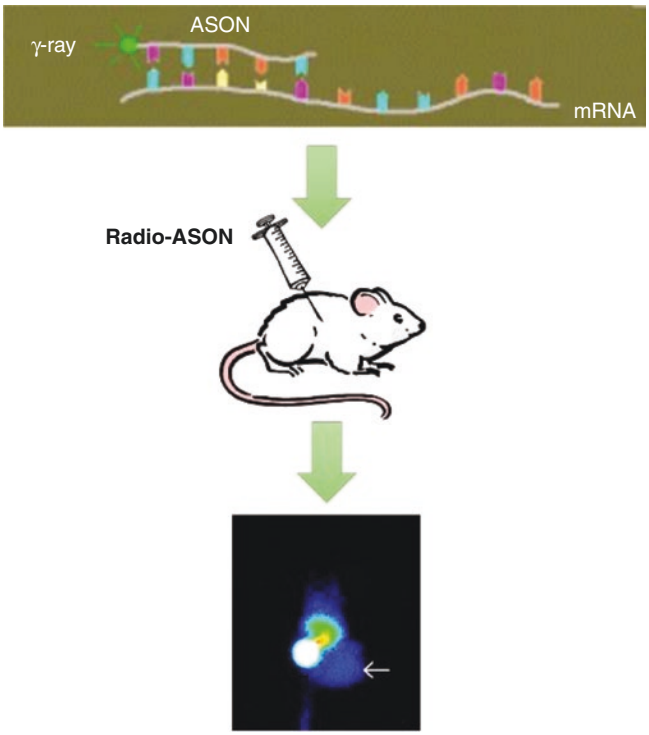

Fig. 15.1 The principle of radionuclide antisense imaging

probes must be able to stay at the targeted site for a longer time while being rapidly cleared in nontargeted organs and tissues so that good contrast can be obtained in SPECT or PET imaging. Although extensive exploration has been performed on imaging probes and some in vitro results have shown positive significance, there are still many challenges in achieving in vivo imaging.

15.1.2.1 The Selection and Design of Antisense Oligonucleotides

Radionuclide antisense imaging is based on the principle of complementary base pairing and specifically binds to the target gene. In theory, as long as there is an overexpression of certain DNA or mRNA in the target tissue, the corresponding oligonucleotide can be artificially synthesized to make a molecular probe labeled with nuclide. But in fact, choosing a suitable antisense sequence is a time-consuming and costly job [3], because antisense DNA has a much weaker affinity for double-stranded regions than single-stranded regions. To increase the stability and recognition by translation regulatory proteins, mRNAs would form in-chain base pairs in many regions, forming complex secondary structures such as hairpins, loops, and corniform, making the antisense mechanisms harder to function. Antisense sequences are usually selected for single-bond regions in mRNAs, such as promoters and their adjacent sequences, 5′ or 3′ end untranslated regions, etc., to reduce interference of secondary structures. Even so, this choice is not necessarily appropriate because proteins are likely to bind to these regions to increase their stability, thereby preventing their binding to antisense DNA [2].

In addition, the specificity of antisense inhibition also depends on the length of the ASON. This is because the length of ASON directly affects the specificity, accessibility, and stability of binding to the target genes, as well as whether it can be recognized by endonucleases, and the permeability to cell membranes. Short ASON will affect the specificity of its binding. If it is too long, it will be easy to distort or form a secondary structure, which will affect its binding to target mRNA. Besides, the length of ASON is also positively correlated with the cost of preparation of antisense probes. When designing ASON, the length is generally controlled at 15–20 base pairs.

15.1.2.2 The Modification of the Antisense Oligonucleotides

In addition to sequence specificity, stability in animals is also an essential requirement of ASON for imaging applications. Natural ASON is extremely sensitive to the degradation of exonuclease and endonuclease in vivo and in vitro. Once ASON is injected into an animal, the effective amount of antisense RNA is rapidly reduced by the RNase in the body, while the remaining antisense RNA that has not been degraded is dispersed throughout the body of the animal [4], rather than being concentrated at the lesion. In order to increase the in vivo stability of antisense oligonucleotide, various structure modifications have been performed in its backbones, such as modifying phosphorus-oxygen bonds, carbon or sulfur atoms substituting phosphorus atoms, and introducing N-containing derivatives into the nucleotide backbone, etc. Among them, the researches of methylation and thiolation in the modification of phosphorus-oxygen bonds are relatively mature. In addition, using methyl groups to replace alcohol groups is called methylation, and substituting P-S bonds by P-O bonds is a process known as thiolation.

Adding phosphate group, glycosyl, or purine, pyrimidine to the oligonucleotide can significantly enhance its ability to resist nuclease, but at the same time, it also affects the ability of the probe to penetrate the membrane and its affinity for the target sequence. Until now, none of the numerous modified structures are perfect, and each has its own pros and cons.

15.1.2.3 The Labeling of Radionuclides

Single-stranded or double-stranded DNA, RNA and antisense oligonucleotides can be labeled with multiple radionuclides for in vitro evaluation [5]. In early antisense hybridization techniques, most radiolabels are made by incorporating ^{3}H-, ^{14}C-, and ^{35}S-labeled nucleotides into

DNA or RNA molecules. Although ^{32}P or ^{35}P emitting β-rays have been used for in vitro hybridization experiments, they are not suitable for in vivo imaging.

The strategy of radionuclide labeling SON or ASON is very limited for the purpose of SPECT or PET in vivo imaging, because only C, H, O, N, and P are the main elements of the oligonucleotide. There is no metal atom in the oligonucleotide body, and it cannot be directly replaced by γ-ray-emitting nuclides, which makes SPECT imaging agent difficult to prepare. When labeled with positron-emitting radionuclides, the half-lives of ^{11}C, ^{15}O, and ^{13}N are very short, which make it difficult to successfully label and image at the desired time. Due to these existing characteristics, ASON needs to be chemically modified at the 3′ or 5′ end to be suitable for radiolabeling, thereby achieving high yield, high specific activity, and high stability characteristics [1, 6]. The selection of suitable radionuclides and appropriate labeling methods is an important issue that must be considered in antisense imaging.

15.1.3 Current Status of Radionuclide Antisense Imaging

Since the concept of antisense imaging was proposed, international and domestic academics conducted a series of tumor antisense imaging studies. Dewanjee [7] first performed a complete antisense imaging study in 1994. They used DTPA as a chelator, and a 15-mer thiol-oligonucleotide with ^{111}In-labeled complementary to the c-myc mRNA sequence was used as the experimental group and a sense oligonucleotide as a control study. The results showed that the uptake of ASON by tumor cells was ten times higher than that of the control group, with fast uptake and high target/nontarget ratio. In vivo imaging shows 8–10% of the thiol-oligonucleotide aggregated in the tumor after 0.5 h since the injection of labeled probe, whereas the control group was less than 1%. The labeled probe ratios on tumor/blood and tumor/muscle were as high as 3.55 ± 0.23 and 24.48 ± 3.27, respectively.

On this basis, with the development of molecular biology and the improvement of antisense imaging technology, more and more scholars have invested in antisense imaging research. In 1996, Cammilleri [8] injected ^{125}I-labeled ASON which were complementary to TGF mRNA into the human breast cancer animal and found that 15% injection dose (ID) was in tumors within 1 h after the injection of the marker; however, 90% of the radioactivity was transferred from the tumor site to the intestine and kidney within 4 h, and only 1% of the radioactivity remained in the tumor at 24 h. The Hantowich DJ team has been working on antisense imaging for a long time, with PNA imaging studies showing that ^{99m}Tc-PNA has higher in vivo stability and better metabolic dynamics for in vivo imaging [9]. The left leg of the mice was intramuscularly injected with polystyrene beads containing the target PNA, and magnetic beads without PNA were injected into the right leg as a control. After tail vein injection of ^{99m}Tc-PNA, the results of 2.5 h and 24 h in vivo distribution studies showed that PNA was rapidly cleared in vivo with a half-life of approximately 2 h. At 2.5 h after injection, the maximum uptake of the kidney was only 1.5% ID/g, and the total radioactivity of all sampling tissues at 24 h was less than 0.07%ID/g. After peritoneal injection of ^{99m}Tc-PNA, at 23 h, whole-body imaging showed only kidney and bladder images, and the ratio of radioactivity in the left leg model tissue/right leg was 6:1. Through this experiment, it is subtly demonstrated that antisense hybridization theory is still feasible in vivo [9].

15.1.4 Problems and Prospects of Radionuclide Antisense Gene Imaging

With the diversification of radionuclide labeling techniques and advances in molecular biology techniques, the concept of antisense imaging has been elucidated in in vitro cell experiments and has been initially successfully demonstrated in in vivo imaging. However, there are still many difficulties in antisense imaging in vivo, including the stability of ASON in vivo, the transfer and transport of labeled probes to target cells, the specific binding to targeted mRNA, and the concentration of targeted mRNA, etc.; one of the most important factors is the inability of the radionuclide labeling ASON to hybridize with the targeted mRNA after internalization into the cell.

Although the use of radiolabeled ASON molecular probes has provided exciting results in both in vitro and in vivo imaging, all studies have been limited to cell and animal experiments, so there is still much work to be done to transform antisense imaging into the clinic. This includes simplification of ASON probe synthesis, chemical modification of radiolabeling processes, increasing the in vivo stability, and enhancing the capability of specific hybridization with target mRNAs and the like. In vivo imaging needs to meet certain conditions, such as the need for labeled probes to overcome biological barriers during transport in vivo, accurate in vivo targeting, in vivo signal amplification, effective retention in target tissues, rapid clearance in nontarget tissues, etc. Almost all diseases are caused by abnormal gene expression or abnormal function of expression products. In theory, antisense imaging can diagnose many diseases including cancer, hereditary diseases, inflammation, and viral infection at the gene level. This huge application prospect deserves more in-depth research and exploration of antisense imaging.

15.2 Reporter Gene Imaging

Reporter gene imaging is an indirect imaging strategy. By combining the reporter gene and probe together, the accumulation of the probe can reflect the activity of the reporter gene product, thereby providing indirect information about the level of reporter gene expression and the endogenous signal or transcription factors that trigger the expression of the reporter gene. A probe that is specifically combined with the product of the reporter gene expression can be used to determine varieties of the target genes of interest coupled with this reporter gene. Also, by having different objects, this probe can also be used to visualize multiple biological and molecular genetic processes without developing different kinds of specific molecular probe. In addition, it's easier to develop a reporter gene which can be applied in clinical practice more quickly than constructing a new molecular probe. Furthermore, it requires less effort and is more economical than the direct imaging strategies [10]. Based on these advantages, reporter gene imaging is widely applied in experimental animal studies.

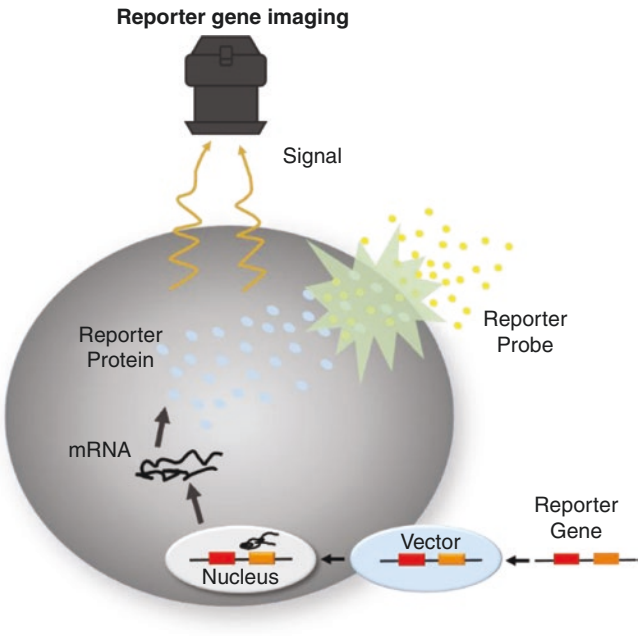

Fig. 15.2 The principle of reporter gene imaging

15.2.1 Principles for Reporting Gene Imaging

Reporter gene imaging is a process which includes transfection of the reporter gene into the target cell, followed by binding of the radiolabeled reporter probe with the expression product of the reporter gene, thereby developing the capabilities of acquiring the imaging signals. The accumulation of the probe reveals the quantity or the activity of the reporter gene product which provides indirect information about the level of reporter gene expression and the endogenous signal or transcription factors which trigger the expression of the reporter gene. What's more, the localization, level, migration, duration, etc. of reporter proteins in vivo that are expressed by the specific gene are also revealed. The most important principle of the reporter gene imaging is that if transcription of the reporter gene doesn't occur in vivo, the reporter probe won't accumulate. Otherwise, if the transcription of the reporter gene occurs under the control of a specific promoter whose product is a single-stranded RNA molecule known as messenger RNA, then the mRNA molecule will be translated to a new protein which will combine with the probe producing a detectable imaging signal. The principle of reporter gene imaging is shown in Fig. 15.2.

The following are the features that an ideal reporter gene imaging should possess. First, the reporter gene should not be expressed in the normal host cells. Second, the specific reporter probe should only accumulate in the site that the reporter gene expression appears. Third, if the reporter gene doesn't express, the probe shouldn't accumulate in vivo. Fourth, the reporter gene product should not be able to trigger an immune response. Fifth, the reporter probe should be stable in vivo, so that it won't be metabolized until it reaches its target. Sixth, the probe should have a rapid blood clearance which contributes to detect the specific signals. Seventh, the reporter gene and its metabolites should not be cytotoxic. Eighth, apart from the transgenic application, the reporter gene and its promoter should be available in different sizes for easy manipulation and construction of reporter vectors, for example, plasmid and virus. Ninth, the probe shouldn't be blocked by the biological barrier before reaching the target site. Tenth, the imaging signal should be well correlated with the amount of the reporter gene product in vivo [11], for instance, the mRNA and its protein. But the problem is there is no such reporter gene or probe which meets these criteria. Therefore, based on different purposes, multi-functional reporter genes are being developed with the aim of monitoring the expression of many kinds of reporter genes and also be used in different imaging systems. In sum, the reporter gene imaging has a promising application prospect in the research of biomedical and translational medicine [12–14].

15.2.2 Classification and Different Imaging Techniques of Reporter Gene Imaging

Currently, the reporter gene imaging can be classified into two categories on the basis of the different kinds of reporter gene-encoding products. These are enzyme-based reporter gene imaging and receptor-based or transporter-based reporter gene imaging. According to different imaging techniques, the reporter gene imaging also has a developed

Table 15.1 The comparison of several imaging techniques of reporter gene imaging

	PET	SPECT	MRI	BLI	FLI
Sensitivity	High 10^{-11}–10^{-12} M	Middling 10^{-9}–10^{-11} M	Low 10^{3}–10^{5} M	Very high	Moderate low
The spatial resolution	Middling	Middling	Excellent three-dimensional spatial resolution	Low imaging depth	Low imaging depth
The time of image acquisition	Quick (min)	Quick (min)	Slow	Very fast (seconds to minutes)	Very fast (seconds to minutes)
The limit of the clinical substrate	+	+++	Contrast medium can be acquired (but it always needs a heavy dosage)	No	No
Reporter gene	Herpes simplex virus type 1 thymidine kinase (HSV1-tk) and its mutant, dopamine-D2 receptor, norepinephrine transporter, sodium iodide symporter (NIS), estrogen receptor (ER), somatostatin subtype 2 receptor (SSTR2)		Transferrin receptors (TfR), beta-galactosidase, tyrosinase ferritin (Tf)	Luciferase (firefly, beetle, renilla, gaussia)	Fluorescent protein (red, green)
Advantages	Direct quantitative, high sensitivity, good spatial resolution	Direct quantitative, the radiopharmaceutical and the imaging system are easily acquired than PET	Best imaging resolution and anatomic information, no radiation	Low cost	Low cost, it doesn't need the substrate
Disadvantages	Radiation, higher cost	Radiation	Higher cost, it doesn't offer the metabolic information	It hasn't been used in clinical practice and can't acquire direct quantitive information	It can't acquire direct quantitive information

complete system of radionuclide imaging, magnetic resonance imaging, and optical imaging. These three imaging techniques have its unique advantages and disadvantages, and the most promising imaging technique among them is the radionuclide imaging system (Table 15.1).

15.2.2.1 Radionuclide Imaging

Radionuclide imaging techniques mainly include single-photon emission computed tomography (SPECT) and positron emission tomography (PET). Based on the nuclear medicine imaging techniques, the reporter gene imaging that monitors the transplanted stem cells in vivo mainly has these four varieties. (1) Enzyme/substrate type: Herpes simplex virus 1 thymidine kinase (HSV1-TK) and its mutant have been used as a reporter gene of nuclear medicine [15–20]. Figure 15.3 shows the principle of this type. (2) Receptor/ligand type: A gene that produces transmembrane receptor has been used as a nuclear medicine reporter gene, for instance, the dopamine-D2 receptor, estrogen receptor (ER), and somatostatin subtype 2 receptor (SSTR2). (3) Transporter type: it is also called transporter/substrate reporter gene system that mainly includes norepinephrine transporter, the sodium iodide symporter (NIS), [21]and so on. (4) Other reporter gene systems contain a fragment of antigen gene or antibody gene, the transferring GGC peptide fusion gene, tyrosine gene, and so on. Table 15.2 illustrates the radionuclide imaging types, reporter genes, and the radiolabeled reporter probes that are frequently used.

15.2.2.2 Optical Imaging

The two popular optical imaging modalities in vivo in living animal models are fluorescence and bioluminescence imaging techniques. The frequently used reporter genes are green fluorescent protein gene and firefly luciferase gene. The main advantages of the optical imaging are the following: There is no radiation, and it can constantly be monitored in real time with high sensitivity. What's more, it's cost-effective. However, the challenge is that the emission light has a limited tissue penetration depth (a few millimeters to a few centimeters), and also there is scattering, so the limited spatial resolution and the poor anatomic localization capability of optical imaging need to be improved. Therefore, this imaging technique is mainly used in the observation of surface lesion and small animal research at present.

15.2.2.3 Magnetic Resonance Imaging Technique

In contrast to radionuclide imaging and optical imaging, the magnetic resonance imaging approaches exhibit a higher spatial resolution and soft-tissue resolution. It can clearly show the anatomic structure, and at the same time, it can also acquire accurate, precise analysis of the anatomic localization and

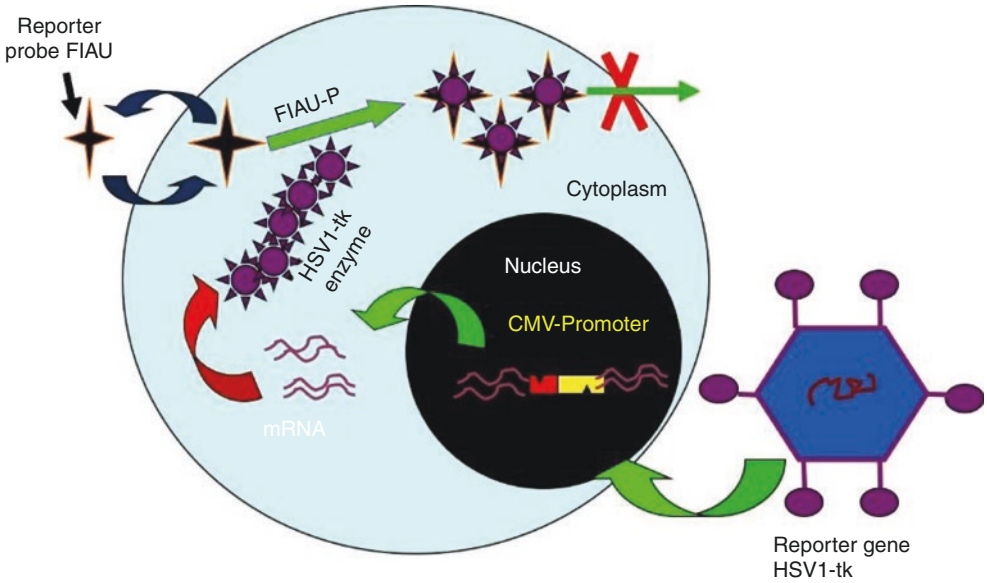

Fig. 15.3 The principle of herpes simplex virus 1 thymidine kinase (HSV1-tk) as a reporter gene for radionuclide reporter imaging with radiolabeled FIAU as probe

Table 15.2 Reporter gene and probe that radionuclide imaging uses

Types	Reporter gene	Radiolabeled reporter probe
Enzyme/ substrate type	HSV1-tk	[^{14}C/^{123}I/^{124}I/^{125}I/^{131}I]FIAU, [^{11}C/^{14}C/^{18}F]FMAU, [^{18}F/^{76}Br]FBAU, [^{18}F]FCAU, [^{3}H]FEAU,[^{3}H/^{18}F] FFAU, [^{18}F]FFEAU,[^{18}F]FPAU, [^{18}F]FBrVAU, [^{18}F]FTMAU, [^{123}I/^{125}I] FIRU, [^{18}F]FGVC, [^{3}H]PCV, [^{18}F]FPCV, [^{18}F]FHPG, [^{18}F]FHBG, [^{11}C]ABE
	HSV1-sr39tk	[^{3}H]PCV, [^{14}C]FIAU, [^{18}F]FHBG
	Cytosine deaminase (CD)	[^{18}F]fluorocytosine
	LacZ	[^{125}I] PETG, [^{11}C] β-galactosyl triazoles
Receptor/ ligand type	Dopamine-D2 receptor (D2R)	[^{18}F]FESP, [^{11}C]Raclopride, [^{11}C]N-methylspiperone
	Somatostatin subtype 2 receptor (SSTr2)	[^{18}F/^{64}Cu/^{67}Ga/^{68}Ga/^{86}Y/^{111}In/^{123}I]-octreotide, ^{99m}Tc-depreotide (P829), ^{99m}Tc-vapreotide, ^{68}Ga-DOTATOC
	Estrogen receptor (ER)	[^{18}F]FES
Transporter type	The sodium iodide symporter (NIS)	^{123}I, ^{124}I, ^{125}I, ^{131}I, ^{99m}TcO4^{-},^{76}Br^{-}
	Norepinephrine transporter (NET)	[^{131}I]MIBG, [^{11}C]mHED
	Dopamine transporter (DAT)	^{99m}Tc-TRODAT-1

quantity from the molecular imaging features of the deep tissue. At present, the reporter genes that can be imaged by MRI frequently are tyrosinase gene, beta-galactosidase gene, and transferrin receptor gene. But the exogenous contrast medium is crucial when these reporter genes are imaged by MRI. The challenges that the MRI reporter gene imaging faces are whether these substances can overcome the biological barrier and be removed from the blood and non-specific tissue.

15.2.3 Application of Reporter Gene Imaging

The reporter gene imaging has several applications. For example, the reporter gene imaging technique is a noninvasive assessment of internal molecular event. And then it can also noninvasively visualize localization, quantification, and duration of the transgene expression that will quantitatively evaluate the transfer rates of gene therapy. Furthermore, it can also be used to study the protein-protein interaction and monitor the migration, localization, and survival rates of the transplanted cells in the cell-based therapy.

15.2.3.1 Monitoring the Gene Therapy

Although the research of gene therapy has been widely conducted, there are still some problems that need to be solved. Therefore, it is unknown whether the therapeutic gene expressions are successful in the target site or the distribution is accurate. What is known is that this information can be acquired by taking samples of the target tissue to evaluate the gene expression and it is an invasive method. In order to

estimate the gene expression over time, several consecutive biopsies need to be done. Combining the reporter gene with therapeutic gene together and then conducting a noninvasive reporter gene imaging will help us indirectly in visualizing the localization, quantification, and duration of the therapeutic gene expression by evaluating the reporter gene expression. This method has an overwhelming advantage in monitoring and evaluating the efficiency of the human gene therapy [22].

15.2.3.2 Tracking the Migration of the Transplanted Cells

Cell-based therapy has received much attention in recent years. Whether the transplanted cells get localized in the target or survive in vivo triggering the therapeutic responses still requires more effective methods to be monitored. Biopsy is the golden standard when assessing these problems, but it is not appropriate to be observed for several consecutive times because of its invasive feature. Reporter gene imaging can noninvasively track the migration, biodistribution, and localization of these cells.

In 2003, Wu [23] initially track the in vivo progression of the stem cells transplanted into the myocardium successfully for 2 weeks by using PET and bioluminescence imaging techniques. Subsequently, Willmann [16] described the feasibility and quantitative analysis of the reporter gene imaging of the human mesenchymal stem cells transplanted into the myocardium in large animals (pig) by using clinical PET. In recent years, with the development of multimodality molecular imaging, multimodal molecular imaging has already been applied to monitor the transplanted stem cells in the myocardium successfully. Higuchi et al. [24] combine PET and MRI techniques to visualize the survival and localization of the transplanted cells in the myocardium of rat. Pei et al. [25] initially used fusion reporter gene(HSV1-tk-eGFP-Fluc, TGF)in the model of myocardial infarction and acquired the micro-PET, fluorescence, and bioluminescence imagings for 7 days and successfully monitored the localization of the transplanted stem cell and provided some correlative quantitative and semiquantitative data (Fig. 15.4).

There are some advantages of applying the reporter gene imaging to track the progression of the cells. First, the reporter gene imaging specifically visualizes the bioactive cells, because only the survival cells in vivo can produce the specific product of the reporter gene. Second, it can monitor the progression of the cells for a long time; that is to say, even if the reporter gene is diluted with the cell proliferation, it can still be monitored. Third, the expression of the reporter gene is increased significantly which contributes to the observation of the imaging. Fourth, using stably transfected cells with reporters under the control of a specific promoter, the differentiation effect of the cells can be monitored.

As the researches go further, some challenges exist that need to be overcome when tracking these cells by using the reporter gene imaging. First, the reporter gene should be transfected into the cell stably for long-term monitoring, but this may increase the risk of gene mutation resulted from insertion of the reporter gene. Second, the nonphysiological overexpression of the reporter gene in vivo may disturb the function of the endogenous cells. Third, the product of the transfected reporter gene may trigger an immune response which may lead to reporter gene inactivation. Fourth, there is a possibility that the transplanted cells may have a malignant transformation depending on the number and site of the insertion of the reporter gene in transplanted stem cells.

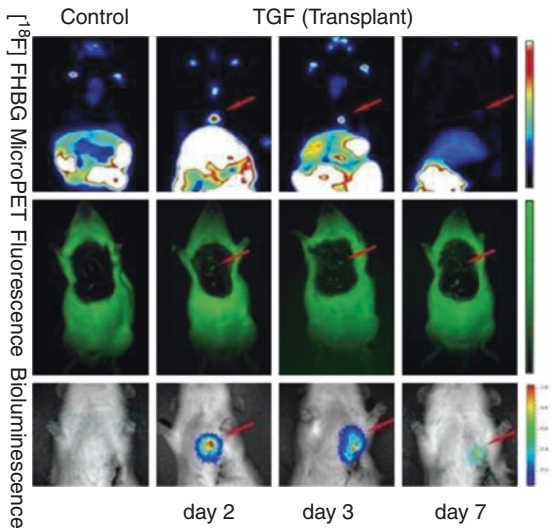

Fig. 15.4 After transplanting TGF to regional myocardium in the model of myocardial infarction, micro-PET, fluorescence, and bioluminescence imaging techniques were used to monitor the progression of the cells. The images of the transplanted cells are indicated by red arrows

15.2.3.3 The Imaging of the Endogenous Gene Expression

The reporter gene imaging can visualize the transcription and posttranscriptional regulation of the target gene, so the biological processes can be clearly understood. Some researchers design specific promoters or enhancers which are on the upstream of the reporter gene in order to initiate the expression of the endogenous gene. This strategy is called cis-promoter/enhancer reporter gene system. Once the promoter or enhancer and the expression of the endogenous gene are activated, it will also induce the expression of the reporter gene. Therefore, the intensity of the imaging signal in the target cells or tissues indicates the level of a specific endogenous gene expression. This imaging method contributes in monitoring and evaluation of the new cloned gene and in signal transduction pathways. In addition, it can also compare images from different types of imaging techniques and quantitatively evaluate the expression of the reporter gene and its spatial distribution.

15.2.3.4 Visualizing the Specific Biological Phenomena

The reporter gene imaging can noninvasively reveal the expression of the endogenous gene and the biological phenomena in the cell, such as signal transduction and the activation of the nuclear receptor, etc. Transforming growth factor-β (TGF-β) can inhibit the growth and progression of the tumor. In the Memorial Sloan Kettering Cancer Center [26], researchers used the reporter gene techniques to visualize the intracellular signal transduction pathways of the transforming growth factor receptors. When the receptor is blocked by the TGF-β, it will activate a specific intracellular signal transduction pathway producing Smad protein. A recombinant retrovirus-containing SV1-tk/GFP and the gene of Smad protein under the control of a specific promoter should be constructed and transfected into the tumor cells. Using ^{18}F-FEAU, a specific reporter probe, can conduce in vivo imaging and confirm if the transfected operation is successful in the xenograft mice.

15.2.3.5 The Application of Drug Screening

The reporter gene imaging also plays an important role in the drug screening. As we all know, the transcription factors and the gene expression are the important targets in the process of drug development, and they vary in the viral infections, tumors, inflammation, and immune system diseases, but the typical method of detecting the gene expression is complicated. If the regulatory sequence of the target gene is linked with the reporter gene, and then they are transfected into the cell, the location and duration of regulatory sequences' effects on transcription factors and gene expression can be dynamically monitored by imaging techniques. In sum, a proper screening model should be constructed and transfected into the specific host cell. And then it can be used to perform a drug screening by activating the target gene. In addition, in the study of the pharmacokinetics of drugs, the drugs can be labeled with a reporter gene and tracked temporally and spatially by imaging techniques to analyze the bioavailability, the excretion pathway, target specificity, drug distribution, the occupancy rate of target, etc. The reporter gene imaging technique provides a new method which will accelerate the process of the identification of drug targets and preclinical testing. So it will undoubtedly accelerate the process of the drug development and its purification to ease the level from cells to animals and humans [27].

15.2.3.6 Assessment of the Protein-Protein Interactions

The biological effects of the unknown functional genes and new functions and effects of the proteins which are already known can be recognized by analyzing the protein-protein interactions. Conventionally, this information will be acquired by using a purely computational model or a large-scale proteomics method. But the noninvasive reporter gene imaging provides a new method to visualize the protein-protein interactions in real time. Ray [28] used yeast two-hybrid system and a cooled charge-coupled device camera to measure the expression of Fluc in a living subject, confirming the interactions between MyoD and ID proteins. Paulmurugan [29] used the methods of protein complementary action and restoration to study protein-protein interactions.

15.2.4 Problems and Prospects of Reporter Gene Imaging

Reporter gene imaging is an indirect imaging which plays a major role in molecular imaging. There are some obvious problems in the current researches: First, the immunogenicity and gene mutation may bring problems; second, whether the transduced or transfected genes are distributed to the target organs or tissues and whether their distribution is optimal are still unknown; third, whether the transduced or transfected genes are localized in the organs or tissues at a sufficiently high level; fourth, whether the process of the reporter gene transduction or transfection is successful; fifth, what is the best time of detecting the reporter gene expression in cells?; sixth, how long can the reporter genes persist being expressed in the target organs or tissues? New methods are needed to solve this series of problems.

The advantages of reporter gene imaging are described as follows: (1) It can noninvasively visualize the location, amount, and duration of transgene expression and also guide the process of gene therapy. (2) Imaging at the transcriptional and translational levels and the noninvasive research of protein-protein interactions contribute to confirm the expression of endogenous genes and specific proteins as a complementary research method of genomics and functional proteomics. (3) It can also visualize the localization and the process of distribution of the transplanted cells in the living subjects in order to better guide the clinical stem cell therapy and bone marrow transplantation. However, these techniques are still in the stage of preclinical research, and there are still so many things to be accomplished before their application in the clinical settings hence benefitting many people. Therefore, the future research should not only focus on increasing and deepening the depth and intensity of the small animal researches of reporter gene imaging but also trying to transform these techniques into clinical imaging methods.

References

1. Tavitian B (2000) In vivo antisense imaging. Q J Nucl Med 44(3):236–255
2. Hnatowich DJ (1999) Antisense and nuclear medicine. J Nucl Med 40:693–703

3. Agrawal S (1999) Importance of nucleotide sequence and chemical modifications of antisense oligonucleotides. Biochim Biophys Acta 1489(1):53–68
4. Mani S, Gu Y, Wadler S et al (1999) Antisense therapeutics in oncology: points to consider in their clinical evaluation. Antisense Nucleic Acid Drug Dev 9(6):543–547
5. Dewanjee MK, Ghafouripour A, Werner R et al (1991) Development of sensitive radioiodinated anti-sense oligonucleotide probes by conjugation techniques. Bioconjug Chem 2(4):195–200
6. Dolle F, Hinnen F, Vaufrey F et al (1997) A general method for labeling oligodeoxynucleotides with 18 F for in vivo PET imaging. J Labelled Comp Radiopharm 39(4):319–330
7. Dewanjee MK, Ghafouripour AK, Kapadvanjwala M et al (1994) Noninvasive imaging of C-myc oncogene messenger RNA with indium-111-antisense probes in a mammary tumor-bearing mouse model. J Nucl Med 35:1054–1063
8. Cammilleri S, Sangrajrang S, Perdereau B et al (1996) Biodistribution of iodine −125 tyramine transforming growth factor alpha antisense oligonucleotide in athymic mice with a human mammary tumour xenograft following intratumoral injection. Eur J Nucl Med 23:448–452
9. Mardirossian G, Lei K, Rusckowski M et al (1997) In vivo hybridization of technetium- 99m labeled peptide nucleic acid (PNA). J Nucl Med 38:907–913
10. Blasberg RG, Tjuvajev JG (2003) Molecular-genetic imaging: current and future perspectives. J Clin Invest 111(11):1620–1629
11. Massoud TF, Gambhir SS (2003) Molecular imaging in living subjects: seeing fundamental biological processes in a new light. Genes Dev 17(5):545–580
12. Ray P, De A, Min JJ et al (2004) Imaging tri-fusion multimodality reporter gene expression in living subjects. Cancer Res 64(4):1323–1330
13. Ponomarev V, Doubrovin M, Serganova I et al (2004) A novel triple-modality reporter gene for whole-body fluorescent, bioluminescent, and nuclear noninvasive imaging. Eur J Nucl Med Mol Imaging 31(5):740–751
14. Kim YJ, Dubey P, Ray P et al (2004) Multimodality imaging of lymphocytic migration using lentiviral-based transduction of a trifusion reporter gene. Mol Imaging Biol 6(5):331–340
15. Sun N, Lee A, Wu JC (2009) Long term non-invasive imaging of embryonic stem cells using reporter genes. Nat Protoc 4(8):1192–1201
16. Willmann JRK, Paulmurugan R, Rodriguez-Porcel M et al (2009) Imaging gene expression in human mesenchymal stem cells: from small to large animals. Radiology 252(1):117
17. Love Z, Wang F, Dennis J et al (2007) Imaging of mesenchymal stem cell transplant by bioluminescence and PET. J Nucl Med 48(12):2011–2020
18. Roelants V, Labar D, de Meester C et al (2008) Comparison between adenoviral and retroviral vectors for the transduction of the thymidine kinase PET reporter gene in rat mesenchymal stem cells. J Nucl Med 49(11):1836–1844
19. Terrovitis J, Kwok KF, Lautamäki R et al (2008) Ectopic expression of the sodium-iodide symporter enables imaging of transplanted cardiac stem cells in vivo by single-photon emission computed tomography or positron emission tomography. J Am Coll Cardiol 52(20):1652–1660
20. Lan X, Liu Y, He Y et al (2010) Autoradiography study and SPECT imaging of reporter gene HSV1-tk expression in heart. Nucl Med Biol 37(3):371–380
21. Hofmann M (2005) Monitoring of bone marrow cell homing into the infarcted human myocardium. Circulation 111(17):2198–2202
22. Blasberg RG (2003) Molecular imaging and cancer. Mol Cancer Ther 2(3):335–343
23. Wu JC (2003) Molecular imaging of cardiac cell transplantation in living animals using optical bioluminescence and positron emission tomography. Circulation 108(11):1302–1305
24. Higuchi T, Anton M, Dumler K et al (2009) Combined reporter gene PET and iron oxide MRI for monitoring survival and localization of transplanted cells in the rat heart. J Nucl Med 50(7):1088–1094
25. Pei Z, Lan X, Cheng Z, Qin C, Wang P, He Y, Yen TC, Tian Y, Mghanga FP, Zhang Y (2012) A multimodality reporter gene for monitoring transplanted stem cells. Nucl Med Biol 39(6):813–820
26. Kang Y, He W, Tulley S et al (2005) Breast cancer bone metastasis mediated by the Smad tumor suppressor pathway. Proc Natl Acad Sci U S A 102(39):13909–13914
27. Ottobrini L, Ciana P, Biserni A et al (2006) Molecular imaging: a new way to study molecular processes in vivo. Mol Cell Endocrinol 246(1-2):69–75
28. Ray P, Pimenta H, Paulmurugan R et al (2002) Noninvasive quantitative imaging of protein-protein interactions in living subjects. Proc Natl Acad Sci U S A 99(5):3105–3110
29. Paulmurugan R, Massoud TF, Huang J et al (2004) Molecular imaging of drug-modulated protein-protein interactions in living subjects. Cancer Res 64(6):2113–2119

Na^+/I^- Symporter Target for Thyroid Disease Imaging and Treatment

16

Rui Huang, Rong Tian, and Zhaowei Meng

Utilizing iodide to synthesize thyroid hormones is a biological signature of thyroid that has been used for the diagnosis and treatment of benign and malignant thyroid diseases [1]. Radioiodine is a classical theranostic representations for personalized targeted therapy and molecular imaging in nuclear medicine history [2]. Thyroid scan with radioiodine or technetium-99m (^{99m}Tc) pertechnetate has unique ability in the assessment of thyroid nodules with anatomical and functional information. Radioiodine whole-body scan (WBS) has played an important role in the detection of normal thyroid tissue remnants and local and distant metastases of differentiated thyroid cancer (DTC) as well as restaging after radioiodine therapy and long-term follow-up.

16.1 Iodine Trapping and Thyroid Handling of Radiotracer

The principle of thyroid imaging mainly depends on its radiotracer can involve on some phase of thyroid hormone synthesis. We need to know the pathophysiological process of different thyroid diseases and how to choose optimal radiopharmaceuticals for them.

16.1.1 Iodine Metabolism

Iodine (stable isotope, iodine-127) is actively accumulated by the thyroid gland for thyroid hormone synthesis from blood pool [3]. Iodine constitutes 65% of the molecular weight of thyroxine (T4) and 59% of the triiodothyronine (T3). Thyroid stores 70–80% of the iodide in the human body. Most of the ingested iodine is rapidly absorbed in the form of iodide and distributed in the blood plasma. The iodide then is transported into the thyroid gland or excreted through the kidneys. Approximately 90% of the excretion is through the kidneys, and 1% of the excretion is through the colon. A small amount of iodide is also excreted through sweat, saliva, and other bodily fluids. When iodide is concentrated from the serum, it is oxidized in apical membrane and then sent to the lumen to incorporate with thyroglobulin (Tg) tyrosyl residues to make diiodotyrosine (DIT) and monoiodotyrosine (MIT). In brief, the ionic form, iodide (I^-), is taken up by thyroid follicular cells through the Na+/I− symporter (NIS), a key transmembrane glycoprotein which is located in the basolateral membrane of the follicular thyroid cell. Next, iodide reaches the apical surface of the follicular cell membrane, where it is oxidized into iodine (I^0) via thyroid peroxidase (TPO), with the presence of hydrogen peroxide. Then, iodine enters into the follicular lumen, via pendrin or other unspecified channels. Iodine is condensed into the tyrosine residues of thyroglobulin to form MIT and DIT. After that, the MIT and DIT are coupled to form T3 and T4. Finally, thyroid hormones are released from the colloid into the bloodstream under the regulation of hypothalamus-pituitary-thyroid axis [4]; see Fig. 16.1.

16.1.2 The Structure, Expression, and Regulation of NIS

The cDNA encoding NIS was isolated in 1996, marking a major breakthrough in thyroid research that led to the subsequent characterization of NIS at the molecular level.

NIS is a member of solute carrier family 5A and has been assigned the designation SLC5A5 by the Gene Nomenclature Committee, according to the Human Genome Organization. Human NIS is a glycosylated protein with 643 amino acids that contains 13 transmembrane domains. Based on the

R. Huang (✉) · R. Tian
Department of Nuclear Medicine, West China Hospital, Sichuan University, Chengdu, P. R. China
e-mail: huang_rui@scu.edu.cn

Z. Meng (✉)
Department of Nuclear Medicine, Tianjin Medical University General Hospital, Tianjin, P. R. China

G. Huang (ed.), *Nuclear Medicine in Oncology*, https://doi.org/10.1007/978-981-13-7458-6_16

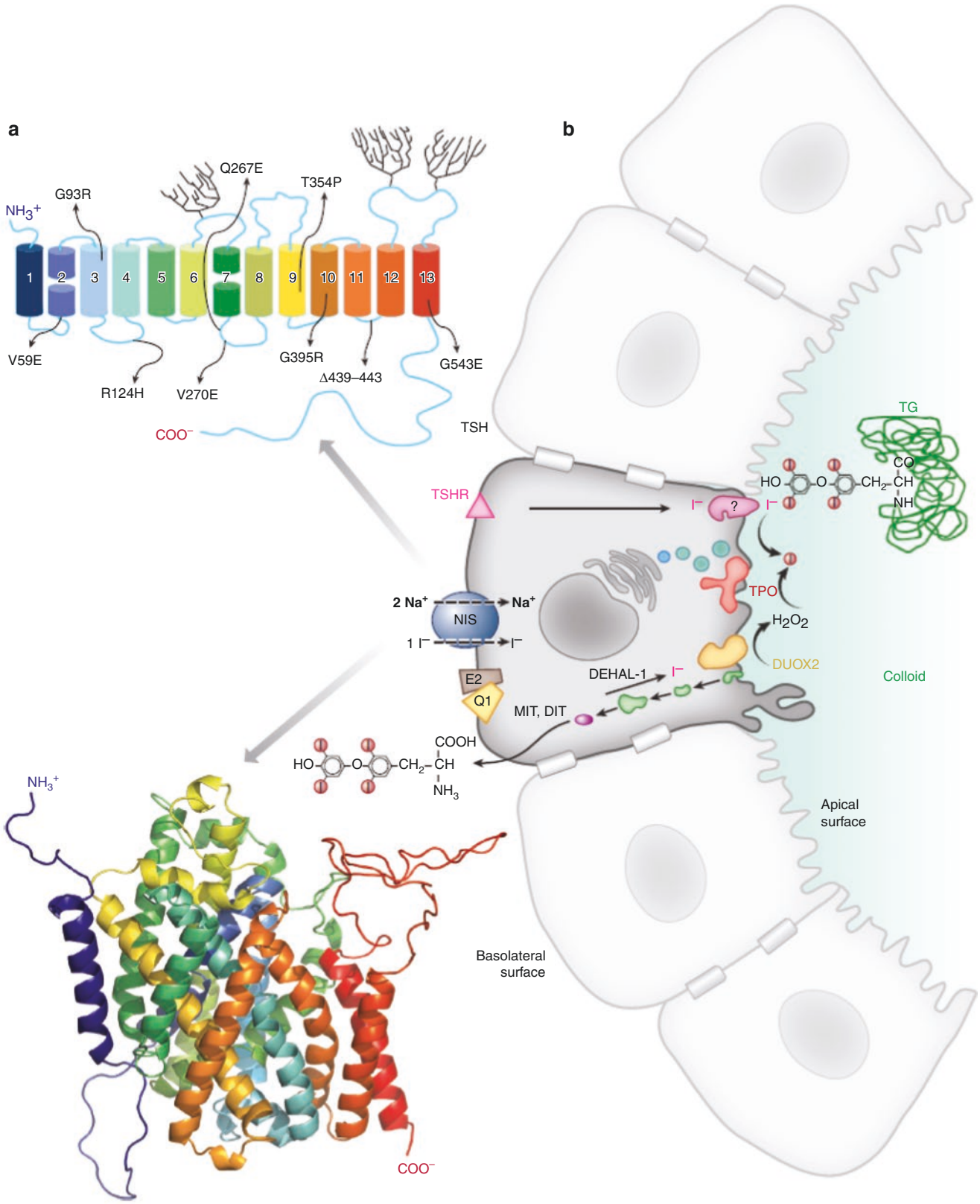

Fig. 16.1 Schematic representation of NIS structure and thyroid hormone biogenesis (Reprint with permission from [4]). (**a**) Secondary structure model (upper left) and crystal structure model (lower left) of NIS. NIS has 13 transmembrane segments, represented by cylinders of different colors (upper left), which match NIS crystal structure model (lower left). (**b**) Schematic representation of thyroid hormone biogenesis. *DEHAL-1* dehalogenase 1; *DIT* 3,5-diiodotyrosine; *DUOX2* dual oxidase 2; *ITD* I– transport defect; *MIT* 3-monoiodotyrosine; *NIS* Na+/I– symporter; *TG* thyroglobulin; *TH* thyroid hormone; *TSHR* TSH receptor; *TSH* thyroid-stimulating hormone; *TPO* thyroid peroxidase

Table 16.1 Physical characteristics of radionuclides for thyroid imaging

Radioisotopes	$T_{1/2}$	Emission	Most abundant energy	Medical use	Cost	Availability
^{123}I	13.2 h	Gamma ray	159 keV	Diagnostic imaging (gamma camera)	Expensive	Limited
^{124}I	4.2 days	Positron/ gamma ray	511 keV/ 602 keV	Diagnostic imaging (PET)	Expensive	Limited
^{131}I	8.0 days	Beta ray/ gamma ray	606 keV/364 keV	Diagnostic imaging (gamma camera) and therapy	Low	Common
^{99m}Tc	6.0 h	Gamma ray	140 keV	Diagnostic imaging (gamma camera)	Lower	Common
^{18}F	109.8 min	Positron	511 keV	Diagnostic imaging (PET) as a form of tetrafluoroborate	Expensive	Common

electrochemical gradient of sodium maintained by Na^+/K^+ ATPase, NIS actively cotransports two Na^+ along with one I^-; see Fig. 16.1 [4]. NIS is mostly expressed in thyroid tissue, which is also expressed in other extra-thyroidal normal tissues, including choroid plexus, lacrimal sac, nasolacrimal duct, salivary glands, gastric mucosa, intestine, kidney, lactating breast, placenta, ovary, and testes. However, the non-thyroid tissues which express NIS do not organify iodide which they traffick.

NIS of the thyroid is mainly regulated by TSH at the transcriptional level and the posttranscriptional levels [5]. The thyroid transcription factor-1 (TTF-1), Pax8, and retinoic acids were also found to activate the transcription of NIS in thyroid cells through the effect on NIS enhancer or promoter [6].

Another regulator of NIS function is I^- itself. At the molecular level, excess I^- may have a deleterious effect on the thyroid by modifying NIS mRNA stability and increasing the production of reactive oxygen species through activation of PI3K/AKT pathway [7].

NIS gene expression is also regulated by RAS/RAF/MAPK pathway. The hyperactivated RAS/RAF/MAPK and PI3K/AKT pathways have been found to be linked to the downregulation of NIS expression and its intracytoplasmic location, which leads to the impairment of NIS-mediated iodide accumulation in patients with DTC [8]. Epigenetic alterations such as NIS promoter or enhancer hypermethylation and histone deacetylation have been shown to be involved in the process of NIS silencing in DTC [9, 10]. Recently aberrant expression of microRNAs, such as mir-146b-3p and mir-106a, is confirmed to direct or indirect posttranscriptional regulation of NIS expression, resulting in the impairment of protein translation and subsequently impairing the ability to transport iodide of the DTC cells [11, 12].

16.1.3 Radiopharmaceuticals for Thyroid Imaging

The principal radiopharmaceuticals employed for thyroid imaging include ^{123}I, ^{124}I, ^{131}I, ^{99m}Tc, and ^{18}F-tetrafluoroborate (TFB).^{123}I, ^{124}I, and ^{131}I are trapped, organified, and then retained in thyroid follicular cells. They are all used to detect ectopic thyroid tissues and thyroid cancer metastases; ^{123}I and ^{131}I are also used for thyroid uptake test. Meanwhile,^{123}I is preferred to be used for thyroid gland imaging; ^{124}I is better in detecting DTC lesions and calculating dosimetry that helps lesions to absorb enough radiation dose from a subsequent treatment of ^{131}I. ^{99m}Tc-pertechnetate and ^{18}F-TFB are also transported into thyroid follicular cells by NIS but do not undergo organification, which means the retention of these two radiotracers is not as long as radioiodine. Imaging with ^{99m}Tc is limited to the intact thyroid gland.^{18}F-TFB has only been evaluated for its safety, biodistribution, and internal radiation dosimetry in DTC patients and needs more clinical trial to demonstrate its utility in DTC metastasis detection [13]. Table 16.1 shows the physical characteristics of radionuclides for thyroid imaging.

16.1.3.1 ^{123}I

^{123}I undergoes electron capture with a principal gamma energy of 159 Kev. It has a short physical half-life of 13 h without beta emission. These physical characteristics make ^{123}I ideally suited for gamma scintillation cameras for imaging the thyroid gland and radioiodine-avid DTC lesions, with fewer radiation safety issues. However, the relatively short half-life limits its routine availability and its utility in performing dosimetry.

16.1.3.2 ^{124}I

^{124}I is a PET radiotracer with a half-life of 4.18 days. PET cameras have better spatial resolution and detective sensitivity that ^{124}I imaging may find more lesions of DTC patients. In addition, ^{124}I has a desired half-life that allows for the evaluation of iodine kinetics in vivo. So, ^{124}I is used as a diagnostic/dosimetric approach for the localization of DTC lesions. However, ^{124}I only has a 23.5% of β+ emitter for positron emission, and a fair amount of high-energy gamma rays it generates may affect the imaging process.

16.1.3.3 ^{131}I

^{131}I undergoes beta minus decay with principal gamma photon energy of 364 KeV. The energy of the principal beta

particle is 0.606 MeV, and the half-life is 8.02 days. ^{131}I is not an ideal radiotracer for routine thyroid imaging with the following two reasons: one is that the high energy of gamma ray is not suitable for gamma scintillation camera, and the other reason is the high absorbed dose in thyroid gland caused by the relatively long physical half-life and beta emissions. However, with high selectively radiation dose and low whole-body dose, ^{131}I is a good radiotherapeutic agent for treating diseases including Graves' disease, toxic nodular goiter, and differentiated thyroid cancer. In addition, the long half-life of ^{131}I is favored for detecting ^{131}I-avid metastatic thyroid carcinoma in delayed scanning studies.

16.2 Radioiodine Imaging and Treatment of DTC

16.2.1 ^{131}I Therapy in DTC

Thyroid cancer is the most common malignancy of endocrine system. More than 90% of thyroid cancer is in the form of DTC, and the other forms contain papillary thyroid carcinoma (PTC), follicular thyroid carcinoma (FTC), Hürthle carcinoma, and anaplastic thyroid carcinoma (ATC). DTC usually has a favorable benign course with a lower risk of death, compared with most other malignancies. Despite the expression and membrane location of NIS in thyroid cancer are impaired, >70% of DTC cells have the ability to accumulate a certain amount of radioiodine, and it is enough to destroy thyroid remnant or metastatic lesions with NIS expression. Radioactive iodine (RAI) is one of the most effective agents used for targeted internal radiation therapy in the nuclear medicine history. Following the complete/partial thyroidectomy with or without lymph node dissection, RAI is chosen for DTC patients. The aims of RAI have been defined as thyroid remnant ablation, adjuvant treatment, and therapy [14]. RAI remnant ablation is to destroy normal remnant thyroid and makes thyroglobulin (Tg) a good tumor marker during follow-up. It also helps to differentiate recurrent in situ from thyroid residue and potentially improve the quality of future whole-body RAI scans. The purpose of RAI adjuvant therapy is to treat potential residual disease with the objective of reducing recurrence and thus improve disease-free survival (DFS) of DTC patients, which is especially useful for patients have an increased recurrence risk. RAI treatment is used for the treatment of unresected local or distant disease to improve DFS [14]. According to the American Thyroid Association (ATA) guideline, RAI ablation is not recommended for patients with low-risk DTC, while RAI adjuvant therapy could be applied on intermediate-risk patients, and RAI treatment is recommended for high-risk patients after total thyroidectomy [14]. There are many controversies about the use or nonuse of RAI in low- and intermediate-risk patients with DTC. For supporting none-RAI group, the data has showed that RAI could not improve recurrence rate and overall survival [15]. However, recurrence risk assessment solely depends on the extent of surgical dissection and pathological examination accuracy. For example, the insufficient lymph node dissection affects TNM staging and recurrence risk stratification; thus, initial risk stratification is not really accurate. Diagnostic or post-RAI WBS would find 5–25% of unsuspected local or distant metastases in low- and intermediate-risk patients with DTC. RAI adjuvant therapy positively improves the overall survival of intermediate-risk PTC patients, reducing 36% death in patients younger than 45 years old [16].

16.2.2 Radioiodine Dosimetry

A high level of TSH is required (more than 30 mU/L) to guarantee a good uptake of radioiodine in remnant tissue, suspected/occult disease, or metastatic sites [17]. Thus, the expression of NIS is increased by TSH stimulation. All patients undergo 2–3 weeks of low-iodine diet and either (a) endogenous TSH elevation after thyroid hormone withdrawal or (b) exogenous stimulation with administration of recombinant human thyrotropin or thyrotropin alfa for injection to avoid hypothyroidism impairing the life quality of patients [18]. However, rhTSH is not recommended for DTC patients with high-risk disease or known distant metastases.

Based on the tumor clinic-pathological features, serum thyroglobulin (Tg) level, US, and radiological results, a proper radioactivity of I-131 is determined. An activity range from 1.1 to 3.7 GBq is often used for the remnant ablation, 3.7–5.5 GBq is recommended for adjuvant therapy, and 3.7–11.1 GBq is given to metastatic disease depending on multiple factors [14]. For the opinion 'less I-131 is more' for intermediate-risk patients with DTC, 1.1 GBq is considered as equally effective as 3.7 GBq; however, many doctors now argue this idea; they proposed that 3.7 GBq is equally as ineffective as 1.1 GBq and that patients need to be administered higher activity of I-131. We need more studies to solve these arguments.

For unresected local lymph node metastases or distant metastases, RAI treatment is usually repeated every 6–12 months if those lesions uptake ^{131}I. To reduce radioresistance and increase success rate of therapeutics with fewer treatments, higher radioiodine activity has been recommended [19]. However, a higher administrated activity may result in complications like sialadenitis, lung fibrosis, bone

marrow suppression, and secondary primary tumor. To keep benefit-risk balance, a dosimetric approach is important for measuring actual absorbed radiation doses to the tumors and the organs at risk.

There are two ways to measure RAI dosimetry in the clinic, the maximum safe dose (MSD) method and the lesion-based dosimetric method. The MSD methodology, based on Benua-Leeper method, emphasizes dose-limiting toxicity on bone marrow. The limitation of absorbed dose is defined as deliver less than 2 Gy to the bone marrow or a whole-body retention less than 4.44 GBq at 48 h post administration or lung retention less than 2.96 GBq at 48 h in cases of diffuse pulmonary metastases [20]. The lesion-based dosimetric method assumes a uniform distribution of ^{131}I in lesions in which the actual dose is calculated on diagnostic ^{131}I SPECT/CT or ^{124}I PET/CT. To achieve successful RAI ablation or treatment, researchers have concluded at least 300 Gy need to be delivered to thyroid remnants and 80 Gy to metastatic sites [21].

Either ^{131}I or ^{124}I can be used for the dosimetric assessment. As discussed above, ^{124}I has a favorable physical half-life of 4.2 days that makes it a good choice for sequential time point imaging and absorbed dose calculations. In addition, ^{124}I PET imaging is better than ^{131}I planar or SPECT [22], due to its higher space discrimination and more accurate quantification of the activity. However, ^{131}I is used more frequently as it is ubiquitously available, and SPECT/CT could also calculate absorbed dose in organs at risk and metastatic lesions.

The absorbed dose is not evenly distributed between different lesions within the same patient, and high variability could be seen within one lesion. The lesion-based dosimetric approach cannot truly reflect the distribution in actual practices [23]. Sgouros et al. used ^{124}I PET/CT to assess the mean absorbed doses which ranged from 1.2 to 540 Gy [24]. Maxon et al. demonstrated that absorbed dose of 80 Gy in lymph node metastases is associated with favorable response [21], while another study reported that 120 Gy is not enough for adequate response [25]. In contrast, Dorn et al. also reported absorbed dose between 100 and 150 Gy is needed for complete responses [26]. Meanwhile, this study also reported a skeletal metastatic lesion that failed to respond to 480 Gy. These findings indicate that even though we use lesion-based dosimetric method to plan the treatment activity, the response of tumor lesions is still variable. In addition, lesion-based dosimetric calculations are considered unreliable for small lesions, even with ^{124}I PET spatial resolution volume of 0.15 mL; only 38% of thyroid remnants and 40% of metastases were able to be accurately calculated [27].

In one large retrospective study to compare the effect of fixed activity with personalized activity in 231 patients with ^{131}I-avid distant metastases who received empiric fixed activity of 3.7 GBq and 121 patients who undertook 2.8–18.6 GBq based on MSD approach, the median cumulative activity was 14.8 GBq and 24.2 GBq, respectively. However, the results concluded that the higher personalized activity based on MSD dosimetric approach didn't provide advantage for overall survival compared with empiric fixed RAI dose [28].

So until now, there is no evidence to support using empiric fixed activity over MSD dosimetry vs lesion-based dosimetry, or vice versa, for measuring administered ^{131}I activity [14].

16.2.3 Radioiodine Scintigrams of Patients with DTC

Radioiodine is also the first theranostic agent [2]. Its imaging can be used for theranostic imaging, which can potentially alter the decision to treat with ^{131}I and finalize the subsequent therapeutic dose of ^{131}I. Radioiodine imaging usually includes diagnostic scan and post-therapy scan. Diagnostic scan is undertaken before radioiodine treatment and surveillance to help determine the existence of thyroid remnant and nodal or distant metastasis. Diagnostic scan is always to be performed 24 h after the oral administration of 74 MBq^{123}I or 48–72 h after the oral administration of 37–185 MBq ^{131}I. Post-therapy scan is performed 3–5 days after the RAI administration (Fig. 16.2). SPECT/CT images are obtained with the diagnostic or post-therapy images if there are equivocal or suspicious findings (Fig. 16.3).

As a diagnostic agent, ^{123}I is preferable to ^{131}I because it has lower gamma energy and no beta rays which provides good-quality images and avoids stunning. However, the high cost of ^{123}I limits its commercial application. In addition, ^{123}I can't be used for sequential imaging because of the short half-life of 13.2 h. Moreover, post-therapy WBS would find more lesions compared with the diagnostic ^{123}I WBS [29]. Hence, ^{131}I is still used for diagnostic WBS in many centers. For PET imaging, ^{124}I has a higher sensitivity to detect more RAI-avid lesions than that of a diagnostic ^{131}I planar WBS [30]. However, ^{124}I is also expensive and not widely available in clinical use.

The radioactivity administered affects the sensitivity of radioiodine imaging and NIS expression of the tumor cells. Increased numbers of lesions were visible on the post-therapeutic ^{131}I scan than using the corresponding diagnostic ^{131}I or ^{123}I scan [29] (Fig. 16.4). When DTC tumor cells lose NIS expression but still express Tg, radioiodine imaging is negative, while serum Tg is positive. In such circumstance, ^{18}F-FDG-PET/CT has a good diagnostic accuracy, showing a sensitivity of 88.5% and a specificity of 84.7% [31]. We can see different uptake patterns of ^{131}I and ^{18}F-FDG, including

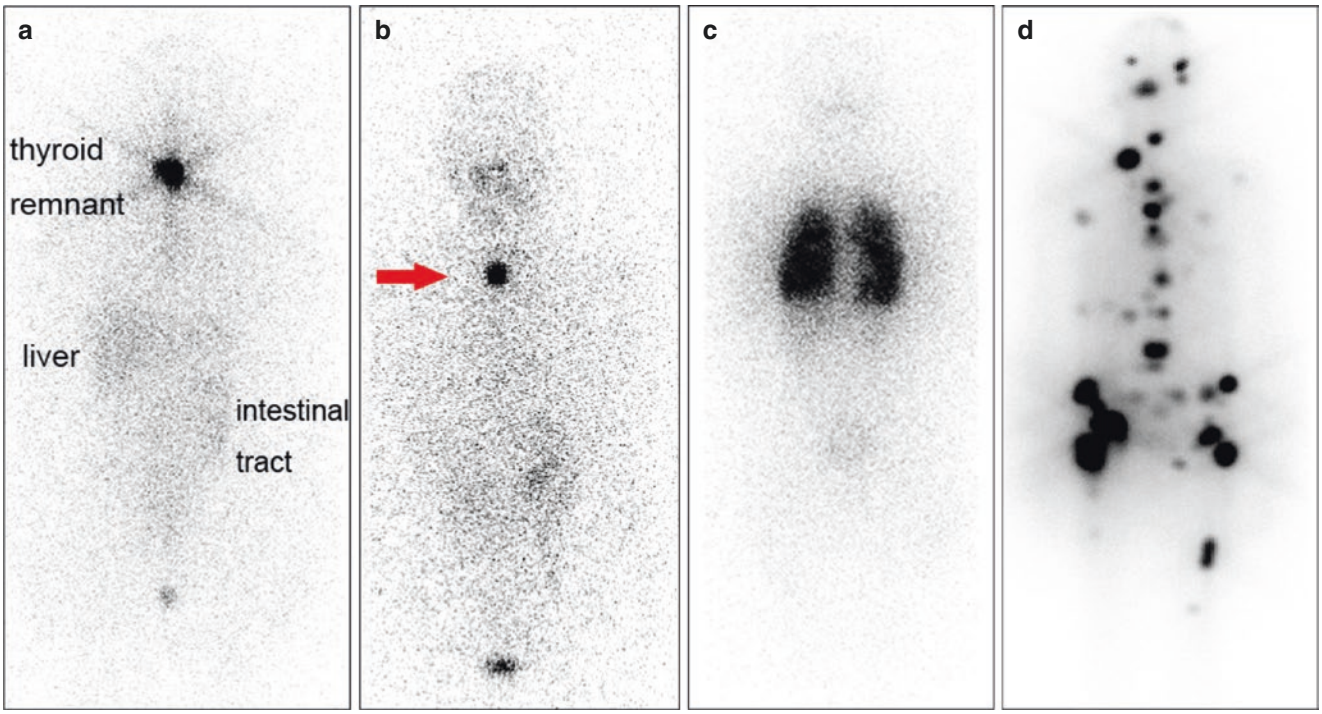

Fig. 16.2 Examples of ^{131}I whole-body scan. (**a**) Physiological biodistribution of radioiodine in the thyroid remnant, the liver, and the gastrointestinal tract; (**b**) upper mediastinum lymph node metastasis uptake of ^{131}I (confirmed by SPECT/CT, but not supplied in this figure); (**c**) diffuse lung metastasis uptake of ^{131}I; (**d**) multiple bone metastasis uptake of ^{131}I

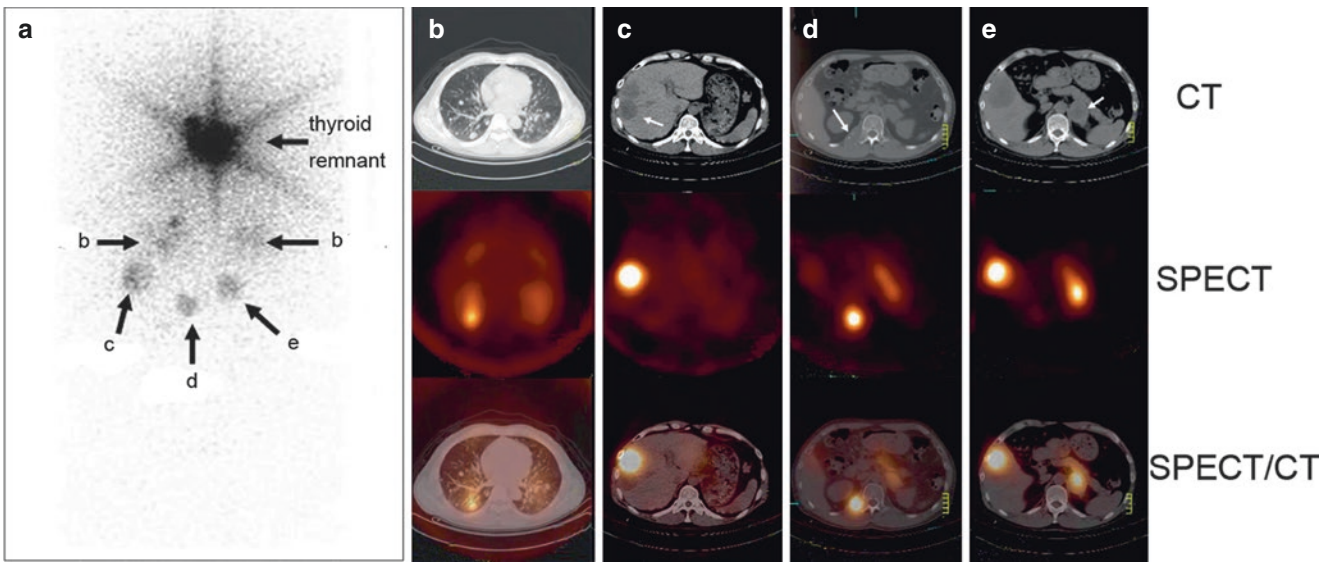

Fig. 16.3 SPECT/CT helps to localize the abnormal uptake sites seen on ^{131}I whole-body scan. (**a**) Post-therapy ^{131}I whole-body scan shows several abnormal uptakes on the chest and abdomen, besides thyroid tissue remnant, of a follicular thyroid cancer patient; (**b**, **c**, **d**, **e**) SPECT/CT demonstrated abnormal ^{131}I uptake belongs to lung, liver, lumbar vertebrae right appendix, and left adrenal gland metastases, respectively

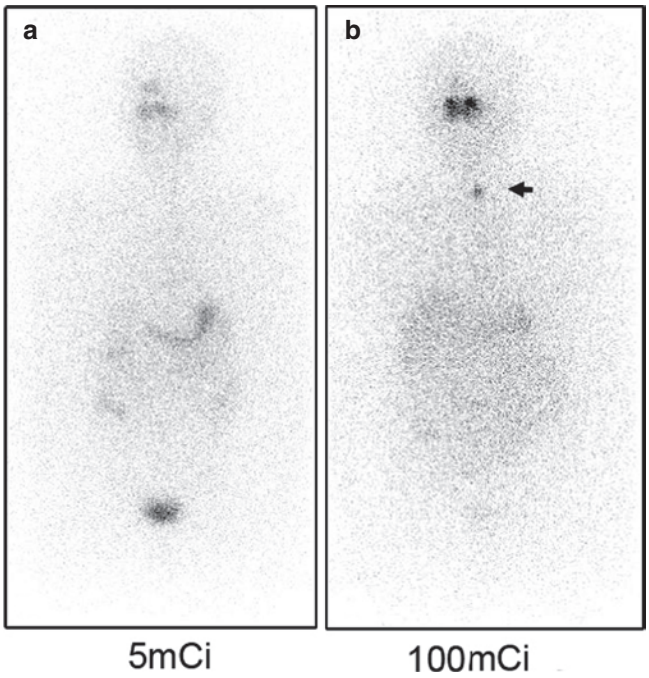

Fig. 16.4 The sensitivity of radioiodine imaging depends on the activity administered. (**a**) 185 MBq ^{131}I diagnostic WBS showed negative finding; (**b**) 3.7 GBq ^{131}I post-therapy WBS showed thyroid remnant

negative on ^{131}I but positive on ^{18}F-FDG (flip-flop phenomena; Figs. 16.5, 16.6 and 16.7) [32], both positive (Fig. 16.8), both negative, or partial coincidence on ^{131}I and ^{18}FDG. If patients with elevated Tg levels but the first RAI treatment WBS was negative, PET/CT, instead of second RxWBS would be used to localize the lesions. When positive lesion is detected on ^{18}F-FDG findings, empiric RAI therapy is not recommended again [33].

16.2.3.1 The Controversies of Diagnostic WBS

There are some controversies about the usefulness of diagnostic WBS before and after RAI. Diagnostic WBS is not commonly performed before RAI in all nuclear medicine centers; the patient with a high risk of recurrence and intermediate-risk (higher-risk) features will still undertake adjuvant RAI therapy for possible suspected lesion even when there is no obvious thyroid remnant or abnormal uptake outside the normal thyroid bed on diagnostic WBS. In our center, we routinely use ^{99m}Tc-pertechnetate scintigraphy and radioiodine uptake test to assess the level of the thyroid remnants, with the aim to better interpret the resource of serum Tg concentration. The decision as to the treatment dose of ^{131}I more depends on patients' surgery and

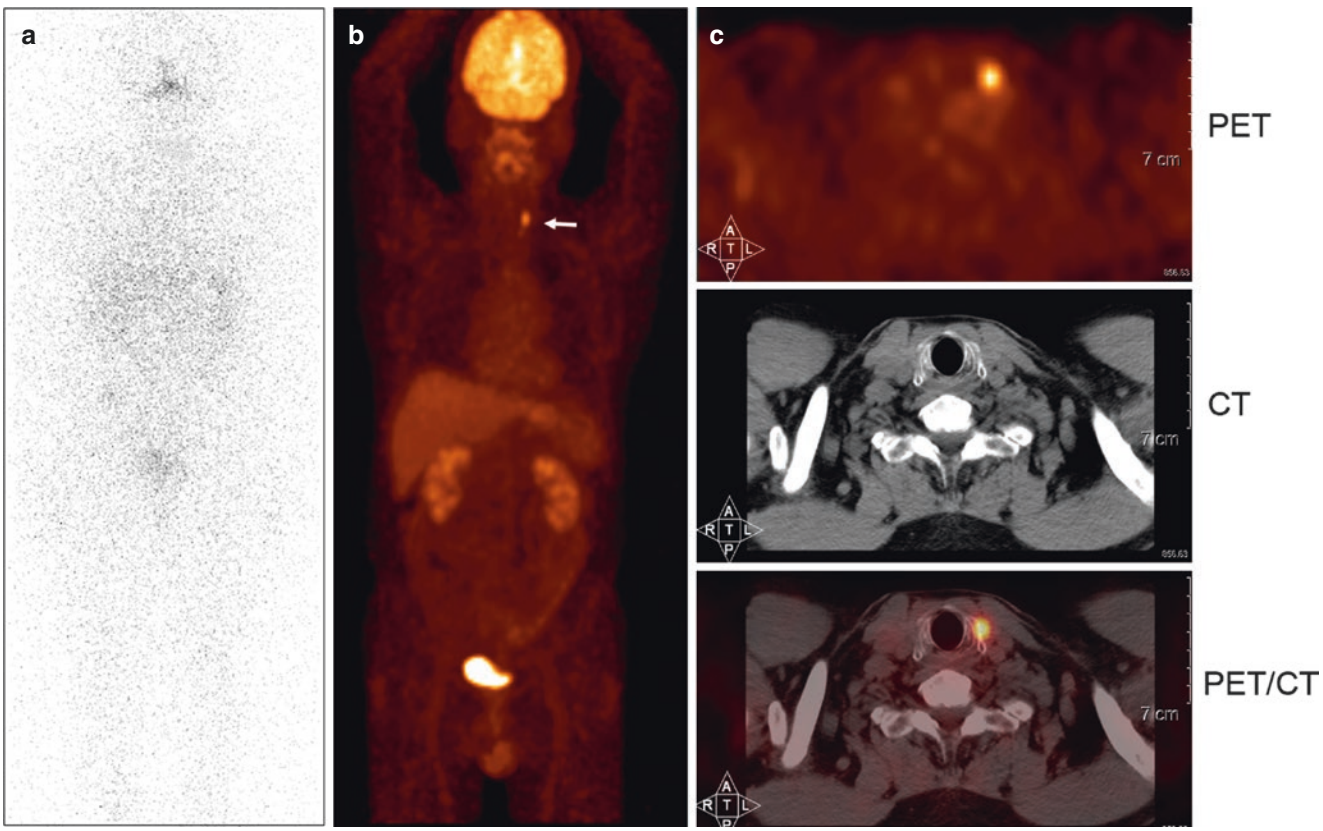

Fig. 16.5 Flip-flop phenomena on ^{131}I WBS and ^{18}F-FDG-PET/CT image. (**a**) A 68-year-old male with PTC ($T_XN_{1b}M_0$, IVa, intermediate-risk). Despite three ^{131}I treatments, his thyroglobulin increased to 40.27 ng/mL under TSH supplement. ^{131}I WBS was negative; (**b**) maximum intensity projection (MIP) of ^{18}F-FDG-PET/CT showed abnormal FDG-avid lesion on the left of thyroid bed, with SUV_{max} = 6.51; (**c**) CT demonstrated one 10 mm-long soft tissue in the left lateral of cricoid cartilage. The diagnosis was PTC recurrence, and he undertook surgery and extra-radiation therapy

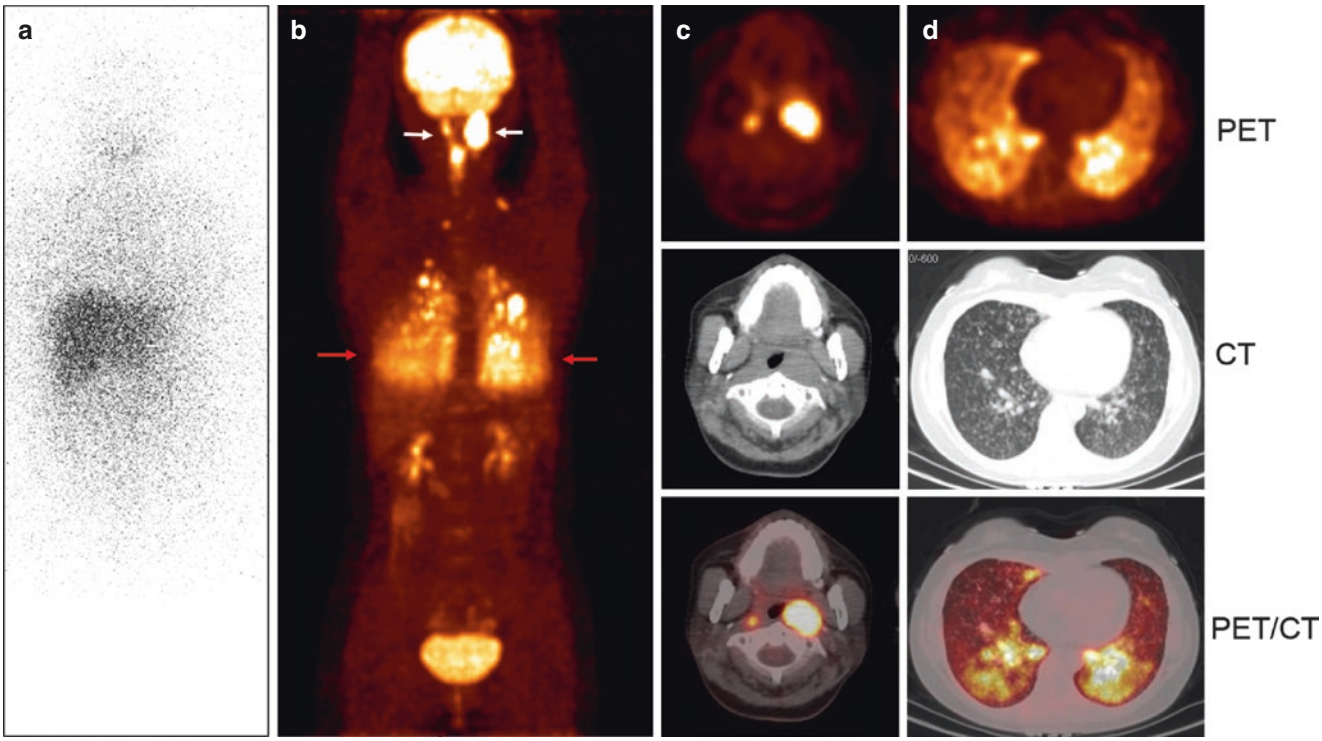

Fig. 16.6 Flip-flop phenomena on ^{131}I WBS and ^{18}F-FDG-PET/CT image. (**a**) A 35-year-old woman with PTC ($T_{4a}N_{1b}M_1$, Stage II, high-risk). Thyroglobulin was 7249 ng/mL under TSH stimulation. ^{131}I WBS was negative; (**b**, **c**, **d**) ^{18}F-FDG-PET/CT showed multiple laryngeal, neck lymph node, and pulmonary metastases. She was enrolled into phase III clinical trial of sorafenib

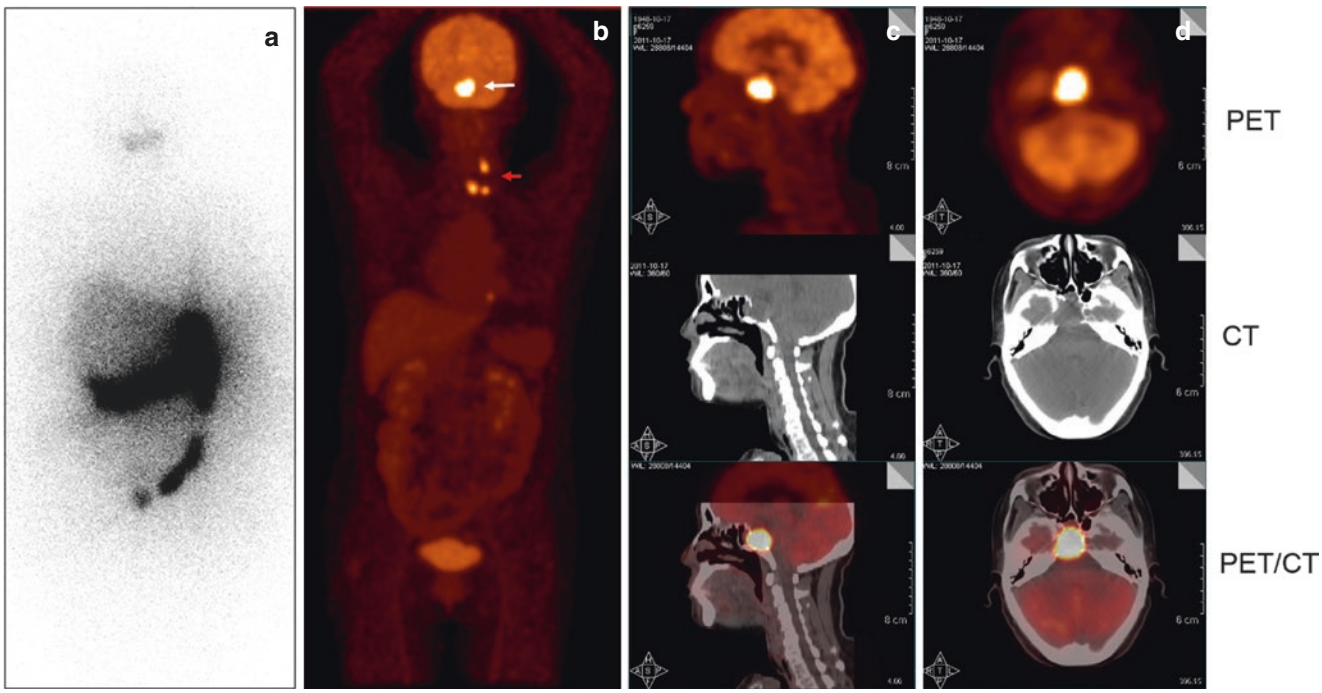

Fig. 16.7 Flip-flop phenomena on ^{131}I WBS and ^{18}F-FDG-PET/CT image. (**a**) A 63-year-old female with PTC ($T_{4a}N_{1b}M_0$, StageIVa, high-risk). Thyroglobulin increased to 123.5 ng/mL under TSH supplement. She had unexplained dizziness and headache. ^{131}I WBS was negative; (**b**) ^{18}F-FDG-PET/CT showed multiple FDG-avid lesions on the head (white arrow) and left neck (red arrow); (**c**, **d**) CT showed sphenoid body, sella turcica, and anterior and posterior clinoid process bony destruction with a 33 mm-diameter soft tissue (SUV_{max} = 45.60) formation in sellar region. The diagnosis was bone metastases; the stage changed into T4aN1bM1. She received gamma knife radiosurgery

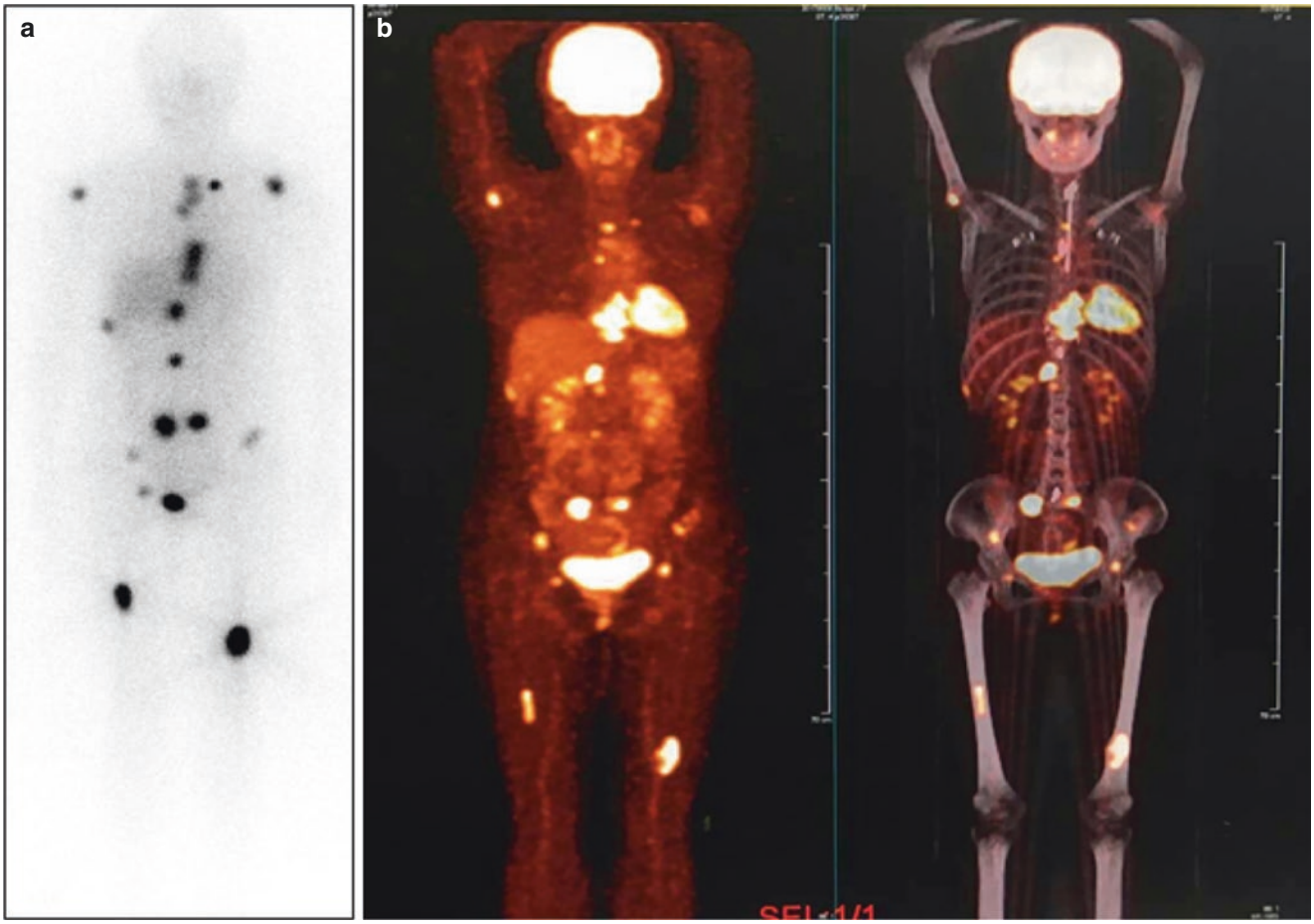

Fig. 16.8 Both positive findings on ^{131}I WBS and ^{18}F-FDG-PET/CT. (**a**) There are widely bone metastases showing radioiodine avid on ^{131}I WBS; (**b**) ^{18}F-FDG-PET/CT shows these radioiodine-avid bone metastatic lesions have obvious FDG metabolism

pathological information, stimulated Tg level, and the abnormal findings on neck US, MRI and thoracic CT scan, etc.

The American Thyroid Association recommends diagnostic WBS for the surveillance of DTC patients with intermediate or high risk of recurrence, 6–12 months following the RAI remnant ablation or adjuvant therapy. However, if the abnormal uptake can be determined as local or distant metastases on the first post-therapy WBS, the patient does not need to undergo diagnostic WBS again before the further RAI, except for dosimetric purpose. A second ablation is not recommended if patients have undetected Tg or antithyroglobulin antibody (TgAb) interference. Thyroid bed uptake on diagnostic WBS had no prognostic value for recurrence [34]. In addition, the quality of patients' life would be impaired after thyroxine withdrawal [35]. So, after the RAI, even with high-risk recurrence, the patients with DTC do not require routine diagnostic WBS during follow-up if there is no abnormal distribution outside the thyroid bed during the first post-therapy scan or have undetectable Tg on TSH suppression (with negative TgAb) and negative findings of other imaging examination during follow-up.

Diagnostic radioiodine WBS could be applied in a few primary clinical situations during follow-up: (1) abnormal uptake outside the thyroid bed that was shown during the first posttreatment WBS has not been well interpreted even under the help of SPECT/CT findings (see discussion on Sect. 16.5.3.2); (2) large thyroid remnants with high uptake of ^{131}I (the administered activity is more than 2% at the time of WBS) that may hamper the local or distant metastases uptake ^{131}I (Fig. 16.9a); and (3) the presence of TgAb to interference with Tg measurement, even there is no suspicious finding on other imaging modality [36].

16.2.3.2 False-Positive Results on Radioiodine WBS of Patients with DTC

As we discussed above, radioiodine scan is a targeted imaging for detecting radioiodine-avid metastasis of DTC. However, variants or pitfalls are common in clinical practice and may be sources of false-positive findings. Table 16.2 summarizes the findings of false-positive radioiodine uptake [37]. The common causes of false-positive findings include:

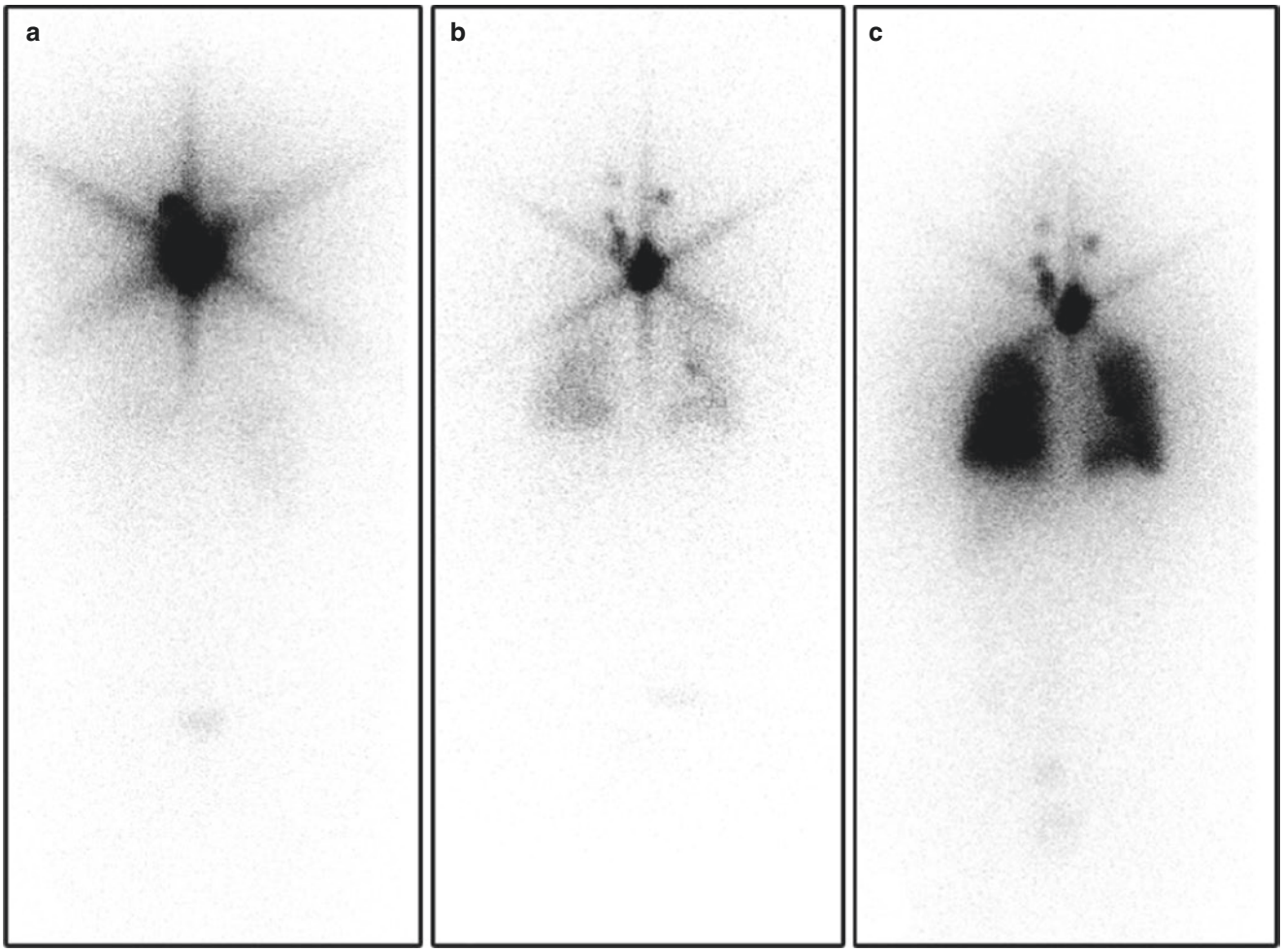

Fig. 16.9 Large thyroid remnant hampers local and distant metastasis uptake. (**a**) The first post-therapy ^{131}I WBS only showed thyroid remnant of a-28-year-old man with PTC, although his thyroglobulin was high (TSH 14.6 mU/L, Tg135.7 ng/mL, TgAb12.41 IU/L). (**b**) Diagnostic ^{131}I WBS after 6 months found thyroid remnant, local lymph nodes, and both lobes of lung uptake ^{131}I. (**c**) The second post-therapy showed the intense uptake of lymph nodes and lung metastases

Table 16.2 Summary of false-positive findings on radioiodine scans

Mechanism of radioiodine uptake	Findings
Functional uptake secondary to sodium-iodide symporter expression (ectopic thyroid or non-thyroid tissues)	Thyroglossal duct remnant, struma ovarii, salivary gland, lactating or nonlactating breast tissue, thymus, Meckel diverticulum, gastrointestinal duplication cysts
Radioiodine retention	Sialolithiasis, salivary gland duct ectasia, carotid artery ectasia, nasolacrimal duct cyst, laryngeal cyst, dental amalgam, retained esophageal or gastric secretions, Zenker diverticulum, hiatal hernia, achalasia, gastric pull-through, pleuropericardial cyst, thymic cyst, bronchogenic cyst, pleural or pericardial effusion, mediastinal blood pool, ectopic kidney, dilated collecting system, urinary tract diverticula, biliary tract retention, endometrial canal during menstruation, renal cyst, hepatic cyst, ovarian cyst, nabothian cyst, gastrointestinal duplication cyst, sebaceous cyst
Inflammatory conditions	Dacryocystitis, sialadenitis, temporomandibular joint effusion, sinusitis, abscess, acute or chronic bacterial or fungal infections, mycobacterial infections, bronchiectasis, rheumatoid lung, sarcoidosis, pulmonary sequestration, post-infectious or post-inflammatory bronchiolitis obliterans, cholecystitis, hydatid cyst, skin abrasions, post-procedural sites, infected sebaceous cyst
Nonthyroid neoplasms	Warthin tumor, salivary gland oncocytoma, meningioma, cavernous hemangioma, nasal polyp, lung adenocarcinoma, lung squamous cell carcinoma, breast fibroadenoma, invasive breast cancers, gastric adenocarcinoma, gallbladder carcinoma, ovarian neoplasms, littoral cell angioma, uterine leiomyoma, benign cystic mesothelioma, malignant fibrous histiocytoma, lipoma, and benign fibrous histiocytoma
Radioiodine contamination	Scalp or hair from sweat; ocular prosthesis; skin contamination with nasal, lacrimal, sweat, breast milk, and tracheobronchial secretions, urine, saliva, or feces; radioactive handkerchief sign

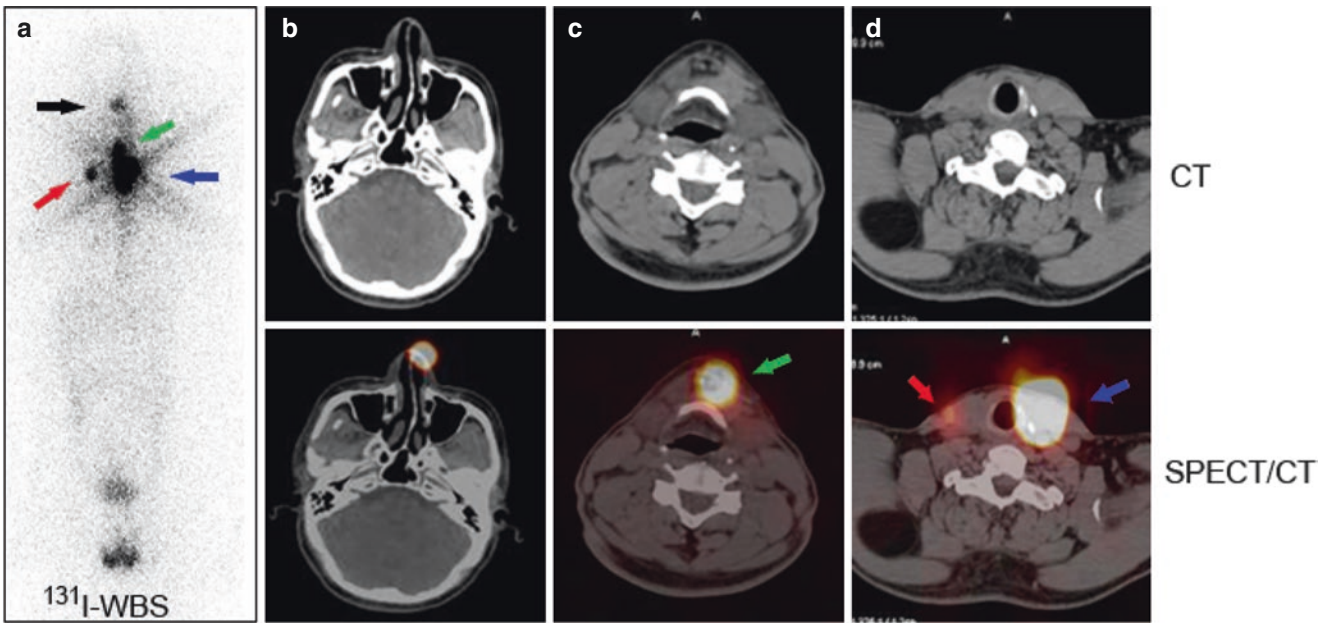

Fig. 16.10 Three types of false-positive uptake on ^{131}I WBS in one DTC patient. (**a**) There are four radioiodine uptakes in the face and neck region on ^{131}I WBS; (**b**) SPECT/CT confirmed radioiodine retention in nasal cavity (black arrow on ^{131}I WBS); (**c**) SPECT/CT localized thyroglossal duct remnant uptake ^{131}I due to NIS expression (green arrow); (**d**) SPECT/CT showed radioiodine uptake localized in the right sternocleidomastoid muscle (red arrow) and right thyroid remnant (purple arrow). The right false radioiodine uptake (red arrow) may be caused by post-surgery inflammation

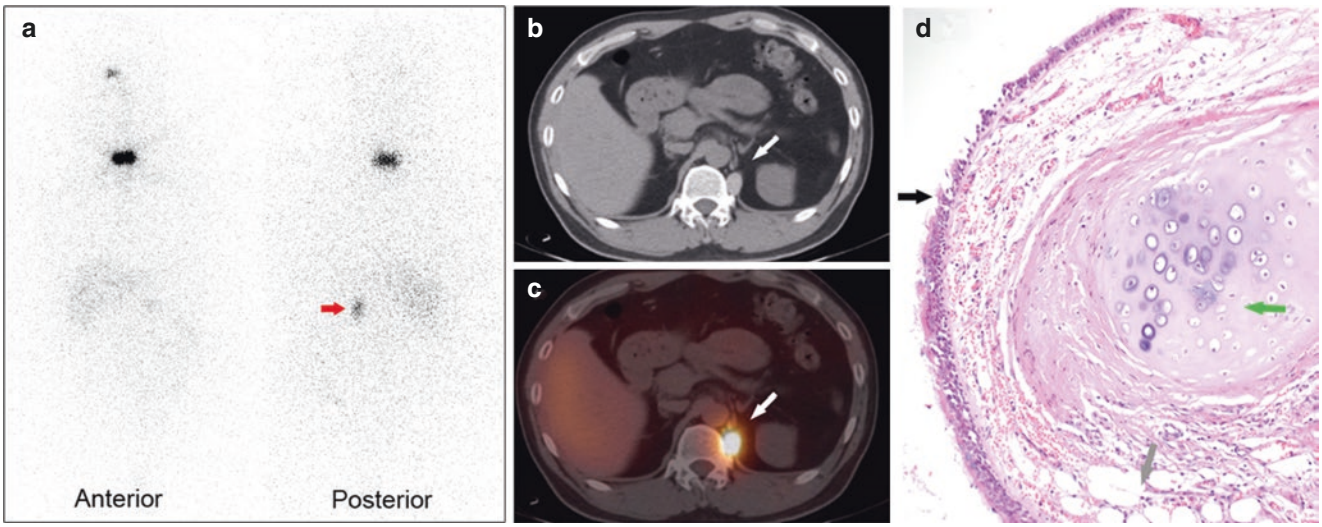

Fig. 16.11 False-positive uptake on radioiodine whole-body scan due to retroperitoneal bronchogenic cyst (Reprint with permission from [38]). (**a**) Post-therapy WBS of a 54-year-old male patient with PTC detected an increased activity in the left abdomen (red arrow) on posterior view; (**b**) CT demonstrated a well-defined soft tissue mass (white arrow) in the retroperitoneal space; (**c**) radioactivity of this mass (white arrow) was confirmed by SPECT/CT; (**d**) the final pathologic nature of this mass is confirmed to be a retroperitoneal bronchial cyst

1. Radioiodine uptake related to NIS expression in ectopic thyroid and non-thyroidal tissues. The most common uptake on WBS is thyroglossal duct remnant (Fig. 16.10) and salivary gland. Sometimes in younger patients, thymus uptake could be seen in the anterior mediastinum as a triangular sail configuration.
2. Radioiodine retention in physiological secretions accumulated in dilated ducts or cavities, such as in nasal cavity (Fig. 16.10), and bronchogenic [38] (Fig. 16.11), hepatic, renal, ovarian, and sebaceous cysts.
3. Radioiodine uptake from inflammatory or infectious causes, such as pulmonary acute or chronic infection,

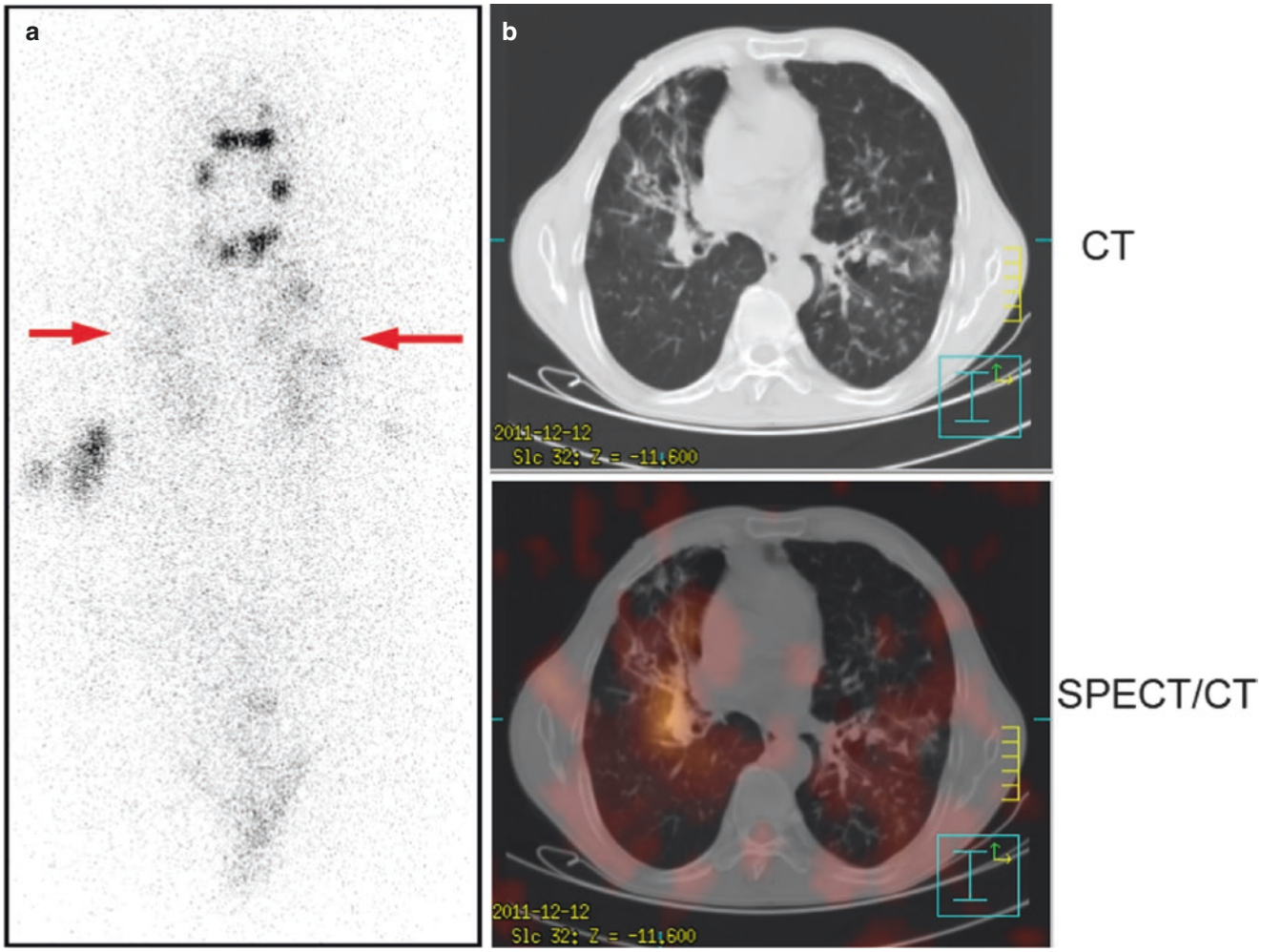

Fig. 16.12 False-positive uptake on radioiodine whole-body scan due to bronchiectasis. (**a**) Post-therapy WBS of a 54-year-old male patient with PTC showed irregular uptake on chest field (red arrow); (**b**) CT showed focal bronchiectasis in the right and left lung. SPECT/CT confirmed that the abnormal pulmonary radioiodine uptake correlates with focal bronchiectasis

bronchiectasis (Fig. 16.12), and skin injury. It is due to vasodilation resulting in increased blood flow and capillary permeability permitting radioiodine uptake.

4. Radioiodine uptake forms neoplasms of non-thyroidal origin. The postulated mechanisms are related to NIS expression (Fig. 16.13 [39]), passive diffusion, and high vascularity of the neoplasm (see Table 16.2). Other neoplasms, such as lipoma [40] (Fig. 16.14) and benign fibrous histiocytoma [41], have been reported as radioiodine avid, without a clearly understood mechanism of uptake.
5. Contamination from radioiodine in bodily secretions or excretions, such as the skin, hair, or cloths contaminated with saliva, sweat, urine, vomitus, or nasal secretions.

To avoid unnecessary further RAI administration, radioiodine scans should be interpreted accurately. We need to understand the physiology and biodistribution of radioiodine and be familiar with the common reasons of false-positive images in conjunction with knowledge of the patient history, tumor histopathologic findings, serum Tg and TgAb level, and other anatomic imaging. SPECT/CT combines

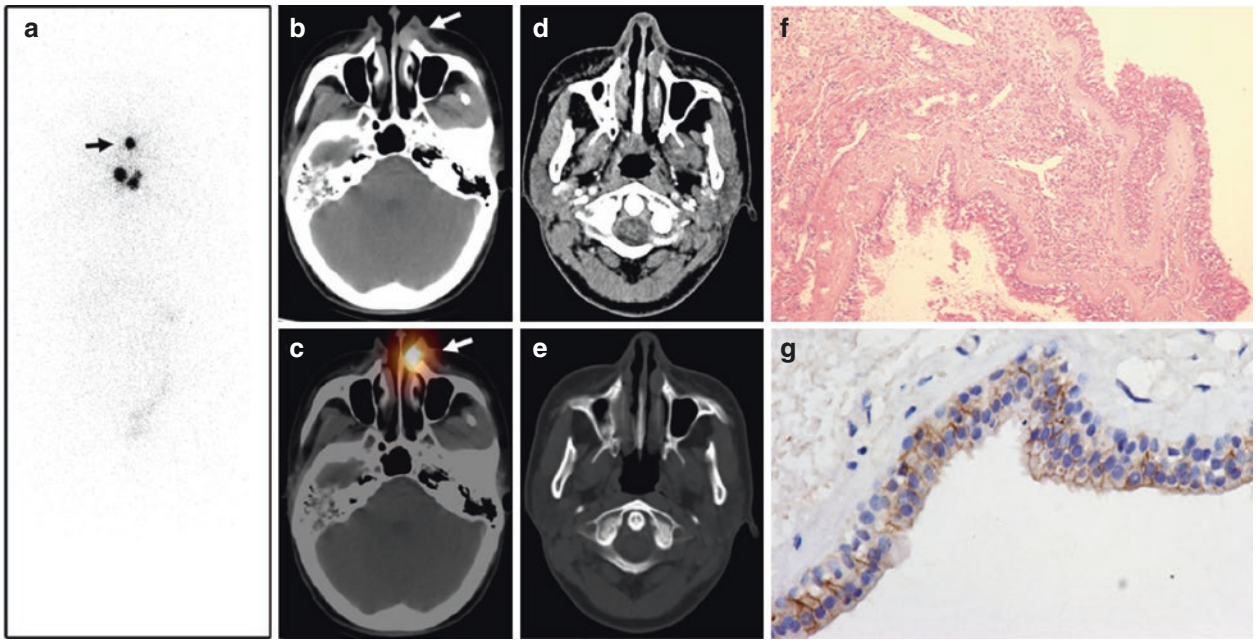

Fig. 16.13 False-positive uptake on radioiodine whole-body scan due to nasal polyp (Reprint with permission from reference [39]). (**a**) Post-therapy WBS of a 35-year-old female patient with PTC showed a focal radioactivity in the facial region (black arrow); (**b** and **c**) CT and SPECT/CT confirmed the radioactivity was from the nodule within the left nasal vestibule; (**d**) the nodule was medium enhanced on contrast-enhanced CT image with minimal absorption of the adjacent maxilla; (**f** and **g**) immunobiological examination revealed a benign nasal polyp with NIS expression on the cell membranes

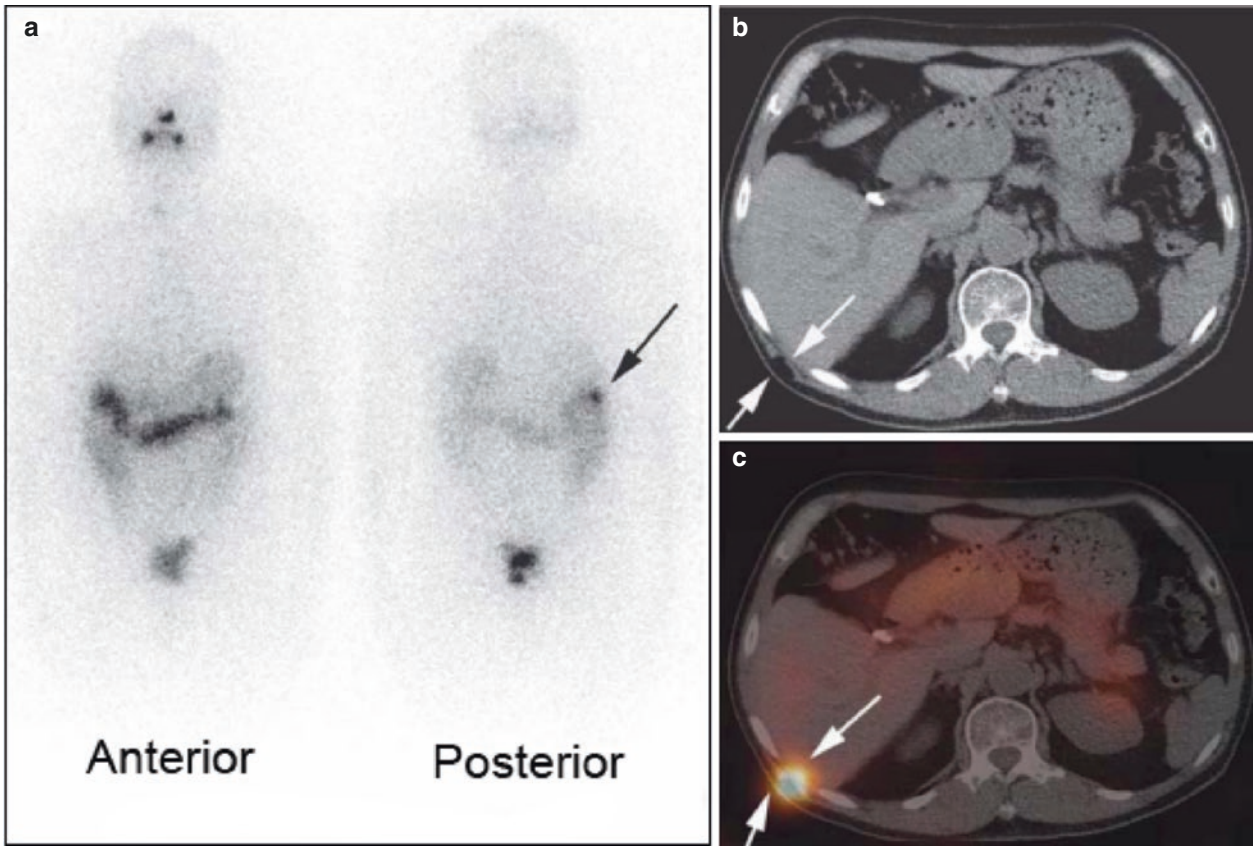

Fig. 16.14 False-positive uptake on radioiodine whole-body scan due to lipoma (Reprint with permission from reference [40]). (**a**) Post-therapy WBS of a 68-year-old male patient with follicular variant PTC showed an abnormal focal uptake located on the right side of the back on posterior view; (**b**) CT scan revealed a small subcutaneous lesion with fat density between the tenth and 11th posterior rib (white arrow); (**c**) fused SPECT/CT image confirmed that the activity was from this lesion (white arrow), which was diagnosed as lipoma by pathological examination

functional information with detailed anatomic location of uptake sites, can help to confirm false-positive results in equivocal cases [37].

16.3 Application of Iodine Metabolic Imaging and Targeted Therapy for Benign Thyroid Diseases

16.3.1 Radioactive Iodine-131 Therapy for Hyperthyroidism

Historically, radiotherapy with radioactive iodine has been used to treat thyroid diseases for roughly 80 years. In fact, the initial radiotherapeutic try was Roentgen treatment. Means and Holmes have suggested that about one third of patients could be cured by Roentgen treatment, another third improved, and the rest not affected [42]. The use of radioactive iodine in the study of thyroid physiology was later undertaken and first reported by Hertz, Roberts, and Evans in 1938. It was found that in untreated hyperthyroidism, thyroid could take up as much as 80% of a given small dose of iodide within a few hours after oral administration. This mechanism established the basis for radioactive iodine therapeutic trials. And in 1942, Saul Hertz and Arthur Roberts published a preliminary report of such treatment on ten patients in Massachusetts General Hospital. The first therapeutic use of radioiodine in clinic was produced by Massachusetts Institute of Technology with 12.5 h half-life ^{130}I with a probable 10% ^{131}I in the regime cocktail. The milestone event happened in the late 1940s when two manuscripts were published regarding the treatment of hyperthyroidism with radioiodine. The first paper was a follow-up study recruiting 29 patients with Graves' disease treated [43]. These patients were administered a dosage of 5–25 mCi of ^{130}I, and the calculated thyroid doses were from 500 to 2500 rads. This study resulted in a therapeutic success rate of 68.97% in patients (20/29). The other paper recruited 22 patients with Graves' disease and treated them with a dosage of 15–45 mCi of ^{130}I (with mixture of ^{131}I). The calculated thyroid dosage was about 4000 rads. The therapeutic response was judged excellent [44]. During the late 1940s and early 1950s, these patients received the 8-day half-life isotope ^{131}I. ^{131}I was established as the most suitable and available isotope for the treatment of hyperthyroid individuals. The reactor-generated radioactive iodine^{131}I was more easily accessible than the cyclotron-generated ^{130}I, and many therapeutic studies were then conducted. In the meantime, thyroid ^{131}I uptake ability was also found to be a feasible approach for the diagnosis of hyperthyroidism [45]. Thanks to the above pioneer works, the US Food and Drug Administration (FDA) approved radioactive iodine for use with thyroid patients in 1951. It was the first FDA-approved radiopharmaceutical for human diseases [46], which should be regarded as the first ever targeted agent to treat diseases. The 2011 American Thyroid Association (ATA) guideline for the management of hyperthyroidism [47] has been the most frequently referred consensus in recent years, which was updated just recently in 2016 [48].

16.3.1.1 Choice of Treatment

In terminology, thyrotoxicosis describes a pathological state that results from the reaction of high thyroid hormone on tissues and organs, the increased thyroid hormone usually caused by increased tissue thyroid hormone production. Hyperthyroidism presents as an inappropriately increased thyroid hormone synthesis and secretion by the thyroid. Appropriate treatment of thyrotoxicosis depends on an accurate diagnosis and is influenced by many factors including coexisting medical conditions and patient preference [47, 48]. Correct diagnosis of endogenous primary hyperthyroidism, which is most commonly caused by disease entities named as Graves' disease (GD) or toxic multinodular goiter (TMNG) disease, is the most important first step. As an autoimmune thyroid disorder, GD development is based on thyrotropin receptor antibodies (TRAb) stimulation on the thyroid-stimulating hormone (TSH) receptor and then the increased thyroid hormone production, storage, and release afterward. The development of toxic nodular thyroid disease is another story, which often includes growth of already established nodules, new thyroidal nodule formation, and progression of autonomous thyroid nodule over time. Less common causes of thyrotoxicosis needing to be differentiated consist of the disease entities of painless thyroiditis as well as subacute thyroiditis, which occur mainly due to inflammation reaction of thyroid tissues and, after the destructive change of the thyroid structure, release of preformed and stored hormone from thyroid follicles into the blood circulation. Hyperthyroidism which can be treated with ^{131}I include GD, solitary hyperfunctioning nodule, and TMNG. ^{131}I may also benefit patients with subclinical hyperthyroidism, particularly patients at risk for cardiac or systemic complications. ^{131}I is used less frequently for the treatment of euthyroid goiters.

The preferred method for treating hyperthyroidism varies in different countries. In a 1991 survey of ATA, European Thyroid Association (ETA), and Japanese Thyroid Association (JTA) members, 69%, 22%, and 11% of respondents, respectively, chose ^{131}I as the therapy of choice for an index patient with GD [49]. In the same survey, anti-thyroid drugs (ATD) were regarded as initial treatment in 30.5%, 77%, and 88% of ATA, ETA, and JTA respondents, respectively. In 2011, another similar survey from clinical endocrinologists was conducted which showed that 59.7% of respondents from the USA used ^{131}I as the choice of primary therapy for GD [50]. Such variation likely stems from differences in perceived risks of prescribing radioactive

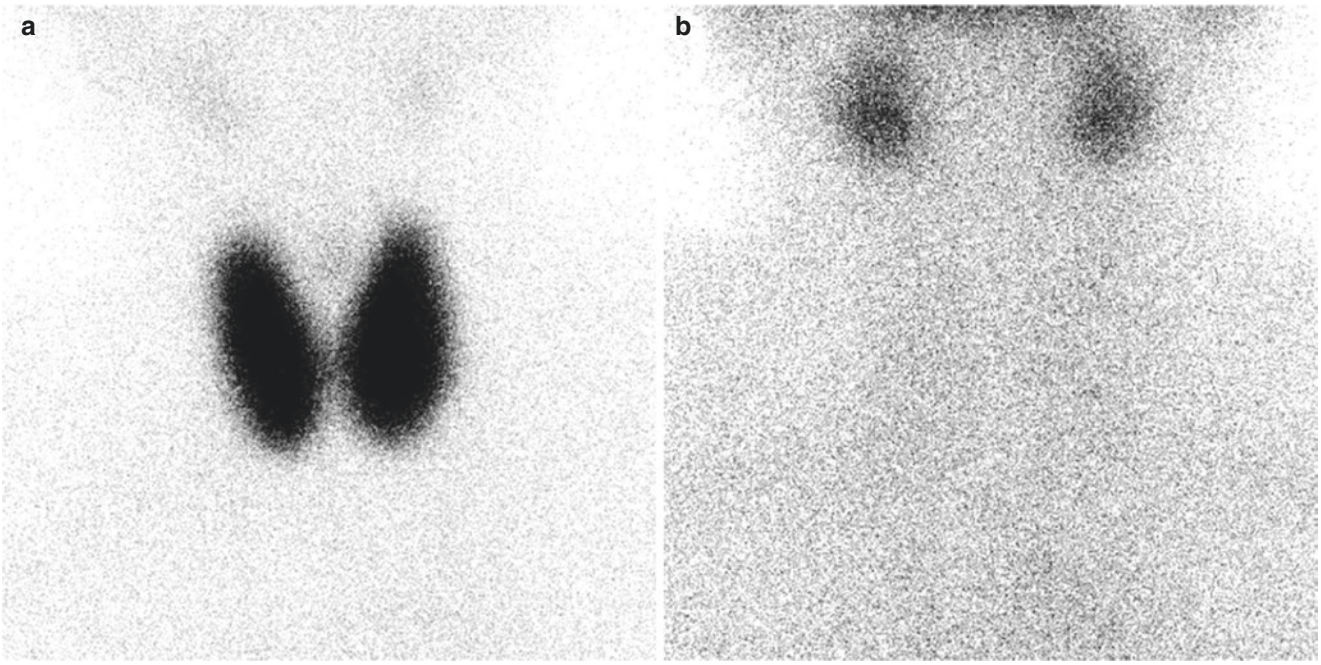

Fig. 16.15 Differentiation between Graves' disease and painless thyroiditis. (**a**) Graves' disease; (**b**) Painless thyroiditis

treatments, differences in cost, local requirements for hospitalization during treatment, patient compliance, response to ATD medications, and natural history of autoimmune thyroid disease in different populations.

Most jurisdictions have specific regulations for possession and use of ^{131}I and other radionuclides. Physicians who use radioisotopes must be knowledgeable and in compliance with all applicable laws. Therapeutic decisions should always be made with consideration for the population from which the patient originates and to local standards of practice.

16.3.1.2 Determination of Etiology

1. Differentiation

   Besides the clinical presentation and initial biochemical evaluation, diagnostic testing should include the following items: (1) measurement of serum TRAb level, (2) determination of the thyroidal radioactive iodine uptake (RAIU) value, or (3) measurement of thyroidal blood flow based on ultrasonography findings. A technetium-99 m pertechnetate ($^{99m}TcO_4$) scan (thyroid scintigraphy) should be obtained when RAIU is not available or the clinical presentation suggests a toxic adenoma (TA) or TMNG [47, 48]. Features of $^{99m}TcO_4$ scan and RAIU for GD and toxic nodular goiter are increased uptake of thyroid tissues, while for subacute thyroiditis, painless thyroiditis, or postpartum thyroiditis, near-absent uptake of thyroid tissues. Factitious ingestion of thyroid hormone tablets or from food source or recent excess amount of iodine intake could also induce a near-absent uptake. Contraindications of $^{99m}TcO_4$ scan and RAIU are pregnancy and lactation. Static thyroid scans provide a planar image of the thyroid gland by using a gamma camera in order to provide a visual view of thyroid uptake display and to assess potential variability in the concentration of radioisotope in different areas of thyroid tissue, and technetium uptake is very similar with iodine uptake.
2. Utility of Thyroid Scan

   Thyroid scan is very reliable for differentiation between GD and thyroiditis [51]. Figure 16.15 demonstrated an example of drug-naïve GD (Fig. 16.15a) and an example of painless thyroiditis (Fig. 16.15b). The difference between the autoimmune-driven hyperthyroidism (Fig. 16.15a) and the destructive thyrotoxicosis (Fig. 16.15b) is obvious in a $^{99m}TcO_4$ thyroid scan; the former is enhanced thyroid uptake, while the latter is decreased thyroid uptake.

16.3.1.3 Biological Basis of ^{131}I Therapy

1. Sodium-Iodide Symporter

   The sodium-iodide symporter (NIS), which gene was characterized in 1996, is responsible for the specific uptake of ^{131}I in thyroid epithelial cells. This transmembrane protein, acting like a pump, can transport iodide against an electrochemical gradient (high concentration of iodine in thyroid versus in blood circulation) via a sodium-dependent active transport mechanism. During the action, two sodium ions are transported along with one iodide ion. The NIS protein is most abundantly expressed in thyroid tissue, although it is also present in some other places such as glandular and mucosal tissue,

thymic tissue, salivary glands, choroid plexus, ciliary body of the eye, and placenta. Position of normal NIS protein expression is limited to the basolateral membrane in a small percentage of thyroid follicular cells. However, in autoimmune thyroid diseases, under thyrotropin receptor-mediated activation by TRAb, increases of the NIS protein expression can be identified on both basolateral and apical surfaces in the majority of thyroid follicular cells. Synthetic mechanisms responsible for iodine organification and incorporation into colloid matrix are also increased.

2. High-Energy β-Particles of ^{131}I

Therapy by ^{131}I relies on the emission of high-energy β-particles to cause damage to thyroid gland tissue. ^{131}I has a physical half-life of 8.1 days, a principal γ-ray energy of 364 keV, and β-particle emission with an average energy of 0.192 MeV. With a tissue range of 0.8 mm, β-particle emission is responsible for the majority of local therapeutic effect. The ensuing inflammation caused by radiation is followed by fibrosis, resulting in the reduction of the synthetic capacity of the thyroid gland. It is important to keep in mind that although hyperthyroidism related to GD may be eliminated by ^{131}I, the underlying autoimmune disease may persist indefinitely and that continued follow-up is necessary to monitor associated autoimmune syndromes, such as Graves' ophthalmopathy (GO).

16.3.1.4 Indications and Contraindications for ^{131}I Therapy and Other Therapies

1. Indication Choices

There are clinical conditions that prefer certain therapy modality for GD [47, 48], which are listed as the following. In addition, patients' personal preference may also impact the choice of therapy.

(a) ^{131}I therapy: Female patients who plan a pregnancy in more than 6 months after ^{131}I administration; patients with co-morbidities which increase surgical risk; patients with previous operation on the neck; patients experiencing external irradiation on neck area; patients who lack of access to a thyroid surgeon with high-volume operations; patients with contra-indications or side-effects because of ATD; or cases who fail to achieve euthyroidism after ATD treatment. Patients with atrial fibrillation, periodic thyrotoxic hypokalemic paralysis, pulmonary hypertension, congestive heart failure, or other complications and comorbidities should also be considered candidates for ^{131}I therapy.

(b) ATD: Patients with high likelihood of remission (mild disease, small goiters, and negative or low-titer TRAb), pregnancy, patients with comorbidities which increase surgical risks, patients with limited life expectancy, individuals who have limited longevity, patients who are unable to follow radiation safety-related regulations, cases with previous operation on the neck or irradiation on the neck area, cases with lack of access to a thyroid surgeon with high-volume operations, patients with moderate active to severe active GO, and patients who need a rapid thyroid hormone level control.

(c) Surgery: Women planning a pregnancy in less than 6 months in condition that thyroid hormone levels are normal, symptomatic compression or large goiters, relatively low RAIU, when thyroid cancer is suspected or confirmed, cases with large thyroid nodules especially diameter larger than 4 cm or if nonfunctioning or hypo-functioning on a $^{99m}TcO_4^-$ thyroid scan, cases with coexisting hyperparathyroidism which also requires surgery removal, cases with particularly high TRAb level, and patients with moderate-to-severe active GO.

2. Contraindications

Contraindications to a particular modality as treatment for GD:

(a) ^{131}I therapy: Definite contraindications include pregnancy, lactation, coexisting thyroid cancer, or suspicious of thyroid cancer, individuals unable to comply with radiation safety guidelines, and used in women planning a pregnancy within 4–6 months.

(b) ATD: Definite contraindications include major adverse reactions to ATDs.

(c) Surgery: Factors against the choice of surgery include substantial comorbidity such as cardiopulmonary disease, end-stage malignancy, or other debilitating disorders or lack of access to a thyroid surgeon with high-volume operations. Pregnancy is a relative contraindication, and surgery should only be applied to cases needing a rapid control of hyperthyroidism, but ATD medications cannot be applied. Thyroidectomy should be avoided in the first and third trimesters of pregnancy due to teratogenic side-effects associated with anesthetic drugs. Besides, increased risk of fetal loss in the first trimester as well as increased risk of preterm labor in the third could occur. If necessarily required, thyroidectomy can be performed in the second trimester which is the safest time, but it is not without any risk.

16.3.1.5 Preparation of Patients with GD for ^{131}I Therapy

Because ^{131}I treatment of GD can induce a transient exacerbation status of hyperthyroidism because of the destructive release of thyroid hormone in the circulation, β-adrenergic blockade drugs should be considered even in asymptomatic patients who are at increased risk for complications due to worsening of hyperthyroidism, especially in elderly patients or cases with comorbidities. In addition to β-adrenergic blockade, a choice of pretreatment with ATD prior to ^{131}I

therapy should be considered to apply to patients who are at increased risk for such complications. ATD should be discontinued 2–7 days prior to ^{131}I treatment. Medical therapies for any comorbid conditions should be optimized before ^{131}I therapy. By the same token of therapeutic safety, in patients who are at an increased risk of complications due to possible worsening of hyperthyroidism, resuming ATD within 3–7 days post-^{131}I administration should be advised. A pregnancy test should be performed prior to ^{131}I treatment compulsorily in any woman with childbearing potential.

16.3.1.6 Dosage of ^{131}I

There are generally two methods of ^{131}I dosage determination for treating hyperthyroidism related to GD. The amount of ^{131}I to be administered could be empirically selected or determined by a dose calculation. Optimal treatment usually involves a single administration of ^{131}I as much as possible. In fact, the goal of ^{131}I therapy in GD is to control hyperthyroidism by rendering the hypothyroid status in the US [47, 48]. This treatment is very effective, provided sufficient radiation dose is achieved in the thyroid. However, the administration of repeated small amounts of ^{131}I activity (e.g., 2 mCi) at frequent intervals is generally not recommended, because by this way, patients will remain to suffer from hyperthyroidism for longer periods of time. This method has not been proven superior at preventing iatrogenic hypothyroidism.

1. Methods for ^{131}I Dosage Determination

   The calculation requires at least two unknown parameters to be acquired: the thyroid uptake of ^{131}I and the thyroid volume (thyroid weight). The therapeutic ^{131}I activity can then be calculated according to these two factors as well as the desired quantity of radiation (μCi or Bq) to be deposited per gram of thyroid [47, 48].

   By empirical method, a mean dosage of 10–15 mCi (370–555 MBq) is prescribed in order to render hypothyroidism to the patient with GD.

   In ATA recommended equation, for instance: ^{131}I activity (μCi) = gland weight (g) × 50 to 200 (μCi/g) × [1/24 h uptake in % of administered activity]. The most frequently used uptake is calculated at 24 h, and the thyroid volume is determined by ultrasound.

   Another example is from Tianjin Medical University Nuclear Medicine Department: activity (mCi) = estimated thyroid weight (g) × absorption dose (Gy/g) × 0.67/ [effective half-life (days) × maximum % uptake]. Absorption dose = 100 Gy/g, 0.67 is a rectified factor [52, 53].
2. Advantages of Either Approach

   Although treatments based on dose calculations appear efficacious, they have not proven superior to the use of empirically selected administered activities. The advantages of using a fixed administered activity for treating hyperthyroidism are its simplicity and successful outcome in an acceptable number of patients. The effectiveness of such an approach appears comparable to a dose calculation method. If a fixed amount of activity is chosen, it is still important to keep in mind that the effectiveness of therapy remains dependent on the total radiation dose to the target tissue. If the estimated dose to the thyroid exceeded 200 Gy in patients receiving a standardized treatment with 15 mCi, a success rate of 80% was obtained.

16.3.1.7 Follow-Up and Efficacy Assessments after ^{131}I Therapy for GD

Follow-up within the first 1–2 months after ^{131}I therapy for GD should include an assessment of free thyroxine, free triiodothyronine, and TSH. Biochemical monitoring should be continued at 4–6-week intervals for 6 months or until the patient becomes hypothyroid and managed as stable on thyroid hormone replacement.

16.3.1.8 Post-^{131}I Therapeutic Hypothyroidism Is Very Often

When adopting a fixed dosage strategy, which is often used in US, most patients respond to ^{131}I therapy with a normalized thyroid function tests and improved clinical symptoms in 4–8 weeks. Hypothyroidism might occur from 1 month on. This transition occurs more commonly between 2 and 6 months, and the timing and dosage of thyroid hormone replacement therapy should be determined by results of thyroid function tests, clinical symptoms, as well as physical examination. Occasionally, hyperthyroidism recurs, which requires a second ^{131}I therapy.

Under a calculation dosage strategy, which is often used in China, the greater the maximum RAIU, and the longer the effective half-life, the higher the possibility of a one-time cure. Elderly patients or patients with a positive TRAb and/or thyroglobulin antibody (TgAb) have a lower possibility of a one-time cure. Women with a positive TRAb should be administered with an increased ^{131}I dosage to improve the curative effect [52, 53]. In China, the incidence of early hypothyroidism (happens within a year of ^{131}I therapy) is higher than that of late hypothyroidism (happens later than a year of ^{131}I therapy). The higher the maximum RAIU, and/or the longer the effective half-life, and/or the higher the thyroid peroxidase antibody level, the higher the possibility of post-therapeutic hypothyroidism [51].

16.3.2 Management of Hyperthyroidism due to Toxic Multinodular Goiter and Toxic Adenoma

Radioactive iodine-131 therapy for toxic multinodular goiter and toxic adenoma is similar to the treatment for Graves' disease.

16.3.2.1 Treatment Modalities

^{131}I therapy and thyroid surgery are two effective and relatively safe therapeutic approaches for TMNG and TA, and the latter is more preferable. In particular, if the nodule or adenoma has thyroid cancer risk, then surgery is the only proper choice. The decision regarding therapeutic option should take into consideration a number of clinical and demographic factors, in addition to patient preference. The therapeutic objective is to achieve a rapid and durable elimination of the hyperthyroid state [47, 48].

For patients with TMNG, treatment failure rate or the need for repeated treatment is less than 1% following near-total and/or total thyroidectomy, compared with a 20% risk of the need for another treatment following ^{131}I therapy.

For patients with TA, the risk of treatment failure is less than 1% after ipsilateral thyroid lobectomy or isthmusectomy. For patients with TA who receive ^{131}I therapy, there is a 6–18% risk of persistent hyperthyroidism and a 3–5.5% risk of recurrent hyperthyroidism.

16.3.2.2 How to Perform ^{131}I Therapy

If ^{131}I is chosen as the therapy, higher dosage should be given. The dosage activity of ^{131}I used to treat TMNG is usually higher than that needed to treat GD. The dosage activity of ^{131}I can be calculated on the basis of goiter size to deliver 150–200 μCi (5.55–7.4 MBq) per gram of tissue, which is usually corrected for 24-h RAIU. ^{131}I administered to treat TA can be given either as a fixed dosage activity of approximately 10–20 mCi (370–740 MBq) or an activity calculated on the basis of nodule size by using 150–200 μCi (5.5–7.4 MBq) ^{131}I per gram after correction with 24-h RAIU.

16.3.3 Management of Hyperthyroidism in Children and Adolescents

Radioactive iodine-131 therapy for children and adolescents with hyperthyroidism is considered as an effective and safe therapeutic option.

16.3.3.1 Treatment Modalities

The treatment of pediatric patients with GD varies considerably among different institutions and physicians. It is important to recognize that lasting remission after even many years of ATD therapy occurs in only a small number of pediatric patients with GD. In determining the initial therapeutic approach, various factors, including the patient's age, clinical status, and likelihood of remission, should be accounted for consideration. Patient and parent values and preferences should also be strongly asked and acknowledged when choosing treatment modalities.

When ATD is chosen, methimazole should be used as the first choice in children. β-adrenergic blockade is always recommended for children who experience symptoms of hyperthyroidism, especially for those with heart rates exceeding 100 beats per minute.

Thyroidectomy is also an effective treatment modality for GD but is usually associated with a higher rate of complications in children than adults. Thyroidectomy should be performed in those children who are too young for ^{131}I therapy; adverse effects happen in ATD therapy.

16.3.3.2 How to Perform ^{131}I Therapy

Children with GD could be treated with the methods of ATD, ^{131}I therapy, or thyroidectomy in preference order. ^{131}I therapy should usually be avoided in very young children (less than 5 years).

^{131}I therapy in children is acceptable when the activity is higher than 150 μCi/g (5.55 MBq/g) of thyroid tissue, as well as for children between 5 and 10 years, if the calculated ^{131}I administered activity is less than 10 mCi (370 MBq). Thyroidectomy should be chosen when treatment is required definitively, and the child is too young for ^{131}I. Surgery can be performed by a high-volume thyroid surgeon. Properly administered, ^{131}I is an effective treatment for GD in the pediatric population [54]. Although ^{131}I is used widely in children, it is still viewed as a controversy by some practitioners owing primarily to a concern of cancer risk. There are sparse clinical data about ^{131}I use in children with GD and subsequent occurrence of thyroid cancer. But, it is known that risks of thyroid cancer after external irradiation are highest in children less than 5 years of age, and the risk declines with aging [55]. In comparison, dosage activities of ^{131}I used are not known to be associated with an increased risk of thyroid cancer in children.

ATA guideline emphasizes that if ^{131}I therapy is chosen as the treatment for GD in children, sufficient ^{131}I should be administered in a single dose to render hypothyroidism to the patient [47, 48]. The procedures are the same as in adults as described above.

16.3.4 Management of Hyperthyroidism Patients with GO

GO is an inflammatory eye disease that develops in the orbit, which is caused in association with and due to autoimmune thyroid disorders. Approximately a third of patients with Graves' hyperthyroidism have signs and/or symptoms of GO with various degrees. Only 5% have moderate-to-severe GO. Current therapeutic approaches to GO include local managements, corticosteroids, orbital radiation, and surgery [56]. Severity of GO is often measured by GO elements generally agreed upon by the European Group on Graves' Orbitopathy (EUGOGO) [56]. Firstly, euthyroidism should be expeditiously achieved and maintained expeditiously in

hyperthyroid patients with GO or in patients with risk factors for the development of GO. Secondly, since smoking is a definite risk factor for GO, patients with GD need to quit smoking and refer to a smoking cessation program. Because both firsthand and secondhand smoking will increase GO risk, patients exposed to secondhand smoking should also be identified and advised of the negative impact. Thirdly, in non-smoking patients with GD without apparent GO, in smoking patients with GD without apparent GO, as well as in patients with Graves' hyperthyroidism who have only mild active ophthalmopathy and no risk factors for deterioration of eye disease, ^{131}I therapy, ATDs, or thyroidectomy should be considered equally acceptable therapeutic options in regard to risk of GO. Fourthly, in GD patients with mild GO who are treated with ^{131}I, steroid usage is recommended when there are concomitant risk factors for GO deterioration. Fifthly, in patients with active and moderate-to-severe GO or sight-threatening situation, ^{131}I therapy is not recommended; surgery or ATDs are preferred treatment options for these patients [47, 48]. Lastly, development of persistent, untreated hypothyroidism after therapy for hyperthyroidism is reported to play a detrimental role in the GO progression. The higher risk of GO development after^{131}I therapy may also be related to the unique increase in TRAb levels observed following this therapy. There are experimental evidence suggesting that TRAb is directly involved in GO pathogenesis.

16.3.5 Cancer Risk and Radiation Safety Regarding Radioiodine Therapy for Hyperthyroidism

In young children after ^{131}I treatment, there is a theoretical risk of thyroid cancer development. Detractors of ^{131}I therapy in children point to the increased rates of thyroid cancer and thyroid nodules observed in young children exposed to radiation from Hiroshima nuclear bomb blast or after the Chernobyl nuclear reactor disaster. However, these data do not apply directly to assessing risks of ^{131}I therapy. Notably, thyroid cancer rate was not increased among children exposed to ^{131}I from the Hanford nuclear reactor accident in an iodine-replete region [57]. Increased thyroid cancer rates also were not seen in children who received ^{131}I diagnostic scanning. In another study, an analysis was carried out on individuals who were exposed to ^{131}I below 20 years of age in Swedish and US populations [58]. The average follow-up period was 10 years, and the mean administered ^{131}I activity to the thyroid was 88 Gy, an activity considered to be associated with thyroid neoplasia and below the recommendation for GD treatment. Two cases of thyroid cancer were identified compared to just 0.1 cases over that period of time. The pediatric study with the longest follow-up time reported 36-year outcomes, after treatment with ^{131}I between 1953 and 1973 [59]. The patients' age at treatment ranged from 3 to 19 years. No patient developed thyroid cancer or leukemia eventually. There was also no increase in the rate of spontaneous abortion or in the number of congenital anomalies in offspring. Another study found that the incidence of thyroid cancer in ^{131}I-treated patients over a 27-year period was not significantly different from its incidence in the general population [60]. One population-based study actually found a small decrease in the risk of several types of cancer following radioiodine therapy [61].

To date, long-term studies of GD children treated with ^{131}I have not demonstrated an increased risk of non-thyroid malignancies. Even a small risk exists; a sample size of more than 10,000 children treated at less than 10 years of age would be needed to identify such a risk, likely exceeding the number of all such treated children. However, based on cancer risk projections from estimated whole-body, low-level radiation exposure related to age, there is a theoretically possibility that there may be a low risk of malignancies in very young children treated with ^{131}I. It is recommended that ^{131}I therapy be avoided in such young children (less than 5 years). If ^{131}I is considered in those children between 5 and 10 years of age, the required activity for treatment should be less than 10 mCi (<370 MBq). It is important to emphasize that these recommendations are only based on theoretical concerns, and further direct study is needed. The theoretical risks of ^{131}I use must be balanced with the known risks inherent in thyroidectomy or prolonged ATD use when choosing among the three different GD treatment options in the pediatric age group.

There is no evidence that exposure to ^{131}I affects subsequent pregnancies and offspring. A 370 MBq (10 mCi) dose of ^{131}I is estimated to deliver a dose of approximately 0.01–0.03 Gy to the ovaries, which mostly came from excreted ^{131}I in the bladder. Therefore, hydration and frequent voiding following treatment are advised to minimize radiation dosage. Women of childbearing age should refrain from becoming pregnant for at least 6 months after ^{131}I therapy.

References

1. Ahn BC (2012) Sodium iodide symporter for nuclear molecular imaging and gene therapy: from bedside to bench and back. Theranostics 2(4):392–402
2. Silberstein EB (2012) Radioiodine: the classic theranostic agent. Semin Nucl Med 42(3):164–170
3. Zhang J, Lazar MA (2000) The mechanism of action of thyroid hormones. Annu Rev Physiol 62:439–466
4. Ravera S, Reyna-Neyra A, Ferrandino G et al (2017) The sodium/iodide symporter (NIS): molecular physiology and preclinical and clinical applications. Annu Rev Physiol 79:261–289
5. Riedel C, Levy O, Carrasco N (2001) Post-transcriptional regulation of the sodium/iodide symporter by thyrotropin. J Biol Chem 276(24):21458–21463

6. Schmutzler C, Schmitt TL, Glaser F et al (2002) The promoter of the human sodium/iodide-symporter gene responds to retinoic acid. Mol Cell Endocrinol 189(1–2):145–155
7. Serrano-Nascimento C, Nicola JP, Teixeira Sda S et al (2016) Excess iodide downregulates Na(+)/I(−) symporter gene transcription through activation of PI3K/Akt pathway. Mol Cell Endocrinol 426:73–90
8. Vu-Phan D, Koenig RJ (2014) Genetics and epigenetics of sporadic thyroid cancer. Mol Cell Endocrinol 386(1–2):55–66
9. Galrao AL, Camargo RY, Friguglietti CU et al (2014) Hypermethylation of a new distal sodium/iodide symporter (NIS) enhancer (NDE) is associated with reduced NIS expression in thyroid tumors. J Clin Endocrinol Metab 99(6):E944–E952
10. Zhang Z, Liu D, Murugan AK et al (2014) Histone deacetylation of NIS promoter underlies BRAF V600E-promoted NIS silencing in thyroid cancer. Endocr Relat Cancer 21(2):161–173
11. Riesco-Eizaguirre G, Wert-Lamas L, Perales-Paton J et al (2015) The miR-146b-3p/PAX8/NIS regulatory circuit modulates the differentiation phenotype and function of thyroid cells during carcinogenesis. Cancer Res 75(19):4119–4130
12. Shen CT, Qiu ZL, Song HJ et al (2016) miRNA-106a directly targeting RARB associates with the expression of Na(+)/I(-) symporter in thyroid cancer by regulating MAPK signaling pathway. J Exp Clin Cancer Res 35(1):101
13. O'Doherty J, Jauregui-Osoro M, Brothwood T et al (2017) (18) F-tetrafluoroborate, a PET probe for imaging sodium/iodide symporter expression: whole-body biodistribution, safety, and radiation dosimetry in thyroid cancer patients. J Nucl Med 58(10):1666–1671
14. Haugen BR, Alexander EK, Bible KC et al (2016) 2015 American Thyroid Association management guidelines for adult patients with thyroid nodules and differentiated thyroid cancer: the American Thyroid Association guidelines task force on thyroid nodules and differentiated thyroid cancer. Thyroid 26(1):1–133
15. Lamartina L, Durante C, Filetti S et al (2015) Low-risk differentiated thyroid cancer and radioiodine remnant ablation: a systematic review of the literature. J Clin Endocrinol Metab 100(5):1748–1761
16. Ruel E, Thomas S, Dinan M et al (2015) Adjuvant radioactive iodine therapy is associated with improved survival for patients with intermediate-risk papillary thyroid cancer. J Clin Endocrinol Metab 100(4):1529–1536
17. Edmonds CJ, Hayes S, Kermode JC et al (1977) Measurement of serum TSH and thyroid hormones in the management of treatment of thyroid carcinoma with radioiodine. Br J Radiol 50(599): 799–807
18. Mazzaferri EL, Kloos RT (2002) Is diagnostic iodine-131 scanning with recombinant human TSH useful in the follow-up of differentiated thyroid cancer after thyroid ablation? J Clin Endocrinol Metab 87(4):1490–1498
19. Bianchi L, Baroli A, Lomuscio G et al (2012) Dosimetry in the therapy of metastatic differentiated thyroid cancer administering high 131I activity: the experience of Busto Arsizio Hospital (Italy). Q J Nucl Med Mol Imaging 56(6):515–521
20. Benua RS, Cicale NR, Sonenberg M et al (1962) The relation of radioiodine dosimetry to results and complications in the treatment of metastatic thyroid cancer. Am J Roentgenol Radium Ther Nucl Med 87:171–182
21. Maxon HR, Thomas SR, Hertzberg VS et al (1983) Relation between effective radiation dose and outcome of radioiodine therapy for thyroid cancer. N Engl J Med 309(16):937–941
22. Kuker R, Sztejnberg M, Gulec S (2017) I-124 imaging and dosimetry. Mol Imaging Radionucl Ther 26(Suppl 1):66–73
23. Chiesa C, Castellani MR, Vellani C et al (2009) Individualized dosimetry in the management of metastatic differentiated thyroid cancer. Q J Nucl Med Mol Imaging 53(5):546–561
24. Sgouros G, Kolbert KS, Sheikh A et al (2004) Patient-specific dosimetry for 131I thyroid cancer therapy using 124I PET and 3-dimensional-internal dosimetry (3D-ID) software. J Nucl Med 45(8):1366–1372
25. Flower MA, Schlesinger T, Hinton PJ et al (1989) Radiation dose assessment in radioiodine therapy. 2. Practical implementation using quantitative scanning and PET, with initial results on thyroid carcinoma. Radiother Oncol 15(4):345–357
26. Dorn R, Kopp J, Vogt H et al (2003) Dosimetry-guided radioactive iodine treatment in patients with metastatic differentiated thyroid cancer: largest safe dose using a risk-adapted approach. J Nucl Med 44(3):451–456
27. Wierts R, Brans B, Havekes B et al (2016) Dose-response relationship in differentiated thyroid cancer patients undergoing radioiodine treatment assessed by means of 124I PET/CT. J Nucl Med 57(7):1027–1032
28. Deandreis D, Rubino C, Tala H et al (2017) Comparison of empiric versus whole-body/-blood clearance dosimetry-based approach to radioactive iodine treatment in patients with metastases from differentiated thyroid cancer. J Nucl Med 58(5):717–722
29. Urhan M, Dadparvar S, Mavi A et al (2007) Iodine-123 as a diagnostic imaging agent in differentiated thyroid carcinoma: a comparison with iodine-131 post-treatment scanning and serum thyroglobulin measurement. Eur J Nucl Med Mol Imaging 34(7):1012–1017
30. Santhanam P, Taieb D, Solnes L et al (2017) Utility of I-124 PET/CT in identifying radioiodine avid lesions in differentiated thyroid cancer: a systematic review and meta-analysis. Clin Endocrinol (Oxf) 86(5):645–651
31. Haslerud T, Brauckhoff K, Reisaeter L et al (2016) F18-FDG-PET for recurrent differentiated thyroid cancer: a systematic meta-analysis. Acta Radiol 57(10):1193–1200
32. Feine U, Lietzenmayer R, Hanke JP et al (1995) 18FDG whole-body PET in differentiated thyroid carcinoma. Flipflop in uptake patterns of 18FDG and 131I. Nuklearmedizin 34(4):127–134
33. Leboulleux S, El Bez I, Borget I et al (2012) Postradioiodine treatment whole-body scan in the era of 18-fluorodeoxyglucose positron emission tomography for differentiated thyroid carcinoma with elevated serum thyroglobulin levels. Thyroid 22(8):832–838
34. Rosario PW, Furtado Mde S, Mineiro Filho AF et al (2012) Value of diagnostic radioiodine whole-body scanning after initial therapy in patients with differentiated thyroid cancer at intermediate and high risk for recurrence. Thyroid 22(11):1165–1169
35. Pacini F, Capezzone M, Elisei R et al (2002) Diagnostic 131-iodine whole-body scan may be avoided in thyroid cancer patients who have undetectable stimulated serum Tg levels after initial treatment. J Clin Endocrinol Metab 87(4):1499–1501
36. Rosario PW, Mineiro Filho AF, Lacerda RX et al (2012) The value of diagnostic whole-body scanning and serum thyroglobulin in the presence of elevated serum thyrotropin during follow-up of anti-thyroglobulin antibody-positive patients with differentiated thyroid carcinoma who appeared to be free of disease after total thyroidectomy and radioactive iodine ablation. Thyroid 22(2):113–116
37. Chudgar AV, Shah JC (2017) Pictorial review of false-positive results on radioiodine scintigrams of patients with differentiated thyroid cancer. Radiographics 37(1):298–315
38. Jiang X, Zeng H, Gong J et al (2015) Unusual uptake of radioiodine in a retroperitoneal bronchogenic cyst in a patient with thyroid carcinoma. Clin Nucl Med 40(5):435–436
39. Jiang X, Wang Q, Huang R (2015) Nasal visualization on radioiodine whole-body scintigraphy due to benign abnormality. Clin Nucl Med 40(4):340–342
40. Shen G, Jing X, Zhang Y et al (2017) Unusual uptake of radioiodine in a subcutaneous lipoma in a patient with differentiated thyroid cancer. Clin Nucl Med 42(1):e75–e76
41. Zhou H, Yan J, Huang R et al (2018) Unusual uptake of 131I in a cutaneous benign fibrous histiocytoma in a patient with thyroid cancer. Clin Nucl Med 43(1):e31–e32

42. Means JH, Holmes GW (1923) Further observations on the Roentgen ray treatment of toxic goiter. Arch Intern Med 31:303
43. Hertz S, Roberts A (1946) Radioactive iodine in the study of thyroid physiology; the use of radioactive iodine therapy in hyperthyroidism. JAMA 131:81–86
44. Chapman EM, Evans RD (1946) The treatment of hyperthyroidism with radioactive iodine. JAMA 131:86–91
45. Crispell KR, Parson W, Sprinkle P (1953) A simplified technique for the diagnosis of hyperthyroidism, utilizing the one-hour uptake of orally administered I131. J Clin Endocrinol Metab 13(2):221–224
46. Becker DV, Sawin CT (1996) Radioiodine and thyroid disease: the beginning. Semin Nucl Med 26(3):155–164
47. Bahn Chair RS, Burch HB, Cooper DS et al (2011) Hyperthyroidism and other causes of thyrotoxicosis: management guidelines of the American Thyroid Association and American Association of Clinical Endocrinologists. Thyroid 21(6):593–646
48. Ross DS, Burch HB, Cooper DS et al (2016) 2016 American Thyroid Association guidelines for diagnosis and management of hyperthyroidism and other causes of thyrotoxicosis. Thyroid 26(10):1343–1421
49. Wartofsky L, Glinoer D, Solomon B et al (1991) Differences and similarities in the diagnosis and treatment of Graves' disease in Europe, Japan, and the United States. Thyroid 1(2):129–135
50. Burch HB, Burman KD, Cooper DS (2012) A 2011 survey of clinical practice patterns in the management of Graves' disease. J Clin Endocrinol Metab 97(12):4549–4558
51. Meng Z, Zhang G, Sun H et al (2015) Differentiation between Graves' disease and painless thyroiditis by diffusion-weighted imaging, thyroid iodine uptake, thyroid scintigraphy and serum parameters. Exp Ther Med 9(6):2165–2172
52. Wang RF, Tan J, Zhang GZ et al (2010) A comparative study of influential factors correlating with early and late hypothyroidism after (131)I therapy for Graves' disease. Chin Med J (Engl) 123(12):1528–1532
53. Zheng W, Jian T, Guizhi Z et al (2012) Analysis of (1)(3)(1)I therapy and correlation factors of Graves' disease patients: a 4-year retrospective study. Nucl Med Commun 33(1):97–101
54. Rivkees SA, Sklar C, Freemark M (1998) Clinical review 99: the management of Graves' disease in children, with special emphasis on radioiodine treatment. J Clin Endocrinol Metab 83(11):3767–3776
55. Boice JD Jr (2005) Radiation-induced thyroid cancer—what's new? J Natl Cancer Inst 97(10):703–705
56. Bartalena L, Baldeschi L, Dickinson AJ et al (2008) Consensus statement of the European group on Graves' orbitopathy (EUGOGO) on management of Graves' orbitopathy. Thyroid 18(3):333–346
57. Davis S, Kopecky KJ, Hamilton TE et al (2004) Thyroid neoplasia, autoimmune thyroiditis, and hypothyroidism in persons exposed to iodine 131 from the Hanford nuclear site. JAMA 292(21):2600–2613
58. Shore RE (1992) Issues and epidemiological evidence regarding radiation-induced thyroid cancer. Radiat Res 131(1):98–111
59. Read CH Jr, Tansey MJ, Menda Y (2004) A 36-year retrospective analysis of the efficacy and safety of radioactive iodine in treating young Graves' patients. J Clin Endocrinol Metab 89(9):4229–4233
60. Ron E, Doody MM, Becker DV et al (1998) Cancer mortality following treatment for adult hyperthyroidism. Cooperative thyrotoxicosis therapy follow-up study group. JAMA 280(4):347–355
61. Angusti T, Codegone A, Pellerito R et al (2000) Thyroid cancer prevalence after radioiodine treatment of hyperthyroidism. J Nucl Med 41(6):1006–1009

Molecular Imaging and Targeted Therapy in Neurology

17

Qian Xu, Weishan Zhang, and Chuantao Zuo

17.1 Parkinson's Disease

As the most common motor neurodegenerative disorder, Parkinson's disease has been the second most common neurodegenerative disorder after Alzheimer's disease (AD). The prevalence of Parkinson's disease (PD) is around 1% at age 60 and 4–5% at 85. Bradykinesia is the most important symptoms in PD, and resting tremor, rigidity, and postural instability are the other three cardinal motor symptoms presented in the disease. Two main neuropathologies of PD are characterized by progressive cell loss of dopaminergic neurons predominately of the ventrolateral part of the pars compacta of the substantia nigra and the presence of Lewy pathology including Lewy bodies (LBs) and Lewy neurites (LNs).

As the accurate diagnosis of PD depends on autopsy of substantia nigra, the current clinical diagnosis of PD is decided by the special motor neurologists by assessing the clinical signs and the response to levodopa therapy. However, only 76% of patients thought clinically to have PD prove to have this diagnosis at postmortem. And it is reported that the misdiagnosis rates are as high as 20–30% in early stages. It is necessary and instrumental to utilize more objective method to in vivo explore the underlying mechanisms and make a better diagnosis. Functional neuroimaging methods, such as PET and SPECT with various radioactive tracers (radioligands), can not only provide objectively quantitative assessment but also demonstrate the prompt and patient-based molecular signaling pattern that is essential for the individualized assessment in different points of care.

Functional imaging methods that we use widely in PD can currently be divided into investigation of glucose metabolism and investigations of receptor binding.

Q. Xu · W. Zhang · C. Zuo (✉)
PET Center, Huashan Hospital, Fudan University, Shanghai, P. R. China

17.1.1 ^{18}F-FDG PET Imaging

^{18}F-FDG PET imaging has been employed to assess regional cerebral glucose metabolism. Myriads of researches utilized it to quantify presynaptic dopaminergic function indirectly through the measurement of changes in brain metabolism occurring downstream from the nigrostriatal lesion and obtained the specific FDG PET imaging in PD patients that showed regionally increased metabolism in the lentiform nucleus, thalamus, pons, and cerebellum and relatively decreased metabolism in the lateral frontal, paracentral, and parietal association areas.

Disease-specific patterns of reduced glucose metabolism have shown higher accuracy in differentiating PD from other Parkinsonism such as multiple system atrophy (MSA) and progressive supranuclear palsy (PSP). From a single case basis, FDG PET was possibly considered to differentiate patients with presumed PD, MSA, PSP, CBGD, and healthy controls with an accuracy of about 90% based on a retrospective analysis of the scan data. As FDG PET imaging can particularly measures the local synaptic activity and biochemical maintenance processes which dominate cerebral function at rest state, the effects of pathology in neurodegenerative diseases on these functions have a greater influence on regional cerebral metabolism than do other factors. It was recognized that neuropathological processes, even if highly localized, could alter regional functional connectivity across the entire brain in a disease-specific manner.

Obviously, pathological occurrence and neurotransmitter system changes ultimately affect brain networks in PD. In this regard, Moeller and colleagues developed the scaled subprofile model (SSM), a spatial covariance mapping method based on principal component analysis (PCA) which was proven to be useful as a means of identifying network abnormalities. Using this network modeling approach, the PD-related pattern (PDRP) was initially identified from region-of-interest (ROI) analysis and subsequently extended to voxel-based analysis over the whole brain. PDRP has been

G. Huang (ed.), *Nuclear Medicine in Oncology*, https://doi.org/10.1007/978-981-13-7458-6_17

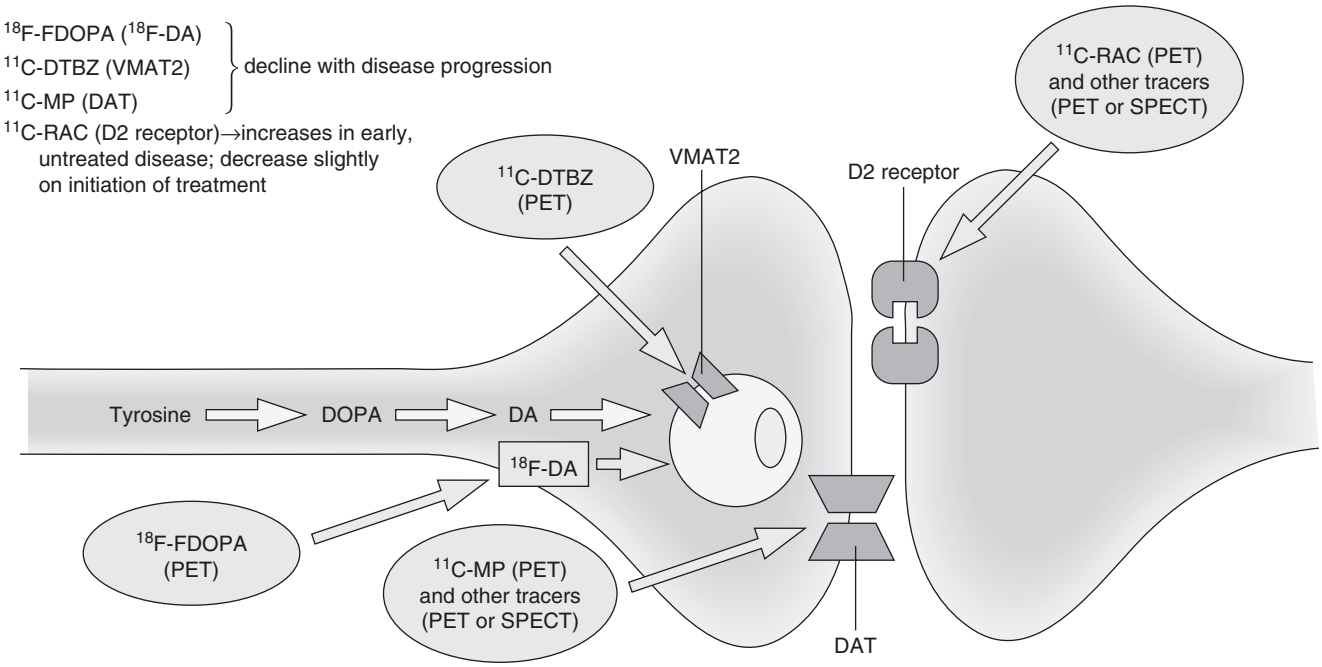

Fig. 17.1 Nigrostriatal dopaminergic tract imaging

characterized by relative increases in pallidothalamic, pontine, and cerebellar metabolism, accompanied with concurrent metabolic decreases in the premotor and posterior parietal areas.

Other more detailed and classified Parkinsonian models expressed in ^{18}F-FDG PET imaging have been proposed including PD tremor-related pattern (PDTP) and PD-related cognitive pattern (PDCP). PDTP refers to increased metabolic activity in the primary motor cortex, anterior cerebellum/dorsal pons, and the caudate/putamen in tremor-dominant PD patients. And PDCP is characterized by metabolic reductions in frontal and parietal association areas and relative increases in the cerebellar vermis and dentate nuclei.

17.1.2 Nigrostriatal Dopaminergic Tract Imaging

The progressive loss of dopaminergic neurons within the SNpc is the most characteristic neuropathology in PD. Moreover, the most profoundly affected area of the SNpc is typically the ventrolateral tier, which contains neurons that project to the dorsal putamen of the striatum. Functional neuroimaging of the nigrostriatal dopaminergic pathway has become an important method for quantification of functional dopaminergic terminals in the striatum. It can be divided into two aspects: presynaptic and postsynaptic dopaminergic imaging.

Presynaptic nigrostriatal neurons can be imaged by measurement of the activity of aromatic-amino-acid decarboxylase (AADC), dopamine transporter (DAT), and vesicular monoamine transporter 2 (VMAT2). Postsynaptic dopaminergic function is assessed by the use of dopamine D2 receptor ligands (Fig. 17.1).

Table 17.1 Radiotracers of presynaptic dopaminergic function

	Radiotracers		
Imaging techniques	DAT	VMAT2	AADC activity
PET	^{11}C-CFT	^{11}C-DTBZ	
	^{11}C-WIN	^{18}F-DTBZ	
	^{11}C-nomifensine		
SPECT	^{123}I-FP-CIT	–	–
	^{123}I-β-CIT		
	^{99m}Tc-TRODAT		

17.1.2.1 Presynaptic Dopaminergic Function

Radiotracers of presynaptic dopaminergic function are presented in Table 17.1.

DOPA Decarboxylase Activity

Aromatic acid decarboxylase (AADC) exists in the presynaptic cytoplasm, and its function is promoting the synthesis of dopamine in the dopaminergic neurons. In the early stage of PD, AADC is upregulated. With the progressive loss of dopaminergic neurons, decarboxylase declines dramatically. ^{18}F-FDOPA PET assesses the rate of decarboxylation of FDOPA to ^{18}F-fluorodopamine, which depends on the function of the dopa decarboxylase activity, and also estimates its storage in dopaminergic nerve terminals. FDOPA uptake is not a direct index for endogenous dopamine synthesis, but

for the current knowledge, it is strongly correlated with dopamine cell counts determined in postmortem specimens.

As representing the activity of dopa decarboxylase, FDOPA signaling correlates with the disease severity and disease progression. In the early stage of PD, FDOPA uptake may increase for the transient upregulation of AADC and then diminished mainly in the posterior putamen and relatively preserved in the anterior putamen and caudate. In relative late stage of disease, PET imaging shows an obvious decrease of ^{18}F-FDOPA uptake in the whole striatum, which is in line with the neuropathological features in PD. Due to its great sensitivity in detecting the loss of dopaminergic neurons, FDOPA PET is a powerful approach to differentiate healthy subjects from PD patients even in early disease stages and from patients with MSA or PSP. Originally, FDOPA has also been used to distinguish among parkinsonian syndromes.

Dopamine Transporter

The dopamine transporter (DAT) lies in the presynaptic membrane on the terminal of dopaminergic neurons and manipulates the release and reabsorption of dopamine in the nigrostriatal inter-synaptic cleft. The expression of DAT that controls the reuptake of synaptic dopamine decreases in the initiation of PD, and the possible explanation is also to compensate the reduced level of dopamine in the synaptic cleft of dopaminergic neurons. And the DAT decreased rapidly with the huge damage to the dopaminergic terminals in striatum. The level of DAT can be measured through a variety of PET ligands, including ^{18}F-FP-CIT, ^{11}C-RTI-32, and FE-CBT, as well as SPECT compounds as β-CIT, FP-CIT, IPT, and TRODAT. Reduction of DAT availability is obvious in parkinsonian patients, which enables this method to differentiate patients with parkinsonian disorders from healthy subjects and patients with essential tremor. Furthermore DAT binding is correlated with the severity of disease in patients with parkinsonian disorder. Differentiating ability of DAT imaging to distinguish PD patients from healthy controls is equivalent to the power of FDOPA PET.

Vesicular Monoamine Transporter 2

Vesicular monoamine transporter type 2 (VMAT2) is a protein that enables the monoamine transportation from cytosol into synaptic vesicles, and it especially existed in the endocrine cells and brain. As VMAT2 functions in vesicular packaging and storage of monoamine neurotransmitters in the synapses of the brain, it plays a key role in the reuptake mechanism, while VMAT2 signaling in the central nervous system could reflect the integrity (total number) of all three monoaminergic neurons. The striatum contained the greatest densities of VMAT2, while both the cortex and cerebellum have relatively sparse VMAT2 levels, only about 1% of the striatal concentration. Since previous reports have demonstrated that drugs for PD did not have a long-term effect on the VMAT2-binding sites, and meanwhile VMAT2 density is correlated to the integrity of SN dopamine neurons, VMAT2 availability may serve as a sensitive measurement of vesicular dopamine levels.

As the latest novel radiotracer for VMAT2, ^{18}F-DTBZ has been designed for a wider clinical utilization. For the features of ^{18}F-DTBZ imaging in patients with PD, the nigrostriatal binding revealed a gradual reduction with the disease progression. Regional integrity of VMAT2 was mostly affected in the posterior *putamen* (PPu) among all patients with PD, followed by the anterior *putamen* (APu), caudate, and SN. This result was in accordance with the postmortem results indicating that the apoptosis of dopaminergic neurons in the lateral ventral tier of the SN projecting to the putamen was most severe.

17.1.2.2 Postsynaptic Dopaminergic Function

The D2 receptors may be upregulated in early-untreated PD patients, probably revealing a means to compensate for presynaptic dopaminergic dysfunction. In later disease stages, this compensating mechanism is lost, leading to a slight reduction or normalization of D2 receptor binding, particularly in patients presenting an unstable levodopa response. The D2 receptor imaging is used primarily in differentiating PD from MSA-P. The fact behind these studies is that D2R-expressing striatal neurons tend to degenerate in MSA-P but not in PD.

Compared with healthy controls, striatal DR2 binding in patients with PD was found to be normal, increased, or decreased. However, D2R binding in the striatum (especially the posterior putamen) of MSA-P patients was reported to reduce. At the same time, most studies found a great overlap of striatal D2R-binding profile between MSA-P and PD patients, which may weaken the diagnostic performance of D2R imaging in individual patients. We summarize the common radiotracers targeted on postsynaptic dopamine receptors in Table 17.2.

Table 17.2 Radiotracers of postsynaptic dopaminergic function

	Radiotracers	
Imaging techniques	D1 receptor probe	D2/3 receptor probe
PET	^{11}C-SCH-23390	^{11}C-raclopride
	^{11}C-NNC-112	^{18}F-fallypride
		^{18}F-desmethoxyfallypride
		^{11}C-N-methylspiperone
		^{18}F-benperidol
		^{11}C-FLB-457
		^{11}C-NPA
		^{18}F-DTBZ
		^{11}C-PHNO
SPECT		^{123}I-IBZM
		^{123}I-epidepride

17.1.3 α-Synuclein Imaging

Apart from the degeneration of dopaminergic neurons, the other hallmark of PD is Lewy pathology. Lewy pathology is the aggregation of abnormally folded proteins, which has been recognized as a common theme in neurodegenerative diseases including PD. Although α-synuclein is an integral part in the pathology of PD, the mechanism(s) whereby aberrant α-synuclein homeostasis causes neurodegeneration remain undetermined. α-Synuclein plays a key role in regulating the size of the vesicular pool, vesicular trafficking to and docking with the presynaptic membrane, and subsequent clathrin-associated formation of synaptic vesicles. Therefore, loss of function may explain the major mechanism underlying α-synuclein toxicity. Besides, α-synuclein is also involved in the regulation of DA biosynthesis and handling. Loss of function results in dysregulated DA handling, as well as the subsequent DA associated toxicity.

Another mechanism underlying the loss of α-synuclein function which produces neurodegeneration is by a destroyed ability to tackle with a variety of cellular stress, including DA toxicity, staurosporine-induced apoptosis, oxidative stress, and serum deprivation. In addition, α-synuclein expression greatly lowers the apoptotic response of neuronal cells by decreasing both p53 expression and p53 transcriptional activity, and there is no doubt that this effect loses when soluble α-synuclein becomes sequestered in aggregates. In summary, loss of α-synuclein function likely results in an increase in DA-mediated cellular stressors, along with a concomitant decrease in the ability of neuronal cells to rebound from the same toxicity. Based on a large number of researches, Braak and colleagues have proposed that the progression of α-synuclein accumulation from preclinical to symptomatic, and subsequently to advanced disease, is not random but spreads along axonal pathways interconnecting vulnerable brain regions in a constant pattern which has been arbitrarily subdivided into six different stages. However, there is no radiotracer specific for α-synuclein being designed today, and it would be beneficial to differentiate PD from other neurodegenerative disorders.

17.1.4 β-Amyloid Imaging

Motor features, for a long time, have been recognized as major symptomatology of PD. But the symptoms of PD are now considered as heterogeneous, as depression and hallucinations are clinically common non-motor features. Similarly, extensive regions within the brain, various neurotransmitters, and toxic protein aggregates are involved in the pathology of PD. For example, β-amyloid plaques and tau-containing neurofibrillary tangles which are regarded as main protein inclusions in Alzheimer's disease (AD) can also exist in the brains of PD patients. Previous study suggested that the amount of associated cortical β-amyloid appears to be the crucial factor for the cognitive decline in PD.

The most widely used molecular probe for β-amyloid imaging was ^{11}C-PIB as it has good affinity to extra-cell β-amyloid plaques but, however, poor to intra-cell or Lewy pathology. So it showed no significant uptake in PD.

17.1.5 Neuroinflammation Imaging

Nowadays, neuroinflammation has also been considered as a key pathological process in many neurodegenerative disorders including PD, while the microglial activation is not only involved in but also regarded as a hallmark of the neuroinflammation in that activated microglia can produce various trophic factors including brain-derived neurotrophic factor and glial-derived neurotrophic factor, as well as the harmful reactive oxygen and nitrogen species and pro-inflammatory cytokines. It is reported that both reactive gliosis induced by activated astrocytes and microgliosis resulting from microglial activation exist in the brain areas of degeneration in PD patients.

Translocator protein 18 kDa (TSPO) is located on the outer membrane of the mitochondria and expresses in a pretty low level in the microglial cells within the healthy human brain, while TSPO can be over expressed on the activated microglial cells. Therefore, the molecular imaging based on TSPO has been commonly used to detect neuroinflammation in various neural disorders. ^{11}C-PK11195 was the first discovered tracer to image TSPO, and ^{11}C-PK11195 PET imaging demonstrated the higher uptake in midbrain of patients with PD compared with the healthy controls. However, ^{11}C-PK11195 reveals some limitations in the clinical application including high level of nonspecific binding, poor signal-to-noise ratio, and relatively short half-life (20.4 min). To improve the quality of TSPO imaging, nearly 100 radiotracers have been developed. The classic new-generation TSPO tracers include ^{11}C-DAA1106, ^{11}C-PBR28, ^{11}C-DPA-713, ^{18}F-PBR06, ^{18}F-FEPPA, ^{18}F-FEDAA106, ^{18}F-DPA-714, and ^{18}F-GE180. Both Annelaure Damont et al. and Frédéric Dollé et al. thoroughly reviewed on this topic.

Apart from TSPO, other targets toward microglial cells including cannabinoid receptor 2 (CB2), cyclooxygenase 2 (Cox-2), and matrix metalloproteinase 9 (MMP9) have been proposed to in vivo activated microglial cells in neuroinflammation. And meanwhile tracers targeted to monoamine oxidase B (MAO-B) that highly expresses in the activated astrocytes during the neuroinflammatory process, like ^{11}C-DED, were also successfully developed to visualize the neuroinflammation.

17.2 Alzheimer's Disease

17.2.1 Background

Dementia is a clinical syndrome characterized by developing cognitive deficits that can severely interfere with daily life and work. There are 35 million patients with dementia and

costs over $600 billion per year, which makes it a major public health concern. Alzheimer's disease (AD) is the most common cause of dementia, following by vascular dementia, dementia with Lewy body (DLB), and frontotemporal dementia (FTD). Two forms of AD are known to us. Most cases are sporadic in nature; other causes can be mutations in the genes of presenilins or amyloid-β protein precursor (AβPP). Various cognitive domains of AD patients can be interfered progressively, including short-term memory, judgment and reasoning, orientation, and personality, and resulted in a total loss of memory and personality change. With abnormal biomarkers, AD is divided into three clinical stages: preclinical (no or subtle cognitive impairment), mild cognitive impairment (MCI) or prodromal AD (episodic memory impairment), and dementia (clear cognitive and functional impairment).

Mechanisms inducing the occurrence of AD are still not so clear, although aggregations of amyloid-β (Aβ) into amyloid plaques and of hyperphosphorylated microtubule-associated protein tau into neurofibrillary tangles (NFTs) are commonly recognized pathological characteristics of AD. Mechanisms thought to be closely related with AD are Aβ peptides and its cascade reaction, tau protein hyperphosphorylation, impairment of cholinergic system, APOE allele status, excessive immune reaction, etc. Moreover, current therapy can neither cure AD or dementia nor modify disease progress of them. By the time AD manifests, irreversible and considerable loss of synapses, neurons, and brain tissue has happened. Therefore, effective treatment needs to be achieved at preclinical stages. Biomarkers that can be applied to infer the preclinical change include Aβ and tau content in CSF, hippocampal atrophy revealed by MRI, temporoparietal hypometabolism, cerebral amyloid, and tau deposition determined by PET.

17.2.2 Hallmarks of AD

17.2.2.1 Aβ Peptide

The most characteristic pathological change of AD is extracellular deposition of Aβ Amyloid plaque, which is mainly composed of Aβ peptides. It is a normal transmembrane protein produced by the sequential proteolytic process of the amyloid-β protein precursor (β-APP), found in most of tissues. Aβ peptides are heterogeneous in peptide length, with the majority of them presenting the Aβ40 form and approximately 5–15% the Aβ42 form. A peptide could form monomers, dimers, oligomers, proto-fibrils, fibrils, and finally fibril aggregates. Both of these two forms of peptides are able to form self-aggregation, but more prone to that is the Aβ42 form, the longer and more amyloidogenic form. In AD pathology, that develops in the brain when the balance of production and clearance is dysregulated. Aβ then become toxic aggregation forms until being insoluble. Moreover, existence of toxic Aβ leads to overproduction of itself and exacerbates oxidative stress, which forms a toxic cycle. The pathology develops slowly, and it may take over two decades before clinical symptoms appear, when synaptic loss and neuronal death, microglial infiltration, and brain shrinkage have been widespread in whole brain.

However, correlation of Aβ deposition and cognitive measurement, synaptic activity, and neurodegeneration in AD is weak, and Aβ deposition is not uncommon in MCI and asymptomatic healthy controls, suggesting that Aβ deposition is a necessary but not sufficient cause for cognitive impairment of AD, indicating other mechanisms such as NFT formation and synaptic failure be involved.

17.2.2.2 Tau Protein

In addition to the amyloid cascade, another characteristic change found in AD brain is intracellular NFTs, which consists of hyperphosphorylated tau protein. The development of Aβ and tau pathologies does not overlap. Tau phosphorylation is regulated by a series of serine-threonine kinases, and tau protein interacts with microtubules of the cytoskeleton leading to the formation of NFTs. The interaction with cytoskeleton causes the destabilization of microtubules and consequently of intracellular trafficking of vesicles and organelles.

17.2.3 Aβ Imaging

Hallmark AD pathologies precede clinical onset by years or decades. The detection of Aβ pathology at the presymptomatic stages is of crucial importance because it provides opportunity for reducing or eliminating Aβ from the brain before irreversible neuronal or synaptic loss occurs. Aβ imaging with PET contributes to the development of more effective therapies by allowing better selection of patients for anti-Aβ therapy trials and providing a means to measure their effectiveness in removing Aβ from the brain.

17.2.3.1 Radioligands

To date, there are several radiolabeled compounds specifically binding to amyloid deposits. The first and most widely used radioligand for PET technique was Pittsburgh Compound B
(2-(4′-[^{11}C]-(methylamino-phenyl-6-hydroxybenzothiazole, PIB))), labeled by ^{11}C. ^{11}C-PIB is suitable for PET imaging because of its high affinity to Aβ aggregates, good brain penetrance, and fast clearance. While its relatively short half-life of 20.4 min limited its further application, it means that it has to be produced on site by PET laboratories equipped with cyclotron. ^{18}F has a longer half-life of 109.8 min, which makes it possible for off-site production and eliminates equipment limitations, hence producing the derivatives of ^{18}F became a subject of interest. The first PET imagining radio-

tracer that has been successfully used is florbetapir ^{18}F (^{18}F-AV-45), which has been approved by the FDA in 2012. Another ^{18}F radioligand flutemetamol has been recently approved by FDA and is in the process of EMA evaluation. Studies have shown that PET tracers mentioned above have similar affinity to amyloid deposits and retention within the brain tissue.

17.2.3.2 Clinical Application

Amyloid PET plays an important role of revealing the Aβ distribution without invasive methods. It has been confirmed that the pattern of binding to Aβ and retention within the brain tissue corresponds with histopathological observations from postmortem examination. PiB binding is low in brain tissues of healthy controls, while in AD it is high in cortical regions with high Aβ deposition evaluated by postmortem studies. Studies have shown that the percentage of healthy control subjects PiB-PET positive was in the range of 10–33%, whereas 65% of MCI and 90–96% of AD patients. PiB positive provides a clue for the diagnosis of AD. However, it should be considered that PiB positive does not necessarily refer to AD, while part of PiB-negative AD patients may have been misdiagnosed. PET studies revealed that PiB binding in the precuneus cortex was significantly higher in AD patients compared with nondemented cohort and patients with MCI, which may be a characteristic of AD. For another, amyloid-positive MCI patients were highly more predisposed to AD conversion during the next 3 years, which gives an insight into the specificity and sensitivity of PiB-PET examination. In this respect, some longitudinal studies suggested that compared with CSF $A\beta_{42}$, amyloid PET may be more sensitive in identifying MCI patients who tend to convert to AD.

^{18}F derivatives including ^{18}F-flumetamol, ^{18}F-florbetapir (AV-45, amyvid), and ^{18}F-florbetaben (AV-1) have been successively identified, and studies have indicated the utility of these new tracers as biomarkers for AD. They have similar effectiveness in detecting fibrillar Aβ pathology as PiB, with high retention in cortical regions while low in white matter, cerebellum, and pons. Several phase II or III trials have already demonstrated high sensitivity and specificity of ^{18}F derivatives to differentiate AD from nondemented cohort.

Nonetheless, amyloid PET examination cannot be used as the only one examination diagnosing AD changes due to the fact that presence of amyloid deposits does not correlate linearly with the severity of neurological symptoms but at some stage reaches plateau level. Taking into account relatively short period and number of longitudinal studies including new ^{18}F-labeled PET radiotracers, the data is still not completely established, and some differences assessing the affinity, sensitivity, or specificity are reported between clinical centers or research groups.

17.2.4 Tau Imaging

The intracellular NFTs consisted of hyperphosphorylated units of tau protein is another well-characterized hallmark of Alzheimer's disease. Interestingly, although Aβ is widely believed to precede tau pathology, NFTs have a greater correlation with the severity of cognitive dysfunction compared to plaque deposits. Established amyloid detection techniques resulted in further development of tau protein radionuclides. Limitation of current AD detection approaches is the low accuracy when used as stand-alone examination. Thus, the combine use of amyloid imaging and tau protein detection has been proposed for early diagnosis in AD. Several imaging compounds selectively bind with tau protein, including ^{18}F-labeled THK compounds [^{18}F]THK-5105 and [^{18}F]THK-5117, ^{18}F-labeled T807 ([^{18}F]AV-1451) and T808 ([^{18}F]AV-680), and PBB compounds. [^{18}F]AV-1451 is a promising ligand that well displays the distribution of NFT in AD brain. [^{18}F]AV-1451 PET shows higher uptake in cortical, parahippocampal, and entorhinal regions in patients with MCI and AD compared with normal individuals. Studies have already shown the positive correlation of tracer retention with tau in CSF and cognitive decline. Limited studies have found AV-1451 bind preferentially to AD tau than non-AD tauopathies. However, to which extent it can discriminate between tau accumulation in AD and other tauopathies requires extensive postmortem validations.

17.2.5 ^{18}F-FDG PET Imaging

[^{18}F]-2-fluoro-2-deoxyglucose (^{18}F-FDG) has been commonly used as a radiotracer in several studies and has been used to demonstrate impaired glucose metabolism. The specific reasons that lead to reduced FDG signals in AD are unclear. Chronic brain tissue loss, reduced glucose uptake, and synaptic function result in progressing memory decline in AD patients. The hippocampus and cortical formations are regions centrally involved in memory formation.

Studies reveal that FDG-PET examination can be used as a tool to diagnose AD at early stage, even years in advance before any significant symptoms of the disease. PET studies allowed to identify specific glucose metabolic patterns, making it feasible to differentiate dementia due to AD from other cognitive disorders. The very first characteristic change of brain tissue in AD patients is hypometabolism in the posterior cingulate cortex and parietal regions; then it is observed in posterior regions and the temporal and prefrontal cortices to overwhelm occipital cortex in advanced stages. This can differentiate AD patients from controls with sensitivity of 90% and specificity of 89%. Decreased uptake in temporoparietal cortices is typical for dementia with Levy bodies (DLB) which is similar to AD. But cerebellum and the

occipital lobes are also affected in DLB, structure which is affected not until late stage of AD. Patients suffering from vascular dementia present uneven hypermetabolism in cortical structures, as well as subcortical structures which are preserved in AD. Frontotemporal dementia (FTD) is characterized by changes in the frontal, anterior temporal, and medial temporal cortices. Patients with depression do not present particular abnormalities. But it still remains to be answered what are the differences between preclinical stage of AD from MCI and if it can be developed to AD.

17.2.6 Cerebral Blood Perfusion Imaging

SPECT examination utilizes the tracers radiolabeled by ^{99m}Tc, usually ^{99m}Tc-ECD (L-ethylcysteinate dimer) or ^{99m}Tc-HMPAO (hexamethylpropyleneamineoxime) to assess the regional cerebral blood flow. It can be used for the differentiation of several dementia types, mainly of DLB, FTD, or vascular dementia, AD, and depression. Classically recognized brain perfusion pattern of AD patients is bilateral hypoperfusion in the parietal and posterior temporal lobes. But results cannot be used as a stand-alone examination, because different diseases may display similar abnormalities. In patients with symptomatic probable Alzheimer's disease, a positive SPECT scan raises the risk of AD diagnosis in postmortem examination from 84 to 92%, whereas a negative SPECT scan reduces this risk to 70%.

17.3 Brain Tumors

The most common type of malignant primary brain tumor is glioma. The annual incidence of gliomas is approximately 5–6/100,000. With current treatment efforts including maximal surgical resection, radiotherapy, and/or chemotherapy, survival time and quality of life remain unsatisfactory. Median survival is only 12–15 months for patients with glioblastoma and WHO grade IV tumors and 2–5 years for patients with WHO grade III tumors. Anaplastic gliomas with oligodendroglial component and 1p/19q codeletion treated with radiotherapy and chemotherapy have better prognosis.

17.3.1 FDG PET Imaging for Brain Tumors

^{18}F-FDG PET may provide useful information for distinguishing WHO grade III/IV gliomas from low-grade gliomas, but its specificity of distinguishing gliomas with other brain tumors or nonneoplastic lesions is limited. Maximum standardized uptake values (SUVmaxs) were significantly higher in primary CNS lymphomas than in glioblastomas, while corticosteroid medication may reduce uptake. Considerable overlap of SUVmax also exists between WHO grades III/IV gliomas and brain metastases. Importantly, increased ^{18}F-FDG metabolism is also seen in nonneoplastic lesions such as brain abscesses, tumefactive demyelination, neurosarcoidosis, etc.

17.3.2 Amino Acid PET Imaging for Brain Tumors

Amino acid PET tracers (Table 17.3), including MET, FET, and FDOPA, are transported via the L-amino acid transporter type 1 (LAT1) system. LAT1 is upregulated in cerebral gliomas, but the expression at the normal blood brain barrier (BBB) is considerably lower. Therefore, they are particularly attractive for gliomas and have relatively low uptake in healthy brain tissue, which result in high tumor-to-background contrast. Moreover, due to the fact that these amino acid tracers are also transported into the normal brain, disruption of the BBB is not a prerequisite for tumor accumulation, which explains uptake of these tracers of low-grade gliomas without BBB leakage.

In general, amino acid tracers that are transported via the LAT1 system have been shown to yield similar results for brain tumor imaging. MET, FET, and FDOPA PET imaging have excellent tumor-to-background contrast and comparable performance in delineating tumor extent. Although SUV of MET and FET PET are not directly comparable, they are strongly correlated. In high-grade gliomas, SUV and tumor-to-background contrast tend to be higher for FET compared with FDOPA PET, but this does not appear to impact tumor visualization.

17.3.2.1 Diagnostic Indexes

Static PET

1. Visual interpretation
2. Semiquantitative analysis of tracer uptake using region-of-interest (ROI) analysis
   SUV: Standardized uptake value
   SUVmax: Maximum standardized uptake value
   T/C: Tumor to normal cerebellum ratio

Table 17.3 Amino acid tracers

^{11}C-tracers		^{18}F-tracers	
^{11}C-AMT	^{11}C-Alpha-methyl-L-tryptophan	^{18}F-FET	^{18}F-O-(2-fluoroethyl)-L-tyrosine
^{11}C-MET	^{11}C-L-methionine	^{18}F-FDOPA	^{18}F-3,4-dihydroxy-6-fluoro-L-phenylalanine
^{11}C-CHO	^{11}C-choline	^{18}F-FLT	^{18}F-3′-deoxy-3′-fluorothymidine

T/N: Tumor to normal brain tissue ratio
T/S: Tumor to normal striatum ratio
T/W: Tumor to normal white matter ratio

Dynamic PET

Dynamic PET imaging for brain tumor involves the collection of a series of frames of PET data over contiguous time intervals, usually in the range of 1–5 min. Data from each of the frames is independently reconstructed to form a set of images.

- TAC: Time-activity curve, curve recording the radioactivity changing with time
- Time-to-peak: Time from the start of the dynamic acquisition till the maximum tumor uptake

17.3.2.2 Clinical Application

Specific PET tracers have addressed numerous molecular targets in the last decades, but only a few have achieved relevance in routine clinical practice. At present, PET studies using radiolabeled amino acids appear to improve clinical decision-making as these tracers can offer better delineation of tumor extent as well as improved targeting of biopsies, surgical interventions, and radiation therapy. Amino acid PET imaging also appears useful for distinguishing glioma recurrence or progression from postradiation treatment effects, particularly radiation necrosis and pseudoprogression, and provides information on histological grading and patient prognosis. In the last decade, the tracers O-(2-[18F] fluoroethyl)-L-tyrosine (FET) and 3,4-dihydroxy-6-[18F]-fluoro-L-phenylalanine (FDOPA) have been increasingly used for these indications.

Diagnostic Performance of Different Amino Acid Tracers Compared with MRI

Response Assessment in Neuro-Oncology (RANO) working group and European Association for Neuro-Oncology (EANO) reported the diagnostic performance of different amino acid tracers compared with MRI in September 2016. For differentiation of gliomas from nonneoplastic lesions, MET and FET PET both have higher diagnostic accuracy than MRI alone. MET and FET PET, especially dynamic FET PET, perform better in glioma grading than MRI alone, but accuracy of differentiation between WHO grades is still limited. As for delineation of glioma extent, amino acid PET reveals metabolically active tumor larger than contrast enhancement in low-grade glioma (LGG) and high-grade glioma (HGG) or delineates tumor in non-enhancing anaplastic glioma, at diagnosis and recurrence. Diagnostic accuracy of amino acid PET is higher than MRI in differentiation of glioma recurrence from treatment-induced changes, such as pseudoprogression and radionecrosis. PET also performs better than MRI in assessment of treatment response. Metabolic active tumor volumes of MET PET, time-activity curve of FET PET or combination with MRI, and maximum uptake of FDOPA PET have higher prognostic value than contrast MRI within HGG and LGG.

Diagnosis

A number of histological studies demonstrated additional amino acid PET help to raise diagnostic accuracy of anatomic MRI alone for the differentiation of gliomas from nonneoplastic lesions. Therefore, amino acid PET would be recommended by RANO and EANO when assessing patients with a suspected primary glioma on MRI. What should be taken in consideration is that majority (>95%) of HGG show increased uptake, while high uptake can also be seen in other brain tumors like lymphoma and metastasis, and moderate uptake can also be seen in nonneoplastic lesions such as active multiple sclerosis and brain abscesses. For another, a good part of LGG is metabolically negative on amino acid PET imaging.

Tumor Grading

Although amino acid uptake is higher in HGG compared with LGG, it is still limited to be used for tumor grading because of significant overlap in uptake values. Dynamic ^{18}F-FET PET analysis is a good choice to improve accuracy of tumor grading. HGG performs an early activity peak around 10–15 min after injection, followed by a decrease of FET uptake, while LGG typically exhibits delayed and steadily increasing tracer uptake. The diagnostic performances of TAC, SUVmax of FET PET, CHO/CR ratio, and ADC of MRI for glioma grading were assessed in comparison to histology. Tumor TAC reached the best accuracy when taken alone to distinguish between LGG and HGG, followed by ADC histogram analysis and combination of TAC and ADC histogram analysis further improved sensitivity and specificity. This special characteristic of FET was not observed from other amino acid tracers such as MET and FDOPA.

Differences in data processing of dynamic FET scans in different PET centers limited the comparability of the results. Thus, standardization of data processing is needed to make clinical results comparable.

Treatment Planning

Either ^{11}C-MET or ^{18}F-FET PET can be used to delineate tumor, because they are both superior to conventional MRI, and both the tracer uptake and tumor to normal tissue contrast are similar. Amino acid PET delineates heterogeneously distributed tumor component, which helps to identify the most aggressive portion of the tumor. For most patients, area of nonspecifically abnormal T2/FLAIR signal and contrast-enhancing area plus a 20–35 mm margin encompassed the PET-positive volumes. Above characteristics of amino acid

PET provide additional biological and metabolic information for better locating the most meaningful biopsy site, deciding maximal resection margin and delineating radiation target volume and boost area, which make it promising for future clinical use.

Treatment Response

Postradiation treatment effects could be summarized as acute effects, subacute effects such as pseudoprogression, and late effects such as radiation necrosis.

Pseudoprogression has been known as a subacute post-treatment reaction (typically regarded as a phenomenon of the first 12 weeks after radiochemotherapy) and occurs in 10–30% of patients with malignant glioma. With increased contrast enhancement and edema, it mimics tumor progression but subsequently stabilizes and/or regresses without further intervention.

Radiation necrosis usually manifests within 6 months after standard radiotherapy and occurs in approximately 5–25% of these patients. It belongs to the late postradiation treatment effects category and may appear months to several years after radiation therapy, later than the typical time period for pseudoprogression. Conventional MRI does not allow a reliable distinction between tumor recurrence and pseudoprogression or radiation necrosis.

MET PET may be effective in differentiating recurrent brain tumor from radiation-induced changes since a simple semiquantitative ROI analysis for the calculation of tumor/normal brain ratios demonstrated a sensitivity and specificity of 70–80%. Based on limited studies with small sample size, there is a sensitivity and specificity of static FET PET of more than 90% for differentiating tumor progression from pseudoprogression in glioblastoma patients after standard radiochemotherapy. Kinetic analysis of FET PET differentiated local recurrent brain metastasis from radiation-induced changes with a sensitivity of 95% and specificity of 91%. FDOPA PET has been shown to differentiate recurrent or progressive brain metastasis from radiation-induced changes with high sensitivity (81%) and specificity (84%).

Prognostication

Prognostication assessment of patients with high-grade and low-grade gliomas may benefit from amino acid PET imaging. For instance, tracer uptake of amino acid is associated with outcome of HGG. Metabolically active tumor volume of glioblastoma is associated with survival. In patients with LGG at initial diagnosis, low tumor MET uptake is associated with longer survival compared with patients exhibiting higher uptake.

Dynamic parameters of FET PET are correlated with outcome of gliomas. Decreasing time-activity curves and early curve decrease of gliomas indicate malignant progression and poor outcome. Combination of FET PET and tumor morphological features derived from MRI can be used to predict survival of patients with newly diagnosed LGG because low baseline FET uptake and a circumscribed growth pattern on T2-weighted MR images are associated with favorable outcome.

17.3.2.3 Limitation and Outlook

A few limitations of amino acid PET need to be considered. The major limitation of MET PET is its requirement of on-site cyclotron. In the case of FDOPA, physiologic uptake in the corpus striatum may obscure margins of tumors that extend into the basal ganglia. For FET, slower renal elimination results in detectable amounts of tracer being present in the blood pool for longer periods of time, which may lead to nonspecific tracer uptake. For another, current PET scanners achieve a lower spatial resolution of about 4–6 mm compared with about 2 mm for MRI, which can lead to false-negative findings because small lesions may be undetectable with PET. Co-registration of PET images with higher spatially resolved images from contrast-enhanced MRI may help to ameliorate difficulties above.

Bibliography

1. Hsiao IT, Weng YH, Hsieh CJ et al (2014) Correlation of Parkinson disease severity and 18F-DTBZ positron emission tomography. JAMA Neurol 71(6):758
2. Niccolini F, Politis M (2016) A systematic review of lessons learned from PET molecular imaging research in atypical parkinsonism. Eur J Nucl Med Mol Imaging 43(12):2244–2254
3. Schreckenberger M, Hägele S, Siessmeier T et al (2004) The dopamine D2 receptor ligand 18F-desmethoxyfallypride: an appropriate fluorinated PET tracer for the differential diagnosis of parkinsonism. Eur J Nucl Med Mol Imaging 31(8):1128–1135
4. George S, Brundin P (2015) Immunotherapy in Parkinson's disease: micromanaging alpha-Synuclein aggregation. J Parkinsons Dis 5(3):413–424
5. Lin KJ, Weng YH, Wey SP et al (2010) Whole-body biodistribution and radiation dosimetry of 18F-FP-(+)-DTBZ (18F-AV-133): a novel vesicular monoamine transporter 2 imaging agent. J Nucl Med 51(9):1480–1485
6. Kim HW, Kim JS, Oh M et al (2016) Different loss of dopamine transporter according to subtype of multiple system atrophy. Eur J Nucl Med Mol Imaging 43(3):517–525
7. Wu P, Wang J, Peng S et al (2013) Metabolic brain network in the Chinese patients with Parkinson's disease based on 18 F-FDG PET imaging. Parkinsonism Relat Disord 19(6):622–627
8. Bohnen NI, Müller MLTM, Frey KA (2017) Molecular imaging and updated diagnostic criteria in Lewy body dementias. Curr Neurol Neurosci Rep 17(10):73
9. Kalia LV, Lang AE (2015) Parkinson's disease. Lancet 386(9996):896–912
10. Hall B, Mak E, Cervenka S et al (2017) In vivo tau PET imaging in dementia: pathophysiology, radiotracer quantification, and a systematic review of clinical findings. Ageing Res Rev 36:50–63
11. Counts SE, Ikonomovic MD, Mercado N et al (2017) Biomarkers for the early detection and progression of Alzheimer's disease. Neurotherapeutics 14(1):35–53

12. Kato T, Inui Y, Nakamura A et al (2016) Brain fluorodeoxyglucose (FDG) PET in dementia. Ageing Res Rev 30:73–84
13. Villemagne VL, Chetelat G (2016) Neuroimaging biomarkers in Alzheimer's disease and other dementias. Ageing Res Rev 30:4–16
14. Villemagne VL (2016) Amyloid imaging: past, present and future perspectives. Ageing Res Rev 30:95–106
15. Weiner MW, Veitch DP (2015) Introduction to special issue: overview of Alzheimer's disease neuroimaging initiative. Alzheimers Dement 11(7):730–733
16. Blennow K, Mattsson N, Scholl M et al (2015) Amyloid biomarkers in Alzheimer's disease. Trends Pharmacol Sci 36(5): 297–309
17. Smailagic N, Vacante M, Hyde C et al (2015) 18F-FDG PET for the early diagnosis of Alzheimer's disease dementia and other dementias in people with mild cognitive impairment (MCI). Cochrane Database Syst Rev (1):D10632
18. Wurtman R (2015) Biomarkers in the diagnosis and management of Alzheimer's disease. Metabolism 64(3 Suppl 1):S47–S50
19. McConathy J, Sheline YI (2015) Imaging biomarkers associated with cognitive decline: a review. Biol Psychiatry 77(8): 685–692
20. Albert NL, Weller M, Suchorska B et al (2016) Response assessment in neuro-oncology working group and European Association for Neuro-Oncology recommendations for the clinical use of PET imaging in gliomas. Neuro Oncol 18(9): 1199–1208
21. Galldiks N, Langen KJ, Pope WB (2015) From the clinician's point of view—what is the status quo of positron emission tomography in patients with brain tumors? Neuro Oncol 17(11):1434–1444
22. Bell C, Dowson N, Puttick S et al (2015) Increasing feasibility and utility of (18)F-FDOPA PET for the management of glioma. Nucl Med Biol 42(10):788–795
23. Glaudemans AW, Enting RH, Heesters MA et al (2013) Value of 11C-methionine PET in imaging brain tumours and metastases. Eur J Nucl Med Mol Imaging 40(4):615–635
24. Dunet V, Rossier C, Buck A et al (2012) Performance of 18F-fluoroethyl-tyrosine (18F-FET) PET for the differential diagnosis of primary brain tumor: a systematic review and metaanalysis. J Nucl Med 53(2):207–214
25. Calabria F, Chiaravalloti A, Di Pietro B et al (2012) Molecular imaging of brain tumors with 18F-DOPA PET and PET/CT. Nucl Med Commun 33(6):563–570
26. Chen W (2007) Clinical applications of PET in brain tumors. J Nucl Med 48(9):1468–1481
27. Damont A, Roeda D, Dollé F (2013) The potential of carbon-11 and fluorine-18 chemistry: illustration through the development of positron emission tomography radioligands targeting the translocator protein 18 kDa. J Labelled Comp Radiopharm 56(3–4):96–104. https://doi.org/10.1002/jlcr.2992
28. Dollé F, Luus C, Reynolds A et al (2009) Radiolabelled molecules for imaging the translocator protein (18 kDa) using positron emission tomography. Curr Med Chem 16(22):2899–2923

Nuclear Cardiology

18

Xu Cheng

18.1 Introduction

Cardiovascular disease (CVD) is a major problem for health of human being. A report [1] from the American Heart Association (AHA) showed the 2009 overall rate of death attributable to CVD was 236.1 per 100,000. In 2009, coronary artery disease (CAD) alone caused about 1 of every 6 deaths in the United States; 386,324 Americans died of CAD. Each year, an estimated of about 635,000 Americans have a new coronary attack, and about 280,000 have a recurrent attack. CVD causes the huge medical expenses and brings the heavy burden to the society. The total direct and indirect cost of CVD and stroke in the United States for 2009 is estimated to be $312.6 billion. CVD costs more than any other diagnostic group [1]. In China, the mortality of CVD is increasing significantly during past three decades, especially for CAD [2]. From 1984 to 1999, the age-adjusted mortality attributable to CAD increased by 41% in 35–74-years-old male population and increased by 39% in female. In 2000, the mortality attributable to CAD was 71.3 per 100,000 for the urban population and 31.6 per 100,000 for the rural population. In 2009, the mortality attributable to CAD increased to 94.96 per 100,000 for the urban population and 71.27 per 100,000 for the urban population [2]. Nuclear cardiology is a mature and widely used diagnostic imaging method and involves a variety of imaging approaches, such as myocardial perfusion imaging (MPI), myocardial metabolic imaging, radionuclide cardiac blood pool imaging, cardiac receptor, etc. Nuclear cardiology plays an important role for CAD and other CVD diagnosis, differential diagnosis, evaluation of treatment response, and assessment of outcome [3].

18.2 Anatomy and Physiology

The heart is the pump that pushes blood flow throughout the blood circulation, and it is also responsible for taking in blood from the veins and delivering it to the arteries. The heart lies in the mediastinum of thoracic cavity behind the sternum, and the 2/3 part of heart is located in the left thoracic cavity and other 1/3 in the right thoracic cavity. The size of human heart is about a closed fist. Myocardium is the middle layer of the heart and composed of myocardial cells. The heart contains valves and four chambers: right atrium, left atrium, right ventricle, and left ventricle. The valve between the right atrium and ventricle is called the tricuspid valve, and the valve between the left atrium and ventricle is called the mitral valve. The valve between right ventricle and the pulmonary artery is called pulmonary artery valve. The valve between the left ventricle and the aorta is called the aortic valve. The apex is mainly composed of the left ventricle, and the septum separates the left and right atriums and ventricles. The function of the valves is mainly to prevent the blood reflux during contraction or relaxation of the atrium and ventricle. The superior and inferior vena cava flow into the right atrium, and the pulmonary veins flow into the left atrium. The left and right ventricles send blood out of the heart and into the arteries.

The conduction system of the heart is consisted of specially differentiated myocardial cells. The main function of conduction system is to generate and conduct electrical impulses. Electrical impulses cause and regulate the heart to contract. The properties of myocardial cells are excitability, conductivity, automaticity, and contractility. The conduction system is composed of sinoatrial (SA) node, atrioventricular (AV) node, atrioventricular bundle, left and right bundle branch, and Purkinje fibers. SA node locates in the wall of the right atrium inferior to the superior vena cava. The electrical signal begins in the SA node and then being picked up by AV node and transmitted through the AV bundle. Finally, the AV bundle splits electrical signals into left and right branches and reaches the apex of the heart. Besides electrical

X. Cheng (✉)
Department of Nuclear Medicine, The First Affiliated Hospital of Nanjing Medical University, Nanjing, P. R. China

G. Huang (ed.), *Nuclear Medicine in Oncology*, https://doi.org/10.1007/978-981-13-7458-6_18

signals from the conduction system, heart rate also depends on physical demands and hormonal and stress factors.

The human heart is supplied by coronary arteries (coronary circulation), which provides oxygen and nutrients for cardiac tissues' metabolism. The aorta branches off into left coronary artery and right coronary artery. The left coronary artery comprises the left main (LM) artery, and LM branches into the left anterior descending (LAD) artery and the left circumflex (LCX) artery. LAD artery branches off into three smaller arteries, diagonal branches, right anterior ventricular branches, and anterior interventricular artery. LAD artery supplies blood flow of anterior wall of left ventricle, anterolateral wall of left ventricle, apex, and the portion of interventricular septum close to apex. LCX artery supplies blood flow of lateral wall of left ventricle and posterior wall of left ventricle. The right coronary artery (RCA) supplies blood flow of right ventricle, inferior wall of left ventricle, and the portion of interventricular septum close to bottom of the heart.

The contraction and relaxation of the heart include the sequential contraction and relaxation of the atriums and ventricles, increasing and decreasing of cardiac chambers pressure, and opening and closing of cardiac valves. The systolic and diastolic of the heart ensure the ejection and congestive function of the heart. Every contraction and diastole of the atrium and ventricle is called one cardiac cycle. The time of cardiac cycle is related to heart rate. The whole cardiac cycle involves three phases: atrial systole phase, ventricular systole phase, and relaxation phase. During the atrial systole phase, the atria contract and push blood into the ventricles and the ventricles remain in the diastole state. During ventricular systole phase, the ventricles contract and push blood into the arteries, and the atria stay in the state of diastole. During the relaxation phase, all four cardiac chambers keep in the diastole state. Stroke volume (SV) is the volume of blood pumped into the aorta by each systole of one ventricle. Cardiac output (CO) is the volume of blood pumped by the heart during 1 min. Ejection fraction (EF) is the ratio of SV to the end-systolic volume of ventricle.

18.3 Myocardial Perfusion Imaging

Myocardial perfusion imaging (MPI) is the most common and important procedure of nuclear cardiovascular imaging methods. In some hospitals and centers, MPI is being responsible for more than three fourths of clinical cardiac imaging, as it has a number of advantages that MPI is difficult to replace by other cardiovascular imaging modalities. In China, the number of MPI is about one fourth of all clinical nuclear imaging. More than 200,000 patients undertake MPI every year in China [4]. MPI is widely used for diagnosis of ischemic heart disease (IHD), risk stratification, evaluation of treatment effect, outcome assessment, and so on.

18.3.1 Radiopharmaceuticals and Principles

18.3.1.1 Technetium-99m Tracers

Technetium-99m (Tc-99m) is produced from a molybdenum-99m Tc-99m generator. The half-life of Tc-99m is 6 h and emits gamma rays at 140 keV energy. Owing to the higher energy gamma rays and better dosimetry of the isotope, the imaging of using Tc-99m-labeled compounds can provide fewer attenuation artifacts and higher imaging quality. Tc-99m-labeled 2-methoxy-isobutyl-isonitrile (^{99m}Tc-MIBI) is the most widely used for MPI worldwide at present, and it is the only currently commercially available for MPI in China. MIBI is a large synthetic molecule of the isonitrile family, which can be labeled with Tc-99m. ^{99m}Tc-MIBI was introduced in 1984 in clinical trials in the late 1980s[5]. After intravenous injection, about 5% ^{99m}Tc-MIBI goes to the heart and gets into the myocardial cells by crossing cell membranes passively and then combines to the mitochondrial negative ion protein. All Tc-99m-labeled agents have the property of becoming "locked" in the myocardium, in proportion to the blood flow delivery and distribution. So ^{99m}Tc-MIBI has no redistribution and imaging can be delayed.

Tc-99m-labeled tetrofosmin (TF) and Tc-99m labeled are also used in MPI; however, the two agents are not supplied commercially in China. The advantage of ^{99m}Tc-TF is of the simple process of labeling without boiling. So it is suitable for 1-day imaging protocol. The uptake rate of ^{99m}Tc-teboroxime is high during first-pass process blood flow in myocardium [6].

18.3.1.2 Thallium-201

Thallium acts as a potassium analogue and is actively transported into tissue by sodium/potassium cellular pump and becomes part of intracellular K^+ pool. The first-pass extraction of thallium is about 90% and is better than other current radiopharmaceuticals in MPI [7]. Thallium-201 (^{201}Tl) is a radionuclide produced by the accelerator. Its half-life is 73.1 h, and decay using electron capture method emits low energy gamma rays. ^{201}Tl uptake by myocyte is linearly proportional to blood flow. Thallium-201 is redistributed along an electrochemical gradient back to the bloodstream after getting in myocardial cells; it takes 3–4 h to achieve equilibrium state in myocardium. The redistribution is usually due to a difference in clearance of thallium, with the normally perfuse areas clearing more rapidly than the ischemic areas [7]. The distribution of thallium-201 in the myocardium can be divided into initial phase and redistribution phase. The initial phase starts as soon as possible after tracer intravenous injection and reflects the distribution of blood flow under stress status. The latter phase is taken as the rest or redistribution images.

The advantage of this tracer is the reflection of lung uptake in patients with high left ventricular end-diastolic

Table 18.1 Characteristics of technetium-99m tracers and thallium-201

	^{99m}Tc-MIBI/TF	^{99m}Tc-teboroxime	Thallium-201
Energy	140 keV	140 keV	70, 167 keV
Half-life	6 h	6 h	74 h
Biological half-life	6 h	6 h	58 h
Dose	740–925 MBq	740–925 MBq	74–111 MBq
Uptake rate of first-pass	65%	80–90%	90%
Radiation dose (whole body)	0.02	NR	0.21

MIBI 2-methoxy-isobutyl-isonitrile, *NR* not report, *TF* tetrofosmin

pressures (EDP). It is a very useful prognostic marker and provides additional information for risk assessment and evaluation of outcome [8]. Another advantage of thallium-201 is it has long accumulated experience and abundant evidence-based data in clinical applications. The main disadvantage of thallium-201 is that the energy is not optimal for gamma camera and only low dose can be used, so the quality of images is inferior. Thallium-201 may lead to a particular artifact known as "upward creep" due to the motion of body during data acquisition [9]. Table 18.1 shows the characteristics of ^{99m}Tc-MIBI, ^{99m}Tc-TF, ^{99m}Tc-TF, and thallium-201.

18.3.1.3 Positron Emitters

Rubidium-82, nitrogen-13, and oxygen-15 can be used in MPI using PET or PET/CT systems. Rubidium-82 (^{82}Rb) is obtained from generator, used in clinical practice is agile. Due to the high energy and noise, these properties affect the spatial resolution of imaging and make images quality inferior. The advantage of oxygen-15 (^{15}O)-labeled H_2O is that ^{15}O-H_2O can be used in calculating quantitative blood flow of coronary artery. Nitrogen-13 (^{13}N)-labeled NH_3 has been used as tracer of MPI from 1972. By using it, ECG-gated acquisition can be performed owing to enough long half-life. However, uptake of liver and lungs may make image quality lower. Table 18.2 shows the characteristics of positron emitters.

Table 18.2 Characteristics of positron emitters

	Rubidium-82	Nitrogen-13	Oxygen-15
Form	Chloride	Ammonia	Water
Half-life	75 s	10 min	110 s
Energy (MeV)	3.15	1.19	1.72
Obtained from	Generator	Cyclotron	Cyclotron
Uptake rate of first-pass	65%	83%	96%
Dose	370–740 MBq	370–555 MBq	

18.3.2 Stress Test

The heart has strong reserve capacity, and it may appear no myocardial ischemia changes on the images of MPI even though 70% stenosis in coronary artery under rest state. Actually, the cardiac reserve capacity has been damaged when there is 40% stenosis exist. During the stress procedure, normal coronary artery has to increase its regional blood flow to supply the increased demands of myocardium; however, coronary artery with stenosis does not. So there represent myocardial ischemia because of the imbalance of the regional myocardial oxygen expenditure. Most stress procedures are performed in patients with symptoms of suspected or known CHD. The purpose of stress test is to provoke symptoms in a safe and controlled environment, and stress test must be performed under direct supervision by a physician. The stress test involves different stress methods, such as exercise stress test and pharmacological stress test.

18.3.2.1 Exercise Stress Test

The most commonly used methods of exercise stress test are treadmill test and bicycle test. In Europe, people prefer to use bicycle test, while treadmill stress test is more commonly used in America. In China, most centers use the latter.

Treadmill Stress Test

The speed and gradient of treadmill are varied. The most commonly used protocols of treadmill stress test are standard Bruce protocol and modified Bruce protocol. The tracer is injected at the peak, and the exercise continues at the same or half speed for 1 min. The uptake of tracer reflects myocardial blood flow perfusion at the moment of injection. The continuation of exercise after tracer injection is to ensure blood clearance of tracer. The advantage of treadmill is that most patients find exercise by walking natural and easy to perform. The disadvantages of it are difficult to obtain blood pressure measurement and ECG tracings due to patient motions.

Bicycle Stress Test

The principle of the bicycle stress test is to gradually increase the resistance to the pedaling following a standardized protocol, hereby controlling the workload the patient is performing. For bicycle stress test, BP measurements are much more reliable, and ECG tracings tend to have less motion artifacts than on a treadmill. The disadvantages involve that many patients are limited by quadriceps femoris fatigue, pain during bicycle exercise, and lower myocardial oxygen consumption compared with treadmill.

End points of exercise:

- Typical chest pain (grade 5 or more on a 0–10 scale)
- Marked fatigue and shortness of breath
- Diagnostic ST depression of >3 mm, horizontal or downsloping

– Significant arrhythmia (e.g., three or more consecutive ventricular beats)
– Reaching at least 85% of age-predicted maximum heart rate: (220 − age = max) × 0.85
– Significant arrhythmia
– If a maximum stress is intended to fatigue

Absolute indications for terminating exercise:
– ST-segment elevation
– Severe angina
– Blood pressure decrease (≥10 mmHg) with symptoms
– Systolic blood pressure > 220 mmHg or diastolic pressure > 110 mmHg
– Serious arrhythmia
– second or third degree AV block

Contraindication of exercise:
– Acute myocardial infarction (within 2 days)
– Unstable angina
– Severe cardiac function damage
– Severe hypertension
– Severe arrhythmia

18.3.2.2 Pharmacological Stress Test

Exercise stress is the preferred stress modality for evaluation of patients with suspected or known coronary artery disease. Similar to exercise stress test, some drugs can induce the increase of the coronary artery blood flow or myocardial contractility. For the patients who are unable or unwilling to perform exercise stress test (musculoskeletal or pulmonary disease), or other conditions (left bundle branch block, paced rhythm or Wolff-Parkinson-White syndrome), pharmacological stress test is used. The most commonly used drugs for stress test involve dipyridamole, adenosine, and dobutamine.

Dipyridamole

Dipyridamole is an indirect vasodilator; it makes the concentration of adenosine in the tissue and blood by reducing decomposition of endogenous adenosine. Exogenous adenosine has the same dilatation effect as the endogenous adenosine and results in obvious dilatation for increasing the blood flow of coronary artery. Before dipyridamole stress test, physician needs to identify contraindications involving recent acute myocardial infarction, unstable angina, heart failure, asthma, and active wheezing. During the procedure of stress test, 12-lead ECT, blood pressure, heart rate, and symptoms must be monitored and recorded continuously during administration. The side effects of dipyridamole are showed in Table 18.3 [10]. If side effects persist, aminophylline should be intravenous injected; it is a specific blocker of adenosine receptor. Because the half-life of aminophylline is shorter than that of dipyridamole, adverse effects may reoccur after 15 min approximately.

Table 18.3 Frequent side effects of dipyridamole, adenosine, and dobutamine (% of patients)

	Dipyridamole	Adenosine	Dobutamine
Cardiac			
Fatal myocardial infarction	0.05	0	0
Nonfatal myocardial infarction	0.05	0	0
Chest pain	19.7	57	31
Tachycardia	3.2	NA	1.4
Hypotension	4.6	NA	0
Hypertension	1.5	NA	1.4
Atrioventricular block	0	10	0.6
Noncardiac			
Headache	12.2	35	14
Nausea	4.6	NA	9
Flushing	3.4	29	14
Dyspnea	2.6	15	14
Fatigue	1.2	NA	NA
Acute bronchospasm	0.15	NA	NA

NA not available

Adenosine

Adenosine is a direct vasodilator and stimulates adenosine receptor. It acts on A2A receptor causing arteriolar vasodilatation in coronary bed. Adenosine must be infused using a pump to ensure dose administration consistently. The dose of adenosine is dependent on patient's weight. Adenosine should not be injected by hand. It is impossible to ensure the steady slow flow of it. Side effects of adenosine are more likely to occur if using hand push because of the rapid action of it. Side effects of adenosine involve non-specific chest pain, flushing, nausea, dyspnea, hypotension, and AV block. Adenosine stress has an excellent safety profile. Because of the short half-life (<10 s), these conditions need not be treated. The contraindications of using adenosine are asthma, hypotension, advanced AV block, recent use of dipyridamole.

Dobutamine

Dobutamine stress test should be used only in patients who cannot undergo exercise stress test and have contraindications to pharmacological vasodilator drugs. It stimulates β_1 receptors of sympathetic nervous system directly and increases heart rate and contractility of myocardium. Primary side effects of dobutamine include those commonly seen for β_1 active sympathomimetics, such as angina, hypertension, arrhythmia, and tachycardia. The most serious side effect of it is increased risk of arrhythmia, including fatal arrhythmias. The half-life of dobutamine is approximately 2 min owing to its rapid hepatic metabolism. It has not been studied as extensively as dipyridamole or adenosine in patients with CAD.

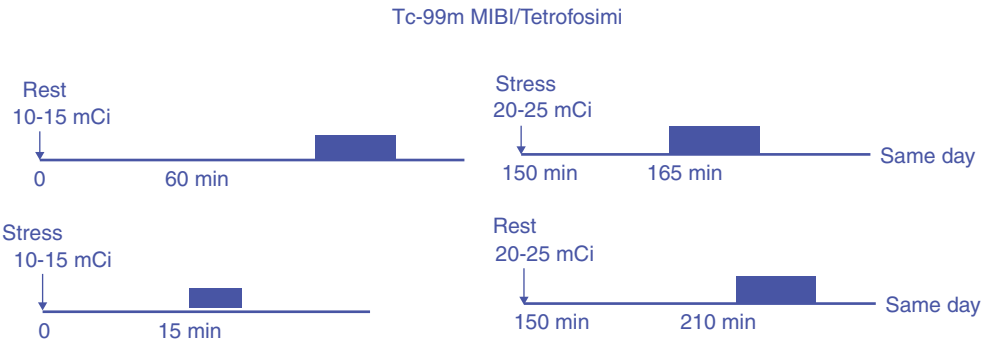

Fig. 18.1 One-day acquisition protocol for Tc-99m-labeled tracers using SPECT

18.3.3 Protocols of Images Acquisition and Processing

Different acquisition methods can be used in clinical practice based on variant tracers and instruments involving planar acquisition, SPECT acquisition, SPECT/CT acquisition, ECG-gated SPECT acquisition, PET and PET/CT acquisition, and so on.

18.3.3.1 Planar Imaging

Due to the widely use of SPECT instruments at present, the application of planar imaging is very few. The projects of planar imaging involve anterior (ANT) view, 45° left anterior oblique (LAO) view, 70° LAO view, and left lateral (LL) view. Equipped with low-energy high-resolution collimators (LEHR), a 128 × 128 matrix is used, and window's width is 20%. The counts of every view should ≥500,000. Tissue attenuation is an important problem with planar imaging. Breast attenuation can result in low counts of anterior wall of left ventricle. Left diaphragm may affect image quality of inferior wall, and we can avoid this problem by acquiring LL images with the patient in a right-side position.

18.3.3.2 SPECT Imaging

The patient is placed in a supine position with arms over the head. SPECT system is equipped with LEHR collimators. Energy width is same as planar imaging. A 64 × 64 matrix is standard used, but a 128 × 128 matrix also can be used. Fields of acquisition range from 45°RAO (right anterior oblique) to 45°LPO (left posterior oblique). Orbit type is circular, and step and shoot/continuous of acquisition type is used. The counts of each project are >100,000. For Tc-99m-labeled tracers, peak is 140 keV. 78 keV centered is used for thallium-201. LEHR collimators provide better spatial resolution but reduced sensitivity. Therefore, LEHR collimators are usually used for the Tc-99m-labeled tracers. Low-energy all-purpose (LEAP) collimators prefer to be used for thallium-201, as it provides higher sensitivity.

For ^{99m}Tc-MIBI and other Tc-99m-labeled agents, stress test and rest acquisition should be performed, respectively, because the tracers have no redistribution. Acquisition protocols involve 1-day protocol and 2-day protocol. Of 1-day protocol, stress and rest imaging are performed within 1 day with low and high dose of tracer (Fig. 18.1). Of 2-day protocol, stress and rest imaging are performed in separate day (Fig. 18.2). ^{99m}Tc-MIBI is excreted by hepatobiliary system, so fat meal or fried eggs should be given 30 min after injection of tracer in order to reduce interference from trace uptake by liver and intestinal tract. Not only for evaluation of myocardial blood flow perfusion but also some acquisition protocols using thallium-201 can be used in evaluating viable myocardium.

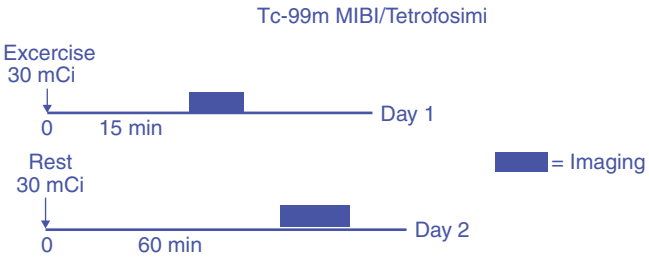

Fig. 18.2 Two-day acquisition protocol for Tc-99m-labeled tracers using SPECT

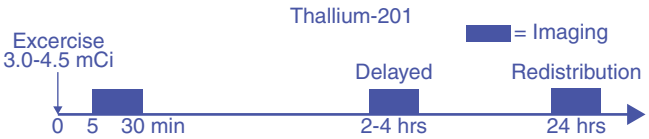

Fig. 18.3 Stress-delayed-redistribution acquisition protocol for thallium-201

For thallium-201, stress test and rest acquisition can be performed in 1 day because of redistribution of the tracer (Fig. 18.3). Acquisition protocols involve stress/redistribution imaging protocol, stress/reinjection imaging protocol, stress/delayed redistribution imaging protocol, and stress/reinjection and delayed imaging protocol.

The image reconstructions use filtered back projection or iterative method. The purpose of filters is to reduce images noise and blur before and after back projection of raw data. The standard filter is Butterworth filter for SPECT imaging. The cutoff and order of Butterworth filter is different for each procedure. Before reconstruction, motion correction can be used for raw image data if motion is detected. The

process of correction should be checked for accuracy. Reconstruction reorients the data to three sets of tomographic images: short axis slices (SA), horizontal long axis slices (HLA), and vertical long axis slices (VLA). It is essential that the stress and rest slices are aligned for comparing.

18.3.3.3 SPECT/CT Imaging

Hybrid imaging techniques allow the direct fusion of functional information and morphologic information. Recently, SPECT/CT scanners have been made available widely. For SPECT/CT imaging, SPECT images are acquired firstly and then do CT images acquisition. CT images are used for attenuation correction and fusion with SPECT images. Combining function and morphology is highly attractive. The reasons involve improvement of diagnostic specificity and accuracy, increase of self-confidence of interpreter, calculation of coronary calcium scores, and performance of CT angiography.

18.3.3.4 ECG-Gated Myocardial Imaging

In a SPECT acquisition, the detectors of scanner rotate around the long axis of the patient, acquiring projection images along the acquisition orbit. In the use of R-wave of ECG as acquisition trigger, the R-R interval was divided into 8 or 16 frames (interval). All projection images of a given interval can be reconstructed into a tomographic image volume using reconstruction techniques, and volumes relative to the various gated SPECT intervals can be showed in time-radioactivity curve. The information of cardiac function and chamber volume can be assessed.

Both blood perfusion and function information of left ventricle (LV) can be obtained by ECG-gated myocardial imaging through one procedure. Information of function involve wall motion of LV, wall thickening of LV, ejection fraction of LV (LVEF), end-systolic volume of LV (LVESV), end diastole volume of LV (LVEDV), and stroke volume of LV (LVSV). The information provides additional value for evaluation of outcome and guides treatment. In additional, ECG-gated imaging can obtain the myocardial systolic and diastolic images in phases, improving the sensitivity and specificity for detecting minimal perfusion defect. But for patients with arrhythmia or atrial fibrillation, ECG-gated is not suitable [11].

18.3.3.5 PET and PET/CT Imaging

SPECT imaging is the most commonly used method for nuclear cardiology procedures in China and worldwide. Comparing with the SPECT imaging, PET or PET/CT imaging can provide higher image quality and a greater efficiency and improve diagnostic accuracy for ischemic myocardium. However, due to limitation of PET systems, radiopharmaceuticals, and expensive cost, the use of PET is infrequent. Recently, using rubidium-82 has made cardiac PET and PET/CT imaging become an important technique in the detection and risk stratification of CAD. People make more and more focus on radiation exposure of medical imaging. For SPECT imaging, thallium-201 results in 15–20 mSv of radiation exposure, and technetium-99m-labeled tracers result in 8–10 mSv. For PET imaging, radiation exposure of rubidium-82 results in 4–6 mSv [12]. Figure 18.4 shows the protocol of ^{82}Rb stress-rest myocardial perfusion PET/CT imaging.

18.3.3.6 Quality Control

Many aspects should be considered to ensure the quality of images, which involve parameters of filter and reconstruction, motion correction, alignment of images of stress study and rest study, count increase, attenuation correction, normalization, and extra-cardiac activity. After acquisition of SPECT imaging, a "sinogram" or cine should be investigated in order to detect motion of patient. If motion is detected, the motion correction program can be applied. It is important that investigator is aware of the results of motion correction. After motion correction, cine should be reviewed to determine if the motion is corrected. There is no evidence of patient motion. Typical motion artifacts are "gaps" at long axis slice images and "breaks" in the short axis slice images. The stress and rest slices must be aligned, and the study may be misinterpreted if the slices are misaligned. The first apical slice of the stress study and rest study must be matched. For 1-day protocol, the myocardial max counts increase in the stress study as expected, especially in obese. For normalized, both studies are normalized to the portion within the myocardium with the highest uptake. In addition, tracer uptake of hepatobiliary system and intestinal tract should be eliminated for ensuring image quality; no significant extra-cardiac activity is shown in perfusion images.

18.3.4 Display and Interpretation of Images

The images should be displayed adjacent to one another and adjusted to optimize match slices. The interpreter should observe the images on a high-resolution computer screen avoiding paper or film shows, as the latter reduces sensitivity of diagnosis.

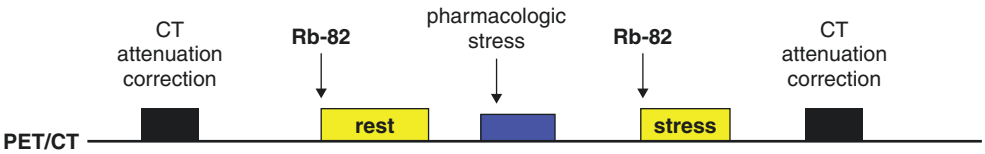

Fig. 18.4 Protocol of stress-rest myocardial perfusion PET/CT imaging with ^{82}Rb

18.3.4.1 Display of Images

After reconstruction, three sets of tomographic slices are obtained for reflection of distribution of radioactivity: short axis slices (SA), horizontal long axis slices (HLA), and vertical long axis slices (VLA). The SA slices are displayed from apex to base perpendicular to the long axis of the heart. On SA slices, apex, anterior wall, inferior wall, posterior wall, septum, and lateral wall of the left ventricle are displayed. The VLA slices are displayed from septum to lateral wall in the shape of horseshoe or from lateral wall to septum, displaying apex, anterior wall, inferior wall, and posterior wall of the left ventricle. The HLA slices are displayed from inferior wall to anterior wall of left ventricle or from anterior wall to inferior wall of left ventricle. Apex, septum, and lateral wall of left ventricle are displayed on it. The stress images and rest or delayed images are displayed in two rows of images to facilitate comparison (Fig. 18.5). ECG-gated SPECT slices are displayed an appropriate color scale. An endless-loop movie are played on processing workstation to investigate wall thickening and wall motion of left ventricle. Images of wall thickening are also displayed in three sets of tomographic slices. Globe and regional ejection fraction and volume information of left ventricle are calculated by ECG-gated analysis software (Fig. 18.6).

The "bull's bye" map or polar image is also a useful display format. Perfusion image data are projected onto one plane, a circular is represented for the left ventricle. The left ventricle is just as if flattened into a pancake. The apex data are projected in the center of the bull's-eye map. The apex is in the center, the anterior wall to the top, the inferior wall to the bottom, the lateral wall to the left, and the septum to the right of map. The periphery is the base of the heart. The bull's-eye map can also be quantitatively studied compared to normal population database (Fig. 18.7). Both on tomographic slices and bull's-eye map the semiquantitative analysis can be applied. 17-Segment model is commonly used model for semiquantitative analysis. In comparison with normal uptake of regional myocardium of LV, scores of each segment of LV are obtained. Thus semiquantitative scores

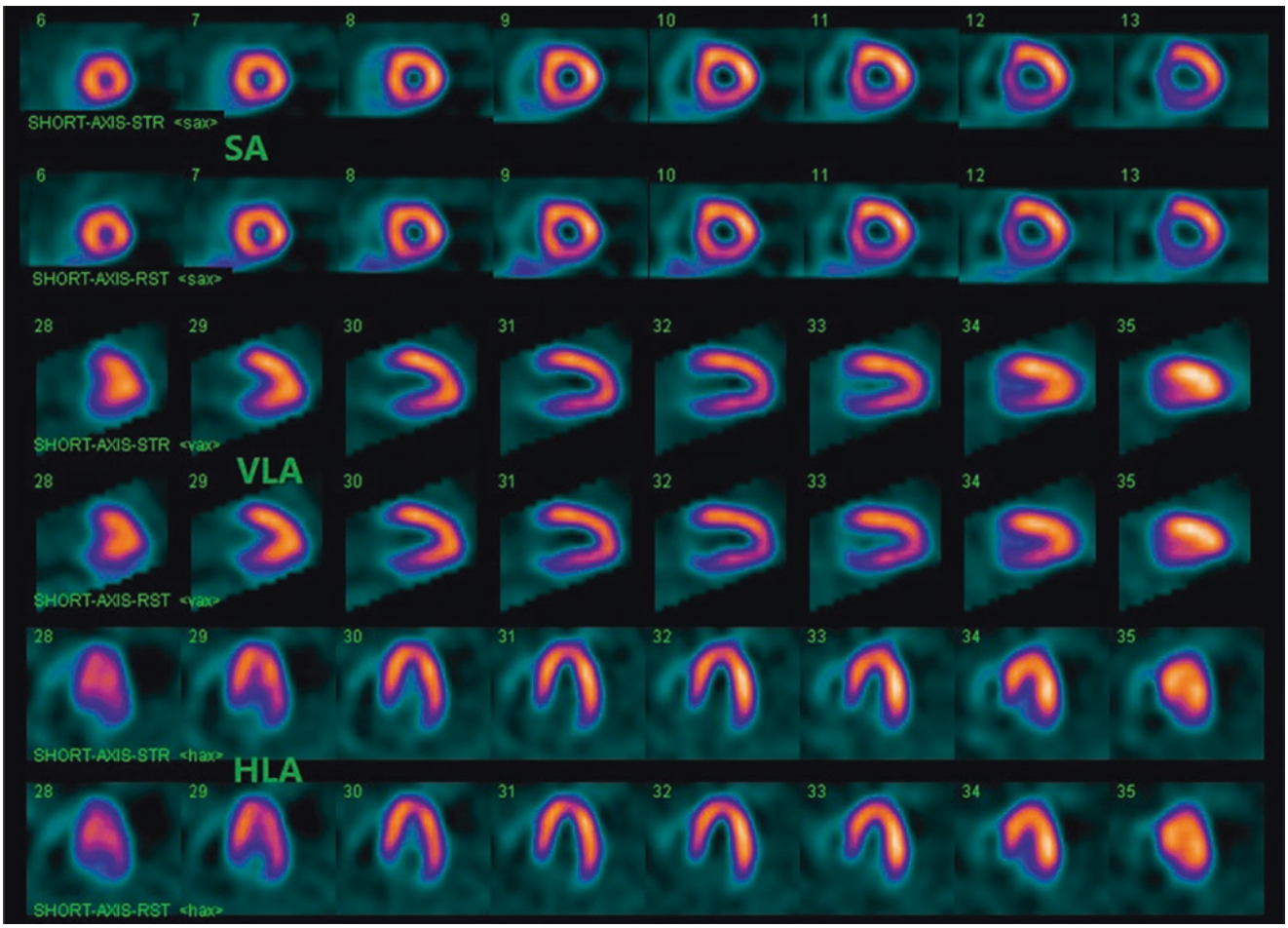

Fig. 18.5 Three sets of tomographic slices of normal stress-rest perfusion imaging. *SA* short axis, *HLA* horizontal long axis, *VLA* vertical long axis. Row 1, 3, and 5 are images of stress study. Row 2, 4, and 6 are images of rest study

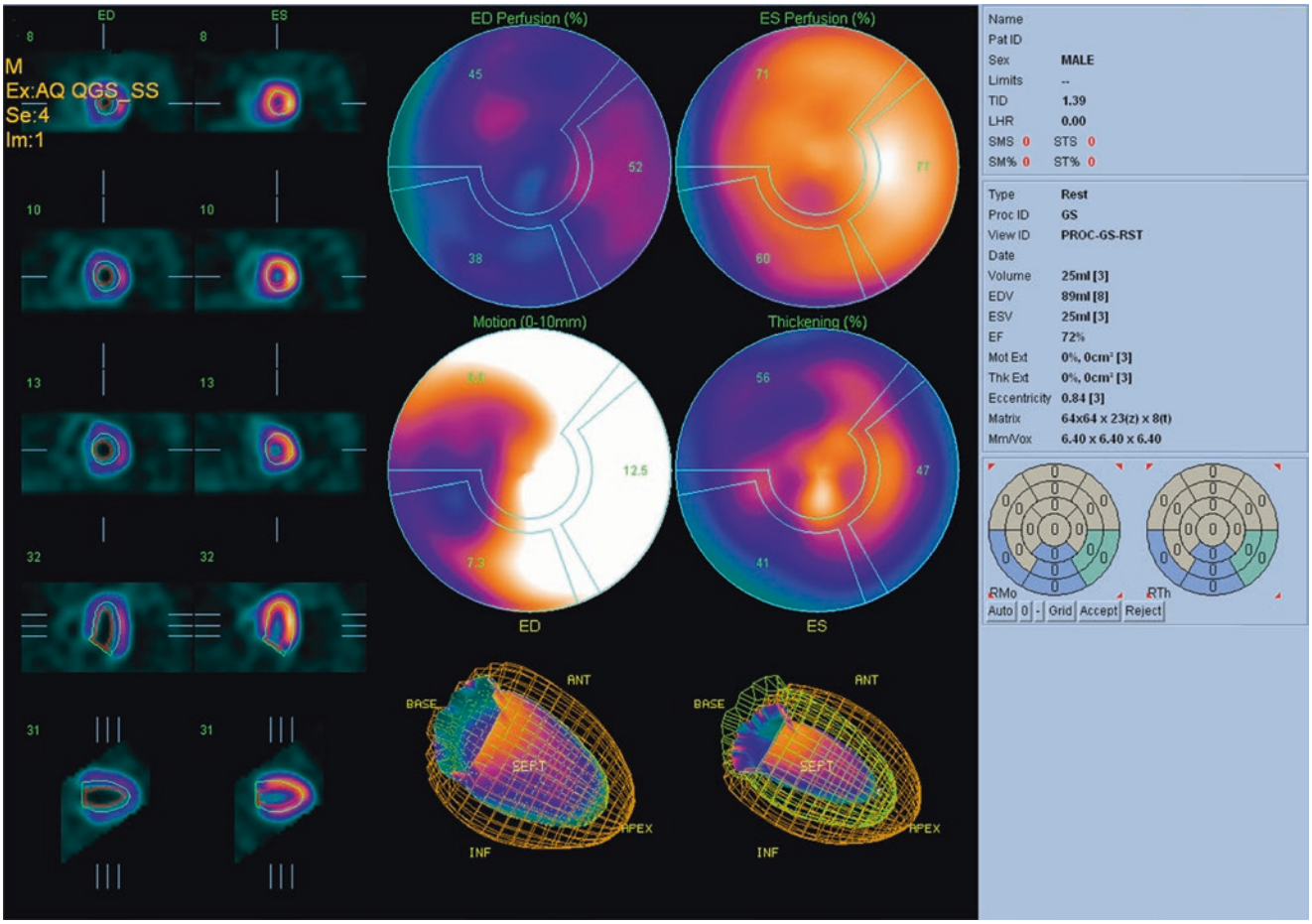

Fig. 18.6 ECG-gated MPI analysis shows "bull's-eye" maps of wall motion and wall thickening. Cavity volumes and EF are also obtained by ECG-gated analysis

are derived, involving a summed stress score (SSS), a summed rest score (SRS), and a summed difference score (SDS). These scores have been shown to provide valuable outcome information.

18.3.4.2 Normal

The radioactivity of tracer is uniform, no abnormal radioactivity decrease, and defect is observed on three tomographic slices. The distribution of radioactivity is slightly decreased in apex of the heart. The intraventricular septum close to the base is consist of membrane tissue; thus the septum close to the base of the heart appears to have radioactivity defect. The perfusion images from a male subject may appear a slight activity reduction in inferior wall of LV; this is a normal variant for a male due to diaphragmatic attenuation. The perfusion images from a female subject may appear a slight activity reduction in regional anterior wall of LV due to breast attenuation. On ECG-gated images and movies, wall thickening and wall motion are normal.

18.3.4.3 Patterns of Abnormal Perfusion

Reduction or defect of radioactivity distribution is appeared more than two planes on the same myocardial segment of two different axis slices. Patterns of abnormal perfusion involve five types: reversible defect, fixed defect, mixed defect, reverse redistribution, and tinea sample change.

Reversible Defect

Defect of regional activity distribution at myocardial segment at stress. However, the abnormal defect of activity distribution recovers to normal distribution at rest. Appearance of reversible defect mainly indicates regional myocardial ischemia (Fig. 18.8).

Fixed Defect

Defect of activity distribution of myocardial segments exist in both stress and rest images. It is also known as nonreversible defect. Appearance of fixed defect indicates myocardial infarction, scar tissue, or severe myocardial ischemia (Fig. 18.9).

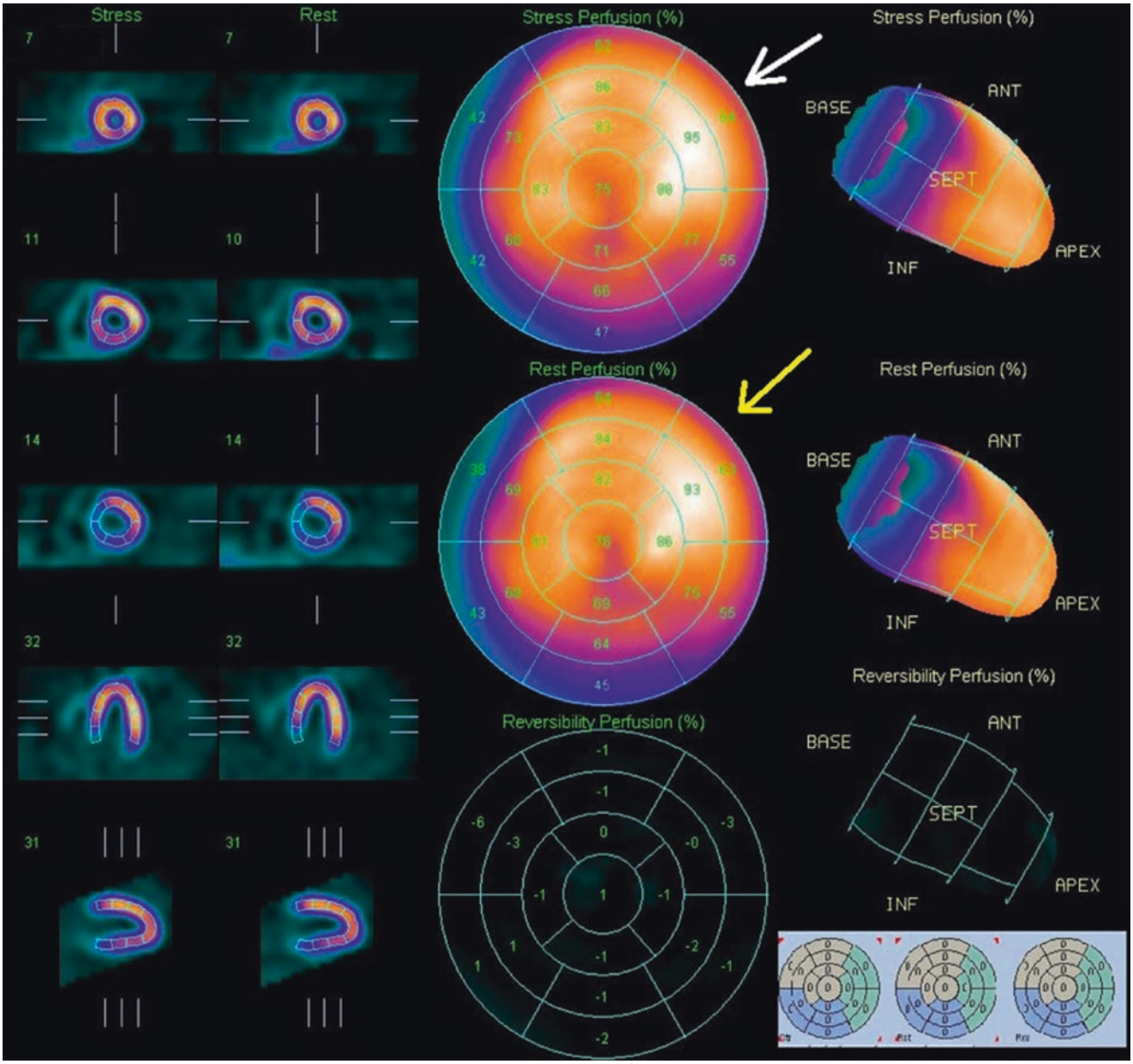

Fig. 18.7 "Bull's bye" maps of stress study (white arrow) and rest study (yellow arrow) in a normal subject

Mixed Defect

Defect of activity distribution of myocardial segments is observed on stress images, while it is partly filled on rest image. Mixed defect indicates myocardial ischemia accompanied with myocardial infarction (Fig. 18.10).

Tinea Sample Change

Both on stress and rest images, the activity distribution appear multiple segmental reduction and defect. The defects do not match to blood flow distribution of coronary artery. Tinea sample change usually appears in cardiomyopathy or myocarditis (Fig. 18.11).

Reverse Redistribution

No reduction or defect of activity distribution is shown on rest images, while abnormal segmental reduction or defect of activity appears on stress images (Fig. 18.12). The abnormal activity distribution of rest images become worsening on stress images also called reverse redistribution. The cause of reverse redistribution is unknown, and the meaning of this appearance is not clear.

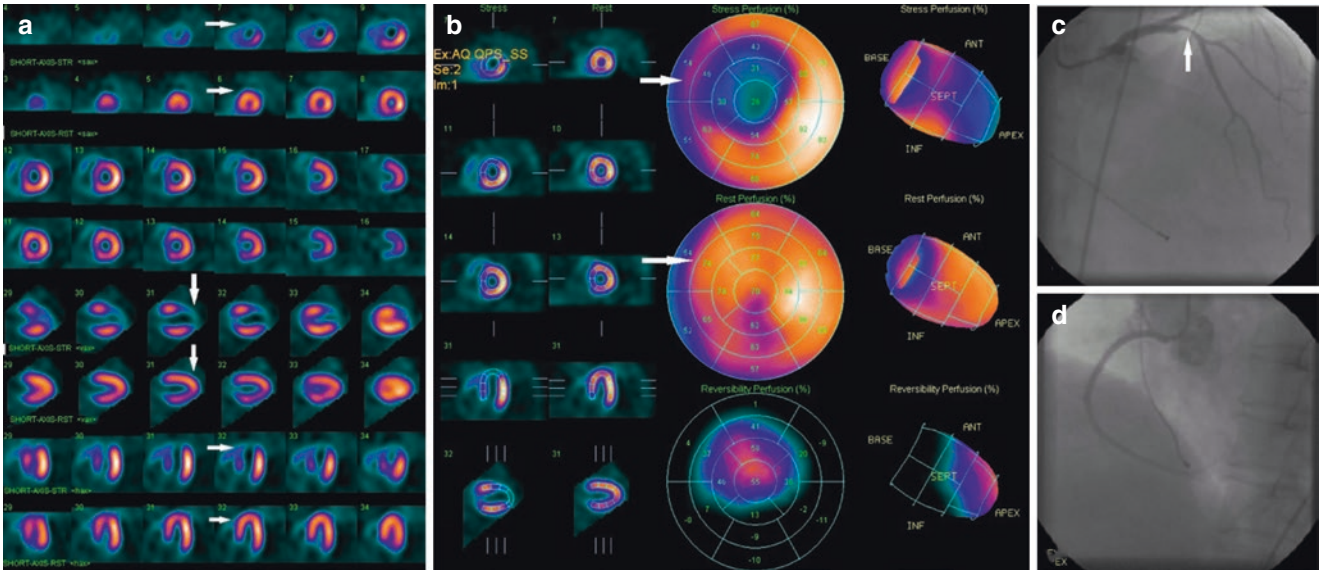

Fig. 18.8 Appearance of reversible defect mainly indicates regional myocardial ischemia. Reversible defects are showed in anterior wall, apex, and septum of three tomographic slices (**a**, arrows) and "bull's-eye" maps (**b**, arrows). CAG shows stenosis in LAD (**c**, arrow) and RCA is normal (**d**)

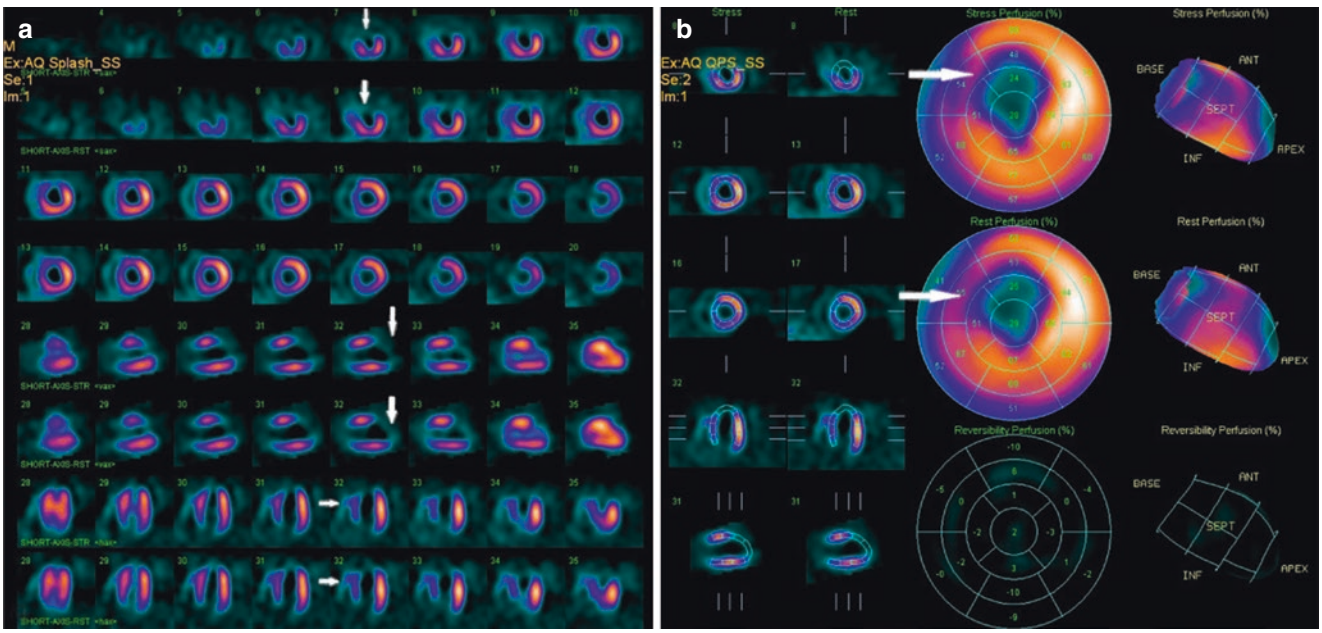

Fig. 18.9 Appearance of fixed defect indicates myocardial infarction, scar tissue, or severe myocardial ischemia. Fixed Defects are showed in anterior wall, apex, septum, and inferior wall of tomographic slices (**a**, arrows) and "bull's-eye" maps (**b**, arrows)

18.3.5 Clinical Applications

The clinical applications of MPI involve diagnosis of CAD, risk stratification, acute coronary syndrome, before and after revascularization, assessment of functional significance of intermediate lesions, and so on.

18.3.5.1 Diagnosis of CAD

With the development of the diagnosis and treatment of coronary heart disease, especially the widely use of percutaneous coronary intervention (PCI) and coronary artery bypass grafting (CABG), mortality from CAD is significantly reduced. MPI is a noninvasive cardiac imaging technique,

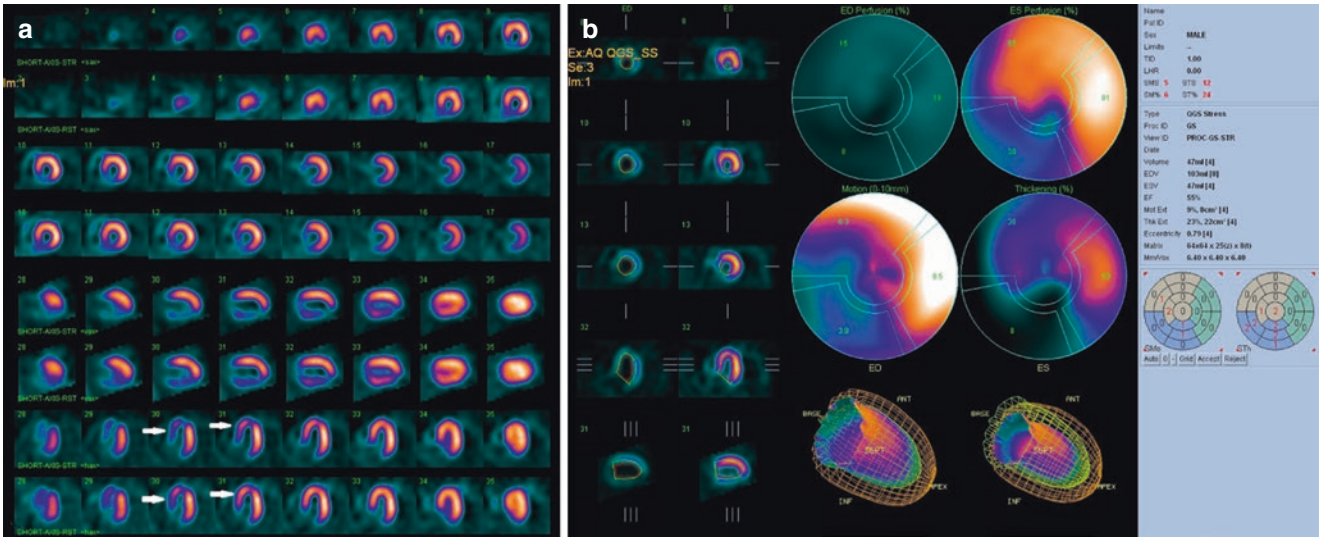

Fig. 18.10 Mixed defects are showed in septum and inferior wall of tomographic slices (**a**) and ECG-gated analysis (**b**)

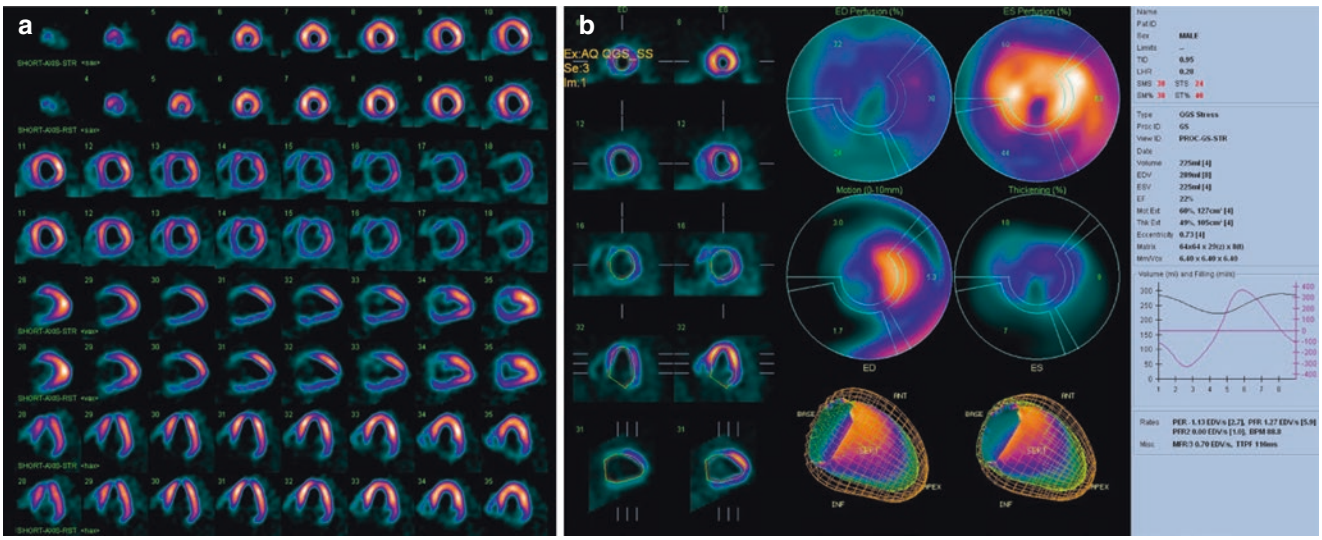

Fig. 18.11 Tinea sample change on tomographic images of MPI (**a**) and results of ECG-gated acquired analysis (**b**)

the diagnostic accuracy of CAD and cost-effective are good. Myocardial ischemia can be detected early using MPI, reducing the mortality of CAD. The pretest probability of CAD is varied; pretest probability of CAD should be estimated for potential subject before MPI exam [13]. Diamond-Forrester predictive model is commonly used methods in clinical practice based on age, gender, symptoms of chest pain, and other factors. Potential CAD population is classed into three grades, low CAD probability, moderate CAD probability, and high CAD probability. In other words, MPI is the most suitable for patients with moderate CAD probability.

The commonly used tracers for MPI involve ^{99m}Tc-MIBI, ^{99m}Tc-tetrofosmin, and thallium-201. In China, ^{99m}Tc-MIBI is the most commonly used tracer. In other countries, the centers prefer to use thallium-201 and ^{99m}Tc-MIBI as tracers. A wealth studies suggest that the sensitivity and specificity of using different tracers are similar. In addition, the sensitivity and specificity of using different stress protocols are also similar. Table 18.4 shows the diagnostic performance of exercise stress MPI using different tracers for CAD (≥50% coronary stenosis defined angiographically) [13]. Table 18.5 shows the diagnostic performance of using different vasodilators (≥50% coronary stenosis defined angiographically) [13]. A Chinese expert consensus [14] published in 2018 showed that the average sensitivity of SPECT MPI for detecting >50% angiography stenosis is 71–97%, whereas the average specificity is 73% (range, 36–100%). The average sensitivity of PET MPI for detecting >50% angiography stenosis is 91% (range, 83–100%), whereas the average specificity is 89% (73–100%).

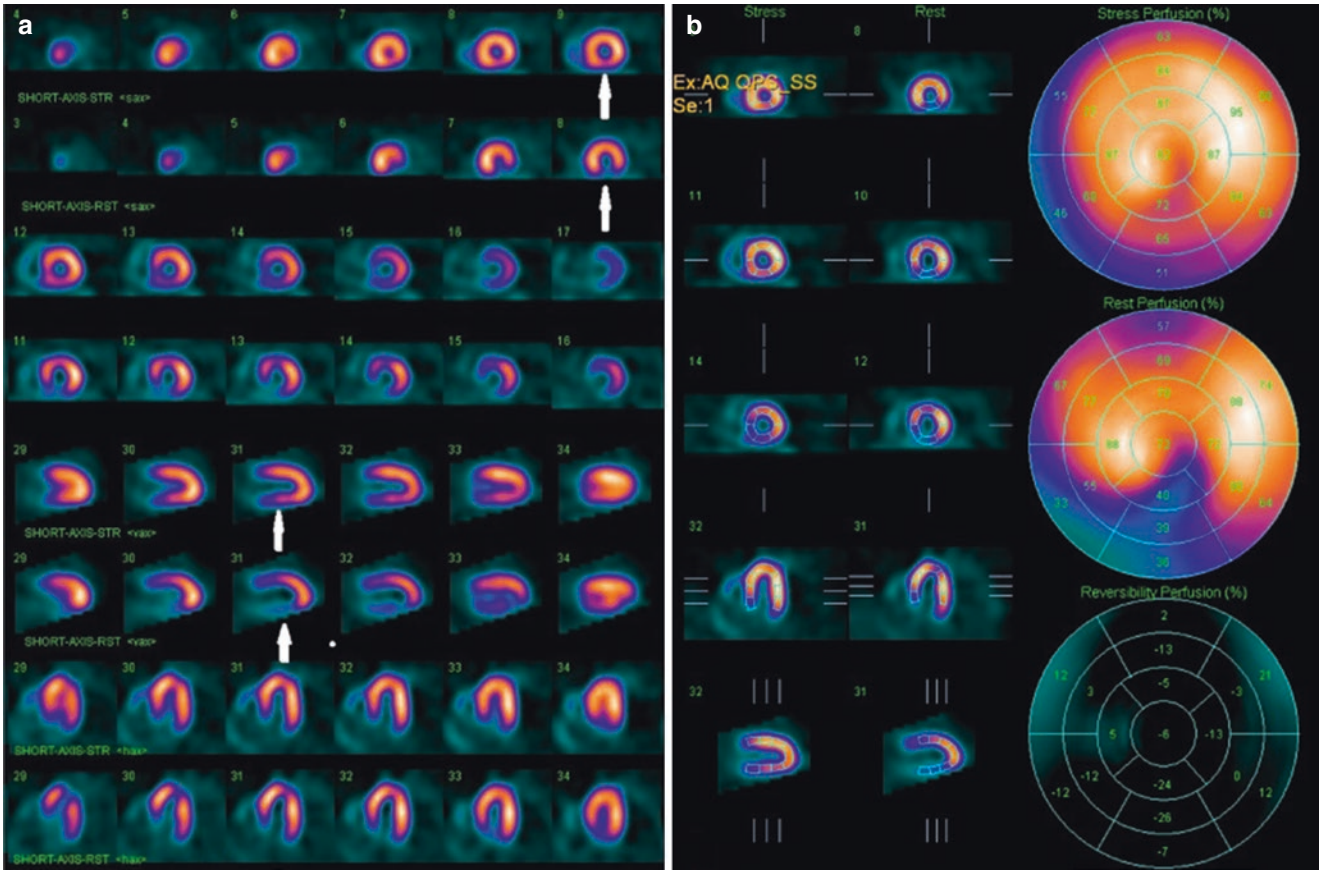

Fig. 18.12 Reverse redistribution is showed in inferior wall (arrows) of three tomographic slices (**a**) and "bull's-eye" maps (**b**)

Table 18.4 Diagnostic accuracy of exercise stress MPI using different tracers for the detection of 50% coronary stenosis defined angiographically

Year	1989–2001
Number of studies	33
Stress protocol	Exercise stress
Number of subjects (range)	21–993
Total number of subjects	4480
Tracer (number of studies)	MIBI (20)
	TF (4)
	^{201}Tl (12)
Range of sensitivity (%)	71–97
Range of specificity (%)	36–100
Average sensitivity (%)	87
Average specificity (%)	73

MIBI 2-methoxy-isobutyl-isonitrile, *TF* tetrofosmin

Table 18.5 Diagnostic accuracy of different vasodilators for the detection of 50% coronary stenosis defined angiographically

Year	1990–2000
Number of studies	17
Number of subjects (range)	26–550
Total number of subjects	2492
Vasodilator (number of studies)	Dipyridamole (5)
	Adenosine (12)
Tracer (number of studies)	MIBI (5)
	TF (3)
	^{201}Tl (10)
Range of sensitivity (%)	72–93
Range of specificity (%)	28–100
Average sensitivity (%)	89
Average specificity (%)	75

MIBI 2-methoxy-isobutyl-isonitrile, *TF* tetrofosmin

MPI, CT angiography (CTA) and coronary angiography (CAG) are used for diagnosing CAD during past decades. At present, CAG is regarded as "golden" standard for CAD diagnosis. CAG and CTA are mainly used for reveal of anatomical and morphological changes in coronary artery (Fig. 18.13). The two techniques cannot reflect the functional significance of coronary artery directly. MPI reveals the blood flow distribution of myocardium and functional significance of myocardial tissue. However, MPI can't show the anatomical information of coronary artery, so MPI is different from other morphological imaging methods. Diagnostic accuracy of different cardiac imaging methods for CAD diagnosis is varied. The result of meta-analysis [15] indicates that diagnostic accuracy of MPI is higher than ECG exercise tests. For pharmacologic stress test, the accuracy of MPI using dipyridamole or adenosine stress is similar to exercise stress test. Study indicates that detection of myocardial ischemia using ^{99m}Tc-MIBI dipyridamole stress

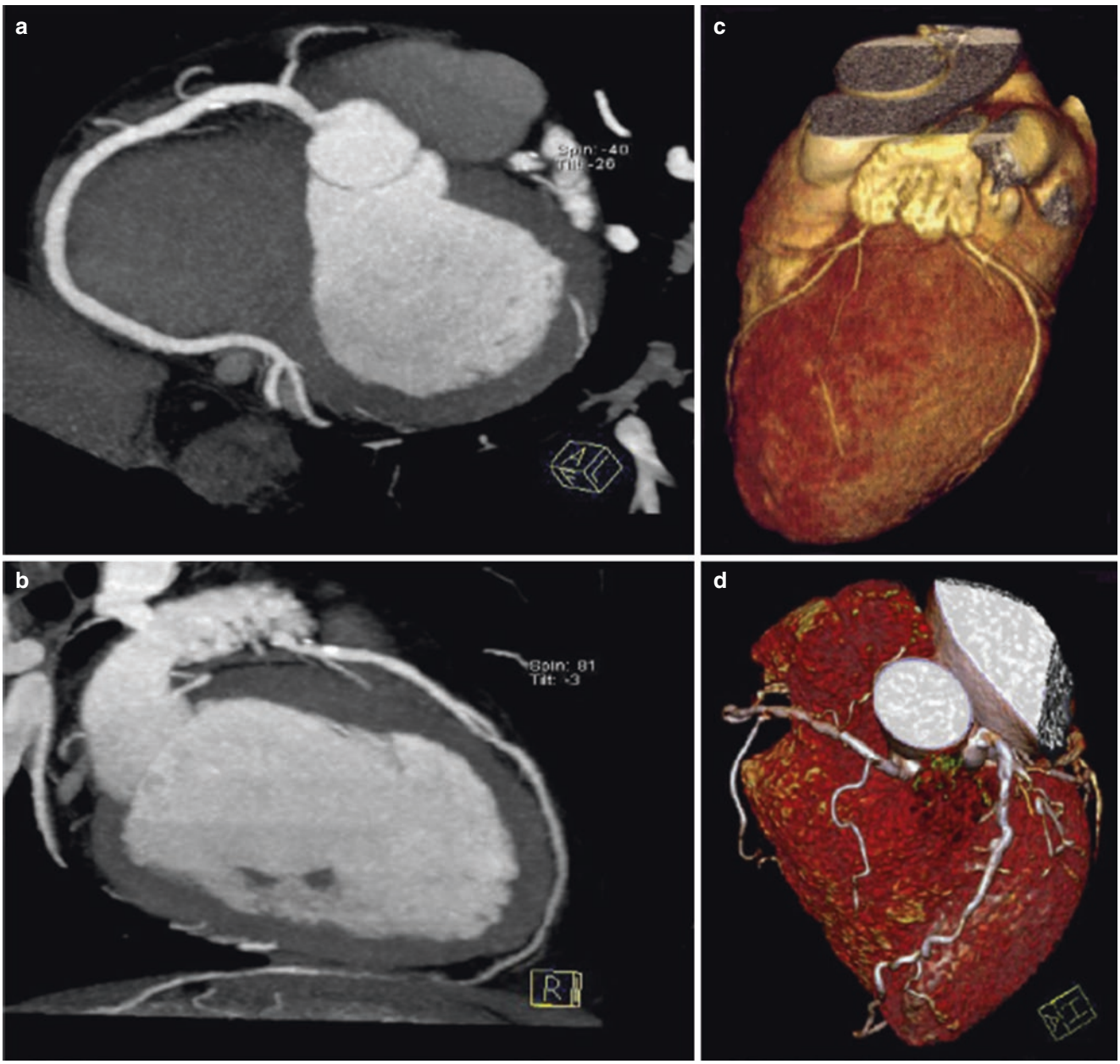

Fig. 18.13 Maximal intensity projection (MIP) images of the heart from contrast-enhanced cardiac CT angiography (**a**, **b**). 3D surface-rendered images of the heart (**c**, **d**)

MPI probably is superior to ^{99m}Tc-tetrofosmin dipyridamole stress MPI; however, the conclusion needs to be confirmed by further study. Detection of myocardial ischemia using MPI is also affected with other factors. These factors involve location of stenosis, degree of stenosis, the number of lesion vessels, status of stress test, and regional wall motion of LV. Research report [13] that the sensitivity of thallium-201 MPI for one-vessel disease, two-vessel disease, and triple-vessel disease is 83%, 93%, and 95%, respectively. For tracer with ^{99m}Tc-MIBI, the sensitivity of MPI is 90% in one-vessel disease and 98% in triple-vessel disease. The overall sensitivity of MPI using exercise stress test for detecting CAD (coronary stenosis ≥50% defined angiographically) is 87%, the overall sensitivity of MPI using pharmacologic stress test is 89%. The overall specificity of MPI using exercise stress test or pharmacologic stress test is 73% and 75%.

ECG-gated acquisition is an effective tool to improve diagnostic specificity and accuracy. It is now routinely used in many centers of China and other countries. Information obtained from ECG-gated analysis does help to distinct true perfusion abnormality and artifact and improve self-confidence of interpreter. These data and indexes provide additional prognostic information from global and regional function of left ventricle. A prospective study performed by Taillefer [16] compared the sensitivity and specificity of

thallium-201, ^{99m}Tc-MIBI, and ECG-gated ^{99m}Tc-MIBI SPECT MPI for detection of CAD, specifically in women. The study included 85 patients with suspected CAD and 30 volunteers. The overall sensitivities for detecting ≥50% and ≥70% stenosis were 75.0% and 84.3%, for thallium-201, and 71.9% and 80.4%. The specificity for detecting lesions ≥50% was 61.9% for thallium-201 and 85.7% for ^{99m}Tc-MIBI. The specificity for stenosis ≥70% was 67.2% for thallium-201, 84.4% for ^{99m}Tc-MIBI SPECT, and 92.2% for ^{99m}Tc-MIBI ECG-gated SPECT MPI. The study indicates specificity of ^{99m}Tc-MIBI SPECT MPI is better than thallium-201, which is further enhanced by the use of ECG-gated method. Smanio et al. [17] investigated how frequently and for what reasons ECG-gated SPECT MPI add value to non-gated SPECT. A total of 285 consecutive patients underwent ECG-gated SPECT. The number of "borderline" interpretations was reduced from 89 to 29; the addition of ECG-gated information added significantly to the percentage of "normal" interpretations (from 74 to 93%, $P < 0.0001$) due to reduce borderline normal and borderline abnormal readings. In patients with a previous infarction, the addition of ECG-gated information changed the percentage of abnormal interpretations from 78 to 92%. The study indicated the addition value of ECG-gated SPECT imaging comparing to the stress/rest MPI alone, significantly reduced the number of "borderline normal" and "borderline abnormal."

18.3.5.2 Risk Stratification

SPECT MPI is commonly used in risk assessment, as an abnormal scan predicts a multifold increase in cardiac risk. Previous studies confirmed value of MPI for risk stratification in patients with myocardial ischemia. If the result of stress MPI is negative, annual incidence of severe heart event (cardiac death or nonfatal myocardial infarction) is lower than 1%. The conclusion is not affected with other factors involving gender, age, symptoms, previous CAD history, result of CAG, tracers of MPI, and procedures of MPI. Table 18.6 shows the risk of severe cardiac event in patients with negative stress MPI [13]. Studies indicate normal or equivocal stress MPI results are associated with a benign prognosis, even in patients with a high likelihood of CAD. Prognostic value is added by nuclear testing in all patient subgroups. Patients with normal stress ^{99m}Tc-MIBI MPI and stable chest pain have very low risk of death or nonfatal MI; coronary revascularization hardly improves survival in such patients. Normal or equivocal exercise stress MPI study results are associated with a benign prognosis, even in patients with a high likelihood of coronary artery disease.

A large samples study [18] determined the predictors of risk with normal SPECT MPI. A total of 7376 consecutive patients with normal exercise stress or adenosine stress MPI were included in the study. The hard event (HE, involves cardiac deaths and nonfatal myocardial infarction) rates were greater in patients with versus without previous CAD. The study identified pharmacologic stress, known CAD, diabetes mellitus, male, and age with interactions between stress type and previous CAD and between gender and DM. The highest risk subgroups had a maximal HE rate of 1.4–1.8%/year. The study revealed that in patients without previous CAD, the risk was uniform with time, while in patients with known CAD, the risk increased with time. Abidov et al. [19] investigated the prognostic importance of hemodynamic responses to adenosine used for stress SPECT MPI. A total of 3444 patients older than age 55 years underwent adenosine stress MPI and were followed up for 2.0 ± 0.8 years. The result showed higher rest heart rate (HR) and to a lesser extent lower peak HR were markers of cardiac death. The HR ratio of peak/rest was an independent predictor of cardiac death. Patients accepted adenosine stress MPI with high rest HR and low peak/rest HR ratio had increased risk of cardiac death. The study indicates the value of MPI data for risk stratification. A Chinese study [20] investigated the predictive value of adenosine triphosphate stress SPECT MPI for risk stratification of suspected CAD patients aged 70 years and older. Four hundred and fifteen consecutive patients underwent ^{99m}Tc-MIBI MPI, and the multivariable analysis showed that abnormal MPI was independently associated with major adverse cardiac events (MACE). The patients with summed stress score (SSS) > 8 had significantly higher cumulative MACE rate than patients with SSS ≤ 8 had. The cumulative MACE-free survival in patients with abnormal MPI was lower than that in normal MPI patients significantly. Adenosine triphosphate stress MPI data are useful for the prediction of MACE in suspected CAD patients aged 70 years and older.

A study [21] investigated the relationship between the amount of inducible ischemia present on stress MPI and the presence of a short-term survival benefit with early revascularization versus medical therapy (MT). A total of 10,627 patients without prior myocardial infarction who underwent adenosine or exercise stress MPI. Treatment received within 60 days

Table 18.6 The risk of severe cardiac event in patients with negative stress MPI

Year	1994–2003
Number of studies	16
Number of subjects (range)	177–15,475
Total number of subjects	31,255
Tracer (number of studies)	MIBI (9)
	^{201}Tl (6)
	TF (2)
Range of average month of F-U	12.8–72
Average F-U month of all studies	26.8
SCE/abnormal SPECT (%/year)	0–1.6
Overall SCE/abnormal SPECT (%/year)	0.6

F-U follow-up, *MIBI* 2-methoxy-isobutyl-isonitrile, *SCE* severe cardiac event, *TF* tetrofosmin

Table 18.7 Diagnostic accuracy of MPI for detection of MI or CAD in patients with suspected ACS

Author	Year	*n*	Sensitivity (%)	Specificity (%)	PPV (%)	NPV (%)	EP
Wackers et al.	1989	203	100	63	55	100	MI
Bilodeau et al.	1991	45	96	79	86	94	CAD
Varetto et al.	1993	64	100	67	43	100	MI
Hilton et al.	1996	102	100	78	38	99	MI
Tatum et al.	1997	532	93	71	15	99	MI
Heller et al.	1998	357	90	60	12	99	MI
Duca et al.	1999	75	100	73	33	100	MI
Kosnik et al.	2001	69	71	92	50	97	MI

EP end point, *MI* myocardial infarction, *CAD* coronary artery disease, *PPV* positive predictive value, *NPV* negative predictive value

after MPI defined subgroups undergoing revascularization (2.8% mortality) or MT (1.3% mortality). The study identified inducible ischemia and anginal symptoms as the most powerful predictors. For predicting cardiac death, patients with MT demonstrated a survival advantage over patients with revascularization in the setting of no or mild inducible ischemia. But in the setting of moderate to severe myocardial ischemia, patients with revascularization had an increasing survival benefit compared to patients with MT. Furthermore, in higher-risk patients (elderly, adenosine stress, women, and diabetes), revascularization had better survival benefit over MT. The size and degree of myocardial ischemia based on MPI are related with risk and outcome of subjects.

18.3.5.3 Acute Coronary Syndrome (ACS)

Chest pain is one of the leading causes of referral to emergency departments worldwide and contributes to 20–37% of medical admissions. An efficient diagnostic method is the key to accurately recognize the patients with ACS, especially those presenting with potentially life-threatening CAD. Diagnostic pathways based on the 12-lead electrocardiogram (ECG) and blood biomarkers of myocardial injury represents missed ACS in part of patients, potentially resulting in inappropriate discharge from hospital. Due to low specificity, ACS can't reliably be excluded from a single blood sample, and current guidelines recommend serial samples test to definite diagnosis. Furthermore, evidence of the diagnostic value of novel blood biomarkers in patients with unstable angina is insufficient; clinical effectiveness needs further to be confirmed. Many noninvasive myocardial ischemia tests are used in suspected ACS, with exercise testing (ET), MPI, stress echocardiography (SE), computed tomography coronary angiography (CTCA), positron emission tomography, and cardiac magnetic resonance (CMR) being the most used in this field. Noninvasive cardiac imaging methods have an important role in the assessment of patients with acute-onset chest pain. Cardiac imaging can complement patient history, ECG, and biomarkers of suspected ACS patients for timely identification or exclusion of ACS. Noninvasive cardiac imaging can avoid missing diagnosis and guide the appropriate management of confirmed ACS patients.

MPI is the most established imaging method for evaluating ischemia and viability. Among the currently available methods in the patients with acute chest pain, MPI has the strongest prognostic data. MPI provides incremental value over routine clinical assessment in suspected ACS patients. Table 18.7 shows the diagnostic performance of MPI for CAD in suspected ACS patients [13]. MPI is endorsed by the guidelines [14] as an appropriate test in suspected ACS patients when ECG and blood biomarkers can't have definite diagnosis. Of the recent systematic review and meta-analysis [22], 77 studies were included for a total of 49,541 patients. The results showed the sensitivity and specificity were 85% (77–91%) and 92% (83–96%), the sensitivity and specificity of troponin T were 89% (79–94%) and 84% (74–90%), and the sensitivity and specificity of CTCA were 93% (81–98%) and 90% (93–94%). Exercise testing showed the lower level of diagnostic accuracy. In subjects without troponin increase, MPI and CTCA showed the highest sensitivity and specificity for detecting ACS. In a pooled analysis [23] of 2465 patients with recent (<6 h) chest pain, the sensitivity and specificity of rest MPI for detecting MI was 90% and 80%, respectively, and the negative predictive value was 99%. Rest MPI is cost-effective, and the use of rest MPI improves the triage of suspected ACS patients. A large multicenter, randomized trial included 2475 patients (the ERASE trail) [24] who showed a 14% reduction using MPI in hospital admission compared with usual care. Cost per patients reduced 17% with the incorporation of MPI.

One of the main limitations of MPI is it required relevant amount of time for its performance, especially when rest imaging or stress imaging is also needed, leading to longer period of hospital stay. Another limitation is that rest MPI alone cannot be used to distinguish between chronic MI and acute, as both of the two conditions appear as myocardial blood flow hypoperfusion areas. Stress-rest SPECT MPI is more accurate and has greater prognostic value for detecting inducible ischemia than rest imaging alone. The stress imaging is usually performed after a normal rest imaging, which can prolong stay time of patients in hospital.

CTCA is feasible with CT scanners acquiring ≥64 slices, and these scanners are now widely available. CTCA offers

an anatomic reconstruction. Of suspected ACS, CTCA also offers the potential to visualize the vulnerable or unstable plaque. It is endorsed by guidelines as an appropriate test in acute chest pain patients with nondiagnostic ECG or biomarkers. CTCA is also endorsed for the evaluation of suspected coronary anomalies in the groups with low or moderate likelihood of and ACS. CTCA is also cost-effective, a meta-analysis ($n = 3266$) showed that incorporating CTCA shortened the hospital stay and save the cost. In addition to coronary imaging, coronary artery calcium scoring has a high negative predictive value in patients presenting with acute chest pain [25].

The role of pharmacological and exercise stress echocardiography (SE) in the assessment of suspected ACS has been studied extensively. The use of stress echocardiography is mainly recommended for patients with no resting chest pain, normal ECG findings, negative troponin, and a low risk score. SE can detect inducible ischemia based on the identification of stress-induced changes of the regional wall motion and wall thickening of the LV. Furthermore, SE is a radiation-free examination and easily used in clinical work.

Cardiac magnetic resonance (CMR) has an emerging role in the assessment and management of patients with ACS. CMR provides structural and functional information about regional myocardial wall motion and wall thickening. Stress CMR is recommend as appropriate for patients with a moderate likelihood of ACS when the ECG is undefinable or the patient is unable to perform stress test. Current ESC guidelines highlight in particular the use of CMR to detect myocardial perfusion and viability in suspected ACS patients [26]. Table 18.8 shows the diagnostic accuracy of different methods in patients without troponin increase [22].

18.3.5.4 Before and After Revascularization

A large number of patients are suffering from CAD with severe ischemia due to multivessel atherosclerotic obstruction. Coronary lesions often lead to impaired myocardial function and heart failure and result in poor outcomes. For these patients, treatments involve drug therapy, percutaneous coronary interventions (PCI), and coronary artery bypass grafting (CABG). Hachamovitch et al. [27] have reported the impact of ischemia and scar on the therapeutic benefit of revascularization and drug treatment in patients undergoing MPI. Their study included total 13,969 patients who underwent exercise or adenosine stress SPECT MPI. Of all included patients, 1226 of them underwent revascularization. The association between post-MPI treatment and survival was determined by early revascularization, the degree of myocardium ischemia, and prior CAD. Increasing amount of myocardium ischemia was associated with lower hazard ratios using early revascularization treatment, without prior CAD. Compared with drug treatment, patients who received the early revascularization resulted in a better disease outcome. The early revascularization is shown to improve the outcome and prolong the survival in patients with substantial inducible myocardium ischemia confirmed by MPI. Drug treatment was preferred for the patients without obvious inducible myocardium ischemia based on the result of MPI. Current guidelines recommend the use of myocardium ischemia evaluation in stable patients prior to the revascularization and recommend medical therapy in overt CAD patients without significant myocardial ischemia. The severity and extent of myocardial ischemia can serve as useful guides for clinicians to make clinical decisions between revascularization and medical therapy. Another retrospective study [28] using SPECT MPI has shown that patients with moderate or severe myocardial ischemia also benefit from receiving the treatment of revascularization. Figure 18.14 demonstrates the results of MPI before and after percutaneous coronary stents implantation.

Restenosis is the major problem of PCI, and disease progressed at untreated sites occurring at a rate of approximately 7% per year. Restenosis usually occurs within 3–9 months after PCI, and incidence of restenosis after PCI without stenting ranges between 20 and 65%. CAG is the "gold standard" for exterminating restenosis, but as an invasive imaging method, the clinical application of CAG is limited in patients following PCI. Chest pain symptoms and exercise electrocardiography (ECG) testing have limited clinical role for evaluating the efficacy of PCI and detecting restenosis. Chest pain following PCI is a poor indicator of restenosis, as asymptomatic restenosis occurs in 18–59% of patients after PCI and in 30–58% of patients after stenting [29]. Exercise testing (ET) is a widely used method in assessing cardiovascular conditions after using therapeutic interventions such as PCI. Symptoms and functional capacity of the patient obtained from ET may provide useful information after PCI procedure. However, two meta-analyses [30, 31] showed that ET had a poor diagnostic performance for myocardial ischemia with a sensitivity of 46% and a specificity of 77%. The

Table 18.8 Diagnostic accuracy of imaging methods for patients presenting with chest pain and without troponin increase

Methods	Sensitivity (95% CI)	Specificity (95% CI)	LR+ (95% CI)	LR− (95% CI)
CCT	0.93 (0.81–0.98)	0.9 (0.93–0.94)	9.4 (5.2–16.5)	0.1 (0.02–0.2)
CCS	0.84 (0.81–0.92)	0.77 (0.66–0.95)	3.75 (2.8–5.2)	0.2 (0.1–0.6)
MPI	0.85 (0.77–0.91)	0.92 (0.83–0.96)	10.48 (5.32–20.6)	0.19 (0.01–0.35)
Stress echo	0.75 (0.59–0.89)	0.96 (0.91–0.98)	18.68 (8.3–42.1)	0.25 (0.14–0.46)

CCS coronary calcium score, *CCT* coronary computed tomography, *CI* confidence interval, *LR−* negative likelihood ratio, *LR+* positive likelihood ratio, *MPI* myocardial perfusion imaging

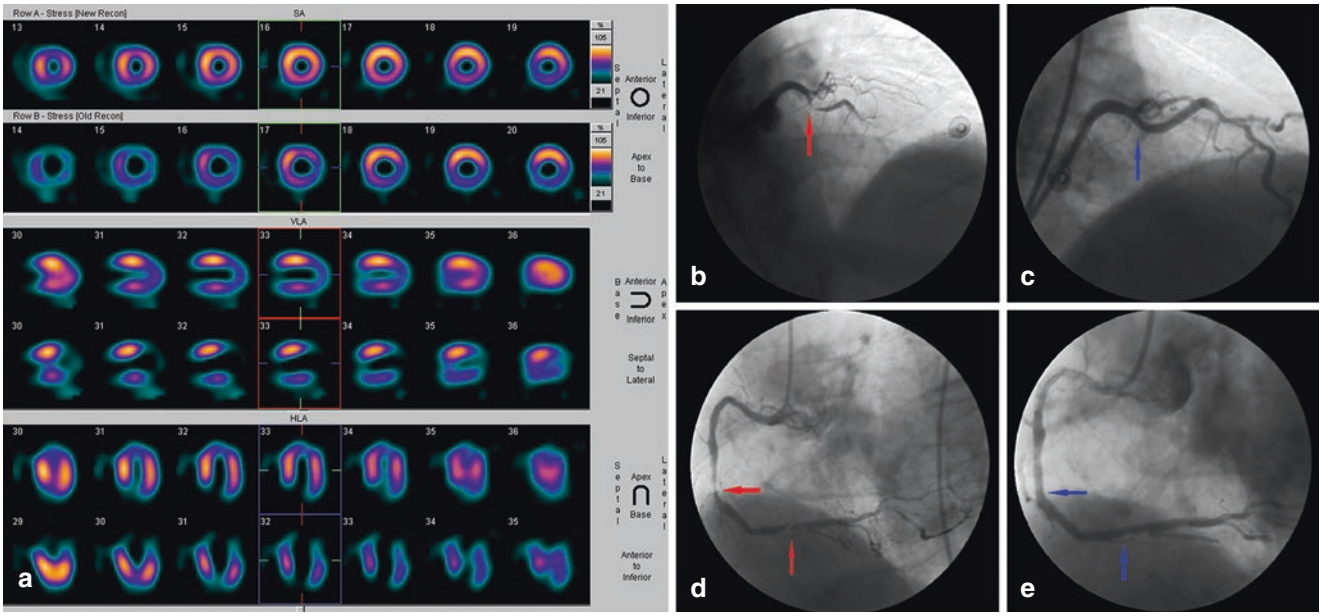

Fig. 18.14 A 79-year-old male, myocardial blood flow perfusion of stress imaging. (**a**) Improves significantly after PCI (after PCI (row 1, 3, 5); before PCI (row 2, 4, 6)). CAG shows proximal 99% stenosis in LAD (**b**, arrow), middle 85% stenosis, and distal 95% stenosis in RCA (**d**, arrows) before revascularization. Coronary artery blood flow recovery after three stents implanted in narrowings of LAD and RCA (**c**, **e**)

use of stress nuclear imaging significantly increased the sensitivity and specificity to 87% and 78%, respectively, while the use of stress echocardiography increased the sensitivity to 63% and the specificity to 87%. Many studies have confirmed the high sensitivity and specificity of MPI in detecting restenosis after PCI. Georgoulias et al. [32] investigated the diagnostic performance of ^{99m}Tc-tetrofosmin MPI in detecting restenosis. The sensitivity, specificity, positive predictive, and negative predictive values were 81.3%, 88%, 81.3%, and 88%, respectively. Diagnostic value of MPI in predicting restenosis after PCI has also been studied. Caner et al. [33] found that the sensitivity, specificity, accuracy, positive predictive, and negative predictive value were 76%, 79%, 77%, 66%, and 86%, respectively. MPI is also used for the detection of in-stent stenosis. Previous study [34] has showed that the mean sensitivity, specificity, positive, and negative predictive values and accuracy of MPI were 95%, 73%, 88%, 89%, and 88%, respectively. SPECT MPI has high sensitivity and specificity in the detection of restenosis after PCI. In patients with typical angina, the sensitivity and specificity were 84% and 80%, respectively. While in patients with atypical chest pain, the corresponding sensitivity and specificity were 70% and 90%, respectively [35].

CABG is a treatment method that frequently performed for the revascularization and management of CAD. Significant multivessel stenosis is a general indication of CABG. At 10 years after CABG, saphenous vein graft (SVG) occlusion rates have been reported to range from 41 to 50%, while symptom of chest pain is not an accurate indicator for detecting graft occlusion. Status of myocardial ischemia has a key role for therapeutic decision-making and outcome evaluation after CABG. Radionuclide imaging method has been recommended to be applied in the follow-up strategy in asymptomatic patients ≥5 years after CABG. Figure 18.15 showed the result of MPI in patient with coronary restenosis after stent implantation.

Studies have demonstrated that the extent of the perfusion abnormality on MPI images is related to the risk of cardiac death and nonfatal myocardial infarction, even in asymptomatic patients. Infarct size and ischemia showed on MPI are important predictors of myocardial infarction and cardiac death. MPI can provide incremental information over clinical and stress data. Shaw et al. [36] investigated the impact of MPI on prognosis and therapeutic risk in a total of 1505 CAD patients after CABG. The result showed that MPI performed 1 year after the CABG provided important information regarding the extent of residual ischemia. MPI can also provide important information regarding stress abnormalities and scarred myocardium, which could be used as effective predictors of long-term outcome. More extensive and severe stress myocardial perfusion abnormalities showed on the 1-year MPI images were associated with higher 5-year rates of death, cardiac death, or MI rates. MPI variables were significantly associated with an increased hazard of cardiac death or MI. Recently, phase analysis using gated SPECT MPI is a tool used for the assessment of left ventricular (LV) dyssynchrony. Park et al. [37] found that 30 of 45 patients showed LV dyssynchrony based on the phase analysis 3 months after CABG. However, 25 out of 45 patients were also found with reverse remodeling 1 year after

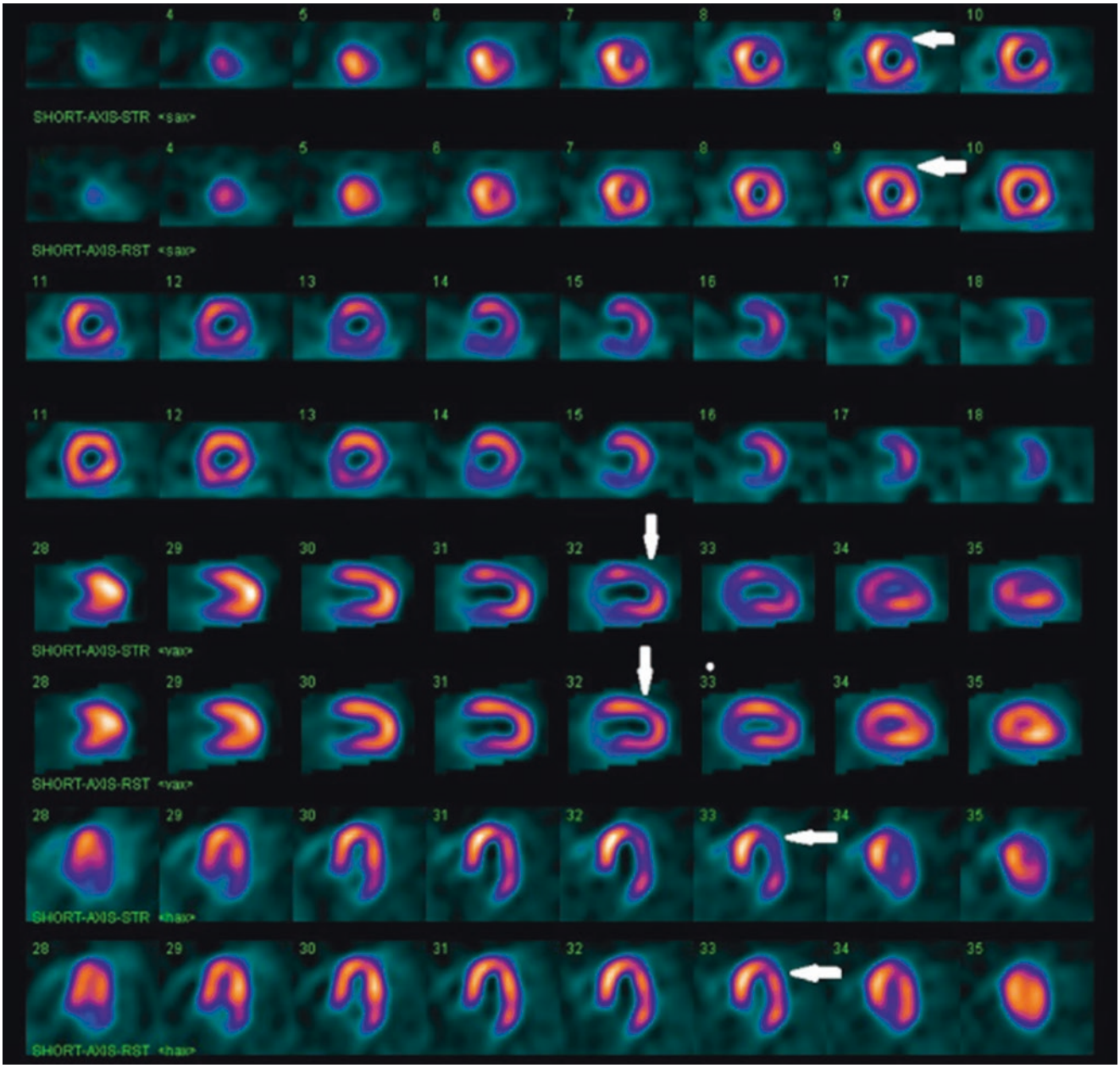

Fig. 18.15 A 53-year-old male with stent implantation in LAD and LCX 1 month ago. Stress (row 1, 3, 5, 7)-rest (row 2, 4, 6, 8) image of MPI shows reversible myocardial ischemia in anterior wall and lateral wall of LV (arrows). Restenosis in-stent are confirmed by CAG

CABG. Among the patients with reverse remodeling, 19 patients had LV dyssynchrony 3 months after CABG. The study indicated phase analysis may reflect late reverse remodeling and potential of further functional improvement after CABG.

18.3.5.5 Intermediate Lesions

Coronary angiography (CAG) is the gold standard for the evaluation of coronary artery stenosis. However, CAG only provides anatomical and morphologic information of coronary lesions. In patients with intermediate lesions (diameter of stenosis 40–70%), the CAG assessment is usually straightforward. CAG cannot reflect the functional significance of intermediate lesion accuracy. Extent and severity of myocardial ischemia obtained from MPI are highly related with outcome and decision-making in CAD patients. A prospective study [38] evaluated the functional significance of intermediate coronary narrowings (40–70% diameter stenosis) for clinical decision-making and risk stratification. The result of the study showed reversible perfusion defects were presented in the area of the intermediate lesion in 30 (16%) patients. Percutaneous transluminal coronary angioplasty (PTCA) of

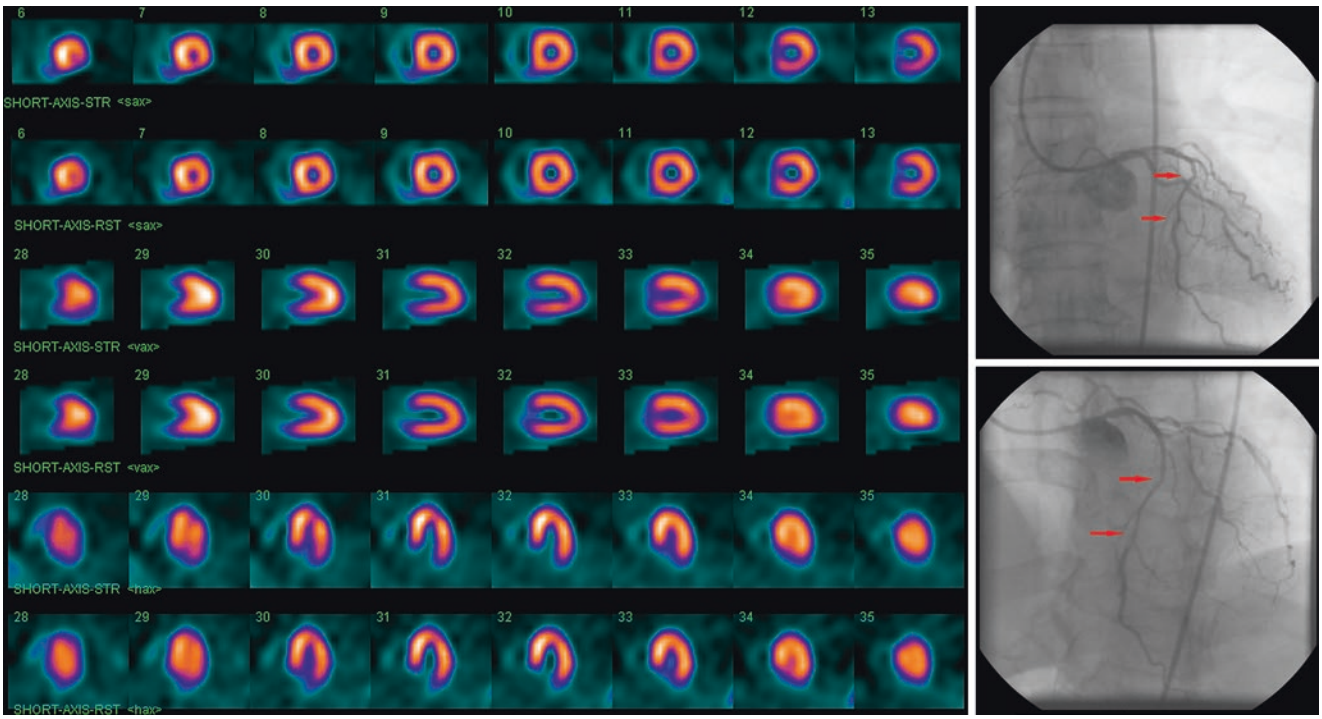

Fig. 18.16 A 65-year-old female with symptom of chest pain. Image of stress-rest myocardial perfusion imaging (**left**) is negative; image of coronary angiography (**right**) shows 60% diameter stenosis in LAD (arrows)

the intermediate lesion was deferred in 182 patients. During 1 year of follow-up, 19 hard heart events occurred (3 myocardial infarctions, 16 revascularizations). The study indicated the value of SPECT MPI for predictive outcome and risk stratification in patients with intermediate lesions. However, the study also found that SPECT MPI is limited for clinical decision-making about intermediate lesions in patients with multivessel CAD. In patients with intermediate lesions, if the result of MPI is negative, the risk of hard heart events is low, and drug treatment may be more suitable than revascularization. The decision-making based on the results of MPI does not adversely affect the prognosis. So MPI can do help to avoid unnecessary cardiac catheterization and CABG, reduce patient discomfort, and save costs. Figure 18.16 showed images of MPI in a patient with intermediate coronary stenosis.

18.4 Radionuclide Cardiac Blood Pool Imaging

Radionuclide cardiac blood pool imaging is also known as radionuclide angiocardiography (RNA). It can be used for evaluating cardiac performance. The commonly used methods involve first-pass radionuclide angiocardiogram (FPRNA) and equilibrium radionuclide angiocardiogram (ERNA).

18.4.1 First-Pass Radionuclide Angiocardiogram (FPRNA)

FPRNA was the first radionuclide technique applied to the study of cardiac physiology. The initial reports of Blumgart and Weiss appeared in 1927. At present, it is performed less frequently than equilibrium radionuclide angiocardiogram (ERNA). However, with the use of technetium-labeled myocardial perfusion agents, FPRNA can evaluate ventricular function at the time of injection of the radionuclide agent before subsequent perfusion imaging.

18.4.1.1 Principle and Radiopharmaceuticals

After injection of radiopharmaceutical with "bolus" in vein, agent passes superior vena cava, right atrium, right ventricle, pulmonary artery, lung, left atrium, left ventricle, aorta, and systemic circulation in turn. Using gamma camera records the whole passage procedure. Time-radioactivity curve is generated by region of interest (ROI) method. Temporal and anatomical separation of radioactivity within each ventricle should be observed during the initial passage. So it is possible to analyze right and left ventricular function independently during this brief transit. Regional function of each ventricle can also be assessed from the generated outlines of ventricles.

^{99m}Tc-labeled radiopharmaceuticals are used for first-pass studies; for the most part, in the past technetium pertechne-

tate or technetium complexed to either diethylenetriaminepentaacetic acid (DTPA) or sulfur colloid was used. The common used tracer is ^{99m}Tc-DTPA, and it is excreted quickly from the kidneys. Rest and stress imaging can be performed in 1 day. For example, ^{99m}Tc-DTPA (740 MBq) is injected at rest; after 20 min ^{99m}Tc-DTPA (740–1110 MBq) is injected at stress again.

18.4.1.2 Protocol and Images Interpretation

Supine position is usually adopted during imaging acquisition; sitting position is also accepted in some special conditions. The acquisition field should cover the atriums, ventricles, lungs, ascending aorta, descending aorta, and abdominal aorta. For the functional evaluation of right ventricle, images of RAO are preferred. Images of anterior view are more suitable for estimating the left ventricle function. The requirement of the injection technique is extremely high for insuring the quality of "bolus." The antecubital and the jugular venous are often selected as the injection sites. Images of 8–10 cardiac cycles are obtained and analyzed.

The FPRAN study is computer processed in frame mode. Regions of interest (ROI) are selected over either the left or right ventricle. Only when the initial bolus passes through the specific chamber of ventricle or atrium, radioactivity is analyzed. This temporal segregation of radioactivity compensates for the potential problem of overlapping regions of interest. Finally, time-activity curve is constructed. Global and regional left ventricular performance can be assessed. Right ventricular function can also be assessed by FPRNA. Cine movie shows regional wall motion of ventricles. Based on time-activity curve, several parameters can be calculated, which involve volume of end-diastolic (ED) and volume of end-systolic (ES). Ejection fraction (EF) is calculated as below (Eq. 18.1).

$$\mathrm{EF} = \frac{\text{counts of ED} - \text{counts of ES}}{\text{counts of ED}} \qquad (18.1)$$

18.4.1.3 Clinical Applications

Applications of FPRNA involve assessment of the right and left ventricles, diastolic as well as systolic function, regional or global performance, ventricular volume, and adaptations for treatment monitoring. Although the radionuclide approach for the evaluation of ventricular function has been challenged by Doppler echocardiography, the former still play a role in the quantitative assessment of cardiac performance.

FPRNA can be used to detect and quantify intracardiac shunts. A ROI is selected over the lung field. A pulmonary time-activity curve from the region is analyzed. Normally, a sharp rise and subsequent falloff of radioactivity are observed when the bolus enters and leaves the pulmonary vasculature. In the presence of a significant left-to-right shunt, persistent radioactivity remains in the lungs, and washout is relatively slow. The degree of shunting correlates extremely well with oximetry measurement. In the presence of right-to-left shunt, early appearance of activity in the aorta is typical appearance. At present, this approach has largely been replaced by Doppler echocardiography.

Diastolic and systolic function of the ventricles can be evaluated from either FPRNA or ERNA study, although the latter has been more frequently used. These indexes are relevant to diagnosis or outcome evaluation in patients with CAD, heart failure, or cardiomyopathy. ED and ES information can do help to diagnose and differential diagnose hypertrophic cardiomyopathy and dilated cardiomyopathy. EF is the most important factor for predicting outcome in CAD patients.

FPRNA is used to diagnose and differential diagnose CAD. The information come from FPRNA and involve wall motion and ventricular volume, and EF can be used for CAD diagnosis. However, with the development of MPI, the application of FPRNA for CAD is rare.

18.4.2 Equilibrium Radionuclide Angiocardiogram (ERNA)

Compared with FPRNA, the advantages of ERNA are better repeatability and higher accuracy. Especially in patients with myocardial infarction, ventricular hypertrophy, or dilation, these lead to volume and sharp of ventricle change.

18.4.2.1 Principle and Tracers

The ERNA uses ECG signal (R-wave) as "trigger" to start the acquisition of imaging data and the information of volume of the cardiac cycle, and the ECG signal is regarded as the "gate." If the R-R interval is within a certain range, acquisition procedure is started, and the whole cardiac cycle data is obtained. Usually, Three hundred to 400 cardiac cycles are performed to ensure adequate radioactivity counts for statistically meaningful analysis. This acquisition technique is also called multiple gated acquisitions (MUGA). Cine movie generated from acquisition quantity data is displayed in an endless-loop format. Visual interpretation and analysis could provide additional information.

^{99m}Tc is usually used for the ERNA labeling. ^{99m}Tc labels with the patient's own red blood cells in vitro. Labeling reaction procedure is facilitated by the unlabeled stannous pyrophosphate. Serial studies can be performed for 4–6 h after the labeling, and the duration of observation can be extended if necessary.

18.4.2.2 Protocol and Images Interpretation

About 15 min after injection of tracer, images of anterior (ANT) view, left anterior oblique (LAO) view, left lateral (LL) view, and right anterior oblique (RAO) view are acquired for observing anatomical structure of the heart using gamma camera. Data from the 45° LAO view are also used for qualitative analysis of global left ventricular function. In this view, overlap of the two ventricles is minimal. Acquire system is equipped with LEAP or LEHR collimator; matrix is 64 × 64 or 128 × 128. 300–400 cardiac circles are acquired. ERNA can be performed at rest status or stress status; bicycle stress method or pharmaceutical stress method is commonly used for stress.

Time-radioactivity curves of left and right ventricles can be constructed by ROI technique. Different parameters reflecting cardiac functions are calculated (Fig. 18.17). Of all these parameters, ventricular ejection fraction (VEF), regional ejection fraction (REF), peak ejection fraction (PER) and first-third ejection fraction (1/3 EF), cardiac output (CO), and stroke volume (SV) can reflect systolic function of ventricle. LVEF is the most important marker reflecting left ventricular systolic function. At rest status, LVEF >55% and RVEF >40% indicate that ventricular function is normal. The finding of a major fall (>5%) in the ejection fraction from rest to exercise carries with it a poor prognosis. Peak filling rate (PFR), first-third filling fraction (1/3 FF), time of peak filling rate (TPFR), and average filling rate (AFR) can reflect diastolic function of ventricles. These indexes play key role in patients with congestive heart failure (CHF). End-diastolic volume (EDV) and end-systolic volume (ESV) reflect volume stress of ventricles. Cine movies can be used for assessing globe and regional wall motion of ventricles. Furthermore, phase analysis, involving phase image, phase histogram, amplitude image and phase cine, can be used for evaluating regional systolic time, sequence, and strength of left and right ventricles. Figure 18.18 showed the result of phase analysis of ERNA in an aneurysm patient.

18.4.2.3 Indications and Contradictions

Indications

- *Coronary artery disease*
- Aneurysm
- *Valvular heart disease*
- Cardiomyopathy
- Congestive heart failure
- Cardiac conduction disease (left bundle branch block)
- Pulmonary heart disease
- Monitor of cardiac drug toxicity

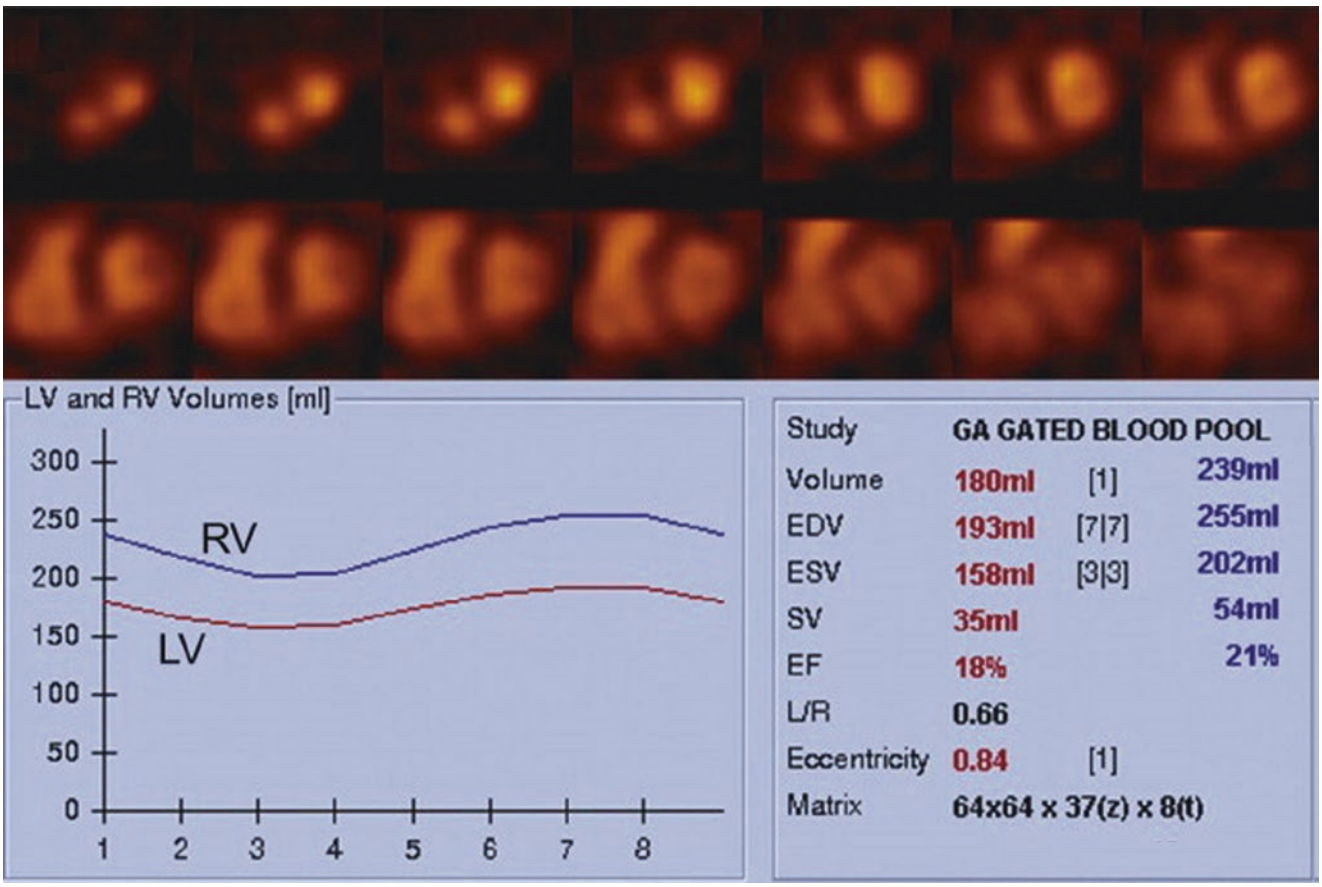

Fig. 18.17 Results of equilibrium radionuclide angiocardiogram. Volume indexes (involve EDV, ESV, SV, and EF) are obtained from time-activity curve

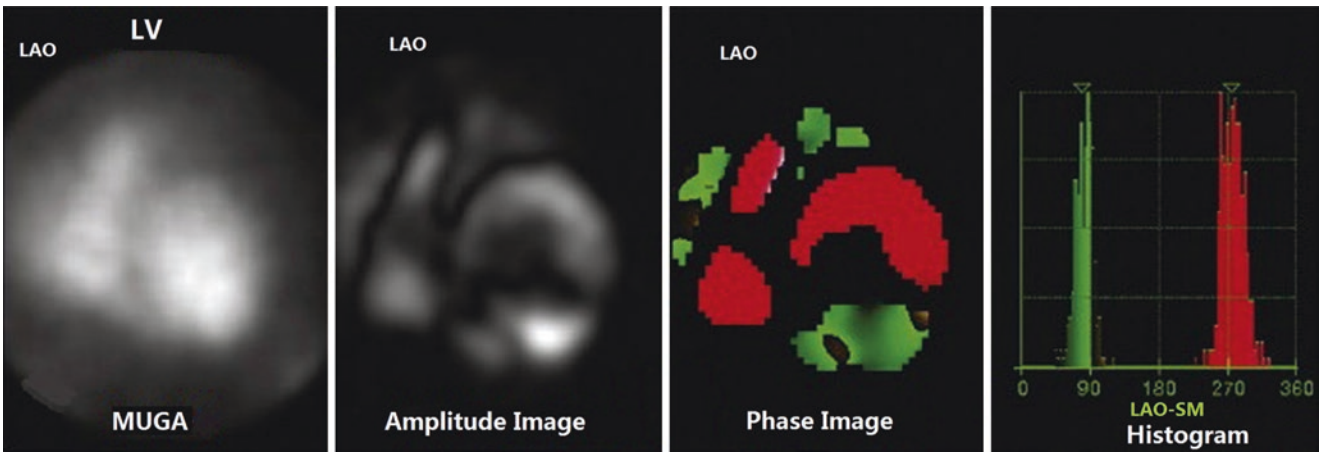

Fig. 18.18 Images of phase analysis of ERNA in an aneurysm patient

Contradictions
- Serious arrhythmia
- Unstable angina
- Decompensated period of congestive heart failure
- Severe hypertension (systolic blood pressure >200/120 mmHg)
- Acute myocardial infarction (within 48 h)

18.4.2.4 Clinical Applications

RNA is mainly used to evaluate cardiac function in clinic. The indexes such as the PFR and TPFR could be obtained from RNA and being widely used to assess diastolic function of ventricles. Diastolic function takes an important role for clinical evaluation of congestive heart failure (CHF) patients with normal systolic function and abnormal diastolic function. Decreased diastolic function is usually appeared in patient with restrictive cardiomyopathy, coronary artery disease, and left ventricular hypertrophy. Improvement of diastolic function obtained from ERNA indicates effective treatment (PCI or drug treatment) and a good prognosis, especially in patients with heart failure. In addition, it is important to notice that indexes of diastolic function are age-dependent.

The EF, especially LVEF, is an important factor in determining prognosis and survival. ERNA accurately reflects the results of EF and LVEF and helps the evaluation of disease prognosis. Studies have documented its prognostic value on the basis of global and regional ventricular function indexes, represented with EF and LVEF obtained from ERNA. LVEF increased by less than 5% or decreased under stress status when comparing with rest status is good diagnostic criteria of myocardial ischemia. The degree of EF reduction determined by ERNA acts as the most important prognostic factor in patients who have survived cardiac arrest performed outside of a hospital setting. In addition, ERNA is a useful tool for the identification of aneurysm of left ventricular. For patients with postinfarction, early recognition of left ventricular aneurysm using ERNA is shown with prognostic significance. Study has indicated, in patients with anterior wall infarction, the findings of left ventricular aneurysm obtained from ERNA provided additional prognostic value compared with using the left ventricular ejection fraction alone. In patients with acute myocardial infarction, performing ERNA at rest can provide valuable information in distinguishing a true aneurysm from a pseudoaneurysm and evaluating the disease outcome.

Evaluation of left ventricular function is key in patients with known or presumed CHF. RNA technique provides relevant systolic and diastolic information. Comparing with using systolic dysfunction alone, the combined use of the diastolic dysfunctional data resulted from RNA provided additional information for clinical decision-making. For valvular heart disease or conditions mimicking heart failure, the RNA study is useful for the disease diagnosis and differential diagnosis. Serial RNA studies provide reliable data for monitoring the treatment effects [39]. RNA studies can be used for identifying the causes of CHF. Results of RNA study indicated that CAD, hypertensive heart disease, cardiomyopathy, or valvular heart diseases are potential causes of CHF.

18.5 Myocardial Metabolic Imaging with ^{18}F-FDG

^{18}F-fluorodeoxyglucose (^{18}F-FDG) PET has a widely range of clinical applications in oncology, neurology, and cardiology. PET imaging using ^{18}F-FDG can assess the status of viable myocardium. PCI and CABG improve the abnormal blood flow perfusion and wall motion of ischemic myocardium. However, revascularization therapy is useless for necrosis myocardium. PET imaging with ^{18}F-FDG with myocardial perfusion imaging is the current gold standard for the assessment of myocardial viability.

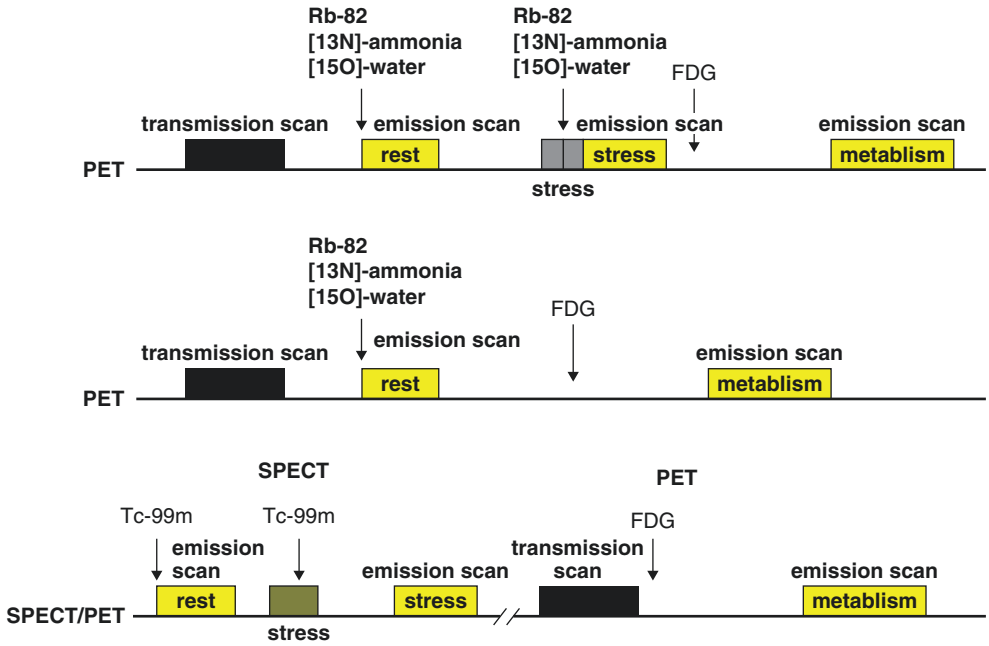

Fig. 18.19 Protocols of ^{18}F-FDG metabolic imaging combined with perfusion imaging for evaluation of myocardial viability

18.5.1 Principle and Radiopharmaceutical

In the fasting state, the major sources of energy of the normal myocardium derives from free fatty acid (FFAs). In the postprandial state, myocardium mainly utilizes glucose to meet its energy need via anaerobic glycolysis. ^{18}F-FDG is an analogue of glucose and crosses cell membrane by glucose transporter protein. After transporting into cells, ^{18}F-FDG is phosphorylated to ^{18}F-FDG-6-PO_4 by hexokinase and cannot undergo any further metabolism. So ^{18}F-FDG-6-PO_4 is essentially trapped within myocardial cells, accumulates, and becomes index of ongoing cellular metabolism.

18.5.2 Protocol and Images Interpretation

Before examination, patient is instructed to fast 6–12 h (preferred) or <6 h (suboptimal) and check the level of blood glucose. If fasting blood glucose <110 mg/dL (6.11 mmol/L) and no known diabetes, administer oral glucose load (typically 25–100 g), and monitor blood glucose. If fasting blood glucose <110–130 mg/dL (6.11–7.22 mmol/L) or known diabetes, administer regular insulin intravenously, and monitor blood glucose. The dose of ^{18}F-FDG is 185–370 MBq (5–10 mCi) for three-dimensional mode and 370–555 MBq (10–15 mCi) for two-dimensional mode. For nondiabetic patients, acquisition is performed 45–60 min after injection of ^{18}F-FDG. For diabetic patients, acquisition is performed 60–90 min after injection. Patients position is supine (arms-up preferred). Image acquisition duration ranges from 10 to 30 min depending on counting rate and dose. Attenuation correction is performed before or immediately after emission scan using radionuclide or CT transmission imaging. Filtered back projection or ordered-subset expectation maximization (iterative reconstruction) is used for reconstruction. Figure 18.19 shows the protocols of ^{18}F-FDG metabolic imaging combined with perfusion imaging.

For evaluation of myocardial viability, the protocol integrates rest myocardial perfusion imaging using PET or SPECT with myocardial glucose metabolism imaging. Blood flow perfusion reduction and FDG activity normal uptake, the partner is termed as perfusion-metabolism "mismatch" (Fig. 18.20), indicates viable myocardium. For reduced blood flow perfusion and reduced FDG activity, the partner is termed as perfusion-metabolism match (Fig. 18.21), which indicates nonviable myocardium (scar or fibrosis).

18.5.3 Clinical Applications

Ischemia leads to a consecutive myocardial for adaptive responses. Animal models have shown that resting contractile dysfunction is dependent on the physiological significance of the coronary artery stenosis. The severity of coronary artery stenosis determines the intrinsic molecular adaptations of the ischemic myocardium, and this course of adaptations may be partly responsible for the myocardial variable time and extent of reversibility of cardiac function after revascularization. Revascularization has the potential to restore and improve contractile function of viable dysfunctional myocardium. For example, myocardial hibernation develops in response to long-term ischemia or chronic coronary stenosis. Hibernating myocardium reduced regional resting blood flow to preserve myocardial viability and accompanied by regional dysfunction. Myocardial hibernation is reversible, which may require

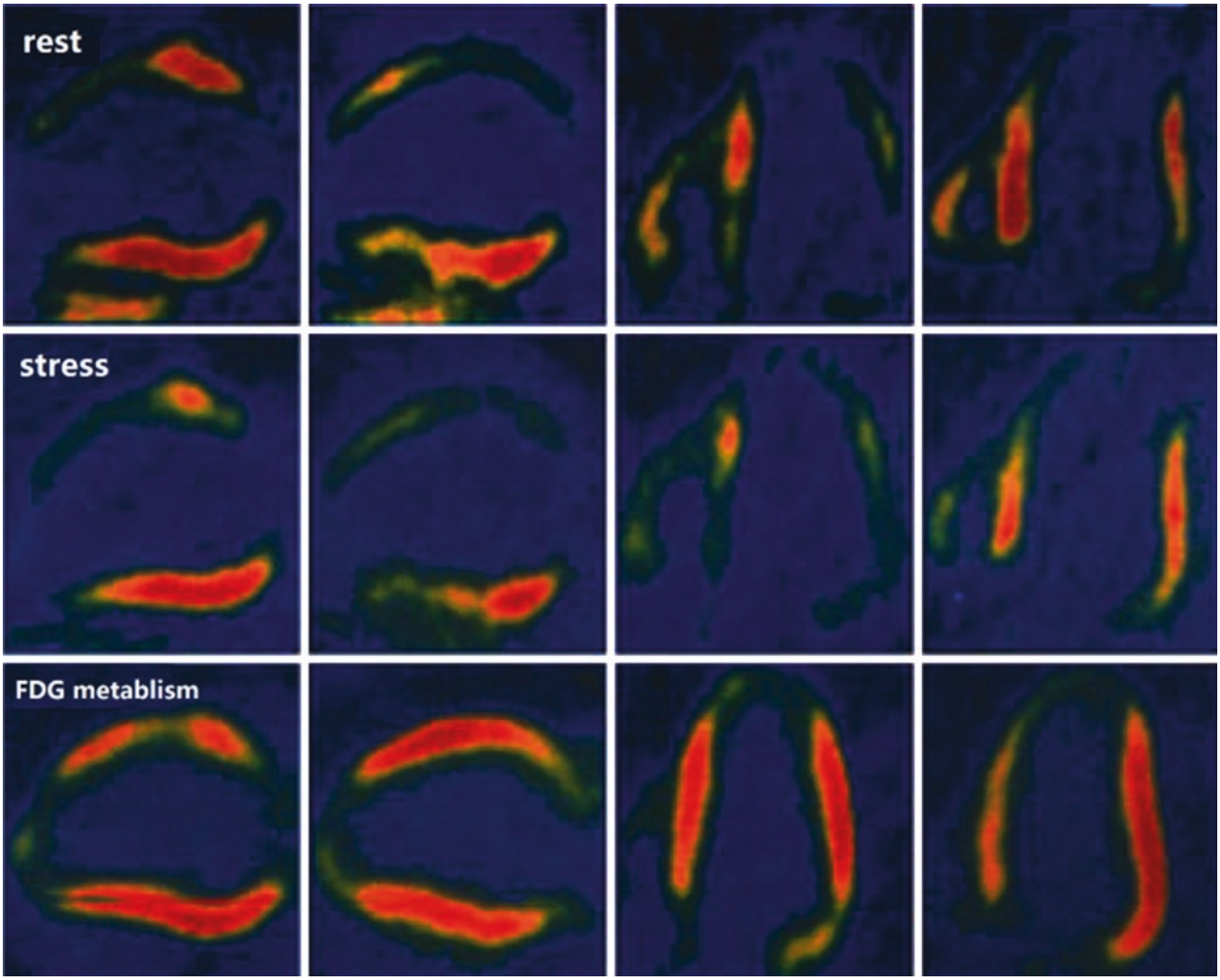

Fig. 18.20 Stress-rest perfusion imaging and ^{18}F-FDG metabolic imaging show perfusion-metabolism "mismatch"

several days to months to recover its function. Hibernating myocardium has important clinical value for prognosis assessment and evaluation of treatment effect after coronary flow recovery.

Marwick et al. [40] investigated the clinical role of viable myocardium assessed by FDG PET and perfusion imaging for predicting the recovery of regional contractile function after revascularization. Sixteen patients with previous infarction were studied before and after revascularization by ^{82}Rb PET perfusion imaging and FDG PET metabolic imaging. The results showed that wall motion and perfusion improve with revascularization of hibernating myocardium. For prediction of recovery of regional function [41], 24 studies (from 2001 to 2007, 756 patients included) used FDG PET to predict recovery of segmental contractile function. Pooled analysis of all studies showed a weighted mean sensitivity, specificity, positive predictive value (PPV), and negative predictive value (NPV) of 92%, 63%, 74%, and 87%, respectively. Magnetic resonance imaging (MRI) techniques are also used to assess myocardial viability. Resting MRI can be used to assess contractile function and wall motion. Dobutamine MRI can be used to assess contractile reserve. Contrast-enhanced MRI using gadolinium-based contrast agents can be used to detect the extent and transmurality of scar. Of all noninvasive imaging modalities, for example, FDG PET, MRI, echocardiography, and SPECT imaging with technetium-99m-labeled agents, FDG PET had the highest sensitivity, NPV, and PPV for the prediction of segmental recovery after revascularization.

For prediction of recovery of global contractile function, the pooled sensitivity, specificity, PPV, and NPV were 83%, 64%, 68%, and 80%, respectively [42]. The sensitivity for FDG PET was higher than the sensitivity for dobutamine echocardiography and no significant difference in the specificity, PPV, and NPV for FDG PET, dobutamine echocardiography, and SPECT perfusion imaging.

For prediction of improvement in heart failure symptoms and exercise capacity, studies [43] using FDG PET indicated

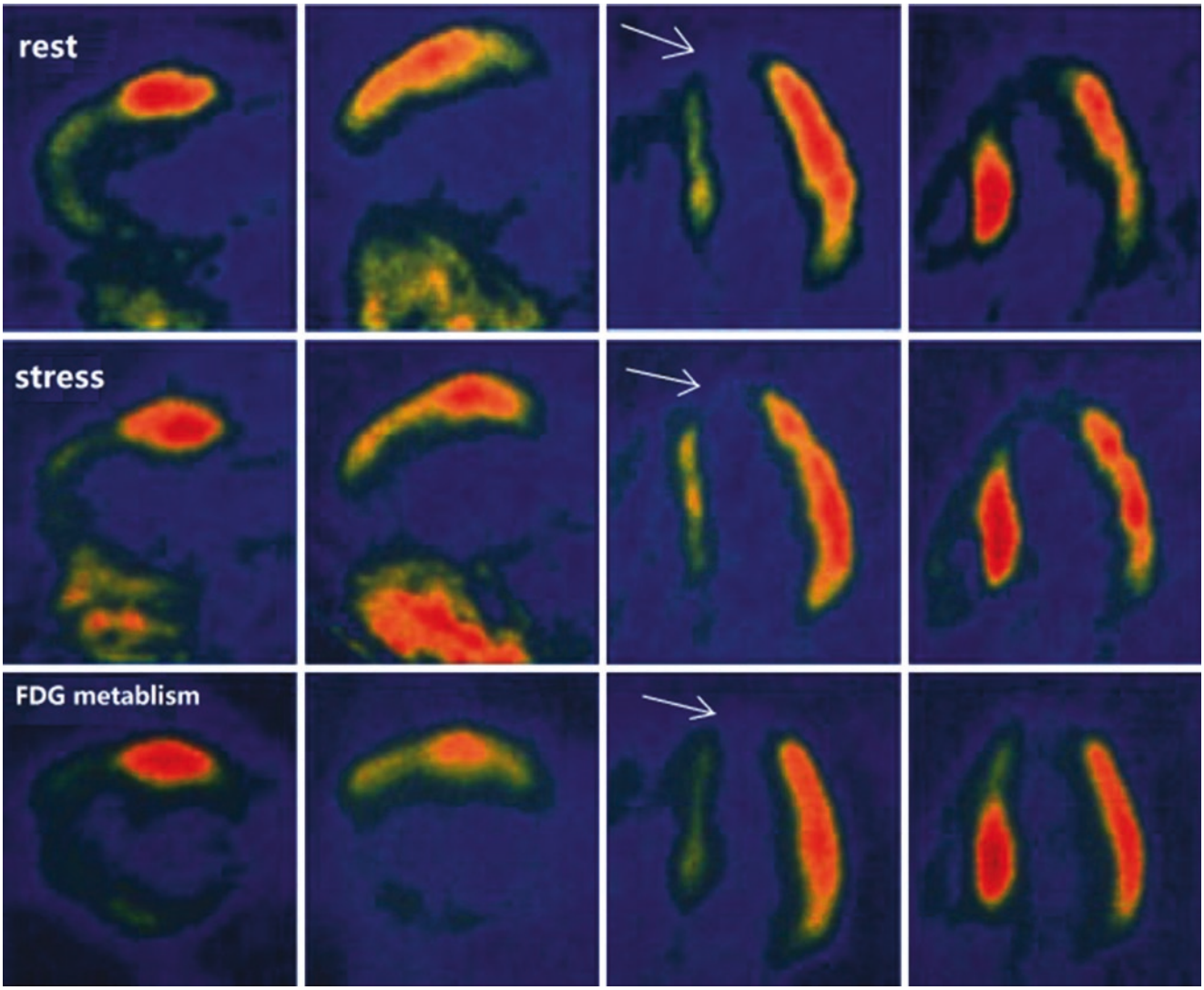

Fig. 18.21 Stress-rest perfusion imaging and ^{18}F-FDG metabolic imaging show perfusion-metabolism "match" (arrows)

that the mean exercise capacity (expressed in METS) was 4.4 before and 5.7 after revascularization in patients with viable myocardium and 5.1 before and 5.9 after revascularization without viable myocardium. For evaluation of prognosis, patients with viable myocardium confirmed by FDG PET who underwent revascularization had the best survival. The highest annualized mortality rate was observed in patients with viable myocardium who underwent medical therapy. Intermediate mortality rates were noted in patient without viable myocardium who underwent medical treatment or revascularization.

18.6 Cardiac Magnetic Resonance (CMR) Imaging

Cardiac magnetic resonance (CMR) imaging is emerging as a radiation-free imaging modality for assessing a variety of cardiac conditions. CMR imaging is considered a gold standard for assessment of cardiac mass, volume, and function. CMR imaging is also used for assessment of myocardial ischemia, myocardial scarring and viability. The clinical applications of CMR involve diagnosis of CAD, evaluation of myocardial viability, nonischemic dilated cardiomyopathy, hypertrophic cardiomyopathy, arrhythmogenic right ventricular cardiomyopathy, non-compaction cardiomyopathy, myocarditis, sarcoidosis, amyloidosis, cardiac iron overload, valvular heart disease, and evaluation of cardiac masses.

For detecting CAD, the CE-MARC study [44] (a prospective trail, a total of 235 women and 393 men included) compared the diagnostic performance of CMR imaging and SPECT imaging. The result showed that CMR had a sensitivity of 86%, specificity of 83%, PPV of 77%, and NPV of 91%. For CMR, the sensitivity in women and men was similar (88.7% versus 85.6%). For SPECT, the sensitivity was significantly lower in women than in men (50.9% versus 70.8%), but the specificities were similar (84.1% versus 81.3%; $P = 0.48$). The sensitivity in both female and male

groups was significantly higher with CMR than SPECT; however, the specificity was similar. Kato et al. [45] performed a national multicenter trial to assess CAD using magnetic resonance coronary angiography (MRCA). The sensitivity, specificity, PPV, NPV, and accuracy of MRCA according to a patient-based analysis in detecting stenosis ≥50% were 88%, 72%, 71%, 88%, and 79%, respectively. The result indicated that the MRCA can detect CAD with high sensitivity and moderate specificity.

Yoon et al. [46] investigated the clinical value of CMR for predicting cardiac events in patients with suspected CAD. 207 suspected CAD patients underwent non-contrast-enhanced free-breathing CMR with a 1.5-T MR system and 32-channel cardiac coils. During a median follow-up of 25 months, for severe events, annual event rate is significant stenosis between patients with significant stenosis (≥50% diameter reduction) and without significant stenosis (3.9% and 0%, respectively), as well as for all cardiac events (6.3% and 0.3%, respectively). Cox regression analysis showed that presence of significant stenosis on CMR was associated with a >20-fold hazard increase for all cardiac events. A meta-analysis [47] included 14 studies and 12,178 patients. Included studies used stress CMR to evaluate patients with known or suspected CAD. The NPV for nonfatal MI and cardiac death of normal CMR was 98.12% during a weighted mean follow-up of 25.3 months. The corresponding annualized event rate after a negative test was 1.03%. The result showed that stress CMR has a high NPV for adverse cardiac events.

For assessment of myocardial viability, CMR plays an important role in the clinical practice. Due to the high spatial resolution, MR has high imaging quality and is able to assess myocardial blood flow at rest in hibernating myocardium. The use of gadolinium as a contrast medium in MR allows detecting the blood flow perfusion, microvascular obstruction, and distinguishing between transmural and subendocardial necrosis. A meta-analysis [48] investigated the diagnostic accuracy of CMR assessing myocardial viability in patients with chronic LV dysfunction due to CAD. Twenty-four studies of CMR evaluating myocardial viability with 698 patients were included. For assessment of myocardial myocardium with delayed enhancement CMR, the weighted mean sensitivity, specificity, PPV, NPV, and accuracy were 95%, 51%, 69%, 90%, and 70%, respectively. For using dobutamine stress CMR, the mean weighted sensitivity, specificity, PPV, NPV, and accuracy were 81%, 91%, 93%, 75%, and 84%, respectively. For using end-diastolic wall thickness CMR, the mean weighted sensitivity, specificity, PPV, NPV, and accuracy were 96%, 38%, 71%, 85%, and 68% respectively. The results indicated that integrating different CMR methods may increase diagnostic accuracy for assessment of myocardial viability in patients being considered for revascularization. Kim et al. [49] performed a prospective study to identify reversible myocardial dysfunction using contrast-enhanced CMR. The study showed the percentage of the LV that was both dysfunctional and not hyperenhanced before revascularization was strongly related to the degree of improvement in the wall motion and EF after revascularization. Reversible myocardial dysfunction can be identified by contrast-enhanced CMR before coronary revascularization. Limitations of CMR, however, include its high cost, unsuitable for patients with implanted devices, and limited availability.

18.7 Cardiac Tumors

Cardiac tumors are divided into primary cardiac tumors and secondary tumors in the heart. Secondary tumors in the heart are significantly more common than primary tumors. Leukemias, melanomas, thyroid carcinomas, lung cancers, sarcomas, renal cell cancer, lymphomas, breast cancer, and malignant mesotheliomas are more common primary cancers. Primary cardiac tumors are extremely rare, with an estimated prevalence of 0.002–0.3% in autopsy reports. About three fourths of these tumors are benign. The benign cardiac tumors include myxomas, fibromas, rhabdomyomas, lipoma, fibroelastomas, and paragangliomas. The primary malignant cardiac tumors include sarcomas, mesotheliomas, and lymphoma. Patients with primary cardiac tumors may present with clinical symptoms that can simulate heart disease. Several imaging methods are used in the evaluation of cardiac and pericardiac tumor. Transthoracic echocardiography is widely available and is the first considered choice for diagnosis of intracardiac tumors. It is radiation-free and provides information about size, mobility, and location of the cardiac mass but limited information on lesion characterization [26]. CT offers a high spatial resolution and sufficient temporal resolution. However, CT cannot reflect functional significance of cardiac masses directly. The advantage of CMR is that CMR has ability to characterize tissue composition, provides excellent temporal and spatial resolution, and evaluates vascular structures and lymph nodes involvement. PET imaging offers an accurate evaluation of the metabolic activity of the tumors. ^{18}F-FDG PET/CT is widely employed for diagnosing and staging of various tumors. In addition, being a whole-body imaging method, ^{18}F-FDG PET/CT is useful for the detection of distant metastases which may be missed on other routine imaging modalities. However, the degree and extent of ^{18}F-FDG cardiac activity may be variable. Patients with myocardial ischemia and atherosclerotic plaques may have a focal increased FDG uptake. ^{18}F-FDG PET/CT has been used for characterization, staging, and restaging of cardiac tumors.

Rahbar et al. [50] investigated diagnostic value of ^{18}F-FDG PET/CT in patients with newly diagnosed cardiac tumors. Of 24 included patients, 7 patients were of benign cardiac tumors, and 17 patients were of malignant cardiac tumors. Malignancy was determined with a sensitivity of 100% and specificity of 86% (accuracy, 96%) with a cutoff

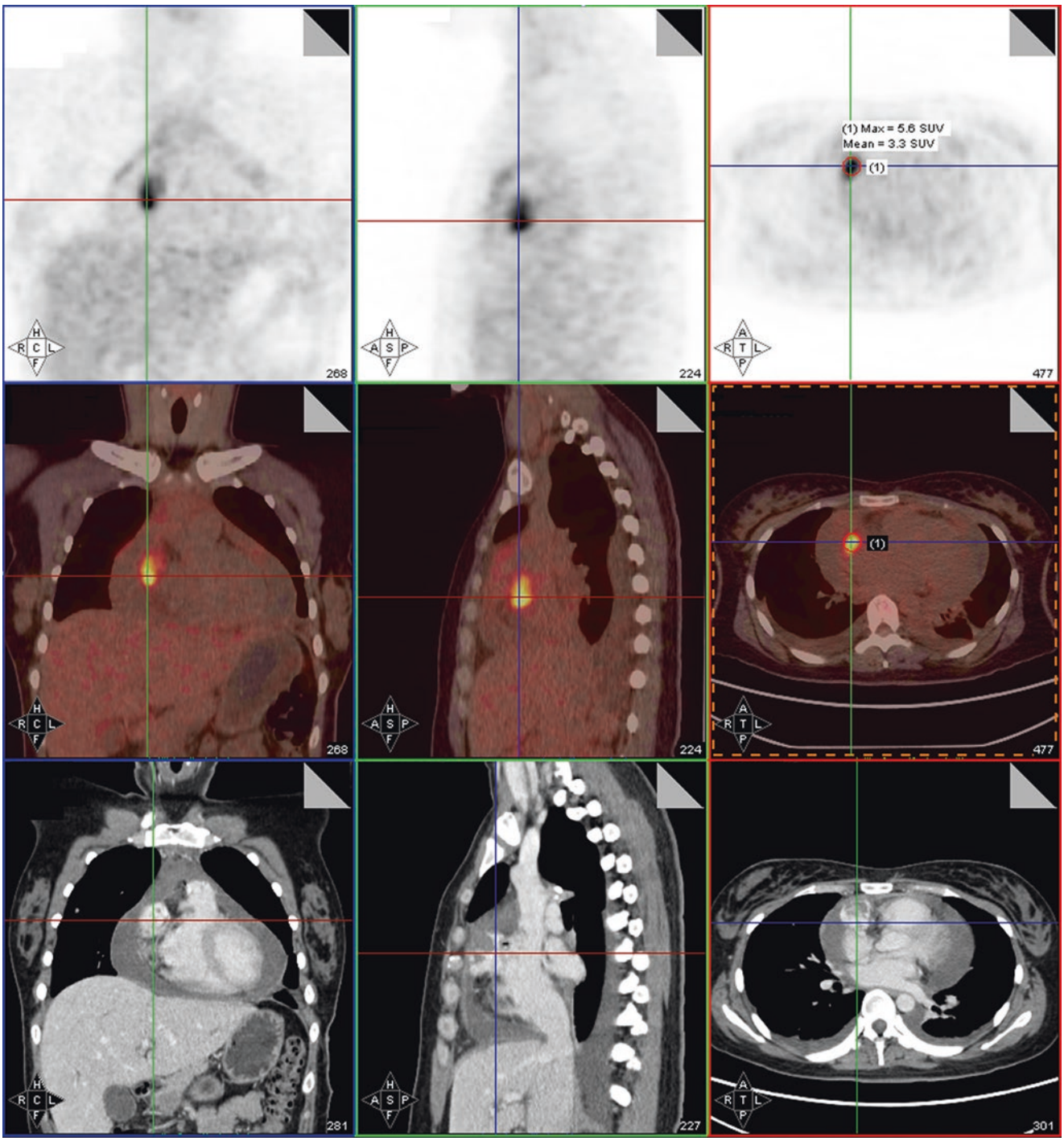

Fig. 18.22 A 45-year-old man with pathological confirmed angiosarcoma of the right atrium. ^{18}F-FDG PET/CT shows increased activity uptake with SUV_{max} of 5.6

SUV_{max} of 3.5. Morphologic imaging reached a sensitivity of 82% and a specificity of 86% (accuracy, 83%). In addition, extra-cardiac tumor manifestations were detected in four patients by whole-body ^{18}F-FDG PET/CT. Figure 18.22 shows the images of ^{18}F-FDG PET/CT of a patient with angiosarcoma.

References

1. Go AS, Mozaffarian D, Roger VL et al (2013) Heart disease and stroke statistics—2013 update: a report from the American Heart Association. Circulation 127:e6–e245
2. Chen HZ (2016) Practice of cardiology. Shanghai Scientific & Technical Publishers, Shanghai

3. De Lorenzo A (2009) The evolving roles of nuclear cardiology. Curr Cardiol Rev 5:52–55
4. Chinese Society of Cardiology, Chinese Medical Association; Editorial Board, Chinese Journal of Cardiology (2007) Guideline for diagnosis and treatment of patients with chronic stable angina. Zhonghua Xin Xue Guan Bing Za Zhi 35:195–206
5. Maublant JC, Gachon P, Moins N (1988) Hexakis (2-methoxy isobutylisonitrile) technetium-99m and thallium-201 chloride: uptake and release in cultured myocardial cells. J Nucl Med 29:48–54
6. Johnson LL (1994) Myocardial perfusion imaging with technetium-99m-teboroxime. J Nucl Med 35:689–692
7. Brown KA (1994) The role of stress redistribution thallium-201 myocardial perfusion imaging in evaluating coronary artery disease and perioperative risk. J Nucl Med 35:703–706
8. Moralidis E, Spyridonidis T, Arsos G et al (2007) Identification of advanced coronary artery disease with exercise myocardial perfusion imaging: the clinical value of a novel approach for assessing lung thallium-201 uptake. Eur J Nucl Med Mol Imaging 34:573–583
9. Friedman J, Van Train K, Maddahi J (1989) Upward creep of the heart: a frequent source of false-positive reversible defects during thallium-201 stress-redistribution SPECT. J Nucl Med 30:1718–1722
10. Wackers FJT (2003) Nuclear cardiology: the basics—how to set up and maintain a laboratory, 2nd edn. Humana Press, Totowa
11. Germano G, Berman DS (2006) Clinical gated cardiac SPECT, 2nd edn. Blackwell Futura Publishing, New York
12. Cerqueira MD, Allman KC, Ficaro EP et al (2010) Recommendations for reducing radiation exposure in myocardial perfusion imaging. J Nucl Cardiol 17:709–718
13. Huang G, Shi HC (2011) Nuclear cardiology. Shanghai Scientific & Technical Publishers, Shanghai
14. Chen YD, Fang WY, Chen JY (2018) Chinese expert consensus on the non-invasive imaging examination pathways of stable coronary artery disease. J Geriatr Cardiol 15:30–40
15. Underwood SR, Anagnostopoulos C, Cerqueira M et al (2004) Myocardial perfusion scintigraphy: the evidence. Eur J Nucl Med Mol Imaging 31:261–291
16. Taillefer R, DePuey EG, Udelson JE et al (1997) Comparative diagnostic accuracy of Tl-201 and Tc-99m sestamibi SPECT imaging (perfusion and ECG-gated SPECT) in detecting coronary artery disease in women. J Am Coll Cardiol 29:69–77
17. Smanio PE, Watson DD, Segalla DL et al (1997) Value of gating of technetium-99m sestamibi single-photon emission computed tomographic imaging. J Am Coll Cardiol 30:1687–1692
18. Hachamovitch R, Hayes S, Friedman JD et al (2003) Determinants of risk and its temporal variation in patients with normal stress myocardial perfusion scans: what is the warranty period of a normal scan? J Am Coll Cardiol 41:1329–1340
19. Abidov A, Hachamovitch R, Hayes SW et al (2003) Prognostic impact of hemodynamic response to adenosine in patients older than age 55 years undergoing vasodilator stress myocardial perfusion study. Circulation 107:2894–2899
20. Yao Z, Zhu H, Li W et al (2017) Adenosine triphosphate stress myocardial perfusion imaging for risk stratification of patients aged 70 years and older with suspected coronary artery disease. J Nucl Cardiol 24:429–433
21. Hachamovitch R, Hayes SW, Friedman JD et al (2003) Comparison of the short-term survival benefit associated with revascularization compared with medical therapy in patients with no prior coronary artery disease undergoing stress myocardial perfusion single photon emission computed tomography. Circulation 107:2900–2907
22. Iannaccone M, Gili S, De Filippo O et al (2018) Diagnostic accuracy of functional, imaging and biochemical tests for patients presenting with chest pain to the emergency department: a systematic review and meta-analysis. Eur Heart J Acute Cardiovasc Care. https://doi.org/10.1177/2048872617754275.
23. Sechtem U, Achenbach S, Friedrich M et al (2012) Non-invasive imaging in acute chest pain syndromes. Eur Heart J Cardiovasc Imaging 13:69–78
24. Udelson JE, Spiegler EJ (2001) Emergency department perfusion imaging for suspected coronary artery disease: the ERASE chest pain trial. Md Med (Suppl):90–94
25. Fernandez-Friera L, Garcia-Alvarez A, Bagheriannejad-Esfahani F et al (2011) Diagnostic value of coronary artery calcium scoring in low-intermediate risk patients evaluated in the emergency department for acute coronary syndrome. Am J Cardiol 107:17–23
26. Douglas PS, Garcia MJ, Haines DE et al (2011) ACCF/ASE/AHA/ASNC/HFSA/HRS/SCAI/SCCM/SCCT/SCMR 2011 appropriate use criteria for echocardiography. A report of the American College of Cardiology Foundation Appropriate Use Criteria Task Force, American Society of Echocardiography, American Heart Association, American Society of Nuclear Cardiology, Heart Failure Society of America, Heart Rhythm Society, Society for Cardiovascular Angiography and Interventions, Society of Critical Care Medicine, Society of Cardiovascular Computed Tomography, and Society for Cardiovascular Magnetic Resonance Endorsed by the American College of Chest Physicians. J Am Coll Cardiol 57:1126–1166
27. Hachamovitch R, Rozanski A, Shaw LJ et al (2011) Impact of ischaemia and scar on the therapeutic benefit derived from myocardial revascularization vs. medical therapy among patients undergoing stress-rest myocardial perfusion scintigraphy. Eur Heart J 32:1012–1024
28. Cremer P, Hachamovitch R, Tamarappoo B et al (2014) Clinical decision making with myocardial perfusion imaging in patients with known or suspected coronary artery disease. Semin Nucl Med 44:320–329
29. Ruygrok PN, Webster MW, de Valk V et al (2001) Clinical and angiographic factors associated with asymptomatic restenosis after percutaneous coronary intervention. Circulation 104:2289–2294
30. Garzon PP, Eisenberg MJ et al (2001) Functional testing for the detection of restenosis after percutaneous transluminal coronary angioplasty: a meta-analysis. Can J Cardiol 17:41–48
31. Dori G, Denekamp Y, Fishman S et al (2003) Exercise stress testing, myocardial perfusion imaging and stress echocardiography for detecting restenosis after successful percutaneous transluminal coronary angioplasty: a review of performance. J Intern Med 253:253–262
32. Georgoulias P, Demakopoulos N, Kontos A et al (1998) Tc-99m tetrofosmin myocardial perfusion imaging before and six months after percutaneous transluminal coronary angioplasty. Clin Nucl Med 23:678–682
33. Caner B, Oto A, Ovunc K et al (1998) Prediction of restenosis after successful percutaneous coronary angioplasty by dobutamine thallium-201 scintigraphy. Int J Cardiol 66:175–181
34. Milavetz JJ, Miller TD, Hodge DO et al (1998) Accuracy of single-photon emission computed tomography myocardial perfusion imaging in patients with stents in native coronary arteries. Am J Cardiol 82:857–861
35. Georgoulias P, Valotassiou V, Tsougos I et al (2010) Myocardial perfusion SPECT imaging in patients after percutaneous coronary intervention. Curr Cardiol Rev 6:98–103
36. Shaw LJ, Cerqueira MD, Brooks MM et al (2012) Impact of left ventricular function and the extent of ischemia and scar by stress myocardial perfusion imaging on prognosis and therapeutic risk reduction in diabetic patients with coronary artery disease: results from the bypass angioplasty revascularization investigation 2 diabetes (BARI 2D) trial. J Nucl Cardiol 19:658–669
37. Park S, Cheon GJ, Paeng JC et al (2016) Phase analysis of gated myocardial perfusion single-photon emission computed tomogra-

phy after coronary artery bypass graft surgery: reflection of late reverse remodeling in patients with patent grafts after coronary artery bypass graft surgery. Nucl Med Commun 37:1139–1147
38. Miller DD et al (2002) Coronary flow studies for risk stratification in multivessel disease. A physiologic bridge too far? J Am Coll Cardiol 39:859–863
39. Mitani I, Jain D, Joska TM et al (2003) Doxorubicin cardiotoxicity: prevention of congestive heart failure with serial cardiac function monitoring with equilibrium radionuclide angiocardiography in the current era. J Nucl Cardiol 10:132–139
40. Marwick TH, MacIntyre WJ, Lafont A et al (1992) Metabolic responses of hibernating and infarcted myocardium to revascularization. A follow-up study of regional perfusion, function, and metabolism. Circulation 85:1347–1353
41. Schinkel AF, Bax JJ, Poldermans D et al (2007) Hibernating myocardium: diagnosis and patient outcomes. Curr Probl Cardiol 32:375–410
42. Slart RH, Bax JJ, van Veldhuisen DJ et al (2006) Prediction of functional recovery after revascularization in patients with chronic ischaemic left ventricular dysfunction: head-to-head comparison between 99mTc-sestamibi/18F-FDG DISA SPECT and 13N-ammonia/18F-FDG PET. Eur J Nucl Med Mol Imaging 33:716–723
43. Marwick TH, Zuchowski C, Lauer MS et al (1999) Functional status and quality of life in patients with heart failure undergoing coronary bypass surgery after assessment of myocardial viability. J Am Coll Cardiol 33:750–758
44. Greenwood JP, Motwani M, Maredia N et al (2014) Comparison of cardiovascular magnetic resonance and single-photon emission computed tomography in women with suspected coronary artery disease from the clinical evaluation of magnetic resonance imaging in coronary heart disease (CE-MARC) trial. Circulation 129:1129–1138
45. Kato S, Kitagawa K, Ishida N et al (2010) Assessment of coronary artery disease using magnetic resonance coronary angiography: a national multicenter trial. J Am Coll Cardiol 56:983–991
46. Yoon YE, Kitagawa K, Kato S et al (2012) Prognostic value of coronary magnetic resonance angiography for prediction of cardiac events in patients with suspected coronary artery disease. J Am Coll Cardiol 60:2316–2322
47. Gargiulo P, Dellegrottaglie S, Bruzzese D et al (2013) The prognostic value of normal stress cardiac magnetic resonance in patients with known or suspected coronary artery disease: a meta-analysis. Circ Cardiovasc Imaging 6:574–582
48. Nagel E, Schuster A et al (2012) Myocardial viability: dead or alive is not the question! JACC Cardiovasc Imaging 5:509–512
49. Kim RJ, Wu E, Rafael A et al (2000) The use of contrast-enhanced magnetic resonance imaging to identify reversible myocardial dysfunction. N Engl J Med 343:1445–1453
50. Rahbar K, Seifarth H, Schäfers M et al (2012) Differentiation of malignant and benign cardiac tumors using 18F-FDG PET/CT. J Nucl Med 53:856–863

Equipment for Imaging and Mechanism of Radiation Protection

19

Rui Li, Qiang Jia, Zhaowei Meng, Shen Wang, Ruiguo Zhang, Wensen Jin, Bin Liu, Yu Chen, Tian Tian, and Rong Tian

19.1 PET System

The use of positron-emitting radionuclide molecular imaging is important in the diagnosis and staging of malignant disease response and monitoring of treatment. In order to cope with emerging clinical needs, the imaging performance has been greatly improved recently. These developments are usually limited by the application of positron emission tomography (PET) physics; hence the primary goal in PET scanner designing is to improve spatial resolution, sensitivity, and the ratio of true coincidence count rate relative to the noise [1]. In addition to the photon counting-related statistical effects, scattered and random coincidence processes also contribute to background noise in PET. Recent advances in new models of scintillator and electronic equipment and statistically based algorithms of PET image reconstruction have greatly improved the clinical performance of PET [2, 3]. Nowadays, the new PET imaging technology is able to complete anatomically and functionally in a few minutes, which largely reduce the waiting time in clinic while maintaining a good imaging quality.

R. Li
Department of Nuclear Medicine, RenJi Hospital, School of Medicine, Shanghai JiaoTong University, Shanghai, P. R. China

Q. Jia (✉) · Z. Meng · S. Wang · R. Zhang
Department of Nuclear Medicine, Tianjin Medical University General Hospital, Tianjin, P. R. China

W. Jin (✉)
Teaching and Research Section of Nuclear Medicine, Anhui Medical University, Hefei, Anhui, P. R. China

B. Liu (✉) · T. Tian · R. Tian
Department of Nuclear Medicine, West China Hospital, Sichuan University, Chengdu, P. R. China

Y. Chen
Department of Operation Management, West China Hospital, Sichuan University, Chengdu, P. R. China

19.1.1 Fundamental Structure and Annihilation Coincidence Detection

19.1.1.1 Fundamental Structure

PET consists of scanning racks, main cabinets and operation consoles, inspection beds, and printing equipment [4, 5]. The rack is the largest component and is the hardware body of PET equipment. It is equipped with transmission sources, partitions, laser locators, detector rings, analog and digital electronics, conforming lines, moving parts (transmission sources, partitions, and beds), control circuit, and other components; its main function is to collect data. The main cabinet and operation console are the software cores of the PET system. They are mainly composed of one or several computers and software systems, including CPUs, input and output systems, and internal and external storage systems. The main functions are data acquisition, data storage, data correction and image reconstruction, display and analysis, and control of PET moving parts such as inspection beds, transmission sources, etc.

The PET detector is a detector module made of strontium bismuth crystals or other crystals. Each module is composed of a plurality of crystal units. Each module is equipped with a plurality of photomultiplier tubes. The working principle of a single module is similar to that of a γ-camera. The scintillation light is used to determine the ray incident crystal unit.

A plurality of detector modules are arranged in a ring to form a detector ring, and a plurality of rings form a cylindrical detector. Each of the crystal units has a fan-shaped field of view and a plurality of crystal units on the same ring and other rings on the opposite side to form a line of coincidence, and the fan-shaped surface thereof is effective to meet the visual field.

19.1.1.2 Annihilation and Coincidence Detection

Positron emission tomography (PET) is an imaging device that is used for the detection of distributions of positron emitter-labeled radiopharmaceuticals [6]. The principle of

G. Huang (ed.), *Nuclear Medicine in Oncology*, https://doi.org/10.1007/978-981-13-7458-6_19

PET imaging is simultaneously detecting pairs of γ-ray photon emitted from the electron-positron annihilation. A positron (β+) is an antiparticle of an electron. It has the same properties as an electron except for a positive charge. Positrons are unstable particles that emitted from the nucleus with different energies during the radioactive decay of unstable, proton-rich isotopes. The energy released during the decay has continuous spectrum and was characterized by a maximum value specific to certain parent isotope [7]. A proton is converted to a neutron through the decay process, and a new positron is created. When a positron-emitting radionuclide (such as ^{11}C, ^{15}O, ^{13}N) decays, a positron is emitted and rapidly (about 10^{-10} s) encounters an electron after traveling a short distance (about 1 mm) in the body and results in the annihilation of both particles. Every annihilation reaction emits two γ-ray photons traveling in almost opposite directions, each with an energy of 511 keV [8]. The two detectors in opposite position surrounding the subject can simultaneously detect the gamma photon. A timed pulse is generated in each detector when an incident photo is recorded, and these timed pulses are selected in coincidence circuitry for the pulses falls within predefined coincidence time window (5–15 ns). The straight line of coincidence, as known as line of response (LOR), is detected between two detectors in opposite direction to localize the annihilation. As the emitted photon pairs are not exactly 180° apart, the LOR has a width apart from zero.

Compared with SPECT that require a physical collimator, PET has a distinctive advantages of employing coincidence detection, which serves as a form of electronic collimation. Temporal coincidence time window is employed to associate pairs of photon events emitted from individual positron decay and allows to distinguish corresponding events from unrelated detection events. The PET system consists of a ring of detectors surrounding the subject, which enables the detection of annihilation photons at any angles within the field of view and used for tomographic reconstruction of activity distribution. During an extended scanning, many coincidence events could be detected and used for the estimation of angular projections and 3D image reconstruction. This mode of coincidence detection is the center of PET scan, which is a powerful means that greatly enhances spatial resolution and statistical accuracy, and hence improves sensitivity and dynamic imaging ability.

19.1.1.3 Types of Coincidence Events

There are four types of coincidence events in PET: true coincidence event, scattered coincidence event, random coincidence event, and multiple coincidence events. In a PET scan, the counts generated from true events, scattered events, and random events are detected along a particular LOR. True coincidence event is the raw data we expect to obtain in PET. Random and scattered coincidence events are two major sources of noise in PET, which are false coincidence event. Noise is an important problem in nuclear medicine imaging. Distinguishing between true and false coincidence event in line with the signal correction is one of the key factors affecting the image quality of photon coincidence detection [9]. Image quality is increased with more true coincidence event.

1. True coincidence event
   Two photons from the annihilation event are detected by the coincidence detector which is counted as true event when there is no interaction that occurred in these photons before the detection, and no other events are captured during the coincidence time window. A true event must fulfill the following three criteria: (1) two γ-photons must be detected simultaneously; (2) two γ-photons are 180° apart; and (3) each γ-photon must have an energy of 511 keV. The numbers of true event only count for a small part in the total counts recorded in each detector.
2. Scattered coincidence event
   Scattered event occurs when at least one of the detected paired photons has undergone Compton scattering event before being recorded. Interaction with any matter in the field of view results in the photon deviation from its previous path and likely to be assigned to a wrong LOR. Scattered event is characterized by photon with an energy level lower than 511 keV and a non-180° angle formed between two photons. LORs of scattered event would change with position and hence affect PET detection accuracy by reducing image resolution and contrast and overestimating isotope concentration. Scattered events increase noise background to the true events and decrease the signal-to-noise ratio. The amount of scattered coincidence events is often related with the morphology and size of the organ being scanned, in addition to the camera geometry. In practice, preprocessing of the data is needed to estimate and correct for scattered events. Other approaches to reduce the numbers of scattered photon include using flat, ring-shaped lead or tungsten septa.
3. Random coincidence event
   Since there is a coincidence time window for detecting coincidence event, any unrelated two photons captured on the probes during this time range will also be recorded. Random coincidence events refer to these photons not producing from the same annihilation event, and it has an fairly uniform distribution in the FOV. Similar to the scattered events, the volume and attenuation characteristics of the object, as well as the camera geometry, would affect the generation of random events. There are two ways to estimate the number of random coincidences. Firstly, mathematical formulas are applied to calculate the count rate and coincidence time collected by the detectors. Another method is using a delayed time window in addi-

tion to the coincidence time window to estimate the number of random coincidences based on count in the delay time window. The presence of random coincidences increases the imaging background, reduces the signal-to-noise ratio, and leads to an overestimation of the isotope concentrations if not corrected. Although random coincidences can be estimated and corrected through the above methods, in practice, the detectors cannot really distinguish random coincidences from true coincidences when a pair of photons is falling within the coincidence time window. When the count rate increases by onefold, random coincidences would increase by twofold correspondingly. Therefore, there is a limit to increase the image quality by increasing the count rate. When the limit is exceeded, the count rate is increased, and the image quality is decreased.

19.1.2 Detection System

In order to improve the efficiency of detection, PET is mostly composed of a number of detector modules which could detect LOR coincidence events in any direction simultaneously, facilitating high sensitivity and rapid imaging speed. By combining multiple rows of detector rings in the axial direction, it is possible to simultaneously image a certain axial length of the object and increase the longitudinal FOV. The detector module is the basic unit of PET and mainly consists of scintillators and photomultiplier tubes.

19.1.2.1 Scintillators and Scintillation Detectors

Scintillation detections are adopted in the majority of current PET systems. The scintillation process refers to the conversion of high-energy γ-photons into scintillation light through a scintillating crystal. A 511 keV photon incident on the scintillator generates an energetic electron, and the electron loses its energy and excites other electrons when it travels through the scintillating crystal. The burst of light is emitted from scintillators when the excited electrons decay and return back to the ground state. Photomultiplier tubes (PMTs) are coupled to the scintillator to capture the visible light and convert the light signal to an electrical signal.

Due to the high energy of annihilation photons, the scintillator crystals of PET detectors mainly use materials with high atomic number and high density such as thallium-doped sodium iodide (NaI(Tl)), bismuth germanate (BGO), cerium-doped lutetium oxyorthosilicate (LSO), or gadolinium oxyorthosilicate (GSO). A scintillator material for PET system should include the following features ideally: firstly, a high linear attenuation coefficient is important to stop high-energy γ-photons; secondly, a short light decay time is essential to reduce dead time (the "cooldown" time of the scintillator after the detection of a photon) in order to reduce coincidence time window and decrease the numbers of random coincidence events; and lastly, a high light output is needed to improve scatter rejection and allow for good energy resolution. The detecting sensitivity can be enhanced by increasing the thickness of the scintillator crystal (usually 1 ~ 3 cm). However, thick crystals tend to have a interaction depth problem. Hence, increasing crystal thickness to an extent may result in a reduction of spatial resolution. In contrast, thin crystals enable an optimal balance of sensitivity and spatial resolution due to a high linear attenuation coefficient for high-energy γ-photons.

NaI(Tl) is a good material for lower-energy single-photon imaging; however, it is not ideal for PET system due to a low linear attenuation coefficient for stopping high-energy γ-photons. BGO crystal is the most commonly used scintillator material for early PET systems. It has a high stopping power for high-energy γ-photons. It can capture 90% of 511 keV photons at a thickness of 2.0 cm and has a good detection efficiency and spatial resolution for high-energy γ-photons. However, BGO has limitations such as relatively poor energy resolution and long decay time, which would reduce its scatter rejecting power and increase dead time. Due to these limitations, BGO is a more suitable material for scanner with physical collimation, which has fewer scatter and count rate. LSO and GSO crystals have now become the mainstream scintillator materials for PET systems [10]. Despite a weaker stopping power of high-energy γ-photons, they have a shorter decay time and increased energy resolution compared to BGO crystal. The fast decay time makes LSO more suitable for the high count rate detection of annihilation coincidence and enabled a time-of-flight (TOF) data acquisition, which makes LSO a suitable choice of scintillator for PET detector applications [11]. It is also worth to notice that LSO contains about 2.6% of ^{176}Lu, which is self-radioactive and contributes to random coincidences [12]. This part of random coincidences would not greatly affect clinical practice of PET detection; in addition, this stable source of radiation could be routinely assessed as a means of quality control. In addition to the above scintillator crystals, cerium-doped lutetium yttrium silicate (LYSO) scintillation crystal is used in some PET systems due to its similar characteristic as LSO.

19.1.2.2 Detector Arrangements

Photodetectors record the scintillation light emitted from the interaction of high-energy γ-photons and scintillator and convert the light signal into electrical signal. In most PET systems, PMTs are the preferred photodetectors due to the combination of high gain of electrical output, high frequency response, and a high signal-to-noise ratio. With the development of technology, the new PET detector module also adopts new technologies to replace traditional photomultiplier

tube. PMTs are highly sensitive to magnetic fields; hence usually they are not used in the PET/MR system with a high magnetic field environment. Multichannel photomultiplier tube, position-sensitive photomultiplier tube, and semiconductor device are applied to increase signal output and spatial resolution, as well as reduce the influence of external magnetic fields. For example, avalanche photodiode (APD) is an alternative to PMTs in some PET applications. Although APD does not have a high gain as PMTs, it has the advantages of small size and a good performance under high magnetic field.

Current PET systems often contain thousands of scintillation detector units, with these scintillation crystals grouped in blocks. Each block unit is coupled to smaller numbers of PMTs (such as four PMTs) due to the space and cost limitations. The design of the combination fashion varies in different PET systems, such as a multichannel PMT coupled to a scintillation crystal assay and a PMT assay coupled to a single crystal plane. A typical model consists of a scintillation crystal matrix, light guide, and four PMTs. Four PMTs are an optimal number to detect light signals from a larger number of scintillation crystals. Encoding ratio means the ratio between the number of scintillation crystals and the number of PMTs; hence a high encoding ratio is more desired due to the higher efficiency. This design enables each block unit to run independently and reduces the interference caused by the transference of light signals between one PMT and other surrounding blocks. The spatial resolution of the detector is affected by the size of the PMTs, with a limit of about 4–5 mm. Quadrant sharing is another agreement for increasing the encoding ratio. Unlike the conventional design, PMTs of the corner blocks located in the quadrant sharing design could detect lights from up to four individual blocks and improve spatial resolution and encoding ratio. However, this design has a dead time problem under high count rates. The Anger-logic design is another method to replace the conventional block design. A number of small scintillation crystals are coupled with a multichannel PMT. It has a greater surface area than conventional block detectors, which in turn collects more uniform light signals and increases the encoding ratio. Using an Anger-logic principle applied in the gamma camera, this design allows the light to spread to a greater area compared to the conventional unit and to obtain the spatial information. Similar to the quadrant sharing design, the Anger-logic design also has the problem of a longer dead time under high count rates.

19.1.2.3 Pulse Processing and Dead Time

When a high-energy photon encountered a scintillation crystal, there is a timing signal being created as the PMTs converted the light signal into electronic signals. It is a digital pulse produced as the electronic pulse travels through the constant fraction discriminator and reaches a stable peak pulse height. These digital pulses are then sent to the coincidence circuitry for analysis. Based on the different levels of pulse height, different discriminators are used to reject or accept these electronic signals, such as upper energy-level discriminator (ULD) and lower energy-level discriminator (LLD). In some cases, these discriminators could be used to analyze acquired pulses according to higher- or lower-energy window. The ULD is useful to refuse the pulses when multiple high-energy photons encountered the block unit simultaneously. Using the LLD to reject pulses with lower energy level is a way to reject scattered events, because some of the scattered photons present with an energy level lower than 511 keV. However, it does have a high enough energy resolution to remove those scattered photons with an energy level around 511 keV. In addition, as a certain amount of the unscattered photons may not reach the exact 511 keV energy level due to potential Compton interactions with scintillator crystals or an incomplete conversion of the crystal, the LLD often used a lower threshold value to not reject potential true events. The energy value of LLD is usually optimized to reach an optimal results of high sensitivity to true events and a low proportion of scattered events [13].

Every detection system has the problem of dead time, as the detection efficient decreases with the activity increases. There is a processing limitation of the detector to separate overlapping light pulses generated from individual annihilations as only one signal could be processed by the PMTs at a time. The phenomenon is known as pileup. The possibility of a detector to miss out a coincidence event increases when the count rate significantly increases. This may cause another problem for coincidence detection when one photon within the pair is missed due to the dead time loss. Due to the random nature of nuclear decay, it is always possible that more than one annihilation reaction could occur around the same time. In addition, the electronics has a limitation of data processing rate, with a maximal rare close to 1 MHz, which may also lead to data loss. These dead time losses still occur under a fairly low count rate and would greatly increase at a high count rate. The losses could be controlled by using multiple independent scintillation detectors and adopting scintillators and electronics with faster processing rate.

19.1.3 PET Image Processing

19.1.3.1 2D and 3D Acquisition

According to different ways of data acquisition, there are two basic types of collecting data in PET, two-dimensional (2D) mode and three-dimensional (3D) mode [5]. Early PET systems usually use 2D mode for data acquisition. In 2D mode, thin septa of lead or tungsten (about 1 mm thick) are

placed in between each detector ring to prevent oblique incident photons from entering the detector [14]. Hence, only the coincidence events that occur between detectors within the same ring or in adjacent rings are recorded. Using 2D mode could effectively reduce random coincidence events and scattered events. Most of the current PET systems use 3D data acquisition. The 3D data acquisition is performed under the condition that the septa are removed and the detector can detect the incident photon at any angle in the axial direction [15]. Compared with 2D data acquisition, the detection rate of photon pairs of 3D mode can be improved by 8~12 times, which helps reduce the acquisition time, reduce the dose of radiopharmaceutical injection, and improve the image signal-to-noise ratio [16]. In 3D mode, the sensitivity for detecting true coincidences greatly increases due to the increased amount of measured LORs. However, the numbers of scattered coincidences and the random coincidences also increase significantly in 3D mode. In order to obtain a better image, an effective correction approach must be performed [17]. In addition, 3D mode requires a high amount of data to complete data acquisition. As the number of crystal ring increases, performing full 3D image reconstruction required a more powerful computer to process.

19.1.3.2 Corrections for Degradation

The image quality in PET can be degraded by a few factors, such as scatter and attenuation. Therefore, both degrading effects should be corrected in PET to obtain high-quality images.

Scatter events could be divided into in-plane and out-plane scatter events. The in-plane scatter event occurs when one photon changed its original path by Compton effect and hit the detector while the other photon of the annihilation remains scattered. The false counts resulted in other LORs may cause the source of the annihilation to appear outside of the subject. In out-plane scatter event, radiation occurs outside the plane of the detector ring. One photon is emitting to the detector ring, while the other photon is scattered back to the detector. The most common way to reduce the out-plane scatter event is to block signals generated outside the ring by using flat, ring-shaped lead or tungsten septa [18]. Septa is able to decrease more than half of the scatter events collected in the detectors. Using septa can physically decrease the total amount of detected scattered events and reduce other radiation events (such as random event) generated outside the FOV. Another common way to reduce scatter event is to use scatter correction algorithm [19]. Adjusting the energy window level of the detector system can help decide whether to accept or reject potential scattered events. As discussed previously, 3D mode is more sensitive to scattered events than 2D mode. The number of scattered events can become really large in the 3D mode and needs to be corrected. The Gaussian fit technique and model-based scatter correction algorithms are the most commonly used methods for scatter correction in 3D mode.

Attenuation is another major factor in PET resulting in data degradation. True events are lost due to photoelectric absorption or scatter during the interaction between annihilation γ-photons and human body. In attenuation, one photon hit direct on the detector when the other photon may not recorded as this photon may stopped or deflected before hit the other detector. The chance of the attenuation effect is much higher in the PET system than in single-photon system, because either of the paired photons from one annihilation event may got lost before leaving the subject. In most attenuation events, at least one of the paired photons need to travel a fairly long distance in the tissue. Annihilation photons emitted from the middle part of the human body are more likely to have attenuation effect than those from the edge part of the body. Hence, attenuation effect may result in uneven reconstructed image as radioactivity generated from deep part of the body may artificially be lost, while a high count of radioactivity is shown on the outer part of the body. As the signals from the center body are affected by the annihilation effect at all directions, the outer body will present as a bright outline in the reconstructed image. It is also noted that an artificially high levels of radioactivity can be observed in the lungs. Due to the hollow structure of lungs, photons are unlikely to have attenuation effect in the lungs than from other surrounding tissues. In addition, the attenuation effect can cause a loss of total counts, increase imaging noise, and result in an incorrect estimation of radioactivity distribution.

Attenuation in PET is often corrected using either calculated correction or measured correction [20]. Practically, the correction process either adds counts back into regions (such as deep body areas) more affected by the attenuation effect or removes counts from regions (such as body edges and lungs) less affected by the attenuation effect. In the calculated correction method, the attenuation effect is treated as a known constant in the outer body contour. Data can be automatically corrected using this method, or non-attenuation-corrected data can be examined by an experienced interpreter. The other measured correction method requires a reference scan of a radioactive source before the actual scan of patient. For all the LORs measured, a correction factor can be calculated by dividing the counts generated in the reference scan by the transmission counts generated in the scan of patient. The reference scan can be operated daily as part of the quality control in PET practices.

19.1.3.3 Image Reconstruction

Following the corrections for scatter, random events, and attenuation effect, parallel collections of counts collected by detectors along the LOR are named as projections. Image

reconstruction from these projections is one of the key factors determining the quality of PET image. The reconstruction algorithm used by PET mainly includes analytical algorithm and iterative algorithm.

Analytic algorithm is mainly based on the Radon line integral model. The relationship between the two-dimensional Fourier transform of the projection data and the three-dimensional Fourier transform of the image is established using this model. The analytical solution of the image reconstruction is then obtained. The analytic algorithm has the advantage of fast reconstruction speed, but there are also statistical noises of PET data, and the accuracy of reconstructing images is limited. Iterative algorithm used the Poisson stochastic model to describe the PET imaging process. It can reduce the statistical data noise but with a relatively slow reconstruction speed. FBP is the most applied analytical method for image reconstruction in the 2D mode [21]. However, this method is easy to implement but also has the characteristics of amplifying signal noises. Currently, the most commonly used iterative reconstruction schema is ordered subsets expectation maximization (OSEM) [22–24]. The OSEM reconstruction algorithm has a better resolution, more accurate positioning and quantification capacity, and anti-noise ability. Using this method, the reconstructed image has clear anatomical structure and layers, less artifacts, and less lesion deformation. The reprojection and filtered back-projection approach is the most commonly used method for 3D image reconstruction.

In addition to the previous methods, time-of-flight (TOF) technology serves as an effective image reconstruction method to reduce image noise. The TOF technology is a method in which PET can accurately detect the time difference between two photons hitting two detectors and accurately calculate the position of the annihilation event on the LOR according to the flying speed of the photon. It is possible to directly determine the location of the annihilation event within the body and obtain a direct distribution profile of the annihilation event. Hence, the TOF technology is used to improve PET image quality and reduce noise. Due to the need of a precise measurement of photon flight time, this method puts higher requirements on the hardware of PET systems. At present, the latest PET system has a time resolution of 580 picoseconds of measuring precise photon flight time. This means a precise positioning ability within a range of 8.7 cm for the annihilation events. Therefore, this method can completely eliminate the effect of image noise outside of this range and enables local image reconstruction. The application of TOF technology improves the image signal-to-noise ratio, and the contrast of the image, which in turn improves the sensitivity of the PET system and shortens the scanning time.

19.1.3.4 Quality Control

PET is a sophisticated imaging equipment, and it is necessary for controlling image quality in PET applications. The most important parameters for PET performance evaluation include spatial resolution, scattering sensitivity, counting characteristics, random coincidence, uniformity, and scatter correction accuracy [25]. (1) High spatial resolution is a key design parameter for PET systems. The spatial resolution reflects the closest distance between two points that the PET system can distinguish. It includes radial, tangential, and axial resolution. The spatial resolution is usually described using indexes including point spread function (PSF), full width at half maximum (FWHM), and equivalent width. The larger the half width, the spread of the point source becomes greater and results in a lower image resolution. (2) Imaging sensitivity refers to the detection ratio of true coincidence of the annihilation event in the PET system when the count loss and the random events are negligible. Several factors can affect the system sensitivity, such as the detecting efficiency covered by the detectors, the attenuation effect, scattering, dead time, and different data acquisition mode. Using 3D acquisition mode instead of 2D acquisition mode will significantly increase the sensitivity. Under a fixed statistical error rate, the sensitivity can affect the scanning time and the required dose of tracer. When a fixed dose of tracer is applied, the increase of imaging sensitivity reduces the scan time. (3) The scattering fraction refers to the percentage of the scattered events in the total coincidence count. It describes the sensitivity of the PET system toward the scattered events. A smaller scatter count means a more powerful ability to reject scattered events. (4) The count rate characteristic reflects the deviation from the radioactivity caused by the count loss. As the intensity of the radiation source in the FOV increases, the count rate of PET system also increases. When the radioactivity reached over a certain limit, the count rate reaches saturation and does not increase due to dead time. If the radiation source continues to increase, the count rate begins to decrease. (5) The noise equivalent count (NEC) reflects the effect of noise on the image quality caused by scattered and random coincidences. It equals to the ratio of true count rate to the total count rate multiplied by the true count rate. (6) Count loss and accuracy of corrections for counts losses and random. These two parameters are used to describe the accuracy of the correction for random coincidence and count loss due to dead time in PET systems. (7) Accuracy of scatter correction describes the ability of the PET system to reject the scattered events. (8) Accuracy of attenuation correction describes the ability of the PET system to correct the attenuation of radiation in the medium. In addition, the image quality is compared among different imaging systems by standard imaging methods within a simulated clinical acquisition condition.

19.2 Internal Radiation Dosimetry

19.2.1 Radiation Units

In nature, ionizing radiation is one process for energy transmitted through some types of radiation including electromagnetic waves (X-ray, γ-ray) and some particles with charges (α-particle, β-particle, heavy ion) or without charges (neutron). When a living organism is irradiated by ionizing radiation, energy might be deposited in the organism or its tissues, subsequently forming biological effect of radiation. Generally, the biological effect of radiation is increasingly strong with more energy transmitted by radiation [18]. It is therefore important to properly quantify radiation so that the effectiveness of radiation on living organism containing human body can be estimated. Some basic quantities for radiation are utilized to measure the energy transferred to other materials from radiation, including energy of radiation, exposure, absorbed dose, equivalent dose, and effective dose.

19.2.1.1 Energy

The radiation biological response of living organism is mainly caused by the deposition of radiation energy. The unit of radiation energy is electron volt (eV), which presents the kinetic energy obtained by acceleration of one electron through an electric pressure of 1 V. In the International System of Units (SI), its unit is expressed in joule (J). One Joule is equivalent to 6.241 × 10^{18} eV. Because 1 eV of energy is very small, some derivative units are commonly used with metric prefixes.

$$\begin{aligned} 1\text{TeV} &= 1\times10^{3}\,\text{GeV} = 1\times10^{6}\,\text{MeV} \\ &= 1\times10^{9}\,\text{keV} = 1\times10^{12}\,\text{eV} \end{aligned} \tag{19.1}$$

$$1\text{MeV} = 1.6\times10^{-13}\,\text{J} \tag{19.2}$$

The radiation energy is related to wavelength (λ) of the photons (electromagnetic waves).

$$\text{Eenergy} = 1.24\times10^{-6}/\lambda \tag{19.3}$$

where λ is in meters and energy is in eV.

19.2.1.2 Exposure (*X*)

The exposure (X) is one of the basic quantities for radiation, which describes the capability of radiation to generate ionization in air under standard temperature and pressure (STP). The exposure is the number of ion pairs produced in certain volume of air at 0 °C and 101.325 kPa by radiation. The traditional unit of exposure is roentgen (R), which is still in extensive use in the radiation field. It is defined as the energy deposited by X-ray or gamma ray in the air at STP, which is equivalent to the deposition of 8.76 × 10^{-6} J per gram of dry air leading to ionization of 1 electrostatic unit of charge per 0.001293 g (1 cm^3) of air. One mR is one thousandth of 1 R. The unit of X in SI is the C/kg, which is defined as the amount of charge in per kilogram air. Conversion of the units is described as

$$1\text{R} = 2.58\times10^{4}\,\text{C/kg} \tag{19.4}$$

Of note, X is only used in the ionization generated by photon radiation (X-ray or gamma ray), meaning not to measure various radiation particles. And it is applied to air rather than other matters. Additionally, the measurement of photons is limited to 3 MeV from 10 keV energy due to practical boundedness of instruments.

The exposure rate ($\dot{X}$) is used to represent radiation intensity, and its units are expressed in R/h or mR/h. In SI system, the unit of exposure rate also is C/kg·h. It is a function between the radiation intensity of source and the distance from the measuring point to the source. The $\dot{X}$ of X-ray or gamma ray is measured on the basic assumptions as the following:

1. Neglecting attenuation in air from the source to the measured point
2. Very small geometric dimensioning of source, namely, point radiation source
3. Negligible scattering [19]

After all of these conditions are satisfied, the function of $\dot{X}$ is described as

$$\dot{X} = \Gamma\frac{A}{D^2} \tag{19.5}$$

The sign of Γ is defined as the $\dot{X}$ constant for every radionuclide, which is generated by 1 Bq of point γ-ray source at 1 m distance. The sign of A represents the activity of the source, and the sign of D is the distance from the measuring point to the source. Γ-values for some common radioisotope γ-ray sources are listed in Table 19.1.

19.2.1.3 Absorbed Dose (*D*)

Since the effectiveness of radiation on matter is related to the amount of energy and kind of radiation, which is far more than photons, one different unit should be utilized to quantify the deposition of energy in matters. In other words, this unit can describe the amount of energy deposed in different materials from different kinds of radiation [21]. Thus the absorbed dose (D) becomes one more universal quantity, which measures the amount of energy from any types of radiation absorbed in mass of any material. So D can be defined as

$$D = \frac{d\bar{\varepsilon}}{dm} \tag{19.6}$$

where $d\bar{\varepsilon}$ is the mean energy imparted to matter by ionizing radiation and dm is the mass of matter. It should be noted that in the physical process, dm isn't allowed to approach zero in mathematical sense.

Table 19.1 Values of Γ for main radioisotope γ-ray sources (C m^2/kg MBq s) [20]

Radionuclide	Γ
Carbon (^{11}C)	1.13×10^{-12}
Sodium (^{22}Na)	2.29×10^{-12}
Sodium (^{24}Na)	3.53×10^{-12}
Chlorine (^{38}Cl)	1.28×10^{-12}
Potassium (^{42}K)	2.65×10^{-13}
Calcium (^{47}Ca)	1.05×10^{-12}
Chromium (^{51}Cr)	3.44×10^{-14}
Cobalt (^{57}Co)	1.09×10^{-13}
Iron (^{59}Fe)	1.20×10^{-12}
Cobalt (^{60}Co)	2.50×10^{-12}
Copper (^{64}Cu)	2.04×10^{-13}
Zinc (^{65}Zn)	5.94×10^{-13}
Gallium (^{67}Ga)	1.55×10^{-13}
Gallium (^{72}Ga)	2.60×10^{-12}
Selenium (^{75}Se)	3.93×10^{-13}
Bromine (^{82}Br)	$2.\ 80 \times 10^{-12}$
Krypton (^{85}Kr)	2.48×10^{-15}
Rubidium (^{86}Rb)	9.60×10^{-14}
Strontium (^{87m}Sr)	3.62×10^{-13}
Yttrium (^{91}Y)	3.16×10^{-15}
Technetium (^{99m}Tc)	1.54×10^{-13}
Tin (^{113}Sn)	2.34×10^{-13}
Iodine (^{125}I)	3.38×10^{-13}
Iodine (^{131}I)	4.26×10^{-13}
Xenon (^{133}Xe)	1.10×10^{-13}
Cesium (^{137}Cs)	6.64×10^{-13}
Gold (^{198}Au)	4.46×10^{-13}

In SI units, the unit of absorbed dose is gray (Gy) to memorize the English physicist Louis Harold Gray. 1 Gy is equivalent to 1 J of radiation energy deposited per kilogram of matter, namely, given by

$$1\text{Gy} = 1\text{J/kg} \tag{19.7}$$

The older unit is the rad, still in common use, which is equivalent to 1×10^{-5} J energy deposited in 1 g of matter. Therefore, the conversion from gray to rad is given by

$$1\text{Gy} = 100\text{rad} = 1\text{cGy} \tag{19.8}$$

Because D is used to measure the amount of the energy absorbed by one medium for any type of ionizing radiation, it isn't sufficient for evaluating the biological consequences of living organism exposure to radiation. If the energy is absorbed by 1 kg air, the conversion from X to D is as follows:

$$1\text{R} = 0.896\text{rad in air} \quad \text{or} \quad 1\text{R} = 0.00869\text{Gy in air} \tag{19.9}$$

19.2.1.4 Radiation Weighting Factors (W_R) and Relative Biological Effectiveness (RBE)

To estimate biological effects caused by different kinds of radiation, the concept of radiation weighting factors (W_R) is introduced for a given type of radiation. The W_R formerly were called quality factors (QFs). In radiobiology, the relative biological effectiveness (RBE) is the ratio of biological effectiveness of one type of radiation relative to the standard radiation, given the same absorbed dose. Alternatively, the ratio of the dose of standard radiation to produce one biological response relative to the dose of another radiation to produce the same biological response is calculated to evaluate RBE. It is usually to use 250 kV of X-radiation or the radiation emitted by ^{60}Co as the standard radiation. The RBE is traditionally defined as

$$\text{RBE} = \frac{D_S}{D_R} \tag{19.10}$$

where D_S is the dose of a standard type of radiation and D_R is the dose of one type of radiation in question. Both doses are measured in the cells.

W_R is closely related to the linear energy transfer (LET) of radiation and has the similar meaning of RBE. It depicts that the deposition of radiation energy causes effects in biological tissues or organs. So W_R is valuable to design shielding of radiation protection and calculate the dose of occupational workers' exposure to radiation. W_R values for various radiations recommended by the International Commission on Radiological Protection (ICRP) are listed in Table 19.2.

Table 19.2 Radiation weighting factors, W_R [22]

Radiation	W_R
Photons (X-ray, γ-ray)	1
β-ray	1
Neutrons	
<10 keV	5
10–100 keV	10
>100 keV to 2 MeV	20
>2–20 MeV	10
>20 MeV	5
Proton >2 MeV	2–5
α-ray, fission fragments, heavy nuclei	20

19.2.1.5 Equivalent Dose (H)

As elaborated above the RBE or W_R of one type of radiation depending largely upon its LET, the more biological response is the type of radiation with higher RBE or W_R in the same radiation dose. In the field of radiation protection and occupational exposure, one purpose is to provide a dosimetric quantity which can evaluate biological effects and risk for the different kinds of radiation. This quantity, named equivalent dose (H), is used to measure the biological effectiveness of different radiation energy causing to tissues or organs. H has the same connotation as absorbed dose (D); its quantity thus is J/kg. H is obtained by D (in Gy) of a given kind of radiation multiplying by its W_R. In SI units, it is expressed in sievert (Sv). Formerly, the unit of H was radiation equivalent man (rem) which was also used to measure

the modification of the doses received by different kinds of radiation. The conversion from different units is given by

$$1\text{J/kg} = 1\text{Sv} = 100\text{rem} \tag{19.11}$$

The W_R for low LET radiation is 1 so that the Sievert is equivalent to the gray, namely, 1 Sv = 1 Gy. The different H values obtained by different types of radiation are calculated as follows:

$$H_T = \sum_R W_R \times D_{T,R} \tag{19.12}$$

where T is target tissue or organ and R is the kind of radiation.

19.2.1.6 Effective Dose (*E*)

Due to the discrepancy in radiosensitivity of various tissues and organs to ionizing radiation, the same type of radiation may cause the variation of damage in different tissues [23]. The effective dose is used to measure the biological effects of a partial or entire body exposure to radiation, which is further used to estimate the risk of radiation for human body. It is the sum of equivalent doses to weighting factor for each tissue and organ and calculated as

$$E = \sum_T W_T \times H_T \tag{19.13}$$

where E is the effective dose, H_T is the equivalent dose to target tissue or organ, and W_T is the radiation weighting factor. W_T for important organs are shown in Table 19.3.

19.2.2 Distribution for Radiation Dose

In nuclear medicine, the biological effect in human for nuclear medicine procedure is induced by utilizing certain radiopharmaceutical. The biological responses of radiation generated from energy absorbed in tissues are dependent upon the following factors: the activity of administrated radiopharmaceutical, the half-life of radiopharmaceutical, the radiosensitivity of target tissue, and the distribution of the radiopharmaceutical in the body [25]. Some common conceptions involving the metabolism and distribution of radiopharmaceuticals are introduced in this section.

Table 19.3 Tissue weighting factor (W_T) for important organs and tissues (ICRP) [24]

Organ or tissue	W_T	Sum of W_T
Bone marrow, colon, lung, stomach, breast	0.12	0.6
Gonads	0.08	0.08
Bladder, esophagus, liver, thyroid	0.04	0.16
Bone surface, brain, salivary glands, skin	0.01	0.04
Adrenals, extrathoracic region, gallbladder, heart, kidney, lymph nodes, muscle, oral mucosa, pancreas, prostate, small intestine, spleen, thymus, uterus, and cervix	0.12	0.12
Whole body		1.0

There are three half-life conceptions for evaluation of the intake and deposition of the radiopharmaceutical in the body after one radiopharmaceutical is administrated, which are physical half-life, biological half-life, and effective half-life.

19.2.2.1 Physical Half-Life

This concept of physical half-life is an intrinsic characteristic of the radionuclide, and it is defined as the time during which one half of the initial activity of the radionuclide is spontaneously decayed.

19.2.2.2 Biological Half-Life

This concept is defined by the time during which the initial quantities of various pharmaceuticals including radiopharmaceuticals are reduced to one half via the biological metabolism (containing exhalation, urination, etc.) in vivo.

19.2.2.3 Effective Half-Life

The concept is defined by the time during which one half of the initial activity of a radiopharmaceutical is reduced via the contribution of both the biological metabolism and spontaneous decay.

The elimination of one radiopharmaceutical from organism is mainly impacted by effective half-life, one shorter time compared with physical half-life or biological half-life. The relationship among half-life time is showed in the following formula:

$$\frac{1}{T_{\text{effective}}} = \frac{1}{T_{\text{physical}}} + \frac{1}{T_{\text{biological}}} \tag{19.14}$$

In clinical nuclear medicine, the main methods for radiopharmaceuticals entering human body are inhalation by the respiratory tract, intravenous injection, and ingestion of the digestive tract. All or partial intake of radiopharmaceutical may enter circulation or tissue, subsequently depositing in special tissues or organs, namely, target organs. In pharmacokinetics, the conception of compartment (or pool) is commonly used in pharmacology, support of technology, and drug discovery. It is very important for radiopharmaceutical research as well.

The meaning of compartment in radiopharmaceutical research isn't an anatomical conception, which is bounded by various anatomic landmarks. One radiopharmaceutical may distribute different tissues and organs and form exchange among these tissues according to certain kinetic parameter. Theoretically, these tissues and organs belong to the same metabolic compartment or pool in radiopharmaceutical research.

For example, after a period of time, the retention of single uptake of one radiopharmaceutical in certain compartment is calculated as

$$A_{\mathrm{T}} = A_0 \mathrm{e}^{-\lambda T_{\mathrm{eff}}} \tag{19.15}$$

$$R_T = \frac{A_T}{A_0} = \mathrm{e}^{-\lambda T_{\mathrm{eff}}} \tag{19.16}$$

where T_{eff} is the effective half-life of radiopharmaceutical and R_T is the effective retention fraction. One radiopharmaceutical may distribute different pools; one organ may contain different pools as well. The radiopharmaceutical is metabolized in compartment in certain clearance rate conforming with special functional law. Hence, it is critical that the retention, transference, and transportation for radiopharmaceutical quantity in tissues and organs can be obtained by establishing the mathematical model for certain compartment.

19.2.3 Calculation for Internal Radiation Dose

Radiopharmaceuticals deposited into human body will be distributed in various tissues and organs of the body. To internal dosimetry calculation, the interest tissues and organs where the quantities of radiopharmaceuticals are calculated and estimated are considered as target tissue or target organ, whereas other regions contributing radiation to the target are considered as source tissues or source organs.

19.2.3.1 Accumulation of Radioactivity in Source Region

As a result of the primary deposition and retention of radiopharmaceutical in source regions, it is very important to calculate the accumulative radioactivity in regions. The number of radioactive decay during a period of time (τ) is commonly calculated by the time integration method as follows:

$$A_S(\tau) = \int_0^{\tau} A_S \cdot dt \tag{19.17}$$

where is the retention of radionuclide in source region (S) at a specific time (t).

If there are i compartments ($i > 1$) in source region, $A_S(\tau)$ is the total sum of accumulative activities in each compartment, defined as

$$A_S(\tau) = \sum_{n=1}^{i} A_{S,n}(\tau) \tag{19.18}$$

where $A_{S,n}(\tau)$ is the accumulative activity of nth compartment in the source containing i compartments.

Because there are several compartments in source region, radiopharmaceutical in one compartment may transfer to the next one by certain rate, ultimately to the last compartment. This transfer process is displayed in the following figure.

As shown in Fig. 19.1, y_1, …, y_i is the rate of radiopharmaceutical transferred into appropriate compartment at certain time (t); and λ_1, …, λ_i is the clearance rate of radiopharmaceutical from appropriate compartment at certain time (t); and A_1, …, A_i is the activity of radiopharmaceutical transferred into appropriate compartment at certain time (t).

If the activity of radiopharmaceutical transferred into second compartment is equal to $A_1\lambda_1 y_2$ at t point, the derivation for radioactivity of pharmaceutical transferred into ith compartment is $A_{i-1}\lambda_{i-1}y_i$. Considering the reduction of radiopharmaceutical quantities ($A_i\lambda_i$) and labeled radionuclide decay, the net increase for radioactivity in ith compartment at t point is defined as

$$dA_i / dt = y_i \cdot \lambda_{i-1} \cdot A_{i-1} - \left(\lambda_i + \lambda_\gamma\right) \cdot A_i \tag{19.19}$$

where λ_γ is the spontaneous decay rate of labeled radionuclide.

In clinical nuclear medicine, short half-life radionuclide is commonly used for diagnosis and treatment. After the above mathematical expression was calculated in differential coefficient, we are going to plug that into Eq. (19.18) to get the following functional expression:

$$A_{S,n}(\tau) = A_{n-1}(\tau) \cdot \lambda_{n-1} \cdot \frac{y_n}{\lambda_{n,\mathrm{eff}}} \tag{19.20}$$

where $A_{n-1}(\tau)$ is the accumulative activity in $(n-1)$th compartment, $\lambda_{n,\ \mathrm{eff}}$ is the effective clearance rate of nth compartment, and y_n is the transfer rate of radiopharmaceutical from $(n-1)$th to nth.

19.2.3.2 Absorbed Dose and Absorbed Fraction in Source Region

The mean absorbed dose in target tissue is often reflected by the sum of mean absorbed dose from each source region. Some ionizing radiation, including X-rays, β-rays, and gamma rays, may penetrate through source regions up to target tissue, whereas α-rays and heavy ions are limited in source regions not to arrive at target tissue. Therefore, the absorbed dose in target tissue from the production of source regions is expressed in

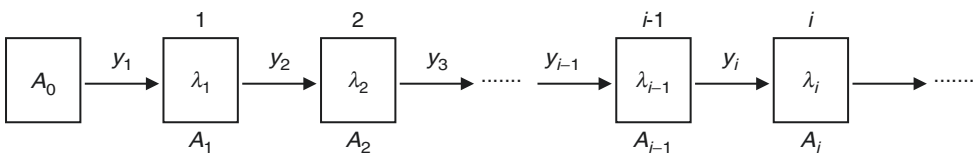

Fig. 19.1 Transference of radiopharmaceutical in several compartments

$$D_{ST} = \sum_j y_j E_j \mathrm{AF}_j \left(T \leftarrow S\right) / M_T \qquad (19.21)$$

where D_{ST} is the absorbed dose of target tissue contributed by per integration activity in source region. y_j is the forming probability of certain ray (j type of ray) per radiation decay. E_j is the transferring energy of certain ray, its unit MeV. $\mathrm{AF}_j(T \leftarrow S)$ is called absorbed fraction and is defined as the ratio of the energy absorbed by the target volume from jth radiation to the energy from the source volume. M_T is the mass of target tissue.

19.2.3.3 Specific Effective Energy of Target Tissue

Specific effective energy (SEE) is the equivalent dose received in target tissue by per decay of radionuclide in source region. It is calculated by

$$\mathrm{SEE}\left(T \leftarrow S\right) = \sum y_j E_j \mathrm{AF}_j \left(T \leftarrow S\right) \omega_{R,j} / M_T \quad (19.22)$$

where $\omega_{R,j}$ is the radiation weighting factors for j kind of radiation. Because most of the radionuclides labeled in radiopharmaceutical emit β-rays and γ-rays in clinical nuclear medicine, $\omega_{R,j}$ is 1 commonly. Simplification of the above function expression is described as follows:

$$\begin{aligned}\mathrm{SEE}\left(T \leftarrow S\right) &= \sum y_j E_j \mathrm{AF}_j \left(T \leftarrow S\right) / M_T \\ &= \sum y_j E \varnothing \left(T \leftarrow S\right)\end{aligned} \qquad (19.23)$$

The meaning of SEE presents 1 Gy of equivalent dose generated by per radiation decay.

19.2.3.4 Committed Equivalent Dose and Total Committed Equivalent Dose

The calculation for the committed equivalent dose in target tissue should be considered to plug the accumulative activity of source region into that function expression. Its formula is described as

$$H\left(T \leftarrow S\right) = 1.6 \times 10^{-10} \times A_S\left(\tau\right) \times \mathrm{SEE}\left(T \leftarrow S\right) \quad (19.24)$$

where 1.6×10^{-10} represents the unit conversion factor from MeV/g to J/kg.

After radiopharmaceutical administrated to patients, it distributes various organs and tissues, followed by the formation of various source regions. The target tissue may be exposed to irradiation emitted by various source regions; total committed equivalent dose thus is calculated as

$$H_T = \sum_S H\left(T \leftarrow S\right) \qquad (19.25)$$

19.2.3.5 Model of Dosimetry in Clinical Nuclear Medicine

In clinical nuclear medicine, based on the difference for the pathway of radiopharmaceutical administration and its metabolism, various models for internal radiation dosimetry are established in human body. These models commonly contain the gastrointestinal tract, the kidney-bladder, the liver-gall, and the brain-spinal cord cavity.

Model for the Gastrointestinal Tract

Supposing the immediate mixture of radiopharmaceutical in each compartment, this model describes the kinetics process of radiopharmaceutical in the region of the gastrointestinal tract, which includes four compartments shown in Fig. 19.2, such as the stomach, small intestine, upper large intestine, and lower large intestine. As for this model, if the clearance rate of radiopharmaceutical in certain compartment is obtained, the activity of radiopharmaceutical may be calculated by initial intake and function expression. The physiology of the gastrointestinal tract can be also studied by the revision of this model, such as transportation of the esophagus, gastroesophageal reflux, gastric emptying, transportation of the small intestine, abnormal permeability of the small intestine, and so on.

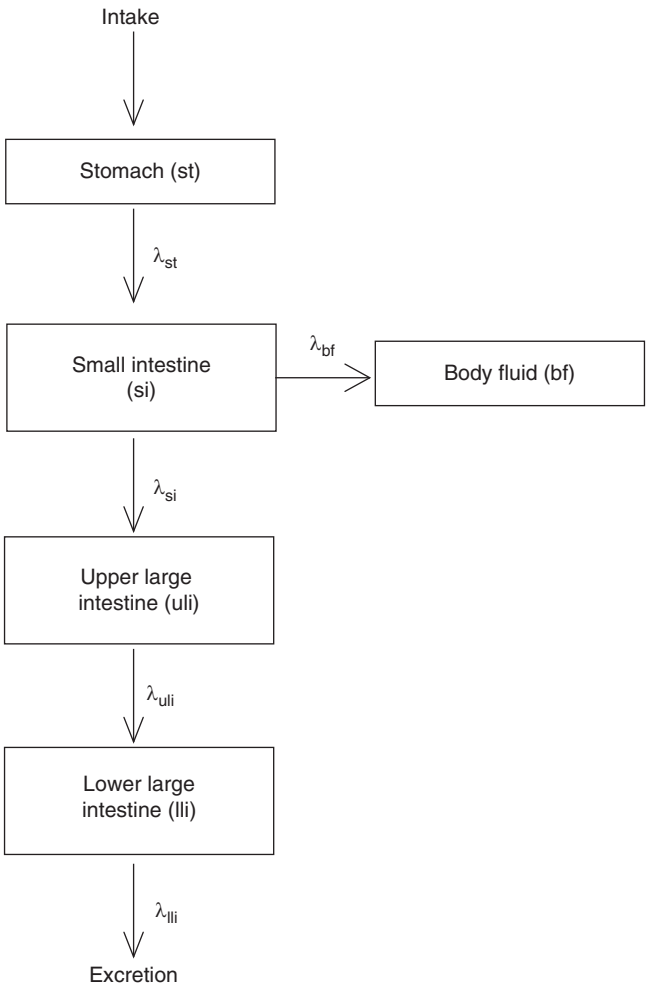

Fig. 19.2 Compartment model for the kinetics of radiopharmaceutical in the gastrointestinal tract

Model for Kidney-Bladder

The model is used to calculate the metabolism of radiopharmaceutical for renal function examination after the ratio of excretion via the kidney-bladder to total excretion is obtained. The excretion rate of radiopharmaceutical can be calculated by total activity in the body (A_{TB}). A_{TB} is defined as

$$A_{TB} = \sum_{i=1}^{n} \alpha_i e^{-(\lambda_i + \lambda_\gamma)t} \tag{19.26}$$

where λ_i is the biological clearance constant of radiopharmaceutical in ith compartment. λ_γ is the radionuclide's decay constant. α_i is the fraction for the activity gained in ith compartment.

Accumulative activity in the kidney is expressed in the following equation:

$$A = f_r \frac{1 - e^{-\lambda_r \overline{T_K}}}{\lambda_r} \sum_{i-1}^{n} \alpha_i \frac{\lambda_i}{\lambda_i + \lambda_r} \tag{19.27}$$

where f_r is the fraction of excretion activity via the kidney and $\overline{T_K}$ represents the time of radiopharmaceutical through the kidney, which is 5 min under normal condition and is 20 min in abnormal renal dysfunction. It should be noted that this equation is the approximation to the practical state owing to the difference of f_r from the clearance of various tissues and organs.

Accumulative activity in the bladder is expressed in the following equation:

$$A_B = f_r \sum_{i=1}^{n} \alpha_i \left[\frac{1 - e^{-\lambda_r t_v}}{\lambda_r} - \frac{1 - e^{-(\lambda_i + \lambda_r)t_v}}{\lambda_i + \lambda_r} \right] \times \left[\frac{1}{1 - e^{-(\lambda_i + \lambda_\gamma)t_v}} \right] \tag{19.28}$$

where t_v is the interval time from filling of the bladder to emptying of the bladder in turn. In this equation, t_v is supposed as one constant about 3.5 h. Meanwhile, the time of renal retention is omitted because it's very short compared with the time of bladder retention.

Model for Liver-Gall

This model describes the metabolic process for radiopharmaceutical absorbed in hepatic cells, subsequently excreting the small intestine via the biliary tract. Radiopharmaceutical is transferred quickly in the liver by blood, and then some of them are preserved temporarily in the gall, which in turn empty to the small intestine by excitation of foods. A partial radiopharmaceutical directly excretes the small intestine via the biliary tract, and a small number of them excrete in urine by the kidney. The metabolism of radiopharmaceutical in pathological state, containing different types of hepatopathy, biliary atresia, biliary obstruction, etc., is also estimated by this model, but the kinetic parameters in diseases are different with those under normal state. The model for liver-gall is displayed in Fig. 19.3.

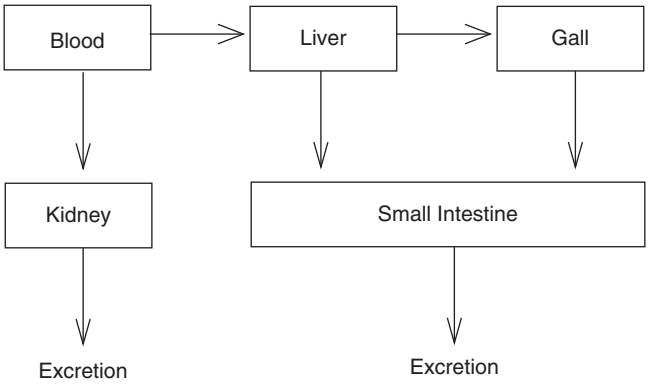

Fig. 19.3 Compartment model for the kinetics of radiopharmaceutical in the liver-gall

The final excretion of radiopharmaceutical from the body confirms with gastrointestinal tract model and kidney-bladder model. Supposing the excretion of radiopharmaceutical at the same way, about 73% of radioactivity is excreted to the outside of the body after 3 h for the initial evacuation of the gall. Nine hours later, 73% of residual radioactivity is excreted to the outside again. Finally, 24 h later, radiopharmaceutical can be excreted completely outside of the body. The primary evacuation of radiopharmaceutical from the gall may be triggered by high-fat diet and cholecystokinin.

19.3 Radiation Protection and Safety in Nuclear Medicine

In both diagnostic and therapeutic nuclear medicine, the patient becomes a source of radiation not only for him/herself but also for the general public and occupational workers. Adequate safeguards against radiation exposure become necessary to minimize the radiation risk to patients, the public, and occupational workers.

19.3.1 Radiation Safety of the Patients

19.3.1.1 Effective Dose for Nuclear Medicine Examinations

It is well recognized that the increasing use of diagnostic imaging procedures has led to a significant increase in the collective radiation dose to the public over the past several decades. Radiation exposure due to medical services consists of nearly 50% of the per capita radiation dose, comparing to that of 15% in the early 1980s [26]. This increased dose has gained concern from the public and regulatory department. As an estimate indicator of potential harm from cancer and hereditary effects, effective dose has been widely used as an important index in determining the appropriateness of medical services related with ionizing radiation [27].

Table 19.4 Representative patient effective doses for various nuclear medicine examinations [28]

Examinations	Radiopharmaceutical	Administered activity (MBq)	Effective dose	
			mSv/MBq	mSv
Brain	^{18}F-FDG	370	0.019	7.0
Biliary	^{99m}Tc-DISIDA	185	0.017	3.1
Bone	^{99m}Tc-MDP	925	0.0057	5.3
Breath test	^{14}C-urea	0.2	0.081	0.02
Cardiac	^{13}N-NH_3	740	0.002	1.48
	^{15}O-water	740	0.00093	0.69
	^{99m}Tc-MIBI	1100	0.0085	9.4
	^{82}Rb	1480	0.0034	5.03
Cardiac ventriculogram	^{99m}Tc-RBC	1110	0.007	7.8
GI bleeding	^{99m}Tc-RBC	1110	0.007	7.8
Lung perfusion	^{99m}Tc-MAA	185	0.011	2.0
Lung ventilation	^{99m}Tc-DTPA	1300	0.0049	0.2
Parathyroid	^{99m}Tc-MIBI	740	0.009	6.7
Renal	^{99m}Tc-DMSA	370	0.0088	3.3
	^{99m}Tc-DTPA	370	0.0049	1.8
	^{99m}Tc-MAG_3	370	0.007	2.6
Thyroid	^{99m}TcO_4	185	0.013	2.4
	^{123}I-NaI	74	0.011[a]	0.81
	^{123}I-NaI	0.74	0.22[b]	0.16
	^{131}I-NaI	185	0.061[a]	11.3
	^{131}I-NaI	0.37	24[b]	8.88
Tumor	^{11}C-acetate	740	0.0035	2.59
	^{11}C-choline	400	0.0047	1.9
	^{18}F-FDG	370	0.019	7.0
	^{18}F-FET	400	0.017	6.8
	^{18}F-FLT	400	0.016	6.4
	^{18}F-L-dopa	400	0.025	10
	^{18}F-NaF	400	0.024	9.6
	^{111}In-octreotide	170	0.054	9.2
	^{123}I-MIBG	400	0.013	5.2

[a]Thyroid uptake = 0%
[b]Thyroid uptake = 35%

The International Commission on Radiological Protection (ICRP) [28] has published standardized organ dose estimates for hundreds of radiopharmaceuticals and developed tables of effective doses for the reference human models. Representative patient effective doses for various nuclear medicine examinations are presented in Table 19.4.

The mean effective dose for most nuclear medicine examinations falls within the range of 1–10 mSv, comparing with the average annual effective dose from background radiation. Emerging evidence has shown the health risks resulted from high-dose radiation exposures [29]. However, risks associated with imaging-related low dose (<50–100 mSv) do not exist or are too minimal to be detected [30, 31]. Based on the current understanding of radiation-related health risks, the Health Physics Society [32] recommended against quantitative estimation of health risks lower than an individual dose of 50 mSv per year or lower than a dose of 100 mSv during lifetime above the background radiation. Medical imaging is intended to achieve a diagnostic purpose. Making accurate diagnoses and avoiding riskier alternatives of medical examinations should be considered of first importance. As such, it is recommended to decrease radiation exposure below the required level [33].

19.3.1.2 Pediatric Radiopharmaceutical Activity

The benefits of nuclear medicine examinations to the care of children have been well established. Meanwhile there has been an increased level of concern and interest about radiation exposures to children from diagnostic imaging examinations. In pediatric nuclear medicine, the effective dose usually falls within the lower range of radiation exposure of general radiologic imaging studies. Although the radiation level in pediatric nuclear medicine is relatively minimal, reducing the radiation exposure to the lowest reasonably achievable levels is suggested. The dose of radiopharmaceutical activity given to the patients is the major factor affecting the radiation exposure they received.

In late 2010, the Society of Nuclear Medicine and Molecular Imaging, the Society for Pediatric Radiology, and the American College of Radiology jointly published consensus guidelines for pediatric administered radiopharmaceutical activities [34]. It recommends the use of doses calculated using maximum doses, doses by body weight (kg), as well as minimum doses for a number of radiopharmaceuticals (Table 19.5).

The nuclear medicine practitioner is allowed to change the administered activity accordingly. For children with a body weight over 70 kg, it is recommended that the maximum administered activity should not exceed the product of the child's weight and the recommended weight-based administered activity. A fixed maximum administered activity equal to 70 times the recommended weight-based administered activity is preferred by some practitioners [35].

19.3.1.3 Imaging Pregnant Patients

The use of diagnostic imaging during pregnancy is not uncommon in clinical practice [36]. Confusion about the safety of nuclear medicine and computed tomography imaging studies for infants often leads to the missing of useful diagnostic information [37]. The ionizing radiation risk received by the fetus is determined by the gestational age at the time of exposure and the dose. In pregnancy, fetal exposure is determined by the physical and biochemical characteristics of the radioisotope. Table 19.6 presents standardized dose estimates to the embryo/fetus for commonly used radiopharmaceuticals [38].

It is widely accepted that a dose of <50 mGy represents no measurable non-cancer risk to the embryo or fetus at any stage of gestation, such as embryonic death, birth defects, or mental retardation [39, 40]. The range of doses received during nuclear medicine examination is far below the threshold for deterministic effects. The ventilation-perfusion lung scintigraphy is the most commonly applied nuclear medicine examination in pregnant women for pulmonary embolism. It usually causes an embryonic/fetal exposure of less than 5 mGy, which is safe in pregnancy.

Radioactive iodine (^{131}I) readily crosses the placenta and causes damage to fetal thyroid, especially after 10–12 weeks of gestation. Hence, it is not allowed to be applied in pregnant women for either diagnostic or therapeutic purposes [41].

In the recently published clinical practice guidelines, the American College of Obstetricians and Gynecologists Committee [42] has stated that radiation exposure resulted from nuclear medicine or computed tomography scans is lower than the harmful amount for fetus, only with a few exceptions. Pregnant patients can receive additional nuclear medicine examinations if other imaging modalities fail to provide sufficient information. It is important to note that the diagnostic radiation exposure is not a sole factor to determine pregnancy termination.

Table 19.5 North American consensus guidelines for pediatric radiopharmaceutical activities [34]

Radiopharmaceutical	Recommended administered activity (MBq/kg weight)	Minimum administered activity (MBq)	Maximum administered activity (MBq)
^{18}F-FDG	Body: 3.7–5.2	37	M[a]
^{18}F-FDG	Brain: 3.7	37	M[a]
^{18}F-NaF	2.22	18.5	M[a]
^{123}I-MIBG	5.2	37	370
^{99m}Tc-MDP	9.3	37	M
^{99m}Tc-DMSA	1.85	18.5	M[a]
^{99m}Tc-MAG_3	5.55	37	148
$^{99m}TcO_4$ Meckel's diverticulum imaging	1.85	9.25	M[a]

[a]Product of patient's weight and recommended weight-based administered activity

Table 19.6 Absorbed dose estimates to the embryo/fetus per unit activity of radiopharmaceutical administered to the mother [38]

Radiopharmaceutical	Administered activity (MBq)	Absorbed dose (mGy)			
		<3 months	3 months	6 months	9 months
^{18}F-FDG	370	8.14	8.14	6.29	6.29
^{18}F-NaF	400	8.8	6.8	3.0	2.72
^{99m}Tc-DTPA	740	8.88	6.43	3.03	3.48
^{99m}Tc-DTPA aerosol	41	0.24	0.18	0.09	0.12
^{99m}Tc-MAA	222	0.62	0.89	1.1	0.14
^{99m}Tc-MDP	740	4.51	3.99	1.99	1.78
^{99m}Tc-MIBI (rest)	370	5.55	4.44	3.11	1.99
^{99m}Tc-MIBI (stress)	740	8.88	7.03	5.11	3.26
$^{99m}TcO_4$	185	2.04	4.07	2.59	1.72

19.3.1.4 Imaging Lactating Patients

Since the radionuclides may be transferred through milk and give rise to an internal dose in the infant, cautions should be taken when administrating radiopharmaceuticals to patients who are breastfeeding. It is not suggested that all patient should stop breastfeeding or avoiding nuclear medicine examination [43]. Using the effective dose limit of the infant (1 mSv), breastfeeding interruption is proposed to be classified into four types: no interruption, 4-h interruption, 12-h interruption and cessation, and interruptions over 3 weeks (Table 19.7) [28].

If the nuclear medicine examination is required and cannot be postponed, it is recommended that the mother could express breast milk that is enough for use during the breastfeeding interruption before the taking the radiopharmaceutical administration. For radioactive iodine (^{123}I or ^{131}I), patients should be suggested to cease breastfeeding or take an interruption for over 3 weeks.

19.3.2 Radiation Protection and Safety of the Public

Doses to the public from patients who have received nuclear medicine procedures primarily result from external exposure. In general, precautions for the public are not needed following the diagnostic nuclear medicine procedure [44]. However, the exposure due to some therapeutic procedures toward the public and patients' relatives needs to be limited, especially for children and pregnant women.

Radioactive iodine (^{131}I) therapy for thyroid cancer and hyperthyroidism patients who accepted unsealed radionuclides is the major source of exposure to the public and patients' relatives. In other circumstances, pure beta emitters including ^{90}Y and ^{89}Sr are commonly used for therapy and present less potential public risks.

A common question after a radionuclide therapy is whether the patient has to be hospitalized or not and which release criteria should be applied. Currently there is still no harmonization of national regulations and not either of ICRP or International Atomic Energy Agency (IAEA) guidelines. ICRP [45] does not explicitly require hospitalization. IAEA [46] does not suggest to release the patient back to home right after the therapy. Instead, the patient should remain hospitalized for hours to days. The decision should be made individually, and the following factors should be considered, including residual activity, patient's opinion, economical burdens, environmental factors, and the public dose limitation [47, 48].

Both the ICRP [45] and IAEA [46] recommend a dose limit of 1 mSv/year for the public (including friends and acquaintances, casual visitors, work colleagues, and those encountered socially or while traveling), infants, and children. In the USA, the Nuclear Regulatory Commission [49] has amended its regulations from an activity-based limit to a dose-based limit in 1997. The later one is based on the concept that the maximally exposed individual is less likely to pass an effective dose of 5 mSv. Unfortunately, a standardized method to reach these goals is still lacking [47, 48].

In China, the regulatory body states that the retained radioactivity in the patient's body should be no more than 400 MBq before releasing patients from hospital following thyroid therapy using radioactive iodine (^{131}I) [44].

Table 19.7 Recommendations on breastfeeding instructions [28]

Interruption	Radiopharmaceutical
No	^{111}In-octreotide, ^{18}F-FDG, ^{11}C-, ^{14}C-, ^{13}N-, ^{15}O-labeled
4 h	^{99m}Tc-labeled: DISDA, DMSA, DTPA, ECD, MDP, SC, MAG_3, MIBI, RBC $_{(in\ vitro)}$, technegas, tetrofosmin
12 h	$^{99m}TcO_4$, ^{99m}Tc-MAA, -RBC $_{(in\ vivo)}$, -WBC, ^{123}I-OIH, ^{131}I-OIH
>3 weeks	^{123}I-MIBG, ^{131}I-MIBG, ^{123}I, ^{131}I

19.3.3 Radiation Protection and Safety of Occupational Workers

It is important to emphasize the occupational radiation protection in clinical practice as related population are potentially exposed to both external and internal radiation; the latter one usually occurs in cases of accidental intake. Contamination generally leads to negligible exposure to staff if adequate protocols are used. Likewise for internal exposure, the effective dose due to external radiation is usually low.

19.3.3.1 Radiation Exposure During Preparation and Administration of Radiopharmaceuticals

During radiopharmaceuticals preparation, the extremities usually receive high levels of radiation exposure. When the workload is high, or without a proper protection, certain parts of extremities (hands and fingertips) are more likely to receive exposure higher than the limited dose. For the assessment of extremity equivalent dose, the personal dose equivalent, $H_p(0.07)$, at a depth (d) of 0.07 mm is used. Sans-Merce et al. [50] have collected data on extremity dosimetry in 139 technologists from 35 nuclear medicine departments in 7 European countries. The mean, median, and range of $H_p(0.07)$ for ^{99m}Tc and ^{18}F investigations are presented in Table 19.8.

Since radiopharmaceuticals preparation requires a longer time, and contains more steps than administration, the

Table 19.8 The mean, median, maximum, and minimum values of $H_p(0.07)$ of all monitored workers classified per procedure [50]

		Maximum doses from all workers (mSv/GBq)			
		Mean	Median	Minimum	Maximum
^{99m}Tc					
	P	0.4	0.25	0.03	2.1
	A	0.2	0.12	0.01	0.9
^{18}F					
	P	1.2	0.83	0.1	4.4
	A	0.9	0.64	0.1	4.1

P stands for preparation, *A* for administration

hands usually received higher doses per unit activity during preparation than administration. ^{18}F involves higher hand doses per unit activity than ^{99m}Tc because of the higher dose rates at contact. The reported hand doses to the technologists from administration of ^{131}I to patients with thyroid diseases ranged from 0.07 to 0.24 mGy/GBq [51].

Shielding is found to be the most important factor affecting hand dose levels. It is reported that the use of shields provided a reduction of a factor from 2 to 5 for diagnostic procedures [52]. The use of automatic devices to avoid worker manipulation is potentially a very efficient mean of dose reduction, provided that appropriate training was given. Training and education in good practices and the worker's experience level are relevant parameters for dose reduction. All practices should avoid direct contact if possible; good practices also include increasing distances to the sources and fastening the procedures [53].

19.3.3.2 Radiation Doses from Patients to Staff Members and Caregivers

Imaging technologists are exposed to external irradiation while performing various tasks near a postinjection patient while escorting the patient to and from the scanner and while positioning him at the scanner or on the scanner bed. For ^{99m}Tc investigations, an average dose to imaging technologists is of the order of nSv/MBq per procedure [54]. While an annual dose will depend on additional factors including workload, typical values for whole-body dose of about 0.3~0.4 mSv are reported by the IAEA [55]. Imaging personnel working on PET generally receive larger annual doses than those working with gamma cameras and SPECT. Reported doses to PET technologists are around 5 μSv per procedure and around 8 mSv annually [56].

Doses to the ward nursing staff from therapeutic procedures are strongly influenced by required level of care. The estimated dose contribution from ambulant patients is of the order of nSv/day, while for totally helpless patients who require hospitalization and high level of care, it can reach around 100 μSv/day [57].

19.3.3.3 Biological and Clinical Effects in Medical Radiation Workers

Radiation has been employed in clinical field for over ten decades. Internationally, it has been estimated that there are 2.3 million medical radiation workers [58]. Despite the significant prolonging in medical radiation procedures, the time trend effective dose data reassuringly show that occupational exposures of radiologists and radiologic technologists have reduced dramatically. Annual effective doses to radiologists reduced significantly from no more than 5 mSv in the early 1960s to around 0.08~0.23 mSv after 2000 [59]. Average annual estimated badge doses received by radiologic technologists greatly dropped from around 100 mSv before the 1940s to 2.3 mSv since the 1980s [60].

It is important to study occupational radiation-related dose-response and lifetime cancer risk in medical radiation workers. Very recently, two comprehensive and systematic studies have assessed the biological and clinical effects in radiologists [61] and physicians performing fluoroscopically guided interventional procedures [62], respectively. Overall, compared with the psychiatrists who are unlikely to have had occupational radiation exposure, total deaths and deaths from specific causes were not elevated neither in radiologists nor in physicians performing fluoroscopically guided interventional procedures.

To date, there is paucity of studies systematically assessing cancer and related risks in workers performing nuclear medicine procedures. Potential reasons include the short on the related clinical, epidemiologic, and dosimetry data of nuclear medicine workers, as well as the complexity of estimating doses from internal and external radiation exposures [63]. There is an urgent need to have long-term evidence regarding the relationship between nuclear medicine practice and radiation-associated disease risks, including cancers, in nuclear medicine physicians and technologists.

References

1. Kanno I, Miura S, Yamamoto S et al (1985) Design and evaluation of a positron emission tomography: HEADTOME III. J Comput Assist Tomogr 9(5):931–939
2. Kwee TC, Torigian DA, Alavi A (2013) Overview of positron emission tomography, hybrid positron emission tomography instrumentation, and positron emission tomography quantification. J Thorac Imaging 28(1):4–10
3. Berg E, Cherry SR (2018) Innovations in instrumentation for positron emission tomography. Semin Nucl Med 48(4):311–331
4. Volkow ND, Mullani NA, Bendriem B (1988) Positron emission tomography instrumentation: an overview. Am J Physiol Imaging 3(3):142–153
5. Porenta G (1994) Positron emission tomography: physics, instrumentation, and image analysis. Wien Klin Wochenschr 106(15):466–477

6. Budinger TF, Derenzo SE, Huesman RH (1984) Instrumentation for positron emission tomography. Ann Neurol 15(Suppl):S35–S43
7. McLean FC (1963) The use of isotopes in orthopaedics. I. The atomic nucleus and isotopes. J Bone Joint Surg Am 45:1067–1072
8. Gambini DJ. [Basic concepts of radiology physics]. J Radiol. 2010;91(11 Pt 2):1186–1188
9. Casey ME, Hoffman EJ (1986) Quantitation in positron emission computed tomography: 7. A technique to reduce noise in accidental coincidence measurements and coincidence efficiency calibration. J Comput Assist Tomogr 10(5):845–850
10. Trebossen R, Comtat C, Brulon V et al (2009) Comparison of two commercial whole body PET systems based on LSO and BGO crystals respectively for brain imaging. Med Phys 36(4):1399–1409
11. Matheoud R, Goertzen AL, Vigna L et al (2012) Five-year experience of quality control for a 3D LSO-based whole-body PET scanner: results and considerations. Phys Med 28(3):210–220
12. Conti M, Eriksson L, Rothfuss H et al (2017) Characterization of (176)Lu background in LSO-based PET scanners. Phys Med Biol 62(9):3700–3711
13. Shao L, Freifelder R, Karp JS (1994) Triple energy window scatter correction technique in PET. IEEE Trans Med Imaging 13(4):641–648
14. Lupton LR, Keller NA (1983) Performance study of single-slice positron emission tomography scanners by Monte Carlo techniques. IEEE Trans Med Imaging 2(4):154–168
15. Colsher JG (1980) Fully three-dimensional positron emission tomography. Phys Med Biol 25(1):103–115
16. Daube-Witherspoon ME, Muehllehner G (1987) Treatment of axial data in three-dimensional PET. J Nucl Med 28(11):1717–1724
17. Ollinger JM (1996) Model-based scatter correction for fully 3D PET. Phys Med Biol 41(1):153–176
18. Derenzo SE (1980) Method for optimizing side shielding in positron-emission tomographs and for comparing detector materials. J Nucl Med 21(10):971–977
19. Bergstrom M, Eriksson L, Bohm C et al (1983) Correction for scattered radiation in a ring detector positron camera by integral transformation of the projections. J Comput Assist Tomogr 7(1):42–50
20. Kinahan PE, Townsend DW, Beyer T et al (1998) Attenuation correction for a combined 3D PET/CT scanner. Med Phys 25(10):2046–2053
21. Oda K, Toyama H, Uemura K et al (2001) Comparison of parametric FBP and OS-EM reconstruction algorithm images for PET dynamic study. Ann Nucl Med 15(5):417–423
22. Morey AM, Kadrmas DJ (2013) Effect of varying number of OSEM subsets on PET lesion detectability. J Nucl Med Technol 41(4):268–273
23. Chism CB, Ravizzini GC, Macapinlac HA et al (2017) Quantitative comparison between regularized time-of-flight and OSEM PET reconstructions for small 18F-FDG-avid lesions. Nucl Med Commun 38(6):529–536
24. Castro P, Huerga C, Chamorro P et al (2018) Characterization and simulation of noise in PET images reconstructed with OSEM: development of a method for the generation of synthetic images. Rev Esp Med Nucl Imagen Mol 37(4):229–236
25. DeGrado TR, Turkington TG, Williams JJ et al (1994) Performance characteristics of a whole-body PET scanner. J Nucl Med 35(8):1398–1406
26. Linet MS, Slovis TL, Miller DL et al (2012) Cancer risks associated with external radiation from diagnostic imaging procedures. CA Cancer J Clin 62(2):75–100
27. Andersson M, Johansson L, Minarik D, Leide-Svegborn S, Mattsson S (2014) Effective dose to adult patients from 338 radiopharmaceuticals estimated using ICRP biokinetic data, ICRP/ICRU computational reference phantoms and ICRP 2007 tissue weighting factors. EJNMMI Phys 1(1):9
28. ICRP (2008) Radiation dose to patients from radiopharmaceuticals. Addendum 3 to ICRP publication 53. ICRP publication 106. Approved by the commission in October 2007. Ann ICRP 38(1–2):1–197
29. Kamiya K, Ozasa K, Akiba S et al (2015) Long-term effects of radiation exposure on health. Lancet 386(9992):469–478
30. Calabrese EJ, O'Connor MK (2014) Estimating risk of low radiation doses—a critical review of the BEIR VII report and its use of the linear no-threshold (LNT) hypothesis. Radiat Res 182(5):463–474
31. Andersson M, Eckerman K, Mattsson LJS (2017) Lifetime attributable risk as an alternative to effective dose to describe the risk of cancer for patients in diagnostic and therapeutic nuclear medicine. Phys Med Biol 62(24):9177–9188
32. Health Physics Society. Radiation risk in perspective: position statement of the health physics society. http://hps.org/documents/radiationrisk.pdf
33. Hendee WR, O'Connor MK (2012) Radiation risks of medical imaging: separating fact from fantasy. Radiology 264(2):312–321
34. Gelfand MJ, Parisi MT, Treves ST et al (2011) Pediatric radiopharmaceutical administered doses: 2010 North American consensus guidelines. J Nucl Med 52(2):318–322
35. Ayres KL, Spottswood SE, Delbeke D et al (2015) Dose optimization of the administered activity in pediatric bone scintigraphy: validation of the North American consensus guidelines. J Nucl Med 56(9):1391–1394
36. Benson CB, Doubilet PM (2014) The history of imaging in obstetrics. Radiology 273(2S):S92–S110
37. Lazarus E, Debenedectis C, North D, Spencer PK, Mayo-Smith WW (2009) Utilization of imaging in pregnant patients: 10-year review of 5270 examinations in 3285 patients—1997-2006. Radiology 251(2):517–524
38. Williams PM, Fletcher S (2010) Health effects of prenatal radiation exposure. Am Fam Physician 82(5):488–493
39. Wang PI, Chong ST, Kielar AZ et al (2012) Imaging of pregnant and lactating patients: part 1, evidence-based review and recommendations. Am J Roentgenol 198(4):778–784
40. Wang PI, Chong ST, Kielar AZ et al (2012) Imaging of pregnant and lactating patients: part 2, evidence-based review and recommendations. Am J Roentgenol 198(4):785–792
41. ICRP (2000) Pregnancy and medical radiation. Ann ICRP 30(1):iii–viii, 1–43
42. Committee on Obstetric Gynecology Committee Opinion No. 723 (2017) Guidelines for diagnostic imaging during pregnancy and lactation. Obstet Gynecol 130(4):e210–e216
43. Liepe K, Becker A (2016) Excretion of radionuclides in human breast milk after nuclear medicine examinations. Biokinetic and dosimetric data and recommendations on breastfeeding interruption. Eur J Nucl Med Mol Imaging 43(5):805–807
44. Liu L, Liu B, Huang R, Kuang A (2017) Radiation protection and safety of nuclear medicine. Chin J Med Imaging Technol 33(12):102–106
45. ICRP (2004) Release of patients after therapy with unsealed radionuclides. Ann ICRP 34(2):v–vi, 1–79
46. IAEA (2009) Release of patients after radionuclide therapy. Safety report series no. 63. Vienna, Austria
47. Liu B, Peng W, Huang R et al (2014) Thyroid cancer: radiation safety precautions in ^{131}I therapy based on actual biokinetic measurements. Radiology 273(1):211–219
48. Liu B, Tian R, Peng W et al (2015) Radiation safety precautions in ^{131}I therapy of Graves' disease based on actual biokinetic measurements. J Clin Endocrinol Metab 100(8):2934–2941
49. NRC (2008) New NRC guidance on release of patients after ^{131}I treatment. J Nucl Med 49(7):16N

50. Sans-Merce M, Ruiz N, Barth I et al (2011) Recommendations to reduce hand exposure for standard nuclear medicine procedures. Radiat Meas 46(11):1330–1333
51. Leide-Svegborn S (2012) External radiation exposure of personnel in nuclear medicine from ^{18}F, ^{99m}TC and ^{131}I with special reference to fingers, eyes and thyroid. Radiat Prot Dosim 149(2):196–206
52. Sans Merce M, Ruiz N, Barth I et al (2011) Extremity exposure in nuclear medicine: preliminary results of a European study. Radiat Prot Dosim 144(1–4):515–520
53. Kaljevic J, Stankovic K, Stankovic J, Ciraj-Bjelac O, Arandjic D (2016) Hand dose evaluation of occupationally exposed staff in nuclear medicine. Radiat Prot Dosim 170(1–4):292–296
54. Krajewska G, Pachocki KA (2013) Assessment of exposure of workers to ionizing radiation from radioiodine and technetium in nuclear medicine departmental facilities. Med Pr 64(5):625–630
55. IAEA (2005) Applying radiation safety standards in nuclear medicine. IAEA safety report series no. 40. Vienna, Austria
56. Feuardent J, Scanff P, Crescini D, Rannou A (2013) Occupational external exposure to ionising radiation in France (2005-2011). Radiat Prot Dosim 157(4):610–618
57. Mattsson S (2013) Radiation protection in nuclear medicine. Springer, Berlin, pp 1–7
58. Rajaraman P, Doody MM, Yu CL et al (2016) Incidence and mortality risks for circulatory diseases in US radiologic technologists who worked with fluoroscopically guided interventional procedures, 1994-2008. Occup Environ Med 73(1):21–27
59. Yoshinaga S, Mabuchi K, Sigurdson AJ, Doody MM, Ron E (2004) Cancer risks among radiologists and radiologic technologists: review of epidemiologic studies. Radiology 233(2):313–321
60. Simon SL, Weinstock RM, Doody MM et al (2006) Estimating historical radiation doses to a cohort of U.S. radiologic technologists. Radiat Res 166(1):174–192
61. Berrington de Gonzalez A, Ntowe E, Kitahara CM et al (2016) Long-term mortality in 43763 U.S. radiologists compared with 64 990 U.S. psychiatrists. Radiology 281(3):847–857
62. Linet MS, Kitahara CM, Ntowe E et al (2017) Mortality in U.S. physicians likely to perform fluoroscopy-guided interventional procedures compared with psychiatrists, 1979 to 2008. Radiology 284(2):482–494
63. Linet MS, Kim KP, Miller DL, Kleinerman RA, Simon SL, Berrington de Gonzalez A (2010) Historical review of occupational exposures and cancer risks in medical radiation workers. Radiat Res 74(6):793–808

Novel Molecular Probes

20

Min Yang, Yuping Xu, Xinyu Wang, Yu Liu, Yanting Wang, Huimin Zhao, Jie Sheng, and Yaoqi Li

Molecular imaging is important for early disease diagnosis, personalized therapy guidance, and new drug development. Nuclear scintigraphy using SPECT or PET is the widely used example in the clinic. To achieve functional visualization, specific probes are indispensable. For nuclear probes, radionuclides and targeting ligands (small compounds, peptide, affibody, etc.) are the main contents (Fig. 20.1). Some popular radioisotopes are listed in Table 20.1. In this chapter, we focused on ^{18}F-, ^{11}C-, ^{68}Ga-, ^{89}Zr-, ^{64}Cu-, ^{90}Y-, and ^{177}Lu-labeled probes.

20.1 Diagnosis

20.1.1 ^{18}F

Min Yang and Yuping Xu

Fluorine-18 is one of the most suitable radioisotopes for PET. It has favorable nuclear and physical characteristics including clean decay profile (97% positron emission and 3% electron capture), low positron energy (β^+max = 0.64 MeV), and high-resolution PET images with a maximum positron range of 2.4 mm in water. Besides, its half-life (109.8 min) allows multistep synthesis and off-site transport. Meanwhile, fluorine forms stronger bond with carbon (C–F energy bond of 112 kcal/mol) than those of carbon–hydrogen bond (C–H = 98 kcal/mol), which is more thermally stable and oxidation resistant. Therefore, fluorine-18 gained high interest in the field of radiochemistry and nuclear medicine.

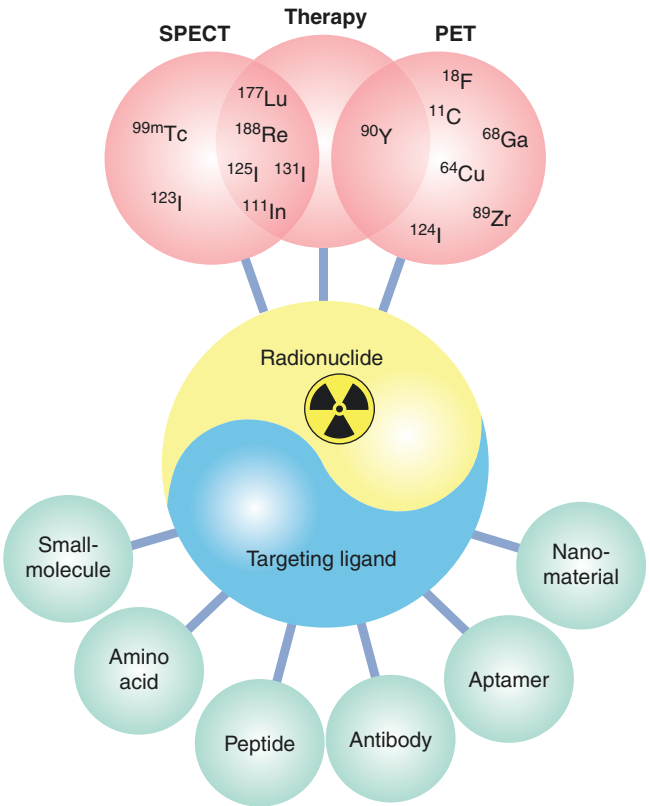

Fig. 20.1 Structure of PET/SPECT imaging and therapy probes

20.1.1.1 Production of ^{18}F

^{18}F can be obtained by an aqueous solution of ^{18}F-fluoride ([^{18}F]F−) or as gaseous [^{18}F]F_2. Due to easy handling and high specific activity (up to 4×10^4 GBq/μmol), no-carrier-added (n.c.a.) ^{18}F fluoride was widely produced through ^{18}O(p, n)^{18}F nuclear reaction on enriched ^{18}O-water in a medical cyclotron. ^{18}F can be incorporated into molecules by radiofluorination chemistry.

M. Yang (✉) · Y. Xu · X. Wang · Y. Liu · Y. Wang · H. Zhao
J. Sheng · Y. Li
Key Laboratory of Nuclear Medicine, Ministry of Health, Jiangsu Key Laboratory of Molecular Nuclear Medicine, Jiangsu Institute of Nuclear Medicine, Wuxi, P.R. China
e-mail: yangmin@jsinm.org

G. Huang (ed.), *Nuclear Medicine in Oncology*, https://doi.org/10.1007/978-981-13-7458-6_20

Table 20.1 Physical characteristics of radionuclides

Nuclide	Half-life	Decay mode	Maximum energy (KeV)
^{18}F	109.7 min	β^+ (97%)	649
^{11}C	20.3 min	β^+	960
^{13}N	10.0 min	β^+	1190
^{15}O	2.0 min	β^+	1700
^{68}Ga	67.8 min	β^+ (90%), EC (10%)	1880
^{64}Cu	12.7 h	EC (41%), β^+ (19%), β^- (40%)	656
^{89}Zr	78.4 h	EC (77%), β^+ (23%)	897
^{177}Lu	159.4 h	β^- (40%)	498
^{90}Y	64.1 h	β^- (100%)	2280
^{223}Ra	11.4 d	α (95.3%)	5750

20.1.1.2 PET Imaging with ^{18}F-Labeled Probes

The best known fluorinated PET probe is 2-[^{18}F]fluoro-2-deoxyglucose ([^{18}F]FDG). Recently, more and more new probes obtain potential medical interest (Table 20.2).

^{18}F-AV45

Alzheimer's disease (AD) is a neurodegenerative disease showing an increasingly high incidence in the older population. The presence of β-amyloid plaques (Aβ plaque) in the brain is a defining pathologic feature for this disease. As such, Aβ deposition appears a suitable target for both early diagnosis and novel AD treatments. Hank F. Kung et al. from the University of Pennsylvania developed a ^{18}F-labeled counterpart (^{18}F-AV45), which is the first FDA-approved commercial radiotracer for Aβ PET imaging in patients (^{18}F-florbetapir commercial name Amyvid™, Eli Lilly) in 2012 owing to its fast kinetics, high selectivity for Aβ plaques, and longer half-life of ^{18}F (110 min) (Fig. 20.2).

Preclinical studies have confirmed the high uptake and rapid washout of ^{18}F-AV45 in the brain of healthy mice. In vitro studies using ^{18}F-AV45 demonstrated the significant differences of plaque labeling between AD brains and healthy brains. An open-label, multicenter trial performed on 16 patients with AD and 16 cognitively healthy controls illustrated that ^{18}F-AV45 was tolerated well and accumulated in cortical regions that were expected to be high in Aβ deposition in AD patients, while minimal accumulation of the tracer was seen in cortical regions of healthy controls. The radioactive uptake of ^{18}F-AV45 in the brain of AD patients showed sustained increases through 30 min after administration and reached an equilibrium in 50 min. Whether using the parametric reference region method (DVR) or the simplified SUVR, PET results showed significant discrimination between patients with AD and healthy controls.

^{18}F-DPA-714 and ^{18}F-FDPA

TSPO is a five-transmembrane domain protein predominantly located on the outer membrane of mitochondria. This protein presents in the peripheral tissues and central nervous system (CNS). TSPO has an important role in the immune and inflammatory response, being upregulated by microglia in neuroinflammatory conditions. Abnormal overexpression of TSPO has been found as a pivotal pathological signal in the progression of many other neurological disorders including Alzheimer's disease, Parkinson's disease (PD), multiple sclerosis, or epilepsy. This characteristic makes TSPO an ideal biomarker for detecting inflammation associated with brain disorders and monitoring treatment response of anti-inflammatory therapies.

^{18}F-DPA-714 is a second-generation tracer for TSPO PET imaging which has shown improved bioavailability, lower nonspecific binding, and higher non-displaceable binding potential. The probe was obtained from the typical nucleophilic substitution, and the non-decay-corrected yield was 16% (Fig. 20.3).

Preclinical studies showed that eightfold higher level of ^{18}F-DPA-714 uptake was observed in the ipsilateral striatum than in the contralateral striatum in rats harboring unilateral quinolinic acid lesions.

Clinical PET studies further demonstrated that ^{18}F-DPA-714 may be useful in assessing the extent of neuroinflammation. Ten patients with probable or definite ALS and eight healthy controls matched for age underwent a PET study. Significant increase of distribution of volume ratio values corresponding to microglial activation was found in the ALS sample in primary motor, supplementary motor, and temporal cortex. Nine patients with cerebral stroke underwent ^{18}F-DPA-714 PET and magnetic resonance imaging (MRI) between 8 and 18 days after the ictus. An increased uptake of ^{18}F-DPA-714 co-localized with the infarct tissue and extension beyond the region corresponding to the damage in the blood-brain barrier was observed.

To optimize the outcomes of radiolabeled compounds, a fluoroaryl analog of ^{18}F-DPA-714, ^{18}F-FDPA, was prepared by precise radiofluorination of non-activated aromatics with spirocyclic iodonium ylide (SCIDY) precursors, and the radiochemical yield was 45 ± 8% (decay-corrected) accompanying with 96 ± 22 GBq/μmol specific activity (Fig. 20.4).

MicroPET imaging showed that ^{18}F-FDPA rapidly crossed the blood-brain barrier (BBB) and increased to 1.50 ± 0.13 SUV at 3 min p.i., demonstrating 1.6-fold higher peak brain uptake and slow washout (possibly attributed to increased specific and nonspecific binding) in APP/PS1 brain compared with age-matched control.

Table 20.2 Overview of novel ^{18}F-labeled probes developed in recent years

Probe	Structure	Application
^{18}F-Florbetapir[a] (^{18}F-AV45)	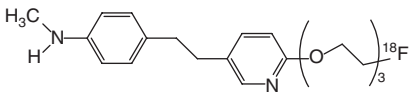	Amyloid-beta imaging
^{18}F-Florbetaben[a]	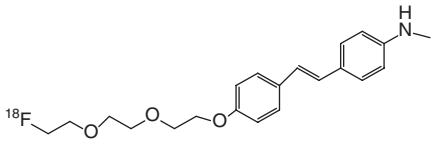	Amyloid-beta imaging
^{18}F-Flutemetamol[a]	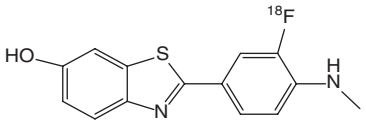	Amyloid-beta imaging
^{18}F-Fluciclovine[a]	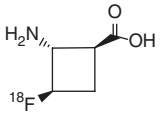	Recurrent prostate cancer
^{18}F-Alfatide	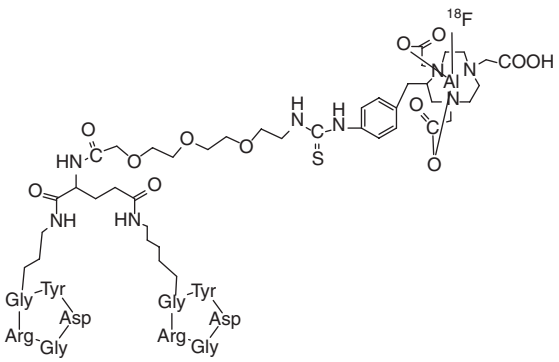	Angiogenesis imaging
^{18}F-BAY864367	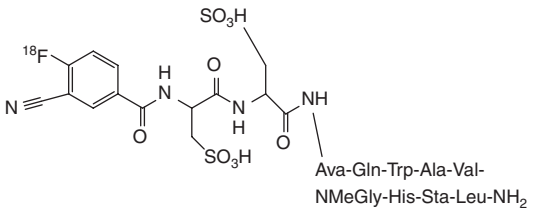	GRPR imaging
^{18}F-PSMA-1007	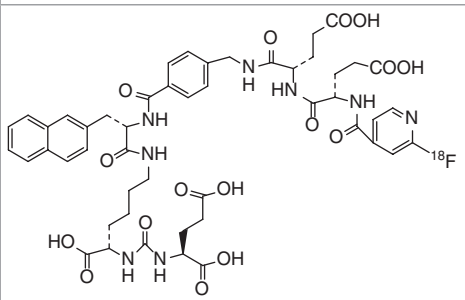	Prostate cancer
^{18}F-ML-10	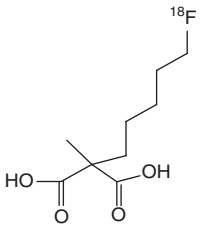	Apoptosis imaging

(continued)

Table 20.2 (continued)

Probe	Structure	Application
^{18}F-DPA-714	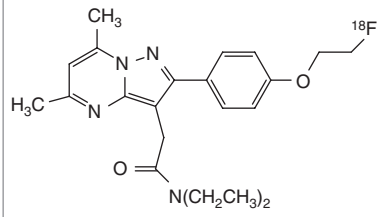	Neuroinflammation
^{18}FAl-NOTA-MATBBN	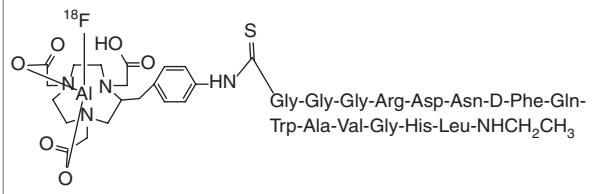	GRPR imaging
^{18}FAl-NOTA-MAL-Cys^{39}-exendin-4	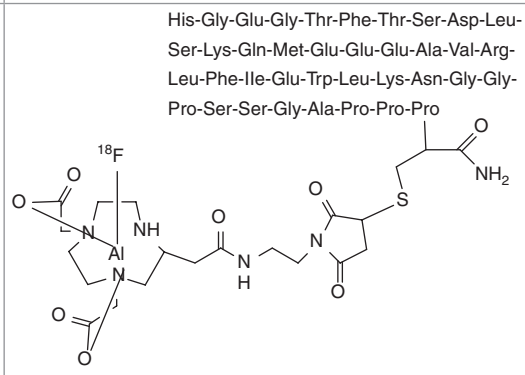	GLP-1R imaging
^{18}FAl-NOTA-MAL-MZHER2	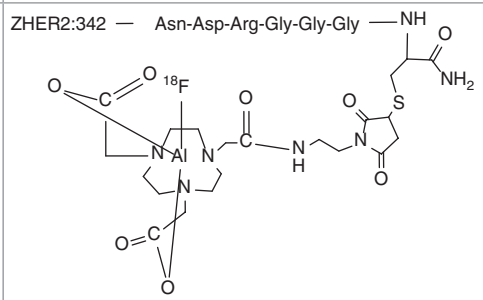	HER2 imaging
^{18}FAl-NOTA-MAL-FSH1	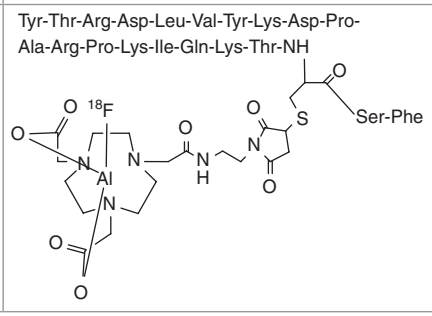	FSHR imaging

[a]FDA Approved

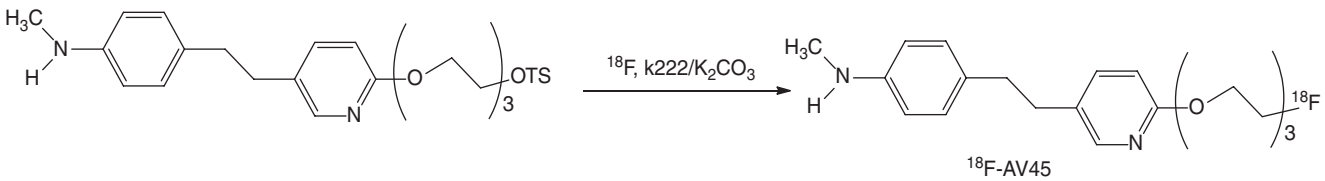

Fig. 20.2 Schematic diagram of synthesis of ^{18}F-AV45

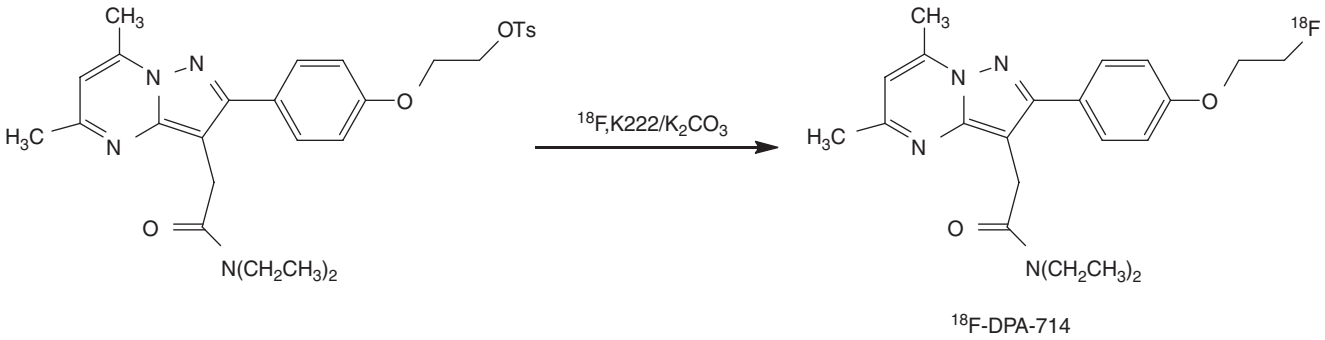

Fig. 20.3 Schematic diagram of synthesis of ^{18}F-DPA-714

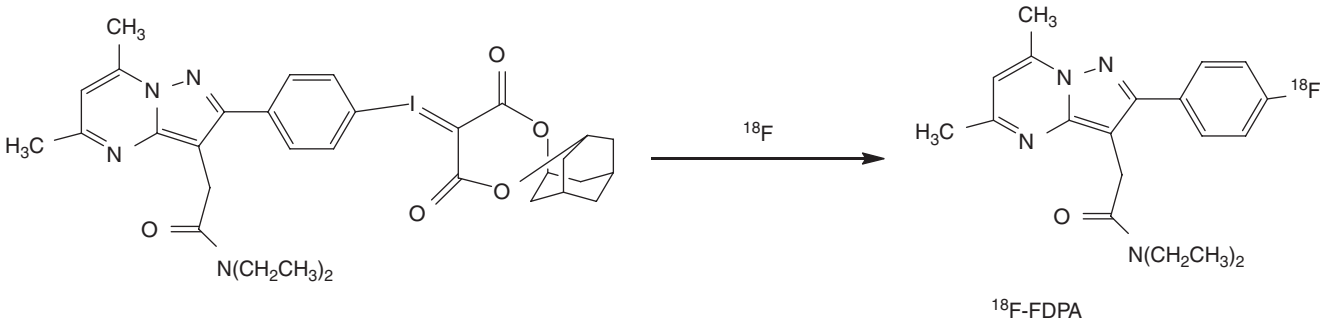

Fig. 20.4 Schematic diagram of synthesis of ^{18}F-FDPA

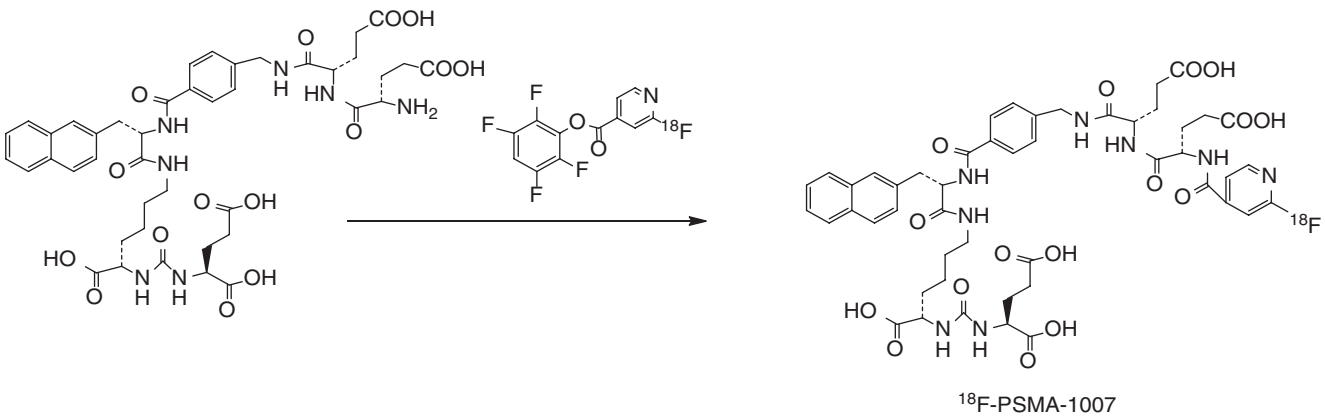

Fig. 20.5 Schematic diagram of synthesis of ^{18}F-PSMA-1007

^{18}F-PSMA-1007

The prostate-specific membrane antigen (PSMA) is overexpressed in most prostate cancers and becomes a versatile target for imaging and therapy. Therefore, several PSMA-targeting tracers have been developed for tumor diagnosis. The urea-based peptidomimetic substances PSMA-11 and its analogs were the candidates for PSMA PET imaging of prostate cancer. Klaus Kopka et al., from Heidelberg University Hospital, designed an ^{18}F-labeled PSMA-targeting radiotracer. A prosthetic group, ^{18}F-Py-TFP, was prepared and then conjugated to the amino group of PSMA-1007 precursor (Fig. 20.5). After HPLC purification and formation, ^{18}F-PSMA-1007 was obtained with the non-decay-corrected yield of 1.5–6.0%.

Preclinical studies showed that high and specific tumor uptake (8.0 ± 2.4 ID%/g) was observed in LNCaP tumor-bearing mice. The first clinical trials on a patient with an elevated prostate-specific antigen levels revealed that PET with ^{18}F-PSMA-1007 detected intraprostatic PSMA accumulation in the peripheral apical zone on the right without any suggestion of tumor spread outside the prostate gland. It clearly underlined successful translation to a clinical setting.

Ten men with biopsy-confirmed high-risk prostate cancer have undergone ^{18}F-PSMA-1007-PET/CT in 2016 by multicenter. Among them, nine patients underwent multiparametric magnetic resonance imaging (mpMRI) in the process of primary diagnosis. Consecutively, radical prostatectomy (RP) histopathology was performed in all ten men. The positive predictive values (PPV) and accuracy for ^{18}F-PSMA-1007-PET/CT and mpMRI were 91% and 93% versus 90% and 87%, respectively. Comparison with RP histopathology demonstrates that ^{18}F-PSMA-1007-PET/CT is promising for accurate local staging of prostate cancer.

^{18}F-Alfatide

Angiogenesis is a key process in tumor growth and metastasis. Targeted imaging of angiogenesis in vivo is an attractive strategy that represents a novel approach to noninvasively monitor angiogenesis and to assess the efficacy of antiangiogenic therapies. Integrin $\alpha_v\beta_3$ are heterodimeric transmembrane glycoproteins and play a key role in the regulation of cellular activation, survival, and migration. Noninvasive imaging of $\alpha_v\beta_3$ expression will be beneficial for evaluating tumor neovascularization and helpful for the diagnosis and treatment of cancers.

The tripeptide sequence of arginine-glycine-aspartic acid (RGD) was a suitable vector for its specific targeting to integrin $\alpha_v\beta_3$. Various ^{18}F-labeled RGD-containing peptide probes have been tested; however, multistep procedures and low yield limited its widespread use in the clinic. Min Yang, from Jiangsu Institute of Nuclear Medicine, cooperated with Xiaoyuan Chen, from NIH, using AlF-labeling strategy to solve this problem. They firstly developed a simple lyophilized kit for labeling PRGD2 peptide (^{18}F-AlF-NOTAPRGD2, denoted as ^{18}F-alfatide). The whole radiosynthesis of ^{18}F-alfatide including purification was accomplished within 20 min with a decay-corrected yield over 40% and radiochemical purity of more than 95% (Figs. 20.6 and 20.7).

The first clinical ^{18}F-alfatide PET/CT scan was performed in a lung cancer patient [1]. ^{18}F-alfatide PET imaging identi-

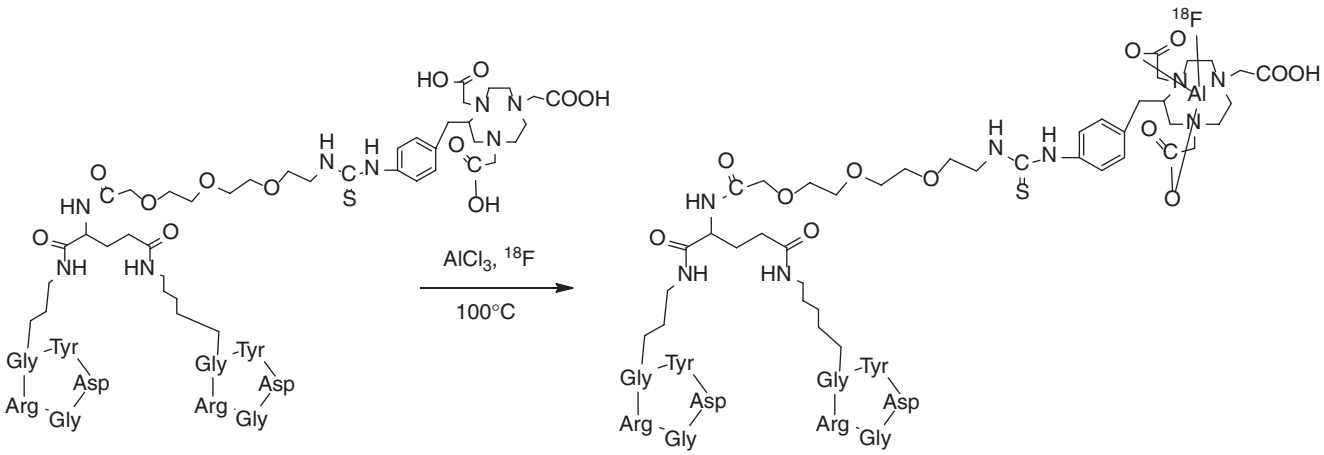

Fig. 20.6 Schematic diagram of synthesis of ^{18}F-alfatide

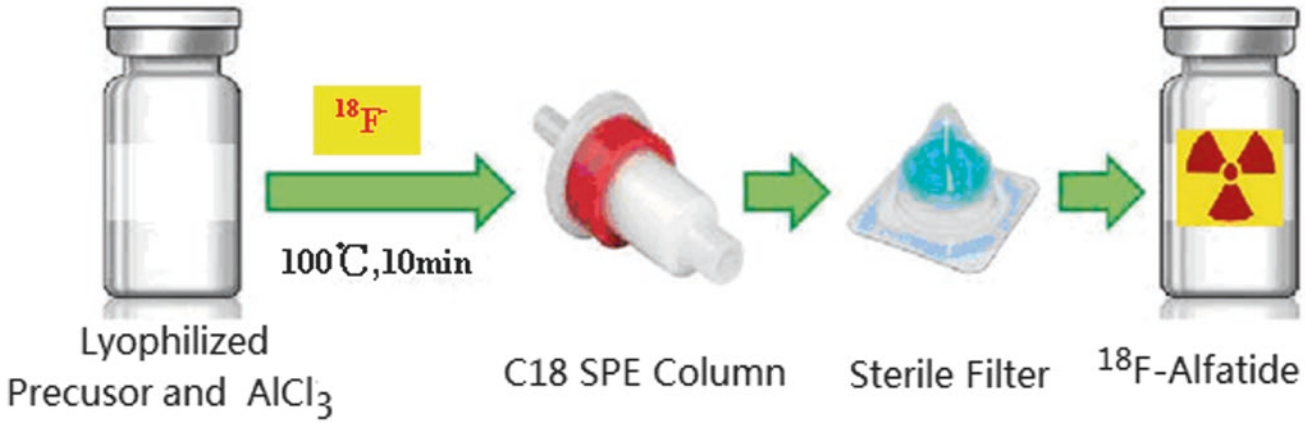

Fig. 20.7 Synthetic procedure for ^{18}F-alfatide

fied all tumors, with mean standardized uptake values of 2.90 ± 0.10. Tumor-to-muscle and tumor-to-blood ratios were 5.87 ± 2.02 and 2.71 ± 0.92, respectively. This first-in-man experience confirms our initial assessment of the suitability of an Al^{18}F-labeled product for in vivo use. Meanwhile, because of the simplicity of the method, additional studies can be easily performed in a single day. Herein, ^{18}F-alfatide was considered as an alternative to ^{18}F-FPPRGD2, which might be used for the assessment of angiogenesis and for planning and response evaluation of cancer therapies.

A further study was performed on 26 patients with suspected lung cancer. The ^{18}F-alfatide PET/CT successfully identified 17 patients with lung cancer, of which 4 patients were true negative (hamartoma) and 5 patients were false positive (4 chronic inflammation and 1 inflammatory pseudotumor). The sensitivity, specificity, positive predictive value (PPV), and negative predictive value (NPV) of ^{18}F-alfatide PET/CT were 100%, 44.44%, 77.27%, and 100%, respectively. In addition, surgery was successfully performed on 16 patients, and pathologic examination confirmed 14 of 152 lymph nodes were positive for metastasis. The sensitivity, specificity, PPV, and NPV of PET/CT for lymph nodes were 92.86%, 95.65%, 61.90%, and 99.25%, respectively. Taken together, these data strongly confirmed that ^{18}F-alfatide PET/CT was safe and effective in suspected lung cancer detection. In another study, static PET imaging of ^{18}F-FDG and ^{18}F-alfatide was performed on nine cancer patients with brain metastases. The results showed that all of the 20 brain lesions could be detected by ^{18}F-alfatide, while ^{18}F-FDG and CT detected only 10 and 13 lesions, respectively (Fig. 20.8) [2]. Thus, ^{18}F-alfatide has potential value in the diagnosis of tumor brain metastasis.

To validate the role of ^{18}F-alfatide in detecting tumor bone metastasis, 30 cancer patients received ^{18}F-FDG and ^{18}F-alfatide PET/CT scan (Fig. 20.8). The results showed that ^{18}F-alfatide had better contrast and higher sensitivity (92%) than ^{18}F-FDG (77%) in detecting bone metastasis [3] especially in the detection of osteoporosis (70% vs. 53%) and bone marrow metastasis (98% vs. 77%). In conclusion, ^{18}F-alfatide PET/CT can be used in the detection of skeletal and bone marrow metastases of cancer, with a nearly 100% sensitivity in osteolytic, mixed, and bone marrow lesions.

Another study was conducted to demonstrate the value of ^{18}F-alfatide in assessing the sensitivity of concurrent chemoradiotherapy (CCRT) in patients with newly diagnostic glioblastoma multiforme (GBM). Twenty-five newly diagnosed GBM patients underwent ^{18}F-alfatide PET/CT during the baseline (T1) assessment and in the third week (T2) following the start of CCRT. Unexpectedly, all GBM residual lesions could be visualized. And both pretreatment

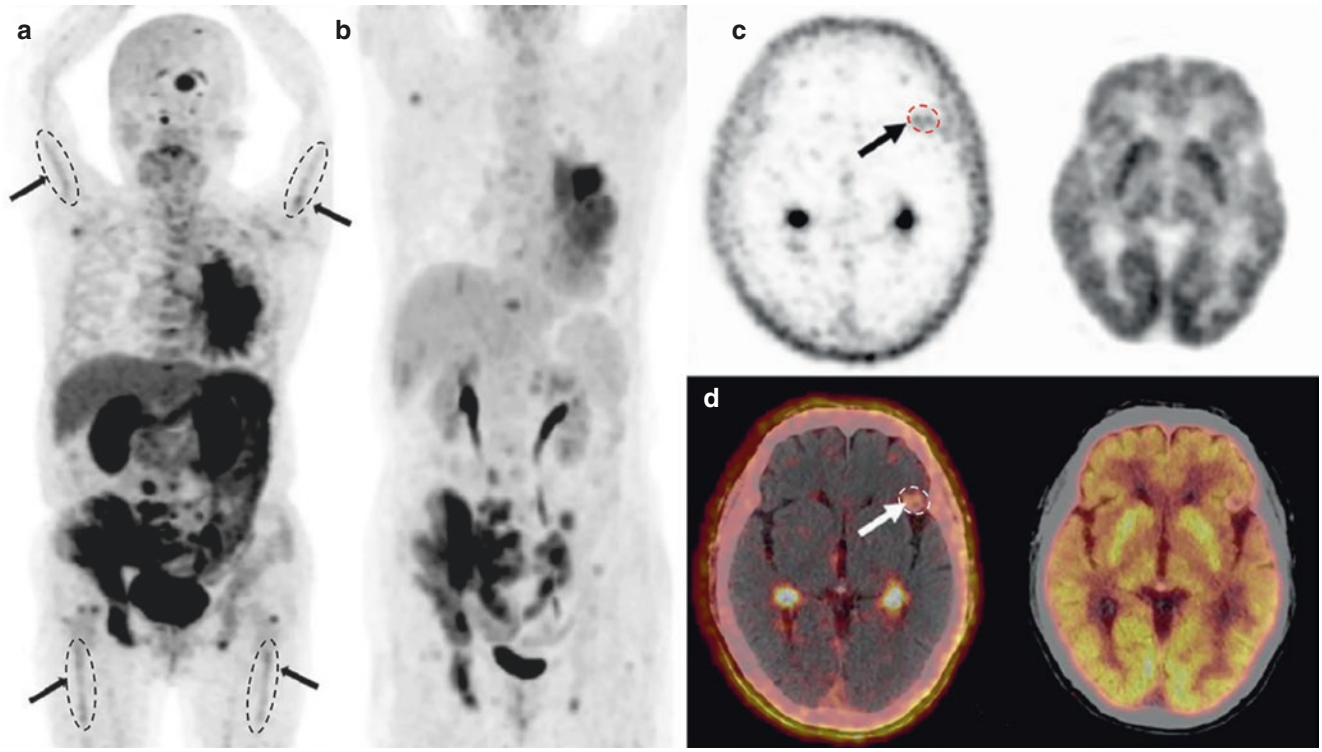

Fig. 20.8 ^{18}F-alfatide (**a**) and ^{18}F-FDG (**b**) PET images of a 68-year-old female patient with lung cancer. Besides the primary tumor in the left lung and multiple bone metastases, the abnormality in bone marrow cavities was also detected by ^{18}F-alfatide PET, which was not shown in ^{18}F-FDG PET. Arrows point to bone marrow cavities. ^{18}F-Alfatide (**c**) and ^{18}F-FDG (**d**) PET/CT images of a 48-year-old male lung cancer patient with left frontal lobe metastasis. Arrows point to brain metastatic lesion

SUVmaxT1 and intra-treatment SUVmaxT2 and T/NTT2 could successfully predict the treatment sensitivity of CCRT. These results indicated that ^{18}F-alfatide PET/CT can achieve the noninvasive visualization of GBM lesions and predict the sensitivity of CCRT within 3 weeks after treatment initiation.

^{18}F-BAY864367

Gastrin-releasing peptide receptor (GRPR) is a G-protein-coupled receptor. It is a potential target for the specific diagnosis and therapy of prostate cancer. Bombesin is a natural GRPR ligand consisted of a 14-amino acid neuropeptide. Michael Honer et al. discovered a newly ^{18}F-labeled bombesin analog ^{18}F-BAY864367 (Fig. 20.9).

Preclinical studies showed that the radioactive uptake of ^{18}F-BAY864367 was significantly higher than that of ^{18}F-fluoroethylcholine and ^{18}F-FDG in prostate cancer xenograft models. In a prospective clinical trial, five patients with primary prostate cancer and five patients with prostate-specific antigen recurrence after radical prostatectomy underwent the examination of ^{18}F-BAY864367 PET/CT. The imaging showed positive lesions in three of the five primary patients and two of the five recurrence patients, with an average tumor-to-background ratio of 12.9 ± 7.0. Among the three patients with radioactive uptake in the primary prostate cancer, the ratio of malignant prostate tissue to normal prostate tissue was 4.4 ± 0.6. These results demonstrated the potential of gastrin-releasing peptide receptor imaging in prostate cancer [4].

^{18}F-Labeled Exendin-4

Endogenously produced GLP-1 interacts with GLP-1 receptor (GLP-1R) to control the production of insulin in response to ingestion of food. GLP-1R exists in pancreatic β-cells and insulinoma and is also expressed in injured myocardium. Thus, GLP-1R is a potential target.

GLP-1 is unstable, while exendin-4 is an agonist of GLP-1R and exhibits great affinity to the receptor with 53% human homologous with GLP-1. Furthermore, it is more resistant to the DPP-IV digestion than GLP-1. Kiesewetter initially modified exendin-4 by adding a cysteine at the C-terminus and labeled with ^{18}F by conjugated with a prosthetic group ^{18}F-FBEM. The resulting probe, ^{18}F-FBEM-Cys^{40}-exendin-4, had significantly higher uptakes in GLP-1R-positive insulinoma xenografts. In spite of these encouraging data, multistep synthetic procedures including twice HPLC purification limited their widespread use in the clinic. Then they prepared [^{18}F]AlF-NOTA-MAL-Cys^{40}-exendin-4. The radiochemical yield was 23.6 ± 2.4%, and the tracer displayed similar biological properties compared to ^{18}F-FBEM-Cys^{40}-exendin-4 (Fig. 20.10).

The 9-amino acid sequence (Pro-Ser-Ser-Gly-Ala-Pro-Pro-Pro-Ser) at C-terminal was not necessary for the specificity and biological activity of exendin-4. In addition, serine has little differences with cysteine except for the hydroxy and sulfhydryl group. Xu et al. from Jiangsu Institute of Nuclear Medicine has confirmed that the replacement of ser^{39} with cys^{39} could provide a unique site for attachment of radiolabeled thiol-reactive groups (such as ^{18}F-FBEM) with little impact on the binding affinity to GLP-1R. Preclinical study showed that after the injection of ^{18}F-FBEM-Cys^{39}-exendin-4, the GLP-1R-positive INS-1 insulinoma could be clearly detected with good contrast, while the GLP-1R-negative MDA-MB435 breast tumor was almost invisible. At the same time, the results of this study indicated that ^{18}F-FBEM-Cys^{39}-exendin-4 may have lower abdominal backgrounds and better contrast compared to ^{18}F-FBEM-Cys^{40}-exendin-4, which may facilitate the diagnosis of tumors.

To accelerate the translation of radiolabeled exendin-4 in clinic, Min Yang, from JSINM, developed NOTA-MAL-conjugated Cys^{39}-exendin-4 and labeled the compounds using the AlF-labeling technology. The tracer, [^{18}F]AlF-NOTA-MAL-Cys^{39}-exendin-4, can be obtained within 30 min with a yield of nearly 20% and radiochemical purity of >95% without HPLC purification [5]. It showed high tumor uptake and highly selective GLP-1R tissue uptake (INS-1 tumor, lung, and pancreas). The favorable preclinical data suggested that the tracer may be a potential GLP-1R radiotracer for the noninvasive visualization of insulinoma in vivo (Fig. 20.11).

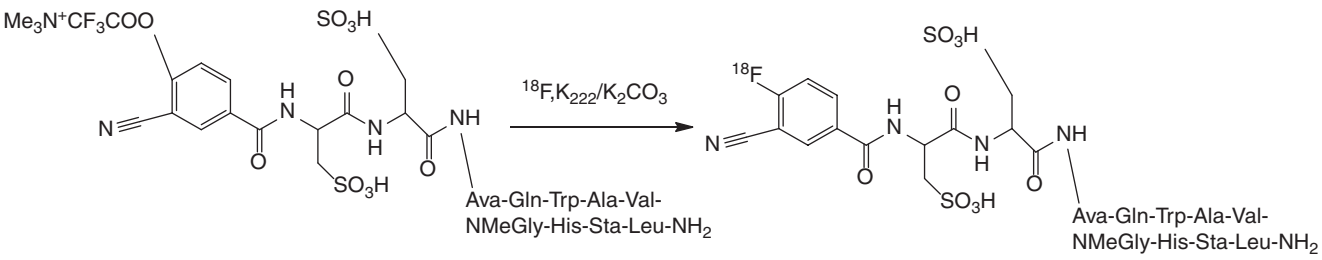

Fig. 20.9 Schematic diagram of synthesis of ^{18}F-BAY864367

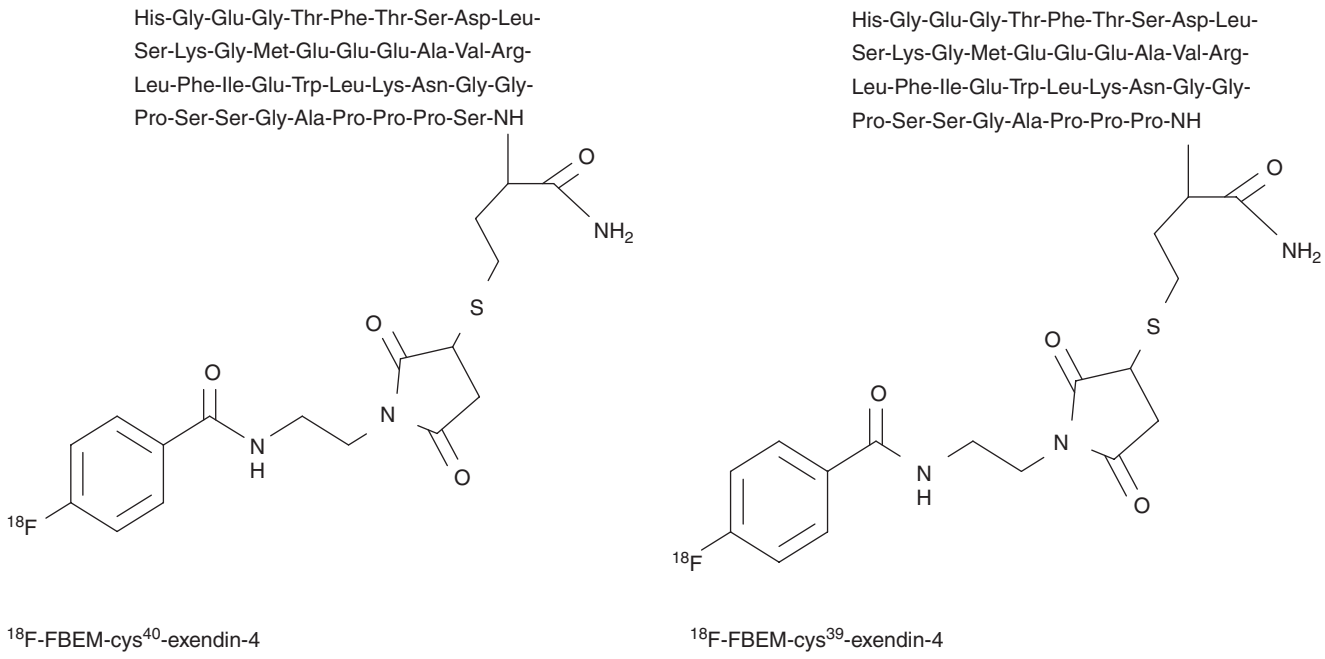

Fig. 20.10 Structure of ^{18}F-FBEM-Cys$^{39/40}$-exendin-4

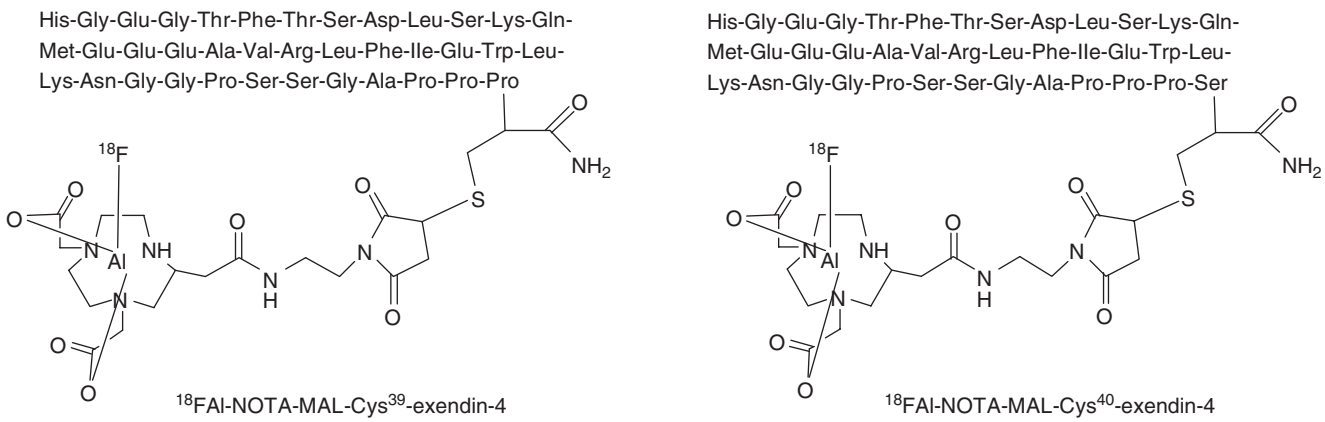

Fig. 20.11 Structure of [^{18}F]AlF-NOTA-MAL-Cys$^{39/40}$-exendin-4

Besides the insulinoma, [^{18}F]AlF-NOTA-MAL-Cys^{39}-exendin-4 showed great promise for monitoring functional pancreatic beta-cells. The pancreas of healthy rats was readily visualized after administration of ^{18}FAl-labeled Cys^{39}-exendin-4, whereas the pancreas of diabetic rats, as well as those from rats co-injected with excess of unlabeled peptides, was barely visible by microPET. Recently, the corresponding lyophilized kit for labeling was undergone by JSINM.

^{18}F-ML-10

Apoptosis is a fundamental biological process of regulated cell death and plays a vital role in many disorders. Several probes have been designed for the detection of apoptosis-associated cell-altering complexes. Among which ^{18}F-ML-10 was the first clinical stage PET probe. The radiosynthesis scheme of ^{18}F-ML-10 was shown in Fig. 20.12. ^{18}F-ML-10 was synthesized from its precursor, ML-10-mesylate, by a nucleophilic substitution reaction. The yield was 30–40% after purification, and the overall time required for radiolabeling was about 75 min.

^{18}F-ML-10 exhibited reliable dosimetry, biodistribution, stability, and safety in vivo. PET imaging of neurovascular apoptosis has been achieved in patients with acute ischemic stroke. ^{18}F-ML-10 PET imaging has the ability to provide early monitoring of the treatment efficacy of whole-brain radiation therapy for the patients with tumor brain metastases, which can further predict the significant anatomical

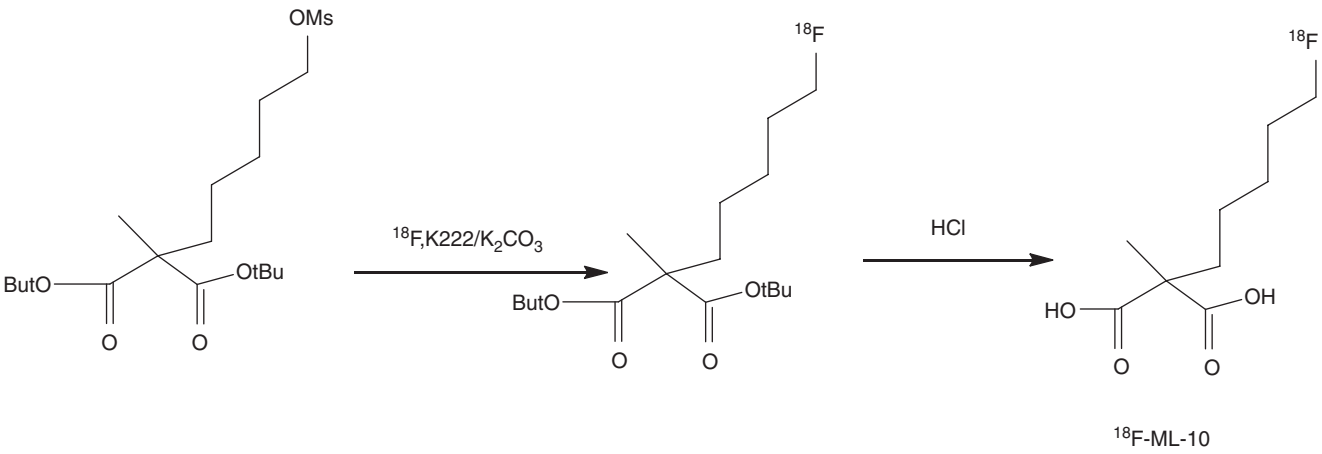

Fig. 20.12 Schematic diagram of synthesis of ^{18}F-ML-10

changes on MRI 2 months later. In a newly diagnosed GBM patient, ^{18}F-ML-10 PET was performed before the start of the treatment (baseline) and in 3 weeks following the whole-brain radiation therapy. The results showed that the radioactive uptake of ^{18}F-ML-10 decreased at the sites with the greatest baseline uptake, but the uptake around the tumor increased at the early treatment time point. The clinical experience of this new probe is currently being further expanded.

20.1.2 ^{11}C

Min Yang and Yanting Wang

^{11}C can be produced in-house using a medical cyclotron. With the short half-life ($T_{1/2}$ = 20.38 min) and emitted β$^+$ (the maximum energy of the positrons is 0.96 MeV), ^{11}C offers the following advantages: lower radiation dose, more injections within the same day, and lower environmental exposure levels. In addition, the carbon atom is widely present in all kinds of molecules such as natural products, synthetic compounds, peptides, and proteins. Radiolabeling carbon-11 to a compound will not change the biological or pharmaceutical properties of that.

20.1.2.1 Radiolabeling of ^{11}C

$^{11}CO_2$ is the most primary labeling precursor, and ^{11}C-labeled synthetic intermediates can be prepared with that (Fig. 20.13). $^{11}CH_3I$ is the most versatile intermediates. It can be synthesized via two distinct methods: gas phase method and wet chemistry route. $^{11}CH_3I$ has been used extensively as an alkylating agent for carbanions and heteroatom nucleophiles. More recently, $^{11}CH_3I$ was used as electrophile in several palladium-mediated cross-coupling reactions to form distinct ^{11}C–C bonds. Finally, $^{11}CH_3I$ is

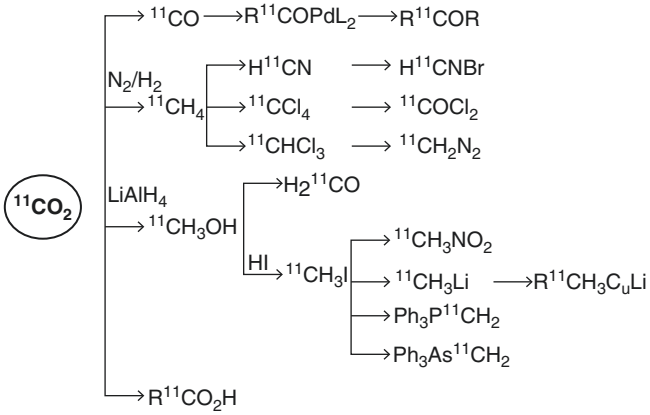

Fig. 20.13 The process of producing intermediates with $^{11}CO_2$ as raw material

needed for the preparation of other labeling precursors such as $^{11}CH_3Li$, $^{11}CH_3NO_2$, $Ph_3P^{11}CH_2$, and $Ph_3As^{11}CH_3$.

20.1.2.2 PET Imaging with ^{11}C-Labeled Probes

^{11}C-probe PET has been used for diagnostic and monitoring anticancer therapies. Main ^{11}C-labeled probes are listed in Table 20.3.

Dopamine Receptor Imaging Agents

Dopamine receptor imaging is the hotspot in molecular and nuclear medicine. In 1983, Wagner HN successfully used ^{11}C-NMSP for D2 receptor PET imaging in human living brain for the first time. ^{11}C-NMSP can be synthesized by using the N-alkylation reaction of spiroperidol and ^{11}C-CH_3I. It can pass through the blood-brain barrier (BBB) and has high affinity to dopamine D2 receptor [6]. ^{11}C-NMSP is suitable for diagnosis of neuropsychiatric diseases such as Parkinson's disease (PD), Huntington's chorea, and multiple system atrophy (MSA). In addition, ^{11}C-NMSP is also used for 5-serotonin receptor (5-HT2) imaging.

Table 20.3 Overview of some ^{11}C-labeled probes developed in recent years

Target	Probe		Application
	Name	Structure	
Dopamine receptor	^{11}C-NMSP	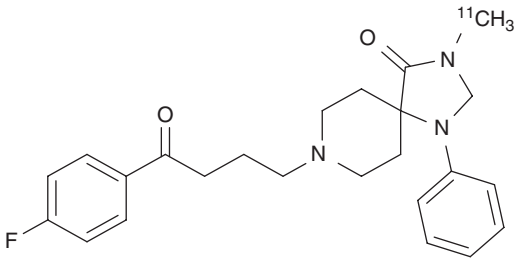	Mental and neurological diseases
	^{11}C-Raclopride	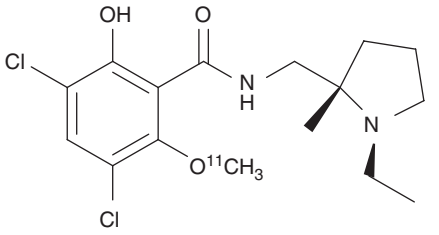	Mental and neurological diseases
Opiate receptor	^{11}C-Carfentanil	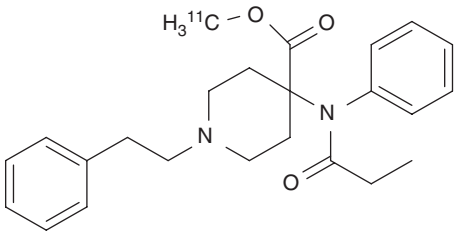	Central and peripheral nervous system
5-HT receptor	^{11}C-WAY-100635 *N*-(2-[4-(2-methoxyphenyl)-1-piperazinyl]ethyl-*N*-(2-pyridinyl) cyclohexanecarboxamide)	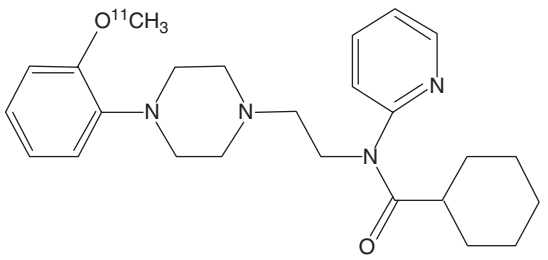	Central nervous system
Benzodiazepine receptor	^{11}C-Flumasini	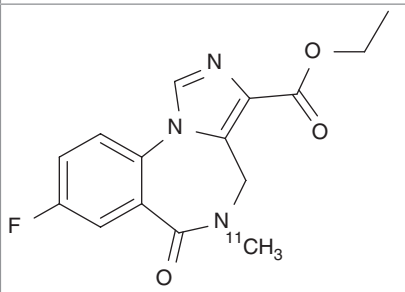	Epileptic lesions and genetic chorea
EGFR receptor	^{11}C-PDl53035 AG1517 (4-(3-bromoanilino)-6,7-dimethoxy-quinazoline)	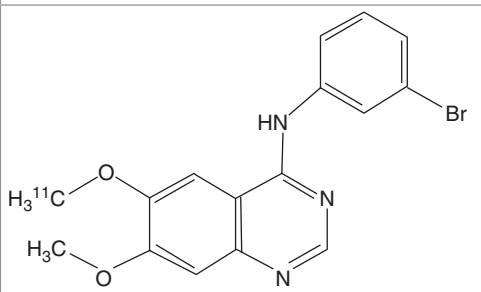	Cancers of epithelial origin

(continued)

Table 20.3 (continued)

Target	Probe		Application
	Name	Structure	
Catecholamine	^{11}C-mHED (^{11}C-meta-Hydroxyephedrine)	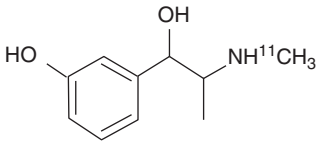	Cardiac sympathetic nerve
	^{11}C-EPI (*R*-(−)-^{11}CEpinephrine)	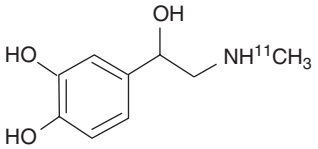	Cardiac sympathetic nerve
	^{11}C-PHEN (1*R*-^{11}C-Phenylephrine)	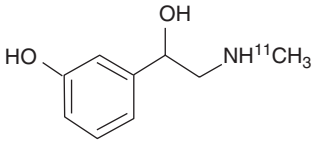	Cardiac sympathetic nerve
	^{11}C-NE (norepinephrine)	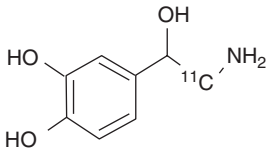	Cardiac sympathetic nerve
	^{11}C-MDA (*N*-^{11}CCH3-Dopamine)	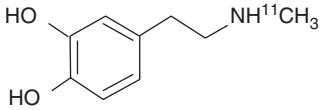	Cardiac sympathetic nerve
Aβ-Amyloid	^{11}C-BTA-1 (Methylamine benzothiazole)	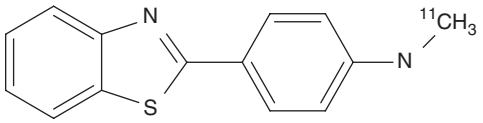	AD (Alzheimer' s disease)
Choline	^{11}C-Choline	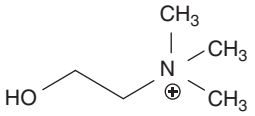	Brain tumors, prostate cancer, and breast cancer
Phospholipid	^{11}C-Acetate (^{11}C-CA)	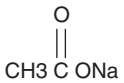	The oxidative metabolism of myocardium
Amino acid	^{11}C-L-MET	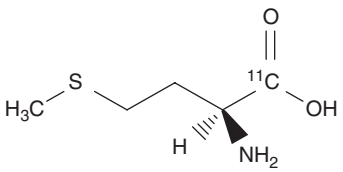	Brain, head and neck, lung and breast cancer
	^{11}C-L-Tyrosine	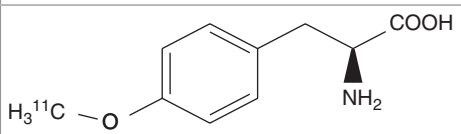	Brain, head and neck, lung and breast cancer
Fatty acid	^{11}C-palmitate (^{11}C-PA)	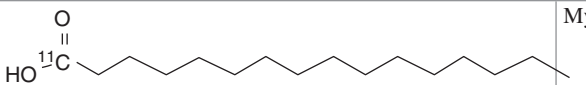	Myocardium
Glucose	[1,2,3-$^{11}C_3$]-glucose	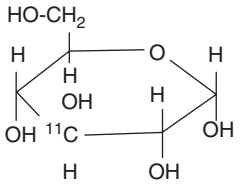	Metabolic research

^{11}C-Raclopride [7] is a specific antagonist of central dopamine D2 receptor. It has higher selectivity and affinity to the receptor. The ratio of striatum to cerebellum is 10 at 30 min after administration. Studies have shown that D2R was upregulated in early-stage PD, while D2R was not upregulated in the striatum of PD patients treated with levodopa for a long time.

Compared with dopamine receptor, the change of DAT (dopamine transporter) is earlier, more direct, and more sensitive. It plays an important role in controlling dopamine release. ^{11}C-CFT is the typical ligand of DAT. Chetti et al. used ^{11}C-CFT to monitor the denaturation of dopamine system in PD. It was found that ^{11}C-CFT binding was reduced in the striatum.

Opiate Receptor Imaging Agents

Opiate receptors are widely expressed in the central nervous system, peripheral nervous system, endocrine system, and gastrointestinal tract. They are divided into six subtypes and related to pain, respiration, thermoregulation, exercise behavior, and other physiological functions. ^{11}C-GR89696 is an ^{11}C-labeled κ receptor imaging agent. It has been shown that approximately 5.4% of radioactivity was concentrated in the brain at 5 min after injection and the ratio of the brain to cerebellum was 7.8 at 90 min. It was indicated that the uptake of ^{11}C-GR89696 was related to the density of κ receptor. ^{11}C-Carfentanil is an ^{11}C-labeled μ receptor imaging agent, which is more uptake in the brain of epilepsy patients than in normal people.

5-HT Receptor Imaging Agents

5-HT receptor (5-HT) is closely associated with many psychiatric disorders. For 5-HT1A receptor PET imaging, ^{11}C-WAY-100635 is commonly used. The human brain imaging showed that the medial cortex/cerebellum ratio was 3. For 5-HT2A receptor PET imaging, ^{11}C-ketoselin and ^{11}C-NMSP are commonly used.

Benzodiazepine Receptor Imaging Agents

The benzodiazepine receptors are only found in the central nervous system. The changes in the density of benzodiazepine receptors were associated with anxiety, insomnia, epilepsy, and chorea. Flumazenil is a benzodiazepine receptor antagonist. ^{11}C-flumazenil [8] is mainly used for PET imaging of epileptic lesions and genetic chorea. PET imaging with ^{11}C-flumazenil can reflect the density of the GABA receptor. Thus, it can contribute to study the pathological basis of epilepsy and the mechanism of antiepileptic drugs.

EGFR Receptor Imaging Agents

Several cancers (lung, breast, and bladder) of epithelial origin have a relatively high expression with EGFR. So, the inhibitor of EGFR is an attractive tool for cancer therapy. ^{11}C-PDl53035 can specifically accumulate in the tumor tissue of non-small cell lung cancer (NSCLC). The uptake of tumor is positively correlated with the EGFR protein expression level and low background radioactivity in the chest.

^{11}C Labeling Catecholamine

Catecholamine is a cardiac sympathetic neurotransmitter, which belongs to adrenergic receptor agonist. It includes norepinephrine (NA), adrenaline (ADR), dopamine (DA), and so on.

^{11}C-labeled cardiac sympathetic nerve imaging agents mainly include ^{11}C-mHED, ^{11}C-EPI, ^{11}C-PHEN, ^{11}C-NE, ^{11}C-MDA, and ^{11}C-GB67. They are prepared by a carbon-11 methyl-substituted catecholamine amino hydrogen atom. HED is an analog of norepinephrine, which has a high uptake in heart and adrenal medulla. ^{11}C-HED can not only be used for imaging of cardiac innervation but also for neuroblastoma. Compared with the ^{123}I-MIBG, ^{11}C-HED imaging was more convenient; the tumor was clearly seen at 5 min.

^{11}C Labeling β-Amyloid

The senile plaque is mainly composed of Aβ, which is an important molecular marker of AD. It is also the gold standard for clinical autopsy and biopsy diagnosis of AD.

Due to the fat solubility (log P = 2.7), affinity constant (Ki = 11 nm), and rapid clearance in the brain, ^{11}C-BTA-1 is an ideal Aβ imaging agent. Klunk et al. found that radioactivity was obviously retained in the related areas of amyloid deposition and the uptake of frontal cortex was the highest. Besides, the study of AD and healthy individuals showed that ^{11}C-BTA-1 remained in the corresponding lesion area of AD and the distribution volume ratio (DVR) of AD was higher than that of healthy.

^{11}C Labeling Choline

Based on the biosynthesis of phosphatidylcholine and the biosynthesis of phospholipid-rich membranes, ^{11}C-choline [9] is used as a cancer imaging PET tracer. As a PET imaging agent, it can effectively differentiate brain tumor, lung cancer, esophageal cancer, colon cancer, prostate cancer, bladder cancer, and so on. Compared with ^{18}F-FDG, ^{11}C-choline has clearer images of tumor, lower radioactivity in normal tissues, and shorter examination time. At the same time, tumor and metastases in the pelvis can be observed. For patients with glioma after treatment, ^{11}C-CHO can not only detect postoperative residual lesions but also monitor the necrosis and recurrence of radiotherapy.

^{11}C Labeling Phospholipid

^{11}C-CA is used to evaluate the oxidative metabolism of myocardium. In the infarcted myocardium, the uptake and clearance of ^{11}C-CA decreased, indicating a decrease of oxygen consumption in the myocardium. Because acetate is a pre-

cursor of amino acid synthesis, it can also be used for the diagnosis of tumors. Liu et al. used ^{11}C-CA for PET imaging with 513 patients. The diagnostic sensitivity was meningioma 97%, nasopharyngeal carcinoma 93%, lymphoma 85%, non-small cell lung cancer 81%, and renal cell carcinoma 80%, respectively. Ho et al. used ^{11}C-sodium acetate for PET imaging on 57 patients with hepatocellular carcinoma (HCC). The diagnostic sensitivity for HCC was 87.3%, while that of ^{18}F-FDG was only 47.3%.

^{11}C Labeling Amino Acid

^{11}C-MET has been used for the classification of tumors and diagnosis of some neurological diseases. It is mainly used for reflecting the amino acid transport activity. Besides, it can indirectly reflect the protein synthesis. Compared with ^{18}F-FDG, ^{11}C-MET can sensitively reflect the change of amino acid metabolism and protein synthesis in tissue cells, T/NT is higher, and imaging is clearer. It is significant that ^{11}C-MET is not concentrated in areas of inflammation. Further, it is easy to distinguish between tumor and inflammation [10].

Because the metabolite of carbon dioxide can be quickly eliminated and its metabolites have little effect on the radioactivity of synthetic proteins, ^{11}C-tyrosine [11] mainly reflects the synthesis of protein in vivo and can be used to determine the rate of protein synthesis (PSR). It has been used in a variety of tumor PET imaging studies. Meanwhile, it demonstrated the superiority of distinguishing tumor and inflammation.

^{11}C Labeling Fatty Acid

^{11}C-PA and ^{11}C-CA were both excellent as myocardial metabolic imaging agents.^{11}C-CA is involved in the oxidation process in vivo and used to determine myocardial oxygen consumption in the clinic. ^{11}C-CA neither participates in beta oxidation of fatty acids nor reflects the oxidation process and oxidation rate. However, ^{11}C-PA can make up for this deficiency. PET imaging showed that the myocardial non-uptake of ^{11}C-PA is a sign of loss of viability of cardiomyocytes.

20.1.3 ^{68}Ga

Min Yang and Yu Liu

^{68}Ga can be produced by a ^{68}Ge/^{68}Ga generator. ^{68}Ge is a long-lived radioisotope with a 271-day half-life, and the generator can be used for about 1 year.^{68}Ga has a physical decay half-life of 68 min which decays by positron emission (89%) and electron capture (11%). The maximum energy of the positrons is 1.92 MeV, while the average energy/disintegration is 0.74 MeV. Compared with ^{18}F, ^{11}C, and other nonmetallic radioisotopes, ^{68}Ga has the advantages of low cost, simple preparation, and high image resolution. As such, ^{68}Ga has been widely used in clinical research in recent years.

20.1.3.1 Production of ^{68}Ga

In a ^{68}Ge/^{68}Ga generator, ^{68}Ge is immobilized on a column filled with inorganic, organic, or mixed matrix where it spontaneously decays to ^{68}Ga extracted by an eluent. The collection of the top fraction can decrease the eluate volume and increase the concentration of ^{68}Ga. The radioactivity of ^{68}Ge and ^{68}Ga would reach equilibrium again at 14 h post elution. If the initial radioactivity of ^{68}Ga is 0, it would take only 68 min to grow to 50% of the maximum radioactivity and 90% after 4 h [12]. Compared with cyclotrons, nuclide generators do not require special sites with radiation shield, nor do they need highly qualified personnel for equipment operation and maintenance.

The preparation of ^{68}Ga radiopharmaceuticals is accomplished by the reaction of $^{68}Ga^{3+}$ with specific chelators such as DOTA, NOTA, DTPA, and EDTA.

20.1.3.2 PET Imaging with ^{68}Ga-Labeled Probes

Over the past decades, ^{68}Ga-labeled probes have undergone a significant increase in preclinical and clinical studies. In Table 20.4, we listed some ^{68}Ga-labeled radiopharmaceuticals.

Targeting SSTR

The diagnosis of neuroendocrine tumors (NETs) by ^{68}Ga-labeled SSTR imaging agents has been widely recognized in clinical research. The most commonly used ^{68}Ga-labeled somatostatin analogs (SSTA) include DOTA-TOC, DOTA-NOC, and DOTA-TATE (Fig. 20.14). Compared with ^{111}In-labeled somatostatin receptor scintigraphy (SRS), ^{68}Ga-SSTA PET/CT imaging has higher sensitivity and specificity for NETs diagnosis [13]. Gabriel et al. compared ^{68}Ga-DOTA-TOC PET/CT with SRS and CT and found that the sensitivity, specificity, and diagnostic accuracy of the former were 97%, 92%, and 96%, respectively, which were all significantly higher than those of SRS (52%, 92%, and 58%) and CT (61%, 71%, and 63%) [14]. Similar results were also validated in ^{68}Ga-DOTA-NOC and ^{68}Ga-DOTA-TATE clinical trials. What's more, different ^{68}Ga-SSTA tracers also have different affinity to different types of SSTRs. ^{68}Ga-DOTA-TATE mainly shows high affinity to SSTR2, while ^{68}Ga-DOTA-TOC has better affinity to SSTR2 and SSTR5.

Targeting GLP-1R

The glucagon-like peptide-1 (GLP-1) is an endogenous 30-amino acid peptide hormone, which is secreted by intestinal epithelial cells. By binding to its receptor, GLP-1 can regulate metabolism and suppress appetite. The GLP-1R agonist, exendin-4, is a polypeptide hormone consisting of 39-amino acid residues which can exert a sustained and stable GLP-1-like effect in vivo. Luo et al. compared ^{68}Ga-NOTA-exendin-4 PET/CT with several traditional imaging examinations such as CT, MRI, EUS, and SRS on 52 cases of insulinoma. They found the diagnostic sensitivity

Table 20.4 Primary applications of ^{68}Ga-labeled probes

Probe	Structure	Applications
^{68}Ga-DOTA-TATE	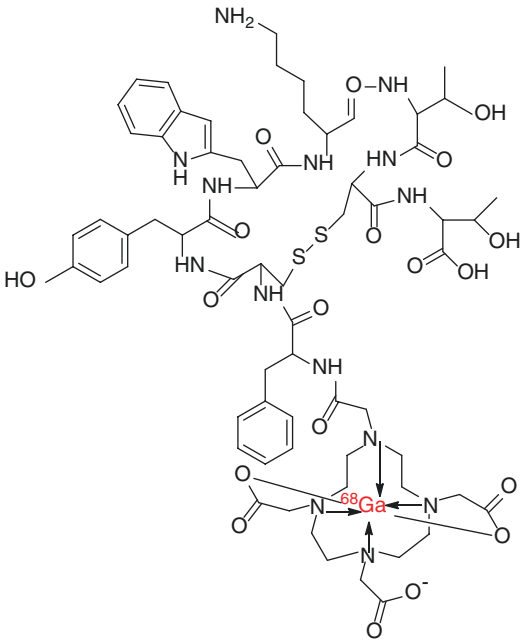	Neuroendocrine tumors (NETs)
^{68}Ga-NOTA-MAL -Cys^{39}-exendin-4	His-Gly-Glu-Gly-Thr-Phe-Thr-Ser-Asp-Leu-Ser-Lys-Gln-Met-Glu-Glu-Glu-Ala-Val-Arg-Leu-Phe-Ile-Glu-Trp-Leu-Lys-Asn-Gly-Gly-Pro-Ser-Ser-Gly-Ala-Pro-Pro-Pro 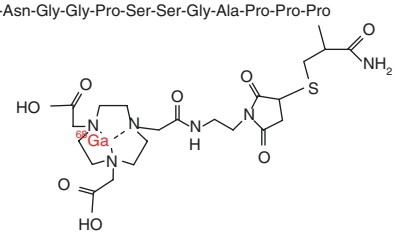	Insulinoma
^{68}Ga-Affibody	Val-Asp-Asn-Lys-Phe-Asn-Lys-Glu-Met-Arg-Asn-Ala-Tyr-Trp-Glu-Ile-Ala-Leu-Leu-Pro-Asn-Leu-Asn-Asn-Gln-Gln-Lys-Arg-Ala-Phe-Ile-Arg-Ser-Leu-Tyr-Asp-Asp-Pro-Ser-Gln-Ser-Ala-Asn-Leu-Leu-Ala-Glu-Ala-Lys-Lys-Leu-Asn-Asp-Ala-Gln-Ala-Pr0-Lys-Asn-Asp-Arg-Gly-Gly-Gly 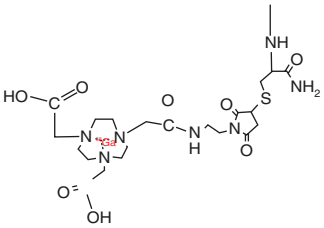	Breast cancer
^{68}Ga-NOTA- MAL -Cys^{59}-MZHER2	ZHER$_{2:342}$ — Asn-Asp-Arg-Gly-Gly-Gly 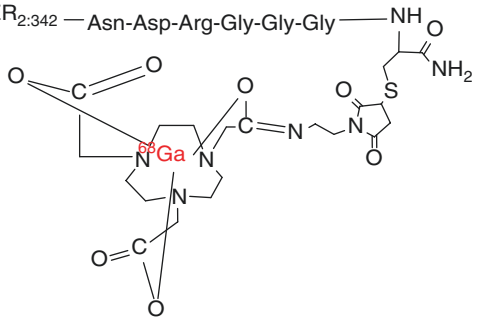	Breast cancer

(continued)

Table 20.4 (continued)

Probe	Structure	Applications
^{68}Ga-RGD	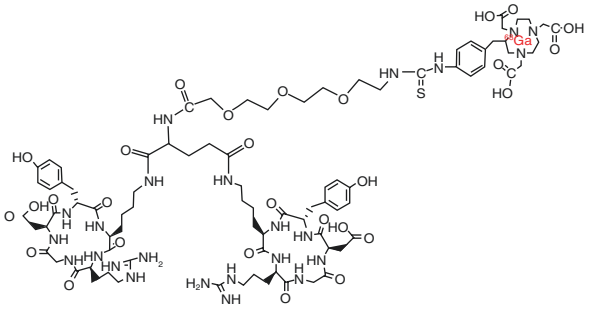	Lung cancer, breast cancer, ovarian cancer, and prostate cancer
^{68}Ga-NOTA-MAL-FSH1	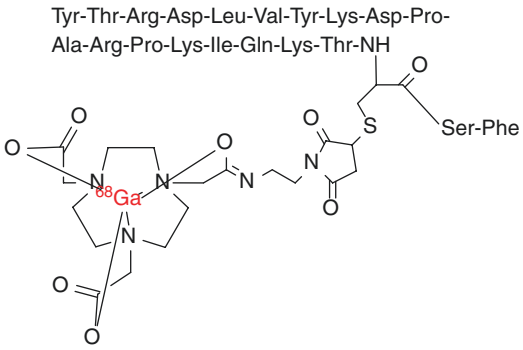	Prostate cancer

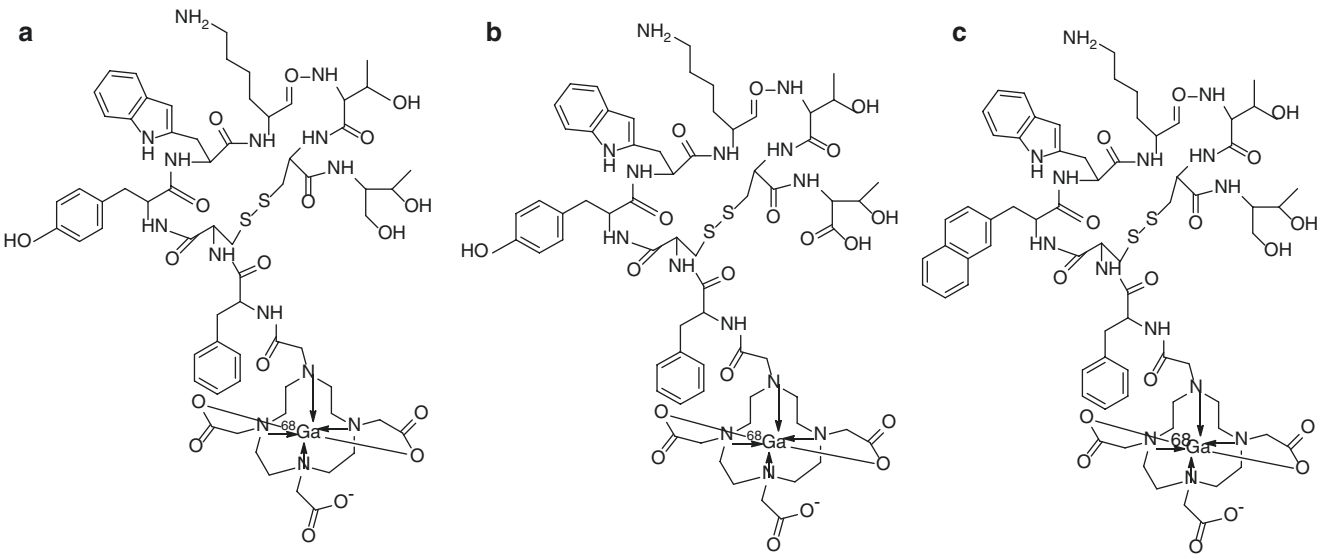

Fig. 20.14 Structure of (**a**) ^{68}Ga-DOTA-TOC, (**b**) ^{68}Ga-DOTA-TATE, and (**c**) ^{68}Ga-DOTA-NOC

of GLP-1R PET/CT for insulinoma reached 97.7%, which was significantly higher than SSTR method (30–50%) and others [15].

Targeting PSMA

^{68}Ga-PSMA has gradually become one of the most popular research hotspots in the field of nuclear medicine. It has been applied to the clinical trial for prostate cancer in 2012 for the first time and showed good diagnostic value. In that study, ^{68}Ga-PSMA successfully detected the relapse and metastasis of prostate cancer with excellent contrast by binding to the extracellular domain of PSMA. Another study performed on 37 patients with biochemical relapse of prostate cancer compared the ^{18}F-fluoromethylcholine and ^{68}Ga-PSMA PET/CT. The results indicated that all lesions detected by ^{18}F-fluoromethylcholine could also be clearly identified by ^{68}Ga-PSMA [16]. Nowadays, ^{68}Ga-PSMA PET/CT can be performed on prostate cancer patients with biochemical

recurrence who has a very low PSA level. With the PSA level increased, the detection rate also increased. In addition, ^{68}Ga-PSMA PET/CT could also be used for primary staging of high-risk prostate cancer patients, which might have a significant impact on the further radiation therapy planning.

Targeting Integrin $\alpha_v\beta_3$

Radionuclide-labeled Arg-Gly-Asp (RGD) peptide can specifically bind to integrin $\alpha_V\beta_3$ receptor and has been proved to be a noninvasive method for early detection of tumor angiogenesis. Zhang Jingjing, from Peking Union Medical College Hospital, assessed ^{68}Ga-BBN-RGD PET/CT imaging in 22 breast cancer patients and found that both primary cancer and metastases showed positive ^{68}Ga-BBN-RGD accumulation. Kang Fei, from Xijing Hospital, compared $\alpha_v\beta_3$ levels in non-small cell lung cancer (NSCLC) and small cell lung cancer (SCLC) patients using ^{68}Ga-RGD$_2$ PET/CT. The results showed that the uptake of ^{68}Ga-RGD$_2$ in SCLC patients is significantly lower than that in NSCLC patients, which meanwhile validated the feasibility of ^{68}Ga-RGD$_2$ PET/CT in lung cancer.

Targeting HER2

Monitoring the expression of HER2 is of great significance for the diagnosis and treatment of HER2-positive tumors. ABY-025 is the second generation of HER2-targeted affibody. ^{111}In-labeled ABY-025 has been used in a first-in-human clinical trial for HER2 receptor expression analysis in patients with breast cancer metastasis. A recent study by Sörensen et al. demonstrated that ^{68}Ga-ABY-025 PET accurately quantifies whole-body HER2 receptor status in metastatic breast cancer. In the study, ^{68}Ga-ABY-025 PET correctly identified conversion and mixed expression of HER2 status at 4 h postinjection [17]. Since ^{68}Ga-ABY-025 specifically targets the HER2 receptor, the radiotracer can be used in place of tissue biopsies to classify tumors based on their molecular expression profiles. In addition, ^{68}Ga-ABY-025 can be used for posttreatment evaluation of HER2 status changes to determine whether ^{68}Ga-ABY-025 PET can be used as a predictive tool for noninvasive treatment evaluation.

Other Applications

In the past few years, ^{68}Ga-labeled radiopharmaceuticals have been increasingly studied in inflammation and infection. Researchers made some preclinical studies in the diffuse *Staphylococcus aureus* tibial osteomyelitis models; the results validate the good specificity and differential diagnostic ability of ^{68}Ga-labeled VAP-1 imaging agents. In addition, ^{68}Ga-labeled citrate was found to play a role in the clinical examination of bone marrow and joint inflammation with a diagnostic accuracy for over 90% [18]. For cardiovascular diseases, ^{68}Ga-Fucoidan has been studied for atherosclerotic plaque, and another ^{68}Ga-labeled peptide, FAMP, has also yielded promising results in preclinical studies which can show the presence of active plaques in the ApoE$^{-/-}$ mice. ^{68}Ga-GallGas, a ^{68}Ga-labeled carbon nanoparticle inhalation aerosol, was tested in piglets of pulmonary obstruction or diffuse airway obstruction. In a self-controlled clinical trial, the investigators performed conventional pulmonary ventilation (V/Q) imaging and PET/CT V/Q imaging after inhalation of ^{68}Ga-labeled carbon nanoparticles in ten patients with suspected pulmonary embolism. The results showed that PET/CT demonstrated higher image resolution and better assessment of pulmonary function, thereby leading to a more accurate diagnosis [19].

20.1.4 ^{89}Zr

Min Yang and Yu Liu

Zirconium is a transition metal in Group IVB of the periodic table. ^{89}Zr, which decays by positron emission (23%) and electron capture (77%) to the stable isotope ^{89}Y, has attractive characteristics for immuno-PET applications. The E_{max} of its positron emission is 897 keV, and E_{ave} is 396.9 keV. The physical decay half-life of ^{89}Zr is 78.4 h, which is compatible with long circulation mAbs [20, 21]. ^{89}Zr labeling is also suitable for in vitro and in vivo PET studies of peptides, peptide polymers, nanoparticles, microspheres, targeted nanotubes, liposomes, and proteins.

20.1.4.1 Production of ^{89}Zr

^{89}Zr has been produced on a cyclotron via both the ^{89}Y (p, n) ^{89}Zr and ^{89}Y (d, 2n) ^{89}Zr reactions. In 1986, Link et al. hit ^{89}Y with 13 MeV photons and produced ^{89}Zr by (p, n) nuclear reaction for the first time. After purification, the yield was 80%, and the radionuclide purity was over 99%. Alternatively, the ^{89}Y (d, 2n) ^{89}Zr reaction can be used to minimize the level of ^{88}Zr. Yttrium pellet is irradiated with a 16 MeV deuteron beam, and ^{89}Zr can be separated from the target by ion exchange chromatography with an overall yield of ~80%. At present, the low-energy cyclotron can produce radionuclide ^{89}Zr with a purity of 99.99%. Wooten et al. [22] reported a custom system for the safe production of ^{89}Zr routinely, which obtained high-purity radionuclides (>99.99%) and a satisfactory effective specific activity of 185–13,100 GBq/mmol.

20.1.4.2 Radiolabeling of ^{89}Zr

Nowadays, ^{89}Zr labeling of antibodies can be achieved through various types of chelators including DTPA, EDTA, DOTA, and DFO (Fig. 20.15). Although the thermodynamic stability constants of ^{89}Zr with EDTA or DTPA are very high, the kinetic reaction rates are low, leading to unsatisfactory labeling rates. Therefore they are not suitable as ^{89}Zr ligands.

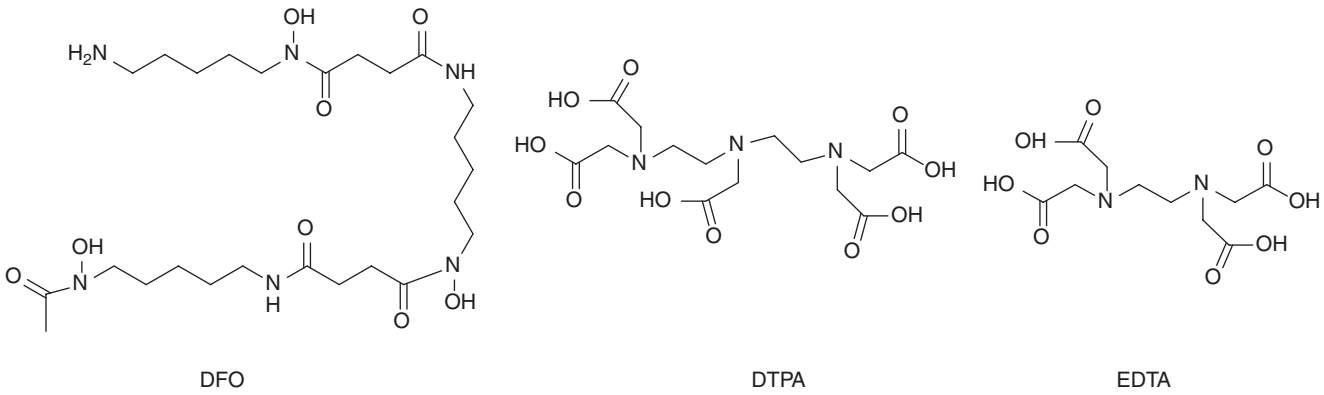

Fig. 20.15 Structure of DFO, DTPA, and EDTA

DFO is a hexadentate siderophore containing three hydroxamate groups for chelating metals and a primary amine tail for conjugation to a biomolecule. When using DFO for labeling, the pH of the solution of [^{89}Zr] zirconium oxalate should be adjusted to 7 by using Na_2CO_3 or HEPES buffer at first, and the bioactive substance containing DFO is then added and reacted for 30–60 min at room temperature. Finally, the product could be obtained with a yield of 35–98% after HPLC purification.

20.1.4.3 PET Imaging with ^{89}Zr-Labeled Probes

Over the last few years, a wide variety of mAbs have been labeled with ^{89}Zr, and many of them have entered preclinical or clinical investigations with promising results (Fig. 20.16). In this section, several developments of ^{89}Zr-labeled antibodies in preclinical studies will be introduced (Table 20.5).

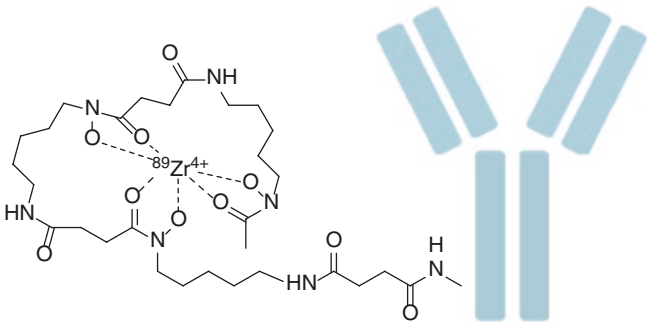

Fig. 20.16 ^{89}Zr-labeled antibody using DFO as chelator

Table 20.5 The primary applications of ^{89}Zr-labeled radiopharmaceuticals

Probes	Applications
^{89}Zr-Ibritumomab	NHL
^{89}Zr-cU36	Head and neck tumor
^{89}Zr-panitumumab	Metastatic colorectal cancer
^{89}Zr-trastuzumab	Ovarian cancer
^{89}Zr-DFO-J591	Prostate cancer
^{89}Zr-bevacizumab	Ovarian cancer
^{89}Zr-R1507	Triple-negative breast cancer
^{89}Zr-cG250-F(ab′)$_2$	Visualize tumor hypoxia

Targeting CD20

^{89}Zr-DFO-labeled rituximab can specifically bind to human cell differentiation antigen CD20 expressed in humanized CD20-expressing transgenic mice (huCD20TM). ^{89}Zr-Ibritumomab can be used to assess the biodistribution and radiation dose of the targeted therapeutic ^{90}Y-ibritumomab. In a clinical study, NHL patients underwent ^{89}Zr-ibritumomab PET scan followed by ^{90}Y-ibritumomab injection 2 weeks later. The results showed that ^{90}Y-ibritumomab treatment did not affect the biodistribution of ^{89}Zr-ibritumomab. This indicates that ^{89}Zr-ibritumomab PET scan can be used to assess, predict, and quantify the biodistribution of ^{90}Y-ibritumomab and optimize the therapeutic dose.

Targeting CD44

Preclinical studies have shown that ^{89}Zr-labeled anti-CD44v6 chimeric monoclonal antibody (^{89}Zr-cU36) can detect HNSCC xenografts. In addition, ^{89}Zr-cU36 PET imaging is a suitable method for the detection of ^{90}Y-cU36 therapeutic doses. A clinical trial showed that the tracer can detect primary tumors and metastases in the head and neck region with similar sensitivity to CT and MRI. ^{89}Zr-cU36 has diagnostic value for HNSCC with cervical lymph node metastasis. ^{89}Zr-cU36 PET imaging cannot effectively distinguish micrometastases; in addition, the average effective radiation dose of ^{89}Zr-cU36 was significantly higher than that of clinical radiation. These shortcomings limit the application of ^{89}Zr-cU36 PET. Preclinical study of ^{89}Zr-RG7356, an antibody directed against the constant part of CD44, has been performed in mice bearing tumor xenografts with different levels of CD44 expression. Whole-body immuno-PET scans of healthy cynomolgus monkeys revealed uptake of ^{89}Zr-RG7356 in the spleen, salivary gland, and bone marrow, indicating that CD44 is also expressed in these organs.

Targeting EGFR

Cetuximab is an IgG chimera that binds to the ligand-binding domain to induce internalization of epidermal growth factor (EGFR) and thus block the signaling system for subsequent reactions. ^{89}Zr-labeled cetuximab has been investigated in several preclinical studies and used as a scouting procedure before radioimmunotherapy (RIT) to confirm tumor targeting and allow estimation of radiation dose delivery to tumors and normal tissues.

Panitumumab is the first human recombinant monoclonal antibody (IgG2) approved by the FDA to treat EGFR-expressing metastatic colorectal cancer (mCRC). In vivo imaging of tumors expressing HER1 was reported in some noninvasive studies with panitumumab. Recently, a comparative assessment of HER1 PET imaging with ^{89}Zr-panitumumab and ^{111}In-panitumumab showed that the biodistribution of ^{89}Zr-panitumumab and ^{111}In-panitumumab in tissue and organs was nearly identical. Moreover, the targeted binding of ^{89}Zr-panitumumab is correlated with the expression of HER1.

Targeting HER2

The radiolabeled trastuzumab has been used for noninvasive HER2 imaging in vivo. ^{89}Zr-trastuzumab has a highly specific uptake in HER2-positive tumors, whereas ^{18}F-FDG and ^{18}F-FLT did not discriminate between HER2-positive tumors and negative tumors. Uptake of ^{89}Zr-trastuzumab by ovarian cancer SK-OV-3 xenografts was as high as 30% ID/g, and its biodistribution was similar to ^{111}In-trastuzumab. Studies have shown that ^{89}Zr-trastuzumab can also quantitatively monitor HER2 expression levels after treatment. For example, ^{89}Zr-trastuzumab imaging showed that HER2 expression was significantly reduced in tumors treated with heat shock protein 90 (hsp90) inhibitors. ^{89}Zr-trastuzumab is also useful in the evaluation of the efficacy of EGFR/HER2/HER4 inhibitors. Uptake of ^{18}F-FDG did not change after afatinib treatment, whereas the uptake of ^{89}Zr-trastuzumab was significantly reduced after treatment [23]. ^{89}Zr-trastuzumab uptake is correlated with HER2 expression. Therefore, ^{89}Zr-trastuzumab PET imaging may be a useful tool for the qualitative characterization, treatment planning, and treatment monitoring of HER2-positive tumors.

Targeting PSMA

The radiochemical yield of ^{89}Zr-labeled monoclonal antibody J591 (^{89}Zr-DFO-J591) is more than 77% with a high radiochemical purity (>99%). In vivo experiments showed that the uptake by prostate cancer was (34.3 ± 3.2) %ID/g, (38 ± 6.2) %ID/g, (40.4 ± 4.8) %ID/g, and (45.8 ± 3.2) %ID/g, respectively at 24, 48, 96, and 144 h after injection. ^{89}Zr-DFO-J591 can qualitatively and quantitatively analyze PSMA-positive or negative prostate cancer tumors in vivo [24].

Targeting VEGF

^{89}Zr-bevacizumab uptake was higher in SK-OV-3 ovarian cancer xenografts compared to ^{89}Zr-IgG. In addition, ^{89}Zr-bevacizumab is also used as a tracer for VEGF expression in the tumor microenvironment, as well as to detect anti-angiogenic responses. Hsp90 plays an important role in VEGF transcription and can treat ovarian cancer. Uptake of ^{89}Zr-bevacizumab in A2780 tumors correlates well with the role of hsp90 inhibitor NVP-AUY922. Another study showed that everolimus, a mTOR inhibitor, reduced tumor uptake of ^{89}Zr-bevacizumab. Thus, ^{89}Zr-bevacizumab can detect tumor VEGF-A levels after early treatment of mTOR inhibitors.

Ranibizumab is a derivative of bevacizumab, and ^{89}Zr-ranibizumab can be used to monitor the early anti-angiogenic response to treatment of sunitinib. The results of ^{89}Zr-ranibizumab PET, as well as cell histology, immunohistochemistry, cell proliferation, and angiogenesis analysis, were more consistent than ^{18}F-FDG PET or ^{15}O-H2O PET. Ranibizumab has a serum half-life of only 2–6 h; therefore, rapid and sequential follow-up PET scans are feasible with ^{89}Zr-ranibizumab.

Targeting IGF-1R

Insulin-like growth factor receptor 1 (IGF-1R) is a transmembrane receptor belonging to the receptor tyrosine kinase (RTK). IGF-1R is expressed in a variety of human tumors, such as triple-negative breast cancers. It is associated with proliferation, apoptosis, angiogenesis, and tumor invasion. IGF-1R not only has a proliferative effect on normal tissues but also is a prerequisite for malignant transformation of cells. IGF-1R is highly expressed in many malignant tumor tissues such as malignant nervous system tumors, malignant melanoma, prostate cancer, breast cancer, colon cancer, lung cancer, and liver cancer. This makes IGF-1R an attractive tumor target, which is expected to serve as an indicator of early diagnosis, treatment, and prognosis. Heskamp et al. reported the uptake of ^{111}In-R1507 and ^{89}Zr-R1507 (targeting IGF-1R) in SUM149 triple-negative breast cancer xenograft mice; the results indicating ^{89}Zr-R1507 for IGF-IR could be used for targeted diagnosis [25].

Targeting CAIX

Carbonic anhydrase (CAIX) is a group of zinc-containing enzymes. At present, it has been found that CA has at least 14 isozymes, among which carbonic anhydrase IX is the most important one. CAIX is a tumor-associated protein which has a high expression in a variety of tumor tissues but scarcely expressed in normal tissues. CAIX is highly expressed in hypoxic cells, which is related to radiotherapy and chemotherapy resistance. Hoeben et al. used ^{89}Zr to label F(ab′)$_2$, a fragment of CG250 antibody, and used microPET to investigate the pharmacokinetics of ^{89}Zr-cG250-F(ab′)$_2$. Four hours after administration, radioactivity aggregation

occurred in the xenografts, and the concentration began to decrease after 24 h. The site of ^{89}Zr-cG250-F(ab′)$_2$ was consistent with the site of CAIX expression. CAIX is also a hypoxia-related cell marker. CAIX radiolabeled monoclonal antibody may be useful for screening patients who are suitable for hypoxia-targeting or hypoxia-modifying treatment combined with radiotherapy. For example, ^{89}Zr-cG250-F(ab′)$_2$ can be used to visualize tumor hypoxia in mice bearing human head and neck squamous cell carcinoma (SCCNij3). Clear cell renal cell carcinoma (ccRCC) rats' studies have shown that ^{89}Zr-cG250 is more sensitive than ^{124}I-cG250. ^{89}Zr-labeled antibody targeting CAIX can be used as a variety of tumor hypoxia PET imaging agent and deserves further study.

20.1.5 ^{64}Cu

Min Yang and Huimin Zhao

Copper (Cu) is a transition metal with atomic number 29 and an important trace element for most organisms. In humans, copper plays a role as a cofactor for numerous enzymes, such as Cu/Zn superoxide dismutase, cytochrome-c oxidase, tyrosinase, ceruloplasmin, and other proteins which is crucial for respiration, iron transport and metabolism, cell growth, and hemostasis. ^{64}Cu is a PET isotope including β$^+$decay (19.3%) with a maximum energy of 0.657 MeV, β$^-$ decay (39.6%) with a maximum energy of 0.571 MeV, and electron capture (EC) decay (19.3%) which emits γ rays with a maximum energy of 1.346 MeV. The energy is appropriate for proper detection by the equipment. The half-life of ^{64}Cu is 12.7 h, which allows sufficient uptake and distribution to yield considerable contrast and quality images.

20.1.5.1 Production of ^{64}Cu

^{64}Cu is a highly unusual isotope because it decays by three processes, namely, positron, electron capture, and β$^-$ decays. This property allows either cyclotron or reactor production. ^{64}Cu can be produced in two ways. One method of ^{64}Cu production is the ^{63}Cu (n, γ) ^{64}Cu reaction and ^{64}Zn (n, p) ^{64}Cu reaction in a nuclear reactor which produced carrier or carrierless ^{64}Cu, respectively. Another method of ^{64}Cu production is the ^{64}Ni (p, n) ^{64}Cu reaction on a cyclotron, which is now widely used to provide carrierless ^{64}Cu.

20.1.5.2 Radiolabeling of ^{64}Cu

^{64}Cu is easy to react with amine, imine, pyridine, and derivatives. It can form a stable coordination bond with nitrogen, oxygen, and sulfur atoms. To achieve high uptake of the copper radionuclide in the tissue or organ of interest and minimize the nonselective binding or incorporation into nontarget organs, ^{64}Cu is utilized to binding with chelators, which are of high specific activity.

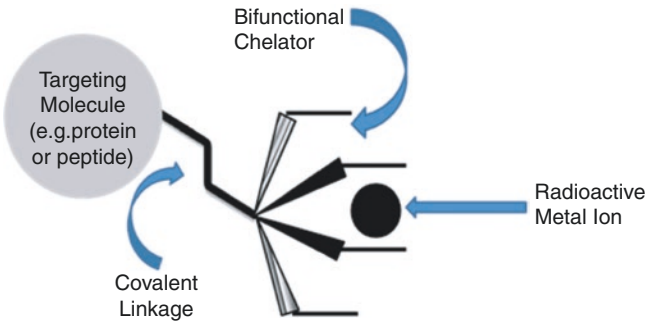

Fig. 20.17 Bifunctional chelator (BFC)

The stability of the radioactive copper complex in vivo is a key factor in optimal ligand design. For example, low electronic resistance and rapid complexation kinetics are crucial to the formation of complexes of ^{64}Cu and chelating agents. In addition, chelators must also be designed with functional groups available to enable covalent attachment to the targeting biomolecule as shown in Fig. 20.17. Therefore, the simplest way to develop a targeted PET tracer is to attach the ^{64}Cu-chelator unit through a pendant arm to an amine on a biomolecule, such as peptides, antibodies, or small molecules with the creation of an amide bond.

Some of the earliest BFC ligand systems used acyclic polyamine carboxylate ligands, including ATSM and PTSM. However, according to relative studies, these chelators labeled by ^{64}Cu were not stable in serum in vivo for long periods. To improve the stability of ^{64}Cu complexes in vivo, researchers have turned study to tetraazamacrocyclic ligands with pendant arms, which can enhance the stability via both the macrocyclic and chelation effects. A series of ^{64}Cu-chelators, macrocyclic polyaminocarboxylates such as DOTA and TETA, are more stable than ^{64}Cu-labeled complexes of acyclic ligands. In addition, it has been also found that the methylenephosphonate pendant-armed tetraaza macrocyclic ligands, DO4P, own relative high stability in vitro and in vivo. Inspired by the findings, Wieghardt and colleagues discovered and synthesized 1,4,7-triazacyclononane-*N*,*N*′,*N*″-triacetate (NOTA), which can also be used as the chelator of ^{64}Cu (Fig. 20.18).

20.1.5.3 PET Imaging with ^{64}Cu-Labeled Probes

^{64}Cu can be used as a PET imaging agent in combination with peptides, antibodies, and small molecules after being linked to a chelating agent so that targeted imaging agents for various clinical diseases can be obtained (Table 20.6).

Targeting VEGFR

Vascular endothelial growth factor receptor (VEGFR) is a type of tyrosine kinase transmembrane glycoprotein, and its extracellular segment can bind to vascular endothelial growth factor (VEGF) to activate downstream signaling. VEGF$_{121}$ has a receptor-binding activity of the larger variants. Cai and

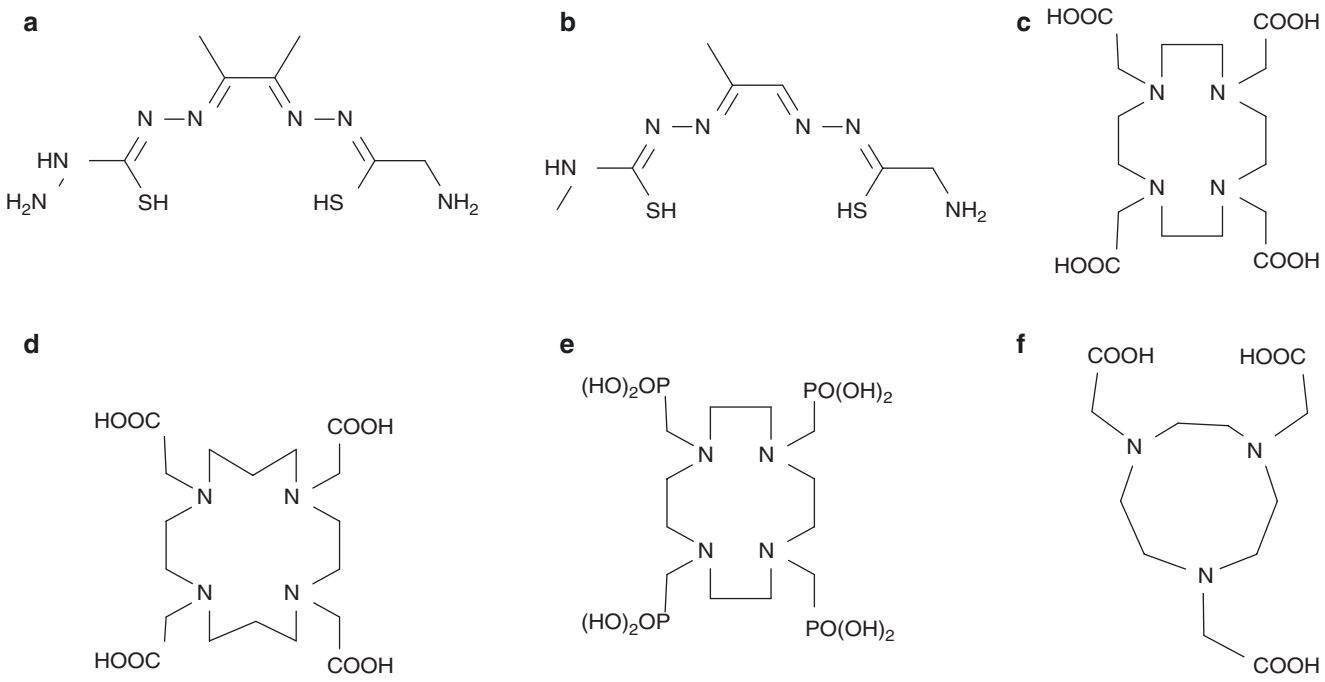

Fig. 20.18 Chelators based on cyclam and cyclen backbones (**a**) ATSM; (**b**) PTSM; (**c**) DOTA; (**d**) TETA; (**e**) DO4P; (**f**) NOTA

Table 20.6 Applications of ^{64}Cu-labeled radiopharmaceuticals

Probe	Structure	Application
^{64}Cu-DOTA-[Lys3]-BBN	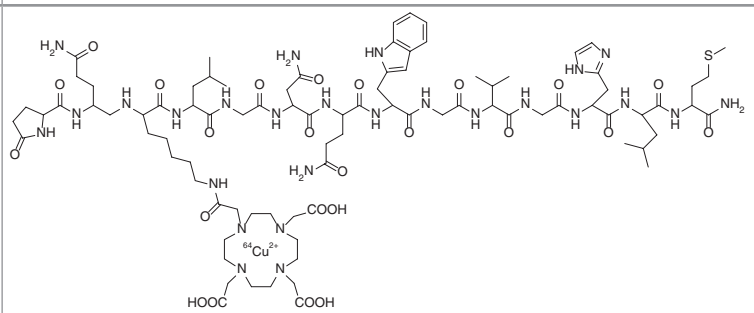	Prostate cancer and GRPR PET imaging
^{64}Cu-DOTA-Aoc-BBN	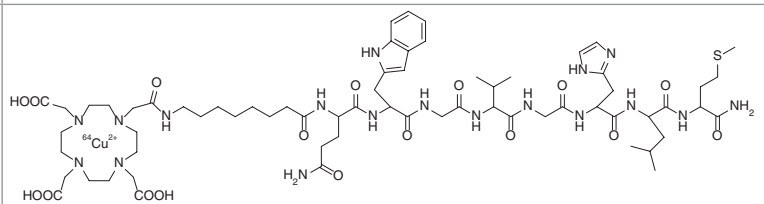	Prostate cancer and GRPR PET imaging
^{64}Cu-DOTA-Aca-BBN	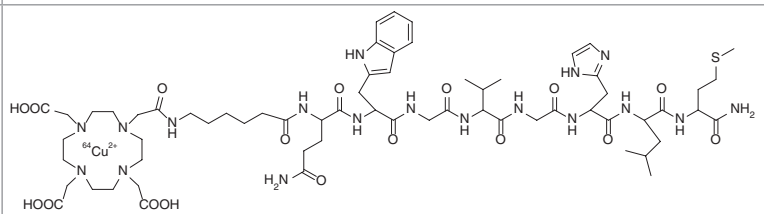	Prostate cancer and GRPR PET imaging

(continued)

Table 20.6 (continued)

Probe	Structure	Application
^{64}Cu-DOTA-RGD tetramer	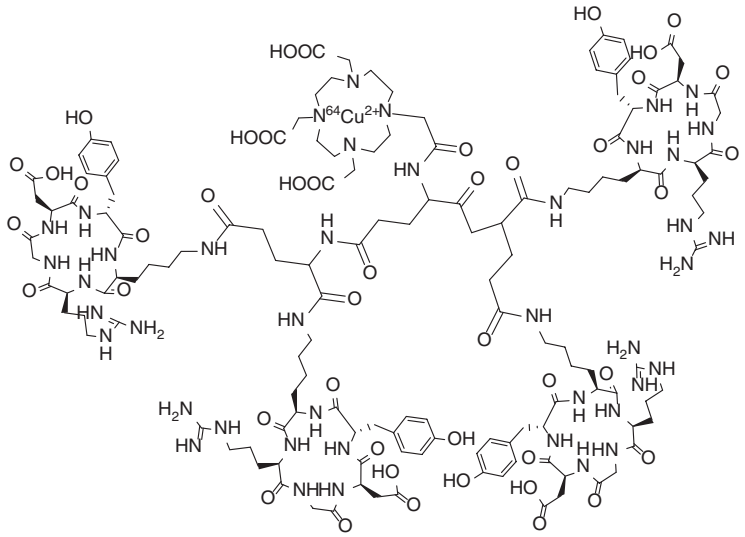	$\alpha_v\beta_3$ PET imaging
^{64}Cu-DOTA-RGD octamer	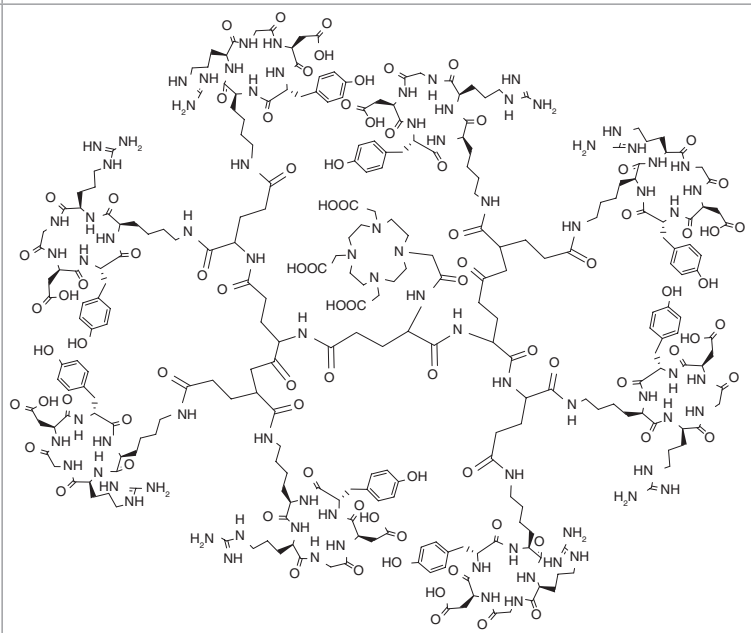	$\alpha_v\beta_3$ PET imaging
^{64}Cu-cuclen-A	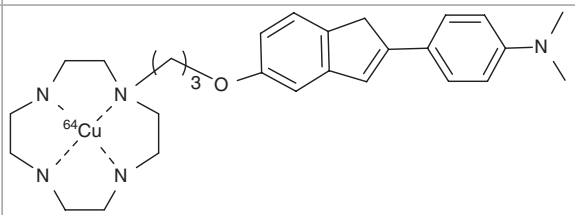	CAA and amylin PET imaging
^{64}Cu-DOTA-A	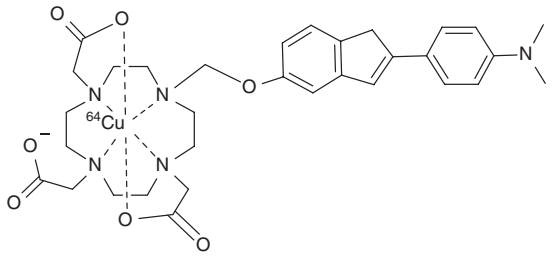	CAA and amylin PET imaging

colleagues reported the first example of ^{64}Cu-labeled $VEGF_{121}$, which used for the expression of VEGFR in PET imaging. MicroPET revealed rapid and high uptake (14.9 ± 0.7, 16.3 ± 0.7, 16.3 ± 0.6, and 15.1 ± 0.8%ID/g at 2, 4, 16, and 23 h after injection) of ^{64}Cu-DOTAVEGF$_{121}$ in small (tumor volume: 64.9 ± 24.6 mm^3, n = 3; high VEGFR expression) U87MG tumors but very low uptake (1–2%ID/g) in large (tumor volume: 1164.3 ± 179.6 mm^3, n = 3; low VEGFR expression) tumors. The results showed that the uptake of ^{64}Cu-DOTA-VEGF$_{121}$ in the tumor was closely related to the expression of VEGFR-2.

Targeting GRPR

The interaction between gastrin-releasing peptide (GRP) and GRP receptor (GRPR) as an autocrine tumor growth stimulating pathway has been repeatedly reported in the pathogenesis of a large number of mammalian carcinomas. Chen and colleagues reported a series of ligands for bombesin, such as ^{64}Cu-DOTA-[Lys3]-BBN, ^{64}Cu-DOTA-Aoc-BBN, and ^{64}Cu-DOTA-Aca-BBN. Bombesin is an analog of human gastrin-releasing peptide (GRP) that binds to the GRP receptor (GRPR) with high affinity and specificity. GRPR is overexpressed in prostate cancer tissues. So ^{64}Cu-chelator-bombesin has the potential of being a prostate cancer imaging agent for its ability to bind to GRPR with a high degree of specificity.

Targeting Integrin $\alpha_v\beta_3$

^{64}Cu-DOTA-RGD has been validated effective for the visualization of $\alpha_v\beta_3$ at a very low integrin concentration. Cai et al. [26] developed a series of ^{64}Cu-labeled multimeric RGD peptides for the PET imaging of integrin $\alpha_v\beta_3$ expression such as RGD tetramer and RGD octamer. The preclinical microPET imaging results demonstrated the promising effects of ^{64}Cu-DOTA-RGD tetramers and octamers in U87MG tumor-bearing nude mice. In detail, U87MG tumors could be clearly detected with high contrast using ^{64}Cu-DOTA-RGD. The specificity of both ^{64}Cu-DOTA-RGD tetramers and octamers was confirmed by receptor-blocking experiments, while RGD octamers had significantly higher affinity and specificity than RGD tetramers. The radioactive uptake of ^{64}Cu-DOTA-RGD octamers in the tumor was 11.7 ± 0.7, 10.6 ± 0.7, 10.6 ± 0.3, 10.5 ± 0.7, and 10.3 ± 1.0%ID/g at 0.5, 1, 2, 6, and 20 h after administration, which were obviously higher than those of ^{64}Cu-DOTA-RGD tetramers. The progress of the series of ^{64}Cu-DOTA-RGD would likely lead to the future development of integrin-based imaging and internal radiotherapy targeting integrin αvβ3.

Targeting CD105

CD105 is a 180 kDa disulfide-linked homodimeric transmembrane protein that is one of the hallmark proteins required for tumor angiogenesis. CD105 is overexpressed only on proliferating tumor endothelial cells, and immunohistochemical studies have demonstrated that CD105 is a recognized standard for the detection of proliferating blood vessels (i.e., neovascular vessels) in tumors. Zhang [27] and colleagues used ^{64}Cu-NOTA-TRC105 as a tumor PET agent, which can bind human CD105 and murine CD105. It has been demonstrated that TRC105 shows anticancer efficacy in animal tumor models. In the study performed by Zhang and colleagues, TRC105 was observed to have significant and sustained uptake (7.5 ± 2.7, 11.4 ± 1.9, and 13.0 ± 1.2% ID/g at 4, 24, and 48 h, respectively, n = 3) of tracer in 4T1 tumors. In addition, blocking experiments using unlabeled TRC105 and ^{64}Cu-NOTA-TRC105 demonstrated the targeting of ^{64}Cu-NOTA-TRC105 as well as good stability in vivo.

Targeting HER2

Trastuzumab is a kind of monoclonal antibody targeting HER2 and now is used as an effective drug for HER2-positive breast tumors. Henry et al. [28] demonstrated the safety, biodistribution, and dosimetry of ^{64}Cu-DOTA-trastuzumab in vivo and get promising PET images by using this novel probe. In their study, six patients with primary or metastatic HER2-positive breast cancer underwent ^{64}Cu-DOTA-trastuzumab PET examination at 1, 24, and 48 h after the administration of this probe. The results indicated that 48 h after ^{64}Cu-DOTA-trastuzumab injection was the best time point for PET scan. The radioactive uptake of ^{64}Cu-DOTA-trastuzumab in nontarget tissues was low except for the blood (9.8 ± 3.3% ID/g, at 48 h after injection). Thus ^{64}Cu-DOTA-trastuzumab could serve as a reliable PET probe for the diagnosis of HER2-positive breast cancer. Similar conclusions have been confirmed in ^{64}Cu-DOTA-hu4D5v8, which had high uptake in HER-positive tumors and could reach 9.0 ± 2.7 and 11.8 ± 1.0%ID/g at 4 and 21 h, respectively, after injection in the tumor-bearing mice [28].

Targeting EGFR

Ayoung Pyo et al. [29] synthesized three different ^{64}Cu-labeled anti-EGFR repebodies (^{64}Cu-rEgA) with three different chelators (NOTA, DOTA, and DTPA) and further demonstrated their biological characteristics in preclinical trials such as cellular uptake studies with the human NSCLC cell line H1650 (high expression of EGFR) and the human colon adenocarcinoma cell line SW620 (low expression of EGFR). Besides, biodistribution and microPET imaging were performed using H1650 tumor-bearing mice. The results demonstrated that the specificity of the rEgA would not be influenced by the various chelators (NOTA, 16.38 ± 1.79%ID/g; DOTA, 13.35 ± 2.32%ID/g; and DTPA, 13.95 ± 6.22%ID/g at 6 h postinjection). The favorable in vivo kinetics and specific tumor uptake of ^{64}Cu-rEgA warrant its further investigation for imaging of EGFR-positive tumors. Therefore, ^{64}Cu-rEgA has potential to serve as a novel scaffold for the development of imaging agents in companion diagnosis.

Targeting Aβ

Imaging of Aβ plaque deposits in the brain in vivo is considered to be a useful tool to study the pathophysiology of neurodegenerative diseases. Ono [30] and colleagues reported two novel ^{64}Cu-labeled 2-phenylbenzofuran derivatives conjugated with ^{64}Cu-cuclen-A and ^{64}Cu-DOTA-A as PET imaging probes for Aβ aggregates, proving suitable for CAA or amylin imaging.

20.2 Therapy

20.2.1 ^{177}Lu

Min Yang and Jie Sheng

^{177}Lu is a medium-energy β-emitter with a maximum energy of 0.5 MeV and a maximal tissue penetration of 2 mm. Its half-life is 6.7 days. ^{177}Lu also emits low-energy γ-rays at 208 and 113 keV with 10% and 6% abundance, respectively, which allows scintigraphy and subsequent dosimetry with the same therapeutic compound. Therefore, studies and application on ^{177}Lu have received more and more attention.

20.2.1.1 Production of ^{177}Lu

Both the "direct" and "indirect" reactor production routes can be followed to obtain ^{177}Lu for nuclear medicine applications. The direct production route is based on neutron irradiation of ^{176}Lu targets by the ^{176}Lu(n,γ)^{177}Lu reaction. The indirect ^{176}Yb(n,γ)^{177}Yb → ^{177}Lu production route necessitates a chemical separation of ^{177}Lu from the target ^{176}Yb target atoms (Fig. 20.19).

20.2.1.2 Radiolabeling of ^{177}Lu

^{177}Lu, as a metal nuclide, are mainly radiolabeled by bifunctional chelating agents. DTPA, EDTA, DOTA, and NOTA are the common chelators. For example, DOTA is mostly used as a chelator in the labeling of octreotate. The [DOTA0, Tyr3] Octreotate and the ^{177}Lu are mixed and heated for 30 min at 80 °C. The labeling yield, which can reach 99%, commonly be checked using instant thin-layer chromatography with 0.1 M sodium citrate (pH 5.0) as a solvent.

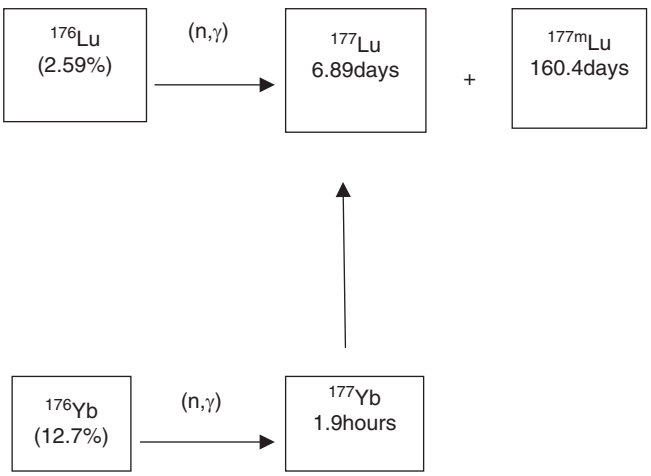

Fig. 20.19 Two methods for preparation of ^{177}Lu

There are still some drugs, which can be labeled with ^{177}Lu by the chelator-free method. EDTMP is a typical one. The whole reaction process is simple and fast. EDTMP and $^{177}LuCl_3$ should be mixed under pH = 8. Labeling yield of ^{177}Lu-EDTMP depends on the pH of the reaction system. With the optimal condition, the labeling yield can reach 99%.

20.2.1.3 Applications of ^{177}Lu-Labeled Probes (Table 20.7)

^{177}Lu-Ethylene Diamine Tetramethylene Phosphonic Acid (EDTMP)

EDTMP, which has a strong affinity to bone, can be labeled with radionuclides to treat pain caused by bone metastasis. Compared with $^{89}SrCl_2$ and ^{153}Sm-EDTMP, which have been used for treating osseous metastasis pain in China, ^{177}Lu-EDTMP has many advantages. First, ^{153}Sm has a short half-life (47 h), which means huge losses during production and supply. To make up for the losses caused by decay, repeated administration is required for the patients. Second, ^{89}Sr has low reaction cross section and production, resulting in the high price. Nowadays, ^{177}Lu-EDTMP has entered into phase 2 clinical trials. Many studies have approved it effective and safe [31–33].

Peptide Receptor Radionuclide Therapy (PRRT)

PRRT, also called radioisotope therapy, is a molecule-related treatment, which is used to treat neuroendocrine, prostate, and pancreatic tumors. PRRT can provide more individualized cancer treatment. Radiopharmaceuticals can be adjusted according to the patients' unique biological features and molecular characteristics of the tumor. Also, it can kill the targeted cancer cells. Compared with chemotherapy, PPRT has relatively mild side effects.

Somatostatin (SST) Labeled by ^{177}Lu

Nowadays, it has been proved that octreotide labeled by ^{177}Lu can be used in octreoscan for tumor location, staging, imaging, and therapy. For treating SSTR-positive tumors,

Table 20.7 Overview of ^{177}Lu-labeled radiopharmaceuticals

Probes	Applications
^{177}Lu-EDTMB	Bone pain
^{177}Lu-DOTATATE	Gastrointestinal neuroendocrine tumors
^{177}Lu-PSMA	Metastatic castration-resistant prostate cancer
^{177}Lu-DOTA-J591	Prostate cancer
^{177}Lu-huA33	Colon tumor
^{177}Lu-J579	Breast cancer
^{177}Lu-CCA9	Prostate cancer

^{177}Lu has following advantages compared with other radionuclides. First, with the ^{177}Lu-labeled analog, it is possible to perform dosimetry and therapy with the same compound, while no PET scans with short-lived radionuclides are needed. Second, the tissue penetration range of ^{177}Lu (maximum range ≈2 mm) is more favorable than that of ^{90}Y (maximum range ≈12 mm), especially for smaller tumors. Third, comparable affinities in In and Y complex [DOTA0, Tyr3] [34] octreotate have implied that the modification of the peptide but not the change in the metal is primarily responsible for the improved affinity. Fourth, ^{177}Lu-octreotate has been reported to have a very favorable impact on tumor regression in a rat model.

In recent years, the treatment of gastrointestinal neuroendocrine tumors using ^{177}Lu-SST has gradually become a research focus. Kwekkeboom [35] performed a study on 76 patients with gastrointestinal neuroendocrine tumors, using [^{177}Lu-DOTA-Tyr3]-octreotate. The patients were administrated 3700, 5550, and 7400 MBq every time, with the cumulated absorbed dose of 22.2–29.6 GBq and the treatment interval of 6–9 months. After finishing the last treatment, 30% patients reached fully effective and partially effective, and 12% patients reached minuteness response. Adverse reactions were rare in the process of treatment, mild bone marrow suppression mostly, which provides a new method for treating gastrointestinal neuroendocrine tumors. In addition, Teunissen [36] used it to treat three thyroid adenocarcinoma patients, with one patient achieving complete healing and another two achieving partial remissions. The *New England Journal of Medicine* reported a three-phase clinical trial of ^{177}Lu-DOTATATE for midgut neuroendocrine tumors [37]. In this randomized, phase 3 trial involving patients with progressive midgut neuroendocrine tumors, treatment with ^{177}Lu-DOTATATE resulted in a risk of progression or death that was 79% lower than the risk associated with high-dose octreotide LAR. The estimated rate of progression-free survival at month 20 was 65.2% (95% CI, 50.0–76.8) in the ^{177}Lu-DOTATATE group and 0.8% (95% CI, 3.5–23.0) in the control group. In January 2018, FDA approved Lutathera for the treatment of somatostatin receptor-positive gastrointestinal cancer (GEP-NETs).

^{177}Lu-GRP Family

Nowadays, the ^{177}Lu-GRP family has made many progresses in animal experiments. Lantry [38], Hu F [39], and many other researchers have studied the effectiveness of ^{177}Lu-GRP family. All the results showed great curative effect on tumor-bearing mice. For patients, it has entered phase 1 clinical trial.

^{177}Lu-PSMA

The therapeutic efficacy of ^{177}Lu-PSMA in advanced prostate cancer has been confirmed by more and more studies. In a recent clinical trial, Madhav Prasad Yadav [40] performed quarterly ^{177}Lu-DKFZ-PSMA-617 treatment on 31 mCRPC patients with progressive disease who had undergone second-line hormonal therapy and/or docetaxel chemotherapy. The results showed that the mean serum PSA levels in baseline and post first cycle therapy were 275 and 141.75 ng/mL, respectively. 2/31, 20/31, 3/31, and 6/31 patients had a complete response (CR), partial response (PR), stable disease (SD), and progressive disease (PD), respectively, based on the biochemical response criteria. The metabolic response showed 2/6 patients with CR, 3/6 patients with PR, and the remaining 1/6 patients with SD. No patients developed nephrotoxicity or hepatotoxicity. Taken together, all of these results demonstrated that ^{177}Lu-DKFZ-PSMA-617 radionuclide therapy could be a safe and promising method for the treatment of mCRPC.

^{177}Lu-Antibodies

Nowadays, epithelial tumors, such as colon cancer, ovarian cancer, and thyroid cancer, received radioimmunotherapy. Carcinoembryonic antigens are the most popular biomarker. For example, tumor-associated antigens 72 are mainly used in colon, ovarian, and breast cancer, mucoprotein-1 is mainly used in ovarian and breast cancer, and antigen 6250 is used in renal cancer.

Bander [41] performed a study on 35 prostate cancer patients (21 cases of bone metastasis, 6 cases of soft tissue metastasis, and 3 cases of bone and soft tissue metastasis) with ^{177}Lu-DOTA-J591. Results showed that part of the prostate-specific antigen has decreased or stabilized for a long time. In addition, ^{177}Lu-huA33 in colon tumor-bearing mice, ^{177}Lu-CCA9 in prostate tumor-bearing mice, and ^{177}Lu-J579 in breast tumor-bearing mice also have achieved favorable curative effect.

20.2.2 ^{90}Y

Min Yang and Yaoqi Li

^{90}Y has an almost pure β emitter (99.98%) and a long half-life of 64.2 h. The mean and maximum energies are 0.94 and 2.28 MeV, respectively, providing mean (maximum) tissue penetration of 2.5 mm (10 mm). Coupled with the proper carrier, it has been shown that ^{90}Y is able to deliver the required dose for the treatment of extended tumor lesions or their metastases.

20.2.2.1 Production of ^{90}Y

There are two kinds of preparation methods. One is through the ^{89}Y (n, γ) ^{90}Y reaction. The irradiation of the Y_2O_3 target was dissolved in dilute HCl, and $^{90}YCL_3$ was obtained with the carrier. The radioactivity specific activity is not high. The other is no-carrier method with leaching ^{90}Sr-^{90}Y gen-

erator through 0.003 mol/L EDTA (where ^{90}Sr content was less than 10^{-8}). Then it was converted to $^{90}YCl_3$ and as a raw material for the synthesis of other organic compounds.

20.2.2.2 Radiolabeling of ^{90}Y

^{90}Y can be linked to many types of monoclonal antibodies (McAbs) using bifunctional chelators such as DOTA and DTPA (Fig. 20.20). Among them, DOTA derivatives are one of the most commonly used chelators for ^{90}Y because of the high stability. In the past few years, several ^{90}Y-McAbs have been demonstrated in clinical and preclinical trials, such as ^{90}Y-DOTA-TOC, ^{90}Y-ibritumomab tiuxetan, ^{90}Y-DTPA-rituximab, ^{90}Y-DOTA-rituximab, ^{90}Y-DOTA-1F5-SA, ^{90}Y-DOTA-30F11, ^{90}Y-DOTA-CD66, ^{90}Y-TSP-A01, ^{90}Y-anti-ROBO1 IgG, ^{90}Y-ITGA6B4, and ^{90}Y-DOTA-biotin. In addition, many new materials such as glass microspheres and colloids have been developed to meet clinic needs.

20.2.2.3 PET Imaging with ^{90}Y

^{90}Y is mainly used for the preparation of therapeutic radiopharmaceuticals. In recent years, researchers have discovered that ^{90}Y can label various antibodies, as well as colloids, microspheres, etc. Here we give some descriptions of these radioactive drugs (Table 20.8).

^{90}Y-Monoclonal Antibodies (McAbs)

^{90}Y-DOTA-Rituximab

B-Cell non-Hodgkin lymphoma (NHL) is the most common hematologic cancer in adults. Rituximab is one type of therapeutics for NHL, but patients might be resistant to it. The association of beta emitter radionuclide to rituximab enhances its therapeutic efficacy. The cells which lack antigen or cells which cannot be reached due to poor vascularization and intratumoral pressure in a bulky tumor would be irradiated and killed by cross fire effect of beta emitter. The purified ^{90}Y-DOTA-rituximab conjugate with a radiochemical purity of >99% exhibited excellent stability when stored at 37 °C up to 72 h. Bioevaluation studies showed the specificity of the radiolabeled conjugate for CD20 antigen. The results indicate the potential of ^{90}Y-DOTA-rituximab for further evaluation as a radioimmunoconjugate for NHL therapy.

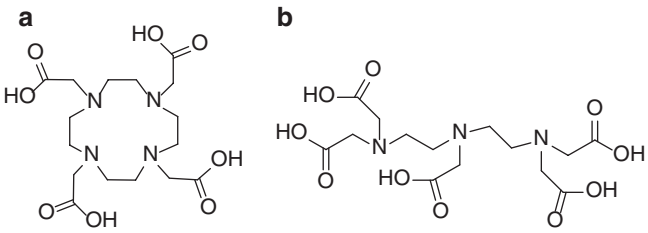

Fig. 20.20 The structural formula of two types of bifunctional chelators (**a**) DOTA; (**b**) DTPA

Table 20.8 Overview of some novel ^{90}Y-labeled probes developed in recent years

Probe	Application
^{90}Y-DOTA-Rituximab	Non-Hodgkin lymphoma
^{90}Y-DOTA-TOC	Meningiomas
^{90}Y-EDTMP	Leukemia
^{90}Y-Colloid	Cancerous pleural effusion or ascites, prophylactic, and advanced brain tumor
^{90}Y-Microspheres	Gastrointestinal malignancies and intrahepatic cholangiocarcinoma

^{90}Y-DOTA-TOC

Somatostatin analog ^{90}Y-labeled tetraazacyclododecanetetraacetic acid [D-Phe1, Tyr3]-octreotide (DOTA-TOC) [42] has shown advantages for treating meningiomas (Fig. 20.21). Fifteen patients with recurrent or progressive meningioma after multimodal pretreatments or unfavorable medical risk profile were treated with systemic ^{90}Y-DOTA-TOC. Stable disease was observed in 13 patients (86.7%) and progressive disease in 2 patients (13.3%). This study demonstrated the feasibility and efficacy of ^{90}Y-DOTA-TOC treatment in patients with complex meningioma.

^{90}Y-EDTMP

Ethylenediaminetetramethylene phosphate (EDTMP) is a tetraphosphonate ligand with great affinity to skeleton and osteoblastic bone metastases. To prepare ^{90}Y-EDTMP, the $^{90}YCL_3$ solution was added into a sterile ampoule containing EDTMP and sterile $NaHCO_3$ solution, then the mixture was shaken and sterilized through microporous membrane to get the final ^{90}Y-EDTMP. ^{90}Y would similarly be able to deliver myeloablative radiation doses. Its higher f-energy (Eha = 2.3 MeV) would achieve more effective penetration of tumor tissue in areas of extensive bone destruction and offer improved cell damage in either leukemia or solid tumors. ^{90}Y-EDTMP is an effective bone pain palliation agent because of its rapid blood clearance, greater uptake in bones, and little absorption in soft tissues. Therefore ^{90}Y-EDTMP can be an effective treatment for leukemia.

^{90}Y-Colloid

Yttrium silicate ^{90}Y-colloid is mainly used for the treatment of cancerous pleural effusion and prophylactic and advanced brain tumors. ^{90}Y-Colloids irradiated 56 brain tumors in close quarters. Most of the cases were tumors and multiple tumors in the deep and important functional areas that were difficult to completely cut by craniotomy. This group was injected ^{90}Y 72 times. After follow-up for 6–15 months, 41 patients (73%) had clinical symptoms improved, and 38 patients (68%) had tumors significantly reduced or disappeared.

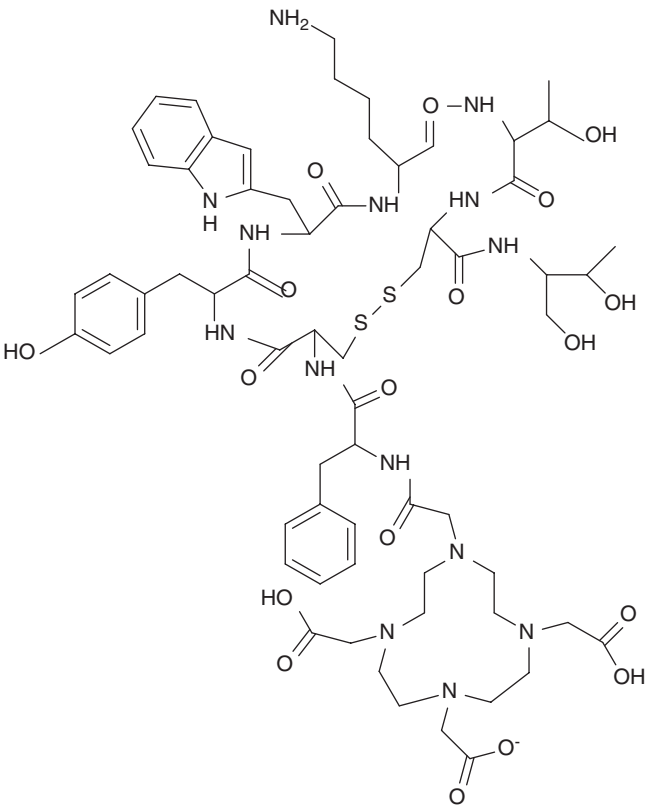

Fig. 20.21 Structure of DOTA-TOC

Another research showed ^{90}Y-colloid [43] offers a local and minimally invasive therapy for treating inflammatory hypertrophy of the synovial membrane of the knee, which has arisen from numerous kinds of disorders such as rheumatoid arthritis (RA), osteoarthritis (OA), spondyloarthropathy, villonodular synovitis, and cystic craniopharyngioma. Sabaté-Llobera [44] presented four cases of patients with cystic craniopharyngiomas treated by intracystic administration with ^{90}Y-colloid and its evolution after treatment. Ultimately they observed that treatment with ^{90}Y-colloid is a useful, axial section of the cranial CT after intracystic irradiation, which shows a very significant reduction in cyst volume. As the size decreases, the symptoms caused by the compression of adjacent structures can be improved.

^{90}Y-Microspheres

There are two types of ^{90}Y microspheres [45]: resin and glass. Because glass microspheres have a higher activity per particle, they can deliver a particular radiation dose with fewer particles, likely reducing embolic effects. Glass microspheres thus are more suitable when early stasis or reflux is a concern, in the setting of hepatocellular carcinoma with portal vein invasion, and for radiation segmentectomy. Radionuclide ^{90}Y glass microspheres (^{90}Y-GTMS) for the treatment of cancer initially began in 1961. Nicholas [46] determined radioembolization using ^{90}Y glass microspheres for the treatment of metastatic, liver-dominant, chemotherapy-refractory gastrointestinal malignancies. They cured 42 adult patients with metastatic chemotherapy-refractory by using ^{90}Y glass microspheres and found the median target dose and activity were 109.4 Gy and 2.6 GBq per treatment session, respectively; patients with colorectal cancer had hepatic objective response rate (ORR) of 25% and a hepatic disease control rate (DCR) of 80%.

In addition, three patients with large (>8 cm) infiltrating HCC were treated with an intrahepatic injection of ^{90}Y microspheres. After 1 year, the first patients showed a 75% HCC reduction with little persistence of tumoral tissue. The remaining two patients show similar results (more than 50% HCC reduction, no recurrence in the contralateral lobe, and preserved liver function). Downstaging of unresectable HCC by intrahepatic injection of ^{90}Y microspheres seems a promising strategy. This technique induces an efficient decrease in tumor size, even in the presence of portal vein thrombosis, without impairing liver function.

As an ideal therapeutic radionuclide, the use of ^{90}Y-labeled radiopharmaceuticals has matured. It is believed that more labeled pharmaceuticals will be available in the future.

20.2.3 Other Therapeutic Radionuclides

Nowadays, many nuclides have been found to be useful in the treatment. Some of them have been applied to clinical therapy, some are currently in various stages of clinical trials, and others are still under preclinical.

^{131}I have been widely applied in hyperthyroidism. It is simple, economic, safe, and effective. ^{89}SrCl and ^{153}Sm-EDTMP have been used for the treatment of bone tumors, and the exact curative effect has been obtained. Meanwhile, ^{125}I can be directly implanted into the tumor tissue to irradiate the tumor. It can be applied to lung cancer, liver cancer, prostate cancer, kidney cancer, bone metastases, and other solid tumors.

In recent years, ^{223}Radium has been approved for the treatment of bone metastases in patients with castration-resistant prostate cancer (CRPC). Based on the data from a phase 3, double-blind, randomized, clinical study of "alpharadin in symptomatic prostate cancer" (ALSYMPCA), the therapy with ^{223}Radium showed an overall survival (OS) benefit of 30.5% (hazard ratio of 2.6) compared to best supportive care [47].

In addition, there are also many therapeutic nuclides in research. The main therapeutic nuclides are shown in Table 20.9.

Table 20.9 Primary therapeutic radionuclides and their applications

Radionuclide	Type of radioactive decay	Half-life	Radiation energies (MeV)	Therapeutic drug	Main application
^{32}P	β− (100%)	14.3 day	1.71	$Na_2H^{32}PO_4$	Hematopathy, tumor
				$Na_3H^{32}PO_4$	Homeopathy, tumor
				Colloid $Cr^{32}PO_4$	Tumor, arthropathy, lymphoma
				^{32}P-HEDP	Painful skeletal metastases
				^{32}P-Microspheres	Tumor
^{89}Sr	β−, γ	50.5 day	β−, 1.488	^{89}SrCl2	Painful skeletal metastases
			γ, 0.908		
$^{117}Sn_m$	IT	13.6 day	Internal conversion electron		
			γ, 0.127, 0.153	$^{117}Sn_m$-DTPA	Painful skeletal metastases
^{125}I	EC	60.2 day	γ, 0.0355	^{125}I-iodipin	Tumor
				$Na^{125}I$	Hyperthyroidism
^{131}I	β−, γ	8.04 day	β−, 0.608, 0.334	$Na^{131}I$	Thyroid disorder
			γ, 0.364, 0.637	^{131}I-iodipin	Tumor
				^{131}I-MIBG	Tumor
^{153}Sm	β−, γ	46.27 h	β−, 0.810, 0.710, 0.640	^{153}Sm-EDTMP	Painful skeletal metastases
			γ, 0.103 (28%)	^{153}Sm-hydroxyapatite	Arthritis
^{165}Dy	β−, γ	2.33 h	β−, 1.305 (80%), 1.215 (16%)	$^{165}Dy(OH)_3$	Tumor
			γ, 0.095		
^{169}Er	β−	9.40 day	β−, 0.340	$^{165}Er(OH)_3$	Tumor
^{186}Re	β−, γ	90.6 h	β−, 1.072, 0.934	^{186}Re-HEDP	Tumor
			γ, 0.137		
^{188}Re	β−, γ	16.9 h	β−, 2.128, 1.973	^{188}Re-HEDP	Tumor
			γ, 0.155		
^{211}At	α, EC	7.21 h	α, 5.866, 5.21	^{211}At-McAb	Tumor
			γ, 0.687		
^{212}Bi	β−, α	60.6 min	β−, 2.25	^{211}Bi-McAb	Tumor
			α, 6.09, 6.05, 5.769		

20.3 Multimodality Molecular Imaging

Min Yang and Xinyu Wang

Multimodality imaging is the diagnostic technology which combined two or more imaging modalities within the setting of a single examination. Among the molecular imaging modalities, single-photon emission computed tomography (SPECT), positron emission tomography (PET), photoacoustic imaging (PAI), near-infrared red fluorescence imaging (NIRFI), and magnetic resonance imaging (MRI) are prominent techniques in today's molecular imaging [48]. PET and SPECT offer good sensitivity and superior quantification. PAI and MRI are noninvasive and nondestructive diagnostic tools with high spatial resolution. NIRFI is also a noninvasive method for diagnostic, however, with limited tissue penetration ability. With different modalities combined, multimodal imaging provides complementary information and achieves synergistic advantages over any single modality alone. Better spatial resolution and biological information at the molecular level with high sensitivity can be obtained using multimodal imaging rather than single modal imaging. Because of the great promising on the clinical diagnosis and on surgical protocol, the development of multimodal contrast agents for in vivo imaging is a rapidly growing field [49, 50]. Up to now, a variety of chemical platforms such as small molecules, proteins, polymers, and nanomaterials have been actively explored to construct multimodality imaging probes. These platforms own different advantages and disadvantages [51].

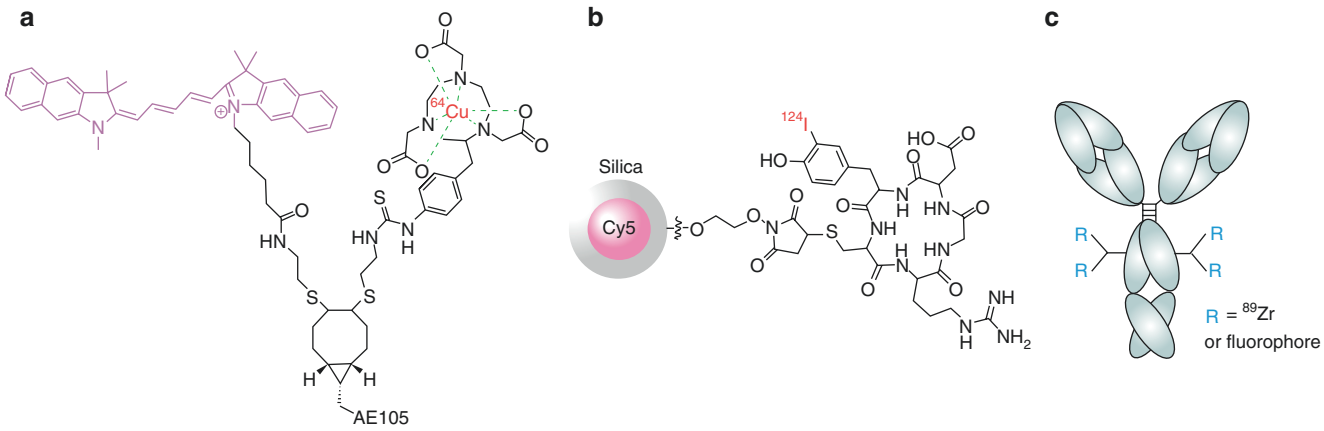

Fig. 20.22 Structure of ^{64}Cu-NOTA-Cy5.5-cyclooctyne-AE105 (**a**), ^{124}I-cRGDY-PEG-C dots (**b**), and ^{89}Zr-ssdual-5B1 (**c**)

20.3.1 PET/NIRFI Probes

Numerous PET/NIRFI contrast agents are developed for multimodality imaging, especially for tumor diagnostics. Sun et al. developed a molecular platform base on cyclooctyne for PET/NIRFI two-modality tumor imaging. PET reporter ^{64}Cu-1,4,7-triazacyclononane-triacetic acid (NOTA), fluorescent dye Cy5.5, and tumor-targeting ligand AE105 peptide were coupled on the same platform. This small molecule scaffold targeted tumor successfully and exhibited excellent imaging characteristics in vivo. Bradbury et al. developed the fluorescent dye Cy5 encapsulated ultrasmall inorganic hybrid nanoparticles which labeled with radioisotope ^{124}I for PET/NIRFI imaging [52]. This nanoparticle ^{124}I-cRGDY–PEG–C has received US Food and Drug Administration (FDA) Investigational New Drug (IND) approval as a drug for targeted molecular imaging of integrin-expressing cancers. It has been applied for melanoma diagnostics and image-guided surgery clinically. Houghton et al. synthesized a probe named as ^{89}Zr-ssdual-5B1 which combined a radioisotope ^{89}Zr and a near-infrared fluorophore on 5B1, a fully human monoclonal antibody that targets pancreatic cancer biomarker CA199 [53] (Fig. 20.22).

20.3.2 PET/MRI and SPECT/MRI Probes

Both PET and MRI are well-established imaging modalities that have been clinically available for more than 30 years. In the recent several years, the combination of PET and MRI attracted more and more attention in the clinical and research fields such as oncology, cardiology, and neurology because of the tremendous potential for clinical application [54]. MRI provides high-resolution, (submillimeter) anatomical information, and PET provides high sensitivity information. Therefore, the combination of high resolution and high sensitivity makes PET/MRI a powerful weapon in the future clinical diagnostic in vivo. The most serious problem for developing PET/MRI probes is the sensitivity difference between PET and MRI (about six orders of magnitude) [55]. Numbers of probes combined with PET contrast agent and MR contrast agent together were developed for PET/MRI multimodality imaging. Frullano et al. developed Gd-DOTA-4AMP-^{18}F as PET/MRI probe as early as 2010. Gros et al. successfully synthesized a DOTA-porphyrin conjugated molecule. This molecule is labeled with Gd^{3+} and Cu^{2+} which have a potential PET/MRI on bimodal imaging. Gd-DTPA-bis(histidylamide)-^{99m}Tc was developed by Park et al. for SPECT/MRI. This system overcame the sensitivity difference problem between MRI and SPECT with "cocktail mixture" formulation. They also synthesized another SPECT/MRI probe Gd-DOTA-cRGDY-^{125}I which exhibited the integrin-specific tumor enhancement both in SPECT and MRI [56] (Fig. 20.23).

20.3.3 Other Multimodality Imaging Probes

Probes applied in more than three modality imaging were developed, mainly based on the nanoparticles. Nanoparticles have advantages as a scaffold for multimodality imaging because of the multifunction characteristics. A lot of probes based on nanoparticle exhibit wonderful multimodal imaging ability, including iron oxides, upconversion nanoparticles, graphene gold nanoparticles, melanin, ferritin, liposome, and so on.

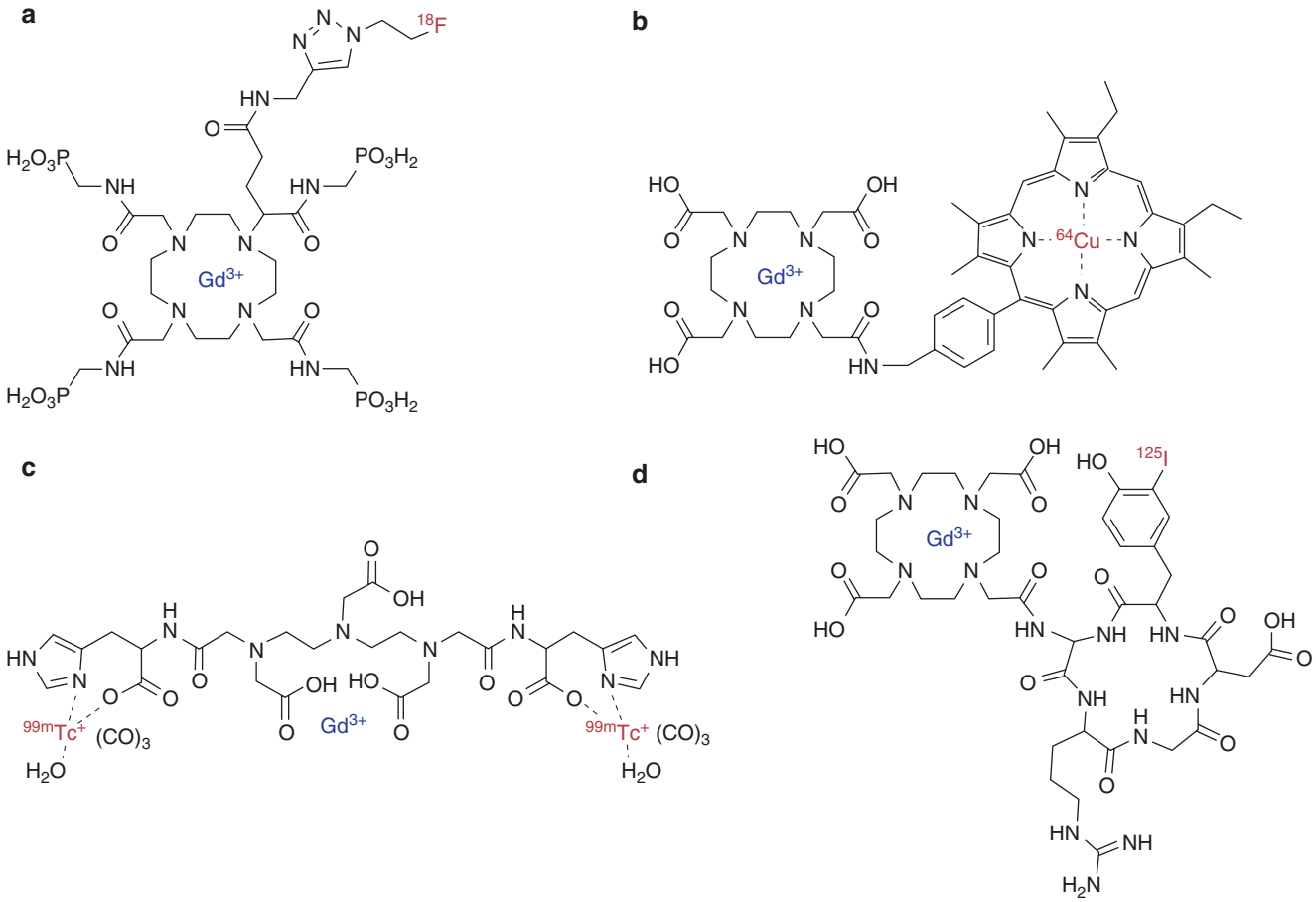

Fig. 20.23 Chemical structure of Gd-DOTA-4AMP-^{18}F (**a**), Gd-DOTA-porphyrin-64Cu (**b**), Gd-DTPA-bis(histidylamide)-^{99m}Tc (**c**), and Gd-DOTA-cRGDY-^{125}I (**d**)

References

1. Wan W, Guo N, Pan D et al (2013) First experience of 18F-alfatide in lung cancer patients using a new lyophilized kit for rapid radiofluorination. J Nucl Med 54(5):691–698
2. Yu C, Pan D, Mi B et al (2015) (18)F-Alfatide II PET/CT in healthy human volunteers and patients with brain metastases. Eur J Nucl Med Mol Imaging 42(13):2021–2028
3. Mi B, Yu C, Pan D et al (2015) Pilot prospective evaluation of (18) F-Alfatide II for detection of skeletal metastases. Theranostics 5(10):1115–1121
4. Sah BR, Burger IA, Schibli R et al (2015) Dosimetry and first clinical evaluation of the new ^{18}F-radiolabeled bombesin analogue BAY 864367 in patients with prostate cancer. J Nucl Med 56(3):372–378
5. Xu Q, Zhu C, Xu Y et al (2015) Preliminary evaluation of [^{18}F] AlF-NOTA-MAL-Cys^{39}-exendin-4 in insulinoma with PET. J Drug Target 23(9):813–820
6. Kaasinen V, Ruottinen HM, Någren K et al (2000) Upregulation of putaminal dopamine D2 receptors in early Parkinson's disease: a comparative PET study with [11C] raclopride and [11C] N-methylspiperone. J Nucl Med 41(1):65–70
7. Talvik M, Nordström AL, Nyberg S et al (2001) No support for regional selectivity in clozapine-treated patients: a PET study with [(11)C] raclopride and [(11)C]FLB 457. Am J Psychiatr 158(6):926–930
8. Froklage FE, Postnov A, Yaqub MM et al (2017) Altered GABAA receptor density and unaltered blood-brain barrier [11C] flumazenil transport in drug-resistant epilepsy patients with mesial temporal sclerosis. J Cereb Blood Flow Metab 37(1):97–105
9. Pieterman RM, Que TH, Elsinga PH et al (2002) Comparison of (11)C-choline and (18)F-FDG PET in primary diagnosis and staging of patients with thoracic cancer. J Nucl Med 43(2):167–172
10. Weber WA, Wester HJ, Grosu AL et al (2000) O-(2-[18F] fluoroethyl)-L-tyrosine and L-[methyl-11C] methionine uptake in brain tumors: initial results of a comparative study. Eur J Nucl Med 27(5):542–549
11. Pieterman R, Willemsen A, Appel M et al (2002) Visualisation and assessment of the protein synthesis rate of lung cancer using carbon-11 tyrosine and positron emission tomography. Eur J Nucl Med Mol Imaging 29(2):243–247
12. Velikyan I (2015) ^{68}Ga-based radiopharmaceuticals: production and application relationship. Molecules 20(7):12913
13. Kowalski J, Henze M, Schuhmacher J, Mäcke HR, Hofmann M, Haberkorn U (2003) Evaluation of positron emission tomography imaging using [^{68}Ga]-DOTA-D Phe(1)-Tyr(3)-Octreotide in comparison to [^{111}In]-DTPAOC SPECT. First results in patients with neuroendocrine tumors. Mol Imaging Biol 5(1):42–48
14. Gabriel M, Decristoforo C, Kendler D, Dobrozemsky G, Heute D, Uprimny C et al (2007) ^{68}Ga-DOTA-Tyr3-octreotide PET in neuroendocrine tumors: comparison with somatostatin receptor scintigraphy and CT. J Nucl Med 48(4):508

15. Luo Y, Pan Q, Yao S, Miao Y, Wu W, Xue H et al (2016) Glucagon-like peptide-1 receptor PET/CT with ^{68}Ga-NOTA-exendin-4 for detecting localized insulinoma: a prospective cohort study. J Nucl Med 57(5):715
16. Afshar-Oromieh A, Haberkorn U, Schlemmer HP, Fenchel M, Eder M, Eisenhut M et al (2014) Comparison of PET/CT and PET/MRI hybrid systems using a ^{68}Ga-labelled PSMA ligand for the diagnosis of recurrent prostate cancer: initial experience. Eur J Nucl Med Mol Imaging 41(5):887–897
17. Sörensen J, Velikyan I, Dan S, Wennborg A, Feldwisch J, Tolmachev V et al (2016) Measuring HER2-receptor expression in metastatic breast cancer using [^{68}Ga]ABY-025 affibody PET/CT. Theranostics 6(2):262–271
18. Nanni C, Errani C, Boriani L, Fantini L, Ambrosini V, Boschi S et al (2010) ^{68}Ga-citrate PET/CT for evaluating patients with infections of the bone: preliminary results. J Nucl Med 51(12):1932
19. Hofman MS, Beauregard JM, Barber TW, Neels OC, Eu P, Hicks RJ (2011) ^{68}Ga PET/CT ventilation-perfusion imaging for pulmonary embolism: a pilot study with comparison to conventional scintigraphy. J Nucl Med 52(10):1513–1519
20. van de Watering FC, Rijpkema M, Perk L, Brinkmann U, Oyen WJ, Boerman OC (2014) Zirconium-89 labeled antibodies: a new tool for molecular imaging in cancer patients. Biomed Res Int 2014:203601
21. Zhang Y, Hong H, Cai W (2011) PET tracers based on Zirconium-89. Curr Radiopharm 4(2):131–139
22. Wooten AL, Madrid E, Schweitzer GD, Lawrence LA, Mebrahtu E, Lewis BC et al (2013) Routine production of ^{89}Zr using an automated module. Appl Sci 3(3):593–613
23. Janjigian YY, Violavillegas N, Holland JP, Divilov V, Carlin SD, Gomesdagama EM et al (2013) Monitoring afatinib treatment in HER2-positive gastric cancer with 18F-FDG and ^{89}Zr-trastuzumab PET. J Nucl Med 54(6):936
24. Zhang Y, Guo Z, Du T, Chen J, Wang W, Xu K et al (2013) Prostate specific membrane antigen (PSMA): a novel modulator of p38 for proliferation, migration, and survival in prostate cancer cells. Prostate 73(8):835–841
25. Heskamp S, van Laarhoven HW, Molkenboer-Kuenen JD, Franssen GM, Versleijen-Jonkers YM, Oyen WJ et al (2010) ImmunoSPECT and immunoPET of IGF-1R expression with the radiolabeled antibody R1507 in a triple-negative breast cancer model. J Nucl Med 51(10):1565
26. Li ZB, Cai W, Cao Q et al (2007) ^{64}Cu-labeled tetrameric and octameric RGD peptides for small-animal PET of tumor αvβ3 integrin expression. J Nucl Med 48(7):1162–1171
27. Hong H, Yang Y, Zhang Y et al (2011) Positron emission tomography imaging of CD105 expression during tumor angiogenesis. Eur J Nucl Med Mol Imaging 38(7):1335–1343
28. Henry KE, Ulaner GA, Lewis JS (2017) Human epidermal growth factor receptor 2-targeted PET/single-photon emission computed tomography imaging of breast cancer. PET Clin 12(3):269–288
29. Eberle AN, Rout B, Bigliardi QM et al (2017) Synthetic peptide drugs for targeting skin cancer: malignant melanoma and melanotic lesions. Curr Med Chem 24(17):1797–1826
30. Chen K, Cui M (2017) Recent progress in the development of metal complexes as β-amyloid imaging probes in the brain. MedChemComm 8(7):1393–1407
31. Agarwal KK et al (2015) (177)Lu-EDTMP for palliation of pain from bone metastases in patients with prostate and breast cancer: a phase II study. Eur J Nucl Med Mol Imaging 42(1):79–88
32. Thapa P et al (2015) Clinical efficacy and safety comparison of 177Lu-EDTMP with 153Sm-EDTMP on an equidose basis in patients with painful skeletal metastases. J Nucl Med 56(10):1513–1519
33. Shinto AS et al (2014) (1)(7)(7)Lu-EDTMP for treatment of bone pain in patients with disseminated skeletal metastases. J Nucl Med Technol 42(1):55–61
34. Kwekkeboom DJ, Bakker WH, Kooij PP, Konijnenberg MW, Srinivasan A, Erion JL, Schmidt MA, Bugaj JL, de Jong M, Krenning EP (2001) [177Lu-DOTA0, Tyr3]octreotate: comparison with [111In-DTPA0]octreotide in patients. Eur J Nucl Med 28(2):1319–1325
35. Kwekkeboom DJ, Bakker WH, Kam BL, Teunissen JJM, Kooij PPM, Herder WW et al (2003) Treatment of patients with gastro-entero-pancreatic (GEP) tumours with the novel radiolabelled somatostatin analogue [177Lu-DOTA0,Tyr3]octreotate. Eur J Nucl Med Mol Imaging 30(3):417–422
36. Tounissen JJ, Kwekkeboom DJ, Kooij PP (2005) Peptide receptor radionuclide therapy for non-radio dine—avid differentiated thyroid carcinoma. J Nucl Med 46(Suppl):107S–114S
37. Strosberg J et al (2017) Phase 3 trial of (177)Lu-Dotatate for Midgut neuroendocrine tumors. N Engl J Med 376(2):125–135
38. Lantry LE, Cappelletti E, Maddalena ME, Fox JS, Feng W, Chen J, Thomas R, Eaton SM, Bogdan NJ, Arunachalam T, Reubi JC, Raju N, Metcalfe EC, Lattuada L, Linder KE, Swenson RE, Tweedle MF, Nunn AD (2006) 177Lu—AMBA:synthesis and characterization of a selective 177Lu—labeled GRP-R agonist or systemic radiotherapy of prostate cancer. J Nucl Med 47:1144–1152
39. Hu F et al (2002) Pm-149 DOTA bombesin analogs for potential radiotherapy. In vivo comparison with Sm-153 and Lu-177 labeled DO3A-amide-betaAla-BBN(7-14)NH(2). Nucl Med Biol 29(4):423–430
40. Yadav MP et al (2017) (177)Lu-DKFZ-PSMA-617 therapy in metastatic castration resistant prostate cancer: safety, efficacy, and quality of life assessment. Eur J Nucl Med Mol Imaging 44(1):81–91
41. Bander NH et al (2005) Phase I trial of 177lutetium-labeled J591, a monoclonal antibody to prostate-specific membrane antigen, in patients with androgen-independent prostate cancer. J Clin Oncol 23(21):4591–4601
42. Gerster-Gilliéron K, Forrer F, Maecke H et al (2015) ^{90}Y-DOTATOC as a therapeutic option for complex recurrent or progressive meningiomas. J Nucl Med 56(11):1748–1751
43. Kampen WU, Voth M, Pinkert J et al (2007) Therapeutic status of radiosynoviorthesis of the knee with yttrium [^{90}Y] colloid in rheumatoid arthritis and related indications. Rheumatology (Oxford) 46(1):16–24
44. Sabaté-Llobera A, Rojas-Camacho JG, Mora Salvadó J et al (2013) Treatment of cystic craniopharyngioma with ^{90}Y-colloid. Four clinical cases. Rev Esp Med Nucl Imagen Mol 32(5):321–323
45. Boas FE, Bodei L, Sofocleous CT (2017) Radioembolization of colorectal liver metastases: indications, technique, and outcomes. J Nucl Med 58(Suppl 2):104S–111S
46. Fidelman N, Kerlan RK, Hawkins RA et al (2016) Radioembolization with ^{90}Y glass microspheres for the treatment of unresectable metastatic liver disease from chemotherapy-refractory gastrointestinal cancers: final report of a prospective pilot study. J Gastrointest Oncol 7(6):860–874
47. Winter BM, von Rundstedt FC, Grimm MO (2017) [Radium-223 dichloride in patients with castration-refractory prostate cancer]. Urologe A 56(11):1435–1439
48. de Jong M, Essers J, van Weerden WM (2014) Imaging preclinical tumour models: improving translational power. Nat Rev Cancer 14(7):481–493
49. Bridot JL, Faure AC, Laurent S et al (2007) Hybrid gadolinium oxide nanoparticles: multimodal contrast agents for in vivo imaging. J Am Chem Soc 129(16):5076–5084
50. Kircher MF, Mahmood U, King RS et al (2003) A multimodal nanoparticle for preoperative magnetic resonance imaging and intraoperative optical brain tumor delineation. Cancer Res 63(23):8122–8125

51. Sun Y, Ma X, Cheng K et al (2015) Strained cyclooctyne as a molecular platform for construction of multimodal imaging probes. Angew Chem Int Ed Engl 54(20):5981–5984
52. Bradbury MS, Phillips E, Montero PH et al (2013) Clinically-translated silica nanoparticles as dual-modality cancer-targeted probes for image-guided surgery and interventions. Integr Biol (Camb) 5(1):74–86
53. Houghton JL, Zeglis BM, Abdel-Atti D et al (2015) Site-specifically labeled CA19.9-targeted immunoconjugates for the PET, NIRF, and multimodal PET/NIRF imaging of pancreatic cancer. Proc Natl Acad Sci U S A 112(52):15850–15855
54. Nensa F, Beiderwellen K, Heusch P et al (2014) Clinical applications of PET/MRI: current status and future perspectives. Diagn Interv Radiol 20(5):438–447
55. Lee SY, Jeon SI, Jung S et al (2014) Targeted multimodal imaging modalities. Adv Drug Deliv Rev 76:60–78
56. Park JA, Kim JY, Lee YJ et al (2013) Gadolinium complex of (125) I/(127)I-RGD-DOTA conjugate as a tumor-targeting SPECT/MR bimodal imaging probe. ACS Med Chem Lett 4(2):216–219